APPLICATIONS OF FLUORESCENCE IN SURGERY AND INTERVENTIONAL DIAGNOSTICS

EDITED BY: Mark Preul, Evgenii Belykh, David Leslie Carr-Locke and Quyen Nguyen
PUBLISHED IN: Frontiers in Surgery and Frontiers in Oncology

frontiers Research Topics

frontiers

ISSN 1664-8714
ISBN 978-2-88966-856-4
DOI 10.3389/978-2-88966-856-4

About Frontiers

Frontiers is more than just an open-access publisher of scholarly articles: it is a pioneering approach to the world of academia, radically improving the way scholarly research is managed. The grand vision of Frontiers is a world where all people have an equal opportunity to seek, share and generate knowledge. Frontiers provides immediate and permanent online open access to all its publications, but this alone is not enough to realize our grand goals.

Frontiers Journal Series

The Frontiers Journal Series is a multi-tier and interdisciplinary set of open-access, online journals, promising a paradigm shift from the current review, selection and dissemination processes in academic publishing. All Frontiers journals are driven by researchers for researchers; therefore, they constitute a service to the scholarly community. At the same time, the Frontiers Journal Series operates on a revolutionary invention, the tiered publishing system, initially addressing specific communities of scholars, and gradually climbing up to broader public understanding, thus serving the interests of the lay society, too.

Dedication to Quality

Each Frontiers article is a landmark of the highest quality, thanks to genuinely collaborative interactions between authors and review editors, who include some of the world's best academicians. Research must be certified by peers before entering a stream of knowledge that may eventually reach the public - and shape society; therefore, Frontiers only applies the most rigorous and unbiased reviews.
Frontiers revolutionizes research publishing by freely delivering the most outstanding research, evaluated with no bias from both the academic and social point of view. By applying the most advanced information technologies, Frontiers is catapulting scholarly publishing into a new generation.

What are Frontiers Research Topics?

Frontiers Research Topics are very popular trademarks of the Frontiers Journals Series: they are collections of at least ten articles, all centered on a particular subject. With their unique mix of varied contributions from Original Research to Review Articles, Frontiers Research Topics unify the most influential researchers, the latest key findings and historical advances in a hot research area! Find out more on how to host your own Frontiers Research Topic or contribute to one as an author by contacting the Frontiers Editorial Office: frontiersin.org/about/contact

APPLICATIONS OF FLUORESCENCE IN SURGERY AND INTERVENTIONAL DIAGNOSTICS

Topic Editors:
Mark Preul, Barrow Neurological Institute (BNI), United States
Evgenii Belykh, Rutgers University, Newark, United States
David Leslie Carr-Locke, Cornell University, United States
Quyen Nguyen, University of California, San Diego, United States

Citation: Preul, M., Belykh, E., Carr-Locke, D. L., Nguyen, Q., eds. (2021). Applications of Fluorescence in Surgery and Interventional Diagnostics. Lausanne: Frontiers Media SA. doi: 10.3389/978-2-88966-856-4

Table of Contents

frontiers in Surgery

EDITORIAL
published: 12 April 2021
doi: 10.3389/fsurg.2021.624124

Editorial: Applications of Fluorescence in Surgery and Interventional Diagnostics

Evgenii Belykh[1], *Mark C. Preul*[2*], *David L. Carr-Locke*[3] *and Quyen T. Nguyen*[4]

[1] *Department of Neurosurgery, New Jersey Medical School, Rutgers University, Newark, NJ, United States,* [2] *The Loyal and Edith Davis Neurosurgical Research Laboratory, Department of Neurosurgery, Barrow Neurological Institute, St. Joseph's Hospital and Medical Center, Phoenix, AZ, United States,* [3] *Center for Advanced Digestive Care, Weill Cornell Medicine, New York, NY, United States,* [4] *Departments of Surgery and Pharmacology, University of California, San Diego, San Diego, CA, United States*

Keywords: fluorescence, diagnostics, optical guidance, vascular neurosurgery, microsurgery

Editorial on the Research Topic

Applications of Fluorescence in Surgery and Interventional Diagnostics

Augmentation of the surgeon's and interventionalist's vision by advanced optical imaging, including fluorescence guidance [i.e., fluorescence-guided surgery (FGS)], is the basis for multiple innovations that will transform the workflow of all subspecialties of surgery and interventional diagnostics. Advanced optical imaging could solve multiple practical problems, making normal and abnormal tissue and cellular structures that are otherwise indistinguishable to an unaided human eye visible and making surgery and interventions for patients safer, more efficient, and successful.

In this *Frontiers* issue, "Applications of Fluorescence in Surgery and Interventional Diagnostics," we are privileged to present a collection of 34 open-access publications that describe the frontiers in research and practice of fluorescence imaging in medicine. These articles were selected through an open peer-review process that unites experts in the field, including 220 authors and 60 reviewers and editors.

The first series of articles addresses the frontiers of wide-field fluorescence imaging in neurosurgical oncology and includes works on the major fluorophores: 5-aminolevulinic acid (5-ALA), fluorescein sodium, indocyanine green (ICG), and talaporfin sodium. 5-ALA-based imaging has seen significant growth in recent years, reflected by the high number of articles submitted for publication. Beginning with a historical review on how 5-ALA was introduced into practice (Georges et al.), we include several clinical studies on its use in various brain tumors (Goryaynov, Okhlopkov et al.), such as low-grade gliomas (Goryaynov, Widhalm et al.). The systematic analysis of a growing body of literature suggests that 5-ALA-guided surgery may impact patients' survival (Gandhi et al.).

Ways to improve fluorescence visualization through the quantification of signal intensity and its spectral signature are reviewed (Valdes et al.). Novel multispectral imaging technology based on these principles is presented for the first time in this collection (Charalampaki, Proskynitopoulos et al.). The latest clinical evidence and experience with the use of ICG is reported (Cho et al.), fluorescein sodium (Falco et al.), and talaporfin sodium (Akimoto et al.) for neurooncological applications are also presented. This subtopic concludes with a group of articles that discuss

Edited and reviewed by:
Elisa Meacci,
Catholic University of Sacred Heart of Rome, Italy

****Correspondence:***
Mark C. Preul
Neuropub@barrowneuro.org

Specialty section:
This article was submitted to Neurosurgery, a section of the journal Frontiers in Surgery

Received: *30 October 2020*
Accepted: *02 March 2021*
Published: *12 April 2021*

Citation:
Belykh E, Preul MC, Carr-Locke DL and Nguyen QT (2021) Editorial: Applications of Fluorescence in Surgery and Interventional Diagnostics. Front. Surg. 8:624124. doi: 10.3389/fsurg.2021.624124

photodynamic therapy (Cramer and Chen), simulation models for fluorescence-guided brain surgery (Valli et al.), and the clinical benefits of integrating FGS in multitechnology surgical workflows (Schebesch et al.). In an invited opinion paper, Duffau discusses the role of fluorescence guidance in the surgery of malignant brain tumors in the context of the current trend for "maximal function-based resections." It could be that the combination of both functional imaging or mapping and fluorescence techniques would be advantageous for a balanced and informed solution to maximize the goals of the surgery. Specifically, this could be achieved by first localizing the brain function through awake or asleep mapping to ensure the safety of resection. Second, localizing tumor extension through advanced optical imaging could ensure no unintentionally missed tumor tissue residuals.

Fluorescence and advance optical guidance will remain relevant and continue advancing within the surgical field as long as surgery remains a part of the neurooncology tumor management strategy. Future developments include more specific optical labels, such as fluorescently labeled peptides and nanoparticles to visualize abnormal and normal tissue better, for example, for peripheral nerves (1), or drug-free optical molecular imaging tools to visualize and discriminate normal (2) and abnormal (3) tissue.

The second series of papers reports on the advances of small-field handheld tools for open and stereotactic (Akshulakov et al.) brain tumor optical imaging, including papers on the frontiers in optical spectroscopy and RAMAN imaging (Lakomkin and Hadjipanayis), small-field confocal microscopy systems with fluorescein sodium (Belykh, Miller et al.), 5-ALA (Wei et al.), and ICG (Charalampaki, Nakamura et al.) used for contrast creation, as well as dyeless cross-polarization optical coherence tomography (Yashin et al.). These papers describe technologies for optical biopsies that are either FDA-approved or are at various stages of development. An exciting development within this realm is improving and optimizing the resection of malignant or invasive tumors by bringing a portable visualizing probe within the surgeon's hand that is a comfortable size and displays real-time *in vivo* fluorescence imaging to detect abnormal histoarchitecture. At least for brain surgery, although such technology could be used to extend the resection margins, which has correlated with increased survival, it may also be used to inform the surgeon of the tumor boundary and thus where to stop resection. These and other technologies within an operating room environment and incorporated into the surgical and pathology workflows effectively link the pathological consultation directly into the operating room. Theoretically, such technology could replace frozen section biopsies with optical biopsies, thereby increasing the yield of biopsies and the speed of surgery. Such technologies will include computer-aided image analysis (Izadyyazdanabadi et al.) and related image assessments that will guide and improve intraoperative diagnostics.

The third set of papers addresses the nuances of fluorescence imaging for vascular neurosurgery. Papers describe the evidence, techniques, and practical pearls of applying ICG contrast to augment visualization of cerebral blood flow in aneurysms (Norat et al.), cerebrovascular bypass (Cavallo et al.), and arteriovenous malformation (Foster et al.) surgeries. Advances in the design of wide-field microscopes, endoscopes, and administration for fluorescein-based angiography are described (Zhao et al.). As surgical techniques become more refined, incorporating such imaging techniques provides a view of the tissue's microvascularity with significant implications for tissue function preservation.

The fourth set of papers relays information on novel molecular fluorescent probes under development to improve FGS. Established and novel ways of imaging probe delivery to brain tumors across the blood-brain barrier are reviewed (Belykh, Shaffer et al.). Investigations of several drug-based strategies to augment already established 5-ALA-based diagnostics are reported [(a) Reinert et al.; (b) Reinert et al.]. Two papers report a new strategy of applying the drugs locally as fluorescent paint to highlight malignant cells (Kitagawa et al.; Byvaltsev et al.). Apart from oncology, a novel application of fluorescence diagnostics for clinically relevant inflammatory cell imaging is presented, which has had a significant impact on medical efficacy and the economics of treating critically ill patients with pulmonary disease (Birch et al.).

The fifth set of papers report on the frontiers of fluorescence-based techniques in visceral surgery (Ferrari-Light et al.; Wu et al.), reconstructive microsurgery (Ludolph et al.), and endoscopic diagnostics (Capuano et al.). These innovative clinical technologies include wide-field and small-field confocal imaging tools with fluorescein and ICG contrast. These fluorescence applications for surgery were among the first to be incorporated into disease diagnostics and therapeutics, such as gastrointestinal disease. They prompted the developments that launched surgical fluorescence handheld endoscopic imaging technology into other surgical disciplines, such as neurosurgery. These imaging techniques are a routine part of disease diagnostics and monitoring in many global locations, especially for precancerous and cancerous lesion management.

This constellation of basic, translational, and clinical papers will facilitate the interdisciplinary exchange of knowledge and will aid in the further progress of advanced optical-aided technologies. These authors and colleagues will lead advanced imaging efforts and champion innovations in optical navigation to improve patient outcomes and benefit healthcare systems.

AUTHOR CONTRIBUTIONS

All authors listed have made a substantial, direct and intellectual contribution to the work, and approved it for publication.

ACKNOWLEDGMENTS

We thank the staff of Neuroscience Publications at Barrow Neurological Institute for assistance with manuscript preparation.

REFERENCES

1. Walsh EM, Cole D, Tipirneni KE, Bland KI, Udayakumar N, Kasten BB, et al. Fluorescence imaging of nerves during surgery. *Ann Surg.* (2019) 270:69–76. doi: 10.1097/sla.0000000000003130
2. Gonsalvez DG, Yoo S, Fletcher JL, Wood RJ, Craig GA, Murray SS, et al. Imaging and quantification of myelin integrity after injury with spectral confocal reflectance microscopy. *Front Mol Neurosci.* (2019) 12:275. doi: 10.3389/fnmol.2019.00275
3. Hollon TC, Pandian B, Adapa AR, Urias E, Save AV, Khalsa SSS, et al. Near real-time intraoperative brain tumor diagnosis using stimulated Raman histology and deep neural networks. *Nat Med.* (2020) 26:52–8. doi: 10.1038/s41591-019-0715-9

Conflict of Interest: The authors declare that the research was conducted in the absence of any commercial or financial relationships that could be construed as a potential conflict of interest.

frontiers in Surgery

TECHNOLOGY REPORT
published: 12 March 2019
doi: 10.3389/fsurg.2019.00011

Indocyanine-Green for Fluorescence-Guided Surgery of Brain Tumors: Evidence, Techniques, and Practical Experience

Steve S. Cho[1,2], *Ryan Salinas*[2] *and John Y. K. Lee*[2]*

[1] Perelman School of Medicine at the University of Pennsylvania, Philadelphia, PA, United States, [2] Department of Neurosurgery at the Hospital of the University of Pennsylvania, Philadelphia, PA, United States

The primary treatment for brain tumors often involves surgical resection for diagnosis, relief of mass effect, and prolonged survival. In neurosurgery, it is of utmost importance to achieve maximal safe resection while minimizing iatrogenic neurologic deficit. Thus, neurosurgeons often rely on extra tools in the operating room, such as neuronavigation, intraoperative magnetic resonance imaging, and/or intraoperative rapid pathology. However, these tools can be expensive, not readily available, time-consuming, and/or inaccurate. Recently, fluorescence-guided surgery has emerged as a cost-effective method to accurately visualize neoplastic areas in real-time to guide resection. Currently, 5-aminolevulinic-acid (5-ALA) remains the only fluorophore that has been approved specifically for fluorescence-guided tumor resection. Its use has demonstrated improved resection rates and prolonged progression-free survival. However, protoporphyrin-IX, the metabolic product of 5-ALA that accumulates in neoplastic cells, fluoresces in the visible-light range, which suffers from limited tissue penetration and significant auto-fluorescence. Near-infrared fluorescence, on the other hand, overcomes these problems with ease. Since 2012, researchers at our institution have developed a novel technique using indocyanine-green, which is a well-known near-infrared fluorophore used traditionally for angiography. This Second-Window-ICG (SWIG) technique takes advantage of the increased endothelial permeability in peritumoral tissue, which allows indocyanine-green to accumulate in these areas for intraoperative visualization of the tumor. SWIG has demonstrated utility in gliomas, meningiomas, metastases, pituitary adenomas, chordomas, and craniopharyngiomas. The main benefits of SWIG stem from its highly sensitive detection of neoplastic tissue in a wide variety of intracranial pathologies in real-time, which can help neurosurgeons both during surgical resections and in stereotactic biopsies. In this review of this novel technique, we summarize the development and mechanism of action of SWIG, provide evidence for its benefits, and discuss its limitations. Finally, for those interested in near-infrared fluorescence-guided surgery, we provide suggestions for maximizing the benefits while minimizing the limitations of SWIG based on our own experience thus far.

Keywords: indocyanine-green, near-infrared, tumor resection, enhanced-permeability and retention effect, fluorescence-guided surgery

OPEN ACCESS

Edited by:
Evgenii Belykh, Barrow Neurological Institute (BNI), United States

Reviewed by:
Peter Nakaji, Barrow Neurological Institute (BNI), United States
Gregory Punisa Lekovic, House Ear Institute, United States

***Correspondence:**
John Y. K. Lee
leejohn@uphs.upenn.edu

Specialty section:
This article was submitted to Neurosurgery, a section of the journal Frontiers in Surgery

Received: *01 January 2019*
Accepted: *19 February 2019*
Published: *12 March 2019*

Citation:
Cho SS, Salinas R and Lee JYK (2019) Indocyanine-Green for Fluorescence-Guided Surgery of Brain Tumors: Evidence, Techniques, and Practical Experience. Front. Surg. 6:11. doi: 10.3389/fsurg.2019.00011

INTRODUCTION

Surgical resection of brain tumors remains an important part of cancer care for pathologic diagnosis, relief of mass effect, and survival benefit (1–9). However, radical resections, such as those practiced in other surgical fields, in the brain could result in neurologic morbidity that may outweigh the benefits of surgery (10). Neurosurgeons must thus balance the goals of maximal resection with minimizing neurologic deficits, which is a difficult task. Indeed, gross-total-resection (GTR) rates for intracranial tumors range from <30% for glioblastoma-multiforme (GBM) and other high-grade gliomas (HGG) to ∼70% for benign meningiomas or pituitary adenomas, and tumors recur even after perceived GTR (11–16). Therefore, it is of paramount importance that neurosurgeons intraoperatively distinguish neoplasm from benign brain parenchyma and surrounding tissue. In addition to enhanced illumination, magnification, and experienced interpretation of tissue color and texture, neurosurgeons often rely on extra tools in the operating room, such as neuronavigation, intraoperative magnetic resonance imaging (MRI), intraoperative rapid pathology, and/or intraoperative ultrasound (17, 18). However, these modalities can have significant drawbacks, such as brain-shifts for neuronavigation and low availability, high cost, and high false-positive rate for intraoperative MRI (17–21). Recently, fluorescence-guided surgery (FGS) has emerged as a rapid and cost-effective alternative to these techniques.

In June 2017, the US Food and Drug Administration (FDA) approved 5-aminolevulinic-acid (5-ALA) as an agent for fluorescence-guided neurosurgery. First tried in neurosurgery in 1998, 5-ALA is a prodrug that leads to selective accumulation of a fluorophore, protoporphyrin IX (PpIX), in malignant cells, which can then be visualized intraoperatively using blue-light excitation (22–28). In a pivotal randomized-control study, Stummer et al. demonstrated that 5-ALA fluorescence-guided surgery led to a 65% GTR rate, compared to 36% in the control group in patients with high-grade gliomas (29). Other studies have replicated the benefits of 5-ALA in high-grade gliomas, as well as potential benefit in other intracranial tumors, such as meningiomas and pituitary adenomas (30–32). Despite the rigorous evidence that 5-ALA use is advantageous, it has visible-light emission that is significantly absorbed by endogenous fluorophores (i.e., heme), limiting its tissue penetration. Furthermore, the brain has numerous endogenous fluorophores, such as lipofuscin or flavin, with excitation/emission spectra that can overlap significantly with PpIX, reducing contrast between the tumor and the background brain (**Figure 1A**).

Fluorescein is another FDA-approved fluorophore that has traditionally been used for angiography in ophthalmology but with recent applications in tumor surgery. Studies have demonstrated that a bolus injection of fluorescein during the operation leads to fluorescein accumulating in areas of blood-brain-barrier breakdown in the peritumoral tissue. Fluorescein has demonstrated a range of sensitivity and specificity for intracranial tumors in prior studies, with generally high sensitivity but lower specificity compared to 5-ALA (33–39). Like 5-ALA, fluorescein is a visible-light fluorophore and suffers from limited visualization through tissue and weak contrast from surrounding normal brain (**Figure 1B**). Some have attempted dual-injections of 5-ALA and fluorescein to enhance detection of neoplastic tissue by increasing the contrast between the neoplastic tissue that uptake 5-ALA and the peritumoral area that uptake fluorescein (40).

More recently, indocyanine-green (ICG), a near-infrared (NIR) fluorophore (peak excitation = 805 nm, peak emission = 835 nm), has demonstrated utility in labeling tumor tissue. Unlike the conventional use of ICG as an angiographic agent, a novel technique using ICG, termed the Second Window ICG (SWIG), has been demonstrated in recent years. Due to the limitations of 5-ALA and fluorescein mentioned earlier, we have focused on NIR fluorophores. Thus, we investigated SWIG in various intracranial tumors, including high-grade gliomas, meningiomas, brain metastases, and pituitary adenomas. In this article, we review the brief history and hypothesized mechanism of action behind SWIG, examine the evidences supporting its use neurosurgery, detail specific operative techniques to minimize errors, and describe our group's practical experience with this novel technique.

HISTORY AND MECHANISM OF ACTION OF SWIG IN INTRACRANIAL TUMORS

Neurosurgeons are familiar with ICG and its role as an angiographic agent since the 1960s. ICG is a small, amphiphilic molecule (<800 daltons) that, when injected intravenously, normally remains within the blood vessel mostly bound to albumin and other plasma proteins. It is removed by biliary excretion and has a very short half-life of <180 s. Due to this short half-life, ICG is usually given as a bolus dose of <0.5 mg/kg and NIR imaging is performed immediately afterwards to delineate the vasculature.

In 1993, Hansen et al. described a technique using ICG boluses to create contrast between neoplastic tissue and brain parenchyma in rat models, rather than just visualizing vasculature (41); this was soon followed by another study by Haglund et al. in rats (42) and in human patients (43). In this last study, patients received a bolus of ICG at 1 mg/kg and then were imaged for up to 10 min after the bolus dosing, allowing ICG to accumulate in the tumor while washing out of the surrounding parenchyma. In patients with HGG, significant contrast between tumor and background was detected, while in patients with low-grade gliomas (LGG), this contrast decreased significantly between 4 and 10 min after ICG injection.

Finally, in a 2012 study, Madajewski et al. proposed that a high-dose infusion of ICG (7.5 mg/kg) given 24 h prior to surgery allows ICG to accumulate in areas of neoplasm, facilitating detection of residual neoplasm after standard resection in murine flank tumor models (44). This effect was confirmed in a follow-up dose-confirmation study in a murine flank tumor model (45) and was further demonstrated in a murine intracranial tumor model by our lab (46). It has been hypothesized that the accumulation of ICG occurs through the well-described enhanced permeability and retention (EPR) effect, which stipulates that solid tumors

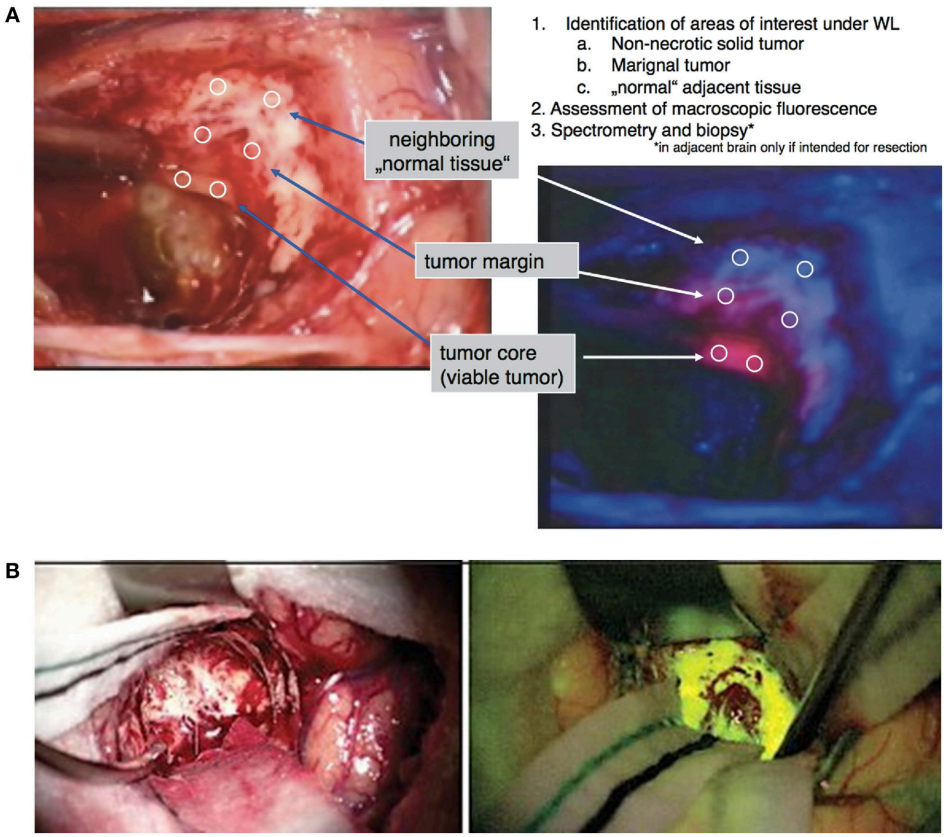

FIGURE 1 | Examples of visible light fluorophores used in brain tumor resection. **(A)** 5-ALA is an oral prodrug that is converted to proptoporphyrin-IX, a visible light fluorophore with red emission, in high-grade neoplastic cells. Under blue-light excitation (400–410 nm), pink areas correspond to areas of neoplasm against the dark-blue background (28). **(B)** Fluorescein is a visible-light fluorophore with yellow emission that highlights areas of blood-brain-barrier damage. When injected intravenously 1–3 h prior to tumor exposure, areas of tumor can be visualized in yellow using yellow-green (460–500 nm) excitation (38).

possess enhanced vascular permeability due to defective vascular structures, impaired lymphatic drainage systems, and increased permeability mediators (47). ICG then accumulates in these areas of enhanced vascular permeability and can be visualized 24-h later (**Figure 2**) (48).

EVIDENCE AND POTENTIAL BENEFITS OF SWIG

SWIG has been investigated in various intracranial applications (**Table 1**). We summarize the results below and discuss potential implications.

Intra-Axial Brain Tumors: Gliomas and Metastases

In 2016, we published the results of the first SWIG study in 15 patients with gliomas (49). An important discovery was that the strongest predictor of positive intraoperative NIR fluorescence was contrast-enhancement on preoperative MRI (p-value = 0.03) (**Figure 3A**). NIR fluorescence could be detected from tumors >1 cm deep and in 8 patients, the tumor could be detected prior to durotomy. In contrast-enhancing gliomas (12/15 in this study), SWIG demonstrated 98% sensitivity, 45% specificity, 82% positive-predictive-value (PPV) and 90% negative-predictive-value (NPV) for detecting areas of neoplasm in biopsy specimens, with an area under the receiver operating characteristic curve (AUROC) of 0.715. In comparison, white-light alone was 84% sensitive and 80% specific for neoplasm, with a PPV of 92%, NPV of 67%, and AUROC of 0.822. Updated data from our group that is yet unpublished shows that SWIG has a PPV of 88% and NPV of 63% for margin specimens in contrast-enhancing gliomas, compared to white-light alone with a PPV of 100% and NPV of 38%. Furthermore, data currently under review for publication suggests that NIR imaging of the surgical bed after resection can increase the surgeon's confidence that GTR has been achieved if there are no residual areas of NIR fluorescence (**Figures 3B–E**).

The utility of SWIG was also investigated in 13 patients with various intracranial metastases in a 2017 study (50). SWIG demonstrated higher sensitivity (96 vs. 82%) and NPV (75 vs. 67%) but lower specificity (27 vs. 91%) and PPV (77 vs. 96%). AUROC with SWIG was 0.619, whereas AUROC with white-light alone was 0.865. NIR signal was visualized through the dura in 11 patients and in patients with sub-surface tumors, NIR signal could be visualized at least to a depth of 6.8 mm below the cortex (**Figure 4**).

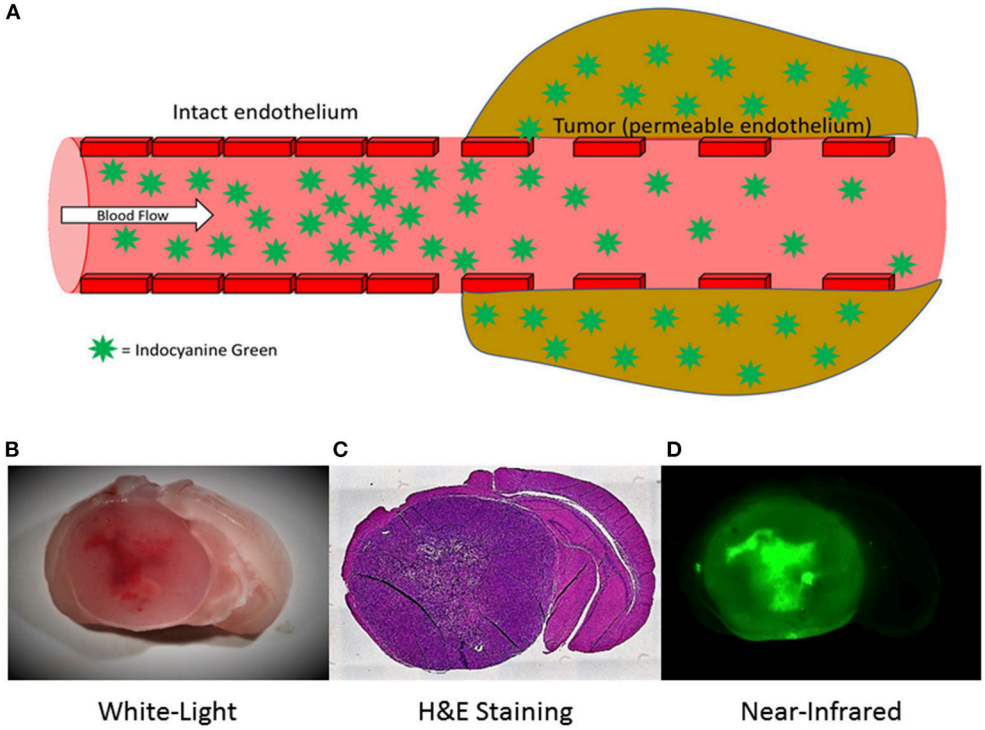

FIGURE 2 | Mechanism of action for Second Window Indocyanine Green (SWIG) **(A)** ICG is hypothesized to accumulate in neoplastic areas via the enhanced permeability and retention effect. In areas of normal brain, with intact endothelium, the ICG remains intravascular and washes away quickly. In areas of tumor, which often have permeable/damaged endothelium, the ICG permeates into the peritumoral tissue and remains in the tissue for a prolonged time (54). **(B–D)** SWIG in murine model of GBM (U87 cells). Under white-light alone **(B)**, it is difficult to visualize the full extent of the tumor, which is demonstrated by hematoxylin and eosin (H&E) staining **(C)**. With SWIG **(D)**, however, both the core of the tumor and the margin are delineated under near-infrared fluorescence.

TABLE 1 | Summary of studies investigating near-infrared fluorescence guided neurosurgery with second-window ICG.

References	Tumor type (n)	Sensitivity (WL, NIR)	Specificity (WL, NIR)	PPV (WL, NIR)	NPV (WL, NIR)
Lee et al. (49)	Gliomas (15)	84% 98%	80% 45%	92% 82%	67% 90%
Lee et al. (50)	Metastases (13)	82% 96%	91% 27%	96% 77%	67% 75%
Lee et al. (51)	Meningiomas (18)	82% 96%	100% 39%	100% 71%	78% 88%
Cho et al. (52)	Varied (6)	NA	NA	NA	NA
Jeon et al. (53)	Skull-base Tumors (15)	NA	NA	NA	NA
Cho et al. (54)	Pituitary Adenomas (16)	88% 100%	90% 29%	96% 82%	73% 100%

NA, Not applicable; NIR, Near-infrared; NPV, Negative-predictive value; PPV, Positive-predictive value; WL, White-light.

The latest application for SWIG under investigation is in stereotactic biopsies of intracranial tumors. Currently, stereotactic brain biopsies may have prolonged operative time due to the need for confirmation of abnormal tissue from frozen pathology. If the result is inconclusive, this may require further biopsy specimens in the operating room. However, using SWIG, the neurosurgeon can examine biopsied specimens *ex-vivo* for NIR fluorescence in the operating room. If the tissue is non-fluorescent, chances are very high that the specimen is not neoplastic or otherwise abnormal due to the highly sensitive nature of SWIG for neoplasm, and thus, another biopsy should be taken; conversely, with fluorescent tissue, the surgeon can be confident that abnormal tissue was biopsied (data under review) (**Figure 5**). Thus, SWIG offers an affordable, rapid, and accurate adjunct to stereotactic biopsies to increase the neurosurgeons' confidence and reduce operating length.

Extra-Axial Brain Tumors: Meningiomas, Pituitary Adenomas, and Others

SWIG has demonstrated sensitive detection of neoplasm in extra-axial tumors as well. In a 2017 study of SWIG in 18 meningioma patients (15 grade I, 3 grade II), NIR imaging detected strong fluorescence in 14 tumors (51). It was noted that 4 tumors demonstrated "inverse" NIR fluorescence, in which the background signal was higher than the signal within the tumor, and linear regression suggested that time from ICG injection was negatively correlated with NIR fluorescence contrast (p-value $= 0.022$, $R^2 = 0.2876$); we have hypothesized that this inverse fluorescence may be due to either quenching of ICG that can occur at concentrations >125 ug/L (52) or the slow permeation of ICG out of the neoplastic tissue into the surrounding area

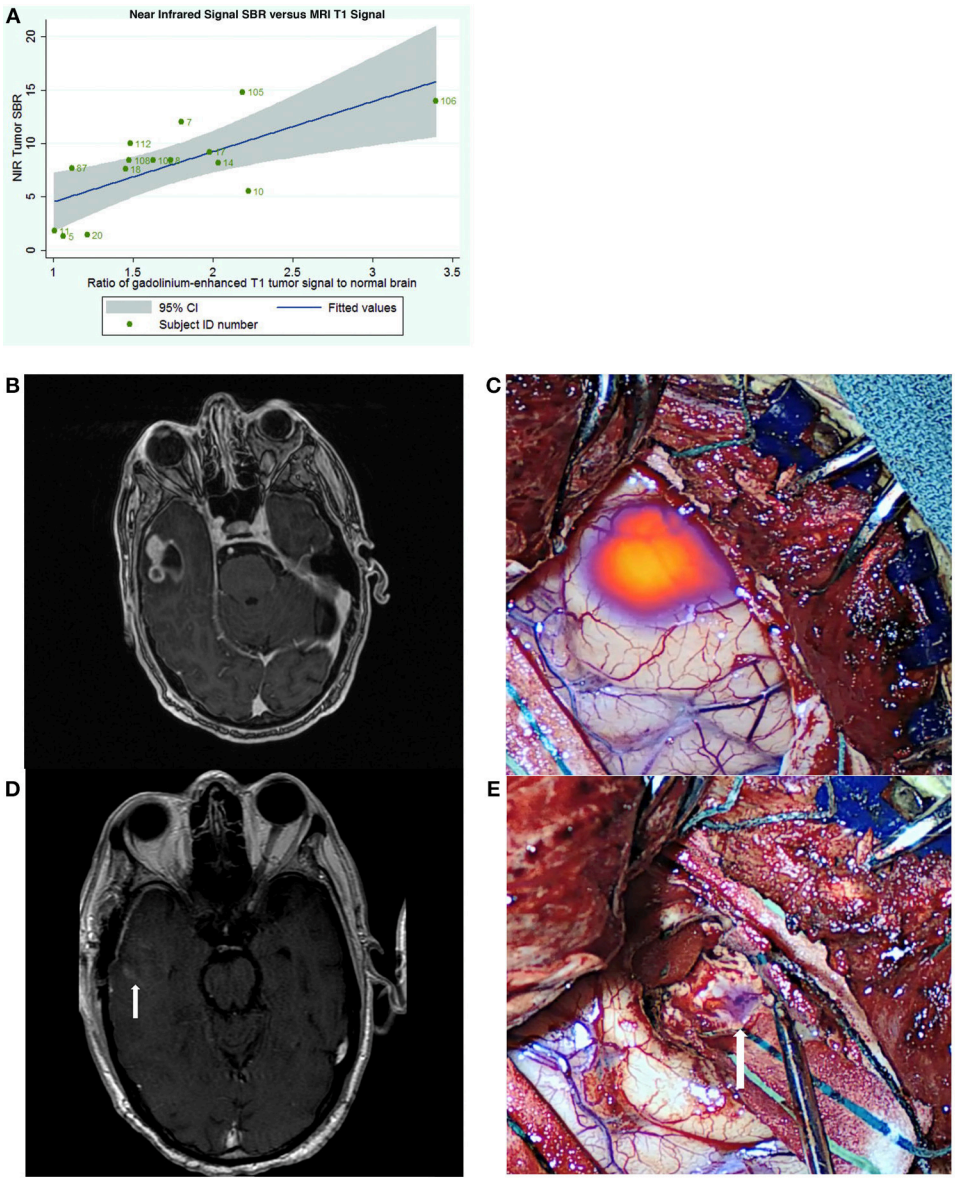

FIGURE 3 | Utility of SWIG in patients with GBM. **(A)** The amount of near-infrared fluorescence detected in tumors after SWIG administration positively correlates with contrast-enhancement on preoperative MRI (p-value 0.03), suggesting that SWIG can label contrast-enhancing tissue in real-time (49). **(B,C)** A contrast-enhancing GBM demonstrates strong NIR fluorescence in the operating room after durotomy. This technique does not suffer from brain-shifts, unlike neuronavigation. **(D,E)** After standard resection, NIR imaging of the surgical bed demonstrates no residual areas of strong NIR fluorescence. Postoperative day-1 MRI demonstrates postoperative changes with gross-total resection. Arrows indicate the orientation of the surgical bed. In patients whom post-resection NIR imaging does not demonstrate residual NIR fluorescence, the neurosurgeon can be more confident that gross-total resection has been achieved.

after 24 h, although neither has been definitively demonstrated. Overall, SWIG demonstrated 96% sensitivity, 39% specificity, 71% PPV, and 88% NPV for detecting neoplasm in these meningioma patients with an AUROC of 0.677, compared to white-light alone, which showed 82% sensitivity, 100% specificity, 100% PPV, and 78% NPV with an AUROC of 0.911.

Finally, SWIG is applicable to skull base tumors, such as pituitary adenomas, chordomas, and craniopharyngiomas, which were accessed via the transnasal/transsphenoidal approach. A 2018 study of 8 pituitary adenomas, 3 craniopharyngiomas, and 4 chordomas demonstrated that all the tumors demonstrated NIR fluorescence (**Figure 6**) (53). Again, contrast-enhancement on preoperative MRI was the best predictor of NIR fluorescence contrast to normal background (p-value = 0.0003). In pituitary adenomas, SWIG demonstrated 100% sensitivity, 20% specificity, 71% PPV, and 100% NPV for neoplasm in biopsy specimens, compared to white-light alone with 90% sensitivity, 100% specificity, 100% PPV, and 83% NPV (n = 15). A more recent study shows that SWIG had 100% sensitivity, 29% specificity, 82% PPV, and 100% NPV (n = 30), whereas white-light

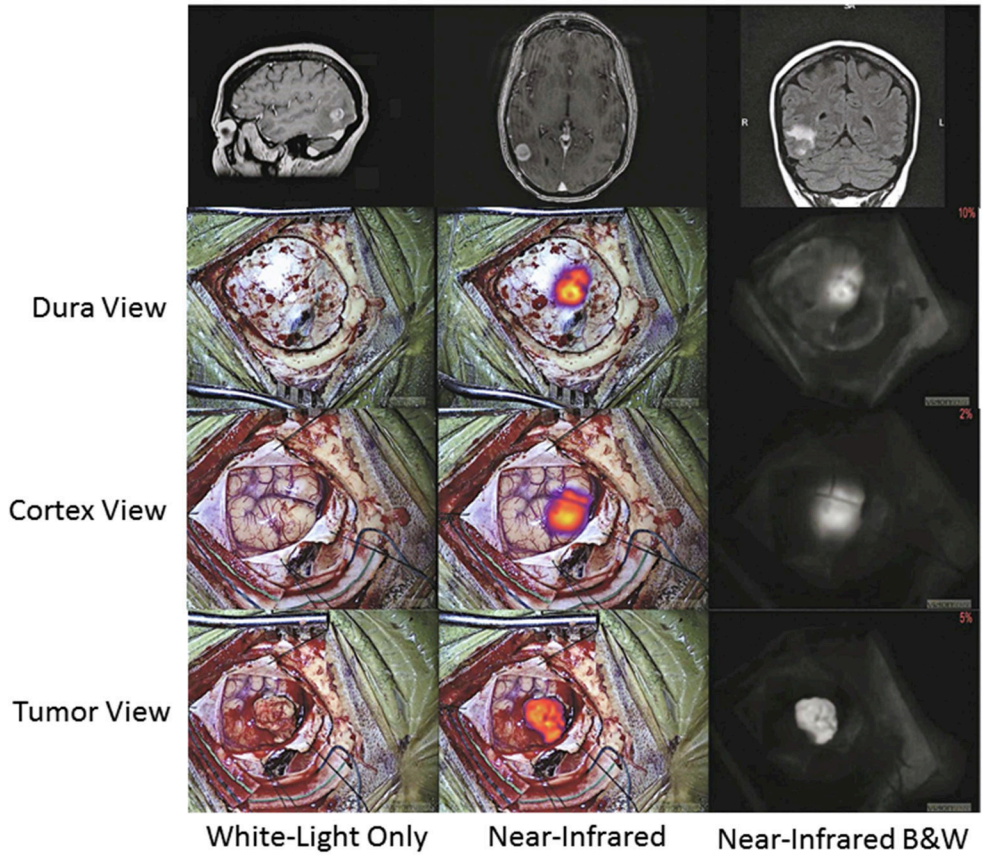

FIGURE 4 | Further clinical applications of SWIG in neurosurgery—trans-dural visualization. In this patient with a subcortical brain metastasis, NIR imaging localized the tumor through intact dura as well as intact cortex. Unlike visible-light fluorescence, NIR fluorescence can travel through tissue up to >1 cm in the brain. Since NIR imaging provides real-time localization of tumor, this can help neurosurgeons better plan the access through the dura and minimize cortical disruption (50).

had 88% sensitivity, 90% specificity, 96% PPV, and 73% NPV ($n = 78$) (54).

Benefits of SWIG in Neurosurgery

Overall, these studies suggest that the main benefit of intraoperative NIR imaging with SWIG is the higher sensitivity and NPV for detecting neoplastic tissue, which may allow surgeons to detect more residual neoplasm at the margins after resection than with white-light alone, increasing the chances of achieving GTR. SWIG studies thus far are all limited by the fact that the scope of surgery was not changed depending on NIR imaging, as SWIG was a technique under investigation at the time. In other words, even if the senior surgeon observed residual areas of fluorescent tissue after standard resection, further resection was not performed. Therefore, it is currently difficult to quantify the effects NIR imaging with SWIG on surgical outcomes. However, given that 5-ALA, with lower sensitivity (∼70–90%), similar PPV (>95%), and much lower NPV (19–24%) has demonstrated benefit in increasing GTR rates and progression-free survival (29), it is not unreasonable to expect that fluorescence-guided surgery with SWIG would lead to equally improved, if not better, surgical outcomes compared to surgery with 5-ALA. Furthermore, the results demonstrating correlation between absence of fluorescence and GTR in HGG is encouraging as well. A study to investigate changing the extent of surgery according to NIR fluorescence with SWIG is currently under way and will better elucidate the effects of fluorescence-guided surgery with SWIG on resection rates and surgical outcomes.

In contrast to PpIX or fluorescein, SWIG imaging utilizes NIR fluorescence, leading to great tissue penetration. The longer NIR wavelength allows the photons to travel further in the body, especially in less dense tissue, because there is less absorption by hemoglobin and other proteins (55, 56). Thus, as demonstrated in the above studies, NIR fluorescence from subcortical tumors can be imaged through intact dura and cortex, which is not possible with white-light visualization or with 5-ALA, except under very limited circumstances with specialized equipment (57). Furthermore, since NIR imaging is performed in real-time, SWIG does not suffer from brain shifts and other inaccuracies in directing the surgeon toward the tumor bulk as can be seen in neuronavigation. Both the deeper tissue signal and the real-time feedback can benefit the surgeon in accurately planning access through the dura and minimizing cortical disruption.

Finally, a defining feature of SWIG is its widespread applicability. Unlike receptor-targeted dyes or metabolic dyes,

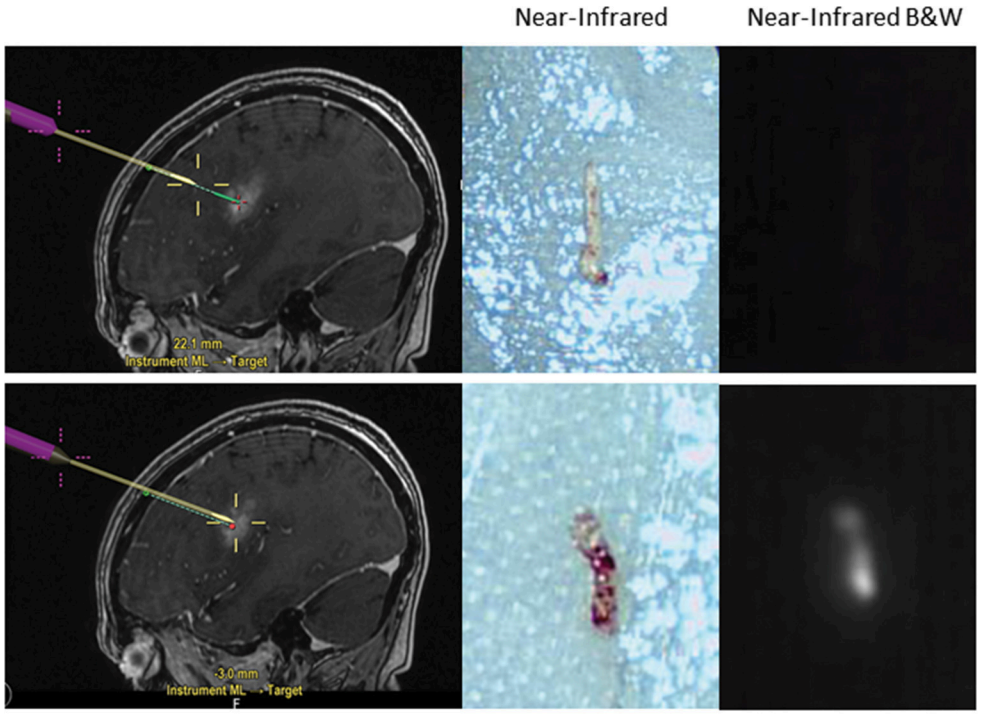

FIGURE 5 | Application of SWIG for stereotactic biopsies. Stereotactic biopsies with SWIG offer rapid confirmation that abnormal tissue was biopsied. When a sample was biopsied outside the contrast-enhancing legion using neuronavigation (top row), it did not demonstrate NIR fluorescence and was normal tissue on the frozen pathology. On the contrary, when a sample was biopsied within the contrast-enhancement (bottom row), it demonstrated NIR fluorescence and pathology diagnosis was GBM. Thus, SWIG offers an affordable, rapid, and accurate adjunct to stereotactic biopsies to reduce operating length.

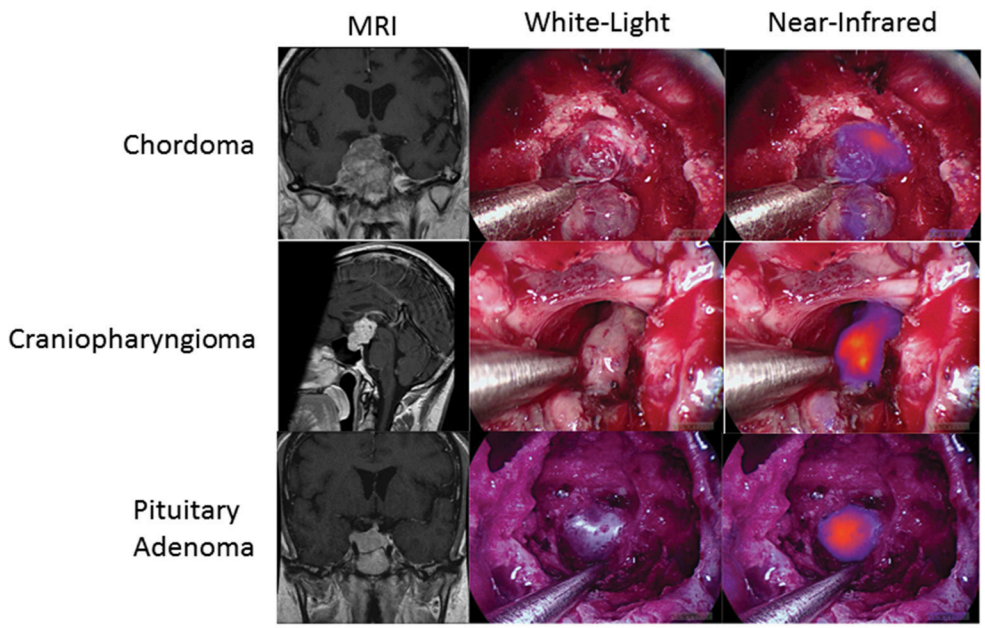

FIGURE 6 | SWIG in extra-axial brain tumors. Patients with chordomas (top row), craniopharyngiomas (middle row), and pituitary adenomas (bottom row) all demonstrate NIR fluorescence with SWIG. Visualization was performed with a NIR-sensitive endoscope system (53).

such as 5-ALA, SWIG has demonstrated nearly equivalent utility in a wide variety of intracranial tumors. This, combined with the high availability of ICG, makes SWIG an easily accessible adjunct to the armamentarium of neurosurgeons world-wide.

TECHNICAL CONSIDERATIONS

SWIG is fundamentally different from traditional angiography with ICG or the minimally delayed imaging performed by Haglund et al. In order to take full advantage of the EPR effect, ICG must be administered between 16 and 30 h prior to the surgery (46). Generally, patients receive an outpatient infusion the day prior to surgery. ICG is administered intravenously over 1 h, at a dose of 5 mg per kg of body weight. The patient is closely monitored throughout the duration of the infusion and for 30 min afterwards for any adverse events. Thus, far, no major complications from ICG administration has been reported. The patient then returns the next day for the surgery. Of note, in a few recent cases, including a spinal cord meningioma and peripheral nerve schwannoma, ICG was administered 6–8 h prior to tumor exposure. While NIR imaging detected pathologic tissue in these cases, there is still insufficient evidence to validate this shorter time window in humans.

Intraoperatively, the surgery setup and procedure proceeds as per standard of care, with the one exception of having a dedicated NIR imaging device present in the operating room. While conventional surgical microscopes have add-on modules that allow NIR imaging of ICG, these were designed for ICG angiography with a much higher concentration of ICG. These modules are not sensitive enough to low concentrations of ICG and do not have a wide dynamic range. Our group uses a dedicated NIR exoscope/endoscope system (VisionSense Iridium^{TM}), which uses a dedicated excitation laser and an integrated post-acquisition image processing. This allows simultaneous visualization of visual light, NIR signal alone, and an overlaid augmented-reality type display of both signals simultaneously. This system was identified as having superior sensitivity and dynamic range compared to other commercial NIR imaging platforms in a comparison study by DSouza et al. (58). Our group further compared the dedicated NIR exoscope system to a commercial neurosurgical microscope module and demonstrated that for SWIG fluorescence-guided surgery, the dedicated NIR system is more suitable, as it can more reliably detect NIR fluorescence through the dura and detect NIR signal from neoplastic tissue with a higher tumor-to-brain contrast over a larger dynamic range of NIR fluorescent signal (**Figure 7**) (52). Other dedicated NIR imaging platforms with strong excitation and high-quality image-processing may also be viable options. More sophisticated add-on modules for surgical microscopes are emerging as well.

In order to minimize background and maximize signal detection, ambient light should be minimized. During the SWIG visualization of the procedure, both room and overhead operating lights are turned off as even these lights can lead to some degree of NIR signal detection. Furthermore, careful consideration should be made if simultaneous neuronavigation is utilized. It has been noted that neuronavigation systems utilizing NIR technology for fiducial detection interfere with NIR signal detection. In some systems, a pulsing NIR light is generated from the neuronavigation "camera" and is visualized by the NIR imaging system as a pulsing, high background signal. Therefore, the neuronavigation camera should be directed away from the field while using any SWIG detection system.

After craniotomy but before durotomy, the NIR imaging modules is introduced into the field to assess whether the tumor can be visualized through the dura. In many cases of superficial tumors, the tumor boundary can be easily delineated through the dura. Durotomy is then performed and repeat NIR imaging is performed to confirm tumor location. In cases of deep tumors, neuronavigation is used to locate and expose the tumor. Once the tumor is exposed, NIR fluorescence of the gross tumor specimen is measured. Then, resection of the tumor proceeds in the standard of care manner, without NIR imaging. After the senior neurosurgeon is satisfied with the resection, NIR imaging is again performed to assess for residual fluorescence. Depending on the protocol, any areas of residual fluorescence can be simply recorded, biopsied, or completely removed. Closure is then performed in a standard manner and the patient undergoes postoperative MRI to assess the extent of resection.

PRACTICAL EXPERIENCE

During our experience with SWIG over the past 4 years, we have come to better understand the various factors that can help or hinder surgeons utilizing SWIG fluorescence-guided surgery, which we detail below.

One of the limitations of SWIG is the higher false-positive detection of neoplasm compared to surgeon judgment with white-light alone. False-positive NIR signal can come from either abnormal or normal tissue. Abnormal tissue, such as neoplasm, inflammation, and necrosis are all associated with endothelial damage and thus, ICG can accumulate in these tissues via the EPR effect, which is not specific to neoplasm, but rather targets areas of blood-brain-barrier breakdown. Since these areas enhance with gadolinium, SWIG will also highlight these areas. The difficulty in distinguishing neoplasm from inflammation and necrosis was noted in murine models as well as canine and human patients with thoracic cancers (59). We have noted a similar phenomenon in neurosurgery, in which SWIG could not distinguish between these abnormal tissues (unpublished data). This is the main limitation of SWIG, as it is not a tumor-targeting dye, and it will likely be difficult to overcome without developing targeting moieties.

False-positive NIR signal can occur in normal tissues as well, especially in the skin, mucosa, and dura. It is believed that due to the negative charges on ICG, it can bind nonspecifically to these tissue with a low affinity, although this has not yet been definitively demonstrated as the cause. Thus, in many cases, we have observed NIR signal from skin, mucosa, and/or dura that are certainly not neoplastic. There are two steps that the surgeon can take in the operating room to minimize these false-positive signals.

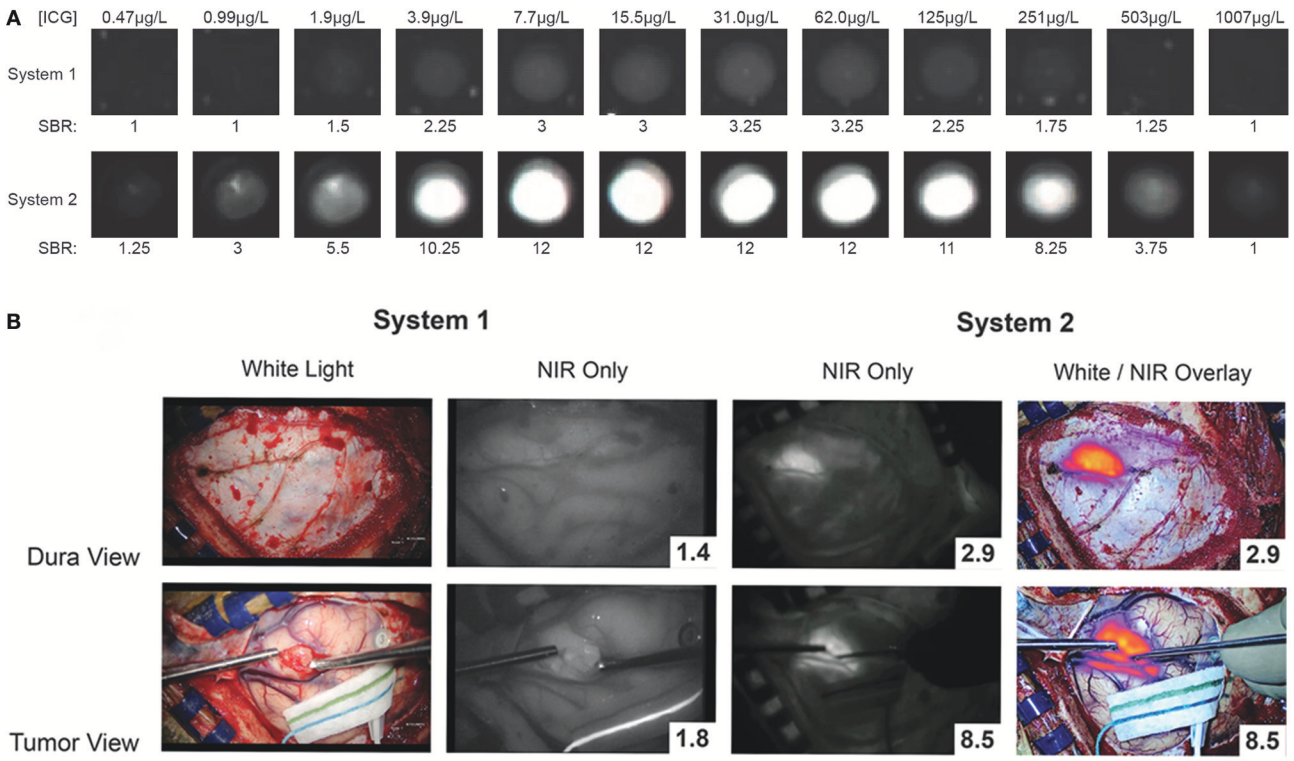

FIGURE 7 | A prior study compared a conventional state-of-the-art microscope (System 1) with a NIR-detecting module to a dedicated NIR-imaging system (System 2). In both *ex-vivo* **(A)** and *in-vivo* visualizations of ICG (**B**; NIR signal-to-background ratio in bottom right corner), System 2 was much more sensitive to NIR fluorescence, with a greater dynamic range. Furthermore, only System 2 was capable of imaging NIR fluorescence through the dura. Thus, for successful surgeries with SWIG, a sensitive, dedicated NIR imaging system is necessary (52).

Many NIR imaging systems have variable gains, which reflect the sensitivity of the camera sensor to the emission photons, that can be adjusted and fixed by the operator. The higher the gain, the more sensitive the camera, and the weaker the signals that can be detected. Thus, a gain that is set too high can result in detection of NIR fluorescence that isn't true neoplasm (**Figures 8A–D**) (51). One way to avoid this problem is to note the gain setting when the tumor is first exposed and then to fix the gain at that level throughout the rest of the surgery. The surgeon can then be confident that any NIR fluorescence that is detected is at the same level of fluorescence as the tumor, increasing the likelihood that the area of fluorescence is neoplastic.

Another factor that can contribute to false-positive NIR signals is the distance between the sensor and the tissue. This is more of a factor with endoscopic surgeries, as the scope is often brought to very close proximity to the tissue of interest for optimal visualization. Since optical signal decays as a factor of distance-squared, simply halving the distance between the endoscope and the tissue of interest can elevate the detected NIR signal 16-fold (4-fold increase in excitation strength, 4-fold increase in emission detection). Thus, similar to the gain above, having the endoscope too proximal to the tissue can cause falsely elevated NIR signal to be detected. In order to avoid this, the surgeon should attempt to visualize areas of suspected NIR fluorescence from a set distance. With the VisionSense Iridium endoscope in transsphenoidal surgeries for pituitary adenomas using a related NIR dye, we demonstrated that having the endoscope at a distance that maintains the distance between the two medial opticocarotid recesses to be <50% of the field of view is ideal for minimizing false-positive NIR signals (**Figures 8E–H**) (60, 61). Endoscopes that offer more precise distance measurements could further help the neurosurgeon to acquire more accurate NIR signals.

Furthermore, there are two factors that can hinder the surgeon's ability to detect true-positive NIR fluorescence: strong signal in the surrounding normal tissue and pooled blood. If the gain is properly set as described above, the surgeon should be able to detect residual areas of NIR fluorescence that is at the same level of fluorescence as the tumor, and thus, likely to be residual neoplasm. However, if there is a significant amount of fluorescence in the skin, mucosa, or dura surrounding the surgical bed, the NIR camera may not properly detect smaller areas of fluorescence. If the surrounding area is covered with surgical towels or gauze to isolate the surgical bed, small areas of residual fluorescence can be detected more easily (**Figures 9A–D**). Pooled blood can also often obscure areas of NIR fluorescence by physically blocking the excitation and emission lights (**Figures 9E,F**). Thus, when imaging for NIR

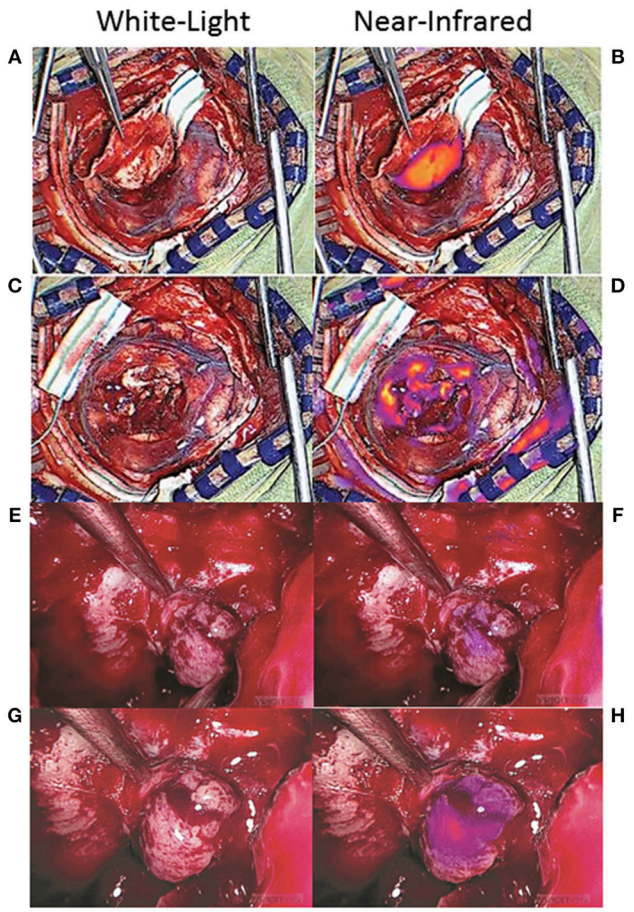

FIGURE 8 | False-positive NIR signal using SWIG. There are two main sources of false-positive signals that may arise during NIR imaging: high gain settings and small distance between the NIR sensor and the tissue. **(A–D)** Some NIR imaging systems have adjustable gain (NIR sensitivity) that need to be fixed in order to avoid detecting false-positive signals. When the tumor was first exposed in this patient with a meningioma **(A)**, the gain was at 15% and strong NIR fluorescence was detected from the tumor **(B)**. After resection **(C)**, NIR fluorescence was again detected, but the gain was at 71% **(D)**. Once the gain was adjusted down to 15%, those areas of NIR fluorescence disappeared, suggesting that the NIR signal had been false-positives (51). **(E–H)** In endoscopic fluorescence-guided surgery, the distance between the scope and the tissue of interest is important as well. Since optical signal decays as a factor of distance-squared, bringing the scope in close proximity to any tissue can result in fluorescence detection. This patient with a pituitary adenoma received a folate-receptor targeted near-infrared dye, but postoperative immunohistochemistry demonstrated no folate-receptor expression; thus, the tumor should not have demonstrated fluorescence. When the tumor was visualized from a distance **(E,F)**, there was minimal NIR signal; however, when the scope was brought closer to the tissue **(G,H)**, the tumor seemed to fluoresce. Thus, maintaining the proper distance between the endoscope and the tissue is of paramount importance in avoiding false-positive NIR signals (61).

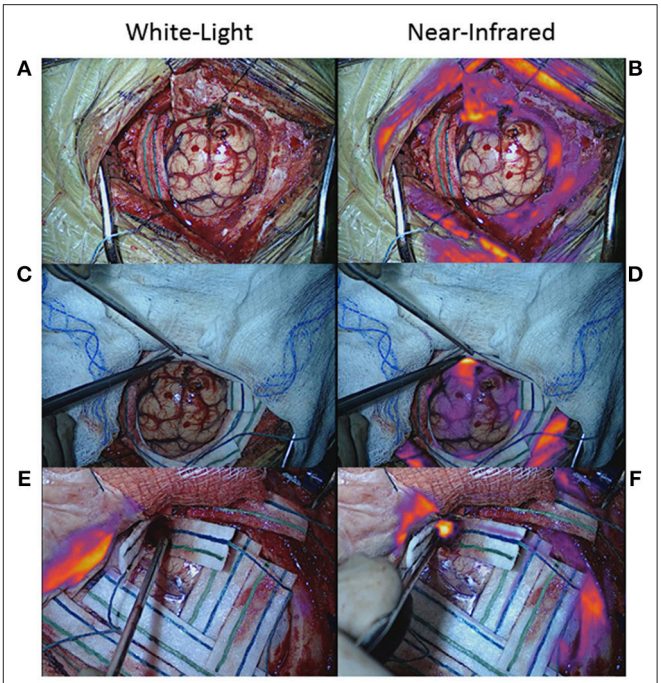

FIGURE 9 | False-negative NIR signal using SWIG. There are two main sources of false-negative signals that may arise during NIR imaging: surrounding, nonspecific NIR signal and blood/fluid. **(A–D)** Upon durotomy in this patient with a GBM, strong but nonspecific NIR signal was observed in the skin and dura, which masked any NIR signal coming from the actual tumor. Once the nonspecific signals were obscured by the surgeon, the NIR fluorescence from the tumor could be detected properly. **(E,F)** Blood and other fluids can obscure NIR fluorescence. In this patient, after standard resection, no NIR fluorescence was detected in the surgical bed initially. However, after removing blood and fluid, the underlying NIR fluorescence was detected.

fluorescence, it is important to achieve hemostasis to clear the field of blood and place the tissue of interest in direct line of the excitation light.

Overall, fluorescence-guided surgery using SWIG has technical intricacies that may require a learning curve. We have detailed the steps that neurosurgeons can take in the operating room to both minimize false-positive signals and to elucidate true-positive signals.

Finally, a consideration for neurosurgeons interested in the technique is the cost of SWIG. As mentioned previously, SWIG requires sensitive NIR imaging capabilities, which is best achieved with a dedicated imaging system, such as the VisionSense Iridium; this system currently costs approximately $100–150 K depending on whether the endoscope function is available. The cost of ICG may vary by institution; a typical patient may need 350–400 mg of ICG (5 mg/kg bodyweight).

FUTURE RESEARCH

There are two main directions in which future research can improve NIR fluorescence-guided neurosurgery. One is improving the specificity of NIR imaging. Despite its potential benefits in the operating room, SWIG is limited mainly by its low specificity as it works through the EPR effect, which is not tumor-specific. One way to overcome this limitation may be to conjugate novel NIR dyes that target specific receptors on neoplastic cell surfaces. In fact, multiple such conjugates are currently being investigated in preclinical and clinical trials for different

intracranial tumors. For instance, folate-receptor overexpression on nonfunctional pituitary adenomas and meningiomas may provide targets for sensitive and specific detection of these tumors in real-time (54, 60–62). An alternative is to use imaging apparatus with higher resolution for fluorescence, which may better distinguish true areas of fluorescence from areas of false-positive fluorescence. This has been demonstrated in murine models with fluorescein and ICG using confocal microscopy and may become applicable clinically (63, 64).

Another limitation of NIR imaging in the operating room is the low sensitivity of the imaging equipment. It is well-acknowledged, and our group has demonstrated, that conventional surgical microscopes with add-on NIR modules are significantly less sensitive for NIR fluorescence, especially at lower concentrations, than dedicated NIR imaging modules. Integrating the high NIR sensitivity into conventional microscopes will hugely increase the applicability of NIR fluorescence-guided neurosurgery, further increasing the potential benefits of this novel technique to improve patient outcomes.

CONCLUSION

Fluorescence-guided surgery with SWIG is a widely applicable technique that allows neurosurgeons to visualize tumors and residual neoplasm at the margins with greater sensitivity than with white-light and microscopy alone. In this review, we have explained the mechanism of SWIG and its potential benefits, as well as steps that neurosurgeons can take to maximize the utility of this novel technique. Results with SWIG thus far are encouraging and suggest potential benefit in improving patient outcomes in neurosurgery.

DATA AVAILABILITY

The datasets generated for this study are available on request to the corresponding author.

AUTHOR CONTRIBUTIONS

SC drafted the manuscript and prepared the figures and tables. RS and JL provided critical revisions for the manuscript. All authors agree to be accountable for the contents of this work.

FUNDING

Supported in part by the National Institutes of Health R01 CA193556, and the Institute for Translational Medicine and Therapeutics of the Perelman School of Medicine at the University of Pennsylvania (JL). In addition, research reported in this publication was supported by the National Center for Advancing Translational Sciences of the National Institutes of Health under Award Number UL1TR000003 (JL). The content is solely the responsibility of the authors and does not necessarily represent the official views of the NIH. No separate funding was used for this review. Open access publication fees supported by the Department of Neurosurgery at the Hospital of the University of Pennsylvania.

ACKNOWLEDGMENTS

We would like to thank Jun Jeon, BS, and Carrie Li, BS who provided some of the figures for this review.

REFERENCES

1. Hammouche S, Clark S, Wong AH, Eldridge P, Farah JO. Long-term survival analysis of atypical meningiomas: survival rates, prognostic factors, operative and radiotherapy treatment. *Acta Neurochir.* (2014) 156:1475–81. doi: 10.1007/s00701-014-2156-z
2. Lacroix M, Abi-Said D, Fourney DR, Gokaslan ZL, Shi W, DeMonte F., et al. A multivariate analysis of 416 patients with glioblastoma multiforme: prognosis, extent of resection, and survival. *J Neurosurg.* (2001) 95:190–8. doi: 10.3171/jns.2001.95.2.0190
3. Patchell RA. The management of brain metastases. *Cancer Treat Rev.* (2003) 29:533–40.
4. Sanai N, Polley, M.-Y., McDermott MW, Parsa AT, Berger MS. An extent of resection threshold for newly diagnosed glioblastomas. *J Neurosurg.* (2011) 115:3–8. doi: 10.3171/2011.2.JNS10998
5. SIMPSON D. The recurrence of intracranial meningiomas after surgical treatment. *J Neurol Neurosurg Psychiatry.* (1957) 20:22–39.
6. Ezzat S, Asa SL, Couldwell WT, Barr CE, Dodge WE, Vance ML, et al. The prevalence of pituitary adenomas. *Cancer.* (2004) 101:613–9. doi: 10.1002/cncr.20412
7. Greenman Y, Cooper O, Yaish I, Robenshtok E, Sagiv N, Jonas-Kimchi T., et al. Treatment of clinically nonfunctioning pituitary adenomas with dopamine agonists. *Eur J Endocrinol.* (2016) 175:63–72. doi: 10.1530/EJE-16-0206
8. Lee JYK, Bohman, L-E, Bergsneider M. Contemporary neurosurgical techniques for pituitary tumor resection. *J Neurooncol.* (2014) 117:437–44. doi: 10.1007/s11060-013-1315-z
9. Stummer W, Kamp MA. The importance of surgical resection in malignant glioma. *Curr Opin Neurol.* (2009) 22:645–9. doi: 10.1097/WCO.0b013e3283320165
10. Zhang C, Zhao Y, Zhang H, Chen X, Zhao N, Tan D., et al. The application of heptamethine cyanine dye DZ-1 and indocyanine green for imaging and targeting in xenograft models of hepatocellular carcinoma. *Int J Mol Sci.* (2017) 18:1332. doi: 10.3390/ijms18061332
11. Schucht P, Beck J, Abu-Isa J, Andereggen L, Murek M, Seidel K., et al. Gross total resection rates in contemporary glioblastoma surgery. *Neurosurgery.* (2012) 71:927–36. discussion 935–6. doi: 10.1227/NEU.0b013e31826d1e6b
12. Pereira BJA, de Almeida AN, Paiva WS, de Aguiar PHP, Teixeira MJ, et al. Natural history of intraventricular meningiomas: systematic review. *Neurosurg Rev.* (2018). doi:10.1007/s10143-018-1019-0. [Epub ahead of print].
13. Aizer AA, Bi WL, Kandola MS, Lee EQ, Nayak L, Rinne ML, et al. Extent of resection and overall survival for patients with atypical and malignant meningioma. *Cancer.* (2015) 121:4376–81. doi: 10.1002/cncr.29639
14. Berkmann S, Schlaffer S, Nimsky C, Fahlbusch R, Buchfelder M. Follow-up and long-term outcome of nonfunctioning pituitary adenoma operated by transsphenoidal surgery with intraoperative high-field magnetic resonance imaging. *Acta Neurochir.* (2014) 156:2233–43; discussion 2243.doi: 10.1007/s00701-014-2210-x
15. Almutairi RD, Muskens IS, Cote DJ, Dijkman MD, Kavouridis VK, Crocker E., et al. Gross total resection of pituitary adenomas after endoscopic vs. microscopic transsphenoidal surgery: a meta-analysis. *Acta Neurochir.* (2018) 160:1005–21. doi: 10.1007/s00701-017-3438-z

16. Seltzer J, Wedemeyer MA, Bonney PA, Carmichael JD, Weiss M, Zada G. Outcomes following transsphenoidal surgical management of incidental pituitary adenomas: a series of 52 patients over a 17-year period. *J Neurosurg.* (2018) 1:1–9.doi: 10.3171/2017.11.JNS171485
17. Wirtz CR, Albert FK, Schwaderer M, Heuer C, Staubert A, Tronnier VM., et al. The benefit of neuronavigation for neurosurgery analyzed by its impact on glioblastoma surgery. *Neurol Res.* (2000) 22:354–60.
18. Sherman JH, Hoes K, Marcus J, Komotar RJ, Brennan CW, Gutin PH. Neurosurgery for brain tumors: update on recent technical advances. *Curr Neurol Neurosci Rep.* (2011) 11:313–9. doi: 10.1007/s11910-011-0188-9
19. Berkmann S, Schlaffer S, Nimsky C, Fahlbusch R, Buchfelder M. Intraoperative high-field MRI for transsphenoidal reoperations of nonfunctioning pituitary adenoma. *J Neurosurg.* (2014) 121:1–10. doi: 10.3171/2014.6.JNS131994
20. Kuo JS, Barkhoudarian G, Farrell CJ, Bodach ME, Tumialan LM, Oyesiku NM., et al. Congress of neurological surgeons systematic review and evidence-based guideline on surgical techniques and technologies for the management of patients with nonfunctioning pituitary adenomas. *Neurosurgery*. (2016) 79:E536–8. doi: 10.1227/NEU.0000000000001390.
21. Sheehan J, et al. Congress of neurological surgeons systematic review and evidence-based guideline for the management of patients with residual or recurrent nonfunctioning pituitary adenomas. *Neurosugery*. (2016) 79:539–40. doi: 10.1227/NEU.0000000000001385
22. Layer G, Reichelt J, Jahn D, Heinz DW. Structure and function of enzymes in heme biosynthesis. *Protein Sci.* (2010) 19:1137–61. doi: 10.1002/pro.405
23. Tran TT, Mu A, Adachi Y, Adachi Y, Taketani S. Neurotransmitter transporter family including SLC6A6 and SLC6A13 contributes to the 5-aminolevulinic acid (ALA)-induced accumulation of protoporphyrin IX and photodamage, through uptake of ALA by cancerous cells. *Photochem Photobiol.* (2014) 90:1136–43. doi: 10.1111/php.12290
24. Nakai Y, Tatsumi Y, Miyake M, Anai S, Kuwada M, Onishi S., et al. Expression of ferrochelatase has a strong correlation in protoporphyrin IX accumulation with photodynamic detection of bladder cancer. *Photodiagnosis Photodyn Ther.* (2016) 13:225–32. doi: 10.1016/j.pdpdt.2015.07.174
25. Collaud S, Juzeniene A, Moan J, Lange N. On the selectivity of 5-aminolevulinic acid-induced protoporphyrin IX formation. *Curr Med Chem Anticancer Agents*. (2004) 4:301–16.
26. Schwake M, Günes D, Köchling M, Brentrup A, Schroeteler J, Hotfilder M., et al. Kinetics of porphyrin fluorescence accumulation in pediatric brain tumor cells incubated in 5-aminolevulinic acid. *Acta Neurochir (Wien).* 156:1077–84.doi: 10.1007/s00701-014-2096-7
27. Stummer W, Stocker S, Wagner S, Stepp H, Fritsch C, Goetz C., et al. Intraoperative detection of malignant gliomas by 5-aminolevulinic acid-induced porphyrin fluorescence. *Neurosurgery*. (1998) 42:518–25; discussion 525–6. doi: 10.1097/00006123-199803000-00017
28. Stummer W, Stepp H, Wiestler OD, Pichlmeier U. Randomized, prospective double-blinded study comparing 3 different doses of 5-aminolevulinic acid for fluorescence-guided resections of malignant gliomas. *Neurosurgery*. (2017) 81:230–9. doi: 10.1093/neuros/nyx074
29. Stummer W, Pichlmeier U, Meinel T, Wiestler OD, Zanella F, Reulen HJ, et al. Fluorescence-guided surgery with 5-aminolevulinic acid for resection of malignant glioma: a randomised controlled multicentre phase III trial. *Lancet Oncol.* (2006) 7:392–401. doi: 10.1016/S1470-2045(06)70665-9
30. Eljamel MS, Leese G, Moseley H. Intraoperative optical identification of pituitary adenomas. *J Neurooncol.* (2009) 92:417–21. doi: 10.1007/s11060-009-9820-9
31. Coluccia D, Fandino J, Fujioka M, Cordovi S, Muroi C, Landolt H. Intraoperative 5-aminolevulinic-acid-induced fluorescence in meningiomas. *Acta Neurochir.* (2010) 152:1711–9. doi: 10.1007/s00701-010-0708-4
32. Valdes PA, Bekelis K, Harris BT, Wilson BC, Leblond F, Kim A., et al. 5-Aminolevulinic acid-induced protoporphyrin IX fluorescence in meningioma: qualitative and quantitative measurements *in vivo*. *Neurosurgery*. (2014) 10(Suppl. 1):74–82; discussion 82–3. doi: 10.1227/NEU.0000000000000117
33. Okuda T, Yoshioka H, Kato A. Fluorescence-guided surgery for glioblastoma multiforme using high-dose fluorescein sodium with excitation and barrier filters. *J Clin Neurosci.* (2012) 19:1719–22. doi: 10.1016/j.jocn.2011.12.034
34. Acerbi F, Broggi M, Eoli M, Anghileri E, Cavallo C, Boffano C, et al. Is fluorescein-guided technique able to help in resection of high-grade gliomas? *Neurosurg. Focus*. (2014) 36:E5. doi: 10.3171/2013.11.FOCUS13487
35. Okuda T, Kataoka K, Yabuuchi T, Yugami H, Kato A. Fluorescence-guided surgery of metastatic brain tumors using fluorescein sodium. *J Clin Neurosci.* (2010) 17:118–121. doi: 10.1016/j.jocn.2009.06.033
36. Chen B, Wang H, Ge P, Zhao J, Li W, Gu H., et al. Gross total resection of glioma with the intraoperative fluorescence-guidance of fluorescein sodium. *Int J Med Sci.* (2012) 9:708–714. doi: 10.7150/ijms.4843
37. Akçakaya MO, Göker B, Kasimcan MÖ, Hamamcioglu MK, Kiriş T. Use of sodium fluorescein in meningioma surgery performed under the YELLOW-560 nm surgical microscope filter: feasibility and preliminary results. *World Neurosurg.* (2017) 107:966–73. doi: 10.1016/j.wneu.2017.07.103
38. Francaviglia N, Iacopino DG, Costantino G, Villa A, Impallaria P, Meli F., et al. Fluorescein for resection of high-grade gliomas: a safety study control in a single center and review of the literature. *Surg Neurol Int.* (2017) 8:145. doi: 10.4103/sni.sni_89_17
39. Bowden SG, Neira JA, Gill BJA, Ung TH, Englander ZK, Zanazzi G., et al. Sodium fluorescein facilitates guided sampling of diagnostic tumor tissue in nonenhancing gliomas. *Neurosurgery*. (2018) 82:719–27. doi: 10.1093/neuros/nyx271
40. Suero Molina E, Wölfer J, Ewelt C, Ehrhardt A, Brokinkel B, Stummer W. Dual-labeling with 5-aminolevulinic acid and fluorescein for fluorescence-guided resection of high-grade gliomas: technical note. *J Neurosurg.* (2018) 128:399–405. doi: 10.3171/2016.11.JNS161072
41. Hansen DA, Spence AM, Carski T, Berger MS. Indocyanine green (ICG) staining and demarcation of tumor margins in a rat glioma model. *Surg Neurol.* (1993) 40:451–6.
42. Haglund MM, Hochman DW, Spence AM, Berger MS. Enhanced optical imaging of rat gliomas and tumor margins. *Neurosurgery*. (1994) 35:930-40; discussion 940–1.
43. Haglund MM, Berger MS, Hochman DW. Enhanced optical imaging of human gliomas and tumor margins. *Neurosurgery*. (1996) 38:308–17.
44. Madajewski B, Judy BF, Mouchli A, Kapoor V, Holt D, Wang MD., et al. Intraoperative near-infrared imaging of surgical wounds after tumor resections can detect residual disease. *Clin Cancer Res.* (2012) 18:5741–51. doi: 10.1158/1078-0432.CCR-12-1188
45. Jiang JX, Keating JJ, Jesus EM, Judy RP, Madajewski B, Venegas O., et al. Optimization of the enhanced permeability and retention effect for near-infrared imaging of solid tumors with indocyanine green. *Am J Nucl Med Mol Imaging*. (2015) 5:390–400.
46. Zeh R, Sheikh S, Xia L, Pierce J, Newton A, Predina J., et al. The second window ICG technique demonstrates a broad plateau period for near infrared fluorescence tumor contrast in glioblastoma. *PLoS ONE*. (2017) 12:e0182034. doi: 10.1371/journal.pone.0182034
47. Maeda H, Wu J, Sawa T, Matsumura Y, Hori K. Tumor vascular permeability and the EPR effect in macromolecular therapeutics: a review. *J Control Release*. (2000) 65:271–84.
48. Ergin A, Wang M, Zhang JY, Bruce JN, Fine RL, Bigio IJ., et al. The feasibility of real-time *in vivo* optical detection of blood-brain barrier disruption with indocyanine green. *J Neurooncol.* (2012) 106:551–60. doi: 10.1007/s11060-011-0711-5
49. Lee JYK, Thawani JP, Pierce J, Zeh R, Martinez-Lage M, Chanin M, et al. Intraoperative near-infrared optical imaging can localize gadolinium-enhancing gliomas during surgery. *Neurosurgery*. (2016) 79:856–71. doi: 10.1227/NEU.0000000000001450
50. Lee JYK, Pierce JT, Zeh R, Cho SS, Salinas R, Nie S, et al. Intraoperative near-infrared optical contrast can localize brain metastases. *World Neurosurg.* (2017) 106:120–30. doi: 10.1016/j.wneu.2017.06.128
51. Lee JYK, Pierce JT, Thawani JP, Zeh R, Nie S, Martinez-Lage M, et al. Near-infrared fluorescent image-guided surgery for intracranial meningioma. *J Neurosurg.* (2018) 128:380–90. doi: 10.3171/2016.10.JNS161636
52. Cho SS, Zeh R, Pierce JT, Salinas R, Singhal S, Lee JYK. Comparison of near-infrared imaging camera systems for intracranial tumor detection. *Mol Imaging Biol.* (2018) 20:213–20. doi: 10.1007/s11307-017-1107-5

53. Jeon JW, Cho SS, Nag S, Buch L, Pierce J, Su YS, et al. Near-infrared optical contrast of skull base tumors during endoscopic endonasal surgery. *Oper. Neurosurg.* (2018) 1–11. doi: 10.1093/ons/opy213. [Epub ahead of print].
54. Cho SS, Jeon J, Buch L, Nag S, Nasrallah M, Low PS, et al. Intraoperative near-infrared imaging with receptor-specific versus passive delivery of fluorescent agents in pituitary adenomas. *J Neurosurg.* (2018) 1:1–11. doi: 10.3171/2018.7.JNS181642.
55. Frangioni JV. *In vivo* near-infrared fluorescence imaging. *Curr Opin Chem Biol.* (2003) 7:626–34.
56. Padalkar M V,Pleshko N. Wavelength-dependent penetration depth of near infrared radiation into cartilage. *Analyst.* (2015) 140:2093–100. doi: 10.1039/c4an01987c
57. Roberts DW, Olson JD, Evans LT, Kolste KK, Kanick SC, Fan X., et al. Red-light excitation of protoporphyrin IX fluorescence for subsurface tumor detection. *J Neurosurg.* (2018) 128:1690–7. doi: 10.3171/2017.1.JNS162061
58. Dsouza AV, Lin H, Henderson ER, Samkoe KS, Pogue BW. Review of fluorescence guided surgery systems: identification of key performance capabilities beyond indocyanine green imaging. *J Biomed Opt.* 21:80901.doi: 10.1117/1.JBO.21.8.080901
59. Hekman MCH, Rijpkema M, Bos DL, Oosterwijk E, Goldenberg DM, Mulders PFA., et al. Intraoperative near-infrared imaging can distinguish cancer from normal tissue but not inflammation. *PLoS ONE.* (2014) 9:e103342. doi: 10.1371/journal.pone.0103342
60. Cho SS, Zeh R, Pierce JT, Jeon J, Nasrallah M, Adappa ND., et al. Folate receptor near-infrared optical imaging provides sensitive and specific intraoperative visualization of nonfunctional pituitary adenomas. *Oper Neurosurg.* (2018) 16:59–70.doi: 10.1093/ons/opy034
61. Lee JY. K. et al. Folate receptor overexpression can be visualized in real time during pituitary adenoma endoscopic transsphenoidal surgery with near-infrared imaging. *J Neurosurg.* (2017) 129:390–403. doi: 10.3171/2017.2.JNS163191
62. Pierce JT, Cho SS, Nag S, Zeh R, Jeon J, Holt D, et al. Folate receptor overexpression in human and canine meningiomas—immunohistochemistry and case report of intraoperative molecular imaging. *Neurosurgery*. (2018) 1–10. doi: 10.1093/neuros/nyy356. [Epub ahead of print].
63. Belykh E, Miller EJ, Patel AA, Yazdanabadi MI, Martirosyan NL, Yagmurlu K., et al. Diagnostic accuracy of a confocal laser endomicroscope for *in vivo* differentiation between normal injured and tumor tissue during fluorescein-guided glioma resection: laboratory investigation. *World Neurosurg.* (2018) 115:e337–48. doi: 10.1016/j.wneu.2018.04.048
64. Martirosyan NL, Cavalcanti DD, Eschbacher JM, Delaney PM, Scheck AC, Abdelwahab MG., et al. Use of *in vivo* near-infrared laser confocal endomicroscopy with indocyanine green to detect the boundary of infiltrative tumor. *J Neurosurg.* (2011) 115:1131–8. doi: 10.3171/2011.8.JNS11559

Conflict of Interest Statement: JL has stock options in VisionSense, which owns VisionSense Iridium^{TM} used extensively in the studies reviewed here.

The remaining authors declare that the research was conducted in the absence of any commercial or financial relationships that could be construed as a potential conflict of interest.

frontiers in Surgery

ORIGINAL RESEARCH
published: 21 March 2019
doi: 10.3389/fsurg.2019.00012

Intraoperative Photodiagnosis for Malignant Glioma Using Photosensitizer Talaporfin Sodium

Jiro Akimoto[1,2]*, *Shinjiro Fukami*[1], *Megumi Ichikawa*[1], *Awad Mohamed*[1,3] and *Michihiro Kohno*[1]

[1] Department of Neurosurgery, Tokyo Medical University, Tokyo, Japan, [2] Department of Neurosurgery, Kohsei Chuo General Hospital, Tokyo, Japan, [3] Department of Neurosurgery, Sohag University, Sohag, Egypt

Objective: The aim of this study was to demonstrate the clinical feasibility of intraoperative photodiagnosis (PD) of malignant brain tumor using talaporfin sodium (TPS), which is an agent used in photodynamic therapy (PDT) for cancers.

Methods: Forty-seven patients diagnosed with malignant gliomas by preoperative imaging (42 patients with gliomas and 5 patients with other brain tumors) received an intravenous injection of TPS at 40 mg/m^2 24 h before resection. During surgery, these patients were irradiated with diode laser light at 664 nm, and tumor fluorescence was observed. The fluorescence intensity was visually rated on a 3-point rating scale [strong fluorescence, weak fluorescence and no fluorescence]. TPS concentrations in 124 samples from 47 cases were measured by HPLC (High performance liquid chromatography).

Results: The fluorescence intensity was confirmed to be weak in all patients with Grade II gliomas and strong in almost all patients with Grade III or IV gliomas, reflecting the histological grade of malignancy. In patients with non-glioma brain tumors except for 1 patient with a metastatic brain tumor, the fluorescence intensity was strong. The mean TPS concentration in tissues was 1.62 μg/g for strong fluorescence areas, 0.67 μg/g for weak fluorescence areas and 0.19 μg/g for no fluorescence areas.

Conclusions: Establishment of an appropriate fluorescence observation system enabled fluorescence-guided resection of malignant brain tumors using TPS, and the fluorescence intensity of tumors correlated with the TPS concentrations in tissues. These results suggest that TPS is a useful photosensitizer for both intraoperative fluorescence diagnosis and photodynamic therapy.

Keywords: malignant glioma, photodiagnosis, talaporfin sodium, fluorescence guided resection, tissue concentration

OPEN ACCESS

Edited by:
Mark Preul,
Barrow Neurological Institute (BNI), United States

Reviewed by:
Prashanth J. Rao,
University of New South Wales, Australia
Peter Nakaji,
Barrow Neurological Institute (BNI), United States

***Correspondence:**
Jiro Akimoto
jiroaki@gmail.com

Specialty section:
This article was submitted to Neurosurgery, a section of the journal Frontiers in Surgery

Received: *29 August 2018*
Accepted: *19 February 2019*
Published: *21 March 2019*

Citation:
Akimoto J, Fukami S, Ichikawa M, Mohamed A and Kohno M (2019) Intraoperative Photodiagnosis for Malignant Glioma Using Photosensitizer Talaporfin Sodium. Front. Surg. 6:12. doi: 10.3389/fsurg.2019.00012

INTRODUCTION

The use of photosensitizers (PSs) for malignant gliomas has been aimed mainly at tumor control by photodynamic therapy (PDT). In 1980, a clinical report related to PDT, in which patients with gliomas underwent helium-neon laser irradiation after the administration of Photofrin II, was submitted by Perria et al. (1) Since this report, clinical studies of PDT with dye laser irradiation mainly using hematoporphyrin derivatives (HpDs) have been reported (2–5). The main mechanism of PDT is based on the generation of cytotoxic singlet oxygen in tissues under aerobic conditions,

as a result of a photochemical reaction induced by the administration of a non-toxic PS in combination with the irradiation of an excitation laser specific to the PS. The cytotoxic effects of this singlet oxygen cause damage to tumor cells and newly formed blood vessels (6, 7).

After administered to a patient, PS is transformed from the ground state to the excited state by laser irradiation, and immediately returns to the ground state with emitting fluorescence. In 2000, Stummer et al. established a methodology called fluorescence-guided resection (FGR) where tumors are resected using an intraoperative photodiagnosis (PD) of malignant gliomas with the fluorescence as a guide (8, 9). The FGR was acclaimed as a breakthrough methodology where PS is used for purposes other than the original intended use in PDT. A phase III study conducted thereafter proved that the improved extent of resection achieved by FGR would prolong progression free survival (PFS), and FGR has gained recognition as a methodology with a high level of evidence (10–12). The PS they used was 5-aminolevulinic acid (5-ALA), which was thereafter approved as an agent for intraoperative localization of malignant gliomas by the European Medicines Agency in 2007, in Korea in 2011 and also in Japan in 2013. Theoretically, 5-ALA can also be applied to PDT, and basic research and clinical research of PDT using 5-ALA in malignant gliomas have been reported. To date, however, no evidence for the usefulness of 5-ALA in PDT comparable to that in PD has been reported (13, 14).

The authors reported the safety and efficacy of PDT using an HpD, talaporfin sodium (TPS), which is a second-generation photosensitizer, by conducting an *in vitro* study in human glioma cells (15), an *in vivo* study in an experimental model of transplanted C6 glioblastoma in rats (16, 17), and furthermore clinical research including investigator-initiated studies in patients with malignant gliomas (18, 19). Partially because TPS had already been approved as an agent for PDT in patients with early stage lung cancer (20), TPS and an excitation diode laser device specific to TPS were approved for health insurance reimbursement in Japan in 2013 as an agent for PDT in patients with primary malignant brain tumors.

In our previous clinical research on PDT, all patients preoperatively predicted to have malignant gliomas received TPS and underwent FGR (18). Then, PDT was performed only for patients suggested to have residual tumor based on PD. In other words, we found TPS to be useful for both PD and PDT and consider TPS an ideal PS to date in the treatment of malignant brain tumors. In this article, we report the usefulness of PD in the treatment of primary malignant brain tumors with TPS administration and excitation laser irradiation, by presenting actual cases. We also report the correlation between PD, which involves gross assessment, and actual TPS concentrations in brain tumor tissues.

MATERIALS AND METHODS

Talaporfin Sodium and Diode Laser

Talaporfin sodium (TPS: Laserphyrin®, Meiji Seika Pharma Co., Ltd., Tokyo, Japan) is a photosensitizer, a hydrophilic compound manufactured by coupling aspartic acid and chlorine, utilized in PDT, which was approved for use in Japan in 2003 as treatment for early-stage lung cancer, in combination with a diode laser (PD Laser®, Panasonic HealthCare Co., Ltd., Ehime, Japan) at a wavelength of 664 nm (**Figures 1A,B**). TPS is a second-generation photosensitizer that is more quickly excreted from the body than the first-generation porfimer sodium (Photofrin®, Pfizer Japan Inc., Tokyo, Japan). It is characterized by rapid resolution of a skin photosensitivity reaction, which is important with the use of photosensitizers. This has enabled the period of necessary light shielding in a room with measurement of $\leqq$ 500 lux to be reduced to 2 weeks for TPS, whereas porfimer sodium requires patients to stay in a semi-dark ($\leqq$ 300 lux) room for 1 month after administration. A diode laser instrument, a compact system weighing 14 kg, has low power consumption, and can easily be maintained without the need for dye exchange.

Operating Microscope Equipped With Diode Laser (Figure 1)

The PD Laser® (Panasonic HealthCare Co., Ltd.), installed in the MM30 microscope (Mitaka Kohki Co., Ltd., Tokyo, Japan), is combined into a system that provides laser irradiation (664 nm) from the operating microscope from a plane nearly coaxial to the surgical view. The laser light is introduced into the microscope by a quartz fiber, and provides a laser transmission path close to an observation light path using a conventional halogen light. This allows surgeons to accurately identify an irradiation target area during surgery. The wavelength of fluorescence from tumor tissues is 672 nm. To detect this fluorescence, a system was established using a very narrow notch filter (Nitto Optical Co., Ltd., Tokyo, Japan) that can capture an 8-nm difference. The system gathers emitted fluorescence through a cooled charge-coupled device (CCD) and visualizes images on the monitor. The system is designed for enhancing the contrast between the brain surface and the tumor, by mounting 6 white light-emitting diodes (LEDs) as light sources (NSPW500BS and NSPW510BS, Nichia Corporation, Tokushima, Japan) around the objective lens to achieve a clear fluorescence observation by brain surface illumination with LEDs allowing 6-level light intensity control (**Figures 1C–F**).

Phantom Experiment

We conducted an experiment to examine whether this microscopic system allows appropriate intraoperative fluorescence observation during brain tumor surgery. TPS at 3 concentrations of 1, 10, and 100 μg/mL each was mixed with 10% bovine serum albumin (BSA; Wako Pure Chemical Industries Ltd., Osaka, Japan). Then, a cotton ball was moistened with each mixture. These cotton balls were irradiated with a diode laser at 664 nm under the irradiation conditions described later, and then observed the emitted fluorescence at 672 nm using the microscopic system to determine whether the dose-dependent fluorescence intensity is grossly detectable.

Subjects

The study subjects were 47 consecutive patients who received the protocol-specified surgery after being diagnosed with glioma by preoperative diagnostic imaging by a single surgeon (JA)

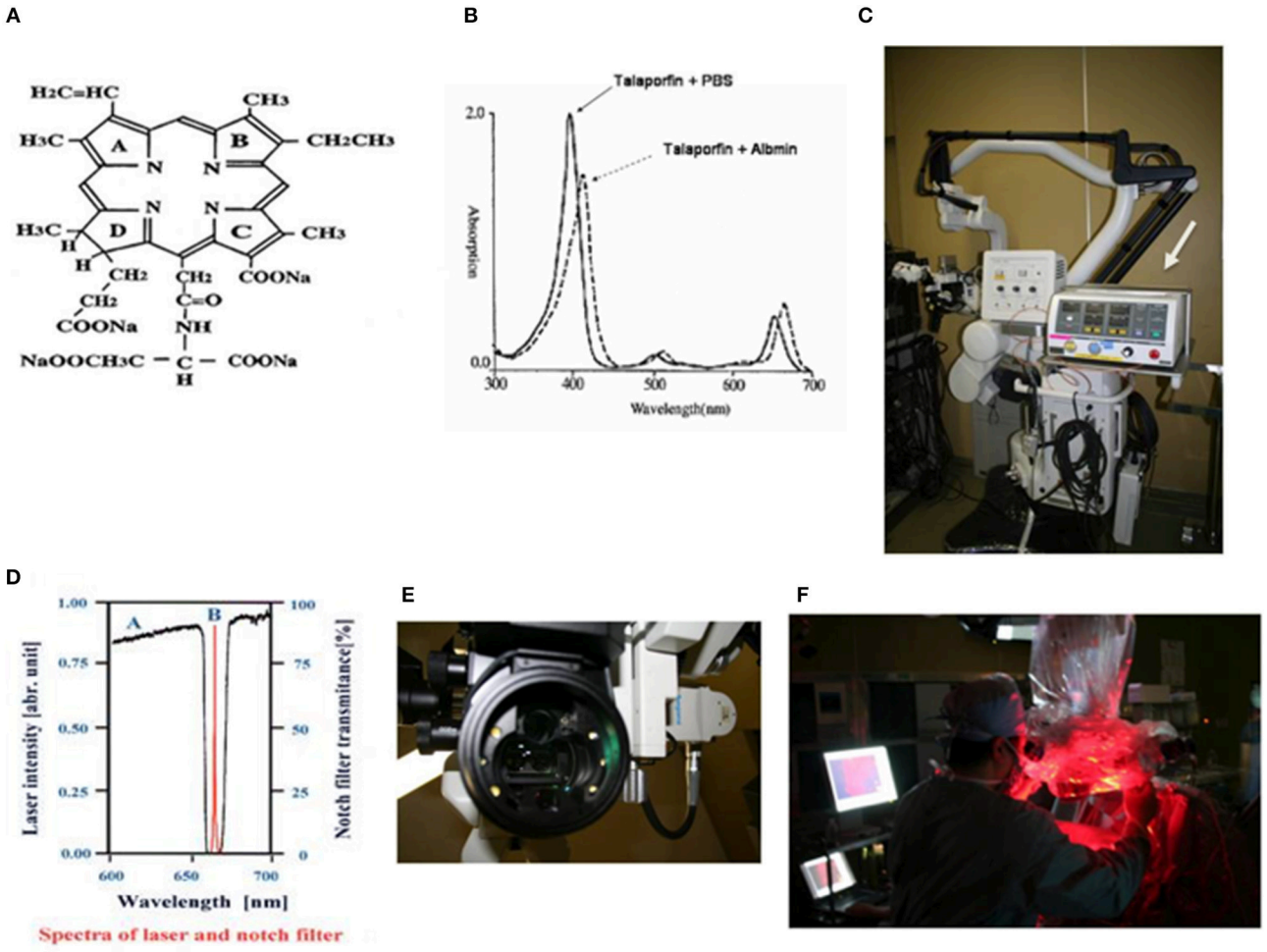

FIGURE 1 | (A) Chemical structure of talaporfin sodium (mono-L-aspartyl chlorine e6, NPe6). **(B)** Absorption spectrum of talaporfin sodium and change in absorption wavelength following conjugation with albumin (solid line: talaporfin sodium and phosphate buffer solution, dotted line: talaporfin sodium conjugated with albumin). Talaporfin sodium has absorption peaks in the Soret band (398 nm) and Q bands (502, 530, 620, and 654 nm) in pH 7.4 phosphate buffer solution (PBS). When it conjugates with albumin, its absorption band wavelength becomes ∼10 nm longer (bathochromic shift). **(C)** MM80® surgical microscope (Mitaka Kohki Co., Ltd.) equipped with a compact diode laser (PD Laser®, Panasonic Health Care Ltd., arrow). **(D)** A very narrow notch filter (Nitto Optical Co. Ltd.) that can cut out light excited at 664 nm and can capture fluorescence emitted at 672 nm is mounted in a surgical microscope. **(E)** Six white LEDs (Nichia Corporation) are mounted as light sources in the applicator at the objective lens side of the microscope, in order to illuminate the brain surface during laser irradiation. **(F)** From the surgical microscope, the diode laser irradiates the surgical field.

from April 2005 to December 2008 at the Department of Neurosurgery, Tokyo Medical University. The final pathological diagnosis was glioma in 42 patients, newly diagnosed tumor in 24 patients, and recurrent tumor in 18 patients. The histological malignancy grade was Grade I in 1 patient, Grade II in 5 patients, Grade III in 8 patients and Grade IV in 28 patients. There were 5 patients whose final pathological diagnosis was not glioma after undergoing the protocol-specified surgery based on the diagnosis of glioma made by preoperative diagnostic imaging. The final pathological diagnosis in these patients was metastatic brain tumor in 2 patients (from lung cancer and mammary gland cancer), primary central nervous system lymphoma in 1 patient and meningioma in 2 patients. The institutional review board approved the participation of humans in research at Tokyo Medical University approved our fluorescence-guided intracranial tumor resection protocol, and all patients gave their informed consent before participating.

PDT and Intraoperative PD Procedures

TPS was administered as a bolus intravenously at a dose of 40 mg/m^2 in light-shielded conditions 24 h prior to surgery. Craniotomy was performed under illumination at ≤500 lux. First, the brain surface was observed under halogen light illumination. Then, the halogen light was turned off, and the brain surface was irradiated with a diode laser at 664 nm at a power density of 10 mW/cm^2, with a beam diameter of 40 mm and an irradiation area of 12.6 cm^2, to observe the presence or absence of tumor fluorescence. The illuminance of the white LEDs was adjusted as appropriate to check the difference in color tone from the brain surface. Every time tumor tissue was

resected, the resected tissue was irradiated with a laser in order to check the intensity of the tumor fluorescence. The fluorescence intensity displayed on the monitor was grossly assessed in three grades: strong fluorescence (S), weak fluorescence (W), and no fluorescence (N). The tumor resection was performed using an optical navigation system (Brainlab K.K., Tokyo, Japan), as awake craniotomy and fluorescence-guided resection, under physiological monitoring. When reaching the limit for resection, the resection cavity was irradiated with a diode laser. When weak or strong fluorescence was grossly detected in the cavity, PDT was performed as reported previously (at a power density of 150 mW/cm^2 and an irradiation energy of 27 J/cm^2, with a beam diameter of 15 mm and an irradiation area of 1.8 cm^2), and the operation was ended. After the operation, the patient was managed in a shielded condition under illumination at $\leq$500 lux, until the result of the skin photosensitivity test turned to negative.

Measurement of Talaporfin Sodium Concentrations in Brain Tumor Tissue

TPS concentrations were measured according to the method reported by Yoshida et al. (21), using 5-mm cubic tissue blocks of 124 samples from 47 cases excised from each area assessed as strong, weak or no during the surgery. To the resected brain tumor tissue per 100 mg, 5 mL of a mixture of HEPES buffer solution and CH_3OH (1:9) was added, then the tissue was homogenized while cooling in ice for 1 min, and the supernatant was used as a measurement sample. The TPS and the internal standard, fluoranthene (Wako Pure Chemical Industries Ltd., Osaka, Japan), in each measurement sample were separated based on the principle of reverse phase liquid chromatography (Inertsil® ODS-2, GL Science Inc., Tokyo, Japan), and detected by a fluorescence detector. Based on each peak area obtained, the peak area ratio relative to fluoranthene was calculated and used the values as TPS concentrations. For patients in whom the concentration was measured at multiple sites in each area assessed as strong, weak or no fluorescence, the mean concentration was used for the evaluation.

Calculation of the Extent Of Resection

Based on MRI images obtained before surgical resection and within 3 days of the resection, the extent of resection was determined. For gadolinium-enhanced tumors, gadolinium-enhanced T1-weighted axial imaging was used. The sum of the products of perpendicular diameters (SPD) of the contrast-enhanced lesions was calculated. Then, the SPD of residual lesions on immediate postoperative imaging was determined, and the extent of resection was calculated. For non-gadolinium-enhanced tumors, the SPD of the areas of prolonged T2 on T2-weighted imaging was assessed to calculate the extent of resection.

Statistical Analysis

A significance test for TPS concentrations in each tissue was performed by Student's *t*-test, using SPSS analysis software (Advanced Statistics Version 17 by SPSS, Chicago, USA).

RESULTS

Phantom Experiment

From the cotton balls impregnated with mixtures of the TPS solutions at 3 concentrations and 10% BSA, red fluorescence with intensities dependent on the concentration of TPS was observed by laser irradiation. A clear fluorescence was observed in light shielded conditions. However, in the case of laser irradiation under halogen light illumination, red fluorescence was visible only from the tissue containing TPS at the concentration of 100 μg/mL, but fluorescence was hardly perceived at other concentrations. In the case of laser irradiation under white LED illumination, both the dose-dependent red fluorescence at all concentrations of TPS and the background are considered observable (**Figures 2A–C**).

Representative Cases

Case 10: A 56-year-old man had glioblastoma in the right parietal lobe, manifested by involuntary twitching at the left corner of the mouth. The tumor was resected en bloc using an optical navigation system under continuous somatosensory evoked potential monitoring. Being irradiated with a laser, resected tissues emitted strong red fluorescence, with weak red fluorescence in the surrounding area. The TPS concentration in tissue was 2.9538 μg/g in the area of strong fluorescence and 1.5765 μg/g in the area of weak fluorescence. The area of strong fluorescence was within the tumor bulk, and the area of weak fluorescence was within the surrounding brain tissues infiltrated with tumor cells. When the resection cavity was observed under laser irradiation, an area of weak fluorescence was detected and therefore was additionally resected. Pathologically, this area was assessed as a tumor infiltration area containing MIB-1 positive cells. A postoperative contrast-enhanced MRI revealed that the tumor was totally resected, and the additionally resected area was clearly identifiable (**Figures 3A–F**).

Case 18: A 41-year-old woman had glioblastoma in the left frontal lobe, manifested by mild motor aphasia and right hemiplegia. She underwent awake surgery, and laser irradiation was performed on the brain surface during the operation. By the laser irradiation, strong red fluorescence suggestive of a localized tumor was observed on the brain surface along with fluorescence from the blood vessels on the brain surface. When a laser was irradiated under white LEDs, a clear contrast was observed between the fluorescence and the surrounding brain surface. The tumor was resected en bloc and examined on the longitudinal cross-section. Strong ring-like red fluorescence was observed, which was similar to the ring-like enhancement surrounding the central necrosis on MRI images. Observation under LED illumination revealed a more detailed relationship with the surrounding brain tissue. The TPS concentration in tissue was 2.1861 μg/g in the strong fluorescence area, 0.9349 μg/g in the weak fluorescence area, and 0.4044 μg/g in the no fluorescence area in the periphery. A postoperative MRI confirmed that the contrast-enhanced lesion was totally resected (**Figures 4A–F**).

Case 2: A 30-year-old man had oligoastrocytoma in the left frontal lobe, manifested by a first episode of generalized tonic-clonic seizures. No obvious contrast enhancement was observed

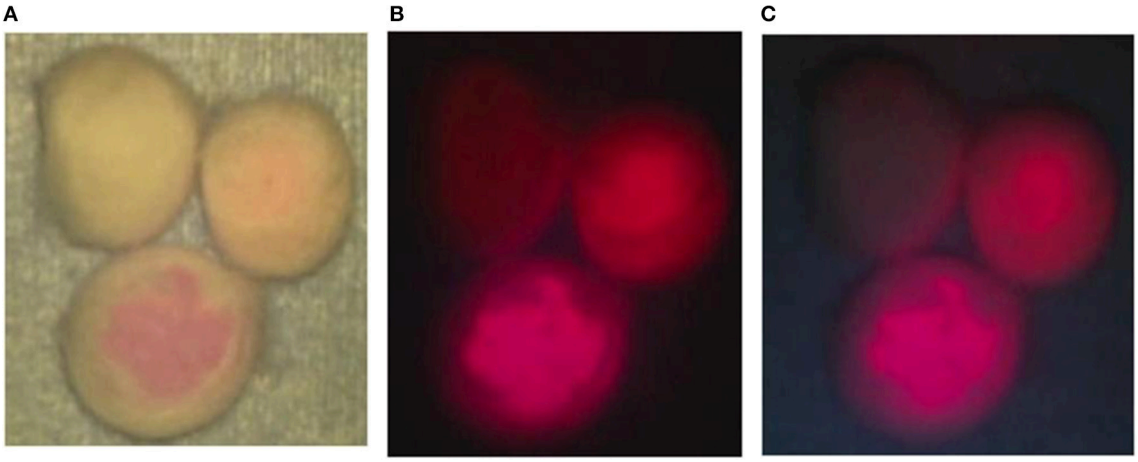

FIGURE 2 | Phantom experiment. **(A)** Talaporfin sodium (TPS) dissolved in 1 mL of physiological saline at 3 concentrations of 1, 10 and 100 μg/mL was mixed with 1 mL of 10% bovine serum albumin (BSA). Then, each mixture was dripped onto a cotton ball. First, when each cotton ball was irradiated with a laser under halogen light illumination of the surgical microscope, clear fluorescence was observed from the cotton ball impregnated with TPS at 100 μg/mL. **(B)** The halogen light illumination of the surgical microscope was turned off, and laser irradiation was performed. Differences in fluorescence intensity dependent on the TPS concentration were clearly identified. **(C)** When laser irradiation was performed while the halogen light was off and the 4 LED light sources were on, color tones of the non-woven fabric on the background were perceived, and differences in concentration among the cotton balls became more distinct.

on the preoperative contrast-enhanced MRI. When the resected tumor tissue was irradiated with a laser, weak red fluorescence was observed at the site where the tumor had been located. The TPS concentration in tissue in this area was 0.6914 μg/g. A postoperative MRI confirmed that the lesion of prolonged T2 was totally resected (**Figures 5A–D**).

Case 1: An 18-year-old man had pilocytic astrocytoma in the vermis cerebelli, manifested by sudden headache and nausea. A preoperative contrast-enhanced MRI showed an enhanced mural nodule. During the surgery, the cyst was opened and irradiated with a laser. As a result, nodular fluorescence, tending to be strong, appeared with weak fluorescence from the surrounding cystic wall. The TPS concentration in tissue was high, being 3.163 μg/g in the strong fluorescence area and 1.614 μg/g in the weak fluorescence area. A postoperative MRI confirmed that the lesion including the cystic wall was totally resected (**Figures 6A–D**).

Results of Intraoperative Observation of Fluorescence From Tumors

Fluorescence Positive Rate (Figure 7, Table 1 and Supplementary Table 1)

In glioma cases, 1 case of Grade I pilocytic astrocytoma showed strong fluorescence. In five Grade II cases, none showed strong fluorescence, but all showed weak fluorescence. In eight Grade III cases, all showed at least weak fluorescence, including 5 cases (62.5%) showing strong fluorescence. In 28 Grade IV cases, 22 cases (78.6%) showed strong fluorescence and 26 cases (92.9%) showed weak fluorescence; thus all showed fluorescence, as seen in Grade III cases. In the Grade IV cases, strong fluorescence was shown in 14 (93.3%) of 15 newly diagnosed cases and 8 (61.5%) of 13 recurrent cases. In the recurrent cases, some showed only weak fluorescence. In the other 5 cases, except for 1 case of metastatic brain tumor, 4 cases showed strong fluorescence.

Correlation Between Fluorescence Intensity and Tissue Concentration (Figure 8, Table 1 and Supplementary Table 1)

The TPS concentrations in tissue in the strong, weak and no fluorescence areas that were assessed grossly were 1.6184 ± 0.9661, 0.6708 ± 0.3765 and 0.1885 ± 0.1253 μg/g, respectively. There were significant differences in concentration between the strong and weak fluorescence areas and between the weak and no fluorescence areas ($P < 0.001$). In the glioma cases, 1 Grade I case showed strong fluorescence with a tissue concentration of 3.1628 μg/g, but all Grade II cases showed weak fluorescence. The tissue concentrations in strong fluorescence areas in Grade III and IV cases were 1.3751 ± 0.7480 and 1.4948 ± 0.7783 μg/g, respectively, showing no significant difference between the Grade III and IV cases ($P = 0.718$). In Grade IV cases, the mean tissue concentrations in strong, weak and no fluorescence areas were 1.4948, 0.6752, and 0.1655 μg/g, respectively, showing significant differences ($P < 0.001$) among the tissue concentrations in these areas. The tissue concentration in the strong fluorescence area in Grade IV cases was 1.5797 ± 0.9082 μg/g in newly diagnosed cases and 1.3589 ± 0.5239 μg/g in recurrent cases, showing no significant difference between the newly diagnosed and recurrent cases ($P = 0.493$). Also in the weak and no fluorescence areas, no significant differences were observed between the newly diagnosed and recurrent cases ($P = 0.821$ for weak fluorescence area and $P = 0.853$ for no fluorescence area). In non-glioma cases, the tissue concentration in the strong fluorescence area was 2.100 ± 1.528 μg/g, showing no significant difference from the result obtained for the strong fluorescence area in Grade IV cases ($P = 0.153$).

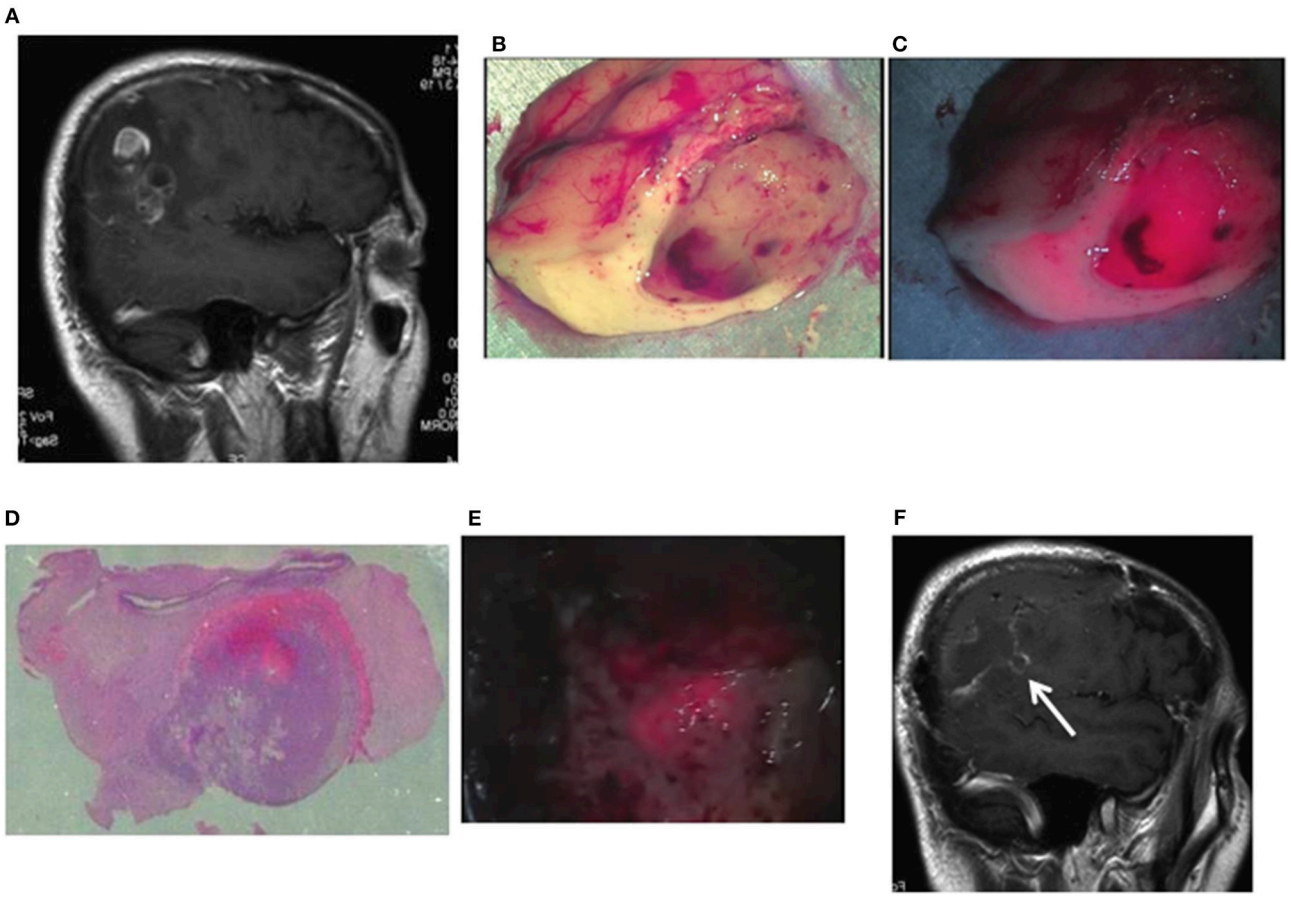

FIGURE 3 | Representative case 10. **(A)** A gadolinium-enhanced T1-weighted sagittal image. The image revealed an irregularly enhanced glioblastoma lesion in the right parietal lobe. **(B)** Brain tissues containing a tumor tissue were resected to the widest extent possible, using an optical navigation system while somatosensory-evoked monitoring was performed. Well-demarcated tumor tissue was observed in the subcortical white matter. **(C)** When laser irradiation was performed under LED illumination, strong fluorescence from the tumor bulk and weak fluorescence from the surrounding white matter were observed. **(D)** A postoperative histopathological image revealed the presence of tumor cells infiltrating from the strong fluorescence area into the weak fluorescence area (hematoxylin and eosin staining). **(E)** When a laser was irradiated to the white matter in the tumor resection cavity under LED illumination, weak fluorescence areas were found in the normal white matter. Therefore, the tissue resection was continued until the fluorescence disappeared. **(F)** The postoperative gadolinium-enhanced MRI confirmed the additionally resected areas (arrow) as well as the total resection of the enhanced lesion.

Extent of Resection (Supplementary Table 1)

By the FGR using TPS, total resection confirmed on imaging was achieved in 22 (52.3%) of 42 patients with gliomas. In most of the 24 newly diagnosed cases, a clear difference in fluorescence intensity was obtained, allowing the resection of not only strong fluorescence areas but also weak to no fluorescence areas. As a result, total resection was achieved in 16 cases (66.7%). Even in cases with residual lesions, the resection of 94 ± 4.3% (89–99%) of the tumor was achieved, according to an SPD analysis. On the other hand, in 18 recurrent cases, it was difficult to obtain a clear difference in fluorescence intensity. In the majority of these cases, weak fluorescence was blurrily spread, making it difficult to grossly determine the disappearance of the fluorescence. Consequently, total resection was achieved only in 6 cases (33.3%), which is an extremely low extent of resection. In cases showing residual lesions, the extent of resection was limited to 81.4 ± 8.9% (63−95%). Of course, when a tumor clearly infiltrates in the functional regions of the brain, it is difficult to resect the tumor even though fluorescence is detected, and PDT should be performed additionally. PDT was performed in 5 newly diagnosed cases and 11 recurrent cases. In most of these recurrent cases, PDT was added due to concern that there may be residual tumors because it was difficult to confirm the disappearance of fluorescence. In non-glioma cases, 1 case with atypical meningioma with repeated recurrences underwent PDT for the residual tumor because total resection had to be abandoned due to intracerebral infiltration of the tumor in the motor cortex, although fluorescence was identified. In this case, however, total resection of other tumor lesions was achieved.

DISCUSSION

In the surgery of glioma, which is characterized by invasive growth, the concept of "maximal safe resection" is important. Evidence for the fact that enhancement of the extent of surgical

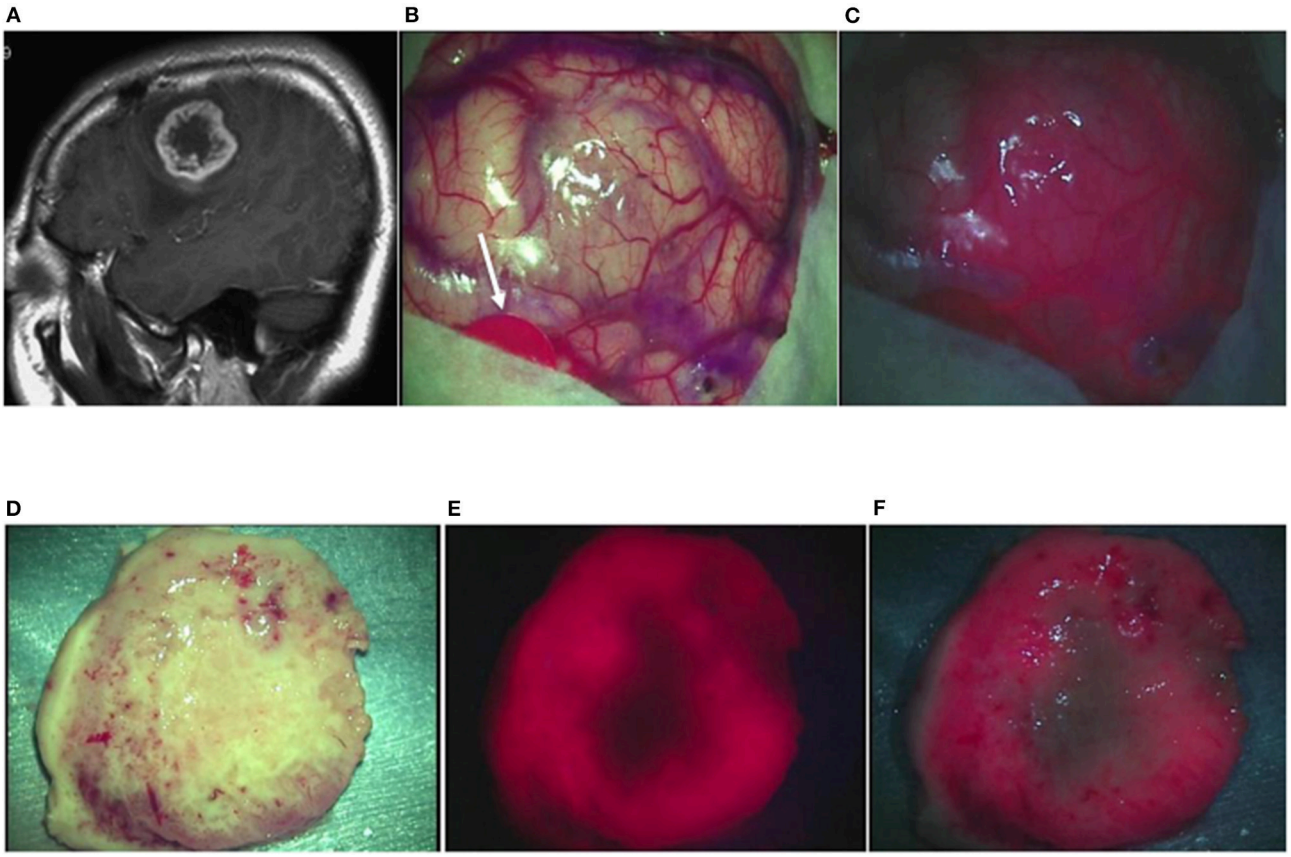

FIGURE 4 | Representative case 18. **(A)** A gadolinium-enhanced T1-weighted sagittal image revealed a ring-like enhanced glioblastoma in the left middle frontal gyrus. **(B)** An image of the brain surface under halogen light illumination showed marked swelling in the left middle frontal gyrus, but tumor tissue was not exposed (arrowed red circle: primary motor cortex). **(C)** In the fluorescence diagnosis under white LED illumination, strong fluorescence from the tumor was observed, and fluorescence from residual TPS in the surrounding blood vessels was identified simultaneously, facilitating the fluorescence-guided resection. **(D)** The tumor together with some surrounding brain tissue attached to the tumor was resected en bloc. The median section observed under halogen light illumination revealed the presence of a light brownish tumor tissue in a doughnut shape. **(E)** Laser irradiation revealed strong fluorescence almost surrounding the central necrotic lesion, clearly identifying the contrast-enhanced lesion on preoperative MRI. **(F)** In the fluorescence diagnosis under white LED illumination, the difference in fluorescence intensity between the strong fluorescence areas and the necrotic lesion or the surrounding brain tissue became more distinct.

resection leads to improved prognosis of malignant gliomas has been accumulating, and there have been a series of discussions regarding how to achieve total resection of gadolinium-enhanced lesions on MRI images and, at the same time, how to protect neurological functions (22–24). FGR using dyes, such as fluorescein and 5-ALA, has been widely accepted as an intraoperative real-time navigation method that visualizes tumor bulk, and many studies on the efficacy of FGR have been reported (25–27). A representative study among these is a randomized controlled trial (RCT) of FGR with 5-ALA, led by Stummer et al. in which FGR has been demonstrated to improve the extent of resection, resulting in significant prolongation of PFS in patients who underwent FGR. Therefore, this methodology has been accepted in many countries (9, 11, 12). However, FGR with 5-ALA alone failed to prolong overall survival (OS). In other words, the results indicate that the total resection of gadolinium-enhanced lesions by FGR only does not prolong OS (10).

A scheme proposed by Wilson for the extent of tumor cell infiltration shows that curative resection cannot be achieved by glioma surgery, as well as that resection of not only contrast-enhanced lesions on imaging but also the surrounding tissue infiltrated by tumor cells can contribute to reducing the residual tumor cells (28). In recent years, a supra-total resection, i.e., an extended resection of high signal-intensity areas on FLAIR images in tissue surrounding the tumor to the extent that the neurological function is not deteriorated, has been reported to prolong OS (29, 30). Therefore, in malignant glioma surgery, in addition to total resection of gadolinium-enhanced lesions using FGR under proper monitoring of neurological functions, the surrounding tissue infiltrated by tumor cells should be resected to the extent possible up to the boundary of the functional regions of the brain (29, 30). For cases where tumor cells have infiltrated in the functional region of the brain, we consider it significant to perform PDT, which is capable of specifically destroying tumor cells (18, 19). In that sense, the TPS we used this time is a PS

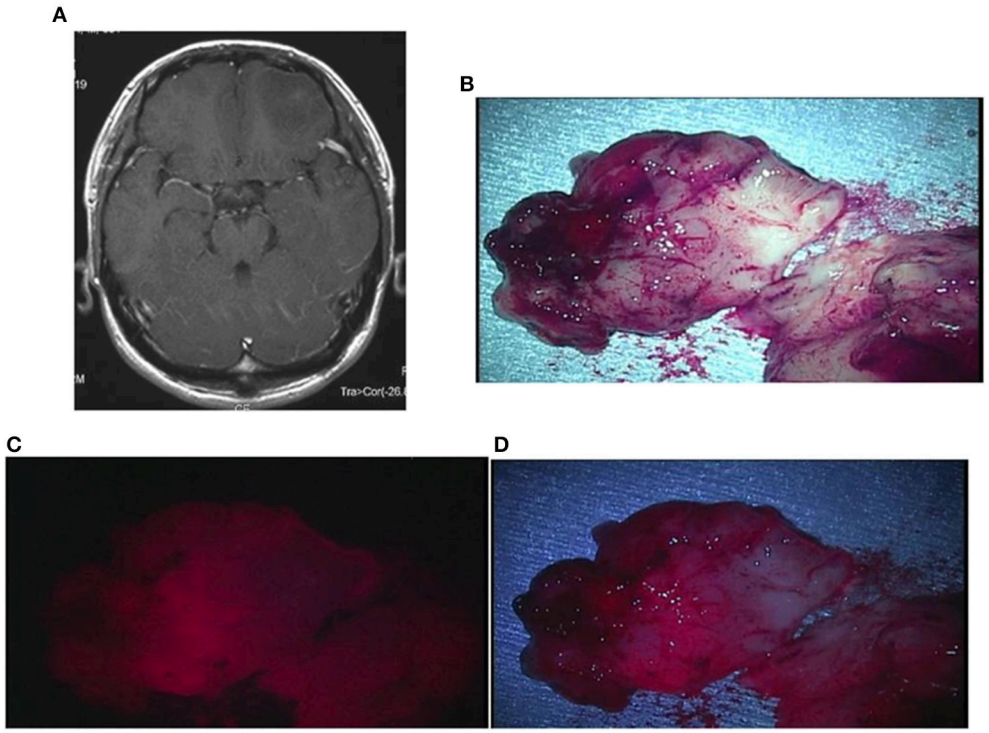

FIGURE 5 | Representative case 2. **(A)** A gadolinium-enhanced T1-weighted axial image showed a slightly enhanced tumor in the left frontal lobe. **(B)** The tumor bulk was resected en bloc. The median section observed under halogen light illumination revealed the presence of a yellowish-gray gelatinous tumor in the cortex. **(C)** By laser irradiation, weak fluorescence from the cortex was detected, and the white matter tended to emit further weaker fluorescence. **(D)** Observed under white LED illumination, the fluorescence from the cortex was enhanced, making the gradation of fluorescence intensity between the cortex and the white matter more distinct.

that can be used in two ways, not only for PD but also for PDT. Thus, TPS is a tool allowing us to carry out the best approach for malignant glioma. In fact, clinical studies of PDT using TPS have reported PFS of 12 months and OS of 24.8 months in patients with newly diagnosed glioblastoma, showing a clear therapeutic add-on effect to the standard treatment, and this method has been rapidly spreading in Japan (19).

In this article, we report that intraoperative PD using TPS and an excitation diode laser can identify gadolinium-enhanced lesions and non-gadolinium-enhanced lesions infiltrated by tumor cells, based on differences in fluorescence intensity, in glioma cases. In particular, a positive correlation was observed between the histological malignancy grade and the fluorescence positive rate or the fluorescence intensity. In particular, in Grade IV cases, strong fluorescence was observed in 93.3% of newly diagnosed cases and 61.5% of recurrent cases, and there were no cases without fluorescence. In recurrent cases, the fluorescence intensity tended to be weaker than that observed in newly diagnosed cases. The reason for this might be associated with the use of radiotherapy in these cases. Even in cases of lower grade gliomas, in which the detection of fluorescence with the use of 5-ALA is difficult, weak fluorescence was observed, although the number of cases was limited. These results suggest the usefulness of FGR using TPS in all glioma surgeries. Very strong fluorescence was observed in 1 case of pilocytic astrocytoma. In addition, strong fluorescence was observed also in cases of malignant lymphoma, metastases and malignant meningioma. These results suggest that FGR using TPS can be performed for tumors enhanced by gadolinium on MRI, regardless of histological type.

Tsurubuchi et al. (31) examined the intracerebral distribution of 5-ALA and TPS, using a glioma rat model, and reported that the lesion-to-normal brain ratio (L/N ratio) in the tumor bulk was 7.78 ± 4.61 at 2 h after administration of 5-ALA and 23.1 ± 11.9 at 12 h after administration of TPS, with the fluorescence intensity being approximately 10-fold stronger with TPS than with 5-ALA (31). On the other hand, both drugs elicited fluorescence even in vasogenic edema in a cold injury model for brain edema. With 5-ALA, the time to peak fluorescence after administration in edema was delayed compared with that in tumor. On the other hand, with TPS, the time to peak fluorescence was 2 h after administration in peritumoral edema and 12 h after administration in tumor tissue. This time course of the fluorescence intensity perfectly reflects the mechanism of TPS uptake by tumor cells, which is considered as follows: TPS, a water-soluble drug, is conjugated with albumin immediately after intravenous injection, and the conjugate circulates in the bloodstream. After leaking from tumor blood vessels due to the disruption of the blood brain barrier (BBB), the conjugate is taken up by tumor cells, mediated by SLC46A1, a heme carrier

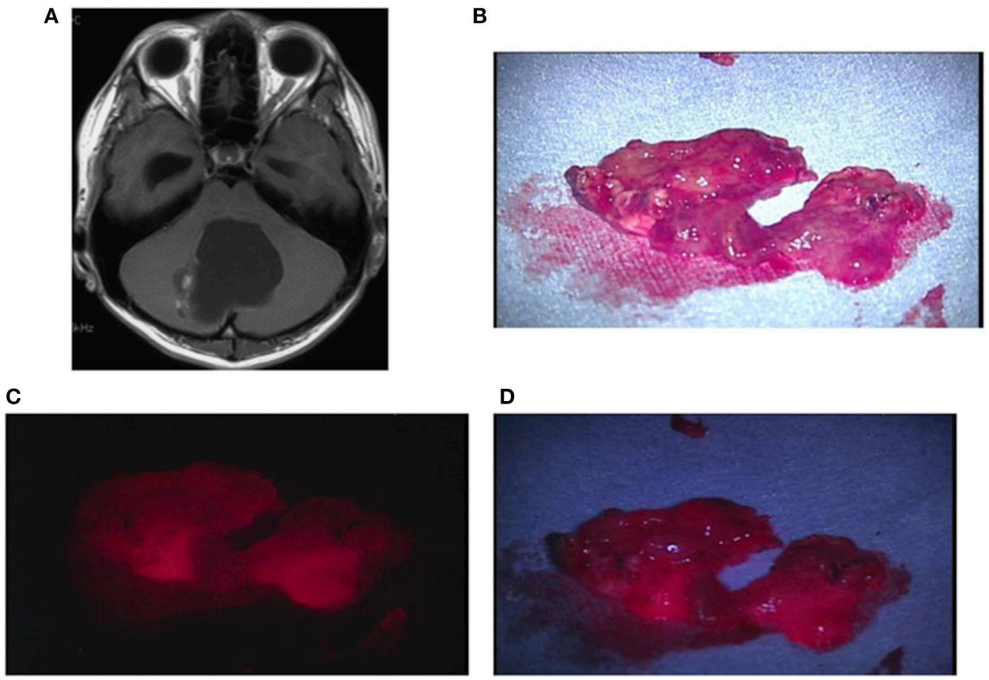

FIGURE 6 | Representative case 1. **(A)** A gadolinium-enhanced T1-weighted axial image showed a cystic tumor with a mural nodule in the vermis cerebelli, in which the nodule was slightly enhanced. **(B)** The resected nodule was rich in blood vessels, exhibiting red color also under halogen light illumination. **(C)** By laser irradiation, strong fluorescence from the nodule was observed. **(D)** Under white LED illumination, strong fluorescence emitted from the entire nodule was clearly observed.

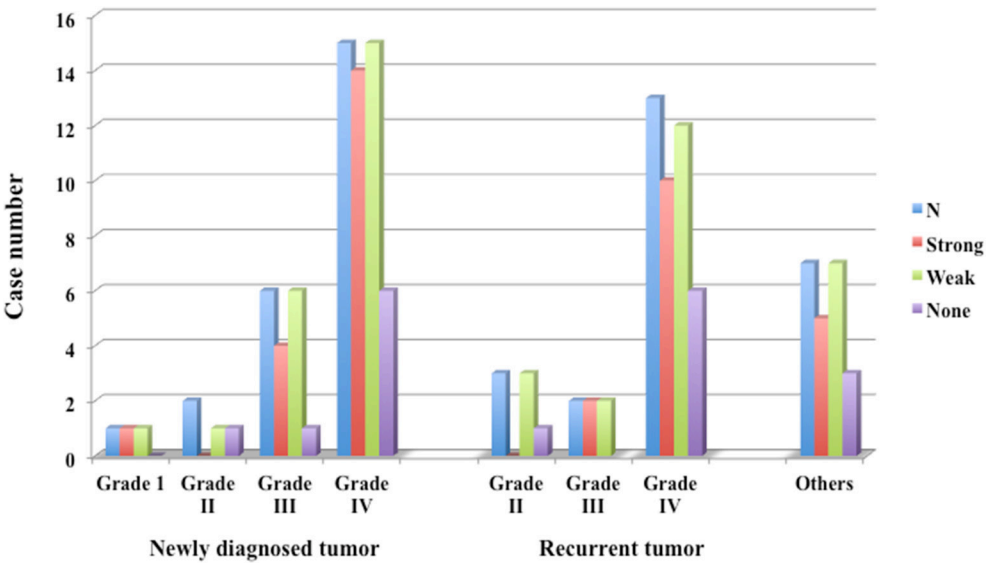

FIGURE 7 | Fluorescence positive rate of newly diagnosed glioma, recurrent glioma and other tumors. In Grade IV, 92.9% of newly diagnosed cases and 61.5% of recurrent cases emitted strong fluorescence.

protein 1, and other factors, and accumulates into the tumor cells due to the enhanced permeability and retention (EPR) effect (31, 32). Comparing the distribution of fluorescence intensity in resected tissues with the images in the clinical cases presented this time, it was confirmed that the gadolinium-enhanced lesions on MRI exhibited strong fluorescence, with high TPS concentrations in these tissues, suggesting that these findings reflect the TPS uptake by tumor cells. In addition, the findings highly suggest that the weak fluorescence in non-enhanced areas is derived from not only the TPS taken up by infiltrating tumor cells but

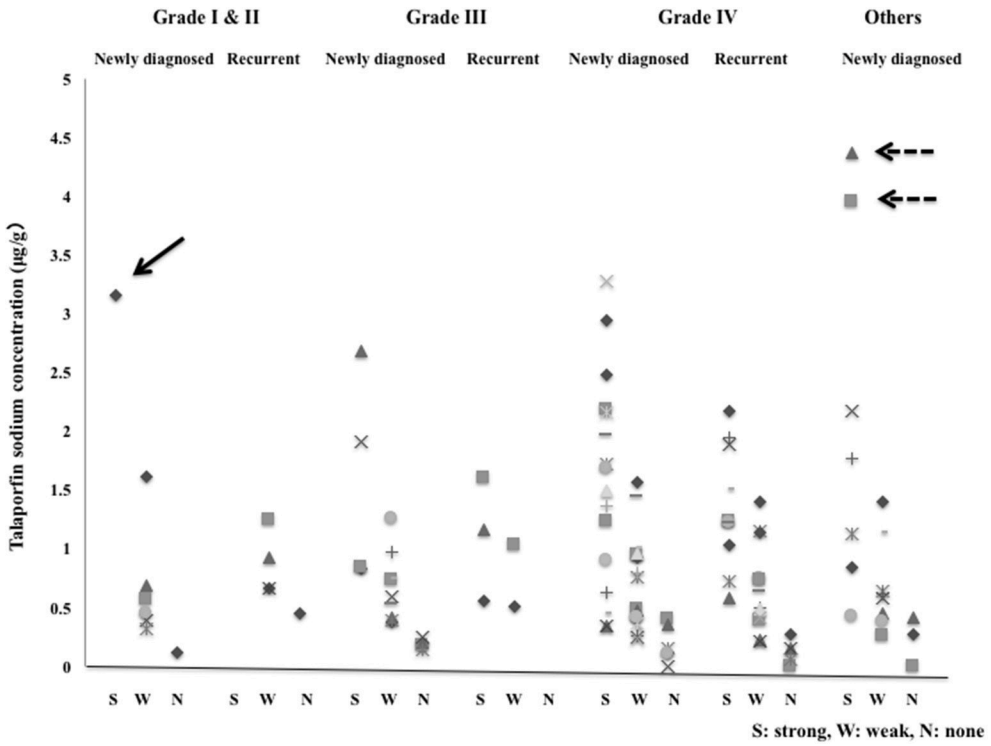

FIGURE 8 | The tissue concentrations of talaporfin sodium in the strong fluorescence (S), weak fluorescence (W) and no fluorescence (N) areas in newly diagnosed cases and recurrent cases with Grade I to IV gliomas and other tumors. Arrow: Pilocytic astrocytoma, Dotted arrow: Primary central nervous system lymphoma.

also the TPS diffused extracellularly. Also in the areas grossly assessed as showing no fluorescence, TPS, which is not present in normal brain tissue, was detected although its concentration was low. The TPS detected may have been trace amounts of TPS diffused outside the tumor cells or the TPS circulating in normal cerebral blood vessels. In addition, since peritumoral brain edema is found also in low-grade gliomas, in which the BBB is generally preserved, it is considered that, as the first step, TPS diffused into the edema fluid emits fluorescence after being taken up by the tumor cells. Particularly in oligodendrogliomas, which is associated with a large volume of the tumor vascular bed, the fluorescence observed may be derived from the TPS present in the tumor blood vessels. This inference is reasonable, because strong fluorescence with a high tissue concentration was observed in pilocytic astrocytoma, although only 1 case was examined.

The finding that the fluorescence intensity was dependent on the histological malignancy grade of glioma cells suggests that the fluorescence intensity of TPS reflects the tumor cell density, proliferative capacity or vascular bed volume, as seen in the studies of 5-ALA (33). Therefore, it is essential to examine the relationship of the fluorescene intensity of TPS with histopathological images in terms of these factors (34).

According to the drug information of TPS, the $t_{1/2\alpha}$ and $t_{1/2\beta}$ of TPS are 14.6 ± 2.96 and 138 ± 21.4 h, respectively (35). Experiments in rats revealed that the TPS concentration in cerebral tissue 24 h after administration of TPS at 40 mg/m^2 was one forty-fifth of the plasma concentration (4.56 ± 0.65 μg/g in plasma and 0.09 ± 0.01 μg/g in cerebral tissue). In humans receiving an intravenous injection of TPS at 40 mg/m^2, the plasma TPS concentration 24 h after administration was 11 μg/g. The TPS concentration in normal cerebral tissue 24 h after administration of TPS at 40 mg/m^2 is calculated to be 0.24 μg/g. On the other hand, the mean TPS concentration in no fluorescence areas measured by the methodology presented in this article was 0.21 μg/g. Since this measured value is very close to the calculated value, this method for measuring TPS concentrations is judged as appropriate.

By the FGR using TPS, total resection on imaging was achieved in 52.3% of glioma cases. Particularly in newly diagnosed cases, a clear difference in fluorescence among tumor areas was easily identified also under a microscope. As a result, total resection was achieved in 66.7% of the cases, and PDT was properly performed for tumors infiltrating in the functional regions in the brain. On the other hand, in the majority of recurrent cases, weak fluorescence appeared blurrily, and even though the resection was continued, the fluorescence persisted. The resection was extended to the boundary of the functional regions in the brain and then PDT was implemented in many cases. The reasons for this may include tumor vascular changes due to radiotherapy and

TABLE 1 | Pathological diagnosis and fluorescence positive rate, tissue TPS concentrations, extent of resection and number of patients who underwent PDT.

	N	Fluorescence			Concentration (μg/g)			Resection		PDT
		Strong	Weak	None	Strong	Weak	None	N of GTR	EOR	*N*
Newly diagnosed tumor	24									
Grade I	1	1	1	0	3.163	1.614		1	100%	0
Grade II	2	0	2	1		0.489 ± 0.145	0.123	1	95% (95–100)	0
Grade III	6	3	6	3	1.573 ± 0.901	0.608 ± 0.304	0.2	3	98% (90–100)	1
Grade IV	15	14	15	6	1.580 ± 0.908	0.675 ± 0.413	0.193 ± 0.156	11	98% (89–100)	4
Recurrent tumor	18									
Grade I	0									
Grade II	3	0	3	1		0.878 ± 0.276	0.46	1	92% (80–100)	1
Grade III	2	2	2	0	1.112 ± 0.529	0.776 ± 0.375		0	88% (80–95)	1
Grade IV	13	8	11	6	1.347 ± 0.524	0.656 ± 0.381	0.132 ± 0.156	5	88% (63–100)	9
Others										
Meta	2	1	2	1	0.851	0.520 ± 0.097		2	100%	0
PCNSL	1	1	1		4.166 ± 0.294	0.647		1	100%	0
MGM	1	1	1	1	1.657 ± 0.735	0.8382 ± 0.807	0.279	1	100%	0
Atypical MGM	1	1	1	1	1.103 ± 0.957	0.720 ± 0.390	0.424	0	75%	1

N, number; Meta, metastatic brain tumor; PCNSL, primary central nervous system lymphoma; MGM, meningioma; GTR, gross total removal; EOR, extent of resection; PDT, photodynamic therapy.

decreased proliferative capacity of recurrent tumors. In fact, TPS concentrations in tumors tended to be lower in recurrent cases than in newly diagnosed cases, although there was no significant difference. This issue also needs to be studied in future.

Yoshida et al. reported 0.36- to 5.69-fold higher TPS concentrations in cancer tissue than in normal tissue, measured 4 h after the administration of TPS at 40 mg/m^2 in 16 patients with early head and neck cancer (21). In addition, they stated, from their experience with PDT performed in these cases, that the TPS concentration in the irradiation target tissue needed to be at least 1 μg/g in order to demonstrate the efficacy of PDT (21). In the present study, the mean TPS concentration in tumor tissue 24 h after the administration of TPS in glioblastoma cases was 1.580 μg/g in strong fluorescence areas and 0.672 μg/g in weak fluorescence areas. The tissue TPS concentration in strong fluorescence areas was 7.52-fold higher than that in normal brain tissue. Although there are differences in the time after the administration of TPS to observation as well as in the PDT implementation conditions, these findings suggest that PDT may not have clinical significance in some cases because, unless the target tissue emits at least weak fluorescence, reactions to PDT are unlikely to occur. This needs to be kept in mind when considering the implementation of PDT after FGR in malignant glioma cases in the future.

There are several limitations to acknowledge in this study. First, since this case group was enrolled only for a certain period of time, it can not deny that there was a limit in the number of cases. In particular, as TPS is a photosensitizer that is used for PDT, which is generally only performed on patients who are suspected of having a malignant brain tumor on preoperative neuroimaging, there is little data on the use of TPS in brain tumors except glioma. Second, there was lack of investigation of relationship between histopathological findings and fluorescence intensity or TPS concentration. Such analysis is the focus of our ongoing study.

CONCLUSION

We examined the fluorescence emission from malignant brain tumors, using TPS, a second-generation photosensitizer, and an excitation laser specific to it, and demonstrated that TPS is applicable to FGR. In glioma cases, the fluorescence intensity and the TPS concentration in tumor tissue have been found to be correlated with the histological malignancy grade, and, particularly in newly diagnosed patients, have been suggested to contribute to improving the extent of resection. We will further investigate the relationship between histopathological images of brain tumors and the fluorescence intensity or tissue TPS concentration, in order to verify the usefulness of FGR using TPS in malignant brain tumor surgery.

AUTHOR CONTRIBUTIONS

MK and AM supervised the project. JA, SF, and MI developed the concept and the design of the study. JA and SF designed and made the experimental set up for data acquisition. JA, SF, and MI carried out patient care, surgery, and sample acquisition. JA performed data collection. JA, SF, MI, AM, and MK analyzed

and interpreted the data. JA drafted the manuscript. SF and MK critically revised the manuscript. AM was contributed to the review of the manuscript and answer to the reviewer's comment. All authors have approved the final manuscript.

ACKNOWLEDGMENTS

The authors are indebted to Associate Professor Edward F. Barroga and Akiko Popiel Helena, Department of International Medical Communications of Tokyo Medical University, for their review of the manuscript. The authors also thank Panasonic HealthCare Co. Ltd., Japan, Mitaka Kohki Co. Ltd., Japan and Meiji Seika Pharma Co. Ltd., Japan for supplies of equipments and drugs.

SUPPLEMENTARY MATERIAL

The Supplementary Material for this article can be found online at: https://www.frontiersin.org/articles/10.3389/fsurg.2019.00012/full#supplementary-material

Supplementary Table 1 | Clinical profile, intensity of emitted fluorescence and tissue concentration of TPS of all cases.

REFERENCES

1. Perria C, Capuzzo T, Cavagnaro G, Datti R, Francaviglia N, Rivano C, et al. First attempts at the photodynamic treatment of human gliomas. *J Neurosurg Sci*. (1980) 24:119–29.
2. Kaye AH, Morstyn G, Appuzo MJ. Photoradiation therapy and its potential in the management of neurological tumors. *J Neurosurg*. (1988) 69:1–14. doi: 10.3171/jns.1988.69.1.0001
3. Stylli SS, Kaye AH, MacGregor L, Howes M, Rajendra P. Photodynamic therapy of high grade glioma- long term survival. *J Clin Neurosci*. (2005) 12:389–98. doi: 10.1016/j.jocn.2005.01.006
4. Muller PJ, Wilson BC. Photodynamic therapy of brain tumor- a work in progress. *Laser Surg Med*. (2006) 38: 384–89. doi: 10.1002/lsm.20338
5. Eljamel MS. Brain photodiagnosis (PD), fluorescence guided resection (FGR) and photodynamic therapy (PDT): past, present and future. *Photodiagnosis Photodyn Ther*. (2008) 5:29–35. doi: 10.1016/j.pdpdt.2008.01.006
6. Nelson JS, Liaw LH, Orenstein A, Berns MW. Mechanism of tumor destruction following photodynamic therapy with hematoporphyrin derivative, chlorine, and phthalocyanine. *J Natl Cancer Inst*. (1988) 80:1599–605. doi: 10.1093/jnci/80.20.1599
7. Castano AP, Demidova TN, Hamblin MR. Mechanism in photodynamic therapy: part one – photosensitizers, photochemistry and cellular localization. *Photodiagnosis Photodyn Ther*. (2004) 1:279–93. doi: 10.1016/S1572-1000(05)00007-4
8. Stummer W, Stocker S, Wagner S, Stepp H, Fritsch C, Goetz C, et al. Intraoperative detection of malignant gliomas by 5-aminolevulinic acid-induced prophyrin fluorescence. *Neurosurgery*. (1988) 42:518–26.
9. Stummer W, Novotny A, Stepp H, Goetz C, Bise K, Reulen HJ. Fluorescence-guided resection of glioblastoma multiforme by using 5-aminolevulinic acid-induced porphyrins: a prospective study in 52 consecutive patients. *J Neurosurg*. (2000) 93:1003–13. doi: 10.3171/jns.2000.93.6.1003
10. Stummer W, Pichlmeier U, Meinel T, Wiestler OD, Zanella F, Reulen HJ. Fluorescence-guided surgery with 5-aminolevulinic acid for resection of malignant glioma: a randomised controlled multicentre phase III trial. *Lancet Oncol*. (2006) 7:392–401. doi: 10.1016/S1470-2045(06)70665-9
11. Widhalm G, Wolfsberger S, Minchev G, Woeher A, Krssak M, Czech T, et al. 5-Aminolevulinic acid is a promising marker for detection of anaplastic foci in diffusely infiltrating gliomas with non-significant contrast enhancement. *Cancer*. (2010) 116:1545–52. doi: 10.1002/cncr.24903
12. Valdes PA, Leblond F, Kim A, Harris BT, Wilson BC, Fan X, et al. Quantitative fluorescence in intracranial tumor: implications for ALA-induced PpIX as an intraoperative biomarker. *J Neurosurg*. (2011) 115:11–17. doi: 10.3171/2011.2.JNS101451
13. Kennedy JC, Pottier RH. Endogeneous protoporphyrin IX, a clinically useful photosensitizer for photodynamic therapy. *J Photochem Photobiol B*. (1992) 14:275–92. doi: 10.1016/1011-1344(92)85108-7
14. Roberts DW, Valdes PA, Harris BT, Fontaine KM, Hartov A, Fan X, et al. Coregistered fluorescence-enhanced tumor resection of malignant glioma: relationship between δ-amino-levulinic acid-induced protoporphyrin IX fluorescence, magnetic resonance imaging enhancement, and neuropathological parameters. *J Neurosurg*. (2011) 114:595–603. doi: 10.3171/2010.2.JNS091322
15. Tsutsumi M, Miki Y, Akimoto J, Haraoka J, Aizawa K, Hirano M, et al. Photodynamic therapy with talaporfin sodium induces dose-dependent apoptotic cell death in human glioma cell lines. *Photodiagnosis Photodyn Ther*. (2013) 10:103–10. doi: 10.1016/j.pdpdt.2012.08.002
16. Matsumura H, Akimoto J, Haraoka J, Aizawa K. Uptake and retention of the mono-L-asparthyl chlorine e6 in experimental glioma. *Lasers Med Sci*. (2008) 23:237–45. doi: 10.1007/s10103-007-0469-3
17. Namatame H, Akimoto J, Matsumura H, Haraoka J, Aizawa K. Photodynamic therapy of C6-implanted glioma cells in the rat brain employing second-generation photosensitizer Talaporfin sodium. *Photodiagnosis Photodyn Ther*. (2008) 5:198–209. doi: 10.1016/j.pdpdt.2008.08.001
18. Akimoto J, Haraoka J, Aizawa K. Preliminary clinical report of safety and efficacy of photodynamic therapy using Talaporfin sodium for malignant gliomas. *Photodiagnosis Photodyn Ther*. (2012) 9:91–99. doi: 10.1016/j.pdpdt.2012.01.001
19. Muragaki Y, Akimoto J, Maruyama T, Iseki H, Ikuta S, Nitta M, et al. Phase II clinical study on intraoperative photodynamic therapy with talaporfin sodium and semiconductor laser in patients with malignant brain tumors. *J Neurosurg*. (2013) 119:845–52. doi: 10.3171/2013.7.JNS13415
20. Usuda J, Tsutsui H, Honda H, Ichinose S, Ishizumi T, Hirata T, et al. (2007) Photodynamic therapy for lung cancers based on novel photodynamic diagnosis using talaporfin sodium (NPe6) and autofluorescence bronchoscopy. *Lung Cancer*. 58:317–23. doi: 10.1016/j.lungcan.2007.06.026
21. Yoshida T, Tokashiki R, Ito H, Shimizu A, Nakamura K, Hiramatsu H, et al. Therapeutic effects of a new photosensitizer for photodynamic therapy of early head and neck cancer in relation to tissue concentration. *Auris Nasus Larynx*. (2008) 35:545–51. doi: 10.1016/j.anl.2007.10.008
22. Sanai N, Polley MY, McDermott MW, Parsa AT, Berger MS. An extent of resection threshold for newly diagnosed glioblastomas. *J Neurosurg*. (2011) 115:3–8. doi: 10.3171/2011.2.JNS10998
23. Chen L, Mao Y. Gross total resection plays a leading role in survival of patients with glioblastoma multiforme. *World Neurosurg*. (2014) 82:105–7. doi: 10.1016/j.wneu.2014.04.074
24. Grabowski MM, Recinos PF, Nowacki AS, Schroeder JL, Angelov L, Barnett GH, et al. Residual tumor volume versus extent of resection: predictors of survival after surgery of glioblastoma. *J Neurosurg*. (2014) 121:1115–23. doi: 10.3171/2014.7.JNS132449
25. Schwake M, Stummer W, Suero Molina EJ, Wolfeer J. Simultaneous fluorescein sodium and 5-ALA in fluorescence-guided glioma surgery. *Acta Neurochir*. (2015) 157:877–79. doi: 10.1007/s00701-015-2401-0
26. Liu JTC, Meza D, Sanai N. Trends in fluorescence image-guided surgery for gliomas. *Neurosurgery*. (2014) 75:61–71. doi: 10.1227/NEU.0000000000000344
27. Zimmermann A, Ritsch-Marte M, Kostron H. mTHPC-mediated photodynamic diagnosis of malignant brain tumors. *Photochem Photobiol*. (2001) 74:611–16. doi: 10.1562/0031-8655(2001)074<0611:MMPDOM>2.0.CO;2
28. Wilson CB. Glioblastoma: the past, the present, and the future. *Clin Neurosurg*. (1992) 38:32–48.
29. Yordanova YN, Moritz SG, Duffau H. Awake surgery for WHO II gliomas within "noneloquent" areas in the left dominant hemisphere: toward a "supratotal" resection. *J Neurosurg*. (2011) 115:232–39. doi: 10.3171/2011.3.JNS101333

30. Li YM, Suki D, Hess K, Sawaya R. The influence of maximum safe resection of glioblastoma on survival in 1229 patients: can we do better than gross-total resection? *J Neurosurg*. (2016) 124:977–988. doi: 10.3171/2015.5.JNS142087
31. Tsurubuchi T, Zoboronok A, Yamamoto T, Nakai K, Yoshida F, Shirakawa M, et al. The optimization of fluorescence imaging of brain tumor tissue differentiated from brain edema- *In vivo* kinetic study of 5-aminolevulinic acid and talaporfin sodium. *Photodiagnosis Photodyn Ther*. (2009) 6:19–27. doi: 10.1016/j.pdpdt.2009.03.005
32. Takada T, Tamura M, Yamamoto T, Matsui H, Matsumura A. Selective accumulation of hematoporphyrin deriveative in glioma through proton-coupled folate transporter SLC46A1. *J Clin Biochem Nutr*. (2014) 54:26–30. doi: 10.3164/jcbn.13-87
33. Stummer W, Tonn JC, Goetz C, Ullrich W, Stepp H, Bink A, et al. 5-Aminolevulinic acid-derived tumor fluorescence: the diagnostic accuracy of visible fluorescence qualities as corroborated by spectrum and histology and postoperative imaging. *Neurosurgery*. (2014) 74:310–9. doi: 10.1227/NEU.0000000000000267
34. Mitra S, Foster TH. *In vivo* confocal fluorescence imaging of the intratumor distribution of the photosensitizer mono-L-aspartylchlorin-e6. *Neoplasia*. (2008) 10:429–38. doi: 10.1593/neo.08104
35. Kessel D. Pharmacokinetics of N-asparthyl chlorin e6 in cancer patients. *J Photochem Photobiol B*. (1997) 39:81–3. doi: 10.1016/S1011-1344(96)00009-7

Conflict of Interest Statement: The authors declare that the research was conducted in the absence of any commercial or financial relationships that could be construed as a potential conflict of interest.

frontiers in Oncology

ORIGINAL RESEARCH
published: 02 April 2019
doi: 10.3389/fonc.2019.00201

Cross-Polarization Optical Coherence Tomography for Brain Tumor Imaging

Konstantin S. Yashin[1], Elena B. Kiseleva[2], Ekaterina V. Gubarkova[2], Alexander A. Moiseev[3], Sergey S. Kuznetsov[4], Pavel A. Shilyagin[3], Grigory V. Gelikonov[3], Igor A. Medyanik[1], Leonid Ya. Kravets[1], Alexander A. Potapov[5], Elena V. Zagaynova[6] and Natalia D. Gladkova[2]*

[1] Microneurosurgery Group, University Clinic, Privolzhsky Research Medical University, Nizhny Novgorod, Russia, [2] Laboratory of Optical Coherence Tomography, Research Institute of Experimental Oncology and Biomedical Technologies, Privolzhsky Research Medical University, Nizhny Novgorod, Russia, [3] Laboratory of High-Sensitivity Optical Measurements, Institute of Applied Physics, Russian Academy of Sciences, Nizhny Novgorod, Russia, [4] Department of Anatomical Pathology, Privolzhsky Research Medical University, Nizhny Novgorod, Russia, [5] Federal State Autonomous Institution "N.N. Burdenko National Scientific and Practical Center for Neurosurgery" of the Ministry of Healthcare of the Russian Federation, Moscow, Russia, [6] Research Institute of Experimental Oncology and Biomedical Technologies, Privolzhsky Research Medical University, Nizhny Novgorod, Russia

OPEN ACCESS

Edited by:
Mark Preul, Barrow Neurological Institute (BNI), United States

Reviewed by:
Eberval Figueiredo, University of São Paulo, Brazil
Gregory Punisa Lekovic, House Ear Institute, United States
Wolfgang Klemens Pfisterer, Medical University of Vienna, Austria

***Correspondence:**
Konstantin S. Yashin
jashinmed@gmail.com

Specialty section:
This article was submitted to Cancer Imaging and Image-directed Interventions, a section of the journal Frontiers in Oncology

Received: *03 December 2018*
Accepted: *11 March 2019*
Published: *02 April 2019*

Citation:
Yashin KS, Kiseleva EB, Gubarkova EV, Moiseev AA, Kuznetsov SS, Shilyagin PA, Gelikonov GV, Medyanik IA, Kravets LY, Potapov AA, Zagaynova EV and Gladkova ND (2019) Cross-Polarization Optical Coherence Tomography for Brain Tumor Imaging. Front. Oncol. 9:201. doi: 10.3389/fonc.2019.00201

This paper considers valuable visual assessment criteria for distinguishing between tumorous and non-tumorous tissues, intraoperatively, using cross-polarization OCT (CP OCT)—OCT with a functional extension, that enables detection of the polarization properties of the tissues in addition to their conventional light scattering.

Materials and Methods: The study was performed on 176 *ex vivo* human specimens obtained from 30 glioma patients. To measure the degree to which the typical parameters of CP OCT images can be matched to the actual histology, 100 images of tumors and white matter were selected for visual analysis to be undertaken by three "single-blinded" investigators. An evaluation of the inter-rater reliability between the investigators was performed. Application of the identified visual CP OCT criteria for intraoperative use was performed during brain tumor resection in 17 patients.

Results: The CP OCT image parameters that can typically be used for visual assessment were separated: (1) signal intensity; (2) homogeneity of intensity; (3) attenuation rate; (4) uniformity of attenuation. The degree of match between the CP OCT images and the histology of the specimens was significant for the parameters "signal intensity" in both polarizations, and "homogeneity of intensity" as well as the "uniformity of attenuation" in co-polarization. A test based on the identified criteria showed a diagnostic accuracy of 87–88%. Intraoperative *in vivo* CP OCT images of white matter and tumors have similar signals to *ex vivo* ones, whereas the cortex *in vivo* is characterized by indicative vertical striations arising from the "shadows" of the blood vessels; these are not seen in *ex vivo* images or in the case of tumor invasion.

Conclusion: Visual assessment of CP OCT images enables tumorous and non-tumorous tissues to be distinguished. The most powerful aspect of CP OCT images that can be used as a criterion for differentiation between tumorous tissue and white

matter is the signal intensity. In distinguishing white matter from tumors the diagnostic accuracy using the identified visual CP OCT criteria was 87–88%. As the CP OCT data is easily associated with intraoperative neurophysiological and neuronavigation findings this can provide valuable complementary information for the neurosurgeon tumor resection.

Keywords: cross-polarization optical coherence tomography (CP OCT), malignant brain tumors, glioblastoma, intraoperative imaging, imaging assessment

INTRODUCTION

Optical coherence tomography (OCT) is a label-free, real-time imaging technique that allows three-dimensional images of biological tissues to be obtained at high resolution (around 2 μm). OCT is similar to ultrasonic imaging, in that both techniques detect reflected waves (light or acoustic). However, OCT uses a near-infrared light source (in the 700–1,300 nm wavelength range). OCT is a promising method for intraoperative guidance during the resection of glial tumors (astrocytomas) (1–3).

Recently, OCT has been proposed for intraoperative use in distinguishing tumorous and non-tumorous tissues using handled probes (4, 5) or microscope-integrated OCT systems (6, 7). OCT can provide differentiation between tumorous and non-tumorous tissues through both quantitative (4, 8) and qualitative (9, 10) assessment of the OCT signals. However, although visual assessment of the OCT data provided by clinically approved systems seems to be less sensitive when compared with the calculation of optical coefficients (which is not approved for clinical use), it is more user-friendly and intelligible. Meanwhile, for the intraoperative application of OCT it is necessary clearly to define the visual assessment criteria required for the OCT images in order to provide precise differentiation between glioma tissue and white matter.

Conventional, intensity-based OCT has demonstrated impressive results in detecting pathological changes in stratified tissues, such as those in the eye. However, the advanced visualization of structureless tissue types (brain, breast) needs novel contrast mechanisms such as can be achieved by using a so-called functional extension of OCT—polarization-sensitive (PS) OCT (11). PS OCT can detect the polarization state changes of the probing light in the tissue and, by means of this, generate tissue-specific contrast (11, 12). Based on the birefringence of the tissue structure, PS OCT provides better visualization of elongated structures and therefore provides advanced imaging of myelinated nerve fibers in nerves and the brain (13, 14), even showing the orientation of white matter tracts (15, 16). Cross-polarization OCT (CP OCT) is a variant of PS OCT that allows imaging of the initial polarization state changes both due to birefringence and cross-scattering in biological tissues (17, 18). In CP OCT two co-registered images are recorded: parallel (conventional OCT image or image in co-polarization) and orthogonal (image in cross-polarization) that detects tissue reflections with polarization state orthogonal to the incident one. Only orthogonally polarized backscattered light which is mutually coherent with the incident is contributing to the cross-polarized OCT image. The origin of such "coherent backscattering" includes random polarization during light propagation in the media, depolarization during the backscattering process, and "regular" polarization changes associated with propagation back and forth in birefringent media (19).

Some studies have demonstrated that tumorous tissue and white matter can be differentiated by visual assessment of such OCT images (8–10). This paper presents criteria based on the results of the CP OCT study of *ex vivo* specimens of human brain samples (20), compared with *in vivo* CP OCT images collected during brain tumor resections.

MATERIALS AND METHODS

This translational research was aimed to discover the CP OCT visual criteria for distinguishing timorous and non-tumorous tissue during surgical removal of a glioma. The study consists of two consecutive stages. During first part the *ex vivo* CP OCT analysis of brain human biopsy specimens matched to the actual histology was performed. Based on this data the visual criteria for distinguishing white matter and timorous tissue was discovered. The task of the second stage of the study was to develop the method of intraoperative using of the CP OCT and to confirm the discovered criteria during glioma removal.

Patients

Ex vivo Study on Human Brain Specimens

The *ex vivo* study was performed on material from human brain specimens that had been obtained during tumor resection from 30 patients with gliomas of differing degrees of malignancy: astrocytoma Grades I-II ($n = 8$), astrocytoma Grade III ($n = 7$), and glioblastoma Grade IV ($n = 15$) (**Figure 1A**). The tumor resections were performed taking into account eloquent brain areas and white matter tracts using a frameless navigation system with uploaded functional MRI data and intraoperative neurophysiological monitoring (also "awake" surgery). The surrounding tumor white matter in the peritumoral area that was routinely subjected to coagulation was accurately marked and removed. Samples were taken from different parts of each tumor.

The removed specimens were immediately placed in Petri dishes and closed to prevent dehydration. Tissues also were kept on ice until transfer to the imaging stage. Before OCT imaging, the tissue surface was cut to create a flat fresh surface of the sample. The CP OCT study of each sample was no longer than 30 min (including tissue preparation). In total, 176 samples of

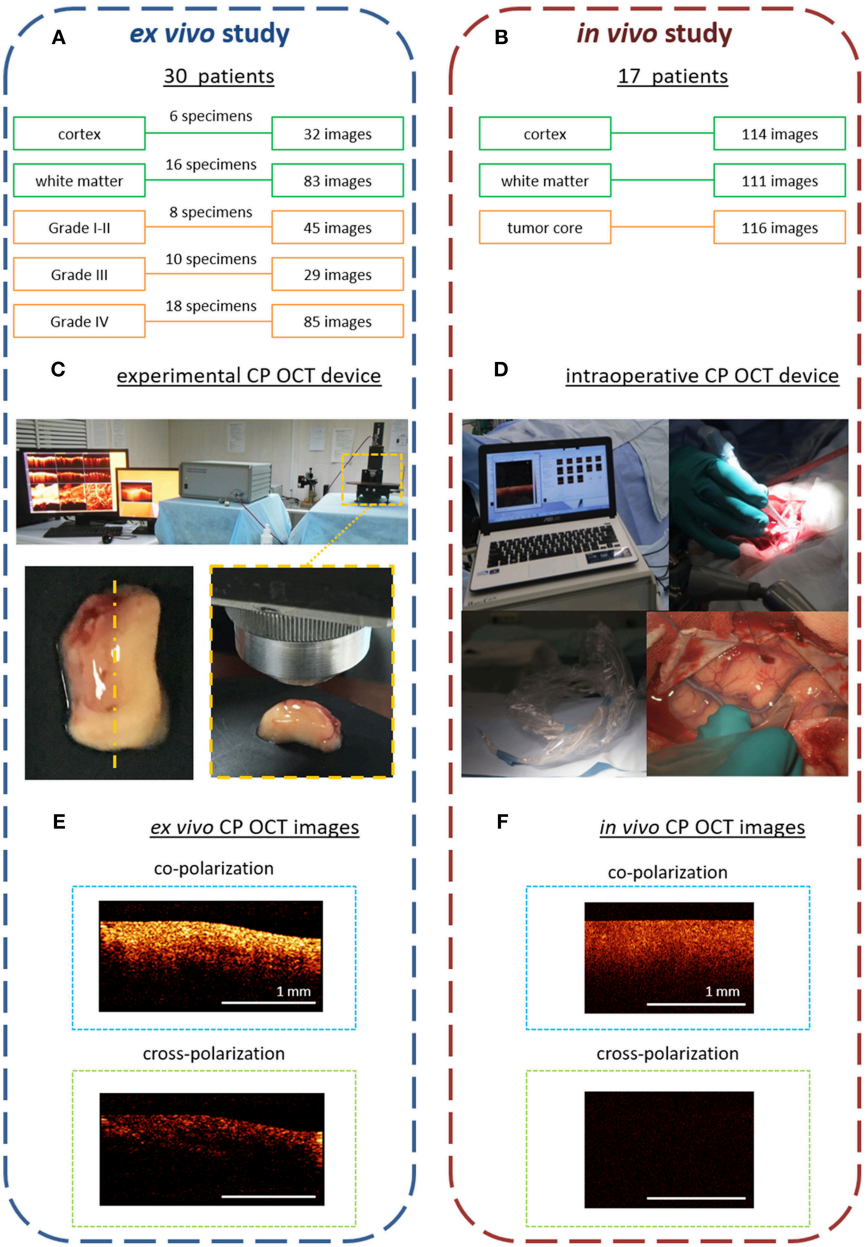

FIGURE 1 | Design of the *ex vivo* and *in vivo* CP OCT study: **(A)** the *ex vivo* study was performed on material from operative biopsies: 30 patients with gliomas of different grades of malignancy; in total 274 *ex vivo* images were analyzed; **(B)** the *in vivo* study was performed on 17 patients with different grades of malignant brain tumors; in total 341 *in vivo* images were analyzed; **(C)** working area for CP OCT scanning with the experimental CP OCT device and on-mount optical probe; specimen with schematic marking of the scanning area along the central line (yellow dotted line); **(D)** CP OCT device approved for clinical use, with a handled OCT probe in a sterile cover; **(F)** *in vivo*, and **(E)** *ex vivo* CP OCT images in co- and cross-polarizations. The signal in cross-polarized image is orthogonally polarized backscattered light, which is mutually coherent with the incident one and can appear if the tissue has anisotropic structures such as myelinated fibers.

different tissue types were studied and 274 *ex vivo* images were obtained. After surgery, any worsening in neurologic state of patients was not recorded.

Intraoperative Study

Here, *in vivo* CP OCT images were collected during tumor resections in 17 patients with different malignant brain tumors: astrocytoma Grades I-II ($n = 5$), astrocytoma Grade III ($n = 9$), glioblastoma Grade IV ($n = 2$), breast cancer metastasis ($n = 1$). During the tumor resections the *in vivo* OCT images were collected using an approved CP OCT device with a handled probe enclosed in a sterile cover. In total, 341 images of three areas of interest were analyzed: cortex−114, white matter−111, tumor core−116 (**Figure 1B**).

This study was carried out in accordance with the recommendations of the World Medical Association's

Declaration of Helsinki. The protocol was approved by the Ethical Committee of the Privolzhskiy Federal Research Medical Center of the Ministry of Health of the Russian Federation. All subjects gave written informed consent in accordance with the Declaration of Helsinki. All studies were performed in accordance with the relevant guidelines and regulations.

Cross-Polarization OCT Devices

The *ex vivo* studies were performed with an multimodal OCT device with cross-polarization detection developed by the Institute of Applied Physics of the Russian Academy of Sciences (Nizhny Novgorod, Russia) (21, 22). The device operates at a central wavelength of 1.3 μm providing axial and lateral resolutions, in air, of 10 and 15 μm, respectively. The probing beam uses circular polarization. The device has a scanning rate of 20,000 A-scans/s and performs 2D lateral scanning within a range of 2.4 × 2.4 mm^2 to obtain the 3D distribution of backscattered light in polarizations parallel and orthogonal to the polarization of the probing beam. Thus, the resulting CP OCT image includes an upper part—co-polarization image and a lower part—cross-polarization image. Scanning was performed in contactless mode (**Figure 1C**).

For *in vivo* study, time-domain "Polarization-sensitive optical coherence tomograph OCT-1300U" (BioMedTech LLC, Nizhny Novgorod, Russia) was used (**Figure 1D**). It is approved for clinical use (product license №FCP 2012/13479 from 30 May 2012) has the same characteristics of laser radiation as the experimental CP OCT device. However, its image data-processing system is not as effective, so the intensity of the intraoperative images in co- and cross-polarization is lower (∼4 times) (**Figure 1F**) compared to those obtained using the experimental CP OCT device (**Figure 1E**).

Histological Study

After imaging the scanning area on the specimen was marked with histological ink, then the specimen was fixed in 10% formalin for 48 h and re-sectioned through the marked area, so that the plane of the histological sections coincided to en-face the CP OCT images. For the histological evaluation, hematoxylin and eosin staining was used. Two histopathologists independently evaluated the histological slides, with their diagnoses coinciding in 98% of cases.

Visual Assessment of CP OCT Images

Based on an initial analysis of the *ex vivo* CP OCT images of the white matter and tumors the parameters of the CP OCT signal for further analysis were selected. The differential criteria for CP OCT images must satisfy the following conditions:

- Simplicity and high speed of evaluation (the signal indicator(s) should be as simple as possible in use, and easy for the operating surgeon to remember);
- Be informative (reflect the histological morphology of the tissue);
- Have a high degree of inter-expert reliability (i.e., not resulting in significant disagreements in interpretation).

Visual assessment of the CP OCT images was performed using two special tests containing a training set and a proper test of 100 images (26 images of white matter and 74 images of tumorous tissue: Grade II−12, Grade III−22, Grade IV−40). The CP OCT images selected for these tests corresponded to specimens with typical histological structures of the tumor and white matter (cropped and damaged images, and images that, according to the histological samples contained large necrotic or hematoma areas were excluded). The first test, aimed at identifying the most useful CP OCT criteria, contained OCT images separately in co- and cross-polarization; the second test, aimed at determining the diagnostic accuracy of distinguishing tumor and white matter, contained OCT images separately in co- and cross-polarization, and simultaneously in both polarizations. Each test was performed by three "blinded" investigators.

In the first test, the visual assessment of the CP OCT image was performed on the basis of the following parameters (**Figure 2**) each with only two possible alternatives, which were selected to satisfy the condition of simplicity and high speed of evaluation (the indicator should be as simple as possible in use, and easy to remember by the operating surgeon):

(1) The signal intensity ("intense"/"non-intense")—the average level of the OCT signal throughout the image.
(2) The homogeneity of intensity ("homogeneous"/"heterogeneous")—the lack of variability of the brightness of the OCT signal.
(3) The attenuation rate ("high"/"low") as estimated by the penetration depth of the probing radiation;
(4) The uniformity of attenuation ("uniform"/"non-uniform")—the uniformity of the OCT signal attenuation along the inferior border of the structural OCT image.

The extent to which the parameters were "informative" was identified based on measuring the degree of association of each visual parameter with the results of the histology during visual assessment by the three "blinded" investigators, between whom the degree of inter-expert reliability was also identified.

The second test was also performed by three "blinded" investigators (neurosurgeons) and was based on the main and additional visual criteria identified during the first test. There were two possible answers: "tumor"/"white matter" (**Figure 3**). The inter-rater reliability between the investigators was also recorded.

Statistical Analysis

The statistical analysis was performed using Statistica 10.0, IBM SPSS Statistics 20. For evaluation of the association ratio of the coefficients Q (Yule) and φ (phi) were used, with a statistically significant value for $Q \geq 0.5$ and for $\varphi > 0.3$. The inter-rater reliability between investigators was registered using the Fleiss' kappa (κ) and Krippendorff's alpha (α) coefficients: $\kappa\ (\alpha) \geq 0.8$—perfect agreement; $0.7 \leq \kappa\ (\alpha) < 0.8$—substantial agreement; $\kappa\ (\alpha) < 0.7$—poor agreement. For the second test the diagnostic test parameters (sensitivity, specificity and accuracy) were calculated.

Intraoperative Application of the CP OCT

There was no histopathological evaluation of the *in vivo* CP OCT images, for error prevention and checking of complementarity between the OCT image and tissue type, the scanning being performed in areas with no doubt about their histology (white

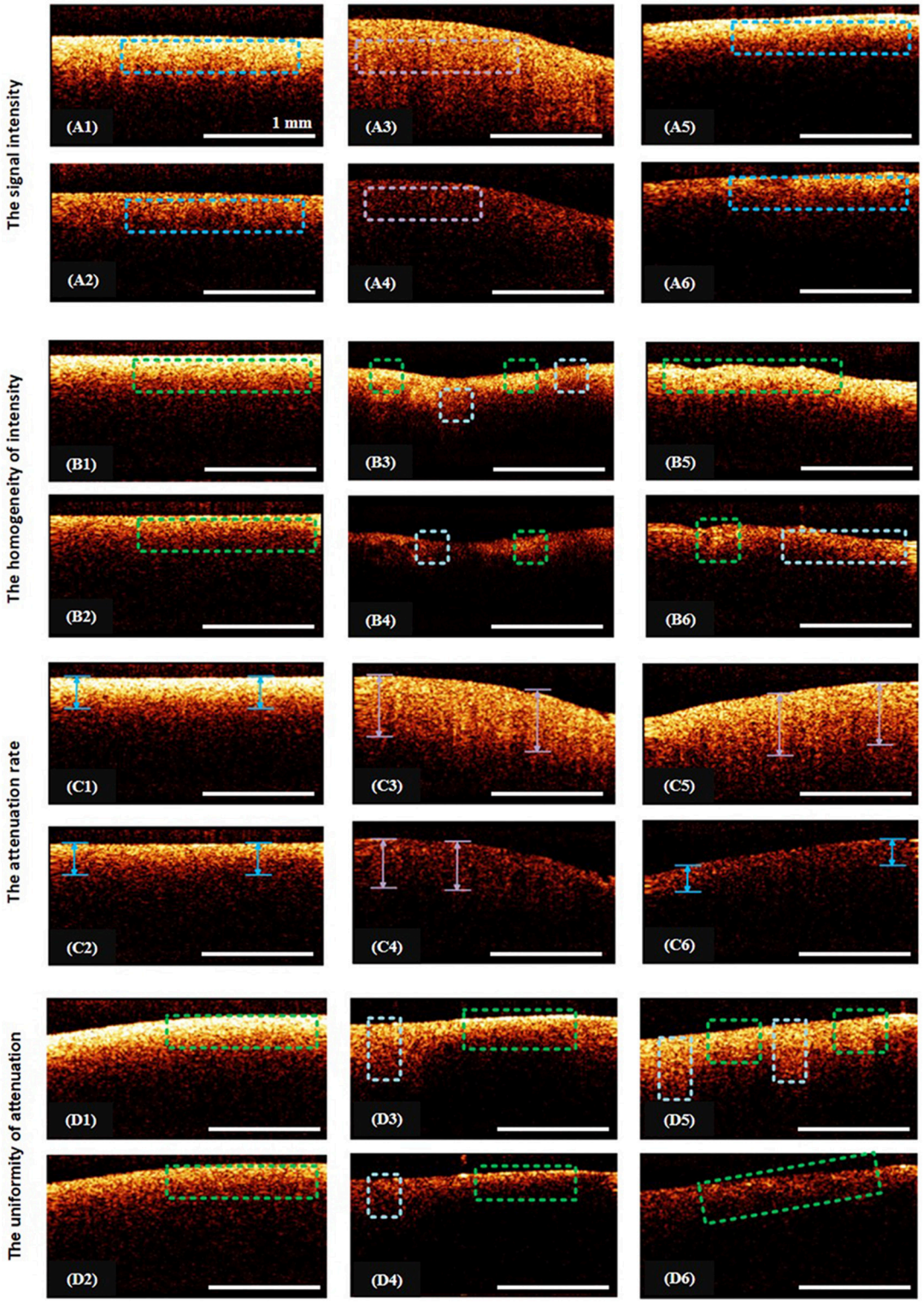

FIGURE 2 | Illustration from the training set of CP OCT images: **(A1–A6)**, **(B1–B6)**, **(C1–C6)**, **(D1–D6)** show examples of the assignment of certain characteristic to the CP OCT signal; **(A1–A6)**—intense signals are marked with blue rectangles, violet—a low-intensity signal; **(B1,B2)**—the regions of homogeneous signals are indicated by green rectangles; **(B3–B6)**—green areas and pale blue squares indicate areas of different intensities; **(C1–C6)**—blue arrows denote regions with high rates of signal attenuation, violet—with low signal attenuation rates; **(D1,D2,D6)**—the green rectangles indicate areas with uniform attenuation of the signal; **(D3–D5)**—rectangles of pale blue and green color indicate regions with different signal attenuation rates.

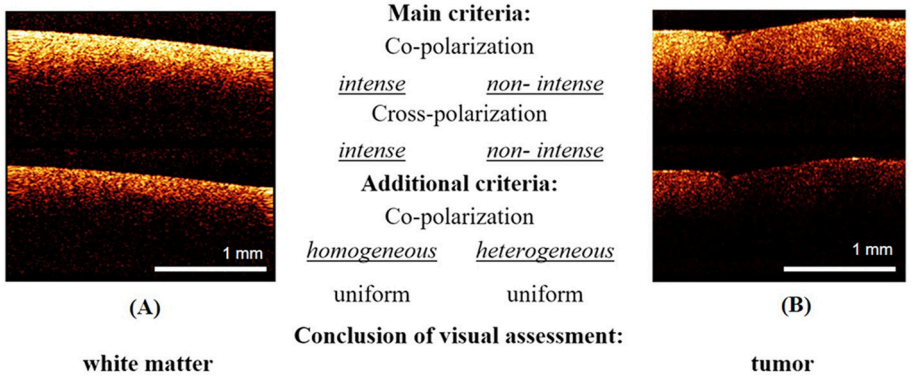

FIGURE 3 | Examples of images from the training set for the second test: **(A)**—white matter, **(B)**—tumor. The responder identifies tissue type using main criteria: white matter is characterized by high intense signal in co- and cross-polarization unlike low intensity signal of tumorous tissue. In the doubtful case, the additional criteria can be used.

matter and cortex far from the tumor mass, and of regions within the tumor core) using image guiding under a neuronavigation system and high magnification of surgical microscope. The *in vivo* CP OCT data were compared with the *ex vivo* set and also combined with surgical microscope view, the preoperative MRI and neuronavigation data, intraoperative neurophysiological and neuronavigation findings.

RESULTS

Ex vivo CP OCT Images of White Matter and Tumorous Tissue

The CP OCT signal of the *ex vivo* specimens is more intense and has a higher attenuation rate (in both the initial and orthogonal polarizations) than those obtained *in vivo*. However, previous comparative analysis of the optical properties of white matter and tumorous tissues has demonstrated that the CP OCT images obtained *ex vivo* show full qualitative similarity to the *in vivo* CP OCT images (23). For the cortex there are also structural differences between the *ex vivo* and *in vivo* images (23). In the *in vivo* studies, the CP OCT images show a specific vertical striation arising from "shadows" of the blood vessels located just under the tissue surface (**Figure 5A1**); this striation is practically invisible on the *ex vivo* images due to vasoconstriction.

White Matter

CP OCY analysis of *ex vivo* specimens showed that the white matter on the CP OCT images in co- and cross-polarizations (**Figures 4A2,B2**) presented by a narrow stripe of high intensity OCT signal. Histologically, the white matter is represented by a regular and dense arrangement of myelinated fibers (**Figure 4C1**) and therefore is characterized by high scattering properties. This explains the presence of a high-intensity homogeneous but rapidly decaying OCT signal in both co- and cross-polarization.

Gliomas

In gliomas the tissue elements are discohesive and disordered (**Figures 4C2–C4**); although there are a few elements with high-scattering properties (**Figure 4C5**). Therefore, the CP OCT images of tumorous tissue are characterized by low signal intensities in co- (**Figures 4A2–A5**) and cross-polarizations (**Figures 4B2–B5**). Grades I-III astrocytomas on the CP OCT images are represented by low intensity and slowly attenuating signals (**Figures 4A2–A4,B2–B4**), however the signal may be homogeneous (**Figures 4A2,A4,B2,B4**) or heterogeneous in the presence of cysts, calcification, and hemorrhaging (**Figures 4A3,B3**). The CP OCT signal of a glioblastoma is of low intensity, and heterogeneous with tessellated areas of high intensity (**Figures 4A5,B5**) corresponding to areas of high cell density, necrosis or hemorrhaging (**Figure 4C5**). The attenuation rate of the CP OCT signal may be high or low with the attenuation along the inferior border of the image being uniform or non-uniform.

The initial comparative analysis of CP OCT images of brain specimens with typical histological structures has demonstrated the capability of OCT to differentiate between white matter and tumorous tissue. However, there are no clear criteria for distinguishing between white matter and tumorous tissue due to the variability of the signal characteristics of the gliomas. Therefore, it is also evident that OCT cannot be used for the intraoperative grading of gliomas.

Visual Assessment Criteria for CP OCT Images for Distinguishing Between White Matter and Gliomal Tissue

Between all investigators the values of the coefficients Q and φ were high for the parameter "signal intensity" in co- and cross-polarization (Qco = 0.91–0.92; φco = 0.64–0.65; Qcross = 0.92–0.94; φcross = 0.64–0.70) and also statistically significant for the parameters "the homogeneity of intensity" (Qco = 0.86–0.94; φco = 0.47–0.50) and "the uniformity of attenuation" (Qco = 0.58–0.82; φco = 0.30–0.44) in co-polarization. The inter-rater reliability between investigators was perfect for the parameter "signal intensity" in both polarizations ($\kappa = 0.90$; $\alpha = 0.90$) and substantial for "the homogeneity of intensity" ($\kappa = 0.79$; $\alpha = 0.79$) and "the uniformity of attenuation" ($\kappa = 0.75$; $\alpha = 0.75$) in co-polarization (**Table 1**).

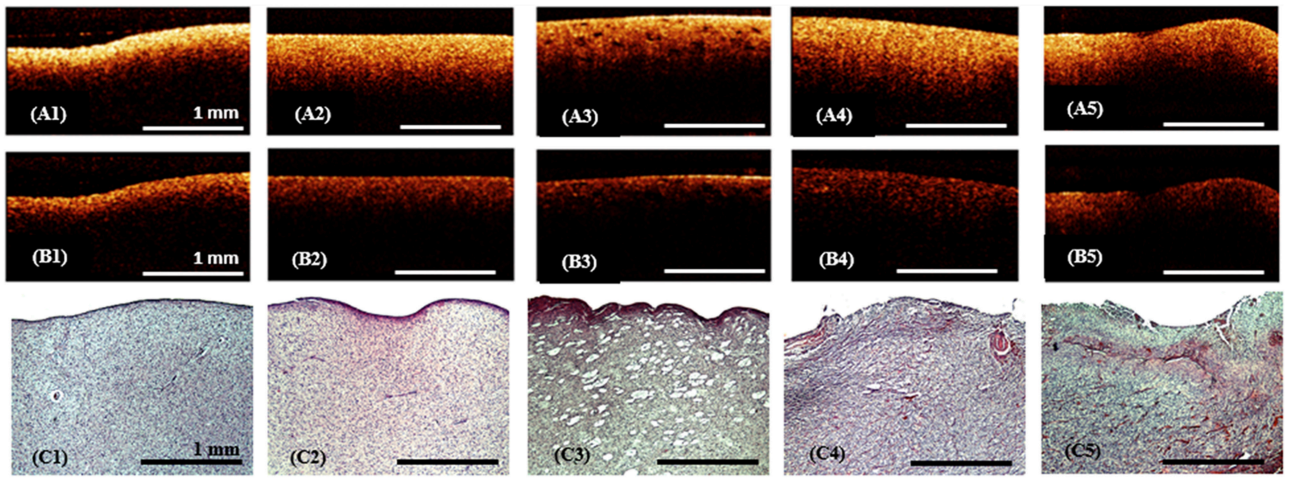

FIGURE 4 | *Ex vivo* CP OCT images **(A1–A5)**, **(B1–B5)** and corresponding histology **(C1–C5)** of white matter **(A1–C1)**, diffuse astrocytoma Grade II **(A2–C2)**, **(A3–C3)**, diffuse astrocytoma Grade III **(A4–C4)** and glioblastoma **(A5–C5)**; on the CP OCT image of diffuse astrocytoma Grade II can be seen microcysts typical for this type of tumor **(A3,C3)**; **(A1–A5)**—CP OCT images in co-polarization and **(B1–B5)**—in cross-polarization. Histological images **(C1–C5)**-hematoxylin and eosin staining.

TABLE 1 | Visual assessment criteria of CP OCT images for distinguishing between white matter and glioma tissue.

CP OCT image parameter	White matter	Tumor
MAIN CRITERIA		
The signal intensity in co-polarization	*Intense*	*Non-intense*
The signal intensity in cross-polarization	*Intense*	*Non-intense*
ADDITIONAL CRITERIA		
The homogeneity of intensity in co-polarization	Homogeneous	Heterogeneous
The uniformity of attenuation in co-polarization	Uniform	Un-uniform

TABLE 2 | The results of diagnostic test by visual assessment of the CP OCT images.

Polarization	Inter-rater reliability rate	Sensitivity, %	Specificity, %	Diagnostic accuracy, %
Co-	0.83/0.83	89–93	67–73	83–84
Cross-	0.86/0.86	80–87	75–89	82–83
Co- and cross- simultaneously	0.92/0.91	82–85	92–94	87–88

Based on the results of the first test the most powerful criteria for the visual assessment of microstructural CP OCT images to enable differentiation between glial tumor tissue and white matter are the CP OCT signal intensities in co- and cross-polarization. Also for this aim, the homogeneity of intensity and the uniformity of attenuation can be used as additional criteria.

Diagnostic Accuracy of CP OCT Based on Visual Assessment of Images

The results of the second set of tests, using the identified main and additional criteria, separately in co- and cross-polarization and simultaneously in co- and cross-polarization (**Table 2**) demonstrate their great inter-rater reliability. The test based on simultaneously assessing CP OCT images in co- and cross-polarization showed a higher diagnostic accuracy (87–88%).

Using co-polarization showed higher sensitivity (89–93%); therefore using this regimen allows minimization of the risk of failure of tumor detection. The high specificity of 92–94% that can be achieved by using simultaneous visual assessment of the images in co- and cross-polarization is associated with the low risk of misguided white matter resection.

Intraoperative Visual Assessment of the CP OCT Images

The intraoperative *in vivo* CP OCT images of white matter and tumors obtained by the certified OCT system with the handled probe show full structural similarity to the *ex vivo* CP OCT images of brain specimens obtained using the laboratory OCT setup, however, owing to differences in image processing between the OCT systems the intensity of the intraoperative images in co- and cross-polarization are lower (∼4 times).

The cortex is characterized by specific vertical striations arising as the "shadows" of the blood vessels located just under the tissue surface (**Figures 5A1**, **6A1**), and these striations can be considered as a specific cortex-indicator. The white matter tissue is characterized by its high attenuation, although the intensity is lower in cross-polarization than for the signal in co-polarization (**Figures 5B1,B2**, **6B1**). Regardless of the glioma grade, the tumorous tissue is characterized by low-intensity, homogeneous or heterogeneous signals with low attenuation rate in co-polarization (**Figures 5C1**, **6A2,A3**, images in co-polarization). Since the OCT device approved for clinical use only provides imaging at low intensity the signal in cross-polarization is therefore almost absent from the tumor (**Figures 5C2**, **6A2,A3**,

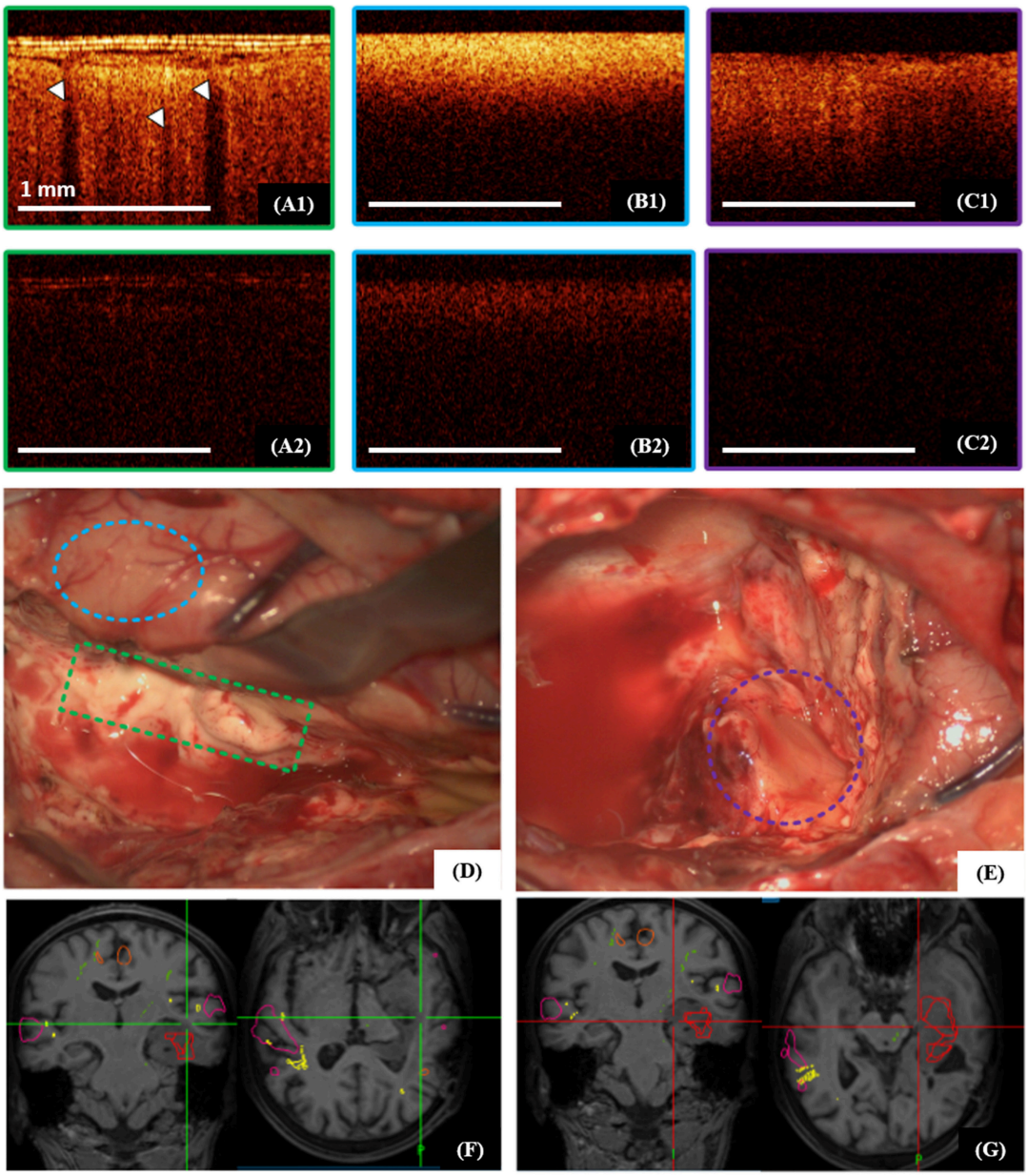

FIGURE 5 | Intraoperative CP OCT images of cortex **(A1,A2)**, white matter **(B1,B2)** and diffuse astrocytoma Grade II **(C1,C2)**; the scanning areas of the corresponding tissue types in the surgical field are marked with green **(A1,A2)**, blue **(B1,B2)** and violet **(C1,C2)** dotted lines **(D,E)**, and interrelated with the neuronavigation data **(F,G)**; **(A1–C1)**—CP OCT images in co-polarization and **(A2–C2)**—in cross-polarization. The white arrows show characteristic vertical striations arising from "shadows" of the blood vessels located just under the tissue surface.

images in cross-polarization) and very low from the cortex (**Figures 5A2**, **6A1**, images in cross-polarization). The scanning areas of the corresponding tissue types in the surgical field are marked with green (cortex, **Figures 5A1,A2**), blue (white matter, **Figures 5B1,B2**) and violet (diffuse astrocytoma Grade II, **Figures 5C1,C2**) dotted lines (**Figures 5D,E**) and interrelated with the neuronavigation data (**Figures 5F,G**).

OCT scanning of the cortex was performed in 9 cases (53%). In all the comparisons, the OCT and neuronavigation data showed that the tumor had widened through the tumor margin that can be detected under the white light of the operating microscope. In the case of visible cortical invasion by the tumor the OCT scanning was performed from this area to visually healthy brain tissue. In the case of visually intact cortex, the scanning was started from the central part of the tumor as detected by the neuronavigation system.

Taking into account the variability of the CP OCT images for a variety of different reasons (e.g., brain swelling), when distinguishing white matter and tumor it is better to commence the OCT scanning of white matter from a control area (where

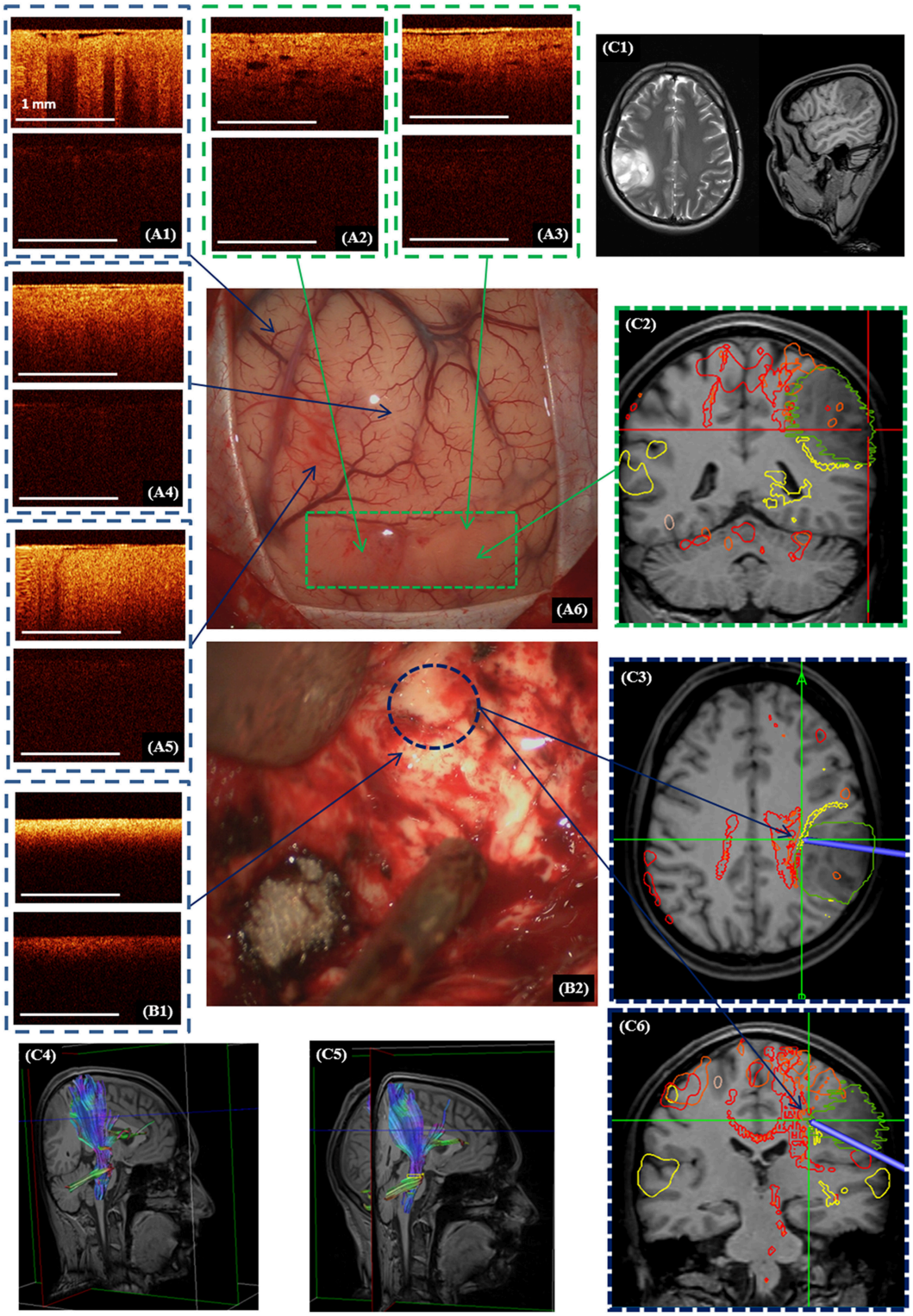

FIGURE 6 | Intraoperative CP OCT images in a patient with diffuse astrocytoma (Grade II): of the cortex **(A1)** with well-defined (**A2,A3**; **A6**—green dotted line) and invisible **(A4,A5)** tumor invasion, white matter **(B1)** close to the right corticospinal tract (**B2**—blue color dotted line; **C3,C4**—marked by red color); the scanning areas of corresponding tissue types in the surgical field **(A6,B2)** are marked with green **(A6)** and, blue **(B2)** dotted lines and interrelated with the neuronavigation data, where the tumor is marked with a green line and the corticospinal tract with a red line **(C2,C3,C6)**. Preoperative MRI in T1 and T2 **(C1)** and the corticospinal tract reconstruction based on the DTI before **(C4)** and after **(C5)** operation. **(A1–A5,B1)**—CP OCT images in co-polarization (upper image) and cross-polarization (lower image).

there is no doubt about the histology) to enable comparison of this scan with following images. In our study scanning of control area before tumor resection was performed only in 9 patients (53%), while in the other cases the identified criteria (**Table 1**) and standard CP OCT images of white matter (**Figures 4A1,B1**, **5B1,B2**) were used.

Perfect detection of white matter by OCT can be useful when tumor resection is performed close to white matter tracts. **Figure 6** shows the process of removal of a diffuse astrocytoma (Grade II) in the right parietal lobe. The preoperative diffusion tensor imaging (DTI) data uploaded in the neuronavigation system demonstrated that the tumor was closely adjacent to right cortico-spinal tract (**Figures 6C2–C4**). Electrical stimulation in this region had shown a response at a current of 5 mA (pulse frequency of 60 Hz, with a single phase duration of 1 ms in trains lasting 4 s), that meant the approximate distance to the tract was about 5 mm. Based on the identified criteria, OCT scanning demonstrated the presence of white matter in this region. It was taken decision to stop further resection. On post-operative DTI, no change in the corticospinal tract was detected. Therefore, the simultaneous use of subcortical electrostimulation and OCT was able to define more exactly the required extent of resection close to eloquent white matter tracts.

DISCUSSION

During surgery of infiltrative brain tumors the benefits of novel intraoperative imaging technologies are self-evident, due to the lack of resolving capacity of the operating microscope for distinguishing tumorous and non-tumorous tissues and the detection of any residual tumor (24–27). In order to overcome this problem, at present, the most commonly used technologies are fluorescent visualization with 5-ALA (28–30) and intraoperative MRI (31, 32). However, these methods have some limitations; therefore, the development of novel intraoperative technologies has become particularly relevant. OCT appears to provide a very promising method for routine neurosurgical practice due to the clear benefits of this method such as: safety (using a near infrared light source does not risk tissue damage); accuracy (high resolution ∼10 micron) the absence of a requirement for contrast agents; imaging depths of more than 1 mm; the ability to obtain images at a distance and therefore the opportunity for integration into a surgical microscope or endoscope (2, 3).

Obviously, the increased interest in OCT has been the result of the continuing improvements in several aspects of OCT, such as imaging speed, sensitivity, the development of functional OCT extensions and signal data processing. The quantitative assessment of OCT with the determination of various optical coefficients such as backscattering (33) and attenuation (4, 10, 34) coefficients provides higher diagnostic accuracy compared with the qualitative assessment of OCT images. Kut et al. have demonstrated the high diagnostic accuracy of OCT for distinguishing tumors from white matter on the basis of the optical attenuation coefficient: for patients with higher-grade tumors the sensitivity/specificity reached 92%/100%; for low-grade tumors sensitivity/specificity values were 100%/80% (4). Unfortunately, at present, clinically approved OCT systems can provide only visual assessment, although that has been sufficient to improve readability for neurosurgeons. Additionally, such visual assessment for distinguishing white matter from tumor tissue also provides high sensitivity of (82–85%), specificity (92–94%), and diagnostic accuracy (87–88%). Therefore, it can be proposed for routine clinical use, although with some restrictions.

This paper deliberately references previously published data (20) with regard to intraoperative approval of the visual CP OCT criteria identified for distinguishing white matter from tumor tissue. These criteria have been specified in place of the previously suggested "loss of normal attenuation" from the tumorous tissue (9, 10). However, this criterion remains relevant for the detection of tumor invasion into the cortex, which is characterized by a "typical view" of vertical striations, disappearing in cases where there are any changes of cortical microarchitecture. The result of this study questions the significance of the "homogeneous" criterion for distinguishing tumor and white matter because of the variability of the characteristics of the OCT signal from gliomas. For example, tumorous tissue may have a quite homogeneous OCT signal, while, on the other hand, white matter in the vicinity of necrotic areas or hematomas can lose its homogeneity.

The study has shown that CP OCT, as an extension of OCT, broadens the functionality of the method. The assessment of CP OCT images simultaneously in co- and cross-polarization has shown a higher specificity (92–94% against 67–73%) and diagnostic accuracy (87–88% against 83–84%) compared with conventional OCT. Therefore, this mode is effective to use during tumor resection closely adjacent to eloquent white matter tracts. Using CP OCT, based on visual assessment along with co-polarization, shows high sensitivity (89–93% against 82–85% when using co- and cross-polarization simultaneously) and therefore it is effective in improving identification of the necessary extent of resection in non-eloquent brain areas.

In this study, discrete histological tissue types such as cortex, white matter and tumor have been described. The formation of the OCT signal and its differences between tumor and white matter can be explained using a simple model of the structural organization of the tissue: tumorous tissue can be represented as an assembly of tumor cells that are characterized by low attenuation, compared to the high attenuation of myelin. However, differentiation using visual assessment can be difficult when comparing white matter with structureless (or intact) myelin and tumorous tissue with necrosis (or necrosis alone), due to their similarity in optical properties. Tumorous tissue without necrosis forms the typical structure of all Grade I-III astrocytomas and the peripherial area of glioblastomas (Grade IV). Necrotic areas characterized by high attenuation (forward cross-scattering) always present in (1) the glioblastoma core, (2) tissues after radiotherapy (e.g., in the case of recurrent astrocytoma after combination treatment) and (3) tissues following bipolar coagulation (total necrosis). The high attenuation (forward cross-scattering) of white matter is

the result of the high-density packaging of its myelin fibers. Some events such as structural damage of the myelin, or cerebral edema related to tumor growth, can lead to a significant decrease of attenuation and of forward cross-scattering (35). These myelin changes are typical of the peritumoral area of high-grade astrocytomas. Probably, improvements in the quantitative assessment of OCT data will allow these tissue types to be clearly distinguished.

At the moment, in all doubtful cases, consideration must be given to the patient's preoperative data, localization of the OCT scanning area, and the distance from eloquent brain areas. For example, if the preoperative clinical data is indicative of a low-grade glioma, during tumor resection no necrotic areas or myelin damage would be expected, so the surgeon would not expect to find necrotic areas or dramatic changes in the myelin structure, meaning that distinguishing between white matter and tumor is not an issue In the case of a glioblastoma, the white matter in the peritumoral area might be characterized by low attenuation and forward cross-scattering, so the intensity of the CP OCT signal could decrease in co- and cross-polarization. On the other hand in the case where there has been previous radiation therapy (e.g., recurrent glioblastoma) the tumor mass could include a vast amount of necrotic tissue and be characterized by high intensity in the CP OCT images. Therefore, in both cases the differentiation between white matter and tumorous tissue can be difficult. Consequently, in these doubtful cases, decisions about the extent of resection should primarily be based on the distance from eloquent brain areas. Hemorrhages can also compromise the interpretability of the OCT signals (10), therefore, before scanning, they should be removed together with any necrotic areas associated with bipolar coagulation.

In contrast to white matter, the cortex does not contain densely packed myelin fibers that might lead to difficulties in distinguishing between cortex and tumor, although tumor is characterized by higher cellularity and nuclear density comparing to cortex. Visual assessment of OCT signals based on the criterion "loss of normal attenuation" allows tumors to be distinguished from the cortex during *in vivo* scanning (10, 23). Probably, additional *in vivo* studies would enable clearer determination of the optical differences between cortex and tumor and offer better definitions for the quantitative OCT criteria (23).

This study was based on *ex vivo* brain specimens for a number of reasons: (1) the possibility of carrying out maximally targeted histological examinations to appropriately validate the OCT; (2) the absence of strict time limitations, which made it possible to perform multiple scans to monitor the image quality. The previously performed comparative analysis of the optical properties of white matter and tumorous tissues of the brain allow us to conclude that the CP OCT images obtained *ex vivo* show a full qualitative similarity to the *in vivo* CP OCT images (23). However, *ex vivo* study is not representative for the cortex by reason of the disappearance of the unique characteristics of the CP OCT signal in *ex vivo* CP OCT images.

The study has several limitations. One of them is the use of different CP OCT devices in the preclinical part and during the intraoperative scanning. Although the experimental device has some advantages due to a better signal characteristics and a more detailed computer processing of the OCT data, using it during surgical procedures was not possible due to its novel character and the absence of permission for its clinical use. Therefore, the study demonstrates the advantages of CP OCT on fresh pathological specimens, but not for intraoperative CP OCT data. In the *ex vivo* CP OCT study based on fresh specimens it is easier to "target" the region of interest and therefore provide advanced histological validation of CP OCT image in comparison with *in vivo* CP OCT study, where image interpretation can be complicated by the impact of several factors such as tissue deformation during its removal, difficulties in access to the region of interest where the white matter is infiltrated by tumor, active bleeding and use of hemostatic materials affecting the quality of the CP OCT images. However, the promising results of this study allow us to recommend implementing a clinical CP OCT prototype based on the experimental one used in this study.

Further, only three raters were tested, therefore the results may be considered as preliminary. Increasing the number of raters may improve the results in terms of visual assessment, diagnostic accuracy, sensitivity and specificity for CP OCT for distinguishing white matter from tumor tissue.

The limitation of the intraoperative phase of the study was lack of morphological verification of scanning areas. Using image guiding under neuronavigation system and high magnification of surgical microscope doesn't provide exact information about tissue morphology.

Nevertheless, while OCT does not provide molecular information and cannot detect individual tumor cells, it looks promising in assisting navigation during neurosurgical procedures such as glioma resection, stereotactic biopsy and the placement of electrodes for deep brain stimulation. For clinical translation, OCT can be integrated into standard operating equipment such as surgical microscopes (6, 7), and probes for stereotactic procedures (36). For the purposes of glioma surgery, the cross-polarization mode provides a good illustration of a functional extension to OCT, which can offer opportunities to improve the visual assessment of OCT data.

CONCLUSION

CP OCT based on the visual assessment of obtained images is a promising imaging tool for distinguishing tumorous and non-tumorous tissues during glioma resection. The most powerful criteria are the signal intensities in co- and cross-polarization. Further to this purpose, additional criteria such as the homogeneity of intensity and the uniformity of attenuation can also be used. The simultaneous assessment of CP OCT images in co- and cross-polarization has demonstrated better diagnostic accuracy for distinguishing white matter from tumor tissue than OCT alone. Differentiation between cortex and white matter can be performed based on the criterion "loss of normal attenuation" (loss of the "typical view" of vertical striations on CP OCT images). In distinguishing white matter and tumors the diagnostic accuracy using the visual CP OCT criteria was 87–88%. The CP OCT data is easily associated with intraoperative neurophysiological and neuronavigation findings and can provide supplementary information for neurosurgeons during tumor resection.

DATA AVAILABILITY

All datasets generated for this study are included in the manuscript and/or the supplementary files.

AUTHOR CONTRIBUTIONS

KY, EK, AM, and NG: study concept and design. KY, EG, PS, IM, and LK: data acquisition and quality control of data. KY, AM, SK, GG, and EK: data analysis and interpretation. KY, EK, AM, and NG: manuscript preparation. AP, EZ, and NG: manuscript review.

FUNDING

Ex vivo human studies were supported by Russian Foundation for Basic Research (Project No. 18-29-01049_mk). Intraoperative CP OCT visualization was funded by Council on grants of the President of the Russian Federation (the Russian President grant for young scientists, project No. MK-6634.2018.7).

ACKNOWLEDGMENTS

We thank Dr. Nikolay N. Karyakin (rector of PRMU, Nizhny Novgorod, Russia) for active supporting translation of CP OCT into clinical usage.

REFERENCES

1. Jenkinson MD, Barone DG, Bryant A, Vale L, Bulbeck H, Lawrie TA, et al. Intraoperative imaging technology to maximise extent of resection for glioma. *Cochrane Database Syst Rev.* (2018) 22:Cd012788. doi: 10.1002/14651858.CD012788.pub2
2. Yashin KS, Kravets LY, Gladkova ND, Gelikonov GV, Medyanik IA, Karabut MM, et al. [Optical coherence tomography in neurosurgery]. *Zhu Vopr Neirokhir Im N N Burdenko.* (2017) 81:107–15. doi: 10.17116/neiro2017813107-115
3. Valdes PA, Roberts DW, Lu FK, Golby A. Optical technologies for intraoperative neurosurgical guidance. *Neurosurg Focus.* (2016) 40:E8. doi: 10.3171/2015.12.FOCUS15550
4. Kut C, Chaichana KL, Xi J, Raza SM, Ye X, McVeigh ER, et al. Detection of human brain cancer infiltration *ex vivo* and *in vivo* using quantitative optical coherence tomography. *Sci Transl Med.* (2015) 7:292ra100. doi: 10.1126/scitranslmed.3010611
5. Sun C, Lee KKC, Vuong B, Cusimano M, Brukson A, Mariampillai A, et al., editors. Neurosurgical hand-held optical coherence tomography (OCT) forward-viewing probe. In: *Proceedings Volume 8207, Photonic Therapeutics and Diagnostics VIII*. San Francisco: *SPIE BiOS* (2012).
6. Lankenau E, Klinger D, Winter C, Malik A, Müller H, Oelckers S, et al. Combining optical coherence tomography (OCT) with an operating microscope. In: Buzug T, Holz D, Bongartz J, Kohl-Bareis M, Hartmann U, Weber S, editors. *Advances in Medical Engineering. Springer Proceedings in Physics*. Vol. 114. Berlin; Heidelberg: Springer (2007). p. 343–8. doi: 10.1007/978-3-540-68764-1_57
7. Lankenau EM, Krug M, Oelckers S, Schrage N, Just T, Hüttmann G. iOCT with surgical microscopes: a new imaging during microsurgery. *Adv Opti Technol.* (2013) 2:233–39. doi: 10.1515/aot-2013-0011
8. Kiseleva EB, Yashin KS, Moiseev AA, Snopova LB, Gelikonov GV, Medyanik IA, et al. Quantitative cross-polarization optical coherence tomography detection of infiltrative tumor margin in a rat glioma model: a pilot study. *Sovremennye Tehnol Med.* (2018) 10:6–14. doi: 10.17691/stm2018.10.1.01
9. Bohringer HJ, Boller D, Leppert J, Knopp U, Lankenau E, Reusche E, et al. Time-domain and spectral-domain optical coherence tomography in the analysis of brain tumor tissue. *Lasers Surg Med.* (2006) 38:588–97. doi: 10.1002/lsm.20353
10. Bohringer HJ, Lankenau E, Stellmacher F, Reusche E, Huttmann G, Giese A. Imaging of human brain tumor tissue by near-infrared laser coherence tomography. *Acta Neurochim.* (2009) 151:507–17; discussion 17. doi: 10.1007/s00701-009-0248-y
11. Baumann B. Polarization sensitive optical coherence tomography: a review of technology and applications. *Appl Sci.* (2017) 7:474. doi: 10.3390/app7050474
12. de Boer JF, Hitzenberger CK, Yasuno Y. Polarization sensitive optical coherence tomography – a review [Invited]. *Biomed Opt Express.* (2017) 8:1838–73. doi: 10.1364/BOE.8.001838
13. Wang H, Akkin T, Magnain C, Wang R, Dubb J, Kostis WJ, et al. Polarization sensitive optical coherence microscopy for brain imaging. *Opt Lett.* (2016) 41:2213–6. doi: 10.1364/OL.41.002213
14. Boas DA, Wang H, Magnain C, Fischl B. Polarization-sensitive optical coherence tomography of the human brain connectome. *SPIE Newsroom.* (2017). doi: 10.1117/2.1201701.006834
15. Wang H, Zhu J, Akkin T. Serial optical coherence scanner for large-scale brain imaging at microscopic resolution. *NeuroImage.* (2014) 84:1007–17. doi: 10.1016/j.neuroimage.2013.09.063
16. Wang H, Zhu J, Reuter M, Vinke LN, Yendiki A, Boas DA, et al. Cross-validation of serial optical coherence scanning and diffusion tensor imaging: a study on neural fiber maps in human medulla oblongata. *NeuroImage.* (2014) 100:395–404. doi: 10.1016/j.neuroimage.2014.06.032
17. Gubarkova EV, Dudenkova VV, Feldchtein FI, Timofeeva LB, Kiseleva EB, Kuznetsov SS, et al. Multi-modal optical imaging characterization of atherosclerotic plaques. *J Biophoton.* (2016) 9:1009–20. doi: 10.1002/jbio.201500223
18. Gladkova N, Kiseleva E, Robakidze N, Balalaeva I, Karabut M, Gubarkova E, et al. Evaluation of oral mucosa collagen condition with cross-polarization optical coherence tomography. *J Biophoton.* (2013) 6:321–9. doi: 10.1002/jbio.201200059
19. Schmitt JM, Xiang SH. Cross-polarized backscatter in optical coherence tomography of biological tissue. *Optics Lett.* (1998) 23:1060–62. doi: 10.1364/OL.23.001060
20. Yashin K, Kiseleva EB, Gubarkova EV, Moiseev AA, Kuznetsov SS, Medyanik IA, et al. Visual assessment criteria of microstructural *ex vivo* co-and cross-polarized optical coherence tomography images in gliomas. In: *Proceedings of SPIE*, Vol 10685. Bellingham, WA (2018). p. 106853F.
21. Gelikonov VM, Gelikonov GV, Shilyagin PA. Linear-wavenumber spectrometer for high-speed spectral-domain optical coherence tomography. *Optics Spectroscopy.* (2009) 106:459–65. doi: 10.1134/S0030400X09030242
22. Moiseev AA, Gelikonov GV, Terpelov DA, Shilyagin PA, Gelikonov VM. Noniterative method of reconstruction optical coherence tomography images with improved lateral resolution in semitransparent media. *Laser Phys Lett.* (2013) 10:125601. doi: 10.1088/1612-2011/10/12/125601
23. Kiseleva EB, Yashin KS, Moiseev AA, Sirotkina MA, Timofeeva LB, Fedoseeva VV, et al. Cross-polarization optical coherence tomography in comparative *in vivo* and *ex vivo* studies of the optical properties of normal and tumorous brain tissues. *Sovremennye Tehnol Med.* (2017) 9:177. doi: 10.17691/stm2017.9.4.22
24. Berger MS. Malignant astrocytomas: surgical aspects. *Sem Oncol.* (1994) 21:172–85.
25. Ducray F, Dutertre G, Ricard D, Gontier E, Idbaih A, Massard C. [Advances in adults' gliomas biology, imaging and treatment]. *Bull du Cancer.* (2010) 97:17–36. doi: 10.1684/bdc.2009.1019
26. Robins HI, Lassman AB, Khuntia D. Therapeutic advances in malignant glioma: current status and future prospects. *Neuroimaging Clin North Am.* (2009) 19:647–56. doi: 10.1016/j.nic.2009.08.015

27. Sanai N, Berger MS. Glioma extent of resection and its impact on patient outcome. *Neurosurgery.* (2008) 62:753–64; discussion 264–6. doi: 10.1227/01.neu.0000318159.21731.cf
28. Hadjipanayis CG, Widhalm G, Stummer W. What is the surgical benefit of utilizing 5-aminolevulinic acid for fluorescence-guided surgery of malignant gliomas? *Neurosurgery.* (2015) 77:663–73. doi: 10.1227/NEU.0000000000000929
29. Potapov AA, Gavrilov AG, Goriainov SA, Gol'bin DA, Zelenkov PV, Kobiakov GL, et al. [Intraoperative fluorescent visualization and laser spectroscopy in intrinsic brain tumor surgery]. *Zh Vopr Neirokhi Im N N Burdenko.* (2012) 76:3–11; discussion 12.
30. Potapov AA, Goryaynov SA, Okhlopkov VA, Pitskhelauri DI, Kobyakov GL, Zhukov VY, et al. [Clinical guidelines for the use of intraoperative fluorescence diagnosis in brain tumor surgery]. *Zh Vopr Neirokhi Im N N Burdenko.* (2015) 79:91–101 doi: 10.17116/neiro201579591-101
31. Fahlbusch R, Samii A. Intraoperative MRI. *Neurosurgical Focus.* (2016) 40:E3. doi: 10.3171/2015.12.FOCUS15631
32. Eljamel MS, Mahboob SO. The effectiveness and cost-effectiveness of intraoperative imaging in high-grade glioma resection; a comparative review of intraoperative ALA, fluorescein, ultrasound and MRI. *Photodiagno Photodyn Ther.* (2016) 16:35–43. doi: 10.1016/j.pdpdt.2016.07.012
33. Boppart SA, Brezinski ME, Pitris C, Fujimoto JG. Optical coherence tomography for neurosurgical imaging of human intracortical melanoma. *Neurosurgery.* (1998) 43:834–41. doi: 10.1097/00006123-199810000-00068
34. Yuan W, Kut C, Liang W, Li X. Robust and fast characterization of OCT-based optical attenuation using a novel frequency-domain algorithm for brain cancer detection. *Sci Rep.* (2017) 7:44909. doi: 10.1038/srep44909
35. Rodriguez CL, Szu JI, Eberle MM, Wang Y, Hsu MS, Binder DK, et al. Decreased light attenuation in cerebral cortex during cerebral edema detected using optical coherence tomography. *Neurophotonics.* (2014) 1:025004. doi: 10.1117/1.NPh.1.2.025004
36. Liang CP, Wierwille J, Moreira T, Schwartzbauer G, Jafri MS, Tang CM, et al. A forward-imaging needle-type OCT probe for image guided stereotactic procedures. *Optics Express.* (2011) 19:26283–94. doi: 10.1364/OE.19.026283

Conflict of Interest Statement: The authors declare that the research was conducted in the absence of any commercial or financial relationships that could be construed as a potential conflict of interest.

frontiers in Surgery

OPINION
published: 12 April 2019
doi: 10.3389/fsurg.2019.00021

Surgery for Malignant Brain Gliomas: Fluorescence-Guided Resection or Functional-Based Resection?

Hugues Duffau [1,2]*

[1] Department of Neurosurgery, Montpellier University Medical Center, Gui de Chauliac Hospital, Montpellier, France, [2] Team "Plasticity of Central Nervous System, Stem Cells and Glial Tumors," U1051 Laboratory, National Institute for Health and Medical Research (INSERM), Institute for Neurosciences of Montpellier, Montpellier University Medical Center, Montpellier, France

Keywords: fluorescence imaging, glioblastoma, functional-based resection, fluorescence-guided resection, brain glioma

The goal of surgery for malignant brain glioma is to optimize the extent of resection (EOR) while preserving the quality of life. A meta-analysis evidenced that gross total resection improves progression free survival and overall survival (OS) in glioblastomas (1). In a consecutive cohort with 500 newly diagnosed glioblastomas, a significant survival benefit was noted with as little as 78% EOR, and stepwise improvement in OS was observed even in the 95–100% EOR range (2). Interestingly, in 243 glioblastomas, survival advantages from total resection remained significant in multivariate analysis after adjustment for bias (3). Concerning anaplastic gliomas, the volume of residual neoplasm on postoperative MRI predicts the time to tumor progression and OS (4).

However, maximal resection can be challenging because it may be difficult to identify the boundaries of glioma due to its infiltrative feature, especially with a white-light microscope. Therefore, to improve the intraoperative real-time visualization of malignant gliomas, the use of fluorescence-guided surgery (FGS) has been advocated, with 5-aminolevulinic acid (5-ALA) as the first option (5, 6). Intrasurgical fluorescence imaging allowed an increase of EOR in high-grade gliomas compared to conventional microsurgery with white-light, as demonstrated by a seminal randomized controlled trial (7). The great merit of this study was also to emphasize the need to objectively assess the EOR on postoperative MRI following glioblastoma surgery. In this Frontiers issue, applications of fluorescence and other optical imaging technology in oncological surgery have been highlighted, especially for malignant brain tumor. Nonetheless, despite a prolific literature on this topic in the past decade, the actual benefit of FGS for glioma patients may be discussed, due to substantial limitations.

From an oncological perspective, beyond the fact that 5-ALA is not adapted to show diffused low-grade gliomas, FGS may paradoxically restrict EOR in high-grade gliomas. Indeed, it has recently been suggested that supracomplete resection, which consists on the removal of a margin around the enhancement, may improve OS in glioblastomas (8). This original concept is based upon the fact that relapses mostly occur at the periphery of the operating cavity, where specific tumor and stromal cells that promote glioblastoma growth and invasion exist (9). In a cohort with 1229 glioblastomas, Li et al. reported a significantly longer OS of 20.7 months when a resection of $\geq$ 53.21% of the surrounding FLAIR-weighted MRI abnormalities was performed in addition to the total contrast-enhancing removal, versus 15.5 months in the case of excision of the enhancement alone (10). Consequently, even though 5-ALA goes beyond the borders of contrast enhancement, because its diffusion is nonetheless reduced, the tumorological risk intrinsically related to this method is to prematurely stop the resection around the tumor mass identified by fluorescence—while optionally, a lobectomy with a (sub)total resection of the FLAIR abnormalities would have been possible in non-eloquent areas, thus with a better impact on OS. From a functional

OPEN ACCESS

Edited by:
Mark Preul,
Barrow Neurological Institute (BNI), United States

Reviewed by:
Shota Tanaka,
The University of Tokyo Hospital, Japan

***Correspondence:**
Hugues Duffau
h-duffau@chu-montpellier.fr

Specialty section:
This article was submitted to Neurosurgery, a section of the journal Frontiers in Surgery

Received: *18 February 2019*
Accepted: *22 March 2019*
Published: *12 April 2019*

Citation:
Duffau H (2019) Surgery for Malignant Brain Gliomas: Fluorescence-Guided Resection or Functional-Based Resection? Front. Surg. 6:21. doi: 10.3389/fsurg.2019.00021

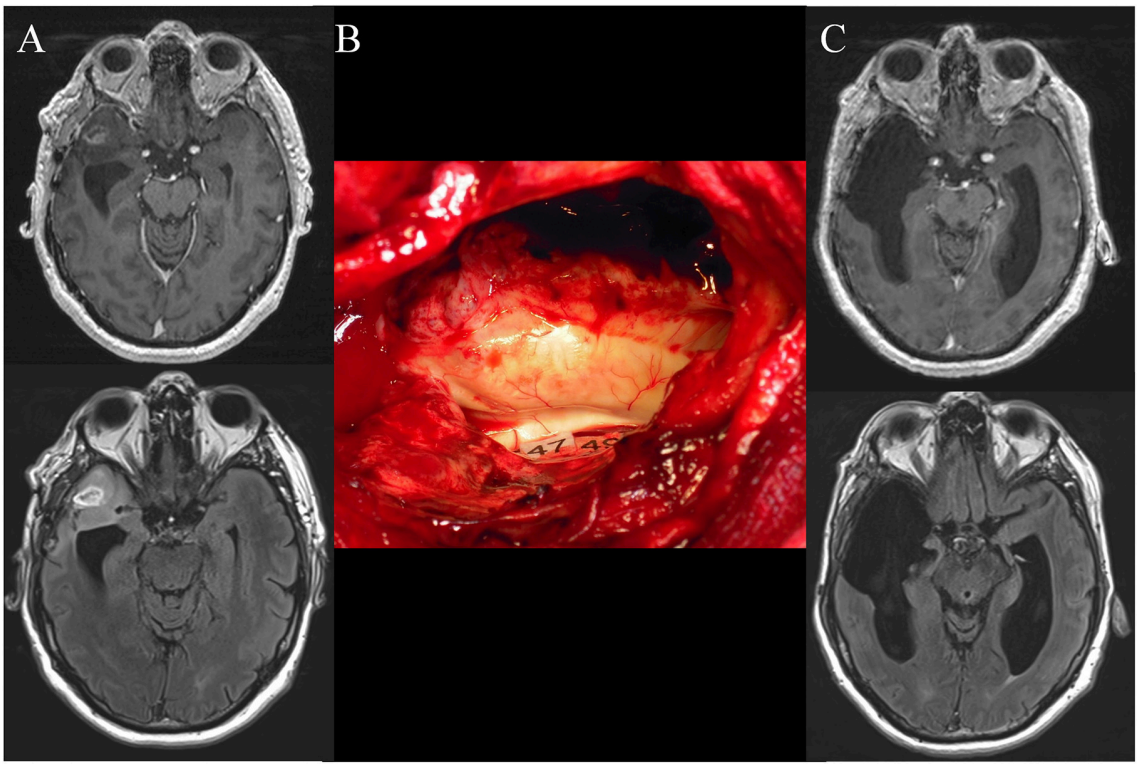

FIGURE 1 | (A) Preoperative axial enhanced T1-weighted MRI (upper) and FLAIR-weighted MRI (lower) achieved in a 50-year-old right-handed man who experienced seizures that allowed the discovery of a right anterior temporal high-grade glioma. The patient underwent a previous "minimal-invasive image-guided surgery" performed under general anesthesia in another hospital with a partial resection of the enhancement and the FLAIR hypersignal. An anaplastic astrocytoma was diagnosed. At that time, the patient was referred to our department and a reoperation was proposed with awake mapping in order to achieve a supratotal resection according to functional boundaries. The neurological examination was normal. Nonetheless, the preoperative neuropsychological evaluation revealed a slight deficit of higher-cognitive functions, that is, theory of mind and semantic processing. **(B)** Intraoperative view after resection, achieved up to eloquent structures, especially at the subcortical level. Indeed, direct electrostimulation of white matter tracts enabled the identification of the subcortical neural networks involved in theory of mind (mentalizing) (tag 47) and non-verbal semantics (tag 49) - which have been mapped according to the results of the presurgical neurocognitive assessment. **(C)** Postoperative axial enhanced T1-weighted MRI (upper) and FLAIR-weighted MRI (lower) (performed 3 months after resection) demonstrating a supracomplete resection of both the enhancement and the FLAIR hypersignal. The patient recovered, with an improvement of the neuropsychological examination thanks to a post-surgical cognitive rehabilitation. A diffuse WHO grade III astrocytoma (IDH1 mutated, non-codeleted) was diagnosed, and postoperative chemotherapy was administrated, with no radiotherapy. The imaging is stable with 4 years of follow-up, and the patient continues to enjoy a normal life, with no symptoms.

point of the view, the same property of 5-ALA going beyond the enhanced part of the glioma can result in permanent neurological deterioration for tumors involving structures essential for brain functions. For example, Díez Valle et al. reported a rate of new or increased neurological worsening of 8.2% in a series with glioblastomas operated on using 5-ALA (11), that is, a higher rate in comparison with series using intraoperative electrical mapping −3.4% in a recent meta-analysis (12).

Therefore, an alternative to overcome these limitations is to switch from a FGS to a functional-guided resection by means of direct electrical stimulation (DES) (13). Indeed, the meta-analysis by De Witt et al. in which the benefit of intraoperative electrical mapping on glioma surgery outcome was investigated on the basis of over 8,000 patients, evidenced that the surgical excision of both high-grade gliomas and low-grade gliomas using DES was correlated with more radical resections and with a significantly lower rate of severe permanent impairment—even for tumors located in eloquent regions (12). It is necessary to stress that such a demonstration of an improved EOR associated with a simultaneous decrease of neurological morbidity thanks to the use of fluorescence *per se*, compared with results reported in series using intraoperative functional mapping [currently considered as the standard of care of glioma surgery (12)], is still lacking.

Of note, it has been proposed to combine 5-ALA and electrophysiological mapping, especially for gliomas invading critical areas (14–17). However, even if technically there is not antagonism to use both methods, FGS is conceptually incompatible with functional mapping-based resection. Indeed, although the aim of 5ALA-guided surgery is to remove the enhanced part of the glioma, with the double risk not to achieve a supramarginal resection when functionally feasible or to induce a persistent deficit in eloquent structures (since it is in essence unable to provide functional information), the purpose of mapping-guided surgery is not to achieve a ≪tumorectomy≫ but to perform the most extensive resection of the parenchyma invaded by a diffuse tumoral disease—on the condition that this part of the brain is not critical for

neural functions (8, 18). In other words, the aim is to push the resection until eloquent structures have been encountered, both at cortical and subcortical levels, with no margin left around these functional boundaries (13). In practice, if there are discrepancies in information given by 5-ALA and DES, neurosurgeons should rely on functional mapping. For instance, if fluorescence reveals residual glioma but electrical mapping shows that it invades functional tissue, resection must be stopped to preserve the neural networks (19). On the other hand, if 5-ALA demonstrates a ≪complete≫ tumoral removal, but the eloquent structures have not yet been reached according to DES, resection should be pursued up to functional limits in order to achieve a supratotal excision (20) (**Figure 1**).

In summary, with the ultimate goal of optimizing the onco-functional balance, namely, to improve both OS and quality of life in patients with malignant brain gliomas, FGS can be questioned by (re)opening the door to functional mapping-guided resection, to be able to maximize the benefit/risk ratio of surgery in high-grade gliomas (12, 18, 21)—as already extensively demonstrated in diffuse low-grade gliomas (22).

AUTHOR CONTRIBUTIONS

The author confirms being the sole contributor of this work and has approved it for publication.

REFERENCES

1. Brown TJ, Brennan MC, Li M, Church EW, Brandmeir NJ, Rakszawski KL, et al. Association of the extent of resection with survival in glioblastoma: a systematic review and meta-analysis. *JAMA Oncol*. (2016) 2:1460–9. doi: 10.1001/jamaoncol.2016.1373
2. Sanai N, Polley MY, McDermott MW, Parsa AT, Berger MS. An extent of resection threshold for newly diagnosed glioblastomas. *J Neurosurg*. (2011) 115:3–8. doi: 10.3171/2011.2.JNS10998
3. Stummer WW, Reulen HJ, Meinel T, Pichlmeier U, Schumacher W, Tonn JC, et al. Extent of resection and survival in glioblastoma multiforme: identification of and adjustment for bias. *Neurosurgery*. (2008) 62:564–76. doi: 10.1227/01.neu.0000317304.31579.17
4. Keles GE, Chang EF, Lamborn KR, Tihan T, Chang CJ, Chang SM, et al. Volumetric extent of resection and residual contrast enhancement on initial surgery as predictors of outcome in adult patients with hemispheric anaplastic astrocytoma. *J Neurosurg*. (2006) 105:34–40. doi: 10.3171/jns.2006.105.1.34
5. Halani SH, Adamson DC. Clinical utility of 5-aminolevulinic acid HCl to better visualize and more completely remove gliomas. *Onco Targets Ther*. (2016) 9:5629–42. doi: 10.2147/OTT.S97030
6. Stummer W, Suero Molina E. Fluorescence imaging/agents in tumor resection. *Neurosurg Clin N Am*. (2017) 28:569–83. doi: 10.1016/j.nec.2017.05.009
7. Stummer W, Pichlmeier U, Meinel T, Wiestler OD, Zanella F, Reulen HJ. Fluorescence-guided surgery with 5-aminolevulinic acid for resection of malignant glioma: a randomised controlled multicentre phase III trial. *Lancet Oncol*. (2006) 7:392–401. doi: 10.1016/S1470-2045(06)70665-9
8. Duffau H. Is supratotal resection of glioblastoma in noneloquent areas possible? *World Neurosurg*. (2014) 82:e101–3 doi: 10.1016/j.wneu.2014.02.015
9. Petrecca K, Guiot MC, Panet-Raymond V, Souhami L. Failure pattern following complete resection plus radiotherapy and temozolomide is at the resection margin in patients with glioblastoma. *J Neurooncol*. (2013) 111:19–23. doi: 10.1007/s11060-012-0983-4
10. Li YM, Suki D, Hess K, Sawaya R. The influence of maximum safe resection of glioblastoma on survival in 1229 patients: can we do better than gross-total resection? *J Neurosurg*. (2016) 124:977–88. doi: 10.3171/2015.5.JNS142087
11. Díez Valle R, Tejada Solis S, Idoate Gastearena MA, García de Eulate R, Domínguez Echávarri P, Aristu Mendiroz J. Surgery guided by 5-aminolevulinicfluorescence in glioblastoma: volumetric analysis of extent of resection insingle-center experience. *J Neurooncol*. (2011) 102:105–13. doi: 10.1007/s11060-010-0296-4
12. De Witt Hamer PC, Gil Robles S, Zwinderman A, Duffau H, Berger MS. Impact of intraoperative stimulation brain mapping on glioma surgery outcome: a meta-analysis. *J Clin Oncol*. (2012) 30:2559–65. doi: 10.1200/JCO.2011.38.4818
13. Duffau H. Mapping the connectome in awake surgery for gliomas: an update. *J Neurosurg Sci*. (2017) 61:612–30. doi: 10.23736/S0390-5616.17.04017-6
14. Della Puppa A, Pellegrin S, d'Avella E, Gioffrè G, Rossetto M, Gerardi A, et al. 5-aminolevulinic acid (5-ALA) fluorescence guided surgery of high-grade gliomas in eloquent areas assisted by functional mapping. Our experience and review of the literature. *Acta Neurochir*. (2013) 155:965–72. doi: 10.1007/s00701-013-1660-x
15. Schucht P, Seidel K, Beck J, Murek M, Jilch A, Wiest R, et al. Intraoperative monopolar mapping during 5-ALA-guided resections of glioblastomas adjacent to motor eloquent areas: evaluation of resection rates and neurological outcome. *Neurosurg Focus*. (2014) 37:E16. doi: 10.3171/2014.10.FOCUS14524
16. Picart T, Armoiry X, Berthiller J, Dumot C, Pelissou-Guyotat I, Signorelli F, et al. Is fluorescence-guided surgery with 5-ala in eloquent areas for malignant gliomas a reasonable and useful technique? *Neurochirurgie*. (2017) 63:189–96. doi: 10.1016/j.neuchi.2016.12.005
17. Corns R, Mukherjee S, Johansen A, Sivakumar G. 5-aminolevulinic acid guidance during awake craniotomy to maximise extent of safe resection of glioblastoma multiforme. *BMJ Case Rep*. (2015) 2015:bcr2014208575. doi: 10.1136/bcr-2014-208575
18. Ferracci FX, Duffau H. Improving surgical outcome for gliomas with intraoperative mapping. *Exp Rev Neurother*. (2018) 18:333–41. doi: 10.1080/14737175.2018.1451329
19. Feigl GC, Ritz R, Moraes M, Klein J, Ramina K, Gharabaghi A, et al. Resection ofmalignant brain tumors in eloquent cortical areas: a new multimodal approachcombining 5-aminolevulinic acid and intraoperative monitoring. *J Neurosurg*. (2010) 113:352–7. doi: 10.3171/2009.10.JNS09447
20. Yordanova YN, Duffau H. Supratotal resection of diffuse gliomas - an overview of its multifaceted implications. *Neurochirurgie*. (2017) 63:243–9. doi: 10.1016/j.neuchi.2016.09.006
21. Sanai N, Berger MS. Surgical oncology for gliomas: the state of the art. *Nat Rev Clin Oncol*. (2018) 15:112–25. doi: 10.1038/nrclinonc.2017.171
22. Duffau H. Diffuse low-grade glioma, oncological outcome and quality of life: a surgical perspective. *Curr Opin Oncol*. (2018) 30:383–9. doi: 10.1097/CCO.0000000000000483

Conflict of Interest Statement: The author declares that the research was conducted in the absence of any commercial or financial relationships that could be construed as a potential conflict of interest.

frontiers in Oncology

ORIGINAL RESEARCH
published: 22 May 2019
doi: 10.3389/fonc.2019.00423

The Role of 5-ALA in Low-Grade Gliomas and the Influence of Antiepileptic Drugs on Intraoperative Fluorescence

Sergey A. Goryaynov[1], Georg Widhalm[2], Maria F. Goldberg[3], Danil Chelushkin[1], Aldo Spallone[4,5], Kosta A. Chernyshov[3], Marina Ryzhova[1], Galina Pavlova[6], Alexander Revischin[6], Ludmila Shishkina[1], Vadim Jukov[1], Tatyana Savelieva[7,8], Loschenov Victor[7] and Alexander Potapov[7]*

[1] N. N. Burdenko Scientific Research Neurosurgery Institute, Moscow, Russia, [2] Department of Neurosurgery, Medical University of Vienna, Vienna, Austria, [3] I.M. Sechenov First Moscow State Medical University, Moscow, Russia, [4] NCL-Institute of Neurological Sciences, Rome, Italy, [5] Department of Biomedicine, University of Rome Tor Vergata, Rome, Italy, [6] Institute of Gene Biology, Russian Academy of Science, Moscow, Russia, [7] Prokhorov General Physics Institute, Russian Academy of Sciences, Moscow, Russia, [8] National Research Nuclear University, Moscow Engineering Physics Institute, Moscow, Russia

OPEN ACCESS

Edited by:
Mark Preul,
Barrow Neurological Institute (BNI), United States

Reviewed by:
Nikolay L. Martirosyan, University of Arizona, United States
Balaji Krishnamachary, Johns Hopkins University, United States

***Correspondence:**
Sergey A. Goryaynov
sgoraynov@nsi.ru

Specialty section:
This article was submitted to Cancer Imaging and Image-directed Interventions, a section of the journal Frontiers in Oncology

Received: *03 February 2019*
Accepted: *03 May 2019*
Published: *22 May 2019*

Citation:
Goryaynov SA, Widhalm G, Goldberg MF, Chelushkin D, Spallone A, Chernyshov KA, Ryzhova M, Pavlova G, Revischin A, Shishkina L, Jukov V, Savelieva T, Victor L and Potapov A (2019) The Role of 5-ALA in Low-Grade Gliomas and the Influence of Antiepileptic Drugs on Intraoperative Fluorescence. Front. Oncol. 9:423. doi: 10.3389/fonc.2019.00423

Objectives: Intraoperative tumor visualization with 5-aminolevulinic acid (5-ALA) induced protoporphyrin IX (PpIX) fluorescence is widely applied for improved resection of high-grade gliomas. However, visible fluorescence is present only in a minority of low-grade gliomas (LGGs) according to current literature. Nowadays, antiepileptic drugs (AEDs) are frequently administered to LGG patients prior to surgery. A recent *in-vitro* study demonstrated that AEDs result in significant reduction of PpIX synthesis in glioma cells. The aim of this study was thus to investigate the role of 5-ALA fluorescence in LGG surgery and the influence of AEDs on visible fluorescence.

Patients and Methods: Patients with resection of a newly diagnosed suspected LGG after 5-ALA (25 mg/kg) administration were initially included. During surgery, the presence of visible fluorescence (none, mild, moderate, or bright) within the tumor and intratumoral fluorescence homogeneity (diffuse or focal) were analyzed. Tissue samples from fluorescing and/or non-fluorescing areas within the tumor and/or the assumed tumor border were collected for histopathological analysis (WHO tumor diagnosis, cell density, and proliferation rate). Only patients with diagnosis of LGG after surgery remained in the final study cohort. In each patient, the potential preoperative intake of AEDs was investigated.

Results: Altogether, 27 patients with a histopathologically confirmed LGG (14 diffuse astrocytomas, 6 oligodendrogliomas, 4 pilocytic astrocytomas, 2 gemistocytic astrocytomas, and one desmoplastic infantile ganglioglioma) were finally included. Visible fluorescence was detected in 14 (52%) of 27. In terms of fluorescence homogeneity ($n = 14$), 7 tumors showed diffuse fluorescence, while in 7 gliomas focal fluorescence was noted. Cell density ($p = 0.03$) and proliferation rate ($p = 0.04$) was significantly higher in fluorescence-positive than in fluorescence-negative samples. Furthermore, 15 (56%)

of 27 patients were taking AEDs before surgery. Of these, 11 patients (73%) showed no visible fluorescence. In contrast, 10 (83%) of 12 patients without prior AEDs intake showed visible fluorescence. Thus, visible fluorescence was significantly more common in patients without AEDs compared to patients with preoperative AED intake (OR = 0,15 (CI 95% 0.012–1.07), $p = 0.046$).

Conclusions: Our study shows a markedly higher rate of visible fluorescence in a series of LGGs compared to current literature. According to our preliminary data, preoperative intake of AEDs seems to reduce the presence of visible fluorescence in such tumors and should thus be taken into account in the clinical setting.

Keywords: low-grade glioma, 5-aminolevulinic acid, protoporphyrin IX, fluorescence, antiepileptic drugs

INTRODUCTION

Gliomas are the most common intracranial tumors representing approximately 70% of all primary brain tumors (1, 2). It is well-known that gross-total resection correlates with improved progression-free and overall survival in patients with low-grade gliomas (LGGs) (3–6). Thus, maximum safe resection of LGGs is regarded nowadays as the recommended primary treatment to delay potential malignant transformation (7, 8). However, such maximum safe resection is only achieved in the minority of LGGs due to their infiltrative growth and undefined borders (9).

Surgery using 5-aminolevulinic acid (ALA) induced protoporphyrin IX (PpIX) fluorescence has been introduced to the neurosurgical field for improved intraoperative tumor visualization (10). In the last two decades, such fluorescence-guided resections were especially applied to optimize surgery of high-grade gliomas (HGGs) (11). In this sense, 5-ALA fluorescence-guided surgery results in a significantly higher frequency of complete resections and a prolonged progression-free survival in HGGs (12–17). In the last years, 5-ALA was also increasingly investigated during surgery of radiologically suspected LGGs (3, 7, 11, 13, 18–21). According to the data of these first clinical studies, 5-ALA induced fluorescence is a powerful marker to identify potential regions of malignant transformation (anaplastic foci) during surgery of suspected LGG and thus to avoid histopathological undegrading. However, the majority of pure LGGs cannot be visualized by visible fluorescence according to the current literature (3, 7, 11, 13, 18, 19, 21, 22).

The exact mechanisms of PpIX accumulation and thus the presence or absence of visible 5-ALA induced fluorescence in gliomas are still unclear. A large variety of factors were suspected to influence visible 5-ALA fluorescence such as increased metabolism and up-regulation of porphyrin-producing enzymes (23), reduced iron metabolism within neoplastic cells (24), and reduction of activity of the ferrochelatase enzyme that converts fluorescing PpIX into heme (25). Recently, an *in-vitro* study reported that antiepileptic drugs (AEDs) result in an injury of the mitochondrial membrane and thus lead to inhibition of PpIX synthesis in glioma cells (26). Nowadays, AEDs are frequently administered to patients suffering from LGG prior to surgery. We hypothesize that administration of AEDs might influence the presence of visible fluorescence in LGGs during surgical resection.

The aim of the present study was thus to investigate the role of 5-ALA induced fluorescence in LGG surgery and analyze the influence of AEDs on the presence of visible fluorescence.

MATERIALS AND METHODS

Patient Population

Patients that underwent resection of a newly diagnosed suspected LGG at the Burdenko Neurosurgical Institute after 5-ALA administration between March 2014 and March 2016 were recruited. In our study, altogether 27 patients with a histopathologically confirmed LGG were finally included. Our study cohort included 19 men and eight women with a median age of 33 years (range: 18–66 year). According to our histopathological analysis, 14 diffuse astrocytomas, 6 oligodendrogliomas, 4 pilocytic astrocytomas, 2 gemistocytic astrocytomas, and one desmoplastic infantile ganglioglioma were diagnosed. The application of 5-ALA during surgery was feasible in all 27 patients. In none of our patients, any significant 5-ALA related side effects occurred in our study. Informed consent for the surgical procedure and administration of 5-ALA was obtained from all patients. The study was approved by the local ethics committee of the N. N. Burdenko National Medical Research Center of Neurosurgery (Moscow, Russia).

Inclusion and Exclusion Criteria

Inclusion criteria for enrolment into this study were age $\geq$18 years, MRI–suspected LGG, possible gross total resection (GTR) (i.e., >90%) as judged by preoperative surgical estimation, absence of any known history of liver disease or signs of significant hepatic dysfunction and Karnofsky scale $\geq$70. Exclusion criteria for the administration of 5-ALA were history of photosensitivity, patient, or family history of porphyria, pregnancy, and breast-feeding. Only patients with diagnosis of LGG after surgery remained in the final study cohort.

Surgical Procedure

Patients were administered orally 25 mg/kg bodyweight 5-ALA ("Alasence" NIOPIK, Moscow, Russia) dissolved in 100 ml of water ~3 h before surgery. Depending on the tumor localization,

intraoperative neuromonitoring with sensory/motor evoked potentials, and/or direct stimulation (Viking Select, Nicolet; $n = 21$ patients) as well as awake surgery ($n = 2$ patients) was performed. A modified neurosurgical microscope (Carl Zeiss OPMI Pentero, Germany) equipped with a fluorescent 400 nm UV light module and specific filters were used. Microsurgical tumor removal was performed using primarily standard white light microscopy with assistance of neuronavigation in most cases ($n = 20$ patients). During surgery, the microscope was switched to violet-blue excitation light repeatedly to visualize potential fluorescence.

Fluorescence intensity was visually assessed by a surgeon and determined as "weak" with only a small tumor part showing pink fluorescence with its bulk not fluorescing at all, "moderate" with more than half of the tumor revealing pink fluorescence, and "bright" with the major part of the tumor looking bright red. Spectroscopy-assisted Fluorescence was quantitatively assessed in 12 patients. The level of fluorescence varied from 0 values up to 15 arbitrary units (after data normalization) regarding the intact brain. We specially did not highlight the role of spectroscopy, as it was performed only in some of our patients. Furthermore, also the intratumoral fluorescence homogeneity of each tumor was determined. In this sense, diffuse fluorescence was defined as homogeneous glowing of the whole tumor. In contrast, focal fluorescence was defined as a circumscribed area of fluorescence within an otherwise non-fluorescing tumor. In the course of surgery, tissue samples from fluorescing and/or non-fluorescing areas within the tumor and/or the assumed tumor border were subsequently collected for histopathological analysis. To avoid potential phototoxicity related to 5-ALA, all patients were protected from strong light sources for at least 24 h after drug administration.

Histopathology

All formalin-fixed, paraffin-embedded tissue samples were processed for hematoxylin and eosin (H & E) staining. Tumor diagnosis was established by an experienced neuropathologist according to the current World Health Organization (WHO) histopathological criteria (27). In our study, cell density and proliferation rate (Ki-67 labeling index) was investigated in each of the collected tissue samples.

Preoperative Intake of AEDs

Since the main focus of our study was to investigate the potential influence of AEDs on 5-ALA induced fluorescence, we documented in each patient if AEDs were administered prior to surgery (yes or no). Patients were ingested average AED dosages: valproic acid (up to 1.5 mg per day), levetiracetam (800 mg per day). We did not study each drug separately, as the general series was not large.

Postoperative Course

The neurological status of each patient was investigated before and after surgery to detect potential postoperative deterioration of neurological symptoms. Additionally, the extent of resection was judged according to the results of an early (up-to 72 h post-surgery) post-operative MRI: (1) GTR was present if at least 90% of the tumor mass was removed, (2) subtotal resection if more than 50% of the tumor mass was resected, and (3) partial resection if <50% of the tumor was removed.

Statistical Analysis

Data processing was performed using R software for statistical computing (version 3.4.4). The continuous variables were compared in groups using Mann–Whitney *U*-test. To analyze the relationship between the categorical variables, a Fisher exact test was applied. A logistic regression analysis was performed to adjust for confounders when testing the effect of AED on fluorescence. The results were considered statistically significant for $p < 0.05$.

RESULTS

5-ALA Induced Fluorescence and Histopathological Diagnosis

We observed visible fluorescence during surgery in 14 (52%) of 27 cases, whereas no fluorescence was detected in the remaining 13 cases (48%).

According to the histopathological tumor diagnosis, all 4 pilocytic astrocytomas, all 2 gemistocytic astrocytomas, and the only desmoplastic infantile ganglioglioma showed visible fluorescence. Furthermore, visible fluorescence was found in 4 (29%) of 14 diffuse astrocytomas, and 3 (50%) of 6 oligodendrogliomas. According to the intratumoral fluorescence homogeneity ($n = 14$ cases), 7 tumors had "diffuse" visible fluorescence, while the other 7 gliomas had "focal" sites of visible fluorescence. Details on the fluorescence data of our cohort are provided in **Table 1** and illustrative cases in **Figure 1**.

5-ALA Induced Fluorescence and Histological Parameters

Altogether, 80 tissue samples were collected during surgery from the 27 patients (median: 3 samples; range 1–12 specimens per patient). Of these, visible fluorescence was found in 21 samples (26%), whereas 59 samples (74%) showed no visible fluorescence. Cell density was significantly higher in fluorescence-positive samples (2,180 mm^2) than in fluorescence-negative samples (1,510 mm^2; $p = 0.03$). Additionally, the proliferation rate assessed by Ki-67 labeling index was also significantly higher in fluorescence-positive samples (2.52%) than in fluorescence-negative samples (0.41%; $p = 0.04$).

5-ALA Induced Fluorescence and AEDs

Due to a prior history of preoperative seizures, 15 patients (56%) of our study cohort were taking AEDs before surgery (finlepsin, levetiracetam, trileptal, and/or valproid acid). Of the 15 patients with preoperative AED intake, 11 patients (73%) showed no visible fluorescence during the resection. In contrast, 10 (83%) of the remaining 12 patients without prior AEDs intake showed visible fluorescence. Thus, visible fluorescence was significantly more common in patients without AEDs intake as compared to patients with preoperative AED intake [OR = 0.15 (CI 95% 0.012–1.07), $p = 0.046$]. The AED showed to be a significant factor ($p =$ 0,048) influencing the probability of

TABLE 1 | Intraoperative fluorescence characteristics.

Histopathology	Fluorescence					
	Visible fluorescence					Absence of fluorescene
	Fluorescence grade			Fluorescence homogeneity		
	1-Mild	2-Moderate	3-Bright	Diffuse	Focal	
Diffuse astrocytoma	1 (3.7%)	2 (7.4%)	1 (3.7%)	2 (7.4%)	2 (7.4%)	10 (37%)
Oligodendroglioma	1 (3.7%)	1 (3.7%)	1 (3.7%)	1 (3.7%)	2 (7.4%)	3 (11.1%)
Gemistocytic atrocytoma	–	–	2 (7.4%)	2 (7.4%)	0	0
Pilocytic astrocytoma	2 (7.4%)	1 (3.7%)	1 (3.7%)	1 (3.7%)	3 (11.1%)	0
Desmoplastic infantile ganglioglioma	–	1 (3.7%)	–	1 (3.7%)	0	0
In total:	4 (14.8%)	5 (18.5%)	5 (18.5%)	7 (25.9%)	7 (25.9%)	13 (48.1%)
In total:		14 (52%)			14 (51.8%)	13 (48%)
In total:				27 (100%)		

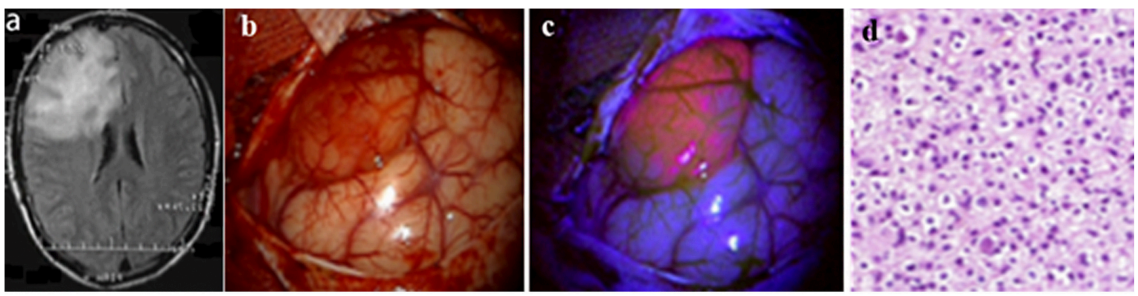

FIGURE 1 | Illustrative case No. 16 (Diffuse fluorescence type). Oligodendroglioma WHO Grade II of the right frontal lobe. **(A)**–Preoperative FLAIR images show a large hyperintense lesion, **(B)**–White light microscopy shows distint cortical abnormalities; **(C)**–The tumor reveals moderate fluorescence with violet-blue excitation light; **(D)**–Histology reveals tumor tissue of a oligodenroglioma WHO grade II. Informed consent has been obtained from the patient for the publication of data, including images.

intraoperative fluorescence when adjusted for other potential confounders (astrocytoma/non-astrocytoma, frontal localization, dexamethasone dose) in a logistic regression model. The other factors included in the model did not show a significant relationship with the fluorescence ($p > 0.05$).

Postoperative Course

After surgery, 21 patients showed stable and four patients improved neurological symptoms. In contrast, deterioration of neurological symptoms was found in the remaining two patients. According to early postoperative MRI, gross total resection was achieved in 16 patients (59%), subtotal resection in 8 patients (30%), and partial resection in three patients (11%). Fluorescence did not correlate with extent of resection.

DISCUSSION

The use 5-ALA induced fluorescence is becoming increasingly popular with the aim of maximizing the extent of resection especially in HGGs and thus improving postoperative patient prognosis. In this sense, fluorescence-guided surgery demonstrated to significantly improve the rate of complete resections in HGGs as compared to microsurgery alone, and this innovative technique also almost doubled the 6-months progression free-survival (16). Recently, visible PpIX fluorescence was found also in other brain lesions such as meningiomas (19), and metastatic tumors (18, 28).

Current Literature: 5-ALA Fluorescence in LGG

So far, the value of 5-ALA induced fluorescence in LGG was only investigated in few studies. In this sense, Ishihara et al. first described in 2007 the application of 5-ALA in two LGG and did not find any visible fluorescence in the multiple collected tissue samples (29). Additionally, Ruge et al. published in 2009 a case report of a 9-year-old girl who underwent fluorescence-guided resection of a pleomorphic xanthoastrocytoma of the right temporal lobe and detected visible fluorescence of the tumor (20). Moreover, Stockhammer et al. published in 2009 a case report of a diffuse astrocytoma WHO grade II with moderate cellular density, higher microvascular density, and visible fluorescence (30). Cases of fluorescence of pilomyxoid astrocytoma and pilocytic astrocytoma were published by Bernal Garcia et al. (31) and Choo et al. (32), respectively. The first series of patients with LGG and 5-ALA was published by Widhalm et al. (33). In this study, all eight diffusely infiltrating WHO grade II gliomas

did not show any visible 5-ALA induced fluorescence during surgery. In a further study, Ewelt et al. reported in 2011 visible fluorescence in only one (8%) of 13 LGGs during surgery (7). Three years after the first patient series, Widhalm et al. published a larger series in 2013 and found visible fluorescence in 4 (9%) of 33 LGGs (34). In another study by Marbacher et al., 8 (40%) of 20 LGGs showed visible fluorescence (18). In 2015, Valdes founded visible fluorescence in 4 (33%) of 12 analyzed LGGs (35). Finally, Jaber et al. found in 2016 in the largest series to date visible fluorescence in 13 (16%) of 82 LGGs (36). Thus, according to the current literature visible fluorescence is observed only in a minority of patients with LGGs.

Current Study: 5-ALA Fluorescence in LGG

Despite of these other studies available in the current literature, our data showed the presence of visible fluorescence in more than half of our cases during surgery. One possible explanation for the higher rate of LGGs with visible fluorescence compared to the current literature might be that we used a slightly higher dose of 5-ALA (25 mg/kg bodyweight) as compared to the other studies (18, 33, 34). However, Stummer et al. compared different doses of 5-ALA in malignant glioma surgery (0.2, 2, 20 mg/kg) and concluded that usage of 5-ALA doses more than 20 mg/kg bodyweight would probably not result in an improved fluorescence effect (37). Another explanation might be that we included also other tumor entities apart from diffusely infiltrating gliomas such as pilocytic astrocytomas or one ganglioglioma. Our promising findings have to be confirmed, however, in independent multicenter studies including a larger cohort of patients suffering from LGG.

Interestingly, we did observe visible fluorescence not only in focal intratumoral areas as previously described (33, 34), but also diffuse fluorescence with homogeneous glowing of the whole tumor. We assume that presence of focal visible fluorescence in LGG might represent areas of potential future malignant transformation. Furthermore, future studies should clarify if the extent of resection could be optimized especially in LGGs with a diffuse fluorescence pattern.

5-ALA Fluorescence and Histopathology

In our study, we observed significantly higher levels of cell density and proliferation in samples with visible fluorescence as compared to no fluorescence. This is in line with the two previous studies by Widhalm et al (33, 34). Similarly, Widhalm et al found a significantly higher mitotic rate, cell density, and nuclear pleomorphism in fluorescing samples as compared to non-fluorescing specimens. Furthermore, the proliferation index assessed by MIB-1 LI was significantly higher in samples with visible fluorescence as compared to non-fluorescing specimens. In this sense, these previous data indicate that visible fluorescence is capable to identify anaplastic foci according to the WHO histopathological criteria (33, 34). Since we also found a significantly higher cell density and proliferation rate in areas of visible fluorescence in a series of LGG, we believe that 5-ALA might serve as an early marker of ongoing malignant transformation of an initial LGG. Future studies with sufficient data on follow-up are needed to clarify this important issue.

5-ALA Fluorescence and AEDs

Nowadays, it is common practice for patients with LGG to have medical treatment of epileptic seizures (38–40). Hefti et al. demonstrated in an *in-vitro* study that the PpIX synthesis was reduced by up to 45% in glioma cells under the effect of phenytoin, but not levetiracetam (26). In our study, we found that visible fluorescence was significantly more common in patients without AEDs intake as compared to patients with preoperative AED intake ($r = 0.56$; $p = 0.045$). Of the 15 patients with preoperative AED intake, 11 patients (73%) showed no visible fluorescence during the resection. In contrast, 10 (83%) of the remaining 12 patients without prior AEDs intake showed visible fluorescence. The underlying mechanisms for the observed influence of AEDs on visible fluorescence is unclear so far. The influence of AEDs on activities of 5-aminolevulinic acid dehydrase and uroporphyrinogen I synthetase in erythrocytes of a Vitamin B6-deficient epileptic boy given valproic acid and carbamazepine was described also by Haust et al. from University of Western Ontario, Canada in 1989 (41). One possible hypothesis might be that AEDs have an influence on the enzyms of the PpIX synthesis in the mitochondria of glioma cells and thus result in presence or absence of fluorescence in LGG. A further study on glioblastoma cell lines found that AEDs (phenytoin/valproates) and dexamethasone may inhibit PpIX synthesis (10). The exact mechanisms for the influence of AEDs on visible fluorescence have to be clarified in future studies.

Future Directions

In future, our first observations should be confirmed in further independent studies with a large cohort of patients. Such larger studies allow also the possibility to analyze the influence of different types of AED separately. Furthermore, the influence of AEDs should also be investigated in HGGs. In cases with lack of visual fluorescence, quantitative detection methods might be useful for improved visualization of LGG tissue. In this sense, confocal microscopy is also a powerful tool to visualize cellular 5-ALA-induced tumor fluorescence within LGGs and at the brain-tumor interface (21). However, convincing data of confocal microscopy in a large cohort of patients with LGG are still missing so far. Another method represents the spectroscopic analysis of PpIX accumulation with specific probes. By this approach, Valdes et al. found that accumulation of PpIX can be detected quantitatively despite the poor diagnostic accuracy of visual fluorescence in LGGs (35, 42). Consequently, this promising approach warrants further investigation in future studies.

CONCLUSIONS

In the present study, we investigated the role of 5-ALA in LGGs and the influence of antiepileptic drugs on intraoperative fluorescence. According to our data, we observed a markedly higher rate of visible fluorescence in our series of LGGs (52%) compared to current literature. Furthermore, increased cell density and proliferation was noted in areas of visible fluorescence. Thus, 5-ALA induced fluorescence might also

improve intraoperative visualization of a subgroup of LGGs and might be also a useful marker for optimized detection of histopathological heterogeneity during surgery of LGGs. Furthermore, preoperative intake of AEDs seems to reduce the presence of visible fluorescence in such tumors according to our preliminary data and thus this issue should be taken into account in the clinical setting. Further, independent multicenter studies including a larger cohort of LGG patients are required to confirm the promising data of this present study.

LIMITATIONS

We understand that the analysis of factors influencing Fluorescence should be multifold. To reach that, we used the model of logistic regression. AED proved to be a significant factor influencing the probability of intraoperative fluorescence, when adjusted for other potential confounders (astrocytoma/non-astrocytoma, frontal localization, dexamethasone dose, IDH1-mutation) in a logistic regression model. The cell density and Ki67 index were revealed only in patients with multiple biopsies (10 patients). It was concluded, that cell density, and Ki67 index were higher for the biopsy samples taken from the fluorescing zone compared to the non-fluorescing one. We've got little evidence on cell density for the rest 17 patients, with their Ki67 index making up mainly 4–5%. As this is a retrospective analysis enrolling 27 patients, we did not plan to study cell density and Ki67 index. Unfortunately, we've got no complete dataset for Ki67 and cell density to include into a logistic regression model.

ETHICS STATEMENT

This study was carried out local committee of the N. N. Burdenko National Medical Research Center of Neurosurgery (Moscow, Russia) with written informed consent from all subjects. All subjects gave written informed consent in accordance with the Declaration of Helsinki. The protocol was approved by the local committee of the N. N. Burdenko National Medical Research Center of Neurosurgery (Moscow, Russia).

AUTHOR CONTRIBUTIONS

SG, GW, and AP designed the study. LS, VJ, and MR collected the date. TS, VL, GP, and AR worked out the technical details. MG and DC analyzed the data and wrote the paper with input from all authors. AS and AP edited the text. KC analyzed the data and wrote the paper with input from all authors.

FUNDING

The reported study was funded by RFBR according to the research projects No. 17-00-00158, No.17-00-00159, and 17-00-00157 [17-00-00162 (K)].

ACKNOWLEDGMENTS

We wish to acknowledge the help provided by our colleagues: Danilov G. V., MD, Ph.D., N. N. Burdenko Scientific Research Neurosurgery Institute, Moscow, Russia for statistic support.

REFERENCES

1. DeAngelis LM. Brain tumors. *N Engl J Med*. (2001) 344:114–23. doi: 10.1056/NEJM200101113440207
2. Ostrom QT, Bauchet L, Davis FG, Deltour I, Fisher JL, Langer CE, et al. The epidemiology of glioma in adults: a "state of the science" review. *Neuro Oncol*. (2014) 16:896–913.doi: 10.1093/neuonc/nou087
3. McGirt MJ, Chaichana KL, Attenello FJ, Weingart JD, Than K, Burger PC, et al. Extend of surgical resection is independently associated with survival in patients with hemispheric infiltraiting low-grade gliomas. *Neurosurgery*. (2008) 63:700–8. doi: 10.1227/01.NEU.0000325729.41085.73
4. Sanai N, Berger MS. Glioma extent of resection and its impact on patient outcome. *Neurosurgery*. (2008) 62:753–66. doi: 10.1227/01.neu.0000318159.21731.cf
5. Schomas DA, Laack NNI, Rao RD, Meyer FB, Shaw EG, O'Neill BP, et al. Intracranial low-grade gliomas in adults: 30-year experience with long-term follow-up at Mayo clinic. *Neuro Oncol*. (2009) 11:437–45. doi: 10.1215/15228517-2008-102
6. Smith JS, Chang EF, Lamborn KR, Chang SM, Prados MD, Cha S, et al. Role of extent of resection in the long-term outcome of low-grade hemispheric gliomas. *J Clin Oncol*. (2008) 26:1338–45. doi: 10.1200/JCO.2007.13.9337
7. Ewelt C, Floeth FW, Felsberg J, Steiger HJ, Sabel M, Langen K-J, et al. Finding the anaplastic focus in diffuse gliomas: the value of Gd-DTPA enhanced MRI, FET-PET, and intraoperative, ALA-derived tissue fluorescence. *Clin Neurol Neurosurg*. (2011) 113:541–7. doi: 10.1016/j.clineuro.2011.03.008
8. Soffietti R, Baumert BG, Bello L, Von Deimling A, Duffau H, Frénay M, et al. Guidelines on management of low-grade gliomas: report of an EFNS–EANO* task force. *Eur J Neurol*. (2010) 17:1124–33. doi: 10.1111/j.1468-1331.2010.03151.x
9. Opoku-Darko M, Lang ST, Artindale J, Cairncross JG, Sevick RJ, Kelly JJP. Surgical management of incidentally discovered diffusely infiltrating low-grade glioma. *J Neurosurg*. (2018) 129:19–26. doi: 10.3171/2017.3.JNS17159
10. Lawrence JE, Steele CJ, Rovin RA, Belton RJ, Winn RJ. Dexamethasone alone and in combination with desipramine, phenytoin, valproic acid or levetiracetam interferes with 5-ALA-mediated PpIX production and cellular retention in glioblastoma cells. *J Neurooncol*. (2016) 127:15–21. doi: 10.1007/s11060-015-2012-x
11. Stummer W, Molina ES. Fluorescence imaging/agents in tumor resection. *Neurosurg Clin*. (2017) 28:569–83. doi: 10.1016/j.nec.2017.05.009
12. Nabavi A, Thurm H, Zountsas B, Pietsch T, Lanfermann H, Pichlmeier U, et al. Five-aminolevulenic acid for fluorescence-guided resection of recurrent malignant gliomas. *Neurosurgery*. (2009) 65:1070–7. doi: 10.1227/01.NEU.0000360128.03597.C7
13. Pichlmeier U, Bink A, Schackert G, Stummer W. Resection and survival in glioblastoma multiforme: an RTOG recursive partitioning analysis of ALA study patients. *Neuro Oncol*. (2008) 10:1025–34. doi: 10.1215/15228517-2008-052
14. Roberts DW, Valdés PA, Harris BT, Hartov A, Fan X, Ji S, et al. Glioblastoma multiforme treatment with clinical trials for surgical resection (aminolevulinic acid). *Neurosurg Clin*. (2012) 23:371–7. doi: 10.1016/j.nec.2012.04.001
15. Roberts DW, Valdés PA, Harris BT, Fontaine KM, Hartov A, Fan X, et al. Coregistered fluorescence-enhanced tumor resection of malignant glioma: relationships between δ-aminolevulinic acid–induced protoporphyrin IX fluorescence, magnetic resonance imaging enhancement, and neuropathological parameters. *J Neurosurg*. (2011) 114:595–603. doi: 10.3171/2010.2.JNS091322
16. Stummer W, Pichlmeier U, Meinel T, Wiestler OD, Zanella F, Reulen H-J. Fluorescence-guided surgery with 5-aminolevulinic acid for resection of

malignant glioma: a randomised controlled multicentre phase III trial. *Lancet Oncol*. (2006) 7:392–401. doi: 10.1016/S1470-2045(06)70665-9
17. Stummer W, Reulen H-J, Meinel T, Pichlmeier U, Schumacher W, Tonn J-C, et al. Extend of resection and survival in glioblastoma multiforme. *Neurosurgery*. (2008) 62:564–76. doi: 10.1227/01.neu.0000317304.31579.17
18. Marbacher S, Klinger E, Schwyzer L, Fischer I, Nevzati E, Diepers M, et al. Use of fluorescence to guide resection or biopsy of primary brain tumors and brain metastases. *Neurosurg Focus*. (2014) 36:E10. doi: 10.3171/2013.12.FOCUS13464
19. Potapov AA, Goryaynov SA, Okhlopkov VA, Shishkina L V, Loschenov VB, Savelieva TA, et al. Laser biospectroscopy and 5-ALA fluorescence navigation as a helpful tool in the meningioma resection. *Neurosurg Rev*. (2016) 39:437–47. doi: 10.1007/s10143-015-0697-0
20. Ruge JR, Liu J. Use of 5-aminolevulinic acid for visualization and resection of a benign pediatric brain tumor: case report. *J Neurosurg Pediatr*. (2009) 4:484–6. doi: 10.3171/2009.6.PEDS08428
21. Sanai N, Snyder LA, Honea NJ, Coons SW, Eschbacher JM, Smith KA, et al. Intraoperative confocal microscopy in the visualization of 5-aminolevulinic acid fluorescence in low-grade gliomas. *J Neurosurg*. (2011) 115:740–8. doi: 10.3171/2011.6.JNS11252
22. Zhang C, Boop FA, Ruge J. The use of 5-aminolevulinic acid in resection of pediatric brain tumors: a critical review. *J Neurooncol*. (2018) 141: 567–73. doi: 10.1007/s11060-018-03004-y
23. Peng Q, Warloe T, Berg K, Moan J, Kongshaug M, Giercksky K-E, et al. 5-Aminolevulinic acid-based photodynamic therapy. *Cancer*. (1997) 79:2282–308.
24. Qian ZM, Chang YZ, Leung G, Du JR, Zhu L, Wang Q, et al. Expression of ferroportin1, hephaestin and ceruloplasmin in rat heart. *Biochim Biophys Acta*. (2007) 1772:527–32. doi: 10.1016/j.bbadis.2007.02.006
25. Kondo M, Hirota N, Takaoka T, Kajiwara M. Heme-biosynthetic enzyme activities and porphyrin accumulation in normal liver and hepatoma cell lines of rat. *Cell Biol Toxicol*. (1993) 9:95–105. doi: 10.1007/BF00755143
26. Hefti M, Albert I, Luginbuehl V. Phenytoin reduces 5-aminolevulinic acid-induced protoporphyrin IX accumulation in malignant glioma cells. *J Neurooncol*. (2012) 108:443–50. doi: 10.1007/s11060-012-0857-9
27. Louis DN, Perry A, Reifenberger G, von Deimling A, Figarella-Branger D, Cavenee WK, et al. The 2016 World Health Organization classification of tumors of the central nervous system: a summary. *Acta Neuropathol*. (2016) 131:803–20. doi: 10.1007/s00401-016-1545-1
28. Kamp MA, Fischer I, Bühner J, Turowski B, Frederick Cornelius J, Steiger H-J, et al. 5-ALA fluorescence of cerebral metastases and its impact for the local-in-brain progression. *Oncotarget*. (2016) 7:66776–89. doi: 10.18632/oncotarget.11488
29. Ishihara R, Katayama Y, Watanabe T, Yoshino A, Fukushima T, Sakatani K. Quantitative spectroscopic analysis of 5-aminolevulinic acid-induced protoporphyrin IX fluorescence intensity in diffusely infiltrating astrocytomas. *Neurol Med Chir*. (2007) 47:53–7. doi: 10.2176/nmc.47.53
30. Stockhammer F, Misch M, Horn P, Koch A, Fonyuy N, Plotkin M. Association of F18-fluoro-ethyl-tyrosin uptake and 5-aminolevulinic acid-induced fluorescence in gliomas. *Acta Neurochir*. (2009) 151:1377. doi: 10.1007/s00701-009-0462-7
31. Bernal García LM, Cabezudo Artero JM, García Moreno R, Marcelo Zamorano MB, Mayoral Guisado C. Fluorescence guided resection with 5-aminolevulinic acid of a pilomyxoid astrocytoma of the third ventricle. *Neurocirugia*. (2017) 28:251–6. doi: 10.1016/j.neucir.2017.03.002
32. Choo J, Takeuchi K, Nagata Y, Ohka F, Kishida Y, Watanabe T, et al. Neuroendoscopic cylinder surgery and 5-aminolevulinic acid photodynamic diagnosis of deep-seated intracranial lesions. *World Neurosurg*. (2018) 116:e35–41. doi: 10.1016/j.wneu.2018.03.112
33. Widhalm G, Wolfsberger S, Minchev G, Woehrer A, Krssak M, Czech T, et al. 5-Aminolevulinic acid is a promising marker for detection of anaplastic foci in diffusely infiltrating gliomas with nonsignificant contrast enhancement. *Cancer Interdiscip Int J Am Cancer Soc*. (2010) 116:1545–52. doi: 10.1002/cncr.24903
34. Widhalm G, Kiesel B, Woehrer A, Traub-Weidinger T, Preusser M, Marosi C, et al. 5-Aminolevulinic acid induced fluorescence is a powerful intraoperative marker for precise histopathological grading of gliomas with non-significant contrast-enhancement. *PLoS ONE*. (2013) 8:e76988. doi: 10.1371/journal.pone.0076988
35. Valdés PA, Jacobs V, Harris BT, Wilson BC, Leblond F, Paulsen KD, et al. Quantitative fluorescence using 5-aminolevulinic acid-induced protoporphyrin IX biomarker as a surgical adjunct in low-grade glioma surgery. *J Neurosurg*. (2015) 123:771–80. doi: 10.3171/2014.12.JNS14391
36. Jaber M, W?lfer J, Ewelt C, Holling M, Hasselblatt M, Niederstadt T, et al. The value of 5-aminolevulinic acid in low-grade gliomas and high-grade gliomas lacking glioblastoma imaging features. *Neurosurgery*. (2016) 78:401–11. doi: 10.1227/NEU.0000000000001020
37. Stummer W, Stepp H, Wiestler OD, Pichlmeier U. Randomized, prospective double-blinded study comparing 3 different doses of 5-aminolevulinic acid for fluorescence-guided resections of malignant gliomas. *Neurosurgery*. (2017) 81:230–9. doi: 10.1093/neuros/nyx074
38. Hirsch LJ. Seizures in patients undergoing resection of low-grade gliomas. *Epilepsy Curr*. (2009) 9:98–100. doi: 10.1111/j.1535-7511.2009.01305.x
39. Kurzwelly D, Herrlinger U, Simon M. Seizures in patients with low-grade gliomas — incidence, pathogenesis, surgical management, and pharmacotherapy. In: Schramm J, editor. *Low-Grade Gliomas. Advances and Technical Standards in Neurosurgery*, vol 35. Vienna: Springer. pp. 81–111. doi: 10.1007/978-3-211-99481-8_4
40. Rudà R, Bello L, Duffau H, Soffietti R. Seizures in low-grade gliomas: natural history, pathogenesis, and outcome after treatments. *Neuro Oncol*. (2012) 14(suppl 4):iv55–64. doi: 10.1093/neuonc/nos199.
41. Haust HL, Poon HC, Carson R, VanDeWetering C, Peter F. Protoporphyrinaemia and decreased activities of 5-aminolevulinic acid dehydrase and uroporphyrinogen I synthetase in erythrocytes of a vitamin B6-deficient epileptic boy given valproic acid and carbamazepine. *Clin Biochem*. (1989) 22:201–11.
42. Valdes PA, Leblond F, Paulsen KD, Kim A, Wilson BC, Conde OM, et al. Combined fluorescence and reflectance spectroscopy for *in vivo* quantification of cancer biomarkers in low-and high-grade glioma surgery. *J Biomed Opt*. (2011) 16:116007. doi: 10.1117/1.3646916

Conflict of Interest Statement: The authors declare that the research was conducted in the absence of any commercial or financial relationships that could be construed as a potential conflict of interest.

frontiers in Surgery

REVIEW
published: 29 May 2019
doi: 10.3389/fsurg.2019.00030

The Use of Spectroscopy Handheld Tools in Brain Tumor Surgery: Current Evidence and Techniques

Nikita Lakomkin[1,2] *and Constantinos G. Hadjipanayis*[1,2]*

[1] Department of Neurosurgery, Mount Sinai Health System, Icahn School of Medicine at Mount Sinai, New York, NY, United States, [2] Department of Neurosurgery, Mount Sinai Health System, Icahn School of Medicine, New York, NY, United States

The fundamental principle in the operative treatment of brain tumors involves achieving maximal safe resection in order to improve postoperative outcomes. At present, challenges in visualizing microscopic disease and residual tumor remain an impediment to complete tumor removal. Spectroscopic tools have the theoretical advantage of accurate tissue identification, coupled with the potential for manual intraoperative adjustments to improve visualization of remaining tumor tissue that would otherwise be difficult to detect. The current evidence and techniques for handheld spectroscopic tools in surgical neuro-oncology are explored here.

Keywords: handheld technologies, gliomas, fluorescence-guided surgery, brain tumors, 5-ALA = 5-aminolevulinic acid, Raman spectroscopy

OPEN ACCESS

Edited by:
Mark Preul,
Barrow Neurological Institute (BNI), United States

Reviewed by:
Jennifer Eschbacher, St. Joseph's Hospital and Medical Center, United States
Nikolay L. Martirosyan, University of Arizona, United States

***Correspondence:**
Constantinos G. Hadjipanayis
constantinos.hadjipanayis@mountsinai.org

Specialty section:
This article was submitted to Neurosurgery, a section of the journal Frontiers in Surgery

Received: *20 January 2019*
Accepted: *09 May 2019*
Published: *29 May 2019*

Citation:
Lakomkin N and Hadjipanayis CG (2019) The Use of Spectroscopy Handheld Tools in Brain Tumor Surgery: Current Evidence and Techniques. Front. Surg. 6:30. doi: 10.3389/fsurg.2019.00030

INTRODUCTION

The fundamental goal in the surgical treatment of brain tumors is achieving the greatest possible extent of resection while minimizing injury to surrounding pathways present in the adjacent brain. Indeed, numerous studies in the literature have demonstrated that the proportion of tumor removed is significantly associated with key postoperative outcome metrics, including overall survival (OS) and progression-free survival (PFS) (1–3). Despite this, however, complete tumor resection remains challenging due to the presence of microscopic disease and infiltrative tumor tissue that is difficult to visually differentiate from the surrounding brain. As such, numerous tools have been developed, for both pre- and intra-operative use [e.g., neuronavigation and intraoperative MRI (iMRI)], in order to assist in the identification and removal of neoplastic tissue (4). More sophisticated MRI techniques, such as whole brain magnetic resonance spectroscopic imaging (MRSI), has allowed for more precise visualization of tumor than would otherwise be possible with standard MRI (5). Multiple studies have highlighted the fact that microscopic involvement of high-grade gliomas (HGGs) extends well-beyond the contrast-enhancing lesion visible on T2-weighted MRI (5, 6). Other techniques, such as neurosurgical virtual reality and simulation have facilitated preoperative visualization and planning (7). Although these instruments have demonstrated utility, intraoperative retraction and tumor resection often result in brain shift, making it challenging to assess the extent of resection in real time. Also, non-specific enhancement after iMRI may be confused with residual tumor. Fluorescence-guided surgery using 5-aminolevulinic acid (5-ALA) has been a crucial addition to the neurosurgeon's toolkit, allowing for direct fluorescence visualization of HGGs using wide-field surgical microscopy (8). However, the infiltrative margin of HGGs and World Health Organization (WHO) grade II low grade gliomas (LGGs) have remained challenging to visualize, since sufficient levels of fluorescence often

cannot be detected using traditionally employed visualization technologies (9). Handheld tools were developed as an adjunct to intraoperative resection, under the premise that real-time use and the ability to adjust the angle of the instrument could facilitate detection of remaining tumor at the time of surgery. Among the most studied techniques has been the use of handheld Raman spectroscopy in the identification of cancer cells during surgery. Other devices aimed at improving visualization in fluorescence guidance surgery have recently been developed. The purpose of this review is to examine the technique and evidence for the utility of handheld spectroscopy tools in neuro-oncologic surgery.

TECHNIQUE

Raman Spectroscopic Probes

Handheld Raman spectroscopic probes harness the traditionally employed Raman spectroscopic technique described decades ago (10). Monochromatic light from a laser is used to shine on an object of interest, resulting in a change in vibrational energy states, which can be detected as electromagnetic radiation that is filtered through a monochromator (11). This results in a molecular fingerprint that can be subsequently harnessed to differentiate various tissue types (12). Neoplastic cells, for instance, have a molecular composition that is distinct from normal brain parenchyma and thus allows for their identification during surgery (13, 14). Glioblastoma (GBM) has been shown to exhibit a decreased lipid band and an increased protein band, while cholesterol bands were found to be absent in metastatic brain lesions (15). One specific advantage of this technique is that water molecules do not interfere with the Raman scattering, thereby increasing its utility in surgical applications. In the operating room, the laser/collection cones, lens, and filter can be combined into a hand-held probe that is then connected to a camera and spectrometer device. This probe can be used intraoperatively during resection in order to both identify tumor cells outside of contrast-enhancing areas on anatomic MRI as well as residual tumor following debulking and resection (16). Unlike the MRI neuronavigation, virtual reality, and other imaging techniques, the handheld probe allows the surgeon to make intraoperative adjustments in terms of positioning and angles following changes in the relative location of anatomic structures during surgery.

5-ALA Fluorescence Visualization

5-ALA is an oral pro-drug and the preoperative administration of this agent results in the accumulation of the fluorescent metabolite protoporphyrin IX in neoplastic lesions, which can be visualized during surgery (17, 18). This is accomplished via excitation of protoporphyrin IX-rich tissue with blue 440 nanometer wavelength light, resulting in the emission of a violet-colored signal (19). Improved visualization of tumors consequently allows for a greater extent of resection than would otherwise be possible under white light. Numerous randomized, controlled trials have demonstrated a benefit to patient survival using this agent, resulting in it gaining recent FDA approval for the treatment of suspected HGGs in the United States (20–22).

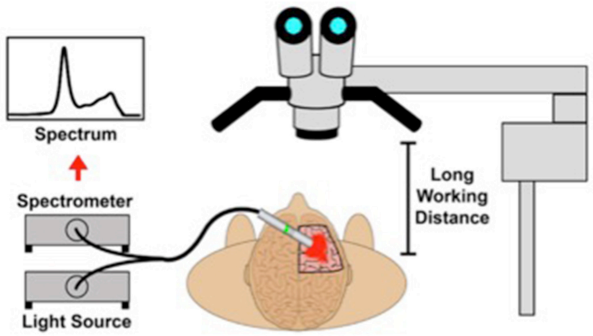

FIGURE 1 | A schematic depicting the intraoperative use of a handheld spectroscopic probe in order to quantify relative protoporphyrin IX levels in various tissues [With permission from Kairdolf et al. (25)].

Despite this, however, the evidence for its utility in the treatment of LGGs is less robust, due to the difficulty in achieving adequate fluorescent signal using wide-field microscopic illumination from a long working distance (9, 23). In addition, visualization of the infiltrative tumor margin becomes more difficult with fluorescence due to the lower number of tumor cells residing away from the tumor bulk. Handheld probes offer distinct advantages in visualizing these tumors, due to both the ability to place the instrument in close proximity to the tissue, as well as potentially generate a precise, quantitative measurement of protoporphyrin IX concentrations (24, 25). These techniques involve utilizing a handheld probe coupled to spectrometer that can be manipulated within the intraoperative field (**Figure 1**) (25, 26).

EVIDENCE

Raman Spectroscopy

Basic Science

An array of *ex-vivo* and animal model studies have demonstrated the value of handheld Raman spectroscopy in differentiating tumor from normal brain tissue. Ji et al. examined the ability of Raman microscopy to discriminate tumor samples from 22 biopsy specimens, and found that Raman spectroscopy detected tumor infiltration in near-perfect agreement with hematoxylin and eosin (H&E) staining (27). The authors concluded that the sensitivity and specificity of the technique was 97.5 and 98.5%, respectively. Similarly, Kalkanis et al. utilized a training set and subsequent validation series in order to employ Raman spectroscopy in distinguishing GBM from gray matter and necrosis. The authors reported 99.6 and 97.8% accuracy in the training and validation cohorts, respectively (28). An *in-vitro* study by Aguiar et al. revealed a sensitivity of 97.4% and a specificity of 100% in the diagnosis of GBM, medulloblastoma, and meningioma (29).

Other studies have revolved around the identification of important biomarkers that could be employed in distinguishing various tumor types. For instance, Zhou et al. demonstrated the utility of Raman spectroscopy in differentiating malignant tissue

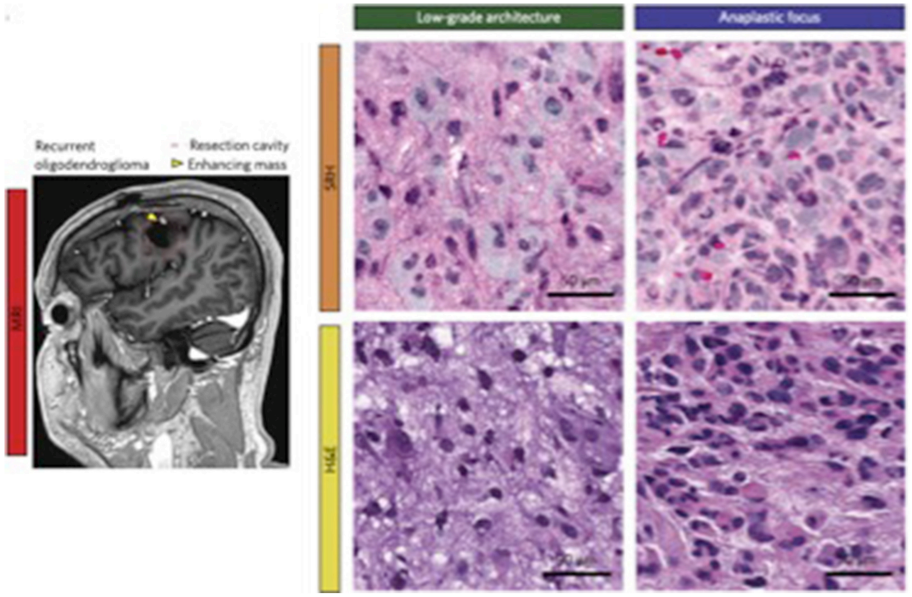

FIGURE 2 | Depiction of Raman-stimulated histology slides alongside traditional haematoxylin and eosin for a patient with a history of recurrent oligodendroglioma [With permission from Orringer et al. (31)].

in 87 samples, revealing the presence of peaks corresponding to lactic acid and ATP in certain tumor tissues when compared to controls (30). These initiatives have been harnessed by investigations focused on their clinical application. Orringer et al. leveraged portable Raman spectroscopy to not only create virtual H&E-stained slides, but to create an algorithm that predicts brain tumor subtypes with 90% accuracy (31). A side-by-side comparison of images generated via Raman-stimulated histology and traditional haematoxylin and eosin staining is depicted in **Figure 2**. These techniques have already been replicated in the pediatric population, where Hollon et al. created a Raman spectroscopic-based algorithm that had near-perfect histologic concordance and could differentiate low and high-grade tumors with 100% accuracy (32). These findings demonstrate the substantial potential of algorithm-driven, handheld spectroscopy tools in providing valuable real-time data that could alter clinical management.

Clinical Studies

Comparatively few studies have examined the feasibility and utility of handheld Raman spectroscopy using real-time, *in-vivo* experimental design. Jermyn et al. employed a handheld probe in 17 patients with grade 2-4 gliomas and compared imaging findings with obtained biopsy specimens (33). The authors concluded that intraoperative Raman imaging facilitated the detection of cancer cells with an accuracy of 92%, compared to 73% using bright microscopy and MRI. The sensitivity and specificity in the differentiation of neoplasia from normal brain parenchyma were 93 and 91%, respectively. Desroches et al. developed a handheld Raman spectroscopy system and demonstrated its preliminary use in a swine brain biopsy model, followed by a human validation study involving 19 grade 2-4 glioma patients. The authors concluded that the handheld spectroscopy was able to detect malignancy during surgery with a sensitivity and specificity of 80 and 90%, respectively (34). Characteristics of selected studies on the role of Raman in diagnosing different types of brain tumors are presented in **Table 1**.

Future Multimodal Techniques

Much of the recent literature on Raman spectroscopy in neurosurgical oncology revolves around the coupling of this technique to other, novel modalities in order to facilitate visualization. For instance, Neuschmelting et al. examined a combined approach of surface-enhanced Raman scattering and multispectral optoacoustic tomography in the detection of GBM cells in mouse brains. The authors reported that this new model exhibited a highly sensitive surface detection of infiltrating GBMs and could be transferrable to other animal models and potentially human trials (35). Meanwhile, Karabeber et al. demonstrated that the use of surface-enhanced Raman nanoparticles in the guidance of mouse GBM resection resulted in greater removal of residual tumor when compared to the use of white light alone (36). Jermyn et al. employed a combined, multimodal spectroscopic technique that incorporated fluorescence spectroscopy, diffuse reflectance spectroscopy, and Raman spectroscopy. The authors described high rates of accuracy, sensitivity, and specificity in differentiating brain, lung, colon, and skin malignancies *in situ* (37).

Visualization in Fluorescence-Guided Surgeries

Basic Science

Numerous laboratory investigations have examined the feasibility and efficacy of handheld probes in detecting protoporphyrin IX. Kim et al. used a handheld, fiberoptic

TABLE 1 | Characteristics of selected studies reporting on the utility of Raman spectroscopy in tumor.

References	Journal	Number of samples	Tumor histology	Relevant outcome metric	Rate	Notes
CLINICAL AND BASIC SCIENCE STUDIES						
Ji et al. (27)	Sci Transl Med	22	Gliomas (both LGG and HGG)	Tumor infiltration (compared to H&E)	Sensitivity = 97.5% Specificity = 98.5%	–
Kalkanis et al. (28)	J Neurooncol	40	GBM	Differentiation of GBM from gray matter and necrosis	99.6 and 97.8% accuracy in training and validation cohorts, respectively	Utilized a training set with subsequent validation series
Aguiar et al. (29)	Photomed Laser Surg	172	GBM, medulloblastoma, meningioma	Diagnosis of tumor types	Sensitivity = 97.4% Specificity = 100%	–
Orringer et al. (31)	Nat Biomed Eng	30	Gliomas (both LGG and HGG) + meningioma, lymphoma, medulloblastoma, and metastases	Prediction of brain tumor subtypes (compared to H&E)	>92% accuracy	–
Hollon et al. (32)	Cancer Res	25	All tumor types	Prediction of brain tumor subtypes (compared to H&E)	92–96% accuracy	Pediatric brain tumor patients
Jermyn et al. (33)	Sci Transl Med	161	Gliomas (WHO grades II-IV)	Detection of malignancy (vs. bright microscopy and MRI)	Sensitivity = 93% Specificity = 91%	*In-vivo* experimental design
Desroches et al. (34)	Sci Rep	280	Gliomas (WHO grades II-IV)	Detection of malignancy (compared to H&E)	Sensitivity = 80% Specificity = 90%	Authors used handheld probe in swine brain biopsy model first, followed by human validation study

GBM, Glioblastoma multiforme; HGG, High grade glioma; LGG, Low grade glioma; MRI, Magnetic resonance imaging; WHO, World Health Organization.

probe in order to quantify the fluorescence signal in *ex vivo* mouse brain tumors (38). They subsequently validated their technique using an *in vivo* rabbit brain tumor surgery model and were able to accurately differentiate tumor tissue from normal brain parenchyma. Cornelius et al. employed this same tool in order to examine its ability to differentiate different tumor types in humans (39). The authors concluded that the probe was a very sensitive tool in detecting 5-ALA-based fluorescence among 17 tumor biopsies, including differentiating between GBM and meningioma samples with the same precision as a laboratory spectrometer. Kairdolf et al. employed a low-cost hand-held spectroscopic instrument in order to compare the sensitivity of the handheld device with traditional surgical microscopes (25). They found that the handheld tool was, at a minimum, 3 times more sensitive and demonstrated strong specificity in differentiating tumor cells from normal brain tissue.

Clinical Studies

These handheld visualization devices have also been studied to assess their use and efficacy in the operating room. Haj-Hosseini et al. employed a handheld spectroscopic tool in order to make intraoperative measurements of white, gray, and known tumor tissue from patients undergoing GBM resection under 5-ALA fluorescence (26). The authors demonstrated the feasibility of this probe to accurately detect protoporphyrin IX fluorescence at the tumor margins *in vivo*. Richter et al. performed a study to directly compare the sensitivity of a hand-held fluorescence probe with fluorescence-guided microscopy in 16 patients undergoing resection of HGGs using 5-ALA. The authors highlighted that they were able to not only successfully integrate the tool into the operative routine, but that the handheld probe was superior to the microscope in sensitivity and detected additional tumor foci after the initial debulking using fluorescence-guided microscopy (40). The intraoperative use of the hand-held fluorescence probe is highlighted in **Figure 3**. These techniques have also been studied in other tumor types. Valdes et al. used a handheld probe tip in the intraoperative resection of low-grade gliomas, meningiomas, metastatic tumors, and GBM in order to compare quantitative fluorescence spectra across tumor types (41). They concluded that there was a significant difference in the quantitative measurements of protoporphyrin IX concentrations for all tumor groups when compared to normal brain tissue, as well as high sensitivity when compared to conventional fluorescence measurements.

DISCUSSION

Tumor Identification Using Raman Probes

Overall, the use of handheld Raman spectroscopic imaging as an adjunct to neurosurgical resection is a promising development in brain tumor treatment and has been corroborated in a variety of clinical and basic science literature. The unique spectra allow for the differentiation of various tissue types. Numerous investigations have identified key biomarkers that can be employed to not only discriminate between tumor and normal parenchyma, but between various tumor types for both intra- and extra-axial lesions. Zhou et al., for instance, reported a detailed

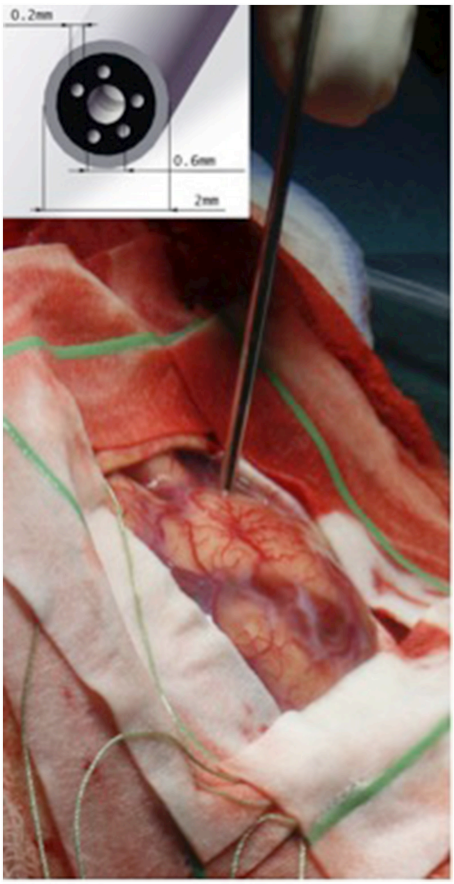

FIGURE 3 | Intraoperative placement of the hand-held fluorescent probe on the cortical surface [With permission from Richter et al. (40)].

analysis of Raman spectra for an array of tumors, including GBM, acoustic neuroma, pituitary adenoma, and meningioma (42). This is turn has been used in several studies to create predictive algorithms with the capability to correctly predict histologic subtype with >90% accuracy (31, 32). The strong predictive capacity of this modality makes it useful in both the diagnosis and subsequent operative treatment of brain tumors.

Intraoperative Advantages

Although numerous other modalities facilitate improved preoperative visualization of tumor, handheld spectroscopic tools offer the advantage of not only strong discriminatory capacity based on molecular footprint, but the ability to make physical adjustments intraoperatively. Unlike other visualization techniques, including intraoperative MRI, handheld probes can be angled away in order to inspect portions of the resection cavity that may not otherwise be visible. This may facilitate the identification of Raman-positive foci and removal of additional tumor. Karabeber et al. performed a study involving the surgical resection of GBM in mice, comparing resection with light microscopy, Raman microscopy, and hand-held Raman scanning (36). The authors demonstrated that the hand-held device was associated with a greater extent of resection, and noted several instances where the hand-held tool detected foci that were missed using microscopy, including the presence of tumor within the right lateral ventricle. This increased flexibility of hand-held devices offers the theoretical advantage of a potential combined therapy, where intraoperative Raman identification may be used alongside 5-ALA fluorescence-guided resection or conventional microscopic imaging. Although the application of 5-ALA has been shown to alter the Raman spectra of bladder tissues, this interference may be improved via fluorescence-subtraction algorithms, making a dual approach potentially viable *in-vivo* (43). Further studies are needed to explore the utility of combined modalities in the resection of brain tumors.

5-ALA Visualization

Other handheld tools have been developed in order to facilitate both visualization and quantification of protoporphyrin IX concentrations for patients undergoing tumor resection with 5-ALA. While the detection of fluorescence using traditional wide-field microscopy has been challenging for LGGs and other tumor types, handheld probes offer several advantages that can improve the utility of 5-ALA for these tumors. First, the ability to place these probes in close proximity to the tissue helps ameliorate the light scatter and suboptimal angle between traditionally employed microscopes and the resection bed (9). Second, the tools can be equipped with spectroscopic instrumentation that allows for the quantification of metabolite concentration, rather than relying on the subjective intraoperative assessment of visualized fluorescent signal (23). These advantages have been demonstrated in numerous studies highlighting the feasibility and efficacy of handheld probes *in vivo*. The ability to directly quantify fluorescence measurements in LGGs, meningiomas, and metastatic lesions, as well as the ability to intraoperatively distinguish them from brain parenchyma may increase the role of 5-ALA for these tumor types in the near future (41).

Clinical Relevance

There is substantial literature reporting the relationship between the extent of resection and subsequent postoperative outcomes in patients with brain tumors (1–3). Identification of microscopic disease and residual tumor remains the primary challenge in neuro-oncology. As such, all tools that facilitate the intraoperative visualization of lesions have the potential to provide clinical benefit to patients. Despite this, however, there is a dearth of literature examining the relationship between the use of spectroscopic handheld tools and improved postoperative clinical endpoints. Additional studies are needed to examine the association between intraoperative Raman spectroscopy, protoporphyrin IX quantification tools, extent of resection, and OS/PFS.

CONCLUSIONS

There is significant evidence demonstrating the utility of Raman spectroscopic imaging in identifying areas of malignancy in both human and animal specimens. Several

studies have highlighted the use of concomitant algorithms in accurately diagnosing histologic tumor subtype and the feasibility of using handheld spectroscopy tools in the operative setting. In addition, numerous studies have demonstrated the efficacy of handheld probes in the operative quantification of protoporphyrin IX levels for patients undergoing 5-ALA fluorescence-guided resection. Further studies exploring the relationship between *in-vivo* spectroscopic use, extent of resection, and postoperative survival are needed to better assess the impact of these tools on patient outcomes.

AUTHOR CONTRIBUTIONS

All authors listed have made a substantial, direct and intellectual contribution to the work, and approved it for publication.

REFERENCES

1. Brown TJ, Brennan MC, Li M, Church EW, Brandmeir NJ, Rakszawski KL, et al. Association of the extent of resection with survival in glioblastoma: a systematic review and meta-analysis. *JAMA Oncol*. (2016) 2:1460–9. doi: 10.1001/jamaoncol.2016.1373
2. Xia L, Fang C, Chen G, Sun C. Relationship between the extent of resection and the survival of patients with low-grade gliomas: a systematic review and meta-analysis. *BMC Cancer*. (2018) 18:48. doi: 10.1186/s12885-017-3909-x
3. Kuhnt D, Becker A, Ganslandt O, Bauer M, Buchfelder M, Nimsky C. Correlation of the extent of tumor volume resection and patient survival in surgery of glioblastoma multiforme with high-field intraoperative MRI guidance. *Neuro Oncol*. (2011) 13:1339–48. doi: 10.1093/neuonc/nor133
4. Schulder M, Carmel PW. Intraoperative magnetic resonance imaging: impact on brain tumor surgery. *Cancer Control J Moffitt Cancer Cent*. (2003) 10:115–24. doi: 10.1177/107327480301000203
5. Cordova JS, Shu HK, Liang Z, Gurbani SS, Cooper LA, Holder CA, et al. Whole-brain spectroscopic MRI biomarkers identify infiltrating margins in glioblastoma patients. *Neuro Oncol*. (2016) 18:1180–9. doi: 10.1093/neuonc/now036
6. Cordova JS, Gurbani SS, Olson JJ, Liang Z, Cooper LA, Shu HG, et al. A systematic pipeline for the objective comparison of whole-brain spectroscopic MRI with histology in biopsy specimens from grade III glioma. *Tomogr Ann Arbor Mich*. (2016) 2:106–16. doi: 10.18383/j.tom.2016.00136
7. Chan S, Conti F, Salisbury K, Blevins NH. Virtual reality simulation in neurosurgery: technologies and evolution. *Neurosurgery*. (2013) 72 (Suppl 1):154–64. doi: 10.1227/NEU.0b013e3182750d26
8. Hadjipanayis CG, Widhalm G, Stummer W. What is the surgical benefit of utilizing 5-ALA for fluorescence-guided surgery of malignant gliomas? *Neurosurgery*. (2015) 77:663–73. doi: 10.1227/NEU.0000000000000929
9. Wei L, Roberts DW, Sanai N, Liu JTC. Visualization technologies for 5-ALA-based fluorescence-guided surgeries. *J Neurooncol*. (2018) 141:495–505. doi: 10.1007/s11060-018-03077-9
10. Raman CV. Part II.—The Raman effect. Investigation of molecular structure by light scattering. *Trans Faraday Soc*. (1929) 25:781–92. doi: 10.1039/TF9292500781
11. Downes A, Elfick A. Raman spectroscopy and related techniques in biomedicine. *Sensors*. (2010) 10:1871–89. doi: 10.3390/s100301871
12. Tu Q, Chang C. Diagnostic applications of Raman spectroscopy. *Nanomed Nanotechnol Biol Med*. (2012) 8:545–58. doi: 10.1016/j.nano.2011.09.013
13. Wills H, Kast R, Stewart C, Rabah R, Pandya A, Poulik J, et al.Raman spectroscopy detects and distinguishes neuroblastoma and related tissues in fresh and (banked) frozen specimens. *J Pediatr Surg*. (2009) 44:386–91. doi: 10.1016/j.jpedsurg.2008.10.095
14. Depciuch J, Kaznowska E, Zawlik I, Wojnarowska R, Cholewa M, Heraud P, et al. Application of Raman spectroscopy and infrared spectroscopy in the identification of breast cancer. *Appl Spectrosc*. (2016) 70:251–63. doi: 10.1177/0003702815620127
15. Uckermann O, Galli R, Meinhardt M, Steiner G, Schackert G, Kirsch M. Path-15. optical analysis of human brain tumors by raman spectroscopy. *Neuro Oncol*. (2017) 19(Suppl 6):vi173–vi173. doi: 10.1093/neuonc/nox168.706
16. Jermyn M, Desroches J, Mercier J, St-Arnaud K, Guiot MC, Leblond F, et al. Raman spectroscopy detects distant invasive brain cancer cells centimeters beyond MRI capability in humans. *Biomed Opt Express*. (2016) 7:5129–37. doi: 10.1364/BOE.7.005129
17. Tonn J-C, Stummer W. Fluorescence-guided resection of malignant gliomas using 5-aminolevulinic acid: practical use, risks, and pitfalls. *Clin Neurosurg*. (2008) 55:20–26. Available online at: https://pdfs.semanticscholar.org/29de/0409643ebcdcc768ade61f30ca33d1296026.pdf
18. Lakomkin N, Hadjipanayis CG. Fluorescence-guided surgery for high-grade gliomas. *J Surg Oncol*. (2018) 118:356–61. doi: 10.1002/jso.25154
19. Ferraro N, Barbarite E, Albert TR, Berchmans E, Shah AH, Bregy A, et al. The role of 5-aminolevulinic acid in brain tumor surgery: a systematic review. *Neurosurg Rev*. (2016) 39:545–55. doi: 10.1007/s10143-015-0695-2
20. Stummer W, Pichlmeier U, Meinel T, Wiestler OD, Zanella F, Reulen HJ, et al. Fluorescence-guided surgery with 5-aminolevulinic acid for resection of malignant glioma: a randomised controlled multicentre phase III trial. *Lancet Oncol*. (2006) 7:392–401. doi: 10.1016/S1470-2045(06)70665-9
21. Stummer W, Tonn JC, Mehdorn HM, Nestler U, Franz K, Goetz C, et al. Counterbalancing risks and gains from extended resections in malignant glioma surgery: a supplemental analysis from the randomized 5-aminolevulinic acid glioma resection study. Clinical article. *J Neurosurg*. (2011) 114:613–23. doi: 10.3171/2010.3.JNS097
22. Díez Valle R, Tejada Solis S, Idoate Gastearena MA, García de Eulate R, Domínguez Echávarri P, Aristu Mendiroz J. Surgery guided by 5-aminolevulinic fluorescence in glioblastoma: volumetric analysis of extent of resection in single-center experience. *J Neurooncol*. (2011) 102:105–13. doi: 10.1007/s11060-010-0296-4
23. Belykh E, Martirosyan NL, Yagmurlu K, Miller EJ, Eschbacher JM, Izadyyazdanabadi M, et al. Intraoperative fluorescence imaging for personalized brain tumor resection: current state and future directions. *Front Surg*. (2016) 3:55. doi: 10.3389/fsurg.2016.00055
24. Stummer W, Tonn JC, Goetz C, Ullrich W, Stepp H, Bink A, et al. 5-Aminolevulinic acid-derived tumor fluorescence: the diagnostic accuracy of visible fluorescence qualities as corroborated by spectrometry and histology and postoperative imaging. *Neurosurgery*. (2014) 74:310–9; discussion 319–20. doi: 10.1227/NEU.0000000000000267
25. Kairdolf BA, Bouras A, Kaluzova M, Sharma AK, Wang MD, Hadjipanayis CG, et al. Intraoperative spectroscopy with ultrahigh sensitivity for image-guided surgery of malignant brain tumors. *Anal Chem*. (2016) 88:858–67. doi: 10.1021/acs.analchem.5b03453
26. Haj-Hosseini N, Richter J, Andersson-Engels S, Wårdell K. Optical touch pointer for fluorescence guided glioblastoma resection using 5-aminolevulinic acid. *Lasers Surg Med*. (2010) 42:9–14. doi: 10.1002/lsm.20868
27. Ji M, Lewis S, Camelo-Piragua S, Ramkissoon SH, Snuderl M, Venneti S, et al. Detection of human brain tumor infiltration with quantitative stimulated Raman scattering microscopy. *Sci Transl Med*. (2015) 7:309ra163. doi: 10.1126/scitranslmed.aab0195
28. Kalkanis SN, Kast RE, Rosenblum ML, Mikkelsen T, Yurgelevic SM, Nelson KM, et al. Raman spectroscopy to distinguish grey matter, necrosis, and glioblastoma multiforme in frozen tissue sections. *J Neurooncol*. (2014) 116:477–85. doi: 10.1007/s11060-013-1326-9
29. Aguiar RP, Silveira L, Falcão ET, Pacheco MTT, Zângaro RA, Pasqualucci CA. Discriminating neoplastic and normal brain tissues *in vitro* through Raman spectroscopy: a principal components analysis classification model. *Photomed Laser Surg*. (2013) 31:595–604. doi: 10.1089/pho.2012.3460
30. Zhou Y, Liu C, Wu B, Zhang C, Yu X, Cheng G, et al. Invited article: molecular biomarkers characterization for human brain glioma grading using

visible resonance Raman spectroscopy. *APL Photonics*. (2018) 3:120802. doi: 10.1063/1.5036637
31. Orringer DA, Pandian B, Niknafs YS, Hollon TC, Boyle J, Lewis S, et al. Rapid intraoperative histology of unprocessed surgical specimens via fibre-laser-based stimulated Raman scattering microscopy. *Nat Biomed Eng*. (2017) 1:0027. doi: 10.1038/s41551-016-0027
32. Hollon TC, Lewis S, Pandian B, Niknafs YS, Garrard MR, Garton H, et al. Rapid intraoperative diagnosis of pediatric brain tumors using stimulated raman histology. *Cancer Res*. (2018) 78:278–89. doi: 10.1158/0008-5472.CAN-17-1974
33. Jermyn M, Mok K, Mercier J, Desroches J, Pichette J, Saint-Arnaud K, et al. Intraoperative brain cancer detection with Raman spectroscopy in humans. *Sci Transl Med*. (2015) 7:274ra19. doi: 10.1126/scitranslmed.aaa2384
34. Desroches J, Jermyn M, Pinto M, Picot F, Tremblay MA, Obaid S, et al. A new method using Raman spectroscopy for *in vivo* targeted brain cancer tissue biopsy. *Sci Rep*. (2018) 8:1792. doi: 10.1038/s41598-018-20233-3
35. Neuschmelting V, Harmsen S, Beziere N, Lockau H, Hsu HT, Huang R, et al. Dual-modality surface-enhanced resonance raman scattering and multispectral optoacoustic tomography nanoparticle approach for brain tumor delineation. *Small*. (2018) 14:e1800740. doi: 10.1002/smll.201800740
36. Karabeber H, Huang R, Iacono P, Samii JM, Pitter K, Holland EC, et al. Guiding brain tumor resection using surface-enhanced raman scattering nanoparticles and a hand-held raman scanner. *ACS Nano*. (2014) 8:9755–66. doi: 10.1021/nn503948b
37. Jermyn M, Mercier J, Aubertin K, Desroches J, Urmey K, Karamchandiani J, et al. Highly accurate detection of cancer *in situ* with intraoperative, label-free, multimodal optical spectroscopy. *Cancer Res*. (2017) 77:3942–50. doi: 10.1158/0008-5472.CAN-17-0668
38. Kim A, Khurana M, Moriyama Y, Wilson BC. Quantification of *in vivo* fluorescence decoupled from the effects of tissue optical properties using fiber-optic spectroscopy measurements. *J Biomed Opt*. (2010) 15:067006. doi: 10.1117/1.3523616
39. Cornelius JF, Placke JM, Knipps J, Fischer I, Kamp M, Steiger HJ. Minispectrometer with handheld probe for 5-ALA based fluorescence-guided surgery of brain tumors: preliminary study for clinical applications. *Photodiagn Photodyn Ther*. (2017) 17:147–53. doi: 10.1016/j.pdpdt.2016.12.007
40. Richter JCO, Haj-Hosseini N, Hallbeck M, Wårdell K. Combination of hand-held probe and microscopy for fluorescence guided surgery in the brain tumor marginal zone. *Photodiagn Photodyn Ther*. (2017) 18:185–92. doi: 10.1016/j.pdpdt.2017.01.188
41. Valdés PA, Leblond F, Kim A, Harris BT, Wilson BC, Fan X, et al. Quantitative fluorescence in intracranial tumor: implications for ALA-induced PpIX as an intraoperative biomarker. *J Neurosurg*. (2011) 115:11. doi: 10.3171/2011.2.JNS101451
42. Zhou Y, Liu CH, Sun Y, Pu Y, Boydston-White S, Liu Y, et al. Human brain cancer studied by resonance Raman spectroscopy. *J Biomed Opt*. (2012) 17:116021. doi: 10.1117/1.JBO.17.11.116021
43. Grimbergen MCM, van Swol CFP, van Moorselaar RJA, Uff J, Mahadevan-Jansen A, Stone N. Raman spectroscopy of bladder tissue in the presence of 5-aminolevulinic acid. *J Photochem Photobiol B*. (2009) 95:170–6. doi: 10.1016/j.jphotobiol.2009.03.002

Conflict of Interest Statement: CH is a consultant for NXDC and Synaptive Medical Inc. He will receive royalties from NXDC. He has also received speaker fees by Carl Zeiss and Leica.

The remaining author declares that the research was conducted in the absence of any commercial or financial relationships that could be construed as a potential conflict of interest.

frontiers in Surgery

REVIEW
published: 06 June 2019
doi: 10.3389/fsurg.2019.00031

Quantitative Wide-Field Imaging Techniques for Fluorescence Guided Neurosurgery

Pablo A. Valdes[1], Parikshit Juvekar[1], Nathalie Y. R. Agar[1], Sylvain Gioux[2] and Alexandra J. Golby[1]*

[1] Department of Neurosurgery, Harvard Medical School, Brigham and Women's Hospital, Boston, MA, United States, [2] ICube Laboratory, University of Strasbourg, Télécom Physique Strasbourg, Alsace, France

Fluorescence guided surgery (FGS) has fueled the development of novel technologies aimed at maximizing the utility of fluorescence imaging to help clinicians diagnose and in certain cases treat diseases across a breadth of disciplines such as dermatology, gynecology, oncology, ophthalmology, and neurosurgery. In neurosurgery, the goal of FGS technologies is to provide the neurosurgeon with additional information which can serve as a visual aid to better identify tumor tissue and associated margins. Yet, current clinical FGS technologies are qualitative in nature, limiting the ability to make accurate, reliable, and repeatable measurements. To this end, developments in fluorescence quantification are needed to overcome current limitations of FGS. Here we present an overview of the recent developments in quantitative fluorescence guidance technologies and conclude with the most recent developments aimed at wide-field quantitative fluorescence imaging approaches in neurosurgery.

Keywords: fluorescence-guided surgery, quantitative fluorescence imaging, protoporphyrin IX, tissue optical properties, brain tumors

OPEN ACCESS

Edited by:
Evgenii Belykh, Barrow Neurological Institute (BNI), United States

Reviewed by:
Leonard Nelson, University of Washington, United States
Kareem Zaghloul, National Institute of Neurological Disorders and Stroke (NINDS), United States
Joseph Georges, Philadelphia College of Osteopathic Medicine, United States

****Correspondence:***
Pablo A. Valdes
pvaldesquevedo@bwh.harvard.edu

Specialty section:
This article was submitted to Neurosurgery, a section of the journal Frontiers in Surgery

Received: *05 February 2019*
Accepted: *15 May 2019*
Published: *06 June 2019*

Citation:
Valdes PA, Juvekar P, Agar NYR, Gioux S and Golby AJ (2019) Quantitative Wide-Field Imaging Techniques for Fluorescence Guided Neurosurgery. Front. Surg. 6:31. doi: 10.3389/fsurg.2019.00031

INTRODUCTION

Fluorescence guided surgery (FGS) has fueled the development of novel technologies aimed at maximizing the utility of fluorescence imaging to help clinicians diagnose and in certain cases treat diseases across a breadth of disciplines such as dermatology, gynecology, oncology, ophthalmology, and neurosurgery. In neurosurgery, FGS has been applied in a variety of diseases including high grade gliomas where the largest experience exists, but also in other brain tumors including low-grade gliomas, meningiomas, lymphomas, and metastases. In addition to the use of FGS for brain tumors, neurosurgeon have used fluorescence for vascular imaging as well (1–11). The most common fluorophores, or fluorescent biomarkers in use include 5-aminolevulinic acid (5-ALA) induced protoporphyrin IX (PpIX), fluorescein sodium, methylene blue, and indocyanine green (ICG) (**Figures 1A–D**). There are also a variety of novel targeted fluorescent agents being tested in clinical trials (4, 9). FGS requires the development of novel agents with the ability to map the biological properties of interest (e.g., high specificity and sensitivity for tissue) as well as accompanying intraoperative instrumentation technologies for accurate, sensitive, specific, and objective assessment of the fluorescence emitted by these biomarkers.

Exciting developments in novel technologies for FGS to treat brain tumors include new wide-field fluorescence microscopes and hand-held devices. The goal of these technologies is to provide the neurosurgeon with additional information which can serve as a visual aid to better identify

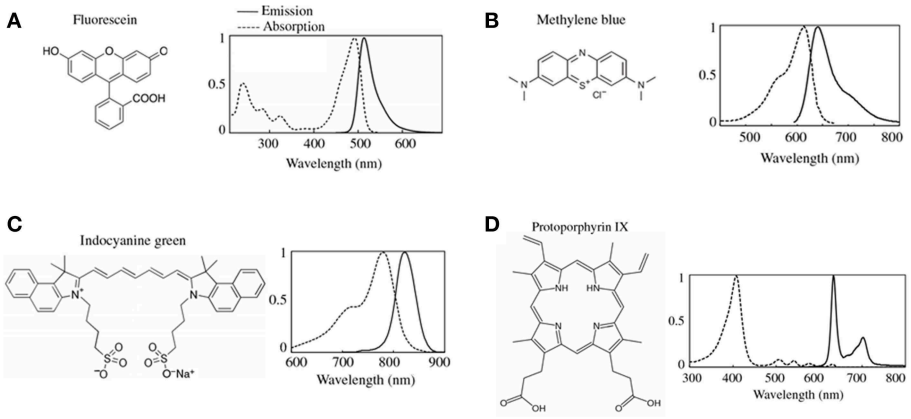

FIGURE 1 | Common fluorophores in clinical use. The chemical formulas and the associated excitation and emission spectra for the most common FDA approved fluorescence dyes are shown in **(A)** fluorescein, **(B)** methylene blue, **(C)** indocyanine green (ICG), and **(D)** protoporphryin IX (PpIX). Figure adapted with permission from DSouza et al. (12).

tumor tissue and associated margins. Beyond implementation of 5-ALA-PpIX across multiple different pathologies (e.g., gliomas, meningiomas, metastases, CNS lymphomas, spinal tumors), quantification of fluorescence in FGS opens a new avenue of research for novel technological development. Fluorescence quantification is needed to overcome current limitations of FGS which has been qualitative in nature, limiting the ability to make accurate, reliable and repeatable measurements. These limitations, in turn, impede consensus, standardization, and adoption of FGS in the field. To this end, various technologies, both pre-clinical and clinical, have been developed which are aimed at quantification and objective means of assessment of intraoperative fluorescence. Here we present an overview of the recent developments in quantitative fluorescence guidance technologies, with a focus on 5-ALA-PpIX, and conclude with the most recent developments aimed at wide-field quantitative fluorescence imaging approaches in neurosurgery.

FUNDAMENTAL CONCEPTS

State-of-the-art, clinically approved systems for FGS using PpIX provide surgeons with qualitative images of the "raw" fluorescence emissions as observed through the oculars of a surgical microscope modified for fluorescence imaging. During surgery, neurosurgeons can switch from conventional, white light illumination imaging mode to fluorescence light illumination mode to visualize either no visible fluorescence, or various graded, qualitative assessments of fluorescence intensities [e.g., in the case of fluorescein green-yellow (**Figure 1A**), or PpIX red-pink (**Figure 1D**)] from low to very bright fluorescence. Surgeons use these qualitative assessments of the fluorescence, herein called visible fluorescence imaging (vFI), to make clinical judgements. Neurosurgeons make qualitative assessments of the fluorescence visualized through the oculars, to ascertain the presence (or absence) of tumor (6, 7, 9, 11). PpIX emits in the 610–720 nm range when excited with 405 nm light to produce a red-pink fluorescence when visualized with state-of-the-art commercial surgical microscopes for FGS (3, 4, 11, 13) (**Figure 1D**). Numerous clinical studies have demonstrated a strong >90% positive predictive value of visible (e.g., bright pink fluorescence) PpIX vFI for predicting the presence tumor. As such, in areas with high or bright levels of visible fluorescence, the surgeon will make the judgement of the presence of tumor. Nevertheless, vFI assessments using state-of-the-art clinical microscopes during PpIX FGS have demonstrated a negative predictive value and sensitivity <50% in numerous studies (4, 11). Therefore, in areas with no visible fluorescence, the surgeon will make the judgement of no tumor present. Yet, given the high false negative rate of vFI PpIX there remains a high likelihood for the presence of residual tumor.

The low negative predictive value and sensitivity of vFI with 5-ALA-PpIX noted in glioma studies sheds light on important fundamental concepts in biomedical optics and on the limits of current state-of-the-art clinical technologies (4, 14, 15). It is well-known in biomedical optics, that multiple factors come into play with respect to *in vivo* fluorescence measurements during surgery or similar applications (3, 4, 14–16). Here, we will elaborate on some of the fundamental principles to consider in the implementation of fluorescence technologies during FGS, with a focus on further needs and developments in terms of quantification, or objective measures of the fluorescence intensity. We will describe the differences between visible fluorescence imaging (vFI) and the concept of quantitative fluorescence imaging (qFI). We will make use of fundamental ideas in biomedical optics to present the key factors to consider when developing quantitative FGS technologies. After building on the fundamental biophysics of tissue fluorescence measurements, we will describe current developments and applications of qFI in neurosurgery.

Tissue Optics

The measured fluorescence intensity, or fluorescence light that reaches the surgeon through the surgical oculars, or which reaches a detector (e.g., camera) and is displayed on a screen depends on multiple factors. These factors may be divided into instrumentation and intrinsic factors. Instrumentation factors include the specific camera properties (e.g., dark noise, pixel size, amplification, binning, etc.), light source excitation power, microscope optics (e.g., filters, mirrors, lenses), and set up (e.g., distance between excitation and tissue, distance between tissue and camera/oculars) (3, 14, 16). Here, we will not elaborate further on these components but acknowledge their significant role in our interpretation of the fluorescence and refer the reader to prior studies (12, 16–18). In the present review, we will focus on intrinsic factors impacting fluorescence, and how we can exploit understanding of these factors in developing quantitative fluorescence technologies.

Endogenous (Auto) Fluorescence

In the intraoperative setting, when tissues are interrogated for a fluorophore of interest (e.g., PpIX), two major intrinsic factors can impact the visualized or detected fluorescence: tissue autofluorescence (***AF***) and tissue optical properties—absorption (μ_a) and reduced scattering (μ_s'). Tissue ***AF*** results from endogenous fluorophores which make up cells and tissues (14). Multiple endogenous fluorophores varying by tissue composition include but are not limited to nicotinamide adenine dinucleotide (NADH), flavin adenine dinucleotide (FAD), aromatic amino acids (e.g., tryptophan), structural proteins (e.g., collagen, elastin), and degradation products (e.g., lipofuscin). These fluorophores have their excitation maxima in the range 200–400 nm and their emission maxima in the range 300–500 nm (14). As such, fluorescence imaging of tissues can have overlapping signal contributions from the fluorophore of interest (e.g., PpIX, fluorescein) and tissue ***AF***, which can lead to overestimation of fluorescence intensity from the fluorophore of interest. Thus, to properly quantify fluorescence, technologies require a means for spectral unmixing of tissue ***AF*** (and additional fluorophore contributions) from fluorescence due to the biomarker of interest such as PpIX, that make up the fluorescence measurements. For example, in the case of PpIX, photobleaching effects produce photoproducts (19–21), which can lead to inaccurate measurements of PpIX fluorescence given overlapping fluorescence emissions in the main PpIX emission peak. Other aspects to consider with fluorophores like fluorescence is fluorophore leakage from the vasculature, unlike PpIX which to the authors' knowledge, no large clinical study has noted leakage of intracellular PpIX contents as with fluorescein (4, 9, 22). Of note, current modified surgical microscopes for FGS provide surgeons with visualization of fluorescence emitted from tissues without any unmixing (e.g., subtraction) of tissue ***AF*** from the fluorescence produced by the fluorophore of interest (e.g., PpIX). These fluorescence measurements can then over or under estimate the actual fluorescence contribution from the fluorophore of interest, leading to inaccurate assessments of biomarker.

Tissue Optical Properties: Absorption and Scattering

The measured fluorescence intensity is significantly affected by tissue optical properties, which include the tissue absorption and reduced scattering at both the excitation ($\mu_{a(x)}$, $\mu_s'(x)$)

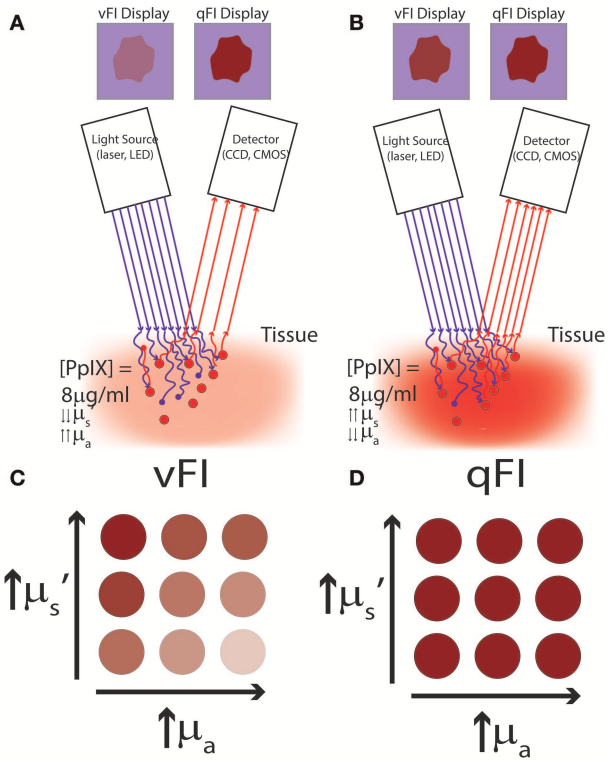

FIGURE 2 | Schematics of vFI and qFI for fluorescence guided surgery. **(A,B)** show schematics of an intraoperative FGS setup, which includes a light source for excitation light (e.g., lasers, light emitting diodes), and a detector to collect the fluorescence emissions (e.g., a CCD or CMOS camera). Tissues are illuminated with 405 nm violet light to excite the fluorophore, PpIX, which emits red to far red fluorescence in the 620–710 nm range. Excitation photons reach tissue and undergo multiple interactions with tissue including absorption and scattering of photons, with only a subset of excitation photons reaching the fluorophore, PpIX. Upon excitation, PpIX emits fluorescent photons which in turn travel through tissue undergoing multiple interactions including absorption and scattering, with only a subset of these fluorescent photons exiting tissue to reach the detector. In **(A)** less excitation photons reach PpIX and less fluorescent photons exit to reach the detector in tissues with high absorption and low reduced scattering. Meanwhile, in **(B)** more excitation photons reach PpIX and more fluorescent photons exit to reach the detector in tissues with low absorption and high reduced scattering, despite both **(A,B)** containing the same concentration and distribution of PpIX fluorophore. In **(A,B)** vFI shows highly different images of the surgical field of view (upper panel labeled vFI Display) despite equal PpIX concentrations, meanwhile, qFI shows equivalent images of the surgical field of view (upper panel labeled qFI Display) by correcting for intrinsic tissue factors including tissue optical properties. Schematics of tissue simulating phantoms containing the same concentration of PpIX but with different optical properties shown in **(C,D)**, with absorption increasing from left to right and reduced scattering increasing from bottom to top. **(C)** Shows images using vFI which either over- (top left corner) or under-estimates (bottom right corner) PpIX fluorescence with different tissue optical properties, meanwhile **(D)** shows images using qFI which performs accurate estimates of PpIX concentrations by correcting for tissue optical properties.

and emission wavelengths ($\mu_{a(m)}$, $\mu_s'(m)$). Tissue optical properties vary with wavelength. For example, hemoglobin has an μ_a (absorption) peak in the ultraviolet region ~10 times greater than its absorption in the red region of the visible spectrum (units cm^{-1}). Meanwhile, reduced scattering, μ_s', has a greater magnitude than absorption with a power law decrease as a function of wavelength. Thus, absorption and scattering will have significantly different effects on fluorescence imaging depending on the fluorophore's excitation and emission wavelengths (14, 15). Absorption and scattering in turn are determined by the biochemical composition of tissue. Absorption (μ_a) of light in tissues is primarily determined by endogenous tissue constituents, e.g., oxy-hemoglobin and deoxy-hemoglobin, melanin, myoglobin, and water. In the brain, the most significant contributors to absorption are oxy- and deoxy-hemoglobin with their largest absorption at <600 nm (9, 14, 23, 24). As a consequence, ultraviolet to near infrared light illuminated on to tissue will travel between ~100 μm to a few millimeters before complete loss due to absorption. In the context of FGS of the brain, a practical translation of the concept of tissue absorption would entail that areas of higher vascularity will have relatively higher levels of hemoglobin compared to other areas with lower vascularity, or areas of greater hypoxia will have higher levels of deoxy-hemoglobin relative to adjacent, better perfused areas. Using optical methodologies, one can then distinguish these different areas by referring to the specific spectra (i.e., optical signatures) of oxy and deoxy-hemoglobin. With respect to fluorophores, in tissues with high absorption (**Figure 2A**), more excitation and emission light would be absorbed relative to tissues with low absorption (**Figure 2B**). Furthermore, tissue with varying scattering will further affect the amount of excitation light that reaches fluorophores for excitation, and in turn, the number of photons which exit the tissue to reach the detector. This means that tissue with the same fluorophore concentration but different absorption and scattering will encounter less excitation light (i.e., fewer photons) reaching the fluorophore to enable excitation, and thus, less emission light would exit the tissue to reach the surgeon's oculars, or detector, leading to decreased detection of fluorescence intensity (4, 9, 14, 25).

Tissue scattering results from structural changes in tissues and is significant in the so called "therapeutic window" from 600 to 1,000 nm, where tissue absorption is small compared to scattering. Tissue scattering is determined by structures such as mitochondria, collagen fiber diameters, cell size and changes in the cell environment and its structures (14). For example, areas of higher cellularity and mitochondria content (e.g., cancerous tissue) will demonstrate different scattering than normal tissue. As such, tissue scattering can be indicative of pathophysiological changes and used as a means for optical contrast between tissues. Areas with higher scattering will allow more excitation light to travel through tissues, and furthermore, more emission light to exit tissues compared to areas with lower scattering (14). Current commercial systems for FGS in neurosurgery do not measure these optical properties or account for them in their fluorescence measurements.

Fluorescence Transport in Tissue

Intrinsic factors include the intrinsic properties of the fluorophore of interest (e.g., PpIX) and intrinsic tissue optical properties. The interplay of these factors determines the measured fluorescence intensity from tissue, $\boldsymbol{F}$ (i.e., the "raw fluorescence" intensity/number of photons measured by a detector or seen via the surgical oculars). Fluorophores possess their own intrinsic properties irrespective of the instrumentation used which include: concentration (**C**), quantum yield ($\boldsymbol{Q}$), and extinction coefficient ($\boldsymbol{\mu}$); such that in the absence of any tissues (or in the setting of pure diluted fluorophore) the emitted (steady state) "raw fluorescence" intensity, $\boldsymbol{F}$, is linearly proportional to the concentration of fluorophore, **C** (Equation 1) (14, 15, 19, 20).

$$F = f = vFI = C * Q * \mu \tag{1}$$

In the absence of tissues (or in the setting of pure diluted fluorophores) without the wavelength-dependent varying effects of tissue optical properties (μ_a, μ_s') and confounding/overlapping autofluorescence, $\boldsymbol{AF}$, from endogenous fluorophores, $\boldsymbol{E_f}$, the "raw" fluorescence intensity, $\boldsymbol{F}$, is equal to the quantitative fluorescence, $\boldsymbol{f}$ (Equation 1). In this ideal state, the fluorescence intensity seen by the surgeon, [i.e., the visible fluorescence (vFI)], is linearly proportional to the concentration of fluorophore in tissue (i.e., the brighter the fluorescence the higher the concentration independent of tissue variations). Nevertheless, in the operative setting, in which the surgeon visualizes different fluorescence intensities in tissue consisting of spatially varying levels of endogenous fluorophores (and in the case of PpIX, PpIX photoproducts), $\boldsymbol{E_f}$, and tissue optical properties, $\boldsymbol{T}$, the "raw" fluorescence intensity (e.g., vFI), is determined by a complex interaction of these factors (Equation 2) (14, 15, 17–21, 26–28).

$$F = f * E_f * T = C * Q * \mu * T \tag{2}$$

During FGS of high-grade gliomas using PpIX as biomarker, the surgeon makes a qualitative assessment, i.e., vFI, of the "raw" fluorescence intensity and visually assessed what he/she sees as levels of red-pink fluorescence (no fluorescence, low fluorescence, high/bright fluorescence). The surgeon uses this information to infer the levels of tumor biomarker, i.e., PpIX, present. That is, tissues with high fluorescence implying high levels of PpIX, will be judged as containing tumor, and those without fluorescence, implying no PpIX, will likely be judged as not having tumor. Nevertheless, the "raw fluorescence" intensity, $\boldsymbol{F}$, as measured using vFI is determined by a variety of factors which include not only the PpIX concentration in tissue but also additional endogenous fluorophores, $\boldsymbol{E_f}$ (e.g., NAD, FADH, PpIX photoproducts) and tissue optical properties, $\boldsymbol{T}$ [absorption (μ_a) and scattering (μ_s')] that vary throughout every region of tissues in a wavelength-dependent manner (5, 8, 11, 14, 15, 17–21, 26–31). This is the critical shortcoming of FGS as currently practiced, because any assessment of the "raw fluorescence" intensity as currently practiced with vFI will be, at best, qualitative and approximate but always inaccurate regarding

the true levels of fluorophore(s) present in tissue. "Raw" fluorescence intensity measurements are in reality an inaccurate estimate since it includes contributions from all these combined factors (fluorophore concentration, ***AF***, and tissue optical properties) (15). The raw fluorescence will always either over- or under-estimate the concentration of fluorescent biomarker, e.g., in glioma surgery under-estimation of fluorophore leads to the incorrect conclusion that the visualized tissue does not contain tumor biomarker, and can result in leaving significant residual tumor tissue unidentified and unresected, increasing the rate of recurrent disease and decreasing patient prognosis (7) (**Figure 2C**).

Inaccurate measurements of fluorescent biomarker levels in tissue has fueled the developing of tools and methods for measuring the quantitative fluorescence, ***f***, in tissues, e.g., quantitative fluorescence imaging (qFI). Quantitative fluorescence measurements are accurate and true assessments of fluorophore(s) fluorescence decoupled from the distorting effects of tissue optical properties and endogenous fluorophores contributions (15). Thus, quantitative fluorescence measurements are linearly proportional to fluorophore concentrations in tissue and Equation (3)

$$\frac{F}{E_{f^*}T} = f = C{*}Q{*}\mu \tag{3}$$

Quantitative fluorescence measurements could provide the surgeon a means for accurate assessment of fluorescent biomarker concentrations. The use of qFI would not have gross over- or under-estimation error in fluorophores levels as seen with vFI; and measurements across surgeons and institutions would be comparable given the objective scale of concentration levels (4, 11, 13, 15, 19, 22, 29, 30, 32–38) (**Figure 2D**).

Here we provided an overview of fundamental concepts in understanding the role of endogenous fluorescence, tissue optical properties, and fluorescence from fluorescent biomarkers currently used for FGS. These concepts provide a framework for understanding the need for quantitative fluorescence imaging (qFI) in neurosurgery. That is, current vFI technologies provide inaccurate assessments of the tissue fluorophore levels, and technological development should be geared toward creating technologies which are quantitative in their assessments of tissue fluorescence. To accomplish the goals of qFI, technologies require a means to correct for tissue optical properties and endogenous ***AF*** in the "raw" fluorescence data. In the next section, we provide an overview of the available technologies for wide-field quantitative fluorescence imaging (qFI) for fluorescence guided neurosurgery. We elaborate on precursors to qFI such as quantitative fluorescence spectroscopy, and subsequently describe technologies and clinical implementations of qFI in neurosurgery.

CLINICAL IMPLEMENTATION OF WIDE-FIELD QUANTITATIVE FLUORESCENCE GUIDED NEUROSURGERY

Quantitative Fluorescence Spectroscopy

To date, most clinical research implementing quantitative fluorescence assessments have used handheld spectroscopic probes (4, 9, 14, 23, 24). These probes consist of a fiber optic bundle for both light delivery and light collection with the tip of the probe held by the surgeon in contact with tissue. These probes are composed of light emitting diodes (LEDs) or laser sources to excite fluorophores and illuminate tissue, and spectrometers to collect the reflected light and/or emitted

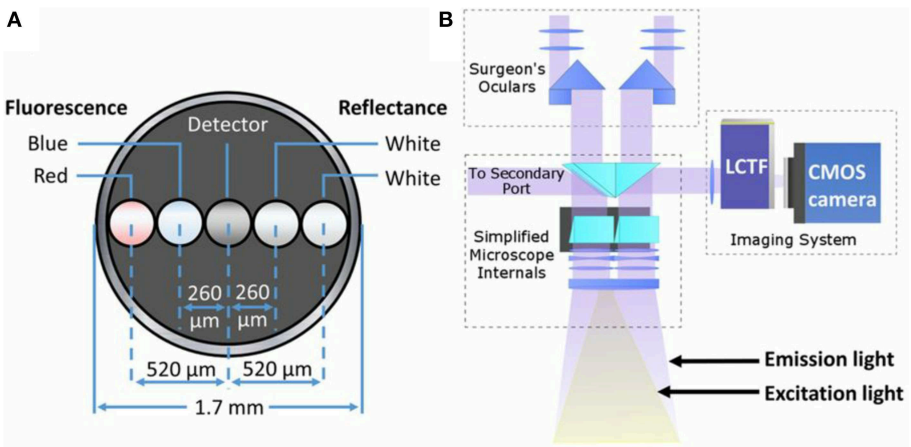

FIGURE 3 | Schematics of common quantitative probe and add-on modules for quantitative fluorescence. **(A)** Schematic of the distal contact end of a quantitative fluorescence probe with a linear arrangement of fibers for white light illumination, fluorescence excitation (violet-blue channel used for surface fluorescence, red channel not used in this study), and detector fiber. **(B)** Schematic of light path set up using a commercial surgical microscope modified for fluorescence imaging with corresponding white light illumination and excitation violet-blue light. A spectrally resolved add-on system connects to a free optical port for quantitative fluorescence imaging. Figure adapted with permission from Bravo et al. (38).

fluorescence in a wavelength-dependent manner (i.e., spectrally-resolved) (**Figure 3A**). A variety of spectroscopy systems have been used (4) in neurosurgery to collect fluorescence for tissue diagnostics and guidance, including probes used to collect the emitted fluorescence of endogenous (e.g., NADH, FADH), exogenously produced endogenous (e.g., PpIX), or exogenous (e.g., fluorescein) fluorophores in a wavelength dependent manner without correction for the distorting effects of tissue optical properties (5). Lin and colleagues detected *in vivo* tissue ***AF*** (i.e., without addition of exogenous fluorophores) as well as white light reflectance at 460 and 625 nm in 26 patients to distinguish normal tissue from tumor with a sensitivity and specificity of 100 and 76%, respectively. Similarly, the same group used the fluorescence peak at 500 nm as a means for identifying specific tissue pathology such as radiated tissue. In subsequent studies the authors developed discrimination algorithms with probe data to achieve sensitivities and specificities of up to 94% in distinguishing tumor from normal brain (39–44). A common theme with spectroscopy probes in neurosurgery is the use of the "raw" (i.e., arbitrary units of fluorescence) PpIX fluorescence intensity peak (5, 31, 45, 46). For example, a study by Stummer et al. (6) used a handheld spectroscopy probe to "quantify" the "raw" fluorescence at 635 nm for intraoperative diagnostic purposes. The authors used the "raw" fluorescence intensity peaks in a total of 33 patients with a receiver operating characteristic curve area under the curve of 88% using a threshold of 0.28 arbitrary units of fluorescence intensity with an associated specificity of 95% and sensitivity of 72%. This probe, like the majority in the neurosurgical literature, collect the "raw" emitted fluorescence from tissue fluorophores and the collected corresponding fluorescence spectra (i.e., wavelength dependent fluorescence light emissions). The collected "raw" fluorescence in these studies is equivalent to the "raw" fluorescence, ***F*** noted in Equation (2), which is a composite of multiple factors and thus, not truly "quantitative" measurements of the fluorescent biomarker. Nevertheless, these demonstrate the utility of improved excitation-collection geometries of contact probe-based systems. Handheld probes are in direct contact with tissue, and thus, are more efficient in both excitation of fluorophores (i.e., more light reaches the fluorophores for excitation) and collection of fluorescent emissions (i.e., more fluorescent light reaches the detector). These systems thus demonstrate the general trend of increased sensitivity compared to vFI using a modified surgical microscope (3, 14, 15, 23).

More recent developments of handheld spectroscopic probes with the aim of more accurate measurements of the true fluorophore-derived fluorescence, i.e., quantitative fluorescence, use algorithms for unmixing (e.g., subtraction) of ***AF***, multiple fluorophores, fluorescent photoproducts, or fluorophore peaks. Montcel et al. used a ratio of the fluorescent emissions collected via a handheld spectroscopic probe at 620 nm divided by the emissions at 634 nm. They corrected this ratio furthermore for tissue ***AF*** following correction of auto fluorescence as a means for more accurate spectroscopic detection (10). In similar fashion, Hosseini et al. used a spectroscopy system to "quantify" PpIX. In their work, they derived a "ratio number" for tissue diagnosis which was the ratio of the fluorescence intensity in arbitrary units at 635 nm minus the auto fluorescence at 635 nm. They then divided by the auto fluorescence at 510 nm to produce the "ratio number." The authors reported a higher "ratio number" in tumor compared to normal brain in a limited number of patients (47). In a subsequent study, they used the ratio of the raw fluorescence intensity at 630 over 600 nm for tissue diagnosis (48). These spectroscopy studies acknowledge the importance of different fluorescent contributions to the collected, "raw" fluorescence, ***F*** (Equation 2), and developed means to correct for them in their processing of fluorescence measurements. The different algorithms account for ***AF***, ***(Ef,*** Equation 2), or for PpIX associated photoproducts in their calculations of the PpIX specific fluorescence. PpIX is known to produce distinct photoproducts and to exist in distinct photochemical states with variation in their spectra depending on factors such as pH (10, 20). This is a significant advancement in spectroscopy probes which allows spectral unmixing of major component(s) in the "raw" fluorescence, ***F***, to arrive at a more quantitative, and accurate measurement of the "quantitative fluorescence," ***f***, and fluorescent biomarker concentrations. Fluorophores exhibit different effects to continuous light excitation, which can lead to irreversible photodamage, or fluorescence quenching, and creation of photoproducts. PpIX is more prone to photobleaching effects than some modern fluorophores used in the basic sciences such as Alexa Fluor agents or quantum dots. In the case of PpIX, multiple photoproducts have been identified with fluorescence emissions which overlap with the main PpIX peak. As such, spectral unmixing is important in accounting for not just tissue autofluorescence, but also for these confounding photoproducts which may lead to inaccurate estimates of PpIX concentrations (4, 19–21). However, these systems do not correct for the non-linear, spatially dependent, and highly variable differences in tissue absorption and scattering, ***T*** (Equation 2), and thus cannot be accurately called "quantitative fluorescence."

Subsequent studies have used developing concepts in biomedical optics to apply correction techniques for the distorting effects of tissue optical properties with handheld spectroscopic tools (15, 26, 49–51). Correction techniques can be broadly categorized as model-based or empirical. The model-based approaches use a model of light transport (e.g., diffuse theory) to correct for tissue optical properties, usually requiring explicit measurement, and calculation of these properties prior to correcting the "raw" fluorescence spectra. Empirical models, rather than explicitly calculating tissue optical properties, will measure or calculate surrogates of these, for example, the use of reflectance measurements at distinct wavelengths. Ratiometric approaches, a common form of the latter, use ratios of the fluorescence emissions over the measured reflectance at specified wavelengths (15). Valdes et al. (33) developed a ratiometric correction approach applied to probe spectroscopy data. The authors collect the spectrally-resolved fluorescence from tissue. They then measure the reflectance near the excitation and main emission peaks; and use the calibrated reflectance correction factor to divide the "raw" fluorescence spectra to derive a "quantitative fluorescence" spectrum and quantitative PpIX concentrations (Equation 4). The "quantitative fluorescence" in this study performs well in phantoms and *in vivo* when

correcting for absorption and scattering, by using the white light reflectance ratio as a surrogate for tissue optical properties effects (33) (Equation 4).

$$\frac{F}{R} = f, \tag{4}$$

Valdes et al. used the same quantitative probe with a model-based correction approach to calculate the quantitative fluorescence in tissues and thus, PpIX concentrations during brain tumor resections (19, 29, 35, 36). This approach used the white light reflectance to measure the reflected white light; and using a spatially resolved model of the diffuse reflectance explicitly calculate the tissue absorption and scattering. The tissue optical properties are used in a light transport model of the fluorescence to correct the "raw" fluorescence for the distorting effects of tissue optical properties and calculate the corrected, or quantitative fluorescence (and PpIX concentrations) at each interrogated site. This group used the probe on a variety of tumor pathologies including low- and high-grade gliomas, meningiomas, and metastases demonstrating improved detection of tumor compared to vFI using commercial systems. For example, the quantitative probe was able to detect significant amounts of PpIX in low grade gliomas which were not identified using vFI, and detection accuracies in low grade gliomas were similar to those using state-of-the-art vFI for high grade gliomas. Similar to the previous approaches which accounted for endogenous or other fluorophore contributions, the authors used a spectral unmixing algorithm to account for autofluorescence, PpIX photoproducts, and PpIX (4, 19–21). These latter two approaches describe the use of a spectroscopic handheld probe similar to the previously mentioned studies. The authors collected both spectrally resolved fluorescence and diffuse white light reflectance. Similar to previous studies, they accounted for additional fluorophore contributions other than PpIX such as the endogenous autofluorescence and PpIX photoproducts. A lesson learned from these later approaches is how they correct for tissue optical properties, either by a ratiometric, and empirical approach, or by means of a model-based, light transport approach. Correction for tissue optical properties in addition to additional fluorescence contributions, enabled the authors to explicitly calculate the quantitative fluorescence and as such, PpIX biomarker concentrations for tumor tissue identification.

Hand-held spectroscopy probes informed the community regarding important factors to consider when developing quantitative technologies and more importantly, the role these measurements might play in helping improve FGS with more accurate (and at times sensitive) measurements. The different probe implementations to date used methodologies to correct for endogenous ***AF***, for fluorophore photoproducts or distinct fluorescence states, the fluorophore of interest (e.g., PpIX), and for tissue optical properties. To accomplish these tasks, spectroscopy probes acquire spectrally-resolved data to analyze the fluorescence spectra in a wavelength dependent manner, and as such, enable such analyses of spectral-fitting. Furthermore, these studies used either surrogates of tissue optical properties in the case of ratiometric approaches, or explicitly measured them using models of light transport. These probes demonstrated improved accuracies for tumor detection across a broad range of pathologies, supporting the need for technologies that are not just more sensitive, but also which perform quantitative fluorescence measurements (4, 9, 14, 23).

Wide-Field Quantitative Fluorescence

Implementation of quantitative fluorescence systems for neurosurgical guidance is limited but included pre-clinical studies in phantoms and animals as well as clinical implementations of these novel imaging systems (3, 4, 15, 52). Yang et al. developed a multispectral fluorescence imaging system that measures fluorescence at multiple wavelengths. They tested this system during brain tumors surgeries using the agent Photofrin. This study used multi-wavelength excitation and emission light in a wide-field FGS imaging setup (53), unlike commercially available surgical microscopes which are single wavelength systems (e.g., a single bandpass for excitation and long pass filters), which limits their utility to one fluorophore at a time (3, 13). Further, as noted with the spectroscopy studies, this system is limited in its ability to correct and account for ***AF*** or additional fluorophore contributions as well as tissue optical properties on the collected fluorescence emissions. In 2011, Saager et al. (54) reported the development of a system capable of dual spatial frequency domain imaging (SFDI) and fluorescence imaging. This system performs patterned illumination at varying spatial frequencies and phases of the field of view (e.g., phantoms, animal brain) to recover the reflected light in a spectrally-resolved manner and calculate the tissue absorption and scattering at every pixel in the entire field of view (SFDI) (55). The authors were able to measure tissue optical properties to calculate a "correction map" and apply this for fluorescence correction and ultimately, quantification of PpIX concentrations. The authors validated their system in phantoms and ultimately applied to optical measurements of skin. Of note, although this study was not applied in neurosurgery or neurosurgical models, it is important because it lays the groundwork for future studies using explicit measurements of tissue optical properties for PpIX quantification. A more recent system (22) collects spectrally resolved white light reflectance and fluorescence emissions using an add-on module that adapts to a commercial surgical microscope (**Figure 3B**). This system collects multiple images at user-specified wavelengths in the visible range of the spectrum (e.g., 400–720 nm) enabling reconstruction of a full reflectance and fluorescence spectrum at each pixel in the image. The authors used an empiric ratiometric approach to correct for tissue optical properties by using a ratio of the "raw" fluorescence, ***F***, to the reflected white light, ***R***, to calculate the quantitative fluorescence in tissues and subsequently, using a calibration factor, calculated the true PpIX in tissues. This approach introduces important concepts in FGS. First, the authors developed a system for spectrally resolved detection of both the white light reflectance and emitted fluorescence, similar to the approach used in spectroscopy systems. Second, the authors use a fluorescence correction technique to derive the "quantitative fluorescence" in tissues. In this work, they used the

reflected fluorescence as a surrogate for tissue optical properties. In the first iteration of their system, the authors used a low sensitivity, CCD camera that enabled detection levels down to ∼100 ng/ml in tissue. Previous work from spectroscopic studies, noted that levels of PpIX in tumor tissues can be as low as 10 ng/ml. A subsequent system update by this team used a more sensitive scientific CMOS camera to improve both the lower threshold of detection and acquisition times by approximately one order of magnitude (19, 22). Jermyn et al developed a similar system for neurosurgical guidance using a more sensitive EMCCD camera (56). The authors noted detection levels down to 10 ng/ml of PpIX, significantly increased speeds for data collection, and improvement in overall system performance and quantification metrics compared to a CMOS based system (34). These latter studies used more sensitive, higher quality cameras, equivalent to those used for benchtop fluorescence microscopy studies, to implement into clinically compatible systems.

Xie et al. (1) developed a pre-clinical system that acquires spectrally resolved white light and fluorescence emissions, similar to Valdes et al. and Jermyn et al., and coupled it to a new algorithm for fluorescence correction. The authors developed an empirical algorithm for fluorescence correction. They correct the "raw" fluorescence by using a calibrated tissue reflectance. They calibrate their system to a known reflectance standard; and use a product of the reflectance at the excitation and emission wavelengths to subsequently correct the fluorescence spectrum. The authors tested the system in phantoms of varying absorption, scattering and PpIX concentrations to demonstrate reliable quantification <100 ng/ml with short acquisition times similar to those reported by prior studies. They noted excellent quantification ($r^2 = 0.94$) down to <100 ng/ml in phantoms, and furthermore, provided pilot data testing of this system in *ex vivo* glioblastoma samples, demonstrating the capabilities to detect PpIX concentrations of tumor infiltrated tissues in wide-field mode. This work presents an important advancement in qFI, by developing a novel algorithm to correct for the non-linear, and confounding effects of tissue optical properties on the measured "raw" fluorescence, further demonstrating the need for techniques to measure the quantitative fluorescence, and providing a detailed account and principles for system calibration

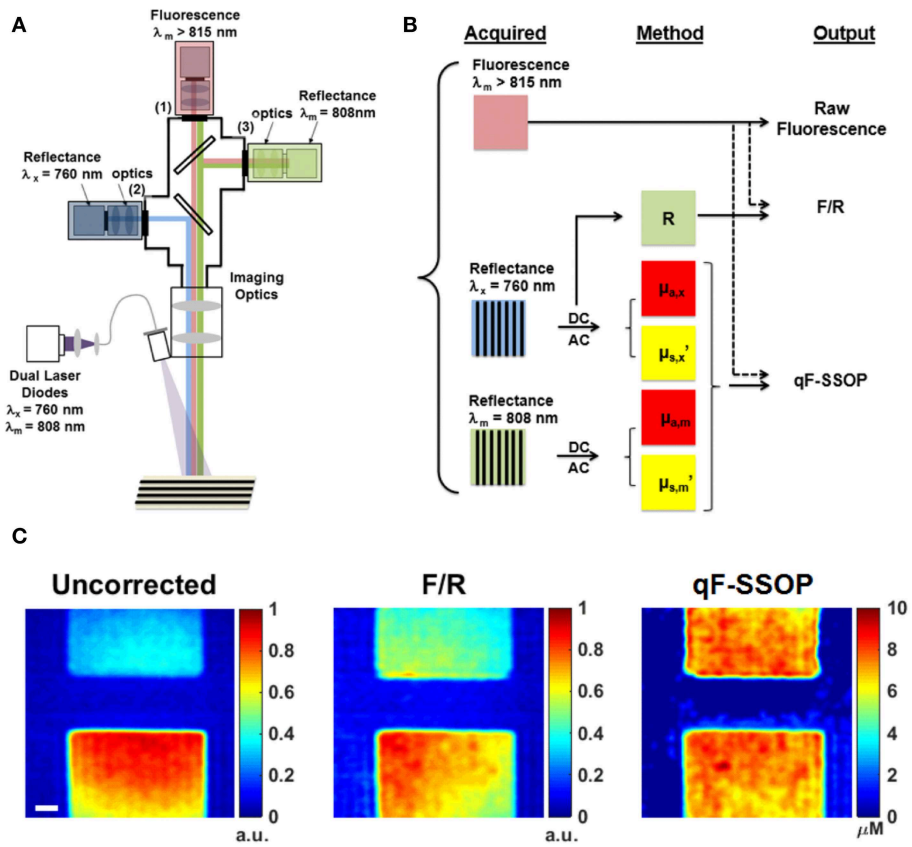

FIGURE 4 | Real time, quantitative fluorescence imaging system coupled with single snapshot optical properties imaging. **(A)** Schematics of a qFI system that performs simultaneous SSOP imaging and fluorescence detection by acquiring simultaneous reflectance and fluorescence imaging under SSOP mode. **(B)** Data processing scheme in which reflectance images are processed under SSOP conditions to estimate the absorption μ_a and reduced scattering μ_s'. **(C)** A light transport model is used to correct the raw fluorescence for the effects of tissue optical properties to calculate the quantitative fluorescence. Bottom panel shows one frame of a real-time dynamic video of tissue simulating phantoms displaying the raw fluorescence (uncorrected), the empirically corrected fluorescence (F/R), and the quantitative fluorescence using SSOP (qF-SSOP). Figure adapted with permission from Valdes et al. (37).

that inform the community when developing such quantitative fluorescence systems.

Sibai et al. (57) developed a bench top pre-clinical system capable of dual spatial frequency domain imaging (SFDI) and fluorescence imaging. This system performs patterned illumination at varying spatial frequencies and phases of the field of view (e.g., phantoms, animal brain) to recover the reflected light in a spectrally-resolved manner and calculate the tissue absorption and scattering at every pixel in the entire field of view (SFDI). In this study, each acquisition takes ∼12 s followed by data processing. The optical properties are used to correct the collected fluorescence using a light transport model of the fluorescence; and reconstruct a qFI image of the full field of view. In this work, the authors validated their system in phantoms with varying optical properties and PpIX concentrations, and subsequently applied their system to a rodent model of glioma. They further validated their imaging results by comparison with the gold standard spectroscopy probe and *ex vivo,* tissue extraction homogenization technique demonstrating differences of μ_a and μ_s' of 14 and 19.4%, respectively and for PpIX of 10.5%. This work makes a significant advancement in quantitative fluorescence techniques in neurosurgery, by using a model-based approach for wide-field quantitative fluorescence imaging. The authors used a rigorous model-based approach for accurate estimates of tissue optical properties using a well-known SFDI technique (28). This is in contrast to the prior studies which use various calibration and empiric correction factors such as the raw reflectance as a surrogate for the tissue optical properties. After explicitly calculating the tissue optical properties across the full surgical field of view, these are integrated into a light transport model of the fluorescence to extract the quantitative fluorescence in tissue and thus, the quantitative PpIX concentrations.

Valdes et al. (37) developed a benchtop pre-clinical system to perform simultaneous single snapshot optical properties (SSOP) imaging and fluorescence imaging in wide field mode (**Figure 4A**). SSOP uses only one single frequency without the need for multiple phases during patterned illumination of tissue, unlike SFDI which uses multiple frequencies and phases to extract the tissue optical properties (28, 58, 59). SSOP enables fast, real time acquisition (milliseconds per acquisition) since it requires only one image to extract optical properties compared to at least 6 required for SFDI. The authors use SSOP imaging to estimate the tissue optical properties in phantoms of varying absorption, scattering and fluorophore concentrations to correct the "raw" fluorescence using a light transport model of the quantitative fluorescence (**Figure 4B**). They further demonstrate the ability to perform quantitative fluorescence imaging in video rate mode as a result of the high speed offered with SSOP imaging across the full field of view in a pixel-wide manner (**Figure 4C**). This work provides a further development in qFI methods by using a model-based approach to estimate tissue optical properties and correct the fluorescence for these effects. Furthermore, they implement this in a wide field of mode at video rate speeds. The ability to perform video rate imaging would

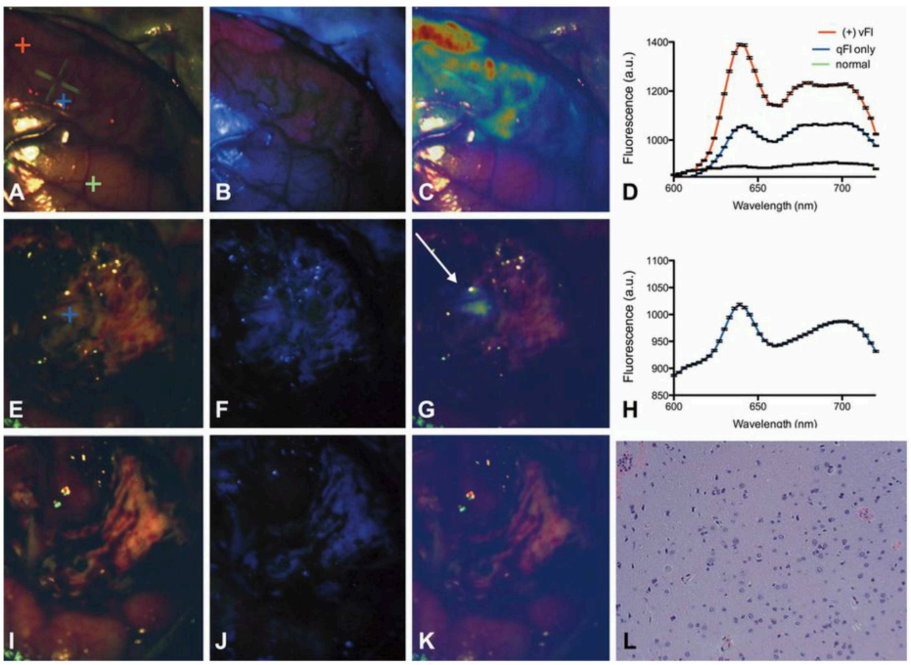

FIGURE 5 | Spectrally-resolved quantitative fluorescence imaging using a ratiometric approach during *in vivo* glioblastoma surgery. Intraoperative images under **(A,E,I)** conventional white light illumination, **(B,F,J)** blue light illumination for vFI using a commercial system, and **(C,G,K)** quantitative fluorescence images using a ratiometric approach at the beginning (top row), near the end (middle row), and at the end (bottom row) of surgery. Near the end of surgery, high levels of PpIX were found using qFI **(G)** but not using vFI **(C)** with histological corroboration of tumor **(L)**. Spectra at the beginning of surgery **(D)** show expected PpIX peaks and near the end of surgery **(H)** in the area of residual tumor **(G)**. Figure adapted with permission from Valdés et al. (22).

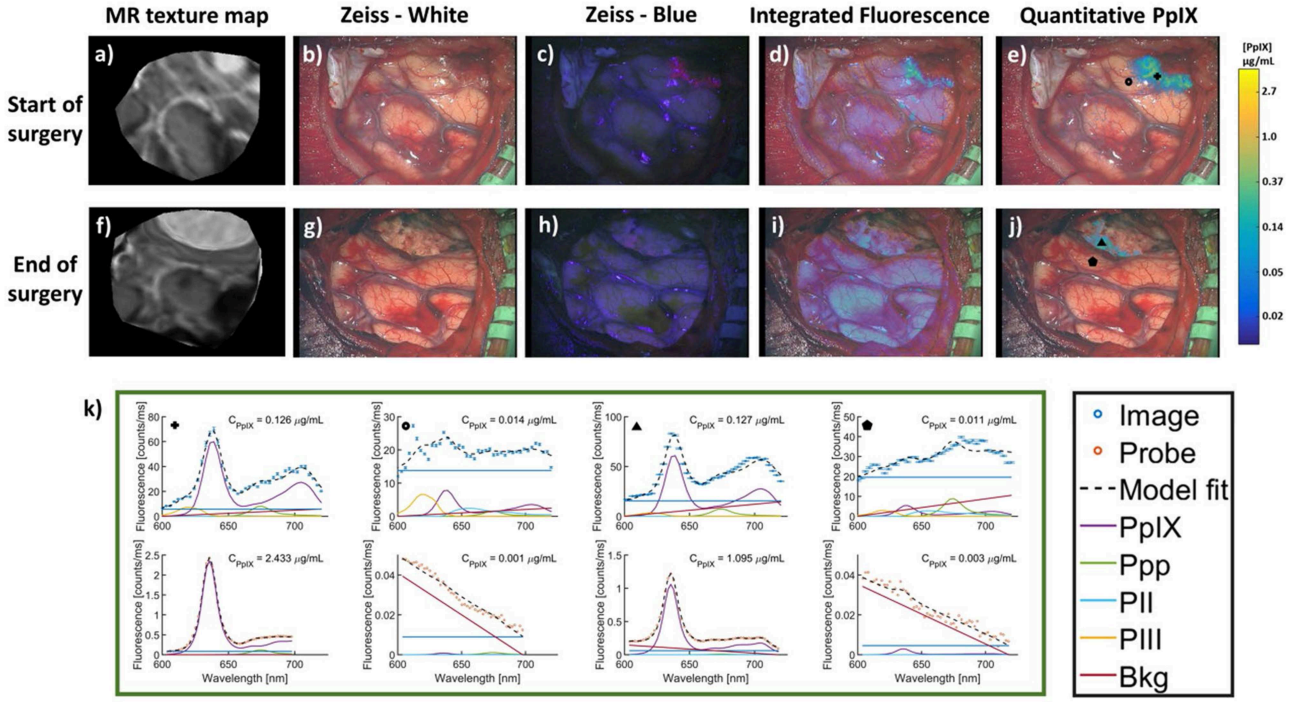

FIGURE 6 | MR images and intraoperative fluorescence using a filter corrected approach. Images were acquired at the start (top row) and end (bottom row) of surgery. **(a,f)**, MR images corresponding to the intraoperative **(b,g)** conventional white light images, **(c,h)** blue light vFI images using a commercial microscope system, **(d,i)** "raw" fluorescence intensity, or integrated fluorescence images, and **(e,j)** quantitative fluorescence images using a ratiometric and filter correction approach. **(k)** PpIX spectra using the qFI system (top row) and spectroscopic quantitative probe (bottom row) at multiple locations and timepoints during surgery [marked by corresponding symbols in images **(e,j)**]. PpIX concentration observed in the C_{PpIX} overlays. Ppp, Photoproduct I; PII, Photoproduct II; PIII, Photoproduct III; Bkg, Background; Offset, linear offset for background signal. Figure adapted with permission from Bravo et al. (38).

enable the surgeon to have immediate feedback regarding tissue in the field of view for real-time qFI.

The work above uses qFI in neurosurgical guidance in the pre-clinical setting, or on *ex vivo* human tissues. A few studies have used the above concepts and technologies and applied these in the intraoperative, clinical scenario. Valdes et al. subsequently used their spectrally-resolved, microscope add on module system in human glioblastoma surgery (22). The authors demonstrate the utility of their qFI system by showing a comparison of the images obtained using a commercially available state-of-the-art surgical microscope enabled to perform vFI and co-registered qFI images at various times points during surgery (**Figures 5A–D**, at the beginning of surgery; **Figures 5E–G**, near the end of surgery; **Figures 5I–K**, at the end of surgery). They demonstrate that the qFI system was able to detect tumor near the end of surgery in areas were vFI left residual tumor unidentified (i.e., vFI showed no visible fluorescence) (**Figure 5F**), but their qFI system was able to detect significant residual tumor (**Figures 5G,H**) which correlated with histopathology (**Figure 5L**). More recently, Bravo et al. (38) used this system *in vivo* to demonstrate the importance of spectral filtering of the fluorescence signals for more accurate PpIX quantification maps. The authors developed a metric called a "confidence ratio," which functions as a filter to remove regions of uncertainty from quantitative PpIX images; by removing those estimates that approach the detection limits of PpIX, the authors show their approach can decrease the rates of false positives (**Figure 6**). This work highlights the value of performing quantitative estimates of the fluorescence to significantly improve our detection of tumor tissue across tumor pathologies compared to the standard of care using commercially available vFI technologies, and the need for complex data processing to maximize qFI detection. Furthermore, this work highlights the importance of performing wide field quantitative detection compared to single small area detection provided by handheld probes.

To date, technologies for fluorescence quantification have used either handheld, contact probes, or wide field, non-contact imaging systems. Each system boasts of their own advantages and disadvantages. Handheld probes are in direct contact with tissue, which provides a geometry for more efficient (i.e., less loss of) light excitation and collection of reflectance and fluorescence emissions from tissue. Furthermore, these systems do not have to account for different distances as they have one distance between excitation and emission sources (since they are in contact with tissue), which simplifies models for fluorescence quantification. As such, these probes have a history of algorithms developed for rigorous model-based quantification, and in more recent developments, are able to

TABLE 1 | Comparative summary of wide-field imaging systems.

Group	Fluorophore	Technical Features and Advantages	Correction Method	Acquisition Time	Processing Time	Cost	Test population	Limitations
RESEARCH SYSTEMS								
Yang et al. (53)	Photofrin	Standalone Multispectral Fluorescence Imaging system—multiple (five band) excitation and emission wavelengths. Long working distance ∼50 cm. Field of view ∼ 3 cm diameter. Detector—CCD camera.	None	15 s	Real-time	∼ $100,000	Phantoms. Human brain (*in vivo*.)	Inability to account and correct for ***AF, Ef***, additional fluorophore contributions and ***T***. Low concentration sensitivity (0.05 to 0.1 μg/g) and low depth sensitivity (0.5 mm.) Stand-alone system not integrated into surgical microscope. Results displayed on a personal computer.
Saager et al. (54)	5-ALA-PpIX	Standalone SFDI system—patterned illumination with varying spatial frequencies and phases of the field of view. Detector—CCD camera.	***T*** calculated as a "correction map" of the field of view using spatial frequency domain imaging	12 s	Not specified	Not specified	Phantoms. Human skin (*in vivo*).	Low concentration specificity (within 0.2 μg/ml of known concentration.) Longer acquisition times since 6 images are required to estimate ***T***. Not tested in human brains.
Valdes et al. (22)	5-ALA-PpIX Fluorescin	Integrated HIS (Hyperspectral Imaging System) for sequential spectrally resolved image acquisition in the range 400–720 nm at 10 nm intervals. Works as a portable, add-on module compatible with commercial surgical microscopes using the microscope optics and light source. Working distance ∼30 cm. Field of view = 10 × 7.5 mm to 50 × 40 mm Allows reconstruction of the field of view with the full reflectance and fluorescence spectrum at each pixel as a 3D image cube. Detector—CCD camera (first iteration, concentration sensitivity ∼100 ng/ml PpIX), sCMOS camera (second iteration, concentration sensitivity ∼10 ng/ml PpIX.) System validated with phantoms, histopathology and comparison with commercial vFI systems.	Spectrally constrained dual-band normalization. Empiric ratiometric approach .	100 ms to 500 ms per wavelength. Up to 2–8 s per white light and fluorescence hyperspectral image capture.	Near real-time	∼20,000–30,000	Phantoms. Rat brain (*in vivo*). Human brain (*in vivo*)	Penetration depth limited to a few hundred microns in depth. Quantification accuracy limited to > 40 ng/ml PpIX using the second generation sCMOS system compared to the gold standard optical probe of ∼10 ng/ml PpIX. Empiric correction algorithm less accurate than model based correction approaches, unable to explicitly measure tissue optical properties and intrinsic tissue biomarkers other than PpIX
Jermyn et al. (56)	5-ALA-PpIX	Integrated HIS for sequential spectrally resolved image acquisition in the range 400–720 nm at 10 nm intervals. Works as a portable, add-on module compatible with commercial surgical microscopes using the microscope optics and light source. Working distance ∼30 cm. Field of view ∼ 20 cm X 20 cm. Allows reconstruction of the field of view with the full reflectance and fluorescence spectrum at each pixel as a 3D image cube . Detector—EMCCD camera (two orders of magnitude lower concentrations detected compared to CMOS, possibly comparable to the ∼1 ng/ml detection limit of point probes) and sCMOS camera connected simultaneously for comparison.s	Spectrally constrained dual-band normalization. Empiric ratiometric approach .	5–100 ms. Up to 2 s per white light and fluorescence hyperspectral image capture.	Near real-time	∼$50,000	Phantoms. Rat brain (*ex vivo*). Human brain (*ex vivo*)	Enhanced sensitivity of EMCCD detectors can be confounded to a greater degree by non-specific ***AF*** signals and ambient light. High cost of EMCCD detectors. Empiric correction algorithm less accurate than model based correction approaches, unable to explicitly measure tissue optical properties and intrinsic tissue biomarkers other than PpIX.

(Continued)

TABLE 1 | Continued

Group	Fluorophore	Technical Features and Advantages	Correction Method	Acquisition Time	Processing Time	Cost	Test population	Limitations
Xie et al. (1)	5-ALA-PpIX	Standalone system conceptually similar to those by Valdes et al and Jermyn et al. Detector—sCMOS camera. Concentration sensitivity ~ 10 ng/ml.	Empirical correction algorithm approach. Calibration to a known tissue reflectance standard and correction of F using a product of the R at excitation and emission wavelengths .	26 s	Not specified	Not specified	Phantoms. Human brain (*ex vivo*).	Penetration depth limited to a few hundred microns in depth. Long acquisition times due to data input/output latencies.
Sibai et al. (57)	5-ALA-PpIX	Standalone SFDI system (similar to Saager et al). Replaces previous approaches of ratiometric or semiratiometric correction in SFDI systems with a more rigorous light transport model. Allows reconstruction of the full-field of view representing qFI data post-correction. Field of view = 3 cm X 3 cm. Detector—CCD camera. System accuracy validated with spectroscopy probe (gold standard) and *ex vivo* homogenized extracted tissue. The method is also able to explicitly measure tissue optical properties and intrinsic tissue biomarkers unlike the systems by Valdes et al, Jermyn et al, and Xie et al.	Light transport model based approach using spatial frequency domain imaging.	36 s	Not specified	Not specified	Phantoms. Rat brains (post mortem in situ, *ex vivo*).	Benchtop preclinical system. Suboptimal results from *in vivo* rat brains (but these limitations may not translate to *in vivo* human experiments as the authors believe the rat glioma model to be the cause, rather than failure of the method or instrumentation). Less sensitive than spectroscopy probes by 2–4 times on account of spill-over or cross talk between image pixels and more tissue distortion and attenuation of weak fluorescence signals. Decreased concentration sensitivity and higher exposure times compared to systems with EMCCD detectors. Penetration depth limited to a few hundred microns in depth. Long acquisition times requiring 6 images to estimate T.
Valdes et al. (37)	5-ALA-PpIX	Standalone qF-SSOP system—single snapshot of optical properties. Able to perform real-time data acquisition since it requires a single image to estimate T (compared to the SFDI systems by Saager et al and Sibai et al which require multiple images).	Light transport model based approach using single snapshot of optical properties imaging	500 ms	21 ms	Not specified	Phantoms.	Benchtop preclinical system. System has not been validated against *ex vivo* or *in vivo* rodent or human brains.
Zeiss Surgical Microscope + Blue 400 module	5-ALA-PpIX	Commercial vFI system as an integrated add-on module for the Zeiss series of surgical microscopes. Real-time visualization of fluorescence through surgical oculars and projected unto a CCD camera.	No correction	Real-time	No processing	Quote requested	Humans (*in vivo*)	Requires purchase of expensive proprietary accessory. Qualitative, subjective information relayed to the surgeon without quantification. High rate of false negatives using PpIX.

(Continued)

TABLE 1 | Continued

Group	Fluorophore	Technical Features and Advantages	Correction Method	Acquisition Time	Processing Time	Cost	Test population	Limitations
COMMERCIAL SYSTEMS								
Leica Surgical Microscope + FL400 module	5-ALA-PpIX	Commercial vFI system as an integrated add-on module for the Leica series of surgical microscopes. Real-time visualization of fluorescence through surgical oculars and projected unto a CCD camera.	No correction	Real-time	No processing	Quote requested	Humans (*in vivo*)	Requires purchase of expensive proprietary accessory. Qualitative, subjective information relayed to the surgeon without quantification.

explicitly measure tissue optical properties and derive intrinsic biomarkers. These, in turn, are used in model-based approaches to correct the fluorescence emissions and quantify fluorophores. Despite the aforementioned advantages, handheld probes face a major disadvantage when it comes to wide-spread surgical implementation and intraoperative diagnostics. They require the surgeon to disrupt the surgical workflow to place the probe in direct contact with tissue, to then interrogate a small field of view (as small as 1 mm in diameter) for each acquisition (10, 14, 15, 19, 23, 31, 39, 43, 44, 47).

Wide-field, quantitative imaging systems allow the surgeons to view a larger area of interrogation up to multiple centimeters in diameter, including the full surgical field of view. This provides a more immediate, intuitive, and less disruptive view of tissue for intraoperative diagnostics. Nevertheless, current systems are limited in their ability to provide instantaneous, real-time quantification of this field of view. Another disadvantage involves a less efficient geometry for light excitation and emission given the ever-changing distances between light sources and the detector resulting from movement of the microscope and the imaging system. This, in turn, presents a challenge to accurate quantification, requiring more complex algorithms to account for these varying distances. Although, various pre-clinical systems (**Table 1**) have been developed that take advantage of model-based approaches for quantification (unlike systems using empiric algorithms), these have not been implemented in a seamless manner for immediate intraoperative surgical feedback. An important consideration with quantitative fluorescence is the need for calibration. Finally, spectroscopy and imaging systems require calibration against known standards of tissue optical properties and fluorophores to ensure accurate estimation of quantitative fluorescence intraoperatively (1, 4, 11, 15, 17, 22, 28, 34, 37, 38, 51, 53, 54, 56, 59). As such, reports on quantitative systems need to provide well-delineated calibration procedures to ensure translation of results between patients and institutions (18, 21, 28, 60).

CONCLUSION

The field of quantitative fluorescence in neurosurgery, with implementation of spectroscopic and wide-field systems is in its infancy. The majority of the literature on fluorescence imaging and its application to neurosurgical guidance in brain tumors uses vFI technologies (3). We have described limitations of vFI including subjectivity and inaccuracy of measurements, inter-observer dependence, and decreased sensitivity for residual disease. This work seeks to first introduce the reader to fundamental concepts in quantitative fluorescence, including concepts of autofluorescence, tissue optical properties and their effects on the fluorescence measurements, and fluorescence correction techniques (14, 15). Second, this study seeks to provide the reader with an overview of the major implementations of quantitative fluorescence in neurosurgery. Since the literature on quantitative fluorescence in neurosurgery is limited, we provide an overview of some of the preliminary studies seeking to arrive at quantitative assessments of the fluorescence

in neurosurgery. We then highlight some lessons learned from each of these studies. Finally, we wish to inform the reader regarding the importance of quantitative fluorescence in neurosurgery both as a means for standardizing measurements across surgeons, but also, as a means for improved detection of residual disease.

The success of vFI has helped fuel technological developments including modified surgical microscopes for fluorescence imaging, exoscopes, and probe-based technologies such as spectroscopic, and confocal systems (3, 4). Furthermore, the success of vFI has subsequently led to development of quantitative fluorescence technologies discussed in this paper, as these technologies have highlighted the intrinsic limitations of vFI (subjectivity, inter-observer dependence, inaccurate measurements, decreased sensitivity for residual disease). Future developments in FGS require that these technologies provide seamless integration to the surgical workflow with fast acquisition times and ease of interpretation of the data to the surgeon. Technologies should provide means for improve visualization, calibration, and heads up display, to enable wide spread use across multiple centers. In summary, the use of qFI in neurosurgery is limited, but continued research and development will provide the neurosurgical community with more accurate technologies to ultimately improve patient outcomes.

AUTHOR CONTRIBUTIONS

All authors listed have made a substantial, direct and intellectual contribution to the work, and approved it for publication.

FUNDING

This work was partially supported by grants received from the Brigham Research Institute and Partners HealthCare Innovation.

REFERENCES

1. Xie Y, Thom M, Ebner M, Wykes V, Desjardins A, Miserocchi A, et al. Wide-field spectrally resolved quantitative fluorescence imaging system: toward neurosurgical guidance in glioma resection. *J Biomed Opt*. (2017) 22:1–14. doi: 10.1117/1.JBO.22.11.116006
2. Whitson WJ, Valdes PA, Harris BT, Paulsen KD, Roberts DW. Confocal microscopy for the histological fluorescence pattern of a recurrent atypical meningioma: case report. *Neurosurgery*. (2011) 68:E1768–72; discussion E1772–3. doi: 10.1227/NEU.0b013e318217163c
3. Wei L, Roberts DW, Sanai N, Liu JTC. Visualization technologies for 5-ALA-based fluorescence-guided surgeries. *J Neurooncol*. (2018) 141:495–505. doi: 10.1007/s11060-018-03077-9
4. Valdés PA, Roberts DW, Lu FK, Golby A. Optical technologies for intraoperative neurosurgical guidance. *Neurosurg Focus*. (2016) 40:E8. doi: 10.3171/2015.12.FOCUS15550
5. Utsuki S, Oka H, Sato S, Suzuki S, Shimizu S, Tanaka S, et al. Possibility of using laser spectroscopy for the intraoperative detection of nonfluorescing brain tumors and the boundaries of brain tumor infiltrates. Technical note. *J Neurosurg*. (2006) 104:618–20. doi: 10.3171/jns.2006.104.4.618
6. Stummer W, Tonn JC, Goetz C, Ullrich W, Stepp H, Bink A, et al. 5-Aminolevulinic acid-derived tumor fluorescence: the diagnostic accuracy of visible fluorescence qualities as corroborated by spectrometry and histology and postoperative imaging. *Neurosurgery*. (2014) 74:310–9; discussion 319–20. doi: 10.1227/NEU.0000000000000267
7. Stummer W, Pichlmeier U, Meinel T, Wiestler OD, Zanella F, Reulen HJ, et al. Fluorescence-guided surgery with 5-aminolevulinic acid for resection of malignant glioma: a randomised controlled multicentre phase III trial. *Lancet Oncol*. (2006) 7:392–401. doi: 10.1016/S1470-2045(06)70665-9
8. Roberts DW, Valdés PA, Harris BT, Fontaine KM, Hartov A, Fan X, et al. Coregistered fluorescence-enhanced tumor resection of malignant glioma: relationships between delta-aminolevulinic acid-induced protoporphyrin IX fluorescence, magnetic resonance imaging enhancement, and neuropathological parameters. Clinical article. *J Neurosurg*. (2011) 114:595–603. doi: 10.3171/2010.2.JNS091322
9. Pogue BW, Gibbs-Strauss S, Valdés PA, Samkoe K, Roberts DW, Paulsen KD. Review of neurosurgical fluorescence imaging methodologies. *IEEE J Sel Top Quantum Electron*. (2010) 16:493–505. doi: 10.1109/JSTQE.2009.2034541
10. Montcel B, Mahieu-Williame L, Armoiry X, Meyronet D, Guyotat J. Two-peaked 5-ALA-induced PpIX fluorescence emission spectrum distinguishes glioblastomas from low grade gliomas and infiltrative component of glioblastomas. *Biomed Opt Express*. (2013) 4:548–58. doi: 10.1364/BOE.4.000548
11. Hadjipanayis CG, Widhalm G, Stummer W. What is the surgical benefit of utilizing 5-aminolevulinic acid for fluorescence-guided surgery of malignant gliomas? *Neurosurgery*. (2015) 77:663–73. doi: 10.1227/NEU.0000000000000929
12. DSouza AV, Lin H, Henderson ER, Samkoe KS, Pogue BW. Review of fluorescence guided surgery systems: identification of key performance capabilities beyond indocyanine green imaging. *J Biomed Opt*. (2016) 21:80901. doi: 10.1117/1.JBO.21.8.080901
13. Stummer W, Stepp H, Möller G, Ehrhardt A, Leonhard M, Reulen HJ. Technical principles for protoporphyrin-IX-fluorescence guided microsurgical resection of malignant glioma tissue. *Acta Neurochir*. (1998) 140:995–1000. doi: 10.1007/s007010050206
14. Richards-Kortum R, Sevick-Muraca E. Quantitative optical spectroscopy for tissue diagnosis. *Annu Rev Phys Chem*. (1996) 47:555–606. doi: 10.1146/annurev.physchem.47.1.555
15. Bradley RS, Thorniley MS. A review of attenuation correction techniques for tissue fluorescence. *J R Soc Interface*. (2006) 3:1–13. doi: 10.1098/rsif.2005.0066
16. Belykh E, Miller EJ, Patel AA, Bozkurt B, Yagmurlu K, Robinson TR, et al. Optical characterization of neurosurgical operating microscopes: quantitative fluorescence and assessment of PpIX photobleaching. *Sci Rep*. (2018) 8:12543. doi: 10.1038/s41598-018-30247-6
17. Gioux S, Choi HS, Frangioni JV. Image-guided surgery using invisible near-infrared light: fundamentals of clinical translation. *Mol Imaging*. (2010) 9:237–55. doi: 10.2310/7290.2010.00034
18. Pogue BW, Zhu TC, Ntziachristos V, Paulsen KD, Wilson BC, Pfefer J, et al. Fluorescence-guided surgery and intervention—An AAPM emerging technology blue paper. *Med Phys*. (2018) 45:2681–8. doi: 10.1002/mp.12909
19. Valdés PA, Leblond F, Kim A, Harris BT, Wilson BC, Fan X, et al. Quantitative fluorescence in intracranial tumor: implications for ALA-induced PpIX as an intraoperative biomarker. *J Neurosurg*. (2011) 115:11–7. doi: 10.3171/2011.2.JNS101451
20. Kim A, Khurana M, Moriyama Y, Wilson BC. Quantification of *in vivo* fluorescence decoupled from the effects of tissue optical properties using fiber-optic spectroscopy measurements. *J Biomed Opt*. (2010) 15:067006. doi: 10.1117/1.3523616
21. Gibbs SL. Near infrared fluorescence for image-guided surgery. *Quant Imaging Med Surg*. (2012) 2:177–87. doi: 10.3978/j.issn.2223-4292.2012.09.04

22. Valdés PA, Leblond F, Jacobs VL, Wilson BC, Paulsen KD, Roberts DW. Quantitative, spectrally-resolved intraoperative fluorescence imaging. *Sci Rep*. (2012) 2:798. doi: 10.1038/srep00798
23. Ramanujam N. Fluorescence spectroscopy of neoplastic and non-neoplastic tissues. *Neoplasia*. (2000) 2:89–117. doi: 10.1038/sj.neo.7900077
24. Sokolov K, Follen M, Richards-Kortum R. Optical spectroscopy for detection of neoplasia. *Curr Opin Chem Biol*. (2002) 6:651–8. doi: 10.1016/S1367-5931(02)00381-2
25. Boas DA, Franceschini MA. Haemoglobin oxygen saturation as a biomarker: the problem and a solution. *Philos Trans A Math Phys Eng Sci*. (2011) 369:4407–24. doi: 10.1098/rsta.2011.0250
26. Müller MG, Georgakoudi I, Zhang Q, Wu J, Feld MS. Intrinsic fluorescence spectroscopy in turbid media: disentangling effects of scattering and absorption. *Appl Opt*. (2001) 40:4633–46. doi: 10.1364/AO.40.004633
27. Marois M, Bravo J, Davis SC, Kanick SC. Characterization and standardization of tissue-simulating protoporphyrin IX optical phantoms. *J Biomed Opt*. (2016) 21:35003. doi: 10.1117/1.JBO.21.3.035003
28. Angelo JP, Chen SJ, Ochoa M, Sunar U, Gioux S, Intes X. Review of structured light in diffuse optical imaging. *J Biomed Opt*. (2018) 24:1–20. doi: 10.1117/1.JBO.24.7.071602
29. Valdés PA, Kim A, Leblond F, Conde OM, Harris BT, Paulsen KD, et al. Combined fluorescence and reflectance spectroscopy for *in vivo* quantification of cancer biomarkers in low- and high-grade glioma surgery. *J Biomed Opt*. (2011) 16:116007. doi: 10.1117/1.3646916
30. Valdés PA, Kim A, Brantsch M, Niu C, Moses ZB, Tosteson TD, et al. Delta-aminolevulinic acid-induced protoporphyrin IX concentration correlates with histopathologic markers of malignancy in human gliomas: the need for quantitative fluorescence-guided resection to identify regions of increasing malignancy. *Neuro Oncol*. (2011) 13:846–56. doi: 10.1093/neuonc/nor086
31. Ishihara R, Katayama Y, Watanabe T, Yoshino A, Fukushima T, Sakatani K. Quantitative spectroscopic analysis of 5-aminolevulinic acid-induced protoporphyrin IX fluorescence intensity in diffusely infiltrating astrocytomas. *Neurol Med Chir*. (2007) 47:53–7; discussion 57. doi: 10.2176/nmc.47.53
32. Valdes PA, Millesi M, Widhalm G, Roberts DW. 5-aminolevulinic acid induced protoporphyrin IX (ALA-PpIX) fluorescence guidance in meningioma surgery. *J Neurooncol*. (2019) 141:555–65. doi: 10.1007/s11060-018-03079-7
33. Valdés PA, Leblond F, Kim A, Wilson BC, Paulsen KD, Roberts DW. A spectrally constrained dual-band normalization technique for protoporphyrin IX quantification in fluorescence-guided surgery. *Opt Lett*. (2012) 37:1817–9. doi: 10.1364/OL.37.001817
34. Valdes PA, Jacobs VL, Wilson BC, Leblond F, Roberts DW, Paulsen KD. System and methods for wide-field quantitative fluorescence imaging during neurosurgery. *Opt Lett*. (2013) 38:2786–8. doi: 10.1364/OL.38.002786
35. Valdés PA, Jacobs V, Harris BT, Wilson BC, Leblond F, Paulsen KD, et al. Quantitative fluorescence using 5-aminolevulinic acid-induced protoporphyrin IX biomarker as a surgical adjunct in low-grade glioma surgery. *J Neurosurg*. (2015) 123:771–80. doi: 10.3171/2014.12.JNS14391
36. Valdes PA, Bekelis K, Harris BT, Wilson BC, Leblond F, Kim A, et al. 5-Aminolevulinic acid-induced protoporphyrin IX fluorescence in meningioma: qualitative and quantitative measurements *in vivo*. *Neurosurgery*. (2014) 10(Suppl. 1):74–82; discussion 82–3. doi: 10.1227/NEU.0000000000000117
37. Valdes PA, Angelo JP, Choi HS, Gioux S. qF-SSOP: real-time optical property corrected fluorescence imaging. *Biomed Opt Express*. (2017) 8:3597–605. doi: 10.1364/BOE.8.003597
38. Bravo JJ, Olson JD, Davis SC, Roberts DW, Paulsen KD, Kanick SC. Hyperspectral data processing improves PpIX contrast during fluorescence guided surgery of human brain tumors. *Sci Rep*. (2017) 7:9455. doi: 10.1038/s41598-017-09727-8
39. Lin WC, Mahadevan-Jansen A, Johnson MD, Weil RJ, Toms SA. *In vivo* optical spectroscopy detects radiation damage in brain tissue. *Neurosurgery*. (2005) 57:518–25; discussion 518–25. doi: 10.1227/01.NEU.0000170559.48166.AC
40. Toms SA, Lin WC, Weil RJ, Johnson MD, Jansen ED, Mahadevan-Jansen A. Intraoperative optical spectroscopy identifies infiltrating glioma margins with high sensitivity. *Neurosurgery*. (2007) 61(1 Suppl):327–35; discussion 335–6. doi: 10.1227/01.neu.0000279226.68751.21
41. Toms SA, Lin WC, Weil RJ, Johnson MD, Jansen ED, Mahadevan-Jansen A. Intraoperative optical spectroscopy identifies infiltrating glioma margins with high sensitivity. *Neurosurgery*. (2005) 57(4 Suppl):382–91; discussion 382–91. doi: 10.1227/01.NEU.0000176855.39826.2D
42. Toms SA, Konrad PE, Lin WC, Weil RJ. Neuro-oncological applications of optical spectroscopy. *Technol Cancer Res Treat*. (2006) 5:231–8. doi: 10.1177/153303460600500306
43. Lin WC, Toms SA, Johnson M, Jansen ED, Mahadevan-Jansen A. *In vivo* brain tumor demarcation using optical spectroscopy. *Photochem Photobiol*. (2001) 73:396–402. doi: 10.1562/0031-8655(2001)0730396IVBTDU2.0.CO2
44. Lin WC, Sandberg DI, Bhatia S, Johnson M, Oh S, Ragheb J. Diffuse reflectance spectroscopy for *in vivo* pediatric brain tumor detection. *J Biomed Opt*. (2010) 15:061709. doi: 10.1117/1.3505012
45. Utsuki S, Oka H, Miyajima Y, Shimizu S, Suzuki S, Fujii K. Auditory alert system for fluorescence-guided resection of gliomas. *Neurol Med Chir*. (2008) 48:95–7; discussion 97–8. doi: 10.2176/nmc.48.95
46. Eljamel MS, Goodman C, Moseley H. ALA and Photofrin fluorescence-guided resection and repetitive PDT in glioblastoma multiforme: a single centre Phase III randomised controlled trial. *Lasers Med Sci*. (2008) 23:361–7. doi: 10.1007/s10103-007-0494-2
47. Haj-Hosseini N, Richter J, Andersson-Engels S, Wårdell K. Optical touch pointer for fluorescence guided glioblastoma resection using 5-aminolevulinic acid. *Lasers Surg Med*. (2010) 42:9–14. doi: 10.1002/lsm.20868
48. Black D, Hahn HK, Kikinis R, Wårdell K, Haj-Hosseini N. Auditory display for fluorescence-guided open brain tumor surgery. *Int J Comput Assist Radiol Surg*. (2018) 13:25–35. doi: 10.1007/s11548-017-1667-5
49. Diamond KR, Patterson MS, Farrell TJ. Quantification of fluorophore concentration in tissue-simulating media by fluorescence measurements with a single optical fiber. *Appl Opt*. (2003) 42:2436–42. doi: 10.1364/AO.42.002436
50. Wu J, Feld MS, Rava RP. Analytical model for extracting intrinsic fluorescence in turbid media. *Appl Opt*. (1993) 32:3585–95. doi: 10.1364/AO.32.003585
51. Weersink R, Patterson MS, Diamond K, Silver S, Padgett N. Noninvasive measurement of fluorophore concentration in turbid media with a simple fluorescence /reflectance ratio technique. *Appl Opt*. (2001) 40:6389–95. doi: 10.1364/AO.40.006389
52. Huang Z, Shi S, Qiu H, Li D, Zou J, Hu S. Fluorescence-guided resection of brain tumor: review of the significance of intraoperative quantification of protoporphyrin IX fluorescence. *Neurophotonics*. (2017) 4:011011. doi: 10.1117/1.NPh.4.1.011011
53. Yang VX, Muller PJ, Herman P, Wilson BC. A multispectral fluorescence imaging system: design and initial clinical tests in intra-operative Photofrin-photodynamic therapy of brain tumors. *Lasers Surg Med*. (2003) 32:224–32. doi: 10.1002/lsm.10131
54. Saager RB, Cuccia DJ, Saggese S, Kelly KM, Durkin AJ. Quantitative fluorescence imaging of protoporphyrin IX through determination of tissue optical properties in the spatial frequency domain. *J Biomed Opt*. (2011) 16:126013. doi: 10.1117/1.3665440
55. O'Sullivan TD, Cerussi AE, Cuccia DJ, Tromberg BJ. Diffuse optical imaging using spatially and temporally modulated light. *J Biomed Opt*. (2012) 17:071311. doi: 10.1117/1.JBO.17.7.071311
56. Jermyn M, Gosselin Y, Valdes PA, Sibai M, Kolste K, Mercier J, et al. Improved sensitivity to fluorescence for cancer detection in wide-field image-guided neurosurgery. *Biomed Opt Express*. (2015) 6:5063–74. doi: 10.1364/BOE.6.005063

57. Sibai M, Fisher C, Veilleux I, Elliott JT, Leblond F, Roberts DW, et al. Preclinical evaluation of spatial frequency domain-enabled wide-field quantitative imaging for enhanced glioma resection. *J Biomed Opt.* (2017) 22:76007. doi: 10.1117/1.JBO.22.7.076007
58. van de Giessen M, Angelo JP, Gioux S. Real-time, profile-corrected single snapshot imaging of optical properties. *Biomed Opt Express*. (2015) 6:4051–62. doi: 10.1364/BOE.6.004051
59. Vervandier J, Gioux S. Single snapshot imaging of optical properties. *Biomed Opt Express*. (2013) 4:2938–44. doi: 10.1364/BOE.4.002938
60. Hoogstins C, Burggraaf JJ, Koller M, Handgraaf H, Boogerd L, van Dam G, et al. Setting standards for reporting and quantification in fluorescence-guided surgery. *Mol Imaging Biol.* (2019) 21:11–18. doi: 10.1007/s11307-018-1220-0

Conflict of Interest Statement: PV reports multiple patents on optical spectroscopy and fluorescence imaging technologies.

The remaining authors declare that the research was conducted in the absence of any commercial or financial relationships that could be construed as a potential conflict of interest.

frontiers in Oncology

ORIGINAL RESEARCH
published: 13 June 2019
doi: 10.3389/fonc.2019.00513

The Probe Based Confocal Laser Endomicroscopy (pCLE) in Locally Advanced Gastric Cancer: A Powerful Technique for Real–Time Analysis of Vasculature

Alessandra Capuano[1†], Eva Andreuzzi[1†], Eliana Pivetta[1], Roberto Doliana[1], Andrea Favero[1], Vincenzo Canzonieri[2], Stefania Maiero[3], Mara Fornasarig[3], Raffaella Magris[3], Renato Cannizzaro[3], Maurizio Mongiat[1‡] and Paola Spessotto[1‡]*

[1] Molecular Oncology, Centro di Riferimento Oncologico (CRO), IRCCS, Aviano, Italy, [2] Pathology, Centro di Riferimento Oncologico (CRO), IRCCS, Aviano, Italy, [3] Oncological Gastroenterology, Centro di Riferimento Oncologico (CRO), IRCCS, Aviano, Italy

OPEN ACCESS

Edited by:
David Leslie Carr-Locke, Weill Cornell Medicine, Cornell University, United States

Reviewed by:
Balaji Krishnamachary, Johns Hopkins University, United States
Massimiliano Cadamuro, University of Padova, Italy

***Correspondence:**
Renato Cannizzaro
rcannizzaro@cro.it

[†] These authors have contributed equally to this work

[‡] These authors share co-last authorship

Specialty section:
This article was submitted to Cancer Imaging and Image-directed Interventions, a section of the journal Frontiers in Oncology

Received: 30 January 2019
Accepted: 29 May 2019
Published: 13 June 2019

Citation:
Capuano A, Andreuzzi E, Pivetta E, Doliana R, Favero A, Canzonieri V, Maiero S, Fornasarig M, Magris R, Cannizzaro R, Mongiat M and Spessotto P (2019) The Probe Based Confocal Laser Endomicroscopy (pCLE) in Locally Advanced Gastric Cancer: A Powerful Technique for Real–Time Analysis of Vasculature. Front. Oncol. 9:513. doi: 10.3389/fonc.2019.00513

Probe based confocal laser endomicroscopy (pCLE) is an advanced technique which provides imaging of gastrointestinal mucosa at subcellular resolution and, importantly, a valid tool for the evaluation of microvasculature during endoscopic examination. In order to assess intratumoral vascularization and the efficiency of blood flow in locally advanced gastric cancer, we examined 57 patients through pCLE imaging. The vascular alterations in gastric cancer were mainly characterized by leakage and by the presence of tortuous and large size vessels. Defects in blood flow were detected very rarely. No association between the angiogenic score and the gastric tumor site or histological type was observed. Interestingly, no correlation was also found with the tumor grading indicating that the vascular angiogenic anomalies in gastric cancer represent an early pathological event to be observed and detected. The majority of patients displayed unchanged vascular alterations following neoadjuvant chemotherapy and this positively correlated with stable or progressive disease, suggesting that an unaltered angiogenic score could *per se* be indicative of poor therapeutic efficacy. Different vascular parameters were evaluated by immunofluorescence using bioptic samples and the vessel density did not correlate with clinical staging, site or histologic type. Interestingly, only CD105, Multimerin-2 and GLUT1 were able to discriminate normal from tumoral gastric mucosa. Taken together, these findings indicate that functional and structural angiogenic parameters characteristic of tumor blood network were fully detectable by pCLE. Moreover, the evaluation of tumor vasculature by real-time assessment may provide useful information to achieve tailored therapeutic interventions for gastric cancer patients.

Keywords: pCLE, gastric cancer, angiogenesis, angiogenic score, CD31, CD34, CD105, MMRN2

INTRODUCTION

Gastric cancer is a major leading cause of cancer-related deaths and a relative common malignancy (1). Surgical resection of the tumor represents the approved option to improve patients' survival (2). At diagnosis, most of the patients display locally advanced or metastatic disease. To improve their chances they are treated with palliative chemotherapy, including cisplatin, docetaxel, oxaliplatin and 5FU, among other drugs (3–5). Unfortunately, at 5 years from the diagnosis only 10% of the patients affected by advanced or metastatic gastric cancer will survive and the median overall survival (OS) is only 1 year (6). Therefore, new therapeutic approaches and more specific targeted therapies are required for the treatment of this type of cancer. Angiogenesis, the development of new blood vessels from pre-existing vasculature, affects tumor growth and the metastatic dissemination of cancer cells and in the latest years has gained attention in gastric cancer research as a promising target (7–9). The angiogenic process is regulated by a plethora of cytokines and growth factors as well as by different cell types (10). Tumor cells will not grow beyond the size of few millimeters unless induce the secretion of angiogenic factors and the development of blood vessel for nutrients and oxygen supply. However, the erratic angiogenic stimulus leads to the formation of an abnormal and not fully functional vascular network (11). An attractive approach that has been advanced in the latest years is the normalization of the aberrant tumor-associated vessels for the induction of a more efficient vasculature. A normalized vasculature would allow an improved delivery of drugs within the tumor and hence a better therapy efficacy (12, 13). One of the major regulators of angiogenesis is the VEGFA/VEGFR2 signaling axis and represents a major target for anti-angiogenic therapy (13, 14). Interestingly, in gastric cancer patients high VEGFA levels have been associated with reduced survival and increased tumor aggressiveness (15). Anti-angiogenic therapy in gastric cancer patients did not so far meet the expectations despite some improvements have been observed (16). Thus, in order to improve the efficacy of anti-angiogenic therapy, it is of major importance to better characterize the vasculature associated with this tumor type.

The probe based Confocal Laser Endomicroscopy system (pCLE) is a highly enhanced endoscopic technique constituted by a confocal scanning microscope integrated into a conventional flexible endoscope. pCLE provides high quality imaging of the tissue, with a resolution of approximately 1 micron of the mucosal layer (17, 18). The main clinical application for which pCLE was developed includes the real-time histopathological diagnosis of gastrointestinal lesions. However, in recent years additional potential application have been proposed and gained attention such as cancer screening on the basis of cellular and vascular changes (19–22). In fact, by using intravenously administered fluorescein sodium (23), images of vascular network can be clearly detected offering the possibility to gain information on the characteristics of gastrointestinal tumor vessels in real time (24). Our group was among the pioneers in exploiting this new promising imaging tool to analyze the angiogenesis pattern in patients with gastric and rectal cancer (25). Unlike conventional immunohistochemistry, the aim was to provide a prompt and accurate evaluation of the pattern and efficiency of intratumoral vessels through a non-invasive technique. The analyses suggested that pCLE was exceptionally powerful tool to visualize and characterize the tumor-associated vasculature. Interestingly, we found that rectal and gastric cancers were highly angiogenic; however, rectal tumors displayed a higher percentage of dilated vessels and presence of defective flow (25).

With the aim of developing new strategies to achieve more efficacious gastric cancer patient-tailored treatments, in this study we thoroughly analyze the vascular characteristics of this type of tumor evaluating the employment of pCLE in the assessment of intratumoral angiogenesis.

MATERIALS AND METHODS

Patients

For this study 57 patients with locally advanced gastric cancer were enrolled to undergo endomicroscopy. Written informed consent was obtained from each patient on the day of the procedure. The methodologies conformed to the standards set by the Declaration of Helsinki. This study was approved by the Institutional Board of CRO-IRCCS, National Cancer Institute of Aviano (PN), Italy (IRB no. CRO-2014-03). The clinical evaluations are reported in **Table 1**. Patients underwent neoadjuvant multiregimen chemotherapy (oxaliplatin, capecitabine, and taxane) followed by surgical resection according to standard guidelines. Laboratory and pathological results were collected by means of the Hospital database.

TABLE 1 | Clinic-pathological characteristics of patients.

	N°	%
GENERAL INFORMATION		
All cases	57	100
Males	28	49
Mean age	62	
Females	29	51
Mean age	61	
HISTOLOGIC TYPE (LAUREN CLASSIFICATION)		
Diffuse	30	52.6
Intestinal	27	47.4
TUMOR SITE		
Body	35	61
Antrum	14	25
Fundus	5	9
Cardias	3	5
STAGING		
Ia-IIa	28	51
IIIa-IV	27	49

Endoscopy Procedures and pCLE Analyses

pCLE analyses were carried out with GastroFlex UHD probe (Cellvizio, Mauna Kea Technology, Paris, France) during gastroscopy (Olympus series 180) and immediately before endoscopic ultrasonography (Olympus series 160) as previously described (25). Patients were examined before chemotherapy or surgical intervention (first pCLE). 13 patients (corresponding to 23% of all patients) were also examined after chemotherapy treatment (second pCLE). Images and sequences of the normal and neoplastic mucosa were taken and the conventional bioptic samples obtained with macrobiopsy (COOK Medical, Ireland) at the end of examination. Images were recorded within the first 10 min following i.v. injection of fluorescein (5 ml of a 10% solution). pCLE images were collected at 12 frames per second to assure high video quality and a direct visualization on a single erythrocyte scale. pCLE recordings were performed for at least 3 min resulting in a real-time imaging of more than 2 thousand frames. Using the videomosaicing function provided by the analysis software, we also obtained the reconstruction of the scanned panoramas of the mucosa. The mucosal architecture, vessel morphology and the efficiency of the blood flow were evaluated. The images were digitally stored and reviewed with the dedicated software package (Cellvizio Viewer, Mauna Kea Technologies) by a single investigator who was blinded to any clinical, endoscopic, or histopathological information. The angiogenic score was assigned on the basis of the presence of tortuous and large sized vessels, the vessels' leakage and the presence of defective flow as previously described (25).

Immunofluorescence

For immunofluorescence (IF) analyses on bioptic samples, serial cryostat sections (7 μm) were collected on positively charged slides (BDH Superfrost Plus), air dried at room temperature (RT) and fixed with PFA for 15 min. After washing with phosphate-buffered saline (PBS), the slices were incubated with 0.5% Triton X-100 in PBS for 5 minutes at RT, saturated with 1% BSA−10% normal goat serum (DAKO) in PBS for 1 h at RT, and stained ON at 4 °C with the appropriate antibodies. Next, the samples were washed with PBS and incubated with the appropriate secondary antibodies and TO-PRO3 to stain the nuclei for 1 hour at RT. After washing with PBS, the slides were mounted in Mowiol containing 2.5% (w/v) of 1,4-diazabicyclo-(2,2,2)-octane (DABCO). Images were acquired with a Leica TCS SP8 Confocal system (Leica Microsystems Heidelberg, Mannheim, Germany), using the Leica Confocal Software (LCS). The monoclonal anti-human CD31, CD34, and CD105 antibodies were from Abcam (Cambridge, UK). The polyclonal anti-human Multimerin-2 (MMRN2) antibody was produced in our laboratories as previously described (26); the polyclonal anti-human GLUT 1 antibody was from Millipore (Temecula, CA, USA). The secondary antibodies conjugated with Alexa Fluor 488, 546 and TO-PRO-3 were from Invitrogen (Milan, Italy).

Quantification Analyses

Fluorescence intensity and quantification were evaluated by means of the Volocity software Version 6.1.1 (PerkinElmer Inc.,Waltham, MA, USA). The expression of CD31, CD34, CD105, MMRN2, and GLUT1 was calculated as pixel positive area of at least four 40x acquired fields. Corresponding values were expressed as mean ± SD.

Statistical Analysis

CD31, CD43, CD105, MMRN2, and GLUT1 expression levels between healthy and tumor mucosa of gastric cancer patients were compared by the Mann-Whitney non-parametric test. Relationships between positivity for vascular and angiogenesis markers and clinic-pathological features were evaluated using Spearman's rank correlation coefficient. Results were considered statistically significant for P-value < 0.05.

RESULTS

pCLE Is a Valuable Tool to Assess the Properties of Gastric Cancer-Associated Vasculature

pCLE has been used in the diagnosis of gastric lesions for the possibility to easily detect with high accuracy the typical morphological alterations of the mucosal architecture (27–33). In **Figure 1** we report representative reconstructions of the scanned panoramas of gastric mucosa obtained using the videomosaicing function which allows the alignment of the input frames. The differences in both morphological and vascular pattern between the normal (**Figure 1A**), atrophic (**Figure 1B**) and neoplastic (**Figure 1C**) gastric mucosa indicate that pCLE is a suitable tool not only for real time histopathological evaluations, but also for the assessment of the gastric cancer-associated vasculature. A thorough and prompt evaluation of the extent and quality of these vessels is in fact important to identify the patients that more likely will respond to anti-angiogenic treatment, as well as to develop new strategies to improve the efficacy of these treatments in non-responders. To this end we exploited the pCLE technology to evaluate the presence of tortuous and large-sized vessels, the presence of vascular leakage, and the efficiency of the vessels in terms of blood flow. We enrolled 57 patients affected by locally advanced gastric cancer and assigned an angiogenic score based on the pCLE analyses. The larger cohort of patients allowed us to confirm with statistical significance the observations gathered from few patients in a previous study aimed at comparing the vasculature of rectal and gastric tumors (25). Representative images of the vascular aberrations in gastric cancer patients characterized by different angiogenic scores are shown in **Figure 2A** (see also **Videos S1**, **S2**). A "3" angiogenic score was assigned to almost 50% of patients indicating that gastric tumors are characterized by a remarkably abnormal and unfunctional vasculature. In fact, a "1" angiogenic score was assigned to only the 11% of all the patients enrolled (**Figure 2B**). The most represented abnormalities were vessel leakage, which was detectable in 55 patients out of 57, the presence of tortuous vessels in 81% of the cases, and the presence of large diameter vessels in 67% of the patients. On the contrary, the presence of aberrant blood flow was detected only in 5% of the patients (**Figure 2C** and **Video S2**). To verify if the vascular pattern could depend on the clinical stage the

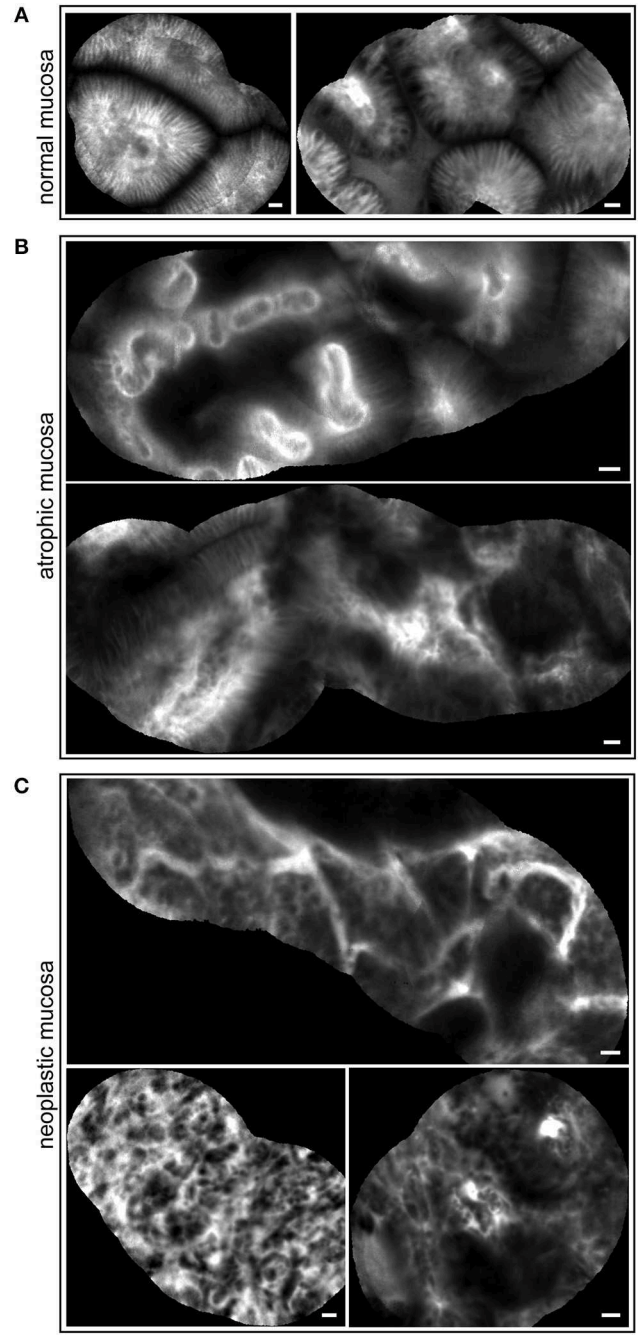

FIGURE 1 | pCLE imaging in gastric mucosa. Representative mosaic reconstructions obtained from scanned panoramas of normal **(A)**, atrophic **(B)**, and tumor **(C)** gastric mucosa. The morphology of regular glands is well defined in **(A)**; some mild to moderate alterations in morphological epithelium architecture as well as unstructured vessels are easily observed in **(B)**; complexity of mucosa with severe cell irregularity and very altered vascular network are shown in **(C)**. Scale bar = 20 μm.

patients were distributed into two categories: Ia-IIb and IIIa-IV. The statistical analyses indicated that there was no association between angiogenic score and staging (**Figure 3A**). In fact, the "2" and "3" angiogenic scores were homogenously distributed in both categories and the "1" and "4" angiogenic scores were not assigned to the low or high clinical stages, respectively. Next, we hypothesized that characteristics of the vasculature could depend on the tumor site or histological type according to Lauren classification (34, 35); however, we found that the angiogenic score did not correlate with these parameters (**Figures 3B,C**). A very high homogeneity was detected when we distributed the patients according to the histological type: no difference in angiogenic score distribution was observed between diffuse and intestinal type (**Figure 3C**). Although not statistically significant, the group characterized by lesions localized in the antrum displayed very frequently a "2" angiogenic score (**Figure 3D**). Taken together, the results from the pCLE analyses indicated that locally advanced gastric cancer is characterized by a remarkably abnormal and unfunctional vasculature.

Neoadjuvant Chemotherapy Does not Significantly Affect the Vascular Properties

Among the enrolled patients a total of 13 (9 with T3N+ and 4 with T3N0, as evaluated during the first endoscopy) completed the neoadjuvant chemotherapy program. The subjects were re-evaluated by pCLE before surgery. These analyses indicated that the chemotherapy treatment did not significantly affect the angiogenic score of the tumors, despite a slight improvement in tumor grading was observed in almost 70% of these patients (**Figure 4**). These results suggest that neodjuvant therapy halted primarily the proliferation of tumor cells without affecting the properties and extent of the vascular network. Interestingly, these findings are in line with the fact that no correlation was found between the results gathered through the pCLE analyses and the tumor staging (**Figure 3A**). Given that locally advanced gastric cancers are characterized by a highly abnormal vasculature, it can be speculated that the slight efficacy of the treatment may depend on a poor delivery of chemotherapy within the tumor of stable or progressive disease patients.

Gastric Cancer Vessels Are Poorly Efficient and Lead to Increased Intratumoral Hypoxia

In order to better define the quality of the gastric cancer associated vasculature we performed IF analyses employing different vascular markers i.e., CD31, CD34, CD105, Multimerin-2. Since Multimerin-2 was previously shown to affect HIF-1α expression (26) we also assessed the hypoxic levels in this tumor. To this end, we employed GLUT1 as a later maker of hypoxia, also in the light of the fact that it was recently reported to be a maker of poor prognosis (36, 37). To this end, during endoscopy and pCLE examination, bioptic samples of healthy and tumor mucosa of 33 patients were collected. First, we evaluated which marker could better detect the vascular density in normal and tumor gastric mucosa. These analyses are shown in **Figure 5** where we report the percentage of positivity relative to the mucosal area for each vascular marker. The results from these analyses indicated that, despite the staining for CD31 and CD34 were higher in the tumor mucosa compared to the normal counterpart, the differences were not statistically significant.

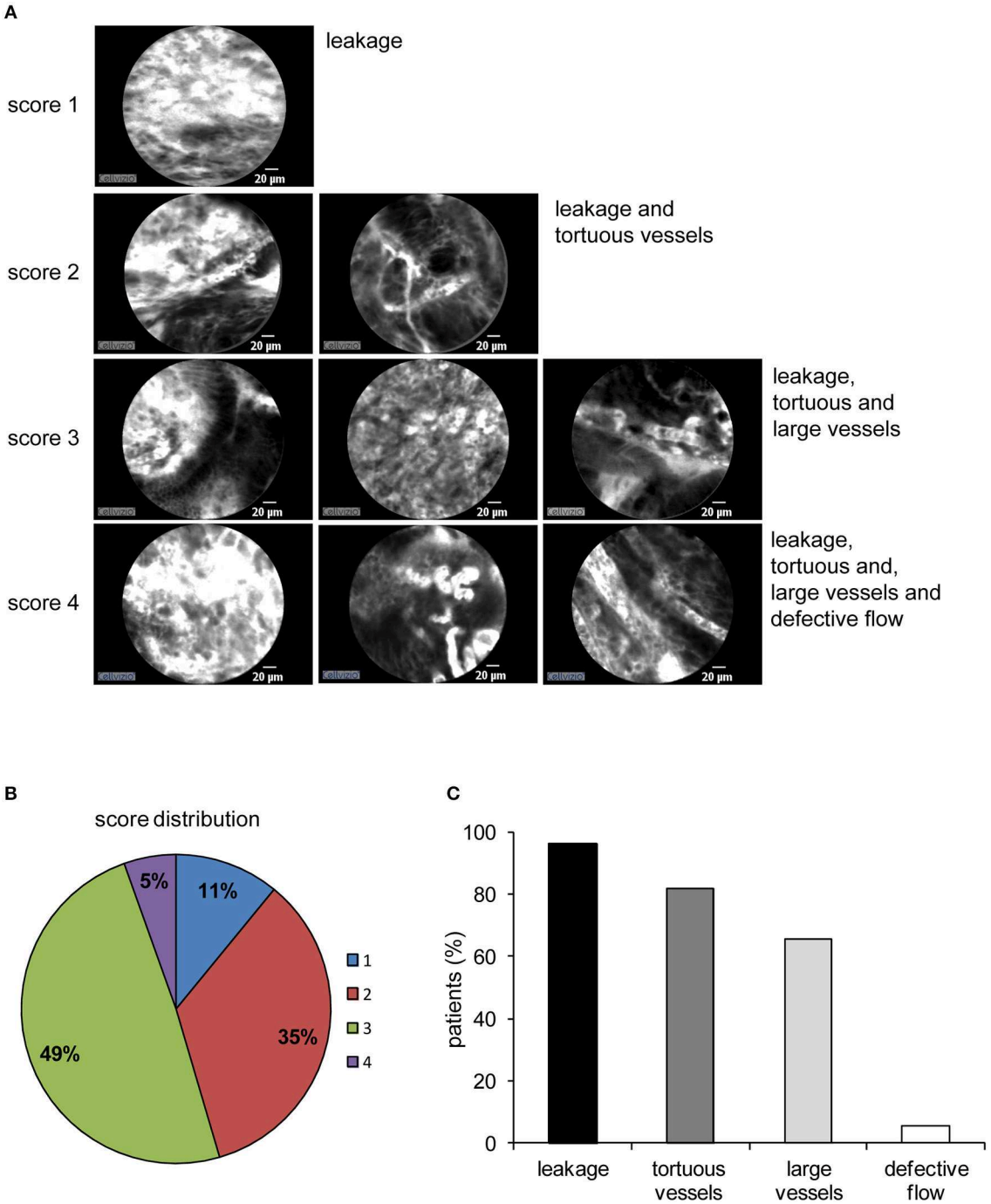

FIGURE 2 | Angiogenic score in gastric cancer. **(A)** Representative images from patients displaying different angiogenic scores (from 1 to 4). The altered features of the tumor vasculature taken into account (leakage, tortuous and large vessels, and aberrant blood flow) are displayed (see also **Videos S1**, **S2**). A value of "1" was assigned to indicate the presence of each vessel feature and a value of "0" for the absence. The angiogenic score is the result of the arithmetical sum of the single features. **(B)** Distribution of the angiogenic score among all 57 gastric cancers analyzed. **(C)** Percentage of gastric cancer patients displaying the morphological and functional features as defined for the angiogenic score assignment. Aberrant blood flow was rarely detectable whereas leakage and the presence of tortuous vessels were the most frequent.

On the other hand, CD105 staining was significantly higher in tumor tissues, suggesting that this marker could better measure the vascular density in gastric tumors. We next assessed the expression of Multimerin-2, an extracellular matrix glycoprotein specifically expressed by endothelial cells exerting an angiostatic and homeostatic function (26, 38–41). We found a striking loss

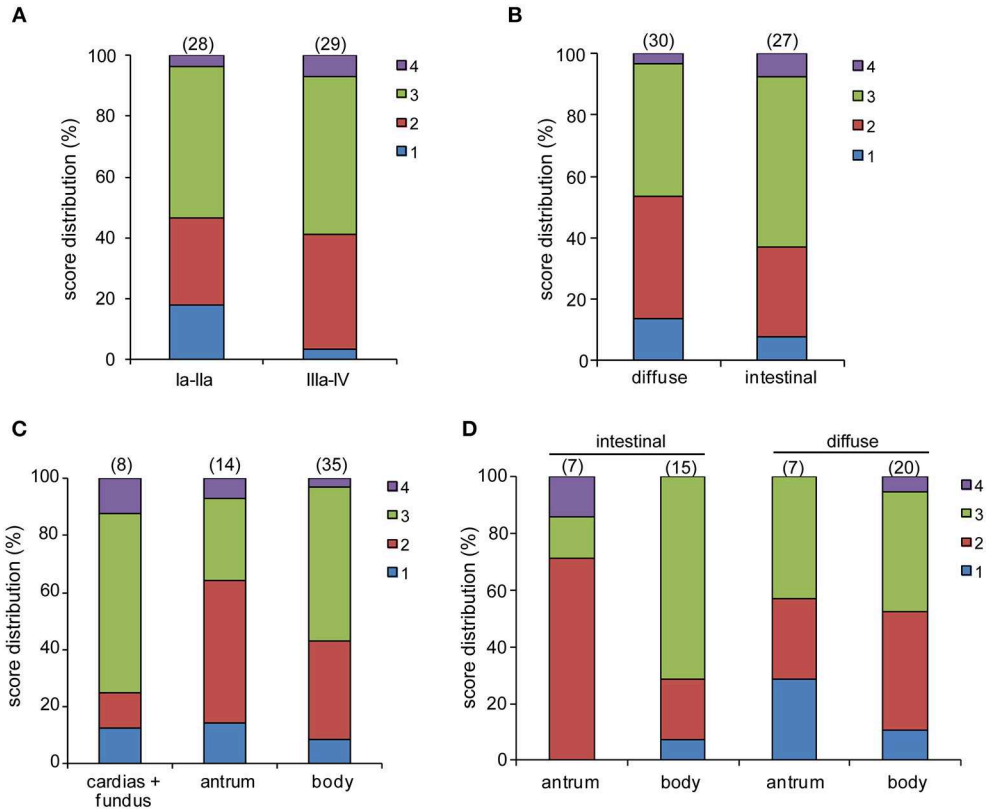

FIGURE 3 | pCLE analysis and patient clinical categories. No statistically significant differences were observed between the score distribution and the tumor staging **(A)**, histologic type **(B)**, or tumor site **(C)**. Although not statistically significant, the percentage of patients with an intestinal type of gastric cancer and a score "3" is more associated with a body than an antrum localization **(D)**.

of Multimerin-2 expression in many gastric tumor associated vessels (**Figure 5**). Another parameter to verify, even if indirectly, the vascular efficiency is to measure the extent of hypoxic regions. To this end, the bioptic samples were stained with GLUT1. As reported in **Figure 5**, most of the gastric cancer samples displayed an increased expression of GLUT1 compared to the normal counterpart. The relative expression of these markers was independent from the tumor staging (**Figure 6A**), similarly to what observed with the angiogenic score determined by pCLE analyses (**Figure 3A**). Also, no correlation between the markers' expression and the histological type and tumor site was detected (**Figures 6B,C**).

These findings encourage the use of pCLE as a powerful tool to detect functional aberrations and other anomalies of the tumor vasculature rather than a mere microscopic system for the assessment of the vascular density.

DISCUSSION

In this study we assessed the possible employment of pCLE as a valid clinical tool to evaluate the vascular properties in gastric cancer. The analyses indicated that this endoscopic technique is indispensable to provide structural and functional insights useful to better characterize the tumor vascular network in locally advanced gastric cancer. Unlike the conventional immunohistochemical approach, which provides a static portrayal of the vasculature, pCLE is a technique able to dynamically visualize the efficiency of the vessels evaluating the extent of vascular leakage and also the efficiency of blood flow within the vessels. Despite markers of vascular leakage are available, such as the erythrocyte marker Ter119, the staining is difficult to interpret and often not reliable. In fact, the use of the Ter119 on the gastric cancer samples did not lead to any detectable specific staining (data not shown). On the contrary, the use of pCLE allows a clear detection of the fluorescein staining outside the vascular wall. It is thus possible to identify the percentage of vessels whose functionality is compromised and characterized by increased leakage. An additional information that can be provided exclusively with the use of pCLE is the efficiency of blood vessels flow. Despite not very frequently, the pCLE analyses in some occasions detected the presence of defective blood flow characterized by an erratic non-directional cell stream. It is conceivable that such vessels are unable to efficiently transport and distribute the blood as well the therapeutic drugs within the tumor, thus leading to increased hypoxia and decreased therapy efficacy, respectively. We subsequently compared the results from the pCLE analyses with those obtained with the use of different vascular markers

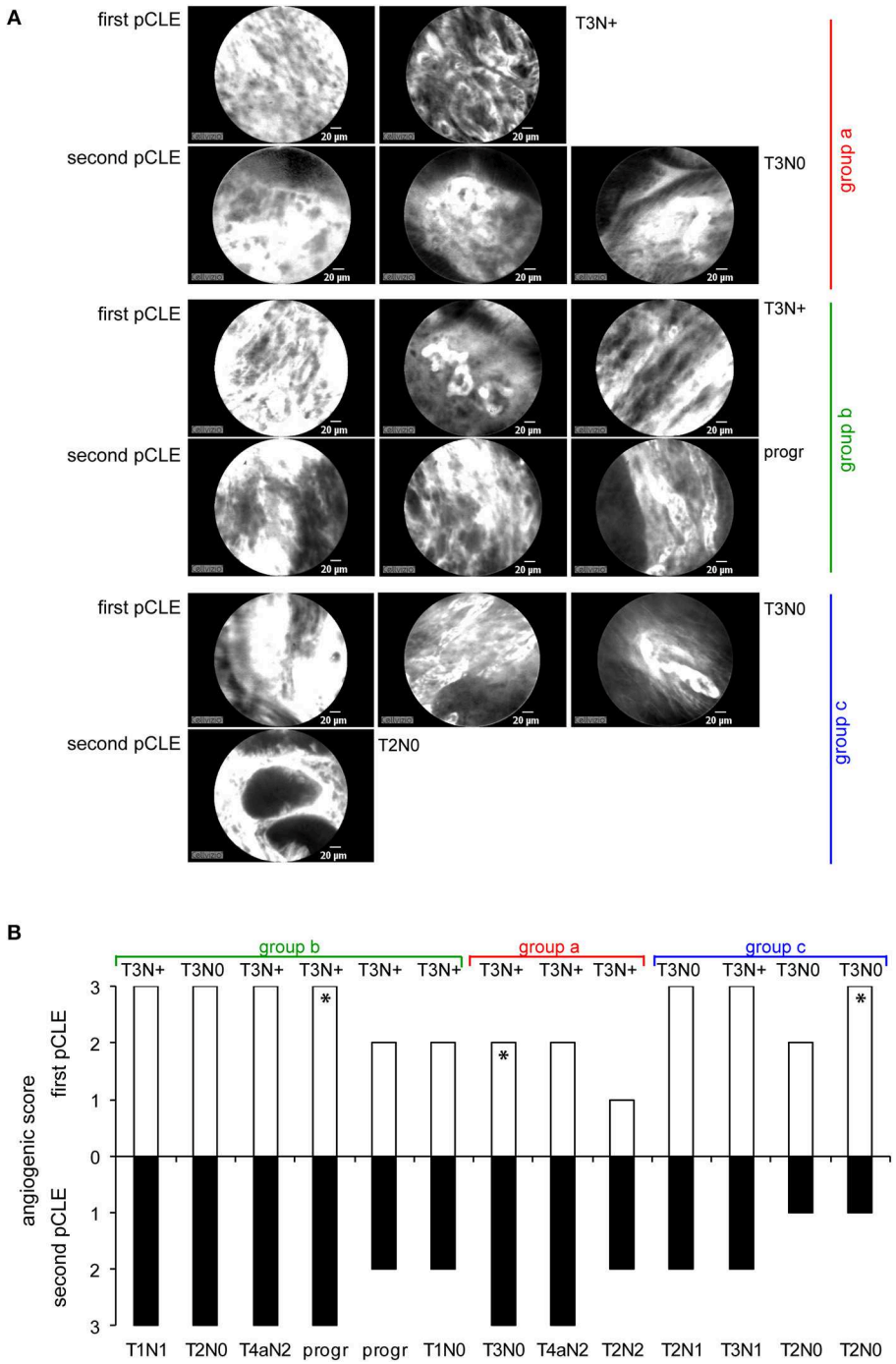

FIGURE 4 | pCLE in patients after chemotherapy treatment. **(A)** Representative pCLE images collected from three patients belonging to three different groups displaying increased (group a), equal (group b) or decreased (group c) angiogenic score after therapy (second pCLE). **(B)** Graph showing the angiogenic score assigned before (first pCLE) and after therapy in 13 gastric cancer patients. Asterisks in the graph indicate the patients whose pCLE images were chosen as representative in **(A)**. For each patients the corresponding tumor grading or disease progression (prog) before and after therapy is reported both in **(A,B)**.

following the immunohistochemical studies. We found that, unlike that of CD105, the analysis of the expression of CD31 and CD34 did not lead to a significant increased staining in gastric tumors, compared to the normal counterpart. Since CD105 is a marker of immature vessels, it is possible that these results depend on the fact that this maker is more appropriate for the detection of the newly formed vessels associated with tumors, as was previously suggested (42). In line with our

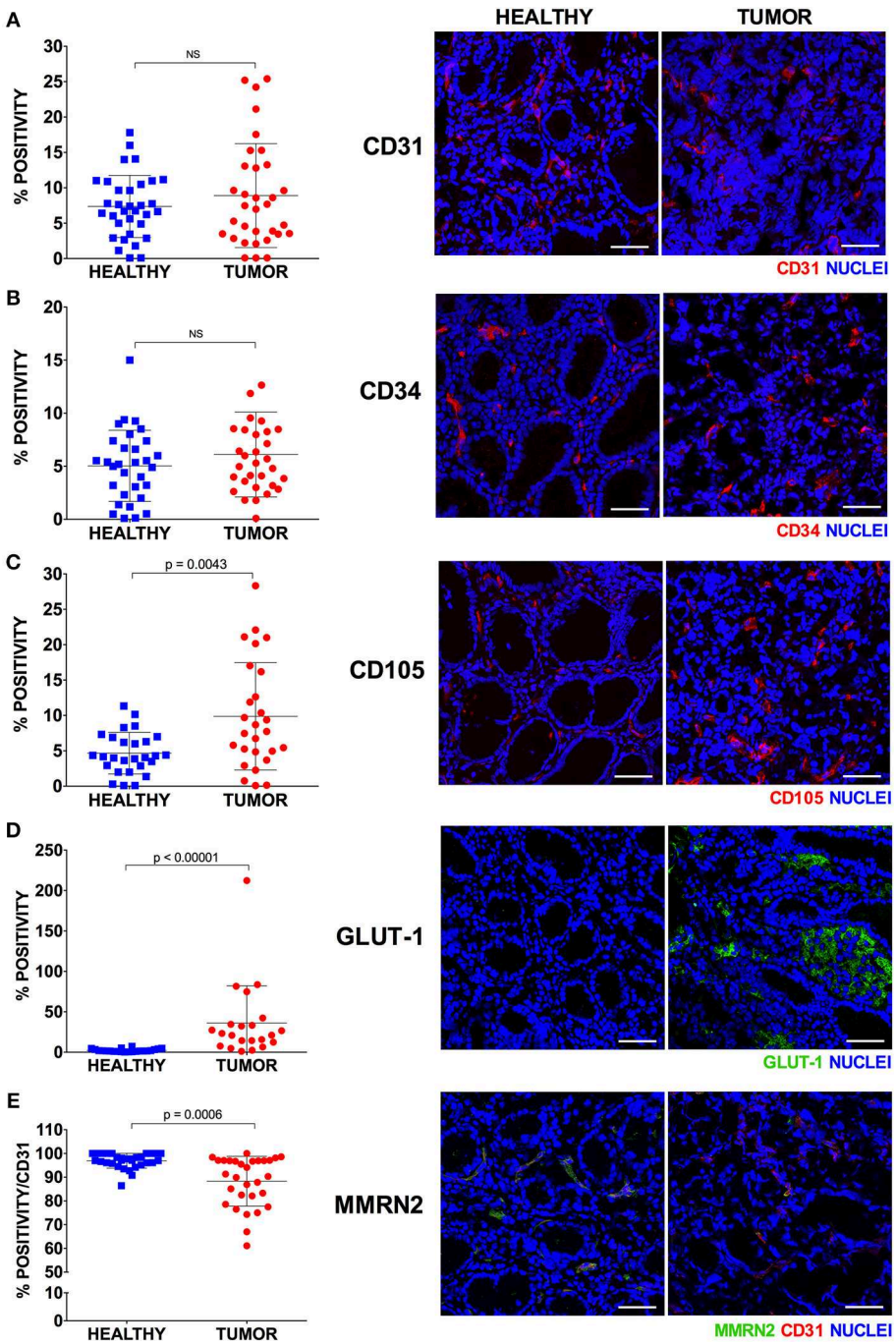

FIGURE 5 | Expression of endothelial cell markers in healthy and tumor gastric tissues. Representative images of healthy and tumor gastric mucosa stained with anti-vascular marker antibodies and scatter plots of the corresponding expression calculated as percentage of IF positive stained area [CD31, **(A)**; CD34, **(B)**; CD105, **(C)**; GLUT-1, **(D)**; MMRN2, **(E)**]. For each marker at least four 40x magnified fields were evaluated. The results are expressed as mean ± SD. Scale bar = 50 μm.

observations it was also reported that CD34 was universally expressed in blood vessels within benign and malignant tissues, whereas CD105 expression was barely detectable in benign tissues and high in gastric carcinoma (43, 44). No clear role for CD34 in angiogenesis has been reported so far (45–48). On the contrary, it has been shown that CD105, as a receptor as TGF-β, may regulate the role of this cytokine in the angiogenic process and be more suitable for detecting newborn blood vessels in gastric and colorectal cancer (49). CD105 expression is strongly upregulated in various tumor tissues, including colon, breast, brain, lung, prostate, and cervix (50, 51). Little is known about the clinical significance of CD105 in gastric carcinomas;

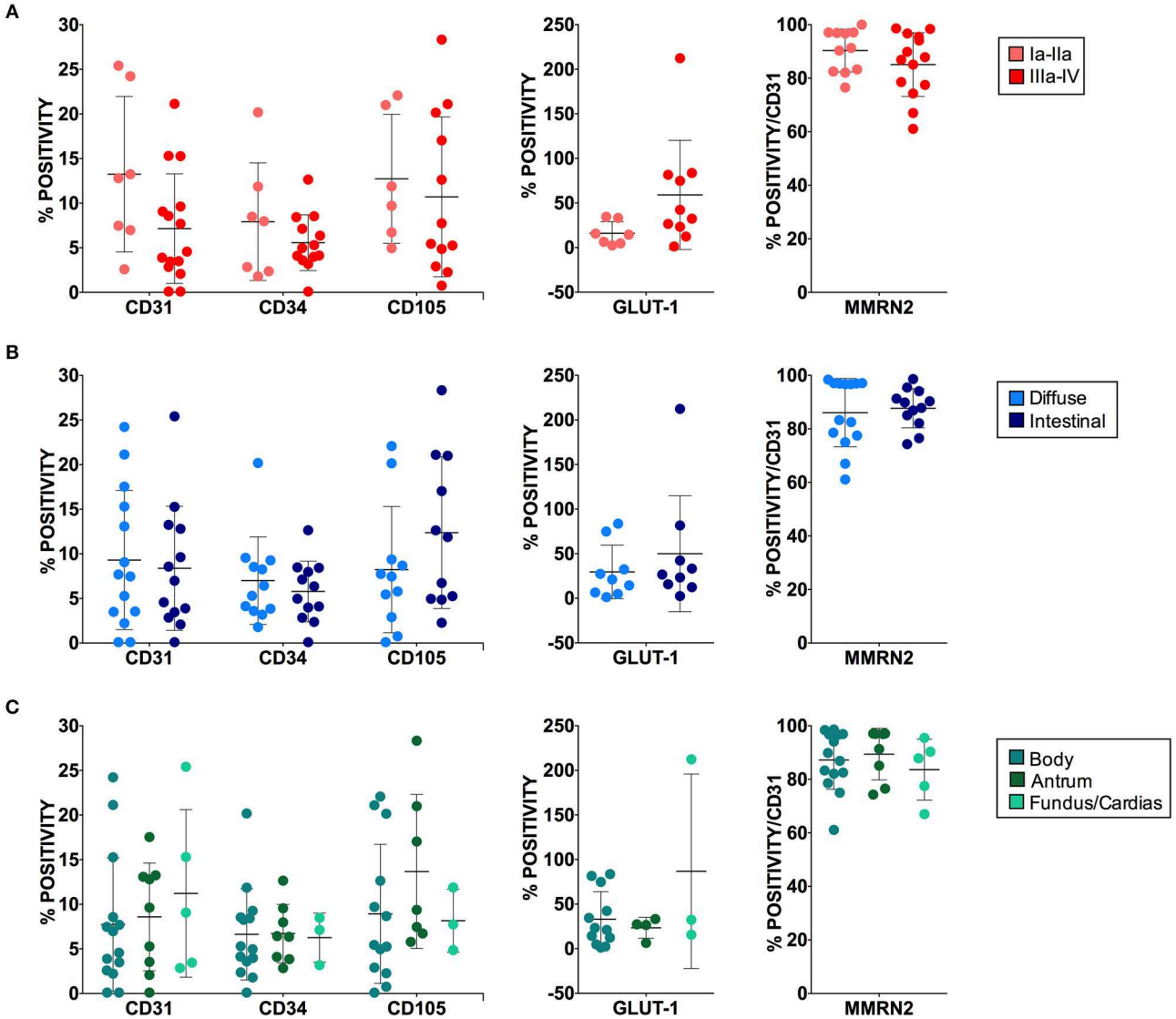

FIGURE 6 | Angiogenesis markers and patient clinical categories. No statistically significant differences were observed between marker positive staining and tumor staging **(A)**, histologic type **(B)**, or tumor site **(C)**. For each marker at least four 40x magnified fields were evaluated. The results are expressed as mean ± SD.

however, Nikiteas et al. have shown that VEGF and CD105 were involved in lymph node metastasis and acted as valuable indicators of the prognosis (52). The fact that high CD105 levels did not correlate with pCLE-based high angiogenic score may depend on the fact that vascular efficiency and stability is affected by several factors being controlled by cytokines, receptors and extracellular matrix components as well as mural cells. Thus, a comprehensive analysis of the proteins and pathways affecting vascular efficiency could be difficult and laborious to perform. On the contrary, the results obtained through the pCLE analyses provide information on the quality and efficiency of the vasculature independently from the molecular cause. In addition, an important advantage of the use of this tool is that the analyses precede the pathology investigations, thus providing a prompt information. We subsequently analyzed the expression of Multimerin-2, an extracellular matrix glycoprotein involved in the maintenance of vascular stability function. We found that many gastric cancer samples displayed loss of Multimerin-2. Since Multimerin-2 is a homeostatic molecule we hypothesize that vessels displaying low expression of this molecule are less efficient. However, no correlation was found between Multimerin-2 expression and the pCLE-based angiogenic score. This could be due to the fact that, as commented for the other vessel markers, vascular efficiency is affected by several molecules. In addition, the IF analyses are performed only in a small area of the tumor. Given the heterogeneity of the tumors it is likely that a more reliable analysis of the expression of the markers should be performed in several areas of the tumor. Interestingly, a stronger association was found between the results from the pCLE analyses and the expression of GLUT1.

Indeed, the presence of abnormal, leaky and poorly perfused vessels, independently from the molecular cause, and the consequent lack of sufficient oxygen supply lead to increased hypoxia and the establishment of an exacerbated mutagenic tumor microenvironment (13). The vascular alterations recorded by pCLE as well as the expression of angiogenic markers did not correlate with clinical staging, histological type and tumor site. Our previous observations indicated that high angiogenic scores as assessed by pCLE analyses associated with tumor progression more in rectal than in gastric cancer patients (25). The larger cohort taken into account in this study confirmed and reinforced these observations.

To better characterize the vasculature associated with gastric cancer is a required clinical need not only to predict which patients will respond to anti-angiogenic therapy, but also to develop new strategies to overcome resistance. The anti-angiogenic drugs employed in gastric cancer clinical trials mainly target VEGFA such as the monoclonal humanized antibody bevacizumab, or the VEGFR2, in particular ramucirumab and selective tyrosine kinase inhibitors such as sunitinib, sorafenib and apatinib. According to a very recent systematic review and meta-analysis the addition of anti-VEGFR2 targeting agents to the first- or second-line chemotherapy could prolong patient's OS and PFS in advanced or metastatic gastric cancer (16). The study also highlighted the inefficacy of anti-VEGFA therapy in this type of tumor, unlike what observed in other type of cancers (53–56). Thus, to better characterize the quality of the gastric cancer-associated vasculature by pCLE may grant the possibility to predict which patients will be more likely to respond to anti-angiogenic therapy, sparing the others from costly ineffective treatments and side effects. In addition, the comparative results from the pCLE and IF analysis may open new avenues toward the development of new strategies to circumvent anti-angiogenic therapy resistance.

ETHICS STATEMENT

This study was carried out in accordance with the recommendations of the Institutional Board of CRO-IRCCS, National Cancer Institute of Aviano (PN), Italy with written informed consent from all subjects. All subjects gave written informed consent in accordance with the Declaration of Helsinki. The protocol was approved by the Institutional Board of CRO- (IRB no. CRO-2014-03).

AUTHOR CONTRIBUTIONS

AC and EA developed the methodology, performed IF staining and graph editing, acquired data, and reviewed the manuscript. EP contributed to IF staining and analyses and critically reviewed the manuscript. RD collected, managed the bioptic samples, and reviewed the manuscript. AF collected data and helped for statistical analyses. VC provided final diagnosis and tumor staging. SM, MF, and RC identified and recruited patients and performed endoscopy and pCLE. RM helped in patient data managing. RC acquired funding, conceptualized the study and critically reviewed the manuscript. MM and PS conceptualized the study, reviewed as blinded investigators all pCLE videos, wrote original draft preparation and supervised investigation and analyses.

FUNDING

This study was supported by Italian Ministry of Health (RF-2016-02361525 to RC and PS) and by Associazione Italiana per la Ricerca sul Cancro (AIRC, IG-2012-12718 to MM).

ACKNOWLEDGMENTS

The authors thank all patients that participated to this study.

SUPPLEMENTARY MATERIAL

The Supplementary Material for this article can be found online at: https://www.frontiersin.org/articles/10.3389/fonc.2019.00513/full#supplementary-material

Video S1 | Representative sequences of normal blood flow in a gastric cancer patient with an angiogenesis score of "2".

Video S2 | Representative sequences of abnormal flow in a gastric cancer patient with an angiogenesis score of "4".

REFERENCES

1. Bray F, Ferlay J, Soerjomataram I, Siegel RL, Torre LA, Jemal A. Global cancer statistics 2018: GLOBOCAN estimates of incidence and mortality worldwide for 36 cancers in 185 countries. *CA Cancer J Clin.* (2018) 68:394–424. doi: 10.3322/caac.21492
2. Rawicz-Pruszynski K, van Sandick JW, Mielko J, Ciseł B, Polkowski WP. Current challenges in gastric cancer surgery: European perspective. *Surg Oncol.* (2018) 27:650–6. doi: 10.1016/j.suronc.2018.08.004
3. Petrioli R, Francini E, Roviello F, Marrelli D, Fiaschi AI, Laera L, et al. Sequential treatment with epirubicin, oxaliplatin and 5FU (EOF) followed by docetaxel, oxaliplatin and 5FU (DOF) in patients with advanced gastric or gastroesophageal cancer: a single-institution experience. *Cancer Chemother Pharmacol.* (2015) 75:941–7. doi: 10.1007/s00280-015-2715-x
4. Buzzoni R, Bajetta E, Di Bartolomeo M, Miceli R, Beretta E, Ferrario E, et al. Pathological features as predictors of recurrence after radical resection of gastric cancer. *Br J Surg.* (2006) 93:205–9. doi: 10.1002/bjs.5225
5. Field K, Michael M, Leong T. Locally advanced and metastatic gastric cancer: current management and new treatment developments. *Drugs.* (2008) 68:299–317. doi: 10.2165/00003495-200868030-00004
6. Lordick F, Allum W, Carneiro F, Mitry E, Tabernero J, Tan P, et al. Unmet needs and challenges in gastric cancer: the way forward. *Cancer Treat Rev.* (2014) 40:692–700. doi: 10.1016/j.ctrv.2014.03.002
7. Pinto MP, Owen GI, Retamal I, Garrido M. Angiogenesis inhibitors in early development for gastric cancer. *Expert Opin Investig Drugs.* (2017) 26:1007–17. doi: 10.1080/13543784.2017.1361926
8. Roviello G, Petrioli R, Marano L, Polom K, Marrelli D, Perrella A, et al. Angiogenesis inhibitors in gastric and gastroesophageal junction cancer. *Gastric Cancer.* (2016) 19:31–41. doi: 10.1007/s10120-015-0537-5

9. Andreuzzi E, Capuano A, Pellicani R, Poletto E, Doliana R, Maiero S, et al. Loss of multimerin-2 and EMILIN-2 expression in gastric cancer associate with altered angiogenesis. *Int J Mol Sci.* (2018) 19:3983. doi: 10.3390/ijms19123983
10. Welti J, Loges S, Dimmeler S, Carmeliet P. Recent molecular discoveries in angiogenesis and antiangiogenic therapies in cancer. *J Clin Invest.* (2013) 123:3190–200. doi: 10.1172/JCI70212
11. Carmeliet P. Mechanisms of angiogenesis and arteriogenesis. *NatMed.* (2000) 6:389–95. doi: 10.1038/74651
12. Wong P-P, Demircioglu F, Ghazaly E, Alrawashdeh W, Stratford MRL, Scudamore CL, et al. Dual-action combination therapy enhances angiogenesis while reducing tumor growth and spread. *Cancer Cell.* (2015) 27:123–37. doi: 10.1016/j.ccell.2014.10.015
13. Jain RK. Antiangiogenesis strategies revisited: from starving tumors to alleviating hypoxia. *Cancer Cell.* (2014) 26:605–22. doi: 10.1016/j.ccell.2014.10.006
14. Park J-S, Kim I-K, Han S, Park I, Kim C, Bae J, et al. Normalization of tumor vessels by Tie2 activation and Ang2 inhibition enhances drug delivery and produces a favorable tumor microenvironment. *Cancer Cell.* (2016) 30:953–67. doi: 10.1016/j.ccell.2016.10.018
15. Park DJ, Seo AN, Yoon C, Ku GY, Coit DG, Strong VE, et al. Serum VEGF-A and tumor vessel VEGFR-2 levels predict survival in caucasian but not asian patients undergoing resection for gastric adenocarcinoma. *Ann Surg Oncol.* (2015) 22(Suppl 3):S1508–15. doi: 10.1245/s10434-015-4790-y
16. Bai Z-G, Zhang Z-T. A systematic review and meta-analysis on the effect of angiogenesis blockade for the treatment of gastric cancer. *Onco Targets Ther.* (2018) 11:7077–87. doi: 10.2147/OTT.S169484
17. Kuiper T, van den Broek FJ, van ES, Fockens P, Dekker E. Feasibility and accuracy of confocal endomicroscopy in comparison with narrow-band imaging and chromoendoscopy for the differentiation of colorectal lesions. *AmJGastroenterol.* (2012) 107:543–50. doi: 10.1038/ajg.2012.14
18. Wallace MB, Fockens P. Probe-based confocal laser endomicroscopy. *Gastroenterology.* (2009) 136:1509–13. doi: 10.1053/j.gastro.2009.03.034
19. Wang KK, Carr-Locke DL, Singh SK, Neumann H, Bertani H, Galmiche JP, et al. Use of probe-based confocal laser endomicroscopy (pCLE) in gastrointestinal applications. a consensus report based on clinical evidence. *United Europ Gastroenterol J.* (2015) 3:230–54. doi: 10.1177/2050640614566066
20. De Palma GD. Confocal laser endomicroscopy in the "*in vivo*" histological diagnosis of the gastrointestinal tract. *World J Gastroenterol.* (2009) 15:5770–5. doi: 10.3748/wjg.15.5770
21. Shahid MW, Buchner AM, Heckman MG, Krishna M, Raimondo M, Woodward T, et al. Diagnostic accuracy of probe-based confocal laser endomicroscopy and narrow band imaging for small colorectal polyps: a feasibility study. *Am J Gastroenterol.* (2012) 107:231–9. doi: 10.1038/ajg.2011.376
22. Shahid MW, Buchner AM, Coron E, Woodward TA, Raimondo M, Dekker E, et al. Diagnostic accuracy of probe-based confocal laser endomicroscopy in detecting residual colorectal neoplasia after EMR: a prospective study. *Gastrointest Endosc.* (2012) 75:525–33. doi: 10.1016/j.gie.2011.08.024
23. Zhang YL, Bai L, Li Z, Ji R, Li CQ, Zuo XL, et al. Lower dose of fluorescein sodium is more suitable for confocal laser endomicroscopy: a feasibility study. *Gastrointest Endosc.* (2016) 84:917–23.e5. doi: 10.1016/j.gie.2016.05.011
24. Cannizzaro R, Mongiat M, Canzonieri V, Fornasarig M, Maiero S, De R V, et al. Endomicroscopy and cancer: a new approach to the visualization of neoangiogenesis. *Gastroenterol Res Pract.* (2012) 2012:537170. doi: 10.1155/2012/537170
25. Spessotto P, Fornasarig M, Pivetta E, Maiero S, Magris R, Mongiat M, et al. Probe-based confocal laser endomicroscopy for in vivo evaluation of the tumor vasculature in gastric and rectal carcinomas. *Sci Rep.* (2017) 7:9819. doi: 10.1038/s41598-017-10963-1
26. Colladel R, Pellicani R, Andreuzzi E, Paulitti A, Tarticchio G, Todaro F, et al. MULTIMERIN2 binds VEGF-A primarily via the carbohydrate chains exerting an angiostatic function and impairing tumor growth. *Oncotarget.* (2016) 7:2022–37. doi: 10.18632/oncotarget.6515
27. Ehling J, Lammers T, Kiessling F. Non-invasive imaging for studying anti-angiogenic therapy effects. *Thromb Haemost.* (2013) 109:375–90. doi: 10.1160/TH12-10-0721
28. Ehling J, Theek B, Gremse F, Baetke S, Mockel D, Maynard J, et al. Micro-CT imaging of tumor angiogenesis: quantitative measures describing micromorphology and vascularization. *Am J Pathol.* (2014) 184:431–41. doi: 10.1016/j.ajpath.2013.10.014
29. Li Z, Zuo XL, Li CQ, Liu ZY, Ji R, Liu J, et al. New classification of gastric pit patterns and vessel architecture using probe-based confocal laser endomicroscopy. *J Clin Gastroenterol.* (2016) 50:23–32. doi: 10.1097/MCG.0000000000000298
30. Safatle-Ribeiro AV, Ryoka Baba E, Corsato Scomparin R, Friedrich Faraj S, Simas de Lima M, Lenz L, et al. Probe-based confocal endomicroscopy is accurate for differentiating gastric lesions in patients in a Western center. *Chin J Cancer Res.* (2018) 30:546–52. doi: 10.21147/j.issn.1000-9604.2018.05.08
31. Goetz M. Characterization of lesions in the stomach: will confocal laser endomicroscopy replace the pathologist? *Best Pract Res Clin Gastroenterol.* (2015) 29:589–99. doi: 10.1016/j.bpg.2015.05.013
32. Goetz M, Malek NP, Kiesslich R. Microscopic imaging in endoscopy: endomicroscopy and endocytoscopy. *Nat Rev Gastroenterol Hepatol.* (2014) 11:11–8. doi: 10.1038/nrgastro.2013.134
33. Wallace M, Lauwers GY, Chen Y, Dekker E, Fockens P, Sharma P, et al. Miami classification for probe-based confocal laser endomicroscopy. *Endoscopy.* (2011) 43:882–91. doi: 10.1055/s-0030-1256632
34. Lauren P. The two histological main types of gastric carcinoma: diffuse and so-called intestinal-type carcinoma. an attempt at a histo-clinical classification. *Acta Pathol Microbiol Scand.* (1965) 64:31–49. doi: 10.1111/apm.1965.64.1.31
35. Zhao L-Y, Wang J-J, Zhao Y-L, Chen X-Z, Yang K, Chen X-L, et al. Superiority of tumor location-modified lauren classification system for gastric cancer: a multi-institutional validation analysis. *Ann Surg Oncol.* (2018) 25:3257–63. doi: 10.1245/s10434-018-6654-8
36. Boström PJ, Thoms J, Sykes J, Ahmed O, Evans A, van Rhijn BWG, et al. Hypoxia marker GLUT-1 (Glucose Transporter 1) is an independent prognostic factor for survival in bladder cancer patients treated with radical cystectomy. *Bladder Cancer.* (2016) 2:101–9. doi: 10.3233/BLC-150033
37. Airley RE, Loncaster J, Raleigh JA, Harris AL, Davidson SE, Hunter RD, et al. GLUT-1 and CAIX as intrinsic markers of hypoxia in carcinoma of the cervix: relationship to pimonidazole binding. *Int J Cancer.* (2003) 104:85–91. doi: 10.1002/ijc.10904
38. Lorenzon E, Colladel R, Andreuzzi E, Marastoni S, Todaro F, Schiappacassi M, et al. MULTIMERIN2 impairs tumor angiogenesis and growth by interfering with VEGF-A/VEGFR2 pathway. *Oncogene.* (2012) 31:3136–47. doi: 10.1038/onc.2011.487
39. Andreuzzi E, Colladel R, Pellicani R, Tarticchio G, Cannizzaro R, Spessotto P, et al. The angiostatic molecule Multimerin 2 is processed by MMP-9 to allow sprouting angiogenesis. *Matrix Biol.* (2017) 64:40–53. doi: 10.1016/j.matbio.2017.04.002
40. Galvagni F, Nardi F, Spiga O, Trezza A, Tarticchio G, Pellicani R, et al. Dissecting the CD93-Multimerin 2 interaction involved in cell adhesion and migration of the activated endothelium. *Matrix Biol.* (2017) 64:112–27. doi: 10.1016/j.matbio.2017.08.003
41. Mongiat M, Andreuzzi E, Tarticchio G, Paulitti A. Extracellular matrix, a hard player in angiogenesis. *Int J Mol Sci.* (2016) 17:1822. doi: 10.3390/ijms17111822
42. Nassiri F, Cusimano MD, Scheithauer BW, Rotondo F, Fazio A, Yousef GM, et al. Endoglin (CD105): a review of its role in angiogenesis and tumor diagnosis, progression and therapy. *Anticancer Res.* (2011) 31:2283–90.
43. Ding S, Li C, Lin S, Yang Y, Liu D, Han Y, et al. Comparative evaluation of microvessel density determined by CD34 or CD105 in benign and malignant gastric lesions. *Hum Pathol.* (2006) 37:861–6. doi: 10.1016/j.humpath.2006.02.006
44. Yu J-X, Zhang X-T, Liao Y-Q, Zhang Q-Y, Chen H, Lin M, et al. Relationship between expression of CD105 and growth factors in malignant tumors of gastrointestinal tract and its significance. *World J Gastroenterol.* (2003) 9:2866–9. doi: 10.3748/wjg.v9.i12.2866
45. Wang JM, Kumar S, Pye D, van Agthoven AJ, Krupinski J, Hunter RD. A monoclonal antibody detects heterogeneity in vascular endothelium of tumours and normal tissues. *Int J Cancer.* (1993) 54:363–70. doi: 10.1002/ijc.2910540303

46. Cheng J, Baumhueter S, Cacalano G, Carver-Moore K, Thibodeaux H, Thomas R, et al. Hematopoietic defects in mice lacking the sialomucin CD34. *Blood.* (1996) 87:479–90.
47. Tasev D, Konijnenberg LSF, Amado-Azevedo J, van Wijhe MH, Koolwijk P, van Hinsbergh VWM. CD34 expression modulates tube-forming capacity and barrier properties of peripheral blood-derived endothelial colony-forming cells (ECFCs). *Angiogenesis.* (2016) 19:325–38. doi: 10.1007/s10456-016-9506-9
48. Rakocevic J, Orlic D, Mitrovic-Ajtic O, Tomasevic M, Dobric M, Zlatic N, et al. Endothelial cell markers from clinician's perspective. *Exp Mol Pathol.* (2017) 102:303–13. doi: 10.1016/j.yexmp.2017.02.005
49. Minhajat R, Mori D, Yamasaki F, Sugita Y, Satoh T, Tokunaga O. Organ-specific endoglin (CD105) expression in the angiogenesis of human cancers. *Pathol Int.* (2006) 56:717–23. doi: 10.1111/j.1440-1827.2006.02037.x
50. Duff SE, Li C, Garland JM, Kumar S. CD105 is important for angiogenesis: evidence and potential applications. *FASEB J.* (2003) 17:984–92. doi: 10.1096/fj.02-0634rev
51. Fonsatti E, Altomonte M, Nicotra MR, Natali PG, Maio M. Endoglin (CD105): a powerful therapeutic target on tumor-associated angiogenetic blood vessels. *Oncogene.* (2003) 22:6557–63. doi: 10.1038/sj.onc.1206813
52. Nikiteas NI, Tzanakis N, Theodoropoulos G, Atsaves V, Christoni Z, Karakitsos P, et al. Vascular endothelial growth factor and endoglin (CD-105) in gastric cancer. *Gastric Cancer.* (2007) 10:12–7. doi: 10.1007/s10120-006-0401-8
53. Assoun S, Brosseau S, Steinmetz C, Gounant V, Zalcman G. Bevacizumab in advanced lung cancer: state of the art. *Future Oncol.* (2017) 13:2515–35. doi: 10.2217/fon-2017-030
54. Rossi L, Verrico M, Zaccarelli E, Papa A, Colonna M, Strudel M, et al. Bevacizumab in ovarian cancer: a critical review of phase III studies. *Oncotarget.* (2017) 8:12389–405. doi: 10.18632/oncotarget.13310
55. Alnimer Y, Hindi Z, Katato K. The effect of perioperative bevacizumab on disease-free and overall survival in locally advanced HER-2 negative breast cancer: a meta-analysis. *Breast Cancer.* (2018) 12:1178223418792250. doi: 10.1177/1178223418792250
56. Xu R, Xu C, Liu C, Cui C, Zhu J. Efficacy and safety of bevacizumab-based combination therapy for treatment of patients with metastatic colorectal cancer. *Onco Targets Ther.* (2018) 11:8605–21. doi: 10.2147/OTT.S171724

Conflict of Interest Statement: The authors declare that the research was conducted in the absence of any commercial or financial relationships that could be construed as a potential conflict of interest.

frontiers in Surgery

REVIEW
published: 20 June 2019
doi: 10.3389/fsurg.2019.00034

Application of Indocyanine Green Videoangiography in Aneurysm Surgery: Evidence, Techniques, Practical Tips

*Pedro Norat†, Sauson Soldozy†, Mazin Elsarrag, Jennifer Sokolowski, Kaan Yağmurlu, Min S. Park, Petr Tvrdik and M. Yashar S. Kalani**

Department of Neurological Surgery, University of Virginia Health System, Charlottesville, VA, United States

Establishing blood vessel patency in neurovascular surgery is an essential component in treating cerebrovascular disorders. Given the difficulty in confirming complete obliteration of the aneurysm sac, ICG videoangiography has emerged as an intraoperative tool that provides neurosurgeons immediate feedback on the status of vessel flow, allowing for surgical modifications to be made without delay. ICG initially emerged as a tool for assessing hepatic, cardiac, and retinovascular function. It is an inert compound with a high affinity for plasma proteins and fluorescence properties making it the ideal candidate for assessment of vessel patency in neurovascular procedures. Requiring only a bolus peripheral vein injection and integration of a near-infrared imaging device into the surgical microscope, ICG can be visualized without disrupting operating room workflow or the surgical field. Quick response time, high-spatial resolution, and low complication rates are features of ICG videoangiography that prove advantageous when compared to the gold standard intra- and postoperative digital subtraction angiography (DSA). Despite this, ICG is not without limitations, specifically in the setting of atherosclerotic vessels, giant, and complex aneurysms. Additionally, there are instances where DSA may prove superior in detecting vessel stenosis and outflow obstruction, prompting the recommendation of ICG as an adjunct to, rather than complete replacement of DSA. In this article, the authors provide a brief overview of the biochemical properties and historical origins of ICG viedoangiography in addition to discussing its current application in aneurysm surgery.

Keywords: cerebral aneurysm, indocyanin green, digital subtraction angiogram, surgical microscope, near infra-red

OPEN ACCESS

Edited by:
Eberval Figueiredo, University of São Paulo, Brazil

Reviewed by:
Jorge Marcelo Mura, Instituto de Neurocirugía, Chile
Hiroki Toda, Fukui Red Cross Hospital, Japan

***Correspondence:**
M. Yashar S. Kalani
kalani@virginia.edu

†These authors have contributed equally to this work

Specialty section:
This article was submitted to Neurosurgery, a section of the journal Frontiers in Surgery

Received: *11 February 2019*
Accepted: *22 May 2019*
Published: *20 June 2019*

Citation:
Norat P, Soldozy S, Elsarrag M, Sokolowski J, Yağmurlu K, Park MS, Tvrdik P and Kalani MYS (2019) Application of Indocyanine Green Videoangiography in Aneurysm Surgery: Evidence, Techniques, Practical Tips. Front. Surg. 6:34. doi: 10.3389/fsurg.2019.00034

INTRODUCTION

Indocyanine green (ICG) is a fluorescent compound that has been utilized for decades in a variety of medical applications. Originally approved by the Food and Drug Administration in 1956, ICG was initially used to evaluate cardiac and hepatic function and later gained extensive use in ophthalmology where it was used to enable angiography (1, 2). More recently, it has been used to enhance tissue visualization in oncology, plastic surgery, neurosurgery, and other fields (3).

Given that the physical properties of ICG may be utilized to facilitate vascular imaging, the utility of ICG angiography in cerebrovascular surgery has become quite apparent.

The first description of ICG angiography for aneurysm surgery was in 2003, where Raabe et al. assessed the feasibility and quality of ICG videoangiography in assessing patency of arterial and venous vessels and exclusion of aneurysm sacs (4). In their study, the ability to visually inspect vessel patency with intraoperative ICG angiography allowed for real-time surgical changes that significantly altered the surgical course in a number of cases. Given the importance of maintaining tissue perfusion in neurovascular surgery and the difficulty associated with ensuring complete obliteration of an aneurysm, a number of studies have since explored and championed the utility of ICG angiography in aneurysm surgery (2, 5–12) as well as in other neurosurgical settings, such as resection of AVMs and AVFs (13–15), vascular bypass surgery (16), and tumor resection (17). With regards to aneurysm surgery, ICG angiography is often contrasted with other intraoperative monitoring techniques such as digital subtraction angiography (DSA) (5), intraoperative computed tomography (6), and microvascular doppler sonography (7), with these studies concluding that ICG angiography should complement rather than replace these alternative imaging methods. In this review, the authors discuss the biochemical properties of ICG dye, provide a brief history of its use in the medical setting, as well as discuss methodology and current applications in aneurysm surgery while considering both the advantages and limitations of this technique.

BIOCHEMICAL PROFILE AND PROPERTIES

Indocyanine green (**Figure 1**) is a water-soluble, odorless or near odorless tricarbocyanine dye with a strong affinity for plasma proteins (primarily albumin and α- and β-lipoproteins) (1, 19, 20). Once administered, ICG remains 98% bound to plasma proteins; this intravascular sequestration of the dye allows blood vessels to be easily visualized using fluorescence imaging techniques. ICG molecules have a spectral absorption range of 750–800 nm, with a peak emission occurring at approximately 832 nm (1, 3, 21). The range of light wavelengths where biological tissue absorption and scattering are minimum is between 650 and 900 nm, otherwise known as the biological "optical window" (3, 22). As a result, light has maximal tissue penetration at this range of wavelengths. As both the excitation and fluorescence wavelengths of ICG lie within the tissue optical window, the dye may be seen beneath several layers of tissue (3, 21). Furthermore, due to minimal light absorption at this wavelength, tissues have a low degree of near infra-red (NIR) autofluorescence in comparison with ICG, resulting in stark contrast of the dye.

ICG is a relatively safe, nontoxic compound with a lethal dosage (LD_{50}) of 50–80 mg/kg. With a typical ICG angiography dose of 0.2–0.5 mg/kg (21), adverse events are seen in <0.1% of patients (primarily hypotension, tachycardia, and urticarial reactions in iodide allergic patients). The dye is quickly removed from circulation by the liver, mostly clearing within 10–20 min (1, 2). Experiments suggest that ICG is excreted exclusively by the liver into bile with no known metabolites (23).

HISTORICAL CONTEXT

Originally introduced for NIR photography by Kodak research laboratories in 1955, ICG was approved for clinical use by the FDA just a year later in 1956 (23). ICG was initially utilized for quantitative measurements in assessing liver function, in the field of cardiology for determining cardiac output in valvular and septal defects (24), and eventually in the field of ophthalmology beginning in the 1970s (3). The first application of ICG in cerebrovascular angiography was experimentally performed on exposed dog brain, reported by Kogure et al. (25). In this study, a wide parietotemporal craniotomy was performed with ICG dye being injected into the left thyroid artery allowing for gross visualization of the middle cerebral artery (MCA) distribution. The authors heralded the "simplicity of technique and employment of standard equipment" noting "it is entirely feasible that a photographic setup such as described in this article could be easily moved into the neurosurgical operating suite." Their prediction would reign true and was made even more feasible given the technological advancements that occurred in the following decades since their experiment was performed. This includes visualizing ICG fluorescence through a surgical microscope as described by Kuroiwa et al. (26), where they reported clear visualization of human brain surface vessels through the dura mater after intravenous injection of ICG.

The first description of NIR videoangiography using ICG dye for intraoperative visualization in aneurysm surgery was described in 2003. Raabe et al. (4) noted that in three cases, the ICG angiographic findings significantly changed the course of the surgical procedure, thereby suggesting that this technique may be implemented as an adjunct in neurovascular procedures (**Figure 2**). In addition, the ICG angiography results were noted to be comparable to DSA in elucidating patency of all vessel types, including small and perforating arteries (<0.05 mm). The integration of NIR technology into the operating microscope would set the stage for ICG videoangiography in neurovascular surgery in the twenty-first century.

TECHNIQUE

Dosage

The recommended dose of ICG injected peripherally for angiography is between 0.2 and 0.5 mg/kg, not to exceed a maximum dose of 5 mg/kg. The standard dose is injected into a peripheral vein as a bolus of 25 mg dissolved in 5 ml of water (2, 3). Within 1–2 s following injection, the ICG dye binds to plasma proteins and has a plasma half-life of 3–4 min. After 10 min, a repeat dose can be administered or until after the ICG dye clears (2). Caloric restriction has been shown to increase plasma clearance at doses below 0.5 mg/kg (27).

Microscopy

The technical integration of ICG videoangiography into the optical path of the surgical microscope was first described

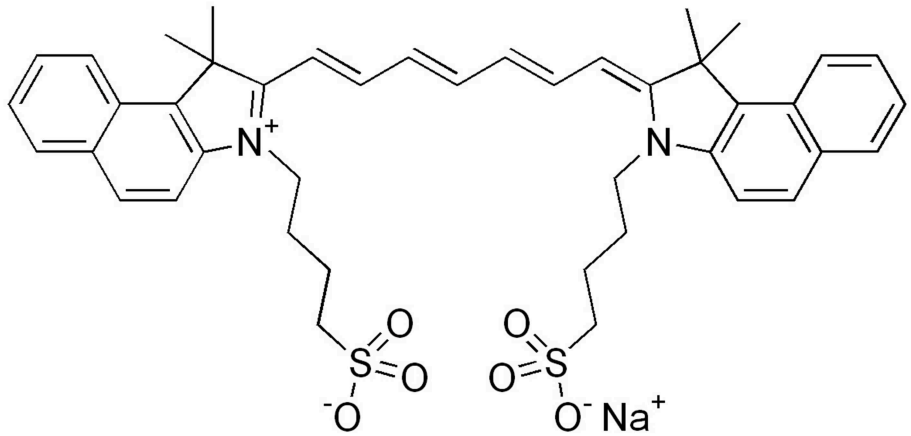

FIGURE 1 | Chemical structure of indocyanine green. Reproduced from File:Indocyanine green.png (18).

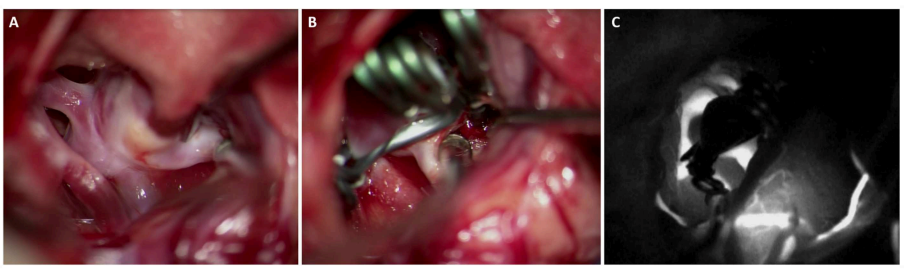

FIGURE 2 | Middle cerebral artery aneurysm with the neck dissected and clear view of the parent vessel, and its two branches **(A)**, after retraction showing the neck of the clipped MCA aneurysm **(B)**, and intraoperative ICG videoangiography showing the patency of the branches of the MCA and complete exclusion of the aneurysm from the circulation **(C)**.

by Raabe et al. (21) and implemented by Carl Zeiss Co. (Oberkochen, Germany). Given that its fluorescent wavelength is in the near-infrared (NIR) spectrum (700–2,500 nm), the dye cannot be seen by the naked eye, and a NIR imaging device must be available to allow vessel visualization. A simple ICG device consists of a NIR light source, an NIR sensitive sensor, and filters used to block light at other wavelengths (3, 21). This allows users to obtain high-resolution NIR images without ambient and excitation light interference. A light source illuminating the operative field has a wavelength comprising the ICG absorption band (range 700–850 nm, peak 805 nm). The setup entails a uniquely designed dielectric filter that allows passage of light in the NIR wavelength that fits the exact absorption band of ICG. An integrated beam splitter in the microscope directs the ICG fluorescence light (range 780–950 nm, peak 835 nm) toward a black-and-white camera, with an observation band-pass filter being used to detect the ICG fluorescence (21).

CURRENT APPLICATIONS

The neurosurgeon's goal for aneurysm surgery is complete exclusion of the aneurysm from the circulation while preserving the parent, perforating, and branching vessels. To achieve this, many intraoperative monitoring techniques, such as microvascular Doppler, monitoring of somatosensory and motor evoked potentials, DSA, and more recently ICG videoangiography, may be utilized. Since the publication of Raabe et al. (4), ICG has been greatly studied and many publications have shown its importance in the microsurgical management of aneurysms; consequently, ICG has become a widely commonplace tool for identification of mis-clipping in aneurysm surgery despite DSA being considered the gold standard technique for intraoperative monitoring in aneurysmal clipping (2, 11, 21, 28, 29). However, intraoperative DSA may be challenging to implement in many centers worldwide due to its requirement of large logistical support, high cost burden, prolonged time frame, and invasive nature. In contrast, ICG is noninvasive with a lower cost burden and quicker image acquisition.

In a prospective two-center trial published in 2005, Raabe et al. (2) directly compared surgical microscope-based ICG videoangiography with intra- or postoperative DSA after aneurysm clipping. The authors described several advantages, including a lower complication rate (0.1% vs. 0.4–2.6%), a faster time frame of 2 min, and higher-spatial resolution that allows for observation of small perforators or cortical arteries of submillimeter diameter that cannot be assessed

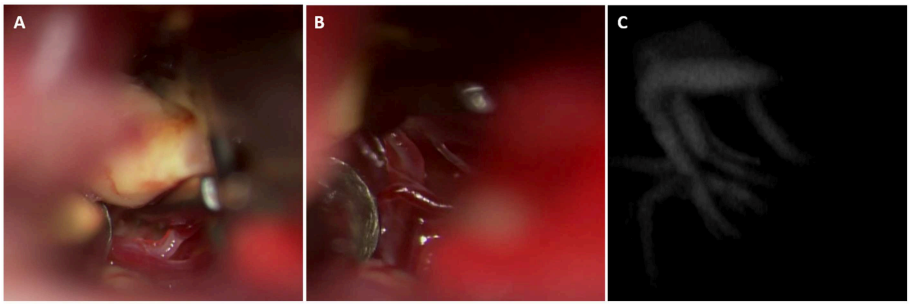

FIGURE 3 | This basilar tip aneurysm was exposed using a modified orbitozygomatic approach. The perforators arising from the posterior aspect of the basilar apex and P1 can be visualized **(A)**. These perforators are dissected from the aneurysm dome and excluded from the clip construct **(B)**. Post clip ICG demonstrates preservation of the perforators **(C)**.

with intraoperative DSA. ICG angiography was reported to be limited in the setting of atherosclerotic or calcified vessels, thrombosed aneurysms, and giant or complex aneurysms; although, ICG disclosed remnant aneurysms mainly in atherosclerotic aneurysms ($p < 0.05$) (30). In cases where ICG angiography missed stenotic vessels, they were found to be likely hemodynamically irrelevant as seen on postoperative DSA. Overall, a correlation of 90% was reported between ICG and DSA, with the authors reporting no cases where inconsistent findings on postoperative DSA lead to reopening and repositioning of the clip (2).

One major utility of ICG is its ability to confirm microsurgical anatomy in a variety of aneurysm cases. de Oliveira et al. (31) have described their experience with 93 ICG videoangiography studies for monitoring the flow in perforating arteries (**Figure 3**) during intracranial aneurysm surgery. They concluded that ICG videoangiography was able to visualize, during the surgical procedure, the small perforating arteries that cannot be detected by intraoperative DSA (31). In addition, Nagai et al. (32) reported a rare case of a ruptured dissecting aneurysm in the A1 segment. Using ICG, the lateral and medial groups of the basal perforating arteries of the anterior communicating artery complex of the ACA were identified prior to clipping, thereby minimizing the risk of complications related to occluding perforator vessels. Other series have been published that further corroborate these findings (8–14, 16, 17, 28, 33–35).

ADVANTAGES AND LIMITATIONS

In concordance with the benefits stated earlier, Sharma et al. (11) demonstrated in 112 patients an 8% clip repositioning rate during surgery after the use of ICG videoangiography, elucidating the clear advantage of having ICG available for use. Despite this, a disagreement between ICG and DSA was observed in 4% of the cases (5 cases−2 patients with anterior communicating aneurysms and ophthalmic ICA aneurysms and 1 middle cerebral artery bifurcation), with discordance being significant higher in ophthalmic ICA when compared with other aneurysm locations ($p = 0.04$; OR = 10.8). Dashti et al. (36) in their series of 239 patients found the rate of unexpected neck residuals to be about 6%; however, neck residuals were significantly more frequent in deep-sited aneurysms (64%). They ultimately concluded that ICG videoangiography is a reliable intraoperative tool for aneurysm surgery, with the exception of giant, complex, and deep-sited aneurysms.

Limitations of ICG videoangiography include trouble visualizing aneurysm residuals after clipping when compared with DSA, inability to visualize areas outside the field of the microscope, and difficulty visualizing of arteries at the depth of the surgical field and residual neck in calcified and thrombosed aneurysms. While Raabe et al. (2) report ICG videoangiography can be used as an independent form of angiography, the majority of other studies recommend this technique as an alternative to or as complementary to intraoperative DSA during aneurysm surgery. In fact, a recent systematic review meta-analysis concluded that ICG videoangiography should serve only a complementary role to DSA rather than fully replace it given a 6.1% rate of mis-clippings not detected by ICG angiography among 1,465 clipped aneurysms as compared to a 4.5% rate of mis-clippings not detected by DSA among 849 clipped aneurysms (5). While not as precise as DSA, the greatest advantage of ICG videoangiography is that it provides real-time information regarding aneurysmal exclusion from the circulation, as well as patency of parent and branch vessels. If necessary, clip repositioning can be performed within minutes given the immediate visual feedback of ICG. Additionally, ICG is susceptible to false negatives further pointing toward its role as an adjunct to DSA (37–39).

FUTURE DIRECTIONS

Given the advantages and ease of use of ICG videoangiography, the dearth of studies examining its utility in other neurovascular procedures suggests that it may be underutilized for these procedures. Examples of these surgeries include ablation of arteriovenous malformations and fistulas along with manipulation and resection of highly vascularized tumors and lesions. The scarcity of data examining ICG videoangiography for these procedures may be a result of their infrequent incidence. Nonetheless, reports on the nuances of employing ICG videoangiography in these procedures may help to further define its specific roles and situational uses. We encourage

groups to publish their techniques and experiences with ICG videoangiography in these areas.

One limitation of ICG videaoangiography is its inability to provide information on unexposed vessels. In order to bypass this limitation, several groups have interfaced the indocyanine NIR imaging technology to neuroendoscopes (8, 40–43). The ICG videoangiography-neuroendoscope may extend the benefits of ICG videoangiography to deep seated lesions and other difficult to visualize vessels without expanding the dissection. Cho et al. (41) report higher detection rates of branch orifices and more exact clip position with the ICG videoangiography-neurendoscope compared with commercial microscopic ICG videoangiography. Another mechanism by which the line of sight limitation has been addressed is with integration of ICG angiography and robotic surgery. The union of ICG angiography with robotic surgery has proven to be valuable in other disciplines such as surgical oncology, (44) demonstrating that this technology is feasible.

In addition to extending ICG videoangiography to lesions and vessels not readily exposed, the robotic system has other benefits which could improve aneurysm surgery. The computer of the robotic console allows additional information to be integrated and simultaneously displayed intraoperatively (44), and the increased precision of movements and ability to navigate narrow anatomical cavities may allow access to deep seated lesions while minimizing brain retraction and dissection. Thus, the expansion of robotics into neurosurgery may be a novel method to incorporate NIR imaging technology and use ICG videoangiography to examine vasculature that is not immediately exposed.

A known drawback to ICG videoangiography is its poor ability to visualize thrombosed, calcified, and buried vessels and aneurysms. This may be in part due to the relatively modest tissue penetration by light at these wavelengths in comparison to other wavelengths. Contrast between ICG and surrounding tissue indeed stems from the fluorescent wavelengths of ICG lying within the tissue optical window. However, Smith et al. (45) discuss the existence of a second optical window, with the first window spanning from 650 to 950 nm and the second from 1,000–1,350 nm. They further state that the first window may not be optimal due to tissue autofluorescence producing substantial background noise and the tissue penetration depth being limited to between 1 and 2 cm. Indocyanine green fluorescing in this first window may significantly detract from the visual quality of ICG angiography. Image acuity may therefore be optimized by utilizing compounds that fluoresce in second optical window. Smith et al. (45) cite simulations and modeling studies suggesting that improvement of signal-to-noise ratios by over 100-fold is possible by using quantum dot fluorophores that emit light at 1,320 nm as opposed to 850 nm. However, currently tested compounds that fluoresce at this range are limited due to safety and toxicity as well as technical challenges associated with imaging technology. Nonetheless, the development of both effective and biologically compatible fluorescent substances that operate within the second optical window may have the potential to greatly enhance fluorescent imaging.

Many of the advantages of ICGVA derive from its safety, convenience and cost effectiveness; preservation of these qualities is necessary for a contrast agent to function optimally. Currently, ICG is the only FDA approved near-infrared dye (3, 22). Investigators have explored both structural analogs of indocyanine as well as novel NIR contrast agents (3). Other areas of improvement include enhancements in NIR imaging technology to capture the broad fluorescence peak of ICG while also effectively filtering out background noise. Lastly, technical developments in flow dynamics analysis may improve visualization after multiple indocyanine loads, since rapid ICG reinjections generally suffer from lower contrast due to residual ICG inside the vessels (3). In addition, the versatility of ICG allows it to be paired with multiple intraoperative monitoring techniques such as somatosensory evoked potential (SSEP) and motor evoked potential (MEP) (46). Overall, there is much that remains to be explored in the field of fluorescent angiography and refinements in technology are inevitable.

CONCLUSION

In this article, the authors review the mechanism of action of ICG angiography and examine the evolution of its applications over time, nuances in technique, and clinical implementation. The reviewed data demonstrates that ICG angiography is indeed quite helpful in vascular mapping for cerebral aneurysm surgery and may certainly alter intraoperative decision making. However, its exact role depends on anatomic features of the particular lesion being treated and the technology is ultimately limited by lower accuracy compared to the gold-standard of digital subtraction angiography. Based on these findings, the highest degree of imaging accuracy may be achieved by employing multiple imaging technologies, and we encourage surgeons to use multimodal imaging when possible during aneurysm clipping surgery.

AUTHOR CONTRIBUTIONS

MK, PN, and SS: conception and design. PN, SS, and ME: acquisition of data and drafting the article. All authors critically revising the article. All authors reviewed submitted version of manuscript. MK approved the final version of the manuscript on behalf of all authors.

REFERENCES

1. Reinhart MB, Huntington CR, Blair LJ, Heniford BT, Augenstein VA. Indocyanine green:historical context, current applications, and future considerations. *Surg Innov*. (2016) 23:166–75. doi: 10.1177/1553350615604053
2. Raabe A, Nakaji P, Beck J, Kim LJ, Hsu FPK, Kamerman JD et al. Prospective evaluation of surgical microscope—integrated intraoperative near-infrared

indocyanine green videoangiography during aneurysm surgery. *J Neurosurg*. (2005) 103:982–9. doi: 10.3171/jns.2005.103.6.0982
3. Alander JT, Kaartinen I, Laakso A, Pätilä T, Spillmann T, Tuchin VV, et al. A review of indocyanine green fluorescent imaging in surgery. *Int J Biomed Imaging*. (2012) 2012:940585. doi: 10.1155/2012/940585
4. Raabe A, Beck J, Gerlach R, Zimmermann M, Seifert V. Near-infrared indocyanine green video angiography: a new method for intraoperative assessment of vascular flow. *Neurosurgery*. (2003) 52:132–9. doi: 10.1227/00006123-200301000-00017
5. Riva M, Amin-Hanjani S, Giussani C, De Witte O, Bruneau M. Indocyanine green videoangiography in aneurysm surgery: systematic review and meta-analysis. *Neurosurgery*. (2018) 83:166–180. doi: 10.1093/neuros/nyx387
6. Schnell O, Morhard D, Holtmannspötter M, Reiser M, Tonn JC, Schichor C. Near-infrared indocyanine green videoangiography (ICGVA) and intraoperative computed tomography (iCT): are they complementary or competitive imaging techniques in aneurysm surgery? *Acta Neurochir*. (2012) 154:1861–8. doi: 10.1007/s00701-012-1386-1
7. Fischer G, Stadie A, Oertel JMK. Near-infrared indocyanine green videoangiography versus microvascular Doppler sonography in aneurysm surgery. *Acta Neurochir*. (2010) 152:1519–25. doi: 10.1007/s00701-010-0723-5
8. Nishiyama Y, Kinouchi H, Senbokuya N, Kato T, Kanemaru K, Yoshioka H, et al. Endoscopic indocyanine green video angiography in aneurysm surgery: an innovative method for intraoperative assessment of blood flow in vasculature hidden from microscopic view. *J Neurosurg*. (2012) 117:302–8. doi: 10.3171/2012.5.JNS112300
9. Washington CW, Zipfel GJ, Chicoine MR, Derdeyn CP, Rich KM, Moran CJ, et al. Comparing indocyanine green videoangiography to the gold standard of intraoperative digital subtraction angiography used in aneurysm surgery. *J Neurosurg*. (2013) 118:420–7. doi: 10.3171/2012.10.JNS11818
10. Özgiray E, Aktüre E, Patel N, Baggott C, Bozkurt M, Niemann D, et al. How reliable and accurate is indocyanine green video angiography in the evaluation of aneurysm obliteration? *Clin Neurol Neurosurg*. (2013) 115:870–8. doi: 10.1016/j.clineuro.2012.08.027
11. Sharma M, Ambekar S, Ahmed O, Nixon M, Sharma A, Nanda A, et al. The utility and limitations of intraoperative near-infrared indocyanine green videoangiography in aneurysm surgery. *World Neurosurg*. (2014) 82:e607–13. doi: 10.1016/j.wneu.2014.05.033
12. Roessler K, Krawagna M, Dörfler A, Buchfelder M, Ganslandt O. Essentials in intraoperative indocyanine green videoangiography assessment for intracranial aneurysm surgery: conclusions from 295 consecutively clipped aneurysms and review of the literature. *Neurosurg Focus*. (2014) 36:E7. doi: 10.3171/2013.11.FOCUS13475
13. Schuette AJ, Cawley CM, Barrow DL. Indocyanine green videoangiography in the management of dural arteriovenous fistulae. *Neurosurgery*. (2010) 67:658–62. doi: 10.1227/01.NEU.0000374721.84406.7F
14. Hänggi D, Etminan N, Steiger HJ. The impact of microscope-integrated intraoperative near-infrared indocyanine green videoangiography on surgery of arteriovenous malformations and dural arteriovenous fistulae. *Neurosurgery*. (2010) 67:1094–4. doi: 10.1227/NEU.0b013e3181eb5049
15. Shah KJ, Cohen-Gadol AA. The application of FLOW 800 ICG videoangiography color maps for neurovascular surgery and intraoperative decision making. *World Neurosurg*. (2019) 122:e186–e197. doi: 10.1016/j.wneu.2018.09.195
16. Schuette AJ, Dannenbaum MJ, Cawley CM, Barrow DL. Indocyanine green videoangiography for confirmation of bypass graft patency. *J Korean Neurosurg Soc*. (2011) 50:23–9. doi: 10.3340/jkns.2011.50.1.23
17. Belykh E, Martirosyan NL, Yagmurlu K, Miller EJ, Eschbacher JM, Izadyyazdanabadi M, et al. Intraoperative fluorescence imaging for personalized brain tumor resection: current state and future directions. *Front Surg*. (2016) 3:55. doi: 10.3389/fsurg.2016.00055
18. File:Indocyanine green.png. *Wikimedia Commons, the Free Media Repository*. (2017). Available online at: https://commons.wikimedia.org/w/index.php?title=File:Indocyanine_green.png&oldid=260065692 (retrieved June 11, 2019).
19. Osol A, Hoover JE. Remington's pharmaceutical sciences. *J Pharm Sci*. (1976) 65:933. doi: 10.1002/jps.2600650641
20. Williams M. The merck index: an encyclopedia of chemicals, drugs, and biologicals. *Drug Dev Res*. (2013) 74:339. doi: 10.1002/ddr.21085
21. Raabe A, Beck J, Seifert V. Technique and image quality of intraoperative indocyanine green angiography during aneurysm surgery using surgical microscope integrated near-infrared video technology. *Zentralbl Neurochir*. (2005) 66:1–6. doi: 10.1055/s-2004-836223
22. Mérian J, Gravier J, Navarro F, Texier I. Fluorescent nanoprobes dedicated to *in vivo* imaging: from preclinical validations to clinical translation. *Molecules*. (2012) 17:5564–91. doi: 10.3390/molecules17055564
23. Engel E, Schraml R, Maisch T, Kobuch K, Konig B, Szeimies RM, et al. Light-induced decomposition of indocyanine green. *Investig Opthalmology Vis Sci*. (2008) 49:1777. doi: 10.1167/iovs.07-0911
24. Yannuzzi LA. Indocyanine green angiography: a perspective on use in the clinical setting. *Am J Ophthalmol*. (2011) 151:745–751.e1. doi: 10.1016/j.ajo.2011.01.043
25. Kogure K, Choromokos E. Infrared absorption angiography. *J Appl Physiol*. (1969) 26:154–7. doi: 10.1152/jappl.1969.26.1.154
26. Kuroiwa T, Kajimoto Y, Ohta T. Development and clinical application of near-infrared surgical microscope: preliminary report. *Minim Invasive Neurosurg*. (2001) 44: 240–2. doi: 10.1055/s-2001-19929
27. Ohkubo H, Musha H, Okuda K. Effects of caloric restriction on the kinetics of indocyanine green in patients with liver diseases and in the rat. *Am J Dig Dis*. (1978) 23:1017–24. doi: 10.1007/BF01263102
28. Chiang VL, Gailloud P, Murphy KJ, Rigamonti D, Tamargo RJ. Routine intraoperative angiography during aneurysm surgery. *J Neurosurg*. (2002) 96:988–992. doi: 10.3171/jns.2002.96.6.0988
29. Gruber A, Dorfer C, Standhardt H, Bavinzski G, Knosp E. Prospective comparison of intraoperative vascular monitoring technologies during cerebral aneurysm surgery. *Neurosurgery*. (2011) 68:657–73. doi: 10.1227/NEU.0b013e31820777ee
30. Della Puppa A, Rossetto M, Volpin F, Rustemi O, Grego A, Gerardi A, et al. Microsurgical clipping of intracranial aneurysms assisted by neurophysiological monitoring, microvascular flow probe, and ICG-VA: outcomes and intraoperative data on a multimodal strategy. *World Neurosurg*. (2018) 113:e336–e344. doi: 10.1016/j.wneu.2018.02.029
31. de Oliveira JG, Beck J, Seifert V, Teixeira MJ, Raabe A. Assessment of flow in perforating arteries during intracranial aneurysm surgery using intraoperative near-infrared indocyanine green videoangiography. *Neurosurgery*. (2008) 62:63–73. doi: 10.1227/01.NEU.0000333795.21468.D4
32. Nagai Y, Goto M, Toda H, Nishida N, Yoshimoto N, Iwasaki K. Indocyanine green videoangiography for surgery of a ruptured dissecting aneurysm in the precommunicating anterior cerebral artery: a technical case report. *Oper Neurosurg*. (2017) 13:E14–E18. doi: 10.1093/ons/opx028
33. Jing Z, Ou S, Ban Y, Tong Z, Wang Y. Intraoperative assessment of anterior circulation aneurysms using the indocyanine green video angiography technique. *J Clin Neurosci*. (2010) 17:26–8. doi: 10.1016/j.jocn.2009.03.034
34. He M, You C, Lan Z, Li J. Assessment of microscope-integrated indocyanine green angiography during intracranial aneurysm surgery: a retrospective study of 120 patients. *Neurol India*. (2009) 57:453. doi: 10.4103/0028-3886.55607
35. Xianli L, Zhongxue W, Sun S, Wang Y, Zang P. Indocyanine green videoangiography in clipping of paraclinoid aneurysms. *Turk Neurosurg*. (2012) 24: 319–22. doi: 10.5137/1019-5149.JTN.6284-12.1
36. Dashti R, Laakso A, Niemelä M, Porras M, Hernesniemi J. Microscope-integrated near-infrared indocyanine green videoangiography during surgery of intracranial aneurysms: the Helsinki experience. *Surg Neurol*. (2009) 71:543–50. doi: 10.1016/j.surneu.2009.01.027
37. Caplan JM, Sankey E, Yang W, Radvany MG, Colby GP, Coon AL, et al. Impact of indocyanine green videoangiography on rate of clip adjustments following intraoperative angiography. *Neurosurgery*. (2014) 75:437–44. doi: 10.1227/NEU.0000000000000468
38. Wang S, Liu L, Zhao Y, Zhang D, Yang M, Zhao J. Evaluation of surgical microscope-integrated intraoperative near-infrared indocyanine green videoangiography during aneurysm surgery. *Neurosurg Rev*. (2011) 34:209–15. doi: 10.1007/s10143-010-0305-2
39. Ma C-Y, Shi J-X, Wang H-D, Hang C-H, Cheng H-L, Wu W. Intraoperative indocyanine green angiography in intracranial aneurysm surgery: microsurgical clipping and revascularization. *Clin Neurol Neurosurg*. (2009) 111:840–6. doi: 10.1016/j.clineuro.2009.08.017

40. Cho W-S, Kim JE, Kim SH, Kim HC, Kang U, Lee D-S. Endoscopic fluorescence angiography with indocyanine green: a preclinical study in the swine. *J Kor Neurosurg Soc*. (2015) 58:513. doi: 10.3340/jkns.2015.58.6.513
41. Cho WS, Kim JE, Kang HS, Son YJ, Bang JS, Oh CW. Keyhole Approach and Neuroendoscopy for Cerebral Aneurysms. *J Korean Neurosurg Soc*. (2017) 60:275–81. doi: 10.3340/jkns.2017.0101.002
42. Bruneau M, Appelboom G, Rynkowski M, Cutsem N, Mine B, Witte O. Endoscope-integrated ICG technology: first application during intracranial aneurysm surgery. *Neurosurg Rev*. (2012) 36:77−84. doi: 10.1007/s10143-012-0419-9
43. Mielke D, Malinova V, Rohde V. Comparison of intraoperative microscopic and endoscopic ICG angiography in aneurysm surgery. *Neurosurgery*. (2014) 10:418–25. doi: 10.1227/NEU.0000000000000345
44. Daskalaki D, Aguilera F, Patton K, Giulianotti PC. Fluorescence in robotic surgery. *J Surg Oncol*. (2015) 112:250–6. doi: 10.1002/jso.23910
45. Smith AM, Mancini MC, Nie S. Bioimaging: second window for in vivo imaging. *Nat Nanotechnol*. (2009) 4:710–1. doi: 10.1038/nnano.2009.326
46. Lin J, Zhao J, Zhao Y, Zhang D, Wang R, Qiao H, et al. Multiple Intraoperative monitoring-assisted microneurosurgical treatment for anterior circulation cerebral aneurysm. *J Int Med Res*. (2011) 39:891–903. doi: 10.1177/147323001103900323

Conflict of Interest Statement: The authors declare that the research was conducted in the absence of any commercial or financial relationships that could be construed as a potential conflict of interest.

frontiers in Oncology

ORIGINAL RESEARCH
published: 25 June 2019
doi: 10.3389/fonc.2019.00519

Fluorescence Image Histology Pattern Transformation Using Image Style Transfer

*Mohammadhassan Izadyyazdanabadi[1,2], Evgenii Belykh[2], Xiaochun Zhao[2], Leandro Borba Moreira[2], Sirin Gandhi[2], Claudio Cavallo[2], Jennifer Eschbacher[3], Peter Nakaji[3], Mark C. Preul[2] and Yezhou Yang[1]**

[1] School of Computing, Informatics, and Decision System Engineering, Arizona State University, Tempe, AZ, United States, [2] The Loyal and Edith Davis Neurosurgery Research Laboratory, Department of Neurosurgery, St. Joseph's Hospital and Medical Center, Barrow Neurological Institute, Phoenix, AZ, United States, [3] Department of Neuropathology, St. Joseph's Hospital and Medical Center, Barrow Neurological Institute, Phoenix, AZ, United States

Confocal laser endomicroscopy (CLE) allow on-the-fly *in vivo* intraoperative imaging in a discreet field of view, especially for brain tumors, rather than extracting tissue for examination *ex vivo* with conventional light microscopy. Fluorescein sodium-driven CLE imaging is more interactive, rapid, and portable than conventional hematoxylin and eosin (H&E)-staining. However, it has several limitations: CLE images may be contaminated with artifacts (motion, red blood cells, noise), and neuropathologists are mainly trained on colorful stained histology slides like H&E while the CLE images are gray. To improve the diagnostic quality of CLE, we used a micrograph of an H&E slide from a glioma tumor biopsy and image style transfer, a neural network method for integrating the content and style of two images. This was done through minimizing the deviation of the target image from both the content (CLE) and style (H&E) images. The style transferred images were assessed and compared to conventional H&E histology by neurosurgeons and a neuropathologist who then validated the quality enhancement in 100 pairs of original and transformed images. Average reviewers' score on test images showed 84 out of 100 transformed images had fewer artifacts and more noticeable critical structures compared to their original CLE form. By providing images that are more interpretable than the original CLE images and more rapidly acquired than H&E slides, the style transfer method allows a real-time, cellular-level tissue examination using CLE technology that closely resembles the conventional appearance of H&E staining and may yield better diagnostic recognition than original CLE grayscale images.

Keywords: confocal laser endomicroscopy, fluorescence, digital pathology, brain tumor imaging, deep learning, image style transfer

OPEN ACCESS

Edited by:
Yin Li,
University of Wisconsin-Madison, United States

Reviewed by:
Yun Gu,
Shanghai Jiao Tong University, China
Guolin Ma,
China-Japan Friendship Hospital, China

***Correspondence:**
Yezhou Yang
yz.yang@asu.edu

Specialty section:
This article was submitted to Cancer Imaging and Image-directed Interventions, a section of the journal Frontiers in Oncology

Received: *28 February 2019*
Accepted: *30 May 2019*
Published: *25 June 2019*

Citation:
Izadyyazdanabadi M, Belykh E, Zhao X, Moreira LB, Gandhi S, Cavallo C, Eschbacher J, Nakaji P, Preul MC and Yang Y (2019) Fluorescence Image Histology Pattern Transformation Using Image Style Transfer. Front. Oncol. 9:519. doi: 10.3389/fonc.2019.00519

INTRODUCTION

Confocal laser endomicroscopy (CLE) is undergoing rigorous assessment for its potential to assist neurosurgeons to examine tissue *in situ* during brain surgery (1–5). The ability to scan tissue or surgical resection bed on-the-fly essentially producing optical biopsies, compatibility with different fluorophores, miniature size of the probe and the portability of the system are essential features of this promising technology. Currently, the most frequent technique used for neurosurgical

intraoperative diagnosis is examination of frozen section hematoxylin and eosin (H&E)-stained histology slides.

Figure 1A shows an example image from a glioma acquired by CLE (left) and a micrograph of an H&E slide (right), acquired by conventional light microscopy. Although generating CLE images is much faster than H&E slides (1 s per image compared to about 20 min per slide), many CLE images may be non-optimal and can be obscured with artifacts including background noise, blur, and red blood cells (6). The histopathological features of gliomas are often more identifiable in the H&E slide images compared to the CLE images generated using non-specific fluorescent dyes such as fluorescein sodium (FNa). Neuropathologists as well are used to evaluating detailed histoarchitecture colorfully stained with H&E for diagnoses, especially for frozen section biopsies. Fluorescent images from intraoperative neurosurgical application present a new digital gray scale (monochrome) imaging environment to the neuropathologist for diagnosis that may include hundreds of images from one case. Recently, the U.S. FDA has approved a blue laser range CLE system primarily utilizing FNa for use in neurosurgery.

Countervailing these diagnostic and visual deficiencies in CLE images requires a rapid, automated transformation that can: (1) remove the occluding artifacts, and (2) add (amplify) the histological patterns that are difficult to recognize in the CLE images. Finally, this transformation should avoid removing the critical details (e.g., cell structures, shape) or adding unreal patterns to the image, to maintain the integrity of the image content. Such a method may present "transformed" CLE images to the neuropathologist and neurosurgeon that may resemble images based on familiar and standard, even colored, appearances from histology stains, such as H&E.

One method for implementing this transformation could be supervised learning, however, supervised learning requires paired images (from the same object and location) to learn the mapping between the two domains (CLE and H&E). Creating a dataset of colocalized H&E and CLE images is infeasible because of problems in exact co-localization and intrinsic tissue movements, although small, and artifacts introduced during H&E slide preparation. "Image style transfer," first introduced by Gatys et al. (7), is an image transformation technique that blends the content and style of two separate images to produce the target image. This process minimizes the distance between feature maps of the source and target images using a pretrained convolutional neural network (CNN).

In this study, we aimed to remove the inherent occlusions and enhance the structures that were problematical to recognize in CLE images. Essentially, we attempted to make CLE images generated from non-specific FNa application during glioma surgery appear like standard H&E-stained histology and evaluate the accuracy and usefulness. We used the image style transfer method since it extracts abstract features from the CLE and H&E image that are independent of their location in the image and thus can operate on the images that are not from the same location. More details about the image style transfer algorithm and the quality assessment protocol follow in section Methods. Our results from a test dataset showed that on average, the diagnostic quality of stylized images was higher than the original CLE images, although there were some cases where the transformed image showed new artifacts.

METHODS

Image Style Transfer

Image style transfer takes a content and style image as input and produces a target image that shows the structures of the content image and the general appearance of the style image. This is achieved through four main components: (1) a pretrained CNN that extracts feature maps from source and target images, (2) quantitative calculation of the content and style representations for source and target images, (3) a loss function to capture the difference between the content and style representation of source and target images, and (4) an optimization algorithm to minimize the loss function. In contrast to CNN supervised learning, where the model parameters are updated to minimize the prediction error, image style transfer modifies the pixel values of the target image to minimize the loss function while the model parameters are fixed.

A 19-layer visual geometry group network (VGG-19), that is pretrained on ImageNet dataset, extracts feature maps from CLE, H&E, and target images. Feature maps in layer "Conv4_2" of VGG-19 are used to calculate the image content representation, and a list of gram matrices from feature maps of five layers ("ReLU1_1", "ReLU2_1", …, "ReLU5_1") are used to calculate the image style representation. To examine the difference between the target and source images, the following loss function was used:

$$Loss_{Total} = \underbrace{\frac{1}{2}\sum\left(C_{CLE} - C_{Target}\right)^2}_{\text{Content Loss: difference between content representation of the CLE and target image}} + \underbrace{\alpha \times \sum_{i=1}^{5} w^i \times \sum\left(S^i_{H\&E} - S^i_{Target}\right)^2}_{\text{Style Loss: difference between style representation of the H\&E and target image}}$$

C_{CLE} and C_{Target} are the content representations of the CLE and target image, $S^i_{H\&E}$ and S^i_{Target} are the style representations of the H&E and target image based on the feature maps of the i^{th} layer, and w^i (weight of i^{th} layer in the style representation) equals 0.2. The parameter α determines relative weight of style loss in the total loss and is set to 100. A limited memory optimization algorithm [L-BFGS (8)] minimizes this loss.

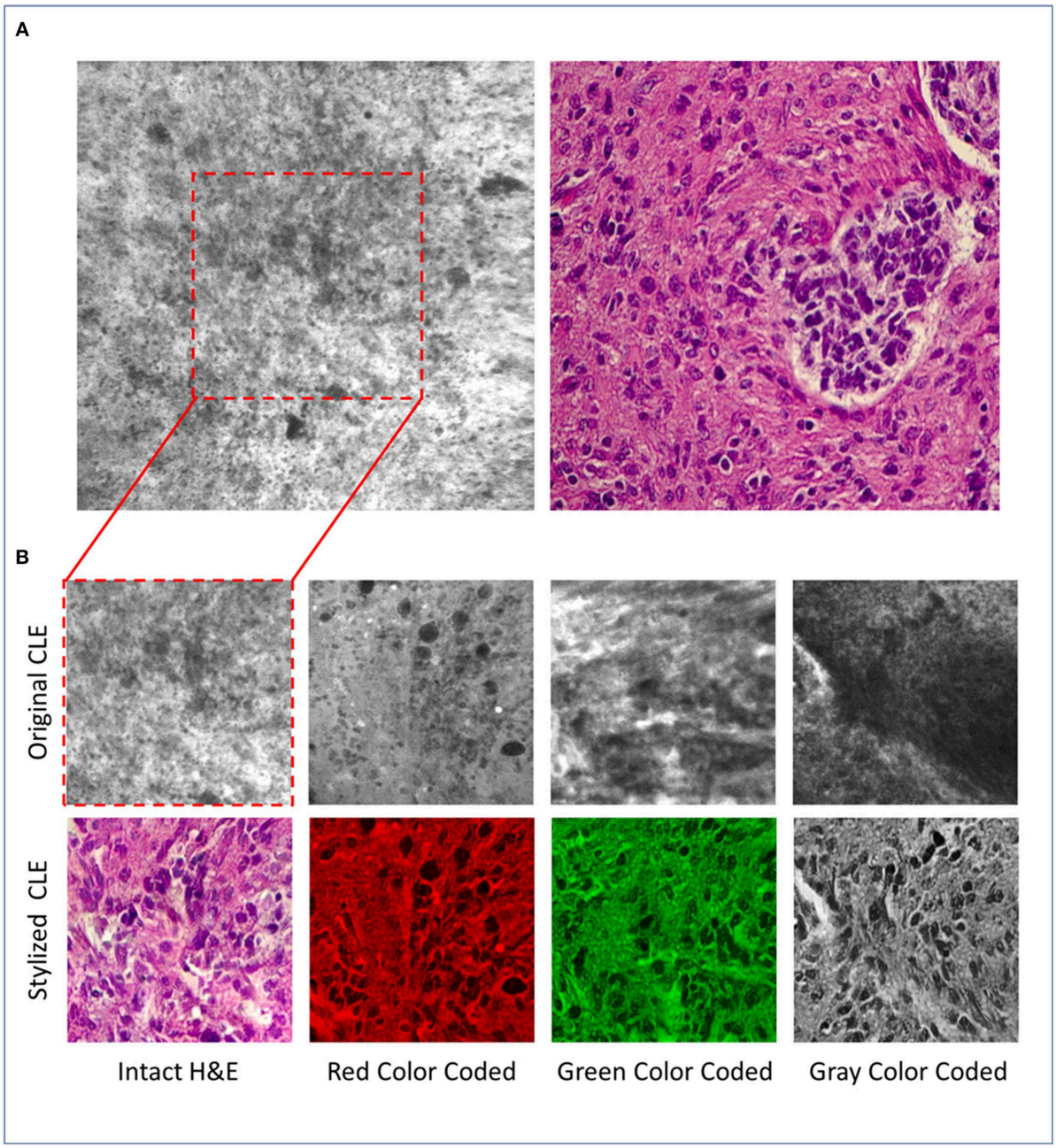

FIGURE 1 | (A) Representative CLE (Optiscan 5.1, Optiscan Pty., Ltd.) and H&E images from glioma tumors. **(B)** Original and stylized CLE images from glioma tumors, in 4 color coding: gray, green, red, intact H&E.

For the experiment, 100 CLE images [from a recent study by Martirosyan et al. (5)] were randomly selected from 15 subjects with glioma tumors as content images. A single micrograph of an H&E slide from a glioma tumor biopsy of a different patient (not one of the 15 subjects) was used as the style image (**Figure 1A**, right). For each CLE image, the optimization process was run for 1,600 iterations and the target image was saved for evaluation and referred to as the "stylized image" in the following sections.

Evaluation

Although the stylized images presented the same histological patterns as H&E images and seemed to contain similar structures to those present in the corresponding original CLE images, a quantitative image quality assessment was performed to rigorously evaluate the stylized images. Five neurosurgeons independently assessed the diagnostic quality of the 100 pairs of original and stylized CLE images. For each pair, the reviewers sought to examine two properties in each stylized image and

provided a score for each property based on their evaluation: (1) whether the stylization process removed any critical structures (negative impact) or artifacts (positive impact) that were present in the original CLE image, and (2) whether the stylization process added new structures that were not present (negative impact) or were difficult to notice (positive impact) in the original CLE image. The scores are between 0 and 6 with the following annotations: 0, extreme negative impact; 1, moderate negative impact; 2, slight negative impact; 3, no significant impact; 4, slight positive impact; 5, moderate positive impact; and 6, extreme positive impact (Further information and instructions about the quality assessment survey is available in the **Supplementary Materials**).

Since the physicians were more familiar with the H&E than the CLE images, it was possible that the reviewers would overestimate the quality of stylized images merely due to their color resemblance to H&E images (during style transfer the color of CLE image is also changed to pink and purple). To explore how the reviewers' scores would change if the stylized images were presented in a different color other than the pink and purple (the common color for H&E images), the stylized images were processed in four different ways: (I) 25 stylized images were converted into gray-scale images (averaging the three red, green, and blue channels), (II) 25 stylized images were color-coded in green (first converted the image to gray-scale and then set red and blue channels to zero), (III) 25 stylized images were color-coded as red (similar approach), and (IV) 25 stylized images were used without any further changes (intact H&E). Since there are too many structures in each CLE image, and to examine the images more precisely, we used the center-crop of each original CLE and its stylized version for evaluation. **Figure 1B** shows some example stylized images used for evaluation.

RESULTS AND ANALYSIS

Figure 2A shows a histogram of all reviewers' scores for the removed artifacts (blue bars) and added structures (orange bars) in the stylized images with different colors. Overall, the number of stylized CLE images that have higher diagnostic quality than the original images (score >3) was significantly larger than those with equal or lower diagnostic quality for both removed artifacts and added structures scores (one-way chi square test $p < 0.001$). Results from stylized images that were color-coded (gray, green, red) showed the same trend for the added structures scores, indicating that the improvement was not just because of color resemblance.

There was significant difference between how much the model added structures and removed artifacts. For all the color-coded and intact stylized images, the average of added structures scores was larger than the removed artifacts scores (t-test $p < 0.001$). This suggests that the model was better at enhancing the structures that were challenging to recognize than removing the artifacts.

Figure 2B shows the frequency of different combinations of scores for removed artifacts and added structures in an intensity map. Each block represents how many times a rater scored an image with the corresponding values on the x (improvement by added structures) and y (improvement by removed artifacts) axes for that block. The most frequent incident across all the stylized images is the coordinates (5,4), which means moderately adding structures and slightly removing artifacts, followed by (5,5) meaning moderately adding structures and removing artifacts. Although the intensity maps derived from different color-coded images were not exactly similar, the most frequent combination in each group still indicated positive impact in both properties. The most frequent combination of scores, for each of the color-coded images, was as follows: gray = (5,4), green = (5,5), red = (5,4), and intact = (5,4).

As a further analysis, we counted the number of images that had an average score of below three to see how often the algorithm removed critical structures or added artifacts that were misleading to the neurosurgeons. From the 100 tested images, 3 images had only critical structures removed, 4 images had only artifacts or unreal added structures, and 2 images had both artifacts added and critical structures removed. On the contrary, 84 images showed improved diagnostic quality through both removed artifacts and added structures that were hard to recognize, 6 images had only artifacts removed, and 5 images had only critical structures added. **Figure 1B** shows some example stylized images with improved quality compared to the original CLE, and **Figure 2C** shows two stylized images with decreased diagnostic quality through removed critical structures (top) and added artifacts (bottom).

DISCUSSION

In this study, image style transfer method was used to improve the diagnostic quality of CLE images from glioma tumors by transforming the histology patterns in CLE images of fluorescein sodium-stained tissue into the ones in conventional H&E-stained tissue slides. From the 100 test images, 90 images showed reduced artifacts and 89 images showed improvement in difficult structures (more identifiable) after the transformation, confirmed by five neurosurgeon reviewers. Similar results in color coded images (gray, green, red) suggested that the improvement was not solely because of the color resemblance of stylized images to the H&E slide images. The same method could be used to transform CLE videos as shown in the **Supplementary Materials**.

In a related study by Gu et al. (9), cycle-consistent generative adversarial network (CycleGAN) was used as a data synthesis method to overcome the limited size of dataset in probe-based CLE (pCLE). A real dataset of pCLE images and histology slide images were used to train a generative model that transformed the histology slide images into pCLE. The pCLE dataset was then augmented with the synthesized images to train a computer aided diagnostic system for classification of breast lesions that are stained with acriflavine hydrochloride. However, for use in the *in vivo* brain, fluorophores are currently extremely limited—only three are approved: 5-ALA, indocyanine green, and fluorescein sodium. Currently CLE in the brain only uses fluorescein sodium. Each of these fluorophores yields completely unique unrelated appearances. However, our aim was to evaluate the diagnostic

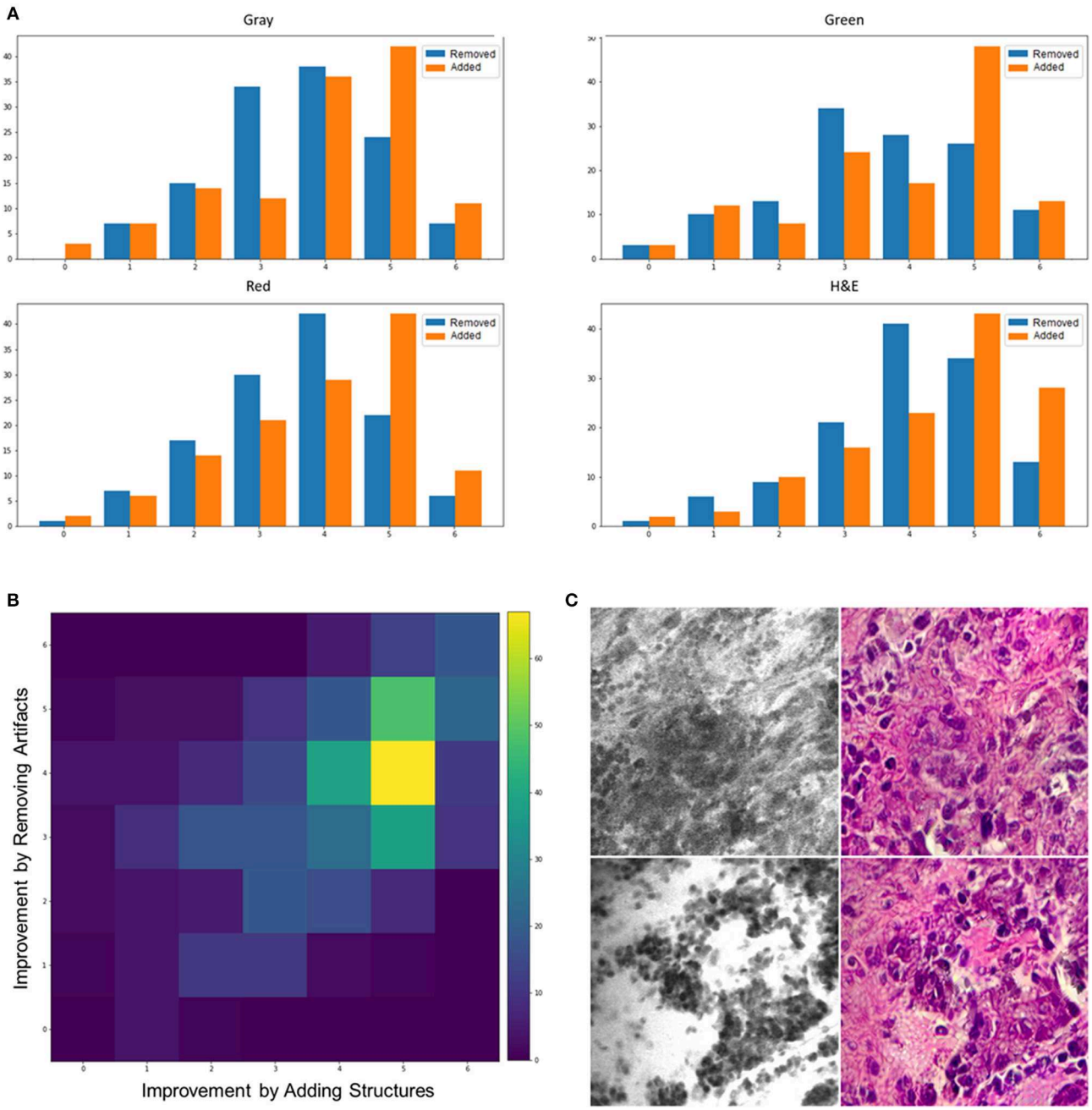

FIGURE 2 | (A) Histogram of scores for added structures and removed artifacts from different color—coded images. **(B)** An intensity map showing the frequency of different combinations of scores for adding structures (x axis) and removing artifacts (y axis). **(C)** Two example images that the stylization process removed some critical details (top) or added unreal structures (bottom).

quality of images that are obtained using fluorescein sodium stained biopsy tissue of brain lesions acquired during intracranial surgery. Fluorescein sodium is a non-specific stain which collects in the tissue background or extracellular space, thus does not produce images such as are stained with acriflavine, which is more specific and stains intracellular structures. Such a situation using fluorescein is thus even more of a diagnostic challenge and for transforming patterns from the CLE image domain to one of the familiar H&E histopathology images.

Although other studies have used CycleGAN for medical domain adaptation (9–11), none has applied "image style transfer" method for transforming CLE to H&E. Despite CycleGAN requirement of many images from both modalities (CLE and H&E) to train the model, image style transfer

can produce transformed images with a single image of each modality. This aspect of efficiency may have an important impact in surgery or pathology interpretation where there is a limited number of images available. Such an aspect of efficiency may lend itself better for inclusion into the CLE operating system for automated decision-making.

The purpose of our study was to evaluate the impact of image style transfer on the diagnostic quality of CLE brain and brain tumor (glioma) images from the neurosurgeons' perspectives. While studies like (9) explore the impact of synthesized data on computer-aided diagnostic methods, our study focused on improving the quality of CLE images from the physician point of view. Due to the intrinsic differences and mechanical limitations between the intraoperative CLE with a field of view of only 400 microns, neurosurgical biopsy instruments that acquire about 1 mL of tissue at minimum, normal physiologic brain movements, and light microscopy imaging of histology sections and slides, it is nearly impossible to image and correlate the same exact location with the two modalities. This limited us to compare the transformed CLE images with the potential real H&E stained sections of the same area, using measures such as structural similarity as performed by Shaban et al. (11) in their study. Indeed, the only available ground truth is the original CLE image (before transformation) which could be used to examine if any critical structures are removed or if unreal cellular architecture is added.

CONCLUSIONS

In this study, image style transfer was applied to CLE images from gliomas to enhance their diagnostic quality. Style transfer with an H&E-stained slide image had an overall positive impact on the diagnostic quality of CLE images. The improvement was not solely because of the colorization of CLE images; even the stylized images that were converted to gray, red, and green, reported improved diagnostic quality compared to the original CLE images. Employment of more specific clinical tasks to explore the advantage of stylization in diagnosing gliomas and other tumor types is underway based on this preliminary success. The fact that the style transfer is based on permanent histology H&E, provides an intraoperative advantage. Initial pathology diagnosis for brain tumor surgery is usually based on frozen section histology, with formal diagnosis awaiting the inspection of permanent histology slides requiring one to several days. The style transfer is based on rapidly acquired, on-the-fly (i.e., real time) *in vivo* intraoperative CLE images that most resemble the permanent histology; therefore, it is a significant advantage for interpretation. Frozen section histology often involves freezing artifact, cutting problems, and may have inconsistent staining for histological characteristics that are important for diagnosis. Style transferred CLE images are then most comparable to the permanent histology, and may be even better because CLE is imaging live tissue without such architectural disturbance.

In the future, application of more advanced methods for transferring patterns in the histology slides to the CLE images will be used to improve their interpretability. Because of the high number of CLE images acquired during a single case, style transfer could add value to such fluorescence images, and allows for computer-aided techniques to play a meaningful, convenient, and efficient role to aid the neurosurgeon and neuropathologist in analysis of CLE images and to more rapidly determine diagnosis.

DATA AVAILABILITY

The datasets generated for this study are available on request to the corresponding author.

AUTHOR'S NOTE

This research article was part of a Ph.D. dissertation (12).

AUTHOR CONTRIBUTIONS

MI, EB, YY, and MP conceived and wrote the article. MI and YY formulated computer learning systems. LM, XZ, SG, CC, and EB assessed the quality of images. PN acquired images from neurosurgical cases. JE examined the CLE and histology images.

FUNDING

This research was supported by the Newsome Chair in Neurosurgery Research held by MP and by the Barrow Neurological Foundation. EB received scholarship support SP-2240.2018.4. YY is partially supported by US National Science Foundation under award #1750082.

SUPPLEMENTARY MATERIAL

The Supplementary Material for this article can be found online at: https://www.frontiersin.org/articles/10.3389/fonc.2019.00519/full#supplementary-material

REFERENCES

1. Martirosyan NL, Georges J, Eschbacher JM, Cavalcanti DD, Elhadi AM, Abdelwahab MG, et al. Potential application of a handheld confocal endomicroscope imaging system using a variety of fluorophores in experimental gliomas and normal brain. *Neurosurg Focus*. (2014) 36:E16. doi: 10.3171/2013.11.FOCUS13486
2. Foersch S, Heimann A, Ayyad A, Spoden GA, Florin L, Mpoukouvalas K, et al. Confocal laser endomicroscopy for diagnosis and histomorphologic imaging of brain tumors *in vivo*. *PLoS ONE*. (2012) 7:e41760. doi: 10.1371/journal.pone.0041760
3. Belykh E, Miller EJ, Patel AA, IzadyYazdanabadi M, Martirosyan NL, Yagmurlu K, et al. Diagnostic accuracy of the confocal laser endomicroscope for *in vivo* differentiation between normal and tumor tissue during fluorescein-guided glioma resection: laboratory investigation.

World Neurosurg. (2018) 115:e337–48. doi: 10.1016/j.wneu.2018.04.048
4. Izadyyazdanabadi M, Belykh E, Mooney M, Martirosyan N, Eschbacher J, Nakaji P, et al. Convolutional neural networks: ensemble modeling, fine-tuning and unsupervised semantic localization for neurosurgical CLE images. *J Vis Commun Image Represent*. (2018) 54:10–20. doi: 10.1016/j.jvcir.2018.04.004
5. Martirosyan NL, Eschbacher JM, Kalani MYS, Turner JD, Belykh E, Spetzler RF, et al. Prospective evaluation of the utility of intraoperative confocal laser endomicroscopy in patients with brain neoplasms using fluorescein sodium: experience with 74 cases. *Neurosurg Focus*. (2016) 40:E11. doi: 10.3171/2016.1.FOCUS15559
6. Izadyyazdanabadi M, Belykh E, Martirosyan N, Eschbacher J, Nakaji P, Yang Y, et al. Improving utility of brain tumor confocal laser endomicroscopy: objective value assessment and diagnostic frame detection with convolutional neural networks. In: *Progress in Biomedical Optics and Imaging - Proceedings of SPIE* (Orlando, FL), (2017).
7. Gatys LA, Ecker AS, Bethge M. Image Style Transfer using convolutional neural networks. In: *2016 IEEE Conference on Computer Vision and Pattern Recognition (CVPR)* (Las Vegas, NV), (2016).
8. Zhu C, Byrd RH, Lu P, Nocedal J. Algorithm 778: L-BFGS-B: fortran subroutines for large-scale bound-constrained optimization. *ACM Trans Math Softw*. (1997) 23:550–60. doi: 10.1145/279232.279236
9. Gu Y, Vyas K, Yang J, Yang G. Transfer recurrent feature learning for endomicroscopy image recognition. *IEEE Trans Med Imaging*. (2019) 38:791–801. doi: 10.1109/TMI.2018.2872473
10. Rivenson Y, Wang H, Wei Z, de Haan K, Zhang Y, Wu Y, et al. Virtual histological staining of unlabelled tissue-autofluorescence images via deep learning. *Nat Biomed Eng*. (2019) 3:466–77. doi: 10.1038/s41551-019-0362-y
11. Shaban MT, Baur C, Navab N, Albarqouni S. Staingan: stain style transfer for digital histological images. *arXiv [Preprint]. arXiv:180401601*. (2018). Available online at: https://arxiv.org/abs/1804.01601
12. Yazdanabadi MI. *Confocal laser endomicroscopy image analysis with deep convolutional neural networks* (Doctoral dissertation). Arizona State University, Tempe, AZ, United States (2019).

Conflict of Interest Statement: The authors declare that the research was conducted in the absence of any commercial or financial relationships that could be construed as a potential conflict of interest.

frontiers in Surgery

ORIGINAL RESEARCH
published: 02 July 2019
doi: 10.3389/fsurg.2019.00039

Enhancing Safety in Reconstructive Microsurgery Using Intraoperative Indocyanine Green Angiography

Ingo Ludolph, Raymund E. Horch, Andreas Arkudas and Marweh Schmitz*

Department of Plastic and Hand Surgery and Laboratory for Tissue Engineering and Regenerative Medicine, University Hospital of Erlangen, Friedrich-Alexander-University of Erlangen-Nuernberg FAU, Erlangen, Germany

Intraoperative assessing and postoperative monitoring of the viability of free flaps is of high relevance in reconstructive microsurgery. Today different methods for the evaluation of tissue perfusion are known. Indocyanine Green angiography is an emerging technique among plastic surgeons with a broad scope of applications especially in microsurgical free flap transfer. We demonstrate the value and clinical application of this technique based on representative selected cases where Indocyanine Green angiography was used in microsurgical free flap transfers from different anatomic donor sites during the operation. Hereby perforator selection, flap tailoring, changes of blood flow and patency of anastomoses was judged and decision making was based on the angiographic findings. This method has proven to be valid, reproducible and easy to use. The application is not limited to the evaluation of skin perfusion, but is also applicable to muscle tissue or chimeric or composite flaps. Reliable judgement is especially given for the extent of arterially perfused tissue following complete flap dissection. Moreover, this real-time angiography revealed a high sensitivity for the detection of poorly perfused flap areas, thus supporting the conventional clinical judgement and reducing complications. In summary Indocyanine Green angiography has the potential to reduce flap related complications and to contribute to enhancing and extending the possibilities of free flap surgery.

Keywords: ICG, Indocyanine Green angiography, microsurgery, free flap, imaging

OPEN ACCESS

Edited by:
Mark Preul,
Barrow Neurological Institute (BNI), United States

Reviewed by:
Hiroo Suami,
Macquarie University, Australia
James Mankin,
Dignity Health, United States

****Correspondence:***
Ingo Ludolph
ingo.ludolph@uk-erlangen.de

Specialty section:
This article was submitted to Reconstructive and Plastic Surgery, a section of the journal Frontiers in Surgery

Received: *06 January 2019*
Accepted: *13 June 2019*
Published: *02 July 2019*

Citation:
Ludolph I, Horch RE, Arkudas A and Schmitz M (2019) Enhancing Safety in Reconstructive Microsurgery Using Intraoperative Indocyanine Green Angiography. Front. Surg. 6:39. doi: 10.3389/fsurg.2019.00039

INTRODUCTION

In plastic reconstructive surgery, the number of free tissue transfers has increased significantly in recent decades. Given the appropriate indication recent advancements in operative techniques and imaging modalities have facilitated microvascular reconstructions to become safer, more reliable procedures almost independent from the patient's age (1–4).

Preoperative assessment of the microvasculature anatomy at the tissue harvesting site with advanced imaging modalities has assisted surgeons in the appropriate selection of the donor site, perforator, and flap and has led to an overall improvement in the flap outcomes (1, 5). Furthermore, the question of the intraoperative decision making especially in critically large free flaps, the individual intraoperative perforator constellation and the patency of anastomoses is as relevant as the question of the postoperative flap monitoring. Since the early days of microsurgical reconstructive procedures postoperative flap monitoring in particular is of high relevance for a successful outcome. Hence many clinical and experimental studies deal with this issue. Therefore,

modern imaging devices ideally should address the entire scope of a reconstructive procedure, from the planning to the postoperative perfusion monitoring. Today several different techniques are available, all of them with the aim of decreasing flap associated complications.

Laser assisted Indocyanine Green angiography (ICG angiography) in its advanced technical version provides real-time angiography, which enables decision making on tissue perfusion in free and pedicled flaps to be made with high reliability both intraoperatively and postoperatively. ICG was introduced into clinical routine in the 1950's. It was initially used in hepatology as a function test, in cardiologic diagnostics and later by ophthalmologists as it shows less leakage from blood vessels as compared to fluorescein (6, 7). In ophthalmology it is valuable because it remains for a long time in more blood-perfused tissues such as the choroid and the blood vessels.

In this study we give insight into the spectrum of the application of ICG angiography in plastic reconstructive surgery based on representative and selected clinical cases and demonstrate the advantages and disadvantages of this procedure in the context of the current literature.

MATERIALS AND METHODS

Among the variety of more than 150 free flaps and pedicled flaps performed in our institution per year four representative clinical cases with different indications for a reconstructive procedure at varying anatomical locations were selected to highlight the status of ICG angiography.

Written informed consent was obtained from all patients in accordance with the Declaration of Helsinki and ICG measurements were performed within a study protocol which was approved by the institutional Review Board (registration number 85_13 B).

As a method for skin perfusion analysis we used ICG-angiography (SPY Elite System, Novadaq Technologies Inc., Toronto, Canada) which has been utilized by our group in more than 300 cases since 2014. Exclusion criteria were solely based on contraindications for the application of Indocyanine Green, e.g., iodine allergy, autonomous adenoma of thyroid gland, hyperthyroidism or due to refusal by the patient. In all free flaps, independent of the anatomic region or the tissue included, it was routinely performed in a standard mode using a 12.5 mg bolus of ICG dye through a venous line.

After intravenous injection of ICG dye, it binds to plasma proteins. The short plasma half-life period of ICG of 3 to 4 min allows repeated injections. It is not metabolized and is excreted by the liver into bile. At the area of interest the ICG is excited by a near-infrared laser. The laser device has no potential for causing damage to the tissue or the observer. The fluorescent substance displays an absorption maximum at 805 nm and an emission maximum at 835 nm. Light at a wavelength of 800 nm in the near-infrared range is minimally absorbed by water or hemoglobin and is not scattered by tissues, which allows visualization of blood vessels (7). The dye highlights vessels up to a minimum of 3 to 5 mm in the tissue. The perfusion pattern, the intensity of the fluorescence as an indicator for dye uptake and the clearance within the tissue is displayed on a video monitor. Well-perfused areas appear bright due to dye uptake, whereas mal-perfused areas are relatively dark. In a standard mode the device displays the video in a gray scale. An additional analysis tool provides color modes and calculation of ingress and egress rates in absolute or relative values. Furthermore, contour levels can be defined for determination of perfusion areas in relation to an automatically or individually set references point in the field of interest. The analysis tool allows the user to work on the videos and pictures at a later time.

RESULTS

Case 1

A 71 year old male patient suffered from an extensive tissue defect at the dorsum of the left hand as a result of a bicycle incident. After multiple debridement and wound conditioning using negative pressure wound therapy the defect had to be reconstructed by a large free anterior lateral thigh flap from the left thigh. During flap harvesting two distant main perforators were detected, located very lateral within the flap. Following complete flap dissection the first ICG measurement was performed with the flap left in place at the thigh. Thus, the special perforator constellation and the borders of the adjacent perforasomes could be determined. **Figure 1** clearly displays the perforasome border nourished by the proximal perforator in the flap which was not to judge sufficiently by clinical signs. After a few seconds the distal perforasome was also perfused shown by an uptake of the ICG dye. Due to this analysis both perforators were then included in the flap.

The flap was anastomosed to the left radial artery in an end-to-side fashion as well as to concomitant recipient veins. Hereupon another ICG measurement revealed a well-perfused flap without changes of blood flow pattern compared to the point after flap harvesting. The perforasome constellation was confirmed and the flap exactly trimmed to the defect size dependent on the ICG perfusion pattern (**Figure 1**).

Case 2

A 49 year old female patient presented a progressive lymphedema at the right leg refractory to conservative measures. In the medical history 4 years ago a laparoscopic hysterectomy and adnexectomy as well as a radical pelvic lymphadenectomy on the right side were performed because of a uterine cervical carcinoma. Despite conservative treatment the lymphedema exacerbated resulting in functional impairment and loss of quality of life. After inconspicuous follow up care and lymphoscintigraphy scan a microsurgically transplanted omentum majus flap containing lymph nodes and lymph vessles was planned. Using a laparoscopic approach the omentum majus flap was raised including the right gastroepiploic artery and vein. The flap was then anastomosed to the right femoral artery and vein. **Figure 2** shows the ICG measurement after anastomosis. The well-perfused vessel arcades via the right gastroepiploic artery could be defined, whereas ICG angiography revealed the mal-perfused parts of the omentum majus which

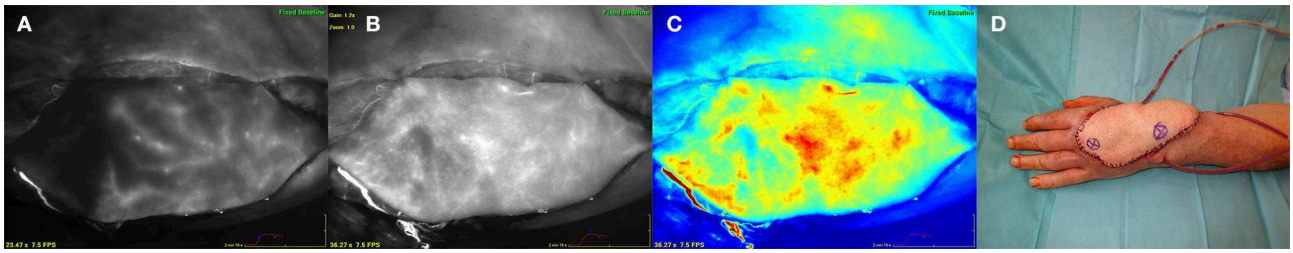

FIGURE 1 | Free anterior lateral thigh flap (ALT) for reconstruction of the dorsum of the left hand. **(A)** (left) ALT flap after harvesting at the left thigh. ICG angiography marking the perforasome perfused by the proximal perforator revealing a distinct perfusion border. **(B)** (middle left) Flap perfused via a proximal and distal perforator showing perfusion of adjacent perforasomes. **(C)** (middle right) ICG angiography color mode. **(D)** (right) ALT flap after inset at the left hand. Asterix within the flap marking the distal (right) and proximal (left) perforator.

FIGURE 2 | Free omentum majus flap at the right inguinal region. **(A)** (left) ICG angiography of the omentum majus after anastomosis to the femoral vessels showing exact perfusion of the vessel arcades and the adjacent tissue. **(B)** (middle) Mal-perfused part of the omentum majus flap. **(C)** (right) Flap at the inguinal region after anastomosis. Red bar indicates the border between well-perfused (top) and mal-perfused (bottom) parts of the omentum majus defined by ICG angiography.

could not be determined by clinical signs. Especially in free flaps where no skin is included and peripheral bleeding on the wound edges is not common as well as residual perfusion is not sufficient for tissue survival, conventional clinical judgement by means of capillary refill or color change is not a reliable option. Discarding of too much or too less tissue is the possible consequence in these cases. Finally after discarding mal-perfused tissue parts the omentum majus was placed and spread out in the subcutaneous tissue to enable lymph vessels to grow in and establish a new lymph collector for the right lower extremity.

Case 3

In a 55 year old female patient invasive breast cancer was diagnosed in her right breast. Neoadjuvant chemotherapy was recommended followed by modified radical mastectomy and radiotherapy. After an uneventful follow up period without tumor relapse during 1 year after mastectomy the patient presented for autologous breast reconstruction with abdominal tissue. A preoperative computed tomography angiography showed a strong lateral perforator from the inferior epigastric artery. Finally a so called DIEP flap (deep inferior epigastric artery perforator flap) was harvested based on the aforementioned lateral perforator on the left side of the abdomen. Because it was hypothesized that lateral located perforators do not constantly perfuse the flap tissue across the midline and often a possibly large flap volume is necessary especially in thin patients, ICG measurement is used to define the perfusion pattern.

In this case ICG angiography showed a well perfused flap area across the midline and flap shaping was performed due to the ICG dye uptake to gain the maximum flap tissue. After anastomosis of the flap to the internal mammary artery and vein in an end-to-end fashion the repeated ICG measurement presented patent anastomoses and a well perfused DIEP flap also in the peripheral zones with no relevant change of the blood flow pattern (**Figure 3**).

Case 4

An 83 year old female patient presented with a skin necrosis at the right knee and an infection of her knee joint prosthesis after multiple operations necessitating replacement of the joint prosthesis due to relapsing implant infections in the past. Because a total knee arthrodesis was not possible due to relevant shortening of the lower extremity and a high risk of osteomyelitis, wound conditioning using negative pressure wound therapy and defect reconstruction was planned to salvage the knee prosthesis and to prevent limb amputation as an ultima ratio procedure. In an interdisciplinary approach with the department of orthopedic surgery the mobile parts of the prosthesis were changed and the defect was closed with a free myocutaneous latissimus dorsi flap. The whole latissimus dorsi muscle was harvested with a large cutaneous flap island as this was necessary due to the defect size. Also in this case ICG measurement was done after harvesting and after anastomosis to the superficial femoral artery and vein.

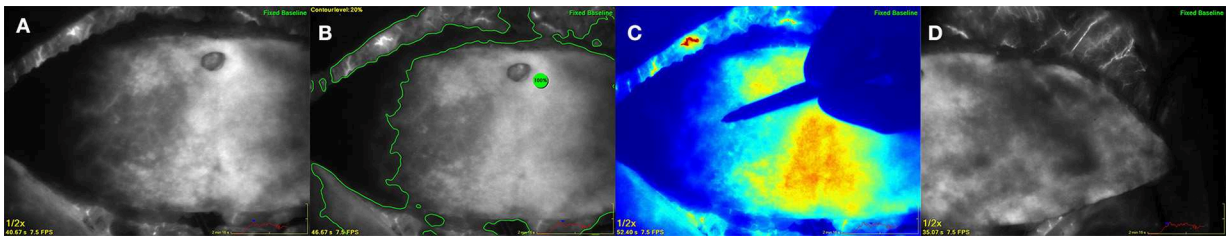

FIGURE 3 | Deep inferior epigastric perforator flap after complete harvesting at the abdomen based on a single lateral located perforator. **(A)** (left) ICG angiography showing the perfusion pattern on the contralateral side of the perforator across the midline. **(B)** (middle left) Analysis by using a contour level of 20% in relation to a reference point of maximum fluorescence within the flap. **(C)** (middle right) Color mode showing the surgeons hand marking the flap borders due to the ICG perfusion pattern. **(D)** (right) ICG angiography of the ipsilateral part of the flap indicating excellent perfusion.

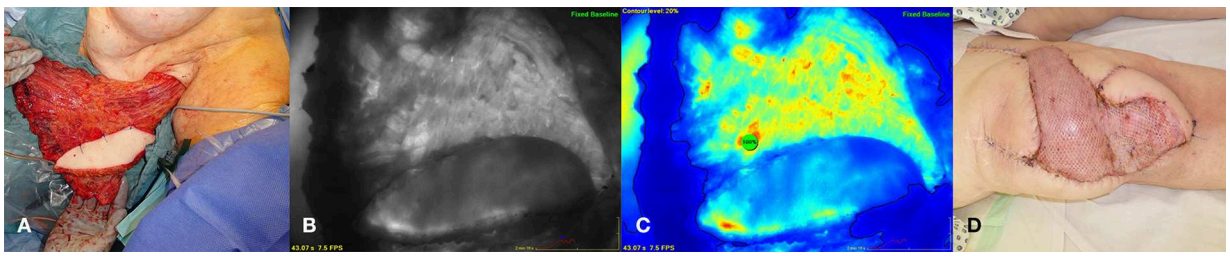

FIGURE 4 | Myocutaneous latissimus dorsi flap for coverage of a defect at the right knee. **(A)** Latissimus flap after complete harvesting at the left axilla. **(B)** (middle left) ICG angiography revealing mal-perfused flap areas at the periphery. **(C)** (middle right) Color mode and contour level at 20% in relation to a reference point of maximum fluorescence within the flap. **(D)** (right) Flap after inset and anastomosis at the right knee.

Based on the perfusion analysis the very peripheral parts of the muscle had to be discarded, whereas the cutaneous island showed normal dispersion of the dye indicating normal perfused tissue (**Figure 4**).

DISCUSSION

Due to technical advancements and the increased knowledge in the field of plastic reconstructive surgery within the last 2–3 decades, the possibilities of microsurgically free tissue transfers have increased massively. As a result, free tissue transfers on the one hand and pedicled flaps on the other hand are now so called standard procedures in a high volume center almost independent of the patient's age (2, 3). In particular, plastic reconstructive surgeons have dealt with the question of flap monitoring since the beginning of microsurgery. In the early 1980s plastic surgeons were already aware of the importance of flap monitoring, which then relied on clinical observation (8). It is generally accepted that nowadays the intraoperative analysis of flap perfusion becomes more and more important in addition to the preoperative perfusion assessment, e.g., the so-called perforator mapping (1, 9–12). Besides the perfusion assessment after flap harvesting and anastomosis, the intraoperative use of imaging techniques is of particular interest in complex constellations of the donor vessels, especially when large flaps are required that challenge the classical perforasomes. It has added a highly valuable tool for intraoperative flap shaping and designing the flaps according to their optimal perfusion zones. Only few imaging methods are actually evaluated and established in clinical routine (9–11, 13, 14). The most common methods today are the laser assisted Indocyanine Green angiography, thermography, combined laser Doppler spectrophotometry, the laser speckle contrast imaging, hyperspectral imaging or near infrared spectroscopy, respectively (15–22). Most techniques are predominantly used in the context of experimental or clinical studies and have their own advantages and disadvantages in the context of the abovementioned fields of application. The ideal monitoring instrument should primarily meet the following requirements: non-invasive and contactless, spatial resolution about the flap, accurate, and easy to use even for inexperienced personnel and providing timely information (17).

ICG angiography has been used for more than 50 years in the clinical assessment of cardiovascular function, hepatic clearance, and retinal angiography. Up to now, it is well-standardized and the laser technologies as well as the analysis options have evolved significantly. The ICG dye itself has proofed to be safe and it features for assessing tissue perfusion have enabled to develop other applications in various surgical procedures, especially in plastic surgery (10).

Denneny et al. performed an experimental study in 1983 (8) using neurovascular island flaps in rats which were transected and re-anastomosed after flap harvesting. Hereafter Fluorescein dye was injected and uptake and elimination of the dye was visualized by a fiberoptic perfusion fluorometer. They stated that this method provides reliable data about flap perfusion and predicts viability. In recent years more studies concerning tissue perfusion analysis were published (23–25). Especially in the field of immediate alloplastic breast reconstruction the perfusion of the mastectomy skin flap was evaluated using ICG angiography,

because judgement of inadequate microcirculatory perfusion can be difficult and may result in skin flap or fat necrosis and reoperation. Nevertheless, for the application in free flap surgery there is still a lack of literature.

As presented in our study the advantages of this method, however, are obvious. ICG angiography offers a real-time determination of tissue vascularity and perfusion, showing a high sensitivity especially in the arterial phase of dye distribution (13). The selected representative cases prove the reproducible practicability for intraoperative perforasome definition in perforator flaps and individualized flap tailoring as well as for the judgement of muscle flaps or even the omentum majus flap.

In autologous breast reconstruction after mastectomy due to breast cancer, microsurgically transplanted tissue from the abdomen, the so-called DIEP- or muscle sparing TRAM flap, represents the gold standard today. Particularly in obese patients or in DIEP flaps where the perforator distribution and the vascular pattern within the fat layer is not predictable, clinical flap tailoring according to the zonal classification by Hartrampf or Holm might be misleading (26, 27). As shown in case 3, individual flap planning is possible by ICG angiography with a high sensitivity for mal-perfused tissue parts. Therefore, partial flap necrosis or fat necrosis can be reduced.

As we could observe in our patients, the initial phase of dye uptake within the flap tissue can be defined as safely perfused tissue. The method is independent of the investigator, reproducible as well as contactless and with a high spatial and temporal resolution. It is an external device and therefore the use is not limited to the operating room. Due to the short half-life, multiple measurements are possible at short intervals. Additionally it can be applied for postoperative flap monitoring in critical cases or if flap perfusion is not distinct by using other methods.

The application possibilities in plastic reconstructive surgery are manifold. Thus, ICG angiography can be applied not only to assess skin or muscle flaps, but also to chimeric flaps, e.g., osteomyocutaneous as well as free vascularized bone grafts such as the free medial femoral condyle bone graft or even after finger replantation (28, 29). If the technique can also contribute to judge flap autonomisation and further clarify the long term vascular changes in transplanted flaps in the long term run seems evident, but is not completely clear yet (30, 31). Further studies are required to address this topic.

However, some inherent limitations regarding ICG angiography need to be discussed also. It represents an invasive procedure in which the intravenous application of a dye is required. Throughout the years of experience with ICG the incidence of adverse effects of the dye has been infrequent and they have generally been of low severity (32, 33). Relative contraindications such as iodide allergy or severe renal failure have to be considered. In addition, the venous phase after dye uptake in the tissue is not comparable in its precision to the very sensitive arterial uptake phase. Thus, the judgement of a venous congestion is more difficult and requires more general experiences with the technique. In addition increasing background fluorescence develops in the tissue when measurements are taken repeatedly in short intervals. The latter can lead to an indistinct perfusion assessment. By using ICG angiography intraoperatively different factors could potentially influence skin perfusion. These included variables such as the use of epinephrine containing tumescent solution, administration of vasopressors, blood pressure, oxygen saturation, fraction of inspired oxygen, temperature and hematocrit as well as individual anatomical differences (34).

Despite the broad application, still no absolute or relative perfusion levels correlating with fluorescence intensity of the dye—which would allow defining parts of the tissue as well-perfused or mal-perfused, respectively—have been standardized. In our experience, a "relative perfusion level" between 20 and 30% in relation to the most fluorescent area within the relevant tissue turned out to be safely perfused tissue. Concerning the postoperative monitoring the non-continuous nature of capturing data and the large size of the device we used the application for a routine bedside monitoring postoperatively is limited (35). Nevertheless, frequent measurements are possible in principle also on the ward or in an outpatient setting.

CONCLUSION

ICG angiography enables a standardized and reproducible real-time angiography of different tissues and provides a high sensitivity in detecting well-perfused and non-perfused tissue in the field of plastic reconstructive surgery. It has the potential to reduce flap related complications and to optimize and extend the possibilities of free flap surgery. Further studies in different applications fields are required to standardize application and enhance the possibilities of this method in plastic surgery.

ETHICS STATEMENT

Written informed consent was obtained from all patients in accordance with the Declaration of Helsinki and ICG measurements were performed within a study protocol which was approved by the institutional Review Board (registration number 85_13 B).

AUTHOR CONTRIBUTIONS

IL: study conception. IL, RH, AA, and MS: acquisition of data. IL, RH, and MS: analysis and interpretation. IL and RH: drafting of manuscript. IL, RH, AA, and MS: critical revision.

REFERENCES

1. Chae MP, Hunter-Smith DJ, Rozen WM. Comparative analysis of fluorescent angiography, computed tomographic angiography and magnetic resonance angiography for planning autologous breast reconstruction. *Gland Surg.* (2015) 4:164–78. doi: 10.3978/j.issn.2227-684X.2015.03.06
2. Ludolph I, Lehnhardt M, Arkudas A, Kneser U, Pierer G, Harder Y, et al. [Plastic reconstructive microsurgery in the elderly patient - consensus

statement of the German Speaking Working Group for Microsurgery of the Peripheral Nerves and Vessels]. *Handchir Mikrochir Plast Chir*. (2018) 50:118–25. doi: 10.1055/s-0043-115730
3. Fried FW, Beier JP, Bohr C, Iro H, Horch RE, Arkudas A. Free latissimus dorsi myocutaneous flap in a 6-month-old child for reconstruction of a temporal fossa defect after teratoma resection. *Ann Plast Surg*. (2019) 82:62–3. doi: 10.1097/SAP.0000000000001629
4. Steiner D, Horch RE, Eyupoglu I, Buchfelder M, Arkudas A, Schmitz M, et al. Reconstruction of composite defects of the scalp and neurocranium-a treatment algorithm from local flaps to combined AV loop free flap reconstruction. *World J Surg Oncol*. (2018) 16:217. doi: 10.1186/s12957-018-1517-0
5. Mathes DW, Neligan PC. Current techniques in preoperative imaging for abdomen-based perforator flap microsurgical breast reconstruction. *J Reconstruct Microsurg*. (2010) 26:3–10. doi: 10.1055/s-0029-1244806
6. Lohman RF, Ozturk CN, Ozturk C, Jayaprakash V, Djohan R. An analysis of current techniques used for intraoperative flap evaluation. *Ann Plast Surg*. (2015) 75:679–85. doi: 10.1097/SAP.0000000000000235
7. Liu DZ, Mathes DW, Zenn MR, Neligan PC. The application of indocyanine green fluorescence angiography in plastic surgery. *J Reconstruct Microsurg*. (2011) 27:355–64. doi: 10.1055/s-0031-1281515
8. Denneny JC III, Weisman RA, Silverman DG. Monitoring free flap perfusion by serial fluorometry. *Otolaryngol Head Neck Surg*. (1983) 91:372–6. doi: 10.1177/019459988309100405
9. Bellamy JL, Mundinger GS, Flores JM, Wimmers EG, Yalanis GC, Rodriguez ED, et al. Do adjunctive flap-monitoring technologies impact clinical decision making? an analysis of microsurgeon preferences and behavior by body region. *Plast Reconstruct Surg*. (2015) 135:883–92. doi: 10.1097/PRS.0000000000001064
10. Burnier P, Niddam J, Bosc R, Hersant B, Meningaud JP. Indocyanine green applications in plastic surgery: a review of the literature. *J Plast Reconstruct Aesthet Surg*. (2017) 70:814–27. doi: 10.1016/j.bjps.2017.01.020
11. Smit JM, Negenborn VL, Jansen SM, Jaspers MEH, de Vries R, Heymans MW, et al. Intraoperative evaluation of perfusion in free flap surgery: a systematic review and meta-analysis. *Microsurgery*. (2018) 38:804–18. doi: 10.1002/micr.30320
12. Saint-Cyr M, Wong C, Schaverien M, Mojallal A, Rohrich RJ. The perforasome theory: vascular anatomy and clinical implications. *Plast Reconstruct Surg*. (2009 124:1529–44. doi: 10.1097/PRS.0b013e3181b98a6c
13. Ludolph I, Arkudas A, Schmitz M, Boos AM, Taeger CD, Rother U, et al. Cracking the perfusion code?: Laser-assisted Indocyanine Green angiography and combined laser Doppler spectrophotometry for intraoperative evaluation of tissue perfusion in autologous breast reconstruction with DIEP or ms-TRAM flaps. *J Plast Reconstruct Aesthet Surg*. (2016) 69:1382–8. doi: 10.1016/j.bjps.2016.07.014
14. Hauck T, Horch RE, Schmitz M, Arkudas A. Secondary breast reconstruction after mastectomy using the DIEP flap. *Surg Oncol*. (2018) 27:513. doi: 10.1016/j.suronc.2018.06.006
15. Beier JP, Horch RE, Arkudas A, Dragu A, Schmitz M, Kneser U. Decision-making in DIEP and ms-TRAM flaps: the potential role for a combined laser Doppler spectrophotometry system. *J Plast Reconstruct Aesthet Surg*. (2013) 66:73–9. doi: 10.1016/j.bjps.2012.08.040
16. Rothenberger J, Amr A, Schaller HE, Rahmanian-Schwarz A. Evaluation of a non-invasive monitoring method for free flap breast reconstruction using laser doppler flowmetrie and tissue spectrophotometry. *Microsurgery*. (2013) 33:350–7. doi: 10.1002/micr.22096
17. Holmer A, Marotz J, Wahl P, Dau M, Kammerer PW. Hyperspectral imaging in perfusion and wound diagnostics - methods and algorithms for the determination of tissue parameters. *Biomed Tech Biomed Eng*. (2018) 63:547–56. doi: 10.1515/bmt-2017-0155
18. Holm C, Mayr M, Hofter E, Dornseifer U, Ninkovic M. Assessment of the patency of microvascular anastomoses using microscope-integrated near-infrared angiography: a preliminary study. *Microsurgery*. (2009) 29:509–14. doi: 10.1002/micr.20645
19. Hardwicke JT, Osmani O, Skillman JM. Detection of perforators using smartphone thermal imaging. *Plast Reconstruct Surg*. (2016) 137:39–41. doi: 10.1097/PRS.0000000000001849
20. Draijer M, Hondebrink E, van Leeuwen T, Steenbergen W. Review of laser speckle contrast techniques for visualizing tissue perfusion. *Lasers Med Sci*. (2009) 24:639–51. doi: 10.1007/s10103-008-0626-3
21. Briers D, Duncan DD, Hirst E, Kirkpatrick SJ, Larsson M, Steenbergen W, et al. Laser speckle contrast imaging: theoretical and practical limitations. *J Biomed Opt*. (2013) 18:066018. doi: 10.1117/1.JBO.18.6.066018
22. Rother U, Gerken ALH, Karampinis I, Klumpp M, Regus S, Meyer A, et al. Dosing of indocyanine green for intraoperative laser fluorescence angiography in kidney transplantation. *Microcirculation*. (2017) 24:1–7. doi: 10.1111/micc.12392
23. Casey WJ III, Connolly KA, Nanda A, Rebecca AM, Perdikis G, Smith AA. Indocyanine green laser angiography improves deep inferior epigastric perforator flap outcomes following abdominal suction lipectomy. *Plast Reconstruct Surg*. (2015) 135:491e-7e. doi: 10.1097/PRS.0000000000000964
24. Swanson E. Comparison of limited and full dissection abdominoplasty using laser fluorescence imaging to evaluate perfusion of the abdominal skin. *Plast Reconstruct Surg*. (2015) 136:31e-43e. doi: 10.1097/PRS.0000000000001376
25. Preidl RH, Schlittenbauer T, Weber M, Neukam FW, Wehrhan F. Assessment of free microvascular flap perfusion by intraoperative fluorescence angiography in craniomaxillofacial surgery. *J Cranio-Max-Facial Surg*. (2015) 43:643–8. doi: 10.1016/j.jcms.2015.03.013
26. Holm C, Mayr M, Hofter E, Ninkovic M. Perfusion zones of the DIEP flap revisited: a clinical study. *Plast Reconstruct Surg*. (2006) 117:37–43. doi: 10.1097/01.prs.0000185867.84172.c0
27. Hartrampf CR, Scheflan M, Black PW. Breast reconstruction with a transverse abdominal island flap. *Plast Reconstruct Surg*. (1982) 69:216–25. doi: 10.1097/00006534-198202000-00007
28. Gould DJ, Mehrara BJ, Neligan P, Cheng MH, Patel KM. Lymph node transplantation for the treatment of lymphedema. *J Surg Oncol*. (2018) 118:736–42. doi: 10.1002/jso.25180
29. Valente SA, Al-Hilli Z, Radford DM, Yanda C, Tu C, Grobmyer SR. Near infrared fluorescent lymph node mapping with indocyanine green in breast cancer patients: a prospective trial. *J Am Coll Surg*. (2018) 228:672-678. doi: 10.1016/j.jamcollsurg.2018.12.001
30. Granzow J, Li AI, Caton A, Boyd JB. Free flap survival following failure of the vascular pedicle. *Ann Plast Surg*. (2015) 75:44–8. doi: 10.1097/SAP.0000000000000136
31. Yoon AP, Jones NF. Critical time for neovascularization/angiogenesis to allow free flap survival after delayed postoperative anastomotic compromise without surgical intervention: a review of the literature. *Microsurgery*. (2016) 36:604–12. doi: 10.1002/micr.30082
32. Newman MI, Samson MC. The application of laser-assisted indocyanine green fluorescent dye angiography in microsurgical breast reconstruction. *J Reconstruct Microsurg*. (2009) 25:21–6. doi: 10.1055/s-0028-1090617
33. Hope-Ross M, Yannuzzi LA, Gragoudas ES, Guyer DR, Slakter JS, Sorenson JA, et al. Adverse reactions due to indocyanine green. *Ophthalmology*. (1994) 101:529–33. doi: 10.1016/S0161-6420(94)31303-0
34. Munabi NC, Olorunnipa OB, Goltsman D, Rohde CH, Ascherman JA. The ability of intra-operative perfusion mapping with laser-assisted indocyanine green angiography to predict mastectomy flap necrosis in breast reconstruction: a prospective trial. *J Plast Reconstruct Aesthet Surg*. (2014) 67:449–55. doi: 10.1016/j.bjps.2013.12.040
35. Karinja SJ, Lee BT. Advances in flap monitoring and impact of enhanced recovery protocols. *J Surg Onco*. (2018) 118:758–67. doi: 10.1002/jso.25179

Conflict of Interest Statement: IL received once-only an honorary for a lecture by Novadaq but has no conflict of interest concerning this study.

The remaining authors declare that the research was conducted in the absence of any commercial or financial relationships that could be construed as a potential conflict of interest.

frontiers in Oncology

SYSTEMATIC REVIEW
published: 02 July 2019
doi: 10.3389/fonc.2019.00585

Robotic-Assisted Sentinel Lymph Node Mapping With Indocyanine Green in Pelvic Malignancies: A Systematic Review and Meta-Analysis

Yuqing Wu[1,2†], Jibo Jing[1,2†], Jinfeng Wang[3†], Bin Xu[1], Mulong Du[4,5*] and Ming Chen[1*]*

[1] Department of Urology, Affiliated Zhongda Hospital of Southeast University, Nanjing, China, [2] Surgical Research Center, School of Medicine, Institute of Urology, Southeast University, Nanjing, China, [3] Department of Urology, School of Medicine, Affiliated Yancheng Hospital, Southeast University, Yancheng, China, [4] Jiangsu Key Laboratory of Cancer Biomarkers, Department of Environmental Genomics, Prevention and Treatment, Collaborative Innovation Center for Cancer Personalized Medicine, Nanjing Medical University, Nanjing, China, [5] Department of Biostatistics, Center for Global Health, School of Public Health, Nanjing Medical University, Nanjing, China

Objective: Newer technologies such as near-infrared (NIR) imaging of the fluorescent dye indocyanine green (ICG) and daVinci Xi Surgical System have become promising tools for sentinel lymph node (SLN) mapping. This meta-analysis was conducted to comprehensively evaluate the diagnostic value of SLN in assessing lymph nodal metastasis in pelvic malignancies, using ICG with NIR imaging in robotic-assisted surgery.

Materials and Methods: A literature search was conducted using PubMed for studies in English before April 2019. The detection rate, sensitivity of SLN detection of metastatic disease, and factors associated with successful mapping (sample size, study design, mean age, mean body mass index, type of cancer) were synthesized for meta-analysis.

Results: A total of 17 articles including 1,059 patients were finally included. The reported detection rates of SLN ranged from 76 to 100%, with a pooled average rate of 95% (95% CI: 93–97; 17 studies). The sensitivity of SLN detection of metastatic disease ranged from 50 to 100% and the pooled sensitivity was 86% (95% CI: 75–94; 8 studies). There were no complications related to ICG administration reported.

Conclusions: NIR imaging system using ICG in robotic-assisted surgery is a feasible and safe method for SLN mapping. Due to its promising performance, it is considered to be an alternative to a complete pelvic lymph node dissection.

Keywords: indocyanine green, robotic surgery, pelvic, sentinel lymph node, cancer

OPEN ACCESS

Edited by:
Evgenii Belykh, Barrow Neurological Institute (BNI), United States

Reviewed by:
James Mankin, Dignity Health, United States
Yasuhiro Fujisawa, University of Tsukuba, Japan

***Correspondence:**
Bin Xu
njxb1982@126.com
Mulong Du
drdumulong@njmu.edu.cn
Ming Chen
mingchenseu@126.com

† These authors have contributed equally to this work

Specialty section:
This article was submitted to Cancer Imaging and Image-directed Interventions, a section of the journal Frontiers in Oncology

Received: *28 May 2019*
Accepted: *17 June 2019*
Published: *02 July 2019*

Citation:
Wu Y, Jing J, Wang J, Xu B, Du M and Chen M (2019) Robotic-Assisted Sentinel Lymph Node Mapping With Indocyanine Green in Pelvic Malignancies: A Systematic Review and Meta-Analysis. Front. Oncol. 9:585. doi: 10.3389/fonc.2019.00585

INTRODUCTION

Pelvic lymphadenectomy (PLND), which remains the most accurate procedure for the detection of lymph node metastasis (LNM) in malignant pelvic tumors, plays an important role in surgical management of endometrial and prostate cancers (1, 2). However, the data from a prospective study suggests that lymphadenectomy is associated with the increasing operative time, blood loss and risk for surgical morbidity (e.g., blood vessel and nerve damage, lymphedema, and lymphocyst formation) (3, 4). Thus, novel nodal assessment techniques should be developed to improve the accuracy of LNM detection with lower surgical morbidity.

The biopsy of SLN which is defined as the first node to receive the drainage from the primary tumor, has been described by Canbanas in 1977 (5). The utility of SLN mapping can avoid the unnecessary LND when the SLN turns out to be negative (6). The different methods used in SLN mapping, such as blue dye, technetium, and ICG with NIR imaging have been investigated, among which ICG has been used clinically for over two decades with an excellent safety profile (7). Also, as one of four fluorochromes approved by US Food and Drug Administration, ICG may be of significant use in pelvic surgery due to its properties (8).

The NIR fluorescence imaging system in daVinci Xi Surgical System (Intuitive Surgical, Sunnyvale, CA, USA) with Firefly technology provides intraoperative ICG near-infrared fluorescence, especially for ICG at low concentrations in lymphatic mapping. While the high concentrations of ICG can be seen directly in green in color on a background of a grayscale image. Moreover, it brings surgeons great convenience to control the scope completely which the infrared and visible light systems are built in.

Nevertheless, although ICG-NIF imaging in SLN detection appears to be superior, there are few studies of meta-analysis on SLN mapping outcomes, and most of them focused on specific one or two types of cancer, especially on endometrial and cervical cancer. Thus, we performed this meta-analysis to evaluate the detection rates and sensitivity of SLN mapping in malignant pelvic tumors, including endometrial, cervical, bladder and prostate cancers.

MATERIALS AND METHODS

Search Strategy

The literature search was conducted on PubMed, only English language studies before April 2019 included. The search terms used are as follow: (robotic OR robot) AND (indocyanine green OR ICG) AND lymph. In addition, the references of included studies were reviewed as supplement.

Inclusion and Exclusion Criteria

Studies were included with the following inclusion criteria: (1) At least 10 patients diagnosed with pelvic malignancies; (2) Robotic-assisted surgery as the surgical approach; (3) Pelvic with or without other lymph node dissection as reference standard; (4) Pathological examination was taken, including hematoxylin-eosin (H&E) staining, immunohistochemistry (IHC) or ultrastaging; (5) ICG was used for SLN mapping; (6) Reported detection rate of SLN. The studies published as reviews and case reports were excluded.

Study Quality Assessment

The quality of enrolled studies was assessed using the QUADAS-2 (Quality Assessment of Diagnostic Accuracy Studies-2) (9) tool by two reviewers independently. The items are shown in the Appendix Table 1 **(Supplementary Material)**.

Data Extraction

The following items were collected from each article: (1) authors; (2) year of publication; (3) sample size; (4) study design; (5) type of cancer; (6) injection site; (7) reference standard; (8) pathology assessment; (9) mean patient age and body mass index (BMI); (10) available outcome data.

The overall detection rate was estimated as the proportion of patients with at least 1 SLN identified among all the patients going though PLND. When assessing sensitivity and specificity, the patients who failed in SLN mapping were excluded, and sensitivity is defined as the percentage of patients with positive SLN divided by all patients with positive lymph nodes. The specificity is defined as the percentage of patients with negative SLN divided by all patients with negative lymph nodes. Studies in which the calculation of sensitivity was based on the number of removed node packets but not on the patients were excluded during assessment.

Statistical Analysis

The Stata 15.0 and meta-disc were used to conduct all data analysis. The overall detection rate was calculated using a random-effects model under meta-analysis. The sensitivity of detection rates of SLN was evaluated using summary receiver operating characteristic curve (SROC). The I^2 index was used to detect the heterogeneity among the studies. The Funnel plots, Egger's regression intercepts were used for the evaluation of publication bias. The univariate meta-regression was applied for the association of SLN detection rate and study characteristics, including sample size, study design, mean age, mean BMI, and type of cancer.

RESULTS

Characteristics of Enrolled Studies

Of the 78 abstracts screened, 17 articles including 1,059 patients with pelvic malignancies were eligible for inclusion as demonstrated in **Figure 1**. The sample size of each study ranged from 10 to 197. SNL was evaluated for endometrial cancer in 9 articles, cervical cancer in 1, prostate cancer in 3 and bladder cancer in 1, with the other 3 articles dedicated in both endometrial cancer, and cervical cancer (10–26) (**Table 1**).

An overall mean of 3.5 SLNs was removed per patient (13 studies). All the studies conducted PLND with or without para-aortic LND, and the mean non-SLNs identified per person was 17.9 (5 studies). The mean age of 1,059 patients was 62 years (17

Abbreviations: SLN, sentinel lymph node; ICG, indocyanine green; NIR, near-infrared; LND, lymph node dissection; PLND, pelvic lymphadenectomy; CI, confidence interval.

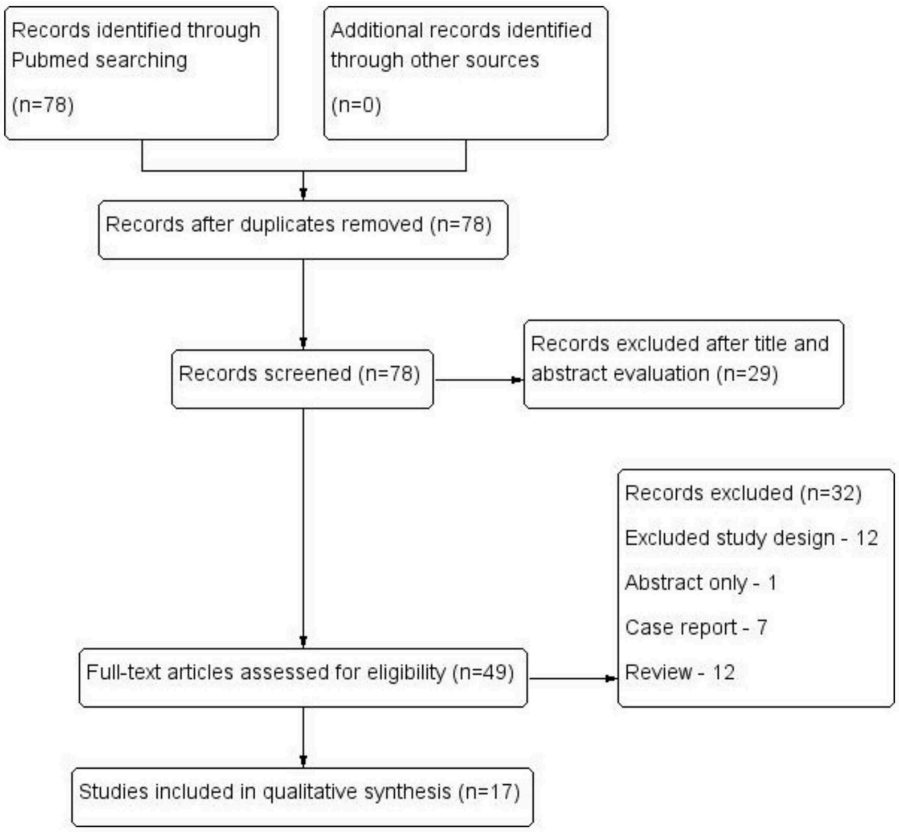

FIGURE 1 | Flow diagram of studies identified, included, and excluded.

studies) and mean BMI was 31.1 kg/m^2 (13 studies) (**Table 1**). No complications, among all 17 articles, were described related to ICG administration.

Data Analysis for the Detection Rate and Diagnostic Accuracy of SLN Mapping

The detection rates of SLN ranged from 76 to 100%, with a pooled average of 95% (95% CI: 93–97; 17 studies) with heterogeneity $I^2 = 56.2\%$ (**Figure 2**). The funnel plot of the pooled overall SLN detection rate is shown in **Figure 3**. The Egger's regression intercept was −4.65 ($p = 0.000$).

Sensitivity of SLN mapping ranged from 50 to 100%. The pooled sensitivity of SLN detection of metastatic disease was 86% (95% CI: 75–94; 8 studies) (**Figure 4**). The funnel plot of the pooled sensitivity is shown in **Figure 3**. The Egger's regression intercept was found out to be −4.85 ($p = 0.003$). The pooled specificity and diagnostic odds ratio were 1.00 (95%Cl: 0.99–1.00) and 381.92 (95%Cl: 111.19–1311.85). The combined positive likelihood ratio and negative likelihood ratio were 67.31 (95% CI: 25.08–180.64) and 0.25 (95% CI: 0.15–0.40), respectively, [Appendix Figure 1 (**Supplementary Material**)]. According to SROC curve, AUC is found to be 0.9971 which is close to 1, showing the high value of ICG in diagnosing lymph node metastasis in pelvic malignancies (**Figure 5**).

Test of Heterogeneity

Due to the heterogeneity I^2 was found to be 56.2% in detection rate a sub-group analysis was conducted to find the reasons for the observed heterogeneity. Univariate meta-regression of SLN detection rate and study characteristics showed that study size, study method, mean patient age, mean patient BMI, and type of cancer were not significantly associated with detection rates (**Table 2**).

DISCUSSION

SLN mapping has been the standard of care for breast cancer and melanoma for a long time (27) and achieved success in many other types of cancer. During the process of assessing the value of SLN mapping, detection rate is taken into consideration in the very first place. Most of meta-analyses on diagnostic efficacy of SLN mapping were focused on uterine cancers, and to our knowledge, this is the first meta-analysis of that in pelvic malignancies.

It should be mentioned that in these previous meta-analyses, studies using both robotic-assisted system and indocyanine green fluorescence tracer in the meantime have not been analyzed statistically before. Compared with prior meta-analyses which studied on tracers including blue dye, ICG and/or 99mTc in

TABLE 1 | Characteristics of included studies.

Author, year	Sample size	Study design	Type of cancer	Injection site	Mean age	Mean BMI (kg/m^2)	Mean number of SLNs detected	Mean number of non-SLNs removed	Reference standard	Pathology assessment	Detection rate	Sensitivity
Rossi et al. (10)	20	Prospective	Endometrium/ cervix	Cervical	61	31	4.5	23.5	Pelvic and para-aortic LND by guidelines	NR	85.0%	50.0%
Holloway et al. (25)	35	Retrospective	Endometrium	Cervical	63	33.1	NR	NR	Complete pelvic and common-iliac LND, aortic LND in high-grade EC	H&E, IHC, ultrastaging	100.0%	90.0%
Manny et al. (11)	50	Prospective	Prostate	Prostate	66	NR	NR	NR	Extended PLND	NR	76.0%	100.0%
Jewell et al. (12)	197	Retrospective	Endometrium/ cervix	Cervical	60	30.2	3	NR	Pelvic and para-aortic LND by guidelines	H&E, ultrastaging	95.0%	NR
Manny et al. (26)	10	Prospective	Bladder	Bladder	71	NR	NR	NR	Complete pelvic and peri-aortic LND	NR	90.0%	100.0%
Sinno et al. (13)	38	Prospective	Endometrium	Cervical	65	31.1	4.8	NR	Complete pelvic and para-aortic LND if preoperative grade 3 endometrioid, serous, clear cell, or carcinosarcoma	H&E, ultrastaging	92.1%	100.0%
Paley et al. (14)	123	Prospective	Endometrium	Cervical	63	32	3	NR	Pelvic and peri-aortic LND if high risk	H&E	96.7%	100.0%
Ehrisman et al. (15)	20	Retrospective	Endometrium	Cervical	67	32.3	2	22	Complete pelvic LND or Memorial Sloan Kettering algorithm	H&E	90.0%	NR
Chennamsetty et al. (16)	20	Prospective	Prostate	Prostate	64	NR	5	NR	Extended PLND	NR	100.0%	NR
Beavis et al. (17)	31	Retrospective	Cervix	Cervical	43	26.5	4	14	Complete pelvic LND, para-aortic LND at surgeon discretion	H&E, IHC, ultrastaging	100.0%	100.0%
Hagen et al. (18)	108	Prospective	Endometrium	Cervical	66	27.5	NR	NR	Surgeon-discretion LND or Memorial Sloan Kettering algorithm	H&E, ultrastaging	96.0%	NR
Erikssion et al. (19)	56	Retrospective	Endometrium/ cervix	Cervical	62	30.6	3	NR	Memorial Sloan Kettering algorithm	H&E, ultrastaging	95.0%	NR
Mendivil et al. (20)	87	Retrospective	Endometrium	Cervical	62	32.9	2	NR	Complete pelvic LND, para-aortic LND if at high risk	H&E	96.5%	NR
Harke et al. (21)	59	Prospective	Prostate	Prostate	64	NR	9	15	Extended PLND	NR	94.9%	78.0%
Rajanbabu and Agarwal (22)	69	Prospective	Endometrium	Cervical	60	27.9	5	NR	Pelvic and para-aortic LND by guidelines	H&E	95.7%	70.0%
Renz et al. (23)	90	Retrospective	Endometrium	Cervical	61	31	2	19	Complete pelvic LND, para-aortic LND by guidelines	H&E	88.0%	83.3%
Rozenholc et al. (24)	46	Prospective	Endometrium	Cervical	64	45	2.4	NR	Pelvic and para-aortic LND by guidelines	H&E, ultrastaging	89.1%	100.0%

NR, not reported; H&E, hematoxylin-eosin; IHC, immunohistochemistry; BMI, body mass index; LND, lymph node dissection; PLND, pelvic lymph node dissection.

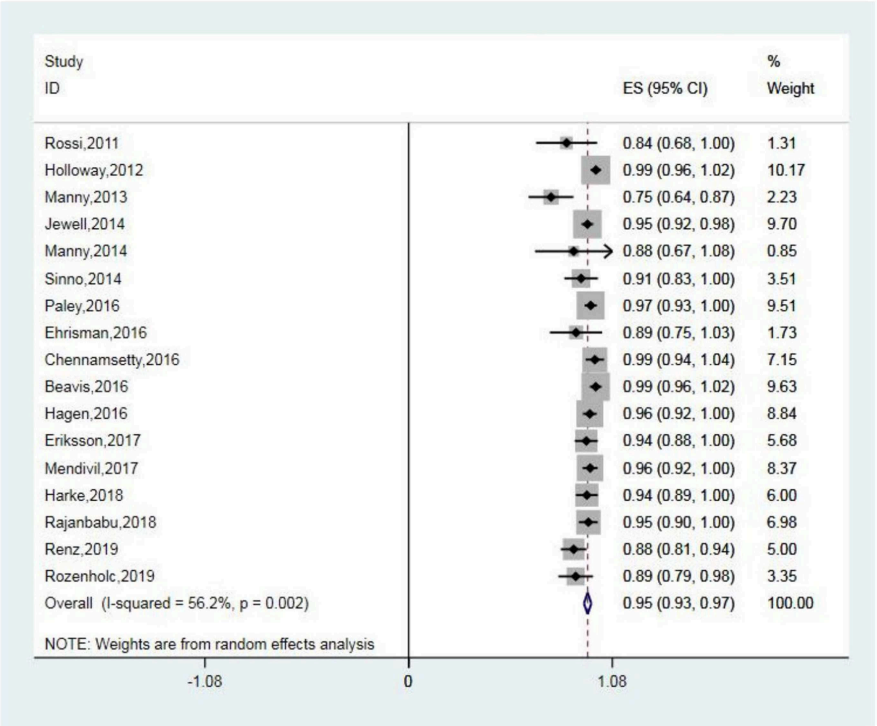

FIGURE 2 | Forest plot of pooled overall detection rate and 95% CI in SLN mapping. CI, confidence interval; SLN, sentinel lymph node.

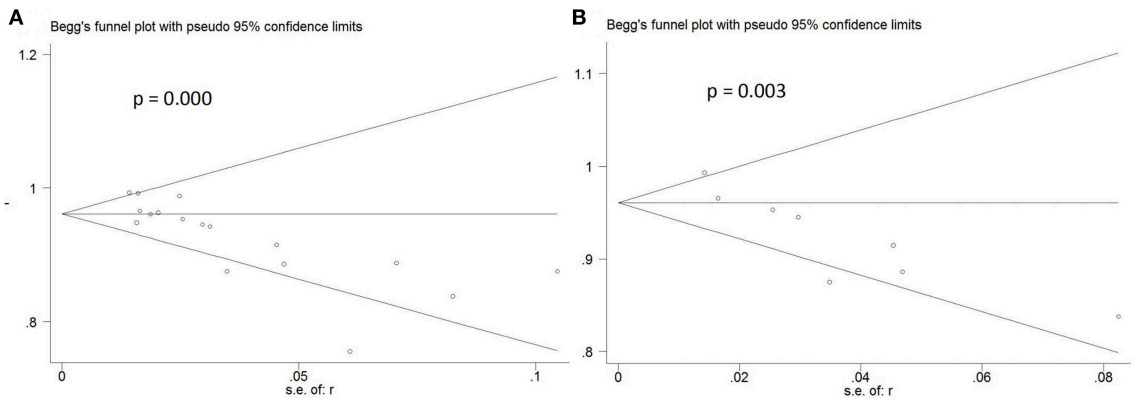

FIGURE 3 | Funnel plot of pooled detection rate and sensitivity. **(A)** Funnel plot of pooled overall detection rate. **(B)** Funnel plot of pooled sensitivity.

endometrial cancer (28–30), this meta-analysis with only ICG used as tracer shows higher detection rate of SLN mapping with detection rate of 95% (95% CI: 93–97), and in study of Lin et al. the detection rate was only 76% (95%: 71–81) with blue dye alone. In their study, detection rates were of 93 and 86% in ICG and 99mTc combined with blue dye, respectively, (28). Moreover, in study of Smith et al. detection rates were found higher of 90.3% in ICG vs. 81% in blue dye (31).

Hybrid image-guided surgery technologies are increasingly gaining interest, such as combined radio- and fluorescence-guidance. In study of KleinJan et al. use of the hybrid tracer ICG-99mTc-nancolloid was evaluated and the detection rate was over 95% (32). Compared with the conventional radioguided SN approach, the additional cost of ICG-99mTc-nancolloid is negligible (33), and use of ICG involves only minor additional costs (34). According to prior studies, the use of ICG also brings several advantages, such as fewer adverse effects, less pain, and quicker transcutaneous real-time visualization (35, 36).

In this meta-analysis, the pooled sensitivity of SLN detection of lymph node metastasis was 86% (95% CI: 75–94). In study of SLN mapping by Rossi et al. there were only two patients with positive lymph nodes in those who had successful mapping

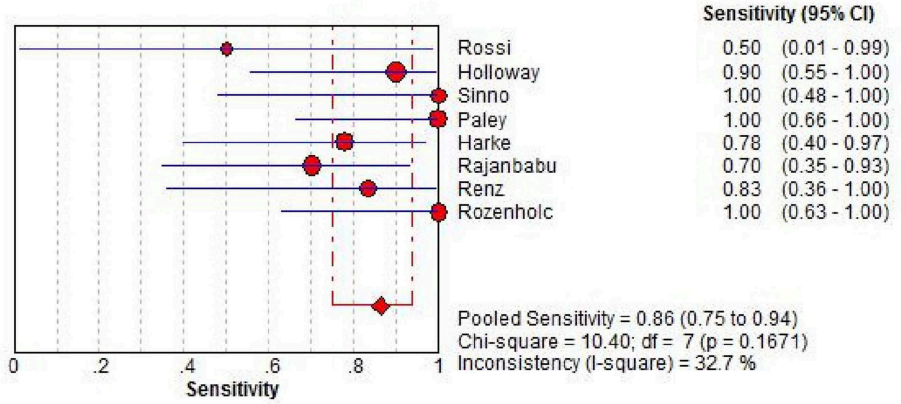

FIGURE 4 | Forest plot of pooled sensitivity of SLN detection and 95% CI in SLN mapping. CI, confidence interval; SLN, sentinel lymph node.

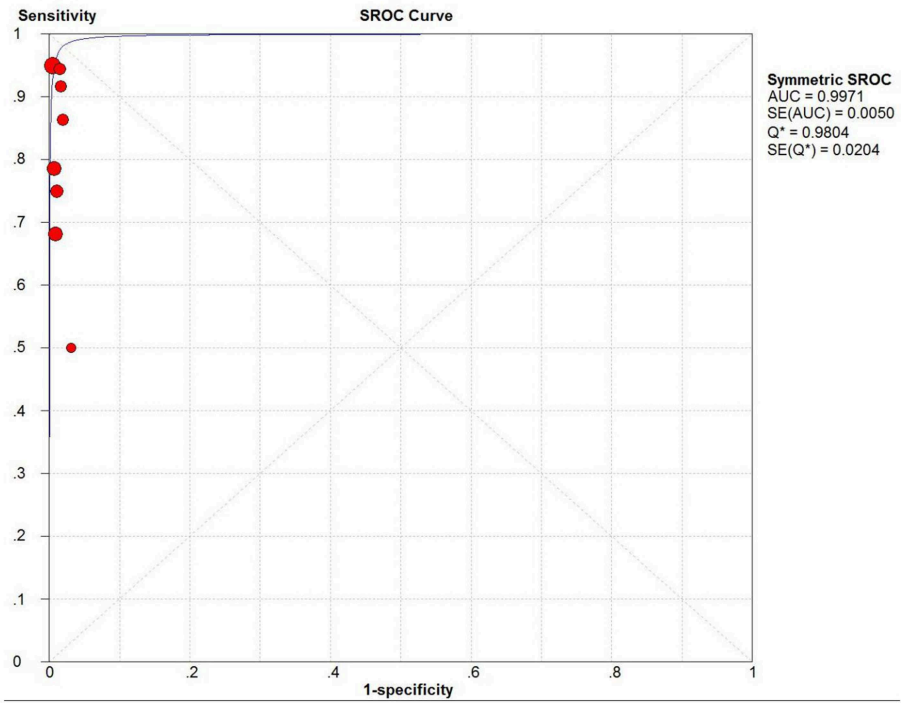

FIGURE 5 | SROC curve. AUC, area under SROC curve; Q* indicates the point at which sensitivity = specificity.

and one of them showed negative SLN, leading to the lowest sensitivity of 50% (10). In other 10 studies with available data, 6 out of them showed the sensitivities of 100% and all of them were over 70% [(11–14, 17, 21–24, 26); **Table 1**]. In previous meta-analyses by Lin et al. and Smith et al. in uterine cancers with several tracers included, sensitivities were found 91% (95% Cl: 87–95) and 96% (95% CI: 93–98), respectively (28, 31).

In pilot meta-analysis, robotic-assisted surgery demonstrated higher detection rates than other modalities. The pilot study conducted by Lin et al. showed that robotic-assisted surgery led to 86% detection rate, when laparoscopy and laparotomy got that of 82 and 77%, respectively, in patients with endometrial cancer (28). In the literature before, a higher BMI is linked to lower detection rate of the SLN (13). However, in the study by Rozenholc et al. there was no difference in the detection rate between surgeries that were robotic (mean BMI 44.6) and laparoscopic (mean BMI 29.4) (24). Moreover, when compared with open surgery, robotic-assisted surgery results in fewer blood transfusions and leads to a slightly shorter hospital stay (37).

However, due to the limitations of robotic-assisted surgery, such as higher costs and the lack of haptic feedback, the current

TABLE 2 | Univariate meta-regression of SLN detection rate and study characteristics.

Characteristics	Detection rate% (95% CI)	*P*-value
Sample size		
<60	0.94 (0.91–0.97)	0.891
≥60	0.95 (0.93–0.97)	
Study design		
Prospective	0.94 (0.91–0.97)	0.456
Retrospective	0.96 (0.93–0.99)	
Mean age		
<63	0.95 (0.92–0.98)	0.985
≥63	0.95 (0.92–0.98)	
Mean BMI		
<32 kg/m^2	0.95 (0.92–0.97)	0.475
≥32 kg/m^2	0.96 (0.94–0.99)	
Type of cancer		
Uterus	0.95 (0.94–0.97)	0.561
Urology	0.91 (0.82–1.00)	

CI, confidence interval; SLN, sentinel lymph node; BMI, body mass index.

robotic technology has not become the standard technique of minimally invasive surgery worldwide. A single robotic surgical system can set a hospital back by about $2 million, and that's just to get started. Some of the instruments are disposable and need to be continually replaced. Additionally, the systems require regular maintenance at rates that can exceed $100,000, which limits the number of hospitals that can buy Da Vinci system (https://www.drugwatch.com/davinci-surgery/).

In a survey of complications of ICG angiography in Japan, the results indicated that indocyanine green was as safe as fluorescein (38), which was reported only 0.05% frequency of severe adverse reactions, such as circulatory shock, bronchospasm, laryngospasm, cardiac arrest, myocardial infarction, and tonic seizure (39).

Our systematic review and meta-analysis has limitations as follow. First, we only included English studies, which may lead to a potential language bias. Second, we didn't have individual patient data, such as age, BMI and so on. The results presented in this study were based on unadjusted estimates. Third, the number of studies included is not sufficient enough so that some subgroup analyses cannot be conducted, and it may contribute to a publication bias.

In conclusion, the NIR imaging system in robotic-assisted surgery with ICG dye is quite easy to master, and the present results confirmed that SLN mapping using ICG alone is a reliable and safe approach that performs well diagnostically when assessing lymph nodal metastasis in pelvic malignancies. Although it is considered to be an alternative to a complete pelvic lymph node dissection, studies with larger patient samples are still needed, especially in urology cancers like prostate and bladder cancer.

DATA AVAILABILITY

All datasets generated for this study are included in the manuscript/**Supplementary Files**.

AUTHOR CONTRIBUTIONS

YW and BX: contributed conception and design of the study. JJ: organized the database. YW and JW: performed the statistical analysis. YW and JJ: wrote the first draft of the manuscript. JW, BX, MD, and MC: wrote sections of the manuscript. All authors contributed to manuscript revision, read, and approved the submitted version.

FUNDING

This study was funded by National Natural Science Foundation of China (Nos. 81872089, 81370849, 81672551, 81300472, 81070592, 81202268, 81202034), Natural Science Foundation of Jiangsu Province (BK20161434).

SUPPLEMENTARY MATERIAL

The Supplementary Material for this article can be found online at: https://www.frontiersin.org/articles/10.3389/fonc.2019.00585/full#supplementary-material

REFERENCES

1. Colombo N, Preti E, Landoni F, Carinelli S, Colombo A, Marini C, et al. Endometrial cancer: ESMO clinical practice guidelines for diagnosis, treatment and follow-up. *Ann Oncol.* (2013) 24:33–8. doi: 10.1093/annonc/mdt353
2. Briganti A, Blute ML, Eastham JH, Graefen M, Heidenreich A, Karnes JR, et al. Pelvic lymph node dissection in prostate cancer. *Eur Urol.* (2009) 55:1251–65. doi: 10.1016/j.eururo.2009.03.012
3. Dowdy SC, Borah BJ, Bakkum-Gamez JN, Weaver AL, McGree ME, Haas LR, et al. Prospective assessment of survival, morbidity, and cost associated with lymphadenectomy in low-risk endometrial cancer. *Gynecol Oncol.* (2012) 127:5–10. doi: 10.1016/j.ygyno.2012.06.035
4. Rousseau B, Doucet L, Perrouin Verbe MA, Papin G, Erauso A, Joulin V, et al. Comparison of the morbidity between limited and extended pelvic lymphadenectomy during laparoscopic radical prostatectomy. *Progres En Urologie J.* (2014) 24:114–20. doi: 10.1016/j.purol.2013.07.018
5. Cabanas RM. An approach for the treatment of penile carcinoma. *Cancer.* (1977) 39:456–66. doi: 10.1002/1097-0142(197702)39:2<456::AID-CNCR2820390214>3.0.CO;2-I
6. Wawroschek F, Vogt H, Weckermann D, Harzmann R. The sentinel lymph node concept in prostate cancer-first results of gamma probe-guided sentinel lymph node identifcation. *Eur Urol.* (1999) 36:595–600. doi: 10.1159/000020054
7. How J, Gotlieb WH, Press JZ, Abitbol J, Pelmus M, Ferenczy A, et al. Comparing indocyanine green, technetium, and blue dye for sentinel lymph node mapping in endometrial cancer. *Gynecol Oncol.* (2015) 137:436–42. doi: 10.1016/j.ygyno.2015.04.004
8. Van den Berg NS, van Leeuwen FW, van der Poel HG. Fluorescence guidance in urologic surgery. *Curr Opin Urol.* (2012) 22:109–20. doi: 10.1097/MOU.0b013e3283501869
9. Whiting PF, Rutjes AW, Westwood ME, Mallett S, Deeks JJ, Reitsma JB, et al. QUADAS-2 Group. QUADAS-2: a revised tool for the quality assessment of diagnostic accuracy studies. *Ann Intern*

Med. (2011) 155:529–36. doi: 10.7326/0003-4819-155-8-201110180-00009
10. Rossi EC, Ivanova A, Boggess JF. Robotically assisted fluorescence-guided lymph node mapping with ICG for gynecologic malignancies: a feasibility study. *Gynecol Oncol.* (2012) 124:78–82. doi: 10.1016/j.ygyno.2011.09.025
11. Manny TB, Hemal AK. Fluorescence-enhanced robotic radical cystectomy using unconjugated indocyanine green for pelvic lymphangiography, tumor marking, and mesenteric angiography: the initial clinical experience. *Urology.* (2014) 83:824–30. doi: 10.1016/j.urology.2013.11.042
12. Jewell EL, Huang JJ, Abu-Rustum NR, Gardner JR, Brown CL, Sonoda Y, et al. Detection of sentinel lymph nodes in minimally invasive surgery using indocyanine green and near-infrared fluorescence imaging for uterine and cervical malignancies. *Gynecol Oncol.* (2014) 133:274–7. doi: 10.1016/j.ygyno.2014.02.028
13. Sinno AK, Fader AN, Roche KL, Giuntoli RL, Tanner EJ. A comparison of colorimetric versus fluorometric sentinel lymph node mapping during robotic surgery for endometrial cancer. *Gynecol Oncol.* (2014) 134:281–6. doi: 10.1016/j.ygyno.2014.05.022
14. Paley PJ, Veljovich DS, Press JZ, Isacson C, Pizer E, Shah C. A prospective investigation of fluorescence imaging to detect sentinel lymph nodes at robotic-assisted endometrial cancer staging. *Am J Obstet Gynecol.* (2016) 215:117 e1–7. doi: 10.1016/j.ajog.2015.12.046
15. Ehrisman J, Secord AA, Berchuck A, Lee PS, Di Santo N, Lopez-Acevedo M, et al. Performance of sentinel lymph node biopsy in high-risk endometrial cancer. *Gynecol Oncol.* (2016) 17:69–71. doi: 10.1016/j.gore.2016.04.002
16. Chennamsetty A, Zhumkhawala A, Tobis SB, Ruel N, Lau CS, Yamzon J, et al. Lymph node fluorescence during robot-assisted radical prostatectomy with indocyanine green: prospective dosing analysis. *Clin Genitourin Cancer.* (2017) 15:e529–34. doi: 10.1016/j.clgc.2016.10.014
17. Beavis AL, Salazar-Marioni S, Sinno AK, Stone RL, Fader AN, Santillan-Gomez A, et al. Sentinel lymph node detection rates using indocyanine green in women with early-stage cervical cancer. *Gynecol Oncol.* (2016) 143:302–6. doi: 10.1016/j.ygyno.2016.08.236
18. Hagen B, Valla M, Aune G, Ravlo M, Abusland AB, Araya E, et al. Indocyanine green fluorescence imaging of lymph nodes during robotic-assisted laparoscopic operation for endometrial cancer. a prospective validation study using a sentinel lymph node surgical algorithm. *Gynecol Oncol.* (2016) 143:479–83. doi: 10.1016/j.ygyno.2016.10.029
19. Eriksson AG, Beavis A, Soslow RA, Zhou Q, Abu-Rustum NR, Gardner GJ, et al. A comparison of the detection of sentinel lymph nodes using indocyanine green and near-infrared fluorescence imaging versus blue dye during robotic surgery in uterine cancer. *Int J Gynecol Cancer.* (2017) 27:743–7. doi: 10.1097/IGC.0000000000000959
20. Mendivil AA, Abaid LN, Brown, JV III, Mori KM, Beck TL, Epstein HD, et al. The safety and feasibility of minimally invasive sentinel lymph node staging using indocyanine green in the management of endometrial cancer. *Eur J Obstet Gynecol Reprod Biol.* (2018) 224:29–32. doi: 10.1016/j.ejogrb.2018.02.027
21. Harke NN, Godes M, Wagner C, Addali M, Fangmeyer B, Urbanova K, et al. Fluorescence-supported lymphography and extended pelvic lymph node dissection in robot-assisted radical prostatectomy: a prospective, randomized trial. *World J Urol.* (2018) 36:1817–23. doi: 10.1007/s00345-018-2330-7
22. Rajanbabu A, Agarwal R. A prospective evaluation of the sentinel node mapping algorithm in endometrial cancer and correlation of its performance against endometrial cancer risk subtypes. *Eur J Obstet Gynecol Reprod Biol.* (2018) 224:77–80. doi: 10.1016/j.ejogrb.2018.03.017
23. Renz M, Marjon N, Devereaux K, Raghavan S, Folkins AK, Karam A. Immediate intraoperative sentinel lymph node analysis by frozen section is predictive of lymph node metastasis in endometrial cancer. *J Robo Surgery.* (2019). doi: 10.1007/s11701-019-00928-z
24. Rozenholc A, Samouelian V, Warkus T, Gauthier P, Provencher D, Sauthier P, et al. Green versus blue: Randomized controlled trial comparing indocyanine green with methylene blue for sentinel lymph node detection in endometrial cancer. *Gynecol Oncol.* (2019) 153:500–4. doi: 10.1016/j.ygyno.2019.03.103
25. Holloway RW, Bravo RA, Rakowski JA, James JA, Jeppson CN, Ingersoll SB, et al. Detection of sentinel lymph nodes in patients with endometrial cancer undergoing robotic-assisted staging: a comparison of colorimetric and fluorescence imaging. *Gynecol Oncol.* (2012) 126:25–9. doi: 10.1016/j.ygyno.2012.04.009
26. Manny TB, Patel M, Hemal AK. Fluorescence-enhanced robotic radical prostatectomy using real-time lymphangiography and tissue marking with percutaneous injection of unconjugated indocyanine green: the initial clinical experience in 50 patients. *Eur Urol.* (2014) 65:1162–8. doi: 10.1016/j.eururo.2013.11.017
27. Mansel RE, Fallowfield L, Kissin M, Goyal A, Newcombe RG, Dixon JM, et al. Randomized multicenter trial of sentinel node biopsy versus standard axillary treatment in operable breast cancer: the ALMANAC Trial. *J Natl Cancer Inst.* (2006) 98:599–609. doi: 10.1093/jnci/djj158
28. Lin H, Ding Z, Kota VG, Zhang X, Zhou J. Sentinel lymph node mapping in endometrial cancer: a systematic review and meta-analysis. *Oncotarget.* (2017) 28:46601–10. doi: 10.18632/oncotarget.16662
29. Kang S, Yoo HJ, Hwang JH, Lim M-C, Seo SS, Park S-Y. Sentinel lymph node biopsy in endometrial cancer: meta-analysis of 26 studies. *Gynecol Oncol.* (2011) 123:522–7. doi: 10.1016/j.ygyno.2011.08.034
30. Ansari M, Rad MAG, Hassanzadeh M, Gholami H, Yousefi Z, Dabbagh VR, et al. Sentinel node biopsy in endometrial cancer: systematic review and meta-analysis of the literature. *Eur J Gynaecol Oncol.* (2013) 34:387–401.
31. Smith BAJ, Fader AN, Tanner EJ. Sentinel lymph node assessment in endometrial cancer: a systematic review and meta-analysis. *Am J Obstet Gynecol.* (2017) 216:459–76. doi: 10.1016/j.ajog.2016.11.1033
32. KleinJan GH, van Werkhoven E, van den Berg NS, Karakullukcu MB, Zijlmans H, van der Hage JA, et al. The best of both worlds: a hybrid approach for optimal pre- and intraoperative identification of sentinel lymph nodes. *Eur J Nucl Med Mol Imaging.* (2018) 45L1915–25. doi: 10.1007/s00259-018-4028-x
33. Lee CM, Park S, Park SH, Jung SW, Choe JW, Sul JY, et al. Sentinel node mapping using a fluorescent dye and visible light during laparoscopic gastrectomy for early gastric cancer: result of a prospective study from a single institute. *Ann Surg.* (2017) 265:766. doi: 10.1097/SLA.0000000000001739
34. Berg NS, Van D, Brouwer OR, Klop WMC, Bari K, Zuur CLI, et al. Concomitant radio- and fluorescence-guided sentinel lymph node biopsy in squamous cell carcinoma of the oral cavity using ICG-(99m)Tc-nanocolloid. *Eur J Nucl Med Mol Imaging.* (2012) 39:1128–36. doi: 10.1007/s00259-012-2129-5
35. Zhang X, Li Y, Zhou Y, Mao F, Lin Y, Guan J, et al. Diagnostic performance of indocyanine green-guided sentinel lymph node biopsy in breast cancer: a meta-analysis. *PLoS ONE.* (2016) 11:e0155597. doi: 10.1371/journal.pone.0155597
36. Ruscito I, Gasparri ML, Braicu EI, Bellati F, Raio L, Sehouli J, et al. Sentinel node mapping in cervical and endometrial cancer: indocyanine green versus other conventional dyes—a meta-analysis. *Ann Surg Oncol.* (2016) 23:3749–56. doi: 10.1245/s10434-016-5236-x
37. Aboumarzouk OM, Bondad J, Ahmed K, Khan MS, Kynaston HG, Dasgupta P, et al. Robotic versus open radical cystectomy for bladder cancer in adults. *Cochrane Database System Rev Ltd.* (2015) 2015: CD011903. doi: 10.1002/14651858.CD011903
38. Obana, A., Miki, T., Hayashi, K., Takeda, M., Kawamura, A., Mutoh, T., et al. Survey of complications of indocyanine green angiography in Japan. *Am J Ophthalmol.* (1994) 118:749–53. doi: 10.1016/S0002-9394(14)72554-1
39. Yannuzzi LA, Rohrer KT, Tindel LJ, Sobel RS, Costanza MA, Shields W, et al. Fluorescein angiography complication survey. *Ophthalmology.* (1986) 93:611–7. doi: 10.1016/S0161-6420(86)33697-2

Conflict of Interest Statement: The authors declare that the research was conducted in the absence of any commercial or financial relationships that could be construed as a potential conflict of interest.

frontiers in Oncology

TECHNOLOGY REPORT
published: 03 July 2019
doi: 10.3389/fonc.2019.00554

Progress in Confocal Laser Endomicroscopy for Neurosurgery and Technical Nuances for Brain Tumor Imaging With Fluorescein

*Evgenii Belykh[1,2], Eric J. Miller[1], Alessandro Carotenuto[1], Arpan A. Patel[1], Claudio Cavallo[1], Nikolay L. Martirosyan[1], Debbie R. Healey[3], Vadim A. Byvaltsev[2], Adrienne C. Scheck[3†], Michael T. Lawton[1], Jennifer M. Eschbacher[4], Peter Nakaji[1] and Mark C. Preul[1]**

[1] Department of Neurosurgery, Barrow Neurological Institute, St. Joseph's Hospital and Medical Center, Phoenix, AZ, United States, [2] Department of Neurosurgery, Irkutsk State Medical University, Irkutsk, Russia, [3] Department of Neuro-Oncology Research, Barrow Neurological Institute, St. Joseph's Hospital and Medical Center, Phoenix, AZ, United States, [4] Department of Neuropathology, Barrow Neurological Institute, St. Joseph's Hospital and Medical Center, Phoenix, AZ, United States

OPEN ACCESS

Edited by:
Sebastian Cerdan,
Spanish National Research Council (CSIC), Spain

Reviewed by:
Samata Kakkad,
Johns Hopkins University, United States
Ana Paula Candiota,
Centre for Biomedical Network Research (CIBER), Spain

***Correspondence:**
Mark C. Preul
neuropub@barrowneuro.org

†Present Address:
Adrienne C. Scheck,
Institute of Molecular Medicine, Phoenix Children's Research Institute, Phoenix Children's Hospital, Phoenix, AZ, United States

Specialty section:
This article was submitted to Cancer Imaging and Image-directed Interventions, a section of the journal Frontiers in Oncology

Received: 07 January 2019
Accepted: 06 June 2019
Published: 03 July 2019

Citation:
Belykh E, Miller EJ, Carotenuto A, Patel AA, Cavallo C, Martirosyan NL, Healey DR, Byvaltsev VA, Scheck AC, Lawton MT, Eschbacher JM, Nakaji P and Preul MC (2019) Progress in Confocal Laser Endomicroscopy for Neurosurgery and Technical Nuances for Brain Tumor Imaging With Fluorescein. Front. Oncol. 9:554. doi: 10.3389/fonc.2019.00554

Background: Previous studies showed that confocal laser endomicroscopy (CLE) images of brain tumors acquired by a first-generation (Gen1) CLE system using fluorescein sodium (FNa) contrast yielded a diagnostic accuracy similar to frozen surgical sections and histologic analysis. We investigated performance improvements of a second-generation (Gen2) CLE system designed specifically for neurosurgical use.

Methods: Rodent glioma models were used for *in vivo* and rapid *ex vivo* CLE imaging. FNa and 5-aminolevulinic acid were used as contrast agents. Gen1 and Gen2 CLE images were compared to distinguish cytoarchitectural features of tumor mass and margin and surrounding and normal brain regions. We assessed imaging parameters (gain, laser power, brightness, scanning speed, imaging depth, and Z-stack [3D image acquisition]) and evaluated optimal values for better neurosurgical imaging performance with Gen2.

Results: Efficacy of Gen1 and Gen2 was similar in identifying normal brain tissue, vasculature, and tumor cells in masses or at margins. Gen2 had smaller field of view, but higher image resolution, and sharper, clearer images. Other advantages of the Gen2 were auto-brightness correction, user interface, image metadata handling, and image transfer. CLE imaging with FNa allowed identification of nuclear and cytoplasmic contours in tumor cells. Injection of higher dosages of FNa (20 and 40 mg/kg vs. 0.1–8 mg/kg) resulted in better image clarity and structural identification. When used with 5-aminolevulinic acid, CLE was not able to detect individual glioma cells labeled with protoporphyrin IX, but overall fluorescence intensity was higher ($p < 0.01$) than in the normal hemisphere. Gen2 Z-stack imaging allowed a unique 3D image volume presentation through the focal depth.

Conclusion: Compared with Gen1, advantages of Gen2 CLE included a more responsive and intuitive user interface, collection of metadata with each image, automatic

Z-stack imaging, sharper images, and a sterile sheath. Shortcomings of Gen2 were a slightly slower maximal imaging speed and smaller field of view. Optimal Gen2 imaging parameters to visualize brain tumor cytoarchitecture with FNa as a fluorescent contrast were defined to aid further neurosurgical clinical *in vivo* and rapid *ex vivo* use. Further validation of the Gen2 CLE for microscopic visualization and diagnosis of brain tumors is ongoing.

Keywords: 5-ALA, brain tumor, confocal, endomicroscopy, fluorescein, fluorescence, glioma, imaging

INTRODUCTION

Intraoperative diagnosis in neurosurgery has traditionally relied on frozen and formalin-fixed, paraffin-embedded section analysis of biopsied tissue samples. Although this technique is considered to be the "gold standard" for establishing a histopathologic diagnosis, it entails a number of significant limitations. These limitations include the time required for transferring, processing, and interpreting the tissue (1); the presence of artifacts and sampling errors (1–3); as well as the differences present when comparing frozen and permanent sections that may lead to misdiagnosis (1, 4). Rapid intraoperative diagnosis has become possible with refinement and miniaturization of the research-type confocal laser scanning microscope into a handheld confocal laser endomicroscopy (CLE) system (5, 6). Combined with appropriate fluorescent stains or labels, CLE provides an imaging technique for real-time intraoperative *in vivo* visualization of histopathologic features of suspected tumor and healthy tissues.

Previous studies using a CLE system originally designed for nonneurosurgical use (e.g., gastrointestinal luminal examination) showed that a blinded review of CLE imaging of brain gliomas and meningiomas by a neuropathologist yielded an accuracy rate of 92.9%, similar to those previously reported with frozen-section analysis (4, 7–9). In terms of analysis of tumor margins, CLE has not yet been thoroughly investigated in human brain tumors; however, in experimental animals, CLE was able to visualize border regions of glioma (10, 11). In humans, CLE was shown to increase accuracy of delineation of margins in early gastric cancer (12). CLE may be used as a diagnostic tool, but it also has the potential to aid in optimizing surgical resection of brain tumors, including maximal safe tumor resection, which is a strategy that would be expected to have a positive impact on long-term neurosurgical patient survival, especially among patients with invasive malignant tumors (10, 13–18).

Various CLE devices have been developed; the proximal scanning fiber optic CLE (19, 20) and distal scanning CLE (1) systems are the most advanced in terms of potential for becoming adopted into wide clinical use (21). Importantly, each CLE system has different pre-set, mostly unchangeable, imaging parameters that may result in unique and different diagnostic performance; therefore, meticulous independent assessment of each microscope system is required. We previously evaluated the diagnostic performance and other application parameters of a handheld scanning CLE system (Optiscan Pty., Ltd., Mulgrave, Australia), referred to in this report as the first-generation (Gen1) device and designed for gastrointestinal use. This system has recently served as the imaging platform for development of a second-generation (Gen2) CLE system specifically aimed at neurosurgery.

The Gen2 CLE device was designed to function specifically for intraoperative application in neurosurgery and to integrate with the robotic operating microscope visualization platform for neurosurgery (22). The goals for this device in neurosurgery are ultimately to increase the positive yield of biopsies and to serve as a tool to microscopically explore, in portable and rapid fashion, for tumor cells beyond the obvious margin of infiltrating tumors, such as cells in and around the surgical resection bed, or to define suspected tumor invasion within eloquent cortex. Previous studies regarding *in vivo* investigation of distal scanning CLE in human and animal model brain tumors were conducted using the Gen1 device, which had several performance characteristics that limited its use in neurosurgery. These included lack of a sterile attachment cover sheath for the imaging probe, a different design and function of the handheld probe that was not optimal for the neurosurgeon's usual hand position, and nonoptimal imaging processing and display (1, 7, 10, 23–25). Therefore, this study was designed to assess performance of the Gen2 CLE system, assess differences in image quality or diagnostic accuracy of the Gen1 and Gen2 systems, and provide additional information on the probe conformation, and optimal handling practices that were designed to produce high-quality confocal intraoperative images for neurosurgery on-the-fly.

Gen1 and Gen2 functionalities were compared using fluorescein sodium (FNa), the primary fluorophore with which they were designed to work, and with 5-aminolevulinic acid (5-ALA)-induced protoporphyrin IX (PpIX) fluorescence. Although the fluorescence signal from PpIX is not within the optimal detection range for these CLE systems, 5-ALA is also of interest in brain tumor surgery, especially for use in invasive gliomas, and our preliminary studies suggested that the PpIX signal may be faintly detected with the CLE systems. This study aimed to expand on the current literature related to CLE for brain tumor imaging, including further investigating the relationship between FNa dosage and image quality, the ability to differentiate cellular structures with CLE and FNa, and the

Abbreviations: 5-ALA, 5-aminolevulinic acid; AF, acriflavine; AO, acridine orange; CLE, confocal laser endomicroscopy; DAPI, 4′6-diamidino-2-phenylindole; FNa, fluorescein sodium; FOV, field of view; Gen1, first generation; Gen2, second generation; H&E, hematoxylin and eosin; LSM, laser scanning microscopy; PpIX, protoporphyrin.

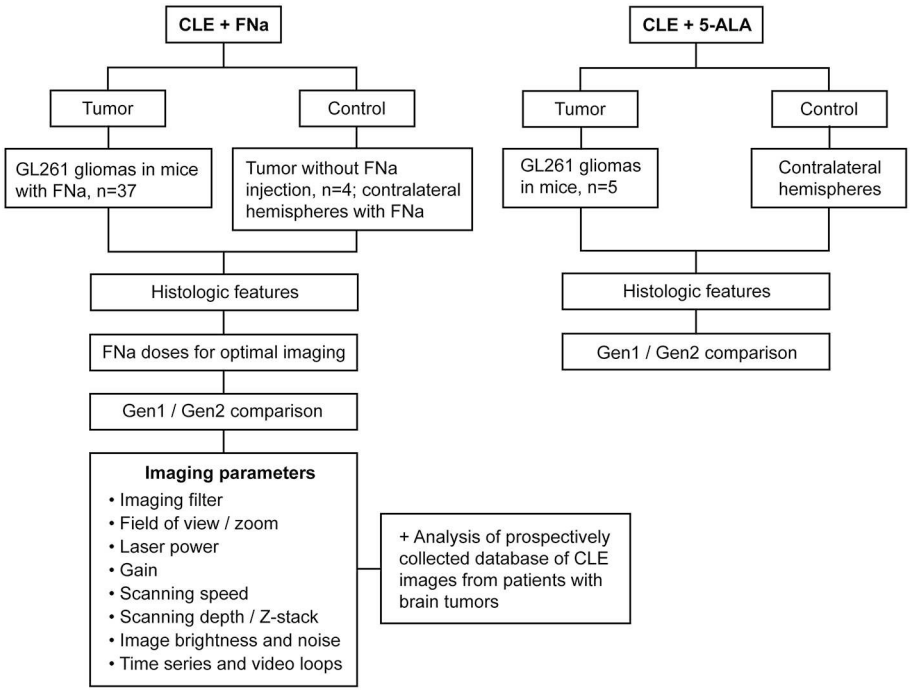

FIGURE 1 | Study design flowchart. CLE, confocal laser endomicroscope; FNa, fluorescein sodium; Gen1, generation 1; Gen2, generation 2; 5-ALA, 5-aminolevulinic acid. Used with permission from Barrow Neurological Institute, Phoenix, Arizona.

utility of both generations of CLE with 5-ALA for the detection of tumor tissue.

METHODS

Ethics Approval

All animal investigations were performed according to the guidelines outlined by the National Institutes of Health *Guide for the Care and Use of Laboratory Animals* and with approval from the Institutional Animal Care and Use Committee of the Barrow Neurological Institute and St. Joseph's Hospital and Medical Center, Phoenix, Arizona. Animals were maintained under approved veterinary care in the vivarium of St. Joseph's Hospital and Medical Center.

Patient tissues used for this project were acquired from a prospective ongoing brain tumor clinical study. Patients with preoperative diagnoses of brain masses requiring surgical removal and for whom the decision was to use the assistance of fluorescence surgical guidance with FNa were prospectively enrolled. Extra biopsies from tumor tissue that would have to be safely removed during the normal course of the surgery were used. De-identified samples were placed on a wet telfa and submitted for immediate *ex vivo* CLE analysis. The same samples were then sent for routine histologic processing and review by a neuropathologist. All patients gave voluntary informed consent as a part of a study protocol approved by the Institutional Review Board of the Barrow Neurological Institute, St. Joseph's Hospital and Medical Center, Phoenix, Arizona. A flowchart describing the study protocol is presented in **Figure 1**.

Mouse Glioma Model

Ten-week-old female B6(Cg)-Tyr^{c-2J}/J mice (albino variant C57BL/6J, The Jackson Laboratory, Bar Harbor, ME) weighing 20 g (mean) were anesthetized and placed in a small-animal stereotactic head frame. Glioma models were created according to the previously described protocol (26). Briefly, 2 μL of GL261-luc tumor cells (1.45×10^7 cells/mL; Division of Cancer Treatment and Diagnosis, National Cancer Institute, Bethesda, MD) were infused 2 mm lateral and 2 mm posterior to bregma at a depth of 2.5 mm from the brain surface through a bur hole at the targeted brain location after the syringe needle was withdrawn 0.5 mm to a total depth of 2 mm below the surface of the brain to create a 0.5 mm pocket for the cells. The 2-μL cell suspension was infused using a controllable microinjector (0.67 μL/min × 3 min with the needle in place for 2 min afterward) (10).

A week prior to surgery, the mice were injected with 15 μg/kg of luciferin (PerkinElmer, Waltham, MA), anesthetized using isoflurane in a 37°C chamber, and glioma growth was confirmed using bioluminescence detection in the IVIS Spectrum *in vivo* imaging system (PerkinElmer). Bioluminescence images were examined and quantified in Living Image 4.3 software (PerkinElmer) (26).

Drug Administration

CLE imaging was performed within the first 2 h after FNa injection. We used escalating dosages of FNa: 0.1 ($n = 4$), 1 ($n = 7$), 2 ($n = 2$), 5 ($n = 7$), 8 ($n = 5$), 20 ($n = 6$), and 40 ($n = 6$) mg/kg. These doses approximate the doses of FNa that can be used in humans, as we have previously used 5 mg/kg IV in clinical

study. The 5-ALA (Clinical grade, NIOPIK, Moscow, Russia) was injected intraperitoneally 2 h before surgery at a dose of 5 mg dissolved in 200 μL of normal saline ($n = 5$). Chosen dosages are similar to those previously used in comparable animal studies with 5-ALA (27–29) and FNa (10, 30–32) and are similar to or higher than those used in humans to compensate for differences in metabolism.

Intraoperative CLE Imaging

After confirmation of tumor growth and size, on average 21 days after implantation, the mice underwent craniectomy. The animals were anesthetized, and their oxygen supply and body temperature were maintained throughout the procedure. An operating microscope (Pentero 900, Carl Zeiss AG, Oberkochen, Germany) was used to visualize the exposed surfaces of both cerebral hemispheres. Brain tumors were identified macroscopically in the right hemisphere of all mice, and the CLE scanning was performed. After imaging was performed, the anesthetized animals were euthanized according to protocol guidelines. Brains were extracted, sliced fresh coronally (1 mm in thickness) through the center of the tumor in a mouse brain slicer matrix (ZIVIC Instruments, Pittsburgh, PA), and imaged rapidly *ex vivo* with CLE again.

Gen1 (Optiscan 5.1, Carl Zeiss AG) and Gen2 CLE (Convivo, Carl Zeiss AG) were compared in terms of intraoperative fluorescence visualization using either FNa ($n = 37$), 5-ALA ($n = 5$), or no dye injection ($n = 4$ control). This comparison was completed initially using the Gen1 CLE in a designated area. Once adequate images were acquired, the Gen2 CLE was used to take further images at the same area. All scanning was performed *in vivo* and then *ex vivo* within the 2-h interval alternating Gen1 and Gen2 confocal microscopes targeting multiple regions of interest. Further testing included evaluation of Gen2 imaging with different available filters (green bandpass or green longpass and red longpass) and with various gain, laser intensity, brightness, acquisition speed, and zoom settings controlling for image quality and noise levels. In 2 animals, topical acridine orange was used for nuclear staining as described elsewhere (10).

Operating Microscopy Fluorescence Imaging

Gross FNa and protoporphyrin IX fluorescence in the brain was assessed with the operating microscopes equipped with the Yellow 560 and Blue 400 filters, respectively (Pentero 900 and Kinevo 900, Carl Zeiss AG).

Benchtop Confocal Laser Microscopy

The benchtop laser scanning microscopy (LSM) imaging (LSM 710 DUO, Carl Zeiss AG) was performed with a C-Apochromat 40×/1.20 W Korr M27 objective. Sliced fresh brain samples were imaged on 35-mm glass-bottom Petri dishes (MatTek, Ashland, MA). For PpIX visualization, the excitation and detection wavelengths used were 405 and 635–750 nm, respectively. Additionally, topical staining was performed with acridine orange (AO), acriflavine (AF), Hoechst 33342 (ThermoFisher Scientific, Waltham, MA), and 4′6-diamidino-2-phenylindole (DAPI). The excitation wavelength was 488 nm for AO, AF, or FNa, and 405 nm for DAPI and Hoechst; and the detection wavelength was 493–625 nm for AO, AF, or FNa, and 410–585 nm for DAPI and Hoechst. Examples of imaging modalities are shown in **Supplemental Figure 1**.

Image Assessment and Statistical Analysis

Imaging analysis and cell and nuclei size measurements were performed in FIJI software (open source software) (33). Statistical analysis was completed in Excel (Microsoft, Redmond, WA). Quality of CLE imaging was scored independently by 5 respondents trained in interpreting CLE images as bad (1), average (2), good (3), or excellent (4), based on the ability to visualize characteristic GL261 tumor histologic characteristics and patterns. Grading was performed based on the assessment of the best confocal images from each animal. Student *t*-test, Mann-Whitney U test, and Kruskal-Wallis analysis of variance (ANOVA) with significance set at $p < 0.05$ were used to establish whether differences were statistically significant, and the Spearman *R*-value was used to assess correlations.

RESULTS

Assessment of CLE Imaging Parameters

To produce clear images, several parameters were controlled in both systems: gain, brightness level, laser power, scanning speed, imaging depth, and Z-stack thickness (Gen2 only). Because many imaging parameters were similar between Gen1 and Gen2 CLE, salient results are presented of observations for Gen2, and are specifically mentioned when differences were observed with Gen1. Gen2 imaging parameters are summarized in **Table 1**.

Field of View

The field of view (FOV) of the Gen2 (475 × 267 μm, 1980 pixels/line) was half the size of the Gen1 image (475 × 475 μm, 1080 pixels/line). Gen2 images were essentially twice the resolution. Gen2 images appear sharper, but upon magnification, they have a grainier appearance compared with Gen1 images. This graininess is due to the raw image TIFF format of Gen2 images, compared to compressed and smoothing JPG formatting of Gen1 images.

Gain

Specimens with grossly average fluorescence brightness produced clear CLE images on Gen2 gain setting of 2,400 (**Table 1**). When the brain tumor appeared grossly intensely bright yellow, lowering the gain allowed imaging with a CLE brightness level within a 20–60% range, which produced optimal quality images without oversaturated pixels and with low noise. However, in specimens with low gross fluorescence intensity, the quality and resolution of CLE images did not improve regardless of the changes in imaging parameters. The increased level of black noise with an increase of brightness level and laser power only lowered image quality in dark images.

Scanning Speed

Scanning speed was critically important for time series imaging. Comparison of imaging speed recorded for both generations of

TABLE 1 | Confocal laser endomicroscopy (CLE) imaging parameters.

Parameter	Gen1	Gen2	Comment
Laser wavelength	488 nm	488 nm	Always the same
Laser power	Range: 0–1,000 μm	Range: 0–100%	Percentages correlate to the actual laser power. Fifty percent results in ∼500 μm laser power; 10%, 100 μm. TIFF image metadata records actual laser power in microwatts, which may be used for further analysis
Depth	Displayed only relative value showing the arrow position on the horizontal scale; not recorded	Range: −50 to 200 μm; also displayed as relative value on the vertical scale	Knowledge of depth position is crucial for understanding of imaging location and adjustment of depth on the fly for optimal image quality. Awareness of depth helps to avoid low-quality images by not imaging too deep into a tissue. The axial imaging resolution is <4.5 μm
Brightness	Range: 0–100%	Range: 0–100%	The brightness is the built-in adjustable proprietary setting parameter used during CLE imaging. Unlike the gain and laser power, the brightness could be adjusted during the imaging. Knowledge of brightness is important to assess the true brightness of the fluorescent staining
Gain	Options: low, normal, high, max	Range: 1,800–3,000	Gain is an important parameter to consider, as it influences the image brightness. We mostly used the system with gain at the midlevel (normal or 2,400). We found it useful to increase or reduce the gain for imaging of very bright and dark fluorescent samples respectively
Speed (resolution)	Options: 1024 × 1024 μm 475 × 475 μm	Options: 1,080 540 270 135	Numbers represent the number of horizontal lines that the laser travels during image acquisition. Acquisition speed 1,080 results in a 1,920 × 1,080 pixel scan at <0.5 μm axial resolution; speed 540 results in a 1,920 × 540 pixel scan, etc. Scan area–aspect ratio is kept the same as 16 × 9. Most images are taken in the "high-image quality low-speed" mode (1,080). Higher speeds (270 and 135) are rarely used and do not produce diagnostic-quality images. Higher speed might be adjusted for an initial search of an optimal imaging position to quickly verify the presence of fluorescence. At the settings window, the user can select two speeds that would be rapidly available to choose from on the primary screen
Zoom	Constant; changes not available	Options: 1× 1.4× 2×	Zoom is usually set at 1× giving a FOV size of 475 × 267 μm (width/height). This FOV size is 2× less compared to Gen1 system; however, with FNa Gen2 provides subjectively similar appearing images to Gen1. We almost never use 2× zoom with FNa, as we feel that a larger field of view is favorable for imaging with FNa. However, 1.4× and 2× zoom are useful with other fluorophores like acridine orange or acriflavine, which bind to the cellular structures and therefore result in more contrasted images
Filter	Options: Green fluoro (505–585 nm) Green-red fluoro (505–750 nm)	Options: Gray filter Green bandpass Green longpass Red filter	Our experience with FNa is that the green longpass filter provides overall brighter images than the green bandpass filter. The red bandpass filter may be unnecessary for the work with FNa. We were not able to detect reliable PpIX (peak emission∼630 nm) signal with red or green longpass filters, which we believe is mostly due to the absence of an appropriate excitation laser source (405 nm for PpIX)
Z-stack	Not available	Start position offset, range: −50 to +47 μm End position offset, range: −47 to +50 μm Step size, range: 3–20 μm	We find that for most cases +10 μm and −15 μm offsets (total depth 25 μm) with the minimally possible (3 μm) Z-step are the most optimal for 3-dimensional reconstruction of the Z-stack
Time stamp	Not available on the image	2017-04-14_12-39-20-34	Time stamp is critical for matching individual CLE images with the time on microscope and navigation in order to track the optical biopsy location

FOV, field of view; FNa, fluorescein sodium; Gen1, first generation; Gen2, second generation; PpIX, protoporphyrin; TIFF, tagged image file format.

CLEs is presented in **Supplemental Table 1**. Scanning speed of Gen1 was 0.8 s per frame for a 1,024 × 512-pixel image and 1.2 s per frame for a 1,024 × 1,024-pixel image. The scanning speed for Gen2 ranged from 1.3 s per frame for the highest quality imaging to 0.27 s per frame for the lowest quality imaging. Despite the difference in scanning speed, all images were recorded and stored as 1,920 × 1,080-pixel red, green, blue (RGB) TIFF files.

Scanning Depth

Optimal imaging depth with FNa was within the first few microns in depth from the surface of the imaged tissue. The CLE Z-stack function (Gen2 only) resulted in a series of images, the first of which was a central image from the current position on the Z axis. A series of images were acquired starting from the surface and ending at the deepest position, with the Z-step image thickness selection to be between 3 and 20 μm. The interval of the scanning depth could be chosen by selecting two offset positions. The maximal range was obtained at the offsets from −47 to +50, which resulted in a 97-μm thick Z-stack. The number of images per Z-stack was limited by the size of the Z-step (3 μm minimum), which for the 97-μm Z-stack resulted in 35 images. Higher ranges are not practically necessary, so the

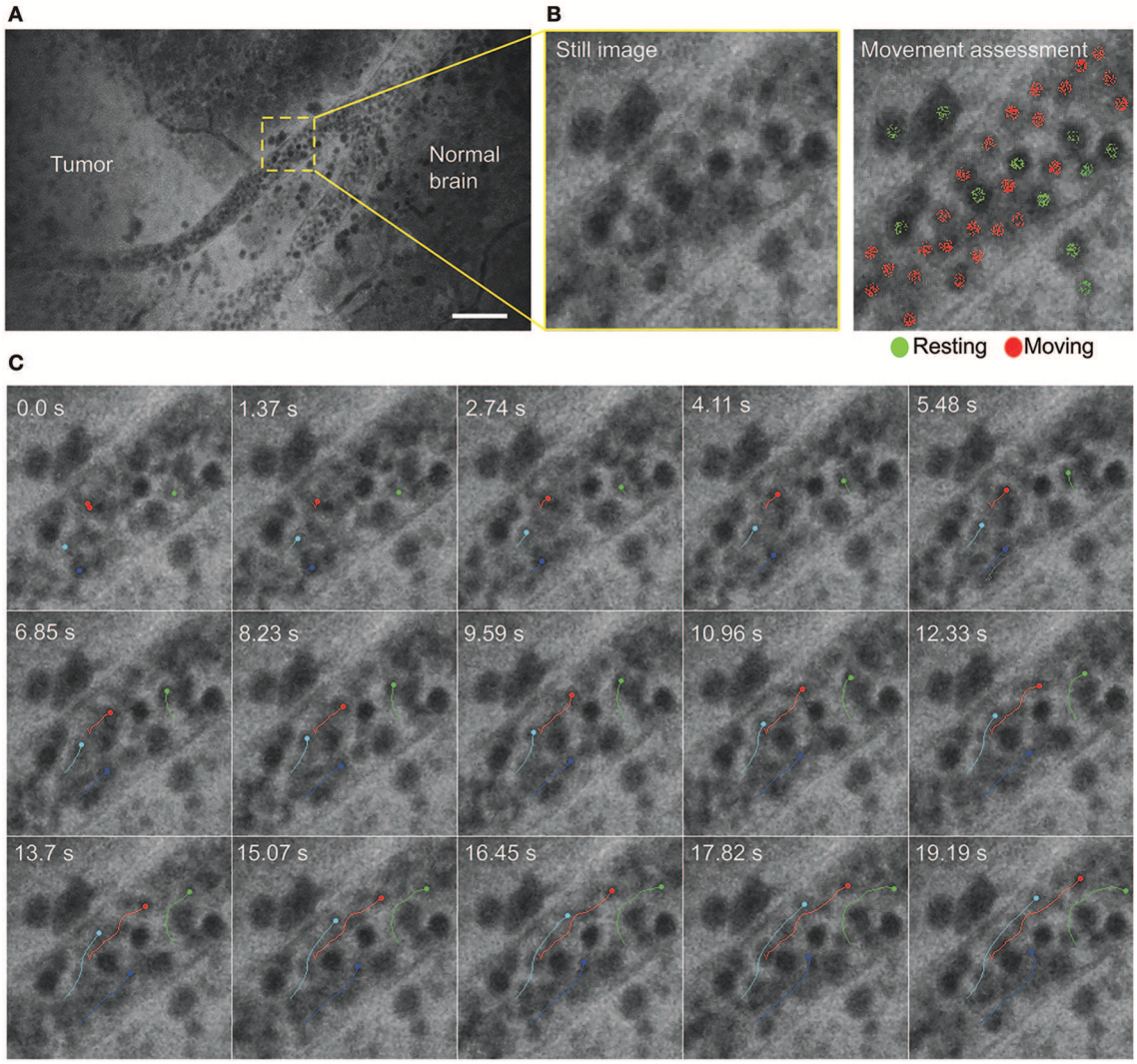

FIGURE 2 | Time series imaging to differentiate stationary and mobile cells using a Gen2 confocal laser endomicroscope. **(A)** Single frame from time-lapse image. **(B)** Enlarged view of the vessel (left) and same image with moving cells labeled red and stationary cells labeled green (right). **(C)** Tracking of the selected cells shows intravascular movement of individual blood cells. Particle tracking performed in FIJI. Scale bar is 50 μm. Used with permission from Barrow Neurological Institute, Phoenix, Arizona.

available CLE Z-stack range is sufficient for use in human brain tissue. Previous experiments have shown that the maximal depth of brain tumor tissue (using FNa) for interrogation through Z-stack imaging is 36 μm in animal and 28 μm in human brain tissue (34).

Probe movements during image capturing produced similar artifacts in both Gen1 and Gen2 CLEs. Although free-hand probe positioning yielded informative images, remaining in a steady position for an optimal Z-stack was difficult for image series acquisition. A semiflexible surgical probe holder was used to decrease movement artifacts.

Time Series and Video Loops

Time series imaging (in both Gen1 and Gen2) allowed observation of blood cell movements inside and outside the vessels (**Figure 2**). Tumor cell movements seen with tissue squeezing under the CLE lens were also noted during *in vivo* imaging, which is not possible on fixed tissues. In contrast to the static hematoxylin and eosin (H&E) slide, *in vivo* CLE revealed histologic features of the living tumor cells and their behavior. In animal gliomas, many tumor cells were actually moving independently, squeezing and pushing each other, captivated by the stream of oozing blood. Such tumor cells were flowing independent of the tumor core, especially when they were at the border of the brain slice. When imaged *in vivo*, GL261 glioma cells were actually not tightly connected to one another, as they appear on H&E slides, although they grow as relatively solid tumors. CLE imaging revealed pericellular spaces that were filled with FNa, which were not previously visualized well on H&E stained slides.

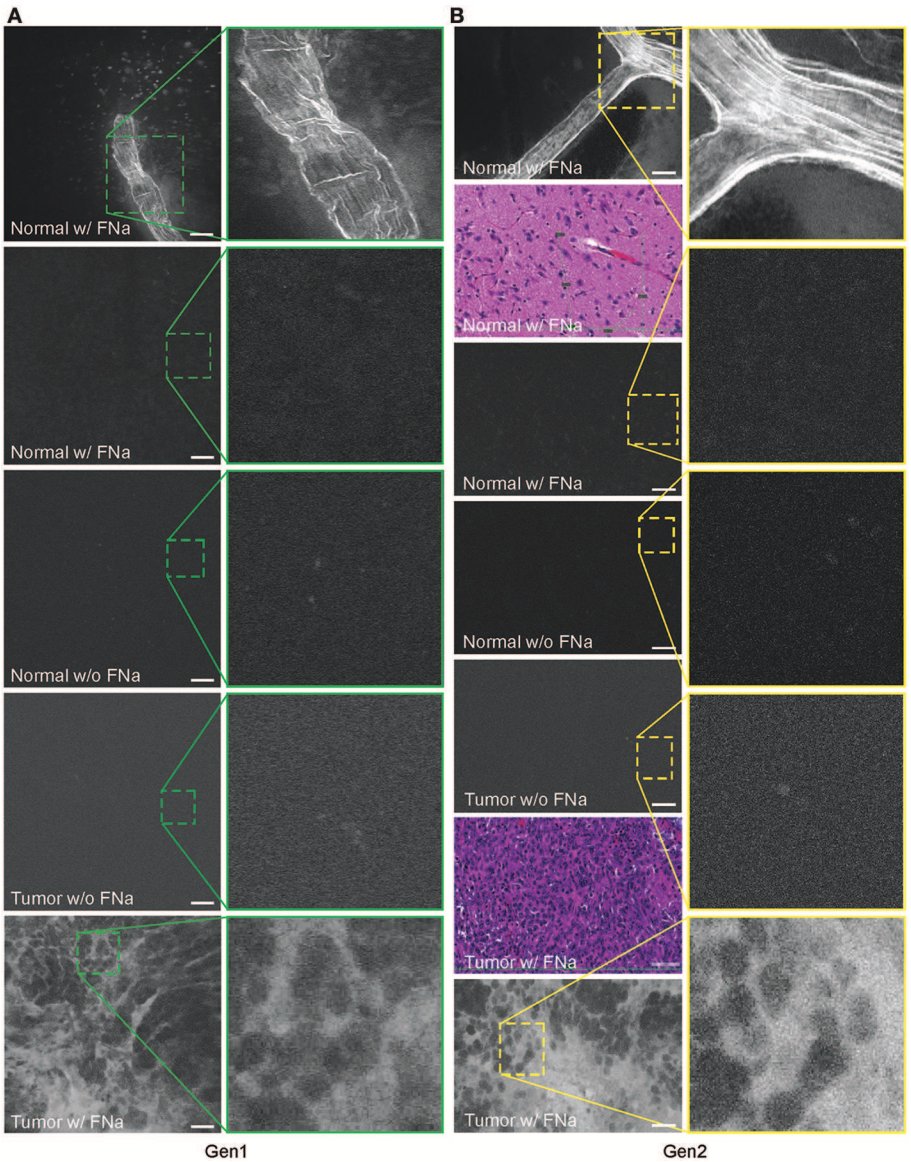

FIGURE 3 | Confocal laser endomicroscopy (CLE) images of normal mouse brain, GL261 brain glioma, visualized with and without fluorescein sodium (FNa), using **(A)** generation 1 (Gen1) and **(B)** generation 2 (Gen2) CLE. Brain vasculature, brain parenchyma, and tumor staining patterns were observed with similar quality between Gen1 and Gen2 systems. The insets show similarly magnified views from Gen1 and Gen2 systems. Additional hematoxylin and eosin (H&E) images are provided from the regions of interest of normal brain and glioma areas scanned with Gen1 and Gen2 CLE. Scale bars are 50 μm. Used with permission from Barrow Neurological Institute, Phoenix, Arizona.

Histologic Features During CLE Imaging With FNa (Gen1 and Gen2)

In no case was the tumor location uncertain based on CLE images after successful intravenous FNa injection. When imaging normal brain without tumor using CLE, FNa could be seen inside blood vessels, and occasionally leaking from vessels because of damage from surgery. Red blood cells could be visualized in these vessels as dark moving objects. No FNa was seen in other areas of the normal brain, other than intravascularly, except for sparse autofluorescent cells. Ultimately, the area of the brain away from the vessels appeared similar to the brain when FNa had not been injected, with both generally lacking fluorescence, except for rare autofluorescent cells and with limited fluorescence (**Figure 3**). After FNa injection, tumor cells were seen as nonfluorescent cells on a highlighted fluorescent background.

Abnormal tumor vasculature was seen in several tumor biopsy spots (**Supplemental Figure 2**). A gradient of FNa in the tumor was observed on images and may suggest proximity to the tumor vessels (**Supplemental Figure 3**).

Average nuclei sizes measured on AO-stained tumor images ($11.9 \pm 2.5\,\mu m$) were not different ($p = 0.10$) from those measured on FNa-contrasted CLE brain tumor images (11.6

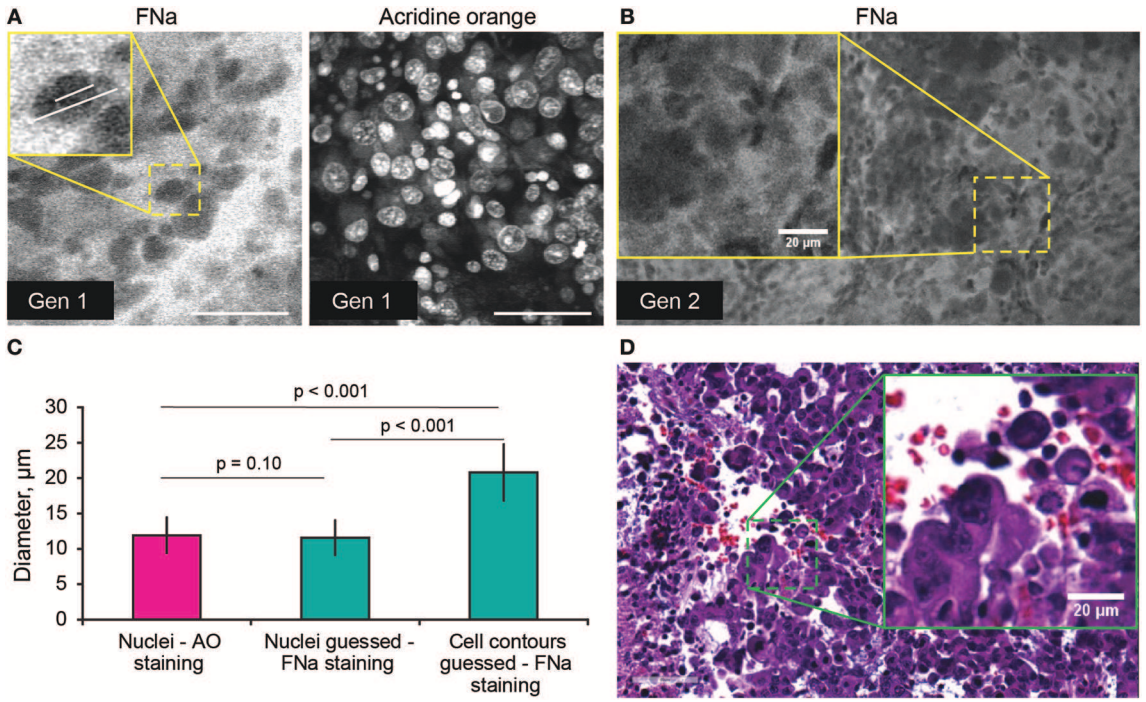

FIGURE 4 | (A,B) Comparison of the tumor cellular features visible on confocal laser endomicroscopy images with fluorescein sodium (FNa) and acridine orange (AO). AO staining of the same specimen shows true nuclei size. Gradient of FNa distribution delineates cell contours with bright gray, while cell nuclei may be visible in some of the cells in a darker gray. **(C)** Comparison of the nuclei size measured on the images with AO staining to the nuclei size measured on the images with the FNa staining ($n = 106$ cells measured with AO stain; $n = 53$ nuclei and $n = 52$ cell diameters were measured with FNa stain). The average nucleus size determined on the FNa images was similar to the true average nucleus size based on the AO staining. Generation (Gen) 2 CLE image **(B)** shows anisocytosis, similar to **(D)** histologic findings. Scale bar in **(A)** is 50 μm. Used with permission from Barrow Neurological Institute, Phoenix, Arizona.

± 2.5 μm), suggesting validity of identification of nuclei on the FNa-based confocal images. The average nuclei size was significantly smaller ($p < 0.01$) than the cell sizes (20.8 ± 3.9 μm) (**Figure 4**). Benchtop confocal LSM of fresh samples stained with FNa (*in vivo*, intravenous) and Hoechst (rapid *ex vivo*, topical live cell nuclear stain) showed images similar to CLE grayscale images and provided additional confirmation regarding the dimensions of nuclei and cells observed with CLE (**Figure 5**).

The tumor margin was visible in the GL261 model with both CLEs. The tumor border region appeared as a nonuniform delineation between the area with low FNa signal that did not contain atypical cellular features (normal brain) and an area with high FNa signal containing silhouettes of the abnormal tumor cells (**Figure 6**). Benchtop confocal microscopy of samples stained with FNa *in vivo* and rapidly counterstained *ex vivo* with Hoechst suggested that FNa signal "followed" invasions of the tumor cells in the normal brain. It confirmed that many small cell contours visible with FNa are actually anuclear red blood cells. A gradient of FNa distribution from the tumor into the normal brain was also visible with the higher FOV confocal microscopy.

When normal brain tissue was injured, leaking FNa signal was visible. Brain regions of injury without tumor could be differentiated from regions of brain with tumor on CLE images by small and nonvariable red blood cells being present, rather than large, numerous, and variable tumor cells (32).

FNa Doses for Optimal CLE Imaging

Different concentrations of intravenous FNa as a contrast for CLE imaging yielded variations in image appearance. Bolus injections of higher concentrations of FNa resulted in brighter images of tumors with less noise, and an overall increase in the fraction of diagnostic frames, compared to lower FNa concentrations ($R = 0.5$, $p < 0.05$) (**Figure 7**). The best working dosages were 20 and 40 mg/kg and are in accordance with previous publications [100 mg/kg (11); 8 mg/kg (24); 7.7 mg/kg (30)]. Based on our experience, imaging closer to the time of FNa injection produced images with greater contrast and overall higher quality compared with images obtained longer after the injection.

Histologic Features During CLE Imaging With 5-ALA (Gen1 and Gen2)

Neither Gen1 nor Gen2 CLE was reliably able to detect PpIX fluorescence in experimental tumors after 5-ALA administration. At the same time, Pentero 900 imaging with a dedicated Blue 400 filter showed very bright red PpIX fluorescence with all tumor masses. Gen2 CLE detected some signal in several tumor areas; however, this signal was not consistent in different locations imaged over the tumor area. Most imaging of the tumor showed dark images without visible signal. In all 5 animals interrogated with both Gen1 and Gen2, reliable histologic features of tumor or normal brain were not discernible with PpIX fluorescence.

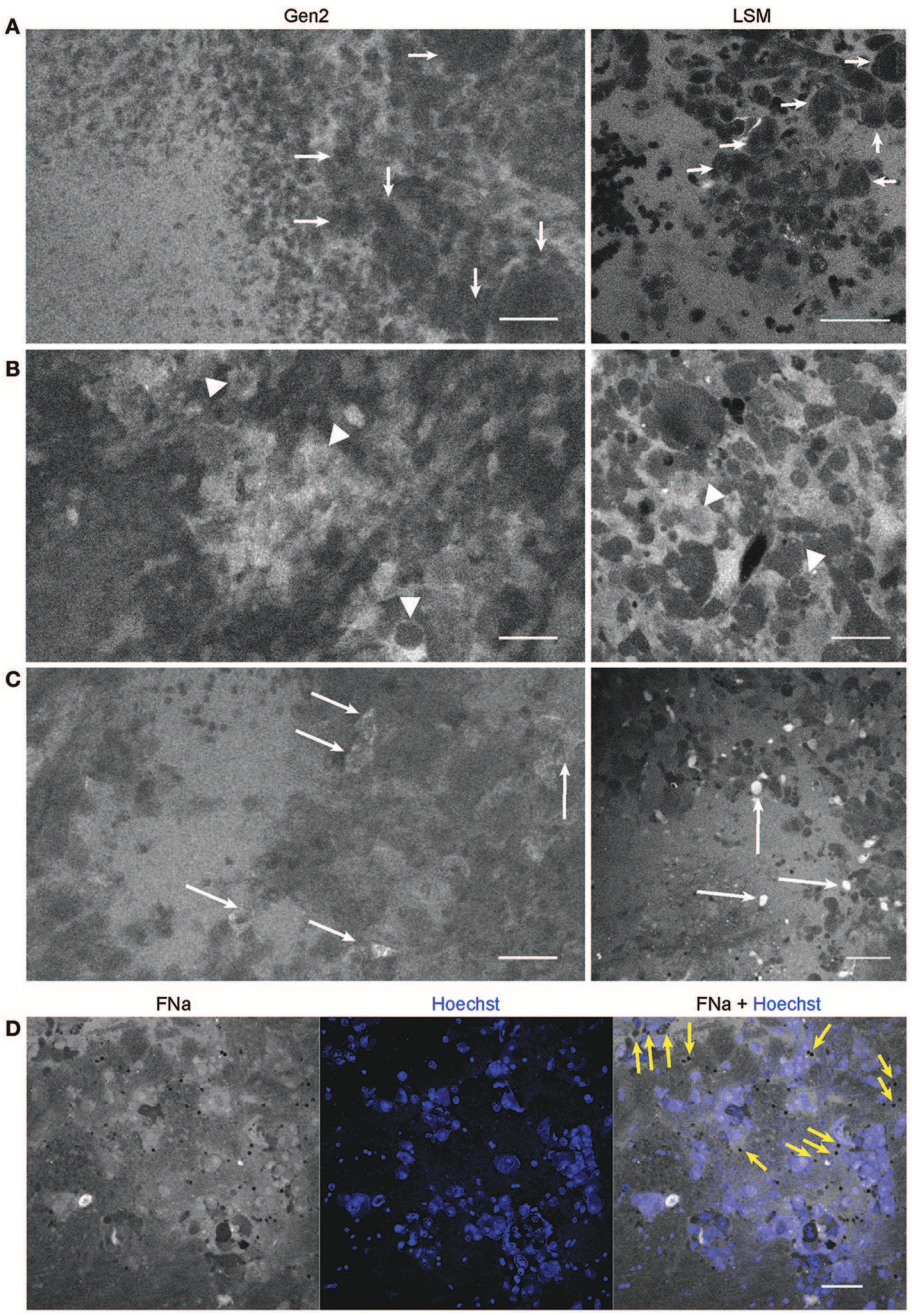

FIGURE 5 | Confocal laser endomicroscopy (CLE) patterns of GL261 glioma core. *In vivo* Gen2 CLE and rapid *ex vivo* laser scanning microscopy (LSM) images show higher fluorescein sodium (FNa) signal in the tumor area and visible contours of the tumor cells. Overall tissue architecture presents similarly in CLE and LSM images. **(A)** Most often tumor cells appeared darker than the background (arrows), while in some areas **(B,C)** tumor cells absorbed FNa and appeared bright. **(D)** Red blood cells, which were not stained by the Hoechst dye, are visible on a bright FNa background (yellow arrows). Scale bars are 50 μm. Used with permission from Barrow Neurological Institute, Phoenix, Arizona.

However, sparse fluorescent spots were observed in normal brain and tumor in experimental animals and were likely autofluorescence (35). When the overall image intensities of normal brain and tumor areas, acquired with similar parameters, were compared, they differed significantly ($p < 0.01$) (**Figure 8**).

Influence of Imaging Parameters on the Image Quality (Gen2 System)

Imaging Filter

Imaging using green bandpass or green longpass filters was compared on both systems to visualize FNa in mouse glioma

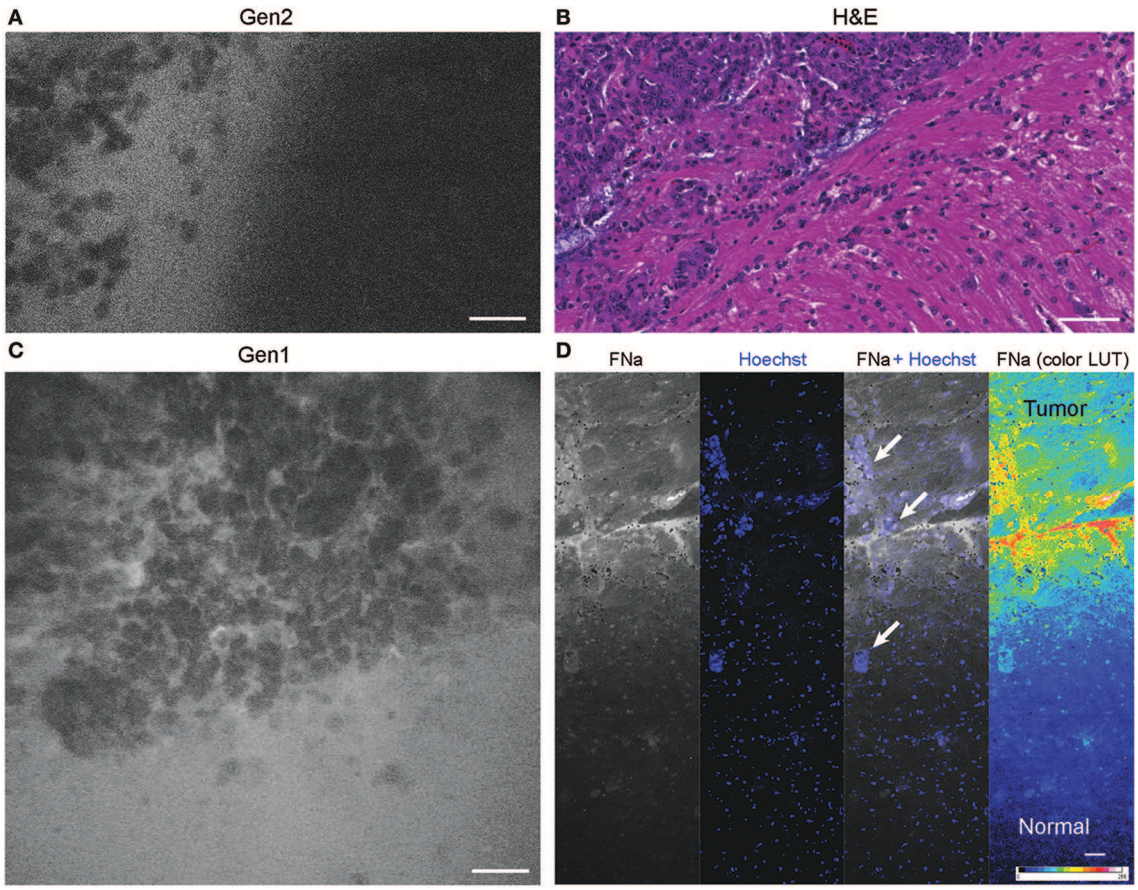

FIGURE 6 | Tumor border 1 h after intravenous fluorescein sodium (FNa) injection. **(A)** Generation 2 (Gen2) and **(C)** generation 1 (Gen1) confocal laser endomicroscopy images show a similar cellular architecture pattern of the GL261 glioma border region. **(B)** Hematoxylin and eosin (H&E) image of the tumor border from a matched sample. **(D)** Larger field of view *ex vivo* benchtop confocal image shows gradient of fluorescein diffusion from the tumor to the normal brain. Arrows indicate invading tumor cell groups. LUT, look-up table. Scale bars are 50 μm. Used with permission from Barrow Neurological Institute, Phoenix, Arizona.

models. Images acquired with the longpass filter appeared brighter. At the same time, quantitative analysis showed that the bandpass filter resulted in significantly better-contrasted images (**Figure 9**). With autobrightness function on, some Gen2 images (using FNa or AO as a contrast) appeared subjectively dark. However, adjusting the brightness during post-processing resulted in significantly better-contrasted images than when using the longpass filter. The red longpass filter was not useful for FNa imaging; however, scant cells and structures emitted light in the red spectrum within normal brain and tumor areas.

Detector Gain

When FNa was used, images were acquired mainly with a gain at the mid-position (2,400). Very bright fluorescent specimens (10–40 mg/kg FNa) required gain adjustments on only rare occasions, as control was usually possible for oversaturated pixels and image quality by lowering the laser power and brightness (**Figure 10**).

Laser Power

For FNa imaging, the laser power was usually at 50% (500 μm). In locations that produced dark images (low FNa or bleached areas), increasing the laser intensity improved image quality and brightness to some extent, but further increases in laser power did not result in quality improvement. The functioning of laser power control was not different between Gen1 and Gen2 systems. Overall, grossly bright fluorescent samples resulted in excellent contrast and quality at 50% laser power and gain position in the midpoint range (2,400) (**Figure 11**).

Image Brightness and Noise

The autobrightness function auto-adjusts the brightness of the image on the fly during continuous imaging based on the brightness histogram of the precedent image, independently from the gain and laser power settings. With one exception, the autobrightness function of the Gen2 was advantageous for rapid image and optimal brightness display, contrasting with the Gen1 that lacked this function and required frequent manual adjustments. The exception occurred when the image had abnormally bright artifacts. In such situations, the autobrightness function decreased the overall image brightness, with the FNa signal in the tumor interstitium becoming low and barely detectable—this was observed both qualitatively in real time and

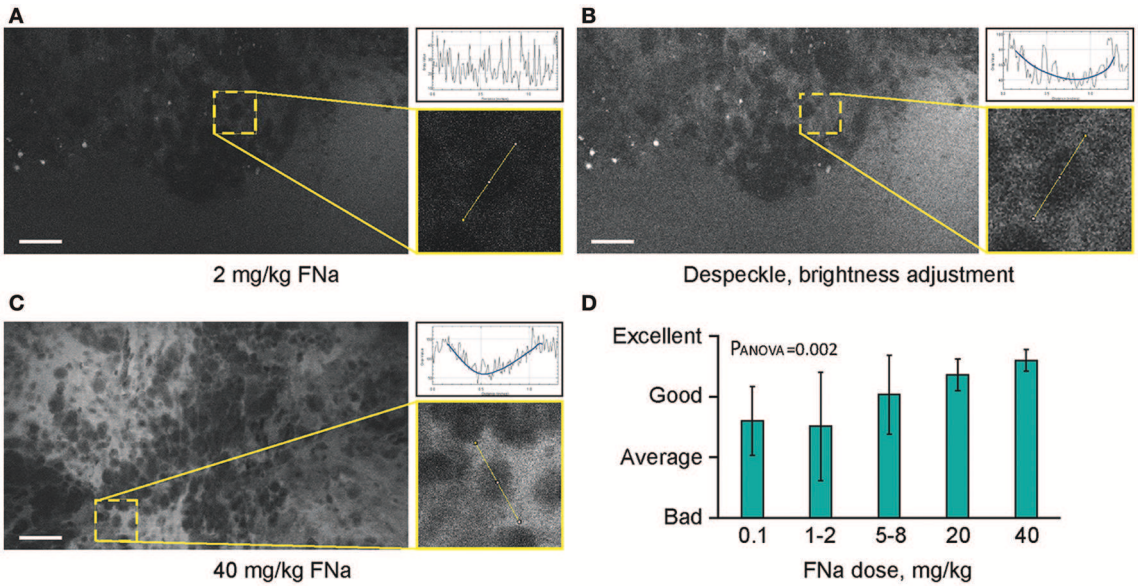

FIGURE 7 | Higher concentrations of fluorescein sodium (FNa) produces images with less noise on a generation 2 confocal laser endomicroscope. Images acquired with a low dose of FNa **(A)** could be post-processed to improve brightness **(B)**, so they appear similar to higher FNa dose images **(C)**. Comparison of the enlarged regions in **(A–C)** shows that cell contours are distinguished on all images; however, noise level [diagrams in **(A–C)**] is less with a higher FNa concentration. **(D)** Subjective grading of overall CLE imaging quality is presented as a mean of all grades from 5 independent raters. The image quality is significantly better with higher FNa dosages ($P_{ANOVA} = 0.002$). Scale bars are 50 μm. Used with permission from Barrow Neurological Institute, Phoenix, Arizona.

quantitatively during post-processing. In such situations, manual brightness setup was used to obtain better overall image quality.

When the autobrightness function was on, the increase in gain resulted in a proportional decrease in automatic brightness level. Brightness values can be indicative of noise level. Brightness levels below 80% were the most optimal with less black noise, compared to a brightness level of 80% and above. The brightness values were maintained below 80% to keep the noise levels low (**Figure 12**).

Background noise levels were further studied to assess the effects of Gen2 imaging parameters on image quality. Imaging of normal brain with various manually set brightness levels revealed that mean image intensity and standard deviation of the individual pixels had a positive correlation with brightness level (**Figure 13**). At a brightness of 91%, laser power of 50% (505 μm), speed of 1080 pixels (∼1.26 seconds per frame), and gain of 2400, the average pixel intensity from a normal brain (black color) was 53.5 arbitrary units, corresponding to about 20% saturation of the 8-bit image.

Image Acquisition Speed

Most images were acquired at a speed setting of 1080 pixels (∼1.26 seconds per frame), which resulted in the best image quality (**Table 1**). Faster scanning at speeds of 135 pixels (∼0.26 seconds per frame) and 270 pixels (∼0.4 seconds per frame) were useful for rapid scanning of large areas to determine the presence or absence of an FNa signal or for blood flow imaging (**Figure 14**). Some gross tumor tissue structures were visible at speeds of 135 and 270 but appeared overly pixelated on the CLE display. Image quality and contrast were significantly better at 1080 pixels (∼1.26 seconds per frame), especially in areas with small vessels contrasted with FNa or when using nuclear stains (AO, AF).

DISCUSSION

The Gen2 CLE system is compatible with the specific demands of neurosurgical use. With the disposable sterile sheath that includes a coverslip, the Gen2 CLE can now be safely used on the human brain during surgery without the need for a complex sterilization procedure after surgery, as was the case with the Gen1 system (**Supplemental Figure 4**). The ergonomics of the probe conformation are such that it resembles a curved, lightweight neurosurgical suction device that will lie comfortably in the hand, grasped by the first few fingers, in a fashion that allows smooth, stabilized movement as a neurosurgeon is used to for surgical instruments. In this study, we performed a preclinical investigation of the Gen2 CLE and characterized its operation, capabilities, and limitations, and compared its performance to the Gen1 CLE system.

Image Quality Comparison (Gen1 vs. Gen2)

Imaging Parameters (Gen1 and Gen2)

Multiple imaging parameters can be adjusted in both Gen1 and Gen2 systems making them flexible and capable of detecting a single-channel fluorescent signal over a broad range of intensity values. Gen2 is more adjustable, as it allows for changing most parameters rapidly during scanning, while with the Gen1, the user is required to create a new imaging session using the operating software interface to change the gain or filter. Another

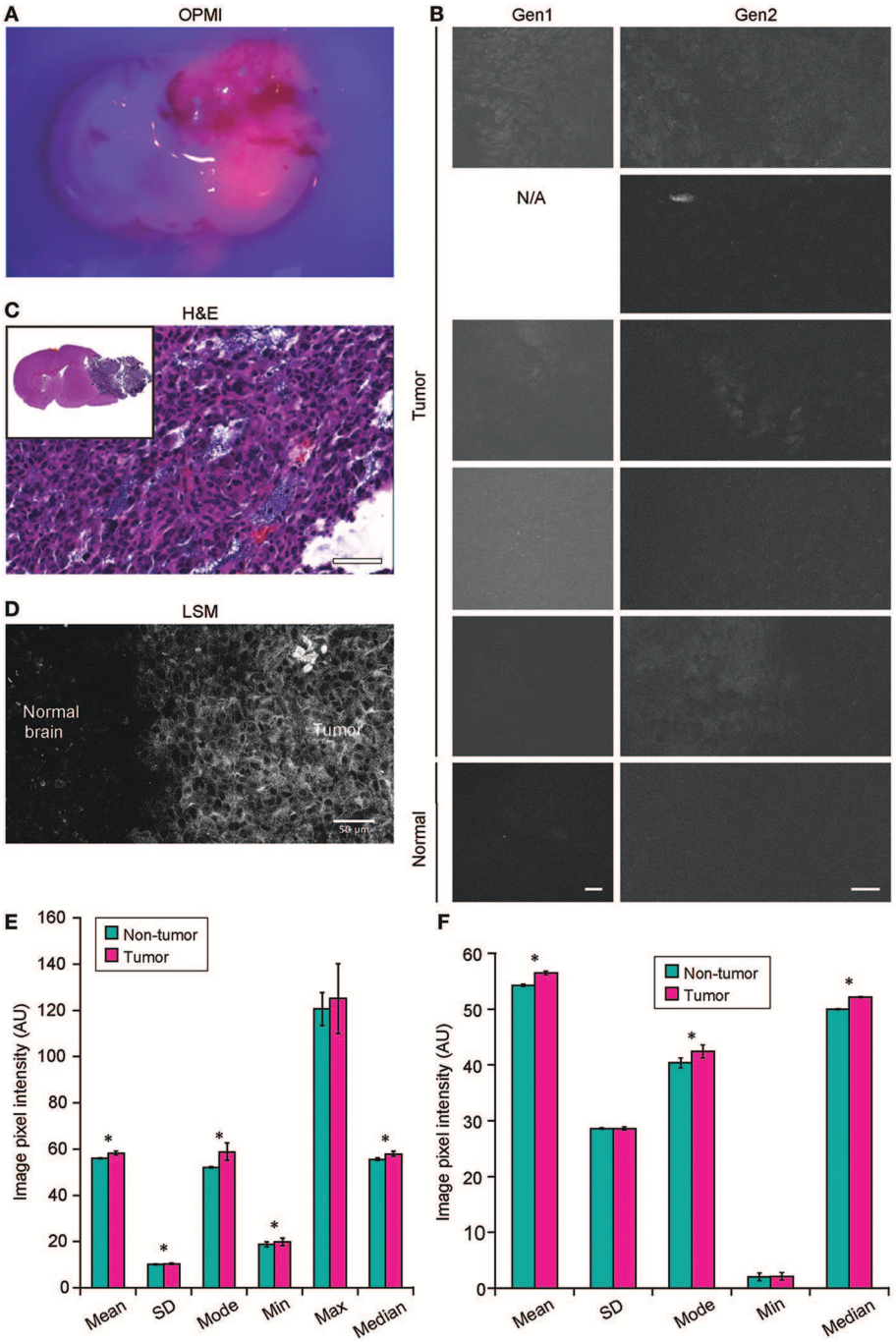

FIGURE 8 | Confocal laser endomicroscopy (CLE) imaging of GL261 glioma with 5-aminolevulenic acid (5-ALA). **(A)** Representative image of a coronal brain slice with a tumor viewed through the Pentero 900 operative microscope in Blue 400 mode shows bright red fluorescence from the tumor. **(B)** The best representative generation 1 (Gen1) and generation 2 (Gen2) CLE images of tumor (rows are 5 separate animals) and normal brain 2 h after intraperitoneal 5-ALA administration. Normal brain shows no fluorescent signal in any of the cases. Fluorescent signal from tumor is very low, visible from only a few areas, and is not consistent across the biopsy locations and across the animals imaged. **(C)** Hematoxylin and eosin (H&E) coronal slice of the brain with a tumor shows hypercellular tumor in the areas from which CLE imaging was performed. **(D)** Laser scanning microscopy (LSM) image at the tumor margin shows the protoporphyrin signal localized to tumor cell cytoplasm. The image displayed in gray scale and size is similar to Gen2 CLE. (Image acquired with 40× 1.2 W objective; 405 nm excitation; 598–740 nm detection range.) **(E)** Gen1 CLE imaging of GL261 gliomas and contralateral normal brain as a control with 5-ALA. Quantification of the images ($n = 54$ control; $n = 59$ tumor images from 5 animals) showed minimal but significant difference in the overall pixel intensities of the images taken from the tumor vs. normal brain. Groups were compared using Student *t*-tests; an asterisk indicates $p < 0.01$. **(F)** Quantification of the Gen2 CLE images ($n = 5$ control; $n = 4$ tumor) showed minimal but significant differences in the overall pixel intensities of the selected best images taken from the tumor and normal brain. Groups were compared using Student *t*-tests; an asterisk indicates $p < 0.01$. Selected images were acquired with similar CLE settings. Scale bars are 50 μm. AU, arbitrary unit. Used with permission from Barrow Neurological Institute, Phoenix, Arizona.

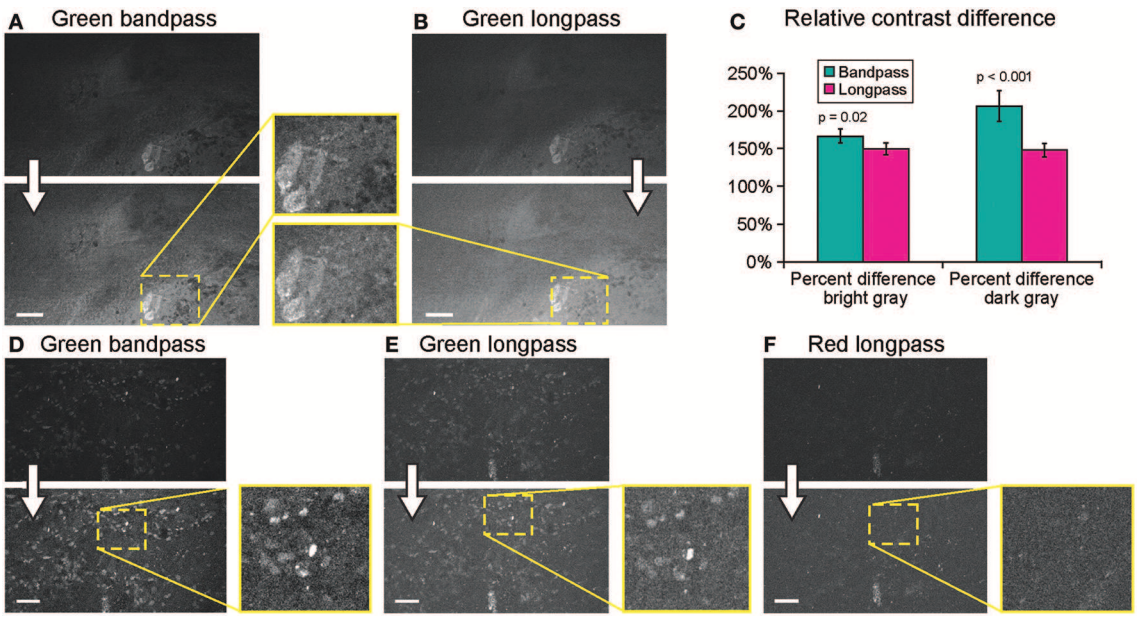

FIGURE 9 | Generation 2 confocal laser endomicroscope (CLE) imaging with various filters. Comparison of the CLE images taken from the same regions of interest with green bandpass **(A,D)**, green longpass **(B,E)**, and red **(F)** optical filters. Human glioma samples (patients were injected with FNa intraoperatively) were used for analysis and illustration. Thick arrows signify post-processing in FIJI, which includes despeckling and maximum brightness adjustment. **(C)** Matching regions of interest (ROI) were selected in FIJI to compare contrast between various structures in longpass and bandpass filters. ROIs were manually drawn over the brightest structures ($n = 5$), over the surrounding gray background ($n = 3$), and on the dark round structures ($n = 5$). Paired Student t-tests were used for comparison. **(D–F)** Green bandpass **(D)**, green longpass **(E)**, and red longpass **(F)** filter images obtained at the same location. Scale bars are 50 μm. Used with permission from Barrow Neurological Institute, Phoenix, Arizona.

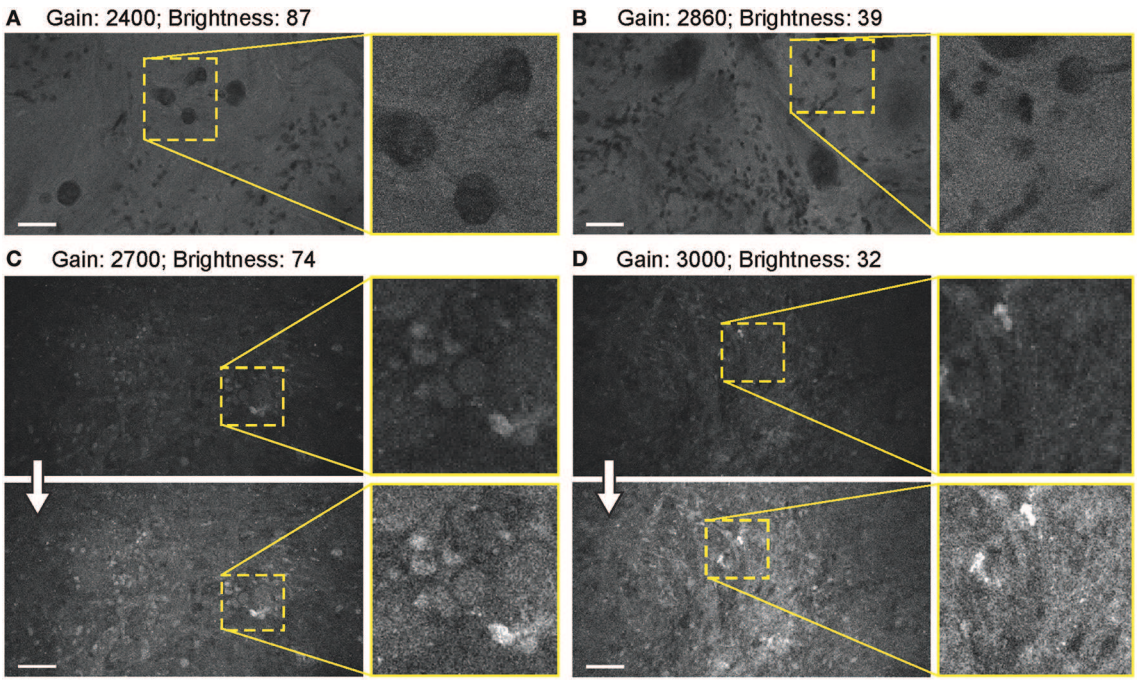

FIGURE 10 | Balanced generation 2 (Gen2) confocal laser endomicroscope (CLE) images with different gain results in comparable image quality. **(A–D)** Comparison of the CLE images taken with various gain setup. Human meningioma **(A,B)** and glioblastoma **(C,D)** samples scanned *ex vivo* 2 h after fluorescein sodium (2-mg/kg) injection are used for analysis and illustration. Increase in the gain requires reciprocal adjustments in the brightness. Overall, the resulting images have comparable quality. **(A,B)** are visualized from one patient, while **(C,D)** are visualized from a different patient. Thick arrows signify post-processing in FIJI, which includes despeckling and maximum brightness adjustment. Scale bars are 50 μm. Used with permission from Barrow Neurological Institute, Phoenix, Arizona.

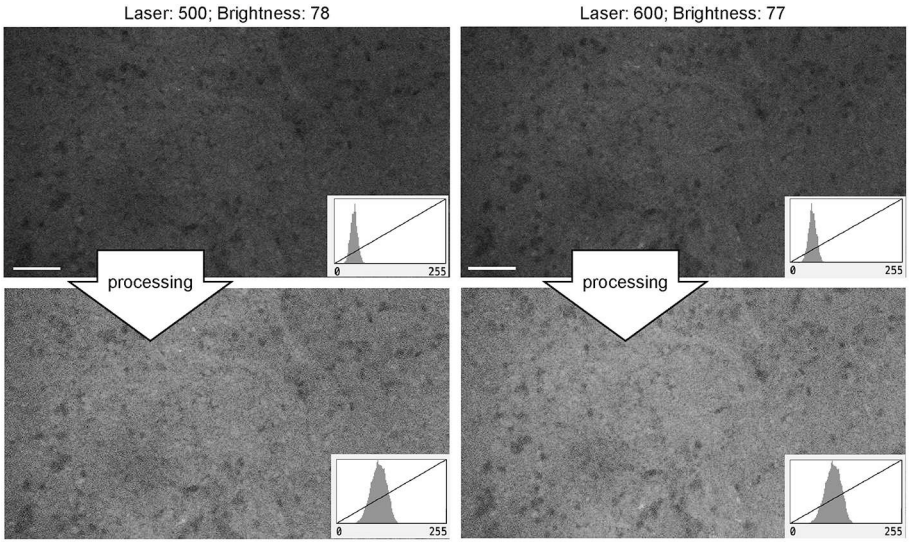

FIGURE 11 | Generation 2 confocal laser endomicroscope images taken at different laser intensity values. A human meningioma sample is used for analysis and illustration. Brightness was kept at a similar level during image acquisition. Increase in the laser intensity from 500 μm (upper left) to 600 μm (upper right) leads to a brighter overall image. Further increase in laser power does not improve contrast. Thick arrows signify post-processing in FIJI, which includes despeckling and maximum brightness adjustment. There are no subjective differences in images after post-processing (lower row). Scale bars are 50 μm. Used with permission from Barrow Neurological Institute, Phoenix, Arizona.

convenient advantage is that, unlike the Gen1, the Gen2 imaging parameters are recorded as part of the file properties. Having access to these parameters is important for quantitative analysis and comparison among various images, especially to evaluate fluorophore signal intensity in the image, which correlates with the concentration of the fluorophore in the sample. For FNa-guided optical biopsy in brain tumors, such information may be used to assess the degree of blood-brain barrier disruption, to eliminate imaging artifacts, to identify potential causes of suboptimal images, or to improve images in post-processing.

Still Images (Gen1 and Gen2)

While continuous imaging occurs at a chosen speed in both CLE systems, the recording options are different. Both systems have the option to record a single still image and time series, while the Gen2 can also automatically record Z-stacks. Still image recordings were used when the sample quality was perfect and when there was no concern about having only a few selected imaging frames recorded while interrogating the tissue. However, in most cases, continuous recording was preferred and advantageous, which is discussed later. Finding the exact same position again is nearly impossible with a CLE system due to the minute dimensions on the order of fractions of a millimeter (475 × 475 μm for Gen1; 475 × 267 μm for Gen2), contact probe design, and pliable nature of unfixed brain tissue. Thus, there was always a concern about not being able to return the CLE to the previous imaging plane. Therefore, still recordings were used less frequently than Z-stacks or time series. Incorporation and registration of the probe into an image-guided surgery navigation system would allow improvement in reassessing tissue imaging location.

Z-Stack Function (Gen2 Only)

A Z-stack is a series of images taken in rapid succession at different depths and a constant position (34). The "Z-step" is the depth distance between images and is a novel feature for handheld CLE imaging with the Gen2 CLE system. The range of the Z-stack can be set by the user, and the Z-step is a constant 3 μm, resulting in 2–35 images per stack. At least several slices (maximum 10–13) from the Z-stack were acquired at optimal Z positions that were in focus, usable, and diagnostic (36). Informative images from a Z-stack can be easily processed into video loops or semitransparent volumetric images for detailed assessment and further interpretation.

It is also worth mentioning that the size of objects becomes larger when they are imaged out of focus and deeper within the tissue. This could potentially make small red blood cells look larger than they are, thus imposing a minor potential for misdiagnosing small cells as tumor cells.

Time Series Recording and Video Loops (Gen1 and Gen2)

Time series (or "cine"-series) recordings were used extensively for post-processing and creation of video loops. Continuous nonstop recording during Gen1 or Gen2 CLE interrogation of the sample was helpful compared with "on-demand" snapshot recording because with the latter technique, some locations were bleached out before the image was recorded. Gradual photobleaching was observed, but with practice, minimizing the scan time avoided this problem. We did not investigate whether laser interrogation results in tissue damage. Although tissue damage is unlikely, we are conducting an ongoing investigation of the potential phototoxicity of CLE scanning. Additionally, minute tissue shifts

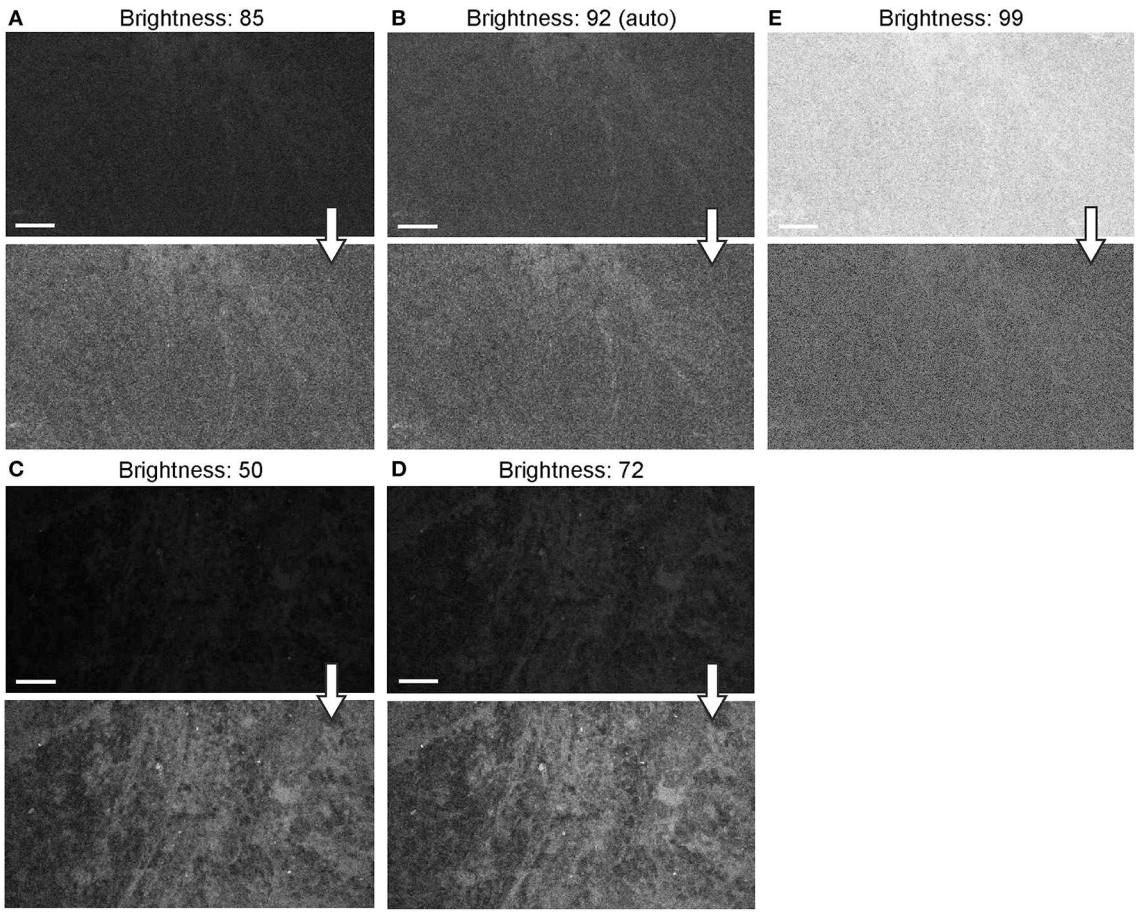

FIGURE 12 | Generation 2 confocal laser endomicroscope (CLE) images taken with different brightness setup. **(A–E)** Comparison of the CLE images taken with various brightness settings. The same fields of view of meningioma **(A–C)** and low-grade glioma **(D,E)** human samples are used for analysis and illustration. Brightness is in the automatic position for **(B)**; in all other figures, brightness is set manually. Increase in brightness higher than automatic position does not increase image quality quantitatively **(C)**. Thick arrows signify post-processing in FIJI, which includes despeckling and maximum brightness adjustment, except for **(C)** in which brightness is decreased with post-processing. Scale bars are 50 μm. Used with permission from Barrow Neurological Institute, Phoenix, Arizona.

changed the observed image before taking a picture, and the probe often could not be returned to the desired location because of the pliable nature of unfixed brain tissue. Z-position, brightness, and laser power can be adjusted during the time series imaging to record optimal quality images.

Notably, time series imaging revealed a "movement" feature of the tissue and supplemented visual information gained from still images. This feature is useful in several aspects for tissue histologic characteristics and CLE image interpretation. Primarily, differentiation of freely moving red blood cells from other moving or stationary cells becomes much easier and thus fosters the diagnostic accuracy of image and tissue interpretation. Additionally, it becomes easier to differentiate real signal from noise. By viewing time series, differentiation is possible between what is meaningful and what is merely stochastic noise. Such judgment is usually difficult on still images because of the nature of FNa. FNa is a nonspecific dye that is not bound to any structure, but rather provides a bright background (i.e., a silhouetted appearance) on which to observe, contrast, and differentiate structures. Noise is an inherent limitation of FNa. *In vivo* CLE demonstrated dynamics of the glioma environment for the first time, something that is not possible in fixed brain tissue.

It should also be noted that CLE allowed for *in vivo* tracking of blood flow in vessels. Tracking of individual blood cells is not always possible because of fast movements that require high-speed scanning confocal imaging systems, such as spinning disk confocal microscopes (37–39).

Histologic Pictures Visualized by CLE With FNa (Gen1 and Gen2)

The use of FNa with both distal scanning CLE systems was effective to visualize brain vasculature, red blood cells, silhouettes of neoplastic cells, nuclear and cell dimensions, GL261 glioma border, and brain injury. FNa aided detection of normal and tumor vessels and did not significantly highlight normal brain tissue. Cell nuclei and cytoplasm may be distinguished in some of the cells by a gradient of FNa penetration through

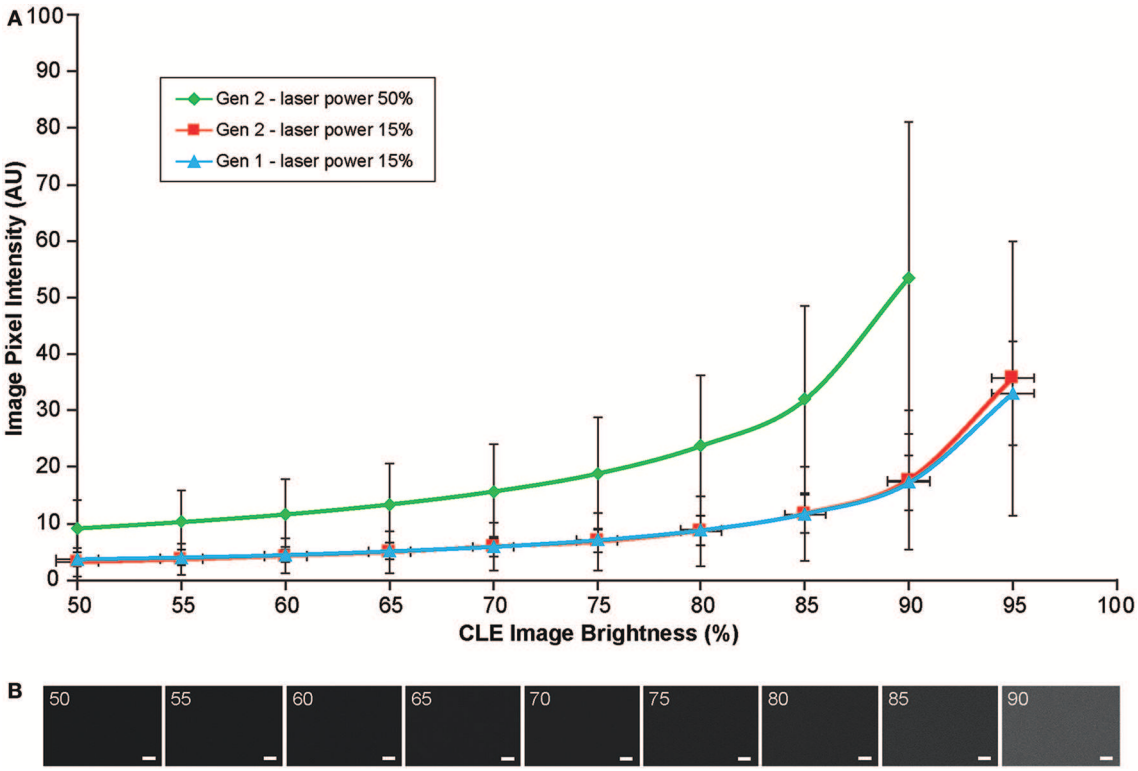

FIGURE 13 | Image brightness and background noise level with the generation 1 (Gen1) and generation 2 (Gen2) confocal laser endomicroscope (CLE). Image brightness and background noise level depend on the laser power and image brightness set up of the CLE. **(A)** Graph showing observed image intensity in arbitrary units (AU) (y axis) at the various brightness positions, while imaging normal brain area. This value represents "black" noise. Brightness setting above 80% results in a significant increase of black noise, which may decrease image quality. Therefore, when imaging, one should aim at getting a picture at a brightness level below 80%. **(B)** Unprocessed Gen 2 CLE images taken at various indicated brightness levels (%) that are set manually. Scale bars are 50 μm. Used with permission from Barrow Neurological Institute, Phoenix, Arizona.

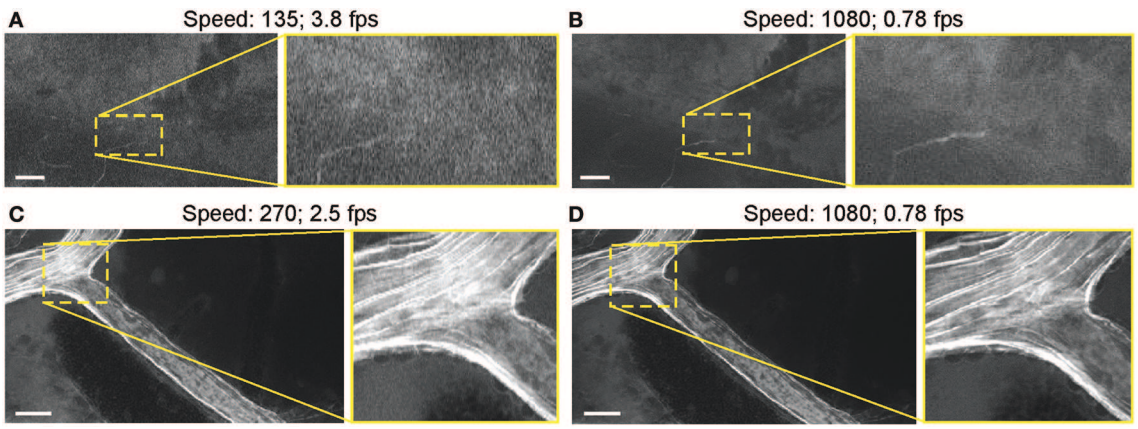

FIGURE 14 | Generation 2 confocal laser endomicroscope (CLE) images taken at different speeds. Comparison of CLE images taken with 3 various acquisition speed settings: **(A)** 135, **(B,D)** 1,080, and **(C)** 270. Images acquired at an intermediate speed setting **(C)** of 270 (calculated mean 2.5 frames per second) are of average quality and are able to resolve more structural details than images taken at the faster speed of 135 **(A)**. Significant improvement in image quality at the slower speed of 1,080 **(B,D)** is mostly apparent in the areas with high contrast, such as small vessels when fluorescein sodium is used. When viewed as smaller pictures, the differences are less pronounced. However, on a large high-definition display, the image quality at different speeds differs substantially. Scale bars are 50 μm. Used with permission from Barrow Neurological Institute, Phoenix, Arizona.

different biological membranes (**Supplemental Figure 5**). FNa extravasation due to injury can be differentiated from the FNa diffusion in the tumor using characteristic histologic patterns on CLE (32). It is worth noting that individual fluorescent cells were frequently observed in both tumor and normal brain (**Supplemental Figure 6**). This phenomenon had various

patterns and was observed more frequently with increased imaging time after FNa injection. Singular and multiple cells were observed that took up FNa on the cut surface of the tumors. Even though such images did not represent a characteristic CLE image of the tumor, they were helpful to assess the cell morphology, tissue architecture, and cytoplasm-to-nucleus ratio. The reason for such FNa uptake by some cells is still unknown because tumor cells do not show FNa uptake *in vitro* (30). However, it might be due to cell membrane disruption caused by injury, as such findings were seen mostly in *ex vivo* samples. Additionally, large singular cells that took up FNa seen in the tumor may be macrophages.

When considering FNa imaging strategies, continuous cine-like time series image recordings and Z-stacks were the most useful and productive. Continuous recordings were used to identify red blood cells and better appreciate cell morphology based on cell movement while reformatted volume views of Z-stacks provided an improved understanding of the 3-dimensional structure of the tissue.

Histologic Pictures Visualized by CLE With 5-ALA (Gen1 and Gen2)

The combination of metabolic dye 5-ALA with either Gen1 or Gen2 was not a reliable method for identification of tumor in our observations, as characteristic histologic features could not be identified. The laser wavelength of both systems (488 nm) is not optimally tuned for excitation of PpIX, and CLE images did not show specific information. CLE images did not reproduce findings when LSM with the appropriate excitation laser was used to image PpIX in the same mouse glioma model (40).

While it was possible to differentiate glioma from normal brain tissue by comparing overall average image intensity, this charcteristic was not deemed useful. Similar "fluorescence intensity" sampling has been shown previously using spectrophotometric methods (41–43). Of note, sparse fluorescent "spots" seen using the Gen2 CLE with 5-ALA were consistent with the previous intraoperative observations of patients with brain tumors with the Gen1 CLE, although the exact identification of these PpIX fluorescent signals is not confirmed (25). These structures are likely autofluorescent due to lipofuscin (35). Imaging of histologic patterns created by 5-ALA-induced PpIX in brain tumors remains limited to benchtop confocal microscopes, or hand-held fluorescence microscopes specifically designed for PpIX excitation and detection, such as a dual axis confocal microscope (44) or a scanning fiber endoscope system (40).

CLE Parameters for Best Image Quality With FNa (Gen2 Only)

Filter

The first parameter to consider during CLE imaging is the filter. Between the two types of green filters (i.e., the longpass filter and bandpass filter), the longpass filter produced brighter images. Although images with such longpass filters may look more pleasing, they include nonspecific light from the background that attenuates FNa-induced contrast. Ultimately, the bandpass filter produced images with higher contrast and was preferable for obtaining better quality and interpretable images.

Gain

Unlike in the benchtop confocal microscope, where the gain is fine-tuned during the constant image capturing, with the Gen2 CLE the gain control is located in a separate window and is not available for rapid adjustments on the fly. However, adjustments of brightness and laser power were enough to obtain quality images in most cases without the need to adjust the gain. Only in a few very bright or very dim specimens was there a need to adjust the gain for optimal image quality.

Laser Power

Laser power at mid-range (50% or 500 μm) was generally optimal for imaging, with increasing intensity providing some improvements in image quality. Lack of significant improvement in image quality with increasing laser power is mainly explained by the nature of FNa, which, after extravasation, is diffused through almost all tissue thickness. Therefore, increased excitation results in increased emission in all image regions, including background and cells. Moreover, autofluorescence and noise begin to be visible at higher laser settings. This association of laser power and gain with contrast and autofluorescence is shown schematically in **Supplemental Figure 7**. Compared with targeted fluorophores or reflectance imaging (45), imaging of FNa is always associated with higher levels of noise.

Brightness

The brightness is the built-in adjustable proprietary setting parameter used during CLE imaging. It has a range of settings from 0 to 100% and, unlike the gain and laser power settings, could be adjusted during the imaging. Brightness was a primary setting of both CLE systems. Autobrightness is a new Gen2 function that saved time and made imaging process faster. Images acquired in autobrightness mode had good quality, comparable with the quality of images acquired at manually set brightness levels. Additionally, an optimal brightness level, or even pseudocoloring, can be applied later during post-processing (34).

Speed

The speed of image acquisition was inversely correlated with image quality. This relationship illustrates the tradeoff of the convenience of using high-speed imaging to locate informative structures quickly within a large area with little detail versus taking more time to look at higher resolution images in greater detail. For areas of high contrast, such as intact vessels with FNa within the normal brain, or pronounced hypercellular tumor areas with bright FNa nearby, high-speed imaging was able to resolve structures well. However, in most cases, fast scanning was not able to resolve red blood cells and fine cellular details.

Zoom

Although the FOV of Gen2 images is about half the size of Gen1 images, it was sufficient to obtain similar image interpretation for corresponding histological structures. Subjective image quality appraisal between the systems is dependent on the display size. The Gen2 is capable of increasing optical zoom by a factor of two, but this results in a corresponding decrease in FOV size, which is not particularly helpful for the identification

of cell or tissue architecture using FNa imaging. However, a zoom function might be advantageous for dyes such as AO or AF (**Supplemental Figure 8**). Unlike benchtop confocal scanning microscope systems, where zoom can be adjusted in real time (45, 46), handheld CLE systems are limited to a preset zoom because of limitations in miniature design and construction.

Because of the inherent cellular composition of different tumor types, including cellular and regional tissue architectural heterogeneity, CLE system functionality may benefit the surgeon or pathologist by use of a lower resolution and larger FOV image assessment. This situation would allow a closer match to the lower power magnification of a conventional pathology microscope, which would allow the surgeon a larger FOV for scanning the tissue surface (40). However, the portability and capability to move the CLE probe compensate for the smaller FOV, along with Z-stack functionality. Combining multiple small FOV frames together using mosaicking computational algorithms has been shown to yield a larger reconstructed FOV (47).

Different Concentrations and Timing of FNa Administration

FNa doses in animals are higher than human doses used in brain tumor surgery either with epifluorescence guidance using the operating microscope with a dedicated filter [2–20 mg/kg (48)] or previously used with CLE [5 mg/kg (1)], which most likely is due to faster metabolism of such fluorophores in rodents. CLE imaging likely requires similar or higher, but not lower, dosages than epifluorescent imaging to obtain informative images. CLE imaging was performed within a period of 5 min to 2 h after FNa injection. This timing was chosen to approximate the duration of tumor surgery in humans and complements the previous data on the biodistribution of FNa in a rodent model (30). Overall, the shorter time periods produced a higher number of diagnostic frames, while imaging at longer time periods produced less contrasted images, which corresponds to the findings by Folaron et al. (31).

Limitations

The current study was performed using a mouse GL261 glioma model. Histologic patterns and the feasibility of FNa imaging with CLE in other experimental tumor models were not addressed in this project. However, clinical experience (1, 7) and the available literature indicate the general feasibility of such an approach for intraoperative brain tumor imaging. The limitations that have not been addressed in this discussion include the need for the development of remote access to the system by another surgeon or neuropathologist or the ability to push images out to cellular devices for rapid assessment or consultation. In addition, the number of images acquired during a case can be very high—in the thousands—and the number of images with artifact caused by motion or other distortions causing them to be unusable is high. Thus, image stabilization control and associated software built into system would be beneficial for quick informative image selection, identification, review, and optimization (49–51).

CONCLUSIONS

Functionality and parameters were assessed for a CLE system (Gen2) designed specifically to perform to the demands and progress of neurosurgery to potentially assist in managing invasive brain tumors in a preclinical setting. Experimental brain tumor models (*in vivo*) and human tumor samples (*ex vivo*) were employed to discern and describe optimal imaging parameters for microscopic histologic visualization with a clinical-grade CLE system and intravenous FNa as a contrast fluorophore. Visualized histologic patterns and pixel intensity values were of comparable quality on Gen1 and Gen2 systems, if not improved with the Gen2 system. The Gen2 had a limitation of a smaller FOV, while having higher resolution, clearer images, and a more responsive user interface, including an autobrightness function and volumetric Z-stack image acquisition that enrich diagnostic possibilities and imaging functionality.

Such portable CLE systems are designed ultimately for *in vivo* use. CLE systems cannot replace the extensive functionality of benchtop confocal scanning microscopes, and they are not designed to accomplish such tasks. CLE systems depend on their specificity, rapid applicability, and portability; their functions, ergonomics, and employment depend on the demands of the surgical or diagnostic specialty. Additionally, the properties of the emitted and detected light range and concomitant fluorophores have a critical impact on use and efficacy.

The CLE provides the neurosurgeon with real-time intraoperative image resolution at the cellular level that is the critical basis of the potential for cell-precision surgery (although neurosurgical instrumentation does not yet provide for precision maneuvers at the cellular level). Although CLE has been used routinely in other medical and surgical specialties, such as for gastrointestinal diagnosis, neurosurgery is in its infancy with respect to CLE use. CLE technology does appear to be responding to the demands of neurosurgeons and neuropathologists for practical introduction into the operating room as an aid in surgery for invasive brain tumors after nearly a decade of developmental exploration and testing.

Concepts for CLE use that must be considered are those that will make the system meaningful in a surgical setting. CLE usefulness to neurosurgery must be proven by being shown to provide a measurable ability to discriminate and guide removal of tumor invasion, thereby extending or optimizing the resection. As much as CLE may provide precise information on where to biopsy or remove tissue, it may be just as crucially used to inform the neurosurgeon where to stop the resection. Further clinical investigation of the diagnostic value of the Gen2 CLE system in fluorescence-guided brain tumor surgery is ongoing.

ETHICS STATEMENT

All patients gave voluntary informed consent as a part of a study protocol approved by the Institutional Review Board of the Barrow Neurological Institute, St. Joseph's Hospital and Medical Center, Phoenix, Arizona.

AUTHOR CONTRIBUTIONS

EB, PN, and MP conception and design. EB, EM, AC, AP, and CC acquisition of data, experiments. EB, EM, NM, VB, JE, PN, and MP analysis and interpretation of data. MP, DH, and AS resources, animal model development. MP, PN, and ML supervision. EB, EM, and CC drafting the article. EB, AC, AP, DH, NM, VB, AS, ML, JE, PN, and MP revising article critically for important intellectual content. All authors final approval of the manuscript.

FUNDING

This research was supported by the Newsome Chair in Neurosurgery Research held by MP and the Barrow Neurological Foundation. This project received materials support from Carl Zeiss AG, Oberkochen, Germany. EB received scholarship support SP-2240.2018.4.

ACKNOWLEDGMENTS

The authors thank the staff of Neuroscience Publications at Barrow Neurological Institute for assistance with manuscript preparation.

SUPPLEMENTARY MATERIAL

The Supplementary Material for this article can be found online at: https://www.frontiersin.org/articles/10.3389/fonc.2019.00554/full#supplementary-material

REFERENCES

1. Martirosyan NL, Eschbacher JM, Kalani MY, Turner JD, Belykh E, Spetzler RF, et al. Prospective evaluation of the utility of intraoperative confocal laser endomicroscopy in patients with brain neoplasms using fluorescein sodium: experience with 74 cases. *Neurosurg Focus*. (2016) 40:E11. doi: 10.3171/2016.1.FOCUS15559
2. Ackerman LV, Ramirez GA. The indications for and limitations of frozen section diagnosis; a review of 1269 consecutive frozen section diagnoses. *Br J Surg*. (1959) 46:336–50.
3. Novis DA, Zarbo RJ. Interinstitutional comparison of frozen section turnaround time. A College of American Pathologists Q-Probes study of 32868 frozen sections in 700 hospitals. *Arch Pathol Lab Med*. (1997) 121:559–67.
4. Plesec TP, Prayson RA. Frozen section discrepancy in the evaluation of central nervous system tumors. *Arch Pathol Lab Med*. (2007) 131:1532–40. doi: 10.1043/1543-2165(2007)131[1532:FSDITE]2.0.CO;2
5. Osman H, Georges J, Elsahy D, Hattab EM, Yocom S, Cohen-Gadol AA. *In vivo* microscopy in neurosurgical oncology. *World Neurosurg*. (2018) 115:110–27. doi: 10.1016/j.wneu.2018.03.218
6. Belykh E, Martirosyan NL, Yagmurlu K, Miller EJ, Eschbacher JM, Izadyyazdanabadi M, et al. Intraoperative fluorescence imaging for personalized brain tumor resection: current state and future directions. *Front Surg*. (2016) 3:55. doi: 10.3389/fsurg.2016.00055
7. Eschbacher J, Martirosyan NL, Nakaji P, Sanai N, Preul MC, Smith KA, et al. *In vivo* intraoperative confocal microscopy for real-time histopathological imaging of brain tumors. *J Neurosurg*. (2012) 116:854–60. doi: 10.3171/2011.12.JNS11696
8. Roessler K, Dietrich W, Kitz K. High diagnostic accuracy of cytologic smears of central nervous system tumors. A 15-year experience based on 4,172 patients. *Acta cytologica*. (2002) 46:667–74. doi: 10.1159/000326973
9. Rao S, Rajkumar A, Ehtesham MD, Duvuru P. Challenges in neurosurgical intraoperative consultation. *Neurology India*. (2009) 57:464–8. doi: 10.4103/0028-3886.55598
10. Martirosyan NL, Georges J, Eschbacher JM, Cavalcanti DD, Elhadi AM, Abdelwahab MG, et al. Potential application of a handheld confocal endomicroscope imaging system using a variety of fluorophores in experimental gliomas and normal brain. *Neurosurg Focus*. (2014) 36:E16. doi: 10.3171/2013.11.FOCUS13486
11. Foersch S, Heimann A, Ayyad A, Spoden GA, Florin L, Mpoukouvalas K, et al. Confocal laser endomicroscopy for diagnosis and histomorphologic imaging of brain tumors *in vivo*. *PLoS ONE*. (2012) 7:e41760. doi: 10.1371/journal.pone.0041760
12. Park JC, Park Y, Kim HK, Jo JH, Park CH, Kim EH, et al. Probe-based confocal laser endomicroscopy in the margin delineation of early gastric cancer for endoscopic submucosal dissection. *J Gastroenterol Hepatol*. (2017) 32:1046–54. doi: 10.1111/jgh.13635
13. Ammirati M, Vick N, Liao YL, Ciric I, Mikhael M. Effect of the extent of surgical resection on survival and quality of life in patients with supratentorial glioblastomas and anaplastic astrocytomas. *Neurosurgery*. (1987) 21:201–6.
14. Devaux BC, O'Fallon JR, Kelly PJ. Resection, biopsy, and survival in malignant glial neoplasms. A retrospective study of clinical parameters, therapy, and outcome. *J Neurosurg*. (1993) 78:767–75.
15. Lacroix M, Abi-Said D, Fourney DR, Gokaslan ZL, Shi W, DeMonte F, et al. A multivariate analysis of 416 patients with glioblastoma multiforme: prognosis, extent of resection, and survival. *J Neurosurg*. (2001) 95:190–8. doi: 10.3171/jns.2001.95.2.0190
16. Nitta T, Sato K. Prognostic implications of the extent of surgical resection in patients with intracranial malignant gliomas. *Cancer*. (1995) 75:2727–31.
17. Rostomily RC, Spence AM, Duong D, McCormick K, Bland M, Berger MS. Multimodality management of recurrent adult malignant gliomas: results of a phase II multiagent chemotherapy study and analysis of cytoreductive surgery. *Neurosurgery*. (1994) 35:378–88; discussion: 88.
18. Wood JR, Green SB, Shapiro WR. The prognostic importance of tumor size in malignant gliomas: a computed tomographic scan study by the Brain Tumor Cooperative Group. *J Clin Oncol*. (1988) 6:338–43.
19. Pavlov V, Meyronet D, Meyer-Bisch V, Armoiry X, Pikul B, Dumot C, et al. Intraoperative probe-based confocal laser endomicroscopy in surgery and stereotactic biopsy of low-grade and high-grade gliomas: a feasibility study in humans. *Neurosurgery*. (2016) 79:604–12. doi: 10.1227/NEU.0000000000001365
20. Charalampaki P, Javed M, Daali S, Heiroth HJ, Igressa A, Weber F. Confocal laser endomicroscopy for real-time histomorphological diagnosis: our clinical experience with 150 brain and spinal tumor cases. *Neurosurgery*. (2015) 62(Suppl. 1):171–6. doi: 10.1227/NEU.0000000000000805
21. Belykh E, Cavallo C, Gandhi S, Zhao X, Veljanoski D, Izady Yazdanabadi M, et al. Utilization of intraoperative confocal laser endomicroscopy in brain tumor surgery. *J Neurosurg Sci*. (2018) 62:704–17. doi: 10.23736/S0390-5616.18.04553-8
22. Belykh EG, Zhao X, Cavallo C, Bohl MA, Yagmurlu K, Aklinski JL, et al. Laboratory evaluation of a robotic operative microscope - visualization platform for neurosurgery. *Cureus*. (2018)10:e3072. doi: 10.7759/cureus.3072.
23. Fenton KE, Martirosyan NL, Abdelwahab MG, Coons SW, Preul MC, Scheck AC. *In vivo* visualization of GL261-luc2 mouse glioma cells by use of Alexa Fluor-labeled TRP-2 antibodies. *Neurosurg Focus*. (2014) 36:E12. doi: 10.3171/2013.12.FOCUS13488
24. Sankar T, Delaney PM, Ryan RW, Eschbacher J, Abdelwahab M, Nakaji P, et al. Miniaturized handheld confocal microscopy for neurosurgery: results in an experimental glioblastoma model. *Neurosurgery*. (2010) 66:410–7; discussion: 7–8. doi: 10.1227/01.NEU.0000365772.66324.6F
25. Sanai N, Snyder LA, Honea NJ, Coons SW, Eschbacher JM, Smith KA, et al. Intraoperative confocal microscopy in the visualization of 5-aminolevulinic acid fluorescence in low-grade gliomas. *J Neurosurg*. (2011) 115:740–8. doi: 10.3171/2011.6.JNS11252

26. Abdelwahab MG, Sankar T, Preul MC, Scheck AC. Intracranial implantation with subsequent 3D *in vivo* bioluminescent imaging of murine gliomas. *J Vis Exp*. (2011) 57:e3403. doi: 10.3791/3403
27. Swanson KI, Clark PA, Zhang RR, Kandela IK, Farhoud M, Weichert JP, et al. Fluorescent cancer-selective alkylphosphocholine analogs for intraoperative glioma detection. *Neurosurgery*. (2015) 76:115–23; discussion: 23–4. doi: 10.1227/NEU.0000000000000622
28. Cho HR, Kim DH, Kim D, Doble P, Bishop D, Hare D, et al. Malignant glioma: MR imaging by using 5-aminolevulinic acid in an animal model. *Radiology*. (2014) 272:720–30. doi: 10.1148/radiol.14131459
29. Fisher CJ, Niu C, Foltz W, Chen Y, Sidorova-Darmos E, Eubanks JH, et al. ALA-PpIX mediated photodynamic therapy of malignant gliomas augmented by hypothermia. *PLoS ONE*. (2017) 12:e0181654. doi: 10.1371/journal.pone.0181654
30. Diaz RJ, Dios RR, Hattab EM, Burrell K, Rakopoulos P, Sabha N, et al. Study of the biodistribution of fluorescein in glioma-infiltrated mouse brain and histopathological correlation of intraoperative findings in high-grade gliomas resected under fluorescein fluorescence guidance. *J Neurosurg*. (2015) 122:1360–9. doi: 10.3171/2015.2.JNS132507
31. Folaron M, Strawbridge R, Samkoe KS, Filan C, Roberts DW, Davis SC. Elucidating the kinetics of sodium fluorescein for fluorescence-guided surgery of glioma. *J Neurosurg*. (2018) 1–11. doi: 10.3171/2018.4.JNS172644
32. Belykh E, Miller EJ, Patel AA, Yazdanabadi MI, Martirosyan NL, Yagmurlu K, et al. Diagnostic accuracy of a confocal laser endomicroscope for *in vivo* differentiation between normal injured and tumor tissue during fluorescein-guided glioma resection: laboratory investigation. *World Neurosurg*. (2018) 115:e337–48. doi: 10.1016/j.wneu.2018.04.048
33. Schindelin J, Arganda-Carreras I, Frise E, Kaynig V, Longair M, Pietzsch T, et al. Fiji: an open-source platform for biological-image analysis. *Nat Methods*. (2012) 9:676–82. doi: 10.1038/nmeth.2019
34. Belykh E, Patel AA, Miller EJ, Bozkurt B, Yağmurlu K, Woolf EC, et al. Probe-based three-dimensional confocal laser endomicroscopy of brain tumors: technical note. *Cancer Manage Res*. (2018) 10:3109–23. doi: 10.2147/cmar.s165980.
35. Croce AC, Bottiroli G. Autofluorescence spectroscopy and imaging: a tool for biomedical research and diagnosis. *Eur J Histochem*. (2014) 58:2461. doi: 10.4081/ejh.2014.2461
36. Belykh E, Patel AA, Miller EJ, Bozkurt B, Yagmurlu K, Woolf EC, et al. Probe-based three-dimensional confocal laser endomicroscopy of brain tumors: technical note. *Cancer Manag Res*. (2018) 10:3109–23. doi: 10.2147/CMAR.S165980
37. Goetz M, Thomas S, Heimann A, Delaney P, Schneider C, Relle M, et al. Dynamic *in vivo* imaging of microvasculature and perfusion by miniaturized confocal laser microscopy. *Eur Surg Res*. (2008) 41:290–7. doi: 10.1159/000148242
38. Norman MU, Hulliger S, Colarusso P, Kubes P. Multichannel fluorescence spinning disk microscopy reveals early endogenous CD4 T cell recruitment in contact sensitivity via complement. *J Immunol*. (2008) 180:510–21. doi: 10.4049/jimmunol.180.1.510
39. Belykh E, Cavallo C, Zhao X, Lawton MT, Nakaji P, Preul MC. 312 Intraoperative imaging of cerebral vasculature and blood flow using confocal laser endomicroscopy: new perspectives in precise real-time brain fluorescence microimaging. *Neurosurgery*. (2018) 65(Suppl. 1):126–7. doi: 10.1093/neuros/nyy303.312
40. Belykh E, Miller EJ, Hu D, Martirosyan NL, Woolf EC, Scheck AC, et al. Scanning fiber endoscope improves detection of 5-aminolevulinic acid-induced protoporphyrin IX fluorescence at the boundary of infiltrative glioma. *World Neurosurg*. (2018) 113:e51–69. doi: 10.1016/j.wneu.2018.01.151
41. Potapov AA, Goryaynov SA, Okhlopkov VA, Shishkina LV, Loschenov VB, Savelieva TA, et al. Laser biospectroscopy and 5-ALA fluorescence navigation as a helpful tool in the meningioma resection. *Neurosurg Rev*. (2016) 39:437–47. doi: 10.1007/s10143-015-0697-0
42. Potapov AA, Goriainov SA, Loshchenov VB, Savel'eva TA, Gavrilov AG, Okhlopkov VA, et al. [Intraoperative combined spectroscopy (optical biopsy) of cerebral gliomas]. *Zh Vopr Neirokhir Im N N Burdenko*. (2013) 77:3–10.
43. Stummer W, Tonn JC, Goetz C, Ullrich W, Stepp H, Bink A, et al. 5-Aminolevulinic acid-derived tumor fluorescence: the diagnostic accuracy of visible fluorescence qualities as corroborated by spectrometry and histology and postoperative imaging. *Neurosurgery*. (2014) 74:310–9; discussion: 9–20. doi: 10.1227/NEU.0000000000000267
44. Wei L, Chen Y, Yin C, Borwege S, Sanai N, Liu JTC. Optical-sectioning microscopy of protoporphyrin IX fluorescence in human gliomas: standardization and quantitative comparison with histology. *J Biomed Opt*. (2017) 22:46005. doi: 10.1117/1.JBO.22.4.046005
45. Martirosyan NL, Georges J, Eschbacher JM, Belykh E, Carotenuto A, Spetzler RF, et al. Confocal scanning microscopy provides rapid, detailed intraoperative histological assessment of brain neoplasms: experience with 106 cases. *Clin Neurol Neurosurg*. (2018) 169:21–8. doi: 10.1016/j.clineuro.2018.03.015
46. Eschbacher JM, Georges JF, Belykh E, Yazdanabadi MI, Martirosyan NL, Szeto E, et al. Immediate label-free *ex vivo* evaluation of human brain tumor biopsies with confocal reflectance microscopy. *J Neuropathol Exp Neurol*. (2017) 76:1008–22. doi: 10.1093/jnen/nlx089
47. Becker V, Vercauteren T, von Weyhern CH, Prinz C, Schmid RM, Meining A. High-resolution miniprobe-based confocal microscopy in combination with video mosaicing (with video). *Gastrointest Endosc*. (2007) 66:1001–7. doi: 10.1016/j.gie.2007.04.015
48. Schebesch KM, Brawanski A, Hohenberger C, Hohne J. Fluorescein sodium-guided surgery of malignant brain tumors: history, current concepts, and future project. *Turk Neurosurg*. (2016) 26:185–94. doi: 10.5137/1019-5149.JTN.16952-16.0
49. Kamen A, Sun S, Wan S, Kluckner S, Chen T, Gigler AM, et al. Automatic tissue differentiation based on confocal endomicroscopic images for intraoperative guidance in neurosurgery. *Biomed Res Int*. (2016) 2016:6183218. doi: 10.1155/2016/6183218
50. Izadyyazdanabadi M, Belykh E, Mooney MA, Eschbacher JM, Nakaji P, Yang Y, et al. Prospects for theranostics in neurosurgical imaging: empowering confocal laser endomicroscopy diagnostics via deep learning. *Front Oncol*. (2018) 8:240. doi: 10.3389/fonc.2018.00240
51. Izadyyazdanabadi M, Belykh E, Cavallo C, Zhao X, Gandhi S, Moreira LB, et al. Weakly-supervised learning-based feature localization for confocal laser endomicroscopy glioma images. In: Frangi A, Schnabel J, Davatzikos C, Alberola-López C, Fichtinger G, editors. *Medical Image Computing and Computer Assisted Intervention – MICCAI 2018, MICCAI 2018. Lecture Notes in Computer Science*. Vol 11071. Springer: Cham. (2018) p. 300–8. doi: 10.1007/978-3-030-00934-2_34

Conflict of Interest Statement: Carl Zeiss AG had no influence on project design, image acquisition, data interpretation and analysis, or manuscript preparation, and has no agreements for marketing or financial incentive with the Barrow Neurological Institute for the technology in this study. PN has a consultant agreement with Carl Zeiss AG. EB and JE have received travel support from Carl Zeiss AG for attendance at a scientific conference.

The remaining authors declare that the research was conducted in the absence of any commercial or financial relationships that could be construed as a potential conflict of interest.

frontiers in Oncology

PERSPECTIVE
published: 03 July 2019
doi: 10.3389/fonc.2019.00592

Toward Quantitative Neurosurgical Guidance With High-Resolution Microscopy of 5-Aminolevulinic Acid-Induced Protoporphyrin IX

Linpeng Wei[1†], *Yoko Fujita*[2†], *Nader Sanai*[2] *and Jonathan T. C. Liu*[1,3*]

[1] Department of Mechanical Engineering, University of Washington, Seattle, WA, United States, [2] Department of Neurological Surgery, Barrow Neurological Institute, Phoenix, AZ, United States, [3] Department of Pathology, University of Washington School of Medicine, Seattle, WA, United States

Low-power fluorescence microscopy of 5-ALA-induced PpIX has emerged as a valuable intraoperative imaging technology for improving the resection of malignant gliomas. However, current fluorescence imaging tools are not highly sensitive nor quantitative, which limits their effectiveness for optimizing operative decisions near the surgical margins of gliomas, in particular non-enhancing low-grade gliomas. Intraoperative high-resolution optical-sectioning microscopy can potentially serve as a valuable complement to low-power fluorescence microscopy by providing reproducible quantification of tumor parameters at the infiltrative margins of diffuse gliomas. In this forward-looking perspective article, we provide a brief discussion of recent technical advancements, pilot clinical studies, and our vision of the future adoption of handheld optical-sectioning microscopy at the final stages of glioma surgeries to enhance the extent of resection. We list a number of challenges for clinical acceptance, as well as potential strategies to overcome such obstacles for the surgical implementation of these *in vivo* microscopy techniques.

Keywords: fluorescence-guided surgery, handheld microscopy, 5-ALA, PpIX, gliomas, quantitative imaging

OPEN ACCESS

Edited by:
Mark Preul,
Barrow Neurological Institute (BNI), United States

Reviewed by:
Guolin Ma,
China-Japan Friendship Hospital, China
Di Dong,
Institute of Automation (CAS), China

***Correspondence:**
Jonathan T. C. Liu
jonliu@uw.edu

[†]*Co-first authors*

Specialty section:
This article was submitted to Cancer Imaging and Image-directed Interventions, a section of the journal Frontiers in Oncology

Received: *02 April 2019*
Accepted: *17 June 2019*
Published: *03 July 2019*

Citation:
Wei L, Fujita Y, Sanai N and Liu JTC (2019) Toward Quantitative Neurosurgical Guidance With High-Resolution Microscopy of 5-Aminolevulinic Acid-Induced Protoporphyrin IX. Front. Oncol. 9:592. doi: 10.3389/fonc.2019.00592

INTRODUCTION

Gliomas are the most common primary malignant brain tumors, with ∼20,000 new cases each year in the United States (1). As the standard-of-care for all grades of gliomas, patients generally receive surgery as a first-line treatment. The goal of this "debulking" surgery is to maximize the extent of resection (EOR) while avoiding neurological damage. Mounting evidence suggests that more-extensive EOR is associated with increased overall survival and progression-free survival for both low- and high-grade gliomas patients (2–11). Unfortunately, optimal EOR is not achieved in many patients due to the lack of effective technologies to delineate tumor margins intraoperatively, with reported rates of gross-total resection (GTR) for high-grade gliomas (HGGs) ranging from 33 to 76% (12–19) and for low-grade gliomas (LGGs) ranging from 14 to 46% (7–9, 20, 21).

In recent years, numerous reports have detailed the benefits of using 5-aminolevulinic acid (5-ALA) for guiding HGG resections (22–38). In brief, 5-ALA is a non-fluorescent prodrug that is orally administered to patients several hours prior to surgery. 5-ALA is then intra-cellularly metabolized to form a fluorescent byproduct, protoporphyrin IX (PpIX), a heme-synthesis pathway

substrate that accumulates preferentially in glioma cells due to metabolic dysregulation (39–43). In most cases, after 5-ALA administration, the bulk of a HGG tumor emits visible red fluorescence (∼630 nm) when excited with blue (∼405 nm) illumination, as viewed by the unassisted eye or with a wide-field fluorescence surgical microscope. A landmark phase III trial in Europe by Stummer et al. demonstrated that the use of this technique resulted in higher rates of GTR (65 vs. 36%) and 6-month progression-free survival (41 vs. 21.1%) compared to control patients (37). Intraoperative 5-ALA-induced fluorescence has since emerged as a valuable adjunct for HGG surgeries (22, 35–38), and has recently been approved by the US Food and Drug Administration (FDA) for neurosurgical guidance in 2017 (44).

In spite of its clear benefits, 5-ALA-based fluorescence-guided surgery (FGS) suffers from a number of shortcomings. First, it remains ineffective for guiding the resections of most LGGs and at the infiltrative margins of all diffuse gliomas (low- and high-grade) due to the fact that PpIX accumulation in these tissues is typically below the detection limit of conventional low-power wide-field surgical microscopes. Second, the visible fluorescence generated by PpIX is interpreted subjectively (45) and is difficult to quantify. This is because the visualized fluorescence is greatly affected by light-tissue interactions such as absorption and scattering, as well as detection parameters such as the angle and working distance of the microscope (46, 47). In light of these concerns, spectroscopy-based methods have been developed to provide a more accurate and reproducible measurement of the absolute concentration of PpIX expression in tissue, in which mathematical models are used to correct for the aforementioned confounding effects (22, 48–51). These quantitative detection methods should enable more-objective decision-making during tumor resection since the degree of PpIX accumulation has been shown to correlate with proliferative index, mitochondrial content, and other clinicopathologic metrics (22, 23, 40, 52, 53). However, while probe-based spectroscopy can provide improved sensitivity to detect weak PpIX fluorescence (i.e., in LGGs or at the tumor margins of all gliomas) in comparison to conventional wide-field surgical microscopy (54), spectroscopic approaches are typically limited to sampling localized points of tissue at low spatial resolution rather than generating an image over an extended field of view (FOV).

As a high-resolution, high-contrast imaging technique, handheld confocal microscopy has been explored as an alternative solution to guide the resection of both LGGs and HGGs. In 2011, a pilot study by Sanai et al. first demonstrated the feasibility of using a handheld *in vivo* confocal microscope to detect PpIX expression in LGGs (55), in which conventional wide-field surgical microscopy lacked the sensitivity to detect the PpIX fluorescence. Although the raw intensity of PpIX fluorescence, as previously mentioned, is subjective and cannot be reliably quantified, the spatial distribution (e.g., size, density, localization, etc.) of the signal can potentially serve as a reproducible tumor biomarker (56). Most recently, high-speed handheld confocal microscopy with video-mosaicking capabilities have also been developed and are continuing to be refined for 5-ALA-based FGS (57). In this perspective article, we outline a vision for a clinical workflow in which quantitative high-resolution microscopy is implemented to achieve optimal EOR for the ultimate benefit of patients suffering from LGGs and HGGs. We also describe key challenges to overcome and potential strategies to facilitate the clinical acceptance of these new technologies.

QUANTITATIVE PPIX VISUALIZATION WITH OPTICAL-SECTIONING MICROSCOPY

Optical-sectioning microscopy enables cross-sectional imaging of intact tissue at shallow depths (<0.5 mm deep) by removing the background "haze" due to out-of-focus and multiply-scattered photons. A technical description of various optical-sectioning approaches has been provided in previous review articles (58–61). In general, optical-sectioning microscopy provides the superior image contrast and spatial resolution that is necessary to detect the weak and sparse PpIX fluorescence generated by LGGs and at the infiltrative margins of all diffuse gliomas (55). An increasing number of studies have showcased the feasibility to examine PpIX expression in human gliomas at the microscopic level using optical-sectioning techniques (55, 56, 62, 63). Microscopic PpIX expression in gliomas is manifested as localized subcellular foci of fluorescence, a pattern that is consistent with our current biological understanding of subcellular PpIX generation by mitochondria (43). Quantification of microscopic PpIX expression based on a tabletop line-scanned dual-axis-confocal (LS-DAC) microscopy—a high-speed, high-contrast optical-sectioning technique—has been shown to agree with conventional fluorescence histology (56), suggesting that a miniature LS-DAC device could serve as a real-time non-invasive alternative to slide-based histopathology. As detailed in a recent review (47) and summarized in **Figure 1**, the main trade-off for high-resolution microscopy is a limited FOV that can lead to sampling bias in glioma tissues that are often spatially heterogeneous. To mitigate this problem, handheld confocal microscopy with video-mosaicking (i.e., stitching overlapping video frames to create an extended FOV over time using image processing algorithms) have been developed to sample a tissue region comparable in size to a physical biopsy specimen (several millimeters in scale) while maintaining high resolution and contrast (57, 64–68).

PROPOSED CLINICAL WORKFLOW

In the current clinical workflow for 5-ALA-based FGS, glioma margins are defined by pre-operative or intraoperative magnetic resonance imaging (MRI), as well as wide-field (low-power) surgical microscopy. However, since all gliomas are diffuse and ill-defined, the contrast-enhancing regions revealed by these wide-field imaging methods (e.g., Gd-enhancement for HGGs, T2-hyperintensity for LGGs, and macroscopic PpIX fluorescence for most HGGs) are not indicative of the actual extent of tumor infiltration. While frozen-section histopathology can confirm

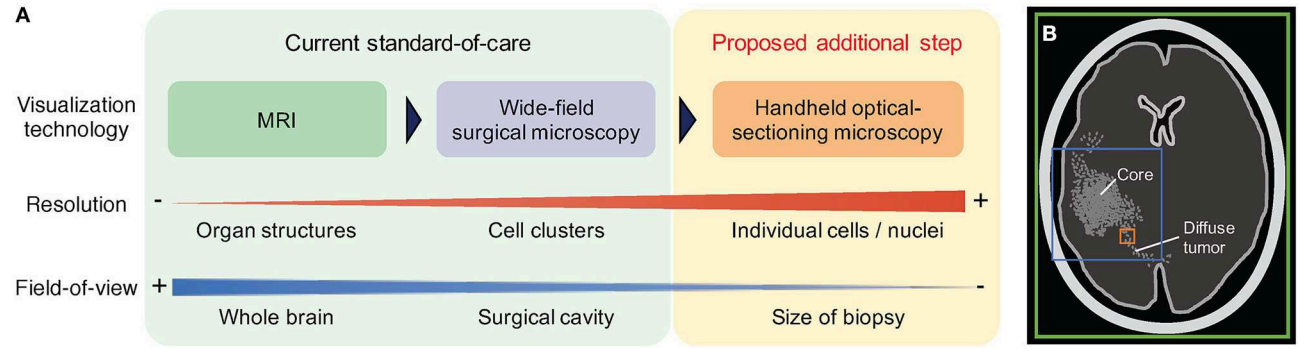

FIGURE 1 | Comparison of routine and emerging imaging techniques for neurosurgical guidance. **(A)** In the current standard-of-care, pre-operative MRI is used to assess the location and size of the bulk tumor, and wide-field surgical microscopy is used intraoperatively to guide debulking. Neither method provides sufficient spatial resolution or sensitivity to effectively visualize diffuse tumors at the surgical margins. Handheld optical-sectioning microscopy is an intraoperative imaging technique that provides superior resolution and sensitivity to detect infiltrating tumor cells at the margins, and can be potentially used to quantify tumor parameters at localized regions at the final stages of resection. **(B)** The colored boxes indicate the relative field-of-view (FOV) of the imaging modalities described. Larger FOVs are advantageous to mitigate sampling errors when imaging heterogeneous tissues, but typically require trade-offs in terms of resolution and sensitivity. Green: MRI. Blue: wide-field microscopy. Orange: optical-sectioning microscopy with mosaicking.

tissue status during the course of glioma resection, this strategy is invasive (requiring a physical biopsy) and time consuming. Our hypothesis, to be investigated in future prospective studies, is that when operating on gliomas adjacent to eloquent cortical and subcortical pathways, quantitative high-resolution microscopy can be used at the final stages of resection to interrogate tumor burden and other quantitative biomarkers at multiple suspicious sites in order to optimize the EOR (including beyond the radiographic margins) without jeopardizing functional pathways. As shown in **Figure 2**, a specific workflow for future clinical use is provided below:

(1) At the initial stages of the surgery, standard neurosurgical methods will be used for debulking the central portions of the tumor. As the neurosurgeon approaches the radiographic or functional boundaries of the tumor (indicated by anatomical/visual cues, MRI-based neuronavigation, intraoperative stimulation mapping, and 5-ALA-based FGS using wide-field surgical microscopy), regions adjacent to non-eloquent brain can be resected more aggressively to minimize residual tumor burden.

(2) At the final stages of surgery, ambiguous regions at critical locations (e.g., near eloquent brain) will be probed with high-resolution video-mosaicked microscopy of the exposed tissue surfaces, enabling a quantitative measure of microscopic PpIX expression that should ideally correlate with clinicopathologic metrics such as tumor burden and proliferative/mitotic index in order to guide operative decision-making. This provides a non-invasive and real-time alternative to intraoperative consultation with frozen-section histology. It should be noted that similar sterile probe-based microscopy/spectroscopy strategies have been implemented during neurosurgeries, as described in several reports (69–73).

(3) Conventional surgical tools (e.g., ultrasonic aspirator, suction catheters, etc.) will be used in an iterative process with intraoperative microscopy until optimal resection has been achieved. Ideally, neuronavigation would be used to track the spatial coordinates of all surgical devices (microscope, suction catheters, etc.) to ensure good co-registration between iterative rounds of imaging and resection.

CHALLENGES AND FUTURE STEPS

A number of translational milestones should ideally be achieved in order to bolster confidence in a high-resolution intraoperative imaging technique for adoption by surgeons. First, and perhaps the most critical step, is to establish a biological context and understanding of the pattern of sub-cellular PpIX expression that is visualized with an optical-sectioning microscope. Note that numerous studies have already shown that PpIX expression provides specific delineation of a variety of neoplasms under wide-field (low-resolution) imaging and spectroscopy (52, 74, 75), including a general correlation between PpIX concentrations and proliferative score as well as World Health Organization (WHO) histologic score (52). Preliminary studies [e.g., using high-resolution *in vivo* microscopy (55), or using fluorescent-activated cell sorting of dissociated human cells [unpublished data]] have also shown that PpIX expression at the cellular level is highly tumor-specific. However, larger-scale correlation studies are needed to improve our ability to interpret high-resolution images of PpIX in gliomas. For example, studies should ideally demonstrate a clear correlation between subcellular patterns of PpIX fluorescence and well-established clinicopathologic metrics such as tumor burden and proliferative/mitotic index (e.g., Ki-67 and pHH3 expression). Facilitated by the recent advancements in both imaging hardware [e.g., open-top light-sheet microscopy (63)] and artificial intelligence (e.g., deep-learning algorithms for classification and regression tasks), it should be possible to perform large correlative studies within a reasonable timeline. A second milestone, as mentioned previously, is to mitigate sampling bias due to tissue heterogeneity and to more-closely match the spatial precision of current surgical tools (typically several millimeters in scale). While it is technically challenging

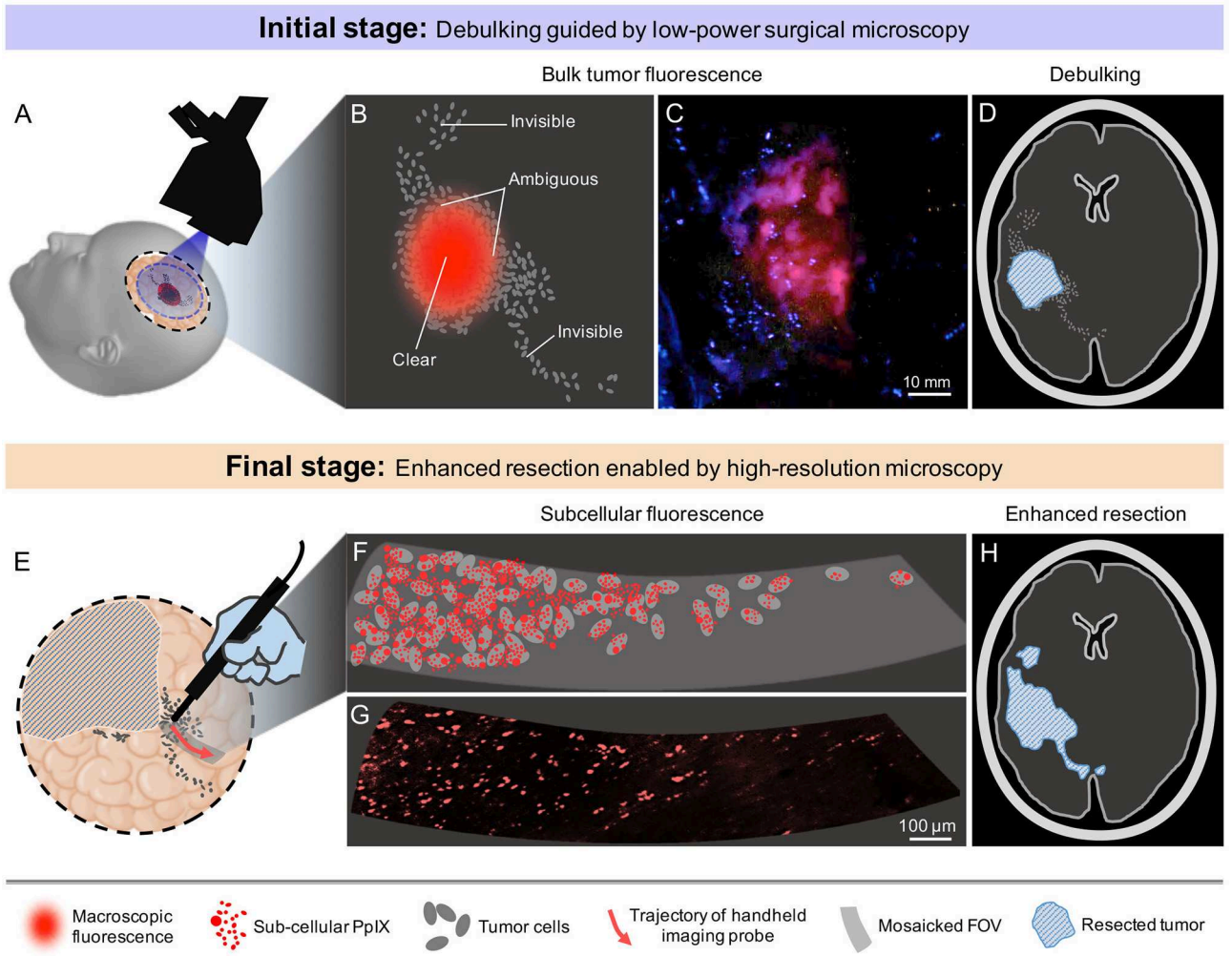

FIGURE 2 | Proposed clinical workflow of 5-ALA-based fluorescence-guided neurosurgery. **(A)** Conventional low-power fluorescence surgical microscopy provides a wide FOV that often covers the entire surgical cavity. **(B)** Macroscopic PpIX fluorescence is visible at the central portions of most HGGs, but not at the infiltrative margins. **(C)** Example low-power fluorescence microscopy image of PpIX expression from a bulk HGG region. The margins of the tumor are subjectively delineated and ambiguous. **(D)** Debulking guided by macroscopic PpIX fluorescence, resulting in residual tumor burden. **(E)** High-sensitivity probe-based optical-sectioning microscopy is used to examine localized regions near the surgical margins, providing a non-invasive alternative to intraoperative frozen section histopathology. **(F)** Visualization of subcellular PpIX fluorescence can potentially enable quantification of tumor parameters in order to guide surgical decisions at the final stages of resection. **(G)** Example image of microscopic PpIX fluorescence in a HGG biopsy using high-resolution optical-sectioning microscopy. **(H)** Optimal extent of resection is achieved after iterative tumor resection guided by video-mosaicked handheld optical-sectioning microscopy.

to engineer high-resolution microscopes with such large FOVs, robust computer vision algorithms have been developed and continue to be refined to stitch overlapping image frames together to create an extended FOV in real time while an imaging device is translated along the tissue surface (57, 64–68).

It bears repeating that the goal of optical-sectioning microscopy is NOT to image deeply, but rather to perform quantitative imaging near the exposed tissue surface, which requires the high contrast of an optical-sectioning device. However, in practice, the ability to image over a shallow range of depths (<150 microns) may be of practical value to identify an optimal depth where image quality and tissue integrity are maximized. Complementary imaging modalities for detecting PpIX fluorescence from deep subsurface tumors (76–78) are beyond the scope of this perspective paper. In terms of resolution, since current resection tools lack the spatial precision of a high-resolution microscope, the value of high-resolution imaging is not to enable cellular-scale resection, but to enable accurate quantification of PpIX, which in turn should correlate with relevant metrics of tumor burden/proliferation to guide surgical decisions. As with all innovative technologies, clinical validation is needed through well-powered and controlled studies. For example, "malignancy scores" based on quantitative PpIX microscopy should agree with traditional assessment methods such as histopathology and post-operative MRI, and should also be predictive of patient outcomes (e.g., recurrence). Note that

for most glioma patients, adjuvant radiotherapy is a logical next-step following tumor resection. The development of technology that enables microscopic quantification of tumor burden and proliferation, and therefore identification of resection cavity regions with high-risk of tumor recurrence, could also inform postoperative radiotherapy planning and improve the efficacy of radiation-based strategies to control tumor progression.

In summary, the recent FDA approval of 5-ALA-based FGS and the advancement of fluorescence imaging technologies have provided a unique opportunity to improve glioma surgeries. We believe that handheld video-mosaicked optical-sectioning microscopy has an important role to play in improving the EOR for glioma surgeries through quantitative and reproducible delineation of the infiltrative margins of diffuse gliomas, for which current techniques fail to provide adequate guidance at the final most-critical stages of resection procedures. The successful translation of this technology will require collaborative efforts amongst multidisciplinary teams that include optical engineers, neurosurgeons, pathologists/biologists, computer scientists, industry partners, and regulatory/reimbursement stakeholders. Together with wide-field imaging techniques such as MRI and low-power surgical microscopy, we have provided a perspective that the use of intraoperative high-resolution microscopy within the surgical armamentarium should yield significant improvements in glioma patient outcomes.

DATA AVAILABILITY

No datasets were generated or analyzed for this study.

AUTHOR CONTRIBUTIONS

All authors listed have made a substantial, direct and intellectual contribution to the work, and approved it for publication.

FUNDING

We acknowledge funding support from the NIH, including grants from the NIDCR (R01 DE023497), the NCI (R01 CA175391), and the NINDS (R01 NS082745).

REFERENCES

1. Ostrom QT, Gittleman H, Liao P, Vecchione-Koval T, Wolinsky Y, Kruchko C, et al. CBTRUS Statistical report: primary brain and other central nervous system tumors diagnosed in the United States in 2010-2014. *Neuro Oncol.* (2017) 19(suppl_5):v1-v88. doi: 10.1093/neuonc/nox158
2. Hervey-Jumper SL, Berger MS. Evidence for improving outcome through extent of resection. *Neurosurg Clin N Am.* (2019) 30:85–93. doi: 10.1016/j.nec.2018.08.005
3. Lau D, Hervey-Jumper SL, Han SJ, Berger MS. Intraoperative perception and estimates on extent of resection during awake glioma surgery: overcoming the learning curve. *J Neurosurg.* (2018) 128:1410–8. doi: 10.3171/2017.1.JNS161811
4. Sharma M, Bellamkonda S, Mohapatra S, Meola A, Jia X, Mohammadi A, et al. Correlation between the residual tumor volume, extent of tumor resection, and O6-methylguanine DNA methyltransferase status in patients with glioblastoma. *World Neurosurg.* (2018) 116:e147-e61. doi: 10.1016/j.wneu.2018.04.134
5. Ahmadi R, Rezvan A, Dictus C, Christine D, Hartmann C, Christian H, et al. Long-term outcome and survival of surgically treated supratentorial low-grade glioma in adult patients. *Acta Neurochir.* (2009) 151:1359–65. doi: 10.1007/s00701-009-0435-x
6. Keles GE, Lamborn KR, Berger MS. Low-grade hemispheric gliomas in adults: a critical review of extent of resection as a factor influencing outcome. *J Neurosurg.* (2001) 95:735–45. doi: 10.3171/jns.2001.95.5.0735
7. McGirt MJ, Chaichana KL, Attenello FJ, Weingart JD, Than K, Burger PC, et al. Extent of surgical resection is independently associated with survival in patients with hemispheric infiltrating low-grade gliomas. *Neurosurgery.* (2008) 63:700–7- author reply 7-8. doi: 10.1227/01.NEU.0000325729.41085.73
8. Sanai N, Polley M-Y, Berger MS. Insular glioma resection: assessment of patient morbidity, survival, and tumor progression. *J Neurosurg.* (2010) 112:1–9. doi: 10.3171/2009.6.JNS0952
9. Smith JS, Chang EF, Lamborn KR, Chang SM, Prados MD, Cha S, et al. Role of extent of resection in the long-term outcome of low-grade hemispheric gliomas. *J Clin Oncol.* (2008) 26:1338–45. doi: 10.1200/JCO.2007.13.9337
10. Stummer W, van den Bent MJ, Westphal M. Cytoreductive surgery of glioblastoma as the key to successful adjuvant therapies: new arguments in an old discussion. *Acta Neurochir.* (2011) 153:1211–8. doi: 10.1007/s00701-011-1001-x
11. Stummer W, Reulen H-J, Meinel T, Pichlmeier U, Schumacher W, Tonn J-C, et al. Extent of resection and survival in glioblastoma multiforme: identification of and adjustment for bias. *Neurosurgery.* (2008) 62:564–76; discussion−76. doi: 10.1227/01.neu.0000317304.31579.17
12. DAmico RS, Englander ZK, Canoll P, Bruce JN. Extent of resection in glioma-a review of the cutting edge. *World Neurosurg.* (2017) 103:538–49. doi: 10.1016/j.wneu.2017.04.041
13. Hervey-Jumper SL, Berger MS. Maximizing safe resection of low- and high-grade glioma. *J Neurooncol.* (2016) 130:269–82. doi: 10.1007/s11060-016-2110-4
14. Sanai N, Berger MS. Operative techniques for gliomas and the value of extent of resection. *Neurother J Am Soc Exp NeuroTher.* (2009) 6:478–86. doi: 10.1016/j.nurt.2009.04.005
15. Brown PD, Maurer MJ, Rummans TA, Pollock BE, Ballman KV, Sloan JA, et al. A prospective study of quality of life in adults with newly diagnosed high-grade gliomas: the impact of the extent of resection on quality of life and survival. *Neurosurgery.* (2005) 57:495–504- discussion 495-504. doi: 10.1227/01.NEU.0000170562.25335.C7
16. Chaichana KL, Halthore AN, Parker SL, Olivi A, Weingart JD, Brem H, et al. Factors involved in maintaining prolonged functional independence following supratentorial glioblastoma resection. *J Neurosurg.* (2011) 114:604–12. doi: 10.3171/2010.4.JNS091340
17. Chaichana KL, Kosztowski T, Niranjan A, Olivi A, Weingart JD, Laterra J, et al. Prognostic significance of contrast-enhancing anaplastic astrocytomas in adults. *J Neurosurg.* (2010) 113:286–92. doi: 10.3171/2010.2.JNS091010
18. Stark AM, Nabavi A, Mehdorn HM, Blömer U. Glioblastoma multiforme-report of 267 cases treated at a single institution. *Surg Neurol.* (2005) 63:162–9-discussion 9. doi: 10.1016/j.surneu.2004.01.028
19. Ushio Y, Kochi M, Hamada J-i, Kai Y, Nakamura H. Effect of surgical removal on survival and quality of life in patients with supratentorial glioblastoma. *Neurol Med Chir.* (2005) 45:454–60- discussion 60-1. doi: 10.2176/nmc.45.454
20. Patel T, Bander ED, Venn RA, Powell T, Cederquist GY-M, Schaefer PM, et al. The role of extent of resection in IDH1 wild-type or mutant low-grade gliomas. *Neurosurgery.* (2018) 82:808–14. doi: 10.1093/neuros/nyx265
21. Wijnenga MMJ, French PJ, Dubbink HJ, Dinjens WNM, Atmodimedjo PN, Kros JM, et al. The impact of surgery in molecularly defined low-grade glioma: an integrated clinical, radiological, and molecular analysis. *Neuro-Oncology.* (2018) 20:103–12. doi: 10.1093/neuonc/nox176
22. Valdes PA, Leblond F, Kim A, Harris BT, Wilson BC, Fan XY, et al. Quantitative fluorescence in intracranial tumor: implications for ALA-induced PpIX as an intraoperative biomarker. *J Neurosurg.* (2011) 115:11–7. doi: 10.3171/2011.2.JNS101451

23. Stummer W, Tonn JC, Goetz C, Ullrich W, Stepp H, Bink A, et al. 5-Aminolevulinic acid-derived tumor fluorescence: the diagnostic accuracy of visible fluorescence qualities as corroborated by spectrometry and histology and postoperative imaging. *Neurosurgery*. (2014) 74:310–9; discussion 9-20. doi: 10.1227/NEU.0000000000000267
24. Stummer W, Novotny A, Stepp H, Goetz C, Bise K, Reulen HJ. Fluorescence-guided resection of glioblastoma multiforme by using 5-aminolevulinic acid-induced porphyrins: a prospective study in 52 consecutive patients. *J Neurosurg*. (2000) 93:1003–13. doi: 10.3171/jns.2000.93.6.1003
25. Panciani PP, Fontanella M, Schatlo B, Garbossa D, Agnoletti A, Ducati A, et al. Fluorescence and image guided resection in high grade glioma. *Clin Neurol Neurosurg*. (2012) 114:37–41. doi: 10.1016/j.clineuro.2011.09.001
26. Yamada S, Muragaki Y, Maruyama T, Komori T, Okada Y. Role of neurochemical navigation with 5-aminolevulinic acid during intraoperative MRI-guided resection of intracranial malignant gliomas. *Clin Neurol Neurosurg*. (2015) 130:134–9. doi: 10.1016/j.clineuro.2015.01.005
27. Roberts DW, Valdes PA, Harris BT, Fontaine KM, Hartov A, Fan X, et al. Coregistered fluorescence-enhanced tumor resection of malignant glioma: relationships between delta-aminolevulinic acid-induced protoporphyrin IX fluorescence, magnetic resonance imaging enhancement, and neuropathological parameters. *J Neurosurg*. (2011) 114:595–603. doi: 10.3171/2010.2.JNS091322
28. Diez Valle R, Tejada Solis S, Idoate Gastearena MA, Garcia de Eulate R, Dominguez Echavarri P, Aristu Mendiroz J. Surgery guided by 5-aminolevulinic fluorescence in glioblastoma: volumetric analysis of extent of resection in single-center experience. *J Neurooncol*. (2011) 102:105–13. doi: 10.1007/s11060-010-0296-4
29. Hefti M, von Campe G, Moschopulos M, Siegner A, Looser H, Landolt H. 5-aminolevulinic acid induced protoporphyrin IX fluorescence in high-grade glioma surgery: a one-year experience at a single institutuion. *Swiss Med Wkly*. (2008) 138:180–5.
30. Acerbi F, Broggi M, Eoli M, Anghileri E, Cuppini L, Pollo B, et al. Fluorescein-guided surgery for grade IV gliomas with a dedicated filter on the surgical microscope: preliminary results in 12 cases. *Acta Neurochir*. (2013) 155:1277–86. doi: 10.1007/s00701-013-1734-9
31. Tsugu A, Ishizaka H, Mizokami Y, Osada T, Baba T, Yoshiyama M, et al. Impact of the combination of 5-aminolevulinic acid-induced fluorescence with intraoperative magnetic resonance imaging-guided surgery for glioma. *World Neurosurg*. (2011) 76:120–7. doi: 10.1016/j.wneu.2011.02.005
32. Hadjipanayis CG, Widhalm G, Stummer W. What is the surgical benefit of utilizing 5-aminolevulinic acid for fluorescence-guided surgery of malignant gliomas? *Neurosurgery*. (2015) 77:663–73. doi: 10.1227/NEU.0000000000000929
33. Rapp M, Kamp M, Steiger HJ, Sabel M. Endoscopic-assisted visualization of 5-aminolevulinic acid-induced fluorescence in malignant glioma surgery: a technical note. *World Neurosurg*. (2014) 82:E277–E9. doi: 10.1016/j.wneu.2013.07.002
34. Belloch JP, Rovira V, Llacer JL, Riesgo PA, Cremades A. Fluorescence-guided surgery in high grade gliomas using an exoscope system. *Acta Neurochir*. (2014) 156:653–60. doi: 10.1007/s00701-013-1976-6
35. Liao H, Noguchi M, Maruyama T, Muragaki Y, Kobayashi E, Iseki H, et al. An integrated diagnosis and therapeutic system using intra-operative 5-aminolevulinic-acid-induced fluorescence guided robotic laser ablation for precision neurosurgery. *Med Image Anal*. (2012) 16:754–66. doi: 10.1016/j.media.2010.11.004
36. Nabavi A, Thurm H, Zountsas B, Pietsch T, Lanfermann H, Pichlmeier U, et al. Five-aminolevulinic acid for fluorescence-guided resection of recurrent malignant gliomas: a phase ii study. *Neurosurgery*. (2009) 65:1070–6; discussion 6-7. doi: 10.1227/01.NEU.0000360128.03597.C7
37. Stummer W, Pichlmeier U, Meinel T, Wiestler OD, Zanella F, Reulen H-J, et al. Fluorescence-guided surgery with 5-aminolevulinic acid for resection of malignant glioma: a randomised controlled multicentre phase III trial. *Lancet Oncol*. (2006) 7:392–401. doi: 10.1016/S1470-2045(06)70665-9
38. Tonn J-C, Stummer W. Fluorescence-guided resection of malignant gliomas using 5-aminolevulinic acid: practical use, risks, and pitfalls. *Clin Neurosurg*. (2008) 55:20–6.
39. Duffner F, Ritz R, Freudenstein D, Weller M, Dietz K, Wessels J. Specific intensity imaging for glioblastoma and neural cell cultures with 5-aminolevulinic acid-derived protoporphyrin IX. *J Neurooncol*. (2005) 71:107–11. doi: 10.1007/s11060-004-9603-2
40. Gibbs SL, Chen B, O'Hara JA, Hoopes PJ, Hasan T, Pogue BW. Protoporphyrin IX level correlates with number of mitochondria, but increase in production correlates with tumor cell size. *Photochem Photobiol*. (2006) 82:1334–41. doi: 10.1562/2006-03-11-RA-843
41. Olivo M, Wilson BC. Mapping ALA-induced PPIX fluorescence in normal brain and brain tumour using confocal fluorescence microscopy. *Int J Oncol*. (2004) 25:37–45. doi: 10.3892/ijo.25.1.37
42. Stummer W, Stocker S, Novotny A, Heimann A, Sauer O, Kempski O, et al. *In vitro* and *in vivo* porphyrin accumulation by C6 glioma cells after exposure to 5-aminolevulinic acid. *J Photochem Photobiol B Biol*. (1998) 45:160–9. doi: 10.1016/S1011-1344(98)00176-6
43. Stepp H, Stummer W. 5-ALA in the management of malignant glioma. *Lasers Surg Med*. (2018) 50:399–419. doi: 10.1002/lsm.22933
44. Aminolevulinic acid hydrochloride, known as ALA HCl (Gleolan, NX Development Corp.) as an optical imaging agent indicated in patients with gliomas (2017).
45. Lau D, Hervey-Jumper SL, Chang S, Molinaro AM, McDermott MW, Phillips JJ, et al. A prospective Phase II clinical trial of 5-aminolevulinic acid to assess the correlation of intraoperative fluorescence intensity and degree of histologic cellularity during resection of high-grade gliomas. *J Neurosurg*. (2016) 124:1300–9. doi: 10.3171/2015.5.JNS1577
46. Valdes PA, Leblond F, Jacobs VL, Wilson BC, Paulsen KD, Roberts DW. Quantitative, spectrally-resolved intraoperative fluorescence imaging. *Sci Rep*. (2012) 2:798. doi: 10.1038/srep00798
47. Wei L, Roberts D, Sanai N, Liu JTC. Visualization technologies for 5-ALA-based fluorescence-guided surgeries. *J Neuro-Oncol*. (2019) 2019:9. doi: 10.1007/s11060-018-03077-9
48. Haj-Hosseini N, Richter J, Andersson-Engels S, Wardell K. Optical touch pointer for fluorescence guided glioblastoma resection using 5-aminolevulinic acid. *Lasers Surg Med*. (2010) 42:9–14. doi: 10.1002/lsm.20868
49. Kim A, Khurana M, Moriyama Y, Wilson BC. Quantification of in vivo fluorescence decoupled from the effects of tissue optical properties using fiber-optic spectroscopy measurements. *J Biomed Optics*. (2010) 15:6. doi: 10.1117/1.3523616
50. Ishihara R, Katayama Y, Watanabe T, Yoshino A, Fukushima T, Sakatani K. Quantitative spectroscopic analysis of 5-aminolevulinic acid-induced protoporphyrin IX fluorescence intensity in diffusely infiltrating astrocytomas. *Neurol Med Chir*. (2007) 47:53–7; discussion 7. doi: 10.2176/nmc.47.53
51. Utsuki S, Oka H, Sato S, Suzuki S, Shimizu S, Tanaka S, et al. Possibility of using laser spectroscopy for the intraoperative detection of nonfluorescing brain tumors and the boundaries of brain tumor infiltrates - Technical note. *J Neurosurg*. (2006) 104:618–20. doi: 10.3171/jns.2006.104.4.618
52. Valdes PA, Kim A, Brantsch M, Niu C, Moses ZB, Tosteson TD, et al. delta-aminolevulinic acid-induced protoporphyrin IX concentration correlates with histopathologic markers of malignancy in human gliomas: the need for quantitative fluorescence-guided resection to identify regions of increasing malignancy. *Neuro Oncol*. (2011) 13:846–56. doi: 10.1093/neuonc/nor086
53. Belykh E, Miller EJ, Hu D, Martirosyan NL, Woolf EC, Scheck AC, et al. Scanning fiber endoscope improves detection of 5-aminolevulinic acid-induced protoporphyrin IX fluorescence at the boundary of infiltrative glioma. *World Neurosurg*. (2018) 113:e51-e69. doi: 10.1016/j.wneu.2018.01.151
54. Valdes PA, Jacobs V, Harris BT, Wilson BC, Leblond F, Paulsen KD, et al. Quantitative fluorescence using 5-aminolevulinic acid-induced protoporphyrin IX biomarker as a surgical adjunct in low-grade glioma surgery. *J Neurosurg*. (2015) 123:771–80. doi: 10.3171/2014.12.JNS14391
55. Sanai N, Snyder LA, Honea NJ, Coons SW, Eschbacher JM, Smith KA, et al. Intraoperative confocal microscopy in the visualization of 5-aminolevulinic acid fluorescence in low-grade gliomas. *J Neurosurg*. (2011) 115:740–8. doi: 10.3171/2011.6.JNS11252
56. Wei L, Chen Y, Yin C, Borwege S, Sanai N, Liu JTC. Optical-sectioning microscopy of protoporphyrin IX fluorescence in human gliomas:

standardization and quantitative comparison with histology. *J Biomed Opt*. (2017) 22:46005. doi: 10.1117/1.JBO.22.4.046005
57. Wei L, Yin C, Fujita Y, Sanai N, Liu JTC. Handheld line-scanned dual-axis confocal microscope with pistoned MEMS actuation for flat-field fluorescence imaging. *Opt Lett*. (2019) 44:671–4. doi: 10.1364/OL.44.000671
58. Conchello JA, Lichtman JW. Optical sectioning microscopy. *Nat Methods*. (2005) 2:920–31. doi: 10.1038/nmeth815
59. Helmchen F, Denk W. Deep tissue two-photon microscopy. *Nat Methods*. (2005) 2:932–40. doi: 10.1038/nmeth818
60. Huisken J, Stainier DY. Selective plane illumination microscopy techniques in developmental biology. *Development*. (2009) 136:1963–75. doi: 10.1242/dev.022426
61. Wei L, Yin C, Liu JTC. Dual-axis confocal microscopy for point-of-care pathology. *IEEE J Select Topics Quantum Electron*. (2019) 25:1–10. doi: 10.1109/JSTQE.2018.2854572
62. Meza D, Wang D, Wang Y, Borwege S, Sanai N, Liu JT. Comparing high-resolution microscopy techniques for potential intraoperative use in guiding low-grade glioma resections. *Lasers Surg Med*. (2015) 47:289–95. doi: 10.1002/lsm.22347
63. Glaser AK, Reder NP, Chen Y, McCarty EF, Yin C, Wei L, et al. Light-sheet microscopy for slide-free non-destructive pathology of large clinical specimens. *Nat Biomed Eng*. (2017) 1:0084. doi: 10.1038/s41551-017-0084
64. Vercauteren T, Perchant A, Pennec X, Ayache N. Mosaicing of confocal microscopic *in vivo* soft tissue video sequences. *Lect Notes Comput Sc*. (2005) 3749:753–60. doi: 10.1007/11566465_93
65. Vercauteren T, Perchant A, Malandain G, Pennec X, Ayache N. Robust mosaicing with correction of motion distortions and tissue deformations for *in vivo* fibered microscopy. *Med Image Anal*. (2006) 10:673–92. doi: 10.1016/j.media.2006.06.006
66. Loewke KE, Camarillo DB, Piyawattanametha W, Mandella MJ, Contag CH, Thrun S, et al. *In vivo* micro-image mosaicing. *IEEE T Bio-Med Eng*. (2011) 58:159–71. doi: 10.1109/TBME.2010.2085082
67. Kose K, Cordova M, Duffy M, Flores ES, Brooks DH, Rajadhyaksha M. Video-mosaicing of reflectance confocal images for examination of extended areas of skin *in vivo*. *Br J Dermatol*. (2014) 171:1239–41. doi: 10.1111/bjd.13050
68. Kose K, Gou M, Yelamos O, Cordova M, Rossi AM, Nehal KS, et al. Automated video-mosaicking approach for confocal microscopic imaging *in vivo*: an approach to address challenges in imaging living tissue and extend field of view. *Sci Rep*. (2017) 7:10759. doi: 10.1038/s41598-017-11072-9
69. Martirosyan NL, Eschbacher JM, Kalani MYS, Turner JD, Belykh E, Spetzler RF, et al. Prospective evaluation of the utility of intraoperative confocal laser endomicroscopy in patients with brain neoplasms using fluorescein sodium: experience with 74 cases. *Neurosurg Focus*. (2016) 40:3. doi: 10.3171/2016.1.FOCUS15559
70. Pavlov V, Meyronet D, Meyer-Bisch V, Armoiry X, Pikul B, Dumot C, et al. Intraoperative probe-based confocal laser endomicroscopy in surgery and stereotactic biopsy of low-grade and high-grade gliomas: a feasibility study in humans. *Neurosurgery*. (2016) 79:604–12. doi: 10.1227/NEU.0000000000001365
71. Belykh E, Cavallo C, Gandhi S, Zhao X, Veljanoski D, Izady Yazdanabadi M, et al. Utilization of intraoperative confocal laser endomicroscopy in brain tumor surgery. *J Neurosurg Sci*. (2018) 2018:8. doi: 10.23736/S0390-5616.18.04553-8
72. Sanai N, Eschbacher J, Hattendorf G, Coons SW, Preul MC, Smith KA, et al. Intraoperative confocal microscopy for brain tumors: a feasibility analysis in humans. *Neurosurgery*. (2011) 68(2 Suppl Operative):282–90; discussion 90. doi: 10.1227/NEU.0b013e318212464e
73. Eschbacher J, Martirosyan NL, Nakaji P, Sanai N, Preul MC, Smith KA, et al. *In vivo* intraoperative confocal microscopy for real-time histopathological imaging of brain tumors. *J Neurosurg*. (2012) 116:854–60. doi: 10.3171/2011.12.JNS11696
74. Yano H, Nakayama N, Ohe N, Miwa K, Shinoda J, Iwama T. Pathological analysis of the surgical margins of resected glioblastomas excised using photodynamic visualization with both 5-aminolevulinic acid and fluorescein sodium. *J Neurooncol*. (2017) 133:389–97. doi: 10.1007/s11060-017-2445-5
75. Yoneda T, Nonoguchi N, Ikeda N, Yagi R, Kawabata S, Furuse M, et al. Spectral radiance of protoporphyrin IX fluorescence and its histopathological implications in 5-aminolevulinic acid-guided surgery for glioblastoma. *Photomed Laser Surg*. (2018) 36:266–72. doi: 10.1089/pho.2017.4384
76. Konecky SD, Owen CM, Rice T, Valdes PA, Kolste K, Wilson BC, et al. Spatial frequency domain tomography of protoporphyrin IX fluorescence in preclinical glioma models. *J Biomed Opt*. (2012) 17:056008. doi: 10.1117/1.JBO.17.5.056008
77. Roberts DW, Olson JD, Evans LT, Kolste KK, Kanick SC, Fan X, et al. Red-light excitation of protoporphyrin IX fluorescence for subsurface tumor detection. *J Neurosurg*. (2018) 128:1690–7. doi: 10.3171/2017.1.JNS162061
78. Kolste KK, Kanick SC, Valdes PA, Jermyn M, Wilson BC, Roberts DW, et al. Macroscopic optical imaging technique for wide-field estimation of fluorescence depth in optically turbid media for application in brain tumor surgical guidance. *J Biomed Opt*. (2015) 20:26002. doi: 10.1117/1.JBO.20.2.026002

Conflict of Interest Statement: The authors declare that the research was conducted in the absence of any commercial or financial relationships that could be construed as a potential conflict of interest.

The handling editor declared a shared institutional affiliation, though no other collaboration, with several of the authors (YF, NS).

frontiers in Surgery

TECHNOLOGY REPORT
published: 16 July 2019
doi: 10.3389/fsurg.2019.00041

Quantitative Modulation of PpIX Fluorescence and Improved Glioma Visualization

Michael Reinert[1,2,3,4]*, *Deborah Piffaretti*[1,5], *Marco Wilzbach*[6], *Christian Hauger*[6], *Roland Guckler*[6], *Francesco Marchi*[1,2] and *Maria Luisa D'Angelo*[1]

[1] Laboratory for Biomedical Neurosciences, Neurocenter of Southern Switzerland, Ente Ospedaliero Cantonale, Torricella-Taverne, Switzerland, [2] Department of Neurosurgery, Neurocenter of Southern Switzerland, Ente Ospedaliero Cantonale, Lugano, Switzerland, [3] Faculty of Biomedical Neurosciences, Università Della Svizzera Italiana, Lugano, Switzerland, [4] Medical Faculty, University of Bern, Bern, Switzerland, [5] Faculty of Medicine, Graduate School for Cellular and Biomedical Sciences, University of Bern, Bern, Switzerland, [6] Carl Zeiss Meditec AG, Oberkochen, Germany

5-Aminolevulinic acid (5-ALA) induced fluorescence to augment surgical resection for high grade glioma has become a standard of care. Protoporphyrin IX (PpIX) visibility is however subject to the variability of the single tumor expression and to the interobserver interpretation. We therefore hypothesized that in different glioma cell lines with variable 5-ALA induced fluorescence, the signal can be pharmacologically increased. We therefore analyzed in three different GBM cell lines, with different expression of epidermal growth factor receptor (EGFR), the variability of 5-ALA induced PpIX fluorescence after the pharmacological blockade at different steps of PpIX breakdown and influencing the outbound transport of PpIX. Using flow cytometry, fluorescence microplate reader, and confocal microscopy the PpIX fluorescence was analyzed after exposure to tin protoporphyrin IX (SnPP), deferoxamine (DFO), and genistein. We furthermore constructed a microscope (Qp9-microscope) being able to measure quantitatively the concentration of PpIX. These values were compared with the extraction of PpIX in tumor biopsy taken during the GBM surgery. Although all three cell lines showed an increase to 5-ALA induced fluorescence their baseline activity was different. Treatment with either SnPP, DFO and genistein was able to increase 5-ALA induced fluorescence. Qp9-microscopy of tumor sample produced a color coded PpIX concentration map which was overlaid on the tumor image. The PpIX extraction from tumor sample analyzed using the plate reader gave lower values of the concentration, as compared to the expected values of the Qp9-microscope, however still in the same decimal range of μg/mL. This may be due to homogenization of the values during extraction and cell disaggregation. In conclusion pharmacological augmentation in GBM cell lines of PpIX signal is possible. A quantitative PpIX map for surgery is feasible and may help refine surgical excision. Further correlations of tumor tissue samples and Qp9-microscopy is needed, prior to develop an intraoperative surgical adjunct to the already existing 5-ALA induced surgery.

Keywords: GBM—glioblastoma multiforme, 5-ALA=5-aminolevulinic acid, protoporphyin IX, quantification, breakdown, visualization, microscope

OPEN ACCESS

Edited by:
Mark Preul,
Barrow Neurological Institute (BNI), United States

Reviewed by:
Claudio Cavallo,
Vanderbilt University, United States
Peter Nakaji,
Barrow Neurological Institute (BNI), United States

***Correspondence:**
Michael Reinert
michael.reinert@eoc.ch

Specialty section:
This article was submitted to Neurosurgery, a section of the journal Frontiers in Surgery

Received: *01 March 2019*
Accepted: *21 June 2019*
Published: *16 July 2019*

Citation:
Reinert M, Piffaretti D, Wilzbach M, Hauger C, Guckler R, Marchi F and D'Angelo ML (2019) Quantitative Modulation of PpIX Fluorescence and Improved Glioma Visualization. Front. Surg. 6:41. doi: 10.3389/fsurg.2019.00041

INTRODUCTION

It is widely accepted that the extent of surgical resection plays an important role in overall survival in patients with glioma, both in IDH wild type and IDH mutated, and both in high grade and low-grade glioma (1, 2). In high-grade glioma, the extent of resection is guided by MRI and directed to the contrast-enhancing portion of the lesion, while in low-grade glioma the resection is decided based on the tumor infiltration shown by T2 sequence alteration (3, 4). New techniques as fluorescence have become a standard of care for intraoperative resection of high grade glioma (4). Nowadays, however, growing evidence support the use of these detection techniques also in low grade glioma (5). PpIX fluorescence and its concentration in tumor cells depends on the balance between its synthesis, catabolism and outflow. The amount of PpIX in tumor cells is favored by both the activity of cytosolic porphobilinogen deaminase (PBGD) during the replication phase, and by the down-regulation of ferrochelatase (FECH) (6). However, other factors such as protein transporters, tyrosine kinase activity and its downstream effect on hemoxygenase-1 (HO-1), availability of free Fe^{2+}-ions and its effect on FECH, are related with PpIX fluorescence (7, 8). Because of the above mentioned factors, the final enhancing results are highly variable and difficult to predict both in clinical and laboratory setting, and might also depend on EGFR expression status in glioma cell lines (7). Proteins transporters such as ATP-binding cassette subfamily G member 2 (ABCG2) regulate intracellular concentration of PpIX. These proteins may also be differently expressed or activated in relation with the epigenetic status of GBM (9) (**Figure 1**).

Further well-known factors such as 5-ALA patient administration concentration, exposure time and tumor cell concentration influence the concentration of PpIX at the local level (4, 10). Furthermore, fading requires also consideration during light exposure. Also, 5-ALA fluorescence may vary spatially from one area to another of GBM (11). Lastly, two further factor that limit the validation of PpIX fluorescence consist in the inter-observer variability and in the different signal imaging obtained by the microscopic view or by the video screen. Based on all above mentioned limitations, there is an urgent need to go beyond the visual capacity of the human eye by measuring more accurately the tumor borders with quantitative pixel based method, and possibly by establishing a definite threshold for tumor activity presence.

The overall purpose of the study was to better understand the metabolic pathway of PpIX, and thereafter to augment pharmacologically its signal in different GBM cell lines in order to increase its visibility. This achievement might be exploited in the future also in photodynamic therapy. We thus selected three compounds: tin protoporphyrin IX (SnPP) a HO-1 blocker, deferoxamine (DFO) an iron chelator, and genistein. Genistein is a natural product (Isoflavone) (12), known as an angiogenesis inhibitor and as an inhibitor of ABCG2 transporter protein, thus influencing the outbound cell traffic of PpIX. All compounds are either FDA approved or previously described in human use. In order to avoid the limit of inter-observer variability and to capture also low concentrations of fluorescence tracer, barely visible by naked eye, a quantification of PpIX during surgical resection is required. We therefore developed a quantitative PpIX microscope (Qp9) according to previously described setup (13–15) aiming to correlate, for the first time, the color coded matrix images with the effective concentration of PpIX is to correlate these matrix images with the effective extraction concentration of PpIX.

METHODS

Cell Culture

Human GBM cell line U87MG obtained from American Type Culture Collection (89081402-1VL, Sigma-Aldrich) was maintained in Dulbecco's Modified Eagle Medium (DMEM, 61965, Gibco® Life technologies Europe), GlutaMAX cell culture medium supplemented with 10% fetal bovine serum (FBS, 10270, Gibco® Life technologies Europe), 1% non-essential amino acids (MEM NEAA, 11140, Gibco® Life technologies Europe), 1 mM sodium pyruvate (S8636, Sigma-Aldrich), penicillin 10,000 units/mL and streptomycin 10,000 µg/mL (15140, Gibco® Life technologies Europe).

The human GBM cell line U87wtEGFR overexpressing the EGFR gene, was generously provided by Prof. Dr. Frank Furnari (Laboratory of Tumor Biology, Ludwig Institute for Cancer Research, University of California-San Diego) and was cultured in DMEM GlutaMAX, 10% FBS and 1% penicillin-streptomycin, supplemented with 100 µg/mL of G418 disulfate salt (A1720, Sigma-Aldrich). U87MG vIII 4.12 cells stably expresses high level of the mutant EGFR variant III (deletion of exons 2-7) (CL 01004-CLTH, Tebu-bio) were maintained in DMEM GlutaMAX, 10% FBS, 1% penicillin-streptomycin and 0.2% of gentamicin 10 mg/mL (15710049, Thermo Fisher Scientific, Life Technologies Europe), enriched with 100 µg/mL of G418. All cells were kept at 37°C, 5% CO_2 atmosphere, in static conditions. Cells were harvested by incubation for 5 min at 37°C with 500 µL TrypLE™ Express Enzyme (1X), no phenol red (12604021, Gibco® Life technologies Europe) and blocked with DMEM supplemented with 10% FBS. During the time of the experiment, the cells were plated and after 24 h the medium was replaced with serum-free DMEM, high glucose, HEPES, no phenol red (21063045, Gibco® Life technologies Europe) for at least 24 h before starting the treatment (16).

Drug Treatment

5-ALA (Fagron DAC 2011), was freshly dissolved in milli-Q water at an intermediate concentration of 1 M and then diluted in serum free medium at a final concentration of 1 mM. DMSO 0.5% (vol/vol) (D2650, Sigma-Aldrich), was added to 5-ALA to increase its permeability into the cells as previously demonstrated by Lawrence et al. (17). Deferoxamine mesylate (492880, Desferal®, DFO, Novartis) was dissolved in milli-Q water. SnPP (sc-203452, Santa Cruz Biotech) and genistein (sc-3515, Santa Cruz Biotechnology) were dissolved in DMSO (16).

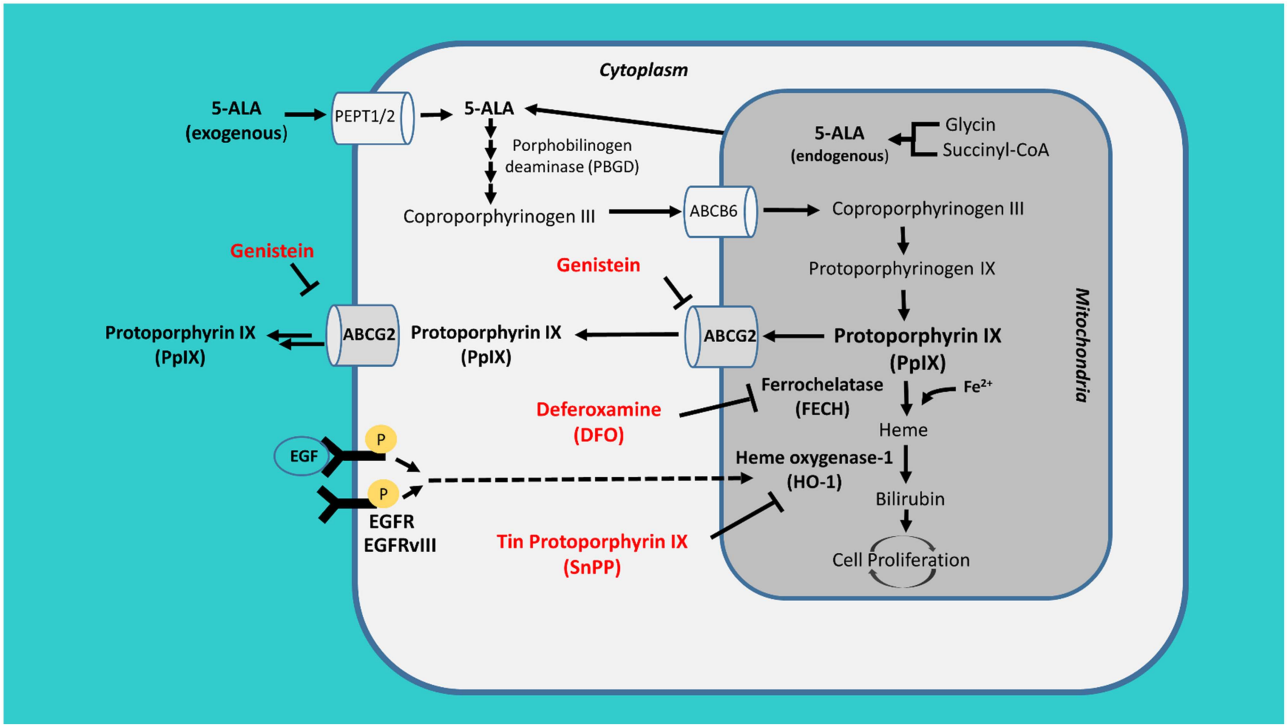

FIGURE 1 | PpIX metabolism. Exogenous 5-aminolevulinic acid (5-ALA) is internalized by tumor cells through the peptide transporter 1 and 2 (PEPT1/2), it is then converted into the fluorescent tracer protoporphyrin IX (PpIX) inside the mitochondrion. The accumulation of PpIX is antagonized by its active conversion through ferrochelatase (FECH) and heme oxygenase-1 (HO-1) and its efflux through ATP-binding cassette sub-family G member 2 (ABCG2). These proteins could be blocked by the action of deferoxamine (DFO), tin protoporphyrin IX (SnPP), and genistein.

PpIX Evaluation by Flow Cytometric Analysis

U87 cells were plated in a 6-well plate and treated with DFO 100 μM, SnPP 100 μM, or genistein 25 μM alone or in combination with 5-ALA at 1 mM or with all combinations of these treatments. After 8 h of treatment, cells were harvested, washed twice with phosphate buffered saline (PBS, 10010056, Gibco® Life technologies Europe) and centrifuged at 2,000 rpm for 5 min. The pellet was resuspended in 100 μL of PBS and the single cells suspension was analyzed by flow cytometry (excitation 408 and emission 630/38; CytoFLEX S, flow cytometry-Beckman Coulter) (16).

Confocal Microscopy

Cells were plated into Ibidi μ-slides VI0.4 (80606, Ibidi). After 24 h in FBS-free medium, cells were treated with DFO 100 μM, SnPP 100 μM, or genistein 25 μM alone or in combination with 5-ALA at 1 mM or with all combinations of these treatments. After 8 h of treatment, cells were washed twice with PBS, fixed with 4% paraformaldehyde for 10 min, washed with PBS. Slides were examined with a confocal line scanning microscope (LSM) Leica TCS SP5 equipped with the objective HCX PL APO lambda blue 40.0 × 1.25 OIL UV and an excitation of 405 nm and an emission of 620–650 nm (16).

Operative Microscope and Quantitative PpIX Microscope

For our tumor resection and cryosectioned slice of GBM xenograft mouse model, an operating microscope (OPMI) Pentero 900 (Carl Zeiss Meditec, AG, Oberkochen, Germany) with a BLUE-400 mode was used for imaging (8-bit RGB, 1,920 × 1,080 pixels) at a 20-cm distance from the target (18). Operative video was registered on BrainLab Buzz for later analysis (**Figure 4**, **Video S1**). For the quantification of the tumor samples taken during the surgery we constructed our custom-made microscope (Qp9) (**Figure 2**) its basic functionality described previously by Valdes et al. (13–15). The Qp9 microscope was calibrated to brain tissue mimicking phantoms with different known PpIX concentrations. The tumor samples were taken (**Video S1**) and then frozen at −80°C for later analysis with color matrix images obtained with Qp9. The sample was processed to trypLE lysis for cell disaggregation, as previously described in cell culture section, and then PpIX was extracted for TECAN analysis, for comparison with the Qp9 microscope.

Qp9 Microscope Setup

Tissue samples and cell cultures are imaged with a hyperspectral camera setup and a color camera attached to a microscope (OPMI pico, Carl Zeiss Meditec) with a fixed working distance of 200 mm. The image is divided by a beam splitter between the

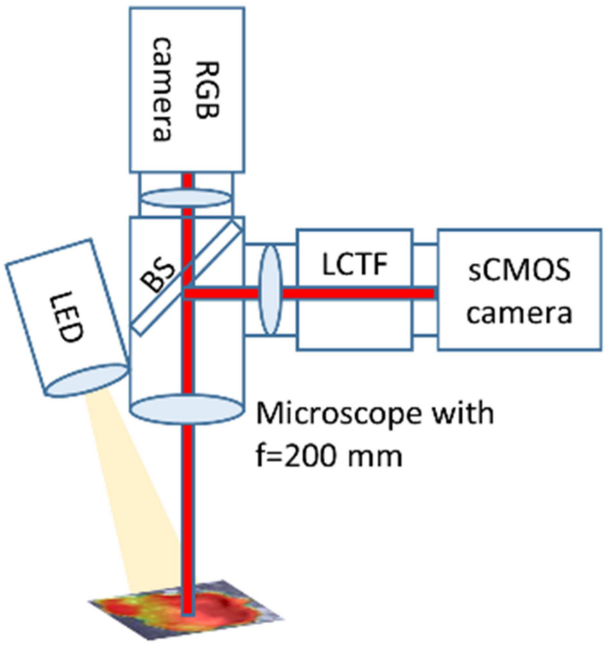

FIGURE 2 | Quantitative PpIX microscope. A tissue sample or cell culture is illuminated by a LED light source with white light or light at 405 nm. The microscope collects the reflected and fluorescent light with an objective lens with f = 200 mm. A beam splitter (BS) splits the light into two paths. One path is imaged with a hyperspectral camera setup. For an overview the second path is imaged on a color camera (RGB camera). The hyperspectral setup consists of a scientific CMOS camera (sCMOS) and a liquid crystal tunable filter (LCTF).

two imaging paths. The LED light source is capable to produce white light and violet light (405 nm) with an intensity of up to 30 mW/cm^2 at the sample.

The hyperspectral setup consists (13) of a scientific CMOS (pco.edge 4.2, PCO AG) camera and a liquid crystal tunable filter (LCTF, Meadowlark Optics, Inc.) (13–15).

The LCTF can be tuned between 420 and 730 nm in one nanometer steps. A typical full width at half maximum (FWHM) of a passband is 12 nm with a transmittance in the range of 5–30%. Outside the passband the transmittance is smaller than 1%.

A standard color camera (uEye CP with IMX252, IDS imaging GmbH) is connected to generate overview images.

With the hyperspectral setup one can record hyperspectral image stacks. The reflectance of the sample can be recorded using white light from the LED light source and fluorescence hyperspectral image stacks can be recorded using 405 nm light from the LED light source. For each pixel a white light reflectance and fluorescence spectrum is available.

These spectra are used to calculate absolute PpIX concentrations (15). So far, the system is calibrated to PpIX brain mimicking phantoms. The fluorescence spectrum is spectrally unmixed, so the pure PpIX signal can be separated from autofluorescence and other background signals such as ambient light. Then the white light spectrum is used to normalize for different tissue properties (different scattering and absorption). We get a PpIX concentration map of the measured samples overlaid on the image of the sample.

Calibration

For calibrating the system, tissue phantoms with defined optical properties were created to mimic brain tissue (19). PpIX was dissolved in dimethyl sulfoxide to get different concentrations (10 ng/ml−5 μg/ml), intralipid and yellow food colorant were used to generate varying scattering (reduced scattering coefficient at 635 nm, μ'_{sm} = 8.7–14.5 cm^{-1}) and absorption properties (absorption coefficient at 405 nm, μ_{ax} = 20–60 cm^{-1}). The lower detection limit of the system at one second integration time is 10 ng/ml of PpIX.

RESULTS

Inhibition of PpIX Metabolism of HO-1 by Tin Protoporphyrin IX (SnPP)

Having previously established the final concentration of 5-ALA at 1 mM for 8 h as the optimal conditions for 5-ALA treatment and quantification of PpIX fluorescence (16), we then proceeded to study the effect of drugs that modulate proteins involved in PpIX conversion into non-fluorescent metabolites. Dose response and cytotoxicity analysis for SnPP showed that the best compromise between PpIX accumulation and cytotoxicity is a concentration of SnPP at 100 μM (16). So, we treated 2 × 10^5 adherent cells/well with SnPP at 100 μM alone or in combination with 5-ALA for 8 h and then determined the mean cellular PpIX fluorescence by flow cytometry for biological duplicates. Based on two independent experiments performed by flow cytometry, we showed that the HO-1 inhibitor SnPP is able to significantly improve 5-ALA-induced PpIX fluorescence in U87MG and U87vIII, alone or in combination with 5-ALA. SnPP and 5-ALA co-treatment augmented the mean PpIX fluorescence by 81% for U87MG cells, by 39% for U87wtEGFR cells and by 48% for U87vIII cells compared to cells treated with 5-ALA alone, set as 100% (**Figure 3A**). The SnPP treatment alone showed an increment of PpIX fluorescence by 358% for U87MG cells, 252% for U87wtEGFR cells and 198% for U87vIII compared to untreated cells, set as 100% (**Figure 3A**) (16).

Inhibition of PpIX Synthesis by Fe^{2+}-Chelation and Inhibitory Effect on FECH

Based on our previous studies on cell cytotoxicity, we selected DFO at 100 μM to test the effect of FECH inhibition for 8 h in the presence or absence of exogenous 5-ALA (16). The treatment with DFO alone compared to control untreated cells showed a non-significant variation in PpIX fluorescence. In contrast, in the presence of exogenous 5-ALA, DFO significantly improved 5-ALA-induced PpIX fluorescence in all the three cell lines. In detail, the increase was of 16% for U87MG, of 6% for U87wtEGFR and of 22% for U87vIII cells when compared to cells incubated with 5-ALA alone, set as 100% (**Figure 3B**) (16).

Inhibition of PpIX Efflux by Genistein Acting on ABCG2

To retain the PpIX accumulated inside the cells, we tested the effect of inhibiting the main PpIX efflux transporter ABCG2 with genistein. Based on our previous cytotoxicity and

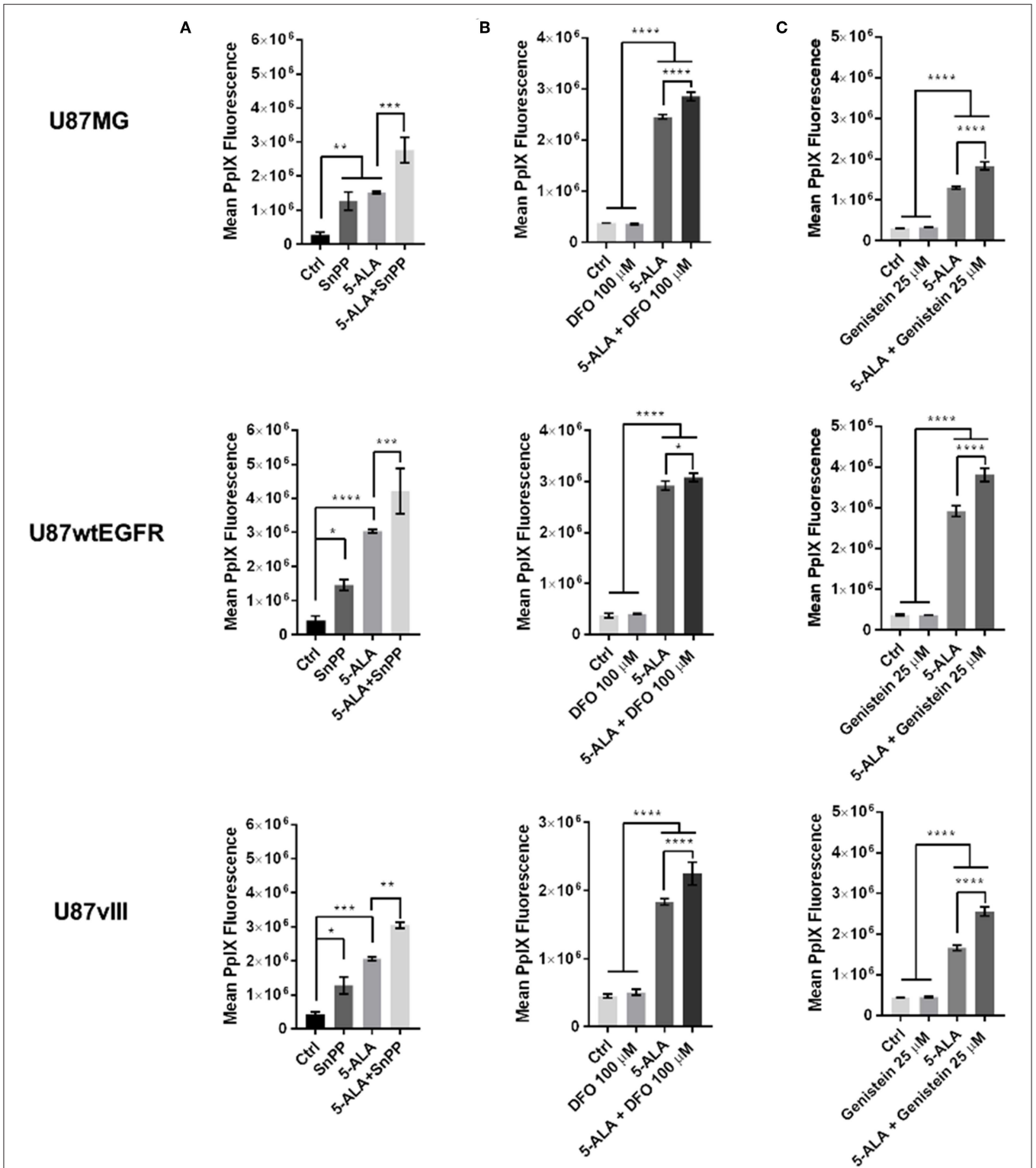

FIGURE 3 | Effect of single treatments on U87 GBM cell lines. Effect of **(A)** tin protoporphyrin IX (SnPP), **(B)** deferoxamine (DFO), and **(C)** genistein on three U87 cell lines differing for EGFR expression. Control untreated cells are compared with cells treated with the selected compound alone and cells treated with 5-ALA alone or with combination of 5-ALA and the indicated drug. Graphs show that all the three treatments in combination with 5-ALA significantly induce the fluorescence compared to 5-ALA alone. Results are expressed as mean ± SD (one-way ANOVA, Sidak's multiple comparison test $^{*}p < 0.05$; $^{**}p < 0.01$; $^{***}p < 0.001$; $^{****}p < 0.0001$). Where not specified the difference is not significant.

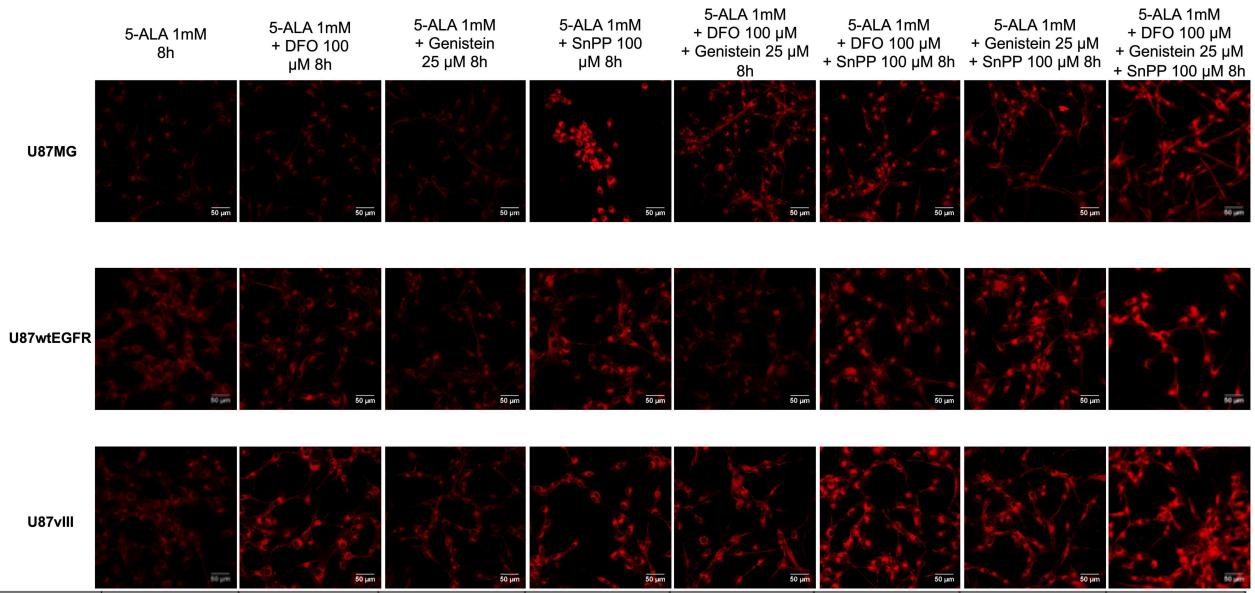

Cell line	5-ALA (alone)	DFO 100 µM	Genistein 25 µM	SnPP 100 µM	DFO 100 µM + Genistein 25 µM	DFO 100 µM + SnPP 100 µM	Genistein 25 µM + SnPP 100 µM	DFO 100 µM Genistein 25 µM SnPP 100 µM
U87MG	0 %	23 %	25 %	48 %	61 %	64 %	75 %	147 %
U87wtEGFR	0%	11%	48%	27%	83%	56%	140%	172%
U87vIII	0 %	26 %	79 %	42 %	161 %	78 %	136 %	228 %

FIGURE 4 | PpIX fluorescence accumulation after single and combined treatments. Confocal images showing the increment in PpIX fluorescence (represented in red, excitation 405 nm and emission 635 nm) in GBM cells after single and combined treatment with two or three drugs compared to 5-ALA alone (represented as 0%). Scale bars represent 50 µm. Table summarizes the increment of PpIX fluorescence in percentage. DFO (deferoxamine), SnPP (tin protoporphyrin IX).

pharmacological studies, we selected a genistein concentration of 25 µM (16). With the selected concentration we performed a more detailed analysis in biological triplicates of PpIX fluorescence by flow cytometry in the absence or presence of exogenous 5-ALA. Endogenous PpIX fluorescence was not affected by the blockade of the ABCG2 transporter in presence of genistein, whilst this was the case when 5-ALA was added to the culture medium for the three cell lines. In fact, the combined treatment with genistein and 5-ALA compared to 5-ALA alone (set as 100%) increased PpIX fluorescence by 42% for U87MG cells, by 31% for U87wtEGFR cells and by 54% for U87vIII cells (**Figure 3C**) (16).

Combined Treatments Improves PpIX Accumulation in U87 Glioblastoma Cell Lines

Detailed flow cytometric analysis led to the identification of combined treatments composed of two drugs leading to significantly increased mean PpIX fluorescence. For all three cell lines, the combination of reduced PpIX metabolism and impaired PpIX efflux resulted in augmented 5-ALA-induced fluorescence. Whilst SnPP and genistein is the best combination for U87MG (75% increase compared to 25% with genistein alone or 48% for SnPP alone) and U87wtEGFR cells (140% increase compared to 48% for genistein and 27% for SnPP), U87vIII cells responded better to DFO combined with genistein (161% increase compared to 79% with genistein and 26% for DFO) in the presence of exogenous 5-ALA, set as 0%. Maximal PpIX fluorescence is observed for the three lines with the combination of all three drugs, indicating that neither SnPP nor DFO, when tested alone, are able to completely block PpIX metabolism. In the presence of the three drugs the increment in PpIX fluorescence reached 147% for U87MG cells, 172% for U87wtEGFR cells and 228% for U87vIII cells as reported in the table of **Figure 4**. These data were confirmed by qualitative confocal microscopy analysis (**Figure 4**). Overall, these data indicated that inhibition of PpIX metabolism coupled to inhibition of PpIX efflux is expected to improve the visualization of GBM cells. Nevertheless, the optimal drug combination may depend on the genotype of the GBM cell, in particular considering the presence of defined gene mutations.

Intraoperative PpIX Fluorescence Guided Tumor Resection and Postoperative Quantification of PpIX Fluorescence of Tumor Samples and Comparison With PpIX Extraction

Figure 5 and **Video S1** show the intraoperative resection of GBM and the tissue which has been taken for later analysis with the Qp9-microscope. **Figure 6A** shows the color-coded image of the tumor samples with the concentration values for PpIX. The color-coded image represents areas of high and low PpIX concentration on its surface. The automated area of investigation of the Qp9

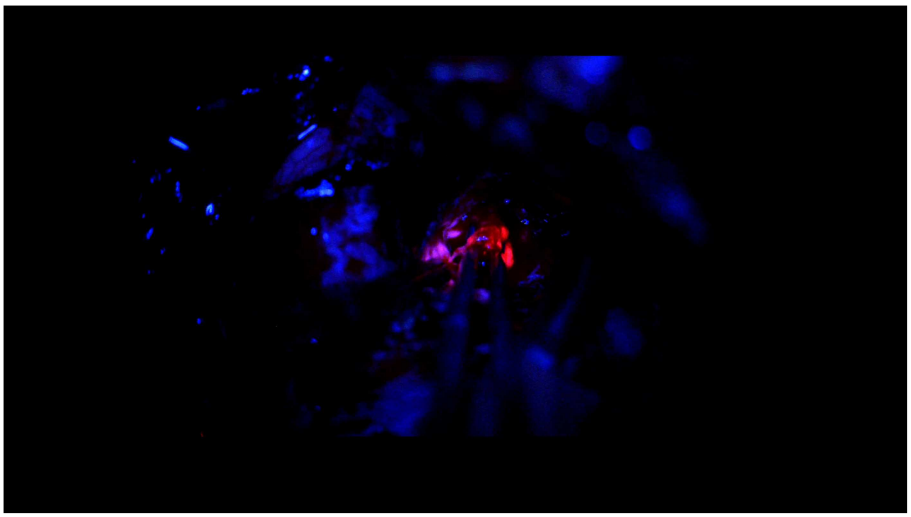

FIGURE 5 | 5-ALA guided surgery with OPMI PENTERO 900. Image of video showing the surgical intervention of glioblastoma removal. Under the blue light the tumor bulk is red, the fluorescence in the tumor margin is pink and more vague.

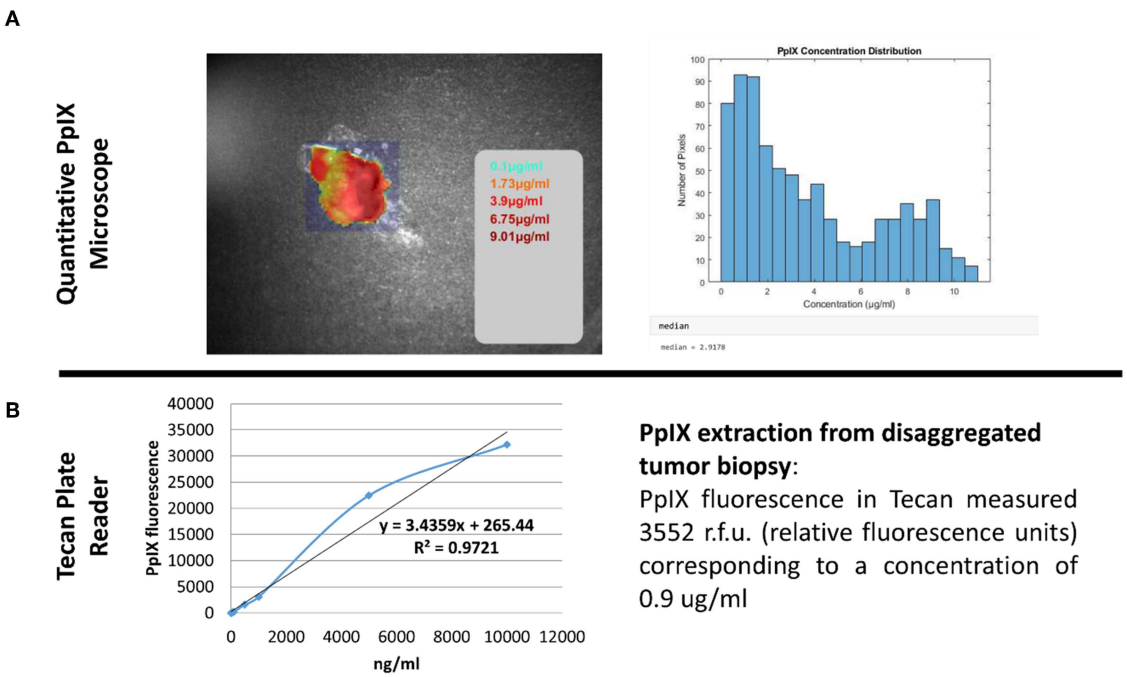

FIGURE 6 | Quantitative PpIX measurement. Comparison of two different methods able to quantitatively measure the accumulated PpIX in tissue biopsy. **(A)** Shows quantitative measurement performed with the Qp9 Zeiss microscope whereas **(B)** shows results obtained after methanolic-perchloric acid extraction from the whole biopsy.

microscope (**Figure 6A**) contains areas outside or at the margin of the tumor specimen and such are practically reported as very low or absence of PpIX (<0.1 μg/ml). This however does not affect the correlation as these very low values are not considered in the sample extraction. Tumor sample has thereafter been disaggregated and analyzed for its PpIX concentration (**Figure 6B**). The values of the disaggregated tumor tissue show concentration below the expected values measured by the Qp9 microscope yet in the same decimal.

DISCUSSION

There is no doubt that 5-ALA induced fluorescence has an impact on augmentation of the surgical resection in GBM surgery (20).

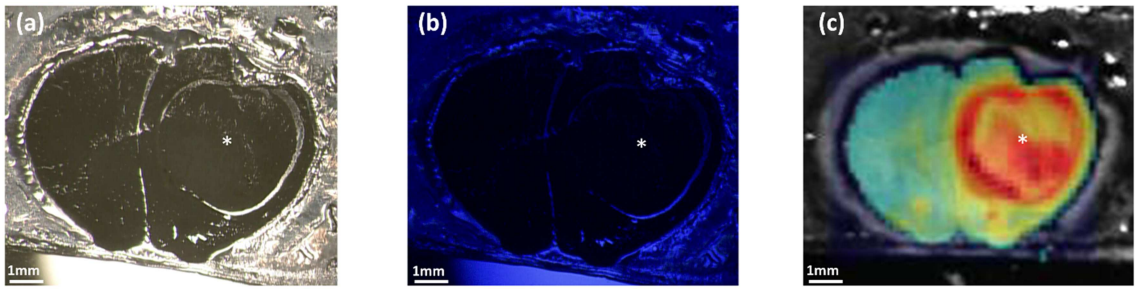

FIGURE 7 | Comparison between OPMI PENTERO 900 and Qp9 Zeiss microscopes. The figures show cryosectioned slice of GBM xenograft mouse model. In **(a,b)** visualization under OPMI PENTERO 900 with white light source and UV laser Blue 400, respectively. **(c)** Shows the color coded matrix image obtained after the PpIX quantification by Qp9. *tumor region. Scale bars = 1 mm.

Additionally, 5-ALA induced fluorescence harbors the potential for photodynamic therapy. For both treatments, a selective and controlled augmentation and especially quantification of the PpIX fluorescence signal is crucial for developing the technologies further. Therefore, we studied, in three different cell lines, the optimal conditions and pharmacological possibilities to augment the signal by influencing the balance of production, consumption and outbound transportation of PpIX. We also identified that different GBM cell lines have different PpIX signal, a phenomenon which has been also observed in the clinical situation (21). The evaluation of PpIX fluorescence positivity during the surgical operation of GBM is especially subjective to the surgeon's eye, limiting the usefulness and thus the impact on resection. Hence user independent evaluation of the operation situs will become necessary. Different groups in the past have described offline imaging techniques or online probes to interpret the quantitative values of PpIX (22). Yet the verification of microscopic arbitrary values as measured in the past and as in our study by the Qp9 microscope need to be further verified by selective tumor tissue analysis and quantitative PpIX extraction.

The values measured after extraction of PpIX from tumor samples were lower than what the values were in the Qp9 analysis. Reasons for that may be divers, resulting from extraction dilution or the disaggregation process. Although approximation of the effective PpIX concentration might technically be possible in the real surgical resection situation, these quantitative values will probably have no effect on the decision making for the tumor resection itself. Furthermore, during surgery of human GBM different factors may influence the visibility, respectively, the detection of PpIX fluorescence both with the naked eye or with the Qp9 microscope. Factors such as bleaching or different focus distance or even fluid covering may influence the signal intensity. Therefore, a sensible detection technique such as Qp9 or a mechanism enhancing the signal intensity such as heme oxygenase-1 blocker, iron chelating agents or PpIX transporter protein blocker may possibly be combined in the future for more sensible detection of different fluorescenting GBM or maybe even lower grade glioma. These findings will however need to be correlated with effective tumor cell infiltration in brain tumor. We have previously demonstrated that different GBM cell lines may have different PpIX signal intensity when treated with the same parameters (7, 16), a phenomenon also described *in vivo* (21). This phenomenon can be also seen in our mice GBM tumor model, as demonstrated in **Figure 7**, where tumor not visible to the naked eye with the conventional blue light of the operation microscope, can be made visible with color coded matrix under the Cp9 microscope. Belykh et al. have previously analyzed three different techniques (Scanning fiber endoscope (SFE), blue light and confocal scanning microscope) and concluded that SFE provides new endoscopic capability to visualize PpIX positivity at cellular levels (18, 23). We agree with Belykh et al. (18) that a more refined technique for visualization of PpIX such as SFE or now Qp9 are necessary. Techniques are complementary and probably cannot replace one with the other. The advantage of Qp9 over SFE may be that it can give the surgeon a faster overall picture of where remaining tumor is to be searched for and resected, however at the fate of more artifacts such as fluids, bleaching and focus distance. SFE will probably result more locally precise. Therefore, possibly a combination of both techniques may prove to be even more effective. Our next steps are passing from the cell cultures and offline tumor samples to immediate intraoperative monitoring first of tumor samples and analyzing the quantitative PpIX matrix color coded images with the effective tumor cell invasion.

DATA AVAILABILITY

The datasets generated for this study are available on request to the corresponding author.

ETHICS STATEMENT

The Ethic Committee of the Canton Ticino approved animal experiments in the animal application TI-05-19 Numero e-TV: 27255.

AUTHOR CONTRIBUTIONS

MR conceived the idea and wrote and edited the manuscript. DP performed experimental work and manuscript editing and reviewing. MW, CH, and RG performed Cp9 design and

manuscript revision. FM and MD performed experimental work and manuscript editing and reviewing.

FUNDING

Lega Cancro Ticinese, Gabriele Charitable Foundation, and Neurosurigcal Fonds, EOC.

SUPPLEMENTARY MATERIAL

The Supplementary Material for this article can be found online at: https://www.frontiersin.org/articles/10.3389/fsurg.2019.00041/full#supplementary-material

Video S1 | 5-ALA guided surgery with OPMI PENTERO 900. Video showing the surgical intervention of glioblastoma removal. Under the blue light the tumor bulk is red, the fluorescence in the tumor margin is pink and more vague.

REFERENCES

1. Peng Q, Warloe T, Berg K, Moan J, Kongshaug M, Giercksky KE, et al. 5-Aminolevulinic acid-based photodynamic therapy: clinical research and future challenges. *Cancer.* (1997) 79:2282–308.
2. Stummer W, Pichlmeier U, Meinel T, Wiestler OD, Zanella F, Reulen HJ, et al. Fluorescence-guided surgery with 5-aminolevulinic acid for resection of malignant glioma: a randomised controlled multicentre phase III trial. *Lancet Oncol.* (2006) 7:392–401. doi: 10.1016/S1470-2045(06)70665-9
3. Fujii Y, Muragaki Y, Maruyama T, Nitta M, Saito T, Ikuta S, et al. Threshold of the extent of resection for WHO Grade III gliomas: retrospective volumetric analysis of 122 cases using intraoperative MRI. *J Neurosurg.* (2018) 129:1–9. doi: 10.3171/2017.3.JNS162383
4. Stummer W, Stepp H, Wiestler OD, Pichlmeier U. Randomized, prospective double-blinded study comparing 3 different doses of 5-aminolevulinic acid for fluorescence-guided resections of malignant gliomas. *Neurosurgery.* (2017) 81:230–9. doi: 10.1093/neuros/nyx074
5. Jaber M, Wölfer J, Ewelt C, Holling M, Hasselblatt M, Niederstadt T, et al. The value of 5-aminolevulinic acid in low-grade gliomas and high-grade gliomas lacking glioblastoma imaging features: an analysis based on fluorescence, magnetic resonance imaging, 18F-fluoroethyl tyrosine positron emission tomography, and tumor molecular factors. *Neurosurgery.* (2016) 78:401–11; discussion 411. doi: 10.1227/NEU.0000000000001020
6. Kim S, Kim JE, Kim YH, Hwang T, Kim SK, Xu WJ, et al. Glutaminase 2 expression is associated with regional heterogeneity of 5-aminolevulinic acid fluorescence in glioblastoma. *Sci Rep.* (2017) 7:12221 doi: 10.1038/s41598-017-12557-3
7. Fontana AO, Piffaretti D, Marchi F, Burgio F, Faia-Torres AB, Paganetti P, et al. Epithelial growth factor receptor expression influences 5-ALA induced glioblastoma fluorescence. *J Neurooncol.* (2017) 133:497–507. doi: 10.1007/s11060-017-2474-0
8. Ogino T, Kobuchi H, Munetomo K, Fujita H, Yamamoto M, Utsumi T, et al. Serum-dependent export of protoporphyrin IX by ATP-binding cassette transporter G2 in T24 cells. *Mol Cell Biochem.* (2011) 358:297–307. doi: 10.1007/s11010-011-0980-5
9. Oberstadt MC, Bien-Möller S, Weitmann K, Herzog S, Hentschel K, Rimmbach C, et al. Epigenetic modulation of the drug resistance genes MGMT, ABCB1 and ABCG2 in glioblastoma multiforme. *BMC Cancer.* (2013) 13:617. doi: 10.1186/1471-2407-13-617
10. Suero Molina E, Wölfer J, Ewelt C, Ehrhardt A, Brokinkel B, Stummer W. Dual-labeling with 5-aminolevulinic acid and fluorescein for fluorescence-guided resection of high-grade gliomas: technical note. *J Neurosurg.* (2018) 128:399–405. doi: 10.3171/2016.11.JNS161072
11. Parker NR, Khong P, Parkinson JF, Howell VM, Wheeler HR. Molecular heterogeneity in glioblastoma: potential clinical implications. *Front Oncol.* (2015) 5:55. doi: 10.3389/fonc.2015.00055
12. Taylor CK, Levy RM, Elliott JC, Burnett BP. The effect of genistein aglycone on cancer and cancer risk: a review of *in vitro*, preclinical, and clinical studies. *Nutr Rev.* (2009) 67:398–415. doi: 10.1111/j.1753-4887.2009.00213.x
13. Valdes PA, Jacobs VL, Wilson BC, Leblond F, Roberts DW, Paulsen KD. System and methods for wide-field quantitative fluorescence imagingduring neurosurgery. *Opt Lett.* (2013) 38:2786–8. doi: 10.1364/OL.38.002786
14. Valdés PA, Leblond F, Kim A, Harris BT, Wilson BC, Fan X, et al. Quantitative fluorescence in intracranial tumor: implications for ALA-induced PpIX as an intraoperative biomarker. *J Neurosurg.* (2011) 115:11–7. doi: 10.3171/2011.2.JNS101451
15. Valdés PA, Leblond F, Kim A, Wilson BC, Paulsen KD, Roberts DW. A spectrally constrained dual-band normalization technique for protoporphyrin IX quantification in fluorescence-guided surgery. *Opt Lett.* (2012) 37:1817–9. doi: 10.1364/OL.37.001817
16. Piffaretti D, Burgio F, Thelen M, Kaelin-Lang A, Paganetti P, Reinert M, et al. Protoporphyrin IX tracer fluorescence modulation for improved brain tumor cell lines visualization. *J Photochem Photobiol B.* (2019).
17. Lawrence JE, Patel AS, Rovin RA, Belton RJ Jr, Bammert CE, Steele CJ, et al. Quantification of protoporphyrin IX accumulation in glioblastoma cells: a new technique. *ISRN Surg.* (2014) 2014:405360. doi: 10.1155/2014/405360
18. Belykh E, Miller EJ, Hu D, Martirosyan NL, Woolf EC, Scheck AC, et al. Scanning fiber endoscope improves detection of 5-aminolevulinic acid-induced protoporphyrin IX fluorescence at the boundary of infiltrative glioma. *World Neurosurg.* (2018) 113:e51–69. doi: 10.1016/j.wneu.2018.01.151
19. Valdés PA, Leblond F, Jacobs VL, Wilson BC, Paulsen KD, Roberts DW. Quantitative, spectrally-resolved intraoperative fluorescence imaging. *Sci Rep.* (2012) 2:798. doi: 10.1038/srep00798
20. Stummer W. Fluorescence-guided resection of malignant gliomas. In: Moliterno Gunel J, Piepmeier J, Baehring J, editors. *Malignant Brain Tumors: State-of-the-Art Treatment*. Springer International Publishing (2017). p. 81–101. doi: 10.1007/978-3-319-49864-5_6
21. Hauser SB, Kockro RA, Actor B, Sarnthein J, Bernays RL. Combining 5-aminolevulinic acid fluorescence and intraoperative magnetic resonance imaging in glioblastoma surgery: a histology-based evaluation. *Neurosurgery.* (2016) 78:475–83. doi: 10.1227/NEU.0000000000001035
22. Richter JCO, Haj-Hosseini N, Hallbeck M, Wårdell K. Combination of hand-held probe and microscopy for fluorescence guided surgery in the brain tumor marginal zone. *Photodiagnosis Photodyn Ther.* (2017) 18:185–92. doi: 10.1016/j.pdpdt.2017.01.188
23. Belykh E, Miller EJ, Patel AA, Bozkurt B, Yağmurlu K, Robinson TR, et al. Optical characterization of neurosurgical operating microscopes: quantitative fluorescence and assessment of PpIX photobleaching. *Sci Rep.* (2018) 8:12543. doi: 10.1038/s41598-018-30247-6

Conflict of Interest Statement: MW, CH, and RG are employed by Carl Zeiss Meditec AG, Oberkochen Germany and declare no further competing interests.

The remaining authors declare that the research was conducted in the absence of any commercial or financial relationships that could be construed as a potential conflict of interest.

frontiers in Surgery

CORRECTION
published: 02 April 2020
doi: 10.3389/fsurg.2020.00014

Corrigendum: Quantitative Modulation of PpIX Fluorescence and Improved Glioma Visualization

Michael Reinert[1,2,3,4]*, *Deborah Piffaretti*[1,5], *Marco Wilzbach*[6], *Christian Hauger*[6], *Roland Guckler*[6], *Francesco Marchi*[1,2] and *Maria Luisa D'Angelo*[1]

[1] Laboratory for Biomedical Neurosciences, Neurocenter of Southern Switzerland, Ente Ospedaliero Cantonale, Torricella-Taverne, Switzerland, [2] Department of Neurosurgery, Neurocenter of Southern Switzerland, Ente Ospedaliero Cantonale, Lugano, Switzerland, [3] Faculty of Biomedical Neurosciences, Università Della Svizzera Italiana, Lugano, Switzerland, [4] Medical Faculty, University of Bern, Bern, Switzerland, [5] Faculty of Medicine, Graduate School for Cellular and Biomedical Sciences, University of Bern, Bern, Switzerland, [6] Carl Zeiss Meditec AG, Oberkochen, Germany

OPEN ACCESS

Edited and reviewed by:
Mark Preul,
Barrow Neurological Institute (BNI), United States

***Correspondence:**
Michael Reinert
michael.reinert@eoc.ch

Specialty section:
This article was submitted to Neurosurgery, a section of the journal Frontiers in Surgery

Received: *12 February 2020*
Accepted: *10 March 2020*
Published: *02 April 2020*

Citation:
Reinert M, Piffaretti D, Wilzbach M, Hauger C, Guckler R, Marchi F and D'Angelo ML (2020) Corrigendum: Quantitative Modulation of PpIX Fluorescence and Improved Glioma Visualization. Front. Surg. 7:14. doi: 10.3389/fsurg.2020.00014

Keywords: GBM—glioblastoma multiforme, 5-ALA=5-aminolevulinic acid, protoporphyin IX, quantification, breakdown, visualization, microscope

A Corrigendum on

Quantitative Modulation of PpIX Fluorescence and Improved Glioma Visualization
by Reinert, M., Piffaretti, D., Wilzbach, M., Hauger, C., Guckler, R., Marchi, F., et al. (2019). Front. Surg. 6:41. doi: 10.3389/fsurg.2019.00041

In the published article there is an error in **Figure 4**. In the images the third and fifth column of the first row are the same. The image in the third column of the first row (Genistein 25 μM) has been corrected. The image in the fifth column of the first row (DFO 100 μM + Genistein 25 μM) remains as it is.

The authors apologize for these errors and state that this does not change the scientific conclusions of the article in any way. The original article has been updated.

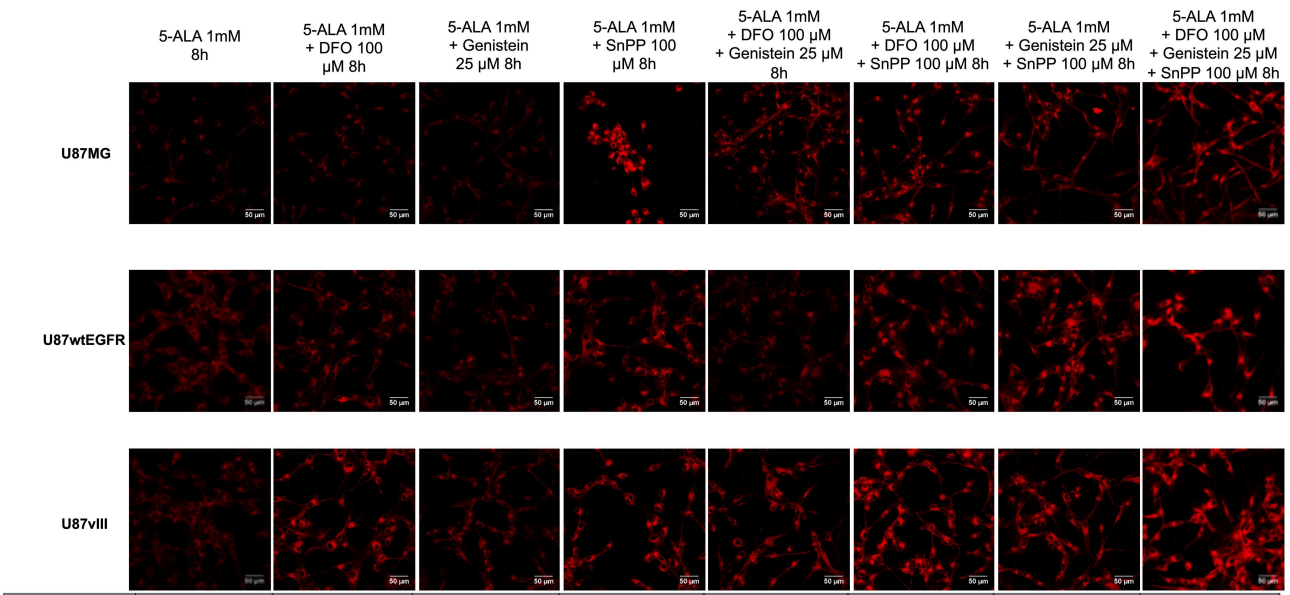

Cell line	5-ALA (alone)	DFO 100 µM	Genistein 25 µM	SnPP 100 µM	DFO 100 µM + Genistein 25 µM	DFO 100 µM + SnPP 100 µM	Genistein 25 µM + SnPP 100 µM	DFO 100 µM Genistein 25 µM SnPP 100 µM
U87MG	0 %	23 %	25 %	48 %	61 %	64 %	75 %	147 %
U87wtEGFR	0%	11%	48%	27%	83%	56%	140%	172%
U87vIII	0 %	26 %	79 %	42 %	161 %	78 %	136 %	228 %

FIGURE 4 | PpIX fluorescence accumulation after single and combined treatments. Confocal images showing the increment in PpIX fluorescence (represented in red, excitation 405 nm and emission 635 nm) in GBM cells after single and combined treatment with two or three drugs compared to 5-ALA alone (represented as 0%). Scale bars represent 50 µm. Table summarizes the increment of PpIX fluorescence in percentage. DFO (deferoxamine), SnPP (tin protoporphyrin IX).

frontiers in Oncology

SYSTEMATIC REVIEW
published: 17 July 2019
doi: 10.3389/fonc.2019.00620

Survival Outcomes Among Patients With High-Grade Glioma Treated With 5-Aminolevulinic Acid–Guided Surgery: A Systematic Review and Meta-Analysis

*Sirin Gandhi[1], Ali Tayebi Meybodi[1], Evgenii Belykh[1,2], Claudio Cavallo[1], Xiaochun Zhao[1], Masood Pasha Syed[3], Leandro Borba Moreira[1], Michael T. Lawton[1], Peter Nakaji[1] and Mark C. Preul[1]**

[1] Department of Neurosurgery, St. Joseph's Hospital and Medical Center, Barrow Neurological Institute, Phoenix, AZ, United States, [2] Department of Neurosurgery, Irkutsk State Medical University, Irkutsk, Russia, [3] Department of Medicine, Saint Vincent Hospital, Worcester, MA, United States

OPEN ACCESS

Edited by:
Sebastian Cerdan,
Spanish National Research Council (CSIC), Spain

Reviewed by:
Brent T. Harris,
Georgetown University, United States
Ana Paula Candiota,
Centre for Biomedical Network Research (CIBER), Spain

***Correspondence:**
Mark C. Preul
neuropub@barrowneuro.org

Specialty section:
This article was submitted to Cancer Imaging and Image-directed Interventions, a section of the journal Frontiers in Oncology

Received: 15 April 2019
Accepted: 24 June 2019
Published: 17 July 2019

Citation:
Gandhi S, Tayebi Meybodi A, Belykh E, Cavallo C, Zhao X, Syed MP, Borba Moreira L, Lawton MT, Nakaji P and Preul MC (2019) Survival Outcomes Among Patients With High-Grade Glioma Treated With 5-Aminolevulinic Acid–Guided Surgery: A Systematic Review and Meta-Analysis. Front. Oncol. 9:620. doi: 10.3389/fonc.2019.00620

Background: High-grade glioma (HGG) is associated with a dismal prognosis despite significant advances in adjuvant therapies, including chemotherapy, immunotherapy, and radiotherapy. Extent of resection continues to be the most important independent prognosticator of survival. This underlines the significance of increasing gross total resection (GTR) rates by using adjunctive intraoperative modalities to maximize resection with minimal neurological morbidity. 5-aminolevulinic acid (5-ALA) is the only US Food and Drug Administration–approved intraoperative optical agent used for fluorescence-guided surgical resection of gliomas. Despite several studies on the impact of intra-operative 5-ALA use on the extent of HGG resection, a clear picture of how such usage affects patient survival is still unavailable.

Methods: A systematic review was conducted of all relevant studies assessing the GTR rate and survival outcomes [overall survival (OS) and progression-free survival (PFS)] in HGG. A meta-analysis of eligible studies was performed to assess the influence of 5-ALA-guided resection on improving GTR, OS, and PFS. GTR was defined as >95% resection.

Results: Of 23 eligible studies, 19 reporting GTR rates were included in the meta-analysis. The pooled cohort had 998 patients with HGG, including 796 with newly diagnosed cases. The pooled GTR rate among patients with 5-ALA–guided resection was 76.8% (95% confidence interval, 69.1–82.9%). A comparative subgroup analysis of 5-ALA–guided vs. conventional surgery (controlling for within-study covariates) showed a 26% higher GTR rate in the 5-ALA subgroup (odds ratio, 3.8; $P < 0.001$). There were 11 studies eligible for survival outcome analysis, 4 of which reported PFS. The pooled mean difference in OS and PFS was 3 and 1 months, respectively, favoring 5-ALA vs. control ($P < 0.001$).

Conclusions: This meta-analysis shows a significant increase in GTR rate with 5-ALA–guided surgical resection, with a higher weighted GTR rate (~76%) than the pivotal phase III study (~65%). Pooled analysis showed a small yet significant increase in

survival measures associated with the use of 5-ALA. Despite the statistically significant results, the low level of evidence and heterogeneity across these studies make it difficult to conclusively report an independent association between 5-ALA use and survival outcomes in HGG. Additional randomized control studies are required to delineate the role of 5-ALA in survival outcomes in HGG.

Keywords: 5-aminolevulinic acid, fluorescence-guided surgery, glioblastoma multiforme, gross total resection, high-grade glioma, meta-analysis, survival outcome

INTRODUCTION

High-grade gliomas (HGGs), including World Health Organization (WHO) grade III and grade IV gliomas, are the most common subtype of primary adult malignant cerebral neoplasms with a poor prognosis. Current management strategies include maximal safe surgical resection along with a combination of chemotherapy and fractionated radiotherapy. Complete resection of enhancing tumor (CRET) or gross total resection (GTR) have been demonstrated to be independent prognosticators of increased progression-free survival (PFS) and overall survival (OS) (1). However, true delineation of the tissue boundaries of HGGs is extremely difficult. Gadolinium enhancement on magnetic resonance imaging (MRI) is conventionally used to determine the tumor boundaries and postoperative resection analysis. In recent years, fluorescence image-guided resection using agents like fluorescein sodium (2), indocyanine green (3, 4), and 5-aminolevulinic acid (5-ALA) (5, 6) has gained significant traction in the treatment of HGGs. These optical agents can augment visual differentiation of the tumor border zone intraoperatively by selective fluorescence of the abnormal diseased tissue (7, 8).

5-ALA is currently approved in many countries, with US Food and Drug Administration (FDA) approval obtained a decade after European Medical Agency (EMA) approval (9). Selective accumulation of protoporphyrin IX (PpIX), which is an endogenous fluorophore and a downstream metabolite of 5-ALA in the heme synthesis pathway, occurs in the malignant glioma cells in HGGs (10). PpIX-fluorescence is best visualized using filtered xenon light with blue-violet light 375–440 nm wavelength and an emission filter for red fluorescence of 635–704 nm (8, 11). The standard dose of 5-ALA oral administration is 20 mg/kg dissolved in 50 mL of water given 3 h prior to surgery with a peak visible fluorescence at 6–8 h after consumption (12). However, photobleaching effects have been observed in this tumor-specific fluorescence, with 36% fluorescence decay in 25 min at an excitation wavelength of 405 nm and after 87 min under unfiltered wide-field illumination (8, 13).

Several studies have suggested that intraoperative PpIX accumulates even in the absence of contrast enhancement on MRI and supersedes the margins of contrast-enhancing tumor in the gadolinium-enhancing tumor subtypes (14, 15). Thus, it is imperative to determine the added surgical benefit of resection of this residual non-enhancing fluorescent tissue while minimizing any postoperative neurological morbidity. This particular question was examined in 50 patients with GBM who underwent operations with 5-ALA-based fluorescence guidance with matched non-surgical prognostic markers, such as age, location, O^6-methylguanine-DNA-methyltransferase status, and Karnofsky Performance Scale score (14). The mean OS was significantly worse in the CRET subgroup (17 months; 95% confidence interval [CI]: 22.4–31.6 months) if patients had persistent residual fluorescence in comparison with maximal safe fluorescent tissue resection (27 months; 95% CI: 12.5–22.5 months) (14). This study demonstrated discrepancy between intraoperative tissue fluorescence and gadolinium contrast enhancement. Use of adjunctive tools like navigation with tractography, somatosensory evoked potential or motor evoked potential mapping, confocal endomicroscopy, intraoperative MRI (iMRI), ultrasound, or awake craniotomy may be beneficial in conjunction with fluorescence-guided surgical resection of aggressive HGGs in eloquent locations. In the current age of personalized and precision medicine, 5-ALA seems to have been identified as a tool in surgical theranostics, with benefits seen during photodynamic therapy using 5-ALA in experimental studies and patients with glioma (16–18).

The current standard of care for HGGs, including GBM, includes the Stupp protocol, which calls for maximal safe surgical resection with concomitant temozolomide and radiation therapy (19). The largest systematic review to date with quantitative analysis of the influence of extent of resection (EOR) on survival outcomes in patients with GBM observed a substantial improvement in PFS and OS in patients undergoing GTR (1). Since 5-ALA has been shown to significantly improve EOR and GTR/CRET in patients with HGG, this would indirectly imply an enhanced survival benefit for this subset of patients. However, there is a paucity of quantitative data analysis in reported systematic reviews owing to the heterogeneity of the patient population and low levels of scientific evidence based on study designs (10, 20–22).

Despite the previous systematic reviews assessing the value of 5-ALA for the treatment of HGG (10, 20, 21), the benefit of 5-ALA to patients (e.g., improvements in neurological outcomes, quality of life, and overall survival) remain inconclusive. The benefit of 5-ALA has so far been demonstrated only indirectly by showing increased GTR rates when using fluorescence guidance. We attempted to bridge the gap and investigate the evidence for 5-ALA benefits on the basis of patient outcome–based metrics. The objective of this study was to conduct a systematic review

Abbreviations: CRET, complete resection of enhancing tumor; EOR, extent of resection; FDA, US Food and Drug Administration; GBM, glioblastoma multiforme; GTR, gross total resection; HGG, high-grade glioma; iMRI, intraoperative magnetic resonance imaging; LGG, low-grade glioma; MRI, magnetic resonance imaging; OS, overall survival; PFS, progression-free survival; PpIX, protoporphyrin IX; RCT, randomized control trial; WHO, World Health Organization; 5-ALA, 5 aminolevulinic acid.

of the literature and perform a quantitative pooled evaluation of survival outcomes and GTR rates of 5-ALA–guided surgical resection in HGGs. Since our pooled cohort included patients with recurrent HGG, a subgroup outcomes analysis among patients with primary HGG was also performed to assess the survival outcomes.

METHODS

This systematic review was conducted in accordance with the Preferred Reporting Items for Systematic Reviews and Meta-Analyses (PRISMA) guidelines. This study was exempt from institutional review board approval as it was a meta-analytical review of literature.

Search Strategy

PubMed, MEDLINE, and EMBASE electronic databases were searched to identify studies from the database inception through December 31, 2018, regarding the use of intraoperative 5-ALA for fluorescence-guided resection of HGGs. No studies were excluded on the basis of publication type or date of publication. However, preclinical and *in vitro* studies involving animals were excluded. MeSH and EMTREE terms relevant to 5-ALA and HGGs were used to search the PubMed, MEDLINE, and EMBASE databases. These terms included "aminolevulinic acid," "levulinic acid," "5ALA" or "5-ALA," "glioma," "high grade glioma," "malignant glioma," and "glioblastoma." The bibliography of all articles meeting the inclusion criteria was examined to identify any missing additional studies. All articles from this search were added to an Endnote library X 8.2 (Clarivate Analytics, Philadelphia, PA). Non-English literature was excluded from this study.

Systematic Review Protocol and Data Extraction

Titles and abstracts were screened by two independent reviewers (SG, ATM) with input from the senior author (MCP) in case of ambiguity. Inclusion criteria for this meta-analysis were as follows: (1) all patients with histopathologically confirmed (WHO grade III and grade IV) HGG including recurrent gliomas and (2) all studies reporting on the GTR or CRET rate and survival outcomes (OS and PFS) pertinent to the use of 5-ALA in the surgical resection of HGGs in adult patients. Laboratory studies, technical reports, review articles including systematic reviews, editorials, commentaries, conference proceedings, and abstracts were excluded from the analyses. Studies were also excluded if there was a lack of clear reporting of HGG type (i.e., whether HGG was primary or recurrent), if they had a small sample size ($n < 10$), if they included overlapping patient populations, and if we were unable to extract analyzable data points.

Full-text review of the studies shortlisted using the above methodology was conducted by two reviewers in an independent fashion, and the relevant data were subsequently extracted from each study for further statistical analyses. The variables of interest included first-author name, year of publication, study design, sample size, demographic distribution, follow-up duration, survival data, EOR, and subtypes and location of glioma. The study design was used as a surrogate marker for assessing any biases. Studies were analyzed quantitatively for three major parameters: GTR (defined as >95% tumor volume resection), PFS, and OS rates. In studies that reported a 95% CI and no standard deviation (SD) in their results, the SD value was obtained from a formula using the standard errors and 95% CI values as follows:

$$\mathrm{SD} = \sqrt{N} \times \frac{(\mathrm{UL} - \mathrm{LL})}{3.92}$$

where N is the number of subjects, UL is the upper limit and LL is the lower limit of the 95% CI.

Additionally, in studies with a lower sample size ($n < 50$), the denominator of 3.92 was replaced with a manual t distribution calculation using the degree of freedom (23). This calculation allowed for inclusion of a few studies in our final analyses that have been excluded in the previously reported studies.

Statistical Analysis of Data

After obtaining the proportional values of GTR >95% and the mean (SD) values for OS and PFS as described above, the statistical analysis was conducted using an open-source meta-analytical software, Open MetaAnalyst for Mac OS Sierra 10.12 (Brown University, Providence, RI). Heterogeneity across the various studies included for the meta-analyses was determined using an I^2 statistical test for inconsistency with an arbitrary cutoff value of $I^2 \geq 50\%$ with a $P < 0.05$ representing significant heterogeneity. A fixed-effect model was used for conducting the meta-analysis in the absence of substantial heterogeneity, and a random-effect model was used for significant heterogeneity across the various combined studies. The random-effect model utilized the DerSimonian-Laird method to evaluate within-study variance (24).

RESULTS

The initial screening using the search strategy described in the Methods section yielded 864 articles, commentaries, and conference proceedings. After removal of duplicates and screening for non-English and non-relevant articles, 88 full-text articles remained. Each full-text article was checked by two independent reviewers to confirm that it met the inclusion criteria (**Figure 1**). Sixty-five articles were excluded because they did not meet the aforementioned eligibility criteria for this study. Twenty-three studies were included in the final meta-analysis of the pooled GTR and survival outcomes analysis.

5-ALA and Gross Total Resection

Of the 23 studies included in the analyses, 19 reported a GTR or CRET rate (5, 25–42). The number of participants who underwent 5-ALA–guided resection in these studies ranged from 10 to 139, with the GTR ranging from 47.6 to 98.5%. The I^2 statistics showed a significant heterogeneity level (90.09%; $P < 0.001$). Therefore, a random-effect model was used for the pooled estimate of these data. In pooled analysis of all HGGs, including

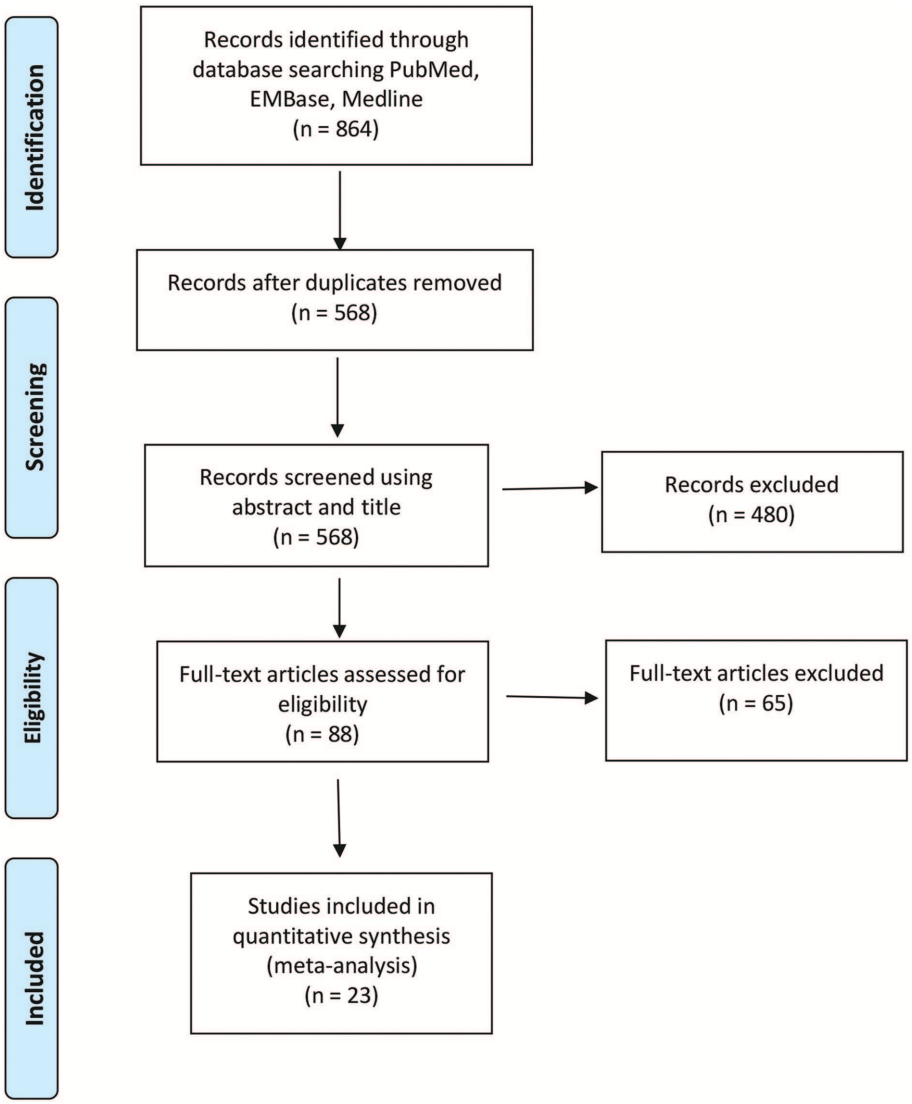

FIGURE 1 | Preferred Reporting Items for Systematic Reviews and Meta-Analyses (PRISMA) flow diagram of the studies included in the meta-analysis of resection and survival outcomes among patients with 5-aminolevulinic acid–guided resection of high-grade glioma. Used with permission from Barrow Neurological Institute, Phoenix, Arizona.

primary and recurrent subtypes, GTR was achieved in 759 of 998 patients, resulting in an overall GTR rate of 76% (95% CI, 69–83%; $P < 0.001$) (**Figure 2**). In the subgroup analysis of primary GBM alone, GTR was achieved in 599 of 796 patients, resulting in a similar GTR rate of 76.8% (95% CI, 68–85%, $P < 0.001$) (**Figure 3**).

Four case-controlled studies were found to be eligible for a meta-analysis of GTR with 5-ALA ($n = 382$) vs. conventional resection ($n = 326$) (31, 34, 37, 43). All other covariates (e.g., use of intraoperative MRI, postoperative treatment with specific chemotherapeutic agents) remained the same within each study but were variable across the studies. However, there was no significant statistical heterogeneity across these studies ($I^2 = 0\%$; $P = 0.57$); hence, we used a fixed-effect model for analysis. GTR was achieved in 302 of 382 (79.1%) patients in the 5-ALA group vs. 172 of 326 (52.8%) patients in the control group. In the pooled estimate of all HGGs (primary and recurrent), 5-ALA was associated with a 26% increase in GTR rate compared with the control group in which surgeries were performed without 5-ALA, resulting in OR = 3.79 (95% CI, 2.65–5.41; $P < 0.001$) for achieving GTR (**Figure 4**).

Overall Survival Data for 5-ALA–Guided Glioma Resection

Of the 23 studies, 9 reported a mean OS period in months ranging from 10 to 22 months (5, 25, 26, 31, 34, 44–47). One of the studies, by Stummer et al. (31), stratified the survival analysis by age (55 years of age and younger vs. older than 55 years). Hence, these

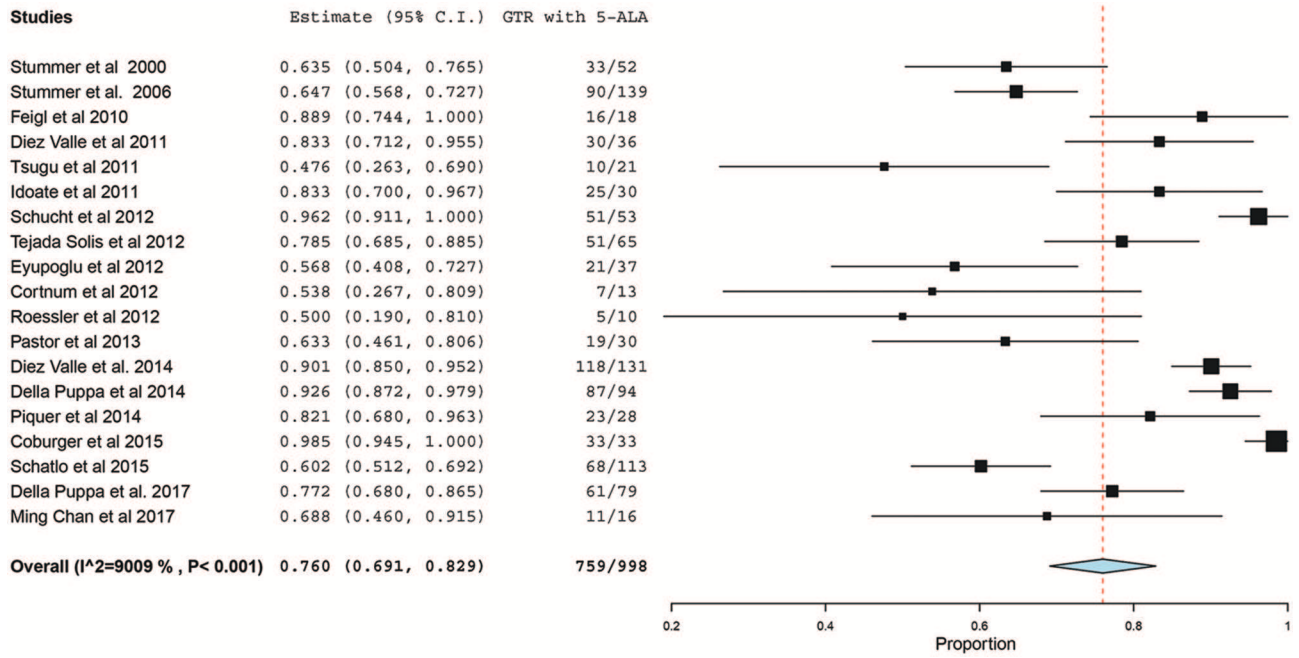

FIGURE 2 | Forest plot graph representing the meta-analysis of gross total resection (GTR) rate (95% confidence interval [CI]) among patients with high-grade glioma, including primary and recurrent cases, treated using 5-aminolevulinic acid (5-ALA)–guided surgical resection. Used with permission from Barrow Neurological Institute, Phoenix, Arizona.

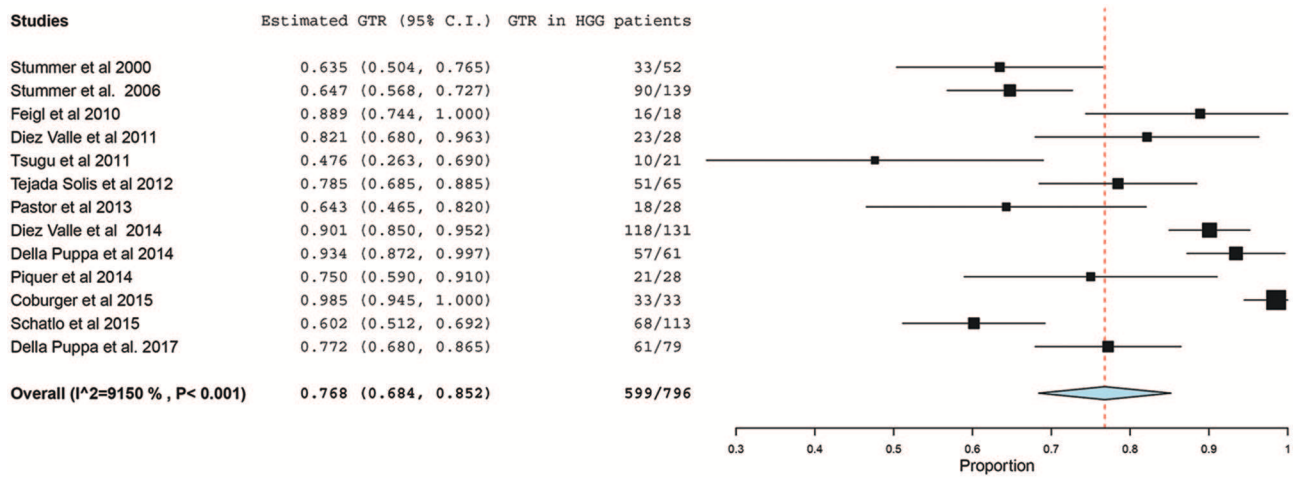

FIGURE 3 | Forest plot graph representing the meta-analysis of gross total resection (GTR) rate (95% confidence interval [CI]) among patients with primary high-grade glioma (HGG) treated using 5-aminolevulinic acid–guided surgical resection. Used with permission from Barrow Neurological Institute, Phoenix, Arizona.

patients were included in our analysis as two independent patient groups conducted by the same methodology used by this phase III randomized control trial (RCT) (31). Similarly, another study had subdivided its patients into two treatment groups (treated using 5-ALA) and one control group (treated without the use of 5-ALA).Thus, we treated the two treatment arms as independent patient groups in our analysis for OS (25). Therefore, 11 distinct groups of patients who underwent 5-ALA–guided resection of primary HGG were extracted for analysis. There was significant heterogeneity across these groups ($I^2 = 96.3\%$; $P < 0.001$); therefore, a random-effects model for continuous variable was used. The meta-analysis in the group of patients with primary HGG who underwent 5-ALA–guided resection showed a mean OS of 16.3 months (95% CI, 14.1–18.5 months; $P < 0.001$) (**Figure 5**). Five studies (seven distinct 5-ALA groups) were available for comparison of OS (measured as a mean survival

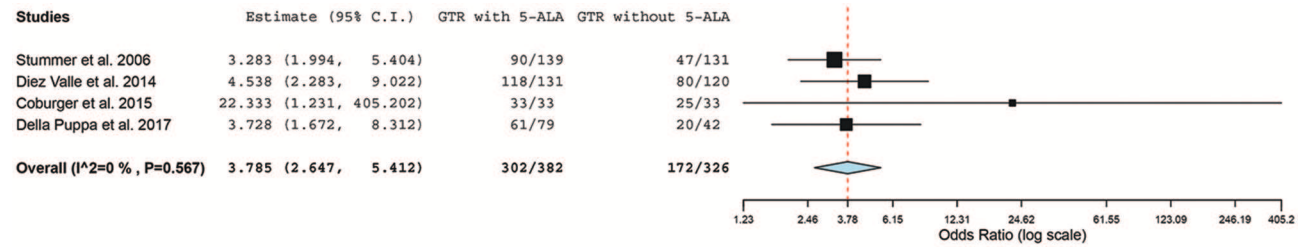

FIGURE 4 | Forest plot graph representing the meta-analysis of the odd ratio (95% confidence interval [CI]) of gross total resection (GTR) among patients with primary high-grade gliomas treated using 5-aminolevulinic acid (5-ALA)–guided surgical resection vs. conventional microsurgical resection. Used with permission from Barrow Neurological Institute, Phoenix, Arizona.

difference) between 5-ALA vs. control groups (25, 31, 34, 46, 47). No significant heterogeneity was noted across these groups ($I^2 = 0\%$; $P = 0.47$); hence, we used a fixed-effects model. The meta-analysis yielded a pooled OS difference of 3.05 months (95% CI, 2.43–3.68 months; $P < 0.001$) favoring 5-ALA-guided resection compared with control groups without 5-ALA (**Figures 6**, **7**).

Progression Free Survival Data for 5-ALA Guided Glioma Resection

Of the 23 papers, three studies reported PFS ranging from 5.1 to 11 months. From these 3 studies, 4 distinct groups of patients who underwent 5-ALA–guided resection of primary HGG were extracted for analysis. Significant heterogeneity was noted across these groups ($I^2 = 96.3\%$; $P < 0.001$), with use of a random-effects model for continuous variables. The meta-analysis of patients with primary HGG who underwent 5-ALA–guided resection showed a mean PFS of 8.4 months (95% CI, 5.9–10.9 months; $P < 0.001$) (**Figure 8**). The mean PFS difference was 1.03 months (95% CI, 0.61–1.45 months; $P < 0.001$) favoring 5-ALA when compared with matched control groups (**Figures 9**, **10**).

DISCUSSION

Interpretation of the Meta-Analytic Data

This meta-analysis was conducted to evaluate the potential survival advantage gained, if any, with the use of 5-ALA–guided resection of HGGs. The pooled analysis of 998 patients with HGG who underwent 5-ALA–guided surgical resection showed a higher rate of GTR in the cohort of all patients with HGG (∼76%) as well as in the subgroup of patients with primary HGG (∼77%), as compared with the phase III RCT conducted by Stummer et al. (31) that reported a GTR rate of 65%. The pooled analysis of the eligible case-controlled studies demonstrated that the estimated GTR rate was significantly higher with the intraoperative use of 5-ALA compared with conventional white light technique surgery (79 vs. 53%; OR = 3.78; $P < 0.001$). As GTR is the most significant independent prognostic marker of survival in patients with HGG (1), these results encourage the utilization of fluorescence-guided resection of these lesions. There was a high level of heterogeneity across the studies included in this pooled GTR analysis, attributable to the observational nature of some of these studies and a multitude of other factors that are difficult to control for. For example, invasion of eloquent cortical tissue by an aggressive lesion, determined by preoperative imaging or intraoperatively, is a critical reason for planned subtotal resection, irrespective of the use of 5-ALA. However, inclusion of such preplanned subtotal resection can contribute to an underestimation of the rate of GTR truly attributable to the use of fluorescence guidance. Unfortunately, owing to the lack of specific data in these studies regarding GTR rate in eloquent cortical locations, an analysis could not be performed on this specific population.

The collated survival analysis demonstrated an overall survival advantage (∼3-months higher mean OS; $P < 0.001$) with the use of 5-ALA. This has been represented using a cumulative meta-analysis that shows a positive trend in the increase in mean survival difference across the studies published over time (**Figure 7**). However, OS is not the most convenient study endpoint owing to the vast heterogeneity and lack of control on the various postoperative adjuvant therapies that can influence the overall survival. Additionally, in recent years, there seems to be an increase in survival for all patients with HGG that is perhaps attributable to the standardization of the Stupp protocol (19), constant evolution of chemotherapeutic agents and radiotherapy modalities, and introduction of immunotherapy and targeted genetic therapies (48, 49). PFS is a better primary study endpoint for survival analysis than OS because of shorter follow-up period, controlling for the effects of non-study-related therapies in influencing survival and avoiding confusion from the multiple reasons for death. Unfortunately, the amount of data available on PFS in controlled studies is limited, as shown by the cumulative meta-analysis (**Figure 10**). Of the three studies included in PFS analysis, a statistically significant delay of 1 month in time to progression was noted in our pooled cohort (25, 26, 31, 34).

Evolution of Evidence on Benefits of 5-ALA–Guided HGG Surgery

The first clinical study on 5-ALA was reported in 1998, which led to the development of the pivotal randomized, multicenter phase III clinical trial in 5-ALA by Stummer et al. (31) in 2006. The study reported a 29% difference in CRET (65% in 5-ALA vs. 36% using white light surgery; $P < 0.001$). This study demonstrated superior clinical outcomes, significantly

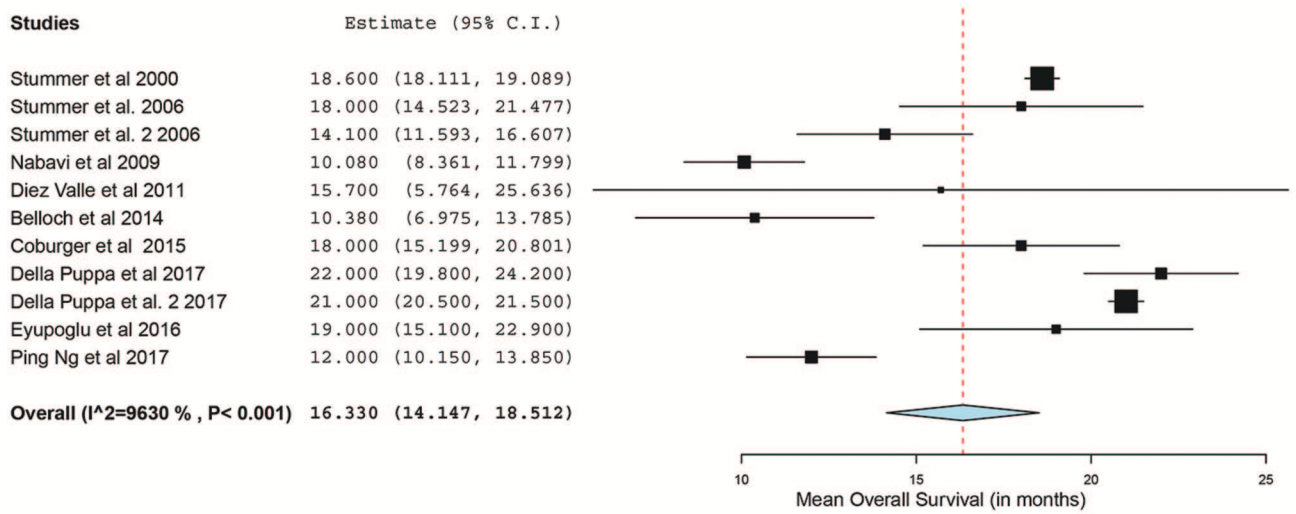

FIGURE 5 | Forest plot graph representing the meta-analysis of mean overall survival (95% confidence interval [CI]) among patients with primary high-grade gliomas treated using 5-aminolevulinic acid–guided surgical resection. Used with permission from Barrow Neurological Institute, Phoenix, Arizona.

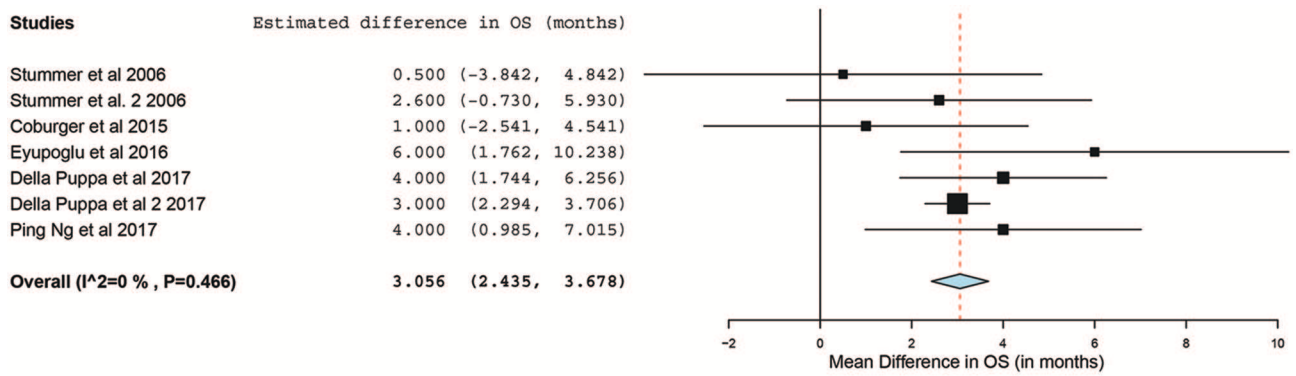

FIGURE 6 | Forest plot graph representing the meta-analysis of mean difference in overall survival (95% confidence interval [CI]) among patients with primary high-grade glioma treated using 5-aminolevulinic acid–guided surgical resection vs. conventional microsurgical resection. Used with permission from Barrow Neurological Institute, Phoenix, Arizona.

higher rates of CRET, and significant improvement in PFS at 6 months using fluorescence-guided surgery vs. the conventional wide-field microsurgical resection (31). In 2007, on the basis of the results of the aforementioned trial, EMA approved the use of 5-ALA. Thereafter, the drug was approved by various countries. In 2011, an FDA request for approval of 5-ALA was filed. The conceptualization of this drug as a therapeutic agent rather than an intraoperative diagnostic tool led to significant delay in the approval of 5-ALA in the United States (9). The drug received FDA approval in June 2017 and became the first optical agent approved by the FDA for use as an intraoperative imaging resource for the resection of HGGs. It is critical to treat 5-ALA and other optical agents as diagnostic markers or tools and not as a means of therapeutic intervention. 5-ALA fluorescence guidance is a modality that is associated with a direct benefit of improving GTR rates and an indirect effect on survival outcomes by increasing maximal safe surgical resection. This is the reason our study chose to assess GTR rates and survival outcomes (OS, PFS) in our final analysis. Concurrently, since the early 2000s, various preclinical and a few clinical studies have investigated the potential therapeutic role of 5-ALA for photodynamic therapy for malignant gliomas with what appear to be advantageous preliminary results (16, 18, 50–59).

Previous Systematic Reviews and Meta-Analyses on 5-ALA–Guided Surgical Resection

Several systematic literature reviews have evaluated the role of fluorescence-guided surgery grouping several optical agents (e.g., fluorescein, 5-ALA, indocyanine green) in terms of GTR, diagnostic metrics (sensitivity and specificity), and survival outcomes (18, 21, 22, 60, 61). Because fluorescein, 5-ALA,

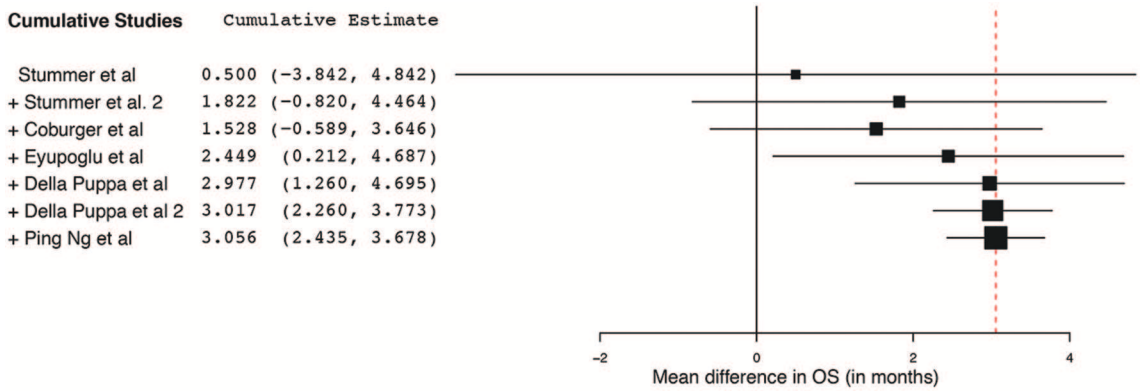

FIGURE 7 | Cumulative regression analysis demonstrating the temporal trend of mean difference (95% confidence interval [CI]) in overall survival among patients with primary high-grade glioma treated using 5-aminolevulinic acid–guided surgical resection vs. conventional microsurgical resection. Used with permission from Barrow Neurological Institute, Phoenix, Arizona.

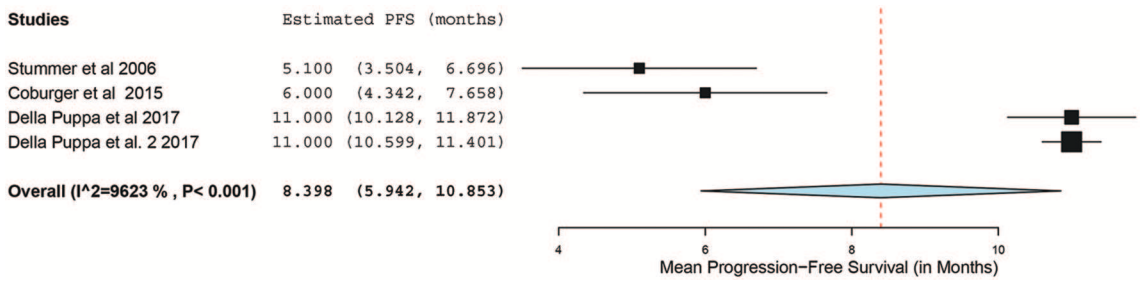

FIGURE 8 | Forest plot graph representing the meta-analysis of mean progression-free survival (95% confidence interval [CI]) among patients with primary high-grade glioma treated using 5-aminolevulinic acid–guided surgical resection. Used with permission from Barrow Neurological Institute, Phoenix, Arizona.

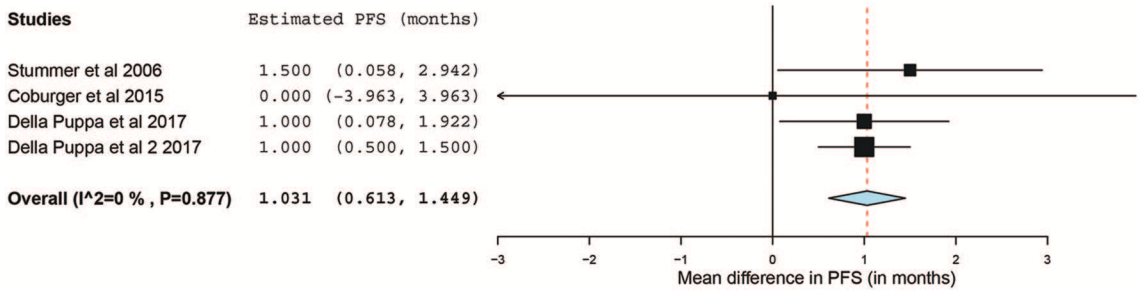

FIGURE 9 | Forest plot graph representing the meta-analysis of mean difference in progression-free survival (95% confidence interval [CI]) among patients with primary high-grade glioma treated using 5-aminolevulinic acid–guided surgical resection vs. conventional microsurgical resection. Used with permission from Barrow Neurological Institute, Phoenix, Arizona.

and indocyanine green have substantially different fluorescent properties and mechanistic behaviors, our study focused on the evaluation of these important study endpoints with the use of 5-ALA as a fluorophore. Eljamel et al. (20) conducted a meta-analysis of 5-ALA–guided resection of GBMs and reported a high sensitivity (82.6%) and specificity (88.9%). The 75% mean GTR rate was in congruence with our results that included a higher sample size. The mean PFS reported in that study was also similar to the PFS reported in our study (∼8 months). In contrast with that study, we calculated the measures of continuous outcomes (e.g., SD) as mentioned in the Methods and included several observational studies that were excluded in the previous analyses.

Mansouri et al. (10) conducted a systematic review of literature to assess the adjunctive intraoperative role of 5-ALA in HGGs. The study included 43 articles (1 RCT, 28

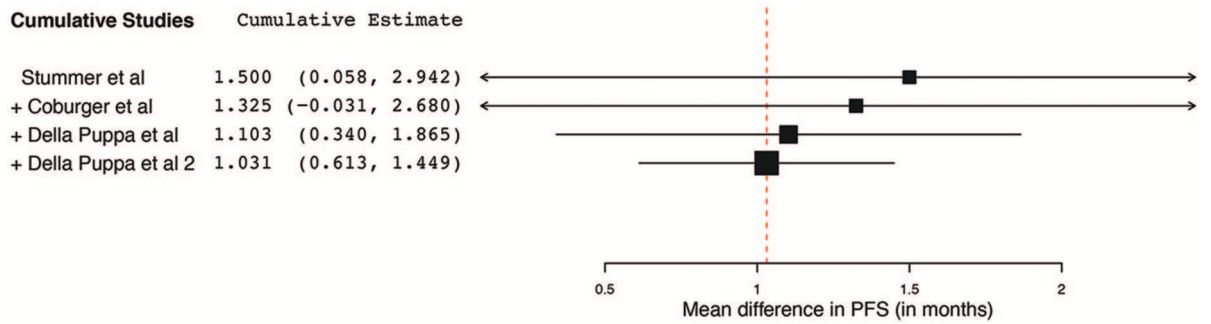

FIGURE 10 | Cumulative regression analysis demonstrating the temporal trend of mean difference in progression-free survival (95% confidence interval [CI]) among patients with primary high-grade glioma treated using 5-aminolevulinic acid–guided surgical resection vs. conventional microsurgical resection. Used with permission from Barrow Neurological Institute, Phoenix, Arizona.

prospective studies, and 14 retrospective studies) and concluded that 5-ALA was associated with improved tumor visualization with a diagnostic accuracy >80%, enabling a greater EOR, that could be indirectly linked to increased survival. Our study had similar inclusion criteria to the aforementioned study. However, we added the quantitative data analyses to objectively evaluate the added benefit of using 5-ALA in HGG surgery.

Potential Limitations of 5-ALA

Fluorophores for intraoperative *in vivo* use in the brain are limited (62). Like other fluorophores in use, 5-ALA has certain drawbacks for its use in a clinical setting. Exogenous administration of 5-ALA leads to selective accumulation of PpIX in the malignant cells of HGG tumors, as mentioned previously (8, 11, 12). From a metabolomic perspective, the molecular mechanism of action of 5-ALA leading to a differential fluorescence of malignant cells can be attributed to the turnover rate of PpIX rather than its accumulation. For instance, in a study of WHO Grade III glioma patients with an *IDH-1* mutation, a depletion of nicotinamide adenine dinucleotide phosphate was hypothesized to mediate the differential temporary accumulation of PpIX (a downstream product of 5-ALA in heme synthesis pathway) in the malignant cells (63). Numerous studies have reported on the potential molecular mechanism for 5-ALA fluorescence properties in malignant cells (63–66). An in-depth analysis of this is beyond the scope of this article.

Blood brain barrier disruption is essential for the accumulation of PpIX in the malignant cells, which is hypothesized to be the cause for lower or negligible fluorescence in LGG cases (8). In addition, the visual PpIX fluorescence signal can be vague or inhomogeneous in appearance with various areas of high and low signal intensity even in HGGs (67, 68). This patchy appearance may be attributed to inhomogeneous tumor growth, glioma cell diversity, overall tissue component heterogeneity (e.g., cysts and necrotic tissue), and differential tumor cellular metabolism. Another level of complexity in accurate detection of fluorescence signal strength originates with the optical detection equipment (e.g., operating microscopes) (7). Limitations of wide-field operating microscopy imaging can, in turn, lead to reduced accuracy of tumor detection at the marginal infiltrative border, especially in eloquent cortical locations. Adjunctive tools that can improve fluorescence detection and provide intraoperative cellular or near-cellular resolution of PpIX fluorescence include the confocal laser endomicroscope (69) and the scanning fiber endoscope (67), whereas implicational or indirect indication of such fluorescent labeling can be correlated with spectroscopy (70–75) and other intraoperative diagnostic adjuncts, such as brain mapping, neuronavigation, ultrasound navigation, and intraoperative MRI (10, 41, 62, 75). These technologies, alone or synergistically, may help to alleviate these limitations and increase the overall EOR.

Photobleaching, defined as the degradation of fluorescence signal of PpIX with prolonged light exposure, is an important limiting phenomenon of which the neurosurgeon should be aware. PpIX photobleaching is directly related to the intensity of the operating microscope light as well as the duration of exposure (7). Photobleaching of PpIX is usually not of major concern during resection of high-grade gliomas, because new tissue layers with unbleached PpIX are exposed with the advancement of resection (11). However, photobleaching may impact accurate quantification or detection of any pathology with low fluorescence signal strength (7). Stummer et al. (11) and Belykh et al. (7) have discussed the potential reasons for insufficient or absent fluorescence and how to circumvent the technical issues, including but not limited to the presence of blood products or overlying soft tissue, photobleaching, improper 5-ALA administration, and incorrect microscope settings. Additionally, the use of 5-ALA requires intermittent switching between the blue light and the white light modes of the neurosurgical operating microscope. Use of 5-ALA likely increases operative time and certainly increases pharmaceutical procedure costs.

Use of Intraoperative MRI in Conjunction With 5-ALA

In addition to neuronavigation and intraoperative cortical (sensory/motor) monitoring, several studies investigated the use

of iMRI with 5-ALA guidance. As gadolinium enhancement on MRI is still the most reliable radiological marker of the EOR, these data are important to consider. Tsugu et al. (42) emphasized the utility of iMRI in patients with negative fluorescence, increasing the GTR to 55.6% from zero. However, the study did not show significant resection benefit with the adjunctive use of iMRI in patients with strong PpIX fluorescence signal. A retrospective study by Roder et al. (76) showed higher CRET rates in patients with iMRI plus 5-ALA vs. 5-ALA alone (74% vs. 45%; $P = 0.02$). Another study with 99 patients with malignant glioma undergoing 5-ALA–guided surgery in conjunction with iMRI reported a mean resection rate of 95% and suggested that 5-ALA allowed marginal tumor identification of the tumor extension beyond its radiological borders on iMRI (77). A recent systematic review by Coburger et al. concluded that the simultaneous use of 5-ALA in conjunction with iMRI can provide superior resection margins beyond radiological contrast enhancement (78). Obvious drawbacks of iMRI would be the added surgical time and significant increase in facilities and procedural costs. Although the assessment of iMRI in conjunction with 5-ALA was beyond the scope of this study, it may play a role in improving EOR and GTR in brain tumors with minimal or negative 5-ALA fluorescence.

Potential Therapeutic Role of 5-ALA

Recent years have witnessed a surge in the institution of novel adjuvant therapies in the management of HGGs, including photodynamic therapy (18, 79). Photodynamic therapy causes direct cytotoxicity by activating cellular death via apoptosis, necrosis, autophagy, and paraptosis through various intrinsic intracellular mechanisms. Several *in vitro* and *in vivo* studies have evaluated the role of 5-ALA as a therapeutic agent for intraoperative photodynamic therapy of the residual tumor (50, 52, 57, 79). Early *in vivo* studies have shown promising results. Because 5-ALA is not cytotoxic on systemic administration and has a better adverse effect profile than the other photosensitizer therapies, it has the potential to function beyond its role as a diagnostic tool by becoming a part of the future armamentarium of adjuvant therapies for aggressive gliomas.

Other Agents for Fluorescence Image-Guided Surgery

Apart from 5-ALA, fluorescein sodium has been used for intraoperative fluorescence-guided resection of HGGs. Fluorescein is an intravenous dye with selective accumulation through a damaged blood-brain barrier in malignant gliomas. A multicenter, controlled, Phase II trial showed complete resection of tumor in 82.6% patients with a 6-month PFS of 56.6%. However, the fluorescence characteristics of fluorescein are different than 5-ALA (2). Both exhibit variable fluorescence signal strength toward the periphery of the tumor, but, while 5-ALA stains cells, fluorescein is a non-specific dye leaked into the extravascular space by means of abnormal tumor vasculature or cortical trauma, with minor uptake by some cells (80). Thus, identification of the tumor marginal zone may be more difficult with fluorescein using wide-field fluorescence detection of the operating microscope, although it presents unique background staining of all cells visualized using confocal laser endomicroscopy (2, 67, 81). An advantage of fluorescein is that dosing can be repeated to a limited degree in the operating room. A pilot study recently investigated the synergistic use of 5-ALA and fluorescein in primary GBM. The complementary properties of these agents were used to capitalize on the advantages of each fluorophore to identify the tumor border zone in these patients (82). There are fewer studies on the use of fluorescein sodium compared to those using 5-ALA. Additional controlled comparative studies with a larger patient cohort are needed to establish the role of other fluorophores in image-guided resection of malignant gliomas.

Study Limitations and Potential Biases

There have been a few publications that have systematically documented the various aspects of the role of 5-ALA in HGGs, as discussed above (10, 20–22). Our study focused on the quantitative data synthesis of EOR, OS, and PFS in HGGs. However, there is a high degree of heterogeneity in the data based on factors such as tumor location, radiological assessment of residual or recurrent tumor, different protocols for neoadjuvant or adjuvant therapy, differential resources or utilization of adjunctive intraoperative tools discussed above, and so on (37, 41, 46, 76). Additionally, the studies were performed at various institutions internationally, imparting a greater degree of diversity in management strategy. The level of evidence supporting the benefit of fluorescence-guided surgery using 5-ALA in HGG is very low to low quality in nature, with the exception of one RCT (31). Therefore, these data must be interpreted with caution. Since 5-ALA is already approved in most of the countries, conducting an additional controlled study might present an ethical problem. Further blinded multicenter RCTs will aid in generating class I level of evidence for the survival outcomes associated with 5-ALA and comparing 5-ALA to the other available intraoperative adjuncts (e.g., iMRI, ultrasound, confocal laser endomicroscopy, and scanning fiber endoscopy) to improve maximal safe EOR (8, 67, 83). Although we attempted careful selection of studies, we cannot control for the inherent limitations and potential risks of surgical trial and retrospective study biases in this pooled analysis of data.

CONCLUSION

Our systematic review and meta-analysis show a modest survival benefit associated with the use of 5-ALA–guided surgery for HGGs. Unfortunately, at this time, the small number of studies and the low level of evidence of the available studies limit the ability to draw firm conclusions about the impact of 5-ALA–guided HGG resection on the OS and PFS of these patients. More high-quality studies with better controlling of confounding factors, such as adjuvant therapies, are needed to delineate the

role of 5-ALA–guided surgery in improving survival of patients with these daunting tumors.

DATA AVAILABILITY

The raw data supporting the conclusions of this manuscript will be made available by the authors, without undue reservation, to any qualified researcher.

AUTHOR CONTRIBUTIONS

SG: literature review and study selection, statistical analysis, figures, manuscript draft, revision, and final draft approval. AT and LB: manuscript draft, review of final draft. EB: manuscript draft, figures, review of final draft. CC: literature review and study selection, review of final draft. XZ: statistical analysis, review of final draft. MS: table for summary of studies, statistical analysis, review of final draft. ML, PN, and MP: study supervision, review and revision of final draft. MP: generation of the topic, approval of final draft.

FUNDING

This research was supported by funds from the Barrow Neurological Foundation, by the Women's Board of the Barrow Neurological Institute, and by the Newsome Chair in Neurosurgery Research to MP. EB acknowledges scholarship support SP-2240.2018.4.

ACKNOWLEDGMENTS

The authors thank the staff of Neuroscience Publications at Barrow Neurological Institute for assistance with manuscript preparation.

REFERENCES

1. Brown TJ, Brennan MC, Li M, Church EW, Brandmeir NJ, Rakszawski KL, et al. Association of the extent of resection with survival in glioblastoma: a systematic review and meta-analysis. *JAMA Oncol.* (2016) 2:1460–9. doi: 10.1001/jamaoncol.2016.1373
2. Acerbi F, Broggi M, Schebesch KM, Hohne J, Cavallo C, De Laurentis C, et al. Fluorescein-guided surgery for resection of high-grade gliomas: a multicentric prospective phase II study (FLUOGLIO). *Clin Cancer Res.* (2018) 24:52–61. doi: 10.1158/1078-0432.CCR-17-1184
3. Li C, Sullivan PZ, Cho S, Nasrallah MP, Buch L, Isaac Chen HC, et al. Intraoperative molecular imaging with second window ICG facilitates confirmation of contrast-enhancing tissue during intracranial stereotactic needle biopsy: a case series. *World Neurosurg.* (2019). 126:e1211–8 doi: 10.1016/j.wneu.2019.02.231
4. Zeh R, Sheikh S, Xia L, Pierce J, Newton A, Predina J, et al. The second window ICG technique demonstrates a broad plateau period for near infrared fluorescence tumor contrast in glioblastoma. *PLoS ONE.* (2017) 12:e0182034. doi: 10.1371/journal.pone.0182034
5. Stummer W, Novotny A, Stepp H, Goetz C, Bise K, Reulen HJ. Fluorescence-guided resection of glioblastoma multiforme by using 5-aminolevulinic acid-induced porphyrins: a prospective study in 52 consecutive patients. *J Neurosurg.* (2000) 93:1003–13. doi: 10.3171/jns.2000.93.6.1003
6. Diez Valle R, Hadjipanayis CG, Stummer W. Established and emerging uses of 5-ALA in the brain: an overview. *J Neuro Oncol.* (2019) 141:487–94. doi: 10.1007/s11060-018-03087-7
7. Belykh E, Miller EJ, Patel AA, Bozkurt B, Yagmurlu K, Robinson TR, et al. Optical characterization of neurosurgical operating microscopes: quantitative fluorescence and assessment of PpIX photobleaching. *Sci Reports.* (2018) 8:12543. doi: 10.1038/s41598-018-30247-6
8. Belykh E, Martirosyan NL, Yagmurlu K, Miller EJ, Eschbacher JM, Izadyyazdanabadi M, et al. Intraoperative fluorescence imaging for personalized brain tumor resection: current state and future directions. *Front Surg.* (2016) 3:55. doi: 10.3389/fsurg.2016.00055
9. Hadjipanayis CG, Stummer W. 5-ALA and FDA approval for glioma surgery. *J Neurooncol.* (2019) 141:479–86. doi: 10.1007/s11060-019-03098-y
10. Mansouri A, Mansouri S, Hachem LD, Klironomos G, Vogelbaum MA, Bernstein M, et al. The role of 5-aminolevulinic acid in enhancing surgery for high-grade glioma, its current boundaries, and future perspectives: a systematic review. *Cancer.* (2016) 122:2469–78. doi: 10.1002/cncr.30088
11. Stummer W, Suero Molina E. Fluorescence imaging/agents in tumor resection. *Neurosurg Clin North Am.* (2017) 28:569–83. doi: 10.1016/j.nec.2017.05.009
12. Stummer W, Stocker S, Novotny A, Heimann A, Sauer O, Kempski O, et al. *In vitro* and *in vivo* porphyrin accumulation by C6 glioma cells after exposure to 5-aminolevulinic acid. *J Photochem Photobiol B Biol.* (1998) 45:160–9. doi: 10.1016/S1011-1344(98)00176-6
13. Stummer W, Stocker S, Wagner S, Stepp H, Fritsch C, Goetz C, et al. Intraoperative detection of malignant gliomas by 5-aminolevulinic acid-induced porphyrin fluorescence. *Neurosurgery.* (1998) 42:518–25; discussion 25–6.
14. Aldave G, Tejada S, Pay E, Marigil M, Bejarano B, Idoate MA, et al. Prognostic value of residual fluorescent tissue in glioblastoma patients after gross total resection in 5-aminolevulinic Acid-guided surgery. *Neurosurgery.* (2013) 72:915–20; discussion 20–1. doi: 10.1227/NEU.0b013e31828c3974
15. Jaber M, Wolfer J, Ewelt C, Holling M, Hasselblatt M, Niederstadt T, et al. The value of 5-aminolevulinic acid in low-grade gliomas and high-grade gliomas lacking glioblastoma imaging features: an analysis based on fluorescence, magnetic resonance imaging, 18F-fluoroethyl tyrosine positron emission tomography, and tumor molecular factors. *Neurosurgery.* (2016) 78:401–11; discussion 11. doi: 10.1227/NEU.0000000000001020
16. Fisher CJ, Niu C, Foltz W, Chen Y, Sidorova-Darmos E, Eubanks JH, et al. ALA-PpIX mediated photodynamic therapy of malignant gliomas augmented by hypothermia. *PLoS ONE.* (2017) 12:e0181654. doi: 10.1371/journal.pone.0181654
17. Kimura S, Kuroiwa T, Ikeda N, Nonoguchi N, Kawabata S, Kajimoto Y, et al. Assessment of safety of 5-aminolevulinic acid-mediated photodynamic therapy in rat brain. *Photodiagn Photodyn Ther.* (2018) 21:367–74. doi: 10.1016/j.pdpdt.2018.02.002
18. Mahmoudi K, Garvey KL, Bouras A, Cramer G, Stepp H, Jesu Raj JG, et al. 5-aminolevulinic acid photodynamic therapy for the treatment of high-grade gliomas. *J Neuro Oncol.* (2019) 141:595–607. doi: 10.1007/s11060-019-03103-4
19. Stupp R, Mason WP, van den Bent MJ, Weller M, Fisher B, Taphoorn MJ, et al. Radiotherapy plus concomitant and adjuvant temozolomide for glioblastoma. *N Engl J Med.* (2005) 352:987–96. doi: 10.1056/NEJMoa043330
20. Eljamel S. 5-ALA Fluorescence image guided resection of glioblastoma multiforme: a meta-analysis of the literature. *Int J Mol Sci.* (2015) 16:10443–56. doi: 10.3390/ijms160510443
21. Barone DG, Lawrie TA, Hart MG. Image guided surgery for the resection of brain tumours. *Cochrane Database System Rev.* (2014) 2014:Cd009685. doi: 10.1002/14651858.CD009685.pub2
22. Jenkinson MD, Barone DG, Bryant A, Vale L, Bulbeck H, Lawrie TA, et al. Intraoperative imaging technology to maximise extent of resection for glioma. *Cochrane Database System Rev.* (2018) 1:Cd012788. doi: 10.1002/14651858.CD012788.pub2
23. Higgins JPTGS. *Cochrane Handbook for Systematic Reviews.* The Cochrane Collaboration. Hoboken, NJ: Wiley-Blackwell (2011).

24. DerSimonian R, Laird N. Meta-analysis in clinical trials. *Controlled Clin Trials.* (1986) 7:177–88. doi: 10.1016/0197-2456(86)90046-2
25. Della Puppa A, Lombardi G, Rossetto M, Rustemi O, Berti F, Cecchin D, et al. Outcome of patients affected by newly diagnosed glioblastoma undergoing surgery assisted by 5-aminolevulinic acid guided resection followed by BCNU wafers implantation: a 3-year follow-up. *J Neuro Oncol.* (2017) 131:331–40. doi: 10.1007/s11060-016-2301-z
26. Diez Valle R, Tejada Solis S, Idoate Gastearena MA, Garcia de Eulate R, Dominguez Echavarri P, Aristu Mendiroz J. Surgery guided by 5-aminolevulinic fluorescence in glioblastoma: volumetric analysis of extent of resection in single-center experience. *J Neuro Oncol.* (2011) 102:105–13. doi: 10.1007/s11060-010-0296-4
27. Eyupoglu IY, Hore N, Savaskan NE, Grummich P, Roessler K, Buchfelder M, et al. Improving the extent of malignant glioma resection by dual intraoperative visualization approach. *PLoS ONE.* (2012) 7:e44885. doi: 10.1371/journal.pone.0044885
28. Feigl GC, Ritz R, Moraes M, Klein J, Ramina K, Gharabaghi A, et al. Resection of malignant brain tumors in eloquent cortical areas: a new multimodal approach combining 5-aminolevulinic acid and intraoperative monitoring. *J Neurosurg.* (2010) 113:352–7. doi: 10.3171/2009.10.JNS09447
29. Idoate MA, Diez Valle R, Echeveste J, Tejada S. Pathological characterization of the glioblastoma border as shown during surgery using 5-aminolevulinic acid-induced fluorescence. *Neuropathology.* (2011) 31:575–82. doi: 10.1111/j.1440-1789.2011.01202.x
30. Schucht P, Beck J, Abu-Isa J, Andereggen L, Murek M, Seidel K, et al. Gross total resection rates in contemporary glioblastoma surgery: results of an institutional protocol combining 5-aminolevulinic acid intraoperative fluorescence imaging and brain mapping. *Neurosurgery.* (2012) 71:927–35; discussion 35–6. doi: 10.1227/NEU.0b013e31826d1e6b
31. Stummer W, Pichlmeier U, Meinel T, Wiestler OD, Zanella F, Reulen HJ, et al. Fluorescence-guided surgery with 5-aminolevulinic acid for resection of malignant glioma: a randomised controlled multicentre phase III trial. *Lancet Oncol.* (2006) 7:392–401. doi: 10.1016/S1470-2045(06)70665-9
32. Tejada-Solis S, Aldave-Orzaiz G, Pay-Valverde E, Marigil-Sanchez M, Idoate-Gastearena MA, Diez-Valle R. Prognostic value of ventricular wall fluorescence during 5-aminolevulinic-guided surgery for glioblastoma. *Acta Neurochirurg.* (2012) 154:1997–2002. doi: 10.1007/s00701-012-1475-1
33. Chan DTM, Yi-Pin Sonia H, Poon WS. 5-Aminolevulinic acid fluorescence guided resection of malignant glioma: Hong Kong experience. *Asian J Surg.* (2018) 41:467–72. doi: 10.1016/j.asjsur.2017.06.004
34. Coburger J, Hagel V, Wirtz CR, Konig R. Surgery for Glioblastoma: Impact of the Combined Use of 5-Aminolevulinic Acid and Intraoperative MRI on Extent of Resection and Survival. *PLoS ONE.* (2015) 10:e0131872. doi: 10.1371/journal.pone.0131872
35. Cortnum S, Laursen RJ. Fluorescence-guided resection of gliomas. *Danish Med J.* (2012) 59:A4460.
36. Della Puppa A, Ciccarino P, Lombardi G, Rolma G, Cecchin D, Rossetto M. 5-Aminolevulinic acid fluorescence in high grade glioma surgery: surgical outcome, intraoperative findings, and fluorescence patterns. *BioMed Res Int.* (2014) 2014:232561. doi: 10.1155/2014/232561
37. Diez Valle R, Slof J, Galvan J, Arza C, Romariz C, Vidal C. Observational, retrospective study of the effectiveness of 5-aminolevulinic acid in malignant glioma surgery in Spain (The VISIONA study). *Neurologia.* (2014) 29:131–8. doi: 10.1016/j.nrleng.2013.05.004
38. Pastor J, Pulido-Rivas P, Sola RG. Neurophysiological assisted transsulcal approach to a high grade glioma without affect neither motor nor somatosensory function. *Rev Neurol.* (2013) 56:370–4. doi: 10.33588/rn.5607.2013008
39. Piquer J, Llacer JL, Rovira V, Riesgo P, Rodriguez R, Cremades A. Fluorescence-guided surgery and biopsy in gliomas with an exoscope system. *BioMed Res Int.* (2014) 2014:207974. doi: 10.1155/2014/207974
40. Roessler K, Becherer A, Donat M, Cejna M, Zachenhofer I. Intraoperative tissue fluorescence using 5-aminolevolinic acid (5-ALA) is more sensitive than contrast MRI or amino acid positron emission tomography ((18)F-FET PET) in glioblastoma surgery. *Neurol Res.* (2012) 34:314–7. doi: 10.1179/1743132811Y.0000000078
41. Schatlo B, Fandino J, Smoll NR, Wetzel O, Remonda L, Marbacher S, et al. Outcomes after combined use of intraoperative MRI and 5-aminolevulinic acid in high-grade glioma surgery. *Neuro Oncol.* (2015) 17:1560–7. doi: 10.1093/neuonc/nov049
42. Tsugu A, Ishizaka H, Mizokami Y, Osada T, Baba T, Yoshiyama M, et al. Impact of the combination of 5-aminolevulinic acid-induced fluorescence with intraoperative magnetic resonance imaging-guided surgery for glioma. *World Neurosurg.* (2011) 76:120–7. doi: 10.1016/j.wneu.2011.02.005
43. Della Puppa A, Rustemi O, Rampazzo E, Persano L. Letter: combining 5-aminolevulinic acid fluorescence and intraoperative magnetic resonance imaging in glioblastoma surgery: a histology-based evaluation. *Neurosurgery.* (2017) 80:E188–e90. doi: 10.1093/neuros/nyw033
44. Nabavi A, Thurm H, Zountsas B, Pietsch T, Lanfermann H, Pichlmeier U, et al. Five-aminolevulinic acid for fluorescence-guided resection of recurrent malignant gliomas: a phase ii study. *Neurosurgery.* (2009) 65:1070–6; discussion 6–7. doi: 10.1227/01.NEU.0000360128.03597.C7
45. Belloch JP, Rovira V, Llacer JL, Riesgo PA, Cremades A. Fluorescence-guided surgery in high grade gliomas using an exoscope system. *Acta Neurochirurg.* (2014) 156:653–60. doi: 10.1007/s00701-013-1976-6
46. Eyupoglu IY, Hore N, Merkel A, Buslei R, Buchfelder M, Savaskan N. Supra-complete surgery via dual intraoperative visualization approach (DiVA) prolongs patient survival in glioblastoma. *Oncotarget.* (2016) 7:25755–68. doi: 10.18632/oncotarget.8367
47. Ng WP, Liew BS, Idris Z, Rosman AK. Fluorescence-guided versus conventional surgical resection of high grade glioma: a single-centre, 7-year, comparative effectiveness study. *Malays J Med Sci.* (2017) 24:78–86. doi: 10.21315/mjms2017.24.2.10
48. Stupp R, Taillibert S, Kanner A, Read W, Steinberg D, Lhermitte B, et al. Effect of tumor-treating fields plus maintenance temozolomide vs maintenance temozolomide alone on survival in patients with glioblastoma: a randomized clinical trial. *JAMA.* (2017) 318:2306–16. doi: 10.1001/jama.2017.18718
49. Weller M, Butowski N, Tran DD, Recht LD, Lim M, Hirte H, et al. Rindopepimut with temozolomide for patients with newly diagnosed, EGFRvIII-expressing glioblastoma (ACT IV): a randomised, double-blind, international phase 3 trial. *Lancet Oncol.* (2017) 18:1373–85. doi: 10.1016/S1470-2045(17)30517-X
50. Fujishiro T, Nonoguchi N, Pavliukov M, Ohmura N, Kawabata S, Park Y, et al. 5-Aminolevulinic acid-mediated photodynamic therapy can target human glioma stem-like cells refractory to antineoplastic agents. *Photodiagn Photodyn Ther.* (2018) 24:58–68. doi: 10.1016/j.pdpdt.2018.07.004
51. Kamoshima Y, Terasaka S, Iwasaki Y. [Photodynamic therapy mediated with 5-aminolevulinic acid for C6 glioma spheroids.] *Hokkaido J Med Sci.* (2008) 83:167–73. [Article in Japanese].
52. Leroy HA, Vermandel M, Vignion-Dewalle AS, Leroux B, Maurage CA, Duhamel A, et al. Interstitial photodynamic therapy and glioblastoma: light fractionation in a preclinical model. *Lasers Surg Med.* (2017) 49:506–15. doi: 10.1002/lsm.22620
53. Madsen SJ, Angell-Petersen E, Spetalen S, Carper SW, Ziegler SA, Hirschberg H. Photodynamic therapy of newly implanted glioma cells in the rat brain. *Lasers Surg Med.* (2006) 38:540–8. doi: 10.1002/lsm.20274
54. Schwake M, Nemes A, Dondrop J, Schroeteler J, Schipmann S, Senner V, et al. In-Vitro Use of 5-ALA for photodynamic therapy in pediatric brain tumors. *Neurosurgery.* (2018) 83:1328–37. doi: 10.1093/neuros/nyy054
55. Tetard MC, Vermandel M, Leroy HA, Leroux B, Maurage CA, Lejeune JP, et al. Interstitial 5-ALA photodynamic therapy and glioblastoma: preclinical model development and preliminary results. *Photodiagn Photodyn Ther.* (2016) 13:218–24. doi: 10.1016/j.pdpdt.2015.07.169
56. Wu SM, Ren QG, Zhou MO, Peng Q, Chen JY. Protoporphyrin IX production and its photodynamic effects on glioma cells, neuroblastoma cells and normal cerebellar granule cells *in vitro* with 5-aminolevulinic acid and its hexylester. *Cancer Lett.* (2003) 200:123–31. doi: 10.1016/S0304-3835(03)00271-4
57. Yamamoto T, Ishikawa E, Miki S, Sakamoto N, Zaboronok A, Matsuda M, et al. Photodynamic diagnosis using 5-aminolevulinic acid in 41 biopsies for primary central nervous system lymphoma. *Photochem Photobiol.* (2015) 91:1452–7. doi: 10.1111/php.12510
58. Yi W, Xu HT, Tian DF, Wu LQ, Zhang SQ, Wang L, et al. Photodynamic therapy mediated by 5-aminolevulinic acid suppresses gliomas growth by

decreasing the microvessels. *J Huazhong Univ Sci Technol Med Sci.* (2015) 35:259–64. doi: 10.1007/s11596-015-1421-6
59. Lakomkin N, Hadjipanayis CG. Fluorescence-guided surgery for high-grade gliomas. *J Surg Oncol.* (2018) 118:356–61. doi: 10.1002/jso.25154
60. Zhao S, Wu J, Wang C, Liu H, Dong X, Shi C, et al. Intraoperative fluorescence-guided resection of high-grade malignant gliomas using 5-aminolevulinic acid-induced porphyrins: a systematic review and meta-analysis of prospective studies. *PLoS ONE.* (2013) 8:e63682. doi: 10.1371/journal.pone.0063682
61. Su X, Cheng K, Wang C, Xing L, Wu H, Cheng Z. Image-guided resection of malignant gliomas using fl uorescent nanoparticles. *Wiley Interdiscipl Rev Nanomed Nanobiotechnol.* (2013) 5:219–32. doi: 10.1002/wnan.1212
62. Martirosyan NL, Georges J, Eschbacher JM, Cavalcanti DD, Elhadi AM, Abdelwahab MG, et al. Potential application of a handheld confocal endomicroscope imaging system using a variety of fluorophores in experimental gliomas and normal brain. *Neurosurg Focus.* (2014) 36:E16. doi: 10.3171/2013.11.FOCUS13486
63. Kim JE, Cho HR, Xu WJ, Kim JY, Kim SK, Kim SK, et al. Mechanism for enhanced 5-aminolevulinic acid fluorescence in isocitrate dehydrogenase 1 mutant malignant gliomas. *Oncotarget.* (2015) 6:20266–77. doi: 10.18632/oncotarget.4060
64. Kitagawa T, Yamamoto J, Tanaka T, Nakano Y, Akiba D, Ueta K, et al. 5-Aminolevulinic acid strongly enhances delayed intracellular production of reactive oxygen species (ROS) generated by ionizing irradiation: quantitative analyses and visualization of intracellular ROS production in glioma cells *in vitro*. *Oncol Rep.* (2015) 33:583–90. doi: 10.3892/or.2014.3618
65. Ju D, Yamaguchi F, Zhan G, Higuchi T, Asakura T, Morita A, et al. Hyperthermotherapy enhances antitumor effect of 5-aminolevulinic acid-mediated sonodynamic therapy with activation of caspase-dependent apoptotic pathway in human glioma. *Tumour Biol.* (2016) 37:10415–26. doi: 10.1007/s13277-016-4931-3
66. Coupienne I, Fettweis G, Rubio N, Agostinis P, Piette J. 5-ALA-PDT induces RIP3-dependent necrosis in glioblastoma. *Photochem Photobiol Sci.* (2011) 10:1868–78. doi: 10.1039/c1pp05213f
67. Belykh E, Miller EJ, Hu D, Martirosyan NL, Woolf EC, Scheck AC, et al. Scanning fiber endoscope improves detection of 5-aminolevulinic acid-induced protoporphyrin IX fluorescence at the boundary of infiltrative glioma. *World Neurosurg.* (2018) 113:e51–69. doi: 10.1016/j.wneu.2018.01.151
68. Motekallemi A, Jeltema HR, Metzemaekers JD, van Dam GM, Crane LM, Groen RJ. The current status of 5-ALA fluorescence-guided resection of intracranial meningiomas-a critical review. *Neurosurg Rev.* (2015) 38:619–28. doi: 10.1007/s10143-015-0615-5
69. Wei L, Chen Y, Yin C, Borwege S, Sanai N, Liu JTC. Optical-sectioning microscopy of protoporphyrin IX fluorescence in human gliomas: standardization and quantitative comparison with histology. *J Biomed Optics.* (2017) 22:46005. doi: 10.1117/1.JBO.22.4.046005
70. Valdes PA, Leblond F, Kim A, Harris BT, Wilson BC, Fan X, et al. Quantitative fluorescence in intracranial tumor: implications for ALA-induced PpIX as an intraoperative biomarker. *J Neurosurg.* (2011) 115:11–7. doi: 10.3171/2011.2.JNS101451
71. Potapov AA, Goryaynov SA, Okhlopkov VA, Shishkina LV, Loschenov VB, Savelieva TA, et al. Laser biospectroscopy and 5-ALA fluorescence navigation as a helpful tool in the meningioma resection. *Neurosurg Rev.* (2016) 39:437–47. doi: 10.1007/s10143-015-0697-0
72. Potapov AA, Goryaynov SA, Okhlopkov VA, Pitskhelauri DI, Kobyakov GL, Zhukov VY, et al. [Clinical guidelines for the use of intraoperative fluorescence diagnosis in brain tumor surgery]. *Zh Vopr Neirokhir Im N N Burdenko.* (2015) 79:91–101. doi: 10.17116/neiro201579591-101
73. Stummer W, Tonn JC, Goetz C, Ullrich W, Stepp H, Bink A, et al. 5-Aminolevulinic acid-derived tumor fluorescence: the diagnostic accuracy of visible fluorescence qualities as corroborated by spectrometry and histology and postoperative imaging. *Neurosurgery.* (2014) 74:310–9; discussion 9–20. doi: 10.1227/NEU.0000000000000267
74. Utsuki S, Oka H, Sato S, Suzuki S, Shimizu S, Tanaka S, et al. Possibility of using laser spectroscopy for the intraoperative detection of nonfluorescing brain tumors and the boundaries of brain tumor infiltrates. Technical note. *J Neurosurg.* (2006) 104:618-20. doi: 10.3171/jns.2006.104.4.618
75. Haj-Hosseini N, Richter J, Andersson-Engels S, Wardell K. Optical touch pointer for fluorescence guided glioblastoma resection using 5-aminolevulinic acid. *Lasers Surg Med.* (2010) 42:9–14. doi: 10.1002/lsm.20868
76. Roder C, Bisdas S, Ebner FH, Honegger J, Naegele T, Ernemann U, et al. Maximizing the extent of resection and survival benefit of patients in glioblastoma surgery: high-field iMRI versus conventional and 5-ALA-assisted surgery. *Eur J Surg Oncol.* (2014) 40:297–304. doi: 10.1016/j.ejso.2013.11.022
77. Yamada S, Muragaki Y, Maruyama T, Komori T, Okada Y. Role of neurochemical navigation with 5-aminolevulinic acid during intraoperative MRI-guided resection of intracranial malignant gliomas. *Clin Neurol Neurosurg.* (2015) 130:134–9. doi: 10.1016/j.clineuro.2015.01.005
78. Coburger J, Wirtz CR. Fluorescence guided surgery by 5-ALA and intraoperative MRI in high grade glioma: a systematic review. *J Neuro Oncol.* (2019) 141:533–46. doi: 10.1007/s11060-018-03052-4
79. Shimizu K, Nitta M, Komori T, Maruyama T, Yasuda T, Fujii Y, et al. Intraoperative photodynamic diagnosis using talaporfin sodium simultaneously applied for photodynamic therapy against malignant glioma: a prospective clinical study. *Front Neurol.* (2018) 9:24. doi: 10.3389/fneur.2018.00024
80. Belykh E, Miller EJ, Patel AA, Yazdanabadi MI, Martirosyan NL, Yagmurlu K, et al. Diagnostic accuracy of a confocal laser endomicroscope for *in vivo* differentiation between normal injured and tumor tissue during fluorescein-guided glioma resection: laboratory investigation. *World Neurosurg.* (2018) 115:e337–48. doi: 10.1016/j.wneu.2018.04.048
81. Martirosyan NL, Eschbacher JM, Kalani MY, Turner JD, Belykh E, Spetzler RF, et al. Prospective evaluation of the utility of intraoperative confocal laser endomicroscopy in patients with brain neoplasms using fluorescein sodium: experience with 74 cases. *Neurosurg Focus.* (2016) 40:E11. doi: 10.3171/2016.1.FOCUS15559
82. Della Puppa A, Munari M, Gardiman MP, Volpin F. Combined fluorescence using 5-aminolevulinic acid and fluorescein sodium at glioblastoma border: intraoperative findings and histopathologic data about 3 newly diagnosed consecutive cases. *World Neurosurg.* (2019) 122:e856–63. doi: 10.1016/j.wneu.2018.10.163
83. Duffau H. The necessity of preserving brain functions in glioma surgery: the crucial role of intraoperative awake mapping. *World Neurosurg.* (2011) 76:525–7. doi: 10.1016/j.wneu.2011.07.040

Conflict of Interest Statement: The authors declare that the research was conducted in the absence of any commercial or financial relationships that could be construed as a potential conflict of interest.

frontiers in Oncology

ORIGINAL RESEARCH
published: 18 July 2019
doi: 10.3389/fonc.2019.00583

Confocal-Assisted Multispectral Fluorescent Microscopy for Brain Tumor Surgery

Patra Charalampaki[1], Makoto Nakamura[1], Dimitrios Athanasopoulos[1] and Axel Heimann[2]*

[1] Department of Neurosurgery, Cologne Medical Center, University Witten-Herdecke, Witten, Germany, [2] Institute of Neurosurgical Pathophysiology, Medical University Mainz, Mainz, Germany

Optimal surgical therapy for brain tumors is the combination of complete resection with minimal invasion and damage to the adjacent normal tissue. To achieve this goal, we need advanced imaging techniques on a scale from macro- to microscopic resolution. In the last decade, the development of fluorescence-guided surgery has been the most influential breakthrough, marginally improving outcomes in brain tumor surgery. Multispectral fluorescence microscopy (MFL) is a novel imaging technique that allows the overlapping of a fluorescent image and a white light image in real-time, with delivery of the merged image to the surgeon through the eyepieces of a surgical microscope. MFL permits the detection and characterization of brain tumors using fluorescent molecular markers such as 5-aminolevulinic acid (5-ALA) or indocyanine green (ICG), while simultaneously obtaining high definition white light images to create a pseudo-colored composite image in real-time. Limitations associated with the use of MFL include decreased light imaging intensity and decreased levels of magnification that may compromise maximal tumor resection on a cellular scale. Confocal laser endomicroscopy (CLE) is another novel advanced imaging technique that is based on miniaturization of the microscope imaging head in order to provide the possibility of *in vivo* microscopy at the cellular level. Clear visualization of the cellular cytoarchitecture can be achieved with 400-fold−1,000-fold magnification. CLE allows on the one hand the intra-operative detection and differentiation of single tumor cells (without the need for intra-operative histologic analysis of biopsy specimens) as well as the definition of borders between tumor and normal tissue at a cellular level, dramatically improving the accuracy of surgical resection. The application and implementation of CLE-assisted surgery in surgical oncology increases not only the number of options for real-time diagnostic imaging, but also the therapeutic options by extending the resection borders of cancer at a cellular level and, more importantly, by protecting the functionality of normal tissue in the adjacent areas of the human brain. In this article, we describe our experience using these new techniques of confocal-assisted fluorescent surgery including analysis on the technology, usability, indications, limitations, and further developments.

Keywords: fluorescent microscopy, brain tumor, surgery, confocal laser endomicroscopy (CLE), meningioma

OPEN ACCESS

Edited by:
Evgenii Belykh, Barrow Neurological Institute (BNI), United States

Reviewed by:
Ryuhei Kitai, University of Fukui, Japan
Chuanming Li, Chongqing Medical University, China

****Correspondence:***
Patra Charalampaki
charalampaki@yahoo.de

Specialty section:
This article was submitted to Cancer Imaging and Image-directed Interventions, a section of the journal Frontiers in Oncology

Received: *03 April 2019*
Accepted: *14 June 2019*
Published: *18 July 2019*

Citation:
Charalampaki P, Nakamura M, Athanasopoulos D and Heimann A (2019) Confocal-Assisted Multispectral Fluorescent Microscopy for Brain Tumor Surgery. Front. Oncol. 9:583. doi: 10.3389/fonc.2019.00583

INTRODUCTION

Microsurgery, the performing of surgical procedures with visualization of the surgical field under a surgical microscope, has nowadays become a standard in neurosurgery. The visualization of specific pathologic entities within the surgical field, such as vascular malformations, benign, and malignant lesions, as well as normal vasculature, can be further facilitated by using different fluorescent dyes, such as indocyanine green (ICG), 5-aminolevulinic acid (5-ALA), and fluorescein (FL). Intra-operative fluorescence uses a surgical microscope with integrated special filters for the visualization of the surgical field under a spectral band that corresponds to the peak spectral emission of a fluorescent agent such as ICG, 5-ALA, or fluorescein (1–3). Previously available fluorescent surgical microscopes have been limited by allowing only the visualization of either white light or the fluorescent signal, but not both. Without simultaneous visualization, the fluorescent image is usually delivered via a separate external monitor and not through the microscope's eyepiece, like the white light image. The surgeon must visualize and process the white light image and the fluorescent image separately, combining the information of both using their perception skills while performing surgery. Secondly, switching between white light imaging and fluorescent imaging is necessary several times during the procedure, since the surrounding anatomical structures (other than the highlighted ones) are not clearly visible under the fluorescent mode. This interchange continually interrupts the workflow of the surgeon.

In order to overcome the limitations and disadvantages associated with the currently available intra-operative fluorescence imaging techniques, we developed and investigated a novel intra-operative advanced imaging technique, multispectral fluorescence microscopy (MFL) (4). MFL uses the ARveo Glow800 surgical microscope (Leica Microsystems, Wetzlar, Germany), which enables the visualization of the surgical field under white light and fluorescence at the same time. This is achieved by the use of different filters integrated into the multispectral fluorescence microscope and a sophisticated software that overlaps the fluorescent image onto the white light image in real-time, creating a composite image. Furthermore, the overlaid image can be delivered to the surgeon directly through the eyepiece of the microscope and not only on an external monitor.

Despite the improvement of fluorescent surgical microscopes, complete surgical resection of central nervous system (CNS) tumors remains challenging. Fluorescence microscopy using markers such as 5-ALA allows for intraoperative macroscopic assessment of tumor tissue and is now routinely used as a marker for resection of high-grade gliomas in neurosurgery (5). Although this has been an important advancement, remaining significant challenges of tumor resection with 5-ALA include the quantitative assessment of the PpIX-fluorescence signal, tumor removal under microscopy "in the dark," and the limited magnification of surgical microscopes.

Therefore, the use of intra-operative histologic analysis of frozen biopsy specimens is the standard of care for the determination of complete surgical resection at the cellular level. This procedure is time-consuming and attended by several limitations, such as the occurrence of freezing artifacts, tissue sampling errors, and poor resolution of the final slide. In order to overcome these limitations, we have used confocal laser imaging for the intra-operative real-time high-resolution optical imaging of CNS tumors at the cellular level (6).

Confocal laser endomicroscopy (CLE) is a promising method that permits *in vivo* cellular and sub-cellular visualization in real-time and in high resolution without any need for special tissue preparation (7). However, CLE requires intra-venous or topical application of fluorescent dyes to achieve high-resolution images during examination (8). Ideal fluorophores should possess specific optical characteristics with a high quantum yield and they should be rapidly cleared from the blood stream and CNS tissue, while having an excellent safety profile for human application (7, 8). CLE works with miniaturized fiber-optic probes and has been successfully used in gastroenterology (7, 9), pulmonology (10, 11), gynecology (12), urology (13–15), otolaryngology (16, 17), and plastic surgery (18). Indeed, CLE has allowed rapid diagnosis of various diseases, such as inflammatory bowel disease (19), Barrett's esophagus (20), coeliac disease, and various types of neoplasias (21). In neurosurgery, CLE could improve the safe removal of tumors in CNS regions by providing real-time differentiation between malignant tissue and healthy tissue at a cellular level (6, 22–25). In addition to the use of CLE, in this article we also describe our experience with MFL using the Glow800 surgical microscope, demonstrating ICG fluorescence under high-definition white light imaging in combination with a confocal endomicroscope for the detection of ICG in the near infrared spectrum (NIR) at a cellular level. Our introduction and development of these innovative techniques, CLE and MFL for neurosurgery, are referred to as confocal-assisted fluorescent microsurgery. The focus of this work is the analysis of the procedural techniques, the combination of both in the same surgical performance, the description of the usability, indications, limitations, and further developments of these new concepts in advanced imaging for neurosurgery.

MATERIALS AND METHODS

Multispectral Fluorescent Surgical Microscope

The MFL microscope has the same basic structure and layout as a standard surgical microscope, capable of visualizing fluorescence, and white light in combination and in real-time. The Glow800 tool (ARveo Glow800, Leica microsystems, Wetzlar, Germany) that we used for our surgeries uses multispectral fluorescence for the excitation of fluorescent molecular markers in the NIR (around 800 nm). By means of custom-built software, it can combine the NIR signal with the white light visual signal (VL) and present an overlaid signal, and finally image, to the end user. Thus, the surgeon receives a combined image, in which both the anatomical orientation of the surgical field, similar to the simple VL image, as well as an artificially colored fluorescence signal are depicted simultaneously and in real-time. A pseudo-coloring algorithm is used to fuse the visible light video signal

with the fluorescence values extracted from the NIR camera. The color choice of the fluorescent signal depends on the end user. In our surgeries we used a standardized bright green color, however surgeons who are red-green color-blind could choose other color options. This technique abolishes the previously usual black and white display of fluorescence images, although the visualization of fluorescence raw data (mere NIR spectrum) on a black background is also possible, depending on the mode the user selects to use for the device.

Confocal Laser Endomicroscope

The Cellvizio®-780 nm system (Mauna Kea Technologies, Paris, France) has a near-infrared scanning unit. The mini-optical probes of the Cellvizio® system are composed of 30,000 optical fibers and are available with various optical properties and lengths according to clinical needs. Confocal imaging was accomplished by the CystoFlex UHD C-R™ probe. The probe is 2 m long, has an internal diameter of 2.6 mm and has a lateral resolution of 1 μm. The maximum field of view is 240 μm with an imaging plane depth of 55–65 μm. To enable real-time imaging, a 4 kHz oscillating mirror has been incorporated for horizontal line scanning and a galvanometric mirror for frame scanning. The device has a frame rate of 12 images per second. A foot pedal allows starting and pausing of video image acquisition. These image files may subsequently be exported using the Cellvizio® software.

Fluorescent Agent Indocyanine Green (ICG)

ICG (Verdye, Germany; λ_{ex} 760–775 nm/λ_{em} 835 nm) was used off label to enhance tumor tissue contrast by highlighting tumor blood vessels. ICG is an approved fluorescent agent for use in everyday neurosurgical practice and has several other medical and diagnostic applications, such as in ophthalmology for the imaging of the retinal blood vessels. It is administered intravenously and tends to bind strongly to specific plasma proteins without being extravasated or binding to atherosclerotic plaques on the walls of blood vessels. This feature results in the fluorescent dye remaining within the vascular system and renders it a very useful tool for contrasting vascular structures and visualization of the blood flow. As it circulates in pathological tumor vessels, ICG extravasation as a tumor staining agent can be visualized. Furthermore, during tumor surgery ICG spreads locally in the tissue and binds to cytoplasmic proteins, which results in staining of the cell cytoplasm around the nucleus. In our study, ICG (50 mg) was administered intravenously 1 h before operative exposure of the tumor.

Confocal-Assisted Fluorescent Technique

All the confocal-assisted fluorescent procedures were performed after permission of the ethical committee of the medical association of Nordrhein-Westfalia, Germany and the ethical committee of the University Witten-Herdecke. The special consent obtained from the participants for participating in the study was both informed and written. Participants under the age of 18 were not included.

We intra-operatively applied the combined use of infrared multispectral fluorescence and CLE on different types of CNS pathologies, using ICG as the fluorescent agent. We first examined 22 rats in the lab with implanted C6 glioma using a combination of the above techniques and transferred our experience to the surgical theater, which is the subject of this study. We describe here our first experience on 13 patients. The pathologies included were gliomas ($n = 5$), meningiomas ($n = 3$), neurinomas ($n = 2$), and metastases ($n = 3$) in different locations within the CNS, such as brain parenchyma, skull base, and spinal cord.

After opening the dura, the tumor was exposed and visualized with the Glow800 microscope. Initial observation was performed for tumor localization and characterization of the lesion's extent within the surgical field, as well as the tumor blood supply and draining vessels in relation to the surrounding structures. Furthermore, we observed tumor vascularization with fluorescent contrast enhancement. During and after tumor resection, the pseudo-colored mode of multispectral fluorescence demonstrated the extent of tumor resection, the tumor margins, and the anatomical properties of the resection cavity, and its vasculature. In a similar fashion, after tumor exposure we used the CLE device to visualize the tumor cellular architecture and performed optical biopsies without the need of real tissue resection. At the end of the fluorescence-assisted removal of the tumor, we inserted the confocal scope again into the surgical field to search for remaining tumor. The endomicroscope was held by hand against the tissue if the tumors were located on the surface or in the parenchyma. Confocal image injection in the surgical microscope was easily possible. If the tumors were located in the skull base and we had to use the endoscope for deep, around the corner visualization, then the endomicroscope was inserted into the working channel of the endoscope (**Figure 1**). Post-operatively, the resected tumor biopsies were fixed with formalin and transported to the neuropathology department for histopathological and immunohistochemical analysis. The extra surgical time was 5–10 min in addition to the normal surgical time for getting the CLE images. The images were selected from three parts of the surgical field: (a) fluorescent part of the tumor, (b) tumor to normal brain transition zone, and (c) normal tissue.

SURGICAL TECHNIQUE ANALYSIS AND CASE DEMONSTRATIONS

The Glow800-mode was used after performing the approach and the initial exposure of the tumor. The VL mode provided an equal image to the standard surgical microscope throughout the entire procedure. Vascular anatomy of the tumors, especially the arterial blood supply of the tumors and their branches, the tumor blood vessels, capillaries, and neovascularization patterns, and the complex venous drainage of the tumors were clearly visible both with the pseudo-colored as well as with the classic NIR-mode. The pseudo-colored mode showed here a significant superiority to the NIR-mode, as it presented the exact localization and anatomical relation of each vascular structure to the tumor mass and the surrounding surgical field in a bright colored image. In cases of extravasation due to bleeding from a local tumor blood vessel, the pseudo-colored mode also assisted the visualization

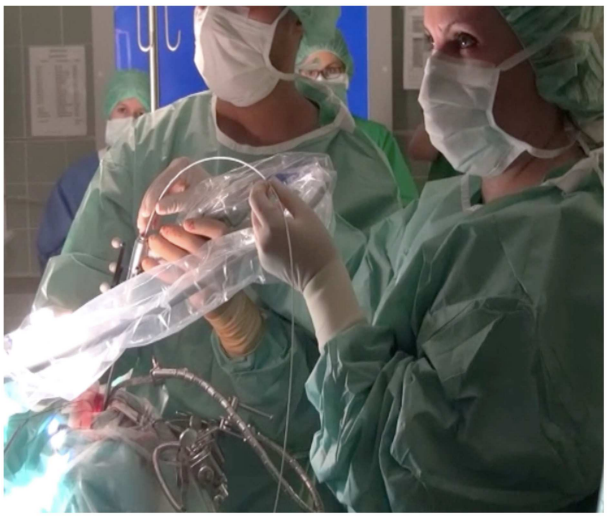

FIGURE 1 | On deep seated lesions, e.g., in the skull base, we inserted the confocal endomicroscope into the working channel of a classic endoscope performing a confocal-assisted endoscopic procedure.

of the bleeding spot and enabled instant hemostasis by the surgeon. After completion of tumor resection, the observation of the tumor margins under the pseudo-colored mode facilitated a better recognition of remaining pathologic tissue and neoplastic blood vessels, and therefore, their further removal. The image overlapping also allowed for quick and efficient recognition of these spots within and close to the resection hole without the need of several manipulations within the surgical field or switching to the VL or NIR-mode. As expected, these advantageous features of the pseudo-colored mode were more profound in more thickly vascularized tumors.

Due to bleeding during tumor removal, ICG was locally distributed in the surgical field and therefore, it could penetrate into the surrounding cells. The use of the CLE tool was important after dural opening and at the end for checking tumor margins at spots in the surgical field where fluorescence was not visible any more. When the probe was held directly with the hand, it was difficult to stabilize the imaging probe, which is a problematic issue. It was also difficult to control the uniform application of pressure of the probe against the tissue to provide artifact-free images. We obtained the best results for the multispectral infrared imaging of meningiomas, neurinomas, and metastatic tumors, while gliomas remained problematic on ICG uptake; high grade (WHO III, IV) gliomas were very marginal and not homogenously highlighted, while low grade gliomas were not highlighted at all. Therefore, we were surprised to see that confocal imaging, in contrast, was able to detect, at a cellular level, even those cells from tumors which were not highlighted at all with the fluorescent surgical microscope. However, the study's subject here is to show how the combination of both technologies together can affect intra-operative decision making on tumor resection and therefore, we present three cases out of 13 patients that demonstrate how we used both novel technologies as a confocal-assisted fluorescent technique.

Patient 1: Convexity Meningioma

This patient was scheduled for resection of a 6 × 5 × 4 cm convexity meningioma. The tumor was macroscopically well-defined. Once the dura was exposed, the Glow800 imaging system was used to demonstrate the accumulation of ICG in the tumor. With the CLE tool we also demonstrated the cytoarchitecture with cellular imaging of the tumor. Psammoma bodies, which are the typical characteristics of meningiomas, were clearly visible. Then, normal resection of the tumor, guided with the Glow800 module, was performed. When complete macroscopic removal was accomplished, CLE optical biopsies were performed to document complete resection with clear margins of normal tissue. *Ex vivo* CLE imaging was also performed on small pieces of the tumor infiltrating the dura matter and on the entire resection specimen by means of an interactive teleconference with the neuropathologists. The tissue areas imaged with CLE *in vivo* were the resection bed and the small parts of the normal brain surrounding the tumor that were exposed after dura opening (**Figure 2**). No residual tumor cells in the resection bed or the dura were seen.

Patient 2: Metastasis of a Ductal Carcinoma of the Breast

This patient was scheduled for the resection of a 5 × 5 × 4 cm metastasis of a ductal carcinoma of the breast located in the right parietal lobe. The tumor was macroscopically well-defined. Once the dura was opened, fluorescent imaging with the Glow800 demonstrated excellent accumulation of ICG onto the tumor surface. Then normal resection of the tumor with the Glow800 module was performed. During the resection, CLE optical biopsies were performed in order to check the histological type of the tumor and the margins between tumor and normal tissue. With the CLE tool we demonstrated the cytoarchitecture of the tumor. Typical cellular architecture of the carcinoma was well-identified with nests of cells featuring prominent nuclei with mitotic activities. *Ex vivo* CLE imaging was performed on the entire resection specimen and discussed in an interactive teleconference with the neuropathologist. The tissue areas visualized before dura closure with CLE *in vivo* were, as usual, the resection bed and the small parts of the normal brain surrounding the tumor on the brain surface exposed after initial dura opening (**Figure 3**).

Patient 3: Sphenoid Wing Meningioma With Compression of the Optic Nerve

This patient was scheduled for resection of a meningioma originating from the sphenoid wing with compression of the optic nerve. Using the fluorescent imaging system with the Glow800, we visualized during the 4 h tumor removal the different uptake steps of ICG into the tumor (**Figure 4**). After completing the tumor resection, CLE was performed on different structures on the skull base, especially on different parts of the exposed optic nerve and chiasm. In this case, the CLE probe was inserted in the operative channel of an endoscope for better stabilization and gentle manipulation of the CLE probe on the optic nerve. CLE video sequences of normal tissue, tumor, nerve,

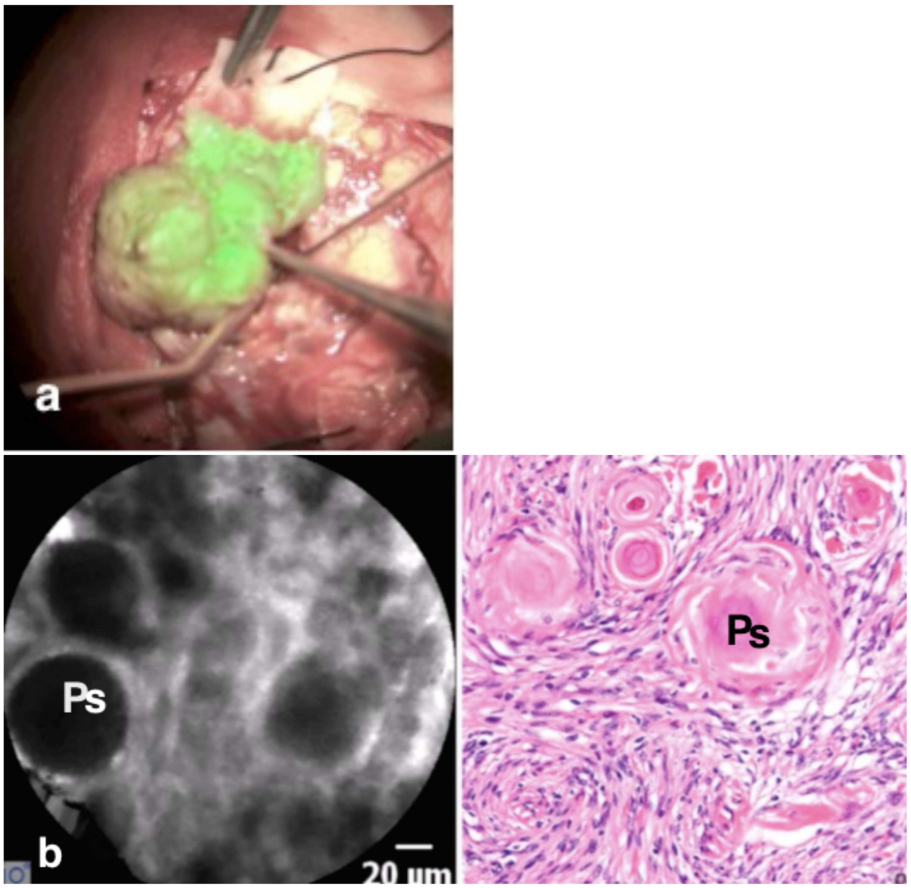

FIGURE 2 | The meningioma is visible as a "green" tumor **(a)** with very clear borders, while the normal brain around is without ICG uptake. *In vivo* confocal image **(b)** shows the cytoarchitecture of the meningioma with big psammoma bodies (Ps), while the H & E staining confirms the diagnosis.

and resection bed were acquired at the beginning, during, and after the resection. **Supplementary Video 1** shows the border between the tumor and nerve fibers (**Supplementary Video 1**). We performed CLE imaging *in vivo* from the resection bed and *ex vivo* directly from the tumor. In the same case, psammoma bodies, nerve, and normal brain tissue from the frontal lobe could be observed. The different cellular perspective pictures in longitudinally and transversely taken slices of the optic nerve were impressive. Within the nerve bundles, we observed insulated nerve fibers from their neighbors by neuroglia. Within the nerve fiber bundles, rows of supporting astrocytes, oligodendrocytes, and some microglial cells were also seen. A continuous glial membrane formed by the astrocytes separated the nerve fibers. ICG highlighted the cytoplasm of the surrounding glia and oligodendrocytes. Therefore, small white rings were visible on the transverse slices of the nerve. Histological sampling (H&E stain) of the optic nerve was not performed as we protected the optic nerve.

DISCUSSION

Over the previous years, the aim of optimizing microsurgery and maximizing its safety and efficiency has brought forward several intra-operative techniques for the visualization and contrast imaging of tumor and normal tissue. In tumor surgery, the visualization of the blood vessels of the tumor and the surrounding tissues has not yet been the major point of interest, with the most cutting edge feature being 5-ALA fluorescence, which uses the metabolic features of tumor cells to help identify neoplastic tissue within the surgical field (5). The currently existing infrared fluorescence surgical microscopes allow fluorescent image delivery through an external monitor and not through the eyepiece of the microscope, thus forcing interruption of the surgical workflow for assessment of the white light and fluorescent images.

The Glow800 tool is a surgical-microscope-integrated software and hardware system that enables the superimposition of an ICG fluorescent image onto a white light image, producing a merged image that delivers both the white light anatomical data as well as the dynamic information of ICG fluorescence in a real-time fashion. It shows the fluorescent signal of ICG in green (also visible in seven different other colors) onto a white light pseudo-colored anatomical background. After visualization of the tumor as a green-colored mass, the confocal endomicroscope was used to characterize the cellular cytoarchitecture of the tumor and scan the intra-operative field for remaining tumor tissue.

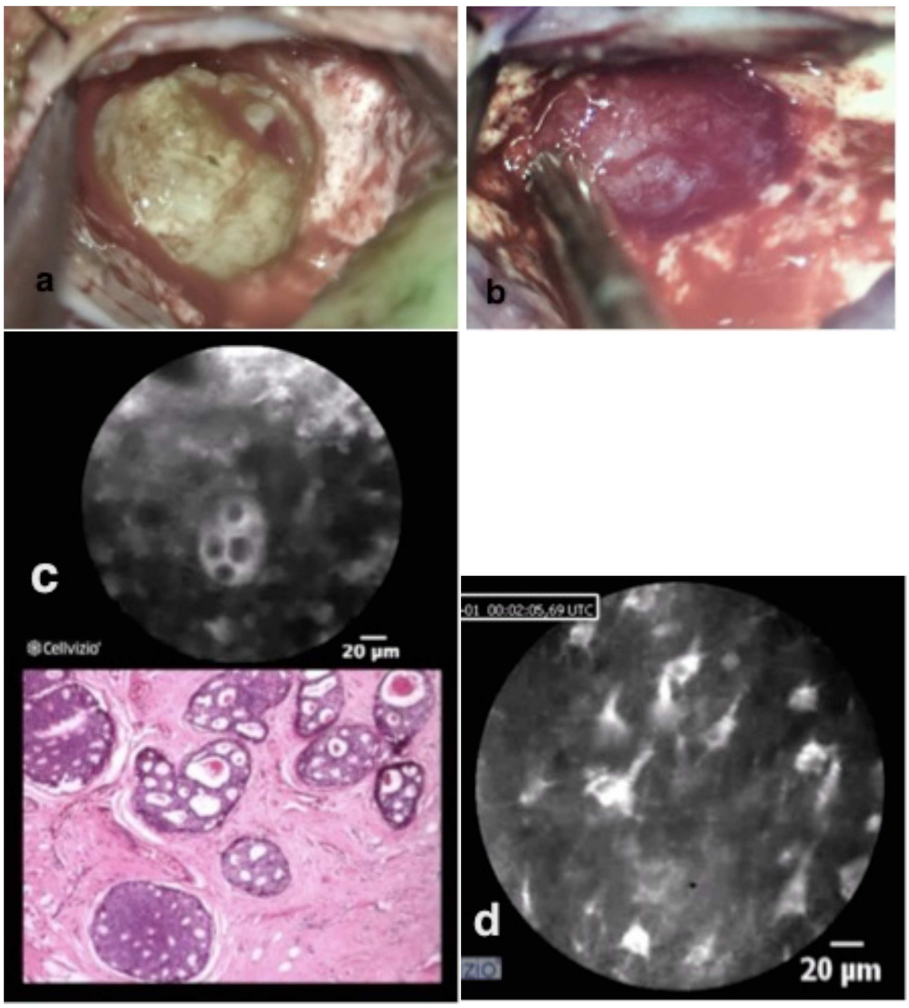

FIGURE 3 | Brain metastasis of ductal breast cancer in two different colors pictured **(a,b)**. *In vivo* confocal imaging **(c)** shows the cell nester with prominent nucleus with the analog H & E staining typical for breast metastasis. The confocal scanning with the scope on the remaining brain tissue shows normal brain structures **(d)** with astrocytes, pyramidal, and bipolar cells.

The current study tested the MFL technique with the Glow800 tool on a series of 13 patients in interaction with confocal endomicroscopy, trying to prove the feasibility and superiority of this so called confocal-assisted fluorescent technique over the existing standard in neurosurgical practice.

In tumor surgery, the presentation of the anatomical structures related to the tumor and the tumor vessels in the pseudo-colored mode provided a substantially larger and crucial amount of information regarding tumor appearance and borders while performing surgery. Although administration of high dose ICG with the second window detection has been reported previously (26–28), a high dose was not necessary in our study. The dose of ICG administered was 50 mg in all cases (two commercially available vials of 25 mg each) and the time of administration was only 1 h before the beginning of the surgical procedure (during introduction of anesthesia). The simultaneous use of CLE with the cellular analysis of tissue brings immediate answers during the surgical session about how far resection has to go.

A further technique, similar to the ICG fluorescence, which has been used by many groups for the visualization of tumor blood vessels, is fluorescein fluorescence (29–33). It also requires a surgical microscope that can detect fluorescent images and delivers the fluorescein highlighting blood vessels over an anatomical white light image of the surgical field. The disadvantages of fluorescein fluorescence, however, include the lack of FDA approval for this fluorescent agent in neurosurgery, the extensive extravasation of fluorescein when injected in high concentrations—and therefore, lack of a quick washout, preventing intravenous injections,—and its extensive binding to atherosclerotic plaques, leading to prolonged highlighting of atherosclerotic blood vessels and potentially generating a false impression of present blood flow. The use of fluorescein in confocal endomicroscopy also faces some limitations in

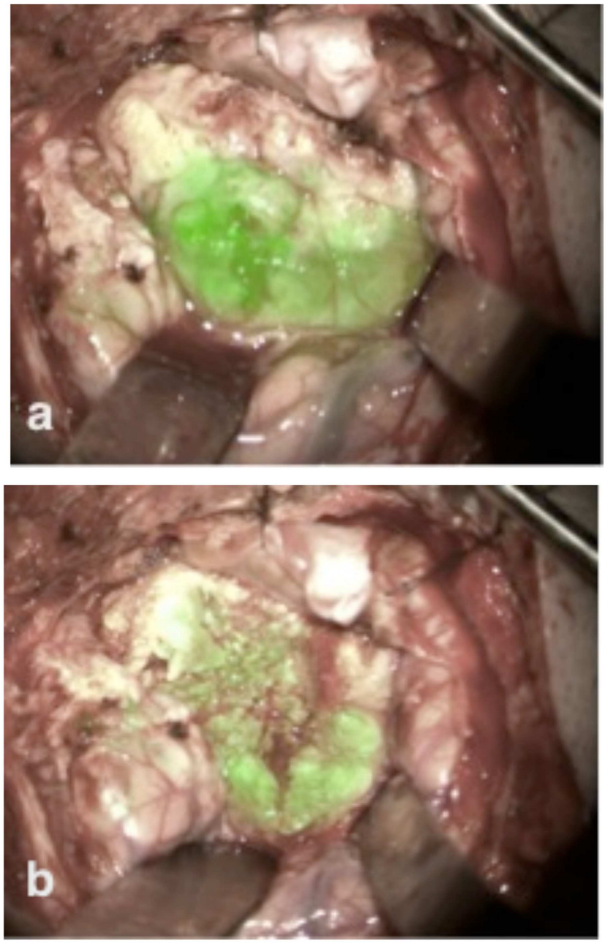

FIGURE 4 | The skull base meningioma shows strong ICG uptake at the beginning of tumor resection immediately after tumor exposure **(a)**. During the tumor resection ICG seemed to be still active in its accumulation into the tumor, as we observed an increased fluorescence signal into the tumor volume **(b)**.

comparison to ICG. Fluorescein remains extracellular and highlights the extracellular space (34). Therefore, cell architecture is not as clearly visible as it is with ICG, which binds intra-cellularly on cytoplasmic proteins and highlights the cell itself. Another disadvantage is that the detection spectrum of fluorescein interacts with the spectrum of hemoglobin on around 530–550 nm. This means that, working with fluorescein intra-operatively at the cellular level, the visualization of fluorescein fluorescence could be blocked due to overlying erythrocytes (hemoglobin), which would not be the case with ICG in infrared (780–800 nm) since confocal endomicroscopes that are able to detect in infrared are "blind" to light emission in lower spectra. In infrared, the view is open to see behind the "wall" of erythrocytes. Furthermore, infrared light (needed for detecting ICG) penetrates deeper in the tissue compared to light at a shorter spectral range (needed for FL). In tumor surgery, even if 5-ALA or ICG fluorescence is not visible, there could be tumor cells present in a depth of 1–2 mm spread behind the tumor bed. Therefore, for cellular imaging we need detection sources able to penetrate as deeply as possible inside the tissue. Those light ranges are found in infrared and beyond.

In oncologic surgery, the CLE-assisted fluorescent technique allows for intra-operative detection of green-colored tumor on a macroscale as well as differentiation and identification of individual tumor cells at a subcellular or subnuclear level. This technique provides immediate online diagnosis without the need for rapid biopsies and therefore, helps to define the borders between tumor and normal tissue at a cellular level. The application and implementation of CLE-assisted surgery in surgical oncology would increase the range of available diagnostic and therapeutic options by extending the resection borders of cancer at a cellular level and, more importantly, by automatically protecting the functionality of normal tissue in eloquent areas of the human brain. Confocal-assisted fluorescent surgery offers, in different regions of the neuronal axis, an excellent addition to the intra-operative navigation because of the cellular confocal-fluorescence guidance, which provides real-time images, so that brain shift is no longer a problem. The surgical CLE prototype device we used in our surgeries provides ∼400-fold magnification of the observed tissue structures during surgery. Widely used microscopy and standard endoscopy offer only a very slight increase in the visualization of structures, about 10-fold and 2-fold, respectively. Therefore, we used the combination of the new fluorescent microscope and the confocal endomicroscope in interaction during surgery. Using the confocal-assisted fluorescent microscopic technique, we were able to clearly identify the tumor on a macroscale while operating with fluorescence-guidance and we were then able to magnify the surrounding environment on a microscale of 400-fold to check the tissue at a cellular level.

There are also limitations in our approach of *in vivo* histopathological imaging with CLE. Intravenous injection and local application of some fluorescent agents such as ICG or fluorescein in tumor surgery are off-label. With the Glow800, we were able to use ICG to detect tumor vascularization and to highlight the tumors while using a small dose of ICG and relatively simple protocol. Although we observed a good accumulation of ICG on benign and metastatic processes, visualization of ICG uptake in gliomas remained problematic. Although we observed the strongest fluorescence signal on the tissue surface, the limited infiltration depth and field of view of the confocal endomicroscope is a drawback if the instrument has to show borders between tumors and normal brain. However, this could be overcome with the next generation of confocal systems, which could be able to penetrate deeper into the tissue and provide larger field of view. In the future, confocal systems with multiple excitation wavelengths, such as in bench-top confocal imaging, may facilitate clinical use, and a combination of a surgical microscope with a confocal endomicroscope could also be of great advantage. Regarding the MFL technique, we are now in the process of extending the usability also to other fluorescent agents like 5-ALA and fluorescein. In the near future, the surgeon will be able to see and operate on the tumor under white light while simultaneously viewing the accumulation 5-ALA or/and fluorescein as colored overlay, therefore, overcoming the individual limitations of dark blue or dark yellow light.

In this study, we described the application of MFL together with confocal laser endomicroscopy as "CLE-assisted fluorescent microsurgical technique," its implementation in the operative theater, its advantages, limitations, and future perspectives with planned developments in oncological surgery. With CLE-assisted fluorescent surgery, we were able to achieve both an improved representation of the borders between tumor (multi-color highlight) and normal tissue as a significant improvement in the representation of immediate histological diagnosis compared with the time-consuming multiple-day hematoxylin and eosin staining.

DATA AVAILABILITY

The raw data supporting the conclusions of this manuscript will be made available by the authors, without undue reservation, to any qualified researcher.

AUTHOR CONTRIBUTIONS

PC: concept design, performance of the clinical testings, and drafted the manuscript. MN: clinical testings and corrected the manuscript. DA: performance of part of clinical testings and edited the manuscript text. AH: contribution on study design according to previous animal experiments.

SUPPLEMENTARY MATERIAL

The Supplementary Material for this article can be found online at: https://www.frontiersin.org/articles/10.3389/fonc.2019.00583/full#supplementary-material

Supplementary Video 1 | (Tumor-optic nerve borders) shows borders between tumor (right side) and nerve fibers (left).

REFERENCES

1. Martirosyan NL, Skoch J, Watson, Lemole GM Jr, Romanowski M, Anton R. Integration of indocyanine green videoangiography with operative microscope. *Neurosurgery*. (2015) 11:252–8 doi: 10.1227/NEU.0000000000000681
2. Raabe A, Nakaji P, Beck J, Kim LJ, Hsu FP, Kamerman JD, et al. Prospective evaluation of surgical microscope-integrated intraoperative near-infrared indocyanine green videoangiography during aneurysm surgery. *J Neurosurg*. (2005) 103:982–9. doi: 10.3171/jns.2005.103.6.0982
3. Raabe A, Beck J, Seifert V. Technique and image quality of intraoperative indocyanine green angiography during aneurysm surgery using surgical microscope integrated near-infrared video technology. *Zentralbl Neurochir*. (2005) 66:1–6. doi: 10.1055/s-2004-836223
4. Nickele C, Nguyen V, Fisher W, Couldwell W, Aboud E, David C, et al. A pilot comparison of multispectral fluorescence to indocyanine green videoangiography and other modalities for intraoperative assessment in vascular neurosurgery. *Oper Neurosurg (Hagerstown)*. (2018) 17:103–9. doi: 10.1093/ons/opy237
5. Stummer W, Pichlmeier U, Meinel T, Wiestler OD, Zanella F, Reulen HJ, et al. Fluorescence-guided surgery with 5-aminolevulinic acid for resection of malignant glioma: a randomised controlled multicentre phase III trial. *Lancet Oncol*. (2006) 7:392–401. doi: 10.1016/S1470-2045(06)70665-9
6. Foersch S, Heimann A, Ayyad A, Spoden GA, Florin L, Mpoukouvalas K, et al. Confocal laser endomicroscopy for diagnosis and histomorphologic imaging of brain tumors *in vivo*. *PLoS ONE*. (2012) 7:e41760. doi: 10.1371/journal.pone.0041760
7. Kiesslich R, Burg J, Vieth M, Gnaendiger J, Enders M, Delaney P, et al. Confocal laser endoscopy for diagnosing intraepithelial neoplasias and colorectal cancer *in vivo*. *Gastroenterology*. (2004) 127:706–13. doi: 10.1053/j.gastro.2004.06.050
8. Zehri AH, Ramey W, Georges JF, Mooney MA, Martirosyan NL, Preul MC, et al. Neurosurgical confocal endomicroscopy: a review of contrast agents, confocal systems, and future imaging modalities. *Surg Neurol Int*. (2014) 5:60. doi: 10.4103/2152-7806.131638
9. Polglase AL, McLaren WJ, Skinner SA, Kiesslich R, Neurath MF, Delaney PM. A fluorescence confocal endomicroscope for *in vivo* microscopy of the upper- and the lower-GI tract. *Gastrointest Endosc*. (2005) 62:686–95. doi: 10.1016/j.gie.2005.05.021
10. Lane PM, Lam S, McWilliams A, Leriche JC, Anderson MW, Macaulay CE. Confocal fluorescence microendoscopy of bronchial epithelium. *J biomed optics*. (2009) 14:024008. doi: 10.1117/1.3103583
11. Thiberville L, Moreno-Swirc S, Vercauteren T, Peltier E, Cave C, Bourg Heckly G. *In vivo* imaging of the bronchial wall microstructure using fibered confocal fluorescence microscopy. *Am j resp crit care med*. (2007) 175:22–31. doi: 10.1164/rccm.200605-684OC
12. Tan J, Quinn MA, Pyman JM, Delaney PM, McLaren WJ. Detection of cervical intraepithelial neoplasia *in vivo* using confocal endomicroscopy. *Bjog*. (2009) 116:1663–70. doi: 10.1111/j.1471-0528.2009.02261.x
13. Sonn GA, Jones SN, Tarin TV, Du CB, Mach KE, Jensen KC, et al. Optical biopsy of human bladder neoplasia with *in vivo* confocal laser endomicroscopy. *J urol*. (2009) 182:1299–305. doi: 10.1016/j.juro.2009.06.039
14. Wiesner C, Jager W, Salzer A, Biesterfeld S, Kiesslich R, Hampel C, et al. Confocal laser endomicroscopy for the diagnosis of urothelial bladder neoplasia: a technology of the future? *BJU inter*. (2011) 107:399–403. doi: 10.1111/j.1464-410X.2010.09540.x
15. Bui D, Mach KE, Zlatev DV, Rouse RV, Leppert JT, Liao JC. A pilot study of *in vivo* confocal laser endomicroscopy of upper tract urothelial carcinoma. *J Endourol*. (2015) 29:1418–23. doi: 10.1089/end.2015.0523
16. Haxel BR, Goetz M, Kiesslich R, Gosepath J. Confocal endomicroscopy: a novel application for imaging of oral and oropharyngeal mucosa in human. *Eur Arch Otorhinolaryngol*. (2010) 267:443–8. doi: 10.1007/s00405-009-1035-3
17. Linxweiler M, Kadah BA, Bozzato A, Bozzato V, Hasenfus A, Kim YJ, et al. Noninvasive histological imaging of head and neck squamous cell carcinomas using confocal laser endomicroscopy. *Eur Arch Otorhinolaryngol*. (2016) 273:4473–83. doi: 10.1007/s00405-016-4145-8
18. Schulz A, Daali S, Javed M, Fuchs PC, Brockmann M, Igressa A, et al. Presurgical mapping of basal cell carcinoma or squamous cell carcinoma by confocal laser endomicroscopy compared to traditional micrographic surgery: a single-centre prospective feasibility study. *Eur J Dermatol*. (2016) 26:572–9. doi: 10.1684/ejd.2016.2874
19. Malmstrom ML, Karstensen JG, A SF, Riis LB, Gogenur I, Vilmann P. Confocal laser endomicroscopy is a new endoscopic technique for diagnosing colorectal neoplasia and inflammatory bowel disease. *Ugeskr Laeger*. (2014) 176:V05130311.
20. Trovato C, Sonzogni A, Ravizza D, Fiori G, Tamayo D, De Roberto G, et al. Confocal laser endomicroscopy for *in vivo* diagnosis of Barrett's oesophagus and associated neoplasia: a pilot study conducted in a single Italian centre. *Dig Liver Dis*. (2013) 45:396–402. doi: 10.1016/j.dld.2012.12.016
21. Buchner AM, Wallace MB. *In-vivo* microscopy in the diagnosis of intestinal neoplasia and inflammatory conditions. *Histopathology*. (2015) 66:137–46. doi: 10.1111/his.12597

22. Charalampaki P, Javed M, Daali S, Heiroth HJ, Igressa A, Weber F. Confocal laser endomicroscopy for real-time histomorphological diagnosis: our clinical experience with 150 brain and spinal tumor cases. *Neurosurgery*. (2015) 62(Suppl 1):171–6. doi: 10.1227/NEU.0000000000000805
23. Martirosyan NL, Georges J, Eschbacher JM, Cavalcanti DD, Elhadi AM, Abdelwahab MG, et al. Potential application of a handheld confocal endomicroscope imaging system using a variety of fluorophores in experimental gliomas and normal brain. *Neurosurg Focus*. (2014) 36:E16. doi: 10.3171/2013.11.FOCUS13486
24. Martirosyan NL, Cavalcanti DD, Eschbacher JM, Delaney PM, Scheck AC, Abdelwahab MG, et al. Use of *in vivo* near-infrared laser confocal endomicroscopy with indocyanine green to detect the boundary of infiltrative tumor. *J neurosurg*. (2011) 115:1131–8. doi: 10.3171/2011.8.JNS11559
25. Eschbacher J, Martirosyan NL, Nakaji P, Sanai N, Preul MC, Smith KA, et al. *In vivo* intraoperative confocal microscopy for real-time histopathological imaging of brain tumors. *J Neurosurg*. (2012) 116:854–60. doi: 10.3171/2011.12.JNS11696
26. Zeh R, Sheikh S, Xia L, Pierce J, Newton A, Predina J, et al. The second window ICG technique demonstrates a broad plateau period for near infrared fluorescence tumor contrast in glioblastoma. *PLoS ONE*. (2017) 12:e0182034. doi: 10.1371/journal.pone.0182034
27. Lee JYK, Pierce JT, Zeh R, Cho SS, Salinas R, Nie S, et al. Intraoperative near-infrared optical contrast can localize brain metastases. *World Neurosurg*. (2017) 106:120–30. doi: 10.1016/j.wneu.2017.06.128
28. Lee JYK, Pierce JT, Thawani JP, Zeh R, Nie S, Martinez-Lage M, et al. Near-infrared fluorescent image-guided surgery for intracranial meningioma. *J Neurosurg*. (2018) 128:380–90. doi: 10.3171/2016.10.JNS161636
29. Belykh E, Cavallo C, Gandhi S, Zhao X, Veljanoski D, Izady Yazdanabadi M, et al. Utilization of intraoperative confocal laser endomicroscopy in brain tumor surgery. *J Neurosurg Sci*. (2018) 62:704–17. doi: 10.23736/S0390-5616.18.04553-8
30. Belykh E, Martirosyan NL, Yagmurlu K, Miller EJ, Eschbacher JM, Izadyyazdanabadi M, et al. Intraoperative fluorescence imaging for personalized brain tumor resection: current state and future directions. *Front Surg*. (2016) 3:55. doi: 10.3389/fsurg.2016.00055
31. Li Y, Rey-Dios R, Roberts DW, Valdés PA, Cohen-Gadol AA. Intraoperative fluorescence-guided resection of high-grade gliomas: a comparison of the present techniques and evolution of future strategies. *World Neurosurg*. (2014) 82:175–85. doi: 10.1016/j.wneu.2013.06.014
32. Lane BC, Cohen-Gadol AA. Fluorescein fluorescence use in the management of intracranial neoplastic and vascular lesions: a review and report of a new technique. *Curr Drug Discov Technol*. (2013) 10:160–9. doi: 10.2174/1570163811310020009
33. Diaz RJ, Dios RR, Hattab EM, Burrell K, Rakopoulos P, Sabha N, et al. Study of the biodistribution of fluorescein in glioma-infiltrated mouse brain and histopathological correlation of intraoperative findings in high-grade gliomas resected under fluorescein fluorescence guidance. *J Neurosurg*. (2015) 122:1360–9. doi: 10.3171/2015.2.JNS 132507
34. Martirosyan NL, Georges J, Eschbacher JM, Belykh E, Carotenuto A, Spetzler RF, et al. Confocal scanning microscopy provides rapid, detailed intraoperative histological assessment of brain neoplasms: experience with 106 cases. *Clin Neurol Neurosurg*. (2018) 169:21–8. doi: 10.1016/j.clineuro.2018.03.015

Conflict of Interest Statement: The authors declare that the research was conducted in the absence of any commercial or financial relationships that could be construed as a potential conflict of interest.

frontiers in Oncology

OPINION
published: 06 August 2019
doi: 10.3389/fonc.2019.00727

Spray Fluorescent Probes for Fluorescence-Guided Neurosurgery

Yosuke Kitagawa[1], Shota Tanaka[1], Yugo Kuriki[2], Kyoko Yamamoto[3], Akira Ogasawara[2], Takahide Nejo[1], Reiko Matsuura[1], Tsukasa Koike[1], Taijun Hana[1,4], Satoshi Takahashi[1], Masashi Nomura[1], Shunsaku Takayanagi[1], Akitake Mukasa[5], Mako Kamiya[3], Yasuteru Urano[2,3] and Nobuhito Saito[1]*

[1] Department of Neurosurgery, Graduate School of Medicine, The University of Tokyo, Tokyo, Japan, [2] Laboratory of Chemistry and Biology, Graduate School of Pharmaceutical Sciences, The University of Tokyo, Tokyo, Japan, [3] Laboratory of Chemical Biology and Molecular Imaging, Graduate School of Medicine, The University of Tokyo, Tokyo, Japan, [4] Genome Science Division, Research Center for Advanced Science and Technology, The University of Tokyo, Tokyo, Japan, [5] Department of Neurosurgery, Graduate School of Medical Sciences, Kumamoto University, Kumamoto, Japan

OPEN ACCESS

Edited by:
Evgenii Belykh, Barrow Neurological Institute (BNI), United States

Reviewed by:
Patra Charalampaki, University of Witten/Herdecke, Germany

***Correspondence:**
Shota Tanaka
tanakas-tky@umin.ac.jp

Specialty section:
This article was submitted to Cancer Imaging and Image-directed Interventions, a section of the journal Frontiers in Oncology

Received: *12 April 2019*
Accepted: *22 July 2019*
Published: *06 August 2019*

Citation:
Kitagawa Y, Tanaka S, Kuriki Y, Yamamoto K, Ogasawara A, Nejo T, Matsuura R, Koike T, Hana T, Takahashi S, Nomura M, Takayanagi S, Mukasa A, Kamiya M, Urano Y and Saito N (2019) Spray Fluorescent Probes for Fluorescence-Guided Neurosurgery. Front. Oncol. 9:727. doi: 10.3389/fonc.2019.00727

Keywords: fluorescent probe, glioma surgery, hydroxymethyl rhodamine green, topical, 5-aminolevulinic acid

Surgery is the initial and most important mode of treatment for glioma, the most common primary brain tumor. The greatest possible extent of resection and preservation of neurological functions are both the primary goals, although they tend to be in the trade-off relationship. Several surgical adjuncts have been developed for maximal safe resection, which include electrophysiological monitoring, navigation system, intraoperative imaging, and fluorescent probes. Intraoperative imaging such as MRI and ultrasound tend to overcome inacuracy due to brain shift during tumor resection. However, these devices tend to be costly. In contrast, fluorescent probes can be implemented to surgery by simply attaching an excitation and emission filters to a preexisting microscope, achieving high versatility with low cost. Fluorescence-guided surgery has been proven effective for radical tumor resection; fluorescent probes effectively visualize the tumor intraoperatively.

Fluorescence probes are useful indicators for biologically relevant targets, being sensitive, rapidly responsive, and capable of affording high spatial resolution via microscopic imaging without destroying structures (1). In surgery, many different types of fluorescent probes have been investigated in preclinical and clinical studies. They are classified based on the mechanisms of their actions into "always-on" probes and activatable probes (2). "Always-on" probes, administered with intravenous injection, readily reveal hypervascularized areas, differentiating the tumor from the normal brain parenchyma. These probes have several disadvantages in their use. They do not necessarily accumulate selectively in tumor tissues (3). Even if they do, they show high background signals, which makes it difficult to identify tumor tissues. On the contrary, activatable probes are efficient in identifying the tumor specifically either with its high substance accumulation or with its metabolic activation, although they often require a considerable time up to several hours in clinical use (4). One such example is activatable cell-penetrating peptide (ACPP) (5). The ACPP probe is a fluorescently labeled, polycationic cell-penetrating peptide coupled with a cleavable linker. When the probe is exposed to a protease being active in the tumor, the linker is cleaved and the inhibitory peptide is dissociated. Then it binds to and enters the tumor cells.

Three types of fluorescent probes are in use in neurosurgical procedures: 5-aminolevulinic acid (5-ALA), indocyanine green (ICG), and fluorescein sodium (6).

ICG and fluorescein sodium are classified as "always-on" probes (7), whereas 5-ALA is classified as an activatable probe. It induces the production of protoporphyrin IX (PpIX), which preferentially accumulates in glioma tissues. It reaches its peak 6 h after 5-ALA administration (8).

A randomized controlled study conducted by Stummer et al. assessed the efficacy of fluorescence-guided resection with 5-ALA in patients with malignant gliomas amenable to complete resection of contrast-enhancing tumor (9). The primary endpoints were the number of patients without contrast-enhancing tumor in early postoperative MRI and 6-month progression-free survival. Secondary endpoints were volume of residual tumor on postoperative MRI, overall survival, neurological deficit, and toxic effects. Patients assigned to fluorescence-guided surgery had a higher 6-month progression-free survival than did those assigned to conventional surgery (41.0 vs. 21.1%, $p = 0.0003$). The complete resection rate of contrast enhancing tumor in the fluorescence-guided surgery group compared favorably with that in the conventional surgery group (65 vs. 36%, $p < 0.0001$). They have shown that the use of 5-ALA resulted in a higher complete resection rate and a longer progression-free survival. Of note, no significant differences in overall survival, neurological deficit, or toxic effects were noted between the two groups. 5-ALA is now routinely used in clinical practice for high-grade glioma surgery. On the contrary, it fails to identify low-grade gliomas. There are some limitations in its use as well, which would include false positivity, false negativity, the need for preoperative oral administration, and the inability for re-administration (10).

We have previously reported on hydroxymethyl rhodamine green (HMRG) probes as activatable fluorescent probes for rapid cancer detection with topical spray (11). They are comprised of HMRG as fluorescent scaffold combined with various types of amino acids or dipeptides. Their fluorescence are completely quenched by spirocyclic caging but are activated rapidly with a one-step enzymatic reaction in the presence of specific aminopeptidase enzymes within a few to tens of minutes (**Figure 1**). Dipeptidylpeptidase IV and γ-glutamyltransferase (GGT) are some examples of dipeptidyl peptidases and aminopeptidases that are known to be expressed at the elevated levels in various types of cancers, such as hepatic cancer, esophagus cancer, ovarian cancer, and glioma as well, as compared to normal tissues (11–15). GGT is present on the plasma membrane and catalyzes the transfer of the N-terminal gamma-glutamyl group of substrates to acceptor molecules. When it encounters GGT on the surface of a cancer tissue, it is hydrolyzed by the enzymatic reaction to yield the highly fluorescent product, HMRG. *In vitro*, when red fluorescent protein was used as a reference for location of a cell of the ovarian cancer cell line SHIN3, sensitivity and specificity of detecting SHIN3-RFP tumors with gGlu-HMRG 10 min after injection were 100 and 100%, respectively. *In vivo*, after establishing the intraperitoneal dissemination mouse model using SHIN3, minute tumors <1 mm in diameter in the peritoneum could be readily identified as early as 30 s after spraying the gGlu-HMRG probe under fluorescence-guided endoscopy and they could be removed easily with forceps. Without fluorescent probes, confirming the completeness of resection would be difficult with naked eyes, and therefore would have to be ascertained by postoperative histological confirmation (16–18).

These HMRG probes can be applied for the detection of a brain tumor. Some probes fluorescence glioma tissue more than the surrounding normal brain tissue after their topical application (**Figure 2**). The biggest advantages of these activatable probes would be that they start to react immediately after spray and can be administered repeatedly during surgery with potentially high specificity and sensitivity. Topical application of spray probes can be performed with a much lower dose than systemic administration, and thus they are deemed safer. On the other hand, one caveat would be that the efficacy of spray fluorescent probes may be diminished by being washed away by active bleeding at the resection cavity before they provoke fluorescence in the tumor. Another concern would be that the surrounding brain tissue may overhang the resection cavity, which makes it difficult to efficiently apply fluorescent probes to the cavity and to accurately evaluate the degree of fluorescence.

We believe that these novel fluorescent probes have a potential as probes complementary to 5-ALA in high-grade glioma surgery. As discussed earlier, 5-ALA is highly effective and routinely administered for resection of high-grade gliomas, but these probes would be worth a try

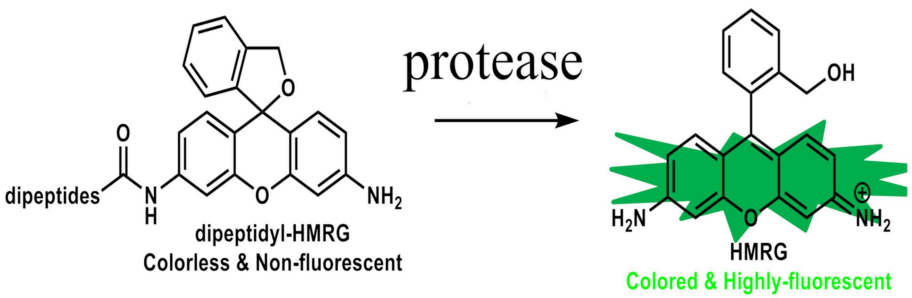

FIGURE 1 | Chemical structures of HMRG-based fluorescent probes. These probes are completely quenched due to spirocyclic caging but are activated with protease reaction.

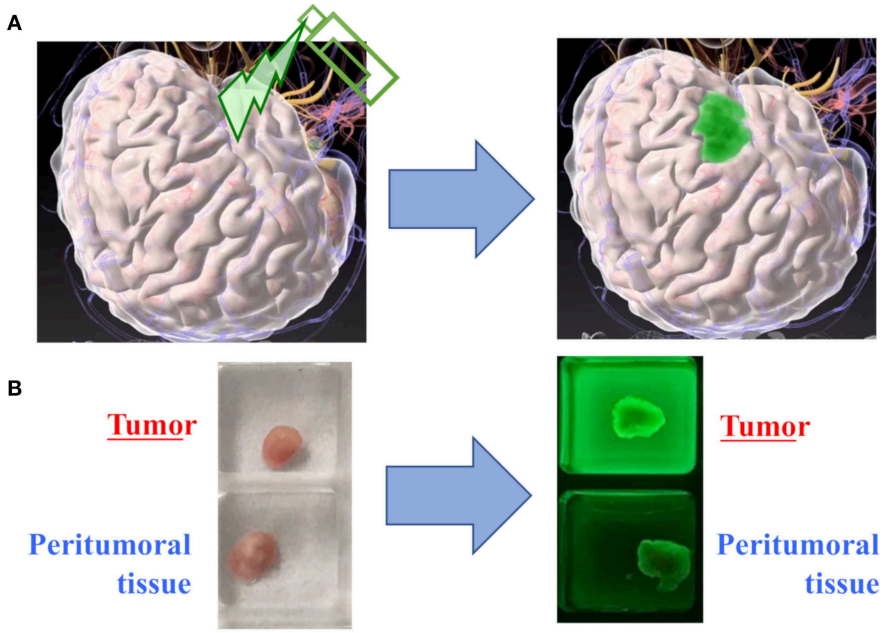

FIGURE 2 | Proof of concept in spray fluorescent probes. **(A)** The conceptual image of tumor detection with topical application of a fluorescent probe. **(B)** In a representative case of glioma, the fresh tumor tissue exhibits significantly stronger fluorescence as compared to the peritumoral tissue.

when the tumor does not fluorescence with 5-ALA or when 5-ALA fluorescence has significantly diminished at the end of tumor resection. In addition, they would be a breakthrough in low-grade glioma surgery, where 5-ALA is largely ineffective. Moreover, they are potentially applicable to virtually all types of brain tumors including malignant lymphoma and brain metastasis, which are the top differential diagnoses of glioma. Novel HMRG probes which specifically detect malignant lymphoma or brain metastasis are currently under investigation. Last but not the least, a larger clinical study is warranted to assess the clinical utility of our probes in brain tumor surgery.

AUTHOR CONTRIBUTIONS

YKi, ShoT, MK, and YU wrote the manuscript. YKu, KY, AO, TN, RM, TK, TH, SatT, MN, ShuT, AM, and NS carefully reviewed the manuscript.

FUNDING

Translational & Clinical Research Core Centers from Japan Agency for Medical Research and Development (AMED) (Seeds A, A105) (ShoT), Japan Society for the Promotion of Science (Grant-in-Aid for Young Scientists (B), 15K19952) (ShoT).

REFERENCES

1. Tsien RY. Fluorescent and photochemical probes of dynamic biochemical signals inside living cells. In: Czarnik AW, editor. *American Chemical Society*. Washington, DC (1993). p. 130–46.
2. Kobayashi H, Ogawa M, Alford R, Choyke PL, Urano Y. New strategies for flourescent probe desogn in medical diagmpstic imaging. *Chem Rev.* (2011) 110:2620–40. doi: 10.1021/cr900263j
3. Diaz RJ, Dios RR, Hattab EM, Burrell K, Rakopoulos P, Sabha N, et al. Study of the biodistribution of fluorescein in glioma-infiltrated mouse brain and histopathological correlation of intraoperative findings in high-grade gliomas resected under fluorescein fluorescence guidance. *J Neurosurg.* (2015) 122:1360–9. doi: 10.3171/2015.2.JNS132507
4. Kobayashi H, Choyke PL. Target-cancer-cell-specific activatable fluorescence imaging probes: rational design and *in vivo* applications. *Acc Chem Res.* (2011) 44:83–90. doi: 10.1021/ar1000633
5. Nguyen QT, Olson ES, Aguilera TA, Jiang T, Scadeng M, Ellies LG, et al. Surgery with molecular fluorescence imaging using activatable cell-penetrating peptides decreases residual cancer and improves survival. *Proc Natl Acad Sci USA.* (2010) 107:4317–22. doi: 10.1073/pnas.0910261107
6. Belykh E, Martirosyan NL, Yagmurlu K, Miller EJ, Eschbacher JM, Izadyyazdanabadi M, et al. Intraoperative fluorescence imaging for personalized brain tumor resection: current state and future directions. *Front Surg.* (2016) 3:55. doi: 10.3389/fsurg.2016.00055
7. Eyupoglu IY, Hore N, Fan Z, Buslei R, Merkel A, Buchfelder M, et al. Intraoperative vascular DIVA surgery reveals angiogenic hotspots in tumor zones of malignant gliomas. *Sci Rep.* (2015) 5:1–7. doi: 10.1038/srep 07958
8. Stummer W, Stepp H, Moller G, Ehrhardt A, Leonhard M, Reulen HJ. Technical principles for protoporphyrin-ix-fluorescence guided microsurgical resection of malignant glioma tissue. *Acta Neurochir.* (1998) 140:995–1000. doi: 10.1007/978-3-319-93698-7_49

9. Stummer W, Pichlmeier U, Meinel T, Wiestler OD, Zanella F, Reulen HJ. Fluorescence-guided surgery with 5-aminolevulinic acid for resection of malignant glioma: a randomised controlled multicentre phase III trial. *Lancet Oncol.* (2006) 7:392–401. doi: 10.1016/S1470-2045(06)70665-9
10. Ferraro N, Barbarite E, Albert TR, Berchmans E, Shah AH, Bregy A, et al. The role of 5-aminolevulinic acid in brain tumor surgery: a systematic review. *Neurosurg Rev.* (2016) 39:545–55. doi: 10.1007/s10143-015-0695-2
11. Urano Y, Sakabe M, Kosaka N, Ogawa M, Mitsunaga M, Asanuma D, et al. Rapid cancer detection by topically spraying a γ-glutamyltranspeptidase-activated fluorescent probe. *Sci Transl Med.* (2011) 3:110ra119. doi: 10.1126/scitranslmed.3002823
12. Stremenova J, Krepela E, Mares V, Trim J, Dbaly V, Marek J, et al. Expression and enzymatic activity of dipeptidyl peptidase-IV in human astrocytic tumours are associated with tumour grade. *Int J Oncol.* (2007) 31:785–92. doi: 10.3892/ijo.31.4.785
13. Onoyama H, Kamiya M, Kuriki Y, Komatsu T, Abe H, Tsuji Y, et al. Rapid and sensitive detection of early esophageal squamous cell carcinoma with fluorescence probe targeting dipeptidylpeptidase IV. *Sci Rep.* (2016) 6:1–7. doi: 10.1038/srep26399
14. Fujii T, Kamiya M, Urano Y. *In vivo* imaging of intraperitoneally disseminated tumors in model mice by using activatable fluorescent small-molecular probes for activity of cathepsins. *Bioconjug Chem.* (2014) 25:1838–46. doi: 10.1021/bc5003289
15. Liu Y, Tan J, Zhang Y, Zhuang J, Ge M, Shi B, et al. Visualizing glioma margins by real-time tracking of γ-glutamyltranspeptidase activity. *Biomaterials.* (2018) 173:1–10. doi: 10.1016/j.biomaterials.2018.04.053
16. Braun S, Vogl FD, Naume B, Janni W, Osborne MP, Coombes RC, et al. A pooled analysis of bone marrow micrometastasis in breast cancer. *N Engl J Med.* (2005) 353:793–802. doi: 10.1056/NEJMoa050434
17. Cote RJ, Rosen PP, Lesser ML, Old LJ, Osborne MP. Prediction of early relapse in patients with operable breast cancer by detection of occult bone marrow micrometastases. *J Clin Oncol.* (1991) 9:1749–56. doi: 10.1200/JCO.1991.9.10.1749
18. Lugo TG, Braun S, Cote RJ, Pantel K, Rusch V. Detection and measurement of occult disease for the prognosis of solid tumors. *J Clin Oncol.* (2003) 21:2609–15. doi: 10.1200/JCO.2003.01.153

Conflict of Interest Statement: The authors declare that the research was conducted in the absence of any commercial or financial relationships that could be construed as a potential conflict of interest.

frontiers in Surgery

REVIEW
published: 09 August 2019
doi: 10.3389/fsurg.2019.00047

The Utility of Near-Infrared Fluorescence and Indocyanine Green During Robotic Pulmonary Resection

Dana Ferrari-Light[1], *Travis C. Geraci*[1]*, *Prabhu Sasankan*[2] *and Robert J. Cerfolio*[1]

[1] *Department of Cardiothoracic Surgery, New York University Langone Health, New York, NY, United States,* [2] *School of Medicine, New York University Langone Health, New York, NY, United States*

During minimally invasive pulmonary resection, it is often difficult to localize pulmonary nodules that are small (<2 cm), low-density/subsolid on imaging, or deep to the visceral pleura. The use of near-infrared fluorescence (NIF) imaging for localizing pulmonary nodules using indocyanine green (ICG) contrast is an emerging technology that is increasingly utilized during pulmonary resection. When administered via electromagnetic navigational bronchoscopy (ENB), ICG can accurately localize pulmonary nodules. When injected intravenously (IV), ICG can also help delineate the intersegmental plane. Research is ongoing regarding the utility of ICG for identification of the sentinel lymph node in lung cancer.

Keywords: electromagnetic, fluorescence, localization, navigational bronchoscopy, lung cancer, pulmonary resection, robotic

OPEN ACCESS

Edited by:
Calvin Sze Hang Ng, The Chinese University of Hong Kong, China

Reviewed by:
J. Matthew Reinersman, University of Oklahoma Health Sciences Center, United States
Nuria Maria Novoa, University of Salamanca Health Care Complex, Spain

***Correspondence:**
Travis C. Geraci
travis.geraci@nyulangone.org

Specialty section:
This article was submitted to Thoracic Surgery, a section of the journal Frontiers in Surgery

Received: *11 June 2019*
Accepted: *23 July 2019*
Published: *09 August 2019*

Citation:
Ferrari-Light D, Geraci TC, Sasankan P and Cerfolio RJ (2019) The Utility of Near-Infrared Fluorescence and Indocyanine Green During Robotic Pulmonary Resection. Front. Surg. 6:47. doi: 10.3389/fsurg.2019.00047

INTRODUCTION

The use of electromagnetic navigational bronchoscopy (ENB) using near-infrared fluorescence (NIF) with indocyanine green contrast (ICG) has emerged as an accurate and efficient method for localizing pulmonary nodules. Indocyanine green is a fluorophore contrast that illuminates in the near infrared spectrum, has a high signal-to-noise ratio, is inexpensive, and relatively non-toxic (although the potential for patient allergy remains) (1). Indocyanine green is approved by the U.S. Food and Drug Administration as an intravenously (IV) injected drug for angiography studies and sentinel node assessments in various cancers. It is theorized that ICG is retained in malignant tissue by a non-specific inflammatory permeability and retention effect. Importantly, infiltration with ICG will not distort the cellular integrity of tissues and therefore will not interfere with the histopathologic characterization of the target specimen, including tumor margins.

Indocyanine green has been used successfully in many areas of medicine including ophthalmic angiography, cerebral perfusion assessment, and for the identification of sentinel lymph nodes and evaluation of anastomotic perfusion in various oncologic resections. However, its utility in pulmonary resection has only recently been explored.

In this review we discuss the multimodal use of ICG during pulmonary resection—transbronchial injection for localization of the primary tumor, delineation of the intersegmental plane, and identification of regional lymph nodes.

INTRAOPERATIVE LOCALIZATION OF PULMONARY NODULES WITH INDOCYANINE GREEN

The management of pulmonary nodules has evolved in synchrony with technological advancements in chest imaging. The increased precision of modern helical computed tomography

(CT) has led to the detection of small pulmonary lesions, ostensibly creating a window of opportunity for curative surgical resection in patients with early stage lung cancer. In 2011, the National Lung Screening Trial (NLST) reported a 20% relative reduction in mortality from lung cancer in high-risk patients screened with low-dose CT (LDCT) rather than chest radiography (2). Now with an exponentially-increasing rate of patients with screening LDCT scans revealing small, ill-defined pulmonary lesions, they increasingly are referred to thoracic surgeons for management. However, the majority of these indeterminate pulmonary nodules do not represent lung cancer. In the NLST, 96.4% of identified lesions were determined to be false-positive results after three screening rounds (2). These patients are continually followed with serial imaging. A minority of patients with more concerning sequential imaging findings require an invasive biopsy or surgical resection for diagnosis and/or definitive treatment.

The current standard of care for patients with small early-stage non-small cell lung cancer (NSCLC) is pulmonary lobectomy (3). This standard, however, is based on data that is over 20 years old, prior to the routine use of preoperative positron emission tomography scans (PET/CT) and the ascendance of minimally-invasive surgical techniques. Sublobar resection such as anatomic segmentectomy is performed more often in patients with small nodules or reduced cardiopulmonary function. Data regarding the efficacy of lobectomy vs. sublobar resection are mixed. Prospective non-randomized data have shown comparable long-term survival in patients with nodules <2 cm without nodal metastasis (4). Two prospective, randomized clinical trials, the Cancer and Leukemia Group B Trial 140503 and the Japan Clinical Oncology Group 0802/WJOG 4607L and JCOG 1211 Trial, are currently being conducted to help address the oncologic superiority or equality of sublobar resection vs. lobectomy, particularly for patients with small, early-stage lung cancer (5).

During sublobar resection, indeterminate lesions are often difficult to localize, particularly when a minimally invasive approach is performed. Nodule characteristics may also make intraoperative localization more difficult, such as when the lesion is smaller than 2 cm, subsolid and/or of low-density on CT scan, or deep to the visceral pleural surface. If performing a segmental resection, the precise location of the lesion may be difficult to determine on CT imaging alone, particularly if it is located between adjacent segments. Additionally, when performing pulmonary resection with robotic assistance, identifying lesions can be difficult due to the system's lack of haptic feedback and reliance on visual cues. These limitations of surgical technique have prompted the development of intraoperative localization techniques to aid in accurate resection. Additional incisions, conversion to thoracotomy for bimanual palpation, or performing a lobectomy to resect an intraoperative non-identifiable lesion are inefficient and morbid strategies. Intraoperative localization avoids these maneuvers and allows for more precise surgery.

Minimally invasive approaches to pulmonary resection are preferred to reduce perioperative morbidity and length of stay, precluding the standard technique of bimanual palpation. A number of preoperative procedures have been developed to aid localization, including CT-guided placement of metallic wires, coils, or markers (6, 7). While these techniques may be accurate, they require coordination with radiology and/or a hybrid operating room, exposes the patient and staff to radiation, requires a significant amount of time to complete, risk migration of the marker, and may be complicated by parenchymal hematoma or pneumothorax.

In 2001, Sakamoto et al. were the first to describe a method for nodule localization using indigo carmine contrast injected via flexible bronchoscopy near the target lesion (8). This study was followed by a series of studies reporting accurate localization of small pulmonary nodules and regional lymph nodes using electromagnetic navigation bronchoscopy (ENB) with transbronchial injection of blue dyes, most commonly, methylene blue or isosulfan blue (9). While the accuracy of these agents range from 79 to 100%, contrast dyes such as indigo carmine and methylene blue are limited by relatively quick diffusion time thereby limiting precision intraoperative visualization. Additionally, unlike color dyes visualized by white light endoscopy, ICG fluorescence is always detectable regardless of color or texture variation in the pulmonary parenchyma such as regions of anthracotic pigmentation, hematoma, or architectural distortion due to underlying pulmonary disease.

In 2015, Anayama et al. confirmed the feasibility of using NIF for lesion localization via ENB-guided ICG injection in a porcine lung model (10). Both *in vitro* and *ex vivo* studies were performed to assess the tissue penetration and spread of ICG in pulmonary parenchyma and to evaluate intraoperative localization. In the same year, Keating et al. published a case report in a human patient of successful intraoperative localization using NIF imaging with ICG during video-assisted thoracoscopic surgery (VATS) (11). In this study, the patient received an intravenous injection of ICG 24 h prior to surgery. Two lesions were successfully visualized and resected, one of which could not be identified with manual palpation through the thoracoscopic port sites.

A number of groups have since reported institutional studies regarding the accuracy of ENB-guided NIF using ICG for intraoperative localization of pulmonary lesions. In 2015 Okusanya et al. reported localization after administering preoperative intravenous ICG (5 mg/kg) followed by open thoracotomy within 24 h (12). NIF detected 16/18 (88%) nodules compared to manual palpation, which achieved a 100% identification rate. Furthermore, ICG identified five additional malignant subcentimeter nodules not readily apparent on CT imaging, three of which were in different lobes than the primary tumor. The authors found that the sensitivity for detecting nodules with NIF was dependent on tissue depth but independent of nodule size, metabolic activity, histology, or vascularity.

In 2017, Abbas et al. reported their institutional experience with ENB, localizing 54 nodules in 51 patients with a success rate of 98.1% and a false negative rate of 1.9% (13). In the first

two patients, methylene blue dye with fiducial markers were used however the markers were found to be of marginal utility and the blue dye diffused quickly, prompting the researchers to switch to an combination of iopamidol (for fluoroscopic identification), methylene blue (for visual identification), and ICG (for fluorescence identification). Two patients required conversion to open thoracotomy for localization and resection due to dense pleural adhesions.

In 2018, Anayama et al. reported a series of 37 patients with nodules <2 cm in size who underwent VATS wedge resection using a mixture of ICG and iopamidol for localization by either CT-guided percutaneous injection or bronchoscopic injection (14). In the CT-guided group, 15/15 (100%) nodules were successfully localized, however a small pneumothorax occurred in three patients (20%) and in one patient this precluded additional marking. In the bronchoscopic group, 20/22 (90.9%) nodules were localized with six patients receiving injections at two anatomic locations. In the two patients unable to be localized, finger palpation was successful after extension of the access port site. The authors concluded that CT-guided localization might not be optimal for patients with multiple nodules, as the risk of pneumothorax may prevent marking of multiple lesions. Additionally, the bronchoscopic method may be preferred for patients with nodules that may be difficult to reach percutaneously, such as lesions adjacent the mediastinum, or posteriorly behind the scapula.

In mid-2019, Chao et al. just recently published their experience with a dual-marker localization technique in a hybrid operating room, using NIF marking with ICG in conjunction with microcoil deployment via CT-guided coaxial needle technique. This dual-marker placement was successful in all 11 patients studied, with a median localization time of 19 min and may be helpful to locate difficult pulmonary nodules (15).

We have recently published our own institutional experience with NIF localization using ICG when administered both via ENB and intravenous injection (16). In our series of patients who underwent planned robotic segmentectomy, 93 were selected for ENB localization with ICG due to small nodule size and/or challenging anatomic location (between segments or deep to the visceral pleural surface). Of the 93 patients undergoing ENB, we successfully identified the pulmonary nodule in 80 patients (86%). We were unable to find a statistically significant variable that would predict success or failure of our method. The most common reasons for localization failure were inaccurate ENB or ICG injection and technical malfunctions of the equipment.

TECHNICAL CONSIDERATIONS FOR ICG LOCALIZATION

At our institution, the decision to use ENB and ICG fluorescence for pulmonary tumor localization is selective. We chose to localize lesions based on size (favored for small lesions <2 cm), lesion morphology (ground-glass opacification), and lesion anatomy (favored in lesions deep to the pleural surface). There is no distance from the pleura that we consider to be an absolute contraindication to lesion localization.

Performing localization starts with a preoperative review of collimated CT scan data using superDimension™ software (Covidien, Minneapolis, MN) to create a virtual bronchoscopic pathway to the target lesion (see **Figure 1**). Identification of the optimal adjacent segmental and/or subsegmental bronchus is important for successful localization. In the operating room, the patient is positioned supine on the operating table and an electromagnetic board is placed beneath. Precordial sensors are attached to the patient which are then registered with the electromagnetic system. The patient is intubated with a single-lumen endotracheal tube. A sensor probe is introduced through the working channel of a flexible bronchoscope and the system is synced with various anatomic coordinates in the proximal and distal airways. Real-time virtual-guided bronchoscopy is then performed to within a goal distance of 1 cm or less to the target lesion (see **Figure 2**). The flexible probe may be extended beyond the end of the bronchoscope, allowing transparenchymal navigation to peripheral lesions and/or those distant from a subsegmental bronchus. In our experience, upper lobe lesions are the most difficult to localize because of the acute bronchoscopic angles required to reach the apical airways. When the lesion is localized, ICG contrast is injected via a bronchoscopic needle. It is prudent to have an assistant hold the bronchoscopic in position during injection to prevent drifting from the target location.

Our method for contrast injection involves an admixture of 10 mL of sterile water in a 25 mg bottled powder of indocyanine green. We inject 0.5 mL of ICG solution followed by a flush of 0.5 mL of sterile water. It is important to use sterile water in the admixture. In our experience, using normal saline will cause the ICG powder to clump and makes it difficult to flush intravenously. The remaining 9.5 mL of ICG solution is given intravenously by the anesthesiologist after control and ligation of the segmental pulmonary artery. During robotic surgery on the Xi version of the da Vinci robotic system, the thoracoscopic camera is equipped with near-infrared technology (Firefly, Intuitive Surgical, Sunnyvale, CA) which illuminates ICG-infiltrated lung parenchyma after peritumoral injection (see **Figure 3**) and ICG-perfused tissue after intravenous administration (see **Figure 4**).

DELINEATION OF THE INTERSEGMENTAL PLANE

During anatomic segmental resection, the corresponding vein, artery, and bronchus are transected and the lung parenchyma is divided with a surgical stapler. During parenchymal division, the surgeon must identify the intersegmental plane while achieving an appropriate tumor margin. Standard techniques for identifying the intersegmental plane such as inflation/deflation of the tissue, are practically cumbersome and may be misleading due to air diffusion through the communicating pores of Kohn. Indocyanine green binds to plasma proteins and when injected intravenously is confined to the vascular compartment. Due to this biochemical property, ICG helps delineate the intersegmental plane after ligation of the segmental artery.

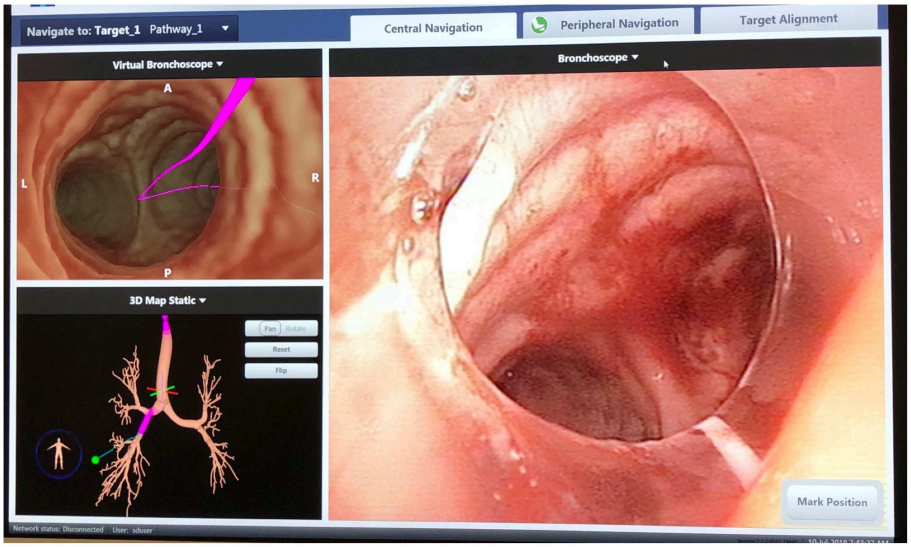

FIGURE 1 | SuperDimension Thoracic Navigation System: electromagnetic bronchoscopic view, showing the pathway to the target nodule in the right lower lobe.

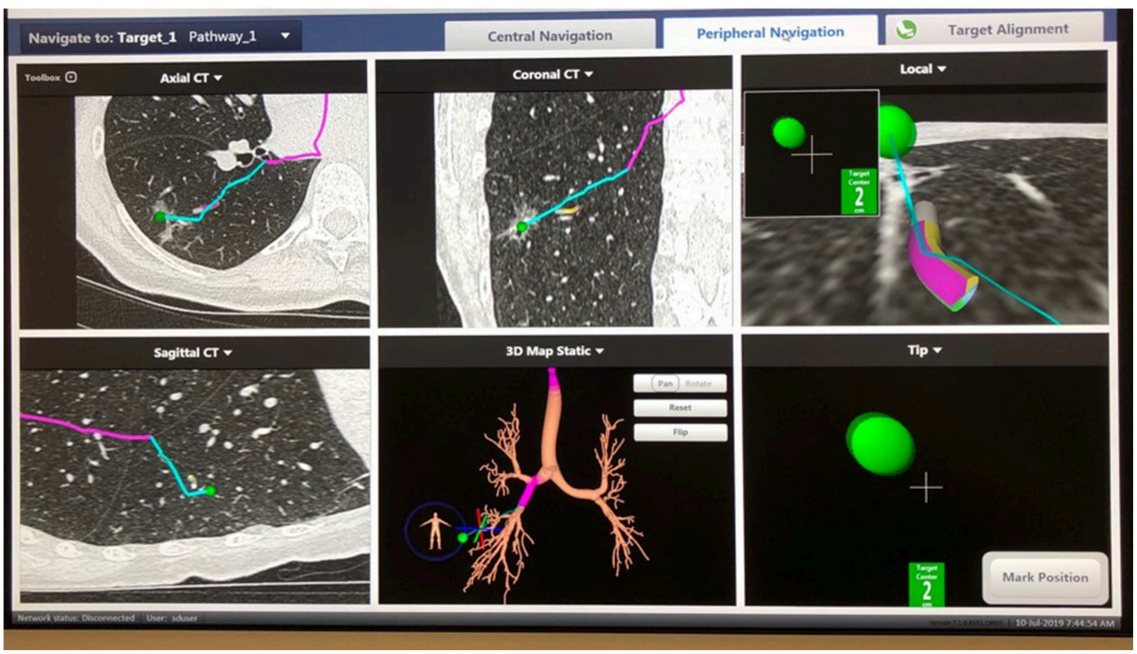

FIGURE 2 | SuperDimension Thoracic Navigation System: image-guided peripheral view, showing electromagnetic probe is 2 cm from the target nodule in the right lower lobe.

Presented in 2017, Mehta et al. conducted a phase II prospective cohort trial evaluating the safety, feasibility, and reproducibility of peripheral venous ICG injection and NIF mapping for delineation of the intersegmental plane during robotic segmental resection (17). Specifically, the researchers assessed whether this technique would increase the oncological margin vs. reliance on visual delineation of the intersegmental plane. In 31 patients who underwent pulmonary resection with ICG injection, 23 (74%) cases resulted in a significant lengthening of the oncologic resection margin. Using a novel 7-point objective rating scale, fluorescent segmental demarcation resulted in an average increase in the oncologic margin of 2.4 cm vs. the predicted plane by a two-surgeon assessment. The long-term significance regarding local control, recurrence, and disease-free survival are unknown, but long-term follow-up is anticipated.

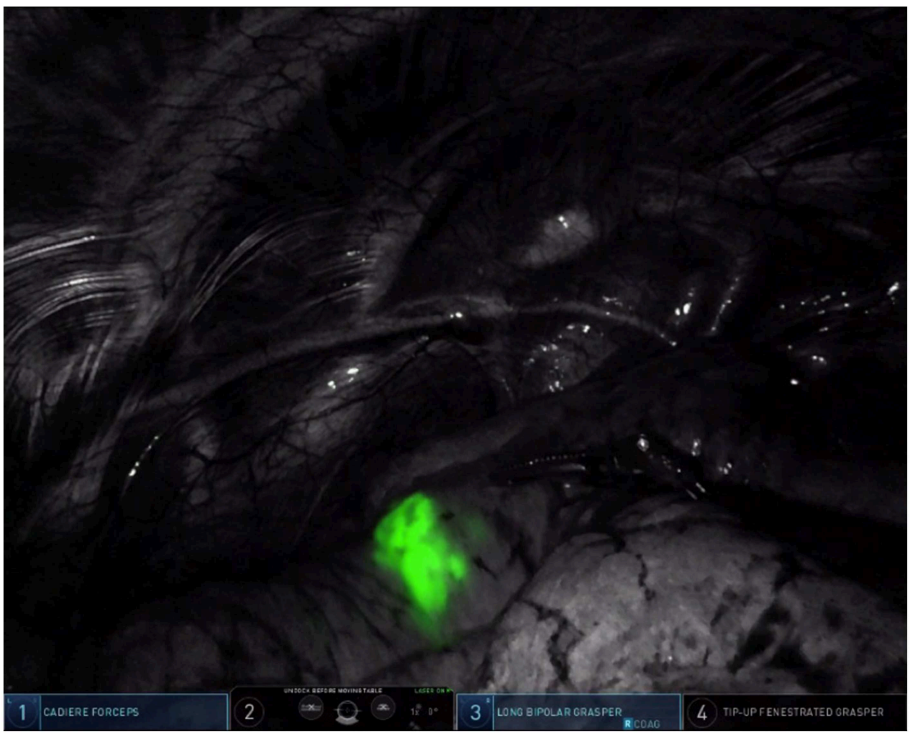

FIGURE 3 | Pulmonary nodule in the left upper lobe, illuminated by ICG fluorescence (firefly mode).

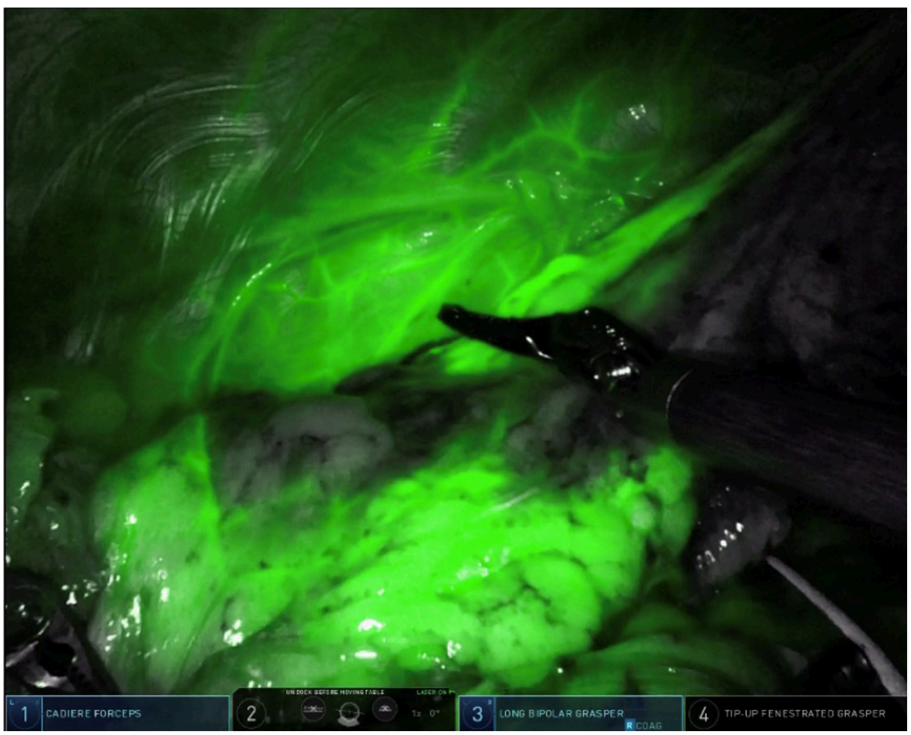

FIGURE 4 | Intravenous ICG delineation of the intersegmental plane between the lingula and the left upper lobe segments during left upper lobe trisegmentectomy. Note the diffusion of ICG contrast around the area of target nodule from **Figure 3**.

In their 2019 report, Sekine et al. report a novel method involving the combined use of 3D image analysis and transbronchial ICG injection to determine surgical margins for pulmonary sublobar resection in patients with early-stage lung cancer. In their method, preoperative 3D image analysis was accomplished using multi-slice enhanced CT imaging to generate pulmonary angiography and virtual bronchoscopy (18). For each case, these virtual models were then used to run several simulations of anatomical sublobar resection in order to determine the appropriate tumor resection margin.

During surgery, transbronchial injection was used to instill ICG into the target segmental bronchus and distribute it throughout the segmental bronchial tree. Following the generation of virtual bronchoscopy from chest CT imaging, sublobar resection simulation was used to identify the segmental area and margins for resection. Intra-operatively, transbronchial ICG injection yielded well-visualized fluorescence and easily definable segmental borders in 55 of 65 cases (84%). A comparison of preoperative simulated resection and postoperative segmental structure found concordance between preoperative virtual segmentectomy and postoperative segmental structures in 54 of the 58 (93.1%) cases. In a propensity-matched comparison of surgical outcomes between patients who underwent fluorescence-guided sublobar resection with patients who underwent traditional VATS segmentectomy, the analysis showed similar operation length, blood loss, length of hospital stay, and postoperative complications.

SENTINEL LYMPH NODE MAPPING

The use of ICG for intraoperative or postoperative identification of the sentinel node is an exciting area of ongoing research, but its role has not been clearly defined in lung cancer. In cancer, the "sentinel node" refers to the lymph node that receives the initial lymphatic flow from a malignant tumor, theoretically representing the first tissue at risk for malignant dissemination of tumor cells. During a resection for certain types of cancer, if a sentinel node is determined to be negative, a less aggressive lymph node dissection is pursued, limiting morbidity. The regional lymph node status is an important prognostic indicator, particularly in lung cancer. Additionally, patients undergoing a lymph node dissection during pulmonary resection may be upstaged based on nodal status and potentially receive adjuvant therapies. However, in the ACOSOG Z4032 multicenter trial of patients undergoing sublobar resection, 35% of patients were found to undergo resection without lymph node assessment (19). With success in identifying the sentinel node in other malignancies using near infrared imaging, there has been progress in the concept of the sentinel lymph node in lung cancer given that ICG often "lights up" an N1 intrasegmental lymph node.

In 2004, Ito et al. utilized sentinel lymph node navigation using ICG in patients with lung cancer, establishing feasibility and safety (20). Presurgical injection of ICG was administered in peritumoral quadrants in 38 patients undergoing pulmonary lobectomy. During lymph node dissection, a sentinel node was identified by visual inspection in 18% of patients. Additionally, sentinel nodes were derived by relative ICG concentration (1.5 × baseline) in 87.5% of patients with a negative predictive rate of 100%. There was a single false-negative result, which the authors posit was due to tumor obstruction of the primary lymphatic flow.

In 2011, Yamashita et al. evaluated the accuracy of ICG to identify the sentinel lymph node in patients with early stage lung cancer undergoing VATS. Peritumoral injection of ICG was performed and a sentinel lymph node was identified with NIF in 25 of 31 patients (80.7%) with a 0% false-negative rate (21). The noted reasons for failure to identify a sentinel lymph node were attributed to intrapleural adhesions or leakage of ICG contrast after injection.

In 2013, Gilmore et al. reported a dose-escalation clinical trial, evaluating the optimal peritumoral injection of ICG to identify sentinel lymph nodes in human patients with lung cancer (22). In 38 patients, the study revealed that sentinel lymph node identification increased with increased dose-response, finding an 89% success rate at a dose of 1,000 μg of ICG. At this dose, 26 sentinel nodes were identified by near infrared imaging in 15 patients, six of which had metastatic disease on histologic analysis. Metastatic nodal disease was not identified in patients with negative sentinel lymph nodes by ICG evaluation.

Recently, Hachey et al. reported a feasibility study using ICG contrast for tumor and sentinel lymph node localization by ENB (23). Performed in 10 patients with early stage NSCLC, the prospective study revealed that ICG accurately and efficiently identifies the target parenchymal lesion by fluorescent flow, with passive drainage to the sentinel lymph node and regional lymph nodes. The technique identified the sentinel node in eight patients (80%) and the sentinel node status was 100% sensitive for overall nodal staging status. Of note, 12.5% of patients were upstaged based on sentinel lymph node mapping.

In a report reviewing the long-term outcomes after NIF-guided sentinel lymph node mapping with peritumoral ICG injection, Digesu et al. compared patients who underwent mediastinal lymph node sampling with or without sentinel lymph node localization (24). Sentinel lymph node mapping was 100% sensitive and specific for local lymph node status; metastatic disease was detected in the sentinel lymph node in all occurrences (7 patients) of positive lymph node disease (pN+) and not detected in the sentinel node in node negative disease. After a median follow-up of nearly 45 months, the study revealed that patients who underwent sentinel node mapping who were found to have pathologic node negative disease (pN0) had an improved estimated overall and disease-free survival than those who were deemed pN0 by lymph node dissection alone (100 vs. 70%, and 100 vs. 66%, respectively). In the non-sentinel lymph node group, 4 of 15 patients (26%) had recurrence of disease despite pN0 status at resection. The authors attribute part of this outcome to improved overall nodal staging with sentinel lymph node mapping, due to the focused histologic analysis of tumor-specific sentinel nodes, thereby shifting patients previously (incorrectly) deemed pN0 to the correct pN+ status.

CONCLUSION

Indocyanine green is emerging as a useful adjunct in the localization of lung nodules and the delineation of

the intersegmental plane when given intravenously, via transbronchial injection, or both. There is significant potential for its utility in localizing pulmonary sentinel lymph nodes and its impact on overall and disease-free survival for lung cancer.

AUTHOR CONTRIBUTIONS

DF-L, TG, PS, and RC contributed equally to the formation, writing, and editing of this manuscript.

REFERENCES

1. Alander JT, Kaartinen I, Laakso A, Patila T, Spillmann T, Tuchin VV, et al. A review of indocyanine green fluorescent imaging in surgery. *Int J Biomed Imag*. (2012) 2012:940585. doi: 10.1155/2012/940585
2. Aberle DR, Adams AM, Berg CD, Black WC, Clapp JD, Fagerstrom RM, et al. Reduced lung-cancer mortality with low-dose computed tomographic screening. *N Engl J Med*. (2011) 365:395–409. doi: 10.1056/NEJMoa1102873
3. Ginsberg RJ, Rubinstein LV. Randomized trial of lobectomy versus limited resection for T1 N0 non-small cell lung cancer. Lung Cancer Study Group. *Ann Thorac Surg*. (1995) 60:615–22; discussion: 22–3. doi: 10.1016/0003-4975(95)00537-U
4. Kodama K, Higashiyama M, Okami J, Tokunaga T, Imamura F, Nakayama T, et al. Oncologic outcomes of segmentectomy versus lobectomy for clinical T1a N0 M0 Non-small cell lung cancer. *Ann Thorac Surg*. (2016) 101:504–11. doi: 10.1016/j.athoracsur.2015.08.063
5. Asamura H. Role of limited sublobar resection for early-stage lung cancer: steady progress. *J Clin Oncol*. (2014) 32:2403–4. doi: 10.1200/JCO.2014.56.4203
6. Lin MW, Chen JS. Image-guided techniques for localizing pulmonary nodules in thoracoscopic surgery. *J Thorac Dis*. (2016) 8(Suppl. 9):S749–55. doi: 10.21037/jtd.2016.09.71
7. Zhao ZR, Lau RW, Ng CS. Hybrid theatre and alternative localization techniques in conventional and single-port video-assisted thoracoscopic surgery. *J Thorac Dis*. (2016) 8(Suppl. 3):S319–27. doi: 10.3978/j.issn.2072-1439.2016.02.27
8. Sakamoto T, Takada Y, Endoh M, Matsuoka H, Tsubota N. Bronchoscopic dye injection for localization of small pulmonary nodules in thoracoscopic surgery. *Ann Thorac Surg*. (2001) 72:296–7. doi: 10.1016/S0003-4975(01)02604-2
9. Cuadrado D, Grogan EL. Localization techniques for small lung nodules. *Oper Tech Thoracic Cardiovasc Surg*. (2014) 19:179–98. doi: 10.1053/j.optechstcvs.2014.08.001
10. Anayama T, Qiu J, Chan H, Nakajima T, Weersink R, Daly M, et al. Localization of pulmonary nodules using navigation bronchoscope and a near-infrared fluorescence thoracoscope. *Ann Thorac Surg*. (2015) 99:224–30. doi: 10.1016/j.athoracsur.2014.07.050
11. Keating JJ, Kennedy GT, Singhal S. Identification of a subcentimeter pulmonary adenocarcinoma using intraoperative near-infrared imaging during video-assisted thoracoscopic surgery. *J Thorac Cardiovasc Surg*. (2015) 149:e51–3. doi: 10.1016/j.jtcvs.2014.10.081
12. Okusanya OT, Holt D, Heitjan D, Deshpande C, Venegas O, Jiang J, et al. Intraoperative near-infrared imaging can identify pulmonary nodules. *Ann Thorac Surg*. (2014) 98:1223–30. doi: 10.1016/j.athoracsur.2014.05.026
13. Abbas A, Kadakia S, Ambur V, Muro K, Kaiser L. Intraoperative electromagnetic navigational bronchoscopic localization of small, deep, or subsolid pulmonary nodules. *J Thorac Cardiovasc Surg*. (2017) 153:1581–90. doi: 10.1016/j.jtcvs.2016.12.044
14. Anayama T, Hirohashi K, Miyazaki R, Okada H, Kawamoto N, Yamamoto M, et al. Near-infrared dye marking for thoracoscopic resection of small-sized pulmonary nodules: comparison of percutaneous and bronchoscopic injection techniques. *J Cardiothorac Surg*. (2018) 13:5. doi: 10.1186/s13019-018-0697-6
15. Chao YK, Leow OQY, Wen CT, Fang HY. Image-guided thoracoscopic lung resection using a dual-marker localization technique in a hybrid operating room. *Surg Endosc*. (2019). doi: 10.1007/s00464-019-06883-y. [Epub ahead of print].
16. Geraci TC, Ferrari-Light D, Kent A, Michaud G, Zervos M, Pass H, et al. Technique, outcomes with navigational bronchoscopy using indocyanine green for robotic segmentectomy. *Ann Thorac Surg*. (2019) 108:363–9. doi: 10.1016/j.athoracsur.2019.03.032
17. Mehta M, Patel YS, Yasufuku K, Waddell TK, Shargall Y, Fahim C, et al. Near-infrared mapping with indocyanine green is associated with an increase in oncological margin length in minimally invasive segmentectomy. *J Thorac Cardiovasc Surg*. (2019) 157:2029–35. doi: 10.1016/j.jtcvs.2018.12.099
18. Sekine Y, Itoh T, Toyoda T, Kaiho T, Koh E, Kamata T, et al. Precise anatomical sublobar resection using a 3D medical image analyzer and fluorescence-guided surgery with transbronchial instillation of indocyanine green. *Semin Thorac Cardiovasc Surg*. (2019). doi: 10.1053/j.semtcvs.2019.01.004. [Epub ahead of print].
19. Kent MS, Mandrekar SJ, Landreneau R, Nichols F, Foster NR, DiPetrillo TA, et al. A nomogram to predict recurrence and survival of high-risk patients undergoing sublobar resection for lung cancer: an analysis of a multicenter prospective study (ACOSOG Z4032). *Ann Thorac Surg*. (2016) 102:239–46. doi: 10.1016/j.athoracsur.2016.01.063
20. Ito N, Fukuta M, Tokushima T, Nakai K, Ohgi S. Sentinel node navigation surgery using indocyanine green in patients with lung cancer. *Surg Today*. (2004) 34:581–5. doi: 10.1007/s00595-004-2780-y
21. Yamashita S, Tokuishi K, Anami K, Miyawaki M, Moroga T, Kamei M, et al. Video-assisted thoracoscopic indocyanine green fluorescence imaging system shows sentinel lymph nodes in non-small-cell lung cancer. *J Thorac Cardiovasc Surg*. (2011) 141:141–4. doi: 10.1016/j.jtcvs.2010.01.028
22. Gilmore DM, Khullar OV, Jaklitsch MT, Chirieac LR, Frangioni JV, Colson YL. Identification of metastatic nodal disease in a phase 1 dose-escalation trial of intraoperative sentinel lymph node mapping in non-small cell lung cancer using near-infrared imaging. *J Thorac Cardiovasc Surg*. (2013) 146:562–70; discussion: 9–70. doi: 10.1016/j.jtcvs.2013.04.010
23. Hachey KJ, Digesu CS, Armstrong KW, Gilmore DM, Khullar OV, Whang B, et al. A novel technique for tumor localization and targeted lymphatic mapping in early-stage lung cancer. *J Thorac Cardiovasc Surg*. (2017) 154:1110–8. doi: 10.1016/j.jtcvs.2016.12.058
24. Digesu CS, Hachey KJ, Gilmore DM, Khullar OV, Tsukada H, Whang B, et al. Long-term outcomes after near-infrared sentinel lymph node mapping in non-small cell lung cancer. *J Thorac Cardiovasc Surg*. (2018) 155:1280–91. doi: 10.1016/j.jtcvs.2017.09.150

Conflict of Interest Statement: DF-L discloses compensation for database entry for an unrelated project from Intuitive Surgical. RC discloses relationships with AstraZeneca, Bard Davol, Bovie Medical Corporation, C-SATS, ConMed, Covidien/Medtronic, Ethicon, Fruit Street Health, Google/Verb Surgical, Intuitive Surgical, KCI/Acelity, Myriad Genetics, Neomend, Pinnacle Biologics, ROLO-7, Tego, and TransEnterix.

The remaining authors declare that the research was conducted in the absence of any commercial or financial relationships that could be construed as a potential conflict of interest.

frontiers in Surgery

ORIGINAL RESEARCH
published: 13 August 2019
doi: 10.3389/fsurg.2019.00049

Fluorescein Application in Cranial and Spinal Tumors Enhancing at Preoperative MRI and Operated With a Dedicated Filter on the Surgical Microscope: Preliminary Results in 279 Patients Enrolled in the FLUOCERTUM Prospective Study

Jacopo Falco[1†], Claudio Cavallo[1,2†], Ignazio G. Vetrano[1], Camilla de Laurentis[1], Lampros Siozos[1], Marco Schiariti[1], Morgan Broggi[1], Paolo Ferroli[1] and Francesco Acerbi[1]*

[1] Department of Neurosurgery, Fondazione IRCCS Istituto Neurologico Carlo Besta, Milan, Italy, [2] Department of Neurosurgery, Barrow Neurological Institute, St. Joseph's Hospital and Medical Center, Phoenix, AZ, United States

OPEN ACCESS

Edited by:
Vernard S. Fennell,
Capital Institute for Neurosciences,
United States

Reviewed by:
Jorge Marcelo Mura,
Instituto de Neurocirugía, Chile
Hiroki Toda,
Fukui Red Cross Hospital, Japan

***Correspondence:**
Francesco Acerbi
francesco.acerbi@istituto-besta.it

[†] These authors have contributed equally to this work

Specialty section:
This article was submitted to Neurosurgery, a section of the journal Frontiers in Surgery

Received: 04 February 2019
Accepted: 29 July 2019
Published: 13 August 2019

Citation:
Falco J, Cavallo C, Vetrano IG, de Laurentis C, Siozos L, Schiariti M, Broggi M, Ferroli P and Acerbi F (2019) Fluorescein Application in Cranial and Spinal Tumors Enhancing at Preoperative MRI and Operated With a Dedicated Filter on the Surgical Microscope: Preliminary Results in 279 Patients Enrolled in the FLUOCERTUM Prospective Study. Front. Surg. 6:49. doi: 10.3389/fsurg.2019.00049

Objective: Sodium fluorescein, a green, water soluble dye, is used as neurosurgical fluorescent tracer thanks to its property to accumulate in cerebral regions of blood-brain barrier (BBB) disruption. The authors report the preliminary results of a prospective observational study regarding the use of fluorescein-guided technique for the resection of suspected malignant neoplasms of the central nervous system (CNS), contrast enhancing at preoperative magnetic resonance imaging (MRI), using a dedicated filter on the surgical microscope.

Methods: In March 2016 the authors started a prospective, observational trial to evaluate intraoperative fluorescence's characteristics of CNS tumors, the percentage of extent of resection thanks to fluorescein aid and side effects related to fluorescein administration. This report is based on a preliminary analysis of the results of first 279 enrolled patients. Fluorescein was intravenously injected after intubation or immediately at the entrance in the operating room for awake procedures; the tumor was removed using a dedicated filter on the surgical microscope in an inside-out fashion until all fluorescent tissue was removed, as considered feasible by the surgeon.

Results: The 279 patients finally enrolled in the trial, both firstly diagnosed and recurrent, were categorized according to WHO pathological classification and there were 212 neuroepithelial tumors, 25 brain metastases, 10 cerebral lymphomas, 7 hemangioblastomas, or hemangioendotheliomas and 25 other tumors and conditions. No adverse reaction related to the administration of fluorescein or to the combined use of fluorescein with other fluorophores was registered. Fluorescein accumulated in cerebral regions where the BBB was damaged, representing a significant surgical aid in most of the CNS tumors with contrast enhancement. In cases of complete removal of all

fluorescent tissue, as intraoperatively judged by the surgeon, postoperative MRI revealed a gross total resection in 181/198 patients (91.4%).

Conclusions: Based on these preliminary results, fluorescein-guided surgery with a dedicated filter on the microscope is a safe and effective technique to improve visualization and resection of different CNS tumors and conditions, based on BBB alteration.

Keywords: biopsy, brain tumors, central nervous system, fluorescein, neuro-oncology, spinal tumors, YELLOW 560

INTRODUCTION

Even if Central Nervous System (CNS) tumors do not represent one of the most frequent kind of cancers, they are a major cause of cancer-related mortality and morbidity (1), with an annual incidence in the Western countries of 16.5 per 100.000 adults and of 2.4 new cases per 100.000 children per year. Surgery is the most important treatment in almost all aggressive brain tumors (2–4). The extent of resection (EOR) is a fundamental topic in neurosurgery; if feasible and safely achievable, the gross total resection (GTR) is the most important predictor of overall survival both in high-grade gliomas (HGG) and in metastases (2, 3, 5–9). Furthermore, GTR reduces the risk of recurrence of low-grade gliomas (LGG) or other benign tumors (10, 11). For solitary metastasis, surgical resection plus adjuvant radiotherapy, in form of whole brain radiotherapy or stereotactic radiosurgery, is considered the gold therapeutic standard (12–14); complete metastases resection associated to a favorable factor for prolonged survival. Also for other astrocytomas or rarer primary brain tumors, such as medulloblastomas or ependymomas, radical resection has been correlated to a better prognosis: regarding pilocytic astrocytoma (PA) and ependymomas, a complete resection can achieve local control improving the survival (15, 16).

This need for a radical tumor removal allowed the flourishing of many tools to better visualize the tumor tissue, improving the extent of resection, such as neuronavigation, intraoperative magnetic resonance imaging (MRI), and intraoperative ultrasounds with contrast-enhanced ultrasound (17–19). Among these, fluorophores have acquired an important role thanks to their ability to discriminate between pathological and normal tissue (20–22). Fluorescein is a green fluorescent synthetic organic compound which has countless medical applications (23–27). In form of fluorescein sodium salt (SF) it represents a water-soluble dye with a major blue excitation peak in the region of 460–500 nm and a major green emission peak in the region of 540 to 690 nm.

Abbreviations: AA, anaplastic astrocytoma; AO, anaplastic oligodendroglioma; AIFA, agenzia italiana del farmaco (Italian Medicine Agency); BBB, blood brain barrier; c.e., contrast enhancement; CNS, central nervous system; CT, computerized tomography; EOR, extent of resection; FET, fluoro-ethyl-tyrosine; GBM, glioblastoma; GTR, gross total resection; HGG, high-grade glioma; ICG, indocyanine green; i.v., intravenous; LGG, low-grade glioma; MET, 11C-methionine; MRI, magnetic resonance imaging; PA, pilocytic astrocytoma; PET, positron emission tomography; PR, partial resection; SF, sodium fluorescein; STR, subtotal resection; 5-ALA, 5-aminolevulenic acid.

Although initially its use has been limited to ophthalmology, with historical and sporadic utilization in neurosurgery (28–30), since the introduction of a dedicated and integrated filter in the surgical microscope (YELLOW 560 –*Pentero 900* and *Kinevo; Carl Zeiss Meditec, Oberkochen, Germany*), SF applications in neurosurgery have increased exponentially (31–42). SF, differently to 5-aminolevulenic acid (5-ALA) which is a metabolic tracer (20), could be considered as a vascular fluorophore and its use as fluorescent tracer in neuro-oncological procedures relies on the property to accumulate in pathological areas of blood-brain barrier (BBB) disruption, as in gliomas, but also in other brain tumors, similar to the process of contrast enhancement (c.e.) on MRI.

In July 2015, based upon preliminary scientific results from different studies published in the international literature (34, 36, 37), including a prospective phase II trial from our group (32, 33, 38, 43–46) the Italian Medicine Agency (AIFA) has extended the indications for the utilization of fluorescein molecule (determination 905/2015, Gazette n.168, 22 July, 2015; http://www.gazzettaufficiale.it/atto/serie_generale/caricaDettaglioAtto/originario;jsessionid=izVcTOmnjOzfNRjjw56kAA__.ntc-as2-guri2b?atto.dataPubblicazioneGazzetta=2015-07-22&atto.codiceRedazionale=15A05620&elenco30giorni=false). According to this determination, the intravenous (i.v.) injection of SF as a neurosurgical tracer during oncological procedures for aggressive tumors of the CNS is approved and its cost are totally reimbursed by the Italian National Health System. Therefore, in March 2016, the authors started a new prospective observational study, called FLUOCERTUM (FLUOrescein in CERebral TUMors), regarding the use of SF as a fluorescent intra-operative tracer in patients with suspected aggressive tumors of the CNS. In this paper, we present the preliminary results of the first 279 patients enrolled in this study, until December 2018.

METHODS

Patients and Inclusion Criteria

The inclusion criteria were as follows: (1) patients of both genders, at any age; (2) patients with suspected aggressive lesions of the CNS, as suggested by preoperative MRI or computerized tomography (CT) with i.v. contrast agent administration. The exclusion criteria were: (1) impossibility to give consent due to cognitive deficits or language disorders; (2) known allergy to contrast agents or history of previous anaphylactic shocks;

(3) known severe previous adverse reactions to SF; (4) acute myocardial infarction or stroke in the last 90 days; (5) severe renal failure; (6) severe hepatic failure; (7) severe heart failure; (8) women in their first trimester of pregnancy or lactation.

The study started in March 2016, when the first patient was enrolled. Written informed consent was obtained from all patients. The FLUOCERTUM study has been approved by the Ethical Committee of the Fondazione IRCCS Istituto Neurologico Carlo Besta.

Three hundred and twenty-eight patients were screened for participation in this prospective trial. Two patients were excluded from the analysis because they refused surgery, seventeen patients were excluded because SF was not intraoperatively injected, while fourteen patients were excluded because the specific YELLOW 560 filter of the microscope was not available or not working properly; finally, we excluded sixteen patients because surgery was performed under 5-ALA guidance but SF was administered only for confocal laser endomicroscopy evaluation. The final enrolment comprised 279 patients: 252 adult patients (145 male and 107 female) from 18 to 82 years (mean age 52.1 years) and 27 pediatric patients (14 male and 13 female) from 2 to 17 years (mean age 9.82 years).

Clinical and Radiological Management

As part of normal clinical practice at our Institution, preoperative assessment included physical and neurological examination, laboratory tests results, preoperative contrast-enhanced MRI or CT scans for neuronavigation, recording of concomitant medications (as steroids) and previous radiation therapies. In pre-operative MRI, patients were categorized based on pre-operative contrast enhancement characteristics and divided in cases with clear contrast enhancement and cases with only minimal/absent contrast enhancement. To evaluate the EOR, a volumetric MRI examination was performed for each patient within 72 h after surgery; in particular, to calculate the residual pathological volume, the hyperintense alterations in volumetric basal T1 acquisitions were subtracted from the volume of hyperintense tissue in post-contrast volumetric T1 images, to avoid the incidental inclusion of blood or blood product. The post-operative clinical evaluation included a standard neurological examination and exclusion of occurrence of any side effect related to fluorescein injection. In particular, according to AIFA determination, arterial blood pressure, heart rate, blood oxygen saturation, temperature, and skin color were monitored pre-operatively and three times per day during the first three post-operative days; plasmatic dosage of creatinine was controlled the first and third post-operative day. The follow-up considered in this trial ended at the completion of the immediate post-operative radiological examination and clinical observation, as in AIFA determination.

Surgical Protocol

Our surgical protocol of fluorescein-guided technique is the same used in the FLUOGLIO trial since 2012 and it has already been described in previous papers (32, 33, 38), and based on i.v. SF (*Monico SpA, Italy*) injection at standard dose of 5 mg/kg, by a central venous line, immediately upon completion of the induction of general anesthesia or anesthetic procedures in awake surgery. The surgery was performed with the aid of a surgical microscope equipped with an integrated fluorescent filter specific for fluorescein (*Pentero* or *Kinevo* microscopes, with YELLOW 560 filter; *Carl Zeiss Meditec, Oberkochen, Germany*). During resection, the microscope could be switched alternatively from fluorescent to white-light illumination; neuronavigation, intraoperative ultrasounds, and contrast-enhanced ultrasound or other tools could be used according to the surgeon's preference. In tumors located in eloquent areas, intraoperative neurophysiological monitoring was used. Tumors were removed in an inside-out fashion until all fluorescent tissue was removed, as considered feasible by the surgeon.

In cases where tumor vessels, or peritumoral arteries and veins needed to be intraoperatively evaluated, indocyanine green (ICG) video-angiography with FLOW 800 analysis (*Carl Zeiss Meditec, Oberkochen, Germany*) and, sometimes, ICG temporary clipping test were performed, as already reported (47–51).

Histological Analysis

Histopathological analysis was performed in each case; tumors were classified according to the 2016 WHO classification by the neuro-pathology group of our Institute, with no additional costs respect to clinical practice (52).

Statistical Analysis

The study population was classified about gender, age, histological subtype, tumor volume and location, and therefore evaluated with descriptive analysis. Fluorescence intensity was graded by the surgeon as intense/bright, inhomogeneous or homogeneous, moderate or slight/absent; surgeons were also asked to classify the use of SF per each procedure as helpful/useful, not essential, not helpful/useless to achieve surgical aims. The EOR was prospectively calculated as a percentage of tumor resection based on early contrast-enhanced postoperative MRI or CT imaging; according to the entity of resection, we distinguished five main categories: GTR (EOR 100%), sub-total resection (STR, with an EOR of 90–100%), partial resection (PR, 30–90%), open biopsy and frameless/stereotactic biopsy. Rate of removal was studied in the different histological subtypes and compared with ANOVA by Prism software.

RESULTS

All the 279 patients finally enrolled in the trial were classified and categorized as stated by the 2016 WHO central nervous system tumors classification; the results about intraoperative fluorescence characteristics, surgical utility and extent of resection, were then related to the different histotypes.

Briefly, there were 212 neuroepithelial tumors, 25 brain metastases, 10 cerebral lymphomas, 7 hemangioblastomas or hemangioendotheliomas and 25 other tumors and conditions in differential diagnosis or in which SF represented a surgical aid (**Tables 1**, **2**).

TABLE 1 | Intraoperative fluorescence characteristics and utility, based on tumor histology, in the surgical group.

HISTOLOGIES		Number of patients	Intraoperative fluorescence	Extent of resection				Surgeon's opinion
				GTR (# - %)	Unexpected STR (no fluorescent residual tissue–not enhancing tumor) (# - %)	Expected STR (fluorescent residual tissue) (# - %)	PR (# - %)	
Tumors of neuroepithelial tissue	Diffuse astrocytic and oligodendro	143	- Heterogeneously intense (HGG) - Absent, only some spots (LGG)	104 (72.7)	13 (9.1)	19 (13.3)	7 (4.9)	- Helpful in HGG (132 cases) - Useless in LGG (11 cases)
	Ependymoma	14	Homogeneously intense	10 (71.5)	1 (7.1)	2 (14.3)	1 (7.1)	Helpful (14 cases)
	Glioneuronal	13	- Homogeneously intense - Slight/Absent (rosette-forming glioneuronal tumor)	9 (69.2)	1 (7.7)	3 (23.1)	0	- Helpful (9 cases) - Partial utility during surgery for drug-resistant epilepsy (3 cases) - Useless in rosette-forming glioneuronal tumor (1 case)
	PA and other astrocytic	18	- Heterogeneously intense (bright cystic fluid if present) - Homogeneously intense (SEGA)	10 (55.6)	2 (11.1)	5 (27.8)	1 (5.5)	Helpful (18 cases)
	Others (Embryonal, PPTID, …)	8	Intense: - Heterogeneously (medulloblastoma, PPTID and angiocentric glioma) - Homogenously (choroid plexus papilloma)	7 (87.5)	0	0	1 (12.5)	- Helpful (7 cases) - Not essential in choroid plexus papilloma (1 case)
Cerebral metastases		25	Heterogeneously intense	24 (96)	0	1 (4)	0	- Helpful (20 cases) - Not essential in 3 skin melanoma metastases and in one hemorrhagic metastasis (4 cases) - Useless in 1 case (previous whole brain radiotherapy and radiosurgery)
Primary CNS lymphomas		4	Homogeneously intense	4 (100)	0	0	0	Helpful (4 cases)
Meningiomas		3	Homogeneously intense	3 (100)	0	0	0	Not essential (3 cases)
Cerebral hemangioblastomas and hemangioendothelioma		7	Moderate (Bright cystic fluid)	7 (100)	0	0	0	Not essential (7 cases)
Tumors of cranial and paraspinal nerves		7	Homogeneously intense	2 (28.6)	0	5 (71.4)	0	Not essential (7 cases)
Tumors of the sellar region		1	Homogeneously intense (motor oil liquid, not enhancing)	1 (100)	0	0	0	Helpful (1 case)
Tumors of soft tissue and bone (Nothocordal)		2	Heterogeneously fluorescent	0	0	2 (100)	0	Not essential (2 cases)

TABLE 2 | Intraoperative fluorescence characteristics and utility, based on histopathological results, in the biopsy group.

Histologies		Open biopsy			Needle biopsy		
		Number of procedures	Intraoperative evaluation	Diagnostic accuracy	Number of procedures	Intraoperative evaluation	Diagnostic accuracy
Tumors of neuroepithelial tissue	Diffuse astrocytic and oligodendro	4	Helpful to highlight the target of biopsy in multifocal presentation	100% (GBM)	10	Bright samples visualized under Y560 filter	70% (6 GBM, 1 AA) 1 choroid plexus 2 reactive gliosis
	Pilocytic astrocytoma	1	Helpful to highlight the fluorescent component in a diffuse spinal lesion	100% (PA)	0	/	/
	Pineal region	1	Helpful to obtain the specimen of the cystic wall	100% (Pineocytoma)	0	/	/
Primary CNS lymphomas		5	Helpful to highlight the target of biopsy in multifocal presentation	100% (B-cell NHL)	1	Bright samples visualized under Y560 filter	100% (B-cell Lymphoma)
Vasculitis processes		5	Helpful to highlight the target of biopsy in multifocal presentation	100% (4 Vasculitis and 1 Cerebral Amyloid Angiopathy)	1	Moderate fluorescence under Y560 filter	100% (Vasculitis)

Tumors of Neuroepithelial Tissue

Diffuse Astrocytic and Oligodendroglial Tumors

One-hundred fifty-seven patients underwent surgery, either for removal and for open or stereotactic biopsy. In 142 cases, the tumor presented inhomogeneous contrast-enhancement, with cystic-necrotic areas and solid components; only 15 selected cases of patients with minimal/absent contrast enhancement were scheduled for fluorescein-guided surgery in this subgroup of patients.

In the 142 cases presenting with intense and inhomogeneous contrast-enhancement, 128 underwent surgery for tumor removal and 14 underwent open (4 cases) or needle biopsy 10 (cases).

In the 128 cases submitted to tumor removal, the histological diagnosis was HGG in all cases. There were 78 primary and 35 recurrent glioblastoma (GBM), 4 newly diagnosed and 1 recurrent anaplastic astrocytoma (AA), 3 newly diagnosed and 5 recurrent anaplastic oligodendrogliomas (AO), 1 newly diagnosed and 1 recurrent NOS high-grade glioma. Intraoperatively (**Figure 1**), these tumors usually presented as brightly fluorescent, with a yellow-green signal clearly distinguishable by pinkish-appearing peritumoral parenchyma under Y560 filter (**Figures 1C,D**). Sometimes, in cases with a clear central necrotic core, this tissue showed a dark pinkish feature with scant fluorescein enhancement (**Figures 1C,D**). This heterogenous appearance was more pronounced in recurrent tumors, already submitted to radiotherapy, although previous fractionated radiation therapy did not determine substantial difference about fluorescence characteristics or usefulness upon surgical evaluation. Finally, in some cases a bright fluid component was reported which was the result of tumor central colliquation. In all these 128 cases, SF was considered helpful by the operating surgeon to help in distinguishing tumor from healthy tissue (100% of the cases). In 95 out of 128 cases (74.2%), fluorescent tissue was completely removed, and the post-operative MRI confirmed a gross-total resection. In 18 out of 128 cases (14.1%) residual fluorescent tissue was deliberately left at the end of surgery, due to the proximity to eloquent areas or the adherence to major brain vessels; in these cases, an expected subtotal resection was achieved at post-operative MRI. In 11 out of 128 cases (8.6%) fluorescent tissue was intraoperatively judged as completely removed, while postoperative MRI showed an unexpected subtotal resection. In 4 out of 128 cases (3.1%) a partial resection was achieved (**Table 1**).

SF was used also in 4 cases of multifocal lesions, to guide open biopsy to highlight the area of fluorescent tissue in the context of the tumor. In all of these cases (100%) SF was considered useful and the histological analysis was possible, with a diagnosis of GBM. Finally, in the 10 cases of needle biopsies, the samples were evaluated under the YELLOW 560 filter of the microscope and resulted to be fluorescent in all cases; however, diagnostic accuracy was confirmed in 7/10 (70%) with a histological diagnosis of GBM in 6 cases and AA in 1 case; in three cases histological analysis was not diagnostic (1 choroid plexus and 2 reactive gliosis) (**Table 2**).

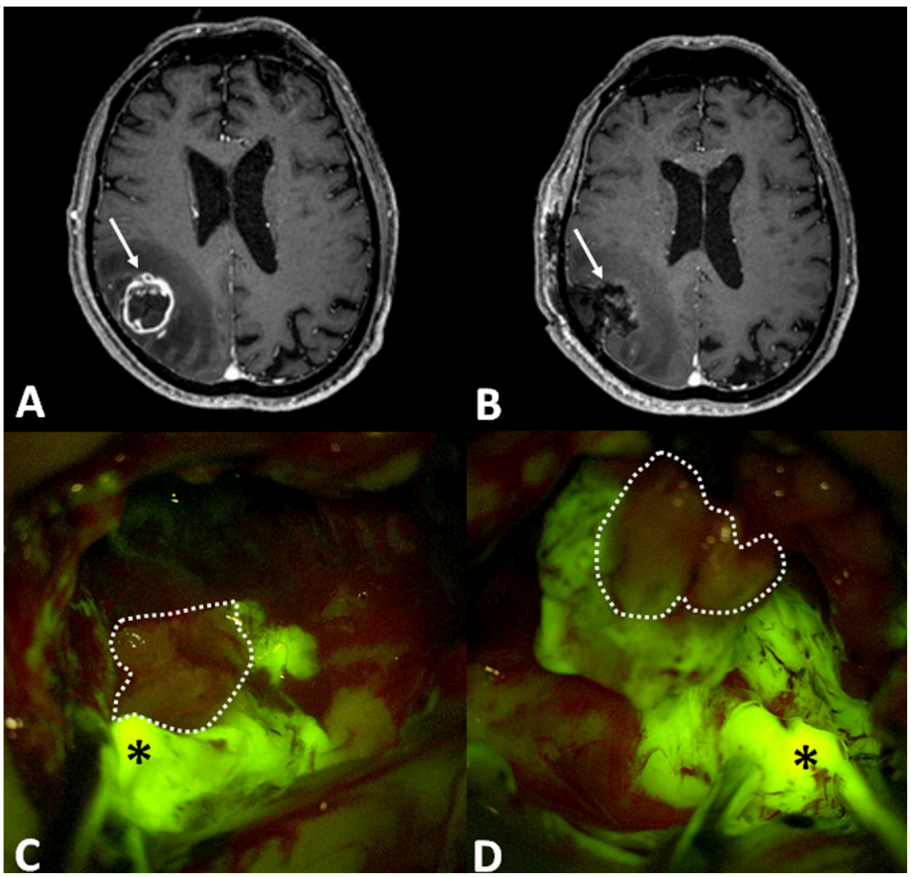

FIGURE 1 | (A) Preoperative post-contrast axial T1-weighted MRI scan showing a right parietal GBM (arrow), that was completely removed, as visible in post-operative T1 with contrast axial scan (**B**: in that case arrow is the surgical cavity). Intraoperative images, under Y560 filter **(C,D)**, depict bright yellow green signal (asterisk), in correspondence of nodular component, and dark pinkish feature in the necrotic core (dotted line).

Fifteen patients with minimal/absent contrast enhancement underwent tumor removal by fluorescein-guided technique. In 10 cases MRI showed a very extensive area of T2/FLAIR hyperintense signal abnormality, which suggested an aggressive behavior. In those cases, SF revealed in 6 out of 10 cases only minimal intralesional fluorescent spots. Therefore, SF was generally judged useless because no adjunctive information about residual tumor volume were provided compared to white light illumination. All that cases were histological grade II lesions (3 NOS grade II glioma, 3 diffuse astrocytomas and 4 oligodendrogliomas). Five patients presented with slight contrast enhancement at pre-operative MRI, and a positive 11C-methionine (MET) or fluoro-ethyl-tyrosine (FET) - Positron Emission Tomography (PET). In all cases, SF highlighted the pathological regions with higher metabolism, as suggested by PET findings, and it was judged useful in 4 patients, in which histopathological analysis revealed grade III lesions (AA in 3 cases and AO in 1 case). One patient affected by recurrent oligodendroglioma presented only few fluorescent spots, such as the MET positive regions, and SF was not judged useful during surgical removal (overall 80% of utility in the population of non-Gadolinium enhancing, but PET positive gliomas).

Other Neuroepithelial Tumors

Fourteen ependymomas, presenting with homogeneous and moderate enhancement at pre-operative MRI were submitted to fluorescein-guided resection. In all cases, the operating surgeon considered SF as a useful adjunct to better identify tumor-healthy tissues interface. GTR was achieved in 10 cases (71.4%); in one case (7.15%), despite the subjective surgical impression of complete fluorescent tissue removal, postoperative MRI showed tiny neoplastic remnants. In two ependymomas of the fourth ventricle (14.3%), there were small fluorescent residual spots due to extremely strong adherence to surrounding health parenchyma. Furthermore, a partial resection was performed in a very huge, recurrent posterior fossa ependymoma (7.15%), due to the significant bleeding (21.45% of expect subtotal or partial removal).

Thirteen neuronal and mixed neuronal-glial tumors were included in this series. Nine patients presented with enhancement (in 7 cases with a diffuse homogeneous

enhancement whereas in the other 2 with a bright nodule associated with enhancing peripheral cyst), while four patients presented with minimal/absent enhancement or with an area of c.e. in the context of a larger not-enhancing tumor at pre-operative MRI. The surgeon found bright and homogeneously fluorescent tissue and SF was judged useful in 12 out of 13 cases, except for one case of a slight enhancing spinal rosette-forming glioneuronal tumor (92.3%). In 6 cases, all fluorescent tissue was removed whereas in 3 patients, small residual tumor was left due to the proximity to eloquent brain areas. Furthermore, in 3 patients scheduled for surgery due to drug-resistant epilepsy affected by supratentorial lesions, located in not-eloquent brain, SF was judged useful to identify the small, pathological nodule but the resection was supramaximal and extended to peritumoral gliosis and dysplastic parenchyma to achieve seizure control. Overall a GTR was achieved in 9 patients out of 12 cases (75%) when SF represented a surgical aid, whereas in 3 cases (25%) an expected STR was achieved (4, 53–56).

Pilocytic astrocytoma, pleomorphic xanthoastrocytoma and sub-ependymal giant cell astrocytoma, presented at pre-operative MRI with well-circumscribed margins, typically having both solid (predominant) and cystic components, with inhomogeneous contrast enhancement at pre-operative MRI. The fluorescein enhancement was typically intense in the vast majority of the solid portion of the neoplasia with characteristic bright fluorescent cystic fluid (**Figure 2**). GTR was achieved in 10 cases out of 19 patients scheduled for tumor removal (52.6%), in 2 cases a minimal residual volume was highlighted by postoperative MRI despite the intraoperative subjective evaluation of complete tumor removal (10.5%); in other 7 cases, the resection was subtotal with fluorescent residual spots to avoid neurological worsening (expected STR in 36.9%). In one case of spinal PA an open biopsy was performed: the most fluorescent component was removed for histological analysis which was diagnostic; the patient did not present any neurological sequelae.

For other neuroepithelial tumors (one choroid plexus papilloma, one recurrent angiocentric glioma and two medulloblastomas), all presenting with inhomogeneous contrast enhancement at pre-operative MRI, intraoperative fluorescein enhancement was intense and judged useful in all cases, even if in the case of choroid plexus papilloma, the tumor tissue was easily recognizable also under white light. SF represented an important surgical aid during pineal surgery, in two intermediate differentiation tumors of the pineal parenchyma, in one papillary pineal tumor and in one cerebellar metastasis of papillary pineal tumor. In these cases, preoperative MRI with Gadolinium showed an intense, inhomogeneous enhancement with cystic regions. Furthermore, SF was used in an open biopsy of a pineocytoma with a voluminous cystic component after its surgical fenestration; radiologically, it appeared as a voluminous cyst with peripheral enhancement. Despite histological differences, all those tumors had a strong and bright fluorescent enhancement and the Y560-guided surgery resulted really useful to identify pathological tissues, preserving normal brain parenchyma.

Metastatic Tumors

Overall 25 patients with cerebral metastasis had undergone fluorescence-guided surgery since 2016; 13 of them underwent previous radiotherapy/radiosurgical treatment. All lesions presented with typical inhomogeneous contrast enhancement at pre-operative MRI. About the primitive tumors, the majority of them were breast (8), lung (5) and colorectal (3) cancers; 3 seminomas, 3 melanomas and also ovarian, renal and thyroid (one case per each histotypes) were present too. GTR was achieved in 96% of patients (24/25); in the remaining one (4%), a right fronto-mesial metastasis enchasing the ipsilateral callosomarginal artery, the surgeon chose to leave lowercase fluorescent residual tissue around the encased artery.

Under YELLOW 560 visualization, metastases appeared intensively fluorescent, with large yellow areas corresponding to the Gadolinium enhancement spots (**Figure 3**). SF was considered really helpful to distinguish tumor or to identify the neoplastic nodules inside infiltrated parenchyma in 20 procedures (80%). In the 3 patients affected by melanoma (12%), visualization with Y560 filter was not essential in melanoma metastases, that showed a characteristic brown-bluish pigmentation; for the patient with a hemorrhagic metastasis (4%), the filter was activated only at the end of the procedure, to verify the absence of residual fluorescence. Finally, in one patient (4%) with a left frontal colorectal metastasis previously submitted to radiosurgery and whole brain radiotherapy, the lesion appeared strongly fluorescent, but this finding was considered not useful due to fluorescein enhancement of peritumoral parenchyma, secondary to radiation damages.

Furthermore, for 3 superficial metastases, after dural opening and YELLOW 560 activation, the surgeon identified an atypical and greater than usual meningeal fluorescence enhancement, in correspondence of the superficial part of the lesion: in these cases, the dura was sacrificed; the histopathological analysis identified leptomeningeal metastasis.

Primary Central Nervous System Lymphoma

Ten patients with radiological diagnosis of lymphoma were enrolled: in four of them, surgery was scheduled due to the spinal localization (two cases: one lumbar and one dorsal localization) or huge dimension of a single lesion in non-eloquent brain region (one left posterior temporal and one right parietal). Six patients had a multifocal presentation and were scheduled for open biopsy in five cases and for stereotactic biopsy of the deep, paraventricular, enhancing component in the remaining one; in every case, biopsies were judged diagnostic by the pathologist. Lymphomas, under YELLOW 560 filter visualization, appeared homogenously and brightly fluorescent: fluorescein guidance was always judged useful.

Cerebral Hemangioblastomas and Hemangioendotheliomas

Six patients with superficial hemangioblastomas and one patient with a left frontal recurrent epithelioid hemangioendothelioma were submitted to fluorescein-guided surgery; GTR was achieved

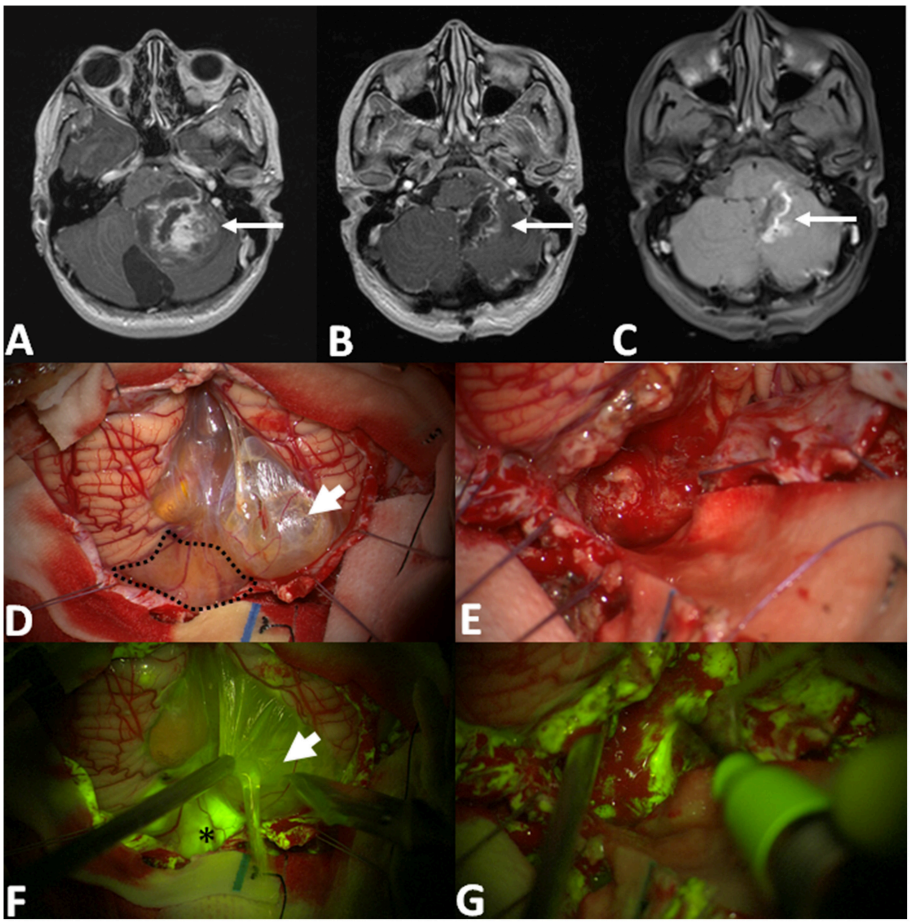

FIGURE 2 | Pre-operative T1 with contrast axial scan **(A)** shows a huge posterior fossa pilocytic astrocytoma (arrow) with a gross-total resection, as detectable by post-operative post-Gadolinium T1 MRI in **(B)**. The area of contrast-enhancement corresponds to the spontaneous hyperintense boundaries of surgical cavity **(C)**. After dural opening **(D,F)**, it is possible to appreciate a multilobulated cyst with a bright fluid (arrowhead in **D**, after its fenestration in **F**) and an inferior vermis nodular component (dotted line in **D**) with an intense fluorescein enhancement (asterisk in **F**). Intraoperative images, under white light **(E)** and Y560 filter **(G)**, during tumor removal with cavitron ultrasound aspirator, showing a bleeding, friable tissue with inhomogeneous fluorescein enhancement.

in all cases. Intraoperatively, the nodular component depicted a slight/moderate and homogenous fluorescence; the intra-cystic fluid, however, when present, appeared intensely fluorescent. Despite these findings, fluorescein was considered not essential because that tumor had a peculiar aspect with the typical orange nodule, that made them easily distinguishable from the surrounding structures. We may speculate that, for deep-seated tumors, SF could help to localize the pathological nodule.

Other Tumors and Conditions

Fluorescein was also used in five vestibular schwannomas, in two lumbar schwannomas and in two chordomas. Although all lesions presented with intense fluorescence, its use for not considered essential to remove the easily recognizable lesion, and because it was not possible to recognize not involved peritumoral cranial or spinal nerve.

SF was used in the only craniopharyngioma approached by craniotomy due to its large dimension and relapse despite the interferon therapy; in this case, the lesion showed an intense and homogeneous fluorescence under the YELLOW 560 filter. SF was considered useful by the surgeon, during the removal, in order to better identify the tumor capsule and to cleave it from the surrounding parenchyma.

SF was also used in three meningiomas: in everyone, it was considered not essential because the tumors were easily recognizable also under white light, even if all showed bright and homogeneous enhancement.

SF was incidentally used in a post-radiation cavernous malformation, located in the superior cerebellar vermis; intra-operatively, after the evacuation of an intra-parenchymal hematoma, the lesion showed an inhomogeneous fluorescence and SF was judged useful to achieve GTR, as confirmed by post-operative MRI, and to distinguish healthy cerebellar tissue.

In other five case, the radiological suspect of cerebral glioma was not confirmed during or after surgery (abscess, inflammatory pseudotumor, radionecrosis with residual pathological vessels of a previously-radiotreated arteriovenous malformation). The abscess appeared heterogeneously, intensely

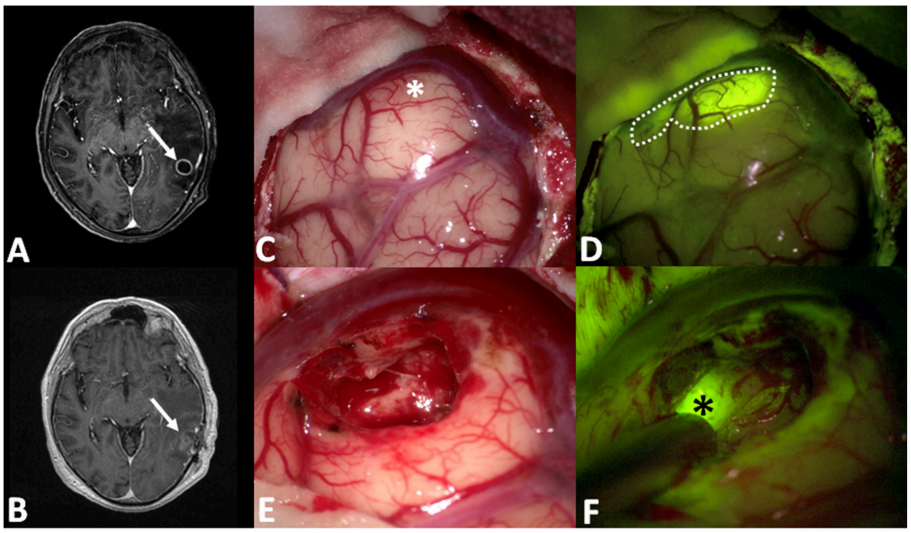

FIGURE 3 | (A,B) Pre- and post-operative post-contrast axial T1-weighted scans showing a left temporal metastasis from lung cancer, completely removed. After dural opening **(C)**, the Y560 filter **(D)** can highlight the superficial part of the metastasis, helping the surgeon in discriminating it from peritumoral brain parenchyma (dotted line in **D**), whereas under white light it is possible to appreciate a grayish, vanishing area (asterisk in **C**). During surgical resection **(E,F)**, fluorescein helps the surgeon to identify residual pathological tissue (black asterisks in **F**), not clearly visible under white light **(E)**.

fluorescent; it was intraoperatively recognized under white light, and, after an extemporaneous histopathological evaluation, the procedure was interrupted, and the material sent for bacteriological analysis. Inflammatory pseudotumor was characterized by a diffuse, moderate fluorescein enhancement which was judged useful by the surgeon during lesion removal. Finally, in the case of radionecrosis, the lesion showed a peripherical zone of strong fluorescein enhancement, with a good demarcation from health parenchyma: in this case, SF was judged not essential.

Six patients with a suspected diagnosis of vasculitis or inflammatory angiopathy, presenting with cerebral lesions at least partly enhancing at pre-operative MRI underwent fluorescein-guided open biopsy. In all cases, SF was helpful in recognizing the enhancing lesion under SF, obtaining a fluorescent sample to be analyzed. Fluorescein-guided biopsy was diagnostic in every case: histopathological analysis confirmed the diagnostic suspicion of cerebral vasculitis in five patient and cerebral amyloid angiopathy in the other one.

Reactions to Fluorescein, to Combined Use of SF With ICG or 5-ALA and Complications

No adverse drug reaction related to SF injection was reported in 309 patients; the only remarkable and visible effect was the transient yellowish staining of urine which disappeared in about 24 h. Moreover, no adverse neurosurgical or clinical event resulted from the combined use of two fluorophores (SF and 5-ALA, SF and ICG) during the same surgical procedure. Preoperative corticosteroid therapy did not affect fluorescence characteristics.

DISCUSSION

In our surgical series, the utilization of SF represented a useful adjunct in most of the CNS tumors presenting with some degree of contrast enhancement at preoperative neuroimaging scans.

During the last years SF has emerged as intraoperative tracer able to improve brain-tumor visualization, due to its non-specific, vascular mechanism of action related to the accumulation in brain regions with BBB disruption, as it happens with MRI contrast enhancement (34, 36, 38, 57). In fact, independently from their grading, the majority of CNS tumors, except for some grade I and II intra-axial histotypes, determine a BBB damage, thus they have a radiological presentation with contrast enhancement at MRI. Previous experiences had suggested that the use SF could be associated with a bright fluorescence of the tumor area in primary and recurrent HGG, in metastases, in lymphomas, and in spinal intramedullary lesions (34–36, 39). This was also associated with good results in term of extent of resection (39). However, there were in the literature significant variations in SF use, considering dosage and time of injections, in the studies published by different research groups (39).

As the reimbursement of SF as a fluorescent tracer in neuro-oncology has been approved by the Italian Drug Agency (AIFA) in July 2015 (determination 905/2015, Gazette n.168, 22 July, 2015), and based on our extensive experience with HGG (32, 33, 38), we decided to start a prospective observational study on the use of SF for the resection of aggressive tumors of the CNS, applying a standardized protocol, with a dosage of 5 mg/kg and an i.v. injection immediately after patient intubation or at the entrance in the OR for awake craniotomies (58).

As expected, the majority of the cases were HGG (51.6% of the total number of patients included in the study). Most of these patients underwent fluorescein-guided tumor resection based on a high suspect for a high-grade lesion based on pre-operative MRI. In all these cases, SF appeared extremely useful to improve the discrimination between tumor tissue and peritumoral brain parenchyma, with a positive impact in term of EOR, with a percentage of GTR in 74.2%. Coming from an unselected series of patients, these results seems to be extremely interesting, and in line with previous published studies (32, 33, 38, 39, 59).

A particular consideration regards instead the population of patients with gliomas with minimal/almost absent enhancement at preoperative MRI. In all that cases we noted that SF was useless due to the unpredictable, and usually focal fluorescence under the specific Y560 filter, except for the cases of patients with FET/MET-PET positive tumor, as suggested by Schebesch et al. (60). In our series of 5 patients with this characteristic, we could confirm a correlation between the positive PET areas and the fluorescein uptake by tumor tissue in all cases. This finding suggests a predictive ability of PET with amino acid tracers to detect areas with minimal BBB disruption, not shown by pre-operative MRI, which can be intra-operatively identified by using fluorescein-guided surgery. In that cases, SF enhancement could be related to the molecular property of SF which has a slightly lower molecular weight than Gadolinium. The intraoperative recognition of these positive PET areas could also be associated to a better diagnostic accuracy, as in 80% of our cases the final histological diagnosis was a grade III glioma.

Regarding brain metastasis, we could also confirm previous experiences (36), showing a very good tumor visualization in most of the cases with a percentage of GTR in 96% of the cases. Of notice, in 3 melanomas we did not find SF to be a useful adjunct, as the tumor was clearly visible under the microscope with white-light illumination.

We also found a good correspondence between pre-operative MRI enhancement and intraoperative fluorescence identification in in neuronal and mixed glioneuronal tumors, in other astrocytic tumors, in other types of neuroepithelial tumors and in lymphomas. SF was useful to identify pathological nodule, but also during surgery and at the end of resection, to verify the absence of residual tumor tissue. We administered fluorescein also in some cases of cranial and spinal schwannomas but, even if they showed an intense and homogeneous fluorescence, at the standard dosage fluorescein failed in distinguishing and identifying normal nerve fibers not related to the tumor. In addition, SF was considered not essential in hemangioblastomas that, despite the moderate but homogenous fluorescence both of nodular and fluid portions, present a peculiar and characteristic nodular component under white-light illumination, such to make not essential the use of fluorescein, at least with our protocol. On the contrary, we believe that a more appropriate application of fluorescein was proposed by Rey-Dios et al. (37) for these tumor subtypes. They reported the intravenous administration of fluorescein in bolus immediately before tumor resection to better visualize its vascular network, including arterial feeders, draining veins, and the nodule, as similarly reported by our group with ICG video-angiography (48, 49) (**Table 1**).

Two hundred and forty-five patients enrolled in the study were scheduled for surgery with a previous planning of macroscopic resection but keeping in mind the philosophy of maximal safe resection: in this series, we obtained a high percentage of GTR (181/245, 73.9%). Minimal residual tumor (lower than 10% of preoperative tumor volume) at postoperative MRI was expected in thirty-seven cases (15.1%), as it was involving eloquent areas or due to the adherences to major brain vessels or cranial nerves and was therefore independent from the use of fluorescein-guided technique. Conversely, in seventeen cases (6.9%), the residual tumor was an unexpected finding, based on the absence of clear residual intraoperative fluorescent tissue: this can be related, as for other fluorophores, to the fact that the residual tissue was not exposed during resection because hidden under the normal brain parenchyma. Finally, in the remaining ten cases (4.1%) the surgical resection was only partial due to the location in eloquent areas, or the significative encasement of major brain vessels or cranial nerves, especially for voluminous posterior fossa tumors (**Table 1**).

Twenty-eight patients were included in our protocol for fluorescein-guided biopsy. Regarding open biopsies, SF was used in four multifocal GBM, in five lymphomas and in five suspected vasculitis process/cerebral angiopathy with a cortico-subcortical component which was chosen as a target, in one pineocytoma with a voluminous cyst, after its surgical fenestration, and in one spinal PA, to identify the enhancing component for histopathological analysis. Regarding patients that underwent open biopsies, SF was always judged useful and, in every case, the tissue specimen was enough for an adequate histopathologic analysis. Regarding frameless/stereotactic biopsies, our series is limited to twelve patients, with a diagnostic accuracy of 75% (9/12): in particular, in two primitive multifocal gliomas, histopathological analysis revealed reactive gliosis despite the fluorescence of specimens, whereas in one recurrent thalamic glioma, the histology suggested choroidal plexus tissue, which can explain the SF enhancement of the samples, due to the absence of BBB, and physiological accumulation of SF in this cerebral area. In two of these patients, a fluorescein-guided diagnostic biopsy was repeated and was successful in obtaining a histological diagnosis (one AA and one oligodendroglioma). Although limited to 28 cases, these results seems to suggest, as already preliminarily shown in previous experiences (61), that SF could assist during biopsies of CNS lesions, for a correct identification of the best target for the histological diagnosis (**Table 2**).

Nobody, between patients of our series, presented fluorescein-related side effects or adverse reactions to SF administration, either singly or combined with other fluorophores. The only visible manifestation of intraoperative fluorescein administration is, as noted, the onset of transient yellowish stain of the urine, that rapidly disappear after 24–48 h : patients should be aware about this particular but totally harmless effect. We believe that the lack of any side effect, in particular any allergic reaction, was predominantly related to the low dosage used in this trial, thanks to the use of a dedicated

filter into the microscope, that allowed a more accurate identification of fluorescent tissue, us suggested firstly by our group (27).

The main limitation of this study presented is represented by the lack of data about overall survival; in fact, the authors considered only a surrogate indicator which is the EOR, and by the lack of the direct comparison of surgery with and without SF aid due to ethical reasons. Furthermore, we did not make any comparison between the use of SF and other available fluorophores, like 5-aminolevulenic acid, that has been established as a surgical adjunct in surgery of HGG (20) and that has been reported as a possible advantage in selected cases of brain metastasis (62). Finally, the utility of SF in stereotactic/frameless biopsies is only descriptively considered without a proper statistical analysis, thus it is not able to establish a predictive value of SF. We have also to stress that, in most of the Countries, SF is still considered off label for neuro-oncological procedures. Thus, a widespread utilization of fluorescence-guided surgery will depend on the definitive approval by the competent authorities.

CONCLUSION

On the basis of its unspecific mechanism of action, the use of SF as fluorescent tracer in neuro-oncology should be considered in several applications. Indeed, as these preliminary results seem to suggest, the same unspecific mechanism may also be seen as its strength since SF can be used as an operative adjunct in every CNS tumor with some degree of BBB disruption as detectable by neuroradiological imaging after contrast medium administration, but also by PET with amino acids positivity. Further studies are required to clarify the field of application of SF in neuro-oncological procedures and definitively assess the value of this technique on improvement of the EOR and overall survival.

ETHICS STATEMENT

The FLUOCERTUM study has been approved by the Ethical Committee of the Fondazione IRCCS Istituto Neurologico Carlo Besta and written informed consent was obtained from all patients, in accordance with the Declaration of Helsinki.

AUTHOR CONTRIBUTIONS

JF, CC, and FA: study concept and design. JF, CC, IV, and FA: critical revision of the manuscript for intellectual content. All authors: acquisition of data, data analysis, and interpretation. PF and FA: study supervision.

FUNDING

This study was partially supported by *Associazione Paolo Zorzi per le Neuroscienze, ONLUS*.

REFERENCES

1. Ostrom QT, Gittleman H, Truitt G, Boscia A, Kruchko C, Barnholtz-Sloan JS. CBTRUS statistical report: primary brain and other central nervous system tumors diagnosed in the United States in 2011–2015. *Neuro Oncol*. (2018) 20:41–86. doi: 10.1093/neuonc/noy131
2. Lacroix M, Abi-Said D, Fourney DR, Gokaslan ZL, Shi W, DeMonte F, et al. A multivariate analysis of 416 patients with glioblastoma multiforme: prognosis, extent of resection, and survival. *J Neurosurg*. (2001) 95:190–8. doi: 10.3171/jns.2001.95.2.0190
3. Weller M, van den Bent M, Tonn JC, Stupp R, Preusser M, Cohen-Jonathan-Moyal E, et al. European Association for Neuro-Oncology (EANO) guideline on the diagnosis and treatment of adult astrocytic and oligodendroglial gliomas. *Lancet Oncol*. (2017) 18:e315–29. doi: 10.1016/S1470-2045(17)30194-8
4. Stone TJ, Rowell R, Jayasekera BAP, Cunningham MO, Jacques TS. Review: Molecular characteristics of long-term epilepsy-associated tumours (LEATs) and mechanisms for tumour-related epilepsy (TRE). *Neuropathol Appl Neurobiol*. (2018) 44:56–69. doi: 10.1111/nan.12459
5. Sanai N, Polley M-Y, McDermott MW, Parsa AT, Berger MS. An extent of resection threshold for newly diagnosed glioblastomas. *J Neurosurg*. (2011) 115:3–8. doi: 10.3171/2011.2.JNS10998
6. Li YM, Suki D, Hess K, Sawaya R. The influence of maximum safe resection of glioblastoma on survival in 1229 patients: can we do better than gross-total resection? *J Neurosurg*. (2016) 124:977–88. doi: 10.3171/2015.5.JNS142087
7. Grabowski MM, Recinos PF, Nowacki AS, Schroeder JL, Angelov L, Barnett GH, et al. Residual tumor volume versus extent of resection: predictors of survival after surgery for glioblastoma. *J Neurosurg*. (2014) 121:1115–23. doi: 10.3171/2014.7.JNS132449
8. Bloch O, Han SJ, Cha S, Sun MZ, Aghi MK, McDermott MW, et al. Impact of extent of resection for recurrent glioblastoma on overall survival. *J Neurosurg*. (2012) 117:1032–8. doi: 10.3171/2012.9.JNS12504
9. Brown TJ, Brennan MC, Li M, Church EW, Brandmeir NJ, Rakszawski KL, et al. Association of the extent of resection with survival in glioblastoma. *JAMA Oncol*. (2016) 2:1460. doi: 10.1001/jamaoncol.2016.1373
10. Aghi MK, Nahed BV, Sloan AE, Ryken TC, Kalkanis SN, Olson JJ. The role of surgery in the management of patients with diffuse low grade glioma. *J Neurooncol*. (2015) 125:503–30. doi: 10.1007/s11060-015-1867-1
11. Yang K, Nath S, Koziarz A, Badhiwala JH, Ghayur H, Sourour M, et al. Biopsy versus subtotal versus gross total resection in patients with low-grade glioma: a systematic review and meta-analysis. *World Neurosurg*. (2018) 120:e762–75. doi: 10.1016/j.wneu.2018.08.163
12. Tsao MN, Xu W, Wong RK, Lloyd N, Laperriere N, Sahgal A, et al. Whole brain radiotherapy for the treatment of newly diagnosed multiple brain metastases. *Cochrane Database Syst Rev*. (2018) 1:CD003869. doi: 10.1002/14651858.CD003869.pub4
13. Brown PD, Ballman KV, Cerhan JH, Anderson SK, Carrero XW, Whitton AC, et al. Postoperative stereotactic radiosurgery compared with whole brain radiotherapy for resected metastatic brain disease (NCCTG N107C/CEC·3): a multicentre, randomised, controlled, phase 3 trial. *Lancet Oncol*. (2017) 18:1049–60. doi: 10.1016/S1470-2045(17)30441-2
14. Mahajan A, Ahmed S, McAleer MF, Weinberg JS, Li J, Brown P, et al. Post-operative stereotactic radiosurgery versus observation for completely resected brain metastases: a single-centre, randomised, controlled, phase 3 trial. *Lancet Oncol*. (2017) 18:1040–8. doi: 10.1016/S1470-2045(17)30414-X
15. Vera-Bolanos E, Aldape K, Yuan Y, Wu J, Wani K, Necesito-Reyes MJ, et al. Clinical course and progression-free survival of adult intracranial and spinal ependymoma patients. *Neuro Oncol*. (2015) 17:440–7. doi: 10.1093/neuonc/nou162
16. Dodgshun AJ, Maixner WJ, Hansford JR, Sullivan MJ. Low rates of recurrence and slow progression of pediatric pilocytic astrocytoma after gross-total resection: justification for reducing surveillance imaging. *J Neurosurg Pediatr*. (2016) 17:569–72. doi: 10.3171/2015.9.PEDS15449

17. Jenkinson MD, Barone DG, Bryant A, Vale L, Bulbeck H, Lawrie TA, et al. Intraoperative imaging technology to maximise extent of resection for glioma. *Cochrane Database Syst Rev*. (2018) 1:CD012788. doi: 10.1002/14651858.CD012788.pub2
18. Senft C, Bink A, Franz K, Vatter H, Gasser T, Seifert V. Intraoperative MRI guidance and extent of resection in glioma surgery: a randomised, controlled trial. *Lancet Oncol*. (2011) 12:997–1003. doi: 10.1016/S1470-2045(11)70196-6
19. Prada F, Del Bene M, Rampini A, Mattei L, Casali C, Vetrano IG, et al. Intraoperative Strain Elastosonography in Brain Tumor Surgery. *Oper Neurosurg*. (2018) 17:227–36. doi: 10.1093/ons/opy323
20. Stummer W, Pichlmeier U, Meinel T, Wiestler OD, Zanella F, Reulen HJ. Fluorescence-guided surgery with 5-aminolevulinic acid for resection of malignant glioma: a randomised controlled multicentre phase III trial. *Lancet Oncol*. (2006) 7:392–401. doi: 10.1016/s1470-2045(06)70665-9
21. Yano H, Nakayama N, Ohe N, Miwa K, Shinoda J, Iwama T. Pathological analysis of the surgical margins of resected glioblastomas excised using photodynamic visualization with both 5-aminolevulinic acid and fluorescein sodium. *J Neurooncol*. (2017) 133:389–97. doi: 10.1007/s11060-017-2445-5
22. Wei L, Roberts DW, Sanai N, Liu JTC. Visualization technologies for 5-ALA-based fluorescence-guided surgeries. *J Neurooncol*. (2019) 141:495–505. doi: 10.1007/s11060-018-03077-9
23. Copeman SM, Coke F, Gouldesbrough C. "Activated" (irradiated) fluorescein in the treatment of cancer. *Br Med J*. (1929) 2:233–42.
24. Siff LN, Hill AJ, Jallad K, Harnegie MP, Barber MD. Intraoperative evaluation of urinary tract injuries at the time of pelvic surgery. *Female Pelvic Med Reconstr Surg*. (2018). doi: 10.1097/SPV.0000000000000679. [Epub ahead of print].
25. O'goshi K, Serup J. Safety of sodium fluorescein for *in vivo* study of skin. *Ski Res Technol*. (2006) 12:155–61. doi: 10.1111/j.0909-752X.2006.00147.x
26. Hara T, Inami M, Hara T. Efficacy and safety of fluorescein angiography with orally administered sodium fluorescein. *Am J Ophthalmol*. (1998) 126:560–4.
27. Keerl R, Weber RK, Draf W, Wienke A, Schaefer SD. Use of sodium fluorescein solution for detection of cerebrospinal fluid fistulas: an analysis of 420 administrations and reported complications in Europe and the United States. *Laryngoscope*. (2004) 114:266–72. doi: 10.1097/00005537-200402000-00016
28. Moore GE. Fluorescein as an agent in the differentiation of normal and malignant tissues. *Science*. (1947) 106:130–1. doi: 10.1126/science.106.2745.130-a
29. Moore GE, Hunter SW, Hubbard TB. Clinical and experimental studies of fluorescein dyes with special reference to their use for the diagnosis of central nervous system tumors. *Ann Surg*. (1949) 130:637–42.
30. Hubbard TB, Moore GE. The use of fluorescein dyes in the diagnosis of malignancy with special reference to tumors of the central nervous system. *J Natl Cancer Inst*. (1949) 10:303–14.
31. Kuroiwa T, Kajimoto Y, Ohta T. Development of a fluorescein operative microscope for use during malignant glioma surgery: a technical note and preliminary report. *Surg Neurol*. (1998) 50:41–8; discussion 48–9.
32. Acerbi F, Broggi M, Eoli M, Anghileri E, Cuppini L, Pollo B, et al. Fluorescein-guided surgery for grade IV gliomas with a dedicated filter on the surgical microscope: preliminary results in 12 cases. *Acta Neurochir*. (2013) 155:1277–86. doi: 10.1007/s00701-013-1734-9
33. Acerbi F, Broggi M, Eoli M, Anghileri E, Cavallo C, Boffano C, et al. Is fluorescein-guided technique able to help in resection of high-grade gliomas? *Neurosurg Focus*. (2014) 36:E5. doi: 10.3171/2013.11.FOCUS13487
34. Schebesch KM, Hoehne J, Hohenberger C, Acerbi F, Broggi M, Proescholdt M, et al. Fluorescein sodium-guided surgery in cerebral lymphoma. *Clin Neurol Neurosurg*. (2015) 139:125–8. doi: 10.1016/j.clineuro.2015.09.015
35. Acerbi F, Cavallo C, Schebesch K-M, Akçakaya MO, de Laurentis C, Hamamcioglu MK, et al. Fluorescein-guided resection of intramedullary spinal cord tumors: results from a preliminary, multicentric, retrospective study. *World Neurosurg*. (2017) 108: 603–9. doi: 10.1016/j.wneu.2017.09.061
36. Höhne J, Hohenberger C, Proescholdt M, Riemenschneider MJ, Wendl C, Brawanski A, et al. Fluorescein sodium-guided resection of cerebral metastases—an update. *Acta Neurochir*. (2017) 159:363–7. doi: 10.1007/s00701-016-3054-3
37. Rey-Dios R, Cohen-Gadol AA. Intraoperative fluorescence for resection of hemangioblastomas. *Acta Neurochir (Wien)*. (2013) 155:1287–92. doi: 10.1007/s00701-013-1723-z
38. Acerbi F, Broggi M, Schebesch K-M, Höhne J, Cavallo C, De Laurentis C, et al. fluorescein-guided surgery for resection of high-grade gliomas: a multicentric prospective phase II study (FLUOGLIO). *Clin Cancer Res*. (2018) 24:52–61. doi: 10.1158/1078-0432.CCR-17-1184
39. Cavallo C, De Laurentis C, Vetrano IG, Falco J, Broggi M, Schiariti M, et al. The utilization of fluorescein in brain tumor surgery: a systematic review. *J Neurosurg Sci*. (2018) 62:690–703. doi: 10.23736/S0390-5616.18.04480-6
40. Neira JA, Ung TH, Sims JS, Malone HR, Chow DS, Samanamud JL, et al. Aggressive resection at the infiltrative margins of glioblastoma facilitated by intraoperative fluorescein guidance. *J Neurosurg*. (2017) 127:111–22. doi: 10.3171/2016.7.JNS16232
41. Rey-Dios R, Cohen-Gadol AA. Technical principles and neurosurgical applications of fluorescein fluorescence using a microscope-integrated fluorescence module. *Acta Neurochir (Wien)*. (2013) 155(4):701-6. doi: 10.1007/s00701-013-1635-y
42. Acerbi F. Fluorescein assistance in neuro-oncological surgery: a trend of the moment or a real technical adjunt? *Clin Neurol Neurosurg*. (2016) 144:119–20. doi: 10.1016/j.clineuro.2016.03.011
43. da Silva CE, da Silva VD, da Silva JLB. Skull base meningiomas and cranial nerves contrast using sodium fluorescein: a new application of an old tool. *J Neurol Surg B Skull Base*. (2014) 75:255–60. doi: 10.1055/s-0034-1372466
44. Bohnstedt BN, Cohen-Gadol AA, Brain C, Lane B, Bohnstedt BN, Cohen-Gadol AA. A prospective comparative study of microscope-integrated intraoperative fluorescein and indocyanine videoangiography for clip ligation of complex cerebral aneurysms. *J Neurosurg*. (2015) 122:618–26. doi: 10.3171/2014.10.JNS132766
45. Li Y, Rey-Dios R, Roberts DW, Valdés PA, Cohen-Gadol AA. Intraoperative fluorescence-guided resection of high-grade gliomas: a comparison of the present techniques and evolution of future strategies. *World Neurosurg*. (2014) 82:175–85. doi: 10.1016/j.wneu.2013.06.014
46. Schebesch K-M, Proescholdt M, Höhne J, Hohenberger C, Hansen E, Riemenschneider MJ, et al. Sodium fluorescein-guided resection under the YELLOW 560 nm surgical microscope filter in malignant brain tumor surgery–a feasibility study. *Acta Neurochir (Wien)*. (2013) 155:693–9. doi: 10.1007/s00701-013-1643-y
47. Ferroli P, Nakaji P, Acerbi F, Albanese E, Broggi G. Indocyanine green (ICG) temporary clipping test to assess collateral circulation before venous sacrifice. *World Neurosurg*. (2011) 75:122–5. doi: 10.1016/j.wneu.2010.09.011
48. Acerbi F, Vetrano IG, Sattin T, Falco J, de Laurentis C, Zattra CM, et al. Use of ICG videoangiography and FLOW 800 analysis to identify the patient-specific venous circulation and predict the effect of venous sacrifice: a retrospective study of 172 patients. *Neurosurg Focus*. (2018) 45:E7. doi: 10.3171/2018.4.FOCUS18120
49. Acerbi F, Vetrano IG, Sattin T, de Laurentis C, Bosio L, Rossini Z, et al. The role of indocyanine green videoangiography with FLOW 800 analysis for the surgical management of central nervous system tumors: an update. *Neurosurg Focus*. (2018) 44:E6. doi: 10.3171/2018.3.FOCUS1862
50. Acerbi F, Restelli F, Broggi M, Schiariti M, Ferroli P. Feasibility of simultaneous sodium fluorescein and indocyanine green injection in neurosurgical procedures. *Clin Neurol Neurosurg*. (2016) 146:123–9. doi: 10.1016/j.clineuro.2016.05.003
51. Ferroli P, Acerbi F, Tringali G, Albanese E, Broggi M, Franzini A, et al. Venous sacrifice in neurosurgery: new insights from venous indocyanine green videoangiography. *J Neurosurg*. (2011) 115:18–23. doi: 10.3171/2011.3.JNS10620
52. Louis DN, Perry A, Reifenberger G, von Deimling A, Figarella-Branger D, Cavenee WK, et al. The 2016 World Health Organization classification of tumors of the central nervous system: a summary. *Acta Neuropathol*. (2016) 131:803–20. doi: 10.1007/s00401-016-1545-1
53. Stone TJ, Keeley A, Virasami A, Harkness W, Tisdall M, Izquierdo Delgado E, et al. Comprehensive molecular characterisation of epilepsy-associated glioneuronal tumours. *Acta Neuropathol*. (2018) 135:115–29. doi: 10.1007/s00401-017-1773-z

54. Giulioni M, Marucci G, Pelliccia V, Gozzo F, Barba C, Didato G, et al. Epilepsy surgery of "low grade epilepsy associated neuroepithelial tumors": a retrospective nationwide Italian study. *Epilepsia*. (2017) 58:1832–41. doi: 10.1111/epi.13866
55. Englot DJ, Berger MS, Barbaro NM, Chang EF. Factors associated with seizure freedom in the surgical resection of glioneuronal tumors. *Epilepsia*. (2012) 53:51–7. doi: 10.1111/j.1528-1167.2011.03269.x
56. Zaghloul KA, Schramm J. Surgical management of glioneuronal tumors with drug-resistant epilepsy. *Acta Neurochir (Wien)*. (2011) 153:1551–9. doi: 10.1007/s00701-011-1050-1
57. Diaz RJ, Dios RR, Hattab EM, Burrell K, Rakopoulos P, Sabha N, et al. Study of the biodistribution of fluorescein in glioma-infiltrated mouse brain and histopathological correlation of intraoperative findings in high-grade gliomas resected under fluorescein fluorescence guidance. *J Neurosurg*. (2015) 122:1360–9. doi: 10.3171/2015.2.JNS132507
58. Acerbi F, Broggi M, Broggi G, Ferroli P. What is the best timing for fluorescein injection during surgical removal of high-grade gliomas? *Acta Neurochir (Wien)*. (2015) 157:1377–8. doi: 10.1007/s00701-015-2455-z
59. Acerbi F, Cavallo C, Broggi M, Cordella R, Anghileri E, Eoli M, et al. Fluorescein-guided surgery for malignant gliomas: a review. *Neurosurg Rev*. (2014) 37:547–7. doi: 10.1007/s10143-014-0546-6
60. Schebesch K-M, Brawanski A, Doenitz C, Rosengarth K, Proescholdt M, Riemenschneider MJ, et al. Fluorescence-guidance in non-Gadolinium enhancing, but FET-PET positive gliomas. *Clin Neurol Neurosurg*. (2018) 172:177–82. doi: 10.1016/j.clineuro.2018.07.011
61. Rey-Dios R, Hattab EM, Cohen-Gadol AA. Use of intraoperative fluorescein sodium fluorescence to improve the accuracy of tissue diagnosis during stereotactic needle biopsy of high-grade gliomas. *Acta Neurochir (Wien)*. (2014) 156:1071-5; discussion 1075. doi: 10.1007/s00701-014-2097-6
62. Ferraro N, Barbarite E, Albert TR, Berchmans E, Shah AH, Bregy A, et al. The role of 5-aminolevulinic acid in brain tumor surgery: a systematic review. *Neurosurg Rev*. (2016) 39:545–55. doi: 10.1007/s10143-015-0695-2

Conflict of Interest Statement: FA received honoraria from the Carl Zeiss Meditec Company for lectures at International Congresses.

The remaining authors declare that the research was conducted in the absence of any commercial or financial relationship that could be constructed as a potential conflict of interest.

frontiers in Oncology

ORIGINAL RESEARCH
published: 16 August 2019
doi: 10.3389/fonc.2019.00748

Development of a Simulation Model for Fluorescence-Guided Brain Tumor Surgery

Daniel Valli[1†], *Evgenii Belykh*[1†], *Xiaochun Zhao*[1], *Sirin Gandhi*[1], *Claudio Cavallo*[1], *Nikolay L. Martirosyan*[2], *Peter Nakaji*[1], *Michael T. Lawton*[1] *and Mark C. Preul*[1*]

[1] *Department of Neurosurgery, Barrow Neurological Institute, St. Joseph's Hospital and Medical Center, Phoenix, AZ, United States,* [2] *Department of Neurosurgery, University of Arizona, Tucson, AZ, United States*

OPEN ACCESS

Edited by:
Jonathan T. C. Liu, University of Washington, United States

Reviewed by:
Mira Sibai, UMR8165 Imagerie et Modélisation en Neurobiologie et Cancérologie (IMNC), France
Sandro M. Krieg, Technical University of Munich, Germany

***Correspondence:**
Mark C. Preul
neuropub@barrowneuro.org

[†]*Co-first authors*

Specialty section:
This article was submitted to Cancer Imaging and Image-directed Interventions, a section of the journal Frontiers in Oncology

Received: *26 April 2019*
Accepted: *25 July 2019*
Published: *16 August 2019*

Citation:
Valli D, Belykh E, Zhao X, Gandhi S, Cavallo C, Martirosyan NL, Nakaji P, Lawton MT and Preul MC (2019) Development of a Simulation Model for Fluorescence-Guided Brain Tumor Surgery. Front. Oncol. 9:748. doi: 10.3389/fonc.2019.00748

Objective: Fluorescence dyes are increasingly used in brain tumor surgeries, and thus the development of simulation models is important for teaching neurosurgery trainees how to perform fluorescence-guided operations. We aimed to create a tumor model for fluorescence-guided surgery in high-grade glioma (HGG).

Methods: The tumor model was generated by the following steps: creating a tumor gel with a similar consistency to HGG, selecting fluorophores at optimal concentrations with realistic color, mixing the fluorophores with tumor gel, injecting the gel into fresh pig/sheep brain, and testing resection of the tumor model under a fluorescence microscope. The optimal tumor gel was selected among different combinations of agar and gelatin. The fluorophores included fluorescein, indocyanine green (ICG), europium, chlorin e6 (Ce6), and protoporphyrin IX (PpIX). The tumor model was tested by neurosurgeons and neurosurgery trainees, and a survey was used to assess the validity of the model. In addition, the photobleaching phenomenon was studied to evaluate its influence on fluorescence detection.

Results: The best tumor gel formula in terms of consistency and tactile response was created using 100 mL water at 100°C, 0.5 g of agar, and 3 g of gelatin mixed thoroughly for 3 min. An additional 1 g of agar was added when the tumor gel cooled to 50°C. The optimal fluorophore concentration ranges were fluorescein 1.9×10^{-4} to 3.8×10^{-4} mg/mL, ICG 4.9×10^{-3} to 9.8×10^{-3} mg/mL, europium 7.0×10^{-2} to 1.4×10^{-1} mg/mL, Ce6 2.2×10^{-3} to 4.4×10^{-3} mg/mL, and PpIX 1.8×10^{-2} to 3.5×10^{-2} mg/mL. No statistical differences among fluorophores were found for face validity, content validity, and fluorophore preference. Europium, ICG, and fluorescein were shown to be relatively stable during photobleaching experiments, while chlorin e6 and PpIX had lower stability.

Conclusions: The model can efficiently highlight the "tumor" with 3 different colors—green, yellow, or infrared green with color overlay. These models showed high face and content validity, although there was no significant difference among the models regarding the degree of simulation and training effectiveness.

They are useful educational tools for teaching the key concepts of intra-axial tumor resection techniques, such as subpial dissection and nuances of fluorescence-guided surgery.

Keywords: europium, fluorescein, fluorescence-guided tumor surgery, fluorophores, high-grade glioma, indocyanine green, protoporphyrin IX, tumor model

INTRODUCTION

Neurosurgery has entered a new era with the application of fluorescence guidance technologies, which are widely applicable in multiple surgical disciplines. To achieve maximal resection, several fluorophores have been introduced into tumor surgery.

1. Fluorescein is a fluorescent dye with an excitation wavelength range of 460–500 nm and emission range of 540–690 nm. It can be visualized under the Yellow 560 filter of the operating microscope. Fluorescein has been used to improve the resection of malignant gliomas by targeting the tumor and margins with doses ranging from 2 to 20 mg/kg administered intravenously (1–3).
2. Indocyanine green (ICG) is widely used in vascular neurosurgery to identify and evaluate the vascular pattern, but it has also been also used for malignant glioma surgeries. It has a peak excitation at a wavelength of 750–800 nm and is visualized by near-infrared cameras at an emission maximum of 850 nm. The usual administration of ICG for vascular application is an intravenous bolus of 5–25 mg, with some tumors remaining fluorescent for about 10 min (4–6). Higher doses of ICG (5 mg/kg) imaged with more sensitive cameras have been used in fluorescence-guided brain tumor resection (6, 7).
3. Protoporphyrin IX (PpIX) is produced from the bioconversion of 5-aminolevulinic acid (5-ALA), which is administered orally at doses of 10–50 mg 4 h before surgery (8). PpIX accumulates in high-grade glioma (HGG) cells and demonstrates red fluorescence with peak emission around 630 nm under blue light (405 nm) excitation, which allows for tumor cells targeted by fluorescence (9–14).
4. Chlorin e6 (Ce6) is a red fluorescent dye, a second-generation photosensitizer, which can be excited with blue light and has an absorption peak of 400 nm. It can be used to target malignant brains tumors or for photodynamic therapy with a dose of 40 mg/m^2 body surface (15–18). Ce6 can be used for fluorescence guidance, but, unlike 5-ALA, its mechanism is not related to bioconversion; rather, similar to fluorescein and ICG, it is related to passive accumulation in the tumor (16, 19, 20).
5. Europium is a photoluminescent lanthanide that emits red light under blue light excitation. It is highly stable and may be used to target tumors in nanoparticles, which can be used in experimental models (21–24). We have demonstrated that europium-based materials have high photostability and can be used for calibration and normalization of quantitative PpIX fluorescence (9).

Abbreviations: 5-ALA, 5-aminolevulinic acid; Ce6, chlorin e6; FNa, fluorescein; FTG, fluorescent tumor gel; HGG, high-grade glioma; ICG, indocyanine green; PpIX, protoporphyrin IX.

It is increasingly important to develop simulative models to educate neurosurgical residents and trainees and to help them develop surgical skills in a safe environment. However, for tumor models, it is challenging to construct a model that can mimic the intra-axial tumor resection process under fluorescence guidance in a laboratory environment. Such teaching models help the trainee to understand the key steps and nuances in fluorescence-assisted tumor resection to achieve maximal resection, especially in the case of invasive tumors, such as malignant gliomas.

In this study, we developed a "tumor gel" based on different combinations of gelatin and agar to mimic the consistency of HGG. Different fluorescent dyes were also tested to simulate the visible fluorescence under microscope magnification. We also built a training model by injecting the tumor gel into fresh sheep/pig brains to simulate a realistic tumor resection (25, 26).

MATERIALS AND METHODS

The development of this model involved two major components: the tumor gel for the consistency of the tumor and the dye for the fluorescent effect. Additionally, we tested the photobleaching effect in the models. Finally, we injected the combination of tumor gel and fluorescent agents into fresh sheep and pig brains and tested the model among neurosurgeons and neurosurgical trainees using a scoring system.

Tumor Gel

A tumor gel was developed based on different combinations of agar (Landor Trading Co. Agar Powder) and gelatin (Knox Original Gelatin, Unflavored) to simulate the consistency and firmness of HGG.

A preliminary experiment was performed to find the optimal proportions of agar and gelatin by mixing different amounts with 100 mL of boiling water. Agar and gelatin were tested separately with amounts of 0.2, 0.3, 0.4, 0.5, and 1–5 g in 0.5 g increments and together in various proportions (**Figure 1**). The powder was dissolved thoroughly in boiling water for 3 min to generate a homogeneous polymer.

After elimination of clearly unworkable combinations (too soft or too hard), 12 different combinations of agar or gelatin or both were included in subsequent tests. Six neurosurgeons with broad experience in brain tumor surgery tested and scored all 12 combinations, using a scoring system from 0 to 10 (10 meant the best simulation of an HGG). Equipment and instruments used to assess the gels included those that would normally be used for resecting an invasive brain tumor, such as operating microscope,

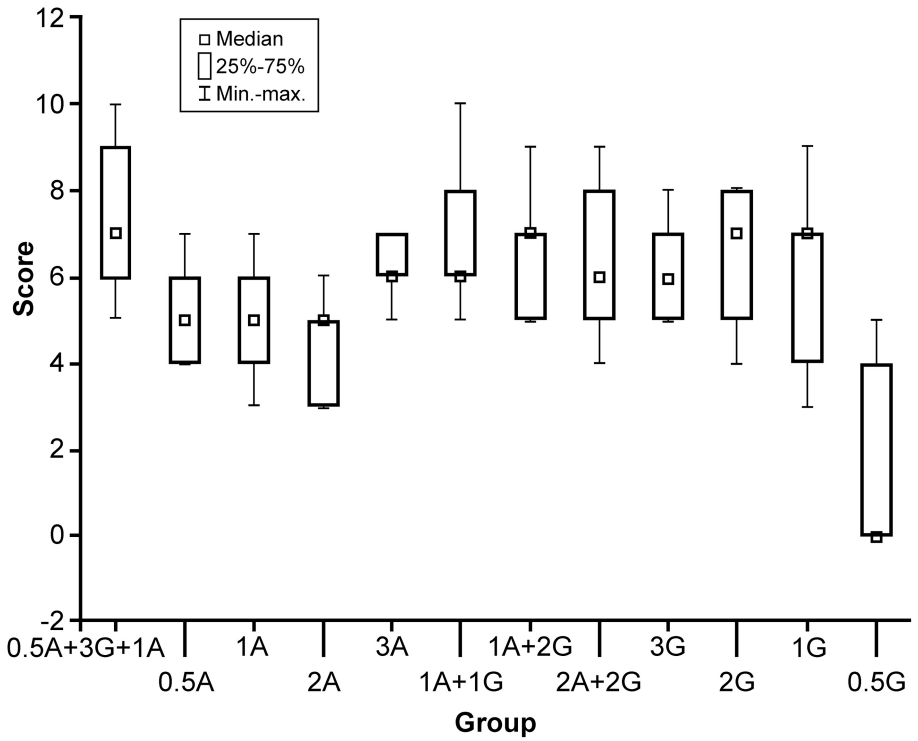

FIGURE 1 | Box plot comparison of 12 solutions with different formulas (horizontal axis) and their scores (0–10, vertical axis). The formula with the highest score was 0.5 g agar and 3 g gelatin with 100 mL boiling water, with additional 1 g of Agar added at 50°C. A, agar; G, gelatin; min-max, minimum to maximum values. *Used with permission from Barrow Neurological Institute, Phoenix, Arizona*.

bipolar forceps, microdissectors, microsuction, microscissors, and microforceps.

To increase the granulation to mimic a real tumor, an additional 1 g of agar was added to the tumor gel (100 mL solution) during cooling (at 50°C).

Optimal Concentrations of Fluorescent Agents

We acquired images of the following dyes at different concentrations: fluorescein (AK-FLUOR Fluorescein Injection, USP), ICG (Cardiogreen Sigma-Aldrich I2633), europium (Sigma-Aldrich), Ce6 (Frontier Scientific), and PpIX (free acid, Enzo Life Sciences). Serial dilutions of the fluorescent dyes were performed to obtain solutions at different concentrations. Normal saline was used as a control for fluorescein and ICG, and dimethyl sulfoxide was used as a control for the remaining three fluorophores. Fluorescein was diluted into 24 shares with concentrations ranging from 1.5×10^{-6} to 12.5 mg/mL. ICG was diluted into 17 shares with concentrations ranging from 3.1×10^{-4} to 10 mg/mL. Europium was diluted into 18 shares with concentrations ranging from 5.5×10^{-4} to 36 mg/mL. Ce6 was diluted into 23 shares with concentrations ranging from 8.6×10^{-6} to 36 mg/mL. PpIX was diluted into 22 shares with concentrations ranging from 1.7×10^{-5} to 36 mg/mL.

Images were captured with an operating microscope (Kinevo 900 OPMI, Carl Zeiss, Oberkochen, Germany) and a camera attached to the observing ocular lens of the microscope (Cannon EOS Rebel T2i, Tokyo, Japan). Different filters of the operating microscope were used with the filters: Blue 400 was used in the analysis of europium, Ce6, and PpIX; Yellow 560 for fluorescein; and Infrared 800 with and without overlay for ICG. A long-wave pass (LWP) filter (B+W F-Pro 58 090 5×E, Schneider Kreuznach, Bad Kreuznach, Germany) was attached to the external camera to accurately measure and analyze PpIX, Ce6, and europium fluorescence.

Settings of the microscope were focus 5× and distance 200 mm, with additional light used when applicable (Blue 400 and Yellow 560), and 1/15 s shutter speed (for the microscope's internal camera) for all images. Procedures using ICG were performed at 25% light intensity (68 mW/cm^2), and the procedures using fluorescein were performed using a Yellow 560 filter at 20% light intensity (9.7 mW/cm^2). The external camera was set at 1/4 s exposure and light sensitivity of the imaging sensor of ISO (International Organization for Standartization) 100 for ICG and fluorescein. Procedures using europium, Ce6, and PpIX were performed under a Blue 400 filter at 100% light intensity (13.4 mW/cm^2), with the red filter attached on the external camera set to 4/5 s exposure and ISO 400. Irradiance was measured using an S120VC photodiode power sensor and a PM400 power meter calibrated to 405 nm for Blue 400, 532 nm for Yellow 560, and 785 nm for Infrared 800 mode (Thorlabs, Dachau, Germany) (9).

Optimal dye concentrations used in the preparation of the fluorescent tumor gels (FTG) were selected by comparing the colors directly under the ocular lens of the microscope. Images were then analyzed in Fiji (27) using the mean pixel signal intensity of the region of interest to confirm the relationship between the relative fluorescence intensity and concentration to select the optimal concentration. Multichannel analysis was used for ICG and single-channel analysis in the others—the green channel for fluorescein and the red channel for europium, Ce6, and PpIX.

Fluorescent Tumor Gel Preparation

The FTG was created by mixing the selected fluorescent dye with the tumor gel immediately after the addition of booster agar at 50°C (see above). To generate the FTG, 5 mL of tumor gel was mixed with each dye at previously selected concentrations.

Photobleaching

A known phenomenon that may affect the interpretation of fluorescence during a period of continuous observation, photobleaching was taken into account and compared among the different FTGs.

Different types of FTG were tested under microscope light with corresponding filters with continuous observation for 5 min, which corresponds to the clinically expected duration of the imaging before altering the microscope position. The photobleaching effect in ICG was recorded using ICG angiography mode as videos, whereas for the remainder of the dyes, a series of images was acquired every 6 s using the external camera. Frames of the ICG video were extracted as images every 6 s using GOM Lab (Gom & Company, South Korea). The settings of the microscope, filter, and camera were the same as above.

The light intensity of each image was extracted during the 5-min continuous observation using Fiji in the region of interest with the same methods as described above.

Tumor Model Preparation

Cooled sheep and pig brains, purchased from a local meat source, were used for the final tumor model preparation to simulate brain tumor resection. A total of 5 mL FTG solution (5 mL FTG and dye at its corresponding concentration) was aspirated in a 5 mL syringe attached to a 21-gauge needle. The FTG was subsequently injected into a fresh sheep and pig brain subcortically; only 1.5–2 mL of the FTG was injected because the size of sheep and pig brain is less than the size of a human brain. The injection was performed meticulously to avoid leakage using a previously described technique (28).

Tumor Model Resection

Three fully trained neurosurgeons and 2 neurosurgical residents (PGY1 and PGY6) assessed the tumor model. Their general information and experience of neurosurgery were collected. They performed simulative tumor resection under microscopic magnification (Kinevo 900 OPMI, Carl Zeiss, Oberkochen, Germany) with and without the assistance of fluorescence guidance. The participants were instructed to perform subpial dissections and to preserve the normal brain tissue. All FTGs were tested by all participants under the corresponding microscopic filters. The simulative operative procedure included operating microscope, and instruments including bipolar forceps, microdissectors, microsuction, microscissors, and microforceps.

Questionnaire of Satisfaction About the Tumor Model

Participants evaluated the model using a questionnaire with items about the face validity, content validity, and white light comparison. Face validity questions evaluate the realism of the model, whereas content validity is a qualitative measure of the appropriateness of the model as a teaching modality (29). The answering system was structured with scores 1–5, in which 1 means "strongly disagree" and 5 means "strongly agree" for all but one question, in which 1 means "easier" and 5 means "more difficult." The questionnaire is shown in **Supplemental Figure 1**.

RESULTS

Tumor Gel

Results of the comparison of all tumor gel formulas are illustrated in **Figure 1**. The best tumor gel formula in terms of consistency and tactile response similar to HGG was the first formula in **Figure 1**: 100 mL 100°C water, 0.5 g of agar, and 3 g of gelatin mixed thoroughly for 3 min ($P_{Kruskal-Wallis} = 0.048$). One gram of agar was added when the tumor gel was at 50°C during the cooling down period.

Optimal Concentrations of Fluorescent Agents

The optimal concentration range of fluorescein was 1.9×10^{-4} to 3.8×10^{-4} mg/mL (**Figure 2**), of ICG was 4.9×10^{-3} to 9.8×10^{-3} mg/mL (**Figure 3**), of europium was 7.0×10^{-2} to 1.4×10^{-1} mg/mL (**Figure 4A**), of Ce6 was 2.2×10^{-3} to 4.4×10^{-3} mg/mL (**Figure 4B**), and of PpIX was 1.8×10^{-2} to 3.5×10^{-2} mg/mL (**Figure 4C**).

During observation of ICG, as the concentration of ICG increased, the fluorescent intensity increased to oversaturation at first, and then decreased as the concentration increased. Two different concentrations produced similar optimal intensity (**Figure 3**), but the solution with a lower concentration was selected for convenience (ICG 4.9×10^{-3} to 9.8×10^{-3} mg/mL).

Because fluorescence intensity was lower in the agar solution than in the normal saline or dimethyl sulfoxide, the following concentrations were selected to create the FTGs: FNa-TG at the concentration of 2.44×10^{-4} mg/mL, ICG-TG 2.5×10^{-2} mg/mL, Eu-TG 1.44×10^{-1} mg/mL, and Ce6-TG 1.125×10^{-2} mg/mL. These FTGs were used to test the effect of photobleaching.

PpIX demonstrated unexpected behavior when mixed with the tumor gel—the red fluorescence disappeared very quickly, with the gel appearing somewhat brown-black. Hydrochloric acid (12M) was added to the FTG in a 1:10 ratio before the dye was mixed (PpIX, 1.1×10^{-3} mg/mL)

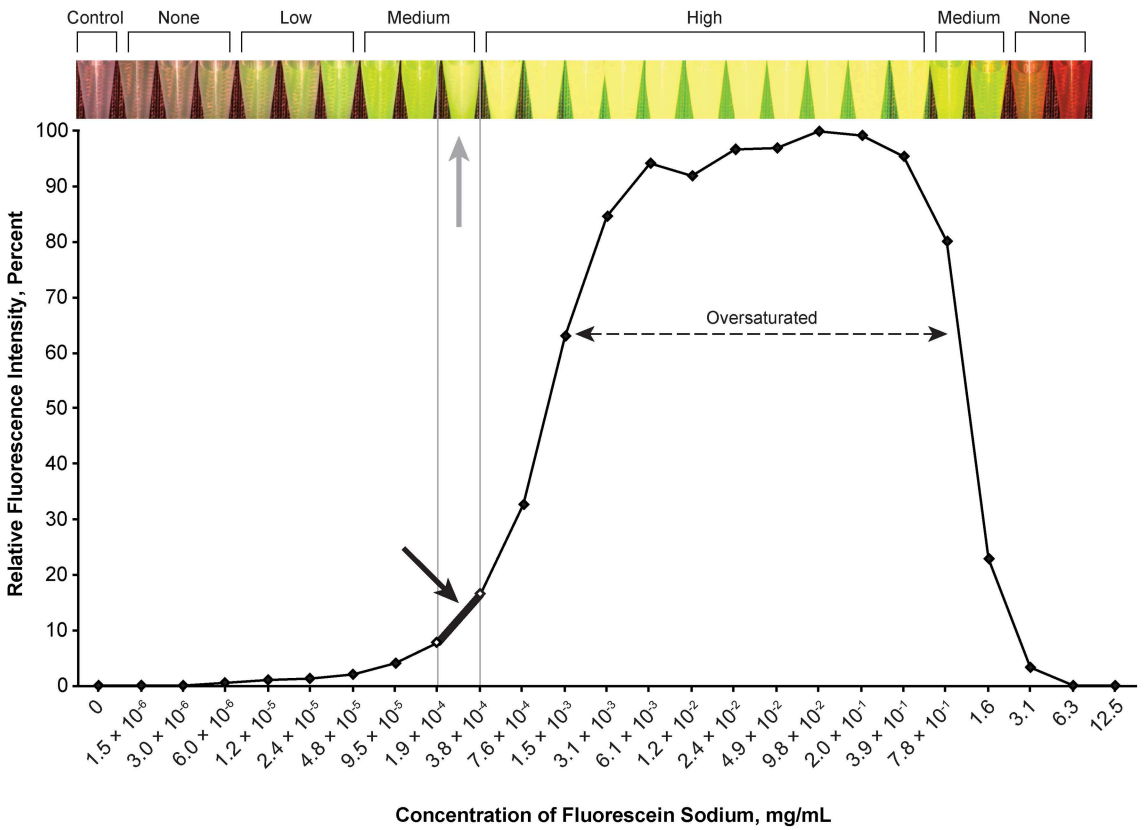

FIGURE 2 | Relationship of relative fluorescence intensity and different concentrations of fluorescein as recorded by the camera. The fluorescence with the concentration ranging from 6.1×10^{-3} mg/mL to ∼4.0 mg/mL is oversaturated. The heading bar shows the fluorescence color and intensity at different concentrations (*gray arrow* indicates optimal intensity). A concentration of 1.9×10^{-4} to 3.8×10^{-4} mg/mL was subjectively selected as the optimal concentration for the tumor model (*black arrow*) by observing the color. *Used with permission from Barrow Neurological Institute, Phoenix, Arizona*.

to circumvent this behavior based on the pH-sensitive property of 5-ALA (30), which eventually prevented the color change.

Photobleaching

During the 5-min photobleaching test, we observed decreases of 22.3% in fluorescein (**Figure 5A**), 10% in ICG (**Figure 5B**), 17.57% in europium (**Figure 5C**, red), 37.56% in Ce6 (**Figure 5C**, orange), and 44.84% in PpIX (**Figure 5C**, light purple). The rate of bleaching effect was higher for PpIX than the rates for europium and Ce6.

Tumor Model Resection Test

Five neurosurgeons and neurosurgical trainees aged 28–37 years tested the tumor model. Every participant performed 5 resections (1 operation per fluorophore). Three out of 5 had at least 2 years of experience in microneurosurgery including glioma resection experience. None had previous experience with any tumor model for resection training. The tumor models under different stages of resection and under different fluorescent modes are shown in **Figure 6**.

Face Validity

Mean scores of the questions for face validity are shown in **Figure 7**. On average, participants answered with a high degree of agreement on the first four questions, which indicates high face validity of the developed model. There were no significant differences among the different dyes for each individual face validity question or for the sum of the four scores ($P_{Kruskal-Wallis} > 0.05$ for all, see **Supplemental Figures 2**, **3**).

Content Validity

Mean scores for the questions for content validity are shown in **Figure 8**. On average, participants answered with a high degree of agreement on the six questions regarding the content validity of the model, which indicates high content validity of the developed model for the purpose of simulating fluorescence-guided surgical tumor resection. There were no significant differences among the different dyes for each individual content validity question or for the sum of the four scores ($P_{Kruskal-Wallis} > 0.05$ for all, see **Supplemental Figure 4**).

Fluorophores Preferences

Results of the subjective comparative evaluation between the fluorophores are shown in **Figure 9**. On average, participants

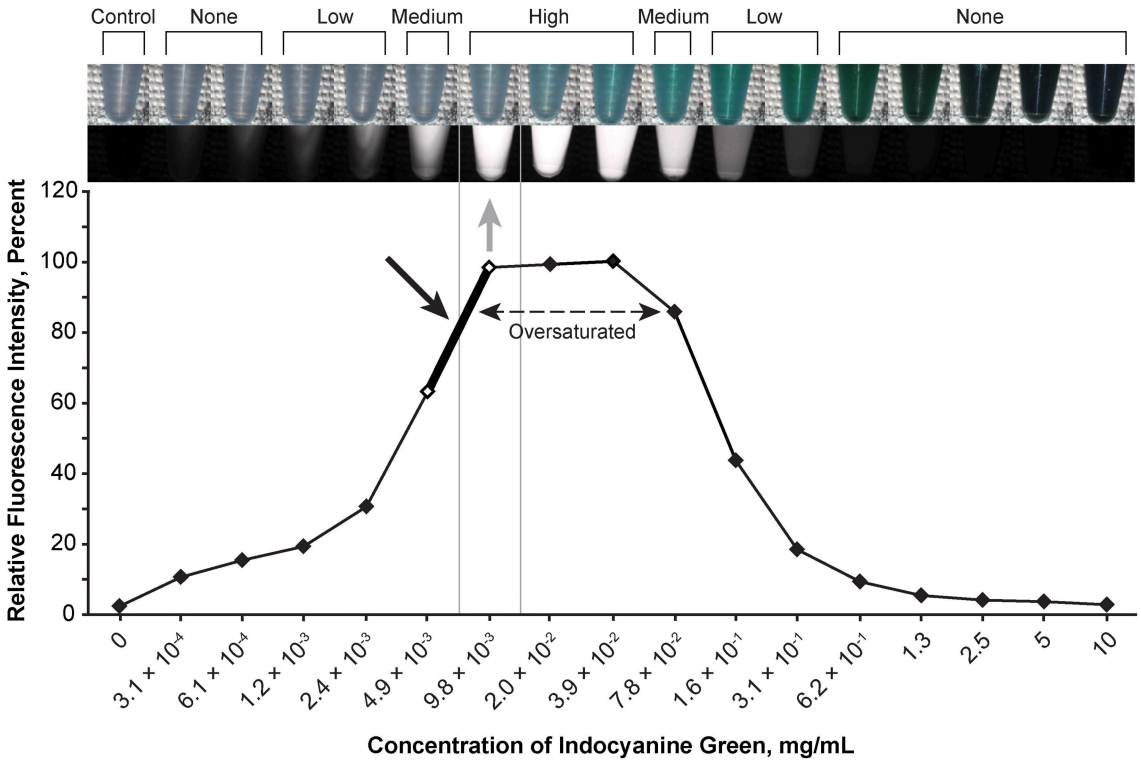

FIGURE 3 | Relationship of the relative fluorescence intensity and different concentrations of indocyanine green as recorded by the camera. The fluorescence with the concentration ranging from 2.0×10^{-2} mg/mL to 3.9×10^{-2} mg/mL is oversaturated. The heading bar shows the fluorescence color and intensity at different concentrations (*gray arrow* indicates optimal intensity). A concentration of 4.9×10^{-3} to 9.8×10^{-3} mg/mL was subjectively selected as the optimal concentration for the tumor model (*black arrow*) by observing the color. *Used with permission from Barrow Neurological Institute, Phoenix, Arizona*.

answered with a high degree of agreement on the questions regarding the convenience, effectiveness, and visual appeal of the fluorescence-guidance of the model. Moreover, when ranking the fluorophores, no fluorophore was significantly better or worse than the others. There were no significant differences among the different dyes for each of the final five questions ($P_{Kruskal-Wallis} > 0.05$ for all, see **Supplemental Figure 5**), indicating that there was no fluorophore that was subjectively superior or inferior to others among the participants.

DISCUSSION

For educational purposes, it is of paramount importance to learn and practice tumor resection prior to a real surgery. Length of survival has been correlated to extent and volume of tumor resection for HGG. Fluorescence techniques add a layer of complexity interpreting tumor boundary in brain tumor surgery, especially for HGG. Previous studies have shown that realistic tumor models can be used in training neurosurgery residents to help them learn the concepts of glioma surgery and the application of fluorescence in neurosurgery (25, 26).

However, those reported models did not include all of the features, such as in real brain tissue simulation and realistic colors of fluorescence-guided tumor surgery (fluorescein, ICG, and europium) along with different filters used in real surgeries. It would arguably be more valuable to have all characteristics in one model to mimic a real neurosurgical scenario. To the best of our knowledge, this is the first report of an in-brain tumor model resembling HGG combined with the use of fluorescence. The tumor model contains 3 parts: the tumor gel, which can offer a tactile response similar to a real tumor during the resection; fluorescent dyes, which can mimic the realistic application of fluorescence; and the actual sheep or pig brains. The FTG was injected in the pig and sheep brains to create a simulation model that replicates the properties of HGG and surrounding brain tissue in a human brain.

Consistency of the Tumor Gel

A tumor model should offer realistic tactile feedback when appropriate instruments are used to help the trainees acquire a simulative experience. We developed a tumor model to simulate HGG. The consistency of HGG may vary from firm to gelatinous and, in general, demonstrates a degree of firmness between normal parenchyma and a firmer, harder metastatic lesion. During the preparation of our tumor gel formula, we created different types of tumor gels of different firmness and consistencies, including those that resemble the metastatic lesions (the solutions of 3 g agar in 100 mL water or 2 g agar plus 2 g gelatin in 100 mL water). The latter recipe results

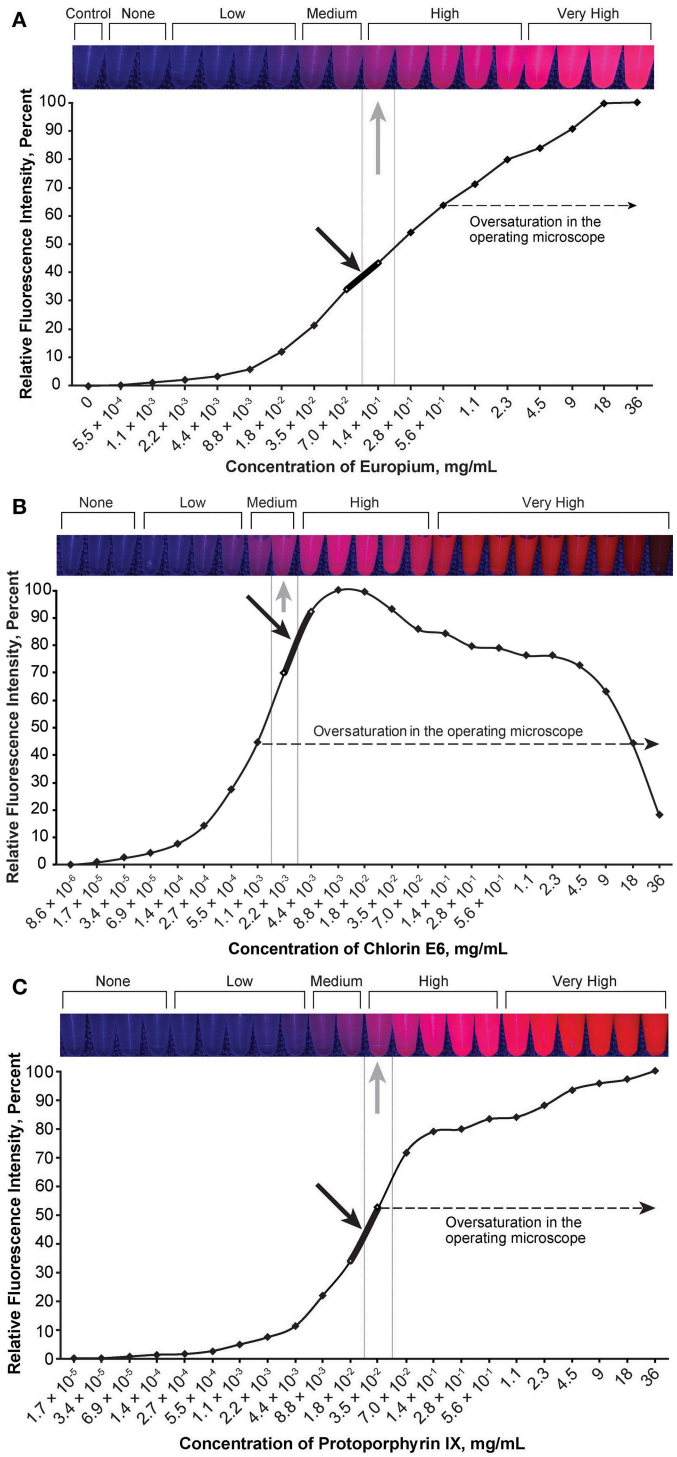

FIGURE 4 | Relationship of the relative fluorescence intensity and different concentrations of europium **(A)**, chlorin e6 **(B)**, and protoporphyrin IX **(C)**. The heading bars show the fluorescence color and intensity at different concentrations (*gray arrows* indicate optimal intensity). For europium **(A)**, the fluorescence was oversaturated when the concentration was higher than 5.6×10^{-1} mg/mL, and the concentration range of 7.0×10^{-2} to 1.4×10^{-1} mg/mL was subjectively selected as the optimal concentration for the tumor model (*black arrow*) by observing the color. For chlorin e6 **(B)**, the fluorescence was oversaturated as recorded through the operating microscope camera when the concentration was above 1.1×10^{-3} mg/mL, and the concentration range of 2.2×10^{-3} to 4.4×10^{-3} mg/mL was subjectively selected as the optimal concentration for the tumor model (*black arrow*) by observing the color. For protoporphyrin IX **(C)**, the fluorescence was oversaturated as recorded by the microscope camera when the concentration was higher than 3.5×10^{-2} mg/mL, and the concentration range of 1.8×10^{-2} to 3.5×10^{-2} mg/mL was subjectively selected as the optimal concentration for the tumor model (*black arrow*) by observing the color. *Used with permission from Barrow Neurological Institute, Phoenix, Arizona*.

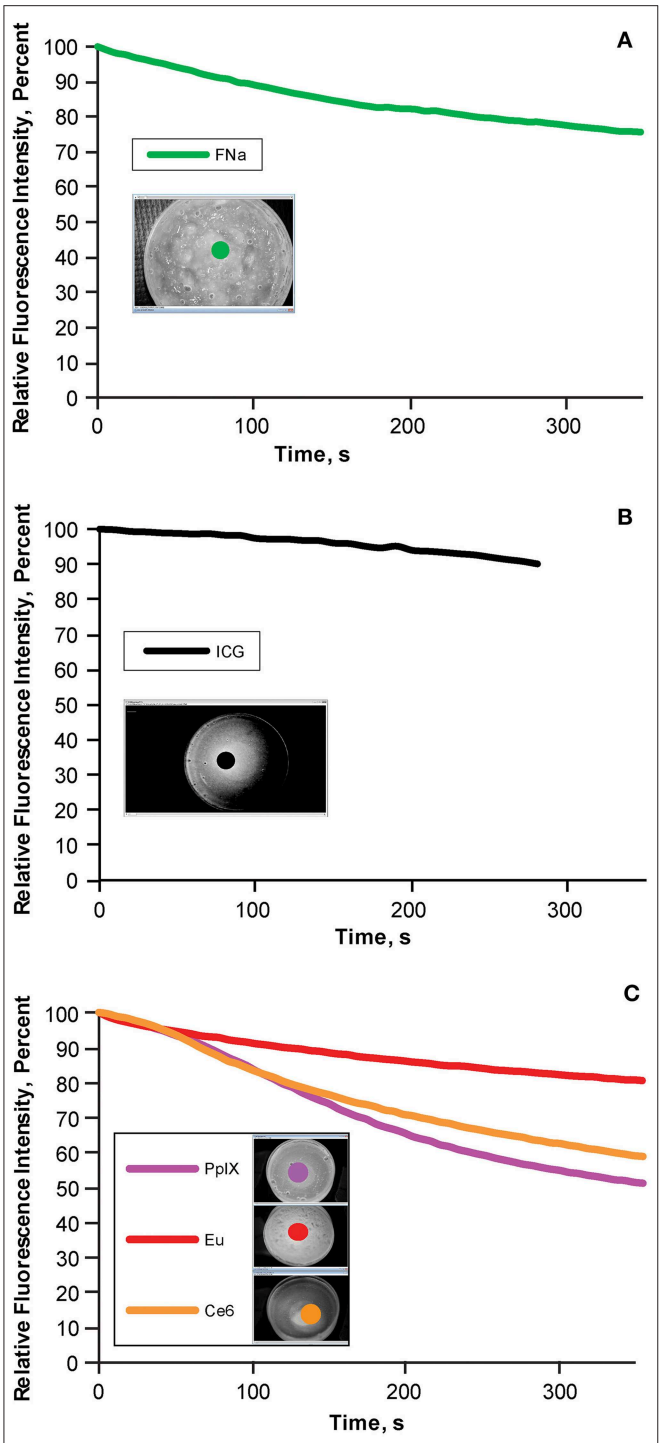

FIGURE 5 | Bleaching phenomena: brightness decrease in different fluorescent tumor gels. **(A)** Fluorescein (FNa); **(B)** indocyanine green (ICG); and **(C)** protoporphyrin IX (PpIX), europium (Eu), and chlorin e6 (Ce6), which are demonstrated together because the same filter was used for all three. During the 5-min (300-s) observation, the decrease in relative fluorescence intensity was approximately 20% for fluorescein, 10% for ICG, 45% for PpIX, 10% for europium, and 35% for Ce6. Inset photographs in each graph show the regions of interests (indicated by colored dots) used to quantify the fluorescence intensity over time. *Used with permission from Barrow Neurological Institute, Phoenix, Arizona*.

in a slightly firmer, more solid consistency that more closely resembles a metastatic lesion, rather than an invading glioma. During preparation of the gel, we also noticed that the thorough mixture of all ingredients in 100°C water produced a tumor gel that was highly homogeneous, whereas a real glioma would be more granulated. In order to create the granularity, we added a booster dose of agar at 50°C during the cooling-down period.

During any intra-axial brain tumor resection, identifying the margin of the tumor and working in the plane between the tumor and normal parenchyma is almost always the principle goal. This technique requires the tumor model to have a similar, but not the same, consistency as normal parenchyma. The margin of the tumor model is easy to locate, especially with the assistance of fluorescence. This goal may be realistic in HGG or metastatic tumors; however, low-grade glioma usually does not have a clear plane of margin, and fluorescence techniques to identify tumor tissue do not appear to work well in such tumors. Our model is not able to mimic the resection of low-grade glioma, which is one of the limitations of the study.

Suitable Color of Fluorescence

A suitable color shown in the tumor model can realistically mimic the fluorescence used in fluorescence-guided surgery. Obtaining a suitable color requires choosing the optimal concentration of each fluorophore. In our study, a series of dilutions were performed to obtain solutions with different levels of concentration. In our experiment, all fluorophores successfully displayed adequate color after mixing with the tumor gel except for PpIX, which had an unexpected behavior. After mixing, the fluorescence of PpIX vanished quickly and the tumor gel turned dark brown. PpIX is an acidophilic substance, which may not work properly in the basic environment of the tumor gel (30). When hydrochloric acid was added into the tumor gel to acidify the tumor gel before adding PpIX, the gel was fluorescent and used in the resection; however, this extra step makes the preparation of PpIX FTG cumbersome, and hydrochloric acid can be dangerous to handle.

The concentrations of fluorophores chosen in our study were selected specifically for application and their functionality with the tumor gels and simulation model development. These concentrations do not represent the concentration of the fluorescent drugs used in actual surgery and accumulated in the tumor tissue, as multiple environmental factors, such as pH, protein binding, and others, affect actual fluorescence intensity in patients. Additionally, brain tumors, especially HGG, are often highly heterogeneous in their cytoarchitecture and present with varying levels of fluorescence intensity within the tumor (31–33).

Advantages and Disadvantages of Fluorophores

Fluorescence techniques are widely used in neurosurgical subdisciplines, and learning to operate under fluorescence is increasingly important for neurosurgeons. The different fluorophores have advantages and disadvantages, and the features of each fluorophore should be well-understood by any neurosurgeon using fluorescent techniques. Recent excellent

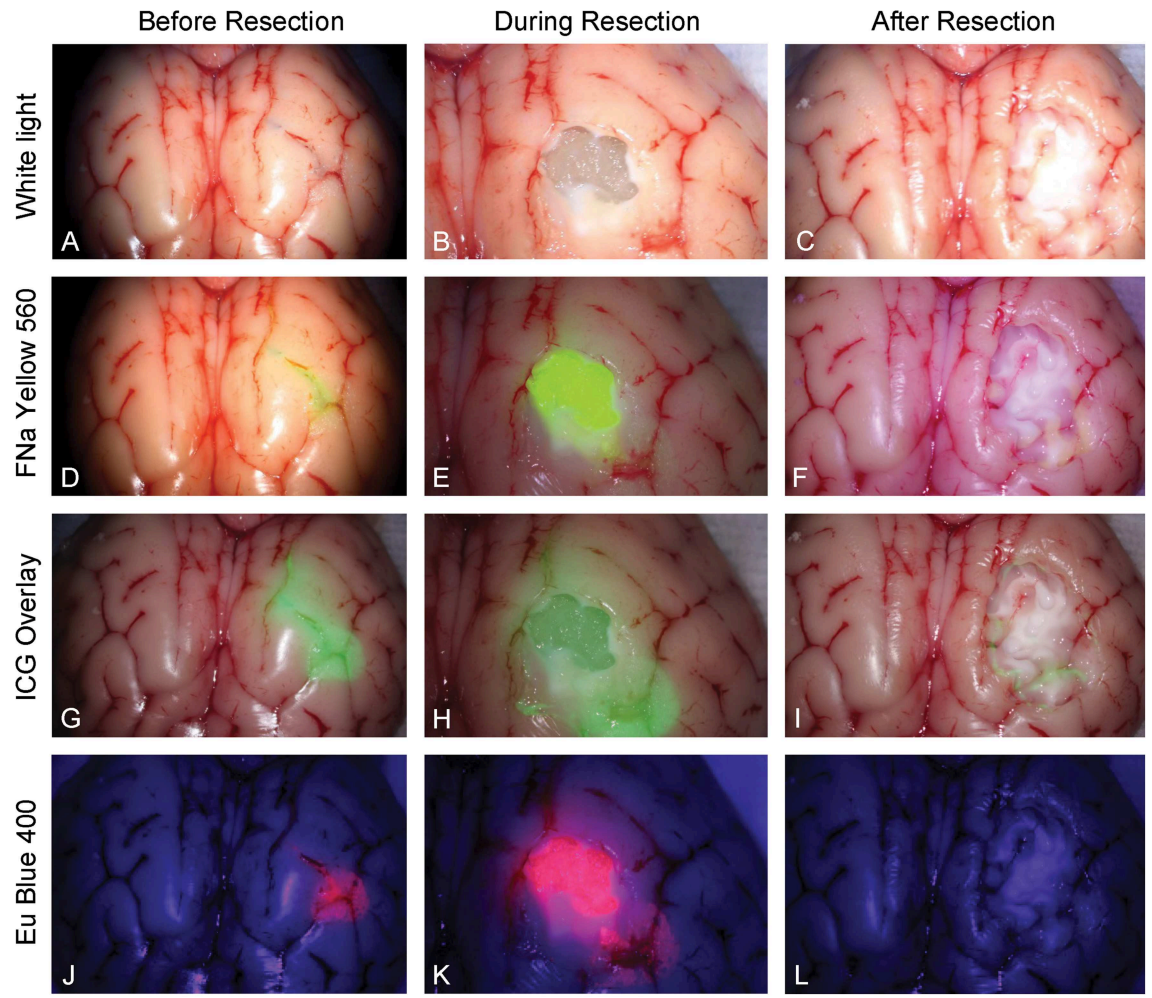

FIGURE 6 | Tumor model in a pig brain at different stages of resection viewed under white light and with the various fluorophores (fluorescein [FNa], indocyanine green [ICG], and europium [Eu]) viewed under their corresponding filters. Tumor model viewed under white light **(A)** before, **(B)** during, and **(C)** after resection. Tumor model after application of fluorescein **(D)** before, **(E)** during, and **(F)** after resection under Yellow 560 filter. Tumor model after application of ICG **(G)** before, **(H)** during, and **(I)** after resection in the ICG overlay mode. Tumor model after application of europium **(J)** before, **(K)** during, and **(L)** after resection under Blue 400 filter. *Used with permission from Barrow Neurological Institute, Phoenix, Arizona*.

reviews discuss fundamental aspects of fluorescence-guided surgery in greater detail (34–36).

Fluorescein is a bright yellow fluorophore used off-label for tumor labeling in neurosurgery, with a growing body of evidence suggesting that its use improves achievement of gross total resection (37–39). Advanced illumination capabilities of the latest operating microscopes allow neurosurgeons to work directly under the Yellow 560 filter throughout the tumor resection (40).

ICG is used in vascular neurosurgery to evaluate the patterns of the vasculature (41), and recent studies suggest its feasibility for brain tumor fluorescence-guided surgery (42). New operating microscopes provide the function of real-time ICG overlay (**Figures 6G–I**), in which the ICG signal is injected into the original white light optical pathway as a semitransparent green overlay (43–45). This enables undistracted continuous manipulations and observation of both normal anatomy and ICG signal, which would be ideal for fluorescence-guided surgery of brain tumors. ICG allows for subsurface imaging as demonstrated by **Figure 6H**. Additionally, there was a tiny rim of residual ICG signal (**Figure 6I**), which represents staining of the pia. Whether this finding represents better sensitivity in detecting ICG signal compared with other fluorophores requires further investigation.

Europium, Ce6, and PpIX are all red fluorophores that can be used for simulation models. We used europium because of its fluorescence spectral similarity to PpIX and the additional benefit that, unlike PpIX, europium is not fast bleaching and can be observed for a relatively longer period than PpIX fluorescence. Ce6 is a photosensitizer that has also been explored which has the same fluorescent color and works under the Blue 400 filter, the illumination of which is blue. Therefore, even though the tumor can be illuminated by fluorescence, it might be challenging

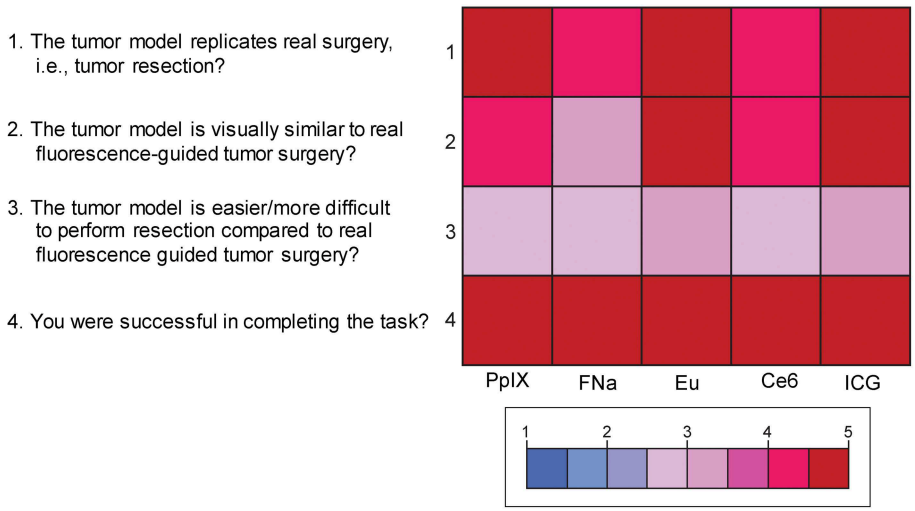

FIGURE 7 | Color-coded plot for questions about face validity. The colored bar shows the scores and their corresponding colors; the score for each question was the average score based on the questionnaire. *Used with permission from Barrow Neurological Institute, Phoenix, Arizona*.

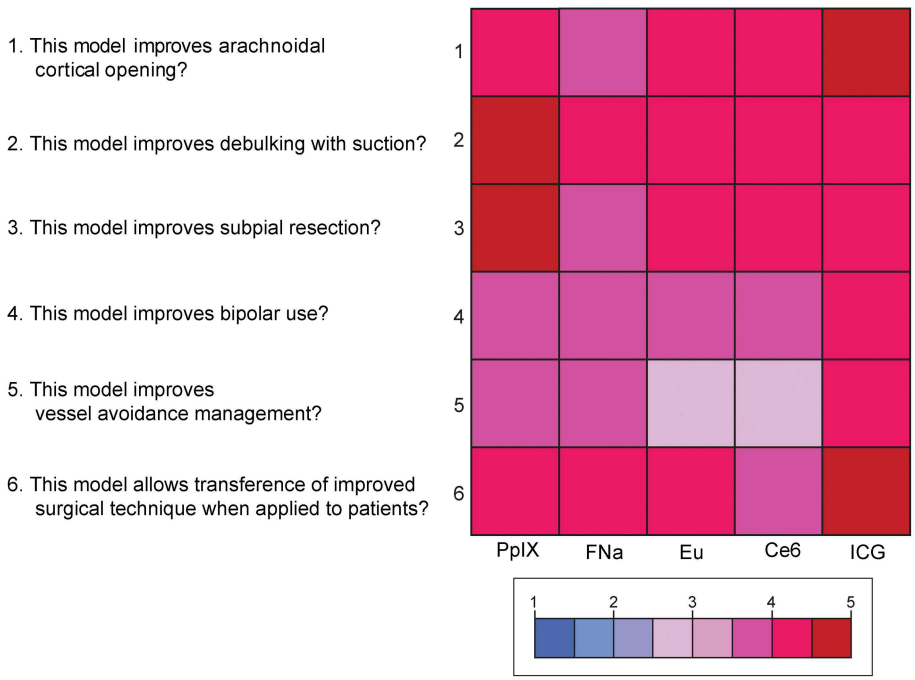

FIGURE 8 | Color-coded plot for questions about content validity. The colored bar shows the scores and their corresponding colors; the score for each question was the average score based on the questionnaire. *Used with permission from Barrow Neurological Institute, Phoenix, Arizona*.

to continuously operate under fluorescence because blood is difficult to visualize. As well, switching between the Blue 400 filter and white light illumination is imperative in real surgery. In our tumor model, there is no bleeding, thus the participants were able to perform the tumor resection under Blue 400 filter without switching, which is not realistic and is one of the major limitations of this model.

Fluorescein and 5-ALA are observed through two separate optical pathways, and therefore can be visualized in stereoscopic three-dimensional mode, which can offer the perception of depth to the observers of the operation. However, ICG, with or without the overlay, is detected through a single optical pathway, and therefore can only be visualized as a two-dimensional image or a semi-transparent pseudo-colored overlay, which lacks

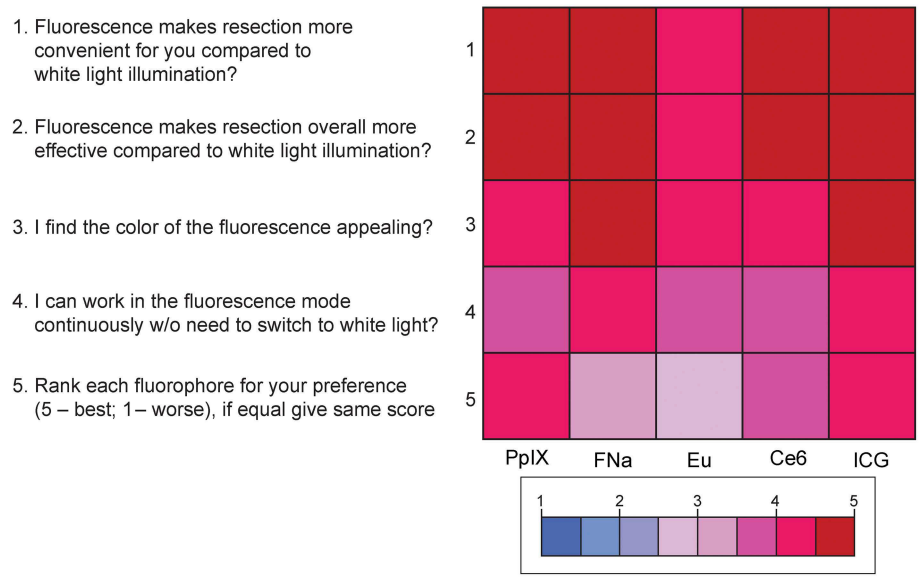

FIGURE 9 | Color-coded plot for questions about fluorophore preferences. The colored bar shows the scores and their corresponding colors; the score for each question was the average score based on the questionnaire. *Used with permission from Barrow Neurological Institute, Phoenix, Arizona*.

depth, making it disadvantageous in terms of practical and educational purposes.

Fluorescence intensity does not necessarily have a linear correlation with the concentration of the fluorophore, which necessitates careful dose selection. With increased concentration, after reaching a peak of fluorescence intensity, all fluorophores are amenable to concentration-dependent quenching, the effect of decreased fluorescence when the concentration of the fluorophore is too high (35). **Figures 2–6** demonstrate this concentration-dependent quenching phenomenon.

Satisfaction scores were relatively high for all the fluorophores. This could mean that, if the tumor cells are labeled with different colors, this sole difference in labeling color would not be likely to affect the efficacy of the resection.

Significance of Photobleaching in Fluorescence Application

Photobleaching is a well-known phenomenon in which the intensity of fluorescence may decrease as the fluorophore is exposed under the excitation light during a prolonged period. This phenomenon may interfere with the interpretation of the fluorescence as the intensity is altered.

Our results demonstrated that fluorescein, ICG, and europium were relatively stable regarding the fluorescence intensity. Among the 3 fluorophores that can mimic the color of 5-ALA, europium is the most stable, which makes it a superior choice for the red fluorescence model.

Realistic Brain Tumor Model: Significance in Practical Education

This project has a potential educational impact for less experienced neurosurgical trainees. They can practice the simulative tumor resection to understand the key concepts of intra-axial brain tumor resection. Subpial resection is a method that can maximize the resection of the lesion while minimizing the risk of damage to the nearby gyrus. It can be deleterious to practice such techniques in real situations, because beginners may not understand the difference between the consistencies of lesions and normal parenchyma. It is certainly valuable for the trainee or less experienced neurosurgeon to practice such concepts prior to the real operation (28).

Because they are hazardous materials, fluorescent dyes are not always available in a laboratory situation for practice. In the tumor model, we created a FTG, that can be shaped and injected easily. Neurosurgical beginners can learn the variations in appearance of fluorescence of different dyes at various positions and light intensities of the microscope while handling a model with a similar consistency to human tissue. The FTG can be widely used in courses because it is an affordable option, is quick and easy to prepare, and has a formula that is replicable. Based on the formula, future models of different types of brain tumors with different consistencies (i.e., metastatic tumor) can be reproduced following the same steps.

Although we did not assess the long-term stability of the FTGs, if necessary, they can be kept in air-tight bags to prevent drying. After being stored for 1 month in a light-protected place, the gels were still fluorescent; however, we believe that freshly prepared gels are better because the tumor gel may dry up, and the concentration of the fluorophore may alter during long-term preservation. Also, sodium azide can be added to the tumor gel to make a 0.01% (weight/volume) solution in order to prevent the growth of mold over time. Caution should be exercised because sodium azide is toxic.

Limitations

The tumor model has several limitations. The tumor model does not permit the practice of skills in identifying and handling vessels; therefore, control of bleeding cannot be taught with this model. Because there is no bleeding, the participants can perform the resection under blue light without switching back to white light (blood is difficult to visualize in the dark fluorescence mode), which is not realistic and may have biased the effectiveness of 5-ALA. After resection, it is difficult to evaluate surrounding brain parenchyma damage. The tumor model cannot mimic the tumor margin of low-grade gliomas. This model cannot represent the normal human brain anatomy because both sheep and pig brains are much smaller. Additionally, assessment of the firmness and consistency of the tumor gels by 6 neurosurgeons was done subjectively. Therefore, the firmness and texture of the selected tumor gel recipe may not accurately represent HGG but can be viewed as a close approximation by neurosurgeons experienced in brain tumor surgery. Finally, the study was probably underpowered for the detection of small subjective differences among the fluorophores. The absence of significant differences among the tested fluorophores reflects the heterogeneity in the questionnaire responses regarding these fluorophores (5-ALA, fluorescein, and to a lesser extent ICG) in the neurosurgical literature (46, 47).

CONCLUSION

In this paper, we present and compare 5 simulation models for fluorescence-guided brain tumor surgery, specifically of HGG. The models efficiently highlighted the "tumor" with 3 different colors—green, yellow, or infrared pseudocolored in green—and multicolor labeling is possible. These models exhibited high face and content validity, and there was no significant difference in the fluorescence-guided surgery performance or fluorescence appearance scores between the models. These models may be effective educational tools for learning the key concepts and technical nuances of fluorescence-guided brain tumor surgery associated with intra-axial tumor resection.

DATA AVAILABILITY

The raw data supporting the conclusions of this manuscript will be made available by the authors, without undue reservation, to any qualified researcher.

AUTHOR CONTRIBUTIONS

EB and MP: conception and design of the study. DV, EB, and XZ: developed the tumor gels and assessed fluorescence measures. SG, CC, NM, PN, EB, and DV: assessed the tumor model. DV and XZ: wrote the first draft of the manuscripts. EB and DV: performed the statistical analysis. PN, ML, and MP: contributed funding, resources acquisition, and supervision. All authors contributed to manuscript revision and read and approved the submitted version.

FUNDING

This study was supported by funds from the Newsome Chair in Neurosurgery Research held by MP and by funds from the Barrow Neurological Foundation.

ACKNOWLEDGMENTS

The authors thank the staff of Neuroscience Publications at Barrow Neurological Institute for assistance with manuscript preparation. EB acknowledges scholarship support SP-2240.2018.4.

SUPPLEMENTARY MATERIAL

The Supplementary Material for this article can be found online at: https://www.frontiersin.org/articles/10.3389/fonc.2019.00748/full#supplementary-material

Supplemental Figure 1 | The questionnaire about the tumor model administered to participants. The answering system was structured with scores 1–5, in which 1 means "strongly disagree" and 5 means "strongly agree" for all but one question, in which 1 means "easier" and 5 means "more difficult." *Used with permission from Barrow Neurological Institute, Phoenix, Arizona*.

Supplemental Figure 2 | Mean scores of answers to questionnaire. *Used with permission from Barrow Neurological Institute, Phoenix, Arizona*.

Supplemental Figure 3 | Scores for the 4 questions for face validity of the tumor model. Scores for the question "The tumor model replicates real surgery?" ranged from 4.4 to 4.8 (highest score was for ICG); from 4 to 5 for the question "The tumor model is visually similar to real fluorescence-guided tumor surgery?" (highest for europium [Eu]); from 2.6 to 3 (3 meaning the most adequate) for the question "The tumor model is easier/more difficult to perform resection compared to real fluorescence-guided tumor surgery?" (most adequate was ICG); and from 4.6 to 5 for the question "You were successful in completing the task?" (highest for ICG). No comparison reached statistical significance. *Used with permission from Barrow Neurological Institute, Phoenix, Arizona*.

Supplemental Figure 4 | Scores for the 6 questions for content validity of the tumor model. Scores for the question "This model improves arachnoidal cortical opening?" ranged from 3.8 to 4.8 (highest score was ICG); from 4 to 4.8 for the question "This model improves debulking with suction?" (highest for ICG); from 3.8 to 4.6 for the question "This model improves subpial resection?" (highest for PpIX); from 3.6 to 4 for the question "This model improves bipolar use?" (highest for ICG); from 3.2 to 4 for the question "This model improves vessel avoidance/management?" (highest for ICG); and from 3.8 to 4.8 for the question "This model allows transference of improved surgical technique when applied to patients?" (highest for ICG). No comparison reached statistical significance. *Used with permission from Barrow Neurological Institute, Phoenix, Arizona*.

Supplemental Figure 5 | Scores for the 5 questions for comparing the fluorophores. The highest and lowest scores for the question "The fluorescence makes resection more convenient for you compared to white light illumination?" were 4.8 (ICG) and 4.2 (europium [Eu]); 5 (ICG) and 4.4 (europium) for the question "The fluorescence makes resection overall more effective compared to white light illumination?"; 4.8 (fluorescein sodium [FNa] and ICG) and 4.2 (chlorin e6 and PpIX) for the question "You find the color of the fluorescence appealing?"; and 4.4 (ICG) and 3.6 (europium and chlorin e6) for the question "You can work in the fluorescence mode continuously without need to switch to white light?" For the question asking participants to rank the fluorophores in order of preference (5 being the best and 1 the worst), ICG had the highest score, followed by PpIX, Ce6, fluorescein sodium, and europium. No comparison reached statistical significance. *Used with permission from Barrow Neurological Institute, Phoenix, Arizona*.

REFERENCES

1. Neira JA, Ung TH, Sims JS, Malone HR, Chow DS, Samanamud JL, et al. Aggressive resection at the infiltrative margins of glioblastoma facilitated by intraoperative fluorescein guidance. *J Neurosurg.* (2017) 127:111–22. doi: 10.3171/2016.7.JNS16232
2. Francaviglia N, Iacopino DG, Costantino G, Villa A, Impallaria P, Meli F, et al. Fluorescein for resection of high-grade gliomas: a safety study control in a single center and review of the literature. *Surg Neurol Int*. (2017) 8:145. doi: 10.4103/sni.sni_89_17
3. Schwake M, Stummer W, Suero Molina EJ, Wölfer J. Simultaneous fluorescein sodium and 5-ALA in fluorescence-guided glioma surgery. *Acta Neurochir*. (2015) 157:877–9. doi: 10.1007/s00701-015-2401-0
4. Senders JT, Muskens IS, Schnoor R, Karhade AV, Cote DJ, Smith TR, et al. Agents for fluorescence-guided glioma surgery: a systematic review of preclinical and clinical results. *Acta Neurochir*. (2017) 159:151–67. doi: 10.1007/s00701-016-3028-5
5. Belykh E, Martirosyan NL, Yagmurlu K, Miller EJ, Eschbacher JM, Izadyyazdanabadi M, et al. Intraoperative fluorescence imaging for personalized brain tumor resection: current state and future directions. *Front Surg*. (2016) 3:55. doi: 10.3389/fsurg.2016.00055
6. Zeh R, Sheikh S, Xia L, Pierce J, Newton A, Predina J, et al. The second window ICG technique demonstrates a broad plateau period for near infrared fluorescence tumor contrast in glioblastoma. *PLoS ONE*. (2017) 12:e0182034. doi: 10.1371/journal.pone.0182034
7. Li C, Sullivan PZ, Cho S, Nasrallah MP, Buch L, Isaac Chen HC, et al. Intraoperative molecular imaging with second window ICG facilitates confirmation of contrast-enhancing tissue during intracranial stereotactic needle biopsy: a case series. *World Neurosurg.* (2019). doi: 10.1016/j.wneu.2019.02.231. [Epub ahead of print].
8. Michael AP, Watson VL, Ryan D, Delfino KR, Bekker SV, Cozzens JW. Effects of 5-ALA dose on resection of glioblastoma. *J Neurooncol.* (2019) 141:523–31. doi: 10.1007/s11060-019-03100-7
9. Belykh E, Miller EJ, Patel AA, Bozkurt B, Yagmurlu K, Robinson TR, et al. Optical characterization of neurosurgical operating microscopes: quantitative fluorescence and assessment of PpIX photobleaching. *Sci Rep*. (2018) 8:12543. doi: 10.1038/s41598-018-30247-6
10. Colditz MJ, Leyen K, Jeffree RL. Aminolevulinic acid (ALA)-protoporphyrin IX fluorescence guided tumour resection. Part 2: theoretical, biochemical and practical aspects. *J Clin Neurosci*. (2012) 19:1611–6. doi: 10.1016/j.jocn.2012.03.013
11. Díez Valle R, Hadjipanayis CG, Stummer W. Established and emerging uses of 5-ALA in the brain: an overview. *J Neurooncol.* (2019) 141:487–94. doi: 10.1007/s11060-018-03087-7
12. Lakomkin N, Hadjipanayis CG. Fluorescence-guided surgery for high-grade gliomas. *J Surg Oncol*. (2018) 118:356–61. doi: 10.1002/jso.25154
13. Pustogarov N, Panteleev D, Goryaynov SA, Ryabova AV, Rybalkina EY, Revishchin A, et al. Hiding in the shadows: CPOX expression and 5-ALA induced fluorescence in human glioma cells. *Mol Neurobiol.* (2017) 54:5699–708. doi: 10.1007/s12035-016-0109-7
14. Hadjipanayis CG, Stummer W. 5-ALA and FDA approval for glioma surgery. *J Neurooncol.* (2019) 141:479–86. doi: 10.1007/s11060-019-03098-y
15. Akimoto J. Photodynamic therapy for malignant brain tumors. *Neurol Med Chir*. (2016) 56:151–7. doi: 10.2176/nmc.ra.2015-0296
16. Shimizu K, Nitta M, Komori T, Maruyama T, Yasuda T, Fujii Y, et al. Intraoperative photodynamic diagnosis using talaporfin sodium simultaneously applied for photodynamic therapy against malignant glioma: a prospective clinical study. *Front Neurol.* (2018) 9:24. doi: 10.3389/fneur.2018.00024
17. Namatame H, Akimoto J, Matsumura H, Haraoka J, Aizawa K. Photodynamic therapy of C6-implanted glioma cells in the rat brain employing second-generation photosensitizer talaporfin sodium. *Photodiagnosis Photodyn Ther*. (2008) 5:198–209. doi: 10.1016/j.pdpdt.2008.08.001
18. Tsutsumi M, Miki Y, Akimoto J, Haraoka J, Aizawa K, Hirano K, et al. Photodynamic therapy with talaporfin sodium induces dose-dependent apoptotic cell death in human glioma cell lines. *Photodiagnosis Photodyn Ther*. (2013) 10:103–10. doi: 10.1016/j.pdpdt.2012.08.002
19. Tzerkovsky DA, Osharin VV, Istomin YP, Alexandrova EN, Vozmitel MA. Fluorescent diagnosis and photodynamic therapy for C6 glioma in combination with antiangiogenic therapy in subcutaneous and intracranial tumor models. *Exp Oncol*. (2014) 36:85–9.
20. Akimoto J, Fukami S, Ichikawa M, Mohamed A, Kohno M. Intraoperative photodiagnosis for malignant glioma using photosensitizer talaporfin sodium. *Front Surg*. (2019) 6:12. doi: 10.3389/fsurg.2019.00012
21. Hu Z, Chi C, Liu M, Guo H, Zhang Z, Zeng C, et al. Nanoparticle-mediated radiopharmaceutical-excited fluorescence molecular imaging allows precise image-guided tumor-removal surgery. *Nanomedicine*. (2017) 13:1323–31. doi: 10.1016/j.nano.2017.01.005
22. Binnemans K. Interpretation of europium(III) spectra. *Coord Chem Rev*. (2015) 295:1–45. doi: 10.1016/j.ccr.2015.02.015
23. Zeng H, Li X, Sun M, Wu S, Chen H. Synthesis of europium-doped fluorapatite nanorods and their biomedical applications in drug delivery. *Molecules*. (2017) 22:753. doi: 10.3390/molecules22050753
24. Galimov DI, Bulgakov RG. The first example of fluorescence of the solid individual compounds of Eu2+ ion: EuCl2, EuI2, EuBr2. *J Luminescence*. (2019) 34:127–9. doi: 10.1002/bio.3580
25. Kamp MA, Knipps J, Steiger HJ, Rapp M, Cornelius JF, Folke-Sabel S, et al. Training for brain tumour resection: a realistic model with easy accessibility. *Acta Neurochir*. (2015) 157:1975–81; discussion 1981. doi: 10.1007/s00701-015-2590-6
26. Mashiko T, Oguma H, Konno T, Gomi A, Yamaguchi T, Nagayama R, et al. Training of intra-axial brain tumor resection using a self-made simple device with agar and gelatin. *World Neurosurg.* (2018) 109:e298–e304. doi: 10.1016/j.wneu.2017.09.162
27. Schindelin J, Arganda-Carreras I, Frise E, Kaynig V, Longair M, Pietzsch T, et al. Fiji: an open-source platform for biological-image analysis. *Nat Methods*. (2012) 9:676–82. doi: 10.1038/nmeth.2019
28. Sabel M. *Getting Ready for Brain Tumor Surgery*. New York, NY: Thieme (2017). doi: 10.1055/b-006-149701
29. Kirkman MA, Ahmed M, Albert AF, Wilson MH, Nandi D, Sevdalis N. The use of simulation in neurosurgical education and training. A systematic review. *J Neurosurg*. (2014) 121:228–46. doi: 10.3171/2014.5.JNS131766
30. Sharma M, Graham JY, Walczak PA, Nguyen R, Lee LK, Carson MD, et al. Optical pH measurement system using a single fluorescent dye for assessing susceptibility to dental caries. *J Biomed Optics*. (2019) 24:017001. doi: 10.1117/1.JBO.24.1.017001
31. Martinez-Moreno M, Kiesel B, Woehrer A, Mischkulnig M, Furtner J, Timelthaler G, et al. *Ex-vivo* analysis of quantitative 5-ALA fluorescence intensity in diffusely infiltrating gliomas with a handheld spectroscopic probe: correlation with histopathology, proliferation and microvascular density. *Photodiagnosis Photodyn Ther*. (2019) 27:354–61. doi: 10.1016/j.pdpdt.2019.05.013
32. Widhalm G, Wolfsberger S, Minchev G, Woehrer A, Krssak M, Czech T, et al. 5-Aminolevulinic acid is a promising marker for detection of anaplastic foci in diffusely infiltrating gliomas with nonsignificant contrast enhancement. *Cancer*. (2010) 116:1545–52. doi: 10.1002/cncr.24903
33. Ross JL, Cooper LAD, Kong J, Gutman D, Williams M, Tucker-Burden C, et al. 5-Aminolevulinic acid guided sampling of glioblastoma microenvironments identifies pro-survival signaling at infiltrative margins. *Sci Rep*. (2017) 7:15593. doi: 10.1038/s41598-017-15849-w
34. Zhang DY, Singhal S, Lee JYK. Optical principles of fluorescence-guided brain tumor surgery: a practical primer for the neurosurgeon. *Neurosurgery*. (2018). doi: 10.1093/neuros/nyy315. [Epub ahead of print].
35. Gioux S, Choi HS, Frangioni JV. Image-guided surgery using invisible near-infrared light: fundamentals of clinical translation. *Mol Imaging*. (2010) 9:237–55. doi: 10.2310/7290.2010.00034
36. Wei L, Roberts DW, Sanai N, Liu JTC. Visualization technologies for 5-ALA-based fluorescence-guided surgeries. *J Neurooncol*. (2019) 141:495–505. doi: 10.1007/s11060-018-03077-9
37. Kaneko S, Eljamel MS. Fluorescence image-guided neurosurgery. *Future Oncol*. (2017) 13:2341–8. doi: 10.2217/fon-2017-0194
38. Acerbi F, Broggi M, Schebesch KM, Hohne J, Cavallo C, De Laurentis C, et al. Fluorescein-guided surgery for resection of high-grade gliomas: a multicentric prospective phase II study (FLUOGLIO). *Clin Cancer Res*. (2018) 24:52–61. doi: 10.1158/1078-0432.CCR-17-1184

39. Xiang Y, Zhu XP, Zhao JN, Huang GH, Tang JH, Chen HR, et al. Blood-brain barrier disruption, sodium fluorescein, and fluorescence-guided surgery of gliomas. *Br J Neurosurg*. (2018) 32:141–8. doi: 10.1080/02688697.2018.1428731
40. Belykh EG, Zhao X, Cavallo C, Bohl MA, Yagmurlu K, Aklinski JL, et al. Laboratory evaluation of a robotic operative microscope-visualization platform for neurosurgery. *Cureus*. (2018) 10:e3072. doi: 10.7759/cureus.3072
41. Ewelt C, Nemes A, Senner V, Wölfer J, Brokinkel B, Stummer W, et al. Fluorescence in neurosurgery: its diagnostic and therapeutic use. Review of the literature. *J Photochem Photobiol B*. (2015) 148:302–9. doi: 10.1016/j.jphotobiol.2015.05.002
42. Acerbi F, Vetrano IG, Sattin T, de Laurentis C, Bosio L, Rossini Z, et al. The role of indocyanine green videoangiography with FLOW 800 analysis for the surgical management of central nervous system tumors: an update. *Neurosurg Focus*. (2018) 44:E6. doi: 10.3171/2018.3.FOCUS1862
43. Martirosyan NL, Skoch J, Watson JR, Lemole GM Jr, Romanowski M, Anton R. Integration of indocyanine green videoangiography with operative microscope: augmented reality for interactive assessment of vascular structures and blood flow. *Neurosurgery*. (2015) 11(Suppl. 2):252–7; discussion 257–8. doi: 10.1227/NEU.0000000000000681
44. Watson JR, Gainer CF, Martirosyan N, Skoch J, Lemole GM Jr, Anton R, et al. Augmented microscopy: real-time overlay of bright-field and near-infrared fluorescence images. *J Biomed Opt*. (2015) 20:106002. doi: 10.1117/1.JBO.20.10.106002
45. Nickele C, Nguyen V, Fisher W, Couldwell W, Aboud E, David C, et al. A pilot comparison of multispectral fluorescence to indocyanine green videoangiography and other modalities for intraoperative assessment in vascular neurosurgery. *Operat Neurosurg*. (2018) 17:103–9. doi: 10.1093/ons/opy237
46. Liu JT, Meza D, Sanai N. Trends in fluorescence image-guided surgery for gliomas. *Neurosurgery*. (2014) 75:61–71. doi: 10.1227/NEU.0000000000000344
47. Brawanski A, Acerbi F, Nakaji P, Cohen-Gadol A, Schebesch KM. Poor man-rich man fluorescence. Is this really the problem? *Acta Neurochir*. (2015) 157:1959–61. doi: 10.1007/s00701-015-2553-y

Conflict of Interest Statement: The authors declare that the research was conducted in the absence of any commercial or financial relationships that could be construed as a potential conflict of interest.

frontiers in Surgery

REVIEW
published: 04 September 2019
doi: 10.3389/fsurg.2019.00045

Delta-Aminolevulinic Acid-Mediated Photodiagnoses in Surgical Oncology: A Historical Review of Clinical Trials

Joseph F. Georges[1,2], Amber Valeri[1,2], Huan Wang[3], Aaron Brooking[1,2], Michael Kakareka[1,2], Steve S. Cho[4,5], Zein Al-Atrache[6], Michael Bamimore[6], Hany Osman[7], Joseph Ifrach[6], Si Yu[3], Carrie Li[4], Denah Appelt[1], John Y. K. Lee[5], Peter Nakaji[8], Kristin Brill[9] and Steven Yocom[2]*

[1] Department of Neurosurgery, Philadelphia College of Osteopathic Medicine, Philadelphia, PA, United States, [2] Department of Neurosurgery, Cooper University Healthcare, Philadelphia, PA, United States, [3] School of Medicine, Cooper Medical School of Rowan University, Camden, NJ, United States, [4] Perelman School of Medicine, University of Pennsylvania, Philadelphia, PA, United States, [5] Department of Neurosurgery, Hospital of the University of Pennsylvania, Philadelphia, PA, United States, [6] School of Medicine, Philadelphia College of Osteopathic Medicine, Philadelphia, PA, United States, [7] Wellman Center for Photomedicine, Massachusetts General Hospital, Boston, MA, United States, [8] Department of Neurosurgery, St. Joseph's Hospital and Medical Center, Barrow Neurological Institute, Phoenix, AZ, United States, [9] Department of Surgery, MD Anderson Cancer Center at Cooper Health Systems, Camden, NJ, United States

OPEN ACCESS

Edited by:
Eberval Figueiredo, Clinical Hospital, Faculty of Medicine, University of São Paulo, Brazil

Reviewed by:
Hiroki Toda, Fukui Red Cross Hospital, Japan
Leonardo Welling, Universidade Estadual de Ponta Grossa, Brazil

***Correspondence:**
Joseph F. Georges
joseph.georges@asu.edu

Specialty section:
This article was submitted to Neurosurgery, a section of the journal Frontiers in Surgery

Received: *15 April 2019*
Accepted: *17 July 2019*
Published: *04 September 2019*

Citation:
Georges JF, Valeri A, Wang H, Brooking A, Kakareka M, Cho SS, Al-Atrache Z, Bamimore M, Osman H, Ifrach J, Yu S, Li C, Appelt D, Lee JYK, Nakaji P, Brill K and Yocom S (2019) Delta-Aminolevulinic Acid-Mediated Photodiagnoses in Surgical Oncology: A Historical Review of Clinical Trials. Front. Surg. 6:45. doi: 10.3389/fsurg.2019.00045

Fluorescence imaging is an emerging clinical technique for real-time intraoperative visualization of tumors and their boundaries. Though multiple fluorescent contrast agents are available in the basic sciences, few fluorescence agents are available for clinical use. Of the clinical fluorophores, delta aminolevulinic acid (5ALA) is unique for generating visible wavelength tumor-specific fluorescence. In 2017, 5ALA was FDA-approved for glioma surgery in the United States. Additionally, clinical studies suggest this agent may have utility in surgical subspecialties outside of neurosurgery. Data from dermatology, OB/GYN, urology, cardiothoracic surgery, and gastrointestinal surgery show 5ALA is helpful for intraoperative visualization of malignant tissues in multiple organ systems. This review summarizes data from English-language 5ALA clinical trials across surgical subspecialties. Imaging systems, routes of administration, dosing, efficacy, and related side effects are reviewed. We found that modified surgical microscopes and endoscopes are the preferred imaging devices. Systemic dosing across surgical specialties range between 5 and 30 mg/kg bodyweight. Multiple studies discussed potential for skin irritation with sun exposure, however this side effect is infrequently reported. Overall, 5ALA has shown high sensitivity for labeling malignant tissues and providing a means to visualize malignant tissue not apparent with standard operative light sources.

Keywords: fluorescence, 5ALA, protoporphyrin IX, surgery, neurosurgery, glioma

INTRODUCTION

Surgeons have utilized light to better visualize their surgical fields since antiquity. Fluorescence, a relatively new discovery, has been studied since the early-to-mid twentieth century as a means for providing better contrast of structures during surgery. Reports from the late twentieth century showing fluorescence contrast could improve intraoperative visualization of tumors during surgery has fueled a renewed interest in further developing clinical fluorescence imaging techniques.

In the United States, few agents are clinically approved for generating intraoperative fluorescence contrast (1). Though novel agents are in various stages of clinical trials, the three agents currently approved for clinical use are fluorescein, indocyanine green, and delta-aminolevulinic acid (5ALA), and of these, only 5ALA has a specific FDA clinical indication for CNS use (2). Of these, 5ALA is also the only agent that produces intracellular tumor-specific fluorescence. Delta-aminolevulinic acid generates this fluorescence by causing tumor-specific accumulation of the fluorescent molecule protoporphyrin IX (PpIX).

Delta-aminolevulinic acid is produced by the condensation of succinate and glycine, and was first reported in a Nature article in 1953 (3, 4). Studies with radiolabeled carbon showed this molecule was involved in porphyrin synthesis (3). Studies during the 1950s and 1960s focused on the role of 5ALA in the heme synthesis pathway (5, 6). The first human studies with 5ALA were conducted in 1956, and were devised to study 5ALA metabolism. In these studies, 5ALA was given orally (7). Skin sensitivity, a well-known complication of 5ALA, was first reported in 1956 (7). This phenomenon occurred 2–11 h after 5ALA administration.

Porphyrin-mediated fluorescence was first reported in the late nineteenth century. However, the potential role porphyrins would have in tumor visualization would not be reported until half a century later in lab-based studies. The earliest clinical studies of 5ALA-mediated tumor visualization were reported for dermatology and urology in 1990 and 1994, respectively (8–10). Throughout the remaining twentieth century and early twenty first century, clinicians and scientists continued to evaluate the role of 5ALA-mediated fluorescence for intraoperative photodiagnosis of neoplasms in neurosurgery, head and neck surgery, cardiothoracic surgery, gastrointestinal surgery and OB/GYN.

This review provides a history of notable findings for 5ALA-mediated photodiagnosis across surgical subspecialties. The information is derived from a PubMed search of all English language clinical trials published between 1950 and 2018. Basic science and animal studies are excluded from this review.

NEUROSURGERY

First Application of 5ALA in Neurosurgery

The first study investigating 5ALA in neurosurgery was published by Stummer et al. (11). In this seminal study, Stummer administered 10 mg/kg of 5ALA orally to 9 patients with high-grade gliomas (HGG) 3 h prior to induction of anesthesia. Using a 375–440 nm bandpass filter, Stummer was able to provide blue-light excitation. A long-pass filter >455 nm blocked the reflected excitation light and allowed the emitted protoporphyrin IX fluorescence to be visualized. From the 9 patients, Stummer took a total of 89 biopsies; in these specimens, 5ALA fluorescence demonstrated 85% sensitivity, 100% specificity, and 90% accuracy. The major contributors to the false-negatives were areas of low-density infiltrates of malignant cells and necrotic areas of the tumors. At the 10 mg/kg dose, no adverse effects were recorded. This study, while small, established the utility of 5ALA as an intraoperative imaging agent and began a new era for fluorescence-guided neurosurgery studies.

Landmark 5ALA Studies in Neurosurgery

Since the first paper in 1998, Stummer et al. and other groups have continued to investigate various aspects of 5ALA in neurosurgery. In 2000, Stummer et al. published a study in a larger cohort of 52 patients with HGGs, this time stratifying fluorescence subjectively into strong, vague, and none (12). The study demonstrated again that 5ALA was highly sensitive and specific for neoplasm and that residual fluorescence after standard resection predicted subtotal resection, seen on postoperative MRI as residual enhancement. The most impactful clinical neurosurgery 5ALA study was the 2006 randomized, controlled, multi-center trial by Stummer et al. (13). In the study, 270 HGG patients were randomized to either fluorescence-guided surgery with 5ALA or conventional surgery with white-light alone. Importantly, the study demonstrated that those in the 5ALA arm achieved gross total resection (GTR) at a much higher rate (65% vs. 36%, $p < 0.0001$) and had significantly higher progression-free survival (PFS) at 6 months (41% vs. 21.1%, $p = 0.0003$) without significant changes in postoperative neurologic deficits. Although the study was underpowered to demonstrate effects on overall survival, the results were nonetheless encouraging. In 2014, Coburger further demonstrated that 5ALA was more accurate than intraoperative MRI for detecting neoplasm at the infiltration zone, establishing 5ALA as both a more cost-effective and superior alternative (14).

Appropriate 5ALA Dose and Route of Administration

The current accepted dose for 5ALA administration in neurosurgery is an oral dose of 20 mg/kg bodyweight ∼3 h before induction of anesthesia, translating to roughly 4–5 h before tumor exposure. In Stummer et al.'s first study in 1998, the dose used was 10 mg/kg. Two later studies investigated different doses of 5ALA in neurosurgery: a 2017 study by Stummer et al. (15) and another 2017 study by Eljamel et al. (16). Stummer et al. studied the efficacy of 0.2, 2, and 20 mg/kg in a total of 21 patients with HGGs and demonstrated that a 10-fold increase in dosage from 2 to 20 mg/kg yielded only a 4-fold increase in signal. They concluded that a dose higher than 20 mg/kg was unlikely to yield significant benefits. Eljamel et al. on the other hand, investigated doses from 10 to 50 mg/kg in 10 mg/kg increments in 19 patients with HGGs. They concluded that a dose of up to 50 mg/kg was safe in patients and suggested that higher doses of 5ALA may increase tumor fluorescence, although their results were not statistically significant in their small sample population. Considering these results, most groups, including Stummer et al.

have transitioned to 20 mg/kg, which seems to be both safe and effective.

In terms of route of administration, 5ALA has always been administered orally for neurosurgical patients. Preclinical studies, and studies in healthy patients, have established that oral 5ALA is rapid and effective (17). Thus, changes to the route of administration have not been considered for 5ALA in neurosurgery.

Imaging 5ALA Fluorescence in Neurosurgery

Neurosurgeons have relied heavily on surgical microscopes for intracranial surgeries since the 1950s (18). Hence, the majority of 5ALA visualization in neurosurgery has been performed with surgical microscopes (**Figure 1A**). In general, add-on modules are attached to existing microscopes to achieve blue-light excitation. Initially, when Stummer et al. first described their experience with 5ALA, a 375–440 nm bandpass filter was placed in front of the Xenon light, which provided UV and blue-light excitation. A long-pass >455 nm filter was used to block the reflected excitation light, in order to better detect the red PpIX fluorescence. This setup was used by Stummer's group and other groups until the mid-2000's, when Zeiss introduced its Blue400 module, which uses a 400–410 nm filter for excitation and 620–710 nm filter for emission and can rapidly toggle between white-light and blue-light illumination. Band pass emission filters at 620–710 nm were initially utilized to specifically visualize the peak red emission of PpIX; however, most surgeons found it difficult to operate with red light only. Hence, emission filters in the next generation of microscopes were changed from the narrow band pass filter to a 444 nm long pass filter. Although the field is illuminated only with blue light, autofluorescence in green and mild yellow provide the surgeon with illumination of surrounding background structures while resecting pink/red fluorescent tissue (**Figure 1B**). Leica has recently offered its FL400 module (380–430 nm excitation filter with a 444 nm long pass emission filter), which, similar to the Zeiss module, provides intraoperative visualization of PpIX.

Although exoscopes are a relatively new addition to the neurosurgeons' armamentarium, at least one group has attempted 5ALA visualization using an exoscope. Piquer et al. demonstrated that a commercial exoscope fitted with a 380–430nm excitation filter and >444 nm emission filter could be used to visualize 5ALA fluorescence reliably in the operating room (19, 20). Their study remains one of few studies to visualize 5ALA fluorescence without standard microscope equipment.

Current Status of 5ALA

In June 2017, 5ALA was FDA-approved as an intraoperative visualizing agent for patients with HGGs. Although 5ALA has been difficult for U.S. neurosurgeons to access outside of research studies, that is slowly changing as of April 2019 (2).

Future Applications of 5ALA Fluorescence in Neurosurgery

Though most clinical 5ALA studies have focused on patients with HGGs, some groups have investigated its application in other intracranial tumors. For instance, Widhalm et al. (21, 22) demonstrated that non-enhancing gliomas are poor targets for 5ALA and Valdes et al. (23) concluded that conventional 5ALA imaging was of limited use in patients with low-grade gliomas. On the other hand, Valdes et al. (24) and Coluccia et al. (25) investigated the utility of 5ALA in meningiomas and concluded that most meningiomas (80 and 94%, respectively) demonstrated PpIX fluorescence. Similarly, Eljamel et al. concluded that 5ALA fluorescence was useful in pituitary adenomas of various subtypes (26). These studies offer encouraging evidence that 5ALA fluorescence may be applicable to other intracranial tumors and may further help neurosurgeons visualize tumors in the operating room.

Technological advances are improving clinical 5ALA fluorescence detection. Thus far, most neurosurgeons have relied on qualitative grading of PpIX fluorescence (i.e., strong, vague, none), which is limited in objectivity and sensitivity. Multiple groups have demonstrated that quantitative grading of fluorescence, achieved with an intraoperative spectrometry probe, increases the sensitivity and accuracy of 5ALA fluorescence (23, 24, 27). Furthermore, an important limitation in 5ALA fluorescence is the micron-scale tissue penetration by ultraviolent excitation light, which can hinder sensitive tumor detection. Therefore, to increase depth penetration of excitation light, Roberts et al. recently demonstrated that using red-light excitation (620–640 nm) and a sensitive spectrally-resolved camera to take advantage of 5ALA's second, smaller excitation/emission peak, neoplastic areas could be visualized up to 5 mm below the tissue surface (28).

Conclusion

Overall, 5ALA has demonstrated utility in increasing GTR rates and PFS in patients with HGGs and may be applicable to other intracranial tumors as well. Along with potential advances in intraoperative visualization techniques, 5ALA may ultimately improve patient outcomes in neurosurgery.

UROLOGY

First Application of 5ALA in Urology

The first study to evaluate 5ALA in Urology was published by Kriegmair et al. (9). In this study, an intravesicular application of 1.5 g of 5ALA dissolved in 50 ml of sodium bicarbonate was instilled. Time of exposure of 5ALA ranged from 15 to 360 min. The mean time between instillation and fluorescence cystoscopy was 204 min. Urologic surgery was performed under violet light from a krypton ion laser with 406.7 nm excitation. This provided visualization of red fluorescence from protoporphyrin IX in the urothelium of the bladder to perform biopsies of the bladder wall in 68 patients who were suspected to have bladder cancer. In this study, photodynamic diagnosis utilizing 5ALA fluorescence-directed urothelium biopsy diagnosed bladder cancer with a high sensitivity of 100% and specificity of 68.5%. No serious side effects were observed with intravesicular instillation of 5ALA. This study generated confidence that 5ALA could provide highly

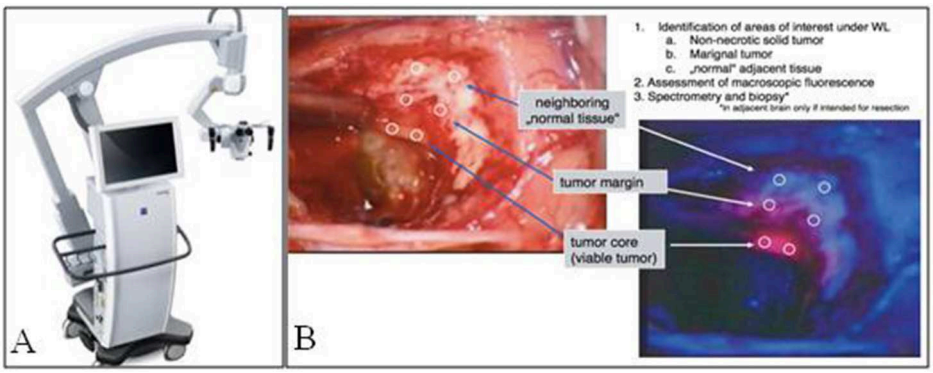

FIGURE 1 | Fluorescence imaging in neurosurgery. **(A)** Zeiss Pentero fluorescence surgical microscope used for intraoperative imaging. **(B)** Brightfield illumination compared to PpIX fluorescence from a malignant glioma, note fluorescence signal of the tumor compared to tumor margin and normal adjacent brain [Intraoperative images courtesy of Stummer et al. (15)].

sensitive visualization and improved resection of difficult-to-detect lesions, such as carcinoma *in situ* and urothelial dysplasia, resulting in diminished recurrence rates.

Appropriate 5ALA Dose and Route of Administration

5ALA can be administered via two routes for the diagnosis of urologic malignancies. In early studies, a 1.5 g, 3% solution of 5ALA was given almost exclusively by direct intravesicular instillation 2–3 h before biopsy was performed. In more recent studies, researchers have transitioned to administering a 20 mg/kg body weight oral solution of 5ALA 3–4 h before biopsy is performed. Inoue et al. evaluated the safety and efficacy of 10 mg/kg vs. 20 mg/kg of oral 5ALA in white light vs. fluorescence cystoscopy in a total of 62 patients (29). The rates of carcinoma *in situ* and high grade non-invasive papillary urothelial carcinoma detected only by white light cystoscopy was 4.0 and 0.0%, respectively in the 10 and 20 mg/kg groups vs. 16.0 an 36.1%, respectively in the 10 and 20 mg/kg fluorescence cystoscopy groups. Inoue et al. performed a follow-up study in 2016 which demonstrated that sensitivity increased in a dose-dependent manner with fluorescence cystoscopy, reporting 83.7% at $\geqq$ 10 mg/kg and $<$15 mg/kg, 86.4% at $\geqq$ 15 mg/kg and $<$20 mg/kg, and 96.3% at $\geqq$ 20 mg/kg (30).

Imaging 5ALA Fluorescence in Urology

In the first study to document the results of 5ALA photodynamic diagnostics in urologic malignancy, Kriegmair et al. utilized a krypton ion laser 406.7 nm excitation. The majority of studies published in this field utilize a xenon arc lamp with a 370–440 nm bandpass filter, with or without long-pass filter to detect the red PpIX fluorescence. A fluorescence cystoscope, sometimes the help of a 0 or 30 telescope is typically employed (**Figure 2**) (32, 33). Fukuhara et al. published a study in 2015 reporting the utility of a flexible fluorescence-cystoscope with a twin-mode monitor in 5ALA photodynamic diagnosis of bladder cancer (31). In this particular study, a new PDD system consisting of a fluorescence endoscope with a SAFE-3000 processor and flexible cystoscope with a xenon lamp and semiconductor laser. Fluorescence images were observed with a charge coupled device image processor. A twin-mode monitor allowed a white light image and fluorescent image to be visualized simultaneously.

Adverse Effects of 5ALA

Intravesicular application of 5ALA is overall, well-tolerated with minimal side effects. Multiple studies reported transient urinary urgency, pollakisuria, and alginuresis (34, 35). With the oral administration of 5ALA, patients are often described as having transient hypotension, transaminitis and skin photosensitivity (29, 31, 36).

Limitations of 5ALA in Diagnosis of Bladder Cancer

Speiss et al. reported in 2006 that fluorescence cystoscopy with 5ALA can have a false-positive rate as high as 40% (37). Possible causes of a false-positive result include: inflammation, urothelial hyperplasia, recent urethral stents, bacteriuria, previous intravesicular therapy within the previous 3 months, and inexperience of the performing Urologist (38, 39).

Current Status of 5ALA in Urology

The United Stated Food and Drug Administration approved 5ALA for intra-operative photodynamic diagnosis of bladder cancers in 1999. Currently, studies are being conducted regarding the use of a 5ALA ester, hexyl aminolevulinate, to compare efficacy and diagnostic accuracy.

Conclusion

Overall, 5ALA has demonstrated increased sensitivity in diagnosis of bladder cancers compared to white-light cystoscopy, especially in the case of carcinoma *in situ* and dysplasia. It has shown to improve visualization of surgical margins at resection and to decrease recurrence rates.

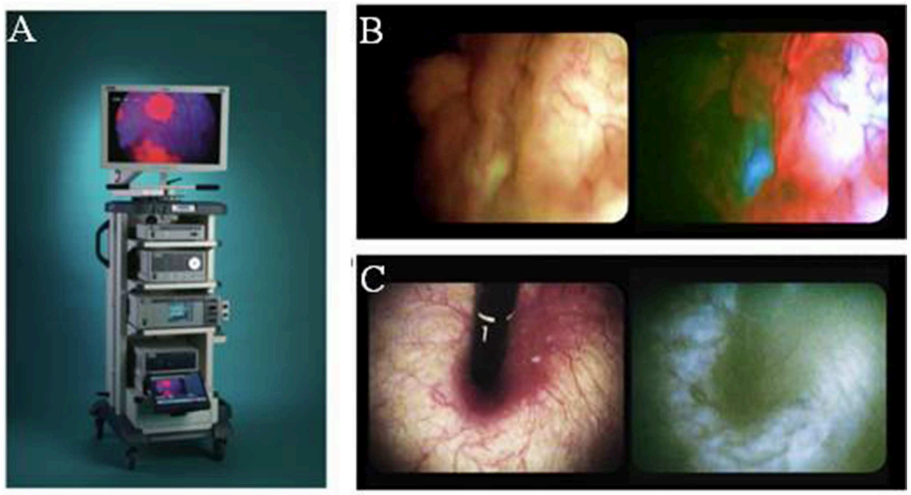

FIGURE 2 | Fluorescence imaging in urology. **(A)** Karl Stortz D-light C used for blue-light cystoscopy as an adjunct to white-light cystoscopy for detection of non-muscle invasive bladder cancer in patients with suspected or known lesion(s). **(B)** White light mode (left side) and blue light mode (right side) images of bladder cancer simultaneously observed using twin mode monitor. Flat lesions show red florescence. **(C)** White light mode (left side) and blue light mode (right side) images of bladder neck using turned back flexible cystoscopy in a vertical direction. No red fluorescence observed [Intraoperative images courtesy of Fukuhara et al. (31)].

DERMATOLOGY

First Application in Clinical Dermatology

The first study investigating 5ALA in dermatology was published by Kennedy et al. (40). Though this study was designed to evaluate the role of 5ALA in photodynamic therapy, fluorescence was reported from tumor areas. In this study, 5ALA was applied topically in a 20% solution to basal cell carcinoma (BCC) lesions. After waiting 3 h, the lesions underwent light exposure. Their initial results were promising. In the first 80 lesions that were treated using this technique, 90% of the lesions had a complete response rate and 7.5% had a partial response rate following a single treatment (40). Significant interest in the dermatologic utility of 5ALA has steadily grown since the work of Kennedy et al.

Landmark 5ALA Studies in Dermatology

Szeimies et al. evaluated tissue localization of protoporphyrin (Pp IX) after topical application of ALA by measuring the fluorescence in different histological types of BCC lesions in 1994. These investigators used a 10% 5ALA and 10% CAB-OSIL M-5 (highly dispersed SiO2, CAB-OSIL Division, Cabot GmbH, Hanau, Germany) in propylene glycol ointment on fifteen patients with BCC lesions undergoing Mohs microsurgical resection (MMS). The area was bandaged after applying 5ALA ointment. Patients then underwent MMS 4–12 h after applying the 5ALA ointment. The control patients did not receive 5ALA prior to MMS. A microscope equipped with a 515–560 nm excitation filter was used during the MMS. The site of red fluorescence was compared to the histopathology. The results showed that tumors undergoing resection after waiting only 4 h had no significant fluorescence, whereas, tumors that underwent resection after 12 h showed a strong tumor-specific red fluorescence (10). These results differed from Kennedy et al. group who appreciated fluorescence of BCC tissue only after 3 h from the application of topical 5ALA. The optimal time required from the application of 5ALA to treatment was still unclear and further clinical studies were needed. The addition of solvents, such as Dimethyl sulfoxide (DMSO) and Ethylenediaminetetraacetic acid (EDTA) to the topical ointment was investigated by Peng et al. to determine if the use of these solvents can enhance the absorbability and specificity of 5ALA in tumor cells. They compared the topical application of 5ALA containing 20% 5ALA alone to 20% 5ALA plus 20% DMSO and 4% EDTA in patients with BCC lesions. They found that 5ALA alone was only located in the superficial layers in the lesion at 3 h post-application and both the penetration into the deeper parts of the lesion along with the degree of fluorescence was improved in the patients who received 20% 5ALA plus 20% DMSO and 4% EDTA after similarly evaluating lesions 3 h post-application. A 99% DMSO wash for 15 min prior to the application of 20% DMSO and 4% EDTA further enhanced the degree of penetration and fluorescence.

Despite apparent accumulation in tumors and improvement in surgical outcomes, 5ALA often showed poor delineation of tumors from normal tissue (41). Poor correlation often results from extension of the PpIX fluorescence beyond the true margins of the tumor and non-specific accumulation in benign lesions such as scars, sebaceous hyperplasia and others (42, 43). A few studies have shown that the accumulation of 5ALA in tumors with an intact epidermis which is usually seen in nodular BCC lesions is less compared to other types of BCC lesions that typical have epidermal ulcerations. This suggests that at the cellular level, the accumulation of 5ALA is not tumor specific but may be related to increased epidermal permeability and cellularity of tumors (44, 45). The use of esters

of ALA, such as Methyl-ALA (MAL) improved delineation and specificity of the BCC lesions most likely secondary to the increased permeability of the molecule (43, 46, 47). Liposome encapsulation of 5ALA further enhances the lipophilicity of 5ALA and requires less time for maximal fluorescence (∼2 h). Although better demarcation of non-melanotic skin lesions was found using liposome encapsulated 5ALA, the increased lipophilicity increases false positives due to the accumulation of Pp IX in sebaceous lesions, such as sebaceous hyperplasia along with viral warts, lichenoid inflammation and melanocytic nevi. Dense hairy areas also showed increased background fluorescence suggesting that this method is not suitable in regions with excess hair (42).

In addition to utility in BCC, topical 5ALA has also been found useful for the demarcation of squamous cell carcinomas (SCC) (48, 49). Delineation and complete excision of SCC lesions can be more challenging compared to BCC lesions due to its frequent irregular margins. Jeon et al. evaluated the use of 5ALA in delineating tumor margins in 64 patients undergoing MMS. Before the application of 5ALA, excessive crusts or scales were scraped off the lesion without causing bleeding and then the lesion cleaned with saline gauze. Nineteen patients received 20% 5ALA, 19 patients received 16% MAL and the remaining control patients did not receive a photosensitizer. The incubation period for the patients that received topical 5ALA was 6 h compared to 3 h for the patients received topical MAL. After the incubation period, a Wood lamp (ultraviolet examination light, model 31602, 356 nm; Burton Medical Products Corp., Chatsworth, CA) was used to determine the margins of the SCC lesion for MMS. The results showed that after MMS, the number of stages required for complete tumor removal was lower in the patients that received either 5ALA or MAL. There was no significant difference between 5ALA and MAL in terms of surgical benefits. A surgical benefit was not seen in all patients that had high-risk histologically SCC features, which may be due to irregular infiltrative patterns for these, PpIX may not penetrate the deeper layers and/or these cells do not produce as much PpIX compared to the cells with histologically low-risk SCC features (48).

Appropriate 5ALA Dose and Route of Administration in Dermatology

As discussed above, topical use is the most common application of 5ALA in dermatology. Prior studies have used 5ALA or methyl ALA, mixed with DMSO/EDTA and or liposomal ALA. Further clinical studies, however, are warranted to determine the optimal clinical dermatology agent that should be used.

Imaging 5ALA Fluorescence in Dermatology

Future development of imaging hardware and techniques to improve PpIX visualization and differentiation of abnormal tissue from normal tissue would be useful. Studies suggest auto-fluorescence is reduced within tumor cells with an excitation wavelength ∼370 nm and an emission wavelength around 455 nm which is different compared to normal tissue (50–52). A few studies have shown improved 5ALA demarcation of BCC lesions when measured in concert with reduced background auto-fluorescence (50–52).

Conclusions and Future Applications of 5ALA Fluorescence in Dermatology

Studies have shown improved surgical outcomes with the use of 5ALA in both photodynamic therapy and delineating tumor margins in MMS, especially in BCC lesions. Fewer studies to date have evaluated the use of 5ALA for SCC, though these studies have shown that 5ALA has potential for improve visualization of SCC. With a better understanding of the kinetics of 5ALA, along with advancements in imaging techniques, 5ALA-mediated visualization has potential for becoming standard practice in the treatment of BCC and SCC lesions, along with expanding use to other skin lesions such as melanoma (**Figure 3**).

OBSTETRICS AND GYNECOLOGY

First Application of 5ALA Imaging in OB/GYN

Use of 5ALA in gynecologic cases now covers a broad spectrum of procedures (54–56) since PpIX was shown to accumulate in endometrial cancer cells by Wyss-Desserich and colleagues at non-toxic doses in 1996 (57). In this study, fluorescence was observed *in vitro* with best results found at 1 mg/ml incubated for 24 h and excited at 488 nm.

There is variation with the amount of 5ALA induced PpIX fluorescence in endometrium throughout the menstrual cycle. Highest fluorescence values are seen in secretory endometrium, followed by hyperplastic endometrium. In atrophic and proliferative phase endometrium fluorescence intensity and rate are the lowest (58).

Landmark Studies and Appropriate 5ALA Dose/Route of Administration

Topical absorption of 5ALA is effective in patients with cervical neoplasia (CIN) II and III, as well as with lichen planus (55, 56). A cervical cap with 2–4 mL of 200 mg/ml 5ALA placed for 1.5 h demonstrates that dysplastic cervical tissue consistently has greater fluorescence than normal tissue. This persists at 1.5, 3, and 6 h after exposure (55). In Women with verified genital erosive lichen planus, 2 ml vaginal suppository of 6.25 mg/ml Hexyl 5-aminolevulinate applied for 3 h shows successful conversion and accumulation PpIX. Superficial fluorescence increases significantly in affected areas, and while this is not statistically significant at 30 min, it becomes so at 3 h. On microscopy, affected mucosa has strong fluorescence originating in submucosal inflammatory cells below the basal membrane (56).

Ovarian carcinoma is a good candidate for early detection with PpIX fluoroscopy as it commonly presents late in course and metastasizes. After initial tumor removal, second look operations can prevent recurrence. Intraperitoneal 5ALA solution given at a concentration of 30 mg/kg 5 h before laparoscopy has been evaluated as a route for administration and has shown systemic distribution comparable to oral/topical preparations. In a third

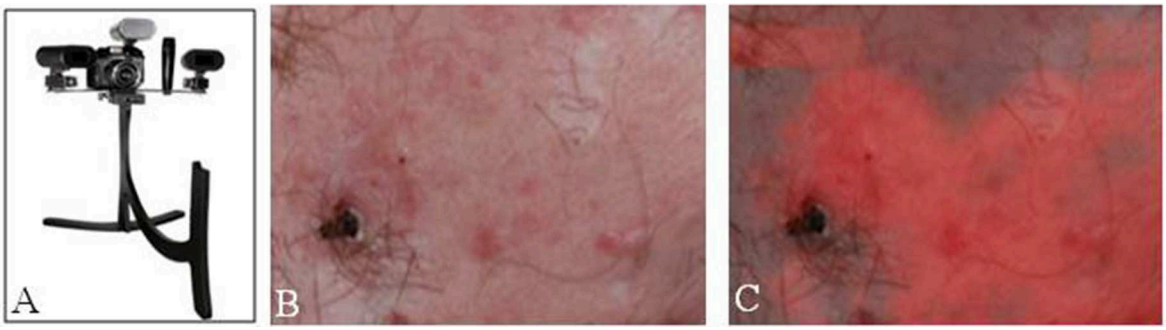

FIGURE 3 | Fluorescence imaging in dermatology. **(A)** Clearstone UV-DA, DigiMed Systems-Medical digital imaging system with ability to take ultraviolet photos. Courtesy of DigiMed Systems. **(B)** Brightfield illumination vs. **(C)** fluorescence-overlay imaging of a facial basal cell carcinoma. [Intraoperative images courtesy of Wan et al. (53)].

of patients with metastases seen at second look operations, PpIX fluorescence was able to detect tumor in a majority of cases that would otherwise have been missed with brightfield illumination alone (59).

5ALA has also been used to delineate peritoneal endometriosis, occasionally as an incidental finding. At doses as low as 10 mg/kg administered orally 4–5 h before laparoscopy there is increased concentration of PpIX fluorescence in peritoneal lesions. These lesions are typically difficult to visualize. 5ALA utility in OB/GYN is limited by increased PpIX concentration in fimbriae and tubal tissue with unknown effects on fertility (54).

Conclusion and Future Applications of 5ALA Fluorescence in OB/GYN

Overall these early studies have shown 5ALA-mediated fluorescence in abnormal ovarian, endometrial, peritoneum and vulva tissue (**Figure 4**). There is potential for widespread and standardized use of 5ALA in OB/GYN especially as it pertains to second look operations in ovarian carcinoma. Further clinical studies are warranted to determine the safety and efficacy of 5ALA-mediated tumor visualization in OB/GYN.

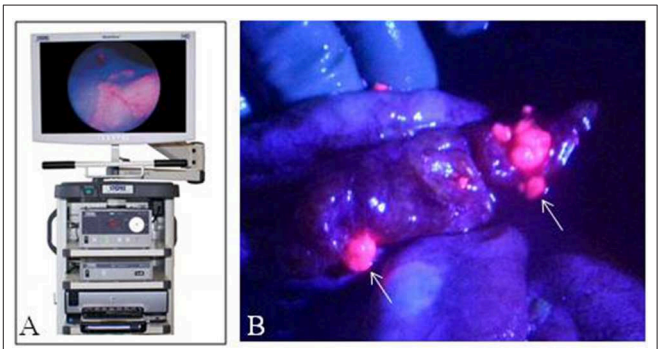

FIGURE 4 | Fluorescence imaging in obstetrics and gynecology. **(A)** Karl Storz D-Light fluorescence endoscopy system. **(B)** Laparoscopic image of peritoneum with ovarian cancer metastases with fluorescence-overlay imaging, Sote small fluorescent metastases (arrows) were histologically consistent with tumor. [Intraoperative images courtesy of Yonemura et al. (60)].

HEAD AND NECK SURGERY

First Application of 5ALA in Head and Neck Surgery

Identifying innovative approaches to labeling and visualizing the borders of oropharynx and laryngeal neoplasms is a significant area of interest in head and neck surgery. The incidence of these neoplasms has increased during the last 2–3 decades secondary to alcohol and tobacco abuse (61). Studies show that survival rates increase with early stage carcinomas; however, the diagnosis of a tumor at the primary stage can be challenging. Earlier researchers used toluidine blue staining and auto-fluorescence imaging to visualize these lesions. However, Sabes et al. found a high false positive and false negative rate with the use of toluidine blue for detecting oral lesions which limited its widespread use. Similarly, Leunig et al. found that autofluorescence between normal and malignant tissue varied significantly between patients. Therefore, toluidine blue staining and autofluorescence never became popular in clinical use. Leunig et al. investigated the local use of 5ALA in patients with head and neck tumors. In this study, 16 patients with histologically confirmed oral SCC were given an oral rinse of 200 mg 5ALA dissolved in 50 ml of mineral oil. A zero- degree endoscope (Art, Nr. 7200 A; Storz, Tuttlingen, Germany) with ultraviolet light filtered xenon-arc lamp system along with an optimal multichannel analyzer (O-SMA 3; SI Instruments, Gilching, Germany) was used to measure the fluorescence contrast between tumor and normal tissue. In all patients, protoporphyin IX fluorescence was detected and significantly higher in the tumor compared to the surrounding healthy tissue. Therefore, the use of oral 5ALA potentially represented a new method for the early detection of oral dysplastic and malignant lesions (61). This study's promising results initiated further research in the use of 5ALA in head and neck surgery.

Landmark 5ALA Studies in Head and Neck Surgery

Since the first paper evaluating the use of 5ALA in head and neck surgery in 1996, Leunig and other groups have continued to investigate the use of 5ALA in head and neck surgery. In 2000, Leunig et al. assessed the use of 5ALA for the detection of oral SCC in 58 patients. These patients rinsed with a 0.4% solution of 5ALA dissolved in mineral oil for 15 min while closely being supervised. After waiting for a 1 to 2.5 h period for incubation, biopsies were taken from red fluorescence areas presumed to represent tumor tissue along with tumor boundaries and normal tissue using a modified 0°degree endoscope equipped with a filter (OG515, Schott, Mainz, Germany). In this study, the topical use of 5 ALA had a sensitivity of 99% and a specificity of 60% in detecting oral squamous cell cancer and dysplasia with no direct side effects of 5 ALA. This study suggests 5ALA can be a useful tool in the early detection of oral malignancy, but further clinical studies were warranted (62). Zheng et al. later further evaluated the use of 5ALA in detecting oral cancer lesions. Their study included 49 patients with either clinically suspicious lesions or pathologically proven malignancies of the oral cavity. The patients rinsed with a 0.4% rinsing solution of 5 ALA dissolved in mineral oil for 15 min. After waiting for an incubation period of 1.5 to 2 h, all patients underwent fluorescence endoscopic-guided biopsies. The malignant and dysplastic histological findings closely correlated with PpIX fluorescence The sensitivity and specificity with the use of 5ALA for separating benign tissue from dysplasia was 92 and 96%, respectively. A sensitivity of 98% and a specificity of 96% was achieved in distinguishing carcinoma *in situ* from SCC with the use of 5ALA, and a sensitivity of 98% and specificity of 92% for distinguishing carcinoma *in situ* and squamous cell carcinoma from dysplasia was achieved with the use of 5ALA (63).

The use of 5ALA for distinguishing laryngeal CA from benign tissue has also been closely evaluated. Mehlmann et al. used a 5 ml 0.9% NaCl solution of 5ALA topically applied in 16 patients with suspected or histologically proven malignancies of the larynx via a nebulized inhaler 1–2 h prior to a microlarnyngoscopy. Microlaryngoscopy was performed through an optimized endoscope (Hopkins 0, Art. No. KSTEXB001-3 or 27005AI, Storz, Tuttlingen German) equipped with a special filter system (D-light, Art No. 20133201, Storz) that was attached to a footswitch that allowed switching between brightfield illumination and fluorescence imaging. Forty-five biopsies were taken. Areas of normal tissue appeared green in color whereas malignant sites showed a strong red fluorescence. The sensitivity and specificity of 5- ALA in separating normal tissue for malignant tissue was 95 and 80%, respectively (64). This was the first clinical study that showed 5ALA utility for the detection of laryngeal cancer. Csanady et al. later further investigated the use of 5ALA in detecting pharyngeal cancer. This study included 31 patients with either precancerous, malignant or benign lesions of the laryngeal or hypopharyngeal cavities. Patients received topical application of 1% 5ALA solution diluted with 0.9% saline solution via nebulizer. After a 1.5–2 h incubation period, fluorescence-guided endoscopic biopsies were performed. With the use of 5ALA, the sensitivity and specificity of detecting laryngeal and pharyngeal cancer from normal tissue was 96 and 76%, respectively. Hence, the laryngeal and hypopharyngeal tumors and their margins were found to be accurately outlined under fluorescence imaging showing the usefulness of 5ALA for intraoperative visualization of neoplastic tissue (65).

Visualizing the parathyroid gland while operating in a small space can be challenging, even for the most experienced surgeons (66). Methylene blue was initially used for identifying the parathyroid gland intraoperatively. However, its clinical use is limited as it is associated with serious side effects including: vascular pain, staining of the skin and urine, and neurological toxicity (66). This intrigued Prosst et al. to investigate the use of 5ALA in a 52 y.o female with refractory secondary hyperparathyroidism for identifying the parathyroid glands. The patient received 30 mg/kg of body weight of 5ALA dissolved in water given orally 4 h prior to surgery. After anterior cervical neck surgical exposure by an otolaryngologists, a 4 mm scope (30; Hopkins II; Karl Stortz CO) connected to D-light fluorescence system was brought into the operative field. Though the parathyroid glands were unable to be identified under white-light mode, they became clearly visible by their typical red fluorescence under 635 nm illumination. The patient did not experience any side effects from 5ALA (67). Suzuki et al. also investigated 5ALA's fluorescence in normal parathyroid glands in 13 patients with thyroid disease undergoing hemithyroidectomy. Patients were orally administered 20 mg/kg body weight of 5ALA dissolved in 10% glucose 5 h prior to surgery. After anterior neck exposure, the room was darkened and the incision was illuminated with a violet-blue light of 405 nm. In all 13 patients, parathyroid glands were easily identified by their red fluorescence, even when they could not be detected under normal light conditions (66). Takeuchi et al. further evaluated the use of 5ALA for identifying parathyroid gland tissue in 20 patients with primary hyperparathyroidism, 6 patients with secondary hyperparathyroidism, and 3 patients with thyroid tumors and normal parathyroid glands. All patients were administered oral 20 mg/kg 45 min to 5 h prior to surgery. In the majority of the cases, 5ALA accurately identified both normal and abnormal parathyroid glands (68).

Appropriate 5ALA Dose and Route of Administration

The preferred application of 5ALA fluorescence during head and neck surgeries depends on the area of surgical interest. For oral lesions, a 0.4% oral solution of 5ALA dissolved in mineral oil rinsed for 15 min followed by 1 to 2.5 h incubation prior to illumination is the most common regime used (61–63). A 0.4–1.0% 5ALA solution diluted with 0.9% saline topically applied via a nebulized inhaler with an incubation period of 1–2 h prior to a microlarnyngoscopy has been reported for oral and pharyngeal lesions (64, 65). Whereas, for parathyroid and thyroid surgery, 20–30 mg/kg of 5ALA given orally with an incubation period between 45 min to 5 h has been reported (66–68). The safety of 5ALA, regardless of the administration

route, has been questioned. Some studies suspected an increase in serum creatinine levels after 5ALA administration; however, this was refuted by Quon et al. when they concluded that the increased creatinine levels represented a false elevation due to substrate competition (69). Evidence in head and neck surgery shows that 5ALA is safe with little to no side effects, with the precaution to avoid sun exposure 24 to 48 h after ingesting 5ALA to avoid the risk of skin bleaching and other phototoxic effects on the skin and eyes (63, 70).

Imaging 5ALA Fluorescence in Head and Neck Surgery

At the molecular level, 5ALA is metabolized by neoplastic or highly metabolic tissues into protoporphyrin IX, a photosensitive metabolite that is excited between wavelengths 375–440 nm and subsequently emits fluorescence between 635 and 700n m (71). The use of an endoscope equipped with a special filter system attached to a footswitch that allows changing between brightfield illumination and fluorescence excitation is the preferred method for detecting the red fluorescence when 5ALA is applied in head and neck surgery.

Conclusions and Future Applications of 5ALA in Head and Neck Surgery

The above studies suggest that 5ALA has potential for improving the early detection of suspected oral and pharyngeal cancerous lesions and may reduce operative time and rate of reoperation in patients with parathyroid and thyroid disease. The disadvantage of 5ALA is the need for patients to avoid sun exposure 24 to 48 h after exposure to 5ALA. More clinical studies are needed to further validate the surgical benefits of 5ALA compared to routine surgery before the use of 5ALA can become FDA-approved for clinical practice in head and neck surgery.

GASTROINTESTINAL SURGERY

First Application of 5ALA in Gastrointestinal (GI) Surgery

The use of 5ALA for photodiagnosis in gastroenterology and gastrointestinal surgery, while broad and encompassing esophageal, gastric, hepatic, and colorectal pathologies, has not yet replaced established standard practice in this field. Interestingly, its first use was aimed at a predominantly preventive strategy during screening colonoscopies to identify mucosal adenomas with malignant potential. Although adenomas are benign, there is no method to distinguish between benign and malignant lesions by conventional colonoscopy. Therefore, Eker et al. (72) described the use of 5ALA to aid in the differentiation of mucosal tissue, potentially as a means to decrease cost and labor involved in removing benign lesions. Of 57 selected patients undergoing laser-induced fluorescence colonoscopy, 41 were ultimately included. Patients were given oral ALA at 5 mg/kg and underwent the study after 2–3 h. A nitrogen laser was tested at excitation wavelengths of 337, 504, and 436 nm. The excitation of tissues at 337 nm was used, as that wavelength yielded the maximum difference in emission between normal and adenomatous tissue. All patient groups were combined at the 337 nm wavelength, including patients who were treated with 5ALA and those who were not. When excited at 337 nm, the sensitivity for adenoma detection was 100% and the specificity was 96%. At the other wavelengths of 405 and 463 nm, the sensitivity and specificity were also higher for 5ALA-treated patients than those without.

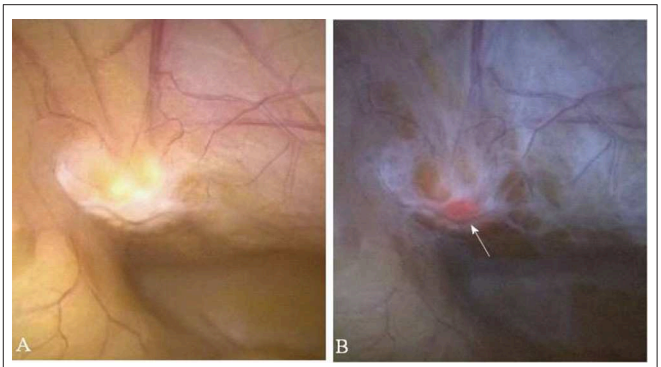

FIGURE 5 | Fluorescence imaging in Gastrointestinal Surgery. **(A)** Non-specific peritoneal area under white light illumination. **(B)** Corresponding fluorescence overlay image shows fluorescence foci histologically consistent with metastatic gastric cancer (arrow). Images obtained with Karl Storz D-light endoscope system. [Intraoperative images courtesy of Namikawa et al. (74)].

The application of 5ALA in predicting the malignant potential of dysplastic epithelial cells associated with ulcerative colitis also demonstrated an efficacious use of the fluorescent molecule. One group evaluated the use of 5ALA to enhance the detection of dysplastic tissue that may otherwise be missed from the conventional standard of care, which is four-quadrant random colon biopsies. In this study, 37 patients underwent 54 colonoscopies and received systemic oral ingestion, a local enema, or a local catheter-directed spray form of 5ALA. The local spray had the highest sensitivity of 100% for detecting malignant tissue. Overall, this serves as a promising modality to increase detection of dysplasia with a reduction of sampling error and unnecessary random biopsies (73).

Landmark 5ALA Studies in GI Surgery

Similar to its use for colorectal cancer, endoscopic 5ALA fluorescence has been explored as a surveillance method for detecting dysplastic, pre-malignant tissue of the esophagus (Barret's), and more recently, assisting in laparoscopy-guided resection of gastric and hepatic malignancies (**Figure 5**). These studies have highlighted the growing number of 5ALA applications in GI surgery while also demonstrating the mild, transient adverse reaction profile with oral administration.

Much of the data pertaining to the use of 5ALA is for the diagnosis and detection of dysplastic tissue in Barrett's esophagus during upper endoscopy. Barrett's esophagus is the replacement of normal esophageal epithelium (stratified squamous) to colonic epithelium (simple columnar), typically due to chronic exposure to acid reflux from the stomach. It is considered a premalignant lesion and requires endoscopic surveillance with biopsy. The

biopsy for Barrett's esophagus is extensive: it involves obtaining 4 random quadrant biopsies for every 2 cm length of the Barrett's esophagus. The tissue within Barrett's esophagus can be classified as a range: nondysplastic, low grade dysplasia, high grade dysplasia, to adenocarcinoma, but these cannot be distinguished by gross examination with standard endoscopy. Given the time and cost required to biopsy Barrett's esophagus via the conventional method, alternative methods are investigated to better pinpoint dysplastic lesions, such as the use of ALA.

Brand et al. (75) evaluated the use of 5ALA to identify dysplasia within Barrett's esophagus, high grade dysplasia in particular. Twenty patients with known Barrett's esophagus were given 5ALA at 10 mg/kg dissolved in orange juice 3 h prior to endoscopy. A nitrogen laser at excitation of 400 nm was used at a total of 97 mucosal sites. The use of 5ALA provided detection of high grade dysplasia from normal tissue at 77% sensitivity and 71% specificity. In nodular high grade dysplasia the sensitivity and specificity of 5ALA-mediated photodiagnosis approaches 100%. Although the use of fluorescence endoscopy may assist in identification of these high grade lesions, there is no definitive data that suggest its use is superior to random biopsies.

Stepinac et al. (76) performed a similar study investigating the fluorescence detection of dysplasia and early cancer in Barrett's esophagus using 20 mg/kg of 5ALA vs. conventional random four-quadrant biopsy. Twenty-eight patients with known Barrett's esophagus were selected for the study. All patients first underwent conventional endoscopy with random four quadrant biopsies at 1 cm intervals approximately 4–6 weeks prior to fluorescence endoscopy. A total of 532 biopsies were taken. During fluorescence endoscopy, a total of 178 biopsies were taken, 81 in fluorescent regions and 97 in non-fluorescent regions. The sensitivity and specificity of fluorescence-guided biopsies were 100 and 63%, respectively. Fluorescence endoscopy identified 5 low grade dysplasia lesions that were not identified by conventional biopsy. Conventional biopsy identified 3 low grade dysplasia lesions that were not detected during fluorescence endoscopy. Both the conventional and 5ALA methods were able to identify high grade dysplasia and adenocarcinoma, but neither is ideal for identification of low grade dysplasia. However, the use of ALA and fluorescence endoscopy may result in fewer biopsies needed to achieve the same diagnosis (81 biopsies vs. 531).

Although the incidence of gastric cancer has decreased overall, it remains one of the most common cancers worldwide. It commonly spreads by peritoneal seeding. The presence of peritoneal dissemination can alter the treatment decision-making between surgery and chemotherapy. In patients with locally advanced disease, performing a staging laparoscopy can help guide treatment. Staging laparoscopy has a sensitivity of ∼30–40% for peritoneal seeding. Kishi et al. (77) has evaluated the use of 5ALA to enhance the tumor detection rate in advanced gastric cancer. Thirteen patients with known gastric cancer were selected to undergo staging laparoscopy. They are given 1 g 5ALA 4 h prior to laparoscopy. The detection rate for metastatic lesions using 5ALA had a sensitivity of 93% and a specificity of 100%. However, there were inconsistencies in the detection of the primary tumors. Although all primary tumors with serosal invasion were detected, 5ALA failed to help identify two primary tumors without serosal invasion and two primary tumors with adjacent organ invasion. This emphasizes the limitation of the use of visible wavelength fluorescence imaging, for while it is useful in detecting surface tumors, it may not visualize tumors that are deeply embedded in tissue.

In 2017, Ushimaru et al. (78) performed 5ALA-assisted staging laparoscopy on 113 patients with advanced gastric cancer and based their treatment strategies on the results of the laparoscopy. They retrospectively evaluated the outcomes, and identified predictive factors for peritoneal metastasis. All patients were given 1 g 5ALA 3–5 h prior to laparoscopy. Observation of abdominal cavity using white light and blue light was done using the Storz D-light System laparoscope. Patients noted to have peritoneal metastasis and/or positive cytology, as diagnosed by 5ALA staging laparoscopy, underwent chemotherapy and an interval gastrectomy if a later laparoscopy revealed negative peritoneal disease. Those without metastasis or cytology underwent definitive gastrectomy during the same procedure. Patients with no peritoneal metastasis had a similar estimated survival than patients with peritoneal metastasis only seen with 5ALA. Factors that were predictive for metastasis were advanced T stage, diffuse-type histology, ascites, and female sex. This study suggests that the use of staging laparoscopy with 5ALA may enhance the diagnostic accuracy for advanced gastric cancer patients and thereby improve their overall treatment outcome.

5ALA-mediated photodiagnosis of hepatic tumors is currently being explored. Kaibori et al. (79) evaluated a total of 134 patients undergoing hepatic resections. They compared the utility of both 5ALA and Indocyanine Green for the intraoperative detection of tumors. Although Indocyanine Green had higher sensitivity of tumor detection (96% vs. 57%), the specificity of detection by 5ALA was 100%. One limitation of photodiagnosis for solid organ tumors is short distance of penetration. 5ALA mediated fluorescence only penetrates 2–5 mm of tissue, limiting its use to superficial tumors. The adverse effects, while transient and self-limited, may also deter patient participation.

A serious complication of hepatic resection is postoperative bile leak. Inoue et al. (80) evaluated 737 patients who underwent hepatic resections. Of these, 109 patients were given oral 1 g 5ALA dissolved in 20 ml of 50% glucose approximately 3 h prior to hepatic resection, which is excreted in the bile. Intraoperatively, patients were evaluated for leaks after resection, first by gross evaluation then by blue light (405 nm) illumination. Fluorescence imaging using 5ALA increased the intraoperative detection rate of bile leaks from 8.3 to 13.7%. Given the mildly increased detection rate, more studies will be needed to justify routine use of 5ALA.

Appropriate Dose of 5ALA and Route of Administration

The optimal dosing of 5ALA in the upper and lower GI tract did not vary significantly from that which was historically used in non-GI related malignancies. Since its earlier application for the photodiagnosis of colorectal (72, 73) and esophageal carcinoma (75, 76), oral administration of 5 and 10 mg/kg, respectively, demonstrated superior sensitivity and specificity in

identifying neoplastic tissue on par with that of tradition biopsy-based surveillance methods. Oral administration of even greater amounts of 5ALA up to 1 g for its more recent gastric and hepatic applications (77–80), including the fluorescence of post-resection bile leaks, has shown equal efficacy.

Conclusions and Future Applications of 5ALA in GI Surgery

Although there is promising data regarding the use of photodiagnosis in gastroenterology and general surgery, there lacks conclusive data to push its use into standard practice. More randomized control trials with larger patient samples are still needed at this time.

CARDIOTHORACIC SURGERY SECTION

First Application of 5ALA in Cardiothoracic Surgery

The first study examining 5ALA's ability to detect early stage lung cancer was published in 1996 by Baumgartner et al. (81). In this study, Baumgartner administered 5–10 wt% (250–500 mg 5ALA in 0.5 ml isotonic saline) through a medical nebulizer to 7 patients with positive or suspicious sputum cytology, but negative white light bronchoscopy, for inhalation for 30–40 min followed by fluorescence bronchoscopy after 3 h. An ultraviolet light with 406.7–413.5 nm was used for excitation. A target integrating color CCD video camera was adapted to the bronchoscope and captured emission wavelength of 635 nm and 705 nm. Baumgartner calculated that the amount of 5ALA inhaled within lung tissue was independent of patients' breathing patterns. Thus, patients can have a wide range of pulmonary function without concern for variability in 5ALA concentration. A peak plasma blood PpIX concentration was found at 3.5 h after inhalation. No side-effects were observed in the 7 patients. A total of 30 tissue samples were taken which showed nine tumors, including seven carcinoma *in situ*, by PpIX fluorescence. Sensitivity was 100% and specificity ranged from 30 to 50% due to five tissue samples exhibiting weak fluorescence with indeterminate diagnoses. This study showed that 5ALA inhalation was safe, could mediate detection of carcinoma *in situ* within lung tissue, and may be used to assist diagnosing early bronchial malignancies.

Follow-Up Study Using Inhaled 5ALA for Bronchial Tumors

Following Baumgartner's study of 7 patients, Piotrowski et al. performed a perspective feasibility study on safety and efficacy of 5ALA for diagnosing bronchial neoplasms (82). Forty-nine patients, divided into four groups, inhaled either 5 or 10 ml of 5ALA solution 3 h before bronchoscopy examination. Xenon short arc lamp with a special filter system was used for fluorescence excitation (λex = 375–440 nm) along with an integrated filter that blocked remitted excitation (long pass = 440 nm). Groups consisted of laryngo-tracheo-bronchial tumors that were previously diagnosed by conventional diagnostic modes ($n = 17$); patients with prior surgery due to bronchial tumors ($n = 6$), patients with prior surgery for laryngeal cancer ($n = 4$); and present or ex-heavy smokers without signs of tumor in conventional examinations ($n = 22$). There was no significant difference between pre and post FEV1 values. The overall sensitivity of 5ALA was 82% and specificity was 62% for all groups, PPV of 45% and NPV of 90%. When brightfield illumination (WLB) plus 5ALA was compared with brightfield alone, there was an increase in sensitivity by 2.1% and NPV by 6%, but decreased specificity by 35.4% and PPV by 53.1%. When the heavy smoker group was excluded (due to increased number of false positives), the WLB+5ALA sensitivity increased by 22% and NPV by 34%, whereas specificity decreased by 26% and PPV by 35%. Due to its higher sensitivity, 5ALA was able to identify recurrent SCC in one patient and a synchronous lesion in another patient that were WLB-negative. Because of the high number of false positive samples, authors concluded that 5ALA should not be used for screening. Rather in combination with WLB, it could be used to guide the physician in choosing proper sites for biopsy due to its higher sensitivity and NPV. Additionally, in this study 5ALA induced transient bronchial obstruction in 2 patients from the heavy smokers group that was reversed with short acting beta agonists.

5ALA Fluorescence for Staging Pleural Malignancies in Patients With Inconclusive Pleural Effusions

Thoracoscopy is often used in patients with negative pleural fluid examinations for staging of malignancies. However, some cases still remain undiagnosed or understaged (83). In 2006, Baas et al. in a feasibility study, incorporated fluorescence and white light inspection on 26 patients with non-diagnostic pleural effusions to test 5ALA's efficacy in diagnosing and staging of pleural malignancies. Three patients were excluded either due to multiple adhesions within thoracic cavity or inability to perform endoscopic inspection. Patients ingested a 2,000 to 2,500 mg capsule of 5ALA depending on body weight followed by thoracoscopy 3–4 h later. Fluorescence images were recorded using the D-LIGHT System with <500 nm for excitation and long-pass filter (470 nm long-pass). In 23 patients, a total of 111 biopsies were taken. Fifteen patients were diagnosed with malignant mesothelioma, 5 with metastases. Three patients had benign plaques and one with empyema. One patient who did not receive initial diagnosis developed mesothelioma 6 months later. A discrepancy between white light and 5ALA occurred in 37 biopsies and further analysis showed there was no improvement using 5ALA to obtain diagnosis. However, with 5ALA, 4 patients upstaged their diagnosis through detection of small lesions (<3 mm) throughout the parietal and visceral pleura as well as the collapsed lung. Complications occurred in 3 patients from thoracoscopy. No side-effects were reported using 5ALA besides grade 1 skin burn in 3 patients 28 to 36 h after 5ALA intake. Authors showed that 5ALA can help improve staging in patients with pleural malignancy and could help guide in choosing proper biopsy sites during thoracoscopy.

In another study of undiagnosed pleural effusions by Pikin et al. 23 patients with non-conclusive pleural effusions received 25 mg/kg of 5ALA 3 h before video-assisted bronchoscopy (84). A total of 118 biopsies were taken. Both white light and fluorescence thoracoscopy detected pleural deposits in 20 patients but fluorescence was able to detect additional lesions in 12 of the 20 patients. In three other patients with macroscopically normal pleura by white-light mode, 5ALA detected micrometastases in one patient that was metastatic lung adenocarcinoma by histological examination. Results from combined conventional and florescence thoracoscopy showed specificity of 88.4%, sensitivity of 89.1% and diagnostic accuracy of 88.9%—results much higher than other studies. Authors pointed out that detecting additional lesions in patients with macroscopic pleural spread does not influence outcome in the majority of cases. However, detection of pleural micometastases in patients with peripheral lung cancer and visceral pleural invasion could improve pre-operative approaches and possible outcomes.

Pharmacokinetics of Inhaled 5ALA for Optimum 5ALA-Induced Protoporphyrin IX Fluorescence in Bronchial Tissue

In Baumgartner et al.'s 1996 study, he first showed that 5ALA was safe for inhalation. In a follow-up study, Hautmann et al. examined *in vivo* kinetics of inhaled 5ALA that generate the greatest difference in fluorescence between tumor and adjacent bronchial tissue. Nineteen patients with known or suspected bronchial carcinoma are given 200 mg of 5ALA dissolved in 5 ml of isotonic NaCl via inhalation. Patients are then randomized to 1,2,3,4, or 6 h before bronchoscopy under local anesthesia.

Excitation wavelength of 380–440 nm was used and emission greater 630 nm, with a peak emission at 635, were measured using Optical Multichannel Analyzer (OMA). Spectroscopy was then analyzed on all macroscopically suspicious areas and areas showing porphyrin fluorescence. A total of 38 biopsies were taken that showed sensitivity that is almost twice that of white light, but with a significant decrease in specificity. This decrease in specificity was explained by the uptake of 5ALA by inflammatory lesions. Spectroscopy showed that normal tissue showed a maximum fluorescence 200 min after 5ALA application and lesions with moderate dysplasia at 160 min after 5ALA application. The spectral data showed significant difference between lesions with moderate dysplasia and normal, as well as lesions with moderate dysplasia and lesions with mild dysplasia 80 to 270 min after 5ALA inhalation. During this time interval, 5ALA fluorescence in lesions with moderate dysplasia can exhibit fluorescence values 5 times higher compared to the normal tissue. No difference was seen in lesions with mild dysplasia and normal tissue (85).

5ALA Facilitates Differentiation of Primary Lung Cancer With Pleural Invasion

Kitada et al. recruited a total of 40 patients diagnosed pre-operatively with lung cancer to undergo white light and 5ALA-mediated photodiagnosis. Patients consisted of 28 cases with primary lung cancer, 8 with metastatic lung tumors, 2 with malignant pleural tumors, and 2 with benign tumors. All lung metastases on the pleural surface, pleural malignant mesotheliomas and benign tumors were visualized under red fluorescence. For primary lung tumors, red fluorescence was confirmed in 15 of 28 patients (53.5%). All P11–P13 (ranging from tumor invading beyond elastic layer to tumors invading parietal pleura) tumors were visualized (10/10). However, visualization decreased to 5/18 (27.7%) for p10 cases (tumor within subpleural parenchyma or superficial invasion of pleural connective tissue). These 5 cases had been previously diagnosed as p11. Authors showed that 5ALA enhances accurate diagnosis of malignant lesions on the pleural surface as well as detection and localization of small disseminated lesions and small metastatic tumors to the lung (86).

Current Status and Future Directions of 5ALA in Cardiothoracic Surgery

Currently, 5ALA is still used as a research tool for photodynamic diagnosis in cardiothoracic surgery. Future direction of 5ALA includes a possible of direct comparison of brightfield vs. 5ALA-mediated fluorescence bronchoscopy in a randomized control trial to determine which yields higher sensitivity and/or specificity.

Conclusion

Clinical studies show 5ALA photodynamic diagnosis yields higher sensitivity but lower specificity in identifying lung and pleural malignancies. When added with conventional brightfield illumination, 5ALA can help visualize small primary tumors (<3 mm), small lung metastases and primary lung cancer with pleural invasions. 5ALA may prove useful for guiding surgeons to specific biopsy sites and in the upstaging of tumors.

DISCUSSION

The clinical use of fluorescent molecules dates back to the start of the twentieth century. Coined "Photodynamic Wirkung," or photodynamic phenomenon, European scientists first described how to utilize these molecules to macroscopically label abnormal tissue (87). While initially a conceptual application, this methodology has driven numerous oncologic investigations of naturally derived fluorescent molecules. Hematoporphyrin derivatives were introduced in the mid-twentieth century as potentially valuable diagnostic tools and treatment modalities. Early studies conducted by Lipson and colleagues (88) using rudimentary, yet novel, endoscopic devices to differentiate neoplastic cells from normal tissue further developed our understanding of hematoporphyrin derivatives in the surgical setting. Currently FDA-approved for its use is glioma surgery, 5ALA has undergone significant advances in its applications to include neurosurgical, head and neck, urological, cardiothoracic, gastrointestinal, and OB/GYN surgery. This historical review of clinical studies highlights the rapidly expanding role of 5ALA in the diagnosis and treatment of neoplastic disease.

Within each surgical field, studies have outlined the advantages and disadvantages 5ALA-mediated photodiagnosis. Due to its ubiquity in the heme synthesis pathway of all cells, and preferential accumulation of PpIX within neoplastic cells, the route and dosage of 5ALA has minimally varied. Intra-venous, oral, intra-peritoneal, intra-vaginal, inhaled, and topically administered 5ALA all demonstrate a similar optimal dosing (5–30 mg/kg), and often, dose-dependent responses. For many 5ALA applications, maximum dose are determined not by increased adverse reactions, but rather plateauing of sensitivity and specificity in neoplastic cell labeling. This phenomenon seems intuitive given 5ALA's role as a naturally occurring PpIX precursor. Studies have noted relatively benign and avoidable adverse reactions including bronchospasm with inhaled variants, and photosensitivity most prevalent with topical and oral administration of 5ALA. Regardless of route of administration, the sensitivity of 5ALA photodiagnosis has varied from 83% with low doses in urologic dysplasia to 100% for most other applications. Albeit rare, a notable disadvantage of using 5ALA is represented in its poor specificity in differentiating moderate dysplasia or cells exhibiting inflammatory changes from normal tissue or higher-grade dysplastic lesions. This limitation is most apparent in labeling urothelial carcinoma and BCC/SCC, resulting in high false positive rates due to epithelial hypercellularity or inadequate depth of topical penetration, respectively. In order to ameliorate non-specific labeling observed with these applications, the composition of 5ALA delivery systems (liposomal) and solvents (EDTA or DMSO) are continuing to be evaluated.

Imaging devices used to visualize 5ALA uptake and PpIX fluorescence are also advancing in their design and implementation. In early clinical applications of hematoporphyrin derivatives, such as PpIX, for malignancies of the upper GI and cardiopulmonary systems, a 400-watt mercury lamp transmitted white light via glass fiber cables through which excitatory (∼400 nm) wavelengths were separated by a quartz rod placed in a rigid bronchoscope (88). Using optical filters in the form of glasses or eye-shields, the surgeon would then visualize only red-fluorescence wavelengths corresponding to PpIX. Current-day fluorescence-guided surgery using commercially available wide-field microscopes is significantly less cumbersome and utilizes more sensitive short pass and long pass filters integrated within the system. Additional imaging hardware designs have aimed to improve on the historical limitations of using 5ALA in its various surgical contexts. While still investigational, newer imaging hardware optimizes the resolution of PpIX in either islands of neoplastic cells or areas of lower-grade lesions where PpIX fluorescence may not be as robust as that of higher-grade lesions. The largest obstacles toward this goal have been to mitigate signal-to-noise ratio of autofluorescent tissue and to achieve a greater sensitivity in localizing deep, labeled tissue (89).

Administration of 5ALA has granted surgeons within multiple subspecialties the ability to more accurately visualize malignant tissue during surgery. The vast data from studies collected during the past 6–7 decades is representative of 5ALA's small side effect profile and reliable efficacy. The growth of 5ALA's intraoperative applications during this timeframe has been paralleled by advancements in imaging technology focused on improving PpIX visualization. These clinical trials suggest 5ALA is a relatively safe molecule for generating intraoperative photodiagnosis of malignant tissues across multiple surgical-oncology subspecialties.

AUTHOR CONTRIBUTIONS

JG, AV, HW, AB, MK, SC, ZA-A, MB, HO, JI, SYu, and CL wrote key portions of the manuscript and created the figures. DA, JL, PN, KB, and SYo oversaw the writing process, provided mentorship, edited, and contributed to manuscript.

FUNDING

Funding for this manuscript was provided by the Philadelphia College of Osteopathic Medicine, Department of Neurosurgery and Center for Chronic Disorders of Aging (CCDA).

REFERENCES

1. Mooney MA, Zehri AH, Georges JF, Nakaji P. Laser scanning confocal endomicroscopy in the neurosurgical operating room: a review and discussion of future applications. *Neurosurg Focus*. (2014) 36:E9. doi: 10.3171/2013.11.FOCUS13484
2. Hadjipanayis CG, Stummer W. 5-ALA and FDA approval for glioma surgery. *J Neurooncol*. (2019) 141:479–86. doi: 10.1007/s11060-019-03098-y
3. Neuberger A, Scott JJ. Aminolaevulinic acid and porphyrin biosynthesis. *Nature*. (1953) 172:1093–4. doi: 10.1038/1721093a0
4. Schiffmann E, Shemin D. Further studies on the utilization of delta-aminolevulinic acid for porphyrin synthesis. *J Biol Chem*. (1957) 225:623–8.
5. Granick S. Porphyrin biosynthesis in erythrocytes. I. Formation of gamma-aminolevulinic acid in erythrocytes. *J Biol Chem*. (1958) 232:1101–17.
6. Granick S, Mauzerall D. Pbrphyrin biosynthesis in erythrocytes. II. Enzymes converting gamma-aminolevulinic acid to coproporphyrinogen. *J Biol Chem*. (1958) 232:1119–40.
7. Berlin NI, Neuberger A, Scott JJ. The metabolism of delta -aminolaevulic acid. 1. Normal pathways, studied with the aid of 15N. *Biochem J*. (1956) 64:80–90. doi: 10.1042/bj0640080
8. Kriegmair M, Baumgartner R, Knuchel R, Ehsan A, Steinbach P, Lumper W, et al. [Photodynamic diagnosis of urothelial neoplasms after intravesicular instillation of 5-aminolevulinic acid]. *Urologe A*. (1994) 33:270–5.
9. Kriegmair M, Baumgartner R, Knuechel R, Steinbach P, Ehsan A, Lumper W, et al. Fluorescence photodetection of neoplastic urothelial lesions following intravesical instillation of 5-aminolevulinic acid. *Urology*. (1994) 44:836–41. doi: 10.1016/S0090-4295(94)80167-3
10. Szeimies RM, Sassy T, Landthaler M. Penetration potency of topical applied delta-aminolevulinic acid for photodynamic therapy of basal cell carcinoma. *Photochem Photobiol*. (1994) 59:73–6. doi: 10.1111/j.1751-1097.1994.tb05003.x
11. Stummer W, Stocker S, Wagner S, Stepp H, Fritsch C, Goetz C, et al. Intraoperative detection of malignant gliomas by 5-aminolevulinic acid-induced porphyrin fluorescence. *Neurosurgery*. (1998) 42:518–25.
12. Stummer W, Novotny A, Stepp H, Goetz C, Bise K, Reulen HJ. Fluorescence-guided resection of glioblastoma multiforme by using 5-aminolevulinic

acid-induced porphyrins: a prospective study in 52 consecutive patients. *J Neurosurg*. (2000) 93:1003–13. doi: 10.3171/jns.2000.93.6.1003
13. Stummer W, Pichlmeier U, Meinel T, Wiestler OD, Zanella F, Reulen HJ, et al. Fluorescence-guided surgery with 5-aminolevulinic acid for resection of malignant glioma: a randomised controlled multicentre phase III trial. *Lancet Oncol*. (2006) 7:392–401. doi: 10.1016/S1470-2045(06)70665-9
14. Coburger J, Engelke J, Scheuerle A, Thal DR, Hlavac M, Wirtz CR, et al. Tumor detection with 5-aminolevulinic acid fluorescence and Gd-DTPA-enhanced intraoperative MRI at the border of contrast-enhancing lesions: a prospective study based on histopathological assessment. *Neurosurg Focus*. (2014) 36:E3. doi: 10.3171/2013.11.FOCUS13463
15. Stummer W, Stepp H, Wiestler OD, Pichlmeier U. Randomized, prospective double-blinded study comparing 3 different doses of 5-aminolevulinic acid for fluorescence-guided resections of malignant gliomas. *Neurosurgery*. (2017) 81:230–9. doi: 10.1093/neuros/nyx074
16. Eljamel S, Petersen M, Valentine R, Buist R, Goodman C, Moseley H, et al. Comparison of intraoperative fluorescence and MRI image guided neuronavigation in malignant brain tumours, a prospective controlled study. *Photodiagn Photodyn Ther*. (2013) 10:356–61. doi: 10.1016/j.pdpdt.2013.03.006
17. Loh CS, MacRobert AJ, Bedwell J, Regula J, Krasner N, Bown SG. Oral versus intravenous administration of 5-aminolaevulinic acid for photodynamic therapy. *Br J Cancer*. (1993) 68:41–51. doi: 10.1038/bjc.1993.284
18. Kriss TC, Kriss VM. History of the operating microscope: from magnifying glass to microneurosurgery. *Neurosurgery*. (1998) 42:899–907. doi: 10.1097/00006123-199804000-00116
19. Belloch JP, Rovira V, Llacer JL, Riesgo PA, Cremades A. Fluorescence-guided surgery in high grade gliomas using an exoscope system. *Acta Neurochir*. (2014) 156:653–60. doi: 10.1007/s00701-013-1976-6
20. Piquer J, Llacer JL, Rovira V, Riesgo P, Rodriguez R, Cremades A. Fluorescence-guided surgery and biopsy in gliomas with an exoscope system. *BioMed Res Int*. (2014) 2014:207974. doi: 10.1155/2014/207974
21. Widhalm G, Wolfsberger S, Minchev G, Woehrer A, Krssak M, Czech T, et al. 5-Aminolevulinic acid is a promising marker for detection of anaplastic foci in diffusely infiltrating gliomas with nonsignificant contrast enhancement. *Cancer*. (2010) 116:1545–52. doi: 10.1002/cncr.24903
22. Widhalm G, Kiesel B, Woehrer A, Traub-Weidinger T, Preusser M, Marosi C, et al. 5-Aminolevulinic acid induced fluorescence is a powerful intraoperative marker for precise histopathological grading of gliomas with non-significant contrast-enhancement. *PloS ONE*. (2013) 8:e76988. doi: 10.1371/journal.pone.0076988
23. Valdes PA, Jacobs V, Harris BT, Wilson BC, Leblond F, Paulsen KD, et al. Quantitative fluorescence using 5-aminolevulinic acid-induced protoporphyrin IX biomarker as a surgical adjunct in low-grade glioma surgery. *J Neurosurg*. (2015) 123:771–80. doi: 10.3171/2014.12.JNS14391
24. Valdes PA, Bekelis K, Harris BT, Wilson BC, Leblond F, Kim A, et al. 5-Aminolevulinic acid-induced protoporphyrin IX fluorescence in meningioma: qualitative and quantitative measurements *in vivo*. *Neurosurgery*. (2014) 10(Suppl. 1):74–82. doi: 10.1227/NEU.0000000000000117
25. Coluccia D, Fandino J, Fujioka M, Cordovi S, Muroi C, Landolt H. Intraoperative 5-aminolevulinic-acid-induced fluorescence in meningiomas. *Acta Neurochir (Wien)*. (2010) 152:1711–9. doi: 10.1007/s00701-010-0708-4
26. Eljamel MS, Leese G, Moseley H. Intraoperative optical identification of pituitary adenomas. *J Neurooncol*. (2009) 92:417–21. doi: 10.1007/s11060-009-9820-9
27. Stummer W, Tonn JC, Goetz C, Ullrich W, Stepp H, Bink A, et al. 5-Aminolevulinic acid-derived tumor fluorescence: the diagnostic accuracy of visible fluorescence qualities as corroborated by spectrometry and histology and postoperative imaging. *Neurosurgery*. (2014) 74:310–9. doi: 10.1227/NEU.0000000000000267
28. Roberts DW, Olson JD, Evans LT, Kolste KK, Kanick SC, Fan X, et al. Red-light excitation of protoporphyrin IX fluorescence for subsurface tumor detection. *J Neurosurg*. (2018) 128:1690–7. doi: 10.3171/2017.1.JNS162061
29. Inoue K, Anai S, Fujimoto K, Hirao Y, Furuse H, Kai F, et al. Oral 5-aminolevulinic acid mediated photodynamic diagnosis using fluorescence cystoscopy for non-muscle-invasive bladder cancer: a randomized, double-blind, multicentre phase II/III study. *Photodiagn Photodyn Ther*. (2015) 12:193–200. doi: 10.1016/j.pdpdt.2015.03.008
30. Inoue K, Matsuyama H, Fujimoto K, Hirao Y, Watanabe H, Ozono S, et al. The clinical trial on the safety and effectiveness of the photodynamic diagnosis of non-muscle-invasive bladder cancer using fluorescent light-guided cystoscopy after oral administration of 5-aminolevulinic acid (5-ALA). *Photodiagn Photodyn Ther*. (2016) 13:91–6. doi: 10.1016/j.pdpdt.2015.12.011
31. Fukuhara H, Kureishi M, Khoda T, Inoue K, Tanaka T, Iketani K, et al. The utility of a flexible fluorescence-cystoscope with a twin mode monitor for the 5-Aminolevulinic acid-mediated photodynamic diagnosis of bladder cancer. *PloS ONE*. (2015) 10:e0136416. doi: 10.1371/journal.pone.0136416
32. Colombo R, Naspro R, Bellinzoni P, Fabbri F, Guazzoni G, Scattoni V, et al. Photodynamic diagnosis for follow-up of carcinoma *in situ* of the bladder. *Ther Clin Risk Manage*. (2007) 3:1003–7.
33. D'Hallewin MA, Vanherzeele H, Baert L. Fluorescence detection of flat transitional cell carcinoma after intravesical instillation of aminolevulinic acid. *Am J Clin Oncol*. (1998) 21:223–5. doi: 10.1097/00000421-199806000-00002
34. Frimberger D, Zaak D, Hofstetter A. Endoscopic fluorescence diagnosis and laser treatment of transitional cell carcinoma of the bladder. *Semin Urol Oncol*. (2000) 18:264–72.
35. Kriegmair M, Baumgartner R, Knuchel R, Stepp H, Hofstadter F, Hofstetter A. Detection of early bladder cancer by 5-aminolevulinic acid induced porphyrin fluorescence. *J Urol*. (1996) 155:105–9. doi: 10.1097/00005392-199601000-00038
36. Osman E, Alnaib Z, Kumar N. Photodynamic diagnosis in upper urinary tract urothelial carcinoma: a systematic review. *Arab J Urol*. (2017) 15:100–9. doi: 10.1016/j.aju.2017.01.003
37. Spiess PE, Grossman HB. Fluorescence cystoscopy: is it ready for use in routine clinical practice? *Curr Opin Urol*. (2006) 16:372–6. doi: 10.1097/01.mou.0000240312.16324.9a
38. Draga RO, Grimbergen MC, Kok ET, Jonges TN, Bosch JL. Predictors of false positives in 5-aminolevulinic acid-induced photodynamic diagnosis of bladder carcinoma: identification of patient groups that may benefit most from highly specific optical diagnostics. *Urology*. (2009) 74:851–6. doi: 10.1016/j.urology.2009.04.095
39. Kata SG, Aboumarzouk OM, Zreik A, Somani B, Ahmad S, Nabi G, et al. Photodynamic diagnostic ureterorenoscopy: a valuable tool in the detection of upper urinary tract tumour. *Photodiagn Photodyn Ther*. (2016) 13:255–60. doi: 10.1016/j.pdpdt.2015.08.002
40. Kennedy JC, Pottier RH, Pross DC. Photodynamic therapy with endogenous protoporphyrin IX: basic principles and present clinical experience. *J Photochem Photobiol B Biol*. (1990) 6:143–8. doi: 10.1016/1011-1344(90)85083-9
41. Fritsch C, Becker-Wegerich PM, Menke H, Ruzicka T, Goerz G, Olbrisch RR. Successful surgery of multiple recurrent basal cell carcinomas guided by photodynamic diagnosis. *Aesthetic Plastic Surg*. (1997) 21:437–9. doi: 10.1007/s002669900153
42. de Leeuw J, van der Beek N, Neugebauer WD, Bjerring P, Neumann HA. Fluorescence detection and diagnosis of non-melanoma skin cancer at an early stage. *Lasers Surg Med*. (2009) 41:96–103. doi: 10.1002/lsm.20739
43. Redondo P, Marquina M, Pretel M, Aguado L, Iglesias ME. Methyl-ALA-induced fluorescence in photodynamic diagnosis of basal cell carcinoma prior to Mohs micrographic surgery. *Arch Dermatol*. (2008) 144:115–7. doi: 10.1001/archdermatol.2007.3
44. Martin A, Tope WD, Grevelink JM, Starr JC, Fewkes JL, Flotte TJ, et al. Lack of selectivity of protoporphyrin IX fluorescence for basal cell carcinoma after topical application of 5-aminolevulinic acid: implications for photodynamic treatment. *Arch Dermatol Res*. (1995) 287:665–74. doi: 10.1007/BF00371740
45. Ericson MB, Sandberg C, Gudmundson F, Rosen A, Larko O, Wennberg AM. Fluorescence contrast and threshold limit: implications for photodynamic diagnosis of basal cell carcinoma. *J Photochem Photobiol B Biol*. (2003) 69:121–7. doi: 10.1016/S1011-1344(02)00413-X
46. Fritsch C, Homey B, Stahl W, Lehmann P, Ruzicka T, Sies H. Preferential relative porphyrin enrichment in solar keratoses upon topical application of delta-aminolevulinic acid methylester. *Photochem Photobiol*. (1998) 68:218–21. doi: 10.1111/j.1751-1097.1998.tb02492.x

47. Tierney E, Petersen J, Hanke CW. Photodynamic diagnosis of tumor margins using methyl aminolevulinate before Mohs micrographic surgery. *J Am Acad Dermatol*. (2011) 64:911–8. doi: 10.1016/j.jaad.2010.03.045
48. Jeon SY, Kim KH, Song KH. Efficacy of photodynamic diagnosis-guided Mohs micrographic surgery in primary squamous cell carcinoma. *Dermatol Surg*. (2013) 39:1774–83. doi: 10.1111/dsu.12359
49. Pugliano-Mauro M, Goldman G. Mohs surgery is effective for high-risk cutaneous squamous cell carcinoma. *Dermatol Surg*. (2010) 36:1544–53. doi: 10.1111/j.1524-4725.2010.01576.x
50. Stenquist B, Ericson MB, Strandeberg C, Molne L, Rosen A, Larko O, et al. Bispectral fluorescence imaging of aggressive basal cell carcinoma combined with histopathological mapping: a preliminary study indicating a possible adjunct to Mohs micrographic surgery. *Br J Dermatol*. (2006) 154:305–9. doi: 10.1111/j.1365-2133.2005.07035.x
51. Andersson-Engels S, Canti G, Cubeddu R, Eker C, af Klinteberg C, Pifferi A, et al. Preliminary evaluation of two fluorescence imaging methods for the detection and the delineation of basal cell carcinomas of the skin. *Lasers Surg Med*. (2000) 26:76–82. doi: 10.1002/(SICI)1096-9101(2000)26:1<76::AID-LSM11>3.0.CO;2-4
52. Na R, Stender IM, Wulf HC. Can autofluorescence demarcate basal cell carcinoma from normal skin? A comparison with protoporphyrin IX fluorescence. *Acta Dermato Venereol*. (2001) 81:246–9. doi: 10.1080/00015550152572859
53. Wan MT, Lin JY. Current evidence and applications of photodynamic therapy in dermatology. *Clin Cosmet Investig Dermatol*. (2014) 7:145–63. doi: 10.2147/CCID.S35334
54. Hillemanns P, Weingandt H, Stepp H, Baumgartner R, Xiang W, Korell M. Assessment of 5-aminolevulinic acid-induced porphyrin fluorescence in patients with peritoneal endometriosis. *Am J Obstetr Gynecol*. (2000) 183:52–7. doi: 10.1067/mob.2000.105897
55. Keefe KA, Chahine EB, DiSaia PJ, Krasieva TB, Lin F, Berns MW, et al. Fluorescence detection of cervical intraepithelial neoplasia for photodynamic therapy with the topical agents 5-aminolevulinic acid and benzoporphyrin-derivative monoacid ring. *Am J Obstetr Gynecol*. (2001) 184:1164–9. doi: 10.1067/mob.2001.113123
56. Helgesen AL, Gjersvik P, Peng Q, Vasovic V, Pripp AH, Jebsen P, et al. Biodistribution of protoporphyrin IX in female genital erosive lichen planus after topical application of hexaminolevulinate. *Photodiagn Photodyn Ther*. (2014) 11:113–7. doi: 10.1016/j.pdpdt.2014.01.005
57. Wyss-Desserich MT, Sun CH, Wyss P, Kurlawalla CS, Haller U, Berns MW, et al. Accumulation of 5-aminolevulinic acid-induced protoporphyrin IX in normal and neoplastic human endometrial epithelial cells. Biochem Biophys *Res Commun*. (1996) 224:819–24. doi: 10.1006/bbrc.1996.1106
58. Degen A, Gabrecht T, Wagnieres G, Caduff R, Imthurn B, Wyss P. Influence of the menstrual cycle on aminolevulinic acid induced protoporphyrin IX fluorescence in the endometrium: *in vivo* study. *Lasers Surg Med*. (2005) 36:234–7. doi: 10.1002/lsm.20139
59. Loning M, Diddens H, Kupker W, Diedrich K, Huttmann G. Laparoscopic fluorescence detection of ovarian carcinoma metastases using 5-aminolevulinic acid-induced protoporphyrin IX. *Cancer*. (2004) 100:1650–6. doi: 10.1002/cncr.20155
60. Yonemura Y, Endo Y, Canbay E, Liu Y, Ishibashi H, Mizumoto A, et al. Photodynamic detection of peritoneal metastases using 5-Aminolevulinic acid (ALA). *Cancers (Basel)*. (2017) 9:23. doi: 10.3390/cancers9030023
61. Leunig A, Rick K, Stepp H, Gutmann R, Alwin G, Baumgartner R, et al. Fluorescence imaging and spectroscopy of 5-aminolevulinic acid induced protoporphyrin IX for the detection of neoplastic lesions in the oral cavity. *Am J Surg*. (1996) 172:674–7. doi: 10.1016/S0002-9610(96)00312-1
62. Leunig A, Betz CS, Mehlmann M, Stepp H, Arbogast S, Grevers G, et al. Detection of squamous cell carcinoma of the oral cavity by imaging 5-aminolevulinic acid-induced protoporphyrin IX fluorescence. *Laryngoscope*. (2000) 110:78–83. doi: 10.1097/00005537-200001000-00015
63. Zheng W, Olivo M, Soo KC. The use of digitized endoscopic imaging of 5-ALA-induced PPIX fluorescence to detect and diagnose oral premalignant and malignant lesions *in vivo*. *Int J Cancer*. (2004) 110:295–300. doi: 10.1002/ijc.20080
64. Mehlmann M, Betz CS, Stepp H, Arbogast S, Baumgartner R, Grevers G, et al. Fluorescence staining of laryngeal neoplasms after topical application of 5-aminolevulinic acid: preliminary results. *Lasers Surg Med*. (1999) 25:414–20. doi: 10.1002/(SICI)1096-9101(1999)25:5<414::AID-LSM8>3.0.CO;2-E
65. Csanady M, Kiss JG, Ivan L, Jori J, Czigner J. ALA (5-aminolevulinic acid)-induced protoporphyrin IX fluorescence in the endoscopic diagnostic and control of pharyngo-laryngeal cancer. *Eur Arch otorhinolaryngol*. (2004) 261:262–6. doi: 10.1007/s00405-003-0660-5
66. Suzuki T, Numata T, Shibuya M. Intraoperative photodynamic detection of normal parathyroid glands using 5-aminolevulinic acid. *Laryngoscope*. (2011) 121:1462–6. doi: 10.1002/lary.21857
67. Prosst RL, Gahlen J, Schnuelle P, Post S, Willeke F. Fluorescence-guided minimally invasive parathyroidectomy: a novel surgical therapy for secondary hyperparathyroidism. *Am J Kidney Dis*. (2006) 48:327–31. doi: 10.1053/j.ajkd.2006.05.002
68. Shahaf G, Pratt H. Thorough specification of the neurophysiologic processes underlying behavior and of their manifestation in EEG - demonstration with the go/no-go task. *Front Hum Neurosci*. (2013) 7:305. doi: 10.3389/fnhum.2013.00305
69. Quon H, Grossman CE, King RL, Putt M, Donaldson K, Kricka L, et al. Interference with the Jaffe method for creatinine following 5-aminolevulinic acid administration. *Photodiagn Photodyn Ther*. (2010) 7:268–74. doi: 10.1016/j.pdpdt.2010.07.008
70. Takeuchi S, Shimizu K, Shimizu K Jr, Akasu H, Okamura R. Identification of pathological and normal parathyroid tissue by fluorescent labeling with 5-aminolevulinic acid during endocrine neck surgery. *J Nippon Med Sch*. (2014) 81:84–93. doi: 10.1272/jnms.81.84
71. Betz CS, Stepp H, Janda P, Arbogast S, Grevers G, Baumgartner R, et al. A comparative study of normal inspection, autofluorescence and 5-ALA-induced PPIX fluorescence for oral cancer diagnosis. *Int J Cancer*. (2002) 97:245–52. doi: 10.1002/ijc.1596
72. Eker C, Montan S, Jaramillo E, Koizumi K, Rubio C, Andersson-Engels S, et al. Clinical spectral characterisation of colonic mucosal lesions using autofluorescence and delta aminolevulinic acid sensitisation. *Gut*. (1999) 44:511–8. doi: 10.1136/gut.44.4.511
73. Messmann H, Endlicher E, Freunek G, Rummele P, Scholmerich J, Knuchel R. Fluorescence endoscopy for the detection of low and high grade dysplasia in ulcerative colitis using systemic or local 5-aminolaevulinic acid sensitisation. *Gut*. (2003) 52:1003–7. doi: 10.1136/gut.52.7.1003
74. Namikawa T, Yatabe T, Inoue K, Shuin T, Hanazaki K. Clinical applications of 5-aminolevulinic acid-mediated fluorescence for gastric cancer. *World J Gastroenterol*. (2015) 21:8769–75. doi: 10.3748/wjg.v21.i29.8769
75. Brand S, Wang TD, Schomacker KT, Poneros JM, Lauwers GY, Compton CC, et al. Detection of high-grade dysplasia in Barrett's esophagus by spectroscopy measurement of 5-aminolevulinic acid-induced protoporphyrin IX fluorescence. *Gastrointest Endosc*. (2002) 56:479–87. doi: 10.1067/mge.2002.128172
76. Stepinac T, Felley C, Jornod P, Lange N, Gabrecht T, Fontolliet C, et al. Endoscopic fluorescence detection of intraepithelial neoplasia in Barrett's esophagus after oral administration of aminolevulinic acid. *Endoscopy*. (2003) 35:663–8. doi: 10.1055/s-2003-41514
77. Kishi K, Fujiwara Y, Yano M, Inoue M, Miyashiro I, Motoori M, et al. Staging laparoscopy using ALA-mediated photodynamic diagnosis improves the detection of peritoneal metastases in advanced gastric cancer. *J Surg Oncol*. (2012) 106:294–8. doi: 10.1002/jso.23075
78. Ushimaru Y, Fujiwara Y, Kishi K, Sugimura K, Omori T, Moon JH, et al. Prognostic significance of basing treatment strategy on the results of photodynamic diagnosis in advanced gastric cancer. *Ann Surg Oncol*. (2017) 24:983–9. doi: 10.1245/s10434-016-5660-y
79. Kaibori M, Matsui K, Ishizaki M, Iida H, Okumura T, Sakaguchi T, et al. Intraoperative detection of superficial liver tumors by fluorescence imaging using indocyanine green and 5-aminolevulinic acid. *Anticancer Res*. (2016) 36:1841–9.
80. Inoue Y, Tanaka R, Komeda K, Hirokawa F, Hayashi M, Uchiyama K. Fluorescence detection of malignant liver tumors using 5-aminolevulinic acid-mediated photodynamic diagnosis: principles, technique, and clinical experience. *World J Surg*. (2014) 38:1786–94. doi: 10.1007/s00268-014-2463-9

81. Baumgartner R, Huber RM, Schulz H, Stepp H, Rick K, Gamarra F, et al. Inhalation of 5-aminolevulinic acid: a new technique for fluorescence detection of early stage lung cancer. *J Photochem Photobiol B Biol*. (1996) 36:169–74. doi: 10.1016/S1011-1344(96)07365-4
82. Piotrowski WJ, Marczak J, Nawrocka A, Antczak A, Gorski P. Inhalations of 5-ALA in photodynamic diagnosis of bronchial cancer. *Monaldi Arch Chest Dis*. (2004) 61:86–93. doi: 10.4081/monaldi.2004.705
83. Baas P, Triesscheijn M, Burgers S, van Pel R, Stewart F, Aalders M. Fluorescence detection of pleural malignancies using 5-aminolaevulinic acid. *Chest*. (2006) 129:718–24. doi: 10.1378/chest.129.3.718
84. Pikin O, Filonenko E, Mironenko D, Vursol D, Amiraliev A. Fluorescence thoracoscopy in the detection of pleural malignancy. *Eur J Cardiothoracic Surg*. (2012) 41:649–52. doi: 10.1093/ejcts/ezr086
85. Hautmann H, Pichler JP, Stepp H, Baumgartner R, Gamarra F, Huber RM. *In-vivo* kinetics of inhaled 5-aminolevulinic acid-induced protoporphyrin IX fluorescence in bronchial tissue. *Respir Res*. (2007) 8:33. doi: 10.1186/1465-9921-8-33
86. Kitada M, Ohsaki Y, Matsuda Y, Hayashi S, Ishibashi K. Photodynamic diagnosis of pleural malignant lesions with a combination of 5-aminolevulinic acid and intrinsic fluorescence observation systems. *BMC Cancer*. (2015) 15:174. doi: 10.1186/s12885-015-1194-0
87. Moghissi K, Dixon K, Gibbins S. A surgical view of photodynamic therapy in oncology: a review. *Surg J*. (2015) 1:e1–15. doi: 10.1055/s-0035-1565246
88. Lipson RL, Baldes EJ, Olsen AM. Hematoporphyrin derivative: a new aid for endoscopic detection of malignant disease. *J Thoracic Cardiovasc Surg*. (1961) 42:623–9.
89. Hosek JE, Todd KS Jr, Kuhlenschmidt MS. Improved method for high-yield excystation and purification of infective sporozoites of *Eimeria* spp. *J Protozool*. (1988) 35:583–9. doi: 10.1111/j.1550-7408.1988.tb04156.x

Conflict of Interest Statement: The authors declare that the research was conducted in the absence of any commercial or financial relationships that could be construed as a potential conflict of interest.

frontiers in Oncology

ORIGINAL RESEARCH
published: 06 September 2019
doi: 10.3389/fonc.2019.00830

Fluorescence Diagnosis in Neurooncology: Retrospective Analysis of 653 Cases

Sergey A. Goryaynov[1], Vladimir A. Okhlopkov[1], Denis A. Golbin[1], Konstantin A. Chernyshov[2], Dmitrij V. Svistov[3], Boris V. Martynov[3], Alexandr V. Kim[4], Vadim A. Byvaltsev[5,6], Galina V. Pavlova[7], Artem Batalov[1], Nikolay A. Konovalov[1], Petr V. Zelenkov[1], Victor B. Loschenov[8,9] and Alexandr A. Potapov[1]*

[1] N. N. Burdenko National Medical Research Center of Neurosurgery of the Ministry of Health of the Russian Federation, Moscow, Russia, [2] I. M. Sechenov First Moscow State Medical University of the Ministry of Health of the Russian Federation, Moscow, Russia, [3] S. M. Kirov Military Medical Academy of the Ministry of Defense of the Russian Federation, St-Petersburg, Russia, [4] V. A. Almazov Federal North-West Medical Research Centre of the Ministry of Health of the Russian Federation, St-Petersburg, Russia, [5] Laboratory of Neurosurgery, Irkutsk Scientific Center of Surgery and Traumatology, Irkutsk, Russia, [6] Department of Neurosurgery, Irkutsk State Medical University, Irkutsk, Russia, [7] Institute of Gene Biology, Russian Academy of Science, Moscow, Russia, [8] Prokhorov General Physics Institute of the Russian Academy of Science, Moscow, Russia, [9] National Research Nuclear University MEPhI, Moscow, Russia

OPEN ACCESS

Edited by:
Mark Preul, Barrow Neurological Institute (BNI), United States

Reviewed by:
Mohamed Labib, Barrow Neurological Institute (BNI), United States
Vernard S. Fennell, Capital Institute for Neurosciences, United States

***Correspondence:**
Sergey A. Goryaynov
sgoraynov@nsi.ru

Specialty section:
This article was submitted to Cancer Imaging and Image-directed Interventions, a section of the journal Frontiers in Oncology

Received: *26 January 2019*
Accepted: *13 August 2019*
Published: *06 September 2019*

Citation:
Goryaynov SA, Okhlopkov VA, Golbin DA, Chernyshov KA, Svistov DV, Martynov BV, Kim AV, Byvaltsev VA, Pavlova GV, Batalov A, Konovalov NA, Zelenkov PV, Loschenov VB and Potapov AA (2019) Fluorescence Diagnosis in Neurooncology: Retrospective Analysis of 653 Cases. Front. Oncol. 9:830. doi: 10.3389/fonc.2019.00830

Objective: This study is to analyze fluorescence sensitivity in the diagnosis of brain and spinal cord tumors.

Material and methods: The authors conducted a multicenter retrospective analysis of data on 653 cases in 641 patients: 553 of them had brain tumors and 88 spinal cord tumors. Brain tumor resection was performed in 523 patients, of whom 484 were adults and 39 children. The analyzed series was presented by 320 gliomas, 101 meningiomas, and 72 metastases. A stereotactic biopsy was performed in 20 patients and endoscopic surgery in 10 patients. In all cases, 20 mg/kg of 5–Aminolaevulinic acid was administered orally 2-h before surgery. All surgical interventions were performed with a microscope BLUE 400 to visualize fluorescence, while endoscopic surgery—with an endoscope equipped with a fluorescent module. Fluorescence spectroscopy was conducted in 20 cases of stereotactic biopsies and in 88 cases of spinal cord tumors.

Results: Among adult brain tumors operated by microsurgical techniques, meningiomas showed the highest 5-ALA fluorescence sensitivity 94% (n = 95/101), brain metastases 84.7% (n = 61/72), low-grade gliomas 46.4% (n = 26/56), and high-grade gliomas 90.2% (n = 238/264). In children the highest 5-ALA visible fluorescence was observed in anaplastic astrocytomas 100% (n = 4/4) and in anaplastic ependymomas 100% (n = 4/4); in low-grade gliomas it made up 31.8% (n = 7/22). As for the spinal cord tumors in adults, the highest sensitivity was demonstrated by glioblastomas 100% (n = 4/4) and by meningiomas 100% (n = 4/4); Fluorescence was not found in gemangioblastomas (n = 0/6) and neurinomas (n = 0/4). Fluorescence intensity reached 60% (n = 6/10) in endoscopic surgery and 90% (n = 18/20) in stereotactic biopsy.

Conclusion: 5-ALA fluorescence diagnosis proved to be most sensitive in surgery of HGG and meningioma (90.2 and 94.1%, respectively). Sensitivity in surgery of intracranial

metastases and spinal cord tumors was slightly lower (84.7 and 63.6%, correspondingly). The lowest fluorescence sensitivity was marked in pediatric tumors and LGG (50 and 46.4%, correspondingly). Fluorescence diagnosis can also be used in transnasal endoscopic surgery of skull base tumors and in stereotactic biopsy.

Keywords: fluorescence diagnosis, 5-Aminolevulinic acid (ALA), glioma, meningioma, neurooncology

INTRODUCTION

In late 90-ies first data on the potential use of 5-ALA in surgery of malignant gliomas have appeared (1, 2). Recently, use of 5-ALA has become more popular for other classes of brain and spinal cord tumors like meningioma (3–7), metastasis (8–11), neurocytoma (12), ependymoma (13, 14), medulloblastoma (15), adenoma (16). Besides microneurosurgery, intraoperative FD has found its application in endoscopic (17–21) and stereotactic surgery (22, 23).

Our study was aimed at analyzing 5-ALA fluorescence sensitivity in patients with brain and spinal cord tumors using microsurgical, endoscopic techniques, along with stereotactic biopsy.

MATERIALS AND METHODS

Patients

The study enrolled 641 patients with brain and spinal cord tumors, operated within 2010–2017 in 3 clinical hospitals: N. N. Burdenko National Medical Research Center of Neurosurgery of the Ministry of Health of the Russian Federation, Moscow; S. M. Kirov Military Medical Academy of the Ministry of Defense of the Russian Federation, St-Petersburg; V. A. Almazov Federal North-West Medical Research Centre of the Ministry of Health of the Russian Federation, St-Petersburg. More data on patients are presented in **Table 1**. The written informed consent to the surgery and 5-ALA administration was obtained from all patients. The study was approved by the local ethics committee of the N. N. Burdenko National Medical Research Center of Neurosurgery.

Drugs and Equipment

Having got the informed consent and data on absence of any significant liver or kidney pathology, patients were administered 20 mg/kg of 5–Aminolevulinic acid ("Alasens," SSC "NIOPIK," Russian Federation) in 2-h before surgery. Contraindications for "Alasens" were: more than 3-or 4-time ALT, AST increase, porphyria, pregnancy, breastfeeding. In children, 5-ALA was ingested after obtaining the informed parents' consent and by the ethics committee approval. All operations were performed with OPMI Pentero (Carl Zeiss Meditec AG, Obrekochen, Germany) microscope equipped with a fluorescent 400-nm UV light and filters (BLUE 400). During stereotactic surgery MRI (magnetic resonance imaging) and PET (positron emission tomography) with methionine were performed to select the target area and to obtain histological samples.

Operations were performed using the stereotactic system "OREOL" ["Elektropribor," St-Petersburg; (24)]. All assessments were made on an optic-fiber fluorescence-reflectance multichannel ≪Skin-AGE≫ spectrometer (25). In patients with spinal cord tumors, laser spectroscopy was performed using LESA-01-BIOSPEK spectrum analyzer (laser electronic-spectral device, "Biospek" company, Moscow). The PpIX level between the tumor tissue and the intact brain was measured during spectroscopy.

For endoscopic procedures there was used an endoscope equipped with a fluorescence filter; in a number of cases, the combined video-recording system was applied, which was developed in the Laboratory of Laser biospectroscopy at the A. M. Prokhorov general physics institute of the Russian Academy of Sciences.

OUTCOMES OF 5-ALA USE IN SURGERY OF BRAIN AND SPINAL CORD TUMORS

5-ALA Fluorescence in Surgery of Brain Tumors in Adults ($n = 493$)

Visible fluorescence was marked in 90.2% ($n = 238/264$) of patients with WHO Grade III-IV gliomas and in 46.4% ($n = 26/56$) of patients with WHO Grade I-II gliomas. More data on patient distribution into subgroups by tumor histology are presented in **Table 1**. Positive fluorescence was marked in 96.2% ($n = 75/78$) of patients with WHO Grade I, in 85.7% ($n = 18/21$) of WHO Grade II, and in 100% ($n = 2/2$) of WHO Grade III meningiomas.

From two to four nodes were revealed in 17 of 63 patients with metastatic brain lesions; overall, 5-ALA fluorescence was measured in 72 tumor cases. Based on tumor location, it was positive in 84.7% ($n = 61/72$) of cases, namely: metastatic lung cancer was positive in 80.7% ($n = 21/26$), metastatic breast cancer in 90% ($n = 18/20$), others in 66.7% ($n = 21/24$).

5-ALA Fluorescence in Surgery of Brain and Spinal Cord Tumors in Children ($n = 42$)

In this subgroup 39 of 42 patients were operated (3 patients underwent repeated surgery). Anaplastic astrocytoma and anaplastic ependymoma demonstrated the maximal sensitivity, which made up 100% ($n = 4/4$), each; sensitivity in glioblastomas reached 80% ($n = 4/5$), and in low-grade gliomas, it averaged 31.8% ($n = 7/22$).

Abbreviations: 5-ALA, 5–Aminolevulinic acid; FD, Fluorescence diagnosis; HGG, High-grade gliomas (WHO Grades III-IV); LGG, Low-grade gliomas (WHO Grades I-II); PpIX, Protoporphyrin IX; PET, Positron Emission Tomography; PDD, Photodynamic diagnosis; STB, Stereotactic Biopsy.

TABLE 1 | Cases.

Object	5-ALA +	5-ALA -
Brain tumors, open resection (*n* = 535)		
Adults (*n* = 493)	420 (85.2%)	73 (14.8%)
Glioma (*n* = 320)	264 (82.5%)	56 (17.5%)
LGG (*n* = 56)	26 (46.4%)	30 (53.6%)
Pilloid astrocytoma	3 (100%)	0 (0%)
Diffuse astrocytoma	6 (25%)	18 (75%)
Gemistocytic astrocytoma	3 (100%)	0 (0%)
Ganglioastrocytoma	0 (0%)	1 (100%)
Non-infantile desmoplastic ganglioglioma	1 (100%)	0 (0%)
Oligoastrocytoma	8 (50%)	8 (50%)
Oligodendroglioma	3 (50%)	3 (50%)
Pleomorphic xanthoastrocytoma	2 (100%)	0 (0%)
HGG (*n* = 264)	238 (90.2%)	26 (9.8%)
Anaplastic astrocytoma	19 (65.5%)	10 (34.5%)
Anaplastic hemangiopericytoma	1 (100%)	0 (0%)
Anaplastic oligoastrocytoma	5 (71.4%)	2 (28.6%)
Anaplastic oligodendroglioma	4 (66.7%)	2 (33.3%)
Glioblastoma (*n* = 211)	203 (94%)	12 (6%)
Gliosarcoma	6 (100%)	0 (0%)
Meningioma (*n* = 101)	95 (94.1%)	6 (5.9%)
Grade I	75 (96.2%)	3 (3.8%)
Grade II	18 (85.7%)	3 (14.3%)
Grade III	2 (100%)	0 (0%)
Brain metastasis (*n* = 72)	61 (84.7%)	11 (15.3%)
Lungs cancer	21 (80.7%)	5 (19.3%)
Breast cancer	18 (90%)	2 (10%)
Other metastases	21 (66.7%)	3 (33.3%)
Pediatric (*n* = 42)	21 (50%)	21 (50%)
LGG (*n* = 22)	7 (31.8%)	15 (68.2%)
Disembrioplastic neuroepithelial tumor	0 (0%)	1 (100%)
Fibrillary protoplasmic astrocytoma	0 (0%)	2 (100%)
Pilocytic astrocytoma	0 (0%)	4 (100%)
Pilomixoid astrpcytoma	4 (57.1%)	3 (42.9%)
Oligoastrocytoma	1 (50%)	1 (50%)
Oligodendroglioma	0 (0%)	1 (100%)
Fibrillary astrocytoma	1 (50%)	1 (50%)
Ependymoma	1 (50%)	1 (50%)
Chorioid papilloma	0 (0%)	1 (100%)
HGG (*n* = 20)	14 (70%)	6 (30%)
Anaplastic astrocytoma	4 (100%)	0 (0%)
Anaplastic ependymoma	4 (100%)	0 (0%)
Glioblastoma	4 (80%)	1 (20%)
Medulloblastoma	1 (16.7%)	5 (83.3%)
Primitive neuroectodermal tumor	1 (100%)	0 (0%)
Brain tumor, Endoscopic surgery (*n* = 10)	6 (60%)	4 (40%)
Meningioma	3 (75%)	1 (25%)
Hordoma	1 (50%)	1 (50%)
Neurinoma	1 (100%)	0 (0%)
Inverted papilloma	1 (100%)	0 (0%)
Other tumors	0 (0%)	2 (100%)
Brain tumor, stereotactic biopsy (*n* = 20)	18 (90%)	2 (10%)
Fibrillary protoplasmic astrocytoma	2 (66.7%)	1 (33.3)
Anaplastic astrocytoma	8 (100%)	0 (0%)
Glioblastoma	7 (100%)	0 (0%)
Other	1 (50%)	1 (50%)
Adults, spinal cord (*n* = 88)	56 (63.6%)	32 (36.4%)
Ependymoma	37 (72.5%)	14 (27.5%)
Astrocytoma	4 (33.3%)	8 (66.7%)
Glioblastoma	4 (100%)	0 (0%)
Gemangioblastoma	0 (0%)	6 (100%)
Meningioma	11 (100%)	0 (0%)
Neurinoma	0 (0%)	4 (100%)
Overall	**653**	

It is interesting to note, that medulloblastomas demonstrated "weak" fluorescence (16.7%, $n = 1/6$) despite their high grade of malignancy.

5-ALA Fluorescence in Endoscopic Neurosurgery ($n = 10$)

Ten operations have been performed: anterior cranial fossa tumor resection by a transnasal approach. By all that, fluorescence was marked in 75% ($n = 3/4$) of meningiomas, in 50% ($n = 1/2$) of chordomas, in 100% ($n = 1/1$) of neurinoma, and in 100% ($n = 1/1$) of inverted papilloma.

Fluorescence-Guided Stereotactic Biopsy of Brain Tumors ($n = 20$)

Stereotactic biopsy and stereotactic fluorescence biospectroscopy revealed positive tumor fluorescence in 90% ($n = 18/20$) of cases. Fluorescence spectroscopy was sensitive for detecting fibrillary-protoplasmatic astrocytomas in 66.7% ($n = 2/3$), anaplastic astrocytomas in 100% [($n = 8/8$), glioblastomas in 100% ($n = 7/7$)] of cases. The false-positive effect was marked in 5.6% ($n = 1/18$) of patients (reactive gliosis after earlier performed radiotherapy).

5-ALA Fluorescence in Surgery of Spinal Cord Tumors in Adults ($n = 88$)

Visible fluorescence was marked in 75% ($n = 33/44$) of intramedullary ependymomas, wherein, a strong PpIX fluorescence, revealed by laser spectroscopy, was observed in 100% ($n = 44/44$) of cases. Astrocytomas have been noted to fluoresce in 33.3% ($n = 4/12$) of cases, spectroscopy has demonstrated PpIX fluorescence in 50% ($n = 6/12$). The highest fluorescence sensitivity was marked in patients with glioblastoma (4/4) and meningioma (11/11). Fluorescence was visible in 57.1% ($n = 4/7$) of cauda equine ependymoma; PpIX fluorescence intensity, revealed by laser spectroscopy, was

($n = 7/7$) in all cases; negative PpIX fluorescence was observed in hemangioblastoma ($n = 0/6$) and neurinoma ($n = 0/4$).

DISCUSSION

At the end of 90-ies first data on the potential use of 5-ALA in neurosurgery appeared, with first publications being devoted to malignant gliomas (1, 22). Today, 5-ALA is applied in surgery of different types of brain and spinal cord tumors for both adults and children, including meningiomas (3–7, 26–28), metastasis (8–11), neurocytomas (12), ependymomas (13, 14), medulloblastomas (15).

Among the publications devoted to application of 5-ALA fluorescence in surgery of CNS tumors, Marbacher et al. (10) (n=458) reports the largest series of patients (10). In contrast to Marbacher et al. (10), our series ($n = 641$) enrolled patients with spinal cord tumors ($n = 88$), children ($n = 39$), and patients who underwent transnasal endoscopic surgery ($n = 10$). The novelty of our research is application of spectroscopy in cases of spinal cord tumors ($n = 88$) and stereotactic biopsy ($n = 20$).

We found it reasonable to combine data on intraoperative fluorescence sensitivity obtained in different tumors of the CNS. In our series, to visualize fluorescence in stereotactic biopsy and in spinal surgery, traditionally, besides microscope, the spectroscopic control is used.

Adults, Brain, Open Resection

High-Grade Gliomas

A number of papers have proved that use of fluorescence diagnosis in surgery of high-grade gliomas results in the increased rate of GTR (gross total resection) and the increased progression-free and overall survival time (29–32). Thus, use of fluorescence diagnosis in surgery of high-grade gliomas is an effective technique.

The results of 5-ALA application in adults with different types of brain tumors were highlighted in detail in our earlier publications (18, 18, 21, 26). In this study, fluorescence sensitivity in the treatment of high-grade gliomas was 90.2% ($n = 238/264$), which corresponded to findings of other authors (22, 32–34).

Low-Grade Gliomas

Whether it is reasonable to use 5-ALA in surgery of non-contrasting gliomas, is still undefined. On the one hand, it is evident knowledge that gross total resection results in the increased progression-free and overall survival time among patients with LGG (31). However, no research has proved that use of fluorescence in LGG results in the increased rate of GTR. For these reasons, there is a strong need for further studying and specifying this problem.

Widhalm et al. have reported that PpIX accumulates in anaplastic focus, where the tumor has higher grade areas of malignancy (Grade III) (23). According to our data, fluorescing focuses in LGG are areas with the Ki 67 index still not exceeding 5% (35). Medical publications provide contradictory opinions on fluorescence sensitivity in LGG, which varies from 7.7 to 40% (10, 36–38). In our group it made up 46.4% ($n = 26/56$), presumably due to comprising different types of gliomas; while the lowest sensitivity was observed in diffuse astrocytomas 25% ($n = 6/18$).

Metastases

In our series, 5-ALA-induced fluorescence for cerebral metastases was 84.7% ($n = 61/72$), which is slightly higher compared to other studies. Thus, according to Kamp and co-authors, fluorescence sensitivity for cerebral metastases varied from 52 to 81% (11). The absence of fluorescence in intracranial metastases indicated a significantly higher incidence of local tumor progression after surgery (11). It might be related to different surgeon's experience in using 5-ALA, which is particularly important when dealing with weak fluorescence intensity. The phenomenon of tumor bed, still fluorescing after metastatic node removal, is still hard to understand (clinical case, **Figure 1**).

Meningiomas

These data prove our previous research on 5-ALA sensitivity in intracranial meningioma surgery (39).

Children, Brain, Open Resection

As was earlier mentioned, use of fluorescence diagnosis in HGG in children results in the increased rate of GTR (gross total resection) and the increased progression-free and overall survival time (40, 41). New data on the clinical use of 5-ALA in children with some other types of brain tumors have been reported (15, 24, 41–43). Thus, fluorescence diagnosis is recommended for HGG. For other classes of tumors, its use is disputable (44).

In our series, fluorescence sensitivity in children with brain tumors was 50% ($n = 21/42$) (45), thus corresponding to other foreign authors' experience (24, 41, 43, 46). Fluorescence sensitivity depends on the tumor morphology and malignancy. According to Stummer et al. fluorescence sensitivity was noted to make up 15% ($n = 2/13$) for Grade I-II astrocytoma, and 85% ($n = 12/14$)—for glioblastoma. In our research, florescence sensitivity for low-grade gliomas was 31.8% ($n = 7/22$), for high-grade gliomas −70% ($n = 14/20$). Maximal sensitivity was revealed in anaplastic astrocytomas 100% ($n = 4/4$) and anaplastic ependymoma 100% ($n = 4/4$).

Still confusing is, that medulloblastomas in children show low fluorescence sensitivity. This high-grade class of tumors, however, reveals "weak" fluorescence (30). For instance, Beez et al. report fluorescence sensitivity reaching 25% ($n = 1/3$) (43). In our series, it made up 16.7% ($n = 1/6$) for medulloblastomas. As Zhang et al. reports, more complete resection rate with the following increased survival time was associated with positive fluorescence (44).

Adults, Spinal Cord

5-ALA fluorescence-assisted technology in adults has proved to be a good method of intraoperative neuroimaging (13, 14, 47–49). In our experience, fluorescence sensitivity for spinal cord tumors was 63.6% ($n = 56/88$), which was similar to other publications (13, 14, 48). Millesi et al. report fluorescence sensitivity to range from 0% ($n = 0/8$) in neurinomas to 100% ($n = 12/12$) in meningiomas (48), thus, also confiding with our

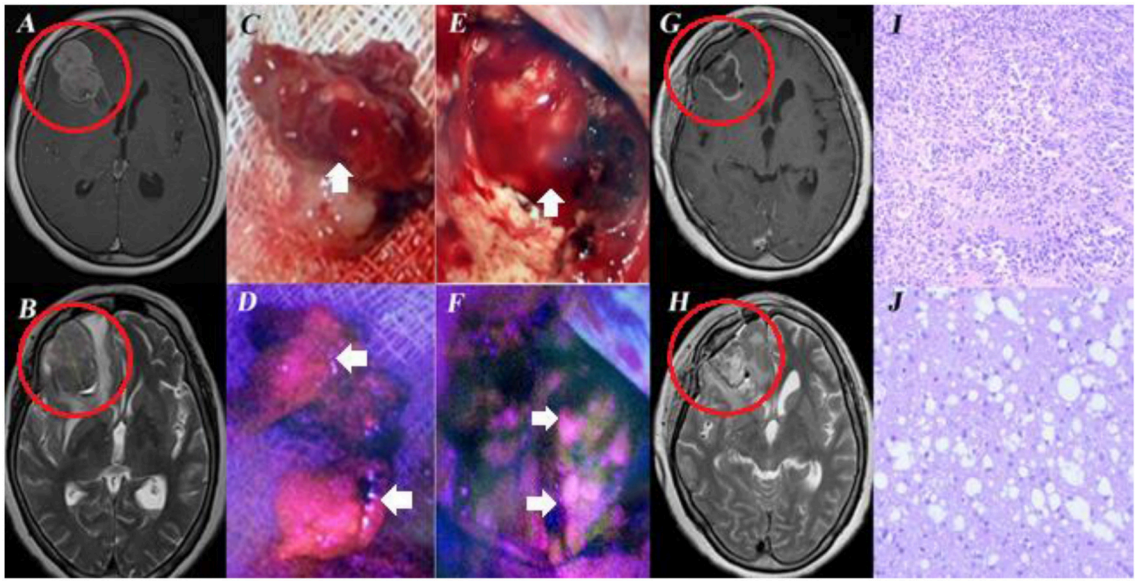

FIGURE 1 | Female, aged 60, admitted to the clinical center with complaints of headaches. In 2009 melanoma of the right lumbar region was removed, in 2017 she underwent resection of the superior lobe of the left lung. MRI of the brain revealed an intracerebral tumor in the right frontal lobe with perifocal edema **(A,B)**. Resection of the right frontal lobe tumor was performed under 5-ALA Fluorescence assistance. During surgery, bright fluorescence of the tumor node was marked **(C,D)**. Biopsy revealed melanoma metastasis **(I)**. immunohistochemical examination showed positive HMB45, MelA expression. After resection, the unchanged white matter of the frontal lobe was exposed in the tumor bed **(E)**. Visible tumor bed fluorescence was observed **(F)**. No tumor tissue was revealed by additional biopsy samples taken from the fluorescing region **(J)**. Postoperative MRI **(G,H)** demonstrated total tumor node resection. This case is interesting, first, by the fact that melanoma metastasis can fluorescence and second, that the resected tumor bed without tumor cells can also fluoresce. Informed consent has been obtained from the patient for the publication of data, including images.

data. Application of spectroscopy in our series allowed us to increase fluorescence sensitivity in astrocytomas (Grade II) from 33.3% (n = 4/12) to 50% (n = 6/12), and in ependymomas from 75% (n = 33/44) to 100% (n = 44/44), including cauda equine ependymoma, the sensitivity of which varied from 57.1% (n = 4/7) to 100% (7/7).

Endoscopic Surgery

The present-day microscope-assisted metabolic navigation possesses the insufficient quality of the fluorescence signal obtained during a deep and narrow approach. To solve this problem, a specific design of fluorescence endoscope has been adopted. 5-ALA fluorescence is known to be useful in visualizing the tumor tissue (18, 19, 50, 51), while fluorescence with indocyanine green (ICG)—for coloration of the vessels (52–55).

There are only a few medical publications devoted to endoscopic surgery with fluorescence assistance in neurooncology. Takeda et al. reported 2 cases of germinomas (56), in which 5-ALA fluorescence-guided endoscopic surgery was used. Cornelius et al. described the procedure of using 5-ALA endoscopic surgery in 2 patients with meningiomas (57). Our series included 10 patients with different skull base tumors; intraoperative fluorescence was visualized in 60% of cases. Alongside with this, meningiomas was visualized in 3 cases out of 4, chordoma in 1 case out of 2, neurinoma in 1 case of 1, inverted papilloma in 1 case of 1.

Patients who underwent microscopic 5-ALA fluorescence-assisted endoscopic surgery for brain tumors did not enter this series. These results were reported in our early publication in 2008 (18). We did not use 5-ALA fluorescence in transventricular endoscopic surgery of intraventricular tumors. Takeda et al. have earlier reported on that (56).

Stereotactic Biopsy

According to the world literature databank, STB proved to be not informative in 24% (58). There are three main methods neurosurgeons have for reduction the incidence of uninformative biopsies: a combination of MRI and PET is used for preoperative planning, biopsy in the operating room and the use 5-ALA fluorescence. A fluorescence-assisted stereotactic biopsy can be obtained in 2 ways: first, by measuring the concentration of PP IX in the tumor tissue along the stereotactic trajectory to the target using a spectral probe before extracting the biopsy (59). Second, by evaluating the tissue sample fluorescence using a neurosurgical microscope with a special fluorescence regimen, as described by Widhalm et al. (23). In the latter, specimens were put under fluorescence light of a surgical microscope to assess their fluorescence. Fluorescence sensitivity, according to Widhalm's report, was 100% for HGG and 0% for LGG. In addition, use of fluorescence was helpful in shortening the operation time and decreasing the average number of biopsies during surgery (60).

In our opinion, the combination of the stereotactic cannula and the spectral probe is easier and does not require an operative

microscope with a fluorescence module. Stereotactic biopsy combined with fluorescence spectroscopy gives a chance when analyzing, to determine the zones of the highest concentration of PPIX and select the tumor site with the highest degree of anaplasia, thus increasing the diagnostic value of stereotactic biopsy as a technique (23, 61).

Fluorescence sensitivity in our series reached 90% ($n = 18/20$), thus corresponding to the world literature data. Marbacher et al. (10) reports fluorescence sensitivity of 88% ($n = 44/50$). Fluorescence sensitivity for a low-grade glioma, particularly for fibrillary protoplasmic glioma, was 66.7% (2/3), while in the study of Marbacher et al. it was 25% (3/12). In our experience, higher fluorescence can be explained by using stereotactic biopsy under spectroscopic, and not only visual, control. A small number of cases in our series does not allow us to perform the comparative analysis of fluorescence sensitivity for patients with low-grade glioma in the STB subgroup.

CONCLUSION

5-ALA fluorescence diagnosis proved to be most sensitive in surgery of HGG and meningioma (90.2 and 94.1%, respectively). Sensitivity in surgery of intracranial metastases and spinal cord tumors was slightly lower (84.7 and 63.6%, correspondingly). The lowest fluorescence sensitivity was marked in pediatric tumors and LGG (50 and 46.4%, correspondingly). Fluorescence diagnosis can also be used in transnasal endoscopic surgery of skull base tumors and in stereotactic biopsy.

LIMITATIONS

There are several limitations our work has. Firstly, we used brain tumor classification of the 2007 year (because it is a retrospective study). Secondly, it common knowledge that medulloblastomas (MB) are recommended to classify into subtypes, according to WHO classification, but our analysis was performed earlier than an official MB sub-type classification was generally accepted. In addition, MB sub-type classification is effective for a traditional classification of patients into moderate or high-grade risk groups and is important for further prognosis and choice of the differentiated treatment modality. In our opinion, the practical value of such a comparative analysis is not so important, because fluorescence degree provides an increase in the radical blastomatous tissue resection rate and not assessment of its molecular genetic features. Our group of MB patients is too small to claim any novelty. We just state that the data obtained can be helpful for a meta-analysis.

ETHICS STATEMENT

All procedures performed in studies involving human participants were in accordance with the ethical standards of the institutional and/or national research committee and with the 1964 Helsinki declaration and its later amendments or comparable ethical standards.

AUTHOR'S NOTE

AK is a corresponding member of RAS. AP is a full member of RAS.

AUTHOR CONTRIBUTIONS

SG and AP: research concept and design. VO, DG, DS, BM, AK, NK, PZ, AP, and AB: data collection and processing. KC: statistic support and writing text. VB, GP, and VL: editing. This work was supported by the ethical committee of Burdenko Neurosurgical Institute.

FUNDING

The reported study was funded by RFBR according to the research projects No 17-00-00158, No 17-00-00159, 17-00-00157 (17-00-00162 (K)), and No 19-29-01154.

ACKNOWLEDGMENTS

We would like to acknowledge the help provided by our colleagues:

A. I. Kholyavin, N. P. Bechtereva Institute of the Human Brain, Russian Academy of Sciences, Saint Petersburg, Russia.

G. V. Papayan, I. P. Pavlov First St. Petersburg State Medical University, Ministry of Health of the Russian Federation, St. Petersburg, Russia.

D. S. Kim, Department of Pathomorphology, Burdenko NSI, Moscow.

I. N. Pronin, Full member of RAS, and A. I. Batalov, Burdenko NSI, Moscow.

Translation from Russian to English – N. A. Pestovskaya.

This work was partially supported by the Competitiveness Program of MEPhI.

REFERENCES

1. Stummer W, Novotny A, Stepp H, Goetz C, Bise K, Reulen HJ. Fluorescence-guided resection of glioblastoma multiforme utilizing 5-ALA-induced porphyrins: a prospective study in 52 consecutive patients. *J Neurosurg.* (2000) 93:1003–13. doi: 10.3171/jns.2000.93.6.1003
2. Stummer W, Goetz C, Stepp H, Stocker S, Reulen HJ. Intraoperative detection of malignant glioma by 5-ALA induced protoporphyrin IX fluorescence. *Clin Neurol Neurosurg.* (1997) 99:S93. doi: 10.1016/S0303-8467(97)81684-8
3. Coluccia D, Fandino J, Fujioka M, Cordovi S, Muroi C, Landolt H. Intraoperative 5-aminolevulinic-acid-induced fluorescence in meningiomas. *Acta Neurochir.* (2010) 152:1711–9. doi: 10.1007/s00701-010-0708-4
4. Foster N, Eljamel S. ALA-induced fluorescence image guided surgery of meningiomas: a meta-analyses. *Photodiagnosis Photodyn Ther.* (2016) 15:73–8. doi: 10.1016/j.pdpdt.2016.05.006
5. Cornelius J, Slotty P, Stoffels G, Galldiks N, Langen K, Steiger H. 5-Aminolevulinic acid and 18F-FET-PET as metabolic imaging tools for surgery of a recurrent skull base meningioma. *J Neurol Surg Part B Skull Base.* (2013) 74:211–6. doi: 10.1055/s-0033-1342918

6. Millesi M, Kiesel B, Mischkulnig M, Martínez-Moreno M, Wöhrer A, Wolfsberger S, et al. Analysis of the surgical benefits of 5-ALA–induced fluorescence in intracranial meningiomas: experience in 204 meningiomas. *J Neurosurg.* (2016) 125:1408–19. doi: 10.3171/2015.12.JNS151513
7. Hefti M, Holenstein F, Albert I, Looser H, Luginbuehl V. Susceptibility to 5-aminolevulinic acid based photodynamic therapy in WHO I meningioma cells corresponds to ferrochelatase activity. *Photochem Photobiol.* (2011) 87:235–41. doi: 10.1111/j.1751-1097.2010.00821.x
8. Utsuki S, Oka H, Sato S, Shimizu S, Suzuki S, Tanizaki Y, et al. Histological examination of false positive tissue resection using 5-aminolevulinic acid-induced fluorescence guidance. *Neurol Med Chir.* (2007) 47:210–3; discussion 213-4. doi: 10.2176/nmc.47.210
9. Belloch JP, Rovira V, Llácer JL, Riesgo PA, Cremades A. Fluorescence-guided surgery in high grade gliomas using an exoscope system. *Acta Neurochir.* (2014) 156:653–60. doi: 10.1007/s00701-013-1976-6
10. Marbacher S, Klinger E, Schwyzer L, Fischer I, Nevzati E, Diepers M, et al. Use of fluorescence to guide resection or biopsy of primary brain tumors and brain metastases. *Neurosurg Focus.* (2014) 36:E10. doi: 10.3171/2013.12.FOCUS13464
11. Kamp MA, Fischer I, Bühner J, Turowski B, Frederick Cornelius J, Steiger H-J, et al. 5-ALA fluorescence of cerebral metastases and its impact for the local-in-brain progression. *Oncotarget.* (2016) 7:66776–66789. doi: 10.18632/oncotarget.11488
12. Song SW, Kim Y-H, Park S-H, Park C-K. 5-Aminolevulinic acid fluorescence discriminates the histological grade of extraventricular neurocytoma. *Brain Tumor Res Treat.* (2013) 1:45. doi: 10.14791/btrt.2013.1.1.45
13. Eicker SO, Floeth FW, Kamp M, Steiger H-J, Hänggi D. The impact of fluorescence guidance on spinal intradural tumour surgery. *Eur Spine J.* (2013) 22:1394–401 doi: 10.1007/s00586-013-2657-0
14. Inoue T, Endo T, Nagamatsu K, Watanabe M, Tominaga T. 5-Aminolevulinic acid fluorescence-guided resection of intramedullary ependymoma. *Oper Neurosurg.* (2013) 72:ons159–68. doi: 10.1227/NEU.0b013e31827bc7a3
15. Skjøth-Rasmussen J, Bøgeskov L, Sehested A, Klausen C, Broholm H, Nysom K. The use of 5-ALA to assist complete removal of residual non-enhancing part of childhood medulloblastoma: a case report. *Child Nerv Syst.* (2015) 31:2173–7. doi: 10.1007/s00381-015-2762-y
16. Eljamel MS, Leese G, Moseley H. Intraoperative optical identification of pituitary adenomas. *J Neurooncol.* (2009) 92:417–21. doi: 10.1007/s11060-009-9820-9
17. Cho W-S, Kim JE, Kang H-S, Ha EJ, Jung M, Lee C, et al. Dual-channel endoscopic indocyanine green fluorescence angiography for clipping of cerebral aneurysms. *World Neurosurg.* (2017) 100:316–24. doi: 10.1016/j.wneu.2017.01.042
18. Potapov AA, Usachev DJ, Loshakov VA, Cherekaev VA, Kornienko VN, Pronin IN, et al. First experience in 5-ALA fluorescence-guided and endoscopically assisted microsurgery of brain tumors. *Med Laser Appl.* (2008) 23:202–8. doi: 10.1016/j.mla.2008.07.006
19. Ritz R, Feigl GC, Schuhmann MU, Ehrhardt A, Danz S, Noell S, et al. Use of 5-ALA fluorescence guided endoscopic biopsy of a deep-seated primary malignant brain tumor. *J Neurosurg.* (2011) 114:1410–3. doi: 10.3171/2010.11.JNS10250
20. Tsuzuki S, Aihara Y, Eguchi S, Amano K, Kawamata T, Okada Y. Application of indocyanine green (ICG) fluorescence for endoscopic biopsy of intraventricular tumors. *Child Nerv Syst.* (2014) 30:723–6. doi: 10.1007/s00381-013-2266-6
21. Belykh E, Miller EJ, Hu D, Martirosyan NL, Woolf EC, Scheck AC, et al. Scanning fiber endoscope improves detection of 5-aminolevulinic acid–induced protoporphyrin IX fluorescence at the boundary of infiltrative glioma. *World Neurosurg.* (2018) 113:e51–69. doi: 10.1016/j.wneu.2018.01.151
22. Stummer W, Pichlmeier U, Meinel T, Wiestler OD, Zanella F, Reulen H-J. Fluorescence-guided surgery with 5-aminolevulinic acid for resection of malignant glioma: a randomised controlled multicentre phase III trial. *Lancet Oncol.* (2006) 7:392–401. doi: 10.1016/S1470-2045(06)70665-9
23. Widhalm G, Minchev G, Woehrer A, Preusser M, Kiesel B, Furtner J, et al. Strong 5-aminolevulinic acid-induced fluorescence is a novel intraoperative marker for representative tissue samples in stereotactic brain tumor biopsies. *Neurosurg Rev.* (2012) 35:381–91. doi: 10.1007/s10143-012-0374-5
24. Stummer W, Rodrigues F, Schucht P, Preuss M, Wiewrodt D, Nestler U, et al. Predicting the "usefulness" of 5-ALA-derived tumor fluorescence for fluorescence-guided resections in pediatric brain tumors: a European survey. *Acta Neurochir.* (2014) 156:2315–24. doi: 10.1007/s00701-014-2234-2
25. Kang U, Papayan GV, Berezin VB, Petrischcv NN, Galagudza MM. Spectrometer for fluorescence-reflectance biomedical research. *Opt J.* (2013) 80:56–67. Available online at: https://yandex.ru/patents/doc/RU2539817C1_20150127
26. Potapov AA, Goryaynov SA, Danilov GV, Chelushkin DM, Okhlopkov VA, Shimanskiy VN, et al. Intraoperative fluorescence diagnostics in surgery of intracranial meningiomas: analysis of 101 cases. *Vopr neirokhirurgii Im NN Burdenko.* (2018) 82:17. doi: 10.17116/oftalma2018821729
27. Belykh E, Martirosyan NL, Yagmurlu K, Miller EJ, Eschbacher JM, Izadyyazdanabadi M, et al. Intraoperative fluorescence imaging for personalized brain tumor resection: current state and future directions. *Front Surg.* (2016) 3:55. doi: 10.3389/fsurg.2016.00055
28. Belykh E, Miller EJ, Patel AA, Bozkurt B, Yagmurlu K, Robinson TR, et al. Optical characterization of neurosurgical operating microscopes: quantitative fluorescence and assessment of PpIX photobleaching. *Sci Rep.* (2018) 8:12543. doi: 10.1038/s41598-018-30247-6
29. Stummer W, Reulen H-J, Meinel T, Pichlmeier U, Schumacher W, Tonn J-C, et al. Extent of resection and survival in glioblastoma multiforme. *Neurosurgery.* (2008) 62:564–76. doi: 10.1227/01.neu.0000317304.31579.17
30. Aldave G, Tejada S, Pay E, Marigil M, Bejarano B, Idoate MA, et al. Prognostic value of residual fluorescent tissue in glioblastoma patients after gross total resection in 5-aminolevulinic acid-guided surgery. *Neurosurgery.* (2013) 72:915–21. doi: 10.1227/NEU.0b013e31828c3974
31. Schucht P, Beck J, Abu-Isa J, Andereggen L, Murek M, Seidel K, et al. Gross total resection rates in contemporary glioblastoma surgery: results of an institutional protocol combining 5-aminolevulinic acid intraoperative fluorescence imaging and brain mapping. *Neurosurgery.* (2012) 71:927–35. doi: 10.1227/NEU.0b013e31826d1e6b
32. Slotty PJ, Siantidis B, Beez T, Steiger HJ, Sabel M. The impact of improved treatment strategies on overall survival in glioblastoma patients. *Acta Neurochir.* (2013) 155:959–63. doi: 10.1007/s00701-013-1693-1
33. Díez Valle R, Slof J, Galván J, Arza C, Romariz C, Vidal C. Estudio observacional retrospectivo sobre la efectividad del ácido 5-aminolevulínico en la cirugía de los gliomas malignos en España (Estudio VISIONA). *Neurología.* (2014) 29:131–8. doi: 10.1016/j.nrl.2013.05.004
34. Chave-Cox DR, Corns MR, Sivakumar MG, Thomson MS. PP36. Improved glioblastoma survival following the introduction of a subspecialised surgical high grade brain tumour service. *Neuro Oncol.* (2017) 19 (Suppl. 1):i11. doi: 10.1093/neuonc/now293.036
35. Goryaynov SA, Widhalm G, Goldberg MF, Chelushkin D, Spallone A, Chernyshov KA, et al. The role of 5-ALA in low-grade gliomas and the influence of antiepileptic drugs on intraoperative fluorescence. *Front Oncol.* (2019) 9:423. doi: 10.3389/fonc.2019.00423
36. Widhalm G, Kiesel B, Woehrer A, Traub-Weidinger T, Preusser M, Marosi C, et al. 5-Aminolevulinic acid induced fluorescence is a powerful intraoperative marker for precise histopathological grading of gliomas with non-significant contrast-enhancement. *PLoS ONE.* (2013) 8:e76988. doi: 10.1371/journal.pone.0076988
37. Ewelt C, Floeth FW, Felsberg J, Steiger HJ, Sabel M, Langen K-J, et al. Finding the anaplastic focus in diffuse gliomas: the value of Gd-DTPA enhanced MRI, FET-PET, and intraoperative, ALA-derived tissue fluorescence. *Clin Neurol Neurosurg.* (2011) 113:541–7. doi: 10.1016/j.clineuro.2011.03.008
38. Jaber M, Wölfer J, Ewelt C, Holling M, Hasselblatt M, Niederstadt T, et al. The value of 5-aminolevulinic acid in low-grade gliomas and high-grade gliomas lacking glioblastoma imaging features. *Neurosurgery.* (2016) 78:401–11. doi: 10.1227/NEU.0000000000001020
39. Potapov AA, Goryaynov SA, Okhlopkov VA, Shishkina LV, Loschenov VB, Savelieva TA, et al. Laser biospectroscopy and 5-ALA fluorescence navigation as a helpful tool in the meningioma resection. *Neurosurg Rev.* (2016) 39:437–47. doi: 10.1007/s10143-015-0697-0

40. Kramm CM, Wagner S, Van Gool S, Schmid H, Sträter R, Gnekow A, et al. Improved survival after gross total resection of malignant gliomas in pediatric patients from the HIT-GBM studies. *Anticancer Res.* (2006) 26:3773–9.
41. Preuß M, Renner C, Krupp W, Christiansen H, Fischer L, Merkenschlager A, et al. The use of 5-aminolevulinic acid fluorescence guidance in resection of pediatric brain tumors. *Child Nerv Syst.* (2013) 29:1263–7. doi: 10.1007/s00381-013-2159-8
42. Bernal García LM, Cabezudo Artero JM, Royano Sánchez M, Marcelo Zamorano MB, López Macías M. Fluorescence-guided resection with 5-aminolevulinic acid of meningeal sarcoma in a child. *Child Nerv Syst.* (2015) 31:1177–80. doi: 10.1007/s00381-015-2703-9
43. Beez T, Sarikaya-Seiwert S, Steiger H-J, Hänggi D. Fluorescence-guided surgery with 5-aminolevulinic acid for resection of brain tumors in children—a technical report. *Acta Neurochir.* (2014) 156:597–604. doi: 10.1007/s00701-014-1997-9
44. Zhang C, Boop FA, Ruge J. The use of 5-aminolevulinic acid in resection of pediatric brain tumors: a critical review. *J Neurooncol.* (2018) 141:567–763. doi: 10.1007/s11060-018-03004-y
45. Khachatryan WA, Kim AV, Samochernich KA, Tadevosian AR, Kazackaya EV, Don OA, et al. Experience with intraoperative fluorescence diagnosis in the surgical treatment of children with tumors of neuroepithelial brain. *Pediatr Neurosergery Neurol.* (2016) N2:37–51.
46. Kim AV, Khachatryan VA. Intraoperative fluorescence diagnosis using 5-aminolevulinic acid in surgical treatment of children with recurrent neuroepithelial tumors. *Zh Vopr Neirokhir Im N N Burdenko.* (2017) 81:51–7. doi: 10.17116/neiro201780751-57
47. De la Garza-Ramos R, Bydon M, Macki M, Huang J, Tamargo RJ, Bydon A. Fluorescent techniques in spine surgery. *Neurol Res.* (2014) 36:928–38. doi: 10.1179/1743132814Y.0000000340
48. Millesi M, Kiesel B, Woehrer A, Hainfellner JA, Novak K, Martínez-Moreno M, et al. Analysis of 5-aminolevulinic acid–induced fluorescence in 55 different spinal tumors. *Neurosurg Focus.* (2014) 36:E11. doi: 10.3171/2013.12.FOCUS13485
49. Rangel-Castilla L, Russin JJ, Zaidi HA, Martinez-del-Campo E, Park MS, Albuquerque FC, et al. Contemporary management of spinal AVFs and AVMs: lessons learned from 110 cases. *Neurosurg Focus.* (2014) 37:E14. doi: 10.3171/2014.7.FOCUS14236
50. Schwartz TH. Endoscopic-Assisted 5-Aminolevulinic Acid Imaging. World Neurosurg. (2014) 82:e117–8. doi: 10.1016/j.wneu.2013.07.110
51. Rapp M, Kamp M, Steiger H-J, Sabel M. Endoscopic-assisted visualization of 5-aminolevulinic acid–induced fluorescence in malignant glioma surgery: a technical note. *World Neurosurg.* (2014) 82:e277–9. doi: 10.1016/j.wneu.2013.07.002
52. Bruneau M, Appelboom G, Rynkowski M, Cutsem N, Mine B, Witte O. Endoscope-integrated ICG technology: first application during intracranial aneurysm surgery. *Neurosurg Rev.* (2012) 36:77–84. doi: 10.1007/s10143-012-0419-9
53. Mielke D, Malinova V, Rohde V. Comparison of intraoperative microscopic and endoscopic icg angiography in aneurysm surgery. *Neurosurgery.* (2014) 10:418–25. doi: 10.1227/NEU.0000000000000345
54. Hide T, Yano S, Kuratsu J. Indocyanine Green fluorescence endoscopy at endonasal transsphenoidal surgery for an intracavernous sinus dermoid cyst: case report. *Neurol Med Chir.* (2014) 54:999–1003. doi: 10.2176/nmc.cr.2014-0087
55. Hide T, Yano S, Shinojima N, Kuratsu J. Usefulness of the indocyanine green fluorescence endoscope in endonasal transsphenoidal surgery. *J Neurosurg.* (2015) 122:1185–92. doi: 10.3171/2014.9.JNS14599
56. Takeda J, Nonaka M, Li Y, Komori Y, Kamei T, Iwata R, et al. 5-ALA fluorescence-guided endoscopic surgery for mixed germ cell tumors. *J Neurooncol.* (2017) 134:119–24. doi: 10.1007/s11060-017-2494-9
57. Cornelius JF, Kamp MA, Tortora A, Knipps J, Krause-Molle Z, Beez T, et al. Surgery of small anterior skull base meningiomas by endoscopic 5-aminolevulinic acid fluorescence guidance: first clinical experience. *World Neurosurg.* (2018) 122:e890–5. doi: 10.1016/j.wneu.2018.10.171
58. Lu Y, Yeung C, Radmanesh A, Wiemann R, Black PM, Golby AJ. Comparative effectiveness of frame-based, frameless, and intraoperative magnetic resonance imaging–guided brain biopsy techniques. *World Neurosurg.* (2015) 83:261–8. doi: 10.1016/j.wneu.2014.07.043
59. Papayan GV, Martynov BV, Kholyavin AI, Nizkovolos VB, Svistov DV, Petrishchev NN, et al. Stereotactic fluorescence biospectroscopy in the diagnosis of brain glial neoplasms. *Top Issues Laser Med.* (2016) 2016:139–51. doi: 10.1093/neuros/nyy315
60. Millesi M, Kiesel B, Wöhrer A, Mercea PA, Bissolo M, Roetzer T, et al. Is intraoperative pathology needed if 5-aminolevulinic-acid-induced tissue fluorescence is found in stereotactic brain tumor biopsy? *Neurosurgery.* (2019) 2019:nyz086. doi: 10.1093/neuros/nyz086
61. Piquer J, Llácer JL, Rovira V, Riesgo P, Rodriguez R, Cremades A. Fluorescence-guided surgery and biopsy in gliomas with an exoscope system. *Biomed Res Int.* (2014) 2014:1–6. doi: 10.1155/2014/207974

Conflict of Interest Statement: The authors declare that the research was conducted in the absence of any commercial or financial relationships that could be construed as a potential conflict of interest.

frontiers in Oncology

REVIEW
published: 12 September 2019
doi: 10.3389/fonc.2019.00882

Optical Molecular Imaging of Inflammatory Cells in Interventional Medicine–An Emerging Strategy

Gavin P. Birch[1,2]*, *Thane Campbell*[2]*, *Mark Bradley*[1] and *Kevin Dhaliwal*[2]

[1] EaStChem School of Chemistry, University of Edinburgh, Edinburgh, United Kingdom, [2] Centre for Inflammation Research, University of Edinburgh, Edinburgh, United Kingdom

The optical molecular imaging of inflammation is an emerging strategy for interventional medicine and diagnostics. The host's inflammatory response and adaptation to acute and chronic diseases provides unique signatures that have the potential to guide interventions. Thus, there are emerging a suite of molecular imaging and sensing approaches for a variety of targets in this area. This review will focus on two key cellular orchestrators that dominate this area, neutrophils and macrophages, with recent developments in molecular probes and approaches discussed.

Keywords: molecular imaging, inflammation, interventional medicine, optical imaging, macrophage, neutrophil

OPEN ACCESS

Edited by:
David Leslie Carr-Locke, Weill Cornell Medicine, Cornell University, United States

Reviewed by:
Wagner Fontes, University of Brasilia, Brazil
Guolin Ma, China-Japan Friendship Hospital, China

***Correspondence:**
Gavin P. Birch
gavin.birch@ed.ac.uk
Thane Campbell
s1003032@sms.ed.ac.uk

Specialty section:
This article was submitted to Cancer Imaging and Image-directed Interventions, a section of the journal Frontiers in Oncology

Received: *05 June 2019*
Accepted: *27 August 2019*
Published: *12 September 2019*

Citation:
Birch GP, Campbell T, Bradley M and Dhaliwal K (2019) Optical Molecular Imaging of Inflammatory Cells in Interventional Medicine–An Emerging Strategy. Front. Oncol. 9:882. doi: 10.3389/fonc.2019.00882

INTRODUCTION

Recent developments in optical molecular imaging are enabling the identification and evaluation of inflammatory cells such as macrophages and neutrophils in a variety of imaging scenarios. This is important as these leukocytes are an important part of host defense and immune homeostasis. Their pivotal roles as professional phagocytes in acute and chronic inflammatory disease may allow their use as versatile interventional biomarkers and as such fluorescent imaging of these cells has the potential to advance disease treatment and management, by producing sub-cellular information in real-time.

Intrinsic tissue autofluorescence adds further value when the structures of extracellular matrix or metabolic activities are of interest. The predominant modality of fluorescence intensity measurements, coupled with recent technological developments such as label-free non-linear optical images and Raman analyses (1, 2), have opened up the possibility of giving the surgeon functional images of the surgical site in real time. Furthermore, exciting developments are resulting from the integration of cell classification and machine learning techniques, allowing deeper analysis of the richness of imaging datasets.

Macroscopic widefield open fluorescence systems and high-resolution endomicroscopy are the predominant systems that have been used clinically to detect optical molecular tracers. The recent advances in imaging technology mean that fluorescence guided surgery is becoming a reality for cancer resection (3). Complete tumor removal is crucial for patient outcomes, but difficult to ensure by conventional microscopy as visual characteristics and palpitation are inadequate to determine tumor-free margin. With fluorescence systems, surgeons have the future ability to assess the extent of tumor excision and local metastases in real-time using a fluorescent label that "lights-up" the tumor and hence delineates its margins. Optical endomicroscopy (OEM) enables optical imaging at high resolution typically via a bundle of optical fibers (although rapidly being replaced by chip-on-tip technologies) to enable imaging with microscopic resolution, with the added ability to explore within a variety of cavities. Recently fiber-bundle endomicroscopy has been used in the lung to

assess alveolar structure in emphysema, neoplastic changes in epithelial cells and real-time *in vivo* detection of bacteria (4–6). As well as in the GI tract, where it has been used to detect changes associated with squamous cell carcinoma and colorectal polyps (7). There are a range of OEM platforms, spanning clinical use and developmental systems (6, 8), although standardization is necessary to generate meaningful diagnostic data (9).

Alongside the devices that enable real-time fluorescence imaging capability, optical molecular probes are required that provide contrast and are suitable for use *in vivo*. Although extensive libraries of optical agents for many targets have been developed (10, 11), none have been licensed for routine clinical use. This review will focus on fluorescent molecular probes for inflammatory cells, in particular neutrophils and macrophages. Recent agents allow the identification of these cells, as well as providing information on dynamic cellular processes such as enzymatic activity, redox processes, and phagocytic ability; processes that impact pathophysiology. Overall, inflammatory cell imaging creates an ideal paradigm for patient-specific disease monitoring and intervention (**Table 1**). Recent advances in the fluorescent and Raman imaging are enabling macrophage and neutrophil burden and activity to be described non-invasively and dynamically with tissue-level resolution.

TABLE 1 | Evidence for the role of neutrophils and macrophages as biomarkers in various diseases.

Cell	Information	Disease	References
Neutrophil	Disease stage	Gastrointestinal tumors	(12)
		Solid tumors	(13)
		Inflammatory bowel disease	(14)
	Disease onset	Bacteremia	(15)
		Sepsis-induced acute kidney injury	(16)
	Critical event	Cardiovascular	(17)
		Diabetic neuropathy	(18)
		Chronic obstructive pulmonary disease	(19)
		Pesticide poisoning	(20)
Macrophage	Disease stage	Solid tumors	(21)
		Sentinel lymph node metastasis (breast cancer)	(22)
		Rheumatoid arthritis	(23)
		Liver fibrosis	(24)

Data referenced to meta-analyses or patient studies in the literature.

NEUTROPHILS AS BIOMARKERS

As cells that migrate to diseased tissues and accumulate, both over the course of a disease and due to chemotactic stimuli, neutrophils can provide meaningful prognostic data just by their enumeration. Neutrophil counts have long been used to stratify patients by scoring disease, for example in ulcerative colitis (25). Several large patient studies and systematic reviews show the neutrophil to lymphocyte ratio is useful in staging inflammatory bowel disease (IBD) and numerous solid tumors (13, 14), as well as predicting cardiovascular disease, diabetic neuropathy, sepsis-induced acute kidney injury, glaucoma and bacteremia (15–19, 26). Simple neutrophil enumeration may even resolve the controversial question of when to intervene in carotid artery disease (27). Using explanted human tissues Ionita et al. evidenced correlations between neutrophil count and several critical factors in atherosclerotic plaque stability (28).

Of course, more sophisticated insights can be drawn from considering the viability status of neutrophils and quantifying neutrophil extracellular traps (NETs) independently of neutrophils in altered activation states. The accumulation of neutrophils on the ocular surface in dry-eye disease (DED) is thought to result in pathological NET formation (29). With the recent success of a phase I/II study evaluating DNase treatment for DED, NET burden is becoming an important clinical parameter in this disease (30). Also, neutrophil nuclei undergo morphological changes in DED that can assist the detection of DED-related hyperosmolarity (31). Due to the abundance of human neutrophil elastase (HNE) in NETs (32) and this enzyme's stimulatory role in mucin production (33), HNE may allow diagnostic disease monitoring in DED. Beyond the conjunctiva, neutrophil infiltration is inversely correlated with neuroprotection D1 and their pro-inflammatory activity has clear implications in retinal vascular and neural degeneration (34). Tumor associated neutrophils (TANs) play a wide array of roles and their investigation can reveal where they act in opposition. For example, in early stage lung cancer TANs were shown to help limit disease progression however animal models have elucidated several pro-tumoral mechanisms (35, 36). Some of the heterogeneity measured may come from relying on the expression of TAN markers which can vary in different tumor microenvironments and no suitable marker exists for distinguishing between the N1 and N2 phenotypes (37).

Another layer of insight may be accessible via measurement of neutrophil activity, as studies of patients with inflammatory bowel disease have demonstrated. Patient studies found changes in fecal lactoferrin, calprotectin and the protease HNE were significantly correlated with endoscopy and could be used to distinguish between mild disease, mucosal healing and clinical remission, and even predict flare onset (38). HNE is further implicated in IBD treatment by cleaving therapeutic monoclonal antibodies Infliximab, Adalumimab, Vedolizumab (39). The varied and clear benefits of such simple and direct analyses highlight the precision of the inflammatory response and the diagnostic potential of optical probes for neutrophil imaging.

NEUTROPHIL IMAGING PROBES

Neutrophils are the first leukocytes to be recruited to an inflammatory site. Their capacities to respond en masse and

Abbreviations: DiD, A lipophilic carbocyanine dye; FAM, Carboxyfluorescein; FITC, Fluorescein isothiocyanate; FLIM, Fluorescence lifetime imaging microscopy; FRET, Förster resonant energy transfer; FR, Folate receptor; HNE/NE, (Human) neutrophil elastase; IBD, Inflammatory bowel disease; MMP, Matrix metalloproteinase; MMR, Macrophage mannose receptor; NIR, Near infrared; OEM, Optical endomicroscopy; PET, Positron emission tomography; TPEM, Two-photon endomicroscopy; UC, Ulcerative colitis.

TABLE 2 | Overview of optical probes for imaging neutrophils.

Target	Molecule class	Optical modality	Models	References
Serprocidins	Quenched dendrimeric probe	Fluorescence	Human cells *ex vivo*	(40)
HNE	Quenched probe	Fluorescence	Mouse	(41)
	Quenched dendrimeric probe	Fluorescence	Sheep, human	(42)
FPR1	Peptide	Fluorescence	Human	(43)
	Radioactive nanoparticle	Dual PET/MRI	Mouse	(44)
Nucleus	Label-free	Raman	Human cells *ex vivo*	(45)
	Label-free	2-photon FLIM	Human	(46)

rapidly underscore their potential as biomarkers capable of producing large readouts in short time-frames—properties that are particularly desirable for surgical guidance. The relatively short neutrophil half-life acts to limit any off-target consequences of labeling to days or hours, whilst the persistence of the neutrophilic influx in inflamed tissues makes neutrophil readouts useful over the entire disease monitoring period, irrespective of its duration. Overall, neutrophil imaging creates an ideal paradigm for patient-specific disease monitoring and intervention. Recent advances in the fluorescent and Raman spectroscopic modes of optical imaging are, for the first time, enabling neutrophil burden and activity to be described non-invasively and dynamically with tissue-level resolution (**Table 2**).

Proteases

Human neutrophil elastase (HNE) is a serprocidin stored at millimolar concentrations in the azurophil granules of neutrophils (47). Although HNE is chiefly a microbicidal protease, its broad substrate specificity allows neutrophils to use it intracellularly, extracellularly and in membrane-bound form for a variety of purposes. Phagocytosis, extravasation (48), extracellular matrix remodeling (49–51), cell-signaling (52), mucus production (53), mucociliary function, (54), and NETosis (55) all have roles for HNE and a host of further interactions give the enzyme utility for other cell-types including monocytes, endothelial, and adenocarcinoma cells. When released by activated neutrophils HNE can be used to destroy pathogens and promote neovascularization as part of tissue repair, however sustained HNE release contributes to the pathophysiological sequalae of acute respiratory distress syndrome, lung adenocarcinoma, atherosclerosis and other chronic inflammatory diseases.

Craven et al. recently reported a probe that revealed neutrophil activation. This was designed to detect the serine proteases (serprocidins) using a pan-serprocidin substrate. A tribranched probe was developed which maintains an optically super-silent ground state with a methyl red and fluorescein FRET pair on each of its three branches (**Figure 1A**) (40). The structure facilitates internalization by activated neutrophils and once in the phagolysosome, active serprocidins cleave the peptide sequences to remove the methyl red quenchers and generate a large fold increase in fluorescence (**Figure 1B**). The probe generates bright intracellular puncta, in human neutrophils, within seconds of activation with pharmacological stimulus or bacterial co-incubation. By adding the probe to whole blood in a simple, no-wash, no-lyse, flow cytometric assay, activated neutrophils could be profiled (**Figure 1C**). Combining rapid signal generation and detailed cell-type specific analysis situates this pan-serprocidin probe as a promising patient-stratification biomarker for several chronic inflammatory diseases.

The neutrophil elastase probe NE680 is a near-infrared multi-branched probe which is sensitive to cleavage by murine NE and HNE, amongst others (**Figure 2**) (41). It consists of a peptide sequence (PMAVVQSVP) flanked by NIR fluorophores and conjugated to a polylysine dendrimer, which lengthens its plasma and tissue half-lives and results in internal quenching. Upon cleavage by proteases, NIR fluorescence emission is generated. NE680's quantification of NE activity was demonstrated by incubating lung sections, from LPS/fMLF challenged mice, in increasing doses of the NE-specific inhibitor, sivelestat (**Figures 2C,D**). Non-invasive, quantitative NE imaging was demonstrated using fluorescence molecular tomography (41). Wang et al. demonstrated a similar dose dependent reduction in NIR fluorescence of NE680 could be achieved under more physiologically relevant conditions, using recombinant alpha 1-antiproteinase (a1PI) instead of sivelestat (56). Further studies using NE680 have revealed roles for NE in promoting neutrophil accumulation in atherosclerotic plaques, insulin resistance and arthritic pain, in murine models (57–59). Although NE680 cleavage by HNE has been demonstrated *in vitro*, structural differences between the murine and human NE active sites and functional differences between murine and human neutrophils mean the clinical utility of NE680 has yet to be demonstrated.

Although a wealth of neutrophil probes have not reached *in vivo* studies, exciting developments in optical probe design provide discriminatory power between related proteases. Despite their concomitant release from degranulating neutrophils, the various serprocidins perform distinct molecular functions (60). Screening combinations of natural and unnatural amino acids by their kinetic affinity and rate constants, Kasperkiewicz et al. designed a HNE probe with a 100-fold sensitivity over the previous champion substrate designed by Korkmaz et al. (61). The group's combinatorial substrate library technique generated substrate-based activatable probes and inhibitory, targeted probes and their approach included counter selection which biases against the interference of substrate cleavage from

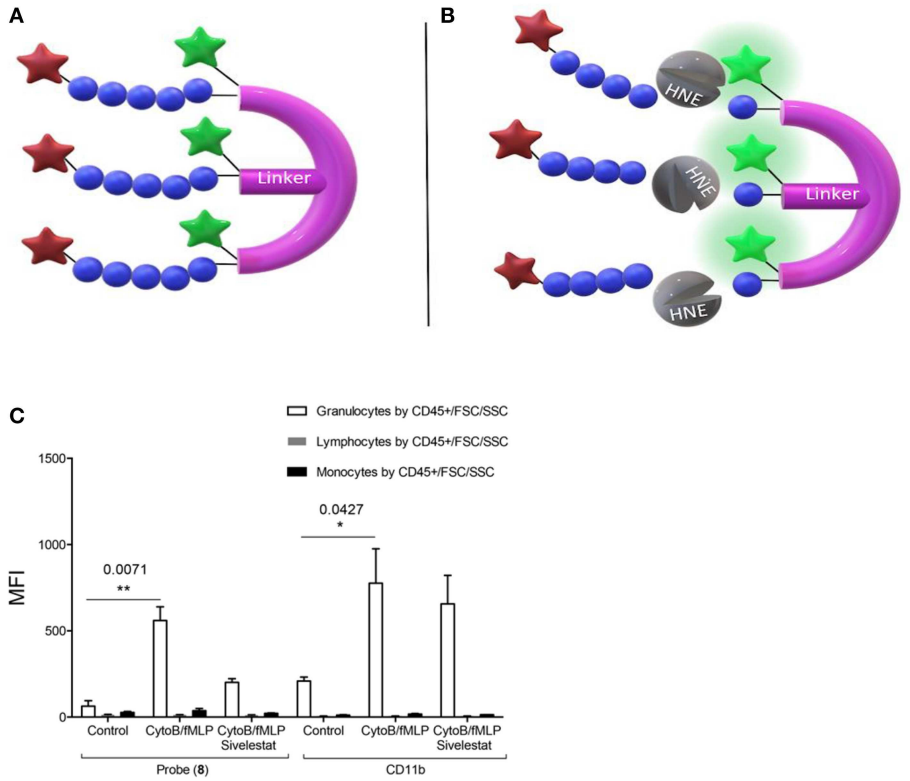

FIGURE 1 | Structure of Craven's neutrophil probe **(A)** before and **(B)** after cleavage by active HNE and indicating the resulting FAM fluorescence. **(C)** In a no-wash, no-lyse whole blood flow cytometric assay, neutrophils activated with bacterial products take up Probe (8) and upregulate CD11b. Fluorescent signal is blocked in activated neutrophils with 100 μM sivelestat co-incubation. MFI = Geometric mean fluorescent index. *$P < 0.05$, **$P < 0.01$, exact multiplicity adjusted p values are shown with the figure. **(C)** Reproduced under the CC BY 4.0 license (40).

similar protease families (62, 63). Finally, the recently synthesized fluorogenic toolbox contained unique substrate-fluorophore combinations for each of the four neutrophil serine proteases (HNE, proteinase 3, cathepsin G and neutrophil serine protease 4) and revealed for the first time their uneven distributions in azurophil granules (64).

To enable clinical, functional neutrophil imaging via HNE activity at inflammatory sites a Neutrophil Activation Probe (NAP) was developed (42). Using static quenching NAP's tribranched structure holds fluorescein moieties in close proximity limiting fluorescence. Each of these SmartProbe's three branches contain an HNE substrate sequence cleaved by the active enzyme to generate large fold increases in fluorescent intensity. Encouraging results with NAP came from synthesizing the SmartProbe to GMP standards and endomicroscopically imaging neutrophil activation in ventilated and perfused *ex vivo* human lungs (37). Craven et al. found NAP to be dequenched within the phagolysosome specifically in response to NE and this lead to a successful phase 1 clinical study (NCT01532024) (42). The ability of NAP to inform clinical decision making is currently being investigated in the phase 2 clinical study, SNAP-IT (number: NCT02804854). SNAP-IT will evaluate the utility of imaging NAP-illumined neutrophils, endomicroscopically, in intensive care unit patients.

Formyl Peptide Receptor 1

NIR imaging is often superior to other wavelengths as tissue autofluorescence is lowest in this region of the visible spectrum. Zhou et al. synthesized a NIR fMLF receptor 1 targeting nanoprobe for imaging inflammation (**Figure 3**) (43). The issue of inflammatory site access was solved by building the labeling (cFLFLF) and fluorophore (Oyster-800) components onto a hydrophilic 8-arm PEG scaffold. There are many benefits to using the cFLFLF ligand: its high affinity FPR1 binding (K_d = 2 nM) generates a sensitive readout of leukocyte distribution (65). The ability of cFLFLF probes to access inflammatory sites with either PET (^{64}Cu, ^{99m}Tc) or NIR (Cy5, Cy7) labels has also been demonstrated. However FPR1 is not cell-type specific and these probes bound macrophages (66) and neutrophils (67, 68). cFLFLF probes may generate a useful readout when information on inflammatory cell accumulation is sought in broad terms but may fail to clarify whether clinical intervention should focus on altering neutrophil or macrophage activity.

Pellico et al. created neutrophil-specific radiotracers with dual PET and MRI signals by coating gallium-doped nanoparticles with cFLFLF for FPR1 labeling (44). Coating with peptide can produce significant probe hydrophobicity which has prevented other radiotracers from reaching the inflammatory site. By citrate-coating nanoparticles, the relatively large nanoparticle

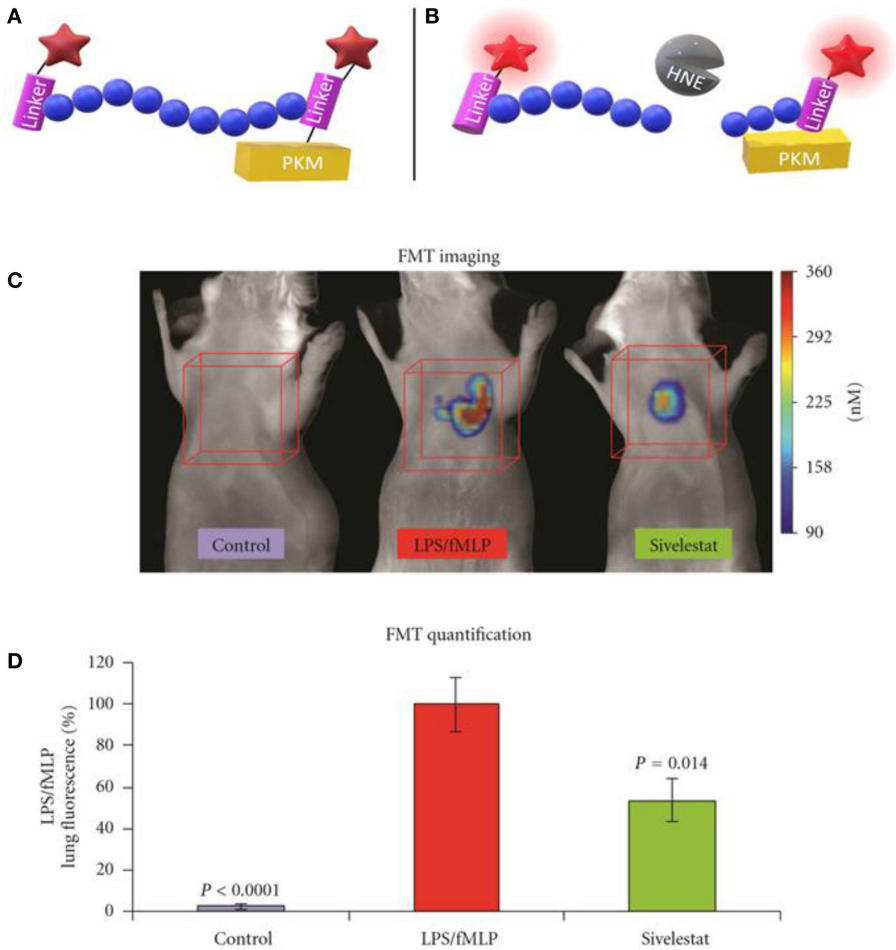

FIGURE 2 | Schematic representation of NE680 FAST before **(A)** and after **(B)** cleavage by active NE which alleviates fluorescence quenching. **(C)** Fluorescence molecular tomography of NE680 FAST (4 nM intranasal) instilled into control, LPS/fMLP and LPS/fMLP mice treated with inhibitor. NIR signal is absent in untreated controls and reduced in sivelestat (5 mg/kg intranasal) treated controls **(D)** and mean concentration of fluorescence (in nM) was quantified in the lung area ROIs (orange cubes) for control ($N = 12$), LPS/fMLP ($N = 16$), and sivelestat ($N = 12$) groups. **(C,D)** Copyright 2011 Kossodo et al. Reproduced under the CC BY 3.0 license (41).

surface confers the necessary solubility for targeting neutrophils *in vivo*. Although neutrophil depletion was capable of removing signal, it also removes important cross-talk from the LPS inflammatory response.

A truly neutrophil specific target has proved elusive. Instead neutrophil specificity has arisen from combinatorial strategies exploiting the unique confirmations of certain targets within neutrophils. For example, HNE reaches such high concentrations in neutrophils that most systems will fail to detect the minority of HNE positive monocytes which bares far lower quantities of the enzyme. Neutrophil specific functions can also be exploited by careful probe design. Phagolysosome alkalinisation does not occur in monocytes and enhance the fluorescence signal of some fluorophores. The super-silent FRET probe combines these structural and functional cellular characteristics to achieve neutrophil specificity. Label-free methods of cell identification have also sought neutrophils using targets found in other cell types but uniquely arranged in neutrophils.

Label Free Neutrophil Imaging

Neutrophil imaging in the context of inflammatory research has aimed at understanding the relevance of cellular components to cell function. Questions of molecular colocalization and characterization are well-served by fluorescent labels for elucidating the spatiotemporal relationships of cells and subcellular structures without altering the processes for investigation. As translational research influences surgical guidance questions of long-term cytotoxicity and ease-of-adoption are more important. Label free imaging, which may seem imprecise for research purposes, is often cheaper, safer and does not require the considerable translation effort of alternative techniques. Molecules such as NADH, elastin, and hemoglobin have been claimed to provide intracellular and extracellular autofluorescence, but signals from cells will always be an amalgamation of signatures of multiple and complex analytes. There is still much characterization to generate clinically meaningful autofluorescence imaging and techniques such as

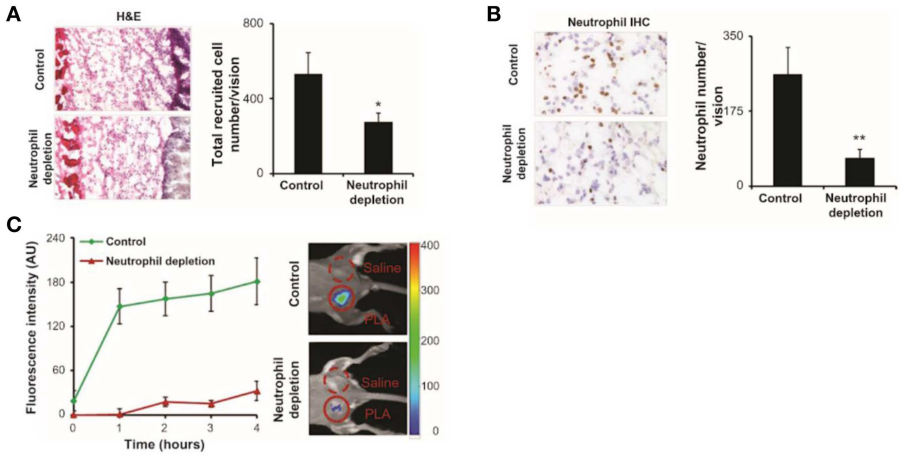

FIGURE 3 | fMLF receptor targeting nanoprobes were implanted in control and neutrophil depleted mice, neutrophils were labeled and quantified. **(A)** Image of hematoxylin and eosin staining and quantification of inflammatory cells. **(B)** Immunohistochemistry and quantification of neutrophils. **(C)** Fluorescence intensities over 4 h post-injection showing the diminished accumulation of the nanoprobe in neutrophil depleted mice compared to control. H&E, hematoxylin and eosin; IHC, immunohistochemistry; PLA, poly(lactic acid); $^{*}P < 0.05$, $^{**}P < 0.01$. Copyright 2012 Zhou et al. Reproduced under the CC BY-NC 3.0 license (43).

fluorescence lifetime imaging may become an important source of differentiation. Reflectance microscopy, which distinguishes between matter of different refractive indices, is now also capable of cellular resolution. For high-resolution imaging, individual molecules can be detected and quantified via Raman spectroscopy. Label free imaging is en route to becoming as informative as fluorescence image-guided surgery can be, a limit it may exceed in a multi-modal platform.

Raman Spectroscopy

By measuring the minute proportion of photons which interact with molecules inelastically, Raman spectroscopy can, non-destructively, describe the chemical composition of unlabeled matter. The first look at a leukocyte using Raman spectroscopy was when Puppels et al. compared eosinophils and Chinese hamster lung cells (69). The group found nuclei spectroscopically distinct from cytoplasm and that distinctions between granulocytes may be made on the basis of their cytoplasmic contents (70). In 1998, Otto et al. collected the first Raman spectrum of activated neutrophils (71). More recently, Ramoji et al. demonstrated the ability to discern between lymphocytes and neutrophils with concomitant Raman mapping of nuclear morphology (45). Using principal components analysis, cells could be classified with 94% accuracy in the validation dataset and predicted with 81% accuracy in a new dataset from a completely different donor. As Raman spectroscopy can describe intracellular contents it may be better suited to quantifying cell function. Instead of identifying cells, Harz et al. used spectrally distinct Raman and fluorescence excitation wavelengths to successfully multiplex these spectroscopic and microscopic techniques (2). Particularly in such a multiplexed system, intracellular localization and oxidation states of functionally significant molecules may be revealed through Raman mapping to imitate whether or not neutrophils are effecting processes such phagocytosis and to what extent (72).

Two-Photon Endogenous FLIM

The question of whether or not technology as nascent and complex as two-photon microscopy can be translated into a clinical endomicroscopy technology is unanswered. Although confocal endomicroscopy is in clinical use, two-photon endomicroscopy (TPEM) carries additional fiber optics challenges such as fiber non-linearity distorting the two-photon excitation light and the low quantum yields of intrinsic fluorophores (73). These and other hurdles were overcome in 2008, when TPEM of human and mouse sarcomeres was conducted using a GRIN lens (74). The technique involved a minimally-invasive needle clad fiber capable of imaging directly beneath the skin. *In vivo* TPEM was performed laparoscopically with a "stick" lens which avoids GRIN lens associated spherical aberrations revealing ovarian cancer through a laparoscopic procedure, centimeters into the body (75). However murine tissues were investigated *in vivo* with a flexible FLIM endomicroscope, of working distance 135 μm in 2011, and the field continues to rapidly improve this label-free technology (76).

Using two-photon excited fluorescence (TPEF), Zeng et al. characterized blood cells by their endogenous fluorescence lifetime signals (**Figure 4**). TPEF fluorescence lifetime imaging can detect differences in bound and unbound NADH such erythrocytes, agranulocytes and granulocytes are distinguishable (46). As proportions of bound and free NADH vary by the dominant metabolic pathway employed by the cell—TPEF FLIM is functional imaging. Metabolic functional imaging may be able to identify granulocytes undergoing phagocytosis but whether or not phagocytosis and other factors affecting the NAD/NADH ratio, such as oxygen availability, can be disentangled remains unclear. By visualizing cytoplasmic protein, TPEF FLIM can identify the size and shape of cells and, by exclusion, their nuclei—detailing the characteristic lobular structure of granulocyte nuclei. With neutrophils comprising 95% of the granulocytes population, these morphological distinctions give TPEF FLIM neutrophil-specificity to rival the

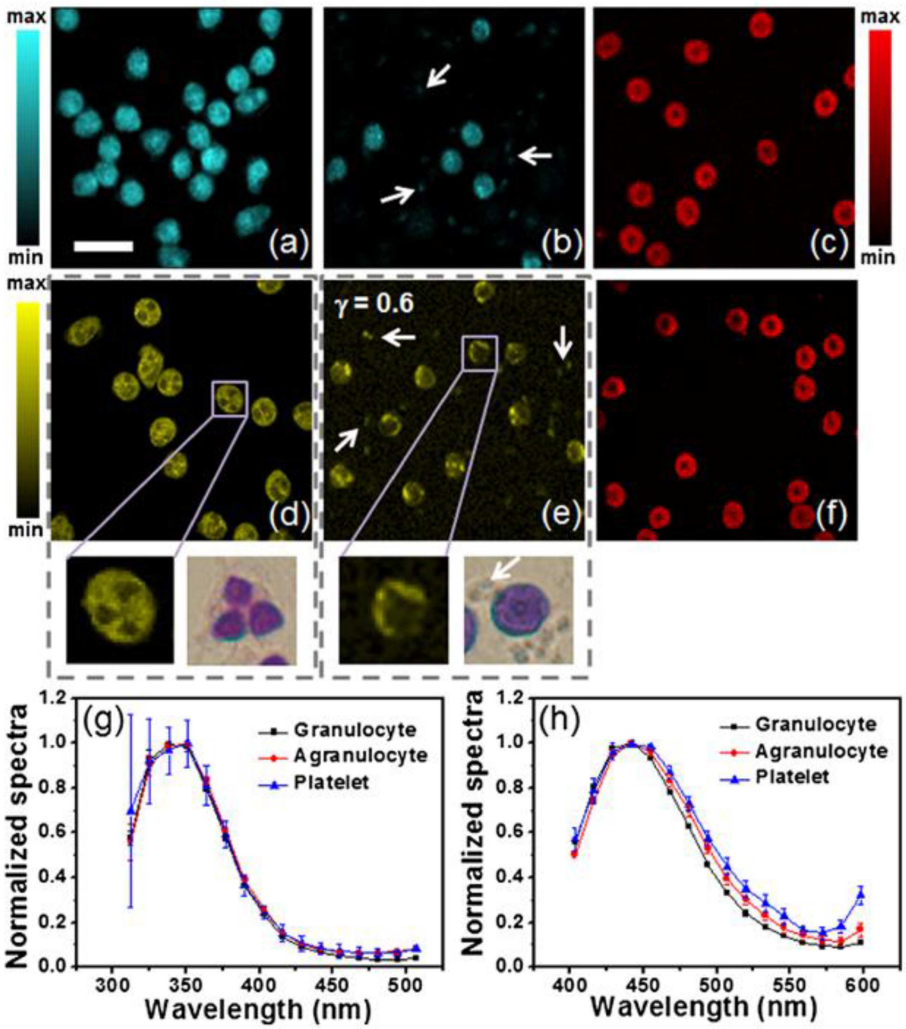

FIGURE 4 | TPEF showing granulocytes, agranulocytes with platelets (white arrows) and erythrocytes **(a–c)** under 600 nM excitation and **(d–f)** under 700 nM excitation, with bright field images in **(d)** and **(e)** showing blood smears granulocytes and agranulocytes with platelets. Normalized spectra of blood cell autofluorescence under 600 nm (5 mW) and 720 nm (10 mW) excitation, are seen in **(g)** and **(h),** respectively. The acquisition time for each TPEF image: 32 s; resolution: 128 × 128 pixels; scale bar: 20 μm; γ is the gamma value in the gamma correction of **(e)**. Reproduced with permission from Zeng et al. Copyright 2013 SPIE (46).

best ligand-based, fluorescent probes. Although the distinction between phagocytic and untreated neutrophils is subtle, this technique can separate untreated from activated neutrophils on morphological grounds. Quiescent neutrophils have a rounded morphology but membrane ruffling characteristic of neutrophil activation was visualized when neutrophils phagocytosed *E. coli* (46).

MACROPHAGES AS BIOMARKERS

Macrophages are readily found at the site of inflammation or infection, forming the first defense against pathogens. Although they play a key role in the initiation of defensive inflammation, recent literature suggests they are also responsible for the resolution of inflammation and repair processes (77). Several large studies show the role of macrophages in solid tumors, sentinel lymph node metastasis, rheumatoid arthritis and liver fibrosis (21–24). In ophthalmology, macrophages have been shown to play a role in preventing ocular infection (78) and contribute to corneal wound healing (79) and biomarkers of macrophage activity have been linked to primary open angle glaucoma and dry eye disease (80, 81).

Macrophages have been broadly classified into two different phenotypes—M1 and M2, with further subsets M2a, M2b, M2c identified, and they display plasticity by moving between these phenotypes (82). Generally, the M1 "classically activated" macrophages are seen as pro-inflammatory and exhibit killing mechanisms against microorganisms, while M2 "alternatively activated" macrophages are anti-inflammatory and exhibit wound healing functions. Further evidence shows that they

TABLE 3 | Overview of optical probes for imaging macrophages.

Target	Molecule class	Optical modality	Models	References
FR-β	Small molecule	SPECT/CT, *in vivo* imaging	Mice/Human (RA)	(85, 86)
CD206	Nanobody (sdAb)	PET	Mice	(87)
	Peptide	Fluorescence	Mice	(88)
MMP-12	Peptidomimetic	Fluorescence	Mice	(89)
Cathepsins	Quenched polymer probe	Fluorescence	Rat	(90)
	Peptide—activity probe	PET/CT and Fluorescence	Mice, Human (PET in IPF patients)	(91)

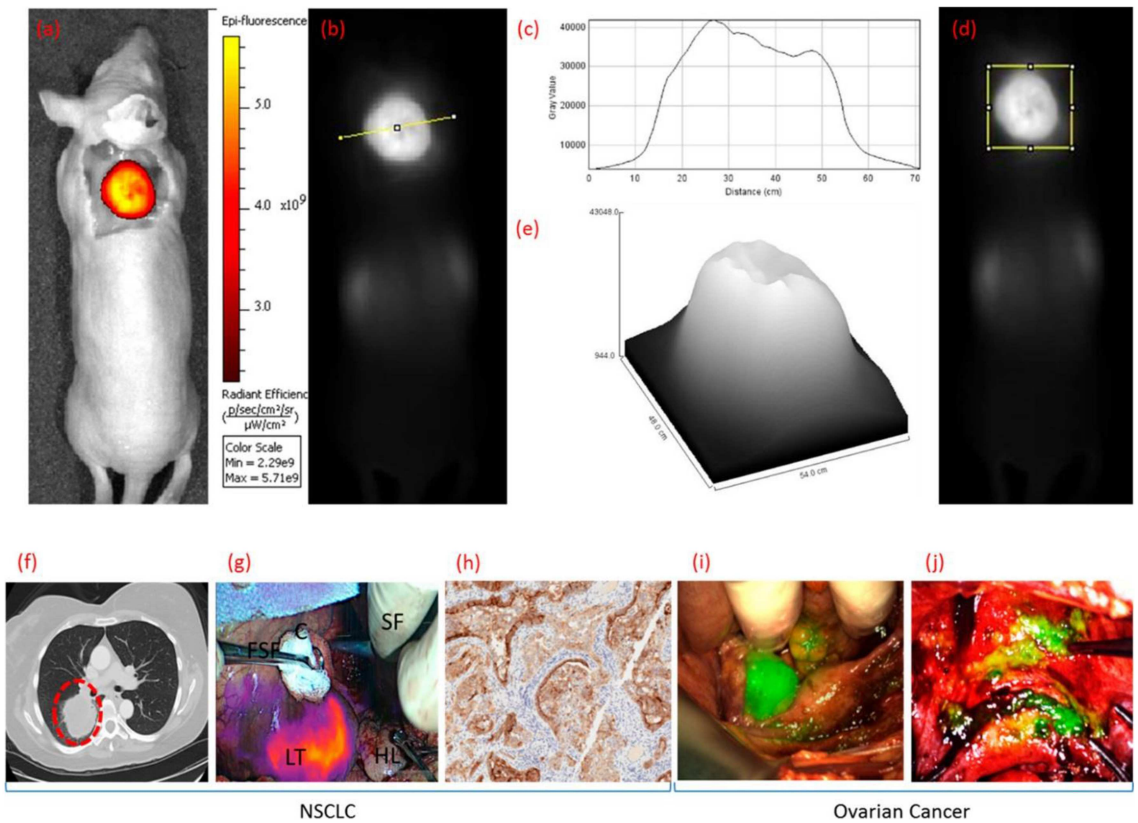

FIGURE 5 | Clinical uses of OTL38 showing whole body fluorescence imaging of a mouse bearing a FRα$^+$ KB tumor in color **(a)** and grayscale **(b,d)** 2 h after administering OTL38. Analysis of gray value vs. distance **(c,e)** [across the line from **(b)** or within the box from **(d)**]. Representative fluorescence images NSCLC and ovarian cancer during image-guided surgery 2 h after administering OTL38. **(f)** Preoperative CT image of pulmonary tumor nodal, **(g)** overlay of fluorescence image over white light image of pulmonary tumor nodal, and **(h)** immunohistochemical (IHC) staining of resected pulmonary tumor nodal indicating tumor is FRα+. Representative fluorescence images over white light images of primary and metastatic ovarian tumors in **(i)** uterine adnexa and **(j)** uterus and bladder peritoneum. LT, lung tumor; HL, healthy lung; FSF, Foerster sponge forceps; SF, surgeons fingers; C, cotton. Adapted with permission from Mahalingam et al. Copyright 2018 American Chemical Society (92).

do not rest in one polarization state, instead they may be reactivated into a different state. The ability to understand the crosstalk between macrophage activation signals and how this alters their phenotypes would be valuable in characterizing disease phenotypes. In oncology, tumor associated macrophages (TAMs) represent a significant imaging target due to their recruitment in the microenvironment of a tumor (83). Their presence contributes to the invasiveness of tumors as they have been linked to angiogenesis, cell proliferation, invasion and immune suppression (84). Targets to visualize macrophages include MMP-12, cathepsin S, the macrophage mannose receptor (CD206), and folate receptor beta (FR-β) (**Table 3**).

Folate Receptor Beta

Folate receptor (FR) targeting is a promising method for visualization of cells that overexpress the folate receptor. Recently, a demonstration of the capabilities of folate targeting during fluorescence guided surgery of cancer was described by Mahalingam (92). OTL-38 is an NIR labeled folate that accumulates in cancer tissue, has a high target affinity and enables the visualization of cancer tissue using image-guided surgery (**Figure 5**). This agent has completed Phase I and II trials for ovarian and lung cancers, and is now in Phase III clinical trials for the detection of FR$^+$ ovarian cancer (NCT03180307). For inflammatory cells, the β isoform (FR-β) is expressed on

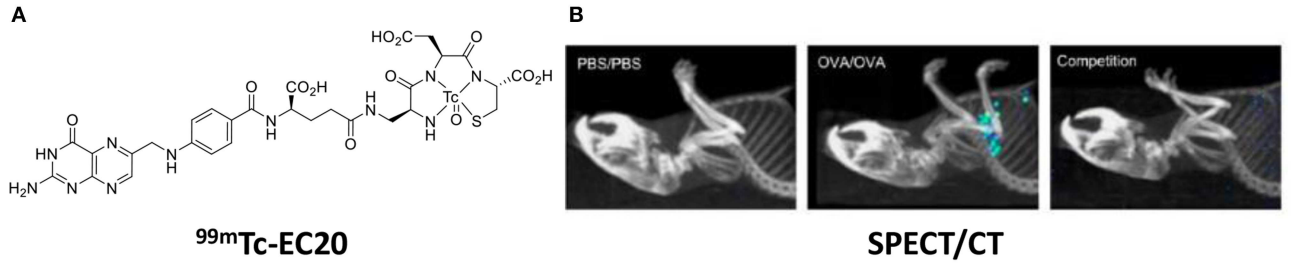

FIGURE 6 | (A) Chemical structure of EC20—a folate radiolabel. **(B)** SPECT/CT images ^{99m}Tc-EC20 uptake in the lung of OVA-induced asthmatic mice, competition experiment with ^{99m}Tc-EC20 plus 100-fold excess folate-glucosamine. Adapted with permission from Shen et al. Copyright 2013 American Chemical Society (86).

activated macrophages and has a high affinity for its ligand folic acid ($K_d = 10^{-10}$ M) (93). Its identification on synovial macrophages in patients with rheumatoid arthritis was first described by Nakashima-Matsushita et al. (94). Studies on both rheumatoid and osteoarthritis in dogs, horses, rats, mice, and humans have demonstrated that essentially all joints experiencing active inflammation uptake folate conjugates (93). A number of studies have reported on the cellular uptake of FR targeted molecules by activated monocytes (95) and macrophages in a number of different diseases (85, 86, 96).

Xia et al. investigated the presence of the folate receptor on activated macrophages from arthritic patients (85). Fluorescence imaging was used to show that the folate receptor was a valid marker for activated macrophages, while non-activated macrophages did not express the folate receptor. After characterizing that bacteria-recruited murine macrophages expressed FR and that these were activated (upregulation of Ly-6C/G, CD80, and CD86), folate-FITC was incubated with the synovial fluid of patients with diagnosed rheumatoid arthritis. A subset of the CD11b$^+$ macrophages was found to uptake folate-FITC, and competition experiments showed that this uptake could be inhibited with the non-conjugated folic acid—showing FR specificity. Finally, a technetium-radiolabelled folate (FolateScan: EC20) was utilized to perform SPECT imaging of human inflamed joints in a Phase II trial (NCT00588393).

In murine models of asthma, Shen et al. showed that *ex vivo* lung macrophages with an M2 phenotype (arginase$^+$, CD206$^+$) bound the green fluorescent probe, folate-Oregon Green. Further, SPECT/CT imaging of ^{99m}Tc-EC20 showed uptake in ovalbumin induced asthmatic lungs, while there was no uptake in the lungs of healthy mice (**Figure 6**) (86).

Recent work by Poh et al. showed that a folate liposome could act as a specific method of targeting FR$^+$ immune cells, specifically in mouse models of colitis and atherosclerosis (97). This study used fluorescent DiD liposomes, labeled with folate, as a demonstration of the ability to deliver payloads via the folate receptor which can accumulate in inflamed tissues. Atherosclerotic mice (ApoE$^{-/-}$ mice fed a high fat diet) were injected via the tail vein with 2 mg/kg of NT-liposome-DiD or Fol-liposome-DiD, respectively. Fluorescence imaging showed selective uptake of Fol-liposomes in the atherosclerotic mice.

To further our understanding of the clinical applicability of folate targeted imaging agents, the field should aim to evaluate their performance in human inflammatory models. It is however also worth mentioning an observation from this field; the use of folate depleted media is necessary for any folate targeting cell studies due to high levels of folic acid in routine media formulations.

CD206

CD206, also known as the macrophage mannose receptor (MMR), is a well-reported marker of M2 differentiated macrophages (82). Its functional role is to recognize mannose lectins found on pathogens. A number of different approaches to probe design have been taken against CD206$^+$ macrophages, from antibodies to a more recent report of a target-binding peptide. The Manocept concept of nanomolecule imaging agents targeting the lectin domain of CD206 has resulted in the FDA approval of γ-Tilmanocept, a ^{99m}Tc-labeled radiolabelled tracer for the imaging of sentinel lymph nodes (98). A similar strategy was applied by Kim et al. who developed a near-infrared MMR targeting polymer and utilized using OCT-NIRF imaging to visualize carotid atheroma plaques (99). However, mannose derivatives are not specific to CD206 and can be recognized by other mannose receptors (100). Therefore, there is a need to develop ligands that are more specific for CD206 which are more suitable for use in the clinic.

Targeted Nanobodies

The most advanced agents for CD206 targeting are labeled nanobodies, which have shown promise as molecular imaging agents (101). Nanobodies (Nb) have been developed as imaging tracers against a number of targets in oncology and inflammation due to their high affinities and small size compared to antibodies (102). Movahedi et al. produced a ^{99m}Tc-labeled nanobody against MMR with an affinity of 2 nM determined by SPR and validated its use for SPECT/micro-CT imaging of tumor-associated macrophages in preclinical models (103). SPECT/CT imaging in tumor-bearing mice showed uptake of the Nb which was significantly higher than uptake of the control Nb with analysis of the dissected tissue confirming these findings.

This nanobody was further developed by Blykers et al. as an ^{18}F-PET tracer for the detection of macrophages in tumor stroma (87). Tumor associated macrophages (TAMs) with upregulated CD206 were found to be tumor promoting. *In vitro* studies with the ^{18}F-fluorobenzoic acid (FB) labeled nanobody (anti-MMR 3.49) showed that it had a high affinity

for human MMR (K_D = 1.8 nM), while *in vivo* biodistribution studies showed fast renal clearance and specific retention in the tumor and MMR-expressing tissue. In a small animal PET imaging study, the nanobody was specifically recognized by MMR in 3LL-R tumor bearing mice, when compared with the uptake in MMR-deficient mice (**Figure 7**). This ligand shows promise as a radiopharmaceutical, while in future it could be developed as an optical probe for highlighting M2 macrophages by fluorescence guided surgery. As noted by Debie et al., the fluorophore chosen and method of conjugation should be carefully considered when developing labeled nanobodies (104).

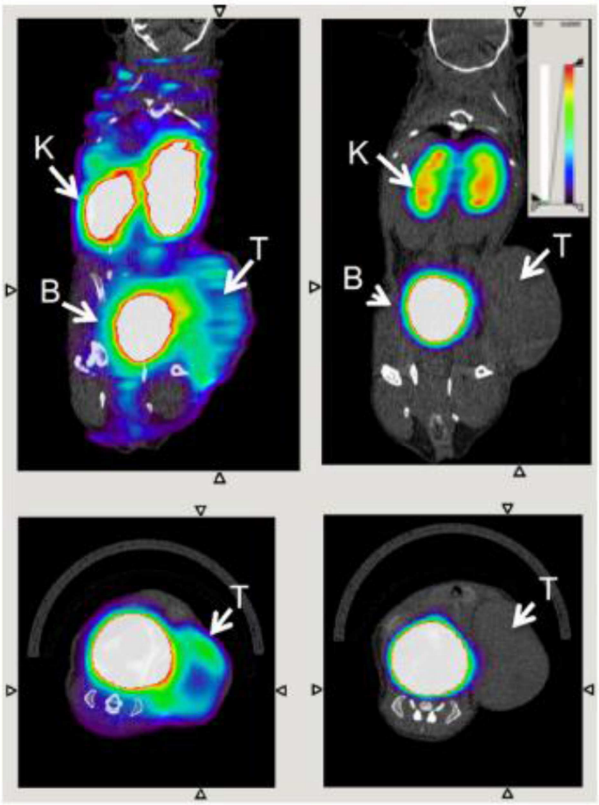

FIGURE 7 | Transverse and coronal PET/CT images of WT (left) vs. MMR-deficient (right) 3LL-R tumor–bearing mice scanned 3 h after injection of ^{18}F-FB-anti MMR 3.49. Arrows point to tumor (T), kidney (K), and bladder (B). Adapted with permission from Blykers et al. Copyright 2015 SNMMI (87).

Peptides

Fluorescent peptides are a widely utilized method for labeling receptors and a number of peptidic agents are under clinical investigation for cancer and bacterial infection imaging (10). Recently, Scodeller et al. showed that M2-like TAMs could be targeted by a "FAM-UNO" fluorescent peptide [sequence: 5(6)-FAM-Ahx-CSPGAKVRC] (88). The peptide sequence was identified by *in vivo* phage display of peptides that bound peritoneal macrophages in 4T1 tumor-bearing mice. FAM-UNO was found to target M2-like TAMs via the CD206 receptor (**Figure 8**) and this binding was confirmed by fluorescence anisotropy. Cargos were delivered to TAMs by coating polymer vesicles with the FAM-UNO peptide and these could be used as a contrast agent for sentinel lymph node imaging. Although this agent is yet to be translated to humans, it could be an attractive method for imaging TAMs. However, green autofluorescence of human tissues means alternative fluorophores may need to be considered to make a case for future clinical applications.

MMP-12

The matrix metalloproteinases (MMPs) are a family of proteases that play a key role in ECM structure, function and remodeling. In the tumor microenvironment macrophages have been found to be potent producers of MMP 2 and 9 (105). It is important to note the pioneering work of the Tsien lab and Avelas Biosciences in advancing activatable cell penetrating peptides (ACPPs) for imaging protease activity. In 2004, the lab demonstrated that an MMP-2 cleavable ACPP could detect tumor cells in resected tissue (106). More recently, Miampamba et al. developed AVB-620, a ratiometric ACPP

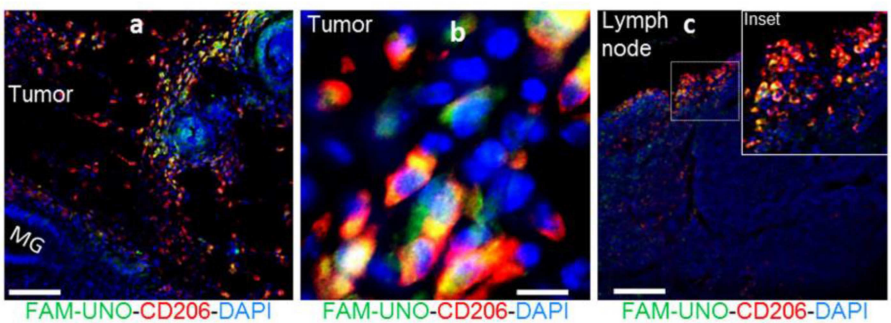

FIGURE 8 | FAM-UNO accumulates in CD206$^+$, TIE2$^+$ macrophages in breast tumors **(a,b)** and lymph nodes **(c)**. 4T1 tumor bearing mice were injected i.v. with FAM-UNO (30 nmol), mice were sacrificed after 2 h and tumor tissues were analyzed by immunofluorescence: rabbit anti-FAM (green), rat anti-CD206 (red) antibodies and counterstained with DAPI. Scale: 100 μm. Reproduced under the CC BY 4.0 license (88).

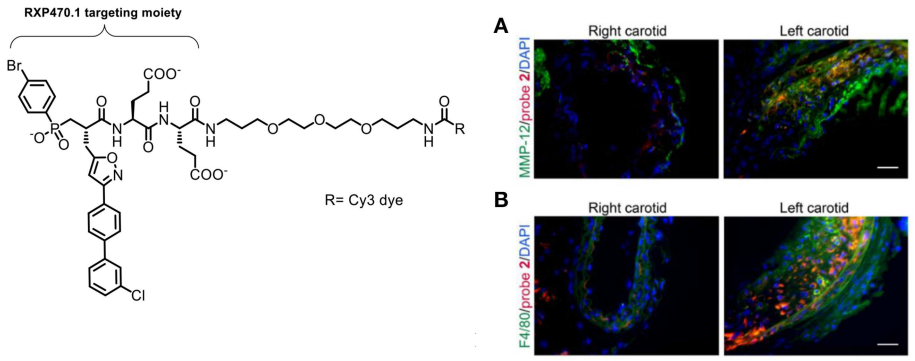

FIGURE 9 | Left: Structure of the Cy3-labeled MMP-12 probe 2. Right: Immunostaining demonstrating that the Cy3-labeled probe 2 (red) binds to carotid arteries and co-localizes with an MMP-12 antibody (**A**, green) and F4/80 positive cells (**B**, green). Nuclei are stained with DAPI (blue). Scale: 50 μm. Reproduced under the CC BY 4.0 license (89).

with Cy5 and Cy7 fluorophores that is a substrate for MMP-2 and -9 (107). This agent has completed Phase I clinical trials for imaging breast cancer tumors in patients undergoing surgery (NCT02391194).

While there are many non-selective imaging agents for MMPs, there is a lack of selective MMP tracers and this may hamper the understanding of the role of a specific MMP in disease. For example MMP-12, macrophage elastase, is responsible for the breakdown of elastin and it is associated with a number of inflammatory pathologies such as aortic aneurysm, emphysema, and rheumatoid arthritis (108). It has been characterized as having a protective role during wound healing in injury models (109).

Bordenave et al. reported the synthesis and evaluation of a Cy5 MMP-12 probe based on a pseudopeptide (RXP470.1) which had previously been shown to inhibit atherosclerotic plaque growth *in vivo* (110). This study noted that the fluorophore used was important to the blood clearance rate and biodistribution of this probe, a factor that has been highlighted by other groups working on the development of fluorescent probes. Further optimization lead to a zwitterionic labeled probe which had good affinity to MMP-12 and fast blood clearance (89). The selectivity of this MMP inhibitor should give advantages over other pan-MMP probes in showing the specific MMP implicated in a disease. Immunostaining showed an analog (probe 2) bound to MMP-12$^+$ and F4/80 macrophages (**Figure 9**). The probe was used for imaging active forms of MMP-12 in murine models. Using a sponge implantation model of sterile inflammation, increased cell infiltration was seen which correlated with mannose receptor positive macrophages. The study was also interested in the role that MMP-12 plays in aneurysm. In a model of carotid aneurysm, significant upregulation of MMP-12 was seen, along with significantly higher signal for the probe, compared to the control (**Figure 9**). Although this was only demonstrated in a mouse model, because of this probe's high selectivity and the clinical relevance of the experimental setup could allow this probe to be used in an intraoperative setting.

Cathepsins

TAMs remodel the extracellular matrix (ECM) through MMPs and cathepsins, specifically during tumor invasion (111). Onda et al. used a commercial NIR fluorescent protease-activatable probe (ProSense), in which they demonstrated imaging of cathepsin activity and confirmed its localization to macrophages. Using *in vivo* and *ex vivo* models of colon cancer they showed that infiltrating TAMs initiate tissue remodeling at the tumor margins by secreting cathepsins. ProSense signal at the tumor margin was shown to be due to cathepsin B$^+$ macrophage infiltration in a rat colon model (90). However, large probes such as ProSense suffer from slow tumor uptake leading to slow rates of activation, as well as demonstrating off-target activation by other proteases which limits their applicability as a fluorescence diagnostic tool.

A number of alternative cathepsin activatable probes are under development (112, 113). Withana et al. investigated the role that macrophages play in idiopathic pulmonary fibrosis (IPF) by staining human biopsy tissue from IPF patients. The optical probe BMV109 is broadly activated by cathepsins B, S, L, and X, was used to validate pan-cathepsin labeling of sectioned frozen tissue. This showed that macrophages expressing active cathepsins were at fibrotic sites in comparison to healthy tissue which showed no cathepsin activity (91). To date, this probe has only been demonstrated in the topical labeling of IPF tissue, further investigation would be necessary to show its utility in fluorescence based diagnostics in the clinic.

CONCLUSION

The nascent field of optical molecular imaging of inflammatory cells appears to be a vibrantly innovative arena full of early-stage biomarkers that offer promise of patient benefits. Targeting neutrophils and macrophages may deliver previously inaccessible measures of disease activity across common and life-threatening diseases. Whilst, in this review, the current stage of neutrophil and macrophage imaging has been discussed, clearly other inflammatory cells such as T cells play major role

in interventional medicine. With many non-redundant targets and readouts available, probe multiplexing seems a particular advantage of this field with the potential to matching monitoring and treatment with immunological precision. As well as being informative in its own right, parallel label-free imaging may become a rapid means of interpreting labeled techniques across multiple contexts and machine learning data-reduction stands to push the power of OMI even further. An exciting therapeutic potential lies in the how imaging agents can impact the drug discovery process—with immune cells. These new technologies stand to enrich assay outputs, accelerate drug development decisions and clinical outputs, and enable better direct drug response metrics in trials.

Future studies will demonstrate the translatability of imaging agents into clinically useful optical probes. Despite the plethora of novel reagents advancing with *in vitro* investigations very few have begun the translational journey. This inertia is perhaps not surprising as the technical demands of translating novel imaging methods can become overwhelming, especially within an academic environment. Probes must be innovative enough to meet clinical needs, yet synthetically feasible and complementary to imaging systems. This is a fiercely interdisciplinary pursuit from start to finish and nearly impossible without optical imaging device standards, as all technologies must meet safety and efficacy standards. Without standardization, investigators risk underestimating translation-ready reagents with "sub-standard" apparatus, or unnecessarily pursue doomed reagents with poor selectivity and specificity (114).

AUTHOR CONTRIBUTIONS

GB and TC wrote the manuscript. KD and MB assisted with proofreading and preparation for publication.

FUNDING

We thank the Engineering and Physical Sciences Research Council Optima CDT (grant: EP/L016559/1) and Biotechnology and Biological Sciences Research Council (grant: BB/N503940/1) for supporting this work, plus additional support from GlaxoSmithKline.

REFERENCES

1. Sun Y, You S, Tu H, Spillman DR, Chaney EJ, Marjanovic M, et al. Intraoperative visualization of the tumor microenvironment and quantification of extracellular vesicles by label-free nonlinear imaging. *Sci Adv.* (2018) 4:eaau5603. doi: 10.1126/sciadv.aau5603
2. Harz M, Kiehntopf M, Stckel S, Rsch P, Deufel T, Popp J. Analysis of single blood cells for CSF diagnostics via a combination of fluorescence staining and micro-Raman spectroscopy. *Analyst.* (2008) 133:1416–23. doi: 10.1039/b716132h
3. Zhang RR, Schroeder AB, Grudzinski JJ, Rosenthal EL, Warram JM, Pinchuk AN, et al. Beyond the margins: real-time detection of cancer using targeted fluorophores. *Nat Rev Clin Oncol.* (2017) 14:347–64. doi: 10.1038/nrclinonc.2016.212
4. Yserbyt J, Dooms C, Janssens W, Verleden GM. Endoscopic advanced imaging of the respiratory tract: exploring probe-based confocal laser endomicroscopy in emphysema. *Thorax.* (2018) 73:188–90. doi: 10.1136/thoraxjnl-2016-209746
5. Fuchs FS, Zirlik S, Hildner K, Schubert J, Vieth M, Neurath MF. Confocal laser endomicroscopy for diagnosing lung cancer *in vivo*. *Eur Respir J.* (2013) 41:1401–8. doi: 10.1183/09031936.00062512
6. Krstajić N, Akram AR, Choudhary TR, McDonald N, Tanner MG, Pedretti E, et al. Two-color widefield fluorescence microendoscopy enables multiplexed molecular imaging in the alveolar space of human lung tissue. *J Biomed Opt.* (2016) 21:046009. doi: 10.1117/1.JBO.21.4.046009
7. East JE, Vleugels JL, Roelandt P, Bhandari P, Bisschops R, Dekker E, et al. Advanced endoscopic imaging: European Society of Gastrointestinal Endoscopy (ESGE) Technology Review. *Endoscopy.* (2016) 48:1029–45. doi: 10.1055/s-0042-118087
8. Thiberville L, Moreno-Swirc S, Vercauteren T, Peltier E, Cavé C, Bourg Heckly G. *In vivo* imaging of the bronchial wall microstructure using fibered confocal fluorescence microscopy. *Am J Respir Crit Care Med.* (2007) 175:22–31. doi: 10.1164/rccm.200605-684OC
9. Koch M, Symvoulidis P, Ntziachristos V. Tackling standardization in fluorescence molecular imaging. *Nat Photonics.* (2018) 12:505–15. doi: 10.1038/s41566-018-0221-5
10. Staderini M, Megia-Fernandez A, Dhaliwal K, Bradley M. Peptides for optical medical imaging and steps towards therapy. *Biorg Med Chem.* (2018) 26:2816–26. doi: 10.1016/j.bmc.2017.09.039
11. Garland M, Yim JJ, Bogyo M. A bright future for precision medicine: advances in fluorescent chemical probe design and their clinical application. *Cell Chem Biol.* (2016) 23:122–36. doi: 10.1016/j.chembiol.2015.12.003
12. Bowen RC, Ann N, Little B, Harmer JR, Ma J, Mirabelli LG, et al. Neutrophil-to-lymphocyte ratio as prognostic indicator in gastrointestinal cancers: a systematic review and meta-analysis. *Oncotarget.* (2017) 8:32171–89. doi: 10.18632/oncotarget.16291
13. Templeton AJ, McNamara MG, eruga B, Vera-Badillo FE, Aneja P, Ocaa A, et al. Prognostic role of neutrophil-to-lymphocyte ratio in solid tumors: a systematic review and meta-analysis. *J Natl Cancer Inst.* (2014) 106:dju124. doi: 10.1093/jnci/dju124
14. Zhao C, Ding C, Xie T, Zhang T, Dai X, Wei Y, et al. Validation and optimization of the Systemic Inflammation-Based modified Glasgow Prognostic Score in predicting postoperative outcome of inflammatory bowel disease: preliminary data. *Sci Rep.* (2018) 8:747. doi: 10.1038/s41598-017-18771-3
15. de Jager CPC, van Wijk PTL, Mathoera RB, de Jongh-Leuvenink J, van der Poll T, Wever PC. Lymphocytopenia and neutrophil-lymphocyte count ratio predict bacteremia better than conventional infection markers in an emergency care unit. *Crit Care.* (2010) 14:R192. doi: 10.1186/cc9309
16. Yilmaz H, Cakmak M, Inan O, Darcin T, Akcay A. Can neutrophil-lymphocyte ratio be independent risk factor for predicting acute kidney injury in patients with severe sepsis? *Renal Fail.* (2015) 37:225–9. doi: 10.3109/0886022X.2014.982477
17. Angkananard T, Anothaisintawee T, Thakkinstian A. Neutrophil lymphocyte ratio and risks of cardiovascular diseases: a systematic review and meta-analysis. *Atherosclerosis.* (2017) 263:e159–60. doi: 10.1016/j.atherosclerosis.2017.06.507
18. Xu T, Weng Z, Pei C, Yu S, Chen Y, Guo W, et al. The relationship between neutrophil-to-lymphocyte ratio and diabetic peripheral neuropathy in Type 2 diabetes mellitus. *Medicine.* (2017) 96:e8289. doi: 10.1097/MD.0000000000008289
19. Teng F, Ye H, Xue T. Predictive value of neutrophil to lymphocyte ratio in patients with acute exacerbation of chronic obstructive pulmonary disease. *PLoS ONE.* (2018) 13:e0204377. doi: 10.1371/journal.pone.0204377
20. Dundar ZD, Ergin M, Koylu R, Ozer R, Cander B, Gunaydin YK. Neutrophil-lymphocyte ratio in patients with pesticide poisoning. *J Emerg Med.* (2014) 47:286–93. doi: 10.1016/j.jemermed.2014.01.034

21. Zhang QW, Liu L, Gong CY, Shi HS, Zeng YH, Wang XZ, et al. Prognostic significance of tumor-associated macrophages in solid tumor: a meta-analysis of the literature. *PLoS ONE.* (2012) 7:e50946. doi: 10.1371/journal.pone.0050946
22. Sondak VK, King DW, Zager JS, Schneebaum S, Kim J, Leong SPL, et al. Combined analysis of phase III trials evaluating [^{99}mTc]tilmanocept and vital blue dye for identification of sentinel lymph nodes in clinically node-negative cutaneous melanoma. *Ann Surg Oncol.* (2013) 20:680–8. doi: 10.1245/s10434-012-2612-z
23. Cook AD, Hamilton JA. Investigational therapies targeting the granulocyte macrophage colony-stimulating factor receptor-α in rheumatoid arthritis: focus on mavrilimumab. *Ther Adv Musculoskeletal Dis.* (2018) 10:29–38. doi: 10.1177/1759720X17752036
24. Friedman SL, Ratziu V, Harrison SA, Abdelmalek MF, Aithal GP, Caballeria J, et al. A randomized, placebo-controlled trial of cenicriviroc for treatment of nonalcoholic steatohepatitis with fibrosis. *Hepatology.* (2018) 67:1754–67. doi: 10.1002/hep.29477
25. Bressenot A, Salleron J, Bastien C, Danese S, Boulagnon-Rombi C, Peyrin-Biroulet L. Comparing histological activity indexes in UC. *Gut.* (2015) 64:1412–8. doi: 10.1136/gutjnl-2014-307477
26. Li S, Cao W, Han J, Tang B, Sun X. The diagnostic value of white blood cell, neutrophil, neutrophil-to-lymphocyte ratio, and lymphocyte-to-monocyte ratio in patients with primary angle closure glaucoma. *Oncotarget.* (2017) 8:68984–95. doi: 10.18632/oncotarget.16571
27. Biller J, Thies WH. When to operate in carotid artery disease. *Am Fam Physician.* (2000) 61:400–6. Available online at: https://www.aafp.org/afp/2000/0115/p400.html
28. Ionita MG, van den Borne P, Catanzariti LM, Moll FL, de Vries JP, Pasterkamp G, et al. High neutrophil numbers in human carotid atherosclerotic plaques are associated with characteristics of rupture-prone lesions. *Atertio Thromb Vasc Biol.* (2010) 30:1842–8. doi: 10.1161/ATVBAHA.110.209296
29. Sonawane S, Khanolkar V, Namavari A, Chaudhary S, Gandhi S, Tibrewal S, et al. Ocular surface extracellular DNA and nuclease activity imbalance: a new paradigm for inflammation in dry eye disease. *Invest Ophthalmol Vis Sci.* (2012) 53:8253–63. doi: 10.1167/iovs.12-10430
30. Mun C, Gulati S, Tibrewal S, Chen Y-F, An S, Surenkhuu B, et al. A Phase I/II placebo-controlled randomized pilot clinical trial of recombinant deoxyribonuclease (DNase) eye drops use in patients with dry eye disease. *Transl Vis Sci Technol.* (2019) 8:10. doi: 10.1167/tvst.8.3.10
31. Tibrewal S, Ivanir Y, Sarkar J, Nayeb-Hashemi N, Bouchard CS, Kim E, et al. Hyperosmolar stress induces neutrophil extracellular trap formation: implications for dry eye disease. *Invest Ophthalmol Vis Sci.* (2014) 55:7961–9. doi: 10.1167/iovs.14-15332
32. Yoo D-g, Winn M, Pang L, Moskowitz SM, Malech HL, Leto TL, et al. Release of cystic fibrosis airway inflammatory markers from Pseudomonas aeruginosa-stimulated human neutrophils involves NADPH oxidase-dependent extracellular DNA trap formation. *J Immunol.* (2014) 192:4728–38. doi: 10.4049/jimmunol.1301589
33. Kohri K, Ueki IF, Nadel JA. Neutrophil elastase induces mucin production by ligand-dependent epidermal growth factor receptor activation. *Am J Physiol Lung Cell Mol Physiol.* (2002) 283:L531–40. doi: 10.1152/ajplung.00455.2001
34. Bazan NG. Neuroprotectin D1-mediated anti-inflammatory and survival signaling in stroke, retinal degenerations, and Alzheimer's disease. *J Lipid Res.* (2009) 50(Suppl.):S400–5. doi: 10.1194/jlr.R800068-JLR200
35. Gregory AD, McGarry Houghton A. Tumor-associated neutrophils: new targets for cancer therapy. *Cancer Res.* (2011) 71:2411–6. doi: 10.1158/0008-5472.CAN-10-2583
36. Gong L, Cumpian AM, Caetano MS, Ochoa CE, De la Garza MM, Lapid DJ, et al. Promoting effect of neutrophils on lung tumorigenesis is mediated by CXCR2 and neutrophil elastase. *Mol Cancer.* (2013) 12:154. doi: 10.1186/1476-4598-12-154
37. Wu L, Saxena S, Awaji M, Singh KR. Tumor-associated neutrophils in cancer: going pro. *Cancers.* (2019) 11:E564. doi: 10.3390/cancers11040564
38. Langhorst J, Boone J, Lauche R, Rueffer A, Dobos G. Faecal lactoferrin, calprotectin, PMN-elastase, CRP, and white blood cell count as indicators for mucosal healing and clinical course of disease in patients with mild to moderate ulcerative colitis: *post-hoc* analysis of a prospective clinical trial. *J Crohns Colitis.* (2016) 10:786–94. doi: 10.1093/ecco-jcc/jjw044
39. Kok K, Curciarello R, Soband T, Jones S, Docena G, MacDonald T. Human neutrophil elastase degrades the therapeutic monoclonal antibodies effective in IBD. *J Crohns Colitis.* (2018) 12(Suppl. 1):S146. doi: 10.1093/ecco-jcc/jjx180.232
40. Craven TH, Avlonitis N, McDonald N, Walton T, Scholefield E, Akram AR, et al. Super-silent FRET sensor enables live cell imaging and flow cytometric stratification of intracellular serine protease activity in neutrophils. *Sci Rep.* (2018) 8:1–10. doi: 10.1038/s41598-018-31391-9
41. Kossodo S, Zhang J, Groves K, Cuneo GJ, Handy E, Morin J, et al. Noninvasive *in vivo* quantification of neutrophil elastase activity in acute experimental mouse lung injury. *Int J Mol Imaging.* (2011) 2011:1–11. doi: 10.1155/2011/581406
42. Craven T, Walton T, Akram A, McDonald N, Scholefield E, Walsh T, et al. *In-situ* imaging of neutrophil activation in the human alveolar space with neutrophil activation probe and pulmonary optical endomicroscopy. *Lancet.* (2016) 387:S31. doi: 10.1016/S0140-6736(16)00418-9
43. Zhou J, Tsai YT, Weng H, Tang EN, Nair A, Dav. Real-time detection of implant-associated neutrophil responses using a formyl peptide receptor-targeting NIR nanoprobe. *Int J Nanomed.* (2012) 7:2057–68. doi: 10.2147/IJN.S29961
44. Pellico J, Lechuga-Vieco AV, Almarza E, Hidalgo A, Mesa-Nuez C, Fernndez-Barahona I, et al. *In vivo* imaging of lung inflammation with neutrophil-specific 68Ga nano-radiotracer. *Sci Rep.* (2017) 7:1–10. doi: 10.1038/s41598-017-12829-y
45. Ramoji A, Neugebauer U, Bocklitz T, Foerster M, Kiehntopf M, Bauer M, et al. Toward a spectroscopic hemogram: Raman spectroscopic differentiation of the two most abundant leukocytes from peripheral blood. *Anal Chem.* (2012) 84:5335–42. doi: 10.1021/ac3007363
46. Zeng Y, Yan B, Sun QQ, Teh SK, Zhang W, Wen ZL, et al. Label-free *in vivo* imaging of human leukocytes using two-photon excited endogenous fluorescence. *J Biomed Opt.* (2013) 18:040504. doi: 10.1117/1.JBO.18.4.040504
47. Hirche TO, Benabid R, Deslee G, Gangloff S, Achilefu S, Guenounou M, et al. Neutrophil elastase mediates innate host protection against Pseudomonas aeruginosa. *J Immunol.* (2008) 181:4945. doi: 10.4049/jimmunol.181.7.4945
48. Young RE, Thompson RD, Larbi KY, La M, Roberts CE, Shapiro SD, et al. Neutrophil elastase (NE)-deficient mice demonstrate a nonredundant role for NE in neutrophil migration, generation of proinflammatory mediators, and phagocytosis in response to zymosan particles *in vivo*. *J Immunol.* (2004) 172:4493–502. doi: 10.4049/jimmunol.172.7.4493
49. Ferry G, Lonchampt M, Pennel La. Activation of MMP-9 by neutrophil elastase in an *in vivo* model of acute lung injury. *FEBS Lett.* (1997) 402:111–5. doi: 10.1016/S0014-5793(96)01508-6
50. Jackson PL, Xu X, Wilson L, Weathington NM, Clancy JP, Blalock JE, et al. Human neutrophil elastase-mediated cleavage sites of MMP-9 and TIMP-1: implications to cystic fibrosis proteolytic dysfunction. *Mol Med.* (2010) 16:159–66. doi: 10.2119/molmed.2009.00109
51. Oltmanns U, Sukkar MB, Xie S, John M, Chung KF. Induction of human airway smooth muscle apoptosis by neutrophils and neutrophil elastase. *Am J Respir Cell Mol Biol.* (2005) 32:334–41. doi: 10.1165/rcmb.2004-0321OC
52. Benabid R, Wartelle J, Malleret L, Guyot N, Gangloff S, Lebargy F, et al. Neutrophil elastase modulates cytokine expression: contribution to host defense against pseudomonas aeruginosa-induced pneumonia. *J Biol Chem.* (2012) 287:34883–94. doi: 10.1074/jbc.M112.361352
53. Shao MXG, Nadel JA. Neutrophil Elastase Induces MUC5AC mucin production in human airway epithelial cells via a cascade involving protein kinase C, reactive oxygen species, and TNF- -converting enzyme. *J Immunol.* (2005) 175:4009–16. doi: 10.4049/jimmunol.175.6.4009
54. Smallman LA, Hill SL, Stockley RA. Reduction of ciliary beat frequency *in vitro* by sputum from patients with bronchiectasis: a serine proteinase effect. *Thorax.* (1984) 39:663–7. doi: 10.1136/thx.39.9.663
55. Papayannopoulos V, Metzler KD, Hakkim A, Zychlinsky A. Neutrophil elastase and myeloperoxidase regulate the formation of neutrophil extracellular traps. *J Cell Biol.* (2010) 191:677–91. doi: 10.1083/jcb.201006052

56. Wang M, Zhan Y, Chen J, Rong H, O'Neil SP, Ghosh B, et al. Understanding lung deposition of alpha-1 antitrypsin in acute experimental mouse lung injury model using fluorescence microscopy. *Int J Mol Imaging.* (2016) 2016:1–11. doi: 10.1155/2016/5768312
57. Glinzer A, Ma X, Prakash J, Kimm MA, Lohfer F, Kosanke K, et al. Targeting elastase for molecular imaging of early atherosclerotic lesions. *Atertio Thromb Vasc Biol.* (2017) 37:525–33. doi: 10.1161/ATVBAHA.116.308726
58. Talukdar S, Oh DY, Bandyopadhyay G, Li D, Xu J, McNelis J, et al. Neutrophils mediate insulin resistance in mice fed a high-fat diet through secreted elastase. *Nat Med.* (2012) 18:1407–12. doi: 10.1038/nm.2885
59. Muley MM, Reid AR, Botz B, Blcskei K, Helyes Z, McDougall JJ. Neutrophil elastase induces inflammation and pain in mouse knee joints via activation of proteinase-activated receptor-2. *Br J Pharmacol.* (2016) 173:766–77. doi: 10.1111/bph.13237
60. Wiedow O, Meyer-Hoffert U. Neutrophil serine proteases: potential key regulators of cell signalling during inflammation. *J Intern Med.* (2005) 257:319–28. doi: 10.1111/j.1365-2796.2005.01476.x
61. Kasperkiewicz P, Poreba M, Snipas SJ, Parker H, Winterbourn CC, Salvesen GS, et al. Design of ultrasensitive probes for human neutrophil elastase through hybrid combinatorial substrate library profiling. *Proc Natl Acad Sci USA.* (2014) 111:2518–23. doi: 10.1073/pnas.1318548111
62. Kasperkiewicz P, Kot S, Janiszewski T, Groborz K, Porba M, Snipas SJ, et al. Determination of extended substrate specificity of the MALT1 as a strategy for the design of potent substrates and activity-based probes. *Sci Rep.* (2018) 8:1–10. doi: 10.1038/s41598-018-34476-7
63. Poreba M, Solberg R, Rut W, Lunde Ngoc N, Kasperkiewicz P, Snipas Scott J, et al. Counter selection substrate library strategy for developing specific protease substrates and probes. *Cell Chem Biol.* (2016) 23:1023–35. doi: 10.1016/j.chembiol.2016.05.020
64. Kasperkiewicz P, Altman Y, D'Angelo M, Salvesen GS, Drag M. Toolbox of fluorescent probes for parallel imaging reveals uneven location of serine proteases in neutrophils. *J Am Chem Soc.* (2017) 139:10115–25. doi: 10.1021/jacs.7b04394
65. Locke LW, Chordia MD, Zhang Y, Kundu B, Kennedy D, Landseadel J, et al. A novel neutrophil-specific PET imaging agent: cFLFLFK-PEG-64Cu. *J Nucl Med.* (2009) 50:790–7. doi: 10.2967/jnumed.108.056127
66. Yang X, Chordia MD, Du X, Graves JL, Zhang Y, Park YS, et al. Targeting formyl peptide receptor 1 of activated macrophages to monitor inflammation of experimental osteoarthritis in rat. *J Orth Res.* (2016) 34:1529–38. doi: 10.1002/jor.23148
67. Xiao L, Zhang Y, Berr SS, Chordia MD, Pramoonjago P, Pu L, et al. A novel near-infrared fluorescence imaging probe for *in vivo* neutrophil tracking. *Mol Imaging.* (2012) 11:372–82. doi: 10.2310/7290.2011.00054
68. Xiao L, Zhang Y, Liu Z, Yang M, Pu L, Pan D. Synthesis of the Cyanine 7 labeled neutrophil-specific agents for noninvasive near infrared fluorescence imaging. *Bioorg Med Chem Lett.* (2010) 20:3515–7. doi: 10.1016/j.bmcl.2010.04.136
69. Puppels GJ, de Mul FF, Otto C, Greve J, Robert-Nicoud M, Arndt-Jovin DJ, et al. Studying single living cells and chromosomes by confocal Raman microspectroscopy. *Nature.* (1990) 347:301–3. doi: 10.1038/347301a0
70. Puppels GJ, Garritsen HS, Segers-Nolten GM, de Mul FF, Greve J. Raman microspectroscopic approach to the study of human granulocytes. *Biophys J.* (1991) 60:1046–56. doi: 10.1016/S0006-3495(91)82142-7
71. Otto C, Sijtsema NM, Greve J. Confocal Raman microspectroscopy of the activation of single neutrophilic granulocytes. *Eur Biophys J.* (1998) 27:582–9. doi: 10.1007/s002490050169
72. van Manen HJ, van Bruggen R, Roos D, Otto C. Single-cell optical imaging of the phagocyte NADPH oxidase. *Antioxidants Redox Signall.* (2006) 8:1509–22. doi: 10.1089/ars.2006.8.1509
73. Ducourthial G, Leclerc P, Mansuryan T, Fabert M, Brevier J, Habert R, et al. Development of a real-time flexible multiphoton microendoscope for label-free imaging in a live animal. *Sci Rep.* (2015) 5:1–9. doi: 10.1038/srep 18303
74. Llewellyn ME, Barretto RPJ, Delp SL, Schnitzer MJ. Minimally invasive high-speed imaging of sarcomere contractile dynamics in mice and humans. *Nature.* (2008) 454:784–8. doi: 10.1038/nature07104
75. Williams RM, Flesken-Nikitin A, Ellenson LH, Connolly DC, Hamilton TC, Nikitin AY, et al. Strategies for high resolution imaging of epithelial ovarian cancer by laparoscopic nonlinear microscopy. *Transl Oncol.* (2010) 3:181–94. doi: 10.1593/tlo.09310
76. Brown CM, Rivera DR, Pavlova I, Ouzounov DG, Williams WO, Mohanan S, et al. *In vivo* imaging of unstained tissues using a compact and flexible multiphoton microendoscope. *J Biomed Opt.* (2012) 17:040505. doi: 10.1117/1.JBO.17.4.040505
77. Pollard JW. Trophic macrophages in development and disease. *Nat Rev Immunol.* (2009) 9:259–70. doi: 10.1038/nri2528
78. Liyanage SE, Gardner PJ, Ribeiro J, Cristante E, Sampson RD, Luhmann UFO, et al. Flow cytometric analysis of inflammatory and resident myeloid populations in mouse ocular inflammatory models. *Exp Eye Res.* (2016) 151:160–70. doi: 10.1016/j.exer.2016.08.007
79. Liu J, Xue Y, Dong D, Xiao C, Lin C, Wang H, et al. CCR2– and CCR2+ corneal macrophages exhibit distinct characteristics and balance inflammatory responses after epithelial abrasion. *Mucosal Immunol.* (2017) 10:1145–59. doi: 10.1038/mi.2016.139
80. Boehm N, Riechardt AI, Wiegand M, Pfeiffer N, Grus FH. Proinflammatory cytokine profiling of tears from dry eye patients by means of antibody microarrays. *Invest Ophthalmol Vis Sci.* (2011) 52:7725–30. doi: 10.1167/iovs.11-7266
81. Sawada H, Fukuchi T, Tanaka T, Abe H. Tumor necrosis factor-α concentrations in the aqueous humor of patients with glaucoma. *Invest Ophthalmol Vis Sci.* (2010) 51:903–6. doi: 10.1167/iovs.09-4247
82. Hussell T, Bell TJ. Alveolar macrophages: plasticity in a tissue-specific context. *Nat Rev Immunol.* (2014) 14:81–93. doi: 10.1038/nri3600
83. Conway EM, Pikor LA, Kung SHY, Hamilton MJ, Lam S, Lam WL, et al. Macrophages, inflammation, and lung cancer. *Am J Respir Crit Care Med.* (2015) 193:116–30. doi: 10.1164/rccm.201508-1545CI
84. Lewis CE, Pollard JW. Distinct role of macrophages in different tumor microenvironments. *Cancer Res.* (2006) 66:605–12. doi: 10.1158/0008-5472.CAN-05-4005
85. Xia W, Hilgenbrink AR, Matteson EL, Lockwood MB, Cheng JX, Low PS. A functional folate receptor is induced during macrophage activation and can be used to target drugs to activated macrophages. *Blood.* (2009) 113:438–46. doi: 10.1182/blood-2008-04-150789
86. Shen J, Chelvam V, Cresswell G, Low PS. Use of folate-conjugated imaging agents to target alternatively activated macrophages in a murine model of asthma. *Mol Pharm.* (2013) 10:1918–27. doi: 10.1021/mp3006962
87. Blykers A, Schoonooghe S, Xavier C, D'Hoe K, Laoui D, D'Huyvetter M, et al. PET imaging of macrophage mannose receptor-expressing macrophages in tumor stroma using 18F-radiolabeled camelid single-domain antibody fragments. *J Nucl Med.* (2015) 56:1265–71. doi: 10.2967/jnumed.115.156828
88. Scodeller P, Simón-Gracia L, Kopanchuk S, Tobi A, Kilk K, Säälik P, et al. Precision targeting of tumor macrophages with a CD206 binding peptide. *Sci Rep.* (2017) 7:14655. doi: 10.1038/s41598-017-14709-x
89. Razavian M, Bordenave T, Georgiadis D, Beau F, Zhang J, Golestani R, et al. Optical imaging of MMP-12 active form in inflammation and aneurysm. *Sci Rep.* (2016) 6:38345. doi: 10.1038/srep38345
90. Onda N, Kemmochi S, Morita R, Ishihara Y, Shibutani M. *In vivo* imaging of tissue-remodeling activity involving infiltration of macrophages by a systemically administered protease-activatable probe in colon cancer tissues. *Transl Oncol.* (2013) 6:628–37. doi: 10.1593/tlo.13430
91. Withana NP, Ma X, McGuire HM, Verdoes M, van der Linden WA, Ofori LO, et al. Non-invasive imaging of idiopathic pulmonary fibrosis using cathepsin protease probes. *Sci Rep.* (2016) 6:19755. doi: 10.1038/srep19755
92. Mahalingam SM, Kularatne SA, Myers CH, Gagare P, Norshi M, Liu X, et al. Evaluation of novel tumor-targeted near-infrared probe for fluorescence-guided surgery of cancer. *J Med Chem.* (2018) 61:9637–46. doi: 10.1021/acs.jmedchem.8b01115
93. Low PS, Henne WA, Doorneweerd DD. Discovery and development of folic-acid-based receptor targeting for imaging and therapy of cancer and inflammatory diseases. *Acc Chem Res.* (2008) 41:120–9. doi: 10.1021/ar7000815
94. Nakashima-Matsushita N, Homma T, Yu S, Matsuda T, Sunahara N, Nakamura T, et al. Selective expression of folate receptor β and its possible role in methotrexate transport in synovial macrophages from patients with

rheumatoid arthritis. *Arthritis Rheum.* (2001) 42:1609–16. doi: 10.1002/1529-0131(199908)42:8<1609::AID-ANR7>3.0.CO;2-L
95. Shen J, Hilgenbrink AR, Xia W, Feng Y, Dimitrov DS, Lockwood MB, et al. Folate receptor-beta constitutes a marker for human proinflammatory monocytes. *J Leukoc Biol.* (2014) 96:563–70. doi: 10.1189/jlb.2AB0713-372R
96. Han W, Zaynagetdinov R, Yull FE, Polosukhin VV, Gleaves LA, Tanjore H, et al. Molecular imaging of folate receptor β-positive macrophages during acute lung inflammation. *Am J Respir Cell Mol Biol.* (2015) 53:50–9. doi: 10.1165/rcmb.2014-0289OC
97. Poh S, Chelvam V, Ayala-López W, Putt KS, Low PS. Selective liposome targeting of folate receptor positive immune cells in inflammatory diseases. *Nanomedicine.* (2018) 14:1033–43. doi: 10.1016/j.nano.2018.01.009
98. Azad AK, Rajaram MVS, Metz WL, Cope FO, Blue MS, Vera DR, et al. γ-tilmanocept, a new radiopharmaceutical tracer for cancer sentinel lymph nodes, binds to the mannose receptor (CD206). *J Immunol.* (2015) 195:2019–29. doi: 10.4049/jimmunol.1402005
99. Kim JB, Park K, Ryu J, Lee JJ, Lee MW, Cho HS, et al. Intravascular optical imaging of high-risk plaques *in vivo* by targeting macrophage mannose receptors. *Sci Rep.* (2016) 6:22608. doi: 10.1038/srep22608
100. Geijtenbeek TBH, Torensma R, van Vliet SJ, van Duijnhoven GCF, Adema GJ, van Kooyk Y, et al. Identification of DC-SIGN, a novel dendritic cell-specific ICAM-3 receptor that supports primary immune responses. *Cell.* (2000) 100:575–85. doi: 10.1016/S0092-8674(00)80693-5
101. Chakravarty R, Goel S, Cai W. Nanobody: the "magic bullet" for molecular imaging? *Theranostics.* (2014) 4:386–98. doi: 10.7150/thno.8006
102. Devoogdt N, Xavier C, Hernot S, Vaneycken I, D'Huyvetter M, De Vos J, et al. Molecular imaging using nanobodies: a case study. In: Saerens D, Muyldermans S, editors. *Single Domain Antibodies. 911. Methods in Molecular Biology*. Totowa, NJ: Humana Press (2012). p. 559–67. doi: 10.1007/978-1-61779-968-6_35
103. Movahedi K, Schoonooghe S, Laoui D, Houbracken I, Waelput W, Breckpot K, et al. Nanobody-based targeting of the macrophage mannose receptor for effective *in vivo* imaging of tumor-associated macrophages. *Cancer Res.* (2012) 72:4165–77. doi: 10.1158/0008-5472.CAN-11-2994
104. Debie P, Van Quathem J, Hansen I, Bala G, Massa S, Devoogdt N, et al. Effect of dye and conjugation chemistry on the biodistribution profile of near-infrared-labeled nanobodies as tracers for image-guided surgery. *Mol Pharm.* (2017) 14:1145–53. doi: 10.1021/acs.molpharmaceut.6b01053
105. Kessenbrock K, Plaks V, Werb Z. Matrix metalloproteinases: regulators of the tumor microenvironment. *Cell.* (2010) 141:52–67. doi: 10.1016/j.cell.2010.03.015
106. Jiang T, Olson ES, Nguyen QT, Roy M, Jennings PA, Tsien RY. Tumor imaging by means of proteolytic activation of cell-penetrating peptides. *Proc Natl Acad Sci USA.* (2004) 101:17867–72. doi: 10.1073/pnas.0408191101
107. Miampamba M, Liu J, Harootunian A, Gale AJ, Baird S, Chen SL, et al. Sensitive *in vivo* visualization of breast cancer using ratiometric protease-activatable fluorescent imaging agent, AVB-620. *Theranostics.* (2017) 7:3369–86. doi: 10.7150/thno.20678
108. Parks WC, Shapiro SD. Matrix metalloproteinases in lung biology. *Respir Res.* (2000) 2:3. doi: 10.1186/rr33
109. Dean RA, Cox JH, Bellac CL, Doucet A, Starr AE, Overall CM. Macrophage-specific metalloelastase (MMP-12) truncates and inactivates ELR+ CXC chemokines and generates CCL2, −7, −8, and−13 antagonists: potential role of the macrophage in terminating polymorphonuclear leukocyte influx. *Blood.* (2008) 112:3455–64. doi: 10.1182/blood-2007-12-129080
110. Bordenave T, Helle M, Beau F, Georgiadis D, Tepshi L, Bernes M, et al. Synthesis and *in vitro* and *in vivo* evaluation of MMP-12 selective optical probes. *Bioconj Chem.* (2016) 27:2407–17. doi: 10.1021/acs.bioconjchem.6b00377
111. Afik R, Zigmond E, Vugman M, Klepfish M, Shimshoni E, Pasmanik-Chor M, et al. Tumor macrophages are pivotal constructors of tumor collagenous matrix. *J Exp Med.* (2016) 213:2315–31. doi: 10.1084/jem.20151193
112. Ofori LO, Withana NP, Prestwood TR, Verdoes M, Brady JJ, Winslow MM, et al. Design of protease activated optical contrast agents that exploit a latent lysosomotropic effect for use in fluorescence-guided surgery. *ACS Chem Biol.* (2015) 10:1977–88. doi: 10.1021/acschembio.5b00205
113. Verdoes M, Edgington LE, Scheeren FA, Leyva M, Blum G, Weiskopf K, et al. A nonpeptidic cathepsin S activity-based probe for noninvasive optical imaging of tumor-associated macrophages. *Chem Biol.* (2012) 19:619–28. doi: 10.1016/j.chembiol.2012.03.012
114. Sevick-Muraca EM, Zhu B. The need for performance standards in clinical translation and adoption of fluorescence molecular imaging. *Med Phys.* (2013) 40:040402. doi: 10.1118/1.4789499

Conflict of Interest Statement: MB and KD are shareholders of Edinburgh Molecular Imaging.

The remaining authors declare that the research was conducted in the absence of any commercial or financial relationships that could be construed as a potential conflict of interest.

frontiers in Surgery

REVIEW
published: 18 September 2019
doi: 10.3389/fsurg.2019.00052

Application of Fluorescein Fluorescence in Vascular Neurosurgery

*Xiaochun Zhao[1], Evgenii Belykh[1,2], Claudio Cavallo[1], Daniel Valli[1], Sirin Gandhi[1], Mark C. Preul[1], Peter Vajkoczy[3], Michael T. Lawton[1] and Peter Nakaji[1]**

[1] Department of Neurosurgery, Barrow Neurological Institute, St. Joseph's Hospital and Medical Center, Phoenix, AZ, United States, [2] Department of Neurosurgery, Irkutsk State Medical University, Irkutsk, Russia, [3] Department of Neurosurgery, Charité – Universitätsmedizin Berlin, Berlin, Germany

Background: Fluorescein sodium (FNa) is a fluorescent drug with a long history of use for assessing retinal blood flow in ophthalmology; however, its application in vascular neurosurgery is only now gaining popularity. This review summarizes the current knowledge about using FNa videoangiography in vascular neurosurgery.

Methods: We performed a literature review on the usage of FNa for fluorescent videoangiography procedures in neurosurgery. We analyzed methods of injection, dosages of FNa, visualizing platforms, and interpretation of FNa videoangiography. We also reviewed practical applications of FNa videoangiography during various vascular neurosurgeries.

Results: FNa videoangiography can be performed with intraarterial (intracarotid) or intravenous dye injections. Both methods provide excellent resolution with enhanced fluorescence that shows intravascular blood flow on top of visible surrounding anatomy, and both allow simultaneous purposeful microsurgical manipulations. Although it is invasive, an intracarotid FNa injection results in faster contrast appearance and higher-intensity fluorescence and requires a lower dose per injection (reported range, 1–50 mg) compared with peripheral intravenous FNa injection (reported range, 75–2,000 mg or 1–1.5 mg/kg body weight). Four optical excitation/detection tools for FNa videoangiography have been successfully used: conventional xenon-light operating microscope with a special filter set, pencil-type light-emitting diode probe with a filter set, laser-illumination operating microscope, and an endoscope with a filter set. FNa videoangiography was reported to be feasible and useful in various clinical scenarios, such as examining the feeders and drainers in arteriovenous malformation surgery, checking the patency of a microvascular anastomosis, and assessing blood flow during aneurysm clipping. FNa videoangiography can be repeated during the same procedure and used along with indocyanine green (ICG) videoangiography.

OPEN ACCESS

Edited by:
William Tupper Couldwell, The University of Utah, United States

Reviewed by:
Jorge Marcelo Mura, Instituto de Neurocirugía, Chile
Min S. Park, University of Virginia Hospital, United States

***Correspondence:**
Peter Nakaji
neuropub@barrowneuro.org

Specialty section:
This article was submitted to Neurosurgery, a section of the journal Frontiers in Surgery

Received: *18 February 2019*
Accepted: *27 August 2019*
Published: *18 September 2019*

Citation:
Zhao X, Belykh E, Cavallo C, Valli D, Gandhi S, Preul MC, Vajkoczy P, Lawton MT and Nakaji P (2019) Application of Fluorescein Fluorescence in Vascular Neurosurgery. Front. Surg. 6:52. doi: 10.3389/fsurg.2019.00052

Conclusions: Compared with ICG videoangiography, FNa videoangiography has the advantages of enabling real-time inspection and better visualization at deep locations; however, thick vessel walls limit visualization of FNa in larger vessels. FNa videoangiography is a useful tool in multiple neurovascular scenarios and merits further studies to establish its clinical value.

Keywords: fluorescein angiography, fluorescein fluorescence, fluorescein sodium, vascular neurosurgery, aneurysm, arteriovenous malformation, arteriovenous fistula

INTRODUCTION

Techniques for evaluating blood flow are essential for successful neurosurgery on vascular lesions. Vascular lesions, such as cerebral aneurysms, arteriovenous malformations (AVMs), and dural arteriovenous fistulas (DAVFs), and other clinical scenarios requiring vascular anastomosis are characterized by unique flow alterations (e.g., aneurysmal turbulent flow). Clinical outcomes may be catastrophic if blood flow is severely compromised or if a vessel is ruptured during these procedures. Surgical intervention in such lesions includes blood flow monitoring to minimize the risk of rupture or to reestablish compromised normal circulation.

Multiple methods have been developed to examine circulation intraoperatively. These methods can be broadly classified on the basis of the principles of physics, drugs, and the devices used.

1. Observation and palpation, using the classic milking test, can assess patency of a dissected vessel. Pulsation waves and the color of blood (bright-red oxygenated vs. dark-red deoxygenated) are qualitative signs that are helpful in flow assessment but have multiple limitations (1).
2. Contact probe-based Doppler angiography can measure the volume and speed of the blood flow (2) using either a point-probe, which measures the target artery from one side, or an intracranial Charbel Micro-Flow probe (Transonic, Ithaca, NY), which measures the target artery from two sides.
3. Wide-field laser speckle imaging (785 nm, 50 mW laser) allows the generation of a real-time two-dimensional color-coded map of perfusion during open surgery and can be used as a noninvasive visualization and measurement of the relative cortical blood flow (3).
4. Digital subtraction angiography (DSA) is a robust but invasive imaging technique that remains the gold-standard examination for many vascular lesions. Intraoperative DSA requires a hybrid room setting (angiography setup in the operating room) and separate sterilization area (i.e., femoral area) (4–6).
5. Fluorescent videoangiography with various wide-field surgical microscopes with appropriate filters includes the use of indocyanine green (ICG) videoangiography and fluorescein sodium (FNa) videoangiography.
6. Confocal laser endomicroscopic angiography can employ FNa or ICG and assess brain microvasculature.

Abbreviations: AVM, arteriovenous malformation; CCA, common carotid artery; DAVF, dural arteriovenous fistula; DSA, digital subtraction angiography; FNa, fluorescein sodium; IA, intraarterial; ICG, indocyanine green; IV, intravenous; LED, light emitting diode.

This paper is a focused review of the history and current applications of FNa videoangiography for intraoperative neurovascular imaging.

HISTORY OF FNa VIDEOANGIOGRAPHY

According to Van Cader (7), the earliest study with FNa was conducted in 1881 by Ehrlich and colleagues, who analyzed the distribution of FNa after intravenous (IV) injection and demonstrated its presence in the anterior chamber of the eye. In ophthalmology, FNa has been extensively used to assess retinal blood flow (8, 9). In the late 1940s, FNa was adopted by Moore et al. to visualize neoplastic tissue in gastric adenocarcinomas and brain tumors (10, 11). Glial tumors were found to produce the most consistent positive fluorescence.

In 1967, FNa was first used to evaluate the intracranial circulation in animals and humans by Feindel et al. (12). A report of an AVM surgery by the same group in 1971 was the first record of FNa application in vascular neurosurgery (13). Since then, the number of studies reporting FNa videoangiography has been relatively limited, with the majority of studies published after 2013 (6, 14–23).

METABOLISM AND SAFETY OF FNa

Upon IV administration, FNa loosely binds to plasma proteins and exists as a protein-bound (80%) and free-salt (20%) substance. FNa is metabolized by glucuronidation in the liver. About 80% of IV FNa is converted to a monoglucuronide within 1 h, which is 95% less fluorescent. FNa is rapidly cleared by the kidneys through filtration and secretion and is almost completely excreted by 24 h (24).

FNa has been shown to be minimally toxic at a dose of 20 mg/kg body weight (1,500 mg for a 75-kg patient) (25). In ophthalmology, however, FNa is used extensively at dosages of 500 mg (26, 27) and as much as 30 mg/kg body weight. Median lethal doses of IV FNa are 2,200 mg/kg for mice, 600 to 1,000 mg/kg in rats, 1,000 mg/kg in dogs, and 350 mg/kg in rabbits (28). Complications such as cardiac effect, respiratory reaction, or seizure have been reported rarely, with the frequency of severe adverse effects reported as 1 in 1,900 and death as 1 in 222,000 (29). Patients injected with doses of more than 5 mg/kg body weight exhibit temporary yellow staining of skin, which disappears within 6 to 24 h as FNa is cleared (10). It was noted that patients with severe liver diseases may experience prolonged yellow skin staining (10). FNa administration for vascular neurosurgical applications requires a relatively low dose,

and no complications related to FNa have been reported in the neurosurgical literature.

DOSAGES OF FNa FOR VASCULAR APPLICATIONS

IV and intraarterial (IA) injections of FNa require different dosages for optimal vascular imaging. IV administration usually requires a higher dosage than IA injection to achieve good contrast, as FNa dilutes during peripheral circulation, and 80% of the FNa binds to albumin and is deactivated in this process (30, 31). Wrobel et al. (32) reported a case of high-dose FNa videoangiography using 2,000 mg IV bolus. In other neurosurgical reports, IV doses range from 75 mg to 500 mg per bolus (6, 18–21, 30, 31, 33) or from 1 mg/kg to 1.5 mg/kg per body weight (16, 34).

Doses for IA injection are low, with 2 studies from the 1970s reporting 10 mg (13) and 50 mg (33) IV boluses, and more recent studies have used a dose as low as 10 ml of 0.01–0.02% FNa solution (0.001–0.002 mg) (20, 31) and 5 ml of 0.5–1% FNa solution (0.025–0.05 mg) (17). After investigating different dosages of FNa, Kuroda et al. reported 10 ml of 0.01–0.02% FNa bolus (0.001–0.002 mg) can be used to sufficiently detect the parent artery and perforating arteries of aneurysms without staining the vessel wall and without persistence in the vessel 5 min after IA injection (31).

SITE OF INJECTION: IV OR IA

IV routes can use central or peripheral venous access, which usually has not been specified in reports. IA injection, however, needs to be made directly into the carotid or vertebral circulation. Thus, the peripheral arterial accesses (radial artery) for blood pressure monitoring would be no different with an IV injection in terms of FNa mixing with blood. However, IA injection requires an additional vascular access site with associated risks, which is a drawback.

Catheterization of the common carotid artery (CCA) may be performed via a direct transcutaneous puncture or transfemoral retrograde catheterization. However, the detailed technique used to access the CCA for FNa injection was not specified in majority of the literature (13, 20, 31, 33). Ichikawa et al. inserted an IA catheter from the superficial temporal artery into the CCA for approximately 5 to 10 cm in a retrograde fashion and then successfully performed FNa videoangiography (17). Other potential retrograde injection sites, such as the occipital artery, merit future feasibility studies.

The major difference between IV injection and IA injection of FNa is the time period from the injection to different phases of FNa appearance in the field of view (**Figure 1**). The arterial phase of IA FNa injection appears immediately after injection (20, 31), usually no more than 2 s (13), and the venous phase fades out in <1 min (17). In comparison, the appearance takes longer in both phases with IV injection—it usually takes at least 10 s for the arterial phase and a minimum of 5 min until the fluorescence fades out (17, 31). The show-up and the fade-out of each phase after an IV injection are steep, and those in IV injection are delayed.

A shorter time period until fade-out is essential if repeated angiography is required, such as for evaluation of a DAVF before and after ligation or when accessing the patency of perforators during a series of clip adjustments in an aneurysm surgery (31). Kuroda et al. reported that IA FNa videoangiography can be repeated at least 5 times without staining the vessel wall in a short period of time, with the total dose significantly below the safety limits (31). However, the length of the period of intravascular stay was under debate; Kakucs et al. advocated that the longer time window of intravascular stay is one of the advantages of the IV injection, which provides more time of the angiography for use in analysis (15).

Because 80% of FNa molecules combine with albumin (30, 31), IV FNa injections usually require a higher dose than IA injections, which may lead to vessel wall staining and decrease the intravascular-extravascular contrast (31, 33). Furthermore, even with a higher IV dose administered, the observed fluorescence decreases as FNa dilutes with blood along the circulation. In IA injection, however, the FNa concentration in cerebral vasculature is high, providing higher contrast to the background anatomy. This is established for both FNa videoangiography (**Figure 1**) and ICG videoangiography (20, 31, 35). However, both IA and IV FNa administration routes can provide sufficient fluorescence intensity and sufficient information for interpretation (20).

In summary, compared with IV injection of FNa, IA injection has the advantage of better contrast, lower required dose, and the ability to be repeatedly performed in a limited time period without staining to the vessel wall. The disadvantage of IA injection is the necessity of additional vascular access to the CCA and its associated risks. Longer intravascular stay may be interpreted differently and can be advantageous or disadvantageous for both methods of administering FNa.

PHASES OF FNa VIDEOANGIOGRAPHY AND FACTORS THAT AFFECT PHASES

As with any angiography, FNa videoangiography has three main phases in which certain vessels are characteristically highlighted by fluorescence: the arterial, capillary, and venous phases. The duration of these phases (i.e., the duration of FNa fluorescence in arterial, capillary, and venous beds) depends on multiple factors. Mindful consideration of these factors is crucial for assessment and differentiation of normal and pathologic conditions. The interrelation of various factors, such as dosage and the route of administration, adds another level of complexity to assessments. Below, we briefly list these factors and discuss those particularly relevant to FNa in more details.

Site of Injection

With IV injections, FNa travels in the cardiopulmonary circulation and then appears in the systemic arterial circulation, which allows FNa to mix with large quantities of blood and thus provides a longer time to peak and less bright fluorescence compared with an IA injection. Additionally, the speed of

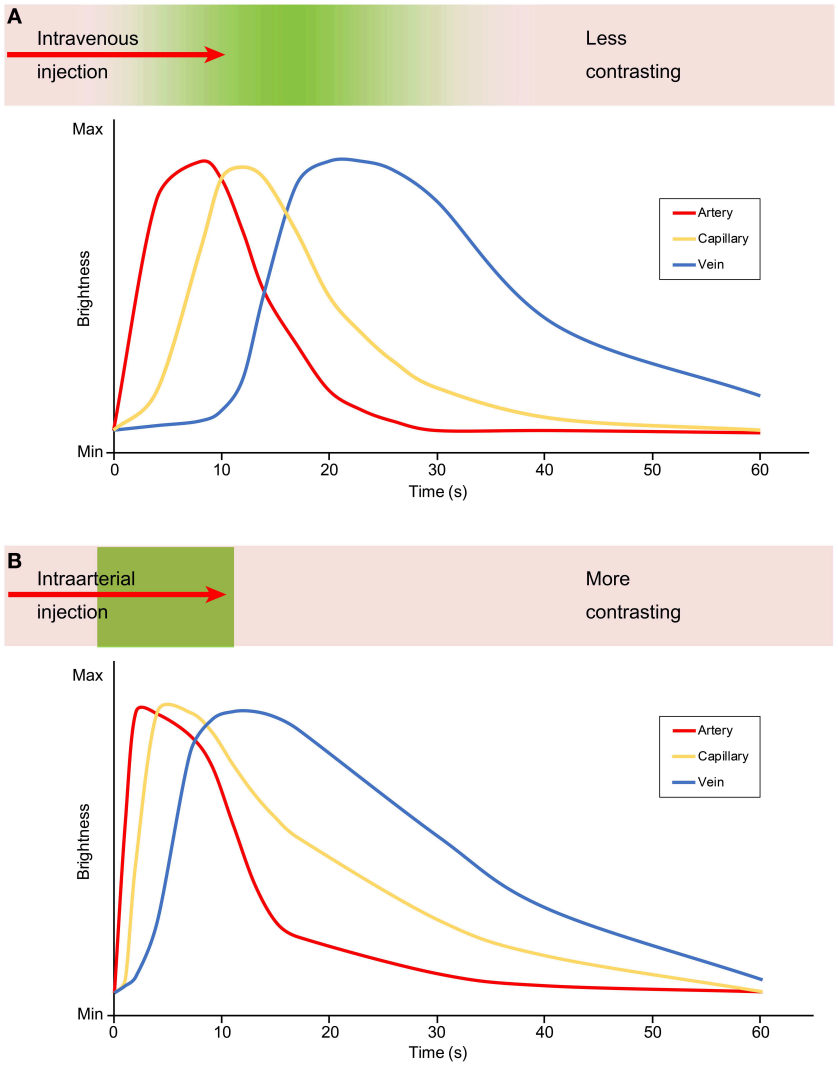

FIGURE 1 | Graphic demonstrating the contrast and brightness changes during angiography with an **(A)** intravenous and **(B)** intraarterial FNa injection. The green color embedded in the bar above the graph represents the flow of the fluorescein. With an intravenous injection, the fluorescein is diluted and contrasts less as shown in the less steep and delayed graph, compared with an intraarterial injection during which the fluorescein is more concentrated and contrasts better as shown by the steep and acute graph. Max, maximum; Min, minimum. Used with permission from Barrow Neurological Institute, Phoenix, Arizona.

injection plays a role in the fluorescence phases and should be standardized as a rapid bolus injection.

Dose

A large dose can prolong the intravascular stay of FNa but has the disadvantage of unspecific vessel wall staining. A dose of 2,000 mg of FNa was reported to remain detectable in the cerebral vessels for 60 min, and the authors suggested that using a lower dose may be better, as used with repetitive angiographies (32).

Vessel Wall Staining

Detected intravascular fluorescence can be due to FNa in the blood or due to the staining of the vessel wall. Stained vessel walls can lower the contrast effect and affect the interpretation of the videoangiography, especially given the impact on quality of subsequent angiographies.

Vascular Abnormalities

The arterial phase appears early when used in a patient with an abnormal connection between the venous and arterial circulations, such as a DAVF or AVM, where the blood flow is aberrantly fast. The arterial phase was reported to be 11 s in a case report of a DAVF (34) and 10–15 s in AVM surgeries (13, 16, 18, 23) after IV FNa injection. These durations are shorter than those reported during IV FNa videoangiography in aneurysm surgeries, in which the arterial phase typically appears for more than 20 s (20, 22, 31, 32).

The effect of a bypass can also influence the arterial phase appearance. Little et al. reported an average 1.7-s time decrease

from the injection to the arterial phase in cortical arteries after superficial temporal artery–middle cerebral artery bypass. This change, along with visual transit of fluorescence signal through an anastomosis, can be used as an indicator of a successful bypass (33).

Cardiovascular Parameters

Cardiovascular parameters, such as arterial blood pressure and heart rate, may affect time-dependent angiographic parameters and should be taken into consideration.

Visualization Platform Parameters

The focus distance of the microscope, its angulation, position within the field of view, photobleaching properties, and irregularities of the surgical field increase the complexity when assessing fluorescence images (36).

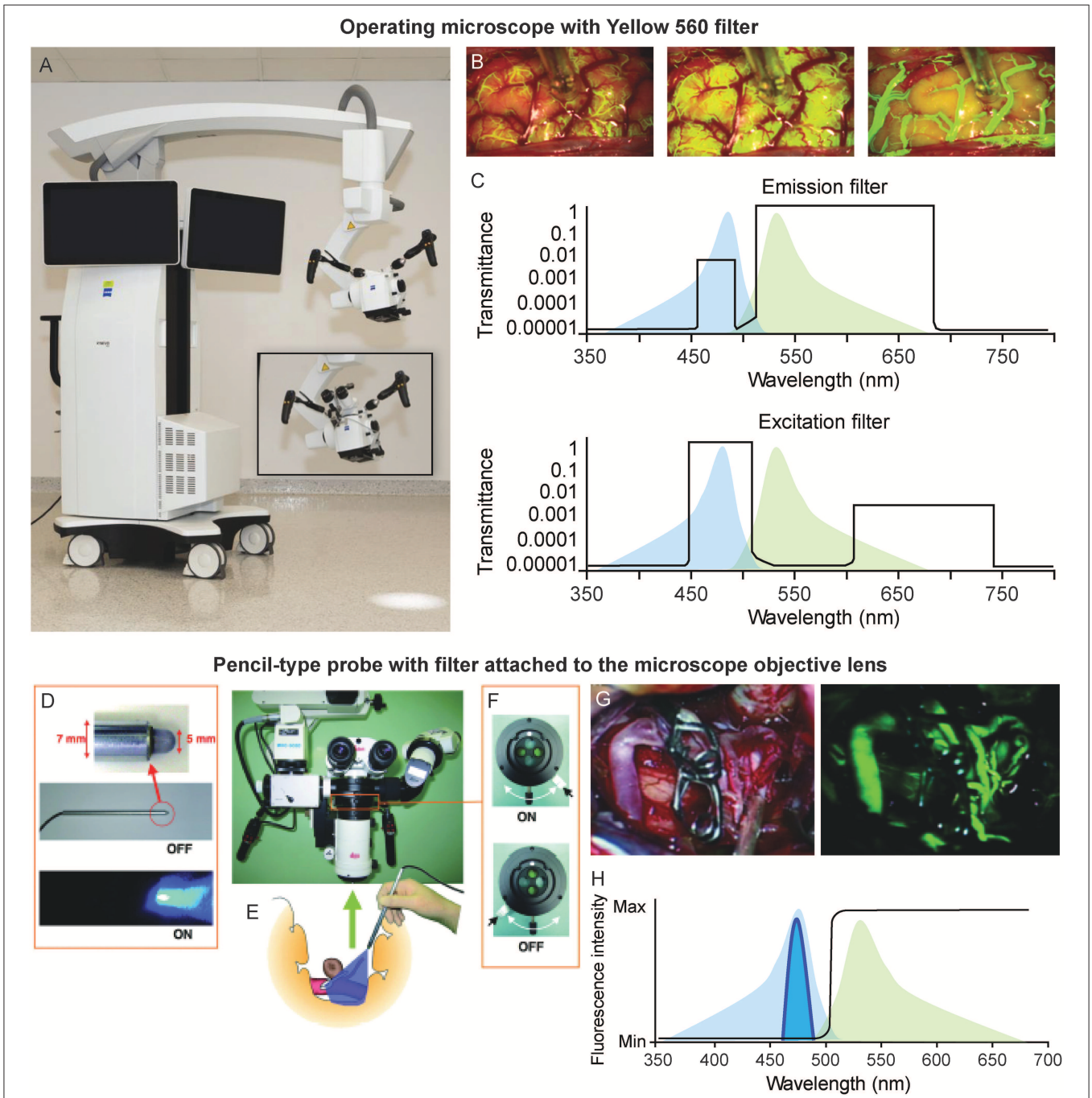

FIGURE 2 | Continued

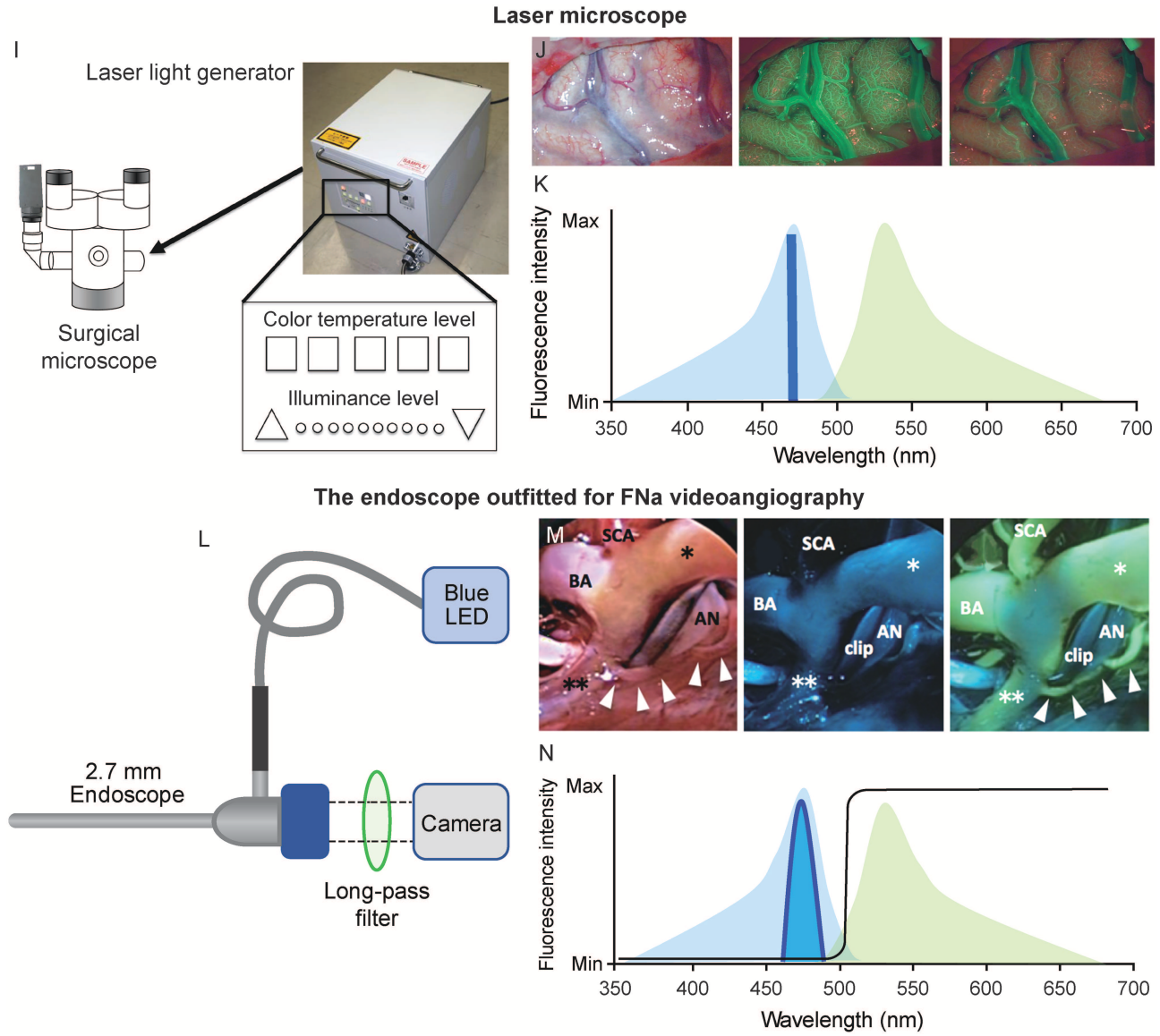

FIGURE 2 | Various platforms used for FNa videoangiography. **(A–C)** Operating microscope. **(A)** The operating microscope with Yellow 560 module (ZEISS KINEVO 900, Carl Zeiss AG, Oberkochen, Germany). **(B)** Intraoperative views of FNa videoangiography (left to right: arterial, capillary, and venous phases). **(C)** Patented filter combinations used in the operative microscope balances the intensities of narrow bands of excitation and emitted light to create a clear operating field view with yellow fluorescence of fluorescein. The excitation (bottom) and emission (top) profiles of fluorescein (peaks are 485 nm, blue; 514 nm, green, respectively) are shown on the background. The transmittance of filters at various wavelengths results in the uniform intensity of all bands, with a higher intensity of emitted yellow light. **(D-H)** Pencil-type probe with filter attached to the microscope objective lens. **(D)** The pencil-type probe with blue LED emission. **(E)** Sketch demonstrating the intraoperative usage of the probe. **(F)** The switch of the filter adapted to the operating microscope. **(G)** The intraoperative view using this device (left, fluorescence off; right, fluorescence on). **(H)** A diagram showing optical setup of the device. Blue LED light is concentrated around 465 nm, and a long-pass filter (black line) allows green emission light into the camera. **(I-K)** The laser microscope. **(I)** The illuminating device. **(J)** Images of the laser FNa videoangiography (left to right: intraoperative image under white light, capillary phase and venous phases of the FNa videoangiography). **(K)** Regular excitation (light blue) overlapping the emission (light green) laser light contains light only at 464 nm wavelength and does not interfere with the emission light; thus, the videoangiogram has good contrast. **(L–N)** An endoscope outfitted for FNa videoangiography. **(L)** A 2.7-mm straight endoscope is connected to a blue LED light source and a long-pass filter is inserted at the camera attachment. **(M)** The intraoperative view of endoscopic FNa videoangiography (left to right: under white light, under the blue LED before FNa injection, and after FNa injection). **(N)** The diagram showing optical setup of the device. Blue LED light is concentrated around 465 nm, and a long-pass filter (black line) allows green emission light into the camera. *, right posterior cerebral artery; **, left posterior cerebral artery; AN, aneurysm; BA, basilar artery; Max, maximum; Min, minimum; SCA, superior cerebellar artery. **(A–C,H,K,L,N)** are used with permission from Barrow Neurological Institute, Phoenix, Arizona. **(D–G)** Are used with permission from Suzuki et al. (37). **(I)** is copyright of Sato et al. (38) and made available under Creative Commons. **(J)** is used with permission from Ito et al. (22). **(M)** is used with permission from Hashimoto et al. (20).

VISUALIZING PLATFORMS

Different visualizing platforms that have been developed for FNa videoangiography are described briefly below (**Figure 2**).

Conventional Operating Microscopes With Fluorescein Filters (Figures 2A–C)

Unlike ICG videoangiography, which requires a separate infrared camera attached to the operating microscope to detect the infrared emission signal (39), the emission light of FNa requires only a filter for fluorescence to be visualized within the visible light spectrum. This may be the reason for the delayed application of ICG into the vascular field (39).

An FNa-specific filter set can be integrated into the surgical microscope to guarantee optimal intraoperative visualization of fluorescence and images superior in clarity. Novel microscopes have improved so much in fluorescence modality, and FNa fluorescence can offer such a brighter view that tumor resection can be performed in fluorescence mode throughout the whole surgery rather than switching between visualization modalities (40).

Pencil-Type Probe With Detachable Filter for the Microscope (Figures 2D–H)

Suzuki et al. used a pencil-type probe with a blue light-emitting diode (LED) at the tip (20, 30, 31); this setup can offer excitatory light while FNa fluorescence can be observed via a filter attached to the microscope (20, 30, 31). This pencil-type probe and filter represent an affordable option, and it enables surgeons to equip existing surgical microscopes with an FNa visualization mode.

A custom long-pass filter inset was designed to be manually installed at the bottom of the surgical microscope cylinder to visualize the FNa fluorescence (41). This device includes optical filters positioned across the three light pathways: two barrier filters for observation within the wavelength of FNa emitted fluorescence and one excitation filter.

Laser Illumination-Based Operating Microscope (Figures 2I–K)

Ito et al. reported the application of the laser microscope for intraoperative fluorescence cerebral angiography (22). Unlike traditional operating microscopes with a xenon lamp-generated light (wide wavelength spectrum), the laser microscope contains only three lasers of 640 nm (red), 532 nm (green), and 464 nm (blue) wavelengths. During illumination, these three wavelengths crosswire, resulting in white light that is similar to the regular xenon-generated light. During FNa videoangiography, the system turns off the green laser while leaving on the blue laser and low-intensity red laser. The peak emission wavelength of the FNa is 520 nm, which does not overlay with reflected blue and red laser lights. Therefore, such illumination offers better contrast. Furthermore, the laser illumination-based microscope produces significantly less tissue heat compared to xenon lamp illumination (38). Although this laser microscope is an early prototype, it provides well-controlled illumination that may benefit future developments of surgical microscopes.

FNa Videoangiography With an Endoscope (Figures 2L–N)

Hashimoto et al. reported their experience of FNa videoangiography visualized through the endoscope (20). A blue LED was adapted to the light source of the 2.7-mm endoscope to offer excitation light, and the emission light passed through a long-pass filter and was received by a camera.

In their detailed report, only three of 18 aneurysms could be completely inspected under the microscope after clipping, and no neck remnant was confirmed. Although microscopic FNa videoangiography showed that in all cases complete aneurysm occlusion had been achieved, subsequent inspection with the endoscopic FNa videoangiography allowed the investigators to detect and correct three of 18 cases with neck remnants and two of 18 cases with incomplete occlusion. Moreover, the perforator origin could be visualized only via endoscopic inspection and

TABLE 1 | Comparison of Advantages and Disadvantages of ICG- and FNa-Based Videoangiography.

Parameter	Fluorescent angiography	
	ICG	**FNa**
Thick vessel wall	Deeper penetration depth; can visualize STA, ICA, VA	Shallow penetration depth; cannot show flow in ICA or VA
Small vessels	Harder to visualize	Easier to visualize
Repeated IV injections or increased dose	Decreased intensity because of quenching	Can stain vessel wall resulting in false-positive fluorescence
Fluorescence detection	Infrared camera only	Eye, camera
Display	Always digital signal; separate LCD display or image injection into microscope eyepieces	Viewed through eyepieces or on any display
On-the-fly angiography	Requires image overlay; otherwise, need to review ICG video separately from natural light view	Can be in real time
View of surgical field	Two-dimensional	Three-dimensional in eyepieces/display
Contrast	Very high contrast	Average to high contrast

FNa, fluorescein sodium; ICA, internal carotid artery; ICG, indocyanine green; STA, superficial temporal artery; VA, vertebral artery.

TABLE 2 | Summary of clinical application of fluorescein videoangiography in the literature.

References	Injection method	Visualizing platform	Dose/concentration	Cases number	Lesion type	Time to arterial phase	Time to fade out	Comments
Feinde et al. (13)	IA	Stroboscopic light with Wratten 2B filter	1–2 ml/1% (10–20 mg)	1	AVM	Less than 2 s	N/A	First report in the literature
Little et al. (33)	IA (CCA)	Strobe light with Kodak-Wratten 47A filter	5 ml/1% (50 mg)	15	STA-MCA bypass	2.4 ± 0.4 s pre-bypass; 0.7 ± 0.3 s post-bypass	N/A	Bypass led to a 1.7 s decrease of the period from injection to arterial phase.
Wrobel et al. (32)	IV	ILC 302 and Oriel liquid light with Wratten 47A filter	20 ml/10% (2 g)	1	Aneurysm	30 s	60 min	2 g FNa caused long-time vessel wall staining
Suzuki et al. (30)	IV	A pencil-type probe with a blue LED/ filter attached to microscope	5 ml/10% (500 mg)	23	Aneurysm	15 s	N/A	The pencil-type probe is an affordable option for FNa videoangiography
Kuroda et al. (31)	IV and IA	A pencil-type probe with a blue LED filter attached to microscope	IV 5 ml/10% (500 mg); IA 10 ml/0.01–0.02% (1–2 mg)	IV, 5; IA, 13	Aneurysm	IV, 30 s; IA, immediately	IV, minimally 5 min; IA, 30 s	First study to report the advantage and disadvantage of IV and IA injections
Rey-Dios and Cohen-Gadol (16)	IV	OPMI Pentero 900	1 mg/kg	2	Aneurysm, 1; AVM, 1	20 s	N/A	
Ichikawa et al. (17)	IA (STA)	OPMI Pentero 900	5 ml/0.5–1%	10	Aneurysm	Immediately	Less than 1 min	3 F catheter inserted 5–10 cm into the STA
Lane and Cohen-Gadol (18)	IV	OPMI Pentero 900	75 mg	4	AVM	10–15 s	N/A	FNa videoangiography has the "real-time inspection" feature which is valuable in AVM surgery
Lane et al. (19)	IV	OPMI Pentero 900	75 mg	22	Aneurysm	20 s	20–30 min	Prospective comparison of FNa and ICG
Misra et al. (34)	IV	N/A	1.5 mg/kg	1	DAVF	11 s	N/A	First case report of use with a spinal AVM
Hashimoto et al. (20)	IV and IA	Olympus endoscope with long-pass filter; blue LED at the light source	IV 5 ml/10% (500 mg); IA 10 ml/0.01–0.02% (1–2 mg)	IV, 5; IA, 13	Aneurysm	IV, 30 s; IA, immediately	IV, N/A; IA 30 s	Endoscope can offer more information such as neck remnant and perforators preservation
Kakucs et al. (15)	IV	OPMI Pentero 900	5 ml/10% (500 mg)	10	Aneurysm	15 s	N/A	
Matano et al. (21)	IV	OPMI Pentero 900	250 mg	23	Aneurysm 18; bypass, 5	NA	N/A	Comparison of ICG and FNa in vascular surgery
Ito et al. (22)	IV	M500 OHS1 Laser microscope	2.5 ml/10% (250 mg)	1	Aneurysm	20 s	N/A	A novel laser microscope examining fluorescein angiography
Narducci et al. (6)	IV	OPMI Pentero 900	500 mg	11	Bypass	15–20 s	20–25 min	
Serrano-Rubio et al. (23)	IV	OPMI Pentero 900	75 mg	12	AVM	11.6 s	N/A	

AVM, arteriovenous malformation; CCA, common carotid artery; DAVF, dural arteriovenous fistula; FNa, fluorescein sodium; IA, intraarterial; ICG, indocyanine green; IV, intravenous; LED, light-emitting diode; MCA, middle cerebral artery; N/A, not applicable; STA, superficial temporal artery.

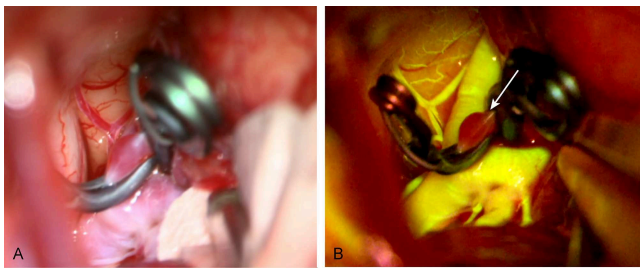

FIGURE 3 | Intraoperative images of an unruptured anterior communicating artery. **(A)** Intraoperative image under normal light. **(B)** Intraoperative image taken during FNa videoangiography; the aneurysm is not filling after being clipped (white arrow). Used with permission from Barrow Neurological Institute, Phoenix, Arizona.

not with the microscope, which allowed the identification and correction of two perforator occlusion events. The authors concluded that endoscopic FNa videoangiography had the same accuracy as DSA.

Although ICG videoangiography can also be obtained via endoscope, such ICG-infrared compatible endoscopes exceed 4 mm in diameter (42–44). Hashimoto et al. reported that in nine of 29 cases, a 4-mm endoscope was too large for visualization at deep locations (20). Therefore, thin endoscopes capable of FNa videoangiography represent a valuable adjunct to visualize blood flow in the vessels that are obscured during wide-field operations using microscope-based angiography.

COMPARISON OF ICG AND FNa VIDEOANGIOGRAPHIES

In vascular neurosurgery, intraoperative DSA remains the gold standard to assess the blood flow, but DSA requires a hybrid operating room and increases operating time (19).

Although ICG was applied to assess cerebral blood flow much later than FNa [ICG in 2003 (39), FNa in 1967 (12)], cerebral fluorescent videoangiography is currently more common with ICG than with FNa. ICG videoangiography can be repeated quickly and can demonstrate the vasculature clearly (45, 46); however, ICG still has several drawbacks. FNa and ICG both have features that can provide benefits in different scenarios—the features of both fluorophores are summarized in **Table 1**.

On one hand, unlike FNa, which can be observed in oculars, ICG requires a dedicated camera to detect the near-infrared signal and a separate display to present a pseudo-colored signal. The ICG signal does not interfere with visible spectral reflectance from the operating field and therefore provides a better contrast than FNa between surrounding structures (signal always = 0) and intravascular ICG (signal is high and always > 0), without the need to sacrifice any wavelength of the visible spectrum.

On the other hand, FNa can be seen as an orange color by the naked eye or as a bright yellow color when fluorescent. Because the excitation and emission wavelengths of FNa are within the visible spectrum, creation of a high contrast for FNa visualization requires the user to sacrifice some portion of the visible spectrum. Improvements with optical filter technologies have made it possible to selectively attenuate or block multiple spectral bands, allowing brighter overall images and making the consequential image demonstrate most of the reflected visible colors (brain, blood, and other tissues) and brighter FNa fluorescence simultaneously.

ICG is a fluorophore that can be visualized only by a near-infrared detector with a complete dark background (45), in which case the relationship of the surrounding anatomy and the vessels cannot be demonstrated. Furthermore, the ICG imaging can be visualized only via a separate infrared camera; therefore, the surgeon cannot change the view or perform real-time dissection on the basis of the information obtained from ICG videoangiography. Although these limitations were partially solved by live ICG-image overlay features on operating microscopes (47), such microscopes are not yet widely available.

FNa videoangiography provides less contrast than ICG but has the advantage of allowing visualization of the angiogram embedded in the thee-dimensional background anatomy within the ocular lens, which can enable real-time manipulation in situations of inadequate exposure, clip adjustment, and so on.

The second ICG injection can be less clear and less contrasting than the first because of quenching effects of dye remaining from the first injection (31). However, higher dosages of FNa with IV injection may stain the vessels for a substantial time, decreasing the specificity of FNa signal. Therefore, in terms of repeating fluorescent videoangiography quickly, ICG videoangiography may be preferred over IV FNa videoangiography (19, 21).

Another advantage of ICG is the longer wavelength emission that could penetrate thick vessel walls. It is reported that ICG is favorable in visualizing major arteries, such as the internal carotid artery and superficial temporal artery (21).

Lane et al. performed a prospective study comparing ICG and FNa videoangiographies in 22 patients and drew the conclusion that FNa can provide better visualization of vasculature at high magnification within deep operative fields (19). The limitation of ICG visualization at deep operative fields has been mentioned as its drawback in multiple studies (48–51). One study reported that inadvertent occlusion of small perforators was encountered in 6% (15/239) of the aneurysm clipping cases despite using ICG videoangiography (49).

ICG videoangiography and FNa videoangiography are valuable and mutually complementary tools in vascular neurosurgery, each with subtle advantages and disadvantages, and neither can yet replace intraoperative DSA as the gold standard. FNa and ICG could be used together sequentially as they do not interfere with each other. As technologies advance, the disadvantages of either modality are becoming less substantial (e.g., real-time ocular overlay of ICG videoangiography and laser illumination system).

CLINICAL APPLICATION OF FNa VIDEOANGIOGRAPHY IN VASCULAR NEUROSURGERY

The use of FNa videoangiography has been reported in many types of vascular neurosurgery, including treating aneurysms, AVMs, and DAVFs and bypass surgeries. A summary of clinical

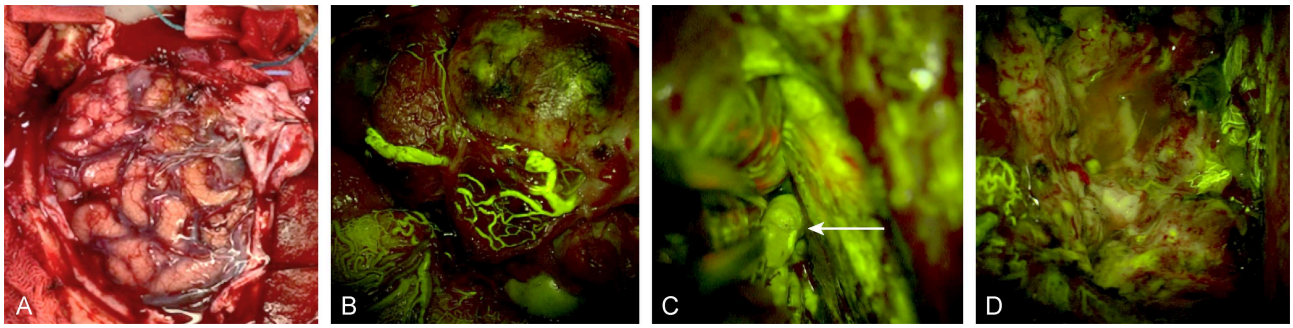

FIGURE 4 | Intraoperative images of a left frontal arteriovenous malformation **(A)** under normal light, **(B)** during FNa videoangiography, **(C)** during real-time inspection of the nidus and the deep feeders (white arrow) under FNa videoangiography during dissection, and **(D)** after total removal of the malformation. Used with permission from Barrow Neurological Institute, Phoenix, Arizona.

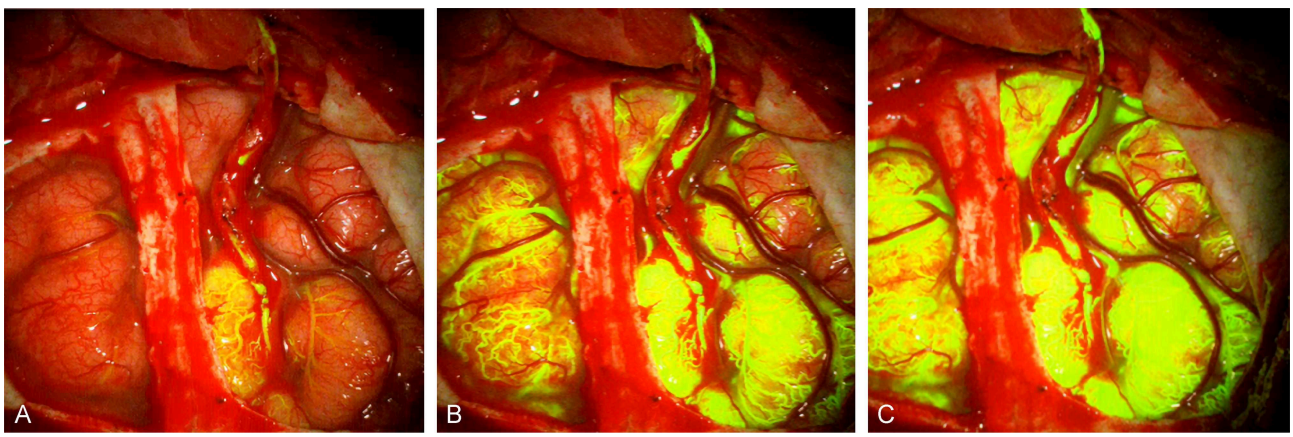

FIGURE 5 | FNa videoangiography images from a patient with moyamoya disease after a superficial temporal artery to middle cerebral artery bypass shows filling of **(A)** donor and recipient arteries, **(B)** cortical capillaries, and **(C)** all cortical vascular networks. Notice the filling starts at the bypass site and spreads around. Used with permission from Charite Universitätsmedizin Berlin, Berlin, Germany.

studies is presented in **Table 2** (6, 13, 15–23, 30–34), and clinical applications of FNa videoangiography are discussed below.

Cerebral Aneurysm Surgery (Figure 3)

For cerebral aneurysm surgery, it is of paramount importance to confirm the obliteration of the aneurysm neck as well as the patency of the parent vessels and small perforators intraoperatively (31). Lane et al. reported that FNa is preferable over ICG in terms of visualizing small perforators and aneurysm obliteration (19). For aneurysms at deep locations requiring a narrow corridor (i.e., anterior cerebral artery aneurysms through the lateral frontal approach), real-time manipulation of the surrounding anatomy under FNa videoangiography allows maximum exposure and inspection of the vessels of interest (19).

As discussed above, the endoscope can offer more information than FNa angiography, such as location of neck remnants and perforator preservation, as the endoscope provides a close and multi-angled inspection (20).

AVM Surgery (Figure 4)

AVMs are usually adhesive to the surrounding brain parenchyma. AVMs can be regarded as "intra-axial lesions" as most require subarachnoid and pial dissection. Numerous feeders can supply the nidus from the deep side, and these feeders may be blocked by brain parenchyma. Such a complex nature means that DSA remains the gold standard for evaluation (52), but it is not always available.

As mentioned above, fluorescence with traditional ICG videoangiography cannot be visualized via an ocular in real time. Deep feeders and the adhesive nature of AVMs make them challenging to operate on because thorough information usually cannot be obtained from a single angiography. Especially after circumferential dissection of the nidus or ligation of the superficial feeders, a premature venous filling indicates the presence of remaining deep feeders. Real-time dissection of the nidus and full inspection around it under videoangiography can facilitate localizing the rest of the feeders as well as provide a thorough examination of the lesion (16, 18). The real-time feature of FNa videoangiography is preferable over

ICG in such scenarios. In the only case of a spinal AVM reported as treated under FNa videoangiography (34), the vascular nidus was well visualized as being embedded in the background anatomy and the AVM was successfully resected.

DAVF Surgery

To date, there is no report of the application of FNa videoangiography for treating a DAVF. Unlike AVMs, DAVFs do not adhere to the surrounding parenchyma. The ligation of the fistula is concise and quick if the fistula can be accurately located; this feature of treating a DAVF requires repeated angiography in a short period of time. Even though IV injection of FNa for videoangiography has a relatively long intravascular stay, IA injection might be suitable in this scenario, and future investigation is merited.

Cerebrovascular Bypass Surgery (Figure 5)

FNa videoangiography can be used to evaluate the patency of the anastomosis and the improvement of the stenosis during cerebrovascular bypass surgery. The feature of real-time manipulation does not make FNa videoangiography differ from the ICG videoangiography in the bypass assessment (6). However, IA injection can be used to evaluate the effectiveness of the bypass apart from the evaluation of the patency. Little et al. carried out a study using IA injection in 1979 and reported that the duration from the injection to the arterial phase decreased from 2.4 ± 0.4 s to 0.7 ± 0.3 s (33). Such a decrease in time can help evaluate the improvement of the ischemic condition and offer another supplementary tool for evaluating the success of the bypass surgery.

CONCLUSION

The FNa-based fluorescent videoangiography techniques reviewed here represent an armamentarium of useful tools for various types of vascular neurosurgeries. Compared with ICG videoangiography, FNa videoangiography has the advantage of three-dimensional visualization of surrounding anatomy and allows real-time surgical manipulation, especially of small vessels in a narrow field. The disadvantages of FNa videoangiography are the incompetence in visualizing flow in thick-walled vessels and the staining of vessel walls at high doses. Advanced microscopy technologies, such as endoscopy and laser microscopy, have the potential to further improve the utility of FNa videoangiography. Finally, FNa videoangiography is affordable and may be complementary to ICG videoangiography for vascular neurosurgery.

AUTHOR CONTRIBUTIONS

PN and MP: conception and design. PN, ML, and PV: providing clinical cases. XZ: drafting the article. EB and CC: figures and graphs producing. EB, CC, DV, and SG: revising the article. PN: study supervision.

FUNDING

This research was supported with funds from the Barrow Neurological Foundation, the Women's Board of the Barrow Neurological Institute, and by the Newsome Chair in Neurosurgery Research to MP. EB acknowledges scholarship support SP-2240.2018.4.

ACKNOWLEDGMENTS

The authors thank the staff of Neuroscience Publications at Barrow Neurological Institute for assistance with manuscript preparation.

REFERENCES

1. Acland R, Raja Sabapathy S. *Acland's Practice Manual for Microvascular Surgery*. 2nd Edn. Mumbai: Medknow (1989).
2. Amin-Hanjani S, Meglio G, Gatto R, Bauer A, Charbel FT. The utility of intraoperative blood flow measurement during aneurysm surgery using an ultrasonic perivascular flow probe. *Neurosurgery*. (2006) 58:ONS-305-ONS-312. doi: 10.1227/01.NEU.0000209339.47929.34
3. Hecht N, Woitzik J, König S, Horn P, Vajkoczy P. Laser speckle imaging allows real-time intraoperative blood flow assessment during neurosurgical procedures. *J Cereb Blood Flow Metab*. (2013) 33:1000–7. doi: 10.1038/jcbfm.2013.42
4. Woitzik J, Horn P, Vajkoczy P, Schmiedek P. Intraoperative control of extracranial—intracranial bypass patency by near-infrared indocyanine green videoangiography. *J Neurosurg*. (2005) 102:692–8. doi: 10.3171/jns.2005.102.4.0692
5. Yanaka K, Fujita K, Noguchi S, Matsumaru Y, Asakawa H, Anno I, et al. Intraoperative angiographic assessment of graft patency during extracranial-intracranial bypass procedures. *Neurol Medico Chir*. (2003) 43:509–13. doi: 10.2176/nmc.43.509
6. Narducci A, Onken J, Czabanka M, Hecht N, Vajkoczy P. Fluorescein videoangiography during extracranial-to-intracranial bypass surgery: preliminary results. *Acta Neurochir*. (2018) 160:767–74. doi: 10.1007/s00701-017-3453-0
7. Van Cader TC. History of ophthalmic photography. *J Ophthalmic Photogr*. (1978) 1:7–9.
8. Norton EW, Gutman F. Diabetic retinopathy studied by fluorescein angiography. *Ophthalmologica*. (1965) 150:5–17. doi: 10.1159/000304822
9. Russell RR, Ffytche T, Sanders M. A study of retinal vascular occlusion using fluorescein angiography. *Lancet*. (1966) 288:821–5. doi: 10.1016/S0140-6736(66)92254-9
10. Moore GE, Peyton WT, French LA, Walker WW. The clinical use of fluorescein in neurosurgery: the localization of brain tumors. *J Neurosurg*. (1948) 5:392–8. doi: 10.3171/jns.1948.5.4.0392
11. Moore GE. Fluorescein as an agent in the differentiation of normal and malignant tissues. *Science*. (1947) 106:130–1. doi: 10.1126/science.106.2745.130-a
12. Feindel W, Yamamoto YL, Hodge CP. Intracarotid fluorescein angiography: a new method for examination of the epicerebral circulation in man. *Can Med Assoc J*. (1967) 96:1.
13. Feindel W, Yamamoto YL, Hodge CP. Red cerebral veins and the cerebral steal syndrome: Evidence from fluorescein angiography and microregional blood flow by radioisotopes during excision of an angioma. *J Neurosurg*. (1971) 35:167–79. doi: 10.3171/jns.1971.35.2.0167

14. Zipfel GJ. Clipping of neurosurgical aneurysms: the dye is cast. *J Neurosurg*. (2015) 122:616–7. doi: 10.3171/2014.8.JNS14957
15. Kakucs C, Florian AI, Ungureanu G, Florian SI. Fluorescein angiography in intracranial aneurysm surgery: a helpful method to evaluate the security of clipping and observe blood flow. *World Neurosurg*. (2017) 105:406–11. doi: 10.1016/j.wneu.2017.05.172
16. Rey-Dios R, Cohen-Gadol AA. Technical principles and neurosurgical applications of fluorescein fluorescence using a microscope-integrated fluorescence module. *Acta Neurochir*. (2013) 155:701–6. doi: 10.1007/s00701-013-1635-y
17. Ichikawa T, Suzuki K, Watanabe Y. Intra-arterial fluorescence angiography with injection of fluorescein sodium from the superficial temporal artery during aneurysm surgery: technical notes. *Neurol Med Chir*. (2014) 54:490–496. doi: 10.2176/nmc.tn.2013-0232
18. Lane BC, Cohen-Gadol AA. A prospective study of microscope-integrated intraoperative fluorescein videoangiography during arteriovenous malformation surgery: preliminary results. *Neurosurg Focus*. (2014) 36:E15. doi: 10.3171/2013.11.FOCUS13483
19. Lane B, Bohnstedt BN, Cohen-Gadol AA. A prospective comparative study of microscope-integrated intraoperative fluorescein and indocyanine videoangiography for clip ligation of complex cerebral aneurysms. *J Neurosurg*. (2015) 122:618–26. doi: 10.3171/2014.10.JNS132766
20. Hashimoto K, Kinouchi H, Yoshioka H, Kanemaru K, Ogiwara M, Yagi T, et al. Efficacy of endoscopic fluorescein video angiography in aneurysm surgery—novel and innovative assessment of vascular blood flow in the dead angles of the microscope. *Operat Neurosurg*. (2017) 13:471–81. doi: 10.1093/ons/opw042
21. Matano F, Mizunari T, Murai Y, Kubota A, Fujiki Y, Kobayashi S, et al. Quantitative comparison of the intraoperative utility of indocyanine green and fluorescein videoangiographies in cerebrovascular surgery. *Operat Neurosurg*. (2017) 13:361–6. doi: 10.1093/ons/opw020
22. Ito Y, Suzuki K, Ichikawa T, Watanabe Y, Sato T, Sakuma J, Saito K. Intraoperative fluorescence cerebral angiography by laser surgical microscopy: comparison with xenon microscopy and simultaneous observation of cerebral blood flow and surrounding structures. *Operat Neurosurg*. (2018) 16:700–6. doi: 10.1093/ons/opy159
23. Serrano-Rubio A, Ruiz-Treviño AS, Orenday-Barraza JM, Vázquez-Gregorio R, Lee A, Nathal E. Sodium fluorescein videoangiography as an adjunct to resection of cerebral arteriovenous malformations. *World Neurosurg*. (2018) 117:e329–34. doi: 10.1016/j.wneu.2018.06.024
24. Dollery C. *Fluorescein, Therapeutic Drugs*. Edinburgh, Churchill Livingstone (1999).
25. Shinoda J, Yano H,Yoshimura SI, Okumura A, Kaku Y, Iwama T, Sakai N. Fluorescence-guided resection of glioblastoma multiforme by using high-dose fluorescein sodium. *J Neurosurg*. (2003) 99:597–603. doi: 10.3171/jns.2003.99.3.0597
26. Bennett TJ, Quillen DA, Coronica R. Fundamentals of fluorescein angiography. *Insight*. (2016) 41:5–11.
27. Kwan AS, Barry C, McAllister IL, Constable I. Fluorescein angiography and adverse drug reactions revisited: the Lions Eye experience. *Clin Exp Ophthalmol*. (2006) 34:33–8. doi: 10.1111/j.1442-9071.2006.01136.x
28. Alford R, Simpson HM, Duberman J, Hill GC, Ogawa M, Regino C, et al. Toxicity of organic fluorophores used in molecular imaging: literature review. *Mol Imaging*. (2009) 8:31. doi: 10.2310/7290.2009.00031
29. Yannuzzi LA, Rohrer KT, Tindel LJ, Sobel RS, Costanza MA, Shields W, et al. Fluorescein angiography complication survey. *Ophthalmology*. (1986) 93:611–7. doi: 10.1016/S0161-6420(86)33697-2
30. Suzuki K, Watanabe Y, Ichikawa T. Usefulness of intraoperative fluorescence cerebral angiography using fluorescein sodium. *Surg Cereb Stroke*. (2009) 37:240–5. doi: 10.2335/scs.37.240
31. Kuroda K, Kinouchi H, Kanemaru K, Nishiyama Y, Ogiwara M, Yoshioka H, et al. Intra-arterial injection fluorescein videoangiography in aneurysm surgery. *Operat Neurosurg*. (2012) 72:ons141–50. doi: 10.1227/NEU.0b013e3182752f32
32. Wrobel CJ, Meltzer H, Lamond R, Alksne JF. Intraoperative assessment of aneurysm clip placement by intravenous fluorescein angiography. *Neurosurgery*. (1994) 35:970–3. doi: 10.1097/00006123-199411000-00027
33. Little JR, Yamamoto YL, Feindel W, Meyer E, Hodge CP. Superficial temporal artery to middle cerebral artery anastomosis: intraoperative evaluation by fluorescein angiography and xenon-133 clearance. *J Neurosurg*. (1979) 50:560–9. doi: 10.3171/jns.1979.50.5.0560
34. Misra BK, Samantray SK, Churi ON. Application of fluorescein sodium videoangiography in surgery for spinal arteriovenous malformation. *J Clin Neurosci*. (2017) 38:59–62. doi: 10.1016/j.jocn.2016.12.004
35. Yamamoto S, Kim P, Kurokawa R, Itoki K, Kawamoto S. Selective intraarterial injection of ICG for fluorescence angiography as a guide to extirpate perimedullary arteriovenous fistulas. *Acta Neurochirurg*. (2012) 154:457–63. doi: 10.1007/s00701-011-1223-y
36. Belykh E, Miller EJ, Patel AA, Bozkurt B, Yagmurlu K, Robinson TR, Nakaji P, et al. Optical characterization of neurosurgical operating microscopes: quantitative fluorescence and assessment of PpIX photobleaching. *Sci Rep*. (2018) 8:12543. doi: 10.1038/s41598-018-30247-6
37. Suzuki K, Kodama N, Sasaki T, Matsumoto M, Ichikawa T, Munakata R, et al. Confirmation of blood flow in perforating arteries using fluorescein cerebral angiography during aneurysm surgery. *J Neurosurg*. (2007) 107:68–73. doi: 10.3171/JNS-07/07/0068
38. Sato T, Bakhit MS, Suzuki K, Sakuma J, Fujii M, Murakami Y, et al. Utility and safety of a novel surgical microscope laser light source. *PLoS ONE*. (2018) 13:e0192112. doi: 10.1371/journal.pone.0192112
39. Raabe A, Beck J, Gerlach R, Zimmermann M, Seifert V. Near-infrared indocyanine green video angiography: a new method for intraoperative assessment of vascular flow. *Neurosurgery*. (2003) 52:132–9. doi: 10.1227/00006123-200301000-00017
40. Belykh EG, Zhao X, Cavallo C, Bohl MA, Yagmurlu K, Aklinski JL, et al. Laboratory evaluation of a robotic operative microscope-visualization platform for neurosurgery. *Cureus*. (2018) 10:e3072. doi: 10.7759/cureus.3072
41. Ichikawa T, Suzuki K, Watanabe Y, Sato T, Sakuma J, Saito K. Development of and clinical experience with a simple device for performing intraoperative fluorescein fluorescence cerebral angiography: technical notes. *Neurol Med Chir*. (2016) 56:141–9. doi: 10.2176/nmc.tn.2015-0188
42. Nishiyama Y, Kinouchi H, Senbokuya N, Kato T, Kanemaru K, Yoshioka H, et al. Endoscopic indocyanine green video angiography in aneurysm surgery: an innovative method for intraoperative assessment of blood flow in vasculature hidden from microscopic view. *J Neurosurg*. (2012) 117:302–8. doi: 10.3171/2012.5.JNS112300
43. Bruneau M, Appelboom G, Rynkowski M, Van Cutsem N, Mine B, De Witte O. Endoscope-integrated ICG technology: first application during intracranial aneurysm surgery. *Neurosurg Rev*. (2013) 36:77–85. doi: 10.1007/s10143-012-0419-9
44. Mielke D, Malinova V, Rohde V. Comparison of intraoperative microscopic and endoscopic ICG angiography in aneurysm surgery. *Operat Neurosurg*. (2014) 10:418–25. doi: 10.1227/NEU.0000000000000345
45. Raabe A, Nakaji P, Beck J, Kim LJ, Hsu FP, Kamerman JD, Seifert V, Spetzler RF. Prospective evaluation of surgical microscope—integrated intraoperative near-infrared indocyanine green videoangiography during aneurysm surgery. *J Neurosurg*. (2005) 103:982–9. doi: 10.3171/jns.2005.103.6.0982
46. de Oliveira JG, Beck J, Seifert V, Teixeira MJ, Raabe A. Assessment of flow in perforating arteries during intracranial aneurysm surgery using intraoperative near-infrared indocyanine green videoangiography. *Operat Neurosurg*. (2007) 61:ONS-63–ONS-73. doi: 10.1227/01.neu.0000289715.18297.08
47. Martirosyan NL, Skoch J, Watson JR, Lemole GM Jr., Romanowski M, Anton R. Integration of indocyanine green videoangiography with operative microscope: augmented reality for interactive assessment of vascular structures and blood flow. *Operat Neurosurg*. (2015) 11:252–8. doi: 10.1227/NEU.0000000000000681
48. Dashti R, Laakso A, Niemelä M, Porras M, Hernesniemi J. Microscope integrated indocyanine green video-angiography in cerebrovascular surgery. *Acta Neurochir Suppl*. (2011) 109:247–50. doi: 10.1007/978-3-211-99651-5_39
49. Dashti R, Laakso A, Niemelä M, Porras M, Hernesniemi J, Microscope-integrated near-infrared indocyanine green videoangiography during surgery of intracranial aneurysms: the Helsinki experience. *Surg Neurol*. (2009) 71:543–50. doi: 10.1016/j.surneu.2009.01.027

50. Gruber A, Dorfer C, Standhardt H, Bavinzski G, Knosp E. Prospective comparison of intraoperative vascular monitoring technologies during cerebral aneurysm surgery. *Neurosurgery*. (2011) 68:657–73. doi: 10.1227/NEU.0b013e31820777ee
51. Washington CW, Zipfel GJ, Chicoine MR, Derdeyn CP, Rich KM, Moran CJ, et al. Comparing indocyanine green videoangiography to the gold standard of intraoperative digital subtraction angiography used in aneurysm surgery. *J Neurosurg*. (2013) 118:420–7. doi: 10.3171/2012.10.JNS11818
52. Yanaka K, Matsumaru Y, Okazaki M, Noguchi S, Asakawa H, Anno I, Nose T. Intraoperative angiography in the surgical treatment of cerebral arteriovenous malformations and fistulas. *Acta Neurochir*. (2003) 145:377–83. doi: 10.1007/s00701-003-0017-2

Conflict of Interest Statement: The authors declare that the research was conducted in the absence of any commercial or financial relationships that could be construed as a potential conflict of interest.

frontiers in Oncology

MINI REVIEW
published: 24 September 2019
doi: 10.3389/fonc.2019.00925

Acridine Orange: A Review of Novel Applications for Surgical Cancer Imaging and Therapy

Vadim A. Byvaltsev[1,2], Liudmila A. Bardonova[1], Naomi R. Onaka[3], Roman A. Polkin[1], Sergey V. Ochkal[1], Valerij V. Shepelev[1], Marat A. Aliyev[1] and Alexander A. Potapov[4]*

[1] Neurosurgery and Innovative Medicine Department, Irkutsk State Medical University, Irkutsk, Russia, [2] Irkutsk Scientific Center of Surgery and Traumatology, Irkutsk, Russia, [3] University of Arizona College of Medicine, Phoenix, AZ, United States, [4] Federal State Autonomous Institution "N. N. Burdenko National Scientific and Practical Center for Neurosurgery" of the Ministry of Healthcare of the Russian Federation, Moscow, Russia

OPEN ACCESS

Edited by:
Jonathan T. C. Liu,
University of Washington,
United States

Reviewed by:
Laurence Gluch,
The Strathfield Breast Centre, Australia
Guolin Ma,
China-Japan Friendship Hospital, China
Joseph Georges,
Philadelphia College of Osteopathic Medicine, United States

***Correspondence:**
Vadim A. Byvaltsev
byval75vadim@yandex.ru

Specialty section:
This article was submitted to Cancer Imaging and Image-directed Interventions, a section of the journal Frontiers in Oncology

Received: 15 April 2019
Accepted: 04 September 2019
Published: 24 September 2019

Citation:
Byvaltsev VA, Bardonova LA, Onaka NR, Polkin RA, Ochkal SV, Shepelev VV, Aliyev MA and Potapov AA (2019) Acridine Orange: A Review of Novel Applications for Surgical Cancer Imaging and Therapy. Front. Oncol. 9:925. doi: 10.3389/fonc.2019.00925

Introduction: Acridine orange (AO) was first extracted from coal tar in the late nineteenth century and was used as a fluorescent dye. In this paper, we review emergent research about novel applications of AO for fluorescence surgery and cancer therapy.

Materials and methods: We performed a systematic search in the MEDLINE, PubMed, Cochrane library, Google Scholar, Embase, Web of Science, and Scopus database using combinations of the term "acridine orange" with the following: "surgical oncology," "neuropathology," "microsurgery," "intraoperative fluorescence," "confocal microscopy," "pathology," "endomicroscopy," "guidance," "fluorescence guidance," "oncology," "surgery," "neurooncology," and "photodynamic therapy." Peer-reviewed articles published in English were included in this review. We have also scanned references for relevant articles.

Results: We have reviewed studies on the various application of AO in microscopy, endomicroscopy, intraoperative fluorescence guidance, photodynamic therapy, sonodynamic therapy, radiodynamic therapy.

Conclusion: Although the number of studies on the clinical use of AO is limited, pilot studies have demonstrated the safety and feasibility of its application as an intraoperative fluorescent dye and as a novel photo- and radio-sensitizator. Further clinical studies are necessary to more definitively assess the clinical benefit AO-based fluorescence guidance, therapy for sarcomas, and to establish feasibility of this new approach for the treatment of other tumor types.

Keywords: acridine orange, radiodynamic therapy, photodynamic therapy, intraoperative fluorescence, surgical cancer imaging

INTRODUCTION

Recent advancements in optical cancer imaging have facilitated the development of novel repurposing of known molecular probes for wide-field and microscopic fluorescence-based surgical guidance that have significant potential to positively impact patient care and to transform the field of surgical oncology. Acridine orange (AO) is a common fluorescent dye that has been well known

for years. It has recently regained attention as a possible innovative drug for clinical applications in the field of oncology, particularly in cancer imaging and photodynamic therapy.

Acridine orange (AO) is a member of the xanthene class of molecules and shares a common aromatic structure with multiple acridine dyes (1, 2). Acridine dyes were first extracted from coal tar at the end of the nineteenth century. And was then used for a period of time as a dye in the fabric industry as well as for biological application. In 1912, Erlich and Beneda proposed to use acridines as antimalarials, with Browning suggesting use as an antimicrobial agent about a decade on in 1922 (3, 4). During World War I and II, the acridine dyes were widely used as antimicrobials prior to the widespread use of penicillin (4). The application of AO has been studied for bacteria detection in clinical specimens with prokaryotes fluorescing bright orange in low pH buffered media, while other cells produce green background fluorescence (5).

The novel research field of acridines is focused on their application in cancer theranostics due to its unique feature of preferential accumulation in the acidic environment of the tumor tissues and strong fluorescent properties (1, 6). AO has been recently explored in several preclinical (**Figures 1A,B**) and clinical studies for specific tumor cells targeting. As the novel diagnostic and therapeutic applications of AO broaden, we thought to review the existing body of knowledge regarding its potential use in various areas of medicine and outline its place and potential future impact on the rapidly growing area of image-guided cancer management. The goal of this paper is to review the current literature on the use of AO for fluorescence-guided surgery and cancer therapy. This review is focused on the clinical and translational studies that described the use of AO-based therapeutic and relevant diagnostic imaging methods.

MATERIALS AND METHODS

Search Strategy

We performed a literature search in MEDLINE, PubMed, Cochrane library, Google Scholar, Embase, Web of Science, and Scopus databases using the combinations of the term "Acridine" with the following: "surgical oncology," "neuropathology," "microsurgery," "intraoperative fluorescence," "confocal microscopy," "pathology," "endomicroscopy," "guidance," "fluorescence guidance," "oncology," "surgery," "neurooncology," and "photodynamic therapy." Peer-reviewed articles published in English till September 2018 were included to compile this review. We have also scanned references for relevant articles. Search strategy is presented in **Supplement 1**.

RESULTS AND DISCUSSION

Chemical Properties

AO ($C_{17}H_{19}N_3$) is a low molecular weight (265.36 g/mol), weakly basic dye that easily penetrates cell membranes. AO has metachromatic properties and upon excitation with blue light, (∼488 nm) emits green fluorescence when in monomer form and orange fluorescence when in dimer form. AO produces orange fluorescence when it binds to RNA and green fluorescence when it binds to DNA. However, this behavior differs significantly in live, apoptotic, and fixed permeabilized cells (6).

In live cells, AO diffuses through the cytoplasmic membrane and is retained in the cellular compartments with low pH, resulting in a bright orange fluorescence of lysosomes when excited with a blue light. AO also intercalates with the cytoplasmic and nuclear RNA molecules and results in a diffuse green fluorescence within all cells (7, 8). AO does not intercalate with DNA of intact living cells (9) and does not accumulate in other non-acidic organelles, such as the mitochondria, endoplasmic reticulum, or Golgi apparatus (7).

In both fixed permeabilized cells and cells undergoing apoptosis, pH compartmentalization is lost. Therefore, AO leaks from acidic lysosomes and diffusely binds to RNA and DNA molecules, resulting in yellow-orange fluorescence in the whole cell (6).

Based on the unique spectral distinctions and differential staining of RNA and DNA molecules, AO can be used to distinguish stages of apoptosis and necroptosis (10). During apoptosis, cells stained with AO demonstrate nuclear shrinkage, cellular fragmentation, and loss of nuclear demarcation, appearing therefore as red cells. Eventually the cellular RNA and red AO emission is lost while fragmented green nucleus remains. In contrast, during necrosis or necroptosis, the orange lysosomal signal is lost due to their disruption and to loss of cellular RNA, while the green signal from smooth and shrunken nuclei remains (11).

Most malignant tumors create an acidic environment due to increased anaerobic glycolysis (Warburg effect). Malignant cells also contain increased amounts of RNA and DNA compared to normal cells. Both factors result in increased accumulation and delayed elimination of AO in tumor cells (12).

Safety

Acridine dyes have a record of a mutagenic effect on certain types of bacteria, which raises a question about AO safety in humans (13). In 1969, Van Duuren showed that AO is neither an irritant nor a carcinogen to the skin of mice after repeated application. However, three out of twenty mice with skin application of AO developed liver tumors, suggesting systemic absorption of AO (14). In the same study, subcutaneous administration of AO lead to two of thirty mice and one of twenty rats developing tumors at the injection site. (14) In1978, the International Agency for Research on Cancer published the opinion that there was insufficient data or evaluation regarding the carcinogenicity of AO (15).

Systemic administration of AO has been investigated in several animal studies. The LD_{50} for intravenous (IV) administration of AO in mice was determined to be 32 and 36 mg/kg for male and female mice, respectively (16). In determining the dose/toxicity relationship, Tatsuta et al. studied mice with gastric cancer and Tomson et al. studied subcutaneously implanted mammary carcinoma tumors treated with intraperitoneal AO application at a dose of 40 mg/kg and showed effectiveness of photodynamic therapy (PDT) without significant toxic effects (17, 18). Udovich et al. also demonstrated the absence of adverse effects of AO administered

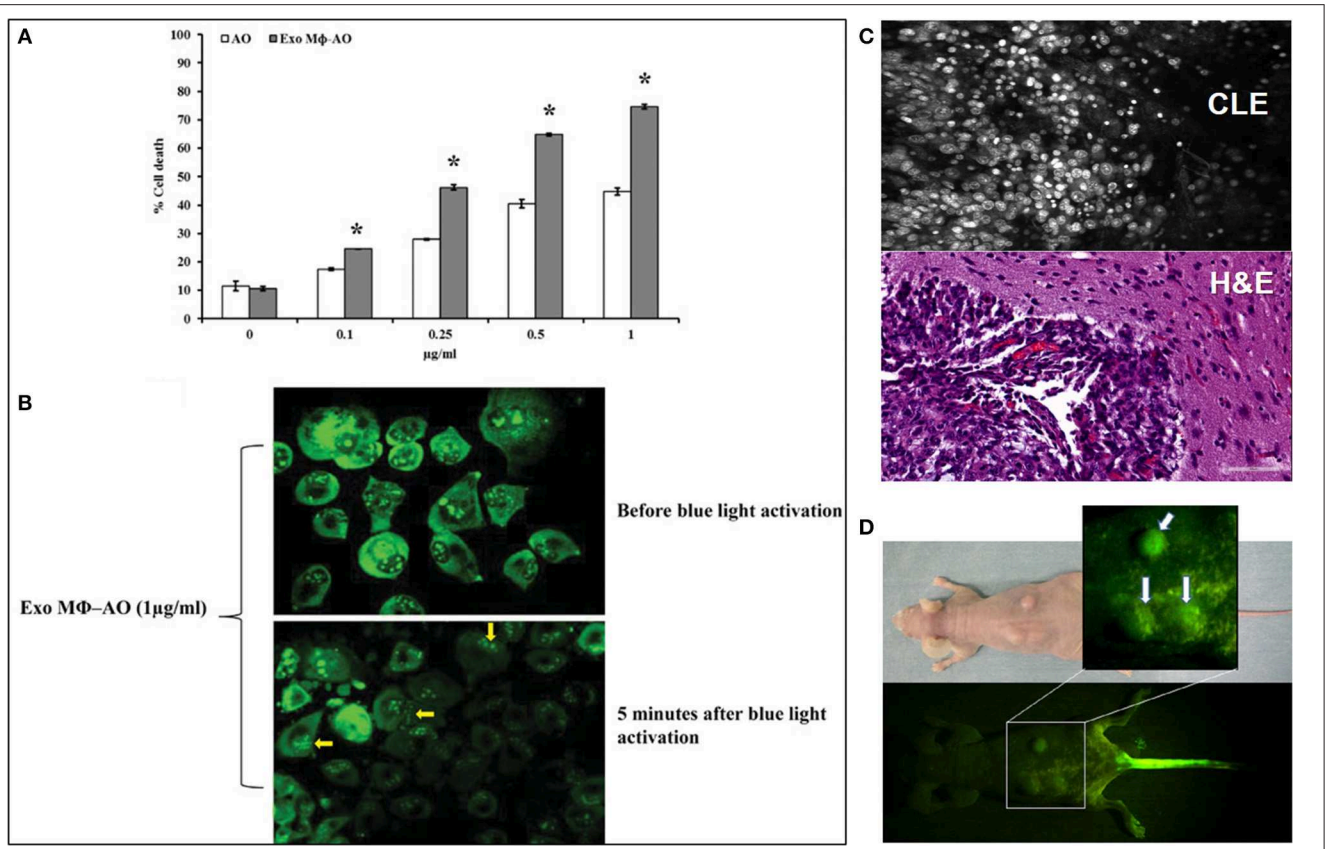

FIGURE 1 | (A) Cytotoxic effect of acridine orange (AO)-charged exosomes derived from macrophages (Exo Mϕ-AO) compared to free AO against melanoma cell monolayer by cytofluorimetry assessment. Columns, mean percentages of cell death of two independent experiments run in triplicate; bars indicate standard deviation. $p < 0.05$. Figure adapted with permission from: Iessi et al. (43) (CC BY 4.0). **(B)** Fluorescence microscopy showing the formation of membrane "blebs" in melanoma cells treated with Exo Mϕ-AO (1 lg/ml) after 5 min of exposition to blue light. Figure adapted with permission from: Iessi et al. (43) (CC BY 4.0). **(C)** Upper image—Confocal laser endomicroscopy image of an animal glioblastoma stained with AO. Lower image—corresponding histology image. Image courtesy of Dr. Mark C. Preul. **(D)** Macroscopic fluorescence view of mouse osteosarcoma subcutaneously inoculated in the back of nude mouse after blue light excitation at 2 h after AO injection through the tail vein. Tumors emit green fluorescence (arrows). Injection site of the tail vein also emits green fluorescence Figure adapted with permission from: Kusuzaki et al. (6) (CC-BY 3.0).

intraperitoneally to mice at dose of 0.33 and 3.3 mM for confocal endomicroscopy imaging (19).

In dogs, IV administration of AO at 0.1 mg/kg showed no clinical signs of toxicity and no abnormalities were seen in the blood within 30 days (20). Serum AO levels decreased rapidly within 30 min and were below the detection limit (5 ng/ml) 2 h after intravenous administration (20). In a case report of AO-based PDT in a cat with cutaneous malignant melanoma, no side effects were reported, where AO was administered locally to the surgical site at a dose of 1 μg/ml (21).

Several human studies have demonstrated the initial safety of AO. Kusuzaki et al. reported a pilot study of eight patients with various malignant neoplasms at the terminal stages (two sarcomas, two pancreatic carcinomas, intrahepatic cholangiocarcinoma, lung, renal, and parotid carcinomas) treated with IV administration of AO at 0.5 or 1 mg/kg and low-dose (with 3 or 5 Gy) radiotherapy (RT) (13). This study did not confirm the assumptions about the toxic effects of the AO (13).

Several studies from Japan [$n = 8$ patients from Teneri, Japan (13) and $n = 51$ from Tsu City, Mie, Japan (22)] investigated the local application of AO solution to tumor cavities following tumor resection at the dosage of 1 μg/ml for 5 min. Subsequent analysis of AO-based photodiagnostics (PD), PDT and RT demonstrated no serious immediate or long-term complications (23–26).

In summary, there is still a lack of convincing data regarding the long-term safety and cancerogenic potential of AO. Future studies are needed to demonstrate if potential toxic effects of AO can be balanced by the benefits of AO-based cytoreduction therapies and diagnostics for various tissue organs, routs of administration, and doses.

Photodiagnostics

AO Use for Microscopy

AO has been extensively studied in pathology as a single dye and in combination with other dyes for specimen assessment using fluorescence microscopy. Differential staining of AO has

been used to differentiate gliosis and glial neoplasms in human specimens with malignant glial cells demonstrating increased red fluorescence secondary to cytoplasmic RNA accumulation compared to reactive glial cells which remained green (27). AO has been used for mapping of GL261 mouse gliomas on 3-D reconstructed confocal imaging following tissue clearing (28). In this application, glioma regions exhibited increased intensity of fluorescence compared to the dimmer surrounding normal brain (28). Additionally, another study demonstrated the ability of AO to effectively differentiate brain tumor types using confocal microscopy of various brain tumor biopsies rapidly stained with AO (29).

Other applications of acridine orange include the simple and sensitive post-mortem detection of early myocardial infarction—normal myocardium fluoresces a golden brown color and myocardial anoxia/ischemia-damaged cells show a shift toward yellow or yellow-green (30). In the 1980's, Tejada et al. developed a specialized test with sperm AO fluorescence staining to determine male fertility (31). Krishnamurthy et al. showed that staining of breast, lung, kidney, and liver tissues with AO alone and subsequent imaging with confocal laser microscopy practically does not differ in efficiency from staining with H&E (32). Moreover, AO staining was much faster and easier than H&E (32). In yet another application, Wang et al. used AO for rapid non-destructive imaging of whole prostate biopsies using video-rate fluorescence structured illumination microscopy and demonstrated its feasibility as an alternative to destructive pathology (33).

In a study investigating surgical treatment of malignant tumors of the skin, AO was used as a nuclear dye in combination with eosin fluorescence (for labeling cytoplasm), and endogenous reflectance (for labeling collagen and keratin) for tri-modal confocal laser scanning microscopy of the skin samples (34). The authors reported that the novel staining method significantly reduced the time of surgical intervention while providing image quality similar to conventional hematoxylin and eosin staining (34). This finding corroborates with the conclusions drawn by Krishnamurthy regarding the non-inferiority of AO and CLE compared to conventional H&E. Another study reported an automatic pipeline that produces rapid, virtual H&E histology of tissue based on a fast, initial confocal staining of a tissue stained with a combination of AO and sulforhodamine 101, with the extrapolated conclusion that CLE with AO improves time to histological diagnosis over H&E (35). The intraoperative direct analysis that CLE can provide, particularly with AO as a contrast agent, has also been studied in the ophthalmological setting. The authors commented that this method provided a fast *ex vivo* preliminary diagnosis of conjunctival lesions, perhaps representing a novel tool for intraoperative as well as postsurgical management of conjunctival tumors (36).

AO is commonly used as a fluorescent dye to stain live tissues for intraoperative confocal endomicroscopy (**Figure 1C**), however, *in vivo* topical application of AO has not been investigated for all organs, and particularly in the brain up to this point due to safety concerns, with the less specific fluorescein sodium being used as a fluorescent contrast (37) In mouse brain glioma models and in fresh human biopsies *ex vivo*, AO staining and imaging with the confocal endomicroscope proved successful for differentiation of normal brain and glioma tissue (38, 39). Notably, *in vivo* AO staining was reported for confocal microlaparoscope imaging of ovarian cancer in 45 patients (40). In this study AO was used under FDA Investigational New Drug approval at a dose of $\leq$1 μL of 330 μM/L applied topically to the surface of the ovary just prior to imaging (40). This study concluded that trained surgeons were able to distinguish between normal and malignant ovarian surface epithelium in AO stained optical biopsies and that accuracy was similar during the *ex vivo* and *in vivo* imaging (40). There are two additional publications regarding AO application for the *in vivo* diagnosis of neoplasia in gynecology (41, 42), but currently, no *in vivo* investigation has been published for brain tissue.

AO Use in Wide-Field Fluorescence Guidance

After intravenous or topical application and soaking of the resection cavity in AO solution, researchers observed increased accumulation of AO in tumor tissue. This allowed accurate identification of the tumor regions as intense green fluorescence in wide field imaging (using specially designed fluorescence imaging operating microscope). AO fluorescence allowed for better tailoring of the resection area while maintaining the maximum amount of healthy tissue. This technology was used to remove breast tumors (35), soft tissue tumors and sarcomas (26, 44, 45), treatment of skin cancer (34, 46), conjunctival tumors (47), renal tumors, lungs, liver (32).

Considering the rapid development of intraoperative optical imaging tools and significant track of publications regarding AO-based microscopy, AO (similarly to fluorescein sodium and indocyanine green) is a promising topical contrast agent for *in vivo* pathology in humans. However, the long-term safety of topical AO should be established before such a method may be used in surgery. Alternatively, novel, dye-less *in vivo* microscopy methods like optical coherent tomography, RAMAN, and multiphoton reflectance microscopy may make any label-based methods obsolete in the future.

AO Use in PDT, SDT, and RDT

Mechanism of Action

The mechanism of AO-based PDT is based on the production of activated forms of oxygen upon AO fluorescence emission when exposed to blue light excitation (488 nm). As AO binds to the increased amount of RNA in tumor cells and also accumulates in lysosomes, released reactive oxygen species damage lipid membranes, leading to the leakage of lysosomal enzymes, and activation of apoptosis in the tumor cells (12). Myotoxicity was also suggested as another potential mechanism of AO (48).

AO can also increase the production of reactive radicals when exposed to low doses of X-ray radiation (26, 44, 49) or to the ultrasound energy (50). The principles of X-ray radiodynamic therapy (RDT) and sonodynamic therapy (SDT) have gained interest because unlike traditional light-based PDT, it has deeper tissue penetration depth. With RDT however, one energy source simultaneously activates both processes of radiotherapy and PDT, maximizing the synergetic treatment effect (49, 51). RDT with

AO shows a similar effect on tumor cells when compared to PDT (52).

Preclinical Studies

One of the earliest studies of PDT with AO by Tomson et al. in the mouse model of undifferentiated carcinoma showed tumor resolution after PDT with AO in 90% of mice (18). Another early study by Ishikawa et al. which suggested the usefulness of PDT investigated photodynamic inactivation of argon laser with topical use of AO in the treatment of bladder cancer. Human bladder cancer cells (MGH-U1) were stained with AO and irradiated with argon laser with wave length of 496.5 nm and the intensity at the sample position about 4.0 mW/cm^2. The result shows that argon laser at the low intensity and with short irradiation time has a sufficient cytocidal effect (53). Satonaka et al. studied the AO-based PDT of pulmonary metastases of osteosarcomas in mice and demonstrated its feasibility (54) (**Figure 1D**). Interestingly, AO alone and AO-PDT inhibited invasion and metastases growth (54).

AO-based PDT and RDT has been advanced to clinical studies for the treatment of sarcomas (osteosarcomas and rhabdomyosarcomas) (1, 7, 12, 23, 25, 55), while its efficacy for brain tumors has been assessed only in preclinical studies. Osman et al. investigated the efficacy of AO-based PDT of glioma cells *in vitro* (56). Treatment of cultured glioblastoma cells with AO at a concentration of 0.001 mg/mL followed by 10 or 30 min incubation with white unfiltered light from light-emitting diode bulbs demonstrated dramatic cytostatic and cytocidal effects and almost complete eradication of glioblastoma cells in 72 h (56).

Local AO Administration

Matsubara et al. investigated the combined use of AO-based PD, followed by PDT and RDT for the treatment of rhabdomyosarcoma (57). After subtotal resection of the tumor, the area of operation was filled with a solution of AO at a concentration of 1 μg/ml and after 5 min, the excess dye was washed off with saline. The first step included the use of wide-field fluorescence microscopy of the surgical area. Authors used a customized operating microscope (Carl Zeiss Co., Ltd, Oberkochen, Germany) with a xenon lamp equipped with an excitation filter (450–490 nm) resulting in a blue excitation light and a long-pass filter (>520 nm) for detection of the green fluorescence emitted by the tumor. After staining, a more thorough curettage of the area was performed until the green glow disappeared. The next step included AO-PDT, a 10 min exposure of the resection cavity to unfiltered light from a xenon lamp with a brightness of 100,000 lx mounted on an operating microscope. After that, a layer of sutures was applied to the wound without rinsing the AO solution. The patient was then transferred to the radiotherapy room where an X-ray exposure was performed (5 Gy) (57).

Matsubara et al. reported long-term results of AO-based PD followed by PDT and RDT in 18 patients from 1996 to 2008, showing that the method allows preservation of more healthy tissue during resection (26, 44). This advantage helped to preserve functionality of the limbs due to more tailored resection compared to the standard wide margin resection method without significant differences in the recurrence rate.

Systemic AO Administration

There was only one study found on the AO-based RDT with systemic administration of AO which included treatment of 8 patients with end-stage cancers. In this study, two patients had sarcomas, two had pancreatic cancer, and one patient each had intrahepatic cholangiocarcinoma, renal, lung, and parotid cancer. (13). Two hours after 1 mg/kg AO was administered IV, the patients received 3–5 Gy X-ray irradiation 3 times within a 3 week period. In 3 out of 5 patients who completed the full course of the proposed therapy, tumors reduced in size and symptoms improved. Notably, this study demonstrated the absence of a toxic effect on the body with the introduction of therapeutic doses of the drug (13).

While some patients benefited in these small pilot studies, further clinical investigation is necessary to assess if the observed cytocidal effect could be achieved in other types of cancer. However, the absence of serious side effects of AO, coupled with the likely cytolytic effect of RDT, together with the radiation, opens up new horizons for exploring its potential in other cancers.

CONCLUSIONS AND FUTURE DIRECTIONS

The use of AO in oncology represents a novel approach but the number of studies is currently limited, likely due to the historical concerns about AO safety. More studies are necessary to identify tumor types and stages where application of AO can be useful to assess its clinical value and identify potential side effects.

There are several promising areas where AO may be beneficial. First, it is worth noting the possibility of macro and confocal fluorescence microscopy for *in vivo* fluorescence guidance during surgical resection. The effect of AO fluorescence guidance has not yet been studied in brain tumors and should be tested in comparison with other fluorescence guidance techniques such as 5-aminolevulinic acid, fluorescein sodium, and indocyanine green, which are already available and have a safety record and established efficacy.

Of particular interest is the effect of intravenously administered AO on tumor cells when exposed to small doses of radiation. If successful, this could dramatically change the approach for cancer treatment. AO-based RDT treatment of distant metastasis is another promising area of application (54). AO fluorescence guidance combined with PDT, SDT, or RDT can be potentially applied to all organs for the surgical treatment of tumor lesions, including brain tumor surgery. Brain gliomas are notorious for their infiltrative growth and thus the possibility of selective killing of any residual tumor cells after surgical resection is encouraging and compelling. However, there are also considerable limitations in that the blood-tumor-brain-barrier at the periphery of the gliomas might decrease efficacy of AO delivery, decreasing its photosensitizing effect (58). It should also be noted that AO is one among many drugs (including

5-ALA) that are in development for PDT, SDA, or RDT for the treatment of various cancers and their comparative efficacy for various cancers is yet to be established (59–63). Future drug developments include nanoparticles and targeted multipurpose theranostic drugs which can be used for intraoperative guidance and subsequent precision treatment of any microscopic residual tumor (36).

AO has demonstrated utility in multiple settings up to this point in time with the majority of applications being *ex vivo*. Although use of AO is not new with practical applications from urology, gynecology, to ophthalmology detailed, repurposing AO for possible specific tumor labeling in the field of neurosurgery has been minimally explored. While there is historical evidence of potentially detrimental health effects of AO dating back to the late 1960s, there is a small body of growing literature in the time since that points to its potential uses *in vivo* without toxic systemic effects. With the evidence presented in this review regarding the role of AO in tumor identification, we are especially interested with respect to brain lesions what AO can possibly provide in terms of specific fluorescent tumor labeling. More data is needed to determine the safety of AO *in vivo* and its future applications, particularly in neurosurgery.

AUTHOR CONTRIBUTIONS

VB, LB, NO, RP, SO, VS, MA, and AP researched the data, wrote the manuscript, generated the figures, provided participation in the discussion of the content, and revised the review.

ACKNOWLEDGMENTS

LB acknowledges scholarship support #SP-2545.2018.4.

SUPPLEMENTARY MATERIAL

The Supplementary Material for this article can be found online at: https://www.frontiersin.org/articles/10.3389/fonc.2019.00925/full#supplementary-material

REFERENCES

1. Kusuzaki K, Murata H, Matsubara T, Satonaka H, Wakabayashi T, Matsumine A, et al. Review. Acridine orange could be an innovative anticancer agent under photon energy. *In Vivo*. (2007) 21:205–14.
2. Sharma VK, Sahare PD, Rastogi RC, Ghoshal SK, Mohan D. Excited state characteristics of acridine dyes: acriflavine and acridine orange. *Spectrochim Acta A Mol Biomol Spectrosc*. (2003) 59:1799–804. doi: 10.1016/S1386-1425(02)00440-7
3. Browning CH, Cohen JB, Gaunt R, Gulbransen R. Relationships between antiseptic action and chemical constitution with special reference to compounds of the pyridine, quinoline, acridine and phenazine series. *Proc R Soc B*. (1922) 93:329–66. doi: 10.1098/rspb.1922.0025
4. Wainwright M. Acridine–a neglected antibacterial chromophore. *J Antimicrob Chemother*. (2001) 47:1–13. doi: 10.1093/jac/47.1.1
5. Kronvall G, Myhre E. Differential staining of bacteria in clinical specimens using acridine orange buffered at low pH. *Acta Pathol Microbiol Scand B*. (1977) 85:249–54. doi: 10.1111/j.1699-0463.1977.tb01970.x
6. Kusuzaki K, Matsubara T, Satonaka H, Matsumine A, Nakamura T, Sudo A, et al. Intraoperative Photodynamic Surgery (iPDS) with acridine orange for musculoskeletal sarcomas. *Cureus*. (2014) 6:e204. doi: 10.7759/cureus.204
7. Kusuzaki K, Murata H, Takeshita H, Hashiguchi S, Nozaki T, Emoto K, et al. Intracellular binding sites of acridine orange in living osteosarcoma cells. *Anticancer Res*. (2000) 20:971–5.
8. Amagasa J. Mechanisms of photodynamic inactivation of acridine orange-sensitized transfer RNA: participation of singlet oxygen and base damage leading to inactivation. *J Radiat Res*. (1986) 27:339–51. doi: 10.1269/jrr.27.339
9. Delic J, Coppey J, Magdelenat H, Coppey-Moisan M. Impossibility of acridine orange intercalation in nuclear DNA of the living cell. *Exp Cell Res*. (1991) 194:147–53. doi: 10.1016/0014-4827(91)90144-J
10. Plemel JR, Caprariello AV, Keough MB, Henry TJ, Tsutsui S, Chu TH, et al. Unique spectral signatures of the nucleic acid dye acridine orange can distinguish cell death by apoptosis and necroptosis. *J Cell Biol*. (2017) 216:1163–81. doi: 10.1083/jcb.201602028
11. Mares I, Drevo M, Adam E, Kubatova M, Casny J. Live measles vaccine from a further attenuated strain SEVAC. *Prog Immunobiol Stand*. (1967) 3:188–91.
12. Kusuzaki K, Hosogi S, Ashihara E, Matsubara T, Satonaka H, Nakamura T, et al. Translational research of photodynamic therapy with acridine orange which targets cancer acidity. *Curr Pharm Des*. (2012) 18:1414–20. doi: 10.2174/138161212799504812
13. Kusuzaki K, Takai T, Yoshimura H, Inoue K, Takai S, Baldini N. Clinical trial of radiotherapy after intravenous injection of acridine orange for patients with cancer. *Anticancer Res*. (2018) 38:481–9. doi: 10.21873/anticanres.12248
14. Van Duuren BL, Sivak A, Katz C, Melchionne S. Tumorigenicity of acridine orange. *Br J Cancer*. (1969) 23:587–90. doi: 10.1038/bjc.1969.72
15. International Agency for Research on Cancer. Acridine orange. In: *IARC Monographs on the Evaluation of Carcinogenic Risk of Chemicals to Man*. Vol. 16. Lyon: IARC Press (1978), 145–52.
16. Nakamura T, Kusuzaki K, Matsubara T, Matsumine A, Asanuma K, Satonaka H, et al. Determination of the LD50 of acridine orange via intravenous administration in mice in preparation for clinical application to cancer therapy. *In Vivo*. (2014) 28:523–7.
17. Tatsuta M, Iishi H, Yamamura H, Yamamoto R, Okuda S. Comparison of photodynamic inactivation of experimental stomach tumors sensitized by acridine orange or hematoporphyrin derivatives. *Oncology*. (1988) 45:35–40. doi: 10.1159/000226527
18. Tomsom SH. Tumor destruction due to acridine orange photoactivation by argon laser. *Ann N Y Acad Sci*. (1976) 267:191–200. doi: 10.1111/j.1749-6632.1976.tb41608.x
19. Udovich JA, Besselsen DG, Gmitro AF. Assessment of acridine orange and SYTO 16 for *in vivo* imaging of the peritoneal tissues in mice. *J Microsc*. (2009) 234:124–9. doi: 10.1111/j.1365-2818.2009.03153.x
20. Maruo T, Shibuya K, Takahashi M, Nakayama T, Fukunaga K, Orito K. Safety of acridine orange intravenous administration in dogs. *Int J Appl Res Vet Med*. (2012) 10:164–8.
21. Hori H, Teramoto Y, Fukuyama Y, Maruo T., Marginal resection and acridine orange photodynamic therapy in a cat with recurrent cutaneous malignant melanoma. *Int J Appl Res Vet Med*. (2014) 12:181–5.
22. Matsubara T, Kusuzaki K, Matsumine A, Nakamura T, Sudo A. Can a less radical surgery using photodynamic therapy with acridine orange be equal to a wide-margin resection? *Clin Orthop Relat Res*. (2013) 471:792–802. doi: 10.1007/s11999-012-2616-9
23. Nakamura T, Kusuzaki K, Matsubara T, Matsumine A, Murata H, Uchida A. A new limb salvage surgery in cases of high-grade soft tissue sarcoma using photodynamic surgery, followed by photo- and radiodynamic therapy with acridine orange. *J Surg Oncol*. (2008) 97:523–8. doi: 10.1002/jso.21025
24. Kusuzaki K, Murata H, Matsubara T, Miyazaki S, Shintani K, Seto M, et al. Clinical outcome of a novel photodynamic therapy technique using acridine orange for synovial sarcomas. *Photochem Photobiol*. (2005) 81:705–9. doi: 10.1562/2004-06-27-RA-218.1

25. Kusuzaki K, Murata H, Matsubara T, Miyazaki S, Okamura A, Seto M, et al. Clinical trial of photodynamic therapy using acridine orange with/without low dose radiation as new limb salvage modality in musculoskeletal sarcomas. *Anticancer Res*. (2005) 25:1225–35.
26. Matsubara T, Kusuzaki K, Matsumine A, Murata H, Nakamura T, Uchida A, et al. Clinical outcomes of minimally invasive surgery using acridine orange for musculoskeletal sarcomas around the forearm, compared with conventional limb salvage surgery after wide resection. *J Surg Oncol*. (2010) 102:271–5. doi: 10.1002/jso.21602
27. Sarnat HB, Curry B, Rewcastle NB, Trevenen CL. Gliosis and glioma distinguished by acridine orange. *Can J Neurol Sci*. (1987) 14:31–5. doi: 10.1017/S0317167100026135
28. Belykh E, Miller EJ, Hu D, Martirosyan NL, Woolf EC, Scheck AC, et al. Scanning fiber endoscope improves detection of 5-aminolevulinic acid-induced protoporphyrin IX fluorescence at the boundary of infiltrative glioma. *World Neurosurg*. (2018) 113:e51–69. doi: 10.1016/j.wneu.2018.01.151
29. Martirosyan NL, Georges J, Eschbacher JM, Belykh E, Carotenuto A, Spetzler RF, et al. Confocal scanning microscopy provides rapid, detailed intraoperative histological assessment of brain neoplasms: experience with 106 cases. *Clin Neurol Neurosurg*. (2018) 169:21–28. doi: 10.1016/j.clineuro.2018.03.015
30. Badir B, Knight B. Fluorescence microscopy in the detection of early myocardial infarction. *Forensic Sci Int*. (1987) 34:99–102. doi: 10.1016/0379-0738(87)90088-0
31. Tejada RI, Mitchell JC, Norman A, Marik JJ, Friedman S. A test for the practical evaluation of male fertility by acridine orange (AO) fluorescence. *Fertil Steril*. (1984) 42:87–91. doi: 10.1016/S0015-0282(16)47963-X
32. Krishnamurthy S, Cortes A, Lopez M, Wallace M, Sabir S, Shaw K, et al. *Ex vivo* confocal fluorescence microscopy for rapid evaluation of tissues in surgical pathology practice. *Arch Pathol Lab Med*. (2018) 142:396–401. doi: 10.5858/arpa.2017-0164-OA
33. Wang M, Kimbrell HZ, Sholl AB, Tulman DB, Elfer KN, Schlichenmeyer TC, et al. High-resolution rapid diagnostic imaging of whole prostate biopsies using video-rate fluorescence structured illumination microscopy. *Cancer Res*. (2015) 75:4032–41. doi: 10.1158/0008-5472.CAN-14-3806
34. Gareau D, Bar A, Snaveley N, Lee K, Chen N, Swanson N, et al. Tri-modal confocal mosaics detect residual invasive squamous cell carcinoma in Mohs surgical excisions. *J Biomed Opt*. (2012) 17:066018. doi: 10.1117/1.JBO.17.6.066018
35. Cahill LC, Giacomelli MG, Yoshitake T, Vardeh H, Faulkner-Jones BE, Connolly JL, et al. Rapid virtual hematoxylin and eosin histology of breast tissue specimens using a compact fluorescence nonlinear microscope. *Lab Invest*. (2018) 98:150–60. doi: 10.1038/labinvest.2017.116
36. Ni K, Lan G, Veroneau SS, Duan X, Song Y, Lin W. Nanoscale metal-organic frameworks for mitochondria-targeted radiotherapy-radiodynamic therapy. *Nat Commun*. (2018) 9:4321. doi: 10.1038/s41467-018-06655-7
37. Belykh E, Martirosyan NL, Yagmurlu K, Miller EJ, Eschbacher JM, Izadyyazdanabadi M, et al. Intraoperative fluorescence imaging for personalized brain tumor resection: current state and future directions. *Front Surg*. (2016) 3:55. doi: 10.3389/fsurg.2016.00055
38. Martirosyan NL, Georges J, Eschbacher JM, Cavalcanti DD, Elhadi AM, Abdelwahab MG, et al. Potential application of a handheld confocal endomicroscope imaging system using a variety of fluorophores in experimental gliomas and normal brain. *Neurosurg Focus*. (2014) 36:E16. doi: 10.3171/2013.11.FOCUS13486
39. Foersch S, Heimann A, Ayyad A, Spoden GA, Florin L, Mpoukouvalas K, et al. Confocal laser endomicroscopy for diagnosis and histomorphologic imaging of brain tumors *in vivo*. *PLoS ONE*. (2012) 7:e41760. doi: 10.1371/journal.pone.0041760
40. Risi MD, Rouse AR, Chambers SK, Hatch KD, Zheng W, Gmitro AF. Pilot clinical evaluation of a confocal microlaparoscope for ovarian cancer detection. *Int J Gynecol Cancer*. (2016) 26:248–54. doi: 10.1097/IGC.0000000000000595
41. Hammond DO. Fluorescence and acridine orange in the diagnosis of gynecologic neoplasia *in vivo*. *Am J Obstet Gynecol*. (1973) 115:272–3. doi: 10.1016/0002-9378(73)90299-8
42. Hoglund A, Joelsson I, Ingelman-Sundberg A, Odeblad E. Acridine orange in gynecologic cancer. I. The proton magnetic resonance spectrum of acridine orange zinc chloride. *Acta Obstet Gynecol Scand*. (1972) 51:309–13. doi: 10.3109/00016347209156864
43. Iessi E, Logozzi M, Lugini L, Azzarito T, Federici C, Spugnini EP, et al. Acridine orange/exosomes increase the delivery and the effectiveness of acridine orange in human melanoma cells: a new prototype for theranostics of tumors. *J Enzyme Inhib Med Chem*. (2017) 32:648–57. doi: 10.1080/14756366.2017.1292263
44. Matsubara T, Kusuzaki K, Matsumine A, Murata H, Marunaka Y, Hosogi S, et al. Photodynamic therapy with acridine orange in musculoskeletal sarcomas. *J Bone Joint Surg*. (2010) 92-B:760–2. doi: 10.1302/0301-620X.92B6.23788
45. Kusuzaki K, Aomori K, Suginoshita T, Minami G, Takeshita H, Murata H, et al. Total tumor cell elimination with minimum damage to normal tissues in musculoskeletal sarcomas following photodynamic therapy with acridine orange. *Oncology*. (2000) 59:174–80. doi: 10.1159/000012156
46. Jain M, Rajadhyaksha M, Nehal K. Implementation of fluorescence confocal mosaicking microscopy by "early adopter" Mohs surgeons and dermatologists: recent progress. *J Biomed Opt*. (2017) 22:24002. doi: 10.1117/1.JBO.22.2.024002
47. Iovieno A, Longo C, De Luca M, Piana S, Fontana L, Ragazzi M. Fluorescence confocal microscopy for *ex vivo* diagnosis of conjunctival tumors: a pilot study. *Am J Ophthalmol*. (2016) 168:207–16. doi: 10.1016/j.ajo.2016.06.001
48. Fotia C, Avnet S, Kusuzaki K, Roncuzzi L, Baldini N. Acridine orange is an effective anti-cancer drug that affects mitochondrial function in osteosarcoma cells. *Curr Pharm Des*. (2015) 21:4088–94. doi: 10.2174/1381612821666150918144953
49. Cline B, Delahunty I, Xie J. Nanoparticles to mediate X-ray-induced photodynamic therapy and Cherenkov radiation photodynamic therapy. *Wiley Interdiscip Rev Nanomed Nanobiotechnol*. (2018) 11:e1541. doi: 10.1002/wnan.1541
50. Suzuki N, Okada K, Chida S, Komori C, Shimada Y, Suzuki T. Antitumor effect of acridine orange under ultrasonic irradiation *in vitro*. *Anticancer Res*. (2007) 27:4179–84.
51. Wilson BC, Pogue BW. Optical and x-ray technology synergies enabling diagnostic and therapeutic applications in medicine. *J Biomed Optics*. (2018) 23:1. doi: 10.1117/1.JBO.23.12.121610
52. Hashiguchi S, Kusuzaki K, Murata H, Takeshita H, Hashiba M, Nishimura T, et al. Acridine orange excited by low-dose radiation has a strong cytocidal effect on mouse osteosarcoma. *Oncology*. (2002) 62:85–93. doi: 10.1159/000048251
53. Ishikawa S, Nemoto R, Kanoh S, Kobayashi K, Ishizaka S. Photodynamic inactivation of bladder cancer cells (MGH-U1) sensitized with acridine orange and irradiated by argon laser. *Tohoku J Exp Med*. (1984) 144:265–71. doi: 10.1620/tjem.144.265
54. Satonaka H, Kusuzaki K, Akeda K, Tsujii M, Iino T, Uemura T, et al. Acridine orange inhibits pulmonary metastasis of mouse osteosarcoma. *Anticancer Res*. (2011) 31:4163–8.
55. Matsubara T, Kusuzaki K, Matsumine A, Shintani K, Satonaka H, Uchida A. Acridine orange used for photodynamic therapy accumulates in malignant musculoskeletal tumors depending on pH gradient. *Anticancer Res*. (2006) 26:187–93.
56. Osman H, Elsahy D, Saadatzadeh MR, Pollok KE, Yocom S, Hattab EM, et al. Acridine orange as a novel photosensitizer for photodynamic therapy in glioblastoma. *World Neurosurg*. (2018) 114:e1310–5. doi: 10.1016/j.wneu.2018.03.207
57. Matsubara T, Kusuzaki K, Matsumine A, Murata H, Satonaka H, Shintani K, et al. A new therapeutic modality involving acridine orange excitation by photon energy used during reduction surgery for rhabdomyosarcomas. *Oncol Rep*. (2009) 21:89–94. doi: 10.3892/or_00000193
58. Randall EC, Emdal KB, Laramy JK, Kim M, Roos A, Calligaris D, et al. Integrated mapping of pharmacokinetics and pharmacodynamics in a patient-derived xenograft model of glioblastoma. *Nat Commun*. (2018) 9:4904. doi: 10.1038/s41467-018-07334-3
59. Costley D, Mc Ewan C, Fowley C, McHale AP, Atchison J, Nomikou N, et al. Treating cancer with sonodynamic therapy: a review. *Int J Hyperthermia*. (2015) 31:107–17. doi: 10.3109/02656736.2014.992484
60. Yoshida M, Kobayashi H, Terasaka S, Endo S, Yamaguchi S, Motegi H, et al. Sonodynamic therapy for malignant glioma using

220-kHz transcranial magnetic resonance imaging-guided focused ultrasound and 5-aminolevulinic acid. *Ultrasound Med Biol*. (2019) 45:526–38. doi: 10.1016/j.ultrasmedbio.2018.10.016

61. Suehiro S, Ohnishi T, Yamashita D, Kohno S, Inoue A, Nishikawa M, et al. Enhancement of antitumor activity by using 5-ALA-mediated sonodynamic therapy to induce apoptosis in malignant gliomas: significance of high-intensity focused ultrasound on 5-ALA-SDT in a mouse glioma model. *J Neurosurg*. (2018) 129:1416–28. doi: 10.3171/2017.6.JNS162398
62. Mahmoudi K, Garvey KL, Bouras A, Cramer G, Stepp H, Jesu Raj JG, et al. 5-aminolevulinic acid photodynamic therapy for the treatment of high-grade gliomas. *J Neurooncol*. (2019) 141:595–607. doi: 10.1007/s11060-019-03103-4
63. Takahashi J, Murakami M, Mori T, Iwahashi H. Verification of radiodynamic therapy by medical linear accelerator using a mouse melanoma tumor model. *Sci Rep*. (2018) 8:2728. doi: 10.1038/s41598-018-21152-z

Conflict of Interest Statement: The authors declare that the research was conducted in the absence of any commercial or financial relationships that could be construed as a potential conflict of interest.

frontiers in Surgery

TECHNOLOGY REPORT
published: 01 October 2019
doi: 10.3389/fsurg.2019.00056

Clinical Benefits of Combining Different Visualization Modalities in Neurosurgery

Karl-Michael Schebesch[1], Katharina Rosengarth[1], Alexander Brawanski[1], Martin Proescholdt[1], Christina Wendl[2], Julius Höhne[1], Christian Ott[1], Hans Lamecker[3] and Christian Doenitz[1]*

[1] Department of Neurosurgery, University Medical Center Regensburg, Regensburg, Germany, [2] Department of Radiology, University Medical Center Regensburg, Regensburg, Germany, [3] 1000shapes GmbH, Berlin, Germany

The prevailing philosophy in oncologic neurosurgery, has shifted from maximally invasive resection to the preservation of neurologic function. The foundation of safe surgery is the multifaceted visualization of the target region and the surrounding eloquent tissue. Recent advancements in pre-operative and intraoperative visualization modalities have changed the face of modern neurosurgery. Metabolic and functional data can be integrated into intraoperative guidance software, and fluorescent dyes under dedicated filters can potentially visualize patterns of blood flow and better define tumor borders or isolated tumor foci. High definition endoscopes enable the depiction of tiny vessels and tumor extension to the ventricles or skull base. Fluorescein sodium-based confocal endomicroscopy, which is under scientific evaluation, may further enhance the neurosurgical armamentarium. We aim to present our institutional workup of combining different neuroimaging modalities for surgical neuro-oncological procedures. This institutional algorithm (IA) was the basis of the recent publication by Haj et al. describing outcome and survival data of consecutive patients with high grade glioma (HGG) before and after the introduction of our Neuro-Oncology Center.

Keywords: fluorescence-guided surgery, fluorescein sodium, YELLOW 560 nm, KINEVO, tumor segmentation, confocal endomicroscopy, CONVIVO, brain tumors

OPEN ACCESS

Edited by:
Evgenii Belykh, Barrow Neurological Institute (BNI), United States

Reviewed by:
Xiaolei Chen, PLA General Hospital, China
Robert Thomas Wicks, Barrow Neurological Institute (BNI), United States

****Correspondence:***
Karl-Michael Schebesch
karl-michael.schebesch@ukr.de

Specialty section:
This article was submitted to Neurosurgery, a section of the journal Frontiers in Surgery

Received: *29 December 2018*
Accepted: *04 September 2019*
Published: *01 October 2019*

Citation:
Schebesch K-M, Rosengarth K, Brawanski A, Proescholdt M, Wendl C, Höhne J, Ott C, Lamecker H and Doenitz C (2019) Clinical Benefits of Combining Different Visualization Modalities in Neurosurgery. Front. Surg. 6:56. doi: 10.3389/fsurg.2019.00056

INTRODUCTION

Modern oncological neurosurgery is marked by the consensus that all surgical interventions should aim to attain complete tumor resection without affecting neurological function. This dogma was finally agreed upon because low tumor burden and good neurological function has been repeatedly shown to form the basis of any successful adjuvant treatment modality and to result in prolonged progression-free and overall survival, whilst preserving good quality of life (1–3).

The combination of different imaging modalities for pre-operative planning and intraoperative guidance should always aim at clearly identifying the targeted tumor that can be extremely heterogeneous. Currently, the integration of various functional imaging data, such as functional magnetic resonance imaging (fMRI), into neuronavigation allows for increased safety when approaching vulnerable, eloquent structures. Fluorescence-guidance can further support the neurosurgeon's eye and experience in visualizing the tumor mass, scattered tumor spots, infiltrated zones and rims, and patterns of blood flow, and can ultimately confirm a tumor-free cavity (4, 5).

However, in the daily routine of a neuro-oncology center (NOC), it is always mandatory to obtain and employ the desired imaging modality in a cost-effective, fast, and uncomplicated manner. Patients must be protected from redundant assessments, and, above all, "technical overkill" in the operating theater must be avoided. Furthermore, critical self-reflection and monocentric or multicenter complication analyses should be consistently generated and published to properly outline advantages and disadvantages, as well as clinical benefits and limitations of the institutional algorithm (IA). This approach is the only way that the most important factors, namely the surgical skills and experiences of neurosurgeons, are effectively supported by innovative technical adjuncts.

In 2017, we published our outcome and survival data of consecutive patients with high grade glioma since the introduction of a certified NOC in 2009. Since 2009, all patients with HGG at our department have been treated according to our IA. The current investigation has shown clear benefits in neurological outcome, progression-free survival, and overall survival in comparison to the equivalent data collected before 2009 (6).

The impact of the NOC organization in terms of improving survival in patients with glioblastoma has been described previously (6), but the detailed description of the workflow and institutional algorithm have yet to be reported. Therefore, the aim of this paper is to present our approach of combining different visualization modalities that are pre- and post-operatively employed not solely for the intraoperative depiction of the targeted area, but also for advanced pre-operative unmasking of the tumor structure, invasiveness, environment, and adherences. This combination enables sophisticated planning of the surgical approach including positioning, craniotomy, and dissection. We strongly believe that the interaction of a visual armamentarium provides neurosurgeons with more sensitivity and purposefulness, especially in complex neuro-oncologic procedures.

RESULTS

When a new patient with a suspected brain tumor is referred to our center, structural MRI is usually initially completed (see **Table 1**). Tumors without Gadolinium enhancement are further analyzed with FET-PET, which influences the choice of intraoperative fluorescent dyes. Proximity of the tumor to eloquent areas results in a functional workup (fMRI and Diffusion Tensor Imaging, DTI). All imaging data are then pre-processed and segmented to provide the essential information of each imaging modality. The final therapeutic decision is made after 3D-visualization and demonstration of the case, followed by stereotactic biopsy, open biopsy/partial resection, or gross tumor removal. The choice of fluorescent dye depends on the level of gadolinium enhancement and the FET-PET result (see **Table 2**).

The following features of the IA (**Table 2**) were selected because of their fundamental scientific interest:

TABLE 1 | Overview of our institutional imaging workup for common intracranial lesions: magnetic resonance imaging (MRI) protocol for patients with intracranial tumors include T1 spin echo and T2 turbo spin echo sequences with 1 mm and isotropic 3D sequences (1 mm) including T1 w/gadolinium contrast (3D multiplane reformation, MPR), T2 (3D sampling perfection with application optimized contrast using different flip angle evolution, SPACE), 3D fluid attenuation inversion recovery, FLAIR, and constructive interference in steady-state (CISS MRI).

Suspected diagnosis	Low grade glioma	High grade glioma/ metastasis	Vascular lesions (aneurysms/ AVM)	Skull base tumor
MRI	SE T1 w/o CM, SE T2, 3D MPR w/contrast, 3D T2, 3D FLAIR	SE T1 w/o CM, T2, 3D MPR w/contrast, 3D T2, 3D FLAIR	SE T1 w/o CM, SE T2, 3D MPR w/contrast, 3D TOF, TWIST	SE T1 w/o CM, SE T2, 3D MPR w/contrast, 3D TOF, T2* CISS
CT thin-sliced skull base (1 mm)	*✓		✓	✓
FET-PET	✓	*✓		
fMRI, rsfMRI	✓	✓	*✓	
DTI	✓	✓	*✓	
CFD simulation			*✓	

*✓ mandatory, *✓ optional.*

3D time-of-flight (TOF) and time-resolved angiography with interleaved stochastic trajectories (TWIST) sequences are obtained in vascularized tumors. Positron emission tomography (PET) with O-(2-[^{18}F]fluoroethyl)-L-tyrosine ([^{18}F]FET) (FET-PET) is used for non-contrast enhancing and recurrent contrast-enhancing gliomas. Functional MRI (fMRI) and resting state (rs) fMRI are conducted for visualizing functional areas.

Pre-operative Workup–Completion of Structural and Metabolic Neuroimaging

When a new patient with a suspicious cranial lesion is referred to our center, neuroimaging is quickly completed according to our institutional imaging requirements (see **Table 1**) that include magnetic resonance imaging plus isotropic 3D sequences, computed tomography (CT), or 18F-fluorethyl tyrosine (FET)-/18F-fluordesoxyglucose (FDG)-positron emission tomography (PET). According to the recommendations of our daily case conference, patients are evaluated neuro-psychologically and consecutively undergo functional MRI and diffusion tensor imaging (DTI).

In 2018, we published a small series of patients with glioma that had not shown any contrast enhancement in the MRI, yet presented with distinct metabolic activity in the FET-PET (7). These patients had been suitable for fluorescence-guided surgery with Fluorescein Sodium (FL) under the YELLOW 560 nm filter (Carl Zeiss Meditec, Oberkochen, Germany). A possible correlation between FET-PET active tumors and fluorescent staining was assumed, facilitating surgical performance. Our results supported the data by Rapp et al. and Pirotte et al. who had outlined the diagnostic value of FET-PET for diagnosing hot spots inside gliomas. Clearly, FET-PET increases intraoperative diagnostic accuracy and helps to establish the most exact histopathological diagnosis (8, 9).

TABLE 2 | Institutional algorithm (IA).

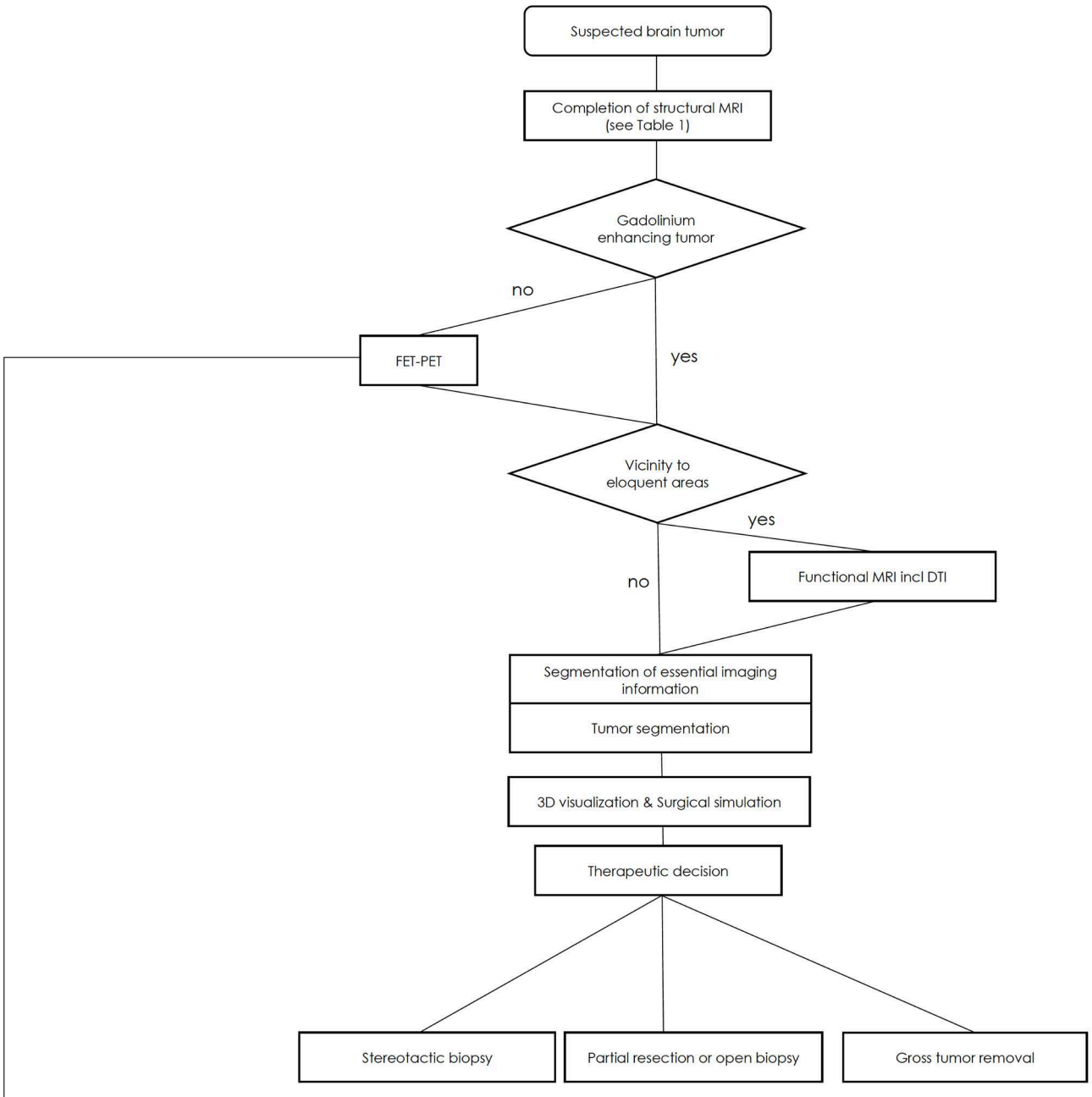

Gadolinium enhancing tumor	FL optional	FL and/or 5-ALA
FET-PET positive tumor	FL optional	FL
FET-PET negative tumor	None	None
Neuronavigation		✓
Confocal endomicroendoscopy		optional
Ultrasound		optional
Awake surgery with direct cortical stimulation		optional
Intraoperative Monitoring		optional

Pre-operative Workup–fMRI and DTI

The aim of pre-surgical functional imaging is to maximize the resection of lesions (tumors or metastases) as well as to minimize post-operative functional deficits. Both factors increase post-operative health-related quality of life (10) and are prognostic factors for successive interventions involving radiation- and/or chemotherapy (11, 12). In our center, pre-surgical functional imaging is conducted with fMRI and resting state functional (rsf) MRI for the functional localization of cortical gray matter; diffusion-weighted imaging is used to determine subcortical white matter tracts. fMRI is exclusively carried out with 3-Tesla Siemens MRI scanners. Protocols

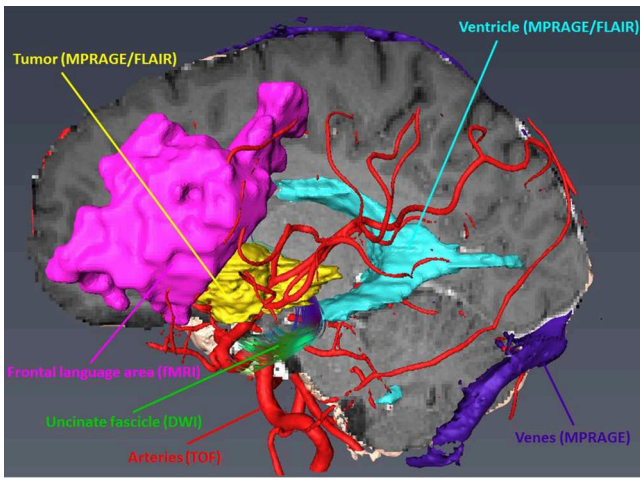

FIGURE 1 | Integration and three-dimensional display of different structural and functional modalities in AMRIA. The original imaging modality used for visualization is annotated in brackets.

for mapping the sensorimotor homunculus, language location and lateralization, and memory or retinotopic organization of the visual cortex depend on the localization of the lesion. Non-compliant or severely disabled patients may undergo rsfMRI that is also used in the case of patients with language barriers or in very young patients, awake patients with their eyes open, or in narcotized patients. fMRI data are analyzed with (S)tatistical(P)arametric(M)apping12 (www.fil.ion.ucl.ac.uk/spm/software/spm12/) including the LI-toolbox (13) and rsfMRI data with in-house generated Matlab scripts including parts of DPARSF and the GIFT-toolbox (http://mialab.mrn.org/software/gift/). According to fiber tracking, diffusion-weighted images (DWI) are acquired by means of 3T and 1.5T MRI scanners, either with 30 directions and 3 mm isotropic resolution or 64 directions with 2 mm isotropic resolution depending on the disease and patient characteristics. The following fiber tracking modeling can be done either deterministically with AMIRA (FEI Visualization Sciences, France) or probabilistically by using a modified FSL pipeline [employing Bayesian Estimation of Diffusion Parameters Obtained using Sampling Technique (BEDPOSTX)]. Fiber tracking is conducted in advance, when mainly pyramidal tracts, arcuate fascicles, uncinated fascicles, and optic tracts are shown. All functional results (fMRI, rsfMRI, and DTI) can be integrated into AMIRA (FEI Visualization Sciences, France) (see **Figure 1**).

Pre-operative Workup–Tumor Segmentation

Automatic pre-operative brain tumor segmentation is a powerful tool for surgical planning that allows the extraction of tumor characteristics (contrast-enhancing and non-contrast-enhancing compartments, edema, and necrosis) from surrounding healthy brain tissue by means of a set of MR modalities (T1 with and without contrast agent, T2, and FLAIR) (14). Such information may be very useful for guiding surgical interventions by defining the extent of resection or the area of resection. There are a number of segmentation and tumor detection algorithms, ranging from classification or clustering approaches to deep learning algorithms (15, 16). In our department, we have established a tumor segmentation pipeline based on ANSTsR [advanced normalization tools (ANTs) and the R statistical project] using random forest-derived probabilities to determine different tumor tissues (17) (see **Figure 2**).

Pre-operative Workup—3D Visualization and Surgical Simulation

Pre-operatively, a special simulation software is employed that condenses the essential information of the different imaging modalities in a 3D-viewer. This software enables the surgeon to pre-operatively envision the operative field as realistically as possible, simulating elements such as patient and head positioning in a virtual clamp, craniotomy, and corticotomy in a virtual OR setting. This software has been developed and modified by our department according to the specific needs of neurosurgeons.

Every pre-operative imaging modality provides unique information to characterize the lesion and its surroundings. For the sake of visual clarity, it is essential to condense and organize the extensive amount of anatomical and functional data. For this reason, we developed an advanced visualization software tool called NeuroVis, aimed at improving the understanding of anatomical and functional relations for pre-operative planning and intraoperative guidance in a virtual reality setting.

The essential information of every image modality is segmented and co-registered with the 3D MPR image stack by means of a semi-automated workflow with AMIRA. Segmented data are then visualized with our browser- based rendering 3D viewer NeuroVis (developed at our institute in collaboration with 1000shapes GmbH, Berlin). This tool enables neurosurgeons to plan individually tailored treatment strategies. Planning steps include skin incision, craniotomy, and intraoperative positioning of the patient and the head clamp in a realistic operative setting. We have also established an interface to a virtual reality setting using UNITY (Unity Tec., USA) and a head-mounted display (HTC, Taiwan). These tools help to pre-operatively envision the operative field as realistically as possible (see **Figure 3**). The prepared plan can also be transferred to a navigation system using the stl format for intraoperative use.

Intraoperative Workup–FET-PET Positive Non-enhancing Tumors and Fluorescence

The question of how to achieve the most effective tumor reduction without affecting relevant motor, language, and visual tracts continues to be highly controversial, particularly in non-contrast enhancing gliomas in eloquent regions of the brain. Besides the integration of functional data into neuro-navigation and conducting surgery in an awake setting, fluorescent visualization of the tumor may significantly increase the quality of resection and speed up surgery. Our recently published

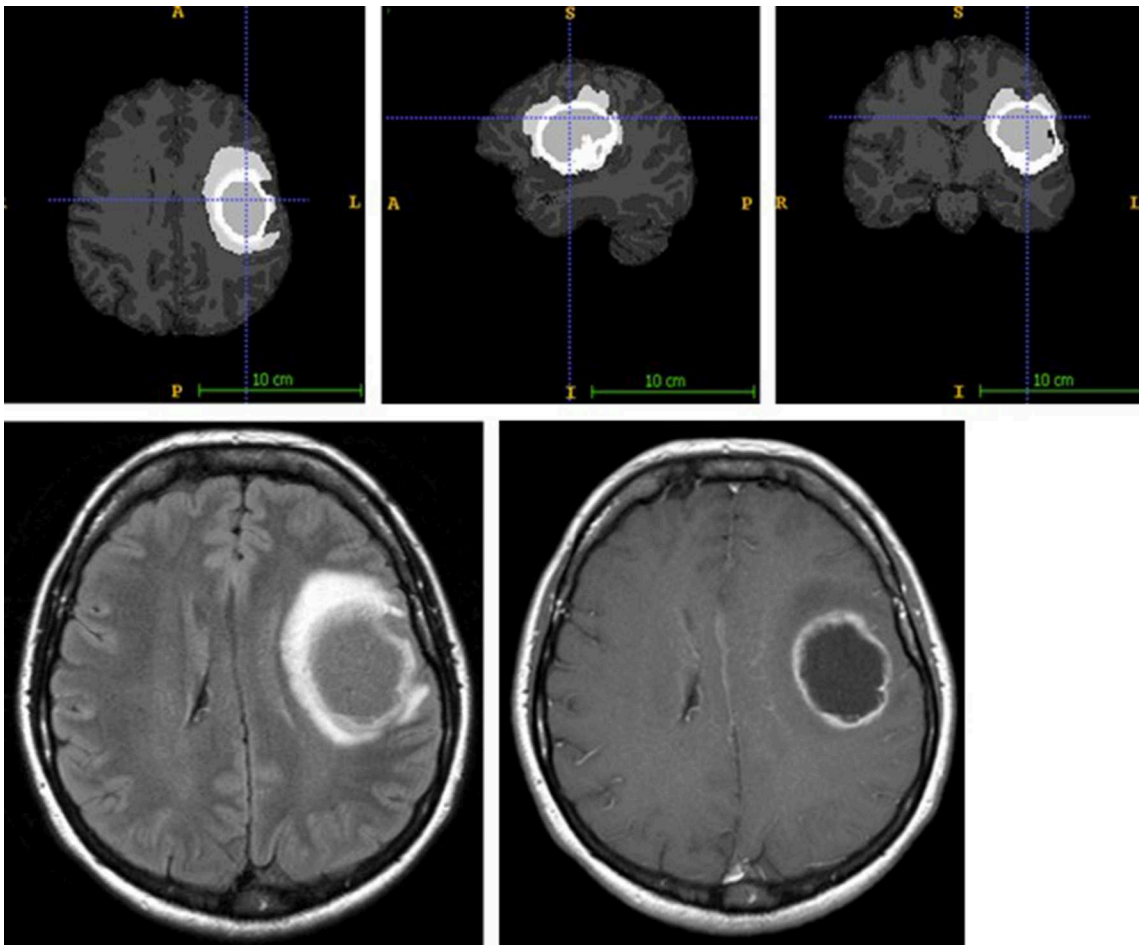

FIGURE 2 | ANTsR tumor segmentation result of glioblastoma, showing labels for contrast-enhancing tumor (very light gray), necrosis (dark gray), edema (light gray) (upper row; contrast non-enhancing tumor label is not depicted), and the corresponding FLAIR (lower row left) and T1 with contrast agency (lower row right) MR image.

experience in patients with non-enhancing gliomas with distinct metabolic activity in FET-PET and clear intraoperative fluorescent staining (7), in addition to the report by Bowden et al. (18), supports the potential supplementary role of FL in cases of low or intermediate grade glioma with high metabolic activity.

Intraoperative Workup–Fluorescein-Enhanced Confocal Endomicroscopy

Because of its unspecific accumulation in areas of disrupted blood-brain barrier (BBB), FL can be applied widely irrespective of the tumor histology in HGG (19–22), cerebral metastases (23, 24), lymphomas (25, 26), meningiomas (27), neuromas (28), and brain abscesses (29) for guiding microsurgical resection under the dedicated light filter. Furthermore, FL-based confocal endomicroscopy can be employed *in vivo* to obtain multiple digital biopsies to visualize the tissue texture, enabling distinct histological evaluation by a (remote) neuropathologist (4, 30–33). This approach circumvents having to wait for the frozen section, enabling the surgeon to rapidly identify the histological origin of the lesion and delineate the tumor border much more precisely. However, since this technique is still under scientific evaluation, clinical data are required to outline the potential significance of this approach (30).

Decision Making

This evaluation and the information provided by our neuropsychologist determine whether surgery is planned in an awake setting or under sedation. Neuro-navigation integrating all neuroimaging devices (fMRI, CT, and PET) is clinically routine.

Prior to surgery, we decide on the intraoperative visualization tools to be used, depending on the suspected etiology of the tumor, the anatomical localization, the expansion into eloquent areas and fiber tracts, and subject to the surgical approach. With the exception of intraoperative magnetic resonance imaging (iMRI), our neurosurgical department comprises all conventional technical adjuncts and personal competences of a tertiary academic neurosurgical center: (a) Fluorescence with dedicated light filters: fluorescein sodium (FL, YELLOW

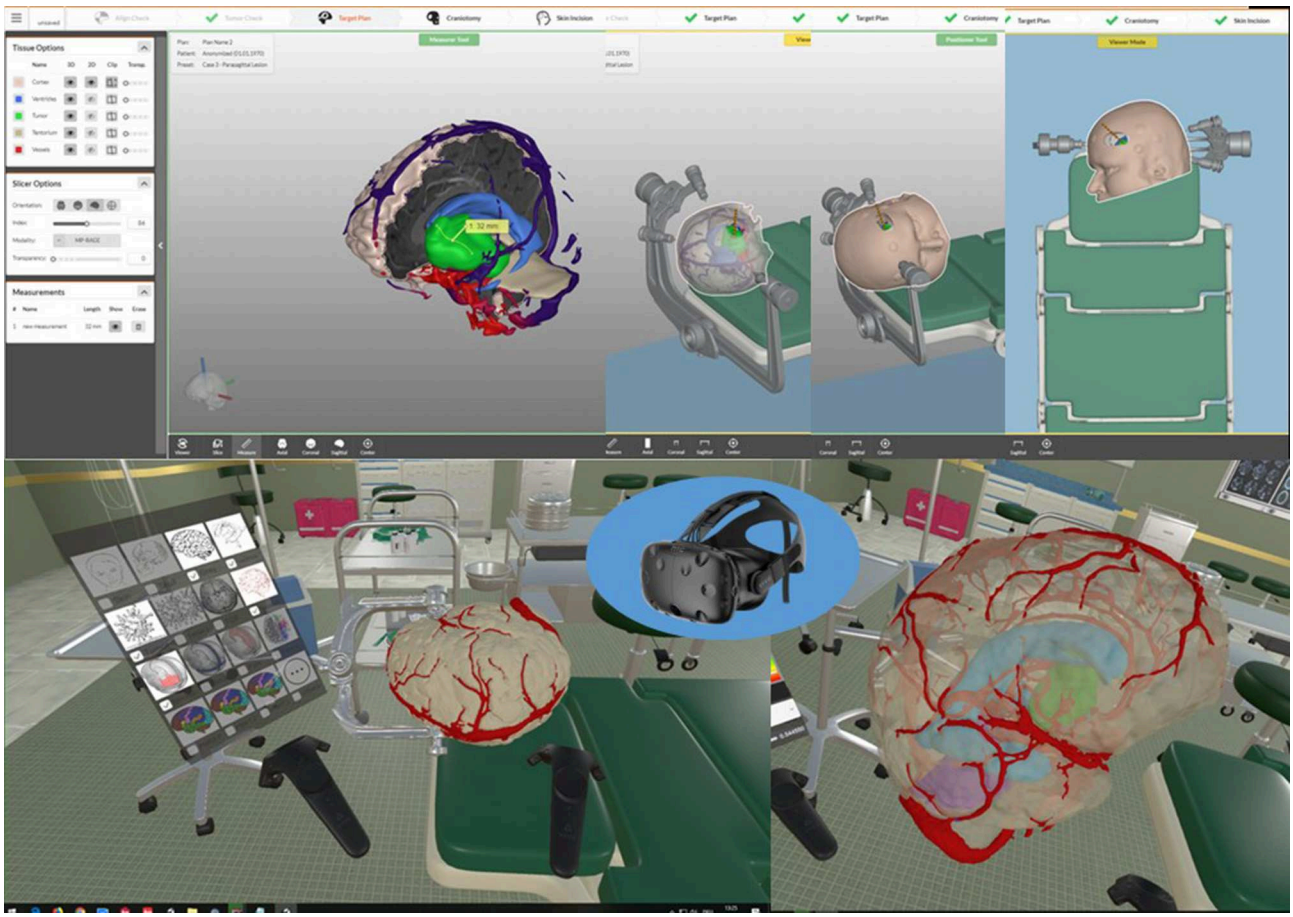

FIGURE 3 | Pre-operative visualization with NeuroVis 3D (upper row) and in a virtual reality setting (lower row) using a head-mounted display.

560 nm filter), 5-aminolevulinic acid (5-ALA, BLUE 400 nm filter), and indocyanine green (ICG, FLOW 800 module); (b) Neuronavigation, ultrasound; (c) Intraoperative monitoring (IOM); (d) Endoscopy; and (e) Confocal endomicroscopy (still under scientific evaluation).

Illustrative Cases

Case #1

This case describes our approach to the treatment of a remotely recurrent, eloquently located, contrast-enhancing astrocytoma WHO III of a 51-year-old female patient. The pre-operative neuroimage-workup consisted of conventional MRI (T1-weighted, axial sequence, **Figure 4**), FET-PET (displayed in navigational software, axial sequence, **Figure 5**), and neuro-navigation with integrated fMRI, DTI, and FET-PET (**Figure 6**). The patient was surgically treated in an awake-awake setting under fluorescence-guidance with FL (5 mg/kg) and the YELLOW 560 nm filter (**Figure 7**), and the removed tumor was examined *ex vivo* with the confocal endomicroscope (**Figure 8**). Early post-operative contrast-enhanced MRI showed complete removal of the contrast-enhanced lesion that was histologically confirmed as astrocytoma WHO III.

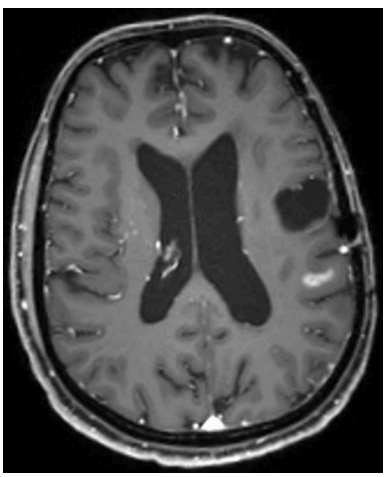

FIGURE 4 | Pre-operative MR image (T1-weighted sequence, axial plane) showing new contrast-enhancement distant to the former resection cavity.

This case was selected because the pre-operative neuroimage-workup distinctively supported the indication for surgery. The FET-PET result ruled out pseudo-progression or

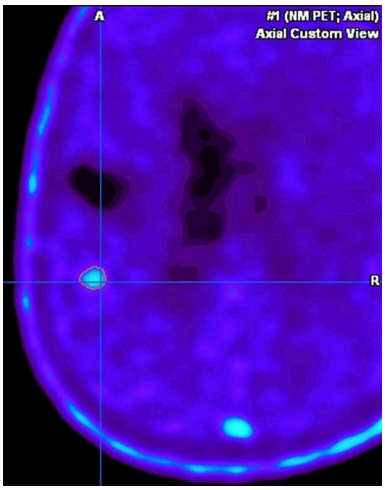

FIGURE 5 | Pre-operative FET-PET image, displayed in the navigational software, showing strong metabolic activity in the suspicious area.

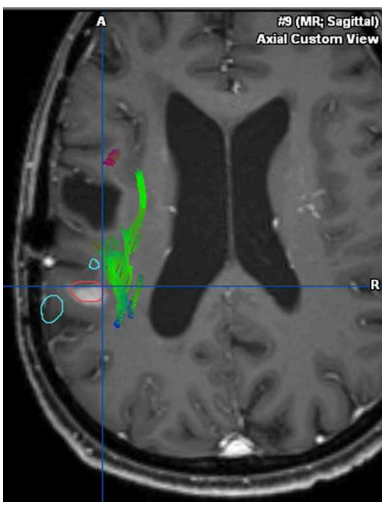

FIGURE 6 | Integration of fMRI, DTI, and FET-PET (in red) into the navigational software, unmasking the proximity to eloquent area (arcuate fasciculus in green, language-associated activation in cyan).

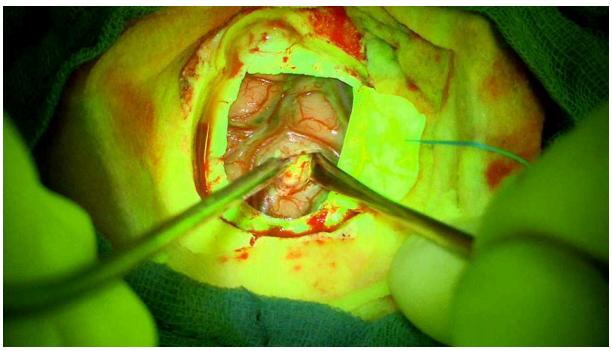

FIGURE 7 | Strong fluorescent staining of the tumor under the YELLOW 560 filter.

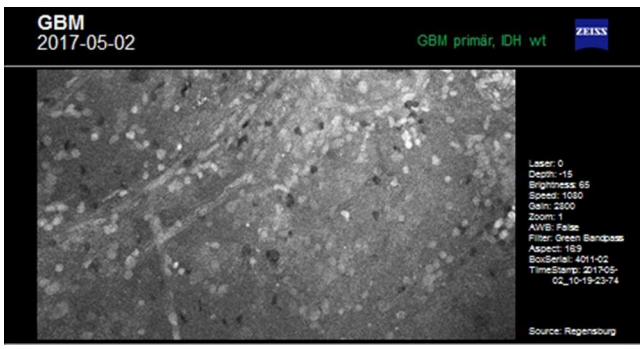

FIGURE 8 | *Ex vivo* examination of tumorous tissue with the confocal endomicroscope.

post-radiation necrosis because of the detected strong metabolic activity that could be matched to the suspicious contrast enhancement in the pre-operative MRI. The functional area was displayed by means of fMRI and DTI, clearly showing proximity but no infiltration to language-associated activation. Finally, fluorescence-guided technique with FL impressively visualized the tumor *in vivo* and *ex vivo*. Taken together, the included imaging modalities resulted in complete removal of the tumor without any functional deterioration.

Case #2

The 65-year-old female patient had a focal seizure with paresthesia of the left upper limb and the face. Initial MRI showed a contrast-enhancing lesion in the left pre- and post-central area, distant to the midline (**Figure 9**). The patient additionally received motor fMRI and DTI of the pyramidal tract that was reconstructed in 3D, including the vasculature (**Figure 10**). Consequently, we indicated awake surgery because of the proximity to the hand and upper limb area. The patient underwent awake craniotomy under fluorescence-guidance with very intensive fluorescence staining (**Figure 11**). The tumor was completely removed, and no new neurological deficits developed. Early post-operative MRI confirmed gross-total resection of the lesion (**Figure 12**), and histology showed glioblastoma WHO IV. According to our institutional algorithm, the patient did not require a PET scan because of the intense contrast-enhancement in the initial MRI; thus, we decided on administering FL (5 mg/kg) and conducting awake surgery because navigational imaging was intraoperatively equipped with functional data (**Figure 13**).

Case #3

This complex case of faintly contrast-enhancing, secondary malignantly transformed oligodendroglioma WHO III, that had been initially diagnosed as astrocytoma WHO II 11 years ago, was additionally chosen to illustrate our workflow. The

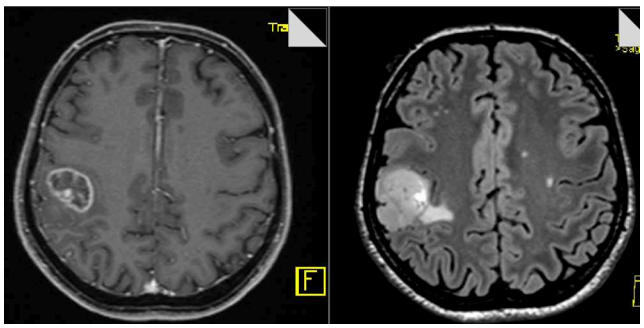

FIGURE 9 | Pre-operative MR image (T1-weighted and FLAIR sequences, axial planes) showing circular contrast-enhancement and moderate edema.

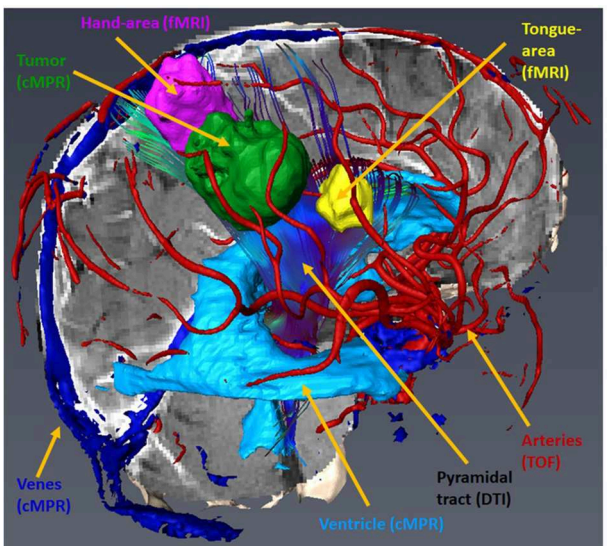

FIGURE 10 | Sagittal view of the Amira 3D-reconstruction of the cortex, the vessels, the ventricle, the tumor (green), the hand motor associations areas (magenta), the tongue motor association area (yellow), and the pyramidal tract.

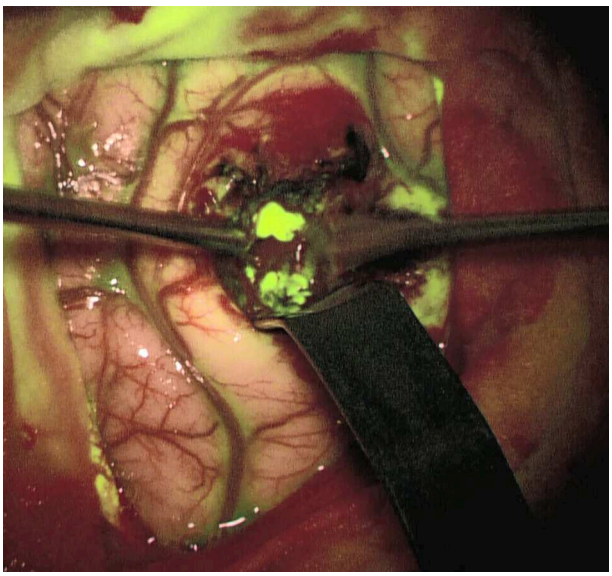

FIGURE 11 | Strong fluorescent staining of the tumor under the YELLOW 560 filter.

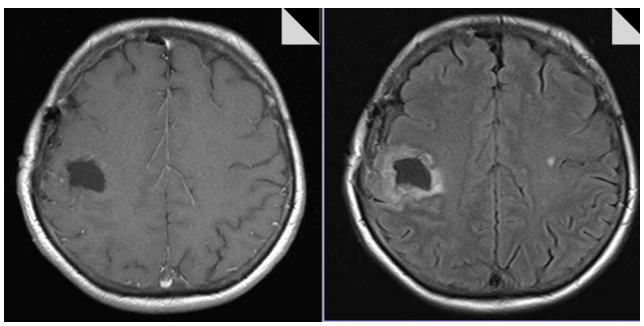

FIGURE 12 | Post-operative MR image (T1-weighted and FLAIR sequences, axial planes) confirming complete removal of the tumor.

tumor—pre-treated with surgery, radiation, and chemotherapy—had recurred, showing marginal contrast-enhancement in the T1-weighted sequence in conventional MRI (**Figure 14**). Consequently, FET-PET was conducted that also showed only marginal metabolic activity (**Figure 15**). However, because of the recent tumor progress and the near-eloquent localization of the tumor in the left frontal cortex, we recommended fMRI followed by subsequent awake craniotomy. Intraoperatively, all imaging modalities were displayed on the navigational screen (**Figure 16**), and we used fluorescence-guidance with FL (5 mg/kg) and ultrasound. Weak but still usable fluorescence was detected, allowing for complete tumor removal based on the early post-operative MRI (**Figure 17**). The neuropathological workup showed anaplastic oligodendroglioma WHO III.

Here, all possible functional and metabolic imaging modalities were included pre- and intraoperatively. Fluorescence-guidance was helpful in this patient, although the initial MRI had only indicated moderate blood brain barrier disruption and the initial PET only demonstrated weak activity.

DISCUSSION

For selected patients with a brain tumor, a detailed, sophisticated workup of different neuroimaging modalities can be of the utmost importance for the pre-operative evaluation and/or simulation of the neurosurgical approach, and for choosing the technique of dissection and removal. This way, the highest possible degree of removal of neoplastic tissue can be attempted with a significant simultaneous increase in safety. Despite pre-operative metabolic and functional visualization of the targeted area by means of PET and fMRI/rsfMRI/DTI and distinctively integrated neuro-navigation, fluorescence-guided surgery with either FL, 5-ALA, or ICG plays a key role in the majority of operations. With this technique,

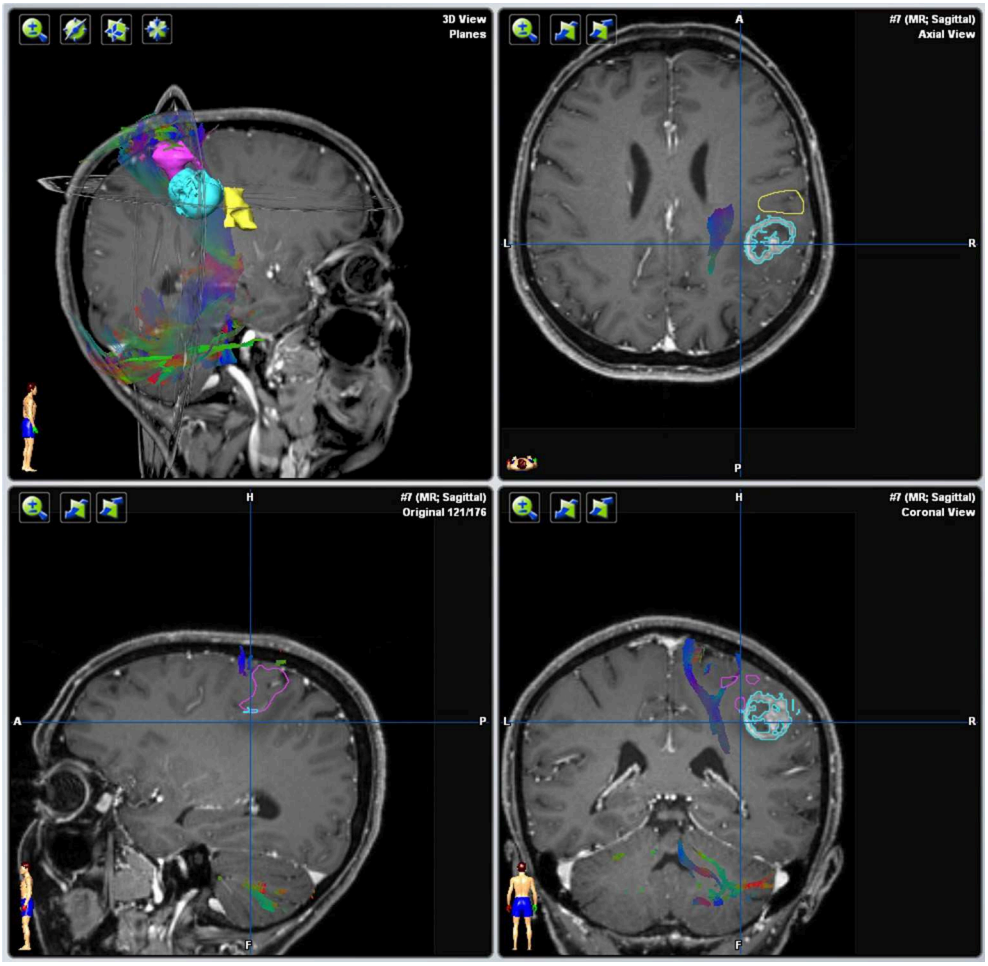

FIGURE 13 | Implementation of fMRI and DTI in the neuro-navigation system [brain tumor (light blue); tumor segmentation based on the 3d cMPR-image, the hand motor association areas (magenta), the tongue motor association area (yellow), and the pyramidal tract (darker blue)].

areas of interest are visualized in real time and according to their specific properties (tumor metabolism with 5-ALA, disrupted BBB with FL, patterns of blood flow with ICG and FL). FL-based confocal endomicroscopy, which is still under scientific evaluation, can further enhance intraoperative accuracy and efficacy.

The discussed imaging modalities, however, should not be arbitrarily applied in every patient with a brain tumor, because such application would counteract the value of an individually tailored combination of these modalities. In most neurosurgical departments, this type of imaging workup is only possible with a high standard of economic and personal competence, and in the case of well-established interdisciplinary collaboration with the departments of neuroradiology, neurology, oncology, nuclear medicine, and neuropathology. Based on this cooperation, the combination of different imaging modalities carries a huge benefit for patients in terms of preserving neurological function while creating the best possible foundation for any type of adjuvant treatment (6).

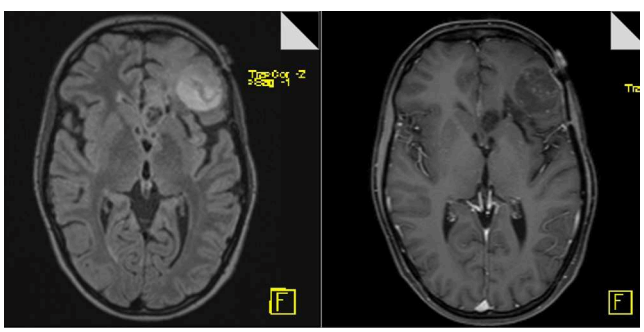

FIGURE 14 | Pre-operative MR image (T1-weighted and FLAIR sequences, axial planes) showing weak contrast-enhancement and marginal edema.

However, some limitations should be clearly stated. Like any academic institution, we can only offer the technical modalities available. For example, there is no

intraoperative MRI to be integrated into our IA. Furthermore, some inter-observer bias cannot be excluded, especially in the interpretation of weak or flaw fluorescence in non-contrast enhancing gliomas. Additionally, the use of fluorescence-guided confocal endomicroscopy is still under scientific evaluation.

Our IA was established 10 years ago and has been adapted according to contemporary scientific perceptions, such as

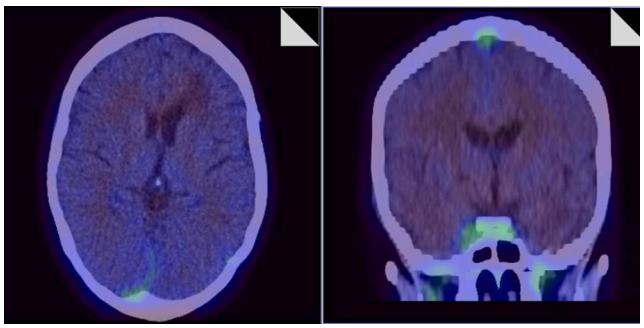

FIGURE 15 | Pre-operative FET-PET showing almost absence of metabolic activity.

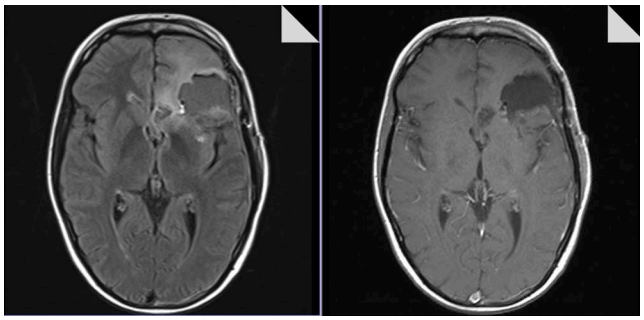

FIGURE 17 | Post-operative MR image (T1-weighted and FLAIR sequences, axial planes) confirming complete removal of the tumor.

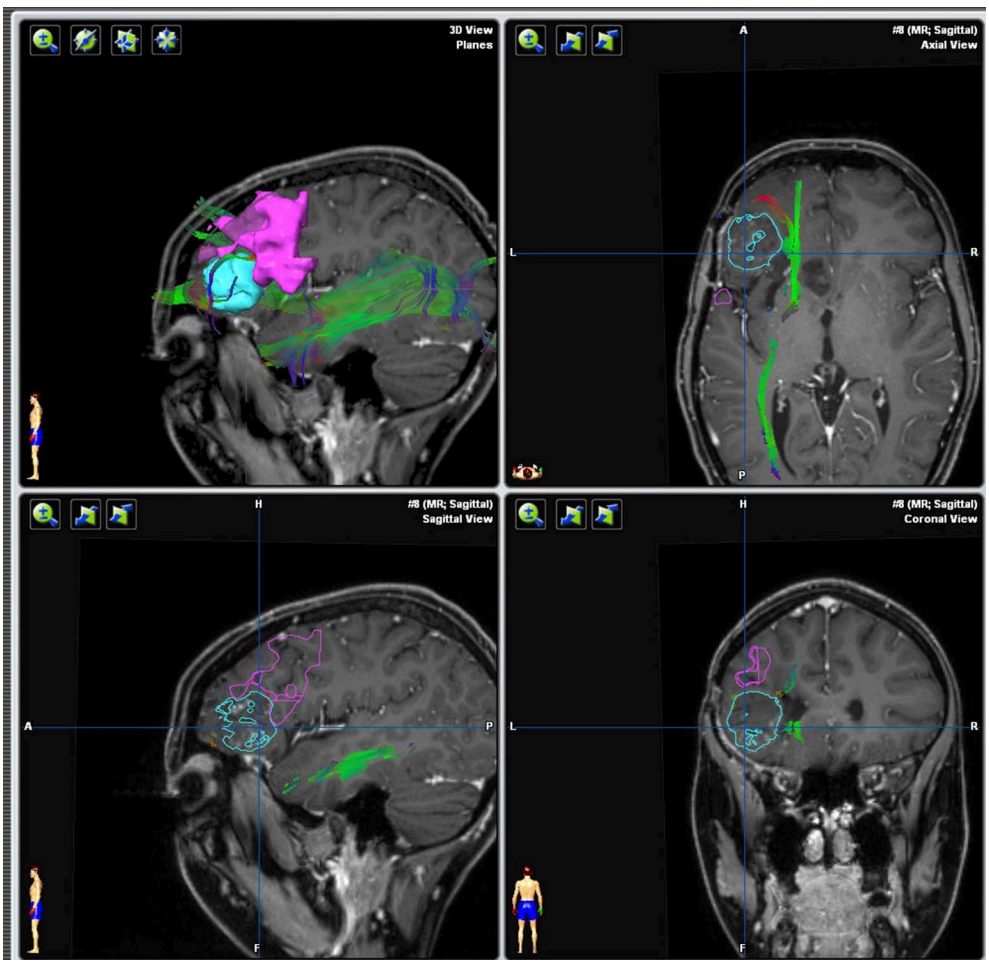

FIGURE 16 | Implementation of fMRI and DTI in the neuro-navigation system [brain tumor (light blue); tumor segmentation based on a FLAIR 3dspace image (not shown), inferior frontal language association area (magenta) and ventral language pathway including uncinate fascicle, extreme capsule, inferior longitudinal fascicle and inferior front-occipital fascicle (green)].

fluorescence-guided surgery and the integration of FET-PET and functional data. In 2017, we published our institutional series before and after the introduction of our IA that was established simultaneously with the opening of the certified neuro-oncologic center in 2009. This analysis confirms that the implementation of the IA has not only greatly contributed to the significantly prolonged PFS and OS, but has also clearly increased the rate of gross-total resections of HGG (6). The IA has been broadly accepted across the disciplines involved in the NOC and serves as the centerpiece of our weekly neuro-oncologic tumor board.

AUTHOR CONTRIBUTIONS

All authors listed have made a substantial, direct and intellectual contribution to the work, and approved it for publication.

FUNDING

Pre-operative simulation research was granted by the German Federal Ministry for Economic Affairs and Energy (Grant number ZF4045803 TS5).

REFERENCES

1. Fujii Y, Muragaki Y, Maruyama T, Nitta M, Saito T, Ikuta S, et al. Threshold of the extent of resection for WHO Grade III gliomas: retrospective volumetric analysis of 122 cases using intraoperative MRI. *J Neurosurg*. (2018) 129:1–9. doi: 10.3171/2017.3.JNS162383
2. Li YM, Suki D, Hess K, Sawaya R. The influence of maximum safe resection of glioblastoma on survival in 1229 patients: can we do better than gross-total resection? *J Neurosurg*. (2016) 124:977–88. doi: 10.3171/2015.5.JNS142087
3. Sanai N, Polley MY, McDermott MW, Parsa AT, Berger MS. An extent of resection threshold for newly diagnosed glioblastomas. *J Neurosurg*. (2011) 115:3–8. doi: 10.3171/2011.2.JNS10998
4. Belykh E, Martirosyan NL, Yagmurlu K, Miller EJ, Eschbacher JM, Izadyyazdanabadi M, et al. Intraoperative fluorescence imaging for personalized brain tumor resection: current state and future directions. *Front Surg*. (2016) 3:55. doi: 10.3389/fsurg.2016.00055
5. Valdes PA, Roberts DW, Lu FK, Golby A. Optical technologies for intraoperative neurosurgical guidance. *Neurosurg Focus*. (2016) 40:E8. doi: 10.3171/2015.12.FOCUS15550
6. Haj A, Doenitz C, Schebesch KM, Ehrensberger D, Hau P, Putnik K, et al. Extent of resection in newly diagnosed glioblastoma: impact of a specialized neuro-oncology care center. *Brain Sci*. (2017) 8:E5. doi: 10.3390/brainsci8010005
7. Schebesch KM, Brawanski A, Doenitz C, Rosengarth K, Proescholdt M, Riemenschneider MJ, et al. Fluorescence-guidance in non-Gadolinium enhancing, but FET-PET positive gliomas. *Clin Neurol Neurosurg*. (2018) 172:177–82. doi: 10.1016/j.clineuro.2018.07.011
8. Pirotte B, Goldman S, Massager N, David P, Wikler D, Vandesteene A, et al. Comparison of 18F-FDG and 11C-methionine for PET-guided stereotactic brain biopsy of gliomas. *J Nucl Med*. (2004) 45:1293–8.
9. Rapp M, Heinzel A, Galldiks N, Stoffels G, Felsberg J, Ewelt C, et al. Diagnostic performance of 18F-FET PET in newly diagnosed cerebral lesions suggestive of glioma. *J Nucl Med*. (2013) 54:229–35. doi: 10.2967/jnumed.112.109603
10. Duffau H, Mandonnet E. The "onco-functional balance" in surgery for diffuse low-grade glioma: integrating the extent of resection with quality of life. *Acta Neurochir*. (2013) 155:951–7. doi: 10.1007/s00701-013-1653-9
11. Sanai N, Berger MS. Extent of resection influences outcomes for patients with gliomas. *Rev Neurol*. (2011) 167:648–54. doi: 10.1016/j.neurol.2011.07.004
12. Stummer W, Kamp MA. The importance of surgical resection in malignant glioma. *Curr Opin Neurol*. (2009) 22:645–9. doi: 10.1097/WCO.0b013e3283320165
13. Wilke M, Lidzba K. LI-tool: a new toolbox to assess lateralization in functional MR-data. *J Neurosci Methods*. (2007) 163:128–36. doi: 10.1016/j.jneumeth.2007.01.026
14. Gordillo N, Montseny E, Sobrevilla P. State of the art survey on MRI brain tumor segmentation. *Magn Reson Imaging*. (2013) 31:1426–38. doi: 10.1016/j.mri.2013.05.002
15. Akkus Z, Galimzianova A, Hoogi A, Rubin DL, Erickson BJ. Deep learning for brain MRI segmentation: state of the art and future directions. *J Digit Imaging*. (2017) 30:449–59. doi: 10.1007/s10278-017-9983-4
16. Bauer S, Wiest R, Nolte LP, Reyes M. A survey of MRI-based medical image analysis for brain tumor studies. *Phys Med Biol*. (2013) 58:R97–129. doi: 10.1088/0031-9155/58/13/R97
17. Tustison NJ, Shrinidhi KL, Wintermark M, Durst CR, Kandel BM, Gee JC, et al. Optimal symmetric multimodal templates and concatenated random forests for supervised brain tumor segmentation (simplified) with ANTsR. *Neuroinformatics*. (2015) 13:209–25. doi: 10.1007/s12021-014-9245-2
18. Bowden SG, Neira JA, Gill BJA, Ung TH, Englander ZK, Zanazzi G, et al. Sodium fluorescein facilitates guided sampling of diagnostic tumor tissue in nonenhancing gliomas. *Neurosurgery*. (2018) 82:719–27. doi: 10.1093/neuros/nyx271
19. Acerbi F, Broggi M, Schebesch KM, Höhne J, Cavallo C, De Laurentis C, et al. Fluorescein-guided surgery for resection of high-grade gliomas: a multicentric prospective phase II study (FLUOGLIO). *Clin Cancer Res*. (2018) 24:52–61. doi: 10.1158/1078-0432.CCR-17-1184
20. Catapano G, Sgulo FG, Seneca V, Lepore G, Columbano L, di Nuzzo G. Fluorescein-guided surgery for high-grade glioma resection: an intraoperative "contrast-enhancer". *World Neurosurg*. (2017) 104:239–47. doi: 10.1016/j.wneu.2017.05.022
21. Hamamcioglu MK, Akcakaya MO, Goker B, Kasimcan MO, Kiris T. The use of the YELLOW 560 nm surgical microscope filter for sodium fluorescein-guided resection of brain tumors: our preliminary results in a series of 28 patients. *Clin Neurol Neurosurg*. (2016) 143:39–45. doi: 10.1016/j.clineuro.2016.02.006
22. Schebesch KM, Proescholdt M, Hohne J, Hohenberger C, Hansen E, Riemenschneider MJ, et al. Sodium fluorescein-guided resection under the YELLOW 560 nm surgical microscope filter in malignant brain tumor surgery–a feasibility study. *Acta Neurochir*. (2013) 155:693–9. doi: 10.1007/s00701-013-1643-y
23. Höhne J, Hohenberger C, Proescholdt M, Riemenschneider MJ, Wendl C, Brawanski A, et al. Fluorescein sodium-guided resection of cerebral metastases-an update. *Acta Neurochir*. (2017) 159:363–7. doi: 10.1007/s00701-016-3054-3
24. Xiao SY, Zhang J, Zhu ZQ, Li YP, Zhong WY, Chen JB, et al. Application of fluorescein sodium in breast cancer brain-metastasis surgery. *Cancer Manag Res*. (2018) 10:4325–31. doi: 10.2147/CMAR.S176504
25. Lin FH, Zhang XH, Zhang J, He ZQ, Duan H, Ke C, et al. Fluorescein sodium-guided biopsy or resection in primary central nervous system lymphomas with contrast-enhancing lesion in MRI. *J Neurooncol*. (2018) 139:757–65. doi: 10.1007/s11060-018-2924-3
26. Schebesch KM, Hoehne J, Hohenberger C, Acerbi F, Broggi M, Proescholdt M, et al. Fluorescein sodium-guided surgery in cerebral lymphoma. *Clin Neurol Neurosurg*. (2015) 139:125–8. doi: 10.1016/j.clineuro.2015.09.015
27. Akcakaya MO, Goker B, Kasimcan MO, Hamamcioglu MK, Kiris T. Use of sodium fluorescein in meningioma surgery performed under the YELLOW-560 nm surgical microscope filter: feasibility and preliminary results. *World Neurosurg*. (2017) 107:966–73. doi: 10.1016/j.wneu.2017.07.103
28. da Silva CE, da Silva JL, da Silva VD. Use of sodium fluorescein in skull base tumors. *Surg Neurol Int*. (2010) 1:70. doi: 10.4103/2152-7806.72247

29. Hohne J, Brawanski A, Schebesch KM. Fluorescence-guided surgery of brain abscesses. *Clin Neurol Neurosurg*. (2017) 155:36–9. doi: 10.1016/j.clineuro.2017.02.014
30. Belykh E, Cavallo C, Gandhi S, Zhao X, Veljanoski D, Izady Yazdanabadi M, et al. Utilization of intraoperative confocal laser endomicroscopy in brain tumor surgery. *J Neurosurg Sci*. (2018) 62:704–17. doi: 10.23736/S0390-5616.18.04553-8
31. Izadyyazdanabadi M, Belykh E, Mooney MA, Eschbacher JM, Nakaji P, Yang Y, et al. Prospects for theranostics in neurosurgical imaging: empowering confocal laser endomicroscopy diagnostics via deep learning. *Front Oncol*. (2018) 8:240. doi: 10.3389/fonc.2018.00240
32. Martirosyan NL, Eschbacher JM, Kalani MY, Turner JD, Belykh E, Spetzler RF, et al. Prospective evaluation of the utility of intraoperative confocal laser endomicroscopy in patients with brain neoplasms using fluorescein sodium: experience with 74 cases. *Neurosurg Focus*. (2016) 40:E11. doi: 10.3171/2016.1.FOCUS15559
33. Martirosyan NL, Georges J, Kalani MY, Nakaji P, Spetzler RF, Feuerstein BG, et al. Handheld confocal laser endomicroscopic imaging utilizing tumor-specific fluorescent labeling to identify experimental glioma cells *in vivo*. *Surg Neurol Int*. (2016) 7:S995–1003. doi: 10.4103/2152-7806.195577

Conflict of Interest Statement: HL was employed by the company 1000shapes GmbH, Berlin, Germany. K-MS, JH, and AB received travel funds and honoraria from Carl Zeiss Meditec, Germany.

The remaining authors declare that the research was conducted in the absence of any commercial or financial relationships that could be construed as a potential conflict of interest.

frontiers in Oncology

MINI REVIEW
published: 02 October 2019
doi: 10.3389/fonc.2019.00947

Current Trends for Improving Safety of Stereotactic Brain Biopsies: Advanced Optical Methods for Vessel Avoidance and Tumor Detection

Serik K. Akshulakov[1], *Talgat T. Kerimbayev*[1], *Michael Y. Biryuchkov*[2], *Yermek A. Urunbayev*[1], *Dara S. Farhadi*[3] *and Vadim A. Byvaltsev*[1,4]*

[1] Department of Neurosurgery, JSC "National Center for Neurosurgery", Nur-Sultan, Kazakhstan, [2] Department of Neurosurgery and Traumatology, West Kazakhstan Marat Ospanov State Medical University, Aktobe, Kazakhstan, [3] University of Arizona College of Medicine, Phoenix, AZ, United States, [4] Department of Neurosurgery and Innovative Medicine, Irkutsk State Medical University, Irkutsk, Russia

OPEN ACCESS

Edited by:
Mark Preul,
Barrow Neurological Institute (BNI),
United States

Reviewed by:
Seyedmehdi Payabvash,
School of Medicine, Yale University,
United States
Arvind P. Pathak,
School of Medicine, Johns Hopkins
University, United States

***Correspondence:**
Vadim A. Byvaltsev
email@uni.edu;
byval75vadim@yandex.ru

Specialty section:
This article was submitted to
Cancer Imaging and Image-directed
Interventions,
a section of the journal
Frontiers in Oncology

Received: 02 April 2019
Accepted: 09 September 2019
Published: 02 October 2019

Citation:
Akshulakov SK, Kerimbayev TT,
Biryuchkov MY, Urunbayev YA,
Farhadi DS and Byvaltsev VA (2019)
Current Trends for Improving Safety of
Stereotactic Brain Biopsies: Advanced
Optical Methods for Vessel Avoidance
and Tumor Detection.
Front. Oncol. 9:947.
doi: 10.3389/fonc.2019.00947

Stereotactic brain needle biopsies are indicated for deep-seated or multiple brain lesions and for patients with poor prognosis in whom the risks of resection outweigh the potential outcome benefits. The main goal of such procedures is not to improve the resection extent but to safely acquire viable tissue representative of the lesion for further comprehensive histological, immunohistochemical, and molecular analyses. Herein, we review advanced optical techniques for improvement of safety and efficacy of stereotactic needle biopsy procedures. These technologies are aimed at three main areas of improvement: (1) avoidance of vessel injury, (2) guidance for biopsy acquisition of the viable diagnostic tissue, and (3) methods for rapid intraoperative assessment of stereotactic biopsy specimens. The recent technological developments in stereotactic biopsy probe design include the incorporation of fluorescence imaging, spectroscopy, and label-free imaging techniques. The future advancements of stereotactic biopsy procedures in neuro-oncology include the incorporation of optical probes for real-time vessel detection along and around the biopsy needle trajectory and *in vivo* confirmation of the diagnostic tumor tissue prior to sample acquisition.

Keywords: fluorescence, 5-aminolevulinic acid, stereotactic, spectroscopy, optical, biopsy, fluorescein sodium

INTRODUCTION

Brain needle biopsies are indicated for deep-seated or multiple brain lesions and for patients with poor prognosis in whom the risks of resection outweigh the potential outcome benefits. A recent systematic review and evidence-based clinical practice guideline investigating the role of stereotactic brain biopsy for low-grade gliomas provided level III evidence in support of brain biopsies and recommended that surgeons consider using advanced imaging techniques to improve diagnostic accuracy (1). In suspected low-grade tumors that are not considered for resection, biopsy location should be planned based on molecular guidance techniques, such as positron emission tomography, magnetic resonance (MR) spectroscopy, or others in order to provide a reliable molecular diagnosis (2).

The current standard-of-care method for stereotactic brain needle biopsy involves a 1.6- to 2-mm-diameter needle cannula insertion through a cranial burr-hole aligned to a predetermined trajectory. The two cannulas have overlapping side windows. When the desired position is reached, these windows are aligned, and brain tissue is lodged into cannula using suction and cut by sliding the inner cannula.

Despite the minimally invasive nature of the needle brain biopsy, the limitations and risks are still present and include the following:

1. Non-diagnostic biopsy yield. The frequency of non-diagnostic biopsies ranges in various studies
   - Not-specified non-diagnostic biopsy rate—5.2% (3), 9% (4), 10.7% (5), 13% (6);
   - Biopsy performed without intraoperative frozen section—11%;
   - Biopsy performed with frozen section on demand—1% (7);
2. Technical failure rate is 2.4–3.7% (7)
3. Complications rate:
   - Overall complications rate—1.2% (3), 7.36% (4);
   - Perioperative—6.3–4.8% (7);
   - Postoperative—10.5–4.8% (7);
   - Hemorrhagic/vessel injury complications: 2.1% (6), 3% (7), 4.35% (4), overall 8.8%, including 1% symptomatic, or >1 cm (8). One study reported the overall rate of hemorrhages on postoperative computerized tomography (CT) as 59.8%, including 41.1% of bleeds <5 mm in diameter and 8.9% of bleeds 3–4 cm in diameter (9).
4. Mortality rate was 0.6% (3), 1.34% (4), and 0.6–3.7% (7) in various studies.

Vessel injury is one of the most feared complications during minimally invasive stereotactic procedures. The rounded tip design of the biopsy needle intends to push aside any vessel encountered along the biopsy needle trajectory. However, such a design does not completely eliminate the potential for vessel injury during the forward movement of the needle. Moreover, the risk of vessel injury is believed to be higher during the side-cutting movement during biopsy acquisition. Therefore, apart from techniques for navigation on the anatomical level, like MR spectroscopy (10, 11), perfusion (12), and metabolism (13), improvements of intraoperative tools for biopsy acquisition and rapid assessment would be beneficial.

This paper aims to provide a concise review of novel fluorescence-based and other optical techniques for improvement of safety and efficacy of minimally invasive stereotactic needle biopsy procedures in neuro-oncology. The main goal of such procedures is not to improve the resection extent but to safely acquire viable tissue representative of the lesion for further comprehensive histological, immunohistochemical, and molecular analyses. Here, we do omit discussion of MR, computed tomography, and ultrasound Doppler (14, 15)-based navigation techniques. Although the potential value of these techniques is undeniable, we focus this review on recently proposed optical methods. The basics of optical techniques are found in recently published reviews of this subject that describe the basics of fluorescence guidance in neuro-oncology (16–21).

Abbreviations: PpIX, protoporphyrin IX; ICG, indocyanine green.

METHODS

We performed a literature search in the PubMed database using the terms "biopsy," "stereotactic," "fluorescence," "Raman," "spectroscopy," "brain," "optical," and "optical probe" in various combinations. Our search included papers published up to November 2018. We did not set a lower bound for this search. The titles were scanned and relevant articles were selected for full-text review, resulting in relevant articles for analysis as presented in the **Supplementary Data 1**. Additional articles were added from reference lists if deemed relevant. After reviewing the articles, the three key areas for analysis and discussion were selected: (1) avoidance of vessel injury during stereotactic biopsies, (2) probe-based guidance methods for biopsy acquisition, and (3) methods for rapid intraoperative assessment of stereotactic biopsy specimens. The latter two areas were united in one section for discussion due to the similarity in the used optical principles toward the common goal for differentiation of tumor and normal tissues, which can be done *in vivo* (using the miniaturized probes) or *ex vivo* after the biopsy has been acquired (using either miniaturized or benchtop systems).

RESULTS AND DISCUSSION

Avoidance of Vessel Injury During Stereotactic Biopsy (Table 1)

Intravascular Contrast Detection

Göbel et al. described a small contact forward-viewing endoscopic probe that can fit into a standard biopsy needle and visualize fluorescence signals of protoporphyrin IX (PpIX) and indocyanine green (ICG) (**Figure 1A**) (22). PpIX is a fluorophore (excitation maximum wavelength is 405 nm; emission maximum, 630 nm) commonly used as the basis of fluorescent-guided neuro-oncology (31), while ICG is a near-infrared fluorophore (excitation maximum wavelength is 780–800 nm; emission maximum, 830 nm) commonly used for vascular flow visualization (32). The multifiber probe includes two excitation diode lasers (405 and 785 nm for PpIX autofluorescence and ICG, respectively) and a charge-coupled device camera for signal detection. This endoscope allowed ICG detection through the brain tissue (about 1 mm thickness) on a phantom model. It also showed reliable detection of a red PpIX fluorescence from the tumor in a mouse glioma model. Subsequently, in a pilot clinical trial ($n = 1$), this needle endoscope was used instead of the standard brain biopsy needle mandarin to visualize fluorescence during probe advancement. The actual biopsy acquisition was performed with a small forward biting biopsy forceps. Although bright

TABLE 1 | Techniques for vessel detection during stereotactic brain biopsies.

Author, year	Technique	Clinical data	Main findings	Limitations	Safety
FLUORESCENT CONTRAST DETECTION					
Göbel et al. (22)	1.5-mm-diameter multifiber forward-viewing needle endoscope for dual fluorescence (PpIX, ICG) and autofluorescence imaging. Results in multicolor images.	Pilot clinical trial ($n = 1$) showed feasibility of autofluorescence and PpIX visualization; however, safety, and vessel detection were not evaluated.	Established feasibility on phantom and characterized detection capability of the vessels, normal brain, and viable tumor tissue.	Forward-viewing probe.	Light power was 10 mW.
Rühm et al. (23)	Fiber-based ICG detection in the vessels for stereotactic procedures.	No. Only computer simulation model.	Established safety corridor for excitation light power to prevent normal brain destruction.	Simulation computer model experiment.	Established light intensity safety corridor for ICG.
STAIN-LESS REFLECTANCE IMAGING APPROACHES					
Pichette et al. (24) Goyette et al. (25)	24-fiber, 1.7-mm-diameter probe for interstitial sub-diffuse optical tomography. Technology is based on the spectroscopic detection of hemoglobin remittance and sub-diffused light spectra. Creates a 2D map visualizing potential locations of vessels and their proximity to the probe's tip.	No. Only preclinical study on phantom models.	Established feasibility and characterized detection capability of the vessels of various locations and sizes.	Extravascular blood could affect interpretation of the data. Complex probe design.	N/R.
Markwardt et al. (26)	Double fiber-based probe inserted in biopsy needle for hemoglobin remission spectrometry. Allows detection of proximity and size of blood vessels.	No. Only preclinical study on phantom models.	Established feasibility and characterized detection capability of the vessels of various locations and sizes.	Extravascular blood could affect interpretation of the data.	Light power intensity below MPE for the skin of 2 kW/m^2.
Ramakonar et al. (27)	Side-viewing fiber OCT probe fitting the standard brain biopsy needle with automatic vessel detection on B-imaging mode.	Pilot clinical trial ($n = 11$) demonstrated feasibility of automatic vessel detection.	Established feasibility and characterized detection capability of the vessels.	No forward viewing.	N/R, although considered safe based on the patient data.
LASER DOPPLER FLOWMETRY					
Haj-Hosseini et al. (28)	9-fiber, forward-viewing probe fitting the biopsy needle for simultaneous laser Doppler flowmetry and PpIX fluorescence spectral detection.	Similar probes for laser Doppler flowmetry imaging have been studied in stereotactic procedures under IRB approval in previous studies (29, 30).	Established feasibility and characterized brain perfusion along the biopsy needle trajectory.	No side viewing.	Light power 10 mW for PpIX excitation.

ICG, indocyanine green; N/R, not reported; PpIX, protoporphyrin IX; ICG, indocyanine green; OCT, optical coherence tomography; MPE, maximal permissible exposure.

PpIX fluorescence from the viable tumor core was visible, no fluorescence in the surrounding needle positions was evident. For vessel visualization, a 200 mg/kg dose of ICG was used in the mouse model. With this, near-infrared ICG fluorescence appeared inside the blood vessels at an excitation of 785 nm (**Figure 1A**, top panel). With autofluorescence at 405-nm excitation, the vessels appear clearer and darker (**Figure 1A**, middle panel). With a combination of autofluorescence and ICG visualization simultaneously, the vessels also display clear visualization (**Figure 1A**, bottom panel). Vessel visualization in a human tissue was not performed.

Ruhm et al. investigated forward-viewing microfiber probe for ICG detection using a computer simulation of ICG fluorescence excited and detected through the same fiber-optic system in homogeneous human brain tissue (23). Although detection of intravascular ICG is widely used in open vascular neurosurgery (33), its application for detection of deep vessels might not be optimal due to the fast redistribution and ICG fluorescence decay. Leakage of blood or trace amounts of blood containing ICG in the vicinity of the probe would result in false-positive measurements. Furthermore, the dosage and timing of ICG administration would need to be optimized, and the necessity for additional drug injection should be considered, especially when comparing to other methods for vessel detection.

Laser Doppler Flowmetry

Another recently reported tool is a 2.2-mm-diameter forward-viewing needle probe that combines fluorescence spectral detection and laser Doppler flowmetry (28). The probe was designed to fit the Leksell® Stereotactic System. By measuring the frequency shift in the 780-nm backscattered laser light caused by the cell movements in the capillaries, the device assesses brain perfusion and blood flow. The pilot study on three patients demonstrated reliable detection of PpIX spectra (405

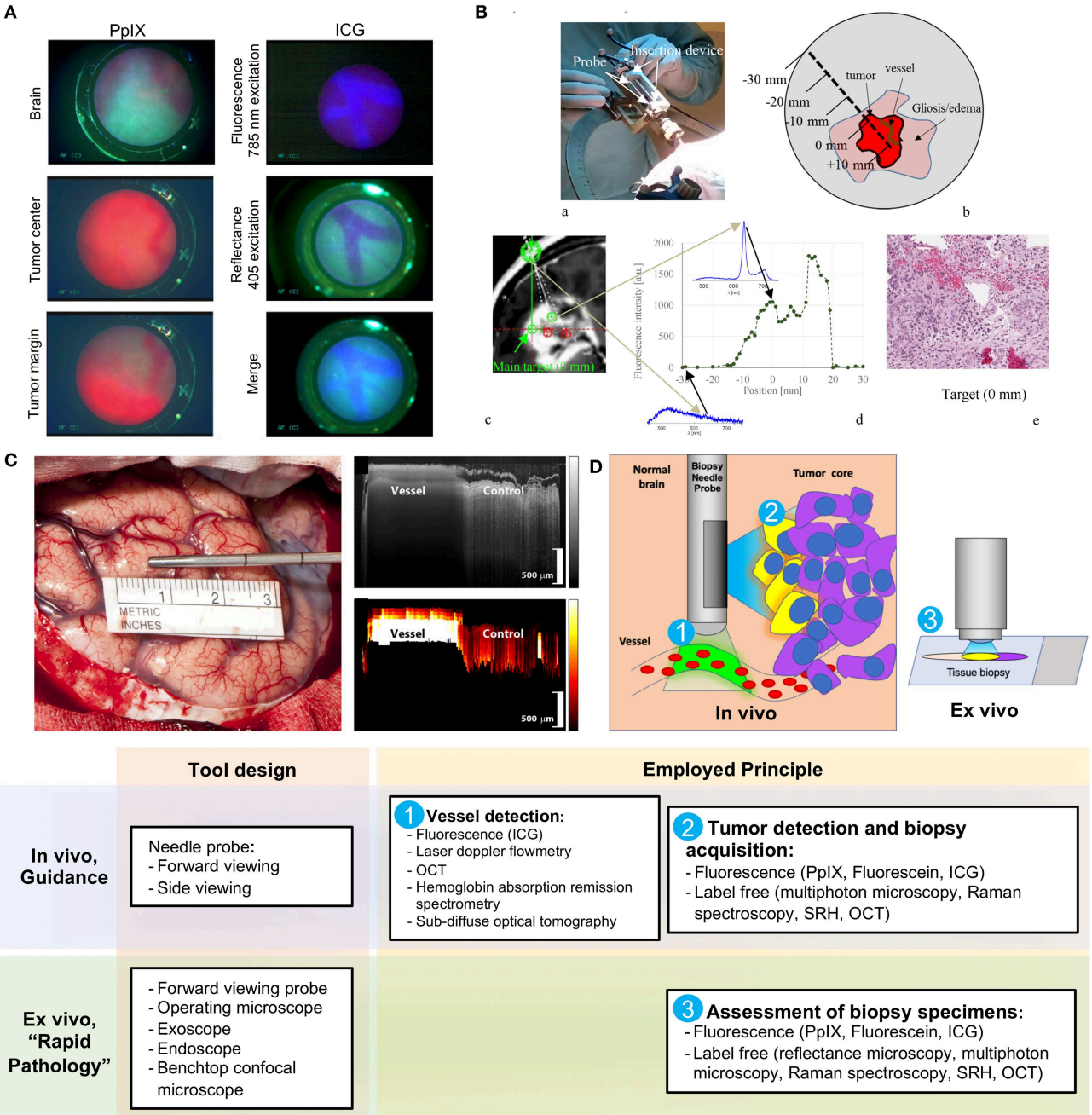

	Tool design	Employed Principle
In vivo, Guidance	Needle probe: - Forward viewing - Side viewing	**1 Vessel detection:** - Fluorescence (ICG) - Laser doppler flowmetry - OCT - Hemoglobin absorption remission spectrometry - Sub-diffuse optical tomography **2 Tumor detection and biopsy acquisition:** - Fluorescence (PpIX, Fluorescein, ICG) - Label free (multiphoton microscopy, Raman spectroscopy, SRH, OCT)
Ex vivo, "Rapid Pathology"	- Forward viewing probe - Operating microscope - Exoscope - Endoscope - Benchtop confocal microscope	**3 Assessment of biopsy specimens:** - Fluorescence (PpIX, Fluorescein, ICG) - Label free (reflectance microscopy, multiphoton microscopy, Raman spectroscopy, SRH, OCT)

FIGURE 1 | Examples of the optical technologies for brain needle biopsies. **(A)** Images from the fluorescence optical needle endoscope described by Göbel et al. (22) for PpIX visualization in the tumor (left column) and vessel visualization using ICG (right column) in a mouse model. Adapted with permission from Göbel et al. (22)© The Optical Society. **(B)** Illustration of PpIX spectroscopy method for tumor detection during stereotactic biopsy described by Haj-Hosseini et al. (28). The top two panels show the probe positioned in the stereotactic frame and the concept of measurements along the trajectory. The bottom panels show an MR image with calculated targets, spectral data of PpIX along the injection trajectory, and the histopathology slide of the target. Adapted with permission from Haj-Hosseini et al. (28)© The Optical Society. **(C)** Stain-less reflectance imaging method from Ramakonar et al. (27). Left panel shows a photo of an imaging needle rolled over a vessel of 650 µm. The imaging window of the probe is not visible and is facing toward the tissue. The upper right panel displays OCT B-scan consisting of A-scans. The tissue surface corresponds to the top of the image. Depth increases going down the image. The bottom right panel displays a speckle decorrelation image calculated form the OCT scan with high decorrelation as white and low decorrelation as dark red. Adapted from Ramakonar et al. (27) under Creative Commons Attribution license. **(D)** Schematic summary of advanced optical methods and tool designs, for increasing safety of stereotactic brain biopsies. OCT, optical coherence tomography; PpIX, protoporphyrin IX; ICG, indocyanine green; SRH, Stimulated Raman Histology.

excitation laser) along the trajectory of the device (**Figure 1B**). Although increased perfusion was detected in two biopsy locations, no information regarding the changes in the surgical plan or needle trajectory was reported (28). A similar stand-alone forward-viewing laser Doppler flowmetry needle probe had been investigated by the same group during the electrode placement for deep brain stimulation in patients (29, 30). Although the main goal of these studies was to establish the link between the measured blood flow and anatomy along trajectories, the authors did encounter one bleeding episode evidenced by significantly increased blood flow measures, which was later confirmed by CT (29). Subsequently, the authors suggested that this method could detect small vessels and thus decrease the risk of bleeding complications in stereotactic procedures (30). Obtaining measurements every 0.5 mm along the injection trajectory was proposed; however, it would result in a significant increase of surgical time (20 s per measurement resulting in at least 33.3 min for 5-cm trajectory) (28). Additionally, this probe has not been integrated into a brain biopsy needle for side view assessment. Future studies are necessary to assess if vascular imaging is helpful to guide intraoperative adjustments of the surgical plan and prevent vessel injury and bleeding.

Stain-Less Reflectance Imaging Approaches

Ramakonar et al. reported the performance of a side-viewing probe that fit a standard side-cutting brain biopsy needle for optical coherence tomography (OCT) imaging and differentiation of solid tissue and vessels (**Figure 1C**) (27). This imaging method is based on the detection and reconstruction of backscattered light from the 1,300-nm near-infrared illumination light, allowing 1–1.5 mm penetration depth and 5–20 μm resolution. OCT imaging was presented in an earlier paper by Kut et al. that demonstrated the modality's efficacy as a label-free technique for differentiating cancer from non-cancer in human brain tissues at a 1- to 1.5-mm penetration depth (34). To overcome the challenge of OCT's shallow depth, Ramakonar et al. was able to develop an optically guided biopsy needle capable of OCT imaging in order to visualize blood vessels at greater tissue depths. The information is then displayed on a monitor as a B-scan acquired during needle movements. Initial analysis of surface cortical vessels in patients that underwent craniotomy showed that the device detected blood vessels with a diameter of >500 μm with a sensitivity of 91.2% and a specificity of 97.7% (27). Furthermore, the authors validated these findings by demonstrating deep brain vessel detection capability (vessels were preselected on MRI) during brain needle biopsies in three patients (27).

Markwardt et al. in a phantom model and in *ex vivo* porcine brains demonstrated that a side-viewing double fiber probe for remission spectrometry inserted in a side-cutting biopsy needle can determine the proximity of the vessel to the needle (26). The method is based on the illumination of the tissue with a light from a broad wavelength light emitting diode (LED) light source (400–700 nm) and spectroscopic analysis of the remitted light. The remitted light is assessed at wavelengths that are characteristic of hemoglobin absorption (578 and 650 nm for oxygenated and deoxygenated, respectively), allowing the estimation of the proximity of the vessels to the probe. The method results are displayed as ratio values that represent the proximity, size, and orientation of the hemoglobin-containing vessels to the probe. Although there is no visual information regarding the appearance of the tissue, the technique is relatively simple and inexpensive.

Pichette et al. in phantom experiments demonstrated that interstitial sub-diffuse optical tomography technology can detect vessels with diameters of more than 300 μm for up to 2 mm from the biopsy needle (24). The 1.7-mm-diameter probe consists of 24 side-viewing fibers that provide circumferential scanning and detection of the spectrally resolved remitted light from the tissue around the needle guide. The main advantage of this method is that the probe scans the whole volume of tissues surrounding the needle, creating a two-dimensional visual signal map across the depth and circumference position. An additional advantage is higher tissue penetration depth when compared to optical coherence tomography (2 vs. ∼1 mm) (24). Remission spectrometry and sub-diffuse optical tomography both rely on the hemoglobin absorption spectra and do not require additional contrast agents (24, 26).

METHODS FOR BIOPSY ACQUISITION GUIDANCE AND FOR RAPID INTRAOPERATIVE ASSESSMENT OF OBTAINED SPECIMENS

Identification of Viable Diagnostic Tissue

Decreasing the number of stereotactic biopsies represents another strategy to minimize the risk of brain and vascular damage. Therefore, technologies that allow for the detection of viable tumor tissue along the biopsy needle trajectory are valuable. Such techniques allow not only to increase accuracy for diagnostic sample acquisition for proper histopathological diagnostics but also to avoid unnecessary repetitive needle biopsies.

Methods Based on the Detection of Molecular Labels in the Tumor Tissue

The presence of 5-aminolevulinic (5-ALA)-induced PpIX fluorescence is diagnostic for malignant tumors and can be used to assess stereotactic biopsy samples before submitting them to pathology, while the absence of fluorescence can filter out necrotic areas and inflammatory reactive tissue without malignant cells. This method was confirmed in multiple studies (35–40). Detection of PpIX fluorescence was highly diagnostic for viable tumor tissue in patients with intracranial lymphomas (41), high-grade gliomas, and anaplastic foci in patients with low-grade gliomas (42). Fluorescence positive samples might even not require intraoperative frozen section analysis and could be sent directly for a permanent section because of the high positive predictive value of PpIX fluorescence (39, 43, 44). In cases of low or negative fluorescence, the intraoperative frozen section analysis is recommended with subsequent biopsies upon the results of the intraoperative histopathological analysis (43).

Excitation of PpIX at 633 nm can further increase the diagnostic utility of such a method, as it allows for deeper imaging through a small layer of blood or tissue, which was previously impossible with 405-nm excitation (45, 46).

Similarly to 5-ALA, fluorescein sodium can be used to assess stereotactic biopsy specimens under the special fluorescence mode of the surgical microscope. High-grade glioma tissue shows strong yellow fluorescence when excited at about 488 nm (47). Being a relatively inexpensive drug, fluorescein sodium could also be visualized using a low-cost miniature device, Fluoropen, which is essentially a LED torch with a blue filter mounted at the light source for excitation and a yellow filter attached around the torch as a cone collar (48). The device is positioned close to the specimen and yellow fluorescence is observed through the yellow filter (48). Observation of fluorescein fluorescence from the specimens had a 100% positive predictive value and a 25% negative predictive value of a lesional tissue (49). Overall, the fluorescein-based method was shown to be as effective as frozen section analysis for the diagnostic biopsy screening (49).

ICG may also be used as a highlighter of the tumor tissue (50–54). Although there are few reports about the ICG use for tumor detection during stereotactic biopsies (16), open surgical visualization showed high sensitivity but low specificity of the second-window ICG (52). Other targeted molecular labels that can be used for open fluorescence-guided surgery, for example, BLZ-100, an ICG-conjugated tumor-targeting peptide chlorotoxin used for imaging, also hold potential for stereotactic needle biopsy procedures (55).

Apart from the macroscopic identification of the retained fluorescent drug, the obtained stereotactic biopsy specimens could be subjected to analysis with other methods alternative to a frozen section. Such methods might be less laborious and time-consuming. Stereotactic samples could be stained with rapid fluorophores *ex vivo* and scanned with a confocal microscope (56, 57). Miniaturized handheld confocal laser endomicroscopy with fluorescein sodium injected intraoperatively as a contrast can visualize the histological architecture of brain biopsies *ex vivo* and *in vivo* (58–62). However, this probe has not been assessed in stereotactic procedures.

A thin forward-viewing fiber-based confocal laser endomicroscope that can fit biopsy needles is available for 488-nm and 660-nm excitable fluorophores (fluorescein sodium and ICG, respectively) (63, 64). A pilot study has demonstrated that such an endomicroscope with fluorescein as a contrast can visualize brain tumor architecture during a stereotactic brain biopsy procedure in humans (65). A similar technique was tested by Lynagh et al. in a proof-of-concept study for the detection of fluorescein and blue-fluorescence protein labeled glioma cells in a rat model using a 0.65-mm fiber microendoscope coupled with a clinical stereotactic biopsy needle (66). Microendoscopy technology is similar to a needle-based contact endoscope (22) and other fiber probes for spectral measurements that were discussed above (28, 35, 44), but is able to provide fluorescence tissue image with higher resolution down to the cellular level.

Label-Free Methods

Various microscopy imaging methods that are not dependent on the drug-induced contrast and instead rely on intrinsic optical properties of the tissues recently received clinical attention. Such methods could be used for rapid intraoperative assessment of the acquired stereotactic brain biopsies to increase diagnostic yield and improve pathology workflow.

It has been shown that measurements of reflectance and fluorescence spectra of unstained brain tissues can differentiate radiation necrosis in brain tumor tissue (67). Reflectance confocal microscopy can differentiate viable brain tumor tissue from necrotic tissue and further characterize histological appearance with high diagnostic accuracy (68, 69). Label-free multiphoton microscopy methods were successfully used for the imaging of Alzheimer's disease brain samples (70). Raman microspectroscopic microscopy imaging has been studied for histological assessment of brain tumor biopsies (71). A notably successful variant of Raman microscopy is the Stimulated Raman Histology (SRH) technique, which has been used for *ex vivo* histological assessment of brain tumor biopsies. SRH provided high-resolution digital images that look similar to the standard hematoxylin and eosin staining (72, 73). SRH is a stand-alone imaging system that can be positioned in the operating room for rapid intraoperative pathological assessment (72, 73). Although most of the imaging studies were performed on benchtop microscopes, some multiphoton microscopy modes (CARS and TREF) will be available in endoscopes and needle-size probes in the near future (74).

Stevens et al. described a 1.8-mm-diameter forward-viewing 830-nm Raman-based spectroscopy probe without fibers that fit a standard brain biopsy needle (75, 76). The new design of the probe resulted in significant noise reduction compared to the silica-fiber-based Raman imaging and demonstrated discrimination of various porcine brain structures including white matter, gray matter, and blood vessels based on the Raman spectra (75).

SUMMARY

Current developments for increasing the safety and efficacy of stereotactic brain biopsy procedures are centered around the two main areas: avoidance of the vessels and detection of the viable diagnostic tissue, which could be achieved *in vivo* or *ex vivo* (**Figure 1D**).

Because vessel avoidance is a major component for the safety of any stereotactic needle-based procedure including needle brain biopsy, deep brain stimulation (77), or interstitial laser thermal therapy (78, 79), advancements in the surgical tools that allow for timely vessel detection is of utmost importance. Several technologies for vessel detection implemented into a biopsy needle included detection of fluorescent intravascular contrast, laser Doppler flowmetry, optical coherence and interstitial sub-diffuse tomography, and remission spectrometry. Non-fluorescence methods based on the blood flow and hemoglobin detection are thought to be the most promising as they avoid dealing with fluctuations in the intravascular contrast

concentrations after injection. It should be noted that the current literature does not provide definitive evidence on the efficacy of such methods for vessel injury avoidance; therefore, more clinical studies are necessary.

Ex vivo confirmation of PpIX or fluorescein fluorescence from biopsy samples has been established to have a high positive predictive value of a diagnostic biopsy in multiple studies and can be recommended as a routine method for stereotactic biopsy at this current stage. However, the possibility for identification of the correct biopsy needle position *in vivo* prior to actual biopsy acquisition with a small optical tool is even more exciting. Most of such reports are based on the detection of the intra-tumoral fluorescent molecules (PpIX, fluorescein, and ICG); however, the development of reflectance and multiphoton microscopy techniques and militarization of microscopes would allow label-free tumor tissue identification through a biopsy needle in the future. There is a marked diversity in qualitative and quantitative optical methods for brain tumor tissue identification, and each of them requires a significant learning curve and dedication. So far, the most progress has been achieved with 5-ALA-induced PpIX, which is highly specific for malignant tissues and can be detected spectroscopically with a single optical fiber inserted in the biopsy needle.

Another limitation is that most of the discussed methods require timely interpretation and adjustments of multiple parameters during the procedure to ensure optimal performance, which is not always practical and may lead to information overload. For example, results of quantitative spectroscopy are usually displayed on the screen in a graph form. This information could be converted into an auditory format, which would be easy to understand and non-disruptive during the surgery (80). Finally, the possibility of light-induced tissue damage should be carefully considered when developing novel optical and fluorescent tools for *in vivo* diagnostics.

When considering the design of an ideal probe, it should incorporate vessel detection as well as tumor detection modules, most likely in forward and side views simultaneously for the safest possible probe insertion and biopsy acquisition. Machine learning, coupled with optical visualization technologies, would be a basis for computer-aided, real-time tissue image analysis for the selection of the best probe trajectory or location for biopsy acquisition. Besides these technologies that are used for vessel avoidance and tumor detection, future development of probes could also include augmented or virtual reality for clinicians to perform more accurate probe trajectory planning.

AUTHOR CONTRIBUTIONS

All authors listed have made a substantial, direct and intellectual contribution to the work, and approved it for publication.

SUPPLEMENTARY MATERIAL

The Supplementary Material for this article can be found online at: https://www.frontiersin.org/articles/10.3389/fonc.2019.00947/full#supplementary-material

REFERENCES

1. Ragel BT, Ryken TC, Kalkanis SN, Ziu M, Cahill D, Olson JJ. The role of biopsy in the management of patients with presumed diffuse low grade glioma. *J Neuro Oncol.* (2015) 125:481–501. doi: 10.1007/s11060-015-1866-2
2. Schwartz C, Kreth FW. Comment on: the role of biopsy in the management of patients with presumed diffuse low grade glioma: a systematic review and evidence-based clinical practice guideline. *J Neuro Oncol.* (2016) 128:173. doi: 10.1007/s11060-016-2086-0
3. Teixeira MJ, Fonoff ET, Mandel M, Alves HL, Rosemberg S. Stereotactic biopsies of brain lesions. *Arq Neuropsiquiatr.* (2009) 67:74–7. doi: 10.1590/S0004-282X2009000100018
4. Chen CC, Hsu PW, Erich Wu TW, Lee ST, Chang CN, Wei KC, et al. Stereotactic brain biopsy: Single center retrospective analysis of complications. *Clin Neurol Neurosurg.* (2009) 111:835–9. doi: 10.1016/j.clineuro.2009.08.013
5. Shastri-Hurst N, Tsegaye M, Robson DK, Lowe JS, Macarthur DC. Stereotactic brain biopsy: an audit of sampling reliability in a clinical case series. *Br J Neurosurg.* (2009) 20:222–6. doi: 10.1080/02688690600875507
6. Bander ED, Jones SH, Pisapia D, Magge R, Fine H, Schwartz TH, et al. Tubular brain tumor biopsy improves diagnostic yield for subcortical lesions. *J Neurooncol.* (2019) 141:121–9. doi: 10.1007/s11060-018-03014-w
7. Dammers R, Schouten JW, Haitsma IK, Vincent AJ, Kros JM, Dirven CM. Towards improving the safety and diagnostic yield of stereotactic biopsy in a single centre. *Acta Neurochir.* (2010) 152:1915–21. doi: 10.1007/s00701-010-0752-0
8. Frati A, Pichierri A, Bastianello S, Raco A, Santoro A, Esposito V, et al. Frameless stereotactic cerebral biopsy: our experience in 296 cases. *Stereotact Funct Neurosurg.* (2011) 89:234–45. doi: 10.1159/000325704
9. Kulkarni AV, Guha A, Lozano A, Bernstein M. Incidence of silent hemorrhage and delayed deterioration after stereotactic brain biopsy. *J Neurosurg.* (1998) 89:31–5. doi: 10.3171/jns.1998.89.1.0031
10. Preul MC, Caramanos Z, Collins DL, Villemure JG, Leblanc R, Olivier A, et al. Accurate, noninvasive diagnosis of human brain tumors by using proton magnetic resonance spectroscopy. *Nat Med.* (1996) 2:323–5. doi: 10.1038/nm0396-323
11. Chernov MF, Muragaki Y, Ochiai T, Taira T, Ono Y, Usukura M, et al. Spectroscopy-supported frame-based image-guided stereotactic biopsy of parenchymal brain lesions: comparative evaluation of diagnostic yield and diagnostic accuracy. *Clin Neurol Neurosurg.* (2009) 111:527–35. doi: 10.1016/j.clineuro.2009.03.006
12. Lefranc M, Monet P, Desenclos C, Peltier J, Fichten A, Toussaint P, et al. Perfusion MRI as a neurosurgical tool for improved targeting in stereotactic tumor biopsies. *Stereotact Funct Neurosurg.* (2012) 90:240–7. doi: 10.1159/000338092
13. Levivier M, Goldman S, Pirotte B, Brucher JM, Baleriaux D, Luxen A, et al. Diagnostic yield of stereotactic brain biopsy guided by positron emission tomography with [18F]fluorodeoxyglucose. *J Neurosurg.* (1995) 82:445–52. doi: 10.3171/jns.1995.82.3.0445
14. Gilsbach J, Mohadjer M, Mundinger F. A new safety device to prevent bleeding complications during stereotactic biopsy—The "stereotactic" Doppler sonography. *Acta Neurochir.* (1987) 89:77–9. doi: 10.1007/BF01406671
15. Virdyawan V, Y Baena FR. Vessel pose estimation for obstacle avoidance in needle steering surgery using multiple forward looking sensors. In: *2018 IEEE/RSJ International Conference on Intelligent Robots and Systems (IROS).* (2018). p. 3845–52. doi: 10.1109/IROS.2018.8594198
16. Cho SS, Salinas R, Lee JYK. Indocyanine-green for fluorescence-guided surgery of brain tumors: evidence, techniques, and practical experience. *Front Surg.* (2019) 6:11. doi: 10.3389/fsurg.2019.00011

17. Zhang DY, Singhal S, Lee JYK. Optical principles of fluorescence-guided brain tumor surgery: a practical primer for the neurosurgeon. *Neurosurgery.* (2019) 85:312–4. doi: 10.1093/neuros/nyy315
18. Wei L, Roberts DW, Sanai N, Liu JTC. Visualization technologies for 5-ALA-based fluorescence-guided surgeries. *J Neurooncol.* (2019) 141:495–505. doi: 10.1007/s11060-018-03077-9
19. Hadjipanayis CG, Stummer W. 5-ALA and FDA approval for glioma surgery. *J Neurooncol.* (2019) 141:479–86. doi: 10.1007/s11060-019-03098-y
20. Valdes PA, Juvekar P, Agar NYR, Gioux S, Golby AJ. Quantitative wide-field imaging techniques for fluorescence guided neurosurgery. *Front Surg.* (2019) 6:31. doi: 10.3389/fsurg.2019.00031
21. Lakomkin N, Hadjipanayis CG. The use of spectroscopy handheld tools in brain tumor surgery: current evidence and techniques. *Front Surg.* (2019) 6:30. doi: 10.3389/fsurg.2019.00030
22. Göbel W, Brucker D, Kienast Y, Johansson A, Kniebühler G, Rühm A, et al. Optical needle endoscope for safe and precise stereotactically guided biopsy sampling in neurosurgery. *Optics Exp.* (2012) 20:26117–26. doi: 10.1364/OE.20.026117
23. Ruhm A, Gobel W, Sroka R, Stepp H. ICG-assisted blood vessel detection during stereotactic neurosurgery: simulation study on excitation power limitations due to thermal effects in human brain tissue. *Photodiagnosis Photodyn Ther.* (2014) 11:307–18. doi: 10.1016/j.pdpdt.2014.03.007
24. Pichette J, Goyette A, Picot F, Tremblay M-A, Soulez G, Wilson BC, et al. Sensitivity analysis aimed at blood vessels detection using interstitial optical tomography during brain needle biopsy procedures. *Biomed Optics Exp.* (2015) 6:4238–54. doi: 10.1364/BOE.6.004238
25. Goyette A, Pichette J, Tremblay MA, Laurence A, Jermyn M, Mok K, et al. Sub-diffuse interstitial optical tomography to improve the safety of brain needle biopsies: a proof-of-concept study. *Optics Lett.* (2015) 40:170–3. doi: 10.1364/OL.40.000170
26. Markwardt NA, Stepp H, Franz G, Sroka R, Goetz M, Zelenkov P, et al. Remission spectrometry for blood vessel detection during stereotactic biopsy of brain tumors. *J Biophoton.* (2017) 10:1080–94. doi: 10.1002/jbio.201600193
27. Ramakonar H, Quirk BC, Kirk RW, Li J, Jacques A, Lind CRP, et al. Intraoperative detection of blood vessels with an imaging needle during neurosurgery in humans. *Sci Adv.* (2018) 4:eaav4992. doi: 10.1126/sciadv.aav4992
28. Haj-Hosseini N, Richter JCO, Milos P, Hallbeck M, Wårdell K. 5-ALA fluorescence and laser doppler flowmetry for guidance in a stereotactic brain tumor biopsy. *Biomed Optics Exp.* (2018) 9:2284–96. doi: 10.1364/BOE.9.002284
29. Wårdell K, Zsigmond P, Richter J, Hemm S. Relationship between laser doppler signals and anatomy during deep brain stimulation electrode implantation toward the ventral intermediate nucleus and subthalamic nucleus. *Oper Neurosurg.* (2013) 72:ons127-ons40. doi: 10.1227/NEU.0b013e31827e5821
30. Wårdell K, Hemm-Ode S, Rejmstad P, Zsigmond P. High-resolution laser Doppler measurements of microcirculation in the deep brain structures: a method for potential vessel tracking. *Stereotact Funct Neurosurg.* (2016) 94:1–9. doi: 10.1159/000442894
31. Stummer W, Pichlmeier U, Meinel T, Wiestler OD, Zanella F, Reulen HJ, et al. Fluorescence-guided surgery with 5-aminolevulinic acid for resection of malignant glioma: a randomised controlled multicentre phase III trial. *Lancet Oncol.* (2006) 7:392–401. doi: 10.1016/S1470-2045(06)70665-9
32. Hanel RA, Nakaji P, Spetzler RF. Use of microscope-integrated near-infrared indocyanine green videoangiography in the surgical treatment of spinal dural arteriovenous fistulae. *Neurosurgery.* (2010) 66:978–84. discussion: 84–5. doi: 10.1227/01.NEU.0000368108.94233.22
33. Raabe A, Beck J, Gerlach R, Zimmermann M, Seifert V. Near-infrared Indocyanine green video angiography: a new method for intraoperative assessment of vascular flow. *Neurosurgery.* (2003) 32–9. discussion: 139. doi: 10.1097/00006123-200301000-00017
34. Kut C, Chaichana KL, Xi J, Raza SM, Ye X, McVeigh ER, et al. Detection of human brain cancer infiltration *ex vivo* and *in vivo* using quantitative optical coherence tomography. *Sci Transl Med.* (2015) 7:292ra100. doi: 10.1126/scitranslmed.3010611
35. Haj-Hosseini N, Richter JCO, Hallbeck M, Wårdell K. Low dose 5-aminolevulinic acid: Implications in spectroscopic measurements during brain tumor surgery. *Photodiagnosis Photodyn Ther.* (2015) 12:209–14. doi: 10.1016/j.pdpdt.2015.03.004
36. Piquer J, Llácer JL, Rovira V, Riesgo P, Rodriguez R, Cremades A. Fluorescence-guided surgery and biopsy in gliomas with an exoscope system. *BioMed Res Int.* (2014) 2014:1–6. doi: 10.1155/2014/207974
37. Hefti M, von Campe G, Moschopulos M, Siegner A, Looser H, Landolt H. 5-Aminolevulinic acid induced protoporphyrin IX fluorescence in high-grade glioma surgery: a one-year experience at a single institutuion. *Swiss Med Wkly.* (2008) 138:180–5. doi: 10.4414/smw.2008.12077
38. Moriuchi S, Yamada K, Dehara M, Teramoto Y, Soda T, Imakita M, et al. Use of 5-aminolevulinic acid for the confirmation of deep-seated brain tumors during stereotactic biopsy. Report of 2 cases. *J Neurosurg.* (2011) 115:278–80. doi: 10.3171/2011.4.JNS102137
39. von Campe G, Moschopulos M, Hefti M. 5-Aminolevulinic acid-induced protoporphyrin IX fluorescence as immediate intraoperative indicator to improve the safety of malignant or high-grade brain tumor diagnosis in frameless stereotactic biopsies. *Acta Neurochir.* (2012) 154:585–8. doi: 10.1007/s00701-012-1290-8
40. Yamaguchi F, Takahashi H, Teramoto A. Photodiagnosis for frameless stereotactic biopsy of brain tumor. *Photodiagnosis Photodyn Ther.* (2007) 4:71–5. doi: 10.1016/j.pdpdt.2006.09.005
41. Kiesel B, Millesi M, Woehrer A, Furtner J, Bavand A, Roetzer T, et al. 5-ALA–induced fluorescence as a marker for diagnostic tissue in stereotactic biopsies of intracranial lymphomas: experience in 41 patients. *Neurosurg Focus.* (2018) 44:E7. doi: 10.3171/2018.3.FOCUS1859
42. Arita H, Kinoshita M, Kagawa N, Fujimoto Y, Kishima H, Hashimoto N, et al. 11C-methionine uptake and intraoperative 5-aminolevulinic acid-induced fluorescence as separate index markers of cell density in glioma. *Cancer.* (2012) 118:1619–27. doi: 10.1002/cncr.26445
43. Widhalm G, Minchev G, Woehrer A, Preusser M, Kiesel B, Furtner J, et al. Strong 5-aminolevulinic acid-induced fluorescence is a novel intraoperative marker for representative tissue samples in stereotactic brain tumor biopsies. *Neurosurg Rev.* (2012) 35:381–91. doi: 10.1007/s10143-012-0374-5
44. Potapov AA, Goryaynov SA, Okhlopkov VA, Pitskhelauri DI, Kobyakov GL, Zhukov VY, et al. [Clinical guidelines for the use of intraoperative fluorescence diagnosis in brain tumor surgery]. *Zh Vopr Neirokhir Im N N Burdenko.* (2015) 79:91–101. doi: 10.17116/neiro201579591-101
45. Markwardt NA, Haj-Hosseini N, Hollnburger B, Stepp H, Zelenkov P, Rühm A. 405 nm versus 633 nm for protoporphyrin IX excitation in fluorescence-guided stereotactic biopsy of brain tumors. *J Biophoton.* (2016) 9:901–12. doi: 10.1002/jbio.201500195
46. Potapov AA, Goriainov SA, Loshchenov VB, Savel'eva TA, Gavrilov AG, Okhlopkov VA, et al. [Intraoperative combined spectroscopy (optical biopsy) of cerebral gliomas]. *Zh Vopr Neirokhir Im Burdenko.* (2013) 77:3–10.
47. Rey-Dios R, Hattab EM, Cohen-Gadol AA. Use of intraoperative fluorescein sodium fluorescence to improve the accuracy of tissue diagnosis during stereotactic needle biopsy of high-grade gliomas. *Acta Neurochir.* (2014) 156:1071–5. doi: 10.1007/s00701-014-2097-6
48. Thien A, Rao JP, Ng WH, King NKK. The fluoropen: a simple low-cost device to detect intraoperative fluorescein fluorescence in stereotactic needle biopsy of brain tumors. *Acta Neurochir.* (2016) 159:371–5. doi: 10.1007/s00701-016-3041-8
49. Thien A, Han JX, Kumar K, Ng YP, Rao JP, Ng WH, et al. Investigation of the usefulness of fluorescein sodium fluorescence in stereotactic brain biopsy. *Acta Neurochir.* (2017) 160:317–24. doi: 10.1007/s00701-017-3429-0
50. Catapano G, Sgulo F, Laleva L, Columbano L, Dallan I, de Notaris M. Multimodal use of indocyanine green endoscopy in neurosurgery: a single-center experience and review of the literature. *Neurosurg Rev.* (2018) 41:985–98. doi: 10.1007/s10143-017-0858-4
51. Hitti FL, Lee JYK. Endoscopic resection of an intraventricular tumor with second window indocyanine green: 2-dimensional operative video. *Oper Neurosurg.* (2018) 15:E53–E4. doi: 10.1093/ons/opy053
52. Lee JY, Thawani JP, Pierce J, Zeh R, Martinez-Lage M, Chanin M, et al. Intraoperative near-infrared optical imaging can localize gadolinium-enhancing gliomas during surgery. *Neurosurgery.* (2016) 79:856–71. doi: 10.1227/NEU.0000000000001450

53. Haglund MM, Hochman DW, Spence AM, Berger MS. Enhanced optical imaging of rat gliomas and tumor margins. *Neurosurgery.* (1994) 35:930–40. discussion: 40–1. doi: 10.1097/00006123-199411000-00019
54. Watson JR, Martirosyan N, Lemole GM, Trouard TP, Romanowski M. Intraoperative brain tumor resection with indocyanine green using augmented microscopy. *J Biomed Optics.* (2018) 23:1–4. doi: 10.1117/1.JBO.23.9.090501
55. Butte PV, Mamelak A, Parrish-Novak J, Drazin D, Shweikeh F, Gangalum PR, et al. Near-infrared imaging of brain tumors using the tumor paint BLZ-100 to achieve near-complete resection of brain tumors. *Neurosurg Focus.* (2014) 36:E1. doi: 10.3171/2013.11.FOCUS13497
56. Martirosyan NL, Georges J, Eschbacher JM, Belykh E, Carotenuto A, Spetzler RF, et al. Confocal scanning microscopy provides rapid, detailed intraoperative histological assessment of brain neoplasms: experience with 106 cases. *Clin Neurol Neurosurg.* (2018) 169:21–8. doi: 10.1016/j.clineuro.2018.03.015
57. Martirosyan NL, Georges J, Eschbacher JM, Cavalcanti DD, Elhadi AM, Abdelwahab MG, et al. Potential application of a handheld confocal endomicroscope imaging system using a variety of fluorophores in experimental gliomas and normal brain. *Neurosurg Focus.* (2014) 36:E16. doi: 10.3171/2013.11.FOCUS13486
58. Martirosyan NL, Eschbacher JM, Kalani MY, Turner JD, Belykh E, Spetzler RF, et al. Prospective evaluation of the utility of intraoperative confocal laser endomicroscopy in patients with brain neoplasms using fluorescein sodium: experience with 74 cases. *Neurosurg Focus.* (2016) 40:E11. doi: 10.3171/2016.1.FOCUS15559
59. Foersch S, Heimann A, Ayyad A, Spoden GA, Florin L, Mpoukouvalas K, et al. Confocal laser endomicroscopy for diagnosis and histomorphologic imaging of brain tumors *in vivo*. *PLoS ONE.* (2012) 7:e41760. doi: 10.1371/journal.pone.0041760
60. Breuskin D, Szczygielski J, Urbschat S, Kim YJ, Oertel J. Confocal laser endomicroscopy in neurosurgery—An alternative to instantaneous sections? *World Neurosurg.* (2017) 100:180–5. doi: 10.1016/j.wneu.2016.12.128
61. Sankar T, Delaney PM, Ryan RW, Eschbacher J, Abdelwahab M, Nakaji P, et al. Miniaturized handheld confocal microscopy for neurosurgery: results in an experimental glioblastoma model. *Neurosurgery.* (2010) 66:410–7. discussion: 7–8. doi: 10.1227/01.NEU.0000365772.66324.6F
62. Sanai N, Eschbacher J, Hattendorf G, Coons SW, Preul MC, Smith KA, et al. Intraoperative confocal microscopy for brain tumors: a feasibility analysis in humans. *Neurosurgery.* (2011) 68(2 Suppl Operative):282–90. discussion: 90. doi: 10.1227/NEU.0b013e318212464e
63. Giovannini M. Needle-based confocal laser endomicroscopy. *Endosc Ultrasound.* (2015) 4:284–8. doi: 10.4103/2303-9027.170405
64. Schneider C, Johnson SP, Gurusamy K, Cook RJ, Desjardins AE, Hawkes DJ, et al. Identification of liver metastases with probe-based confocal laser endomicroscopy at two excitation wavelengths. *Lasers Surg Med.* (2017) 49:280–92. doi: 10.1002/lsm.22617
65. Pavlov V, Meyronet D, Meyer-Bisch V, Armoiry X, Pikul B, Dumot C, et al. Intraoperative probe-based confocal laser endomicroscopy in surgery and stereotactic biopsy of low-grade and high-grade gliomas: a feasibility study in humans. *Neurosurgery.* (2016) 79:604–12. doi: 10.1227/NEU.0000000000001365
66. Lynagh R, Ishak M, Georges J, Lopez D, Osman H, Kakareka M, et al. Fluorescence-guided stereotactic biopsy: a proof-of-concept study. *J Neurosurg.* (2019) 22:1–7. doi: 10.3171/2018.11.JNS18629
67. Lin W-C, Mahadevan-Jansen A, Johnson MD, Weil RJ, Toms SA. *In vivo* optical spectroscopy detects radiation damage in brain tissue. *Neurosurgery.* (2005) 57:518–25. doi: 10.1227/01.NEU.0000170559.48166.AC
68. Eschbacher JM, Georges JF, Belykh E, Yazdanabadi MI, Martirosyan NL, Szeto E, et al. Immediate label-free *ex vivo* evaluation of human brain tumor biopsies with confocal reflectance microscopy. *J Neuropathol Exp Neurol.* (2017) 76:1008–22. doi: 10.1093/jnen/nlx089
69. Georges J, Zehri A, Carlson E, Nichols J, Mooney MA, Martirosyan NL, et al. Label-free microscopic assessment of glioblastoma biopsy specimens prior to biobanking [corrected]. *Neurosurg Focus.* (2014) 36:E8. doi: 10.3171/2013.11.FOCUS13478
70. Lee JH, Kim DH, Song WK, Oh M-K, Ko D-K. Label-free imaging and quantitative chemical analysis of Alzheimer's disease brain samples with multimodal multiphoton nonlinear optical microspectroscopy. *J Biomed Optics.* (2015) 20:056013. doi: 10.1117/1.JBO.20.5.056013
71. Krafft C, Belay B, Bergner N, Romeike BFM, Reichart R, Kalff R, et al. Advances in optical biopsy—Correlation of malignancy and cell density of primary brain tumors using Raman microspectroscopic imaging. *Analyst.* (2012) 137:5533–7. doi: 10.1039/c2an36083g
72. Hollon TC, Lewis S, Pandian B, Niknafs YS, Garrard MR, Garton H, et al. Rapid intraoperative diagnosis of pediatric brain tumors using stimulated Raman histology. *Cancer Res.* (2018) 78:278–89. doi: 10.1158/0008-5472.CAN-17-1974
73. Orringer DA, Pandian B, Niknafs YS, Hollon TC, Boyle J, Lewis S, et al. Rapid intraoperative histology of unprocessed surgical specimens via fibre-laser-based stimulated Raman scattering microscopy. *Nat Biomed Eng.* (2017) 1:0027. doi: 10.1038/s41551-016-0027
74. Romeike BFM, Meyer T, Reichart R, Kalff R, Petersen I, Dietzek B, et al. Coherent anti-stokes raman scattering and two photon excited fluorescence for neurosurgery. *Clin Neurol Neurosurg.* (2015) 131:42–6. doi: 10.1016/j.clineuro.2015.01.022
75. Mahadevan-Jansen A, Petrich W, Stevens OAC, Hutchings J, Gray W, Day JC. A low background Raman probe for optical biopsy of brain tissue. *Biomed Vibrational Spectrosc.* (2014). doi: 10.1117/12.2044139. [Epub ahead of print].
76. Stevens OAC, Hutchings J, Gray W, Vincent RL, Day JC. Miniature standoff Raman probe for neurosurgical applications. *J Biomed Optics.* (2016) 21:087002. doi: 10.1117/1.JBO.21.8.087002
77. Giller CA, Liu H, German DC, Kashyap D, Dewey RB. A stereotactic near-infrared probe for localization during functional neurosurgical procedures: further experience. *J Neurosurg.* 110:263–73. doi: 10.3171/2008.8.JNS08728
78. Lee I, Kalkanis S, Hadjipanayis CG. Stereotactic laser interstitial thermal therapy for recurrent high-grade gliomas. *Neurosurgery.* (2016) 79 (Suppl 1):S24–S34. doi: 10.1227/NEU.0000000000001443
79. Ashraf O, Patel NV, Hanft S, Danish SF. Laser-induced thermal therapy in neuro-oncology: a review. *World Neurosurg.* (2018) 112:166–77. doi: 10.1016/j.wneu.2018.01.123
80. Black D, Hahn HK, Kikinis R, Wårdell K, Haj-Hosseini N. Auditory display for fluorescence-guided open brain tumor surgery. *Int J Comput Assisted Radiol Surg.* (2017) 13:25–35. doi: 10.1007/s11548-017-1667-5

Conflict of Interest: The authors declare that the research was conducted in the absence of any commercial or financial relationships that could be construed as a potential conflict of interest.

frontiers in Surgery

REVIEW
published: 28 November 2019
doi: 10.3389/fsurg.2019.00059

Applications of Microscope-Integrated Indocyanine Green Videoangiography in Cerebral Revascularization Procedures

*Claudio Cavallo, Sirin Gandhi, Xiaochun Zhao, Evgenii Belykh, Daniel Valli, Peter Nakaji, Mark C. Preul and Michael T. Lawton**

Department of Neurosurgery, St. Joseph's Hospital and Medical Center, Barrow Neurological Institute, Phoenix, AZ, United States

Indocyanine green videoangiography (ICG-VA) is a near-infrared range fluorescent marker used for intraoperative real-time assessment of flow in cerebrovascular surgery. Given its high spatial and temporal resolution, ICG-VA has been widely established as a useful technique to perform a qualitative analysis of the graft patency during revascularization procedures. In addition, this fluorescent modality can also provide valuable qualitative and quantitative information regarding the cerebral blood flow within the bypass graft and in the territories supplied. Digital subtraction angiography (DSA) is considered to be the gold standard diagnostic modality for postoperative bypass graft patency assessment. However, this technique is time and labor intensive and an expensive interventional procedure. In contrast, ICG-VA can be performed intraoperatively with no significant addition to the total operative time and, when used correctly, can accurately show acute occlusion. Such time-sensitive ischemic injury detection is critical for flow reestablishment through direct surgical management. In addition, ICG has an excellent safety profile, with few adverse events reported in the literature. This review outlines the chemical behavior, technical aspects, and clinical implications of this tool as an intraoperative adjunct in revascularization procedures.

Keywords: indocyanine green videoangiography, cerebral revascularization, extracranial-intracranial bypass, intracranial-intracranial bypass, graft patency

OPEN ACCESS

Edited by:
Philipp Taussky, The University of Utah, United States

Reviewed by:
Hans-Jakob Steiger, Heinrich Heine University of Düsseldorf, Germany
Jorge Marcelo Mura, Instituto de Neurocirugía, Chile

****Correspondence:***
Michael T. Lawton
neuropub@barrowneuro.org

Specialty section:
This article was submitted to Neurosurgery, a section of the journal Frontiers in Surgery

Received: *14 May 2019*
Accepted: *02 October 2019*
Published: *28 November 2019*

Citation:
Cavallo C, Gandhi S, Zhao X, Belykh E, Valli D, Nakaji P, Preul MC and Lawton MT (2019) Applications of Microscope-Integrated Indocyanine Green Videoangiography in Cerebral Revascularization Procedures. Front. Surg. 6:59. doi: 10.3389/fsurg.2019.00059

INTRODUCTION

Revascularization procedures are considered in the management of various cerebrovascular disorders, including complex intracranial aneurysms, moyamoya disease (MMD), symptomatic cerebral ischemia recalcitrant to standard medical therapy, and cranial base tumors that require a proximal major vessel sacrifice. MMD is a pathological condition that is characterized by a bilateral progressive narrowing at the terminal portion of the intracranial internal carotid arteries. This stenosis may lead to occlusion of the vessel lumen and a consequent abnormal, compensatory collateral neovascularization at the base of the brain. Superficial temporal artery (STA)-middle cerebral artery (MCA) bypass is the main direct revascularization procedure performed, and it is effective in reducing the risk of ischemic and hemorrhagic strokes as well as in improving cerebral ischemia (1–3).

Microscope-integrated indocyanine green videoangiography (ICG-VA) is a relatively recent technique used as an intraoperative adjunct for real-time assessment of anastomotic patency. Indocyanine green was approved by the US Food and Drug Administration (FDA) in 1956 for the evaluation of cardio-circulatory and liver functions. In addition, the FDA approved ICG for use in ophthalmic angiography in 1975 (4). Since then, ICG has been extensively used for retinal angiography (5, 6). Raabe et al. revived this technique to document intravascular flow in cerebral vessels to establish vascular patency (4). ICG-VA was also used for the intraoperative assessment of dural arteriovenous fistulas, for confirming complete aneurysm obliteration, and avoiding perforator or branch vessel compromise on microsurgical clipping (7). Over the years, ICG-VA has become an effective low-cost, non-invasive technique for confirming real-time intravascular flow in bypasses, with a good safety profile. The objective of our study was to present a focused review of the application of ICG-VA in cerebral bypass procedures and to describe the current diagnostic and therapeutic modalities of this technique.

CHEMICAL PROPERTIES, PHARMACOKINETICS, AND ADVERSE-EFFECT PROFILE OF ICG

ICG ($C_{43}H_{47}N_2NaO_6S_2$) is a tricarbocyanine dye with near-infrared fluorescent properties.

The absorption and emission peaks of ICG are 805 and 835 nm, respectively, which fall in the near-infrared (NIR) light range. The NIR peaks allow greater transmission of the fluorescence signal through the native tissue compared with the fluorophores, with peaks in the visible light range (6, 8–10). In theory, ICG fluorescence has a penetration depth of 10–20 mm in human tissues (11). This two-dimensional fluorescence imaging provides high spatial resolution and image quality compared with other intraoperative techniques.

On intravenous administration, ICG binds to alpha-1 lipoproteins, belonging to the globulin family, and remains intravascular as long as the vascular wall integrity is preserved. This fluorescent compound does not enter the enterohepatic circulation and is not metabolized in the body. It has a plasma half-life of 3–4 min and is excreted exclusively by the liver. Despite its relatively good safety profile, the ICG molecule or the 5% sodium iodine contained in the drug can potentially cause adverse reactions (4). Mild reactions, such as nausea, vomiting, pruritus, and sneezing, have been reported in ∼0.15% of cases. Severe adverse reactions, including bronchospasm, laryngospasm, anaphylaxis, shock, myocardial infarction, cardiovascular arrest, and tonic clonic seizures have occurred in ∼0.05% of cases (4). Overall, ICG is associated with a low rate of adverse reactions, comparable to other contrast media. Iodine allergy or prior adverse reactions to contrast media are contraindications for the administration of ICG.

Abbreviations: CBF, cerebral blood flow; CFI, cut flow index; CSF, Cerebrospinal fluid; DSA, Digital subtraction angiography; EC-IC, Extracranial-intracranial; FDA, US Food and Drug Administration; HP, hyperperfusion; ICG-VA, indocyanine green videoangiography; IC-IC, Intracranial-intracranial; MCA, Middle cerebral artery; MMD, Moyamoya disease; NIR, near infrared; PCA, Posterior cerebral artery; STA, Superficial temporal artery; TNE, transient neurological event.

TECHNICAL ASPECTS OF ICG-VA

Intraoperative technology for visualization of fluorescence is an integrated component of the currently available surgical microscopes. An excitation light in the NIR range is transmitted through the microscope optics to generate ICG fluorescence. This emitted electromagnetic radiation is invisible to the human eye and passes through the NIR optical filter (INFRARED 800. Zeiss AG, Oberkochen, Germany) that blocks both the excitation and the ambient light. An infrared-sensitive camera on the surgical microscope detects the ICG fluorescence and translates the signal into a real-time white image on a black background. Recently, an innovative dual-image videoangiography system was developed to overlay visible light and NIR fluorescence images and allow the simultaneous intraoperative visualization of both ICG fluorescence and surrounding anatomical structures (12).

Before activating the INFRARED 800 mode to perform ICG-VA, the focus distance and the magnification should be set at <300 mm and less than 5×, respectively. Afterward, the surgeon can adjust these two parameters during the INFRARED 800 recording to optimize the image. However, modern surgical microscopes usually assist the user with an automatic function that fine-tunes the settings to render the highest quality images. The KINEVO 900 (Carl Zeiss) provides an AutoZoom function that automatically adjusts the total magnification and diaphragm opening to the preconfigured values at the start of ICG-VA and an AutoGain function that automatically adjusts the camera gain to fit the NIR signal intensity within the dynamic range of the camera as the ICG-VA progresses. Chromatic aberration due to higher magnification and surgical field depth account for the inability of electromagnetic radiation of different wavelengths to focus on the same positions in the focal plane. Through the use of special lenses, apochromatic optics adjust light arrays of different colors to converge to the same focal point. This method achieves a variable degree of compensation that is more significant in the visible light spectrum (400–700 nm). Chromatic aberration of NIR light, like the ICG emission light (820–900 nm) can be compensated the most at working distances of <300 mm and at low magnification (<5×). The use of zoom and focal values other than those recommended can increase the focal point discrepancy between the NIR and visible light images and affect the quality of ICG-VA, resulting in a blurry NIR image.

The usual dose of ICG used is 0.2–0.5 mg/kg. At the time of administration, 25 mg of the dye is dissolved in 5 mL water and flushed with 10 mL of normal saline as a single intravenous bolus. Once the INFRARED 800 mode is activated, the ICG solution is injected through a peripheral line. ICG can cause lower values of peripheral oxygen saturation to be falsely displayed. The surgeon should manipulate and mobilize anatomical structures through the operating oculars of the surgical microscope to

ensure that the bypass graft is visible. Although NIR fluorescence has significantly greater penetration depth than visible light, the blood flow can be appreciated only in exposed blood vessels that are not obscured by anatomical structures, brain parenchyma, surgical instruments, or patties. The ICG fluorescence signal cannot be visualized directly through the operating oculars but is seen on the monitor of the surgical microscope following image processing (13, 14). The operating neurosurgeon can manipulate the vessels while the assistant reports the ICG-VA findings displayed on the screen with the ICG module activated.

An ICG-VA image takes ∼10–30 s to appear on the screen. Once the recording is ended by the user, the automatic playback mode of the operating microscope allows the surgeon to assess the quality of the imaging in detail. ICG-VA can be repeated over time without any significant interference from the residual fluorescence of the previous injection. However, ICG should be reinjected after 20 min to guarantee adequate clearance of the tracer and optimize contrast enhancement (13, 14). Repeated administration of the dye should not exceed a total cumulative dose of 5 mg/kg.

ICG-VA can also analyze the intraluminal flow rate and flow velocity in selected regions of interest. In addition, a graph is generated to display the results of this quantitative analysis in a map delay time. The time characteristics of the graph allow the evaluation of the time to peak, defined as the interval from uprise of a wave to highest signal intensity, and washout time, represented by the interval from uprise of a wave to the time of rapid fall of signal intensity.

APPLICATION OF ICG-VA

Assessment of Graft Patency

During bypass surgery, the assessment of intravascular graft patency is essential to reduce the rate of graft failure. Early intraoperative identification of an occluded graft artery is critical for prompt surgical correction and for early restoration of blood flow to ensure a successful bypass. Several characteristics of the donor and graft vessels have been found to affect bypass function, including the graft diameters and the extent of focal atherosclerotic change (15). Other critical factors that play a role in intraoperative bypass patency include the cerebral blood flow demand of the downstream vascular territory and the direction of blood flow—antegrade vs. retrograde (15, 16). Technical aspects related to the surgical procedure or hypercoagulable states may also be responsible for the occurrence of a graft occlusion (17). Early intraoperative detection of an immediate bypass occlusion using ICG allows us to potentially identify and restore the patency of the bypass to prevent iatrogenic brain ischemia. Early detection may also impact the functional outcome for the patient and decrease the morbidity and mortality associated with revascularization procedures.

Direct intraoperative visual inspection of the anastomotic site cannot always accurately determine the patency of the graft vessel. The postoperative graft patency rate reported in the existing literature for an extracranial-intracranial (EC-IC) bypass is 87–96% (18–22). However, the aforementioned rate varies depending on the intraoperative diagnostic tool used to detect this complication. There are numerous intraoperative monitoring techniques for the evaluation of the graft patency. Among all of them, digital subtraction angiography (DSA) is considered to be the gold standard (23). Despite its diagnostic accuracy in identifying an intraoperative graft occlusion, this diagnostic imaging technique has several limitations, including its invasive nature and the associated risks; high procedural costs; the need for dedicated, trained personnel; and exposure of the patient to prolonged ionizing radiation (18). Moreover, DSA is time-consuming and detects the vessel occlusion in a delayed fashion, in contrast to ICG, which allows for an intraoperative diagnosis and immediate intervention. Other intraoperative monitoring techniques include Doppler ultrasonography (24) and thermal artery imaging (25). Intraoperative microvascular Doppler ultrasonography can be done directly on the bypass graft to assess its patency and quantitatively evaluate the blood flow metrics (26–28). The blood flow values can then be used to calculate the intraoperative cut flow index (CFI), which is the ratio of flow through the graft to the flow through the donor vessel prior to bypass (cut flow). CFI seems to be a sensitive parameter for postoperative bypass patency (29). Indeed, a previous study evaluating 51 bypass procedures for flow augmentation demonstrated that a CFI < 0.5 and CFI > 0.5 were associated with patency rates of 50 and 92%, respectively (28). Alternatively, an ultrasound system with a multifrequency linear probe can be used to perform a standard B-mode acquisition and a color Doppler evaluation with or without ultrasound contrast agents. This technique allows the intraoperative assessment of the arterial course and flow through the intracranial vessels present in the depth of the surgical field, which are deeper than the cortical surface in contact with the probe (30).

However, these techniques have major drawbacks in terms of spatial resolution and image quality, such that blood flow in small perforating arteries cannot be evaluated.

MR and CT angiography are effective non-invasive radiological modalities for evaluation of the patency of the bypass in the early postoperative period (18). Conventional DSA can be employed in the postoperative period to obtain valuable information regarding the graft patency and the dynamics of the bypass functionality (23). Other diagnostic adjuncts like functional cerebral blood flow (CBF) studies, SPECT, and Xe-enhanced CT are indicated to assess the postoperative cerebral perfusion.

As mentioned earlier, ICG-VA is a cost-effective and easy-to-use technique that provides real-time visualization of the fluorescent tracer inflow within cerebral vessels. ICG-VA is ideal for the intraoperative assessment of graft patency, and it seems to be superior to standard angiographic techniques (18). It consists of three different phases: arterial, capillary, and a combined arteriovenous phase generated by the recirculation of the dye. The early arterial phase is the most critical to detect delay or cessation of flow in the bypass graft, arterial branches, or perforators (4). Surgical microscope settings for fluorescence detection might differ substantially from the standard ones adopted for intraoperative visualization under conventional white light. Indeed, flow in perforating vessels is better visualized with a lower magnification and a shorter focus distance (4).

The remarkable spatial resolution of ICG-VA allows assessment of the morphology of graft patency and the hemodynamic of the bypass functioning (18). This diagnostic information is based on the pattern of filling of the graft with the fluorescent tracer compared with the contrast enhancement of the surrounding cerebral blood vessels. Moreover, this property allows the localization of the graft occlusion in real time in case of early bypass failure (13). Revision of the bypass graft might resolve this early intraoperative complication and improve surgical results related to revascularization procedures. Several clinical factors may influence the image quality with ICG-VA, such as the cardiovascular dynamics and cerebrospinal fluid (CSF) accumulation. The technical factors that qualitatively alter ICG-VA images include the speed of ICG injection and microscope settings, such as light intensity, working distance, magnification, and the diameter of the luminous field diaphragm opening. A previous study reported that ICG-VA image quality was notably affected by high magnification and depth of field based on chromatic aberration, as previously elaborated (13, 14).

In a previous series, Woitzik et al. reported bypass function in 31 of 35 (89%) STA-MCA bypasses, 2 of 2 (100%) STA-PCA bypasses, and 6 of 8 (75%) high-flow bypasses (18). Four STA-MCA bypasses had intraoperative occlusion, whereas 2 saphenous vein high-flow bypasses demonstrated moderate graft filling. In all these cases, ICG-VA localized the site of bypass failure at the anastomotic site, and timely surgical revision restored the flow through the bypass. Patency of the graft was subsequently documented by postoperative DSA or CT angiography.

Intraoperative Flow Analysis

Januszewski et al. described three different types of flow through a graft: Type I, robust anterograde flow; Type II, delayed anterograde flow; and Type III, anterograde delayed flow but with no continuity to the bypass site or no convincing flow. This study analyzed 36 EC-IC and intracranial-intracranial (IC-IC) bypasses performed in 33 ischemic patients with hemodynamic compromise despite maximal medical therapy (7). In their cohort, 8% of patients with Type II flow on ICG-VA had CTA findings indicating a graft occlusion within 72 h. Interestingly, none of the patients with Type II or Type III flow pattern had any clinical or radiological evidence of stroke in the postoperative period. This finding may be justified by the presence of competitive collateral flow leading to a lack of demand through the graft. Type III flow can also be caused by either technical surgical complications at the anastomosis or poor arterial graft quality and is associated with a higher probability of eventual graft failure (7). In contrast, failure in a Type II flow pattern is less likely to be related to the presence of competitive regional flow from collateral vessels. Therefore, the authors recommend reexploration of anastomoses in a Type II flow category to detect any early signs of bypass failure with the goal of immediate revision to salvage the bypass. If the quantitative flow characterization on ICG-VA images can be standardized for use across various medical centers, it would overcome a possible observer bias (7). Despite the results of this pilot study, a correlation between the flow characterization and the eventual clinical outcome is yet to be proven.

A quantitative analysis of flow was performed by Awano et al. using a specialized image analysis software (17). The ICG signal was quantified and the perfusion area of ICG was calculated at the point of maximal fluorescence intensity in specific regions of interest on the cortical surface (17). Awano et al. developed an innovative system based on visual light spectroscopy to continuously record hemodynamic changes of cortical blood flow during STA-MCA bypass surgery (17). Two groups of patients were included in this study, patients with and patients without MMD (with other indications for revascularization). The authors demonstrated that the ICG perfusion area was larger with a significant increase in cortical oxygen saturation in the MMD cohort. This could be attributable to the increase of blood flow demand and the larger pressure gradient between the anastomosed STA and the recipient vessels.

ICG-VA Role in Predicting Postoperative Neurological Complications

In recent years, several studies investigated the role of semi-quantitative and quantitative analysis of intraoperative ICG-VA findings in predicting the occurrence of postoperative neurological events after revascularization surgery in MMD. A variety of transient neurological events (TNEs) have been reported in the immediate postoperative period after STA-MCA bypass, which is most commonly employed in MMD treatment. TNEs occur in 14–77% of patients after MMD bypass surgery (3) and include extremity numbness, weakness, and episodic severe headaches (31–34), which could potentially have permanent neurological sequelae (31–34). The underlying causative mechanisms of TNEs are yet to be elucidated. However, the postoperative hemodynamic changes after revascularization procedures suggest that these complications might be related to local cerebral hyperperfusion (HP) (31, 35) or regional inflammation or due to a watershed shift (33, 36). In addition, extravasation of contrast materials in radiological imaging was found to be associated with cerebral HP after revascularization, suggesting a possible role for the breakdown of the blood-brain barrier (37, 38). Horie et al. described the diagnostic criteria for postoperative symptomatic HP as (1) the presence of focal neurologic deficits and/or severe headache, (2) confirmed graft patency by magnetic resonance angiography, (3) evident postoperative increase in CBF, and (4) absence of any ischemic changes and other pathologies (31, 32, 39–41). Postoperative HP occurs more frequently in adults than in pediatric patients in MMD (29, 31, 35). Postoperative radiological HP has been reported to occur in ∼60% of the adult MMD population overall, and ∼30% of the adult MMD population experiences symptomatic HP (35). Some diagnostic adjunct intraoperative laser Doppler or thermal diffusion probe (42) can detect an increase in intraoperative CBF in the anastomotic site, indicative of postoperative HP (43, 44). In addition, the use of infrared imaging, electromagnetic flowmetric, and Adobe Photoshop (Adobe Inc., San Jose, California) software have also been reported for the evaluation of hemodynamics (43–45). In patients

undergoing a STA-MCA bypass for intracranial atherosclerotic disease or symptomatic carotid stenosis, a reduction in CBF and cerebrovascular reserve can be predictive of postoperative HP. However, this phenomenon does not apply to MMD patients (35, 41). In their prospective study, Horie et al. performed ICG-VA after STA-MCA anastomosis and compared cortical perfusion between the adult and pediatric populations with MMD as well as in adult patients with atherosclerotic disease (46). On evaluation of ICG intensity-time curves of the donor (STA), recipient (MCA), and the surrounding vessels, the postoperative HP was assumed to depend on the donor vessel caliber and on the poor integrity of the blood-brain barrier in the recipient. In this context, ICG-VA can be potentially utilized to predict postoperative HP in MMD patients. Similarly, a study by Uchino et al. suggested that semiquantitative analysis of ICG-VA is useful in predicting potential occurrence of HP after STA-MCA anastomosis in occlusive carotid artery disease (47). ICG-VA is effective in assessing intraoperative hemodynamic changes. Moreover, the blood flow index, calculated on the basis of the ICG intensity-time curve, can document the augmentation of cortical perfusion. A blood flow index increase greater than 3-fold from the baseline preoperative value may predict the occurrence of HP, whereas repeated SPECT is necessary to diagnose delayed postoperative HP.

Similarly, Uda et al. analyzed ICG-VA using specialized software (FlowInsight, Infocom Corporation, Shibuya, Tokyo, Japan) that allows the recording of several parameters in different regions of interest around the anastomotic site, including CBF, mean transit time, mean gradation time (Grad), and time to peak (TTP). Percentage change of these parameters after bypass was calculated using the formula ($\Delta X = (Xafter - Xbefore)/Xbefore$). They demonstrated that patients with $\Delta TTP \leq -12$, $\Delta CBF \geq 8$, or $\Delta Grad \geq 30$ have a higher risk of developing postoperative TNEs (3). Hemodynamic changes after bypass surgery, analyzed through ICG and FlowInsight, were predictive of postoperative TNE and correlated with their duration. Optimization of the clinical management of these patients may further reduce TNE-related complications after revascularization procedures. Despite several reports demonstrating the role of hemodynamic changes detected by ICG-VA image analysis in potentially predicting postoperative HP and TNEs, there is no current evidence showing a correlation with improved treatment outcomes. Moreover, the role of ICG-VA in predicting delayed postoperative HP several days after surgery remains uncertain (47). Larger studies are warranted to confirm these results and further elucidate the contribution of this fluorescent intraoperative technique.

Intraoperative Vessel Identification

EC-IC bypass surgery, in particular STA-MCA anastomosis, is the most common revascularization procedure for the treatment of cerebral ischemia. Designed and successfully performed for the first time by Yaşargil in 1967 (48–50), this surgery is aimed at providing alternative blood supply in patients with an underlying hemodynamic cerebrovascular insufficiency (51). Visualization of STA and its branches is critical, and an adequate donor artery can be selected preoperatively using different imaging modalities, including DSA, CTA, and magnetic resonance angiography (49). In addition, the course of STA from the underside of the frontotemporal skin flap can be mapped intraoperatively by light palpation, continuous Doppler ultrasound, or through the assistance of frameless electromagnetic neuronavigation to guarantee a safe dissection (49, 52). The parietal branch of STA is the more commonly used donor graft. However, in certain cases with a planned double-barrel STA-MCA bypass or with an atrophic or damaged parietal STA, the frontal branch of the artery is used. ICG-VA can aid in the intraoperative visualization of STA and assist in the identification of the donor artery, especially when the anterior frontal branch is selected. In addition, ICG-VA provided valuable intraoperative information for the mapping and preparation of the donor vessel (50).

Peña-Tapia et al. first described a new application of ICG-VA to identify a cortical target point and find an adequate recipient vessel (51). They used a rectangular template made of transparent plastic material that can be applied to both sides of the head and with a handle centered on the outer auditory canal. This template-based approach allows the preoperative identification of the end of the sylvian fissure, accurately relying on external landmarks (51). Two different highlighted lines are engraved on the surface of the plastic, and their overall orientation is aimed at identifying several M4 (segment of the MCA) branches emerging from the sylvian fissure, which can be selected as recipient vessels and marked on the patient's scalp.

Previous studies have shown that the application of ICG-VA is not limited to the identification or safe dissection of the STA in bypass procedures. In fact, this intraoperative technique has also been used to selectively target the most suitable cortical M4 recipient artery for flow-preserving bypass to trap complex MCA aneurysms (53). Alternatively, M2-M3 segments of the MCA could also be selected if the anatomy is favorable and the microsurgical dissection of the sylvian fissure is safe (53). However, M2-M3 segments may feed cortical M4 vessels and the STA-MCA anastomosis may redirect the blood supply to uninvolved vascular territories despite the use of anatomical landmarks, neuroimaging, and neuronavigation (52, 54). For this reason, a terminal branch of the MCA (M4) is preferred as a recipient vessel. Moreover, temporary ischemia is considered less invasive and is better tolerated in M4 superficial cortical arteries than in M2-M3 segments (54, 55). During intraoperative ICG-VA, the cortical surface in the surrounding area of the sylvian fissure is analyzed to detect the direction of the flow and possible delayed or reversed filling time of M4 branches during the arterial phase and other vascular structures during the capillary and venous phase (52, 54). Esposito et al. described a primary and a secondary identification in their surgical protocol for intraoperative ICG-VA (53). The primary identification consists of performing a baseline ICG-VA without any temporary occlusion of arterial vessels. On the contrary, the secondary identification consists of intraoperative ICG-VA with a "provocative" temporary occlusion. Delayed fluorescent filling of superficial M4 branches during either primary or secondary identification demarcates the cortical territory supplied, and any artery confined within this area can be selected as the recipient vessel (53). ICG-VA can be repeated

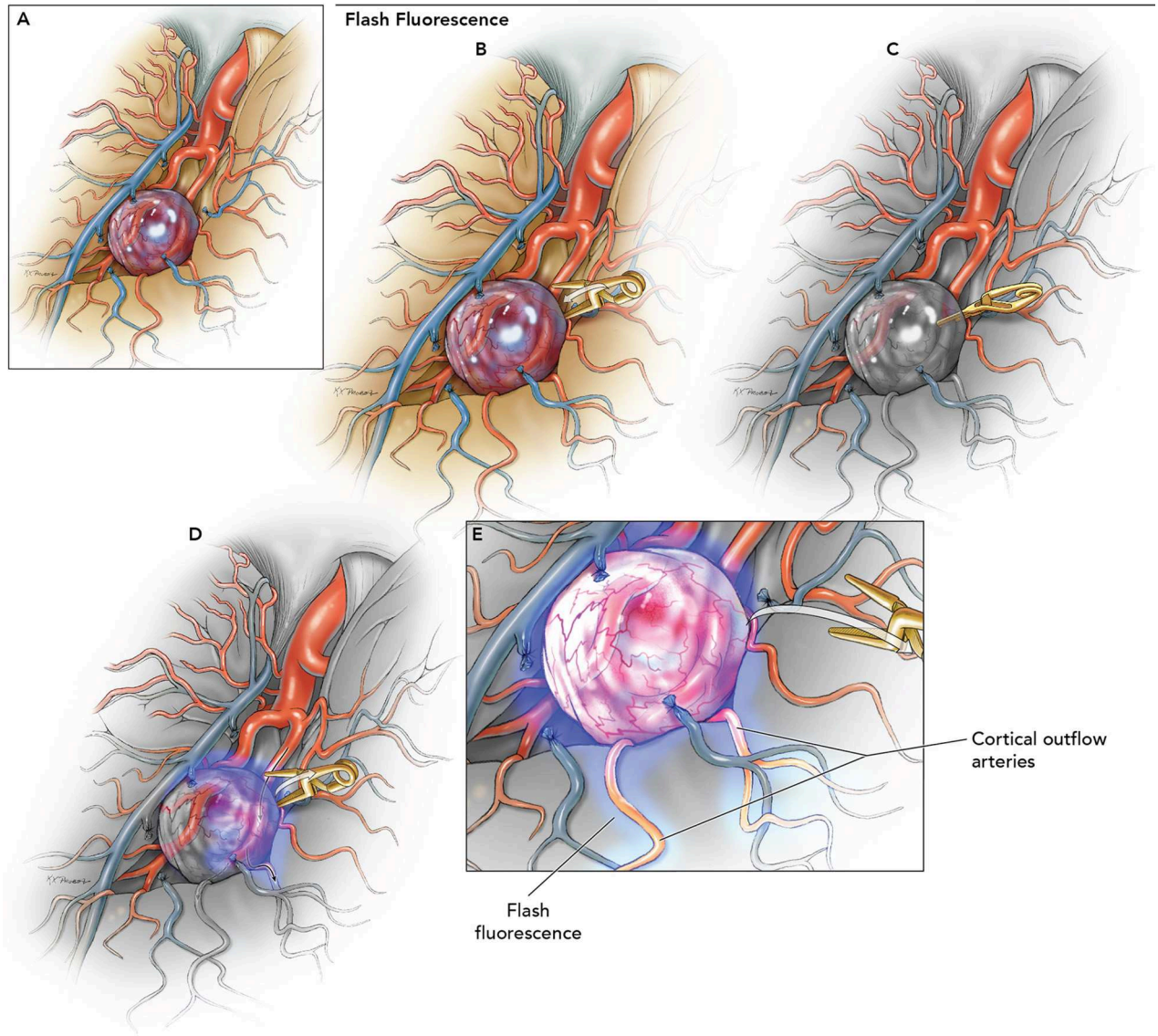

FIGURE 1 | Use of flash fluorescence technique to identify the efferent arteries of the aneurysm using ICG-VA. **(A)** Identification of candidate bypass recipient arteries among the surface M4 branches is difficult but could be improved using the following steps. **(B)** Temporary clip occlusion of the aneurysm inflow (afferent arteries) proximal to the aneurysm. **(C)** ICG-VA demonstrating initial fluorescence in uninvolved arterial branches. **(D)** Removal of temporary clip for aneurysm reperfusion. **(E)** Fluorescence seen in the efferent arteries to identify the most suitable recipient on the cortical surface for the bypass. Used with permission from Lawton (56).

after anastomosis to rule out any residual filling in the complex MCA aneurysm.

The senior author has previously introduced the "flash fluorescence" technique (**Figures 1**, **2**) to select an adequate recipient artery for bypass. The application of this technique is summarized in the three following surgical steps: (1) proximal temporary occlusion of the afferent artery of the aneurysm, (2) ICG-VA to define the uninvolved cortical arteries, and (3) temporary clip removal for reperfusion of the afferent artery and concomitant flash fluorescence ICG run in efferent arteries on the cortical surface (57). The recipient artery is initially dark during the ICG-VA and flash fluorescence. This direct technique enables the selection of the distal recipient artery. An alternative, indirect technique has been described that relies on temporary occlusion of the uninvolved arteries adjacent to the aneurysm's afferent artery. In this case, the efferent arteries illuminate first and simultaneously flash fluorescence with temporary clip removal to highlight the arteries that should not be considered as recipients for the bypass. The direct technique is preferred, as it requires a more limited ischemia time and only one temporary clip. Flash fluorescence is especially valuable with distal MCA aneurysms that require bypass because the identification of a distal cortical recipient prevents unnecessary sylvian fissure dissection. Moreover, brain retraction is not

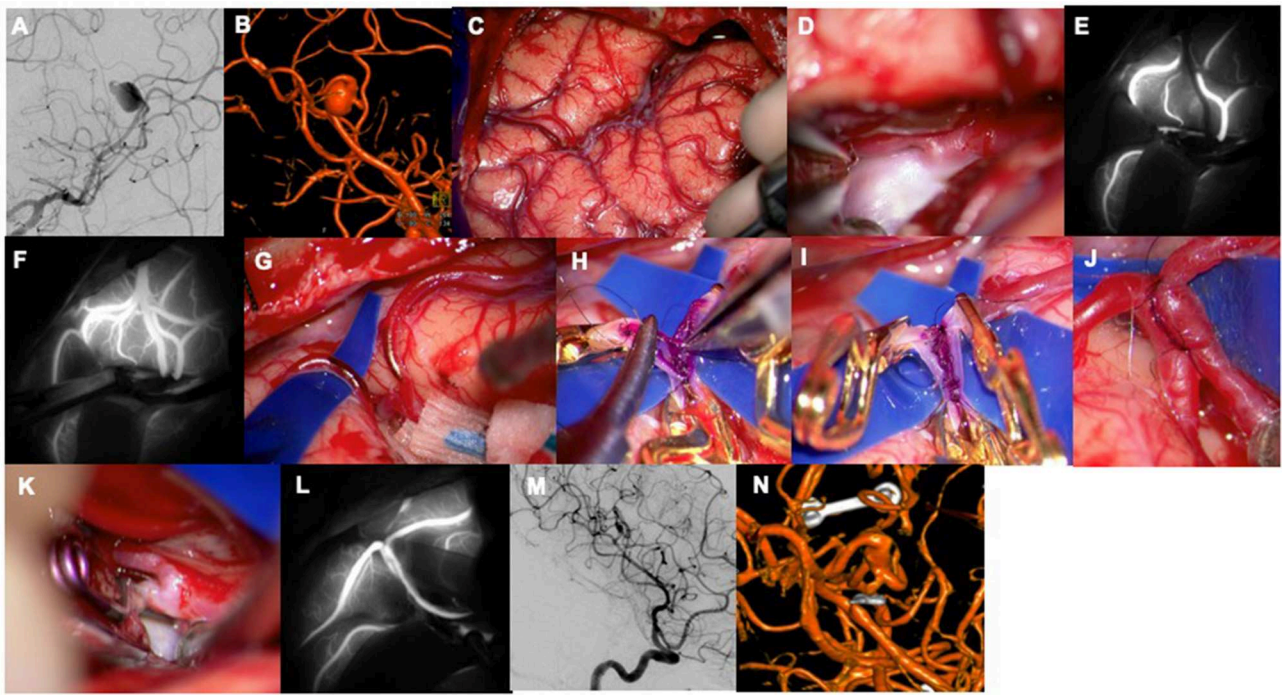

FIGURE 2 | A 47-year-old woman presented with a sudden headache suspicious for sentinel hemorrhage. **(A)** An aneurysm was found at the distal M2 segment with dolichoectatic morphology and two efferent branches (left ICA, AP view). **(B)** Left ICA, 3D reconstruction. **(C)** Sylvian fissure split to access the insular recess. **(D)** Aneurysm with parent artery. **(E)** Flash fluorescence technique was used to identify the efferent vessel to be used as a bypass recipient with proximal temporary clip occlusion. **(F)** Temporary clip removal led to flash ICG filling of this vascular territory and showed the angular artery as the outflow vessel. **(G)** *In situ* bypass of angular artery with posterior temporal artery was performed. **(H)** The intraluminal suture line was sewn with a single anchoring stitch to better visualize the walls. **(I,J)** The extraluminal suture line was sewn loosely, tightened, and tied. **(K)** Proximal aneurysm occlusion. **(L)** M3 MCA-M3 MCA *in situ* bypass perfused the donor angular artery as seen with ICG-VA. **(M)** Left ICA, lateral view. **(N)** Left ICA, 3D reconstruction. Used with permission from Lawton (56).

needed, and the anastomosis is more easily performed on the cortical surface than in the deep sylvian location. Compared with the conventional pterional craniotomy, the bone flap should be extended posteriorly to accommodate the more distal location of the anastomotic site. Other authors reported the use of transdural ICG-VA in STA-MCA bypass procedures to expose the appropriate cortical recipient distributing from the sylvian fissure and superficial vessels anatomy. The location of the recipient was then marked on the dura mater with pyoktanin blue to tailor the dural incision and prevent possible damage during dural opening and microsurgical dissection (58). ICG-VA has also been used to trace the course of the middle meningeal artery (MMA) for use in indirect bypass, encephalo-duro-myo-arterio-pericranial synangiosis for MMD (59). This MMA anterior branch provides collateral flow through the dura mater to the anterior cerebral artery territory both spontaneously and through indirect bypass (60, 61). The standard fronto-temporal craniotomy can damage the anterior branch of MMA given its course within the lesser wing of the sphenoid bone in 50–75% of patients (62, 63). Based on the ICG-VA findings, the craniotomy has been customized into a heart-shaped bone flap to prevent damage to the anterior MMA.

ICG-VA vs. FLUORESCEIN VIDEOANGIOGRAPHY

Fluorescence videoangiography has gained significant traction in the recent years in the practice of complex cerebrovascular neurosurgery. Despite the widespread acceptance of ICG-VA in neurosurgical procedures, the recent reemergence of fluorescein sodium as a fluorescent tracer has prompted authors to investigate and compare fluorescein videoangiography (FL-VA) with ICG-VA. An objective analysis was recently conducted by applying quantitative metrics to data derived from video capture images, which were subsequently elaborated by pixel intensity-analyzing software (62). In this fluorescence study, ICG-VA demonstrated a greater potential for allowing the robust visualization of the extracranial arteries, including the STA and thick intracranial vessels. On the contrary, FL-VA provided superior intraoperative information regarding perforating arteries, distal branches, and small vessels at high magnification deep in the surgical field (62). In addition, FL-VA allows the surgeon to perform a real-time flow assessment and manipulation of vessels of interest by direct intraoperative visualization through the operating microscope oculars.

The widespread acceptance of ICG-VA is attributable to its ease of use along with its diagnostic accuracy, low cost, and good safety profile (64). Another important advantage of ICG-VA is the ability to perform repeated injections with a short refractory period for intraoperative blood flow reassessment (64). The limitations of fluorescein in vascular neurosurgery are mainly related to its tendency to leak more readily into the extravascular space, resulting in a more persistent fluorescent signal in the surgical field that prevents repeated injections (64). Despite their differences, these two fluorescent modalities are complementary in nature, and their application should be based on the surgical procedure, the depth of the operative field, and the size of the vessels of interest.

FUTURE DIRECTION FOR APPLICATION OF ICG-VA

In recent years, a few novel techniques in the application of ICG-VA have been described. These techniques include the introduction of a "second window" ICG technique for glioblastoma resection that capitalizes on the inherent property of permeability of the tumor vasculature. A high dose of ICG is delivered ∼24 h before surgery, leading to non-specific accumulation of the tracer within the tumor tissue. This technique may allow real-time intraoperative tumor identification to optimize surgical resection (65). Additionally, ICG-VA has been used to identify the venous drainage pattern and collateral circulations during tumor resection for possible venous sacrifice to predict and minimize the potential side effects (66). However, the role of these techniques in the setting of revascularization has yet to be elucidated.

Other Applications of ICG-VA

The contribution of ICG-VA has also been investigated for other types of revascularization procedures including coronary artery bypass. The calculated sensitivity and specificity of ICG in detecting 50% stenosis were 83.3 and 100%, respectively (67). However, ICG-VA is associated with several limitations that preclude its widespread acceptance and use in this subspecialty, in contrast to neurosurgery. ICG visualization of pedicle conduits is poorer when compared with skeletonized conduits, and each graft requires up to 4 min to be evaluated, resulting in a significant effect on the operative time (68). Moreover, the "semi-quantitative assessment" of graft patency with ICG-VA provides inadequate information on the distal coronary vasculature as well as competitive flow and transit times (69). Despite other studies showed promising results, the use of ICG for detecting coronary bypass patency has yet to be definitively proven (70).

CONCLUSION

ICG-VA has been widely established as a useful technique to perform qualitative analyses of graft patency and CBF during revascularization procedures. The widespread incorporation of ICG-VA is attributable to its ease of use, diagnostic accuracy, low cost, and excellent safety profile.

AUTHOR CONTRIBUTIONS

CC: literature review, manuscript draft, revision, and final draft approval. SG: manuscript draft, revision, and review of final manuscript. XZ and EB: manuscript draft and review of final draft. DV: literature review and final draft review. PN, MP, and ML: study supervision, review, and revision of the final draft.

FUNDING

EB acknowledges scholarship support (SP-2240.2018.4).

ACKNOWLEDGMENTS

The authors thank the staff of Neuroscience Publications at Barrow Neurological Institute for assistance with manuscript preparation.

REFERENCES

1. Kuroda S, Kashiwazaki D, Hirata K, Shiga T, Houkin K, Tamaki N. Effects of surgical revascularization on cerebral oxygen metabolism in patients with Moyamoya disease: an 15O-gas positron emission tomographic study. *Stroke.* (2014) 45:2717–21. doi: 10.1161/strokeaha.114.006009
2. Miyamoto S, Yoshimoto T, Hashimoto N, Okada Y, Tsuji I, Tominaga T, et al. Effects of extracranial-intracranial bypass for patients with hemorrhagic moyamoya disease: results of the Japan Adult Moyamoya Trial. *Stroke.* (2014) 45:1415–21. doi: 10.1161/strokeaha.113.004386
3. Uda K, Araki Y, Muraoka S, Ota S, Wada K, Yokoyama K, et al. Intraoperative evaluation of local cerebral hemodynamic change by indocyanine green videoangiography: prediction of incidence and duration of postoperative transient neurological events in patients with moyamoya disease. *J Neurosurg.* (2019) 130:1367–75. doi: 10.3171/2017.10.JNS171523
4. Raabe A. *INFRARED 800 Video Angiography a Practical Guide for the Surgeon*. Bern: University Clinic for Neurosurgery (2010).
5. Kogure K, David NJ, Yamanouchi U, Choromokos E. Infrared absorption angiography of the fundus circulation. *Arch Ophthalmol.* (1970) 83:209–14. doi: 10.1001/archopht.1970.00990030211015
6. Sakatani K, Kashiwasake-Jibu M, Taka Y, Wang S, Zuo H, Yamamoto K, et al. Noninvasive optical imaging of the subarachnoid space and cerebrospinal fluid pathways based on near-infrared fluorescence. *J Neurosurg.* (1997) 87:738–45. doi: 10.3171/jns.1997.87.5.0738
7. Januszewski J, Beecher JS, Chalif DJ, Dehdashti AR. Flow-based evaluation of cerebral revascularization using near-infrared indocyanine green videoangiography. *Neurosurg Focus.* (2014) 36:E14. doi: 10.3171/2013.12.Focus13473
8. Jobsis FF. Noninvasive, infrared monitoring of cerebral and myocardial oxygen sufficiency and circulatory parameters. *Science.* (1977) 198:1264–7. doi: 10.1126/science.929199
9. McCormick PW, Stewart M, Goetting MG, Balakrishnan G. Regional cerebrovascular oxygen saturation measured by optical spectroscopy in humans. *Stroke.* (1991) 22:596–602. doi: 10.1161/01.STR.22.5.596
10. Reynolds EO, McCormick DC, Roth SC, Edwards AD, Wyatt JS. New non-invasive methods for the investigation of cerebral oxidative metabolism and haemodynamics in newborn infants. *Ann Med.* (1991) 23:681–6. doi: 10.3109/07853899109148103
11. Miwa M. The principle of ICG fluorescence method. *Open Surg Oncol J.* (2010) 2:26–8. doi: 10.2174/1876504101002020026

12. Feletti A, Wang X, Tanaka R, Yamada Y, Suyama D, Kawase T, et al. Dual-image videoangiography during intracranial microvascular surgery. *World Neurosurg.* (2017) 99:572–9. doi: 10.1016/j.wneu.2016.12.070
13. Kim DL, Cohen-Gadol AA. Indocyanine-green videoangiogram to assess collateral circulation before arterial sacrifice for management of complex vascular and neoplastic lesions: technical note. *World Neurosurg.* (2013) 79:404.e1–6. doi: 10.1016/j.wneu.2012.07.028
14. Shah KJ, Cohen-Gadol AA. The application of FLOW 800 ICG videoangiography color maps for neurovascular surgery and intraoperative decision making. *World Neurosurg.* (2019) 122:e186–97. doi: 10.1016/j.wneu.2018.09.195
15. Vajkoczy P, Horn P, Schmiedek P. Standard superficial temporal artery-middle cerebral artery bypass surgery in hemodynamic cerebral ischemia: indication and technique. *Operat Techn Neurosurg.* (1999) 2:106–15. doi: 10.1016/S1092-440X(99)80002-4
16. Yoon S, Burkhardt JK, Lawton MT. Long-term patency in cerebral revascularization surgery: an analysis of a consecutive series of 430 bypasses. *J Neurosurg.* (2019) 131:86–7. doi: 10.3171/2018.3.Jns172158
17. Awano T, Sakatani K, Yokose N, Kondo Y, Igarashi T, Hoshino T, et al. Intraoperative EC-IC bypass blood flow assessment with indocyanine green angiography in moyamoya and non-moyamoya ischemic stroke. *World Neurosurg.* (2010) 73:668–74. doi: 10.1016/j.wneu.2010.03.027
18. Woitzik J, Horn P, Vajkoczy P, Schmiedek P. Intraoperative control of extracranial-intracranial bypass patency by near-infrared indocyanine green videoangiography. *J Neurosurg.* (2005) 102:692–8. doi: 10.3171/jns.2005.102.4.0692
19. EC/IC Bypass Study Group. Failure of extracranial-intracranial arterial bypass to reduce the risk of ischemic stroke. Results of an international randomized trial. *New Engl J Med.* (1985) 313:1191–200. doi: 10.1056/nejm198511073131904
20. Mendelowitsch A, Taussky P, Rem JA, Gratzl O. Clinical outcome of standard extracranial-intracranial bypass surgery in patients with symptomatic atherosclerotic occlusion of the internal carotid artery. *Acta Neurochir.* (2004) 146:95–101. doi: 10.1007/s00701-003-0154-7
21. Sundt TM Jr, Siekert RG, Piepgras DG, Sharbrough FW, Houser OW. Bypass surgery for vascular disease of the carotid system. *Mayo Clin Proc.* (1976) 51:677–92.
22. Schmiedek P, Piepgras A, Leinsinger G, Kirsch CM, Einhupl K. Improvement of cerebrovascular reserve capacity by EC-IC arterial bypass surgery in patients with ICA occlusion and hemodynamic cerebral ischemia. *J Neurosurg.* (1994) 81:236–44. doi: 10.3171/jns.1994.81.2.0236
23. Yanaka K, Fujita K, Noguchi S, Matsumaru Y, Asakawa H, Anno I, et al. Intraoperative angiographic assessment of graft patency during extracranial-intracranial bypass procedures. *Neurol Med Chir.* (2003) 43:509–12; discussion 13. doi: 10.2176/nmc.43.509
24. Badie B, Lee FT Jr, Pozniak MA, Strother CM. Intraoperative sonographic assessment of graft patency during extracranial-intracranial bypass. *AJNR Am J Neuroradiol.* (2000) 21:1457–9.
25. Nakagawa A, Hirano T, Uenohara H, Sato M, Kusaka Y, Shirane R, et al. Intraoperative thermal artery imaging of an EC-IC bypass in beagles with infrared camera with detectable wave-length band of 7-14 microm: possibilities as novel blood flow monitoring system. *Minim Invasive Neurosurg.* (2003) 46:231–4. doi: 10.1055/s-2003-42357
26. Charbel FT, Hoffman WE, Misra M, Ostergren L. Ultrasonic perivascular flow probe: technique and application in neurosurgery. *Neurol Res.* (1998) 20:439–42. doi: 10.1080/01616412.1998.11740545
27. Nakayama N, Kuroda S, Houkin K, Takikawa S, Abe H. Intraoperative measurement of arterial blood flow using a transit time flowmeter: monitoring of hemodynamic changes during cerebrovascular surgery. *Acta Neurochir.* (2001) 143:17–24. doi: 10.1007/s007010170133
28. Amin-Hanjani S, Du X, Mlinarevich N, Meglio G, Zhao M, Charbel FT. The cut flow index: an intraoperative predictor of the success of extracranial-intracranial bypass for occlusive cerebrovascular disease. *Neurosurgery.* (2005) 56(1 Suppl.):75–85; discussion 75–85. doi: 10.1227/01.neu.0000143032.35416.41
29. Fujimura M, Inoue T, Shimizu H, Saito A, Mugikura S, Tominaga T. Efficacy of prophylactic blood pressure lowering according to a standardized postoperative management protocol to prevent symptomatic cerebral hyperperfusion after direct revascularization surgery for moyamoya disease. *Cerebrovasc Dis.* (2012) 33:436–45. doi: 10.1159/000336765
30. Prada F, Del Bene M, Casali C, Saladino A, Legnani FG, Perin A, et al. Intraoperative navigated angiosonography for skull base tumor surgery. *World Neurosurg.* (2015) 84:1699–707. doi: 10.1016/j.wneu.2015.07.025
31. Fujimura M, Kaneta T, Mugikura S, Shimizu H, Tominaga T. Temporary neurologic deterioration due to cerebral hyperperfusion after superficial temporal artery-middle cerebral artery anastomosis in patients with adult-onset moyamoya disease. *Surg Neurol.* (2007) 67:273–82. doi: 10.1016/j.surneu.2006.07.017
32. Hayashi K, Horie N, Suyama K, Nagata I. Incidence and clinical features of symptomatic cerebral hyperperfusion syndrome after vascular reconstruction. *World Neurosurg.* (2012) 78:447–54. doi: 10.1016/j.wneu.2011.10.041
33. Hamano E, Kataoka H, Morita N, Maruyama D, Satow T, Iihara K, et al. Clinical implications of the cortical hyperintensity belt sign in fluid-attenuated inversion recovery images after bypass surgery for moyamoya disease. *J Neurosurg.* (2017) 126:1–7. doi: 10.3171/2015.10.Jns151022
34. Machida T, Nakano S, Ishige S, Ono J, Fujikawa A. Subcortical low-intensity lesions on fluid-attenuated inversion recovery images after revascularization surgery for moyamoya disease. *World Neurosurg.* (2017) 98:512–9. doi: 10.1016/j.wneu.2016.11.058
35. Uchino H, Kuroda S, Hirata K, Shiga T, Houkin K, Tamaki N. Predictors and clinical features of postoperative hyperperfusion after surgical revascularization for moyamoya disease: a serial single photon emission CT/positron emission tomography study. *Stroke.* (2012) 43:2610–6. doi: 10.1161/strokeaha.112.654723
36. Hayashi T, Shirane R, Fujimura M, Tominaga T. Postoperative neurological deterioration in pediatric moyamoya disease: watershed shift and hyperperfusion. *J Neurosurg Pediatr.* (2010) 6:73–81. doi: 10.3171/2010.4.Peds09478
37. Sharma P, Poppe AY, Eesa M, Steffanhagan N, Hudon M, Morrish W. Extravasating contrast material on angiography following carotid angioplasty and stenting: not necessarily subarachnoid hemorrhage. *J Neuroimaging.* (2010) 20:180–2. doi: 10.1111/j.1552-6569.2008.00316.x
38. Takayama K, Nakagawa H, Iwasaki S, Taoka T, Wada T, Myouchin K, et al. Cerebral hemorrhage with angiographic extravasation immediately after carotid artery stenting. *Radiat Med.* (2007) 25:359–63. doi: 10.1007/s11604-007-0147-1
39. Fujimura M, Mugikura S, Kaneta T, Shimizu H, Tominaga T. Incidence and risk factors for symptomatic cerebral hyperperfusion after superficial temporal artery-middle cerebral artery anastomosis in patients with moyamoya disease. *Surg Neurol.* (2009) 71:442–7. doi: 10.1016/j.surneu.2008.02.031
40. Fujimura M, Shimizu H, Inoue T, Mugikura S, Saito A, Tominaga T. Significance of focal cerebral hyperperfusion as a cause of transient neurologic deterioration after extracranial-intracranial bypass for moyamoya disease: comparative study with non-moyamoya patients using N-isopropyl-p-[(123)I]iodoamphetamine single-photon emission computed tomography. *Neurosurgery.* (2011) 68:957–64; discussion 64–5. doi: 10.1227/NEU.0b013e318208f1da
41. Kaku Y, Iihara K, Nakajima N, Kataoka H, Fukuda K, Masuoka J, et al. Cerebral blood flow and metabolism of hyperperfusion after cerebral revascularization in patients with moyamoya disease. *J Cereb Blood Flow Metab.* (2012) 32:2066–75. doi: 10.1038/jcbfm.2012.110
42. Mukerji N, Cook DJ, Steinberg GK. Is local hypoperfusion the reason for transient neurological deficits after STA-MCA bypass for moyamoya disease? *J Neurosurg.* (2015) 122:90–4. doi: 10.3171/2014.8.Jns132413
43. Nakagawa A, Fujimura M, Arafune T, Sakuma I, Tominaga T. Clinical implications of intraoperative infrared brain surface monitoring during superficial temporal artery-middle cerebral artery anastomosis in patients with moyamoya disease. *J Neurosurg.* (2009) 111:1158–64. doi: 10.3171/2009.4.Jns08585
44. Kawamata T, Kawashima A, Yamaguchi K, Hori T, Okada Y. Usefulness of intraoperative laser Doppler flowmetry and thermography to predict a risk of postoperative hyperperfusion after superficial temporal artery-middle cerebral artery bypass for moyamoya disease. *Neurosurg Rev.* (2011) 34:355–62; discussion 62. doi: 10.1007/s10143-011-0331-8

45. Mizumura S, Nakagawara J, Takahashi M, Kumita S, Cho K, Nakajo H, et al. Three-dimensional display in staging hemodynamic brain ischemia for JET study: objective evaluation using SEE analysis and 3D-SSP display. *Ann Nucl Med.* (2004) 18:13–21. doi: 10.1007/BF02985609
46. Horie N, Fukuda Y, Izumo T, Hayashi K, Suyama K, Nagata I. Indocyanine green videoangiography for assessment of postoperative hyperperfusion in moyamoya disease. *Acta Neurochir.* (2014) 156:919–26. doi: 10.1007/s00701-014-2054-4
47. Uchino H, Kazumata K, Ito M, Nakayama N, Kuroda S, Houkin K. Intraoperative assessment of cortical perfusion by indocyanine green videoangiography in surgical revascularization for moyamoya disease. *Acta Neurochir.* (2014) 156:1753–60. doi: 10.1007/s00701-014-2161-2
48. Yaşargil MG. *Microsurgery Applied to Neurosurgery*. Stuttgart: Georg Thieme Verlag (1969). Available online at: https://books.google.com/books?id=K_ogBQAAQBAJ&printsec=frontcover&dq=yasargil+microsurgery+applied+to+neurosurgery&hl=en&newbks=1&newbks_redir=0&sa=X&ved=2ahUKEwiE6bzxlKrlAhVDqJ4KHVLaCQEQuwUwAHoECAYQBQ#v=onepage&q=yasargil%20microsurgery%20applied%20to%20neurosurgery&f=false.
49. Newell DW, Vilela MD. Superficial temporal artery to middle cerebral artery bypass. *Neurosurgery.* (2004) 54:1441–8; discussion 8–9. doi: 10.1227/01.NEU.0000124754.84425.48
50. Esposito G, Burkhardt JK, Bozinov O, Regli L. Indocyanine green videoangiography for the identification of superficial temporal artery branches in EC-IC bypass surgery. *Acta Neurochir.* (2016) 158:565–70. doi: 10.1007/s00701-016-2703-x
51. Peña-Tapia PG, Kemmling A, Czabanka M, Vajkoczy P, Schmiedek P. Identification of the optimal cortical target point for extracranial-intracranial bypass surgery in patients with hemodynamic cerebrovascular insufficiency. *J Neurosurg.* (2008) 108:655–61. doi: 10.3171/jns/2008/108/4/0655
52. Esposito G, Durand A, Van Doormaal T, Regli L. Selective-targeted extra-intracranial bypass surgery in complex middle cerebral artery aneurysms: correctly identifying the recipient artery using indocyanine green videoangiography. *Neurosurgery.* (2012) 71(2 Suppl.):ons274–84; discussion ons84–5. doi: 10.1227/NEU.0b013e3182684c45
53. Esposito G, Dias S, Burkhardt JK, Bozinov O, Regli L. Role of indocyanine green videoangiography in identification of donor and recipient arteries in cerebral bypass surgery. *Acta Neurochir Suppl.* (2018) 129:85–9. doi: 10.1007/978-3-319-73739-3_12
54. Esposito G, Regli L. Selective Targeted cerebral revascularization via microscope integrated indocyanine green videoangiography technology. *Acta Neurochir Suppl.* (2014) 119:59–64. doi: 10.1007/978-3-319-02411-0_10
55. Kronenburg A, Esposito G, Fierstra J, Braun KP, Regli L. Combined bypass technique for contemporary revascularization of unilateral MCA and bilateral frontal territories in moyamoya vasculopathy. *Acta Neurochir Suppl.* (2014) 119:65–70. doi: 10.1007/978-3-319-02411-0_11
56. Lawton MT. Seven Bypasses: Tenets and Techniques for Revascularization. New York, NY: Thieme (2018).
57. Rodriguez-Hernandez A, Lawton MT. Flash fluorescence with indocyanine green videoangiography to identify the recipient artery for bypass with distal middle cerebral artery aneurysms: operative technique. *Neurosurgery.* (2012) 70(2 Suppl.):209–20. doi: 10.1227/NEU.0b013e31823158f3
58. Yokota H, Yonezawa T, Yamada T, Miyamae S, Kim T, Takamura Y, et al. Transdural indocyanine green videography for superficial temporal artery-to-middle cerebral artery bypass-technical note. *World Neurosurg.* (2017) 106:446–9. doi: 10.1016/j.wneu.2017.07.004
59. Tanabe N, Yamamoto S, Kashiwazaki D, Akioka N, Kuwayama N, Noguchi K, et al. Indocyanine green visualization of middle meningeal artery before craniotomy during surgical revascularization for moyamoya disease. *Acta Neurochir.* (2017) 159:567–75. doi: 10.1007/s00701-016-3060-5
60. Dusick JR, Gonzalez NR, Martin NA. Clinical and angiographic outcomes from indirect revascularization surgery for Moyamoya disease in adults and children: a review of 63 procedures. *Neurosurgery.* (2011) 68:34–43; discussion. doi: 10.1227/NEU.0b013e3181fc5ec2
61. Kuroda S, Houkin K. Bypass surgery for moyamoya disease: concept and essence of sugical techniques. *Neurol Med Chir.* (2012) 52:287–94. doi: 10.2176/nmc.52.287
62. Matano F, Mizunari T, Murai Y, Kubota A, Fujiki Y, Kobayashi S, et al. Quantitative comparison of the intraoperative utility of indocyanine green and fluorescein videoangiographies in cerebrovascular surgery. *Oper Neurosurg.* (2017) 13:361–6. doi: 10.1093/ons/opw020
63. Ma S, Baillie LJ, Stringer MD. Reappraising the surface anatomy of the pterion and its relationship to the middle meningeal artery. *Clin Anat.* (2012) 25:330–9. doi: 10.1002/ca.21232
64. Lane B, Bohnstedt BN, Cohen-Gadol AA. A prospective comparative study of microscope-integrated intraoperative fluorescein and indocyanine videoangiography for clip ligation of complex cerebral aneurysms. *J Neurosurg.* (2015) 122:618–26. doi: 10.3171/2014.10.Jns132766
65. Zeh R, Sheikh S, Xia L, Pierce J, Newton A, Predina J, et al. The second window ICG technique demonstrates a broad plateau period for near infrared fluorescence tumor contrast in glioblastoma. *PLoS ONE.* (2017) 12:e0182034. doi: 10.1371/journal.pone.0182034
66. Acerbi F, Vetrano IG, Sattin T, Falco J, de Laurentis C, Zattra CM, et al. Use of ICG videoangiography and FLOW 800 analysis to identify the patient-specific venous circulation and predict the effect of venous sacrifice: a retrospective study of 172 patients. *Neurosurg Focus.* (2018) 45:E7. doi: 10.3171/2018.4.Focus18120
67. Desai ND, Miwa S, Kodama D, Koyama T, Cohen G, Pelletier MP, et al. A randomized comparison of intraoperative indocyanine green angiography and transit-time flow measurement to detect technical errors in coronary bypass grafts. *J Thorac Cardiovasc Surg.* (2006) 132:585–94. doi: 10.1016/j.jtcvs.2005.09.061
68. Taggart DP, Choudhary B, Anastasiadis K, Abu-Omar Y, Balacumaraswami L, Pigott DW. Preliminary experience with a novel intraoperative fluorescence imaging technique to evaluate the patency of bypass grafts in total arterial revascularization. *Ann Thorac Surg.* (2003) 75:870–3. doi: 10.1016/s0003-4975(02)04669-6
69. Leacche M, Balaguer JM, Byrne JG. Intraoperative grafts assessment. *Semin Thorac Cardiovasc Surg.* (2009) 21:207–12. doi: 10.1053/j.semtcvs.2009.08.007
70. Ohmes LB, Di Franco A, Di Giammarco G, Rosati CM, Lau C, Girardi LN, et al. Techniques for intraoperative graft assessment in coronary artery bypass surgery. *J Thorac Dis.* (2017) 9(Suppl. 4):S327–32. doi: 10.21037/jtd.2017.03.77

Conflict of Interest: The authors declare that the research was conducted in the absence of any commercial or financial relationships that could be construed as a potential conflict of interest.

frontiers in Surgery

REVIEW
published: 11 December 2019
doi: 10.3389/fsurg.2019.00070

Application of Indocyanine Green During Arteriovenous Malformation Surgery: Evidence, Techniques, and Practical Pearls

Chase H. Foster[1], *Peter J. Morone*[2], *Samuel B. Tomlinson*[3] *and Aaron A. Cohen-Gadol*[4]*

[1] Department of Neurological Surgery, George Washington University Hospital, Washington, DC, United States, [2] Department of Neurological Surgery, Vanderbilt University Medical Center, Vanderbilt University, Nashville, TN, United States, [3] School of Medicine and Dentistry, University of Rochester Medical Center, Rochester, NY, United States, [4] Goodman Campbell Brain and Spine, Department of Neurological Surgery, Indiana University, Indianapolis, IN, United States

OPEN ACCESS

Edited by:
Evgenii Belykh, Barrow Neurological Institute (BNI), United States

Reviewed by:
Robert Thomas Wicks, Barrow Neurological Institute (BNI), United States
Jinbing Zhao, Nanjing Brain Hospital Affiliated to Nanjing Medical University, China

***Correspondence:**
Aaron A. Cohen-Gadol
acohenmd@gmail.com

Specialty section:
This article was submitted to Neurosurgery, a section of the journal Frontiers in Surgery

Received: *05 June 2019*
Accepted: *20 November 2019*
Published: *11 December 2019*

Citation:
Foster CH, Morone PJ, Tomlinson SB and Cohen-Gadol AA (2019) Application of Indocyanine Green During Arteriovenous Malformation Surgery: Evidence, Techniques, and Practical Pearls. Front. Surg. 6:70. doi: 10.3389/fsurg.2019.00070

Indocyanine green (ICG) is a fluorescent molecule that enables visualization of hemodynamic flow through blood vessels. The first description of its application to the resection of arteriovenous malformations (AVMs) did not occur until 2007. Since then, industry leaders have rapidly integrated this optical technology into the intraoperative microscope, and the use of ICG videoangiography (VA) has since become routine in AVM surgery among some academic centers. A number of case series have been published since the introduction of ICG VA to AVM neurosurgery. These early reports with small sample sizes were largely qualitative, assigning to the technology "usefulness" and "benefit" scores as perceived by the operators. This lack of objectivity prompted the development of FLOW 800 software, a proprietary technology of Carl Zeiss Meditec AG (Oberkochen, Germany) that can quantify relative fluorescence intensity under the microscope to generate color maps and intensity curves for *ad hoc* and *post hoc* analyses, respectively. However, subsequent case series have done little to quantify the effect of ICG VA on outcomes. The available literature predominately concludes that ICG VA, although intuitive to deploy and interpret, is limited by its dependence on direct illumination and visualization. The subcortical components of AVMs represent a natural challenge to ICG-based flow analysis, and the scope of ICG VA has therefore been limited to AVMs with a high proportion of superficial angioarchitecture. As a result, digital subtraction angiography has remained the gold standard for confirming AVM obliteration. In this review, we provide an overview of the existing literature on ICG VA in AVM resection surgery. In addition, we describe our own experiences with ICG VA and AVMs and offer the senior author's surgical pearls for optimizing the marriage of fluorescence flow technology and AVM resection surgery.

Keywords: AVM, fluorescence, indocyanine green, neurosurgery, resection, videoangiography

INTRODUCTION

A tenant of any neurosurgical operation is the maintenance of perfusion by way of avoiding undue vascular compromise. In the resection of intracerebral arteriovenous malformations (AVMs), this means the exclusion of en passage (i.e., uninvolved) vessels as well as the protection of nidal draining veins until arterial feeders have been disconnected (1). Indocyanine green (ICG) is a non-specific fluorescein-like dye that can be injected systemically to help delineate the margins of vascular anatomy under direct visualization and represents one such maneuver to successfully accomplish these goals. ICG videoangiography (VA) specifically is useful in this endeavor in that it enables the operator to directly and immediately assess the integrity of vessels under the intraoperative microscope.

Since its introduction to the field, the utility of ICG VA in optimizing the margins of safety during AVM resection has become more widely accepted. Now, some authors would posit that ICG VA is a standard component of AVM resection surgery (2). Both single-institution (3) and expert-driven (1) reports of the practicality of ICG VA as an intraoperative armament have been bolstered by larger reviews of the topic by various research cooperatives in recent years (2, 4, 5). A contemporaneous review of the topic is warranted to refresh neurosurgeons' understanding of ICG's important role in neurosurgery as it relates to AVM resection surgery and to provide an updated synthesis of available data.

HISTORY OF ICG

ICG dye was first introduced to the field of medicine after its approval by the Food and Drug Administration in 1956 (6). Providers soon discovered it to be helpful in a variety of specialties, beginning with cardiology and ending, for our purposes, in neurosurgery in 1995, when Hongo et al. (7) applied ICG to the study of cerebral hemodynamics. Their seminal work was followed by that of Raabe et al. (8), who in 2003 used ICG VA during the microsurgical clipping of intracerebral aneurysms. The use of ICG VA in neurovascular surgery has become ubiquitous, if not expected, since the subsequent introduction of an ICG VA integrated microscope to the neurosurgical operating room by Carl Zeiss Meditec. Its usefulness for excluding residual nidus in AVM resection has been endorsed repeatedly since the formative work by Takagi et al. (9) in 2007 and by Killory et al. (10) 2 years later. Part of ICG VA's appeal stems from data suggesting that it can produce results somewhat comparable to those of digital subtraction angiography (DSA) (8), which is considered the gold-standard method of assessing AVM resection completeness (11). The relatively recent development of FLOW 800 quantitative software (Carl Zeiss Meditec) has perhaps helped to mitigate some of the often-cited shortcomings of ICG VA (discussed below) by providing a measure of objectivity to this otherwise subjective auxiliary (12).

Abbreviations: AVM, arteriovenous malformation; DSA, digital subtraction angiography; ICG, indocyanine green; SMG, Spetzler-Martin grade; VA, videoangiography.

ICG PHARMACOLOGY

ICG ($C_{43}H_{47}N_2NaO_6S_2$) is a water-soluble molecule with a molecular weight of 744 g/mol (13). ICG is similar to the perhaps more familiar fluorescein in that the fluorescent properties of both are exploited to define vascular borders intraoperatively (13). Specifically, the tricarbocyanine structure of ICG is responsible for its near-infrared fluorescence, having peak excitation and emission wavelengths at 800 and 830 nm, respectively (11, 14). ICG becomes highly bound to plasma proteins such as albumin immediately after systemic intravenous injection, with a 95% rate of binding after just 1–2 s (6, 13). Physically, the molecule is too large to cross the blood–brain barrier and thus collects and concentrates only in intravascular compartments without invading surrounding parenchyma (14). ICG travels uninhibited and unfiltered through intracranial vessels after the standard 2-mL (i.e., 5 mg ICG/1 mL H_2O) bolus (15–17) is injected into a peripheral vein and appears in as little as 2–3 s under the fluorescent surgical microscope, lasting for a matter of several moments (6, 11). It also harbors favorable pharmacokinetic properties for its purpose of highlighting intraluminal flow. The biological activity of ICG is largely nil inside the body; although it is widely distributed, the liver is the only organ to actively take up ICG (6). Furthermore, the toxicity of ICG is low (2), meaning that several rounds of ICG infusion are generally well-tolerated by the majority of patients, and adverse effects occur only very rarely (17). The most likely adverse effect is allergic cross-reaction in patients with hypersensitivity to iodinated compounds; this, too, has been only very rarely documented (16). With its low side effect profile and negligible overall biologic activity (and thus, toxicity) successive rounds of ICG infusions are limited mainly by parameters such as time until already-present videoangiographic fluorescence dissipates. Practically, because ICG may accumulate in tissues where the blood-brain barrier has been disrupted, the consequential pooling of fluorescence in these areas may obfuscate nearby anatomy if multiple rounds of ICG VA are performed (14).

This combination of physical and pharmacological characteristics makes ICG an ideal choice for delineating superficial AVM anatomy and excluding intervening brain parenchyma. Although near-infrared fluoroscopy has been shown to "penetrate several centimeters into tissue" (18, 19), the obfuscation of deeper anatomy by dilated cortical vessels limits its utility during AVM resection to only real-time evaluation of superficial vascular topography (20). This limitation will be discussed further.

EVIDENCE FROM AND APPLICATIONS DURING AVM RESECTION

The 2007 report by Takagi et al. (9) is the often-cited first publicized use of ICG VA in AVM surgery. In their case report, the authors described the then-novel application of ICG to detect residual nidus during the resection of a Spetzler-Martin grade (SMG) III AVM from a 2-year-old child that was otherwise

missed by intraoperative angiography. In their astute recognition of the potential that this newly integrated ICG VA technology might hold, this case report laid the foundation as the first documented use of ICG, and underscored its ancillary use as an immediately available intraoperative adjunct to the angiographic gold standard. Since 2007, several groups of seasoned operators have applied ICG VA to cohorts of patients afflicted with an AVM (1, 3, 10, 12, 15, 21–25).

Killory et al. (10) were the next to publish their experience; they reported their experience with ICG VA used in 10 consecutive AVM resections. Building on the anecdotal success of their predecessors, they effectively applied intraoperative fluorescence and found it subjectively useful for the detection of feeding arteries into the AVM nidus. They also detected a small residual nidus in 1 case. However, they were also the first to draw attention to this technique's major limitation. Namely, deeper vessels could not be visualized with ICG VA in 2 of their patients; those vessels were detected only after they resorted to DSA.

One year later, Ferroli et al. (23) published a case report detailing the use of ICG VA during microvascular decompression for trigeminal neuralgia in a 52-year-old woman in whom a micro-AVM was the unexpected etiology. In this article, they described the usefulness of ICG VA's ability to provide data about flow dynamics of visualized vessels (more specifically, to enable the operator to diagnose the malformation on the basis of an arterialized petrosal vein). Although fluorescent videoangiography did not ultimately surmount the technical challenges of completely resecting this lesion, it did provide data to help the surgeon avoid making the potentially morbid or mortal error of incorrectly ligating the vessel. Their case highlighted a major advantage of ICG VA: its availability and intuitiveness in the operating room, even when its use was not predicted a priori.

That same year, more than 500 miles away, neurosurgeons in Germany reported similar results in 15 patients with an AVM (22). The resolution of resultant videospatial output was graded by researchers in this series, who found ICG injection runs to be of "excellent" quality in the large majority of cases. In 2 of these cases, the ICG VA elucidated information that affected the operative plan, but it failed to fully visualize draining vessels in 1 case (reportedly secondary to the field depth and insufficient illumination).

Nearly 9,000 miles from their German colleagues, Khurana et al. (16) assessed the intuitiveness and usefulness of ICG VA with a "benefit" grade in 4 Australian patients undergoing 5 AVM resection surgeries. The perceived benefit grade was described as a numerical scale from 1 to 4 with the following criteria: "1" indicated that the ICG application was "not useful"; "2" indicated that the fluorescence was seen as "useful, but not affecting surgical management"; a "3" meant that ICG VA was both "useful and affected surgical management"; and a benefit grade of "4" indicated that it provided "false reassurance" (16). ICG VA received a benefit score of 3 in 3 of these patients, indicating that the surgeons found the fluorescence both useful for and influential in surgical management. However, these positive data are tempered by the outcome of the fourth patient; a 22-year-old woman who had a ruptured SMG III insular AVM. ICG VA initially falsely reassured the operators, and a repeat elective resection was necessary (benefit score of 4). In fact, of the 46 operations in which ICG VA was used (which included open aneurysm repair, bypass operations, and tumor resections), this case was the only instance of ICG VA directly misleading the researchers.

Perhaps summarizing 2010's international experience with ICG VA in AVM surgeries, Wang et al. (26) concluded, after retrospective analysis of 43 AVM resections, that no one adjunctive intraoperative modality, ICG VA included, could persistently delineate anatomy and lesional boundaries with the fidelity of DSA. Other groups, such as Taddei et al. (27) on the basis of their own success in 9 AVM operations in India, contrarily maintained that ICG VA might subvert DSA in some cases.

FLOW 800 QUANTIFICATION

The first article describing the use of FLOW 800 quantitative software was published in 2011. Just 4 years after the first publication on ICG VA and AVM surgery, Faber et al. (1) sought to address the subjectivity shortcoming of the technology. Prior to their group's contribution to the methodology, flow quantification had been attempted in several ways as far back as 1998 (28) via laser Doppler perfusion imaging in murine models (29), and diffuse optical spectroscopy with concurrent magnetic resonance correlation in both murine and porcine subjects (28, 30). These methods, however, were impractical in their complexity, requiring both sophisticated technologies and extensive time for interpretation. These obstacles made these earlier methods impractical in the operating room, in which rapid yet accurate assessment would be required. FLOW 800 software was developed to this end. The software is currently available on the OPMI Pentero and Kinevo 900 microscopes (12). FLOW 800 is an analytical software integrated into the intraoperative fluorescent microscope that transcribes the visual data obtained during ICG-laden vessel perfusion into arbitrary intensity units, which then are mathematically corrected for variance in native physiologic flow and fed through a proprietary algorithm to generate a color-coded tissue perfusion map in real time (31). The output of this process can only be considered "semi-quantitative" at best, as the arbitrary intensity units that inform the outputted data are themselves imprecise, non-real data (32). This calculated map also provides information about ICG dye intensity, time to change in intensity from 10 to 90% (i.e., "rise time"), and transit time, which is then interpreted post hoc and used to guide further surgical maneuvers (17, 32).

In the report by Faber et al. (1), this technology was applied during 2 AVM resections: an SMG I incidental malformation in a 38-year-old woman's left frontal lobe, and an epileptogenic SMG III lesion in the right temporal lobe of a 26-year-old man. It is notable that the authors specifically stated that their report was limited to these 2 cases because the lesions therein had characteristics amenable to trialing the newly developed color-encoded flow technology. Nevertheless, the authors described their inaugural experience favorably. In one respect, they

commended the ergonomics of the FLOW 800 application in the operating room, even for novice users. In another, they found that quantitation of flow provided valuable insight to understanding how hemodynamics into and out of the AVM nidus were affected by ligation and resection as the procedure progressed. However, these advantages were not enough to overcome the inability of ICG VA to provide data about complex 3-dimensional structures; it remains ill-equipped to assess along the z-axis of deep-seated AVMs. As stated by Kalyvas and Spetzler (33), because FLOW 800 output is calculated from ICG VA input, it will inevitably suffer from the same lack of penetrance.

After their influential first report, Takagi et al. (15) and Kamp et al. (31) reported in 2012 on their continued experiences with 27 runs of ICG VA with FLOW 800 analysis and DSA in a series of 11 and 2 AVM resections, respectively. The researchers used ICG VA at various time points during their procedures, split roughly equally between uses before dissection, after arterial feeder clippings, and after dissection, as guided by perceived need and experience. When compared to DSA, ICG VA performed comparably, visualizing nidal filling before dissection and reliably excluding residual nidal filling after resection in 100% of cases. However, even in experienced hands, ICG VA fell short of matching the ability of DSA to visualize arterial feeding vessels (33 vs. 100%, respectively) and venous drainage vessels (89 vs. 100%, respectively). Although the authors praised ICG VA's intraoperative facility, they concluded by noting its inferiority to the DSA gold standard, particularly in regard to the detection of feeders. Furthermore, the small cohort of patients was specifically chosen for the superficial drainage patterns of their lesions, which might have further biased their opinion about the usefulness of ICG VA.

Ng et al. (21) further discussed the limitations of ICG in AVM resection in their retrospective study published the following year. Over 3 years, ICG VA with FLOW 800 quantification was performed 49 times in their cohort of 24 patients with AVMs. Their experience in many ways mirrored that of previous publications. Namely, ICG VA was useful primarily in confirming totality of resection by way of the absence of fluorescent flow through the primary draining vein. The authors found ICG VA in the detection of arterial feeders before dissection less useful than others had reported before them. In this cohort, 15% of predissection ICG runs were considered not useful by researchers because of "a thin layer of adherent clot" (21). Furthermore, although the authors endorsed FLOW 800 quantitative analysis for helping to distinguish between entering and exiting vessels on the basis of flow delay and intensity, they also lamented the need for relatively trivial maneuvers (i.e., removal of cottonoids, blood, and cerebrospinal fluid from the operative field) to prevent inaccurate ICG intensity readings during quantification. This study was unique in that it did not use concomitant DSA in validating the results of ICG VA. A study of 25 AVM surgeries by Ye et al. (25) that same year recapitulated these data closely, reporting that quantification and emulation of transit time was more useful than visualization on normal playback mode alone in differentiating pathologic from native vessels *in situ*.

In 2014, the Spetzler group published what is thought to be the largest consecutive case series of ICG VA in AVM surgery to date (3). They retrospectively reviewed data from 130 patients divided nearly equally into ICG and no-ICG groups that were otherwise similar according to patient and baseline lesion characteristics, and their results revealed no statistically significant difference between the extent of AVM resection or improvement in functional outcome as measured by the modified Rankin score at 6 weeks (12.5 vs. 14.9%, respectively) (3). Despite these equivocal data, the authors maintained that the results were at least in part attributable to the poor penetrance of direct light and consequent ICG fluorescence in deeper vasculature. The study encouraged its continued use in surgery to treat superficially seated AVMs.

A 2015 study of 7 patients who underwent ICG VA–mediated AVM resection by Fukuda et al. (34) resulted in the first detailed quantitative assessment of flow delay (measured by time to half-maximum fluorescence intensity) at various stages of the operation. Their data revealed that these calculated parameters are reliable and intuitive indicators of decreased intranidal flow after sequential and successful feeder clipping. The authors recommended FLOW 800 as reasonable inclusion in the cerebrovascular neurosurgeon's AVM armamentarium given its ability to provide data on changing hemodynamics as the resection progresses. However, a commentary on this study by Kalyvas and Spetzler (33) throttled this notion to a degree by reiterating that FLOW 800 will share the same limitations as non-quantitative ICG VA, because its output also relies on what fluorescence can be directly observed on the surface.

SPINAL AVMs

Vascular malformations of the spinal cord are grossly similar to their intracranial counterparts, yet are also distinct entities that require a specialized surgical approach. There are far fewer available data regarding the application of ICG VA techniques to these lesions in the neurosurgical library because, in part, of their overall lower incidence (35). Nevertheless, several recent case series have described institutional-specific techniques for ICG application to spinal AVMs in larger cohorts (35–37). Similar to the relationship between DSA and ICG VA of cerebral vessels, ICG VA of spinal vasculature is an increasingly employed intraoperative alternative to the "gold standard" of selective spinal angiography. ICG VA has been used adjunctively in the operating room even after preoperative selective spinal angiography was performed, particularly when the lesion of interest has multiple feeders or appears to be primarily irrigated via the indispensable Artery of Adamkiewicz (36, 37). The arguments for and against ICG VA in spinal AVMs are likewise remarkably similar, with advocates championing ICG VA's practicality and ease of rapid intraoperative interpretation to help inform safe surgical resection and preservation of uninvolved angioarchitecture (37). The technique for its infusion during surgery is also similar, and follows a regimented paradigm of a 25 mg bolus diluted in 50 mL of sterile normal saline via a peripheral vein (35, 37). The slightly modified semi-quantitative

software, IR800 (also a product of Carl Zeiss Meditec), may also be readily employed through equipped intraoperative surgical microscopes to aid in the often-challenging identification of niduses and fistulas.

These published reports, though limited to single institution case series, reflect on several years of operator experience in applying ICA VA to the resection of spinal AVMs. They represent a small but apparently growing consensus on ICG VA's usefulness to these challenging operations. Although far more research is needed to address the current paucity of published data on the matter, these foundational case series are sparking innovation and unique applications of their own. In a recent study by Hamauchi et al. (38), ICG was used in combination with catheter-based intraoperative super-selective spinal angiography and high frame rate videography to help identify abnormal vasculature in a single thoracic intramedullary AVM. The slow-motion replaying of the captured video data was reportedly influential in the surgeons' resection approach, and provided crucial qualitative feedback in real-time to help guide an effective operation. This report on a single patient and lesion obviously warrants further rigorous investigation to prove its merits, but is representative of the ongoing interest in applying ICG VA to help treat challenging vascular malformations of the spinal cord.

SURGICAL PEARLS

The limitations previously discussed are perhaps unsurprising to the neurosurgical community at large. The predominately deep-to-superficial anatomical arrangement of intracranial vessels inherently limits any modality that relies on direct visualization and illumination. Today, no means to fully rectify this limitation has been found, but it still might be attenuated by a combination of operator experience and deft applications of the technology. For example, in 2017, one such experienced group published a video documenting their surgical treatment of a large, eloquently located frontoparietal SMG III AVM in a 31-year-old man who presented with hemiparesis after the malformation ruptured (24). The challenges of the case included the largely subcortical focus of the AVM and its proximity to the central sulcus. Despite these challenges, the surgeons prudently used ICG VA to detect a superficial arterialized draining vein from the lesion and simultaneously differentiated it from the nearby vein of Trolard. The authors used this finding to navigate a subcortical dissection path for the complete resection of the AVM per standard resection techniques. Aptly named the "safe sulcus" approach, this clever application of ICG VA exploits its aforementioned superficial limitation to identify an appropriate starting point for subcortical dissection. This approach has since been adopted by other groups with similar success (39). It represents a novel application of a no-longer-novel neurosurgical technology.

The senior author recently published his experience using ICG VA in a small group of patients who were undergoing cerebrovascular neurosurgery (12) (**Figure 1**). FLOW 800 software was used in 10 patients with an AVM in this case series of 23 for the purpose of guiding intraoperative planning and progression. It is the senior author's practice to use only the color maps that are output after semi-quantification because the fluorescence curves that are produced, although valuable in their own right, are not amenable to rapid intraoperative evaluation and thereby extend the patient's time in surgery. ICG was injected intravenously before dissection of the malformation to delineate the angioarchitecture of the lesion and to reliably differentiate involved structures including the feeding arteries from arterialized veins and the uninvolved *en passage* vessels. Of note, to accurately evaluate ICG VA intraoperatively, it is necessary to position the operative microscope at a predefined distance from the operative field and adjust the zoom and focus accordingly. These variables are dependent upon the microscope, and one should consult the microscope's user manual prior to the case.

In 2 of these cases, careful study of the resultant maps enabled the disconnection of an arterialized draining vein and preservation of crucial normal venous drainage. In another illustrative case of a medial parasagittal AVM, mobilization of the hemisphere was made possible after ICG VA enabled the operator to discern high-throughput cortical arterialized bridging veins from those less vigorously irrigated and therefore safe for sacrifice. To our knowledge, this application of the technology is not represented elsewhere in the literature. Although it requires a coupling of comfort with the interhemispheric approach and confidence in interpreting color map data, quantified ICG VA can be cautiously adapted for this purpose.

Nuanced quantitative ICG VA color mapping is particularly useful in a subset of AVMs with specific characteristics, as previous studies have concluded. Intraoperative fluorescent flow analysis directly influenced dissection strategies in each of the cases in the senior author's study. We find ICG VA to be most effective when judicious patient and lesion selection has occurred. For example, superficial AVM anatomy may appear obscured to the naked eye because of overlying dense arachnoid bands. In these cases, ICG VA makes an important contribution to the surgical stratagem by providing real-time data on vascular structures that would otherwise have to be dissected blindly and therefore haphazardly, guided by direct visualization alone. It is also regularly used, in our experience, when there is concern for inadvertent clip-induced *en passage* vessel stenosis. The integrated FLOW 800–capable operative microscope makes evaluation in these cases especially easy by obviating the need to rearrange surgical equipment during the operation. In fact, at least 1 study found ICG VA to be statistically significantly faster to deploy than DSA (34).

The additional time needed to perform DSA might nevertheless be warranted by the equipoise of safety in some situations. For example, in a 2013 article, Kono et al. (40) described the intra-arterial infusion of ICG into the common carotid and vertebral arteries. Although this technique successfully differentiated AVM feeding vessels from normal native arteries, we opine that the additional risk of arterial catheterization in the neck likely nullifies the benefit gained and can be performed more safely via standard DSA. For these reasons, we respectfully do not recommend this form of ICG VA technique.

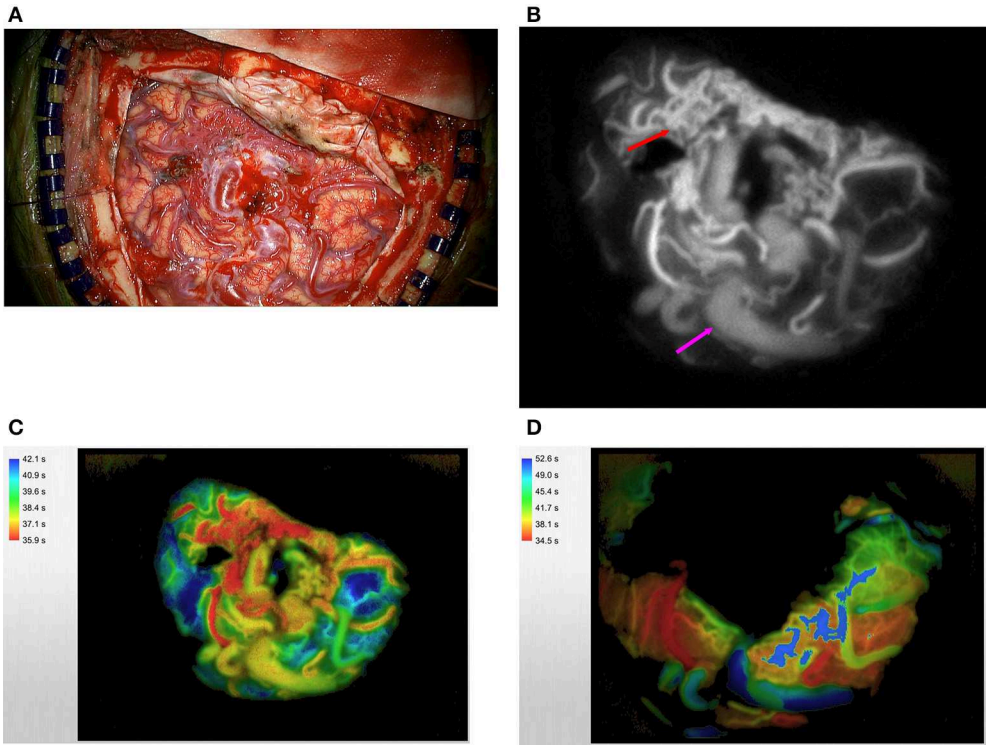

FIGURE 1 | A large right temporoparietal AVM is exposed **(A)**. ICG videoangiography **(B)** demonstrates the early filling of the arterial feeders (red arrow) and delayed filling of arterialized veins (purple arrow); this technique can confirm the identity of these vessels more accurately especially if they are covered by thick arachnoid bands. This information can also guide the early steps of disconnection to start in the area where the concentration of feeding arteries is most (red arrow). The same AVM was analyzed via the use of FLOW 800 software. Please note the feeding arteries in red, arterialized veins in yellow, and normal veins in blue **(C)**. Post-resection FLOW 800 analysis demonstrates that the primary vein is now blue **(D)**.

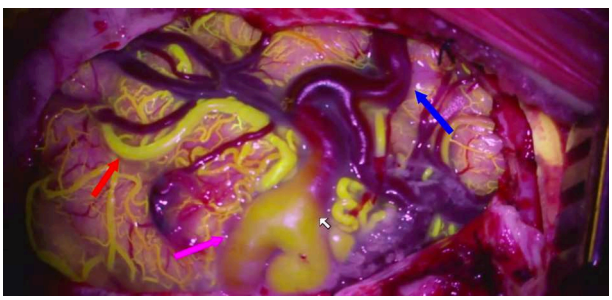

FIGURE 2 | Fluorescein videoangioram of a parietal AVM demonstrates the relative flow in different components of the AVM: feeding artery (red arrow), arterialized vein (purple arrow), and normal vein (blue arrow).

Our team has also used fluorescein in place of the ICG and has found reasonable results similar to those of the ICG (41, 42). The advantage of fluorescein over ICG is that the dye can be visualized through the microscope's binoculars (**Figure 2**) (43).

Altogether, these data make a strong argument for the role of ICG VA as an adjunct modality in AVM surgery, fulfilling a specific purpose with relative ease in a specific group of lesions. This general gestalt seems to be shared by other experienced operators at high-volume centers (3, 33). Despite the strides made toward objectifying ICG VA with FLOW 800 and the new applications being conceived by shrewd surgeons, current data suggest that ICG VA cannot emulate AVM anatomy with fidelity superior to that of DSA, especially for subcortical structures.

CONCLUSION

Studies unanimously agree that ICG VA with FLOW 800 quantitative analysis is an accurate method of delineating superficial AVM structures, but it suffers in regard to deeper structures. In our opinion and experience, it can be used effectively to guide cortical entry points for subcortical dissections and to inform the safe sacrifice of tethering secondary cortical arterialized veins in certain surgical approaches. Likewise, the generated color maps of FLOW 800 are practical, easily interpreted intraoperatively, and sufficient for guiding surgical resection. Although ICG VA has advantages over DSA in terms of deployment speed and ease of use, its inability to visualize subcortical AVM components remains a looming obstacle. Therefore, DSA remains the gold-standard method of confirming complete AVM occlusion (33).

Only 1 systematic review (4) and 2 general reviews (2, 5) of the data on ICG VA in AVM surgery exist in the neurosurgical

literature. The systematic review by Scerrati et al. (4), which was published in 2014 and included 7 of the AVM studies available at the time, succinctly concluded that ICG VA might portend a "modest benefit" during AVM resection. Indeed, there is a paucity of adequately powered, prospective, multicenter studies that have investigated the true effect size that this fluorescent technology has on various outcome measures. Although current data on the topic are an amalgam of anecdotes and subjectivity, experienced groups of surgeons worldwide seem to agree that the low toxicity, non-invasiveness, intuitiveness, and real-time feedback offered by ICG VA make it a reasonable tool in the cerebrovascular neurosurgeon's repertoire for open AVM resection. Although the margins and magnitude of this role have yet to be established, it is a meritorious goal for future research.

AUTHOR CONTRIBUTIONS

CF performed literature review, synthesized data, and prepared the draft of the final manuscript. PM reviewed, edited, and augmented the drafted manuscript. ST assisted with gathering and contributing data for the drafting of the manuscript. AC-G reviewed and edited the drafted manuscript, provided expertise to technical portions of the manuscript, and provided supervisory support.

REFERENCES

1. Faber F, Thon N, Fesl G, Rachinger W, Guckler R, Tonn JC, et al. Enhanced analysis of intracerebral arterioveneous malformations by the intraoperative use of analytical indocyanine green videoangiography: technical note. *Acta Neurochir*. (2011) 153:2181–7. doi: 10.1007/s00701-011-1141-z
2. Cenzato M, Dones F, Boeris D, Marcati E, Fratianni A, Crisa FM, et al. Contemporary tools in arteriovenous malformations surgery. *J Neurosurg Sci*. (2018) 62:467–77. doi: 10.23736/S0390-5616.18.04398-9
3. Zaidi HA, Abla AA, Nakaji P, Chowdhry SA, Albuquerque FC, Spetzler RF. Indocyanine green angiography in the surgical management of cerebral arteriovenous malformations: lessons learned in 130 consecutive cases. *Neurosurgery*. (2014) 10:246–51. doi: 10.1227/NEU.0000000000000318
4. Scerrati A, Della Pepa GM, Conforti G, Sabatino G, Puca A, Albanese A, et al. Indocyanine green video-angiography in neurosurgery: a glance beyond vascular applications. *Clin Neurol Neurosurg*. (2014) 124:106–13. doi: 10.1016/j.clineuro.2014.06.032
5. Balamurugan S, Agrawal A, Kato Y, Sano H. Intra operative indocyanine green video-angiography in cerebrovascular surgery: An overview with review of literature. *Asian J Neurosur*. (2011) 6:88–93. doi: 10.4103/1793-5482.92168
6. Bervini D, Raabe A. Principles of indocyanine green videoangiography. In: Hadjipanayis CG, Stummer W, editors. *Fluorescence-Guided Neurosurgery: Neuro-oncology and Cerebrovascular Applications*. 1st ed. New York, NY: Thieme Medical Publishers, Inc. (2018). p. 125–31.
7. Hongo K, Kobayashi S, Okudera H, Hokama M, Nakagawa F. Noninvasive cerebral optical spectroscopy: depth-resolved measurements of cerebral haemodynamics using indocyanine green. *Neurol Res*. (1995) 17:89–93. doi: 10.1080/01616412.1995.11740293
8. Raabe A, Beck J, Gerlach R, Zimmermann M, Seifert V. Near-infrared indocyanine green video angiography: a new method for intraoperative assessment of vascular flow. *Neurosurgery*. (2003) 52:132–9. doi: 10.1227/00006123-200301000-00017
9. Takagi Y, Kikuta K, Nozaki K, Sawamura K, Hashimoto N. Detection of a residual nidus by surgical microscope-integrated intraoperative near-infrared indocyanine green videoangiography in a child with a cerebral arteriovenous malformation. *J Neurosurg*. (2007) 107:416–8. doi: 10.3171/PED-07/11/416
10. Killory BD, Nakaji P, Gonzales LF, Ponce FA, Wait SD, Spetzler RF. Prospective evaluation of surgical microscope-integrated intraoperative near-infrared indocyanine green angiography during cerebral arteriovenous malformation surgery. *Neurosurgery*. (2009) 65:456–62. doi: 10.1227/01.NEU.0000346649.48114.3A
11. Yeung JT, Kalani MY, Nakaji P. Applications of indocyanine green video angiography in neurovascular surgery. In: Spetzler RF, Kalani MYS, Nakaji P, editors. *Neurovascular Surgery*. 2nd ed. New York, NY: Thieme Medical Publishers, Inc. (2015). p. 194–200.
12. Shah KJ, Cohen-Gadol AA. The application of FLOW 800 ICG videoangiography color maps for neurovascular surgery and intraoperative decision making. *World Neurosurg*. (2018) 122:e186–97. doi: 10.1016/j.wneu.2018.09.195
13. Pogue BW, Gibbs-Strauss S, Valdes PA, Samkoe K, Roberts DW, Paulsen KD. Review of neurosurgical fluorescence imaging methodologies. *IEEE J Sel Top Quantum Electron*. (2010) 16:493–505. doi: 10.1109/JSTQE.2009.2034541
14. Roberts DW, Valdes PA. Indocyanine green. In: Bernstein M, Berger MS, editors. *Neuro-Oncology: The Essentials*. 3rd ed. New York, NY: Thieme Medical Publishers, Inc. (2014). p. 136–46.
15. Takagi Y, Sawamura K, Hashimoto N, Miyamoto S. Evaluation of serial intraoperative surgical microscope-integrated intraoperative near-infrared indocyanine green videoangiography in patients with cerebral arteriovenous malformations. *Neurosurgery*. (2012) 70:34–42. doi: 10.1227/NEU.0b013e31822d9749
16. Khurana VG, Seow K, Duke D. Intuitiveness, quality and utility of intraoperative fluorescence videoangiography: Australian neurosurgical experience. *Brit J Neurosurg*. (2010) 24:163–72. doi: 10.3109/02688690903518247
17. Kato N, Prinz V, Dengler J, Vajkoczy P. Blood flow assessment of arteriovenous malformations using intraoperative indocyanine green videoangiography. *Stroke Res Treat*. (2019) 2019:7292304. doi: 10.1155/2019/7292304
18. Desmettre T, Devoisselle JM, Mordon S. Fluorescence properties and metabolic features of indocyanine green (ICG) as related to angiography. *Surv Ophthalmol*. (2000) 45:15–27. doi: 10.1016/S0039-6257(00)00123-5
19. Liebert A, Wabnitz H, Obrig H, Erdmann R, Moller M, Macdonald R, et al. Non-invasive detection of fluorescence from exogenous chromophores in the adult human brain. *Neuroimage*. (2006) 31:600–8. doi: 10.1016/j.neuroimage.2005.12.046
20. Mascitelli JR, Burkhardt J-K, Lawton MT. Indocyanine green videoangiography and arteriovenous malformations. In: Hadjipanayis CG, Stummer W, editors. *Fluorescence-Guided Neurosurgery: Neuro-Oncology and Cerebrovascular Applications*. 1st ed. New York, NY: Thieme Medical Publishers, Inc. (2018). p. 133–40.
21. Ng YP, King NK, Wan KR, Wang E, Ng I. Uses and limitations of indocyanine green videoangiography for flow analysis in arteriovenous malformation surgery. *J Clin Neurosci*. (2013) 20:224–32. doi: 10.1016/j.jocn.2011.12.038
22. Hanggi D, Etminan N, Steiger HJ. The impact of microscope-integrated intraoperative near-infrared indocyanine green videoangiography on surgery of arteriovenous malformations and dural arteriovenous fistulae. *Neurosurgery*. (2010) 67:1094–103. doi: 10.1227/NEU.0b013e3181eb5049
23. Ferroli P, Acerbi F, Broggi M, Broggi G. Arteriovenous micromalformation of the trigeminal root: intraoperative diagnosis with indocyanine green videoangiography: case report. *Neurosurgery*. (2010) 67:(3 Suppl Operative):onsE309–10; discussion: onsE10. doi: 10.1227/01.NEU.0000381769.15291.4C
24. Rustemi O, Scienza R, Della Puppa A. Utility of indocyanine green videoangiography in subcortical arteriovenous malformation resection. *Neurosurg Focus*. (2017) 43:V10. doi: 10.3171/2017.7.FocusVid.1774
25. Ye X, Liu XJ, Ma L, Liu LT, Wang WL, Wang S, et al. Clinical values of intraoperative indocyanine green fluorescence video angiography with Flow 800 software in cerebrovascular surgery. *Chin Med J*. (2013) 126:4232–7. doi: 10.3760/cma.j.issn.0366-6999.20131649

26. Wang S, Liu L, Zhao YL, Zhang D, Wang R, Zhao JZ. Strategy for assisted cerebral arteriovenous malformation surgery. *Zhonghua yi xue za zhi*. (2010) 90:869–73.
27. Taddei G, Tommasi CD, Ricci A, Galzio RJ. Arteriovenous malformations and intraoperative indocyanine green videoangiography: preliminary experience. *Neurology India*. (2011) 59:97–100. doi: 10.4103/0028-3886.76878
28. Kuebler WM, Sckell A, Habler O, Kleen M, Kuhnle GE, Welte M, et al. Noninvasive measurement of regional cerebral blood flow by near-infrared spectroscopy and indocyanine green. *J Cerebral Blood Flow Metab*. (1998) 18:445–56. doi: 10.1097/00004647-199804000-00013
29. Wuestenfeld JC, Herold J, Niese U, Kappert U, Schmeisser A, Strasser RH, et al. Indocyanine green angiography: a new method to quantify collateral flow in mice. *J Vascular Surg*. (2008) 48:1315–21. doi: 10.1016/j.jvs.2008.06.049
30. Cuccia DJ, Bevilacqua F, Durkin AJ, Merritt S, Tromberg BJ, Gulsen G, et al. *In vivo* quantification of optical contrast agent dynamics in rat tumors by use of diffuse optical spectroscopy with magnetic resonance imaging coregistration. *Appl Optics*. (2003) 42:2940–50. doi: 10.1364/AO.42.002940
31. Kamp MA, Slotty P, Turowski B, Etminan N, Steiger HJ, Hanggi D, et al. Microscope-integrated quantitative analysis of intraoperative indocyanine green fluorescence angiography for blood flow assessment: first experience in 30 patients. *Neurosurgery*. (2012) 7065–73. doi: 10.1227/NEU.0b013e31822f7d7c
32. Prinz V, Hecht N, Kato N, Vajkoczy P. FLOW 800 allows visualization of hemodynamic changes after extracranial-to-intracranial bypass surgery but not assessment of quantitative perfusion or flow. *Neurosurgery*. (2014) 10(Suppl. 2):231–8; discussion: 8–9. doi: 10.1227/NEU.0000000000000277
33. Kalyvas J, Spetzler RF. Does FLOW 800 technology improve the utility of indocyanine green videoangiography in cerebral arteriovenous malformation surgery? *World Neurosurgery*. (2015) 83:147–8. doi: 10.1016/j.wneu.2014.09.010
34. Fukuda K, Kataoka H, Nakajima N, Masuoka J, Satow T, Iihara K. Efficacy of FLOW 800 with indocyanine green videoangiography for the quantitative assessment of flow dynamics in cerebral arteriovenous malformation surgery. *World Neurosurgery*. (2015) 83:203–10. doi: 10.1016/j.wneu.2014.07.012
35. Rangel-Castilla L, Russin JJ, Zaidi HA, Martinez-Del-Campo E, Park MS, Albuquerque FC, et al. Contemporary management of spinal AVFs and AVMs: lessons learned from 110 cases. *Neurosurgical Focus*. (2014) 37:E14. doi: 10.3171/2014.7.FOCUS14236
36. Walsh DC, Zebian B, Tolias CM, Gullan RW. Intraoperative indocyanine green video-angiography as an aid to the microsurgical treatment of spinal vascular malformations. *Brit J Neurosurg*. (2014) 28:259–66. doi: 10.3109/02688697.2013.829556
37. Jing L, Su W, Guo Y, Sun Z, Wang J, Wang G. Microsurgical treatment and outcomes of spinal arteriovenous lesions: learned from consecutive series of 105 lesions. *J Clin*. (2017) 46:141–7. doi: 10.1016/j.jocn.2017.09.003
38. Hamauchi S, Osanai T, Seki T, Kawabori M, Okamoto M, Hida K, et al. Intraoperative real-time identification of abnormal vessels within the bright field by superselective arterial injection of saline and its slow-motion recording using a high frame rate digital camera during surgical treatment of spinal arteriovenous shunts: technical note. *J Neurosurg Spine*. (2018) 29:576–81. doi: 10.3171/2018.3.SPINE1854
39. Muhammad S, Niemela M, Lehecka M. Utility of video indocyanine angiography to detect the cortical entry point of a draining vein with a superficial vein during arteriovenous malformation surgery. *World Neurosurgery*. (2019) 122:428. doi: 10.1016/j.wneu.2018.11.054
40. Kono K, Uka A, Mori M, Haga S, Hamada Y, Nagata S. Intra-arterial injection of indocyanine green in cerebral arteriovenous malformation surgery. *Turkish Neurosurg*. (2013) 23:676–9. doi: 10.5137/1019-5149.JTN.6420-12.0
41. Lane BC, Cohen-Gadol AA. A prospective study of microscope-integrated intraoperative fluorescein videoangiography during arteriovenous malformation surgery: preliminary results. *Neurosurg Focus*. (2014) 36:E15. doi: 10.3171/2013.11.FOCUS13483
42. Lane BC, Cohen-Gadol AA. Fluorescein fluorescence use in the management of intracranial neoplastic and vascular lesions: a review and report of a new technique. *Curr Drug Discov Technol*. (2013) 10:160–9. doi: 10.2174/1570163811310020009
43. Rey-Dios R, Cohen-Gadol AA. Technical principles and neurosurgical applications of fluorescein fluorescence using a microscope-integrated fluorescence module. *Acta Neurochir*. (2013) 155:701–6. doi: 10.1007/s00701-013-1635-y

Conflict of Interest: AC-G is a consultant for Carl Zeiss Meditec AG.

The remaining authors declare that the research was conducted in the absence of any commercial or financial relationships that could be construed as a potential conflict of interest.

frontiers in Surgery

REVIEW
published: 21 January 2020
doi: 10.3389/fsurg.2019.00081

Photodynamic Therapy for the Treatment of Glioblastoma

*Samuel W. Cramer and Clark C. Chen**

Department of Neurosurgery, University of Minnesota, Minneapolis, MN, United States

Glioblastoma is the most common form of adult brain cancer and remains one of the deadliest of human cancers. The current standard-of-care involves maximal tumor resection followed by treatment with concurrent radiation therapy and the chemotherapy temozolomide. Recurrence after this therapy is nearly universal within 2 years of diagnosis. Notably, >80% of recurrence is found in the region adjacent to the resection cavity. The need for improved local control in this region, thus remains unmet. The FDA approval of 5-aminolevulinic acid (5-ALA) for fluorescence guided glioblastoma resection renewed interests in leveraging this agent as a means to administer photodynamic therapy (PDT). Here we review the general principles of PDT as well as the available literature on PDT as a glioblastoma therapeutic platform.

Keywords: brain tumor, photodynamic therapy (PDT), glioblastoma multiforme (GBM), tumor-targeting, neurosurgery

OPEN ACCESS

Edited by:
Eberval Figueiredo, University of São Paulo, Brazil

Reviewed by:
Konstantin Slavin, University of Illinois at Chicago, United States
Mario Ganau, University of Trieste, Italy

***Correspondence:**
Clark C. Chen
ccchen@umn.edu

Specialty section:
This article was submitted to Neurosurgery, a section of the journal Frontiers in Surgery

Received: *26 September 2019*
Accepted: *23 December 2019*
Published: *21 January 2020*

Citation:
Cramer SW and Chen CC (2020) Photodynamic Therapy for the Treatment of Glioblastoma. Front. Surg. 6:81. doi: 10.3389/fsurg.2019.00081

INTRODUCTION

Glioblastoma is a malignant central nervous system (CNS) neoplasm with histologic features resembling astrocytic cells. It is the most common form of primary brain cancer, with an incidence of 3.19 per 100,000 people in the United States (1). Glioblastomas are aggressive and infiltrative, with microscopic extension into normal brain parenchyma (2, 3). Invading tumor cells exhibit characteristic migratory patterns, including spread beneath the pial margin (subpial spread), along neurons (perineuronal spread), along cerebrovasculature (perivascular satellitosis), or along white matter tracts (intrafascicular spread) (4). Microscopic, infiltrating cells are found centimeters from the margin of the visible tumor mass (5). As such, surgical resection is not curative. The current standard-of-care involves maximal, safe surgical resection followed by concurrent chemotherapy (temozolomide) and fractionated radiotherapy (FRT) (6–9). The overall prognosis for glioblastoma patients is poor, with reported median survival of 14.6 months (7), and tumor recurrence near universal.

The observation that >80.0% of the recurrences are located adjacent to the resection cavity suggests utility for therapeutic platforms targeting this region (10–13). The recent United States Food and Drug Administration (FDA) approval of 5-aminolevulinic acid (5-ALA) for fluorescence guided resection (FGR) of tumors renewed interests in leveraging this agent as a means to administer photodynamic therapy (PDT). In principle PDT to the resection cavity can minimize the risk of local recurrence. In this article, we will review the current state of the literature as it pertains to PDT as a glioblastoma therapeutic platform.

METHODS

The goal of this article is to provide a current state of the art review of photodynamic therapies for the treatment of glioblastoma. To this end, we aim to provide an overview of the

development of photodynamic therapy for glioblastoma, describe the physical mechanism of the therapeutic approach, describe known interactions between PDT and pharmacological treatments, as well as predict future developments in this field. Therefore, a comprehensive literature search was performed in PubMed (MEDLINE) using MeSH terms "photodynamic therapy gliomas" which resulted in 480 articles. The type of publications considered included clinical and pre-clinical trials, systematic reviews and case series. Relevant publications were then selected based upon validated academic metrics including journal impact factor and i10 factor.

Principle of Photodynamic Therapy (PDT)

PDT involves photo-activation of a photosensitizer molecule that is selectively incorporated into neoplastic cells. Photo-irradiation activates the photosensitizer by transfer of energy to the sensitizer resulting in excitation of molecular oxygen to a singlet or triplet state. In the singlet state the energy is converted to heat (internal conversion) or is emitted as light (fluorescence). In the triplet state, the energy generates reactive oxygen species (ROS) necessary to induce cell death (**Figure 1**). ROS rapidly react with macromolecules containing unsaturated double bonds, including proteins, unsaturated fatty acids and cholesterols. These reactions damage the membranes of intracellular organelles, such as mitochondria, lysosomes, and the endoplasmic reticulum (8), ultimately triggering necrosis, apoptosis, local ischemia (due to occlusion of neoplastic vessels) as well as subsequent immunological reactions (14).

Singlet oxygen diffuses over short distances (i.e., ∼0.02–1.00 μm) and has a limited lifespan (i.e., ∼0.04–4.0 μs) contributing to local tumor ablation while minimizing risk of damage to adjacent normal tissue (15). The type of photosensitizer and photo-activation determines the specific intracellular components affected as well as the degree and type of damage incurred by those components.

Like ionizing radiation, the cytotoxic effects of PDT requires the presence of molecular oxygen. Thus, the degree of oxygenation with the tumor microenvironment is a key determinant of PDT's tumoricidal activity. In this context, PDT is often delivered through multi-session treatment in order to facilitate re-oxygenation between treatments (16, 17). Pre-clinical and clinical trials of PDT performed in combination with hyperbaric oxygen demonstrate improved tumoricidal activity (18).

Though both radiation and PDT require molecular oxygen for their respective anti-neoplastic activities, their modes of action fundamentally differ. The available data suggest that ionizing radiation triggers cell death through induction of DNA damage (19). In contrast, the predominant model of cytotoxicity by PDT involves damage of cell membranes, proteins, and organelles (20). As such, PDT potentially synergizes with DNA

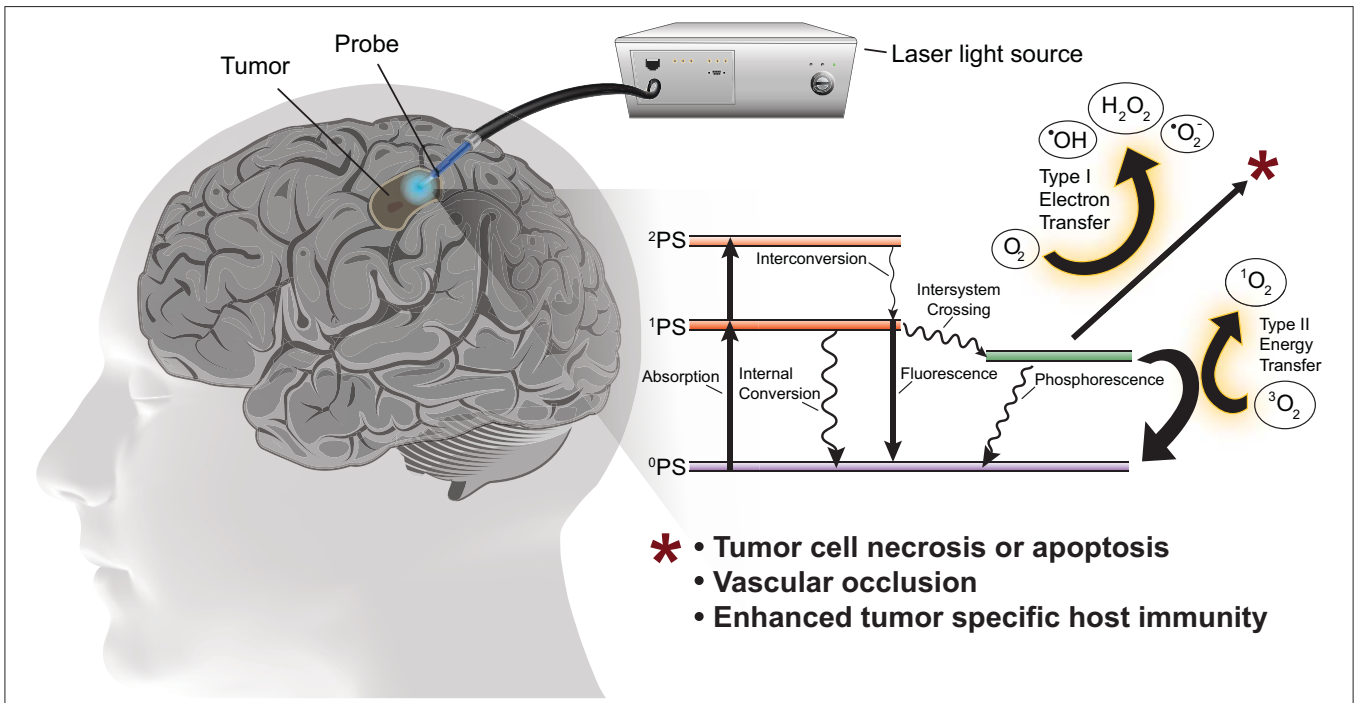

FIGURE 1 | Schematic of PDT for the treatment of glioblastoma with simplified energy diagram of the oxygen dependent photodynamic response. The photosensitizer in the ground state (^{0}PS) is excited to one of two states by the appropriate wavelength and power photostimulation, the first excited singlet state (^{1}PS) or the second excited singlet state (^{2}PS). The ^{1}PS may then convert to the excited triplet state (^{3}PS) via intersystem crossing. In the presence of molecular oxygen, the ^{3}PS may undergo Type I or Type II redox reactions producing reactive oxygen species which cause tumor cell death.

damaging agents routinely used as standard-of-care treatment for glioblastoma (21).

Photo-Activation

The light source may be incoherent or coherent (i.e., laser). The efficacy of PDT is not affected by the coherence of the light source. The emission wavelength of the light source is adjusted to the absorption spectrum of the photosensitizer. Photo-irradiation with longer wavelength light is preferred because it penetrates more deeply and delivers sufficiently energetic photons to activate the photosensitizer. Given the excitation peaks of clinically available photosensitizers and the limitations of photon propagation through biological tissues, PDT generally utilizes wavelengths between ∼400 and 900 nm, with an optimal window of 600–800 nm (15). PDT stimulation may be applied in a continuous or pulsed fashion (14), with consideration that pulsed delivery may facilitate tumor re-oxygenation between pulses.

First, Second, and Third Generation Photosensitizers

First-generation photosensitizer molecules consist of naturally occurring porphyrins, including hematoporphyrin (**Table 1**). These compounds have a strong absorption around 400 nm but have limited excitation absorption at longer wavelengths of light (22). HpD is an example of a first generation photosensitizer. It consists of a proprietary combination of monomers, dimers and oligomers derived from hematoporphyrin (23). HpD is an inefficient producer of singlet oxygen requiring extended photo-stimulation to achieve adequate therapeutic effect (23).

Second-generation photosensitizers were developed to overcome the inherent limitations of first-generation sensitizers. They are usually activated by wavelengths >600 nm and are more potent in generating singlet oxygen. Chlorins (talaporfin sodium and temoporfin) and 5-Aminolevulinic acid (5-ALA) are examples of second-generation photosensitizers (15).

Talaporfin sodium and temoporfin are clinically used to treat dermatologic diseases. Talaporfin is water soluble and administered intravenously. As such, it is quickly cleared from the body. Talaporfin is activated by 664 nm light (23, 24). Temoporfin is the most potent of the clinically available photosensitizers (activated by 652 nm photostimulation). Temoporfin is generally well-tolerated but does confer photosensitivity for up to 6 weeks post-administration.

Among the commercially available photosensitizers, 5-ALA is commonly utilized (25). The clinical utility is driven by oral bioavailability and a highly favorable safety profile. Pertaining to glioblastomas, 5-ALA exhibits high selectivity in terms of preferential accumulation in malignant gliomas (15). 5-ALA is the first compound in the synthesis of porphyrin, a component required for heme synthesis. Porphyrins are assembled into porphobilinogen, which is converted to protoporphyrin IX (PpIX) by porphobilinogen deaminase. The expression of this deaminase is elevated in glioblastomas, resulting in increased synthesis of PpIX. PpIX is normally converted to heme by the enzyme ferrochelatase (26). Decreased expression of ferrochelatase in glioblastoma arrests this conversion, further augmenting the accumulation of PpIX in glioblastomas (15).

PpIX absorbs blue light (404 nm) and emits fluorescence in the red spectrum (635 nm). When excited by 635 nm light, PpIX generates triplet oxygen and produces cytotoxicity as a photosensitizer (27). Of note, there is significant inter-tumoral heterogeneity in PpIX concentration after 5-ALA administration (25). The molecular underpinning of this variation remains poorly understood though may involve inter-tumoral expression differences in ATP-binding cassette transporters (28).

Third generation photosensitizers are characterized by enhanced tumor cell selectivity achieved through the conjugation of modifiers including nanoparticles and antibodies (15, 23). Development of third generation photosensitizers has also emphasized the design of prodrugs that are only activated by neoplastic cells. The goal of rational design of third generation photosensitizers is to reduce off target effects while optimizing pharmacokinetics and excitation-absorption properties to maximize the effective PDT window while minimizing side-effects. At this time, no third generation photosensitizers are approved for PDT in humans.

Blood-Brain Barrier

In the normal brain, endothelial cells exhibit morphological specializations including the expression of tight junctions that

TABLE 1 | Properties of clinically relevant photosensitizers.

Photosensitizer	Trade name(s)	Excitation wavelength(s)	Treatment window[a]	Clearance time	Side effects
Talaporfin sodium	Laserphyrin, Aptocine™, Litx™, LS11, Photolon®	664	2–4 h	15 days	Skin sensitization for 2 weeks
HpD	Photofrin®, Photogem®	408, 510, 630[b]	24–48 h	4–6 weeks	Skin sensitization for several weeks
5-ALA (PpIX)	Levulan®	410, 510, 635[b]	4–8 h	2 days	Skin sensitization for few days, nausea, elevated liver enzymes, anemia,
Porfimer sodium	Photofrin II®	630	48–150 h	4–6 weeks	Skin sensitization for several weeks
BOPP	n/a	630	24 h	4–6 weeks	Skin sensitization for several weeks, thrombopenia
Temoporfin	Foscan®	652	4 days	2–6 weeks	Skin sensitization for several weeks

[a] *Latency after drug administration and accumulation of photosensitizer in the tumor.*

[b] *Optimal excitation wavelength for clinical application.*

HpD, Hematoporphyrin derivative; BOPP, Boronated porphyrin.

contribute to the formation of the blood-brain barrier (BBB). There is no active transport system for 5-ALA across the BBB. As such, there is little spontaneous diffusion of 5-ALA into normal brain tissue (25). Break-down in the BBB which frequently occurs in the glioblastoma microenvironment facilitates diffusion of 5-ALA into the tumor mass. In this context, 5-ALA guided surgical resection facilitates removal of the contrast enhancement, which is typically observed in these regions of BBB breakdown.

Whether 5-ALA is a true proxy for tumor mass or simply the region of BBB breakdown remains an open question. The therapeutic window for 5-ALA mediated PDT depends on the extent that PpIX is preferentially accumulated in the glioblastoma cell relative to the cellular constituents of the tumor microenvironment (29).

Medications That May Affect PDT for Glioblastoma

Glioblastoma patients are commonly prescribed anti-epileptic drugs (AEDs, such as phenytoin and levetiracetam) as well as corticosteroid therapy. There are pre-clinical data that suggests these drugs interact with 5-ALA metabolism. In pre-clinical investigation, phenytoin administration after 5-ALA infusion suppressed PpIX synthesis by 31.0% (30). In contrast, levetiracetam did not affect PpIX synthesis or the response to PDT (30).

The interaction between corticosteroid and PpIX synthesis is more complex. PpIX production in response to 5-ALA was reduced by dexamethasone administration. However, the cellular retention of PpIX retention was increased (30). The complexity is further layered in the observation that corticosteroid administration reduced BBB permeability, which may hinder uptake of 5-ALA (15). Pre-clinical studies suggest that this effect is most prominent for dexamethasone (a commonly used corticosteroid in glioblastoma patients) with doses exceeding 12 mg per day (31).

Additionally, other FDA approved medications increase PpIX accumulation in tumor cells, including iron chelators (deferoxamine and deferiprone), vitamin D, ciprofloxacin, 5-fluorouracil, and febuxostat. Combination of these drugs has been proposed as a means to augment efficacy of 5-ALA in PDT (32).

CLINICAL APPLICATIONS

Infiltrating glioblastoma cells can be found 4.0 cm beyond the border of radiologically or histologically identifiable tumor lesions (33). Infiltrating tumor growth and extent of resection is difficult to assess intraoperatively and infiltrative tumor cells are always left behind when using traditional surgical and imaging approaches. Therefore, a method that affords the visual identification of neoplastic tissue and the simultaneous ability to selectively destroy that tissue would likely improve the success of glioblastoma resection. The joint clinical application of fluorescence guided surgery (FGS) and PDT confers the ability to both visualize tumor cells and selectively destroy them.

Interstitial PDT

Interstitial PDT (iPDT) is applied via the stereotactic insertion of fiber optic cable(s) into the tumor to deliver photostimulation to the tumor mass after the patient has been administered a photosensitizer (25). The application of iPDT is similar to laser interstitial thermal therapy (LITT) for the treatment of glioblastoma as both are minimally invasive stereotactic techniques, however, iPDT has the added benefit of selective neoplastic cell targeting. Several technical considerations are unique to iPDT. For example, selecting a light diffuser with the appropriate geometry to apply optimal photostimulation to the target tumor, determining the optimal number of diffusers to insert into the tumor to maximize therapy while minimizing the harm associated with insertion of the diffuser through normal brain tissue and, finally, proper selection of tumors of the appropriate size, anatomic location, and geometry to maximize the safety and efficacy of iPDT.

A challenge of iPDT is the even delivery of photostimulation to achieve adequate fluence over a maximal volume of tumor without causing thermal injury to the normal brain tissue. Modeling experiments have examined light delivery and determined the optimal geometry of light guides for the delivery of iPDT. Cylindrical light diffusers have a larger emitting surface area with a lower fluence rate at the tissue/light emitter interface than flat cleaved fibers (34). Therefore, light delivery via cylindrical diffuser improves photon distribution with a reduced sensitivity to local tissue absorption variability thereby distributing photostimulation over a greater tissue volume than flat, cleaved fibers. However, the light fluence drops off more rapidly from the flat fiber which is useful when treating a tumor in close proximity to eloquent brain tissue. Therefore, the geometry of the light diffuser as well as the total number of diffusers needed to safely treat a tumor are factors to consider preoperatively in order to achieve optimal iPDT.

The dose of light delivered during PDT is another important consideration. A dosimetry model was developed which is specific to 5-ALA but the underlying principle must be considered for iPDT performed with any photosensitizer. To achieve the maximal therapeutic effect of PDT, the goal is to achieve "advanced photobleaching" (based on an established dosimetry model of the same name) of the photosensitizer. Advanced photobleaching is defined as the fluence rate at which causes $\geq$95% photobleaching of photosensitizer and is associated with better outcomes (35, 36). In the case of 5-ALA mediated PDT, simulations suggest advanced photobleaching is achieved to a distance of $\sim$4 mm from the surface of a light diffuser emitting a power of 200 mW/cm for 1 h. Based upon the estimated volume of tissue affected by photo-irradiation, the optimal interfiber distance of the photo diffusers for iPDT is $\sim$10 mm and maximum power of photostimulation should not exceed 200 mW/cm as the threshold at which the risk of increasing tissue temperatures $>48^{\circ}$C (the threshold at which thermal side-effects become a factor) increases significantly (25, 37).

Software for optimization of iPDT delivery has been in development for several decades (31, 36). One approach utilizes the co-registration of contrasted magnetic resonance imaging and positron emission tomography imaging with stereotactic

computed tomography images to allow virtual trajectory planning and positioning of light diffusers within tumors (37). The goal is to virtually plan the implantation of the optimal number of light diffusers for tumor ablation without causing injury to the adjacent vasculature or traversing eloquent cortex.

Post-resection PDT

After maximal safe tumor resection, PDT may be applied to the resection cavity in the operating room or during post-operative recovery. Cavitary PDT is commonly applied by placing a balloon filled with diffusing liquid (typically a lipid suspension) coupled to a fiber optic guide and an external light source into the intracranial resection cavity. After tumor resection, the balloon is positioned in the cavity and inflated to conform with the geometry of the cavity without causing excessive compression of surrounding brain tissue. In one photostimulation paradigm utilizing the diffuser balloon, total treatment time was derived from the volume of the diffusing media in the balloon and applied in five fractions to the tumor. Between photo-irradiation fractions, 2.0 min pauses are applied allowing brain tissue reoxygenation. All photostimulation fractions are delivered in the operating room. This is the approach being utilized in the Intraoperative Photodynamic Therapy of glioblastoma (INDYGO) clinical trial which is currently ongoing (17).

Another method for cavitary PDT is to apply fractions of photostimulation out of the operating room during the post-operative recovery period. After FGS, a balloon diffuser is placed in the resection cavity and inflated with a radio-opaque lipid emulsion until the resection cavity is filled. Fluoroscopy is used to verify balloon inflation and later complete deflation, prior to removal. The first PDT treatment is applied in the recovery area with daily PDT treatments delivered subsequently at the bedside for a total of 5 treatments. A key consideration for applying PDT over a prolonged time period is the effective half-life of the photosensitizer (in this example porfimer sodium was used). After the total number of treatments are delivered, the balloon diffuser is deflated and removed at the bedside (38, 39).

CLINICAL OUTCOMES OF PDT TREATED GLIOBLASTOMAS

Outcomes after PDT in glioblastoma patients are generally favorable compared to historical data, however, the quality of the studies is limited by the lack of randomized controlled trials. The Royal Melbourne Hospital group has the most extensive clinical experience with PDT for gliomas with a series of more than 350 patients and report overall survival rates of those with newly diagnosed and recurrent glioblastomas of 28.0 and 40.0%, at 2 years and 22.0 and 34.0% at 5 years, respectively, an improvement compared to historical controls. Similarly, a meta-analysis of more than 1,000 patients enrolled in observational studies of PDT for high-grade gliomas reported median survival of newly diagnosed and recurrent glioblastomas of 16.1 and 10.3 months, respectively (40). A summary of a summary of clinical trials evaluating PDT for the treatment of glioblastomas is found in **Table 2**.

HpD Mediated PDT for Glioblastoma

An early study evaluating the efficacy of HpD mediated PDT enrolled 18 glioblastoma patients. HpD was administered via direct arterial puncture during preoperative angiogram, IV or directly into the tumor during craniotomy for tumor resection. Cavitary PDT was applied intraoperatively after tumor resection. Patients were brought back to the operating room 3 days later for redo-craniotomy and administered another round of PDT. At publication, six patients with primary glioblastomas were surviving at 22.0 months (43).

The effects of HpD or porfimer sodium mediated PDT on glioblastomas was evaluated in 17 patients. Patients were administered the photosensitizer 18–24 h prior to undergoing maximal tumor resection and intraoperative, cavitary PDT was applied via an inflatable balloon diffuser. For glioblastoma patients that died during follow-up, mean survival was 6.3 months post-PDT (46).

HpD concentration in tumor tissue compared to survival after PDT was evaluated in 58 glioblastoma patients. Patients underwent maximal safe tumor resection, then intraoperative, cavitary PDT was administered by filling the resection cavity with a continuously circulating lipid emulsion while photostimulation was applied. There was a strong association between HpD uptake and survival among treated patients (Hazard Ratio $= 0.26$, $p = 0.001$) and the median overall survival for glioblastoma patients after PDT was 24.0 months (57). A similar study evaluating HpD mediated PDT for high grade gliomas including 78 glioblastoma patients was performed. Patients underwent maximal safe tumor resection followed by intra-operative photoirradiation. The median overall survival for glioblastoma patients treated with PDT was 14.3 months (58).

Porfimer Sodium Mediated PDT for Glioblastoma

A case series reports the efficacy of porfimer sodium mediated PDT for newly diagnosed and recurrent glioblastomas in 49 patients. After the maximal tumor resection, either a balloon diffuser was placed in the resection cavity or the resection cavity itself was filled with a continuous infusion of lipid emulsion and photo-irradiation was applied. The median survival of glioblastoma patients was 30 weeks, with 1- and 2-years actuarial survival of 22.0 and 2.0%, respectively (48).

A small study was conducted to evaluate porfimer sodium or temoporfin mediated PDT for malignant primary brain tumors, including 20 glioblastoma patients. Patients underwent tumor resection followed by photo-irradiation to the resection cavity. Light was delivered with a 630 nm laser with a fluence of 75 J/cm^2 in porfimer sodium patients and at 652 nm with a fluence of 20 J/cm^2 in the temoporfin patients. A continuous infusion of lipid emulsion was applied to the resection cavity during photo-irradiation to minimize the risk of thermal injury to brain tissue. Post-operatively, patients were kept in a unique ICU room with no exposure to sun-light. Sunlight was avoided for 4 weeks (porfimer sodium) or 2 weeks (temoporfin). Patients received standard temozolomide chemotherapy and FRT post-operatively. Median OS for these patients was 17 months (59).

TABLE 2 | Summary of clinical trials using PDT for the treatment of GBM.

References	Number of patients		Photosensitizer		Photo-irradiation		Median overall survival (mo)
	New GBM	rGBM	Drug	Dose, route of administration	Wavelength, nm	Energy density (J/cm^2)	
Stupp et al. (6)	287		n/a	n/a	n/a	n/a	14.6[c] newly diagnosed
Akimoto et al. (41)	6	8	Talaporfin sodium	40 mg/m^2, IV	664	27	n/a
Beck et al. (37)[a]		10	5-ALA	20 mg/kg, PO	633	100	15 rGBM
Eljamel et al. (39)	13		5-ALA and Porfimer sodium	2 mg/kg Photofrin IV; 20 mg/kg 5-ALA, PO	630	100	13.2[d] newly diagnosed
Johansson et al. (36)[a]	1	4	5-ALA	20–30 mg/kg	635	720 J/cm	n/a
Kaye et al. (42)	13	6	HpD	5 mg/kg, IV	630	70–120 or 120–230 J/cm^2	n/a
Kostron et al. (43)	18		HpD	1 mg/cm^3 of tumor IA and/or 1 mg/cm^3 into tumor and/or IV mg/cm^3	630	40–120	n/a
Kostron et al. (44)		26	Temoporfin	0.15 mg/kg, IV	652	20	8.5 rGBM
McCulloch et al. (45)	9		HpD	5 mg/kg, IV	627.8[b]	n/a	n/a
Muller and Wilson (46)	17		HpD or Porfimer sodium	1.4–2.7 mg/kg, IV	630	8–68	n/a
Muller and Wilson (47)		32	HpD or Porfimer sodium	5 mg/kg, IV; 2 mg/kg, IV	630	8–110	7.5 (29.5 from diagnosis) rGBM
Muller and Wilson (48)	12	37	Porfimer sodium	2 mg/kg, IV	n/a	58 (mean)	8.25 newly diagnosed, 7.25 rGBM
Muller and Wilson (49)	11		Porfimer sodium	2 mg/kg, IV	630	8–110	9.25 newly diagnosed
Muller et al. (50)		37	Porfimer sodium	2 mg/kg, IV	n/a	8–150	7.75 rGBM
Muragaki et al. (51)	13		Talaporfin sodium	40 mg/m^2, IV	664	27	24.8 newly diagnosed
Nitta et al. (52)	30		Talaporfin sodium	40 mg/m^2, IV	664	27	27.4 newly diagnosed
Origitano et al. (31)[a]		8	Porfimer sodium	2 mg/kg, IV	630	50 (100 J/cm interstitial)	n/a
Popovic et al. (53)	38	40	HpD	5 mg/kg, IV	628	72–260	24 newly diagnosed, 9 rGBM
Powers et al. (54)	2		Porfimer sodium	2 mg/kg, IV	630	400 J/cm	n/a
Rosenthal et al. (55)	7	9	Boronated porphyrin	0.25–8.0 mg/kg, IV	630	25–100	5 newly diagnosed, 11 rGBM
Schwartz et al. (56)[a]	15		5-ALA	20–30 mg/kg, PO	633	12.960 J	n/a
Stylli et al. (57)	58		HpD	5 mg/kg, IV	n/a[b]	240 J/cm^2 (median)	24 newly diagnosed
Stylli et al. (58)	31	55	HpD	5 mg/kg, IV	n/a[b]	230 J/cm^2 (median)	14.3 newly diagnosed, 14.9 rGBM
Vanaclocha et al. (59)	20		Porfimer sodium or temoporfin	2 mg/kg, IV; 0.15 mg/kg, IV	630; 652	20–75	17 newly diagnosed

[a] *iPDT.*
[b] *Multiple lasers used.*
[c] *Reference survival time for newly diagnosed GBM.*
[d] *Mean.*
rGBM, recurrent GBM; HpD, hematoporphyrin derivative.

A phase II study evaluated porfimer sodium mediated PDT for newly diagnosed and recurrent supratentorial gliomas including 37 recurrent and 11 newly diagnosed glioblastomas. Subjects enrolled in the study underwent tumor resection followed by intraoperative placement of expandable balloon irradiator filled with a light dispersion medium for photo-irradiation (49, 50). Those with recurrent glioblastomas who had failed prior surgical resection and FRT (with or without chemotherapy) underwent PDT while patients with newly diagnosed tumors underwent surgical resection with intraoperative PDT. The median survival for newly diagnosed glioblastoma patients was 7.75 months while those with recurrent glioblastomas had a median survival of 9.25 months.

The application of PDT as treatment for glioblastomas was first evaluated in a randomized, controlled trial by Muller and Willson (40, 48). The treatment arm enrolled 43 patients who underwent glioblastoma resection followed by porfimer sodium mediated PDT and was compared to 34 patients who underwent tumor resection alone. Post-operative FRT was administered to all patients. Median survival was 11.0 months (95% CI 6.0–14.0

months) in the treatment group compared to 8.0 months (95% CI 3.0–10.0 months) in the control group. A 38.0% increase in median survival with PDT as well as >6.0-months survival rate in the treatment group were statistically significant, but Kaplan–Meier curves crossed over at 15 months (14, 40, 48).

Eljamel et al. conducted a single-center, randomized controlled phase III trial to evaluate porfimer sodium mediated PDT after 5-ALA FGS for newly diagnosed glioblastomas. In the study, 13 patients underwent FGS for glioblastoma resection followed by intracavitary placement of a balloon diffuser to provide repetitive PDT (1 session per day, 100 J/cm^2 applied per session) for 5 days during the post-operative period. The control arm underwent FGS for tumor resection without PDT. Post-operatively, all patients underwent FRT and were followed clinically and radiographically every 3 months until death. There was no statistically significant difference in the frequency of adjuvant and salvage treatments between the two cohorts. The mean survival of patients in the PDT and surgery only groups was 52.8 weeks (95% CI 40.0–65.0 weeks) and 24.2 weeks (95% CI 18.0–30.0 weeks), respectively ($p < 0.001$). Despite an overall worse functional status in the study group prior to FGS and PDT, their functional status improved to a much higher level post-operatively compared to the surgery only group. There was no residual tumor on discharge in 10 out of 13 patients in the PDT group and in 4 out of 14 patients in the surgery only group. There was also no difference between the groups in the average length of stay in the hospital or in the complication rate.

Talaporfin Sodium Mediated PDT for Glioblastoma

Talaporfin sodium accumulates selectively in high grade gliomas and is useful for intraoperative photodiagnosis of malignant brain tumors (60). Furthermore, several small case series report the safety and efficacy of talaporfin sodium mediated PDT as glioblastoma treatment. Thirty newly diagnosed glioblastoma patients treated with PDT in addition to standard FRT and temozolomide were compared to 164 patients with newly diagnosed glioblastomas who received standard therapy alone. The median survival time was 27.4 months for PDT patients compared to 22.1 months for those receiving standard therapy (52).

Another case series reported a median survival of 26.0 months (with one patient surviving >38.0 months) for four newly diagnosed glioblastoma patients treated with maximal safe tumor resection followed by talaporfin sodium mediated PDT while six patients with recurrent glioblastomas who underwent the same treatment had a median survival of 8.5 months (41). Muragaki et al. report their experience with talaporfin sodium PDT for the treatment of newly diagnosed or recurrent malignant primary brain tumors (including 13 glioblastoma patients). Patients underwent craniotomy and tumor resection followed by intraoperative cavitary PDT. The photostimulation was targeted to regions with high risk of tumor recurrence including the genu of the corpus callosum. In total, 1–3 regions within the resection cavity were targeted with photo-irradiated. All patients with newly diagnosed glioblastomas underwent FRT and adjuvant chemotherapy with temozolomide in addition to PDT. The median overall survival for patients with newly diagnosed glioblastomas was of 24.8 months with a median progression free survival of 12.0 months (51).

5-ALA Mediated PDT for Glioblastoma

Two series report their experience with 5-ALA mediated iPDT for malignant gliomas. In a pilot study, the efficacy of 5-ALA mediated iPDT for small (maximum diameter <3 cm), circumscribed recurrent malignant gliomas was evaluated in 10 patients. Based upon 3-D photoirradiation simulations during preoperative planning, 4–6 fiber diffusers were stereotactically placed per patient to achieve complete photo-irradiation of the tumors. The 1-year survival rate was 60.0% with a median survival of 15.0 months (37). A similar series in 15 patients with small newly diagnosed (<4 cm) and unresectable glioblastomas who underwent 5-ALA iPDT and were compared to glioblastoma patients ($n = 112$) who underwent complete tumor resection alone. All patients received standard radiotherapy and temozolomide. The iPDT group demonstrated significantly longer median progression free survival of 16.0 vs. 10.2 months and a 3-years survival of 56.0 vs. 21.0% (56). Of note, 6 of the 15 patients in the iPDT group experienced progression free survival >30 months.

Boronated Porphyrin and Temoporfin Mediated PDT for Glioblastoma

A phase I trial evaluated the safety of boronated porphyrin (BOPP) for the treatment of high-grade gliomas including seven patients with newly diagnosed and 9 patients with recurrent glioblastomas. The dose of BOPP and photo-irradiation were varied incrementally with the goal of determining the maximum safe doses. The median overall survival for newly diagnosed glioblastomas was 5.0 months and the median overall survival for those with recurrent glioblastomas after PDT was 11.0 months (55).

A non-randomized controlled phase II study evaluated temoporfin mediated PDT in 26 patients with recurrent glioblastomas. Prior to enrollment, all patients had received standard surgical, chemo and radiation therapy. The PDT consisted of FGS (classified as a macroscopically total resection in 75.0% of cases) followed by the administration of intraoperative PDT. The median survival was 8.5 months, and the 2-years survival rate was 15.0%. The median survival rates for the PDT treated patients was significantly better than the survival in the control group (44).

Efficacy of PDT for Glioblastoma

Despite sample size limitations and few randomized controlled studies of PDT, the data suggest potential beneficial effect of PDT for improving survival in glioblastoma patients when compared to standard therapy. The extent of PDT's practical application is hindered by the depth of light penetration into brain and tumor tissue with an estimated effective therapeutic spatial window for PDT limited to ∼0.75–1.5 cm from the light source (16, 41, 61). At this time given the above limitations of light delivery

and photosensitizer properties, aggressive tumor resection is necessary prior to application of PDT except in the case of very small tumors.

Safety of PDT for the Treatment of Glioblastomas

Beyond complications associated with brain tumor resection, adverse events uniquely related to PDT include the systemic administration of a photosensitizer, the application of photostimulation and photochemical reactions. Each photosensitizer confers a slightly different safety profile. A risk common to all photosensitizers is retinal and cutaneous photosensitivity which occurs for several days in the case of 5-ALA to up to 6 weeks for temoporfin, during which time exposure to direct sunlight should be avoided (23).

A phase I–II study conducted by Kaye et al. that examined the efficacy of high-dose PDT using the photosensitizer HpD in 23 patients with malignant brain tumors found no evidence of increased cerebral edema nor any other adverse events, including hematological, hepatic and renal dysfunction (42). In another case series of 20 patients, side-effects of HpD administration included one patient with dermatotoxicity consisting of swelling of the head and hands after sun-exposure despite the application of sun blocking agents, which lasted for 1 week and three patients experienced meningeal symptoms (stiff neck, fever, headache) after direct injection of HpD into the tumors which lasted for 3 days (43). There was no mortality associated with PDT, however, three patients experienced symptomatic cerebral edema that responded to medical management. Another series reports a cerebral edema incidence of 0.04% cerebral edema after HpD PDT (58).

Reports of stereotactic iPDT suggest it is safe when applied to appropriately selected patients. One of the primary considerations is post-iPDT edema. In the experience at Kashiwaba Neurosurgical hospital with porfimer sodium mediated iPDT, cerebral edema was observed post-operatively in 46.0%, though the swelling was mild and did not require therapeutic intervention in 42.0% of cases (14).

Evaluation of 112 brain tumor patients treated with porfimer sodium mediated PDT yielded adverse events in 25.0% of cases (48). Among the adverse events were death (2.7%), post-operative hemorrhage (2.7%), neurological deficit (6.2%), deep venous thrombosis (3.6%), infection (3.6%), and light sensitivity reactions, such as hand burns, facial erythema, and facial pruritus 3.6% of patients. The majority of adverse events, however, were surgical and not directly related to photo-irradiation except for light sensitivity (48).

In a series of 365 PDT applications with 5-ALA and porfimer sodium in 150 brain tumor patients, adverse events occurred in 4.7% of patients (40). Deep venous thrombosis occurred in 2.0% of patients after administration of porfimer sodium, while no cases were observed after 5-ALA administration. Serious skin photosensitivity reactions developed in 1.3% of patients after non-adherence to light protection precautions. The photosensitivity reactions were considered avoidable had precautions been taken. Cerebral edema occurred after porfimer sodium mediated PDT in 1.3% of patients with recurrent tumors requiring intervention. In 0.7% of patients, there was rupture of the balloon diffuser used for photo-irradiation during PDT or cerebrospinal fluid leak (40).

In another series of 41 patients treated with porfimer sodium or temoporfin PDT, two patients with thalamic tumors died post-operatively due to significant post-treatment cerebral edema (59). Several adverse events were encountered during the trial. First, one scalp burn required plastic surgery with a cutaneous graft for repair. Other cutaneous toxicities were observed including blisters on the forearm and cutaneous erythema. A case of burn injury on the thumbnail from pulse oximeter was observed (59).

In another large case series of 100 patients with primary brain tumors who underwent HpD or porfimer sodium PDT, the authors report a mortality of 3.0% and combined serious morbidity-mortality rate of 8.0% (50). Of note, mean post-operative ICP is significantly higher after HpD or porfimer sodium mediated PDT compared to control patients (46).

Overall, porfimer sodium PDT has been associated with more adverse events than other photosensitizers, such as 5-ALA. For example, porfimer sodium is associated with increased risk of neurological deficits at a total photo-irradiation dose above 4,000 J (62). However, the apparent increased risk of adverse events with porfimer sodium mediated PDT compared to the use of other photosensitizers PDT may be due to the larger number of patients treated with porfimer sodium PDT.

There have been no systematic reviews of PDT safety. Overall, the common risks of PDT are retinal and cutaneous photosensitivity after administration of the photosensitizer. However, the risk of photosensitivity reactions are time limited and may be mitigated by avoidance of direct sun-light. The most serious safety risk of PDT is uncontrolled cerebral edema. The exact rate of cerebral edema after PDT is not known since it varies by photosensitizer as well as with the mode of delivery and intensity of photo-stimulation utilized during therapy.

EMERGING TECHNOLOGIES, ADVANCEMENTS IN PDT FOR GLIOBLASTOMAS

PDT Mediated Immune Response

PDT has several unique properties that induce effective anti-tumor responses, such as apoptosis, autophagy, and necrosis as well as immunogenic cell death (ICD) (8). The unique modes of cell death evoked by PDT are thought to underlie a robust tumor-specific immune response which potentially leads to sustained immune mediated surveillance and suppression of neoplastic cell growth.

A mouse model cured of brain tumor by PDT provided the first evidence for induction of a tumor-specific immune response by resisting subsequent tumor cell re-challenge a tumor-specific manner while immunosuppressed mice did not resist the re-challenge (63). Several years later, the cellular mechanism of the anti-tumor immunity was further elucidated. Among the different modes of PDT induced cell death, ICD is a type of cell death whereby neoplastic cells expose and/or

release of tumor antigens molecules known as damage associated molecular patterns (DAMPs) (64, 65) which activate both innate and adaptive immune responses (66). DAMPs are integral components of cells that are only exposed on the plasma membrane and/or released in response to injury, such as the oxidative damage caused by PDT. DAMPs play a key role in cell mediated immunity by causing the activation and stimulation of antigen processing/presentation by antigen presenting cells (APCs). The activation of APCs causes their migration and proliferation in local lymph nodes where the APCs then present the tumor antigens to $CD8^+$ T cells (8). Activated $CD8^+$ T cells actively surveil the body for neoplastic cells and induce apoptosis whenever tumor cells are encountered, thereby providing long-term tumor control. Therefore, ICD induced by PDT has the potential to stimulate immune activation and surveillance, contributing to long term tumor control is observed in pre-clinical models (63, 66–69).

Overall, the survival benefit of PDT trials for malignant gliomas has been modest, thus providing the rationale for adjuvant therapies, such as further augmentation of the immune response initiated by PDT. There have been few experimental studies exploring the effects of direct PDT mediated immune response on brain tumor growth and to our knowledge no clinical studies to date.

Nanoparticle Photosensitizers

Nanoparticle technology provides several opportunities to improve upon the delivery, bio-availability, selectivity, and functionality of currently available photosensitizing molecules while reducing side-effects (70–72). Selective drug delivery using nanotechnology is an area of active research that may provide functional tumor cell type specific delivery capabilities as well as provide improved systemic pharmacokinetics of photosensitizer molecules (73–75). For example, nanoparticle-conjugated photosensitizers are in development to exploit tumor specific cell surface receptors which would deliver the photosensitizer directly to the tumor cell (76). The goal is to develop nanoparticles that are able to cross the BBB and selectively enter tumor cells. The availability of a photosensitizer capable of crossing the BBB and selectively entering tumor cells would broaden the spectrum of brain tumor targets to lower grade tumors for PDT as the requisite tumor mediated disruption of the BBB would be eliminated.

Upconverting nanoparticles, nanoparticles that convert multiple incident photons (generally in the infrared range) into an emitted photon (in the visible light range) of higher energy for PDT is an area of active research (77, 78). Another shortcoming of clinically available photosensitizers is the peak excitation wavelength necessary for activation requires wavelengths of light that poorly penetrate brain tissue. To address this limitation, nanoparticles are in development that are activated by deeper-penetrating near infrared light which causes the nanoparticles to release photons at the photosensitizer excitation wavelengths (78). The goal is to achieve a higher degree of tumor cell specificity (even in regions with intact BBB) while being able to apply PDT at greater distances from the light source and, therefore, over a larger tissue volume than can be achieved using current PDT techniques.

CONCLUSION

Following on the heels of the recent FDA approval of 5-ALA for fluorescent guided glioblastoma resection, there is emerging interest in leveraging this agent toward administering photodynamic therapy (PDT) to the resection cavity. Review of the available literatures suggests that such PDT can be safely delivered to prevent local tumor recurrence. However, it is difficult to extrapolate the efficacy of the regimen given significant heterogeneity in study design, patient cohort, and PDT agents. This review provides data spanning over 25 years of technological sophistication of PDT, hence overlaps with extension in life expectancy and quality of life parameters conferred to glioblastoma patients by optimization of their multispecialistic care are difficult to evaluate. However, lack of clear efficacy of PDT in overall survival has limited the wide-spread adaption of this technology and implementation as a standard treatment of glioblastoma. Furthermore, technical limitations in light delivery and photosensitizer design have blunted the impact that this technology might have in the treatment of glioblastoma.

The immunological effects of PDT is of particular interest given recent studies demonstrating the importance of these processes in glioblastoma. Further studies of PDT in glioblastoma after stratification of pertinent molecular biomarkers, including isocitrate dehydrogenase mutation status and methyl-guanine-methyl transferase (MGMT) promoter methylation status is warranted. Incorporation of PDT into the current standard-of-care therapy should be explored in this context. Furthermore, exploration of next generation photosensitizer agents with increased specificity to glioblastoma is equally warranted.

AUTHOR CONTRIBUTIONS

All authors listed have made a substantial, direct and intellectual contribution to the work, and approved it for publication.

ACKNOWLEDGMENTS

We thank Alexander Cramer for generating graphics.

REFERENCES

1. Tamimi AF, Juweid M. Epidemiology and outcome of glioblastoma. In: De VleeSchouwer S, editor. *Glioblastoma*. Brisbane, QLD: Codon Publications (2017). p. 143–53. doi: 10.1016/B978-0-323-47660-7.00006-9
2. Claes A, Idema AJ, Wesseling P. Diffuse glioma growth: a guerilla war. *Acta Neuropathol.* (2007) 114:443–58. doi: 10.1007/s00401-007-0293-7
3. Sahm F, Capper D, Jeibmann A, Habel A, Paulus W, Troost D, et al. Addressing diffuse glioma as a systemic brain disease with single-cell analysis. *Arch Neurol.* (2012) 69:523–6. doi: 10.1001/archneurol.2011.2910

4. Scherer HJ. The forms of growth in gliomas and their practical significance. *Brain.* (1940) 63:1–35. doi: 10.1093/brain/63.1.1
5. Kelly PJ, Daumas-Duport C, Kispert DB, Kall BA, Scheithauer BW, Illig JJ. Imaging-based stereotaxic serial biopsies in untreated intracranial glial neoplasms. *J Neurosurg.* (1987) 66:865–74. doi: 10.3171/jns.1987.66.6.0865
6. Stupp R, Mason WP, van den Bent MJ, Weller M, Fisher B, Taphoorn MJB, et al. Radiotherapy plus concomitant and adjuvant temozolomide for glioblastoma. *N Engl J Med.* (2005) 352:987–96. doi: 10.1056/NEJMoa043330
7. Stupp R, Hegi ME, Mason WP, van den Bent MJ, Taphoorn MJB, Janzer RC, et al. Effects of radiotherapy with concomitant and adjuvant temozolomide versus radiotherapy alone on survival in glioblastoma in a randomised phase III study: 5-year analysis of the EORTC-NCIC trial. *Lancet Oncol.* (2009) 10:459–66. doi: 10.1016/S1470-2045(09)70025-7
8. Hirschberg H, Berg K, Peng Q. Photodynamic therapy mediated immune therapy of brain tumors. *Neuroimmunol Neuroinflamm.* (2018) 5:27. doi: 10.20517/2347-8659.2018.31
9. Pellerino A, Franchino F, Soffietti R, Rudà R. Overview on current treatment standards in high-grade gliomas. *Q J Nucl Med Mol Imaging.* (2018) 62:225–38. doi: 10.23736/S1824-4785.18.03096-0
10. Petrecca K, Guiot MC, Panet-Raymond V, Souhami L. Failure pattern following complete resection plus radiotherapy and temozolomide is at the resection margin in patients with glioblastoma. *J Neurooncol.* (2013) 111:19–23. doi: 10.1007/s11060-012-0983-4
11. Ganau M, Foroni RI, Gerosa M, Zivelonghi E, Longhi M, Nicolato A. Radiosurgical options in neuro-oncology: a review on current tenets and future opportunities. Part I: therapeutic strategies. *Tumori.* (2014) 100:459–65. doi: 10.1700/1636.17912
12. Ganau M, Foroni RI, Gerosa M, Ricciardi GK, Longhi M, Nicolato A. Radiosurgical options in neuro-oncology: a review on current tenets and future opportunities. Part II: adjuvant radiobiological tools. *Tumori.* (2015) 101:57–63. doi: 10.5301/tj.5000215
13. Thon N, Tonn JC, Kreth FW. The surgical perspective in precision treatment of diffuse gliomas. *Onco Targets Ther.* (2019) 12:1497–508. doi: 10.2147/OTT.S174316
14. Kaneko S, Fujimoto S, Yamaguchi H, Yamauchi T, Yoshimoto T, Tokuda K. Photodynamic therapy of malignant gliomas. *Prog Neurol Surg.* (2018) 32:1–13. doi: 10.1159/000469675
15. Mahmoudi K, Garvey KL, Bouras A, Cramer G, Stepp H, Jesu Raj JG, et al. 5-Aminolevulinic acid photodynamic therapy for the treatment of high-grade gliomas. *J Neurooncol.* (2019) 141:595–607. doi: 10.1007/s11060-019-03103-4
16. Bechet D, Mordon SR, Guillemin F, Barberi-Heyob MA. Photodynamic therapy of malignant brain tumours: a complementary approach to conventional therapies. *Cancer Treat Rev.* (2014) 40:229–41. doi: 10.1016/j.ctrv.2012.07.004
17. Dupont C, Vermandel M, Leroy HA, Quidet M, Lecomte F, Delhem N, et al. INtraoperative photoDYnamic Therapy for GliOblastomas (INDYGO): study protocol for a phase I clinical trial. *Neurosurgery.* (2019) 84:E414–9. doi: 10.1093/neuros/nyy324
18. Al-Waili NS, Butler GJ, Beale J, Hamilton RW, Lee BY, Lucas P. Hyperbaric oxygen and malignancies: a potential role in radiotherapy, chemotherapy, tumor surgery and phototherapy. *Med Sci Monit.* (2005) 11:RA279–89. Available online at: https://www.medscimonit.com/abstract/index/idArt/428463
19. Maier P, Hartmann L, Wenz F, Herskind C. Cellular pathways in response to ionizing radiation and their targetability for tumor radiosensitization. *Int J Mol Sci.* (2016) 17:E102. doi: 10.3390/ijms17010102
20. Robertson CA, Evans DH, Abrahamse H. Photodynamic therapy (PDT): a short review on cellular mechanisms and cancer research applications for PDT. *J Photochem Photobiol B.* (2009) 96:1–8. doi: 10.1016/j.jphotobiol.2009.04.001
21. Zhang X, Guo M, Shen L, Hu S. Combination of photodynamic therapy and temozolomide on glioma in a rat C6 glioma model. *Photodiagnosis Photodyn Ther.* (2014) 11:603–12. doi: 10.1016/j.pdpdt.2014.10.007
22. de Paula LB, Primo FL, Tedesco AC. Nanomedicine associated with photodynamic therapy for glioblastoma treatment. *Biophys Rev.* (2017) 9:761–73. doi: 10.1007/s12551-017-0293-3
23. Allison RR, Sibata CH. Oncologic photodynamic therapy photosensitizers: a clinical review. *Photodiagnosis Photodyn Ther.* (2010) 7:61–75. doi: 10.1016/j.pdpdt.2010.02.001
24. Wang S, Bromley E, Xu L, Chen JC, Keltner L. Talaporfin sodium. *Expert Opin Pharmacother.* (2010) 11:133–40. doi: 10.1517/14656560903463893
25. Stepp H, Stummer W. 5-ALA in the management of malignant glioma. *Lasers Surg Med.* (2018) 50:399–419. doi: 10.1002/lsm.22933
26. Lakomkin N, Hadjipanayis CG. Fluorescence-guided surgery for high-grade gliomas. *J Surg Oncol.* (2018) 118:356–61. doi: 10.1002/jso.25154
27. Ewelt C, Nemes A, Senner V, Wölfer J, Brokinkel B, Stummer W, et al. Fluorescence in neurosurgery: its diagnostic and therapeutic use. Review of the literature. *J Photochem Photobiol B Biol.* (2015) 148:302–9. doi: 10.1016/j.jphotobiol.2015.05.002
28. Kawai N, Hirohashi Y, Ebihara Y, Saito T, Murai A, Saito T, et al. ABCG2 expression is related to low 5-ALA photodynamic diagnosis (PDD) efficacy and cancer stem cell phenotype, and suppression of ABCG2 improves the efficacy of PDD. *PLoS ONE.* (2019) 14:e0216503. doi: 10.1371/journal.pone.0216503
29. Hirschberg H, Uzal FA, Chighvinadze D, Zhang MJ, Peng Q, Madsen SJ. Disruption of the blood-brain barrier following ALA-mediated photodynamic therapy. *Lasers Surg Med.* (2008) 40:535–42. doi: 10.1002/lsm.20670
30. Lawrence JE, Steele CJ, Rovin RA, Belton RJ, Winn RJ. Dexamethasone alone and in combination with desipramine, phenytoin, valproic acid or levetiracetam interferes with 5-ALA -mediated PpIX production and cellular retention in glioblastoma cells. *J Neurooncol.* (2016) 127:15–21. doi: 10.1007/s11060-015-2012-x
31. Origitano TC, Karesh SM, Henkin RE, Halama JR, Reichman OH. Photodynamic therapy for intracranial neoplasms: investigations of photosensitizer uptake and distribution using indium-111 Photofrin-II single photon emission computed tomography scans in humans with intracranial neoplasms. *Neurosurgery.* (1993) 32:357–63; discussion 363–4. doi: 10.1227/00006123-199303000-00004
32. Kast RE, Skuli N, Sardi I, Capanni F, Hessling M, Frosina G, et al. Augmentation of 5-aminolevulinic acid treatment of glioblastoma by adding ciprofloxacin, deferiprone, 5-fluorouracil and febuxostat: the CAALA regimen. *Brain Sci.* (2018) 8:E203. doi: 10.3390/brainsci8120203
33. Silbergeld DL, Chicoine MR. Isolation and characterization of human malignant glioma cells from histologically normal brain. *J Neurosurg.* (1997) 86:525–31. doi: 10.3171/jns.1997.86.3.0525
34. Baran TM, Foster TH. Comparison of flat cleaved and cylindrical diffusing fibers as treatment sources for interstitial photodynamic therapy. *Med Phys.* (2014) 41:1–8. doi: 10.1118/1.4862078
35. Johansson A, Palte G, Schnell O, Tonn JC, Herms J, Stepp H. 5-aminolevulinic acid-induced protoporphyrin IX levels in tissue of human malignant brain tumors. *Photochem Photobiol.* (2010) 86:1373–8. doi: 10.1111/j.1751-1097.2010.00799.x
36. Johansson A, Faber F, Kniebühler G, Stepp H, Sroka R, Egensperger R, et al. Protoporphyrin IX fluorescence and photobleaching during interstitial photodynamic therapy of malignant gliomas for early treatment prognosis. *Lasers Surg Med.* (2013) 45:225–34. doi: 10.1002/lsm.22126
37. Beck TJ, Kreth FW, Beyer W, Mehrkens JH, Obermeier A, Stepp H, et al. Interstitial photodynamic therapy of nonresectable malignant glioma recurrences using 5-aminolevulinic acid induced protoporphyrin IX. *Lasers Surg Med.* (2007) 39:386–93. doi: 10.1002/lsm.20507
38. Eljamel MS. Photodynamic assisted surgical resection and treatment of malignant brain tumours technique, technology and clinical application. *Photodiagnosis Photodyn Ther.* (2004) 1:93–8. doi: 10.1016/S1572-1000(04)00014-6
39. Eljamel MS, Goodman C, Moseley H. ALA and Photofrin® fluorescence-guided resection and repetitive PDT in glioblastoma multiforme: a single centre phase III randomised controlled trial. *Lasers Med Sci.* (2008) 23:361–7. doi: 10.1007/s10103-007-0494-2
40. Eljamel S. Photodynamic applications in brain tumors: a comprehensive review of the literature. *Photodiagnosis Photodyn Ther.* (2010) 7:76–85. doi: 10.1016/j.pdpdt.2010.02.002
41. Akimoto J, Haraoka J, Aizawa K. Preliminary clinical report on safety and efficacy of photodynamic therapy using talaporfin sodium for malignant gliomas. *Photodiagnosis Photodyn Ther.* (2012) 9:91–9. doi: 10.1016/j.pdpdt.2012.01.001
42. Kaye AH, Morstyn G, Brownbill D. Adjuvant high-dose photoradiation therapy in the treatment of cerebral glioma: a phase 1-2 study. *J Neurosurg.* (1987) 67:500–5. doi: 10.3171/jns.1987.67.4.0500

43. Kostron H, Fritsch E, Grunert V. Photodynamic therapy of malignant brain tumours: a phase I/II trial. *Br J Neurosurg.* (1988) 2:241–8. doi: 10.3109/02688698808992675
44. Kostron H, Fiegele T, Akatuna E. Combination of FOSCAN® mediated fluorescence guided resection and photodynamic treatment as new therapeutic concept for malignant brain tumors. *Med Laser Appl.* (2006) 21:285–90. doi: 10.1016/j.mla.2006.08.001
45. McCulloch GA, Forbes IJ, See KL, Cowled PA, Jacka FJ, Ward AD. Phototherapy in malignant brain tumors. *Prog Clin Biol Res.* (1984). 170:709–17.
46. Muller PJ, Wilson BC. Photodynamic therapy of malignant primary brain tumours: clinical effects, post-operative ICP, and light penetration of the brain. *Photochem Photobiol.* (1987) 46:929–35. doi: 10.1111/j.1751-1097.1987.tb04871.x
47. Muller PJ, Wilson BC. Photodynamic therapy for recurrent supratentorial gliomas. *Semin Surg Oncol.* (1995) 11:346–54. doi: 10.1002/ssu.2980110504
48. Muller PJ, Wilson BC. Photodynamic therapy of brain tumors–a work in progress. *Lasers Surg Med.* (2006) 38:384–9. doi: 10.1002/lsm.20338
49. Muller PJ, Wilson BC. Photodynamic therapy of supratentorial gliomas. In: *Proceedings of SPIE 2972, Optical Methods for Tumor Treatment and Detection: Mechanisms and Techniques in Photodynamic Therapy VI, 8 May 1997* (San Jose, CA) (1997). doi: 10.1117/12.273505
50. Muller PJ, Wilson BC, Lilge LD, Yang VX, Hetzel FW, Chen Q, et al. Photofrin photodynamic therapy for malignant brain tumors. *Opt Methods Tumor Treat Detect Mech Tech Photodyn Ther X.* (2001) 4248:34. doi: 10.1117/12.424454
51. Muragaki Y, Akimoto J, Maruyama T, Iseki H, Ikuta S, Nitta M, et al. Phase II clinical study on intraoperative photodynamic therapy with talaporfin sodium and semiconductor laser in patients with malignant brain tumors. *J Neurosurg.* (2013) 119:845–52. doi: 10.3171/2013.7.JNS13415
52. Nitta M, Muragaki Y, Maruyama T, Iseki H, Komori T, Ikuta S, et al. Role of photodynamic therapy using talaporfin sodium and a semiconductor laser in patients with newly diagnosed glioblastoma. *J Neurosurg.* (2018) 1–8. doi: 10.3171/2018.7.JNS18422. [Epub ahead of print].
53. Popovic EA, Kaye AH, Hill JS. Photodynamic therapy of brain tumors. *Semin Surg Oncol.* (1995) 11:335-45. doi: 10.1002/ssu.2980110503
54. Powers SK, Cush SS, Walstad DL, Kwock L. Stereotactic intratumoral photodynamic therapy for recurrent malignant brain tumors. *Neurosurgery.* (1991) 29:688-95; discussion: 695–6. doi: 10.1097/00006123-199111000-00008
55. Rosenthal MA, Kavar B, Uren S, Kaye AH. Promising survival in patients with high-grade gliomas following therapy with a novel boronated porphyrin. *J Clin Neurosci.* (2003) 10:425–7. doi: 10.1016/S0967-5868(03)00062-6
56. Schwartz C, Ruhm A, Tonn J-C, Kreth S, Kreth F-W. Interstital photodynamic therapy of *de-novo* glioblastoma multiforme WHO IV. *Neurooncology.* (2015) 17:v214–20. doi: 10.1093/neuonc/nov235.25
57. Stylli SS, Howes M, MacGregor L, Rajendra P, Kaye AH. Photodynamic therapy of brain tumours: Evaluation of porphyrin uptake versus clinical outcome. *J Clin Neurosci.* (2004) 11:584–96. doi: 10.1016/j.jocn.2004.02.001
58. Stylli SS, Kaye AH, MacGregor L, Howes M, Rajendra P. Photodynamic therapy of high grade glioma–long term survival. *J Clin Neurosci.* (2005) 12:389–98. doi: 10.1016/j.jocn.2005.01.006
59. Vanaclocha V, Sureda M, Azinovic I, Rebollo J, Cañón R, Sapena NS, et al. Photodynamic therapy in the treatment of brain tumours. A feasibility study. *Photodiagnosis Photodyn Ther.* (2015) 12:422–7. doi: 10.1016/j.pdpdt.2015.05.007
60. Akimoto J, Fukami S, Ichikawa M, Mohamed A, Kohno M. Intraoperative photodiagnosis for malignant glioma using photosensitizer talaporfin sodium. *Front Surg.* (2019) 6:12. doi: 10.3389/fsurg.2019.00012
61. Akimoto J, Fukami S, Suda T, Ichikawa M, Haraoka R, Kohno M, et al. First autopsy analysis of the efficacy of intra-operative additional photodynamic therapy for patients with glioblastoma. *Brain Tumor Pathol.* (2019) 36:144–51. doi: 10.1007/s10014-019-00351-0
62. Krishnamurthy S, Powers SK, Witmer P, Brown T. Optimal light dose for interstitial photodynamic therapy in treatment for malignant brain tumors. *Lasers Surg Med.* (2000) 27:224–34. doi: 10.1002/1096-9101(2000)27:3<224::AID-LSM4>3.0.CO;2-#
63. Canti G, Lattuada D, Nicolin A, Taroni P, Valentini G, Cubeddu R. Antitumor immunity induced by photodynamic therapy with aluminum disulfonated phthalocyanines and laser light. *Anticancer Drugs.* (1994) 5:443–7. doi: 10.1097/00001813-199408000-00009
64. Krysko DV, Garg AD, Kaczmarek A, Krysko O, Agostinis P, Vandenabeele P. Immunogenic cell death and DAMPs in cancer therapy. *Nat Rev Cancer.* (2012) 12:860–75. doi: 10.1038/nrc3380
65. Kroemer G, Galluzzi L, Kepp O, Zitvogel L. Immunogenic cell death in cancer therapy. *Annu Rev Immunol.* (2013) 31:51–72. doi: 10.1146/annurev-immunol-032712-100008
66. Castano AP, Mroz P, Hamblin MR. Photodynamic therapy and anti-tumour immunity. *Nat Rev Cancer.* (2006) 6:535–45. doi: 10.1038/nrc1894
67. Garg AD, Nowis D, Golab J, Agostinis P. Photodynamic therapy: illuminating the road from cell death towards anti-tumour immunity. *Apoptosis.* (2010) 15:1050–71. doi: 10.1007/s10495-010-0479-7
68. Yi W, Xu HT, Tian DF, Wu LQ, Zhang SQ, Wang L, et al. Photodynamic therapy mediated by 5-aminolevulinic acid suppresses gliomas growth by decreasing the microvessels. *J Huazhong Univ Sci Technol Med Sci.* (2015) 35:259–64. doi: 10.1007/s11596-015-1421-6
69. Shibata S, Shinozaki N, Suganami A, Ikegami S, Kinoshita Y, Hasegawa R, et al. Photo-immune therapy with liposomally formulated phospholipid-conjugated indocyanine green induces specific antitumor responses with heat shock protein-70 expression in a glioblastoma model. *Oncotarget.* (2019) 10:175–83. doi: 10.18632/oncotarget.26544
70. Ganau L, Prisco L, Ligarotti G, Ambu R, Ganau M. Understanding the pathological basis of neurological diseases through diagnostic platforms based on innovations in biomedical engineering: new concepts and theranostics perspectives. *Medicines.* (2018) 5:22. doi: 10.3390/medicines5010022
71. Ganau M. Tackling gliomas with nanoformulated antineoplastic drugs: suitability of hyaluronic acid nanoparticles. *Clin Transl Oncol.* (2014) 16:220–3. doi: 10.1007/s12094-013-1114-1
72. Ganau M, Syrmos NC, D'Arco F, Ganau L, Chibbaro S, Prisco L, et al. Enhancing contrast agents and radiotracers performance through hyaluronic acid-coating in neuroradiology and nuclear medicine. *Hell J Nucl Med.* (2017) 20:166–8. doi: 10.1967/s002449910558
73. Huang X, Wu J, He M, Hou X, Wang Y, Cai X, et al. Combined cancer chemo-photodynamic and photothermal therapy based on ICG/PDA/TPZ-loaded nanoparticles. *Mol Pharm.* (2019) 16:2172–83. doi: 10.1021/acs.molpharmaceut.9b00119
74. Yang Y, Tu J, Yang D, Raymond JL, Roy RA, Zhang D. Photo- and sono-dynamic therapy: a review of mechanisms and considerations for pharmacological agents used in therapy incorporating light and sound. *Curr Pharm Des.* (2019) 25:401–12. doi: 10.2174/1381612825666190123114107
75. Zhang H, Wang T, Liu H, Ren F, Qiu W, Sun Q, et al. Second near-infrared photodynamic therapy and chemotherapy of orthotopic malignant glioblastoma with ultra-small Cu^{2-}: X Se nanoparticles. *Nanoscale.* (2019) 11:7600–8. doi: 10.1039/c9nr01789e
76. Kruger CA, Abrahamse H. Utilisation of targeted nanoparticle photosensitiser drug delivery systems for the enhancement of photodynamic therapy. *Molecules.* (2018) 23:E2628. doi: 10.3390/molecules23102628
77. Tang XL, Wu J, Lin BL, Cui S, Liu HM, Yu RT, et al. Near-infrared light-activated red-emitting upconverting nanoplatform for T1-weighted magnetic resonance imaging and photodynamic therapy. *Acta Biomater.* (2018) 74:360–73. doi: 10.1016/j.actbio.2018.05.017
78. Tsai YC, Vijayaraghavan P, Chiang WH, Chen HH, Liu TI, Shen MY, et al. Targeted delivery of functionalized upconversion nanoparticles for externally triggered photothermal/photodynamic therapies of brain glioblastoma. *Theranostics.* (2018) 8:1435–48. doi: 10.7150/thno.22482

Conflict of Interest: The authors declare that the research was conducted in the absence of any commercial or financial relationships that could be construed as a potential conflict of interest.

frontiers in Oncology

REVIEW
published: 05 June 2020
doi: 10.3389/fonc.2020.00739

Blood-Brain Barrier, Blood-Brain Tumor Barrier, and Fluorescence-Guided Neurosurgical Oncology: Delivering Optical Labels to Brain Tumors

Evgenii Belykh[1], Kurt V. Shaffer[1], Chaoqun Lin[2], Vadim A. Byvaltsev[3], Mark C. Preul[1†] and Lukui Chen[4*†]*

[1] Department of Neurosurgery, Barrow Neurological Institute, St. Joseph's Hospital and Medical Center, Phoenix, AZ, United States, [2] Department of Neurosurgery, School of Medicine, Southeast University, Nanjing, China, [3] Department of Neurosurgery, Irkutsk State Medical University, Irkutsk, Russia, [4] Department of Neurosurgery, Neuroscience Center, Cancer Center, Integrated Hospital of Traditional Chinese Medicine, Southern Medical University, Guangzhou, China

Recent advances in maximum safe glioma resection have included the introduction of a host of visualization techniques to complement intraoperative white-light imaging of tumors. However, barriers to the effective use of these techniques within the central nervous system remain. In the healthy brain, the blood-brain barrier ensures the stability of the sensitive internal environment of the brain by protecting the active functions of the central nervous system and preventing the invasion of microorganisms and toxins. Brain tumors, however, often cause degradation and dysfunction of this barrier, resulting in a heterogeneous increase in vascular permeability throughout the tumor mass and outside it. Thus, the characteristics of both the blood-brain and blood-brain tumor barriers hinder the vascular delivery of a variety of therapeutic substances to brain tumors. Recent developments in fluorescent visualization of brain tumors offer improvements in the extent of maximal safe resection, but many of these fluorescent agents must reach the tumor via the vasculature. As a result, these fluorescence-guided resection techniques are often limited by the extent of vascular permeability in tumor regions and by the failure to stain the full volume of tumor tissue. In this review, we describe the structure and function of both the blood-brain and blood-brain tumor barriers in the context of the current state of fluorescence-guided imaging of brain tumors. We discuss features of currently used techniques for fluorescence-guided brain tumor resection, with an emphasis on their interactions with the blood-brain and blood-tumor barriers. Finally, we discuss a selection of novel preclinical techniques that have the potential to enhance the delivery of therapeutics to brain tumors in spite of the barrier properties of the brain.

Keywords: fluorescence-guided surgery, blood-brain barrier, blood-tumor barrier, 5-aminolevulinic acid, fluorescein sodium, indocyanine green, enhanced permeability and retention, drug delivery

OPEN ACCESS

Edited by:
Bo Gao,
Affiliated Hospital of Guizhou Medical University, China

Reviewed by:
Sandro M. Krieg,
Technical University of Munich, Germany
Pilar López-Larrubia,
Consejo Superior de Investigaciones Científicas (CSIC), Spain
Andre Bongers,
University of New South Wales, Australia

***Correspondence:**
Lukui Chen
neuro_clk@hotmail.com
Mark C. Preul
neuropub@barrowneuro.org

† These authors share senior authorship

Specialty section:
This article was submitted to Cancer Imaging and Image-directed Interventions, a section of the journal Frontiers in Oncology

Received: *23 October 2019*
Accepted: *17 April 2020*
Published: *05 June 2020*

Citation:
Belykh E, Shaffer KV, Lin C, Byvaltsev VA, Preul MC and Chen L (2020) Blood-Brain Barrier, Blood-Brain Tumor Barrier, and Fluorescence-Guided Neurosurgical Oncology: Delivering Optical Labels to Brain Tumors. Front. Oncol. 10:739. doi: 10.3389/fonc.2020.00739

INTRODUCTION

Gliomas account for nearly 80% of primary malignant tumors in the central nervous system (CNS) (1). Current recommended treatment for glioblastoma includes maximal safe resection, radiotherapy, temozolomide, and alternating electric field therapy (2). Despite all treatment efforts, glioma recurrence is inevitable due to the invasive nature of the tumor hampering complete tumor resection (3). Although it is practically impossible to eradicate every glioma cell surgically, increasing the precision of glioma removal with more accurate margin delineation predicts better treatment outcomes and preservation of quality of life (4–7). Because of the infiltrative growth pattern of gliomas, the tumor boundary is a mixture of tumor cells, reactive glial and immune cells, as well as normal brain cells. Such architecture complicates delivery of drugs to the invasive border region and restricts complete tumor resection. Margin delineation during resection is difficult and is inherently biased by both the subjective experience of the surgeon and the technical limitations of the operating microscope. Because of these factors, the goal of maximal safe resection of gliomas remains difficult to achieve, if not elusive.

In recent years, a number of intraoperative optical techniques, including fluorescence-guided surgery, have been developed to improve intraoperative visualization of cancers. These techniques can specifically label tumor cells, helping neurosurgeons to more objectively determine the boundary between the abnormal and surrounding normal tissues and to achieve more informed, maximum, and safe tumor resection. The impact of fluorescence techniques on extending progression-free and overall survival in high-grade gliomas is yet to be fully realized (8, 9). The most common drugs used for fluorescence-guided resection of high-grade gliomas are 5-aminolevulinic acid (5-ALA), fluorescein sodium (FLS), and indocyanine green (ICG), while multiple other fluorescent probes are currently in Phase I-II stages of investigation. Despite their mitigated success in clinical application for high-grade gliomas, current fluorescent labels often do not stain the overall area of the tumor, especially near the tumor margin, and do not delineate tumor margins in low-grade brain tumors. These difficulties are likely due to the effects of the blood-brain barrier (BBB), which maintains the sensitive environment of the brain by preventing the passage of blood-borne proteins, drugs, inflammatory cells, and other solutes. Consequently, delivery of fluorescent markers into the brain is also prevented, limiting the effectiveness of optical imaging techniques. Breakdown of the BBB is common in high-grade gliomas and brain metastases, producing what is known as the blood-brain tumor barrier (BBTB). It is this dysfunctional barrier that enables the extravasation of fluorescent markers into tumor tissue. However, the BBTB is more competent in low-grade gliomas and at the invasive border of high-grade gliomas (10, 11), complicating tumor staining (12, 13). Clearly, it would be advantageous to understand and manipulate the BBB and BBTB to overcome regional barriers to drug delivery and to target tumor cells where the BBTB is less disrupted.

In this review, we summarize the structure and function of the BBB and BBTB and their interactions with fluorescence visualization techniques for the optical guidance of invasive brain tumor resection. We review novel techniques that show potential for trans-BBB delivery of labels and therapeutics to elucidate the extent of brain tumors and to guide brain tumor surgery.

THE BLOOD-BRAIN BARRIER

The BBB is primarily composed of a continuous layer of non-fenestrated capillary endothelial cells covered by the glycocalyx and securely connected by a net of intercellular tight junctions (TJs) and adherens junctions, a basement membrane, pericytes, and perivascular astrocyte end-foot processes. Conceptually, the BBB contains three barriers arranged sequentially from the blood to the brain: the glycocalyx, endothelium, and extravascular compartment (14). A scaled schematic of these barriers is shown in **Figure 1**. Knowledge of the structure and function of these barriers is important not only for understanding the pharmacology of optical tracers in brain tumors and surrounding normal brain, but also for informing the design of novel drugs that can efficiently target invading tumor cells hidden behind regions of relatively intact BBTB.

Glycocalyx

The glycocalyx is an ∼300-nm thick (15), gel-like structure on the luminal membrane of the endothelium consisting of negatively charged proteoglycans, glycosaminoglycans, and glycoproteins anchored in the luminal membrane by transmembrane proteins (16). A functional glycocalyx prevents the adhesion of circulating cells to the endothelium and serves as an initial malleable, sieve-like barrier to large molecules. For example, the concentration of intravascularly administered 150-kDa dextrans decreases by almost 50% within the glycocalyx layer, while the concentration of FLS (376 Da) remains above 90%, when compared to the center of the vessel (14, 17).

Endothelium

Endothelial cells create an ∼200-nm thick, highly functionalized wall with luminal and abluminal membranes. These cells are tightly interconnected by TJs, lack fenestrations, and have a diminished number of pinocytic vesicles, limiting the transport of solutes across the BBB (18). Given these barrier properties, there are two main ways molecules pass the endothelial layer: via paracellular diffusion or using transcellular mechanisms.

Paracellular diffusion is significantly limited by the fence created by the continuous network of TJ complexes. TJs seal interendothelial clefts and anchor to the cytoskeleton, providing structural support. Brain endothelium differs from peripheral endothelium and epithelium in its expression of TJ proteins (high expression of occludin and claudin-5), which creates a tighter TJ network (19). Furthermore, alteration in the expression of the transmembrane proteins composing the TJs and their interactions modulate the gating of paracellular diffusion, allowing for dynamic control of paracellular diffusion (**Figure 2A**).

Transcellular diffusion is limited to those molecules that are relatively small, uncharged, and lipophilic (**Figure 2B**). More specifically, the intact BBB allows diffusion of hydrophobic

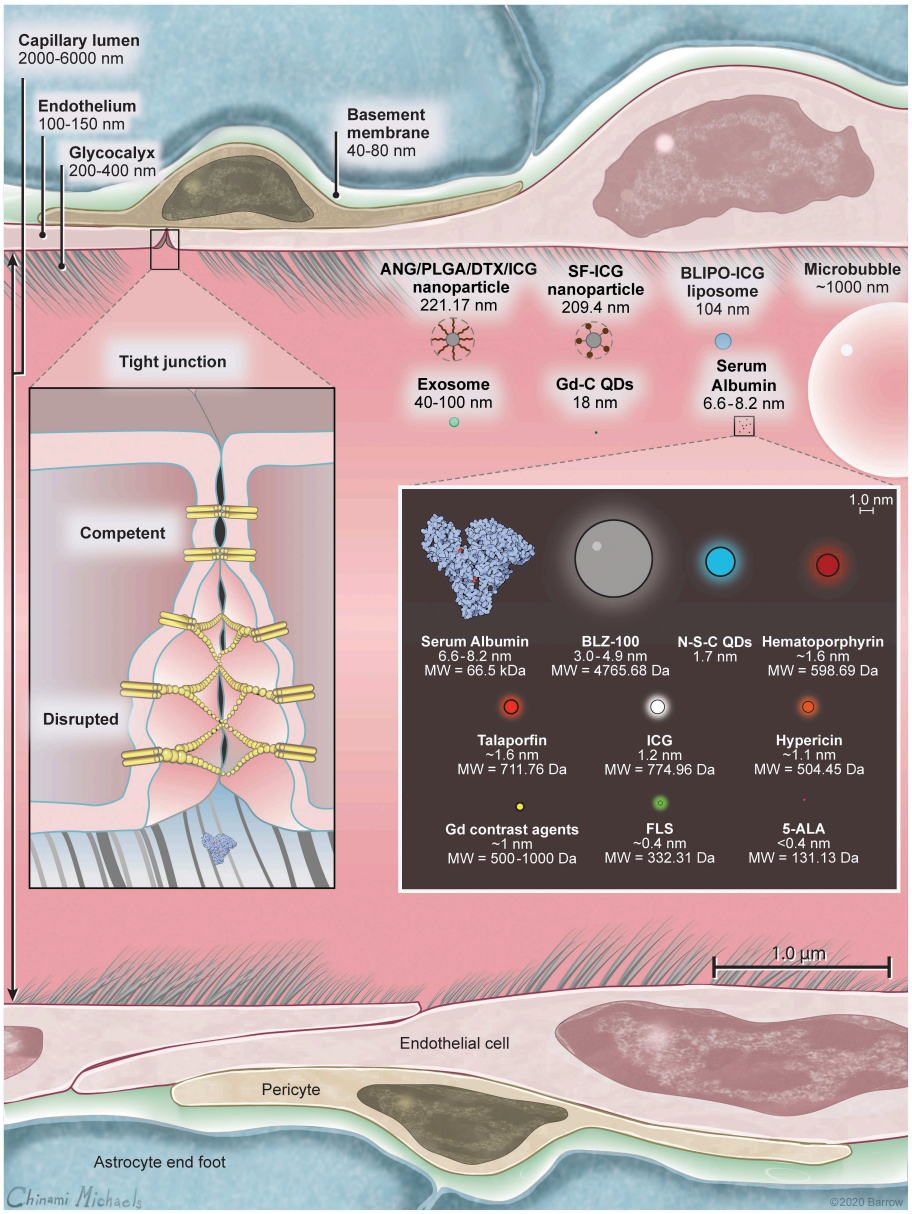

FIGURE 1 | A scale illustration of blood-brain barrier (BBB) structure with a selection of drugs and fluorescent markers discussed in this paper. Left inset shows the structure of the BBB including luminal glycocalyx, tight junctions (TJs), and the membranes of the neighboring endotheliocytes. In intact BBB, TJs secure the paracellular transport, while in disrupted BBB or in BBTB, TJs are deficient and allow for paracellular transport of large molecules through the interendothelial slits and pores. Human serum albumin is included because many small-molecule drugs (including ICG and FLS) bind extensively to serum proteins upon intravascular administration, thus changing their ability to cross the BBB. Right inset is scaled relative to the molecules within. Listed in nanometers are hydrodynamic diameters of molecules, when available, or molecular chain length estimated using PyMOL (The PyMOL Molecular Graphics System, Version 2.3 Schrödinger, LLC). 5-ALA, 5-aminolevulinic acid; ANG/PLGA/DTX/ICG, angiopep2/poly(lactic-co-glycolic acid)/docetaxel/indocyanine green; BLIPO-ICG, biomimetic liposome conjugated to indocyanine green; FLS, fluorescein sodium; Gd, gadolinium; Gd-C QD; gadolinium-carbon quantum dot; ICG, indocyanine green; N-S-C QD, nitrogen and sulfur co-doped carbon quantum dot; SF-ICG, silk fibroin indocyanine green conjugated. *Used with permission from Barrow Neurological Institute, Phoenix, Arizona*.

molecules that are less than 400–500 Da in size and form fewer than 8 to 10 hydrogen bonds with water (20). For ideal delivery, a drug should have an octanol:water partition coefficient (P_{ow}) of between 10:1 and 100:1 (21) or a total polar surface area less than 90 $Å^2$ (22). Coupled with endothelial TJs, this barrier to diffusion allows the endothelial expression and modulation of select transporters and receptors to dictate the flow of large molecules across the BBB (**Figures 2C–G**). Transporters at the endothelial cell membrane are primarily members of the solute carrier (SLC) family of passive membrane transporters (23–25) or of the adenosine triphosphate-binding cassette (ABC) family of active transporters (26–28). In contrast, the receptors

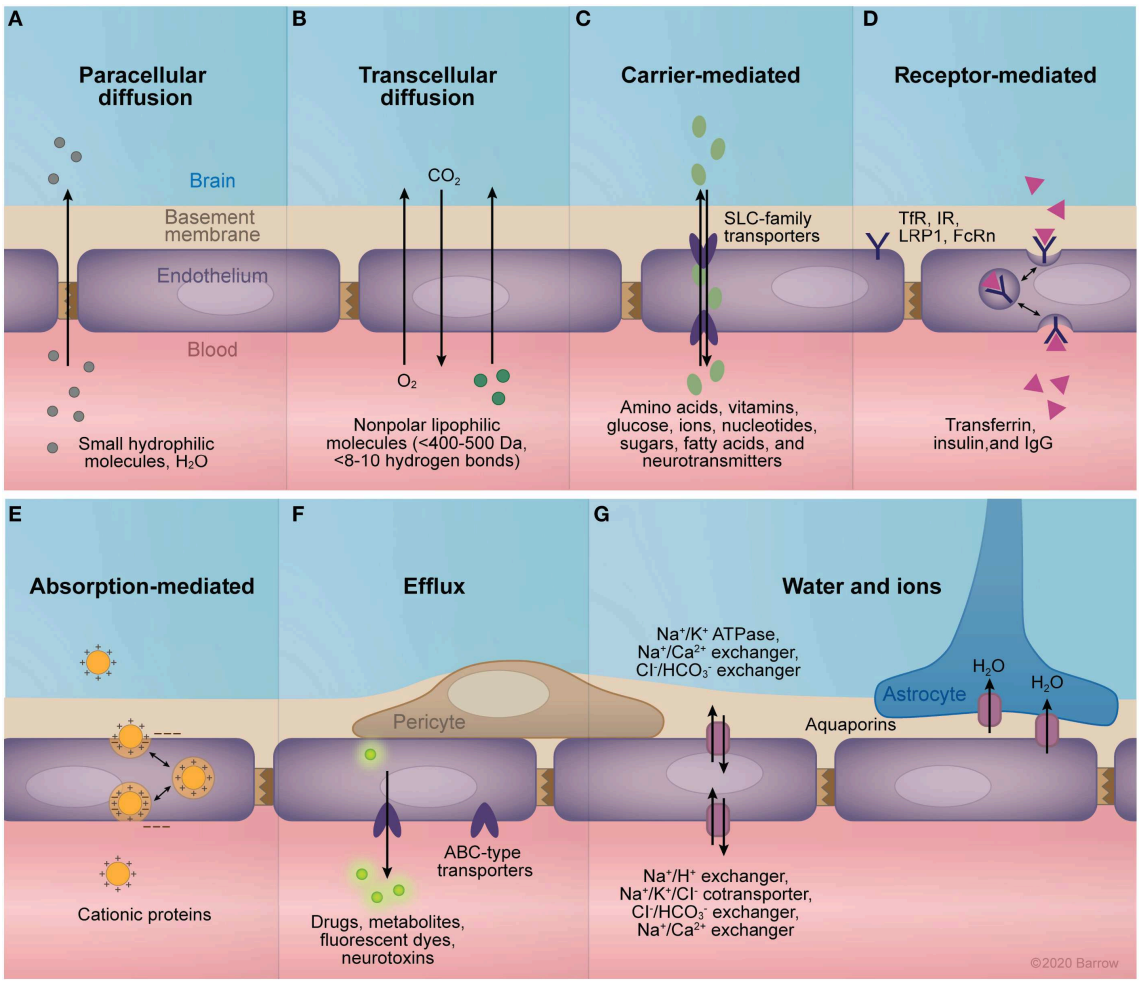

FIGURE 2 | Transport mechanisms of the blood-brain barrier (BBB). **(A)** Paracellular diffusion through intact tight junctions is possible for small, hydrophilic molecules and water. **(B)** Transcellular diffusion of small non-polar lipophilic molecules. **(C)** The facilitated diffusion of small molecules across the endothelium is mediated primarily by members of the solute carrier family of transporters, which transport a range of molecules including amino acids, vitamins, glucose, ions, nucleotides, sugars, fatty acids, and neurotransmitters. **(D)** Receptor-mediated transport allows for the transcellular passage of larger molecules across the endothelium via their binding to specific receptors. These receptors trigger endocytosis by conformational changes in cytoplasmic domains, allowing for the transcytosis or endocytosis of bound molecules. Examples of receptors expressed at the BBB include the transferrin receptor, insulin receptor, low-density lipoprotein related receptor 1, and the neonatal Fc receptor. **(E)** Cationic proteins can traverse the BBB via binding to negatively charged cell-surface molecules expressed in the capillary lumen, allowing for their transcytosis across the endothelium. **(F)** Members of the adenosine triphosphate (ATP) binding cassette family of transporters are expressed at the central nervous system endothelium, mediating the active efflux of a large selection of drugs, metabolites, neurotoxins, and fluorescent markers. **(G)** Proper osmolarity of the endothelial basement membrane and the adjacent brain interstitium is mediated by the selective expression of ion pumps and channels. Namely, the Na^+/K^+ ATPase, Na^+/Ca^{2+} exchanger, and Cl^-/HCO_3^- exchanger regulate abluminal ion equilibrium, while the Na^+/H^+ exchanger, $Na^+/K^+/Cl^-$ cotransporter, Cl^-/HCO_3^- exchanger, and Na^+/Ca^{2+} control ionic equilibrium with the blood. Additionally, expression of aquaporins 1 and 4 mediate the passive flow of water across endothelial cell and astrocyte membranes, respectively. ABC, adenosine triphosphate–binding cassette; FcRn, neonatal Fc receptor; IgG, immunoglobulin G; IR, insulin receptor; LRP1, low-density lipoprotein related receptor; SLC, solute carrier; TfR, transferrin receptor. *Used with permission from Barrow Neurological Institute, Phoenix, Arizona*.

expressed at the BBB are diverse, including the transferrin receptor (29), neonatal Fc receptor (30, 31), and low-density lipoprotein receptor 1 (LRP1) (25).

Extravascular Compartment

Other components of the BBB are pericytes, which cover 22–32% of the surface of the capillaries (32), the foot processes of neighboring astrocytes that completely encase the brain microvasculature (33), microglia, and neurons. These surrounding cells secrete signals that contribute to BBB development, provide physical and metabolic support, and are necessary to maintain dynamic integrity of the BBB (34–40). Altogether, these elements form a so-called neurovascular unit, capable of responding dynamically to local changes in physiology and environment (38, 41, 42). The composition, development, and regulation of the BBB have been previously reviewed in greater detail (21, 25, 38, 41–44), including a recent review of BBTB (45).

THE BLOOD-BRAIN TUMOR BARRIER

The Role of Vascular Endothelial Growth Factor in the BBTB

A major driver of BBB compromise, especially in high-grade gliomas, is tumor-secreted vascular endothelial growth factor (VEGF). The increased metabolic rate of high-grade gliomas results in local hypoxia and upregulation of hypoxia inducible factor-1, which stimulates the production of VEGF. Secreted VEGF then induces breakdown of existing BBB architecture and growth of structurally altered capillaries from the existing vessels (46, 47). This induced tumoral vascular endothelium displays an abnormal expression profile of transporters and receptors in order to accommodate the high metabolic demands of associated tumor cells (48–52). Unlike the normal brain vessels from which they originate, newly formed capillaries are structurally altered and are more permeable than even non-BBB peripheral capillaries (53). Although the abnormal microvasculature of high-grade brain neoplasms is different from that of non-brain solid tumors, both are similarly hyper-permeable when compared with normal capillaries.

Degree of BBTB Endothelium Permeability

The large size of interendothelial clefts and transendothelial fenestrations as well as their increased number contribute to the high degree of BBTB permeability. The degree of BBB and BBTB permeability is traditionally measured by using different-sized fluorescently labeled dextrans (54–58). The customizability of uniformly sized dextrans and their reactivity with fluorescent molecules such as fluorescein isothiocyanate (FITC) create easily assembled probes that can be visualized for interrogating BBB permeability. The average transendothelial pore size in intracranially implanted tumors is significantly smaller than that of extracranially implanted tumors (210–550 nm compared to 380–2,000 nm) (53). However, the hyperpermeability of the tumor capillaries to fluorescently labeled albumin (≈7 nm, 66 kDa) was associated with the number of pores, rather than their size (53). In average-size tumor vessels, about 30% had fenestrations and about 10% had open junctions (53). In a series of experiments with nine various-sized nanoparticles that tried to identify the maximal fenestration size in RG-2 glioma BBTB, 597 kDa molecules did not transgress the BBTB, while 330 kDa and smaller nanoparticles passed the BBTB (59).

To better portray the degree of BBTB hyperpermeability, tumor endothelium could be compared to non-brain endothelium, which is categorized into three groups based on permeability. (1) *Continuous non-fenestrated endothelium* is found in skin, heart, and lungs and is usually impermeable to molecules larger than 4–6 nm in diameter, but it may have intermittent discontinuities in TJs that create intercellular slits of up to 20 nm (60). (2) F*enestrated endothelium* of the intestines, kidneys, and choroid plexus has transcellular pores 25–60 nm in diameter, which are sealed by 5–6 nm thick diaphragms (61). (3) *Discontinuous endothelium* of the liver, spleen and bone marrow has large, 100–200 nm fenestrations without an underlying basement membrane (61). Consideration of the permeability of the various capillary types is important for the development of drugs, especially those that rely on the enhanced permeability and retention (EPR) effect for delivery.

Heterogeneity of the BBTB

Tumor-mediated changes in the BBB may vary with tumor type, volume, stage, and anatomical location, or even within the same tumor (62). The severity of barrier compromise ranges significantly, from critical disruption comparable to the vasculature in solid, non-brain neoplasms to mild compromise found in neurodegenerative disease, stroke, diabetes, and obesity, among other pathologies (18, 21, 43). Indeed, studies have shown that brain tumors possess all three distinct types of endothelium: non-fenestrated continuous, similar to normal cerebral blood vessels; continuous fenestrated; and discontinuous endothelium (63–65).

In low-grade gliomas, the structure and function of the BBTB largely resembles that of the normal BBB (66). In grade III gliomas, the microvasculature surface area and vascular diameter are higher compared with low-grade gliomas (67). In high-grade gliomas, the BBB is significantly altered, leading to associated edema (68) and gadolinium-based contrast accumulation. However, even in high-grade gliomas there are regions with vascular density and integrity within the same range as that of normal cerebral white matter, especially in non-enhancing regions or necrotic, avascular regions with decreased perfusion (10, 69, 70). Interestingly, this disruption does not necessarily correlate with the degree of infiltration of normal brain by tumor cells. A single infiltrating glioblastoma cell can cause the foot processes of astrocytes to migrate away from vascular endothelial cells, leading to the formation of localized fractures in the BBB (71). Alternatively, infiltrating glioma cells may be shielded by an intact BBB from intravascularly administered diagnostic and therapeutic agents (72, 73). This spectrum of BBB disruption seen in glioma is shown in **Figure 3**. An additional layer of complexity is added by the regional heterogeneity of immune cell populations that influence the BBTB in gliomas (74–76).

Glucocorticoids that are frequently used to manage peritumoral edema also influence the BBTB, reducing transendothelial flow by shrinking interendothelial gaps and increasing formation of intercellular junctions (77). However, preoperative steroid use was not associated with the efficacy of FLS staining of high-grade glioma tissue for wide-field fluorescence guidance and thus is unlikely to affect delivery of optical agents to the core of the tumor (78).

These characteristics depict the BBTB as a heterogeneous combination of preexisting and newly formed blood vessels, which provide nutrients and oxygen to the tumor. Although the BBTB is disrupted in the tumor core, it may retain characteristics of an intact BBB in certain areas, thus creating a barrier that, while compromised, still hinders delivery of diagnostic agents to the tumor, diminishing the diagnostic accuracy of intraoperative optical guidance techniques (52, 79). The fact that the BBTB is so disrupted in the core of high-grade gliomas leads some scientists to question the BBB as the major factor that limits the effectiveness of chemotherapy in these tumors (11). Therefore, in order to improve these techniques for brain tumor surgery, we

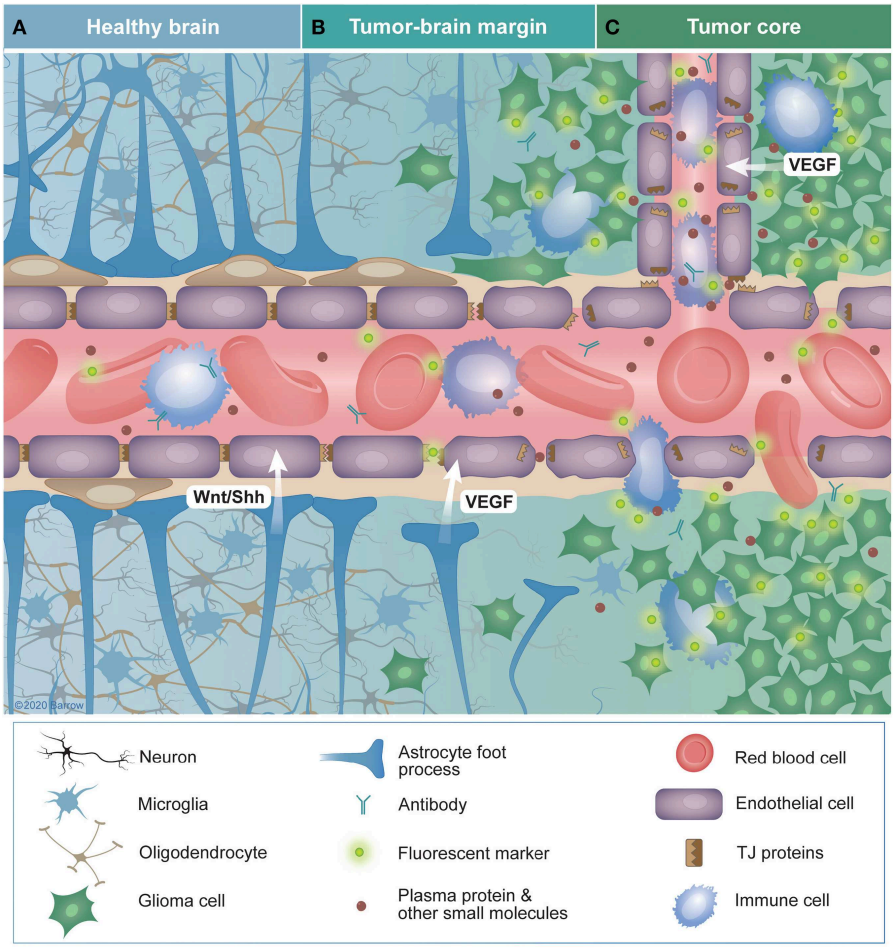

FIGURE 3 | Characteristics of the blood-brain (BBB) and blood-brain tumor barriers (BBTB) in glioma. **(A)** The healthy BBB selectively impedes the diffusion of blood contents across the central nervous system (CNS) endothelium. Controlled expression of tight-junction proteins and the endothelial cells themselves provide a physical barrier to the passage of these solutes into the brain parenchyma. Additionally, intimate associations among endothelial cells, pericytes, astrocytes, and neurons (the neurovascular unit) promote the continued integrity of the BBB. Sonic hedgehog and Wnt-family proteins secreted by astrocytes and pericytes are crucial for BBB maintenance. **(B)** In tumor margin zones, glioma cells may infiltrate into otherwise healthy parenchyma, causing disruption of local neural structures, including the BBB. This infiltration disrupts the connections between members of the neuro vascular unit, leading to the downregulation of tight-junction proteins and degradation of the BBB through tumor-secreted vascular endothelial growth factor. The resulting vascular permeability leads to the extravasation of blood contents, including solutes, antibodies, fluorescent markers, and immune cells. Alternatively, glioma cells may infiltrate in such a way that they do not disrupt the BBB, effectively shielding themselves with an intact BBB. **(C)** Within the tumor core, BBB disruption is often the greatest, especially in high-grade gliomas. The increased density of highly metabolically active cells in this area promotes hypoxia-driven expression of VEGF that promotes angiogenesis. These new vessels are often immature, lacking typical CNS barrier properties, leading to characteristics such as aberrant transporter expression, increased interstitial pressure, and edema. TJ, tight junctions; VEGF, vascular endothelial growth factor; Wnt/Shh, Wnt and sonic hedgehog family proteins. *Used with permission from Barrow Neurological Institute, Phoenix, Arizona*.

first need to understand the mechanisms that govern delivery of various optical labels across the heterogeneous BBTB in various tumor types. We also discuss approaches to circumvent the intact portions of the BBTB for more effective delivery of optical agents.

CURRENT STRATEGIES FOR DELIVERY OF TUMOR MARKERS ACROSS THE BBB AND BBTB

Efficacious drug delivery to the CNS has been difficult. The disrupted nature of the BBTB in high-grade gliomas permits increased delivery of drugs to the tumor core compared to surrounding normal brain, where the BBB is generally intact. Still, the invasive nature of high-grade gliomas and other non-enhancing brain tumors (80), in which cells migrate beyond the visible borders of gadolinium enhancement (81), presents a challenge for accurate delineation of the extent of tumor growth, for accurate diagnosis, and for intraoperative guidance.

Although many methods have been explored for drug delivery across the heterogeneous BBB and BBTB, these barriers remain a major obstacle (20, 21, 24, 52, 64, 82–92). In general, such methods can be classified into five broad categories: (1) passive delivery, (2) EPR of the BBTB, (3) BBTB disruption, (4) BBTB

bypass, (5) BBTB targeting. We briefly discuss these categories of drug delivery and relate them to the current clinical tools and novel advancements for intraoperative optical guidance in neuro-oncology. Tumor markers reviewed in this manuscript are summarized in the **Table 1**.

Passive Delivery

Passive delivery through the intact BBTB is challenging, as most small lipophilic drugs that could diffuse through the BBB are not targeted and exhibit toxicity in high doses, and most hydrophilic molecules do not pass through the narrow TJs of the BBB (140, 141).

Passive delivery of small molecules (<40 kDa) through the disrupted BBTB proceeds down a blood-tumor diffusion gradient, similarly to drug delivery to non-brain tumors. Interestingly, low-molecular-weight drugs usually have a lower "tumor-to-normal brain" distribution ratio compared with larger molecules. This difference is due to the rapid wash out of the small-molecule drugs from the extracellular space and clearance from the blood (142). Accumulation of small molecular labels in tumor tissues peaks within minutes and gradually decreases within 4–6 h. Fluorescence-guided surgery within this time window of first-pass accumulation and clearance is still feasible, mainly because a healthy BBB limits the extravasation of these labels (for example FLS, ICG, and others) to areas of tumoral BBB degradation.

Enhanced Permeability and Retention

The EPR mechanism was initially described for non-brain solid tumors in 1986 (142, 143). This mechanism is based on four main components: (1) hypervascularization of the tumor, (2) enhanced permeability of tumor vasculature, (3) hampered absorption of macromolecules back into the vasculature, and (4) reduced drainage of molecules through the lymphatic system. Because the BBTB in high-grade gliomas is even more permeable than fenestrated non-brain capillaries, many optical guidance drugs reach the tumor via this mechanism. Furthermore, the lack of a lymphatic system in tumors prevents the clearance of large molecules and lipids from the interstitial space, greatly contributing to drug retention (142, 143). It is worth noting that some tumors do not have increased vascularity, and therefore the EPR effect is not observed in them. For example, metastatic prostate and liver cancers have low vascular densities (144, 145). This low vascular density potentially explains the lack of FLS-, ICG-, and 5-ALA-labeling of some brain metastases.

In order for the EPR effect to occur, the injected molecule should be biocompatible, have no clearance by the reticuloendothelial system, and be non-reactive to blood cells or the endothelium (142). The molecule should be large enough (>40 kDa) to avoid renal clearance through the pores in glomerular endothelium and have a weakly negative or neutral surface charge (142, 146). With respect to the upper limit of size of a molecule for EPR, researchers have demonstrated that 1-μm diameter *Lactobacilli* can be selectively delivered into the tumor with additional dilation of the tumor endothelial cell junctions by an angiotensin-converting enzyme inhibitor (147). Many drugs, including polymer conjugates, bind to albumin (60 kDa), increasing their molecular weight, thus satisfying the criteria for EPR delivery. For example, immunoglobulin G (160 kDa), polymer-drug conjugates, and liposome-encapsulated drugs fit the above-mentioned criteria.

Distinct accumulation of a high-molecular-weight drug via EPR can be seen within half an hour, with a maximum tumor-to-normal tissue ratio within hours to days after administration (142). The retention time usually ranges from hours to days. In comparison, low-molecular-weight contrast agents, including gadolinium-based contrast agents (500–1,000 Da in size) are capable of freely diffusing through the peripheral endothelium (148). These agents accumulate within the tumor because of a first-pass effect, but are not retained. Thus, compared to smaller molecules, the model EPR macromolecule is small enough to enter endothelial pores of the abnormal tumor vasculature, where it more preferentially accumulates, but large enough to avoid renal clearance, allowing prolonged circulation (142, 143).

Of note, all current clinically employed optical tracers for brain tumor imaging (FLS, ICG, and 5-ALA) rely to some degree on the EPR effect to exit the tumor microvasculature through a compromised BBTB.

BBB Disruption

Hyperosmolar Opening

Focus on drug delivery via disruption of the BBB began in the 1970s by Rapoport (149) and Rapoport et al. (150), establishing the effectiveness of temporary TJ opening with intraarterial infusion of a bolus of hyperosmolar mannitol (**Figure 4A**) (151). This method was subsequently adapted to increase the delivery of chemotherapeutics to brain tumors (152, 153). Although there are reports on the safety and efficacy of the selective endovascular hyperosmolar opening of the BBB for chemotherapeutics in cases of CNS lymphoma, anaplastic oligodendroglioma, and other brain malignancies (154, 155), overall effectiveness of this method is still debatable (91). The non-selective opening of the BBB allows for indiscriminate influx of blood-borne molecules, causing neurotoxicity, vasculopathy, seizure, and chronic neurologic defects, which limit its widespread clinical use (20, 91, 156). However, since the inception of this idea, there has been considerable advancement in other techniques to disrupt the BBB for theranostic applications.

Microbubble-Enhanced Focused Ultrasound

Microbubble-enhanced focused ultrasound (MEUS) techniques rely on the application of low-power ultrasound to a specific brain region in combination with intravenous (IV) administration of preformed, lipid-coated, echogenic microbubbles (**Figure 4A**) (160). The focused ultrasound induces stable cavitation in the bubbles as they pass through the ultrasound field, mediating precise and transient disruption of the BBB via the downregulation of TJ proteins (82), suppression of P-glycoprotein expression (161), and facilitation of pinocytosis (162). MEUS has been used recently in animal models to enhance BBB permeability to an array of therapeutics (160). Furthermore, this technique can be used under magnetic resonance imaging (MRI) guidance to evaluate the effectiveness of BBB opening. Such a combination has been explored clinically for targeted

TABLE 1 | Preclinical and early clinical agents for delivery of optical labels to brain tumors discussed in this review.

Agent	Interaction with BBB/BBTB	Stage of development	References
UNTARGETED AGENTS			
[^{18}F]-1; an [^{18}F]-labeled dasatinib derivative for ^{18}F-PET and fluorescence visualization *in vivo*	None; investigated using CED to bypass the BBB in mouse models	Preclinical	(93)
Collagen-based, ^{131}Cs-laden wafer for intracranial brachytherapy	None; intracranial implant to bypass the BBB	Clinical	(94)
PEGylated FLS	None; improved passive accumulation within tumor tissues via the EPR effect in U251 orthotopic mouse glioma	Preclinical	(95)
Albumin-bound 5-aminoFLS	None; improved passive accumulation within tumor tissues via the EPR effect intraoperatively	Clinical	(96, 97)
Second-window ICG	None; passive accumulation within tumor tissues via a delayed EPR effect	Clinical	(98–102)
Aptamer-conjugated PEGylated quantum dots	None; passive accumulation via the EPR effect and targeting via EGFRvIII-targeted aptamers in orthotopic mouse gliomas	Preclinical	(103)
Silk fibroin-ICG nanoparticles	None; improved passive accumulation within orthotopic C6 mouse glioma cells via the EPR effect	Preclinical	(104)
EPR Enhancers			
PGI2 agonists	Dilation of tumor vasculature to increase extravasation and accumulation via the EPR effect	Preclinical	(105)
TNF-a		Preclinical	(106)
Intraarterial angiotensin II		Clinical	(107)
ANTIBODY/AFFIBODY-BASED AGENTS			
ABY-029, an anti-EGFR affibody conjugated to the near infrared probe IRDye 800CW	Targeting to EGFR receptors overexpressed on glioma cells	Clinical	(108), NCT02901925
FITC-conjugated anti-EGFR antibody		Preclinical	(109)
IRDye 800CW-conjugated anti-EGFR antibody		Preclinical	(110)
OTHER TARGETED AGENTS			
ANG2, a synthetic peptide shown to target the BBB	RMT via low-density lipoprotein receptor 1 targets both BBB and BBTB	Clinical	(111, 112), NCT01967810, NCT02048059
ANG2/PLGA/DTX/ICG probe, an ANG2-coated, ICG- and docetaxel-laden PLGA nanoparticle	RMT via low-density lipoprotein receptor 1 targets both BBB and BBTB	Preclinical	(113)
ANG2/PEG-UCNP, an ANG2-conjugated, gadolinium-laden fluorescent upconversion nanoparticle	RMT via low-density lipoprotein receptor 1 targets both BBB and BBTB	Preclinical	(114)
AsT, a TGN- and AS1411-conjugated Cy3 fluorescent probe	Endothelial cell uptake and transcytosis into the brain via TGN-conjugation by an unknown mechanism and AS1411 aptamer-mediated glioma cell targeting	Preclinical	(115)
Lysine-methotrexate prodrug	CMT via L-type amino acid transporter 1 targets the BBB in a mouse model	Preclinical	(116)
Aspartate-, 2-amino-apidic acid-, and phenylalanine-conjugated dopamine prodrugs	CMT via large neutral amino acid transporter 1 targets BBB	Preclinical	(117)
ApoE3-labeled porphyrin-lipid nanoparticles	RMT via low-density lipoprotein receptor 1 targets both BBB and BBTB in a mouse model	Preclinical	(118)
Transferrin-functionalized lipid nanoparticles laden with temozolomide and bromodomain inhibitor JQ1	RMT via transferrin receptor in a mouse model	Preclinical	(119)
BLZ-100 (tozuleristide), ICG-conjugated chlorotoxin	RMT via binding to chloride channels to trigger endocytosis at the BBB or BBTB and MMP-2 binding for targeting of glioma cells	Clinical	(120–123), NCT03579602
IRDye 800CW-cyclic-RGD peptide	Targeting to integrin receptor overexpression on tumor vasculature and on tumor cells in a mouse glioma model	Preclinical	(124)
BLIPO-ICG, ICG-laden biomimetic proteolipid liposomes	Passive accumulation via the EPR effect and targeting to glioma cells via functionalization with glioma-derived surface markers in a mouse glioma model	Preclinical	(125)
5-ALA-COUPLED AGENTS			
5-ALA + MEK inhibitor selumetinib	Inhibition of ABCB1-mediated PpIX efflux and ferrochelatase-mediated PpIX metabolism at the BBB or BBTB in a mouse model	Preclinical	(126)

(Continued)

TABLE 1 | Continued

Agent	Interaction with BBB/BBTB	Stage of development	References
5-ALA + efflux pump inhibitors			
Ko143	Inhibition of ABCG2-mediated PpIX efflux at the BBB or BBTB	Preclinical	(127, 128)
Gefitinib		Preclinical	(129)
Imatinib mesylate		Preclinical	(130)
5-ALA + iron chelators	None; inhibition of PpIX metabolism to heme via ferrochelatase in tumor cells	Preclinical	(131–134)
5-ALA + differentiation agents			
Calcitriol	None; enhanced PpIX accumulation via upregulation of coproporphyrinogen oxidase in epithelial cancer and glioma cell cultures	Preclinical	(135, 136)
Vitamin E	None; enhanced PpIX accumulation via upregulation of coproporphyrinogen oxidase in epithelial cancer cell culture	Preclinical	(137)
5-ALA + heme oxygenase inhibitors	None; accumulation of PpIX via inhibition of downstream metabolism of heme by heme oxidase	Preclinical	(138, 139)

^{18}F, Fluorine-18; ^{131}Cs, Cesium-131; 5-ALA, 5-aminolevulinic acid; ABCB1, ATP-binding cassette subfamily B member 1; ABCG2, ATP-binding cassette subfamily G member 2; ANG2, angiopep-2; ApoE3; apolipoprotein E3; BBB, blood-brain barrier; BBTB, blood-brain tumor barrier; CMT, carrier-mediated transport; DCT, docetaxel; EPR, enhanced permeability and retention; FLS, fluorescein sodium; ICG, indocyanine green; MEK, mitogen-activated protein kinase kinase; MMP-2, matrix metalloproteinase 2; PEG, polyethylene glycol; PET, proton emission tomography; PLGA, poly(lactic-co-glycolic acid); PpIX, protoporphyrin IX; RMT, receptor-mediated transport; UCNP, up-conversion nanoparticle.

neuromodulation (163) and drug delivery in Alzheimer's disease (164). MEUS is designed for a non-invasive and highly targeted approach, mitigating the risks of non-specific hyperosmolar BBB disruption and surgical methods of drug delivery (165, 166).

Neurogenic Methods

Transcranial magnetic stimulation and sphenopalatine ganglion stimulation (**Figure 4D**) are novel methods that can affect neurovascular unit function and BBB permeability by acting on its neuronal component. Transcranial magnetic stimulation effects are based on neuronal activity and are mediated by an N-methyl-D-aspartate-receptor-dependent mechanism (167, 168). Transcranial magnetic stimulation has been used for the treatment of neurological disorders, including depression, but its potential for improving drug delivery to the brain has become a subject of recent studies (167). Sphenopalatine ganglion stimulation is a novel technique for transient (4 h) BBB disruption via neural stimulation (57). Sphenopalatine ganglion stimulation caused downregulation of TJ proteins, similar to that seen in hyperosmolar disruption, and resulted in ipsilateral, hemispheric extravasation of a 70-kDa FLS-labeled dextran in a rat model (57). The safety and clinical efficacy of this method, especially compared to the more focused MEUS, is yet to be established.

Photodynamic Method

Photodynamic opening of the BBB using 5-ALA has been described in a mouse model (169). Irradiation with a 635-nm laser, 30 min after IV administration of 5-ALA resulted in a transient (4 h) increased BBB permeability to Evans blue dye, 70-kDa FITC-dextrans, and intravascular solutes. Histological analysis demonstrated complete recovery from the induced perivascular edema within 3 days. Implications of these findings for the current 5-ALA-based fluorescence-guided surgical techniques or photodynamic therapy should be investigated further. However, 5-ALA is mostly cleared from the blood by the time of glioma resection (∼6 h after oral administration).

Clinical Applicability of BBB Disruption for Fluorescence-Guided Surgery

With regard to optically guided brain tumor resection, techniques for BBB disruption may be used to enhance the delivery of targeted optical markers, improving the sensitivity of tumor visualization, especially in low-grade gliomas and at the border of high-grade gliomas, where the BBTB remains largely intact. However, clinical procedures for BBB disruption may be too invasive and time consuming to warrant their application solely to improve fluorescence-guided surgery. Preoperative BBB disruption for delivery of targeted optical drugs should ideally be combined with therapeutic agents in order to take full advantage of transient BBB opening. Further, wider adoption of MEUS and transcranial magnetic stimulation should stimulate the clinical translation of novel combinatory drugs that include not only therapeutic agents, but also optical fluorescent tracers for better intraoperative visualization of brain tumor margins. However, major efforts are directed toward development of molecular techniques for bypassing and targeting the BBB/BBTB without destroying its integrity (170).

Bypassing the BBB

Techniques to bypass the BBB entirely are primarily surgical in nature (**Figure 4B**). These include methods such as intrathecal/intraventricular injection, transnasal administration, convection-enhanced delivery (CED), and intracerebral or topical implantation.

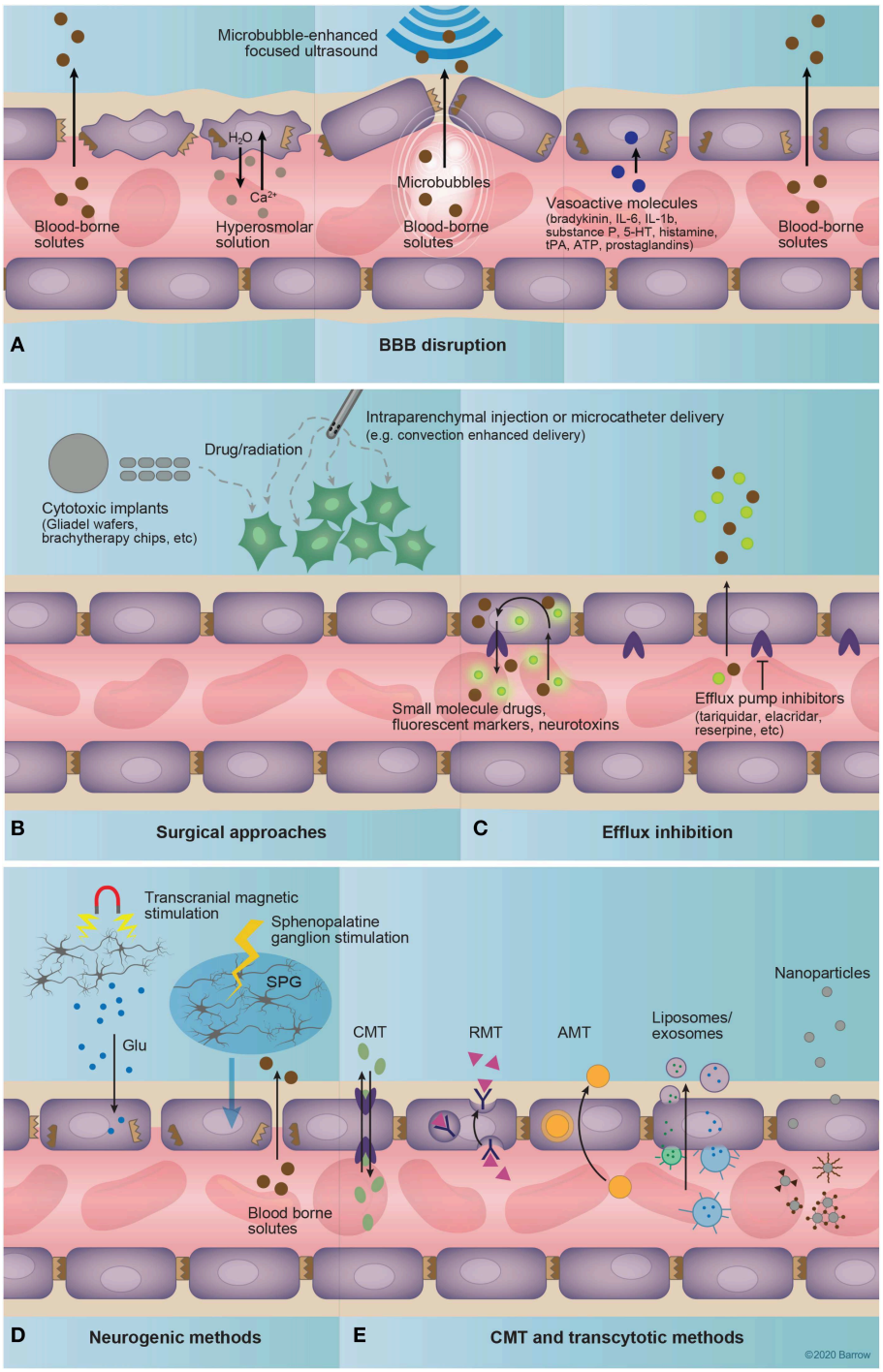

FIGURE 4 | Drug delivery to the central nervous system. **(A)** Techniques that involve coadministration of a drug coupled to disruption of the blood-brain barrier (BBB) include hyperosmolar disruption, microbubble-enhanced focused ultrasound (MEUS), and administration of vasoactive substances. The intravascular injection of a hyperosmolar solution dehydrates endothelial cells, shrinking them and causing strain at tight junctions, and ultimately causing tight-junction protein displacement and BBB disruption. MEUS involves the intravascular administration of small (~1 μm) bubbles that are targeted by focused ultrasound to induce cavitation, creating tight-junction strain and resulting in BBB permeation. Finally, vasoactive molecules including bradykinin, interleukins 6 and 1β, substance P, serotonin, histamine, tissue plasminogen activator, adenosine triphosphate, and prostaglandins, alter the expression of tight-junction proteins, affecting BBB permeability. **(B)** Surgical approaches deliver drugs by circumventing the BBB entirely. These approaches include the implantation of a polymer with delayed drug release [for example, radioactive brachytherapy (157) or chemotherapeutic-loaded implants (157, 158)] into the brain or the injection of a drug into the brain via microcatheter. **(C)** Efflux inhibition aims to augment the diffusion of a drug across the BBB via the inhibition of efflux pumps that mediate its active removal from the brain. Examples of known efflux pump

(Continued)

FIGURE 4 | inhibitors include tariquidar, elacridar, and reserpine (159). **(D)** Neurogenic methods of increasing BBB permeability include transcranial magnetic stimulation and sphenopalatine ganglion stimulation. Transcranial magnetic stimulation is thought to increase BBB permeability through the endothelial binding of glutamate released from magnetically excited neurons. The exact mechanisms of sphenopalatine-mediated BBB permeability are currently unknown, but likely involve sympathetic innervation of intracranial vasculature provided through the sphenopalatine ganglion. **(E)** Carrier-mediated and transcytotic methods involve the targeted binding of drug-bearing molecules to structures expressed on the luminal surface of the endothelium. This delivery system includes freely soluble drug molecules that bind to expressed transporters or surface molecules, drug-delivery vehicles such as liposomes or exosomes, or nanoparticles. Importantly, these drug-delivery methods often incorporate transporter or receptor substrates or molecular probes for targeting to specific structures at the BBB/BBTB. 5-HT, serotonin; AMT, adsorption-mediated transport; ATP, adenosine triphosphate; BBB, blood-brain barrier; CMT, carrier-mediated transport; Glu, glutamate; IL, interleukin; RMT, receptor-mediated transport; SPG, sphenopalatine ganglion; tPA, tissue plasminogen activator. *Used with permission from Barrow Neurological Institute, Phoenix, Arizona*.

Intrathecal or Intraventricular Administration

Intrathecal or intraventricular administration theoretically bypasses the BBB, but diffusion from the cerebrospinal fluid (CSF) to the brain parenchyma is limited by a relatively rapid bulk flow of CSF and a slow rate of diffusion into brain tissue (87). Thus, drugs administered to the CSF are ultimately redistributed to the blood where they must cross the BBB to be effective. While intrathecal or intraventricular drug delivery is effective for leptomeningeal diseases, it is not suitable for parenchymal brain tumors (64, 171).

Transnasal Drug Administration

Transnasal drug administration and mucosal engrafting (172, 173) techniques initially avoid the BBB, but the drug must still cross into the subarachnoid space, where it will face the same obstacles as intrathecally administered drugs while providing only limited focal drug distribution.

Convection-Enhanced Delivery

CED involves surgical insertion of a semipermeable catheter into the area of drug administration in the brain or tumor with a constant administration of drug solution under a positive-pressure gradient (174, 175). Over 20 clinical studies used CED for delivery of therapeutic agents in high-grade gliomas and showed moderate clinical efficiency (158). A few studies have used coinfusion with gadolinium to monitor infusate distribution (176, 177). Wang et al. (93) investigated CED of an ^{18}[F]-positron-emitting, fluorescent derivative of the Abl-kinase inhibitor dasatinib in a mouse glioma model. Similar to other studies (178, 179), the main purpose of coadministration of the fluorescent agent is to monitor drug distribution in experimental settings. As trials for the delivery of novel therapeutics using CED are still being conducted (180, 181), the utilization of CED with fluorescent markers for optical image guidance, for example in recurrent gliomas, is yet to be explored.

Another method for circumvention of the BBB is to deliver drug directly into the resection cavity intraoperatively. This technique has seen relative success with current therapeutic agents, such as an implantable, biodegradable polyanhydride polymer infused with the alkylating agent carmustine (Gliadel) (182–184) or a collagen wafer embedded with x-ray-emitting cesium-131 (94). Such administration promotes delayed diffusion of the drug that creates areas of increased drug concentration and CED in the peritumoral bed over time. Direct intracavitary delivery of optical imaging agents, especially "activatable" fluorescence probes that turn on upon specific binding to a targeted molecular motif, is also being explored (185, 186). Although promising, local application of fluorescent markers to the surface of a resection cavity is inherently limited in that it requires some incubation time and would leave any subsurface tumor unlabeled. On the other hand, topical staining could still be useful to identify any apparent residual tumor. Furthermore, such staining could be used for a small-field, intraoperative, digital biopsy assessment of selected regions of interest (187, 188).

Targeting the BBB

Recent technologies have adopted a strategy of targeting existing transporters, receptors or other molecules expressed on the luminal surface of the CNS endothelium to facilitate drug delivery (**Figures 4C,E**). Importantly, these techniques allow for crossing of the BBB without disrupting interendothelial TJs, thereby avoiding the potential efflux of neurotoxic substances from the blood into the brain.

Carrier-Mediated Transport

Carrier-mediated transport (CMT) takes advantage of an array of small-molecule transporters expressed at the BBB. Through the conjugation of small-molecule drugs to or the mimicking of the ligands of these transporters, selective movement of drugs across the BBB may be achieved. Classically, drugs such as L-3,4-dihydroxyphenylalanine, melphalan, and gabapentin take advantage of CMT for CNS activity. Singh and Subudhi (116) have demonstrated this by delivering a methotrexate-lysine conjugate prodrug across the BBB via L-type amino acid transporter 1. In a similar approach, Peura et al. (117) synthesized amino acid prodrugs of dopamine to increase uptake across the BBB via the large amino acid transporter 1. While these early results have been successful in animal models, clinical application of CMT-based delivery may be difficult. Examination of the expression profiles of these receptors in a given tumor or BBTB might be needed prior to determination of a therapeutic target. Further, CMT-based strategies are limited to small-molecule drugs or prodrugs, as transporters will not support the passage of larger molecules.

Receptor-Mediated Transport

Receptor-mediated transport (RMT) strategies target receptors expressed on the luminal surface of CNS endothelium in order to initiate endocytosis or transcytosis for transport of the molecule to the abluminal surface. Often, these strategies involve the

linking of an effector molecule to a receptor ligand or antibody that can bind and initiate endocytosis.

An example of a molecule used successfully for RMT is angiopep-2 (ANG2), a synthetic peptide that targets LRP1 at the BBB. Importantly, LRP1 is a shuttling receptor, able to mediate transcytosis while avoiding the destructive lysosomal compartment (111, 189). LRP1 has also been shown to be overexpressed on glioblastoma cells (190), giving ANG2 tumor-specific targeting capabilities. So far, ANG2 has proven capable of delivering paclitaxel to glioma and brain metastases, avoiding P-glycoprotein-mediated paclitaxel efflux (90), and is currently in Phase II clinical trials for recurrent high-grade glioma (NCT01967810) and breast cancer with recurrent brain metastases (NCT02048059).

Rajora et al. (118) reported the successful targeting of LRP-1 expressed on orthotopic U87 glioblastoma cells in mice using apolipoprotein E3 porphyrin-lipid nanoparticles. Glioblastoma cells readily took up the nanoparticles, exhibiting near-infrared fluorescence and sensitization to photodynamic therapy. In another study, Lam et al. (119) reported the success of transferrin-functionalized nanoparticles bearing temozolomide and bromodomain inhibitor JQ1 to selectively target and kill glioblastoma cells in a mouse model. These studies both demonstrate the efficacy of RMT-mediated targeting of tumors *in vivo*. Importantly, these therapies have a potential to traverse the intact portion of the BBTB for treatment of otherwise shielded tumor cells.

The Future and Caveats of Techniques for Transcellular Transport

Increasingly, CMT- and RMT-based therapeutic strategies are incorporating delivery vehicles such as nanoparticles, liposomes, or exosomes to target brain tumors. These strategies involve the assembly of a custom-built molecular vehicle, often housing an effector molecule, that is coated with receptor ligands or other targeting molecules to facilitate the precise targeting of the vehicles to the endothelium of the BBB or tumor cells. A detailed review of liposome-based drug vehicles was recently published (141), and several have been published regarding nanoparticle-based drug delivery to the brain (85, 89, 170, 191–196). The main advantage of nanoparticle technology is its customizability, as the size, composition, cargo, and target are tunable, affecting changes in BBB permeability, therapeutic effect, or drug pharmacokinetics. However, several caveats to these strategies need to be carefully considered.

Bypassing the endothelial barrier with an optical or other diagnostic agent only informs about the location and degree of BBB disruption and not necessarily about the tumor cells themselves. In order to achieve better selectivity and ability to target tumor cells beyond the competent BBTB, the agent should dissociate from the encapsulating vehicle, travel through the extracellular space and, ideally, label the tumor cells. Given the complexity of the underlying mechanisms of drug delivery, many obstacles must be overcome. If the vehicle is too stable, the drug is not released and does not react with the target (197, 198). However, if the drug has low molecular weight, it risks diffusion back to the circulation upon dissociation from the large carrier (197, 199, 200). Large molecular constructs, and especially micelles, should additionally withstand shear stress of the microvascular circulation (201). For example, it has been demonstrated that a significant amount of doxorubicin has leaked out of encapsulating micelles within a few hours after administration because of shear stress (200). These problems are only a few considerations that hinder the safety and efficacy of these therapies, but nonetheless, they must be reconciled before clinical application.

MECHANISMS OF FLUORESCENT LABELING OF BRAIN TUMORS

5-Aminolevulinic Acid

General Characteristics

5-ALA ($C_5H_9NO_3$, 131.13 Da), is an endogenous metabolite and a precursor for the biosynthesis of heme *in vivo* (**Figure 5A**). Under the action of intracellular enzymes in the heme biosynthetic pathway, 5-ALA is converted to an endogenous fluorophore, protoporphyrin IX (PpIX) (excitation: 405 nm; emission: 635 nm, with a minor emission peak at 710 nm). Intraoperatively, the blue excitation light contrasts well with the red fluorescence of PpIX, facilitating tumor margin delineation. 5-ALA was initially investigated for use in photodynamic therapy (202–205), whereby absorption of light by PpIX mediates the production of tumor-killing reactive oxygen species, but became a drug for improved visualization of high-grade gliomas during resection (206, 207) approved by the US Food and Drug Administration (FDA) (208). The mechanisms of 5-ALA passage through the BBTB (209) and intracellular metabolism (127, 210) have been previously reviewed in detail, so here we provide a brief summary of the key steps.

5-ALA Delivery Across the BBTB

The oral bioavailability of 5-ALA is around 60% in healthy subjects (127). Plasma half-life of 5-ALA after oral administration is about 45 min and plasma concentration approaches zero after about 6.5 h (211, 212). Experiments with radioactive 5-ALA in mice showed that 5-ALA does not penetrate an intact BBB but accumulates and undergoes conversion to PpIX in brain regions with a diminished BBB, such as the ependyma, choroid plexus, arcuate nucleus, and median eminence. (213, 214) PpIX visualization in high-grade gliomas correlates well with gadolinium-enhanced MRI (215), suggesting that the main mechanism of accumulation of PpIX in glioma is leakage of free 5-ALA through the altered BBTB. The lack of PpIX accumulation in low-grade gliomas is likely due to the presence of a more competent BBTB that prevents 5-ALA delivery and a lack of severe alterations in heme metabolism that would result in PpIX accumulation. So far, it is hard to elucidate which mechanism is most determinate of 5-ALA accumulation. Observed foci of fluorescence in low-grade gliomas were correlated with anaplastic transformation and increased cellularity (216, 217), which in turn may result in a less competent BBTB that is permeable to 5-ALA but not to gadolinium-based contrast.

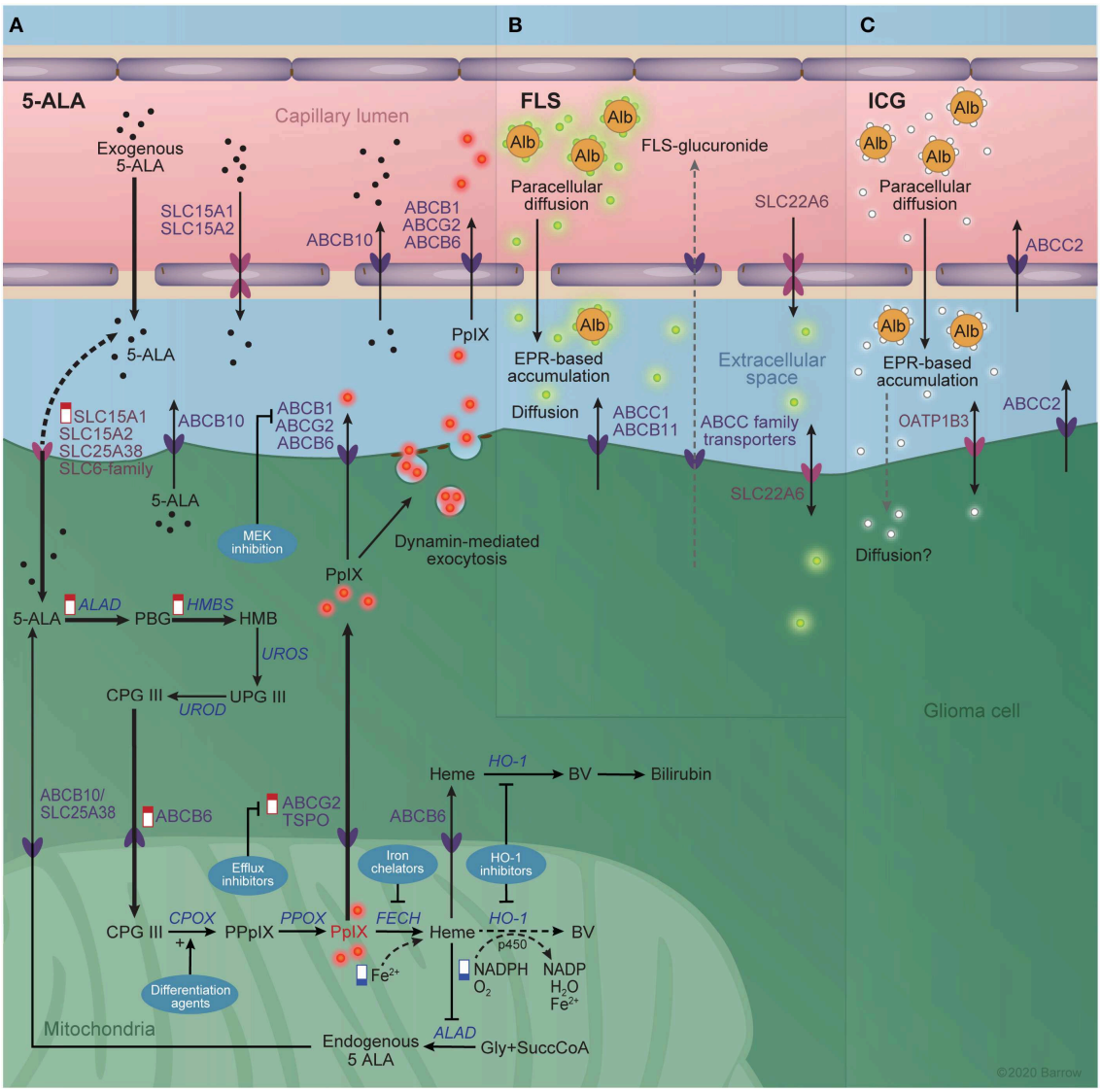

FIGURE 5 | Interaction between imaging agents and the blood-brain barrier. **(A)** The known transporters of 5-aminolevulinic acid (5-ALA) and protoporphyrin IX (PpIX) at the blood brain barrier and glioma cell membrane are shown schematically. The heme biosynthetic pathway is shown in the glioma cell cytoplasm and mitochondrial matrix. Alterations in the heme biosynthesis pathway responsible for increased PpIX accumulation in the tumor are indicated by "low" (blue) and "high" (red) signs. Thick arrows represent increased rate reactions after exogenous 5-ALA administration that contribute to the excess PpIX accumulation. Dotted arrows represent reduced rate reactions contributing to PpIX accumulation. Techniques for augmenting 5-ALA-mediated PpIX accumulation are shown in blue bubbles and include MEK inhibition, efflux inhibitors, differentiation agents, iron chelators, and heme oxygenase 1 inhibitors. **(B)** The known transporters of fluorescein and **(C)** indocyanine green are shown similarly. Active efflux pumps of the ATP-binding cassette family are depicted in dark violet and solute carrier family transporters in pink. Alb, albumin; ABC, ATP-binding cassette; ALAD, aminolevulinic acid dehydrogenase; BV, biliverdin; CPG III, coproporphyrinogen III; CPOX, CPG III oxidase; FECH, ferrochelatase; Gly, glycine; HO-1, Heme Oxygenase 1; HMB, hydroxymethylbilane; HMBS, HMB synthase; PBG, porphobilinogen; PpIX, protoporphyrinogen IX; PPOX, PpIX oxidase; SLC, solute carrier; SuccCoA, Succinyl Coenzyme A; UPG III, uroporphyrinogen III; UROD, UPG III decarboxylase; UROS, UPG III synthase. *Used with permission from Barrow Neurological Institute, Phoenix, Arizona*.

5-ALA Metabolism

Once inside the cell, 5-ALA enters the heme biosynthetic pathway, where it is converted sequentially to porphobilinogen, hydroxymethylbilane, uroporphyrinogen III, coproporphyrinogen III, protoporphyrinogen IX, PpIX, and heme (**Figure 5A**). Peak fluorescence intensity of PpIX in the tumor core is observed about 7 to 8 h after oral 5-ALA administration, while in the marginal tumor area the peak of weaker fluorescence is observed after about 8 to 9 h (218, 219).

In normal non-erythroid cells, heme biosynthesis is regulated by negative feedback mechanisms, mainly negative feedback of heme on the enzyme ALA synthase, controlling the intracellular levels of PpIX (220). In cancer cells, however, these systems are dysregulated, leading to PpIX accumulation and fluorescence. A

recent examination of various human tumor samples suggests that the kinetics of PpIX accumulation are determined primarily by alterations in PpIX efflux, conversion of PpIX to heme, and PpIX biosynthesis (221). Interestingly, fluorescence was not shown to be dependent on the rate of 5-ALA uptake (221).

Heterogeneity in tumor cell signaling, protein expression, and metabolism are responsible for variations in PpIX accumulation. In this way, differential expression of transporters for elements of the heme biosynthetic pathway at the BBTB or tumor cell membrane is a source of modulation of the accumulation of PpIX. Notably, 5-ALA is a substrate of SLC15A1 and SLC15A2 (222), SLC36A1 (223), SLC6A6 and SLC6A13 (224), and ABCB10 (210), while PpIX is a substrate of ABCB6, ABCG2 (225) and ABCB1 (126). Of these, SLC15A1, SLC15A2, ABCB10, ABCB1, ABCG2, and ABCB6 are known to be expressed at the BBB (226), and therefore likely influence levels of PpIX accumulation. Kitajima et al. (227) showed that dynamin 2-mediated exocytosis plays a role in PpIX efflux from cancer cell lines in the JFCR39 panel, which includes six brain tumor lines. Interestingly, they failed to show a correlation between ABCG2 expression levels and PpIX efflux, although ABCG2 inhibition led to enhanced PpIX accumulation. This is in contrast to previous results by Hagiya et al. (228) that showed ABCG2 expression to be a major determinant of PpIX fluorescence in gastric cancer cell lines *in vitro*.

PpIX Excretion

PpIX may be converted to heme in mitochondria via the action of ferrochelatase or may be subject to active efflux from the cell by the ABCG2 efflux pump. Once in the blood, the plasma half-life of PpIX is around 8 h (229). If not further metabolized to heme, PpIX is taken up and excreted into bile by the liver (210).

Approaches to Augment PpIX Accumulation

The complex metabolism and transport of PpIX precursors create opportunities for the pharmacologic augmentation of PpIX accumulation in tumors that bear relevance for photodiagnostic and photodynamic applications of PpIX. At least five mechanisms have been identified (**Figure 5A**).

Mitogen-Activated Protein Kinase Kinase (MEK) inhibition

Yoshioka et al. (126) demonstrated enhancement of PpIX accumulation in a murine mammary tumor model via the inhibition of oncogenic Ras/MEK. MEK inhibition decreased expression of the ABCB1 efflux pump and reduced activity of ferrochelatase, the enzyme responsible for converting PpIX to non-fluorescent heme. Importantly, these changes were not observed in normal tissues, highlighting a targetable difference in regulatory mechanisms for heme biosynthesis between tumor and normal cells.

Efflux inhibition

Efflux pump inhibition relies on the principle that a known set of targetable transporters are responsible for the efflux of PpIX or its precursors from the brain or tumor tissues (**Figure 4C**). Kawai et al. (230) demonstrated that expression of the efflux pump ABCG2 was associated with a cancer stem cell phenotype and decreased 5-ALA fluorescence in a human pancreatic cancer cell line. Studies in peripheral tumors (127, 128) and with tumor cells *in vitro* (129, 130) share these results, showing an increase in 5-ALA-mediated PpIX accumulation in tumor tissue when combined with ABCG2 inhibitors. However, these studies do not necessarily account for the added heterogeneity of transporter expression at the BBB or within tumors *in vivo*.

Iron chelators

Augmentation of PpIX fluorescence by ferrochelatase inhibition using iron chelators has been demonstrated *in vitro* in glioma cell cultures (131–133). Wang et al. (134) showed that glioma stem cell escape from PpIX fluorescence could be overcome with the use of iron chelation to inhibit ferrochelatase, but not with administration of an ABCG2 inhibitor. In fact, contrary to the abovementioned reports, ABCG2 inhibition was shown to slightly decrease PpIX accumulation in these cells. The authors suggest that these results are likely due to the off-target inhibition of ABCB6, required for trafficking of coproporphyrinogen III across the mitochondrial membrane, leading to decreased PpIX synthesis overall. These results emphasize the importance of targeting specific transporters if efflux inhibition is to be employed and also raise questions about the viability of this approach in all tumors.

Differentiation agents

Differentiation therapy (calcitriol, vitamin E) has been shown to increase the cytotoxic effects of 5-ALA-mediated photodynamic therapy via upregulation of coproporphyrinogen oxidase in epithelial cancers (135, 137). Calcitriol was also shown to enhance 5-ALA-induced fluorescence and photodynamic therapy in human glioma cells *in vitro* (136).

Heme oxygenase 1 (HO-1) inhibition

Inhibition of HO-1 has also been shown to increase PpIX accumulation in melanoma (138). This strategy has the added benefit of disabling the cytoprotective and anti-inflammatory properties of HO-1, making tumor cells more prone to lysis by oxidative stress (139).

Opportunities and Limitations of 5-ALA Augmentation

Overall, the intricacy of cell-signaling pathways and transporter expression that governs heme biosynthesis complicates PpIX-based fluorescence visualization. Notably, elements of the heme biosynthetic pathway are substrates of a diverse set of transporters that modulate their intracellular accumulation. Furthermore, heme biosynthetic enzymes are often aberrantly expressed or active in tumor cells, hampering the reliable prediction of PpIX fluorescence status. For example, Lai et al. (231) demonstrated that selective inhibition of SLC15A1 and SLC36A1 expressed in normal but not cancerous lung and prostate cell lines allowed for augmentation of PpIX accumulation in tumor cells. This approach may actually hinder PpIX accumulation in glioma, though, as SLC15A1 is expressed at the BBB and may mediate 5-ALA accumulation in the brain (231). Nevertheless, the general approach of inhibiting transporters selectively expressed in normal cells versus tumor cells may still prove useful to augment tumor-selective accumulation of PpIX.

The described approaches provide tools for control of the selective augmentation of PpIX fluorescence in tumor cells. While these results remain to be evaluated amidst the added complexity of the BBB and BBTB in humans, they support the viability of pharmacological strategies to enhance PpIX fluorescence. Further research may one day see the ultimate translation of these approaches to the operating room, where they can help to augment the sensitivity and utility of 5-ALA-guided brain tumor resection.

Fluorescein Sodium

General Characteristics

FLS ($C_{20}H_{10}Na_2O_5$, 376.5 Da) is a yellow-green fluorescent dye (excitation 460–490 nm, emission 510–530 nm) (232) whose derivatives, such as FITC and Alexa 488, are used widely in research. The LD_{50} of IV FLS is 300 mg/kg in rabbits (233). FLS-guided resection of high-grade glioma was successful in a recent Phase II clinical trial ($n = 46$ patients) (234) and in a prospective observational study ($n = 279$ patients) (78), indicating its clinical applicability. FLS has also been used as a contrast for intraoperative assessment of tissue microstructure using confocal laser endomicroscopy (235, 236).

Pharmacokinetics

After IV administration, FLS weakly binds to serum albumin and rapidly distributes throughout the central circulation. FLS has a volume of distribution of 0.5 L/kg (237), indicating an even distribution between blood and interstitial spaces. FLS exists in the circulation in both a free unbound fraction and a serum-protein bound fraction. The small size of unbound FLS allows for rapid diffusion into the tumor due to first-pass extravasation, creating a large early peak in tumor fluorescence (**Figure 5B**). In contrast, the larger effective diameter of protein-bound FLS leads to a later smaller peak that is facilitated by the EPR effect. The unbound fraction of FLS only minimally crosses the intact BBB when administered in high doses (95) but is not readily detected within the normal brain using the operative microscope at the time of surgery. Unspecific leakage of unbound FLS through a heterogeneous and dynamic BBB/BBTB explains reports of unspecific FLS staining in peritumoral areas (238). Compared to unbound FLS, a PEGylated form of FLS with a molecular weight similar to that of gadolinium-based contrast agents (939 Da) showed improved specificity of accumulation in U251 orthotopic mouse gliomas 1 h after administration (95). An albumin-bound formulation of 5-aminofluorescein (66,950 Da) was investigated in a Phase I/II study in Germany (96, 97), where bright fluorescence was observed in 10 of 10 patients with high-grade gliomas 0.5 to 4 days after IV administration. These results highlight the utility of the EPR effect for prolonging the fluorescent staining window for small non-targeted molecules.

Optimal FLS Timing and Dosage

Increasing the dose of FLS (5 vs. 20 mg/kg human equivalent) results in an increase in unbound FLS in the blood and normal brain tissue (95). Therefore, the dose and timing of FLS administration should be considered to optimize fluorescent contrast during surgery. Thus far, the optimal strategy is to use lower doses of FLS [1–2 mg/kg (239), 3 mg/kg (240), and 5 mg/kg (234)] to minimize unspecific extravasation and to administer FLS 2 to 4 h before visualization, which corresponds to the wash-out period of the FLS from the normal brain (78).

FLS and BBTB Heterogeneity

FLS tends to accumulate in extravascular spaces and not within tumor cells. Accordingly, FLS-defined high-grade glioma margins correlate well with gadolinium-based MRI results (240). Reports on the use of FLS for the visualization of brain metastases demonstrated that the majority of them were fluorescent [90/95 (95%) (241) and 16/17 (94%) (242)]. However, surrounding normal brain also showed a low degree of fluorescence (241). Data on FLS efficacy in low- and intermediate-grade gliomas show that about half of tumors are not labeled with FLS, likely because the BBTB is not sufficiently disrupted (243). However, some non-gadolinium-enhancing gliomas can still be labeled with FLS (244, 245). These findings support the hypothesis that the unbound, low-molecular-weight fraction of FLS plays an important role in labeling tumors with minimally disrupted BBTB. Such tumors and peritumoral brain regions may allow extravasation or convection-based transport of the smaller unbound FLS molecules but not gadolinium-based contrast. Thus, a balance must be struck between dosing that creates an increased proportion of unbound FLS that is more likely to unspecifically stain normal brain but more readily stain marginal tumor and dosing in which a smaller dose of free and protein-bound FLS promotes EPR-based labeling of the tumor core but less labeling of the surrounding normal brain.

Potential Molecular Transporters and Clearance of FLS

Molecular transporters may also play a role in FLS pharmacokinetics. In the liver, FLS is conjugated to glucuronide before being excreted in the urine. FLS has a plasma half-life of 23.5 min, while minimally fluorescent FLS-glucuronide has a plasma half-life of 264 min (237). The small size and relative lipophilicity of FLS may allow for greater BBB permeability compared to ICG or gadolinium-based agents, but the activity of certain transporters at the BBB or BBTB may limit unaided extravasation. FLS is a substrate for the SLC22A6 transporter (237), the bile salt export pump, ABCB11 (246), and multidrug resistance-associated protein 1 (ABCC1) (247). Notably, SLC22A6 is involved in drug clearance from the CSF (248) and is expressed at low levels in CNS endothelium (226), and ABCC1 is expressed at the BBB (25). FLS-glucuronide is also likely a substrate of other members of the ABCC-subfamily of multidrug resistance proteins that are responsible for transporting conjugated metabolites (249), although, to our knowledge, this has not been shown. As such, these transporters likely alter the BBB permeability of unbound FLS.

Indocyanine Green

General Characteristics

ICG ($C_{43}H_{47}N_2NaO_6S_2$, 774.96 Da) is a water soluble, unstable [half-life in aqueous solution is 20 h (250)], amphiphilic fluorescent dye. The LD_{50} of IV ICG is 50 to 75 mg/kg

(251). After IV injection, ICG rapidly binds to plasma proteins and is distributed throughout the circulation with a volume of distribution of 0.035 L/kg (252), reflecting a high degree of plasma protein binding (140). The excitation and emission maximums of bound ICG exist in the near-infrared range (805 and 830 nm, respectively) thus enabling greater tissue penetration than markers that fluoresce in the visible range (253, 254).

Pharmacokinetics

ICG binding with plasma proteins increases the brightness of ICG fluorescence nearly 3-fold. Although it was initially thought that IV-injected ICG binds to albumin (255), later studies of blood samples following IV ICG injection suggested that ICG binds more intensely to high density lipoproteins (175–360 kDa, 7–14 nm) and moderately to low-density lipoproteins (256, 257). The larger size of bound ICG and the fact that, unlike FLS, ICG is almost completely bound to plasma proteins are important considerations for understanding the transport of ICG across the BBTB (**Figure 5C**).

Bound ICG gradually traverses the incompetent BBTB and accumulates in brain tumors such as high-grade gliomas and meningiomas, primarily due to the EPR effect (258). The timing of ICG accumulation in the tumor and optimal dosing of ICG was the subject of animal and human studies that could be grouped into three categories based on the imaging time: imaging immediately after ICG injection, delayed imaging within a few hours after injection, and imaging within a day after injection, termed the second-window ICG (251, 259, 260).

A study by Haglund et al. (251) investigated ICG in low- and high-grade gliomas using a charge-coupled device camera attached to a standard operating microscope within the first 10 min after IV ICG administration at 1 mg/kg. They observed progressively increased ICG signal within 10 min of recording in a high-grade glioma.

A study by Charalampaki et al. (261) demonstrated ICG accumulation in high-grade gliomas and meningiomas 1 h after IV injection of 50 mg ICG (<1 mg/kg). They used a commercially available operating microscope with a near-infrared imaging mode (ARveo Glow800, Leica microsystems, Wetzlar, Germany). In a study by Eyüpoglu et al. (262), 5 mg/kg ICG was administered intravenously at the end of high-grade glioma resection. Using this technique and a standard operating microscope (OPMI Pentero, Carl Zeiss AG, Oberkochen, Germany) the authors were able to highlight PpIX-negative, hypervascularized transitional tumor zone (262).

Several studies (98–102) assessed high-dose ICG (5 mg/kg administered IV over 1 h, 24 h prior to surgery) with a dedicated commercial near-infrared exoscope/endoscope imaging system (Iridium, VisionSense, Medtronic, Dublin, Republic of Ireland) in various brain tumors to take advantage of EPR-based drug accumulation.

ICG and BBTB Heterogeneity

It is worth noting that in all three ICG-based tumor-imaging methods described, high-grade gliomas were efficiently labeled with ICG. In low-grade gliomas, fluorescence intensity returned to the baseline within 5 min after a slight delay in clearance compared to the adjacent normal brain (251). Extravascular ICG in the tumor region does not specifically bind to brain tumor cells; however, it does penetrate certain cells, creating cytoplasmic contrast for confocal imaging and histopathologic tissue analysis (261, 263).

Potential Molecular Transporters and Clearance of ICG

ICG is rapidly and exclusively cleared by the liver. There is evidence in animal models that ICG clearance proceeds in a biphasic method, with an initial phase of rapid clearance resulting in a half-life of 2 to 4 min and a secondary phase with a half-life of more than an hour at low concentrations (264–266). Uptake into hepatocytes and excretion into bile is mediated by two members of the ABC transporter family: the canalicular multispecific organic anion transporter 1 (ABCC2) and the bile salt export pump (ABCB11) (267, 268).

There is also evidence that ICG-uptake is enhanced in peripheral hepatocellular carcinoma cells expressing organic anion transporting polypeptide 1B3 (SLCO1B3), a member of the SLC family of membrane transporters (269). Importantly, ABCC2 is expressed at the BBB (27), and so may mediate the active efflux of ICG. While SLCO1B3 and ABCB11 are not significantly expressed at the BBB, their aberrant expression in tumor cells would likely modulate the dynamics of ICG-staining, warranting investigation of their expression if ICG visualization is to be used.

OPTIMIZING DELIVERY OF OPTICAL AGENTS TO BRAIN TUMORS ACROSS THE BBB AND BBTB

Various fluorophores, including currently approved ICG and FLS, could be conjugated to other molecules or packed in molecular vehicles with two main goals: first, to improve tumor-to-normal brain contrast by increasing delivery efficiency compared to a fluorophore alone and, second, to improve the specificity of delivery by including targeting mechanisms. Here, we discuss the vehicles irrespective of the optical agent, assuming that criteria and considerations for optical agent selection are a completely separate issue mostly related to the detection methodology and tools. These optical considerations were reviewed previously (270–273). It is worth noting that any study of novel molecular vehicles, even for non-imaging purposes of brain tumor treatment, is relevant to the development of fluorescence-guided surgical technology and strategy because localization experiments are necessarily involved as part of the study. Among the available localization methods that include electron microscopy, radioactive tracers, and MRI, optical imaging methods and fluorescence microscopy are arguably among the most widely used and convenient approaches.

Creating Small-Size Molecules

Efforts in nanotechnology research have been directed toward creating molecules small enough to pass the BBB and BBTB. Even if a molecule is designed that may pass the ∼6-nm pore

restriction in healthy BBB endothelium, it is unlikely that such a nanoparticle could achieve targeted delivery to tumor cells, as the size restriction greatly limits targeting options. However, several nanoparticles that are <100 nm in size have shown good tumor penetration in solid orthotopic animal gliomas.

One potential solution to this problem is quantum dots (QDs). QDs are nanoscale semiconductor crystals that can be excited to emit fluorescence. A unique property of QDs is that their absorption and emission wavelengths are functions of both the size and shape of the QD, allowing for the tailoring of emission and absorption spectra for desired applications (274). Tang et al. (103) report the use of aptamer-conjugated PEGylated QDs (∼20-nm size) for the fluorescent visualization of epidermal growth factor receptor (EGFR)-expressing glioma. In this study, QDs were conjugated to a deoxyribonucleic acid oligonucleotide aptamer designed to bind to EGFR variant III (EGFRvIII), which is known to be expressed specifically on glioma cells. The authors showed that the QD-aptamer probe was able to cross the BBTB to highlight tumor cells in an orthotopic mouse model *in vivo*. Whether a nanoparticle of this size could pass the competent portions of a BBTB to label invading tumor cells *in vivo* still needs to be investigated.

Although QDs represent a novel class of nanoscale, highly stable, fluorescent molecules that have been stably conjugated to antibodies, peptides, and small molecule drugs (275, 276), several issues related to QDs specifically have to be addressed for clinical translation. Namely, stability within the pH-range in normal and tumor tissues, biosafety, stability within the circulation and clearance by the reticuloendothelial system are all characteristics that must be evaluated before clinical application. Furthermore, some QDs are composed of heavy metals including cadmium, lead, or mercury, which raises biosafety questions. While such QDs have yet to be tested clinically, successful preclinical studies warrant their further investigation.

Enhancing EPR

Malignant tumors are notorious for disorganized and functionally abnormal vasculature that has sluggish blood flow, but which is a target for EPR optimization methods (142). The main strategies to improve permeability via EPR are directed toward dilating tumor vasculature, such as with nitric oxide-mediated vasodilation (angiotensin-converting-enzyme inhibitors, nitroglycerin, etc.), prostaglandin I2 agonists (105), tumor necrosis factor-a (106), or increasing systemic blood pressure by intraarterial administration of angiotensin II (107). The latter method improves tumor perfusion through unreactive tumor vessels that remain dilated while systemic vessels constrict and develop even tighter interendothelial connections. Such methods have commonalities with BBB disruption techniques and might be useful for enabling EPR through a relatively intact BBTB.

Increasing the molecular weight and size of a drug above 40 kDa by conjugating optical labels to targeting molecules or combining optical labels with large molecular vehicles would prolong drug circulation, increase the specificity of extravasation, and promote retention within high-grade gliomas and other tumors with severely disrupted BBTB for improved EPR-based drug delivery (277).

Xu et al. (104) developed silk fibroin nanoparticles loaded with ICG for imaging-guided photothermal therapy of orthotopic C6 glioma cells. Silk fibroin (200–350 kDa) is a biocompatible natural protein originating from silkworm cocoons. Conjugation with ICG created nanoparticles of about 200 nm in diameter, with improved EPR delivery in flank C6 gliomas, resulting in eight times higher intensity compared with free ICG injection 8 h after IV injection.

Nanoparticle delivery can enhance the circulation time and photostability of ICG (278) and offers a method for the specific targeting of ICG to tumor tissues. A drawback to this approach is limitation of drug delivery to the larger pores of the BBTB. Therefore, large molecules that are not targeted for transendothelial BBB or BBTB transport are unlikely to have better sensitivity in labeling glial tumors than already existing non-specific FLS, ICG, and metabolic 5-ALA.

Tumor Targeting Coupled With Passive BBTB Transport

Molecular probes are molecules that bind specifically to a second target molecule, allowing for the interrogation of the properties of that molecule. Recent experimental studies have developed fluorescent molecular probes for labeling glioma. In general, fluorescent molecular probes are made up of two components: a signaling component (label) and an affinity component. The signaling component is a contrast agent or marker, such as a radionuclide, luciferin, or a paramagnetic molecule, that can generate a detectable signal, while the affinity component is a targeting molecule, such as an oligonucleotide or antibody, that specifically binds to and labels a molecule of interest. Importantly, the affinity component of these molecules is customizable, allowing for the precise targeting of minute differences in protein or cell-surface marker expression in tumor cells, thus providing contrast between tumor and normal tissue. These probes can be additionally classified based on structure, binding affinity, or type of signaling component (279, 280). Fortunately, advances in genome sequencing have allowed for better characterization of the aberrant genetic environment of gliomas, uncovering potential probe targets. Thus, molecular probes may provide a highly targeted labeling technique for the fluorescence visualization of glioma.

Peptide-Based Labels

BLZ-100 or tozuleristide (4,766 Da) is a protein composed of chlorotoxin (CTX), a 36-residue neurotoxic peptide found in scorpion venom, conjugated to ICG. As a neurotoxin, CTX works to block small-conductance chloride channels, triggering internalization by endocytosis (281). CTX has been shown to selectively localize to gliomas via inhibitory binding of matrix metalloproteinase 2 that is frequently upregulated by glioma cells to facilitate tissue invasion (282). Thus, BLZ-100 is a high-affinity, targeted fluorescent probe that has shown specificity for glioma cells and is capable of near-infrared fluorescence, making it viable for applications of fluorescence-guided glioma resection. BLZ-100 has seen success in preclinical studies for resection of

glioma (120), head and neck carcinoma (121), and soft-tissue sarcoma (122). Liposomes targeted with CTX were also tested in mouse glioblastoma (283). BLZ-100 has also passed a Phase I clinical trial, showing no toxicity for doses up to 30 mg (123). When administered in doses of >9 mg, BLZ-100 fluorescence was detected *ex vivo* or *in vivo* in 4 of 7 grade-2 gliomas and 4 of 4 grade-4 gliomas, demonstrating potential transport across the relatively competent BBTB in these tumors and optimism for sensitive and specific brain tumor labeling. Currently, BLZ-100 is undergoing a joint Phase II/III trial for fluorescence-guided resection of pediatric CNS tumors (NCT03579602).

Another fluorescent molecular probe that falls in this category is IRDye 800CW-cyclic-RGD. This probe employs a recognition motif containing a tripeptide sequence (Arg-Gly-Asp) that binds integrin receptors that are overexpressed on the tumor surface. Huang et al. (124) tested this near-infrared probe in three mouse glioblastoma models, including a transgenic glioblastoma mouse model (RCAS-PDGF-driven/tv-a glioblastoma), which mimics the infiltrative growth pattern of human glioblastomas and associated heterogeneity of the BBTB. In this model, the label demonstrated great delineation of tumor margin and tumor cells.

Affibody-Based Labels

Elliott et al. (108) reported on the simultaneous administration of an anti-EGFR affibody conjugated to a near-infrared fluorescent probe, named ABY-029 (7,914.95 Da), a marker of perfusion, IRDye680RD (927.13 Da), and 5-ALA, for the fluorescent visualization of F98 orthotopic gliomas in rats. All three labels were administered simultaneously, 3 h before imaging, thus relying on passive targeting and EPR mechanisms. The results of the study showed significant but complementary differences in staining patterns of the three markers. As measured by histological analysis, ABY-029 performed expectedly better in the visualization of EGFR-expressing tumors (91% accuracy, 80% overall accuracy), while 5-ALA performed better in the visualization of the tumor margins of non-EGFR-expressing tumors (87% accuracy, 84% overall accuracy). ABY-029 is currently undergoing a Phase I clinical trial for the fluorescent-guided resection of recurrent glioma (NCT02901925). We expect this affibody to have a good correlation with a gadolinium-based contrast imaging based on similar molecular weights and therefore expected similarity in crossing the BBTB.

Antibody-Based Labels

Martirosyan et al. (109) reported the use of an FITC-conjugated anti-EGFR antibody (∼70,000 Da) for the identification of EGFR-expressing F98 tumor cells using confocal laser endomicroscopy in rats 24 h after IV administration of the FITC-conjugated antibodies. Warram et al. (110) investigated IRDye 800CW conjugated to an anti-EGFR antibody for fluorescence guidance in orthotopic mouse gliomas 3 days after IV administration. In both studies, EGFR-expressing tumor cells were readily visualized *in vivo*, confirming the viability of antibody-conjugated fluorescent tumor identification in the presence of a BBTB. While these studies are preclinical, there is significant potential for the application of this technique clinically for resection of high-grade glioma, but not for low-grade glioma, where the BBTB more closely resembles an intact BBB. Future applications of this technique may be as a part of a theranostic approach, whereby characterization of tumor protein expression guides the selection of appropriate antibodies for targeted fluorescence visualization.

Liposomal-Based Labels

Liposomes represent a class of highly modifiable nano- to micro-scale carriers that have a bi-lipid membrane. The size, composition of the lipid membrane, surface charge, mechanical properties, and anchoring of biologically active ligands can each be adjusted to optimize pharmacokinetics (141). Importantly, some liposome formulations are already FDA approved.

Jia et al. (125) investigated ICG-laden, biomimetic proteolipid liposomes (BLIPO-ICG, 104 ± 3 nm size) for the fluorescence-guided resection of C6 orthotopic mouse gliomas. These nanoparticles were infused with cell-surface proteins harvested from C6 glioma cells, enabling them to evade phagocytosis and to precisely target tumor cells via the homotypic interaction of surface proteins. Further, the authors were able to achieve complete surgical resection of tumors, guided by BLIPO-ICG and validated with histology. These results did not extend to resection guided by control nanoparticles without tumor-derived cell-surface markers, indicating that the cell-surface proteins contributed to greater tumor-specificity. Despite this, the invasiveness of C6 glioma cells in this study likely does not accurately replicate the invasiveness of high-grade human gliomas. As such, further testing is needed to evaluate the effectiveness of this nanoparticle beyond intact regions of BBTB and for further clinical applicability.

The design of fluorescent molecular probes for brain tumor visualization warrants consideration of the wide variation in structural characteristics of these molecules as they relate to interactions with the BBB. The barrier properties of the CNS endothelium severely restrict passive diffusion of molecules across the BBB, and transporters such as the neonatal Fc receptor and ABC-type efflux pumps work to actively remove antibodies and other large molecules from the brain. Absent any mechanisms for selective targeting of probes to tumor cells, accumulation via the EPR effect is likely not sufficient to stain high-grade brain tumor margins and low-grade gliomas, which are the main areas of difficulty for current fluorescent markers. As such, methods to functionalize markers for delivery across the BBB are warranted to ensure adequate BBB permeability and marker accuracy.

Functionalizing Particles for BBB Passage in Gliomas

Crucially, functionalization of nanoparticles can allow for effective extravasation despite an intact BBB, increasing the utility of fluorescence-guided glioma resection. Identifying a family of peptides with structural homology to the ligands that induce endothelial transcytosis is an important step to deliver drugs across the intact BBB and BBTB endothelium. ANG2, a member of the angiopep family of proteins, was identified to exhibit high transcytosis capacity via LRP-1 and is actively used for

functionalization of various molecular vehicles that can carry therapeutic or diagnostic agents or both (112).

Hao et al. (113) demonstrated the efficacy of a combined chemo-phototherapy technique using ANG2-coated polylactide-co-glycolide (PLGA) nanoparticles loaded with ICG and the microtubule toxin docetaxel (DTX) (ANG2/PLGA/DTX/ICG probe) in a U87MG mouse orthotopic glioma model. Ni et al. (114) investigated an ANG2-targeted dual MRI-optical nanoprobe consisting of a fluorescent up-conversion nanoparticle loaded with gadolinium (ANG2/PEG-UCNP probe) in an orthotopic mouse glioblastoma model. The ANG2 coating facilitated the selective uptake of these labels across the BBB in both studies, as visualized by fluorescence imaging.

Ma et al. (115) described a fluorescent probe conjugated with TGN, a BBB targeting peptide selected from a library of phage display. In their experiments, TGN was conjugated with glioma targeting aptamer AS1411 and Cy3 orange fluorescent dye and showed some glioma cell-labeling capacity in an orthotopic C6 mouse glioma model.

These nanoparticles are examples of an extensively functionalized drug-delivery system, where a BBB-targeting motif potentially allows for better labeling of the marginal tumor zone. Unfortunately, all three studies were performed in orthotopic glioblastoma models that display disrupted BBTB, which might not fully represent the heterogeneous BBTB and especially its competent regions. The additional complexity of the probes raises further concerns about stability, toxicity, and clearance that have to be further investigated. Overall, functionalization of the labels with BBB-targeted molecules is a significant advance for trans-BBB drug delivery.

CONCLUSION

The optimal surgical treatment of invasive brain tumors requires accurate visualization of tumor margins to maximize cytoreductive resection within functionally safe borders. Optically guided brain tumor surgery is an intriguing method for improving resection and has seen a number of exciting advancements within the last few years. Despite the initial enthusiasm in some of these techniques, the diversity and heterogeneity of gliomas complicate the consistent and accurate labeling of all tumors and limit clinical success. These difficulties require visualization agents to cross the BBB or BBTB to reach target tumor tissues. Not only do these barriers physically limit passive diffusion of many therapeutics, but also the dynamic expression of a vast network of transporters and junctional proteins further complicates drug delivery to gliomas. Thus, the efficacy of labels for optically guided glioma surgery will vary depending on tumor- and patient-specific BBB and BBTB properties. In this review, we described the barrier properties of the CNS and gliomas and discussed a number of technologies that have potential in overcoming these barriers for better fluorescence-visualization of gliomas.

Many novel tumor-targeted labels that have a large molecular weight do not cross competent BBTB regions in low-grade gliomas. Given that these areas of competent BBB or BBTB are where currently used markers struggle, it is important that novel tumor labels address this impediment. Novel BBB disruption techniques could be used to improve brain tumor labeling using these labels. Alternative BBB-targeted drugs with optical imaging properties are promising new tools. While many of these technologies are still in the preclinical stages of development and, therefore, require additional time and development before they may be available clinically, these advances offer a number of solutions for BBB-mediated brain tumor labeling and therapy.

AUTHOR CONTRIBUTIONS

EB and CL: conception and design. KS, EB, VB, and CL: acquisition of data and drafting the article. All authors critically revised the article. All authors reviewed and edited the manuscript. LC and MP: supervision. All authors approved the final version of the manuscript.

FUNDING

This research was supported by the National Natural Science Foundation of China (No. 81671819) held by LC, scholarship SP-2240.2018.4 to EB and the Newsome Chair in Neurosurgery Research held by MP, and the Barrow Neurological Foundation.

ACKNOWLEDGMENTS

The authors thank the Neuroscience Publications staff at Barrow Neurological Institute for assistance with manuscript preparation.

REFERENCES

1. Ostrom QT, Cioffi G, Gittleman H, Patil N, Waite K, Kruchko C, et al. CBTRUS statistical report: primary brain and other central nervous system tumors diagnosed in the United States in 2012-2016. *Neuro Oncol.* (2019) 21:v1–100. doi: 10.1093/neuonc/noz150
2. Taylor OG, Brzozowski JS, Skelding KA. Glioblastoma multiforme: an overview of emerging therapeutic targets. *Front Oncol.* (2019) 9:963. doi: 10.3389/fonc.2019.00963
3. Deng Z, Yu H, Wang N, et al. Impact of preoperative Karnofsky Performance Scale (KPS) and American Society of Anesthesiologists (ASA) scores on perioperative complications in patients with recurrent glioma undergoing repeated operation. *J Neurorestoratol.* (2019) 7:143–52. doi: 10.26599/JNR.2019.9040015
4. Hervey-Jumper SL, Berger MS. Evidence for improving outcome through extent of resection. *Neurosurg Clin N Am.* (2019) 30:85–93. doi: 10.1016/j.nec.2018.08.005
5. Clark VE, Cahill DP. Extent of resection versus molecular classification: what matters when? *Neurosurg Clin N Am.* (2019) 30:95–101. doi: 10.1016/j.nec.2018.08.006
6. Lu VM, Goyal A, Graffeo CS, Perry A, Burns TC, Parney IF, et al. Survival benefit of maximal resection for glioblastoma reoperation in the temozolomide era: a meta-analysis. *World Neurosurg.* (2019) 127:31–7. doi: 10.1016/j.wneu.2019.03.250

7. Mampre D, Ehresman J, Pinilla-Monsalve G, Osorio MAG, Olivi A, Quinones-Hinojosa A, et al. Extending the resection beyond the contrast-enhancement for glioblastoma: feasibility, efficacy, and outcomes. *Br J Neurosurg*. (2018) 32:528–35. doi: 10.1080/02688697.2018.1498450
8. DeLong JC, Hoffman RM, Bouvet M. Current status and future perspectives of fluorescence-guided surgery for cancer. *Expert Rev Anticancer Ther*. (2016) 16:71–81. doi: 10.1586/14737140.2016.1121109
9. Gandhi S, Tayebi Meybodi A, Belykh E, Cavallo C, Zhao X, Syed MP, et al. Survival outcomes among patients with high-grade glioma treated with 5-aminolevulinic acid-guided surgery: a systematic review and meta-analysis. *Front Oncol*. (2019) 9:620. doi: 10.3389/fonc.2019.00620
10. Nduom EK, Yang C, Merrill MJ, Zhuang Z, Lonser RR. Characterization of the blood-brain barrier of metastatic and primary malignant neoplasms. *J Neurosurg*. (2013) 119:427–33. doi: 10.3171/2013.3.JNS122226
11. Stewart DJ. A critique of the role of the blood-brain barrier in the chemotherapy of human brain tumors. *J Neuro Oncol*. (1994) 20:121–39. doi: 10.1007/BF01052723
12. Colditz MJ, Leyen Kv, Jeffree RL. Aminolevulinic acid (ALA)–protoporphyrin IX fluorescence guided tumour resection. Part 2: theoretical, biochemical and practical aspects. *J Clin Neurosci*. (2012) 19:1611–6. doi: 10.1016/j.jocn.2012.03.013
13. Roberts DW, Valdés PA, Harris BT, Hartov A, Fan X, Ji S, et al. Glioblastoma multiforme treatment with clinical trials for surgical resection (aminolevulinic acid). *Neurosurg Clin North Am*. (2012) 23:371–7. doi: 10.1016/j.nec.2012.04.001
14. Kutuzov N, Flyvbjerg H, Lauritzen M. Contributions of the glycocalyx, endothelium, and extravascular compartment to the blood-brain barrier. *Proc Natl Acad Sci USA*. (2018) 115:E9429–38. doi: 10.1073/pnas.1802155115
15. Ando Y, Okada H, Takemura G, Suzuki K, Takada C, Tomita H, et al. Brain-specific ultrastructure of capillary endothelial glycocalyx and its possible contribution for blood brain barrier. *Sci Rep*. (2018) 8:17523. doi: 10.1038/s41598-018-35976-2
16. Reitsma S, Slaaf DW, Vink H, van Zandvoort MA, oude Egbrink MG. The endothelial glycocalyx: composition, functions, and visualization. *Pflugers Archiv Eur J Physiol*. (2007) 454:345–59. doi: 10.1007/s00424-007-0212-8
17. Haeren RH, van de Ven SE, van Zandvoort MA, Vink H, van Overbeeke JJ, Hoogland G, et al. Assessment and imaging of the cerebrovascular glycocalyx. *Curr Neurovasc Res*. (2016) 13:249–60. doi: 10.2174/1567202613666160504104434
18. Sweeney MD, Sagare AP, Zlokovic BV. Blood–brain barrier breakdown in Alzheimer disease and other neurodegenerative disorders. *Nat Rev Neurol*. (2018) 14:133–50. doi: 10.1038/nrneurol.2017.188
19. Tietz S, Engelhardt B. Brain barriers: crosstalk between complex tight junctions and adherens junctions. *J Cell Biol*. (2015) 209:493–506. doi: 10.1083/jcb.201412147
20. Pardridge WM. The blood-brain barrier: bottleneck in brain drug development. *NeuroRX*. (2005) 2:3–14. doi: 10.1602/neurorx.2.1.3
21. Banks WA. From blood-brain barrier to blood-brain interface: new opportunities for CNS drug delivery. *Na Rev Drug Discov*. (2016) 15:275–92. doi: 10.1038/nrd.2015.21
22. Hitchcock SA, Pennington LD. Structure–brain exposure relationships. *J Med Chem*. (2006) 49:7559–83. doi: 10.1021/jm060642i
23. Hediger MA, Clémençon B, Burrier RE, Bruford EA. The ABCs of membrane transporters in health and disease (SLC series): introduction. *Mol Aspects Med*. (2013) 34:95–107. doi: 10.1016/j.mam.2012.12.009
24. Pardridge WM. Blood–brain barrier endogenous transporters as therapeutic targets: a new model for small molecule CNS drug discovery. *Expert Opin Ther Targets*. (2015) 19:1059–72. doi: 10.1517/14728222.2015.1042364
25. Zhao Z, Nelson AR, Betsholtz C, Zlokovic BV. Establishment and dysfunction of the blood-brain barrier. *Cell*. (2015) 163:1064–78. doi: 10.1016/j.cell.2015.10.067
26. Chen Z, Shi T, Zhang L, Zhu P, Deng M, Huang C, et al. Mammalian drug efflux transporters of the ATP binding cassette (ABC) family in multidrug resistance: a review of the past decade. *Cancer Lett*. (2016) 370:153–64. doi: 10.1016/j.canlet.2015.10.010
27. Löscher W, Potschka H. Blood-brain barrier active efflux transporters: ATP-binding cassette gene family. *NeuroRX*. (2005) 2:86–98. doi: 10.1602/neurorx.2.1.86
28. Mahringer A, Fricker G. ABC transporters at the blood–brain barrier. *Expert Opin Drug Metab Toxicoly*. (2016) 12:499–508. doi: 10.1517/17425255.2016.1168804
29. Zhang Y, Pardridge WM. Rapid transferrin efflux from brain to blood across the blood-brain barrier. *J Neurochem*. (2001) 76:1597–600. doi: 10.1046/j.1471-4159.2001.00222.x
30. Schlachetzki F, Zhu C, Pardridge WM. Expression of the neonatal Fc receptor (FcRn) at the blood-brain barrier. *J Neurochem*. (2002) 81:203–6. doi: 10.1046/j.1471-4159.2002.00840.x
31. Zhang Y, Pardridge WM. Mediated efflux of IgG molecules from brain to blood across the blood–brain barrier. *J Neuroimmunol*. (2001) 114:168–72. doi: 10.1016/S0165-5728(01)00242-9
32. Dore-Duffy P. Pericytes: pluripotent cells of the blood brain barrier. *Curr Pharm Design*. (2008) 14:1581–93. doi: 10.2174/138161208784705469
33. Mathiisen TM, Lehre KP, Danbolt NC, Ottersen OP. The perivascular astroglial sheath provides a complete covering of the brain microvessels: an electron microscopic 3D reconstruction. *GLIA*. (2010) 58:1094–103. doi: 10.1002/glia.20990
34. Abbott NJ, Rönnbäck L, Hansson E. Astrocyte–endothelial interactions at the blood–brain barrier. *Nat Rev Neurosci*. (2006) 7:41–53. doi: 10.1038/nrn1824
35. Alvarez JI, Katayama T, Prat A. Glial influence on the blood brain barrier. *GLIA*. (2013) 61:1939–58. doi: 10.1002/glia.22575
36. Armulik A, Genové G, Mäe M, Nisancioglu MH, Wallgard E, Niaudet C, et al. Pericytes regulate the blood–brain barrier. *Nature*. (2010) 468:557–61. doi: 10.1038/nature09522
37. Banerjee S, Bhat MA. Neuron-glial interactions in blood-brain barrier formation. *Annu Rev Neurosci*. (2007) 30:235–58. doi: 10.1146/annurev.neuro.30.051606.094345
38. Bauer H-C, Krizbai IA, Bauer H, Traweger A. "You Shall Not Pass" - tight junctions of the blood brain barrier. *Front Neurosci*. (2014) 8:392. doi: 10.3389/fnins.2014.00392
39. Daneman R, Zhou L, Kebede AA, Barres BA. Pericytes are required for blood–brain barrier integrity during embryogenesis. *Nature*. (2010) 468:562–6. doi: 10.1038/nature09513
40. Obermeier B, Daneman R, Ransohoff RM. Development, maintenance and disruption of the blood-brain barrier. *Nat Med*. (2013) 19:1584–96. doi: 10.1038/nm.3407
41. Daneman R, Prat A. The Blood–Brain Barrier. *Cold Spring Harbor Perspect Biol*. (2015) 7:a020412. doi: 10.1101/cshperspect.a020412
42. Komarova YA, Kruse K, Mehta D, Malik AB. Protein interactions at endothelial junctions and signaling mechanisms regulating endothelial permeability. *Circ Res*. (2017) 120:179–206. doi: 10.1161/CIRCRESAHA.116.306534
43. Luissint AC, Artus C, Glacial F, Ganeshamoorthy K, Couraud PO. Tight junctions at the blood brain barrier: physiological architecture and disease-associated dysregulation. *Fluids Barriers CNS*. (2012) 9:23. doi: 10.1186/2045-8118-9-23
44. Reinhold AK, Rittner HL. Barrier function in the peripheral and central nervous system—a review. *Pflugers Archiv Eur J Physiol*. (2017) 469:123–34. doi: 10.1007/s00424-016-1920-8
45. Arvanitis CD, Ferraro GB, Jain RK. The blood–brain barrier and blood–tumour barrier in brain tumours and metastases. *Nat Rev Cancer*. (2019) 20:26–41. doi: 10.1038/s41568-019-0205-x
46. Hardee ME, Zagzag D. Mechanisms of glioma-associated neovascularization. *Am J Pathol*. (2012) 181:1126–41. doi: 10.1016/j.ajpath.2012.06.030
47. Plate KH, Scholz A, Dumont DJ. Tumor angiogenesis and anti-angiogenic therapy in malignant gliomas revisited. *Acta Neuropathol*. (2012) 124:763–75. doi: 10.1007/s00401-012-1066-5
48. Madden SL, Cook BP, Nacht M, Weber WD, Callahan MR, Jiang Y, et al. Vascular gene expression in nonneoplastic and malignant brain. *Am J Pathol*. (2004) 165:601–8. doi: 10.1016/S0002-9440(10)63324-X
49. Ningaraj NS, Rao M, Hashizume K, Asotra K, Black KL. Regulation of blood-brain tumor barrier permeability by calcium-activated potassium channels. *J Pharmacol Exp Ther*. (2002) 301:838–51. doi: 10.1124/jpet.301.3.838
50. Nishio S, Ohta M, Abe M, Kitamura K. Microvascular abnormalities in ethylnitrosourea (ENU)-induced rat brain tumors: structural basis for altered blood-brain barrier function. *Acta Neuropathol*. (1983) 59:1–10. doi: 10.1007/BF00690311

51. Phoenix TN, Patmore DM, Boop S, Boulos N, Jacus MO, Patel YT, et al. Medulloblastoma genotype dictates blood brain barrier phenotype. *Cancer Cell*. (2016) 29:508–22. doi: 10.1016/j.ccell.2016.03.002
52. Zhan C, Lu W. The blood-brain/tumor barriers: challenges and chances for malignant gliomas targeted drug delivery. *Curr Pharm Biotechnol*. (2012) 13:2380–7. doi: 10.2174/138920112803341798
53. Hobbs SK, Monsky WL, Yuan F, Roberts WG, Griffith L, Torchilin VP, et al. Regulation of transport pathways in tumor vessels: role of tumor type and microenvironment. *Proc Natl Acad Sci U.S.A*. (1998) 95:4607–12. doi: 10.1073/pnas.95.8.4607
54. Hoffmann A, Bredno J, Wendland M, Derugin N, Ohara P, Wintermark M. High and low molecular weight fluorescein isothiocyanate (fitc)–dextrans to assess blood-brain barrier disruption: technical considerations. *Transl Stroke Res*. (2011) 2:106–11. doi: 10.1007/s12975-010-0049-x
55. Mayhan WG, Heistad DD. Permeability of blood-brain barrier to various sized molecules. *Am J Physiol Heart Circ Physiol*. (1985) 17:H712–8. doi: 10.1152/ajpheart.1985.248.5.H712
56. Natarajan R, Northrop N, Yamamoto B. Fluorescein isothiocyanate (FITC)-dextran extravasation as a measure of blood-brain barrier permeability. *Curr Protoc Neurosci*. (2017) 9.58.51-59.58.15. doi: 10.1002/cpns.25
57. Schmidt RF, Theofanis TN, Lang MJ, Stricsek GP, Lin R, Lebrun A, et al. Sphenopalatine ganglion stimulation is a reversible and frequency-dependent modulator of the blood-brain barrier. *Brain Res*. (2019) 1718:231–41. doi: 10.1016/j.brainres.2019.04.030
58. Yuan W, Lv Y, Zeng M, Fu BM. Non-invasive measurement of solute permeability in cerebral microvessels of the rat. *Microvasc Res*. (2009) 77:166–73. doi: 10.1016/j.mvr.2008.08.004
59. Sarin H, Kanevsky AS, Wu H, Brimacombe KR, Fung SH, Sousa AA, et al. Effective transvascular delivery of nanoparticles across the blood-brain tumor barrier into malignant glioma cells. *J Transl Med*. (2008) 6:80. doi: 10.1186/1479-5876-6-80
60. Firth JA. Endothelial barriers: from hypothetical pores to membrane proteins. *J Anat*. (2002) 200:541–8. doi: 10.1046/j.1469-7580.2002.00059.x
61. Aird WC. Phenotypic heterogeneity of the endothelium. *Circ Res*. (2007) 100:158–73. doi: 10.1161/01.RES.0000255691.76142.4a
62. Nir I, Levanon D, Iosilevsky G. Permeability of blood vessels in experimental gliomas: uptake of 99mTc-glucoheptonate and alteration in blood-brain barrier as determined by cytochemistry and electron microscopy. *Neurosurgery*. (1989) 25:523-31; discussion 531–22. doi: 10.1227/00006123-198910000-00004
63. Blasberg RG, Nakagawa H, Bourdon MA, Groothuis DR, Patlak CS, Bigner DD. Regional localization of a glioma-associated antigen defined by monoclonal antibody 81c6 *in vivo*: kinetics and implications for diagnosis and therapy. *Cancer Res*. (1987) 47:4432–43.
64. Groothuis DR. The blood-brain and blood-tumor barriers: A review of strategies for increasing drug delivery. *Neuro Oncol*. (2000) 2:45–59. doi: 10.1215/15228517-2-1-45
65. Schlageter KE, Molnar P, Lapin GD, Groothuis DR. Microvessel organization and structure in experimental brain tumors: microvessel populations with distinctive structural and functional properties. *Microvasc Res*. (1999) 58:312–28. doi: 10.1006/mvre.1999.2188
66. Machein MR, Kullmer J, Fiebich BL, Plate KH, Warnke PC. Vascular endothelial growth factor expression, vascular volume, and capillary permeability in human brain tumors. *Neurosurgery*. (1999) 44:732–40. doi: 10.1097/00006123-199904000-00022
67. Guo H, Kang H, Tong H, Du X, Liu H, Tan Y, et al. Microvascular characteristics of lower-grade diffuse gliomas: investigating vessel size imaging for differentiating grades and subtypes. *Eur Radiol*. (2019) 29:1893–902. doi: 10.1007/s00330-018-5738-y
68. Dhermain FG, Hau P, Lanfermann H, Jacobs AH, van den Bent MJ. Advanced MRI and PET imaging for assessment of treatment response in patients with gliomas. *Lancet Neurol*. (2010) 9:906–20. doi: 10.1016/S1474-4422(10)70181-2
69. Groothuis DR, Molnar P, Blasberg RG. Regional blood flow and blood-to-tissue transport in five brain tumor models. Implications for chemotherapy. *Prog Exp Tumor Res*. (1984) 27:132–53. doi: 10.1159/000408227
70. Wesseling P, van der Laak JA, de Leeuw H, Ruiter DJ, Burger PC. Quantitative immunohistological analysis of the microvasculature in untreated human glioblastoma multiforme. *J Neurosurg*. (1994) 81:902–9. doi: 10.3171/jns.1994.81.6.0902
71. Watkins S, Robel S, Kimbrough IF, Robert SM, Ellis-Davies G, Sontheimer H. Disruption of astrocyte-vascular coupling and the blood-brain barrier by invading glioma cells. *Nat Commun*. (2014) 5:1–15. doi: 10.1038/ncomms5196
72. Hambardzumyan D, Bergers G. Glioblastoma: defining tumor niches. *Trends Cancer*. (2015) 1:252–65. doi: 10.1016/j.trecan.2015.10.009
73. la Fougère C, Suchorska B, Bartenstein P, Kreth FW, Tonn JC. Molecular imaging of gliomas with PET: opportunities and limitations. *Neuro Oncol*. (2011) 13:806–19. doi: 10.1093/neuonc/nor054
74. Kushchayev SV, Sankar T, Eggink LL, Kushchayeva YS, Wiener PC, Hoober JK, et al. Monocyte galactose/N-acetylgalactosamine-specific C-type lectin receptor stimulant immunotherapy of an experimental glioma. Part II: combination with external radiation improves survival. *Cancer Manage Res*. (2012) 4:325–34. doi: 10.2147/CMAR.S33355
75. Kushchayev SV, Sankar T, Eggink LL, Kushchayeva YS, Wiener PC, Hoober JK, et al. Monocyte galactose/N-acetylgalactosamine-specific C-type lectin receptor stimulant immunotherapy of an experimental glioma. Part 1: stimulatory effects on blood monocytes and monocyte-derived cells of the brain. *Cancer Manage Res*. (2012) 4:309–23. doi: 10.2147/CMAR.S33248
76. Kushchayev SV, Kushchayeva YS, Wiener PC, Scheck AC, Badie B, Preul MC. Monocyte-derived cells of the brain and malignant gliomas: the double face of janus. *World Neurosurg*. (2014) 82:1171–86. doi: 10.1016/j.wneu.2012.11.059
77. Underwood JL, Murphy CG, Chen J, Franse-Carman L, Wood I, Epstein DL, et al. Glucocorticoids regulate transendothelial fluid flow resistance and formation of intercellular junctions. *Am J Physiol Cell Physiol*. (1999) 277:C330–42. doi: 10.1152/ajpcell.1999.277.2.C330
78. Falco J, Cavallo C, Vetrano IG, de Laurentis C, Siozos L, Schiariti M, et al. Fluorescein application in cranial and spinal tumors enhancing at preoperative mri and operated with a dedicated filter on the surgical microscope: preliminary results in 279 patients enrolled in the FLUOCERTUM prospective study. *Front Surg*. (2019) 6:49. doi: 10.3389/fsurg.2019.00049
79. Yuan F, Salehi HA, Boucher Y, Vasthare US, Tuma RF, Jain RK. Vascular permeability and microcirculation of gliomas and mammary carcinomas transplanted in rat and mouse cranial windows. *Cancer Res*. (1994) 54:4564–8.
80. Claes A, Idema AJ, Wesseling P. Diffuse glioma growth: a guerilla war. *Acta Neuropathol*. (2007) 114:443–58. doi: 10.1007/s00401-007-0293-7
81. Eidel O, Burth S, Neumann JO, Kieslich PJ, Sahm F, Jungk C, et al. Tumor infiltration in enhancing and non-enhancing parts of glioblastoma: a correlation with histopathology. *PLOS ONE*. (2017) 12:e0169292. doi: 10.1371/journal.pone.0169292
82. Dong X. Current strategies for brain drug delivery. *Theranostics*. (2018) 8:1481–93. doi: 10.7150/thno.21254
83. Ha D, Yang N, Nadithe V. Exosomes as therapeutic drug carriers and delivery vehicles across biological membranes: current perspectives and future challenges. *Acta Pharm Sin B*. (2016) 6:287–96. doi: 10.1016/j.apsb.2016.02.001
84. Hendricks BK, Cohen-Gadol AA, Miller JC. Novel delivery methods bypassing the blood-brain and blood-tumor barriers. *Neurosurg Focus*. (2015) 38:E10. doi: 10.3171/2015.1.FOCUS14767
85. Juillerat-Jeanneret L. The targeted delivery of cancer drugs across the blood–brain barrier: chemical modifications of drugs or drug-nanoparticles? *Drug Discov Today*. (2008) 13:1099–106. doi: 10.1016/j.drudis.2008.09.005
86. Mäger I, Meyer AH, Li J, Lenter M, Hildebrandt T, Leparc G, et al. Targeting blood-brain-barrier transcytosis – perspectives for drug delivery. *Neuropharmacology*. (2017) 120:4–7. doi: 10.1016/j.neuropharm.2016.08.025
87. Pardridge WM. CSF, blood-brain barrier, and brain drug delivery. *Expert Opin Drug Deliv*. (2016) 13:963–75. doi: 10.1517/17425247.2016.1171315
88. Pardridge WM. Drug transport across the blood–brain barrier. *J Cereb Blood Flow Metab*. (2012) 32:1959–72. doi: 10.1038/jcbfm.2012.126
89. Parveen S, Misra R, Sahoo SK. Nanoparticles: a boon to drug delivery, therapeutics, diagnostics and imaging. *Nanomed Nanotechnol Biol Med*. (2012) 8:147–66. doi: 10.1016/j.nano.2011.05.016

90. Pulgar VM. Transcytosis to cross the blood brain barrier, new advancements and challenges. *Front Neurosci*. (2019) 12:1019. doi: 10.3389/fnins.2018.01019
91. van Tellingen O, Yetkin-Arik B, de Gooijer MC, Wesseling P, Wurdinger T, de Vries HE. Overcoming the blood–brain tumor barrier for effective glioblastoma treatment. *Drug Resist Updates*. (2015) 19:1–12. doi: 10.1016/j.drup.2015.02.002
92. Zhu Z, Kalyan BS, Chen L. Therapeutic potential role of exosomes for ischemic stroke. *Brain Sci Adv*. (2020) 5:128–43. doi: 10.1177/2096595820902588
93. Wang M, Kommidi H, Tosi U, Guo H, Zhou Z, Schweitzer ME, et al. A murine model for quantitative, real-time evaluation of convection-enhanced delivery (RT-CED) using an 18[F]-positron emitting, fluorescent derivative of dasatinib. *Mol Cancer Ther*. (2017) 16:2902–12. doi: 10.1158/1535-7163.MCT-17-0423
94. Brachman DG, Youssef E, Dardis CJ, Sanai N, Zabramski JM, Smith KA, et al. Resection and permanent intracranial brachytherapy using modular, biocompatible cesium-131 implants: results in 20 recurrent, previously irradiated meningiomas. *J Neurosurg*. (2019) 2019:1–10. doi: 10.3171/2018.7.JNS18656
95. Folaron M, Strawbridge R, Samkoe KS, Filan C, Roberts DW, Davis SC. Elucidating the kinetics of sodium fluorescein for fluorescence-guided surgery of glioma. *J Neurosurg*. (2019) 131:724–34. doi: 10.3171/2018.4.JNS172644
96. Ding R, Frei E, Fardanesh M, Schrenk HH, Kremer P, Haefeli WE. Pharmacokinetics of 5-aminofluorescein-albumin, a novel fluorescence marker of brain tumors during surgery. *J Clin Pharmacol*. (2011) 51:672–8. doi: 10.1177/0091270010372626
97. Kremer P, Fardanesh M, Ding R, Pritsch M, Zoubaa S, Frei E. Intraoperative fluorescence staining of malignant brain tumors using 5-aminofluorescein-labeled albumin. *Oper Neurosurg*. (2009) 64:ons53–61. doi: 10.1227/01.NEU.0000335787.17029.67
98. Cho SS, Jeon J, Buch L, Nag S, Nasrallah M, Low PS, et al. Intraoperative near-infrared imaging with receptor-specific versus passive delivery of fluorescent agents in pituitary adenomas. *J Neurosurg*. (2018) 1:1–11. doi: 10.3171/2018.7.JNS181642
99. Jeon JW, Cho SS, Nag S, Buch L, Pierce J, Su YS, et al. Near-Infrared Optical Contrast of Skull Base Tumors During Endoscopic Endonasal Surgery. *Oper Neurosurg*. (2019) 17:32–42. doi: 10.1093/ons/opy213
100. Lee JY, Thawani JP, Pierce J, Zeh R, Martinez-Lage M, Chanin M, et al. Intraoperative near-infrared optical imaging can localize gadolinium-enhancing gliomas during surgery. *Neurosurgery*. (2016) 79:856–71. doi: 10.1227/NEU.0000000000001450
101. Lee JYK, Pierce JT, Zeh R, Cho SS, Salinas R, Nie S, et al. Intraoperative near-infrared optical contrast can localize brain metastases. *World Neurosurg*. (2017) 106:120–30. doi: 10.1016/j.wneu.2017.06.128
102. Lee JYK, Pierce JT, Thawani JP, Zeh R, Nie S, Martinez-Lage M, et al. Near-infrared fluorescent image-guided surgery for intracranial meningioma. *J Neurosurg*. (2018) 128:380–90. doi: 10.3171/2016.10.JNS161636
103. Tang J, Huang N, Zhang X, Zhou T, Tan Y, Pi J, et al. Aptamer-conjugated PEGylated quantum dots targeting epidermal growth factor receptor variant III for fluorescence imaging of glioma. *Int J Nanomedicine*. (2017) 12:3899–911. doi: 10.2147/IJN.S133166
104. Xu HL, ZhuGe DL, Chen PP, Tong MQ, Lin MT, Jiang X, et al. Silk fibroin nanoparticles dyeing indocyanine green for imaging-guided photo-thermal therapy of glioblastoma. *Drug Deliv*. (2018) 25:364–75. doi: 10.1080/10717544.2018.1428244
105. Tanaka S, Akaike T, Wu J, Fang J, Sawa T, Ogawa M, et al. Modulation of tumor-selective vascular blood flow and extravasation by the stable prostaglandin 12 analogue beraprost sodium. *J Drug Target*. (2003) 11:45–52. doi: 10.1080/1061186031000086072
106. Seki T, Carroll F, Illingworth S, Green N, Cawood R, Bachtarzi H, et al. Tumour necrosis factor-alpha increases extravasation of virus particles into tumour tissue by activating the Rho A/Rho kinase pathway. *J Controlled Release*. (2011) 156:381–9. doi: 10.1016/j.jconrel.2011.08.022
107. Nagamitsu A, Greish K, Maeda H. Elevating blood pressure as a strategy to increase tumor-targeted delivery of macromolecular drug SMANCS: cases of advanced solid tumors. *Jpn J Clin Oncol*. (2009) 39:756–66. doi: 10.1093/jjco/hyp074
108. Elliott JT, Marra K, Evans LT, Davis SC, Samkoe KS, Feldwisch J, et al. Simultaneous *in vivo* fluorescent markers for perfusion, protoporphyrin metabolism, and EGFR expression for optically guided identification of orthotopic glioma. *Clin Cancer Res*. (2017) 23:2203–12. doi: 10.1158/1078-0432.CCR-16-1400
109. Martirosyan NL, Georges J, Kalani MY, Nakaji P, Spetzler RF, Feuerstein BG, et al. Handheld confocal laser endomicroscopic imaging utilizing tumor-specific fluorescent labeling to identify experimental glioma cells *in vivo*. *Surg Neurol Int*. (2016) 7:995. doi: 10.4103/2152-7806.195577
110. Warram JM, de Boer E, Korb M, Hartman Y, Kovar J, Markert JM, et al. Fluorescence-guided resection of experimental malignant glioma using cetuximab-IRDye 800CW. *Br J Neurosurg*. (2015) 29:850–8. doi: 10.3109/02688697.2015.1056090
111. Demeule M, Currie JC, Bertrand Y, Ché C, Nguyen T, Régina A, et al. Involvement of the low-density lipoprotein receptor-related protein in the transcytosis of the brain delivery vector Angiopep-2. *J Neurochem*. (2008) 106:1534–44. doi: 10.1111/j.1471-4159.2008.05492.x
112. Demeule M, Régina A, Ché C, Poirier J, Nguyen T, Gabathuler R, et al. Identification and design of peptides as a new drug delivery system for the brain. *Jf Pharmacol Exp Ther*. (2008) 324:1064–72. doi: 10.1124/jpet.107.131318
113. Hao Y, Wang L, Zhao Y, Meng D, Li D, Li H, et al. Targeted imaging and chemo-phototherapy of brain cancer by a multifunctional drug delivery system. *Macromol Biosci*. (2015) 15:1571–85. doi: 10.1002/mabi.201500091
114. Ni D, Zhang J, Bu W, Xing H, Han F, Xiao Q, et al. Dual-targeting upconversion nanoprobes across the blood-brain barrier for magnetic resonance/fluorescence imaging of intracranial glioblastoma. *ACS Nano*. (2014) 8:1231–42. doi: 10.1021/nn406197c
115. Ma H, Gao Z, Yu P, Shen S, Liu Y, Xu B. A dual functional fluorescent probe for glioma imaging mediated by blood-brain barrier penetration and glioma cell targeting. *Biochem Biophys Res Commun*. (2014) 449:44–8. doi: 10.1016/j.bbrc.2014.04.148
116. Singh VK, Subudhi BB. Development and characterization of lysine-methotrexate conjugate for enhanced brain delivery. *Drug Deliv*. (2014) 23:1–11. doi: 10.3109/10717544.2014.984369
117. Peura L, Malmioja K, Huttunen K, Leppänen J, Hämäläinen M, Forsberg MM, et al. Design, synthesis and brain uptake of LAT1-targeted amino acid prodrugs of dopamine. *Pharm Res*. (2013) 30:2523–37. doi: 10.1007/s11095-012-0966-3
118. Rajora MA, Ding L, Valic M, Jiang W, Overchuk M, Chen J, et al. Tailored theranostic apolipoprotein E3 porphyrin-lipid nanoparticles target glioblastoma. *Chem Sci*. (2017) 8:5371–84. doi: 10.1039/C7SC00732A
119. Lam FC, Morton SW, Wyckoff J, Vu Han TL, Hwang MK, Maffa A, et al. Enhanced efficacy of combined temozolomide and bromodomain inhibitor therapy for gliomas using targeted nanoparticles. *Nat Commun*. (2018) 9:1991. doi: 10.1038/s41467-018-04315-4
120. Butte PV, Mamelak A, Parrish-Novak J, Drazin D, Shweikeh F, Gangalum PR, et al. Near-infrared imaging of brain tumors using the Tumor Paint BLZ-100 to achieve near-complete resection of brain tumors. *Neurosurg Focus*. (2014) 36:E1. doi: 10.3171/2013.11.FOCUS13497
121. Baik FM, Hansen S, Knoblaugh SE, Sahetya D, Mitchell RM, Xu C, et al. Fluorescence identification of head and neck squamous cell carcinoma and high-risk oral dysplasia with BLZ-100, a chlorotoxin-indocyanine green conjugate. *JAMA Otolaryngol Head Neck Surg*. (2016) 142:330. doi: 10.1001/jamaoto.2015.3617
122. Fidel J, Kennedy KC, Dernell WS, Hansen S, Wiss V, Stroud MR, et al. Preclinical validation of the utility of BLZ-100 in providing fluorescence contrast for imaging spontaneous solid tumors. *Cancer Res*. (2015) 75:4283–91. doi: 10.1158/0008-5472.CAN-15-0471
123. Patil CG, Walker DG, Miller DM, Butte P, Morrison B, Kittle DS, et al. Phase 1 Safety, pharmacokinetics, and fluorescence imaging study of tozuleristide (BLZ-100) in adults with newly diagnosed or recurrent gliomas. *Neurosurgery*. (2019) 2019:1–9. doi: 10.1093/neuros/nyz125

124. Huang R, Vider J, Kovar JL, Olive DM, Mellinghoff IK, Mayer-Kuckuk P, et al. Integrin αvβ3-targeted IRDye 800CW near-infrared imaging of glioblastoma. *Clin Cancer Res*. (2012) 18:5731–40. doi: 10.1158/1078-0432.CCR-12-0374
125. Jia Y, Wang X, Hu D, Wang P, Liu Q, Zhang X, et al. Phototheranostics: active targeting of orthotopic glioma using biomimetic proteolipid nanoparticles. *ACS Nano*. (2019) 13:386–98. doi: 10.1021/acsnano.8b06556
126. Yoshioka E, Chelakkot VS, Licursi M, Rutihinda SG, Som J, Derwish L, et al. Enhancement of cancer-specific protoporphyrin ix fluorescence by targeting oncogenic ras/MEK pathway. *Theranostics*. (2018) 8:2134–46. doi: 10.7150/thno.22641
127. Yang X, Palasuberniam P, Kraus D, Chen B. Aminolevulinic acid-based tumor detection and therapy: molecular mechanisms and strategies for enhancement. *Int J Mol Sci*. (2015) 16:25865–80. doi: 10.3390/ijms161025865
128. Palasuberniam P, Yang X, Kraus D, Jones P, Myers KA, Chen B ABCG2 transporter inhibitor restores the sensitivity of triple negative breast cancer cells to aminolevulinic acid-mediated photodynamic therapy. *Sci Rep*. (2015) 5:13298. doi: 10.1038/srep13298
129. Sun W, Kajimoto Y, Inoue H, Miyatake S, Ishikawa T, Kuroiwa T. Gefitinib enhances the efficacy of photodynamic therapy using 5-aminolevulinic acid in malignant brain tumor cells. *Photodiagn Photodyn Ther*. (2013) 10:42–50. doi: 10.1016/j.pdpdt.2012.06.003
130. Liu W, Baer MR, Bowman MJ, Pera P, Zheng X, Morgan J, et al. The tyrosine kinase inhibitor imatinib mesylate enhances the efficacy of photodynamic therapy by inhibiting ABCG2. *Clin Cancer Res*. (2007) 13:2463–70. doi: 10.1158/1078-0432.CCR-06-1599
131. Blake E, Curnow A. The hydroxypyridinone iron chelator CP94 can enhance PpIX-induced PDT of cultured human glioma cells. *Photochem Photobiol*. (2010) 86:1154–60. doi: 10.1111/j.1751-1097.2010.00770.x
132. Blake E, Allen J, Curnow A. An *in vitro* comparison of the effects of the iron-chelating agents, CP94 and dexrazoxane, on protoporphyrin IX accumulation for photodynamic therapy and/or fluorescence guided resection. *Photochem Photobiol*. (2011) 87:1419–26. doi: 10.1111/j.1751-1097.2011.00985.x
133. Reinert M, Piffaretti D, Wilzbach M, Hauger C, Guckler R, Marchi F, et al. Quantitative modulation of PpIX fluorescence and improved glioma visualization. *Front Surg*. (2019) 6:41. doi: 10.3389/fsurg.2019.00041
134. Wang W, Tabu K, Hagiya Y, Sugiyama Y, Kokubu Y, Murota Y, et al. Enhancement of 5-aminolevulinic acid-based fluorescence detection of side population-defined glioma stem cells by iron chelation. *Sci Rep*. (2017) 7:42070. doi: 10.1038/srep42070
135. Anand S, Hasan T, Maytin EV. Mechanism of differentiation-enhanced photodynamic therapy for cancer: upregulation of coproporphyrinogen oxidase by C/EBP transcription factors. *Mol Cancer Ther*. (2013) 12:1638–50. doi: 10.1158/1535-7163.MCT-13-0047
136. Chen X, Wang C, Teng L, Liu Y, Chen X, Yang G, et al. Calcitriol enhances 5-aminolevulinic acid-induced fluorescence and the effect of photodynamic therapy in human glioma. *Acta Oncol*. (2014) 53:405–13. doi: 10.3109/0284186X.2013.819993
137. Kouchesfehani HM, Nabiuni M, Majlesara MH, Amini E, Irian S. Effect of vitamin E succinate as a differentiation agent on the efficacy of 5-ALA-PDT on prostate cancer cells in culture. *J Paramed Sci*. (2011) 2:16–23.
138. Frank J, Lornejad-Schäfer MR, Schöffl H, Flaccus A, Lambert C, Biesalski HK. Inhibition of heme oxygenase-1 increases responsiveness of melanoma cells to ALA-based photodynamic therapy. *Int J Oncol*. (2007) 31:1539–45. doi: 10.3892/ijo.31.6.1539
139. Podkalicka P, Mucha O, Józkowicz A, Dulak J, Łoboda A. Heme oxygenase inhibition in cancers: possible tools and targets. *Współczesna Onkol*. (2018) 2018:23–32. doi: 10.5114/wo.2018.73879
140. Maeda H, Nakamura H, Fang J. The EPR effect for macromolecular drug delivery to solid tumors: Improvement of tumor uptake, lowering of systemic toxicity, and distinct tumor imaging *in vivo*. *Adv Drug Deliv Rev*. (2013) 65:71–9. doi: 10.1016/j.addr.2012.10.002
141. Vieira DB, Gamarra LF. Getting into the brain: liposome-based strategies for effective drug delivery across the blood-brain barrier. *Int J Nanomedicine*. (2016) 11:5381–414. doi: 10.2147/IJN.S117210
142. Maeda H, Tsukigawa K, Fang J. A retrospective 30 years after discovery of the enhanced permeability and retention effect of solid tumors: next-generation chemotherapeutics and photodynamic therapy–problems, solutions, and prospects. *Microcirculation*. (2016) 23:173–82. doi: 10.1111/micc.12228
143. Matsumura Y, Maeda H. A new concept for macromolecular therapeutics in cancer chemotherapy: mechanism of tumoritropic accumulation of proteins and the antitumor agent smancs. *Cancer Res*. (1986) 46:6387–92.
144. Fang J, Nakamura H, Maeda H. The EPR effect: unique features of tumor blood vessels for drug delivery, factors involved, and limitations and augmentation of the effect. *Adv Drug Deliv Rev*. (2011) 63:136–51. doi: 10.1016/j.addr.2010.04.009
145. Maeda H. Nitroglycerin enhances vascular blood flow and drug delivery in hypoxic tumor tissues: analogy between angina pectoris and solid tumors and enhancement of the EPR effect. *J Controlled Release*. (2010) 142:296–8. doi: 10.1016/j.jconrel.2010.01.002
146. Noguchi Y, Wu J, Duncan R, Strohalm J, Ulbrich K, Akaike T, et al. Early phase tumor accumulation of macromolecules: a great difference in clearance rate between tumor and normal tissues. *Jpn J Cancer Res*. (1998) 89:307–14. doi: 10.1111/j.1349-7006.1998.tb00563.x
147. Fang J, Liao L, Yin H, Nakamura H, Shin T, Maeda H. Enhanced bacterial tumor delivery by modulating the EPR effect and therapeutic potential of *Lactobacillus casei*. *J Pharm Sci*. (2014) 103:3235–43. doi: 10.1002/jps.24083
148. Quarles CC, Bell LC, Stokes AM. Imaging vascular and hemodynamic features of the brain using dynamic susceptibility contrast and dynamic contrast enhanced MRI. *Neuroimage*. (2019) 187:32–55. doi: 10.1016/j.neuroimage.2018.04.069
149. Rapoport SI. Effect of concentrated solutions on blood-brain barrier. *Am J Physiol*. (1970) 219:270–4. doi: 10.1152/ajplegacy.1970.219.1.270
150. Rapoport SI, Hori M, Klatzo I. Testing of a hypothesis for osmotic opening of the blood-brain barrier. *Am J Physiol*. (1972) 223:323–31. doi: 10.1152/ajplegacy.1972.223.2.323
151. Nduom EK, Zhuang Z, Lonser RR. Blood-brain barrier. response. *J Neurosurg*. (2014) 120:291.
152. Neuwelt EA, Frenkel EP, Diehl J, Vu LH, Rapoport S, Hill S. Reversible osmotic blood-brain barrier disruption in humans. *Neurosurgery*. (1980) 7:44–52. doi: 10.1227/00006123-198007000-00007
153. Williams JA, Roman-Goldstein S, Crossen JR, D'Agostino A, Dahlborg SA, Neuwelt EA. Preirradiation osmotic blood-brain barrier disruption plus combination chemotherapy in gliomas: quantitation of tumor response to assess chemosensitivity. *Adv Exp Med Biol*. (1993) 331:273–84. doi: 10.1007/978-1-4615-2920-0_43
154. Neuwelt E, Ambady P, Muldoon L, McConnell H, Doolittle N. Outwitting the blood-brain barrier. *Oncology*.(2016) 30:963, 966–7.
155. Priest R, Ambady P, Neweult E. ACTR-23. safety of intra-arterial chemotherapy with osmotic opening of the blood-brain barrier. *Neuro Oncology*. (2018) 20:vi16. doi: 10.1093/neuonc/noy148.057
156. Oberoi RK, Parrish KE, Sio TT, Mittapalli RK, Elmquist WF, Sarkaria JN. Strategies to improve delivery of anticancer drugs across the blood–brain barrier to treat glioblastoma. *Neuro Oncology*. (2016) 18:27–36. doi: 10.1093/neuonc/nov164
157. Bartek J Jr, Alattar AA, Dhawan S, Ma J, Koga T, Nakaji P, et al. Receipt of brachytherapy is an independent predictor of survival in glioblastoma in the Surveillance, Epidemiology, and End Results database. *J Neuro Oncol*. (2019) 145:75–83. doi: 10.1007/s11060-019-03268-y
158. Shi M, Sanche L. Convection-enhanced delivery in malignant gliomas: a review of toxicity and efficacy. *J Oncol*. (2019) 2019:9342796. doi: 10.1155/2019/9342796
159. Ughachukwu P, Unekwe P. Efflux pump-mediated resistance in chemotherapy. *Ann Med Health Sci Res*. (2012) 2:191–8. doi: 10.4103/2141-9248.105671
160. Burgess A, Shah K, Hough O, Hynynen K. Focused ultrasound-mediated drug delivery through the blood–brain barrier. *Expert Rev Neurother*. (2015) 15:477–91. doi: 10.1586/14737175.2015.1028369
161. Aryal M, Fischer K, Gentile C, Gitto S, Zhang YZ, McDannold N. Effects on P-glycoprotein expression after blood-brain barrier disruption using focused ultrasound and microbubbles. *PLOS ONE*. (2017) 12:e0166061. doi: 10.1371/journal.pone.0166061
162. Zhang J, Liu H, Du X, Guo Y, Chen X, Wang S, et al. Increasing of blood-brain tumor barrier permeability through transcellular and paracellular pathways

by microbubble-enhanced diagnostic ultrasound in a C6 glioma model. *Front Neurosci*. (2017) 11:86. doi: 10.3389/fnins.2017.00086
163. di Biase L, Falato E, Di Lazzaro V. Transcranial focused ultrasound (tFUS) and Transcranial unfocused ultrasound (tUS) neuromodulation: from theoretical principles to stimulation practices. *Front Neurol*. (2019) 10:549. doi: 10.3389/fneur.2019.00549
164. Lipsman N, Meng Y, Bethune AJ, Huang Y, Lam B, Masellis M, et al. Blood–brain barrier opening in Alzheimer's disease using MR-guided focused ultrasound. *Nat Commun*. (2018) 9:1–8. doi: 10.1038/s41467-018-04529-6
165. Gallay MN, Moser D, Jeanmonod D. Safety and accuracy of incisionless transcranial MR-guided focused ultrasound functional neurosurgery: single-center experience with 253 targets in 180 treatments. *J Neurosurg*. (2019) 130:1234–43. doi: 10.3171/2017.12.JNS172054
166. Krishna V, Sammartino F, Rezai A. A review of the current therapies, challenges, and future directions of transcranial focused ultrasound technology advances in diagnosis and treatment. *JAMA Neurol*. (2018) 75:246–54. doi: 10.1001/jamaneurol.2017.3129
167. Levi D, Raffa G, Periti M, Broggi G. A New possible application of transcranial magnetic stimulation: case report. *EC Neurol*. (2018) 10:1000–5.
168. Pell G, Zangen A, Roth Y, Friedman A, Vazana U, inventors; Brainsway Ltd, assignee. *Use of transcranial magnetic stimulation tomodulate permeability of the blood-brain barrier*. United States patent US 9636517B2 (2017). Available online at: https://patents.google.com/patent/US9636517B2/en
169. Semyachkina-Glushkovskaya O, Kurths J, Borisova E, Sokolovski S, Mantareva V, Angelov I, et al. Photodynamic opening of blood-brain barrier. *Biomed Optics Express*. (2017) 8:5040. doi: 10.1364/BOE.8.005040
170. Tang W, Fan W, Lau J, Deng L, Shen Z, Chen X. Emerging blood-brain-barrier-crossing nanotechnology for brain cancer theranostics. *Chem Soc Rev*. (2019) 48:2967–3014. doi: 10.1039/C8CS00805A
171. Witham TF, Fukui MB, Meltzer CC, Burns R, Kondziolka D, Bozik ME. Survival of patients with high grade glioma treated with intrathecal thiotriethylenephosphoramide for ependymal or leptomeningeal gliomatosis. *Cancer*. (1999) 86:1347–53. doi: 10.1002/(SICI)1097-0142(19991001)86:7<1347::AID-CNCR34>3.0.CO;2-M
172. Bleier BS, Kohman RE, Feldman RE, Ramanlal S, Han X. Permeabilization of the blood-brain barrier via mucosal engrafting: implications for drug delivery to the brain. *PLOS ONE*. (2013) 8:e61694. doi: 10.1371/journal.pone.0061694
173. Miyake MM, Bleier BS. Bypassing the blood-brian barrier using established skull base reconstruction techniques. *World J Otorhinolaryngol Head Neck Surg*. (2015) 1:11–6. doi: 10.1016/j.wjorl.2015.09.001
174. Stine CA, Munson JM. Convection-enhanced delivery: connection to and impact of interstitial fluid flow. *Front Oncol*. (2019) 9:966. doi: 10.3389/fonc.2019.00966
175. Platt S, Nduom E, Kent M, Freeman C, Machaidze R, Kaluzova M, et al. Canine model of convection-enhanced delivery of cetuximab-conjugated iron-oxide nanoparticles monitored with magnetic resonance imaging. *Clin Neurosurg*. (2012) 59:107–13. doi: 10.1227/NEU.0b013e31826989ef
176. Saito R, Sonoda Y, Kumabe T, Nagamatsu K, Watanabe M, Tominaga T. Regression of recurrent glioblastoma infiltrating the brainstem after convection-enhanced delivery of nimustine hydrochloride. *J Neurosurg Pediatr*. (2011) 7:522–6. doi: 10.3171/2011.2.PEDS10407
177. Sampson JH, Brady M, Raghavan R, Mehta AI, Friedman AH, Reardon DA, et al. Colocalization of gadolinium-diethylene triamine pentaacetic acid with high-molecular-weight molecules after intracerebral convection-enhanced delivery in humans. *Neurosurgery*. (2011) 69:668–76. doi: 10.1227/NEU.0b013e3182181ba8
178. Pang HH, Chen PY, Wei KC, Huang CW, Shiue YL, Huang CY, et al. Convection-enhanced delivery of a virus-like nanotherapeutic agent with dual-modal imaging for besiegement and eradication of brain tumors. *Theranostics*. (2019) 9:1752–63. doi: 10.7150/thno.30977
179. Weng KC, Hashizume R, Noble CO, Serwer LP, Drummond DC, Kirpotin DB, et al. Convection-enhanced delivery of targeted quantum dot-immunoliposome hybrid nanoparticles to intracranial brain tumor models. *Nanomedicine*. (2013) 8:1913–25. doi: 10.2217/nnm.12.209
180. Souweidane MM, Kramer K, Pandit-Taskar N, Zhou Z, Zanzonico P, Donzelli M, et al. A phase I study of convection-enhanced delivery of 124I-8H9 radio-labeled monoclonal antibody in children with diffuse intrinsic pontine glioma: An update with dose-response assessment. *J Clin Oncol*. (2019) 37:2008. doi: 10.1200/JCO.2019.37.15_suppl.2008
181. Vogelbaum MA, Brewer C, Barnett GH, Mohammadi AM, Peereboom DM, Ahluwalia MS, et al. First-in-human evaluation of the Cleveland Multiport Catheter for convection-enhanced delivery of topotecan in recurrent high-grade glioma: results of pilot trial 1. *J Neurosurg*. (2019) 130:476–85. doi: 10.3171/2017.10.JNS171845
182. Ashby LS, Smith KA, Stea B. Gliadel wafer implantation combined with standard radiotherapy and concurrent followed by adjuvant temozolomide for treatment of newly diagnosed high-grade glioma: a systematic literature review. *World J Surg Oncol*. (2016) 14:225. doi: 10.1186/s12957-016-0975-5
183. McGirt MJ, Than KD, Weingart JD, Chaichana KL, Attenello FJ, Olivi A, et al. Gliadel (BCNU) wafer plus concomitant temozolomide therapy after primary resection of glioblastoma multiforme. *J Neurosurg*. (2009) 110:583–8. doi: 10.3171/2008.5.17557
184. Westphal M, Hilt DC, Bortey E, Delavault P, Olivares R, Warnke PC, et al. A phase 3 trial of local chemotherapy with biodegradable carmustine (BCNU) wafers (Gliadel wafers) in patients with primary malignant glioma. *Neuro Oncology*. (2003) 5:79–88. doi: 10.1215/15228517-5-2-79
185. Byvaltsev VA, Bardonova LA, Onaka NR, Polkin RA, Ochkal SV, Shepelev VV, et al. Acridine orange: a review of novel applications for surgical cancer imaging and therapy. *Front Oncol*. (2019) 9:925. doi: 10.3389/fonc.2019.00925
186. Kitagawa Y, Tanaka S, Kuriki Y, Yamamoto K, Ogasawara A, Nejo T, et al. Spray fluorescent probes for fluorescence-guided neurosurgery. *Front Oncol*. (2019) 9:727. doi: 10.3389/fonc.2019.00727
187. Cutter JL, Cohen NT, Wang J, Sloan AE, Cohen AR, Panneerselvam A, et al. Topical application of activity-based probes for visualization of brain tumor tissue. *PLOS ONE*. (2012) 7:e33060. doi: 10.1371/journal.pone.0033060
188. Martirosyan NL, Georges J, Eschbacher JM, Cavalcanti DD, Elhadi AM, Abdelwahab MG, et al.MPotential application of a handheld confocal endomicroscope imaging system using a variety of fluorophores in experimental gliomas and normal brain. *Neurosurg Focus*. (2014) 36:E16. doi: 10.3171/2013.11.FOCUS13486
189. Candela P, Gosselet F, Miller F, Buee-Scherrer V, Torpier G, Cecchelli R, et al. Physiological pathway for low-density lipoproteins across the blood-brain barrier: transcytosis through brain capillary endothelial cells *in vitro*. *Endothelium J Endothelial Cell Res*. (2008) 15:254–64. doi: 10.1080/10623320802487759
190. Yamamoto M, Ikeda K, Ohshima K, Tsugu H, Kimura H, Tomonaga M. Increased expression of low density lipoprotein receptor-related protein/alpha2-macroglobulin receptor in human malignant astrocytomas. *Cancer Res*. (1997) 57:2799–805.
191. Blasi P, Giovagnoli S, Schoubben A, Ricci M, Rossi C. Solid lipid nanoparticles for targeted brain drug delivery. *Adv Drug Deliv Rev*. (2007) 59:454–77. doi: 10.1016/j.addr.2007.04.011
192. Gao H. Progress and perspectives on targeting nanoparticles for brain drug delivery. *Acta Pharm Sin B*. (2016) 6:268–86. doi: 10.1016/j.apsb.2016.05.013
193. Harilal S, Jose J, Parambi DGT, Kumar R, Mathew GE, Uddin MS, et al. Advancements in nanotherapeutics for Alzheimer's disease: current perspectives. *J Pharm Pharmacol*. (2019) 71:1370–83. doi: 10.1111/jphp.13132
194. Masserini M. Nanoparticles for brain drug delivery. *ISRN Biochem*. (2013) 2013:238428. doi: 10.1155/2013/238428
195. Saraiva C, Praça C, Ferreira R, Santos T, Ferreira L, Bernardino L. Nanoparticle-mediated brain drug delivery: overcoming blood-brain barrier to treat neurodegenerative diseases. *J Control Release*. (2016) 235:34–47. doi: 10.1016/j.jconrel.2016.05.044
196. Nduom EK, Bouras A, Kaluzova M, Hadjipanayis CG. Nanotechnology applications for glioblastoma. *Neurosurg Clin N Am*. (2012) 23:439–49. doi: 10.1016/j.nec.2012.04.006
197. Hollis CP, Weiss HL, Leggas M, Evers BM, Gemeinhart RA, Li T. Biodistribution and bioimaging studies of hybrid paclitaxel nanocrystals: lessons learned of the EPR effect and image-guided drug delivery. *J Controlled Release*. (2013) 172:12–21. doi: 10.1016/j.jconrel.2013.06.039

198. Park K. Questions on the role of the EPR effect in tumor targeting. *J Controlled Release*. (2013) 172:391. doi: 10.1016/j.jconrel.2013.10.001
199. Maeda H, Khatami M. Analyses of repeated failures in cancer therapy for solid tumors: poor tumor-selective drug delivery, low therapeutic efficacy and unsustainable costs. *Clin Transl Med*. (2018) 7:11. doi: 10.1186/s40169-018-0185-6
200. Nakanishi T, Fukushima S, Okamoto K, Suzuki M, Matsumura Y, Yokoyama M, et al. Development of the polymer micelle carrier system for doxorubicin. *J Controlled Release*. (2001) 74:295–302. doi: 10.1016/S0168-3659(01)00341-8
201. Takeda KM, Yamasaki Y, Dirisala A, Ikeda S, Tockary TA, Toh K, et al. Effect of shear stress on structure and function of polyplex micelles from poly(ethylene glycol)-poly(l-lysine) block copolymers as systemic gene delivery carrier. *Biomaterials*. (2017) 126:31–8. doi: 10.1016/j.biomaterials.2017.02.012
202. Mahmoudi K, Garvey KL, Bouras A, Cramer G, Stepp H, Jesu Raj JG, et al. 5-aminolevulinic acid photodynamic therapy for the treatment of high-grade gliomas. *J Neurooncol*. (2019) 141:595–607. doi: 10.1007/s11060-019-03103-4
203. Namikawa T, Yatabe T, Inoue K, Shuin T, Hanazaki K. Clinical applications of 5-aminolevulinic acid-mediated fluorescence for gastric cancer. *World J Gastroenterol*. (2015) 21:8817–25. doi: 10.3748/wjg.v21.i29.8769
204. Lucena SR, Salazar N, Gracia-Cazaña T, Zamarrón A, González S, Juarranz Á, et al. Combined treatments with photodynamic therapy for non-melanoma skin cancer. *In J Mol Sci*. (2015) 16:25912–33. doi: 10.3390/ijms161025912
205. Lakomkin N, Hadjipanayis CG. Fluorescence-guided surgery for high-grade gliomas. *J Surg Oncol*. (2018) 118:356–61. doi: 10.1002/jso.25154
206. Hadjipanayis CG, Stummer W, Sheehan JP. 5-ALA fluorescence-guided surgery of CNS tumors. *J Neurooncol*. (2019) 141:477–8. doi: 10.1007/s11060-019-03109-y
207. Hadjipanayis CG, Widhalm G, Stummer W. What is the surgical benefit of utilizing 5-aminolevulinic acid for fluorescence-guided surgery of malignant gliomas? *Neurosurgery*. (2015) 77:663–73. doi: 10.1227/NEU.0000000000000929
208. Hadjipanayis CG, Stummer W. 5-ALA and FDA approval for glioma surgery. *J Neurooncol*. (2019) 141:479–86. doi: 10.1007/s11060-019-03098-y
209. Novotny A, Stummer W. 5-Aminolevulinic acid and the blood-brain barrier – A review. *Med Laser Appl*. (2003) 18:36–40. doi: 10.1078/1615-1615-00085
210. Sachar M, Anderson KE, Ma X. Protoporphyrin IX: the good, the bad, and the ugly. *J Pharmacol Exp Ther*. (2016) 356:267–75. doi: 10.1124/jpet.115.228130
211. Dalton JT, Yates CR, Yin D, Straughn A, Marcus SL, Golub AL, et al. Clinical pharmacokinetics of 5-aminolevulinic acid in healthy volunteers and patients at high risk for recurrent bladder cancer. *J Pharmacol Exp Ther*. (2002) 301:507–12. doi: 10.1124/jpet.301.2.507
212. Rick K, Sroka R, Stepp H, Kriegmair M, Huber RM, Jacob K, et al. Pharmacokinetics of 5-aminolevulinic acid-induced protoporphyrin IX in skin and blood. *J Photochem Photobiol B Biol*. (1997) 40:313–9. doi: 10.1016/S1011-1344(97)00076-6
213. Olivo M, Wilson BC. Mapping ALA-induced PPIX fluorescence in normal brain and brain tumour using confocal fluorescence microscopy. *Int J Oncol*. (2004) 25:37–45. doi: 10.3892/ijo.25.1.37
214. Terr L, Weiner LP. An autoradiographic study of delta-aminolevulinic acid uptake by mouse brain. *Exp Neurol*. (1983) 79:564–8. doi: 10.1016/0014-4886(83)90234-0
215. Valdés PA, Moses ZB, Kim A, Belden CJ, Wilson BC, Paulsen KD, et al. Gadolinium- and 5-aminolevulinic acid-induced protoporphyrin IX levels in human gliomas: an *ex vivo* quantitative study to correlate protoporphyrin IX levels and blood-brain barrier breakdown. *J Neuropathol Exp Neurol*. (2012) 71:806–13. doi: 10.1097/NEN.0b013e31826775a1
216. Goryaynov SA, Widhalm G, Goldberg MF, Chelushkin D, Spallone A, Chernyshov KA, et al. The role of 5-ALA in low-grade gliomas and the influence of antiepileptic drugs on intraoperative fluorescence. *Front Oncol*. (2019) 9:423. doi: 10.3389/fonc.2019.00423
217. Widhalm G, Olson J, Weller J, Bravo J, Han SJ, Phillips J, et al. The value of visible 5-ALA fluorescence and quantitative protoporphyrin IX analysis for improved surgery of suspected low-grade gliomas. *J Neurosurg*. (2019) 2019:1–10. doi: 10.3171/2019.1.JNS182614
218. Kaneko S, Suero Molina E, Ewelt C, Warneke N, Stummer W. Fluorescence-based measurement of real-time kinetics of protoporphyrin IX after 5-aminolevulinic acid administration in human *in situ* malignant gliomas. *Neurosurgery*. (2019) 85:E739–46. doi: 10.1093/neuros/nyz129
219. Tonn JC, Stummer W. Fluorescence-guided resection of malignant gliomas using 5-aminolevulinic acid: practical use, risks, and pitfalls. *Clin Neurosurg*. (2008) 55:20–6.
220. Ajioka RS, Phillips JD, Kushner JP. Biosynthesis of heme in mammals. *Biochim Biophys Acta Mol Cell Res*. (2006) 1763:723–36. doi: 10.1016/j.bbamcr.2006.05.005
221. Nakanishi T, Ogawa T, Yanagihara C, Tamai I. Kinetic evaluation of determinant factors for cellular accumulation of protoporphyrin IX induced by external 5-aminolevulinic acid for photodynamic cancer therapy. *J Pharm Sci*. (2015) 104:3092–100. doi: 10.1002/jps.24462
222. Döring F, Walter J, Will J, Föcking M, Boll M, Amasheh S, et al. Delta-aminolevulinic acid transport by intestinal and renal peptide transporters and its physiological and clinical implications. *J Clin Invest*. (1998) 101:2761–7. doi: 10.1172/JCI1909
223. Frølund S, Marquez OC, Larsen M, Brodin B, Nielsen CU. Delta-aminolevulinic acid is a substrate for the amino acid transporter SLC36A1 (hPAT1). *Br J Pharmacol*. (2010) 159:1339–53. doi: 10.1111/j.1476-5381.2009.00620.x
224. Tran TT, Mu A, Adachi Y, Adachi Y, Taketani S. Neurotransmitter transporter family including SLC6A6 and SLC6A13 contributes to the 5-aminolevulinic acid (ALA)-induced accumulation of protoporphyrin IX and photodamage, through uptake of ALA by cancerous cells. *Photochem Photobiol*. (2014) 90: 1136–43. doi: 10.1111/php.12290
225. Krishnamurthy P, Schuetz JD. The role of ABCG2 and ABCB6 in porphyrin metabolism and cell survival. *Curr Pharm Biotechnol*. (2011) 12:647–55. doi: 10.2174/138920111795163995
226. Geier EG, Chen EC, Webb A, Papp AC, Yee SW, Sadee W, et al. Profiling solute carrier transporters in the human blood–brain barrier. *Clin Pharmacol Ther*. (2013) 94:636–9. doi: 10.1038/clpt.2013.175
227. Kitajima Y, Ishii T, Kohda T, Ishizuka M, Yamazaki K, Nishimura Y, et al. Mechanistic study of PpIX accumulation using the JFCR39 cell panel revealed a role for dynamin 2-mediated exocytosis. *Sci Rep*. (2019) 9:8666. doi: 10.1038/s41598-019-44981-y
228. Hagiya Y, Endo Y, Yonemura Y, Takahashi K, Ishizuka M, Abe F, et al. Pivotal roles of peptide transporter PEPT1 and ATP-binding cassette (ABC) transporter ABCG2 in 5-aminolevulinic acid (ALA)-based photocytotoxicity of gastric cancer cells *in vitro*. *Photodiagn Photodyn Ther*. (2012) 9:204–14. doi: 10.1016/j.pdpdt.2011.12.004
229. Webber J, Kessel D, Fromm D. Plasma levels of protoporphyrin IX in humans after oral administration of 5-aminolevulinic acid. *J Photochem Photobiol B Biol*. (1997) 37:151–3. doi: 10.1016/S1011-1344(96)07348-4
230. Kawai N, Hirohashi Y, Ebihara Y, Saito T, Murai A, Saito T, et al. ABCG2 expression is related to low 5-ALA photodynamic diagnosis (PDD) efficacy and cancer stem cell phenotype, and suppression of ABCG2 improves the efficacy of PDD. *PLOS ONE*. (2019) 14:e0216503. doi: 10.1371/journal.pone.0216503
231. Lai HW, Sasaki R, Usuki S, Nakajima M, Tanaka T, Ogura SI. Novel strategy to increase specificity of ALA-Induced PpIX accumulation through inhibition of transporters involved in ALA uptake. *Photodiagn Photodyn Ther*. (2019) 27:327–35. doi: 10.1016/j.pdpdt.2019.06.017
232. Li Y, Rey-Dios R, Roberts DW, Valdés PA, Cohen-Gadol AA. Intraoperative fluorescence-guided resection of high-grade gliomas: a comparison of the present techniques and evolution of future strategies. *World Neurosurg*. (2014) 82:175–85. doi: 10.1016/j.wneu.2013.06.014
233. Emerson GA, Andersen HH. Toxicity of certain proposed antileprosy dyes: fluorescein, eosin, erythrosin and others. *Int J Leprosy*. (1934) 2:257–63.
234. Acerbi F, Broggi M, Schebesch KM, Höhne J, Cavallo C, De Laurentis C, et al. Fluorescein-guided surgery for resection of high-grade gliomas: a multicentric prospective phase II study (FLUOGLIO). *Clin Cancer Res*. (2018) 24:52–61. doi: 10.1158/1078-0432.CCR-17-1184
235. Belykh E, Miller EJ, Carotenuto A, Patel AA, Cavallo C, Martirosyan NL, et al. Progress in confocal laser endomicroscopy for neurosurgery and technical

nuances for brain tumor imaging with fluorescein. *Front Oncol*. (2019) 9:554. doi: 10.3389/fonc.2019.00554
236. Martirosyan NL, Eschbacher JM, Kalani MY, Turner JD, Belykh E, Spetzler RF, et al. Prospective evaluation of the utility of intraoperative confocal laser endomicroscopy in patients with brain neoplasms using fluorescein sodium: experience with 74 cases. *Neurosurg Focus*. (2016) 40:E11. doi: 10.3171/2016.1.FOCUS15559
237. Blair NP, Evans MA, Lesar TS, Zeimer RC. Fluorescein and fluorescein glucuronide pharmacokinetics after intravenous injection. *Invest Ophthalmol Vis Sci*. (1986) 27:1107–14.
238. Stummer W. Fluorescein in brain metastasis and glioma surgery. *Acta Neurochir*. (2015) 157:2199–200. doi: 10.1007/s00701-015-2576-4
239. Fan C, Jiang Y, Liu R, Wu G, Wu G, Xu K, et al. Safety and feasibility of low-dose fluorescein-guided resection of glioblastoma. *Clin Neurol Neurosurg*. (2018) 175:57–60. doi: 10.1016/j.clineuro.2018.10.011
240. Diaz RJ, Dios RR, Hattab EM, Burrell K, Rakopoulos P, Sabha N, et al. Study of the biodistribution of fluorescein in glioma-infiltrated mouse brain and histopathological correlation of intraoperative findings in high-grade gliomas resected under fluorescein fluorescence guidance. *J Neurosurg*. (2015) 122:1360–9. doi: 10.3171/2015.2.JNS132507
241. Höhne J, Hohenberger C, Proescholdt M, Riemenschneider MJ, Wendl C, Brawanski A, et al. Fluorescein sodium-guided resection of cerebral metastases-an update. *Acta Neurochir*. (2017) 159:363–7. doi: 10.1007/s00701-016-3054-3
242. Xiao SY, Zhang J, Zhu ZQ, Li YP, Zhong WY, Chen JB, et al. Application of fluorescein sodium in breast cancer brain-metastasis surgery. *Cancer Manage Res*. (2018) 10:4325–31. doi: 10.2147/CMAR.S176504
243. Xiang Y, Zhu XP, Zhao JN, Huang GH, Tang JH, Chen HR, et al. Blood-brain barrier disruption, sodium fluorescein, and fluorescence-guided surgery of gliomas. *Br J Neurosurg*. (2018) 32:141–8. doi: 10.1080/02688697.2018.1428731
244. Schebesch KM, Rosengarth K, Brawanski A, Proescholdt M, Wendl C, Höhne J, et al. Clinical benefits of combining different visualization modalities in neurosurgery. *Front Surg*. (2019) 6:56. doi: 10.3389/fsurg.2019.00056
245. Schebesch KM, Brawanski A, Doenitz C, Rosengarth K, Proescholdt M, Riemenschneider MJ, et al. Fluorescence-guidance in non-Gadolinium enhancing, but FET-PET positive gliomas. *Clin Neurol Neurosurg*. (2018) 172:177–82. doi: 10.1016/j.clineuro.2018.07.011
246. Wang EJ, Casciano CN, Clement RP, Johnson WW. Fluorescent substrates of sister-P-glycoprotein (BSEP) evaluated as markers of active transport and inhibition: evidence for contingent unequal binding sites. *Pharm Res*. (2003) 20:537–44. doi: 10.1023/a:1023278211849
247. Sun H, Johnson DR, Finch RA, Sartorelli AC, Miller DW, Elmquist WF. Transport of fluorescein in MDCKII-MRP1 transfected cells and mrp1-knockout mice. *Biochem Biophy Res Commun*. (2001) 284:863–9. doi: 10.1006/bbrc.2001.5062
248. Zhang Z, Tachikawa M, Uchida Y, Terasaki T. Drug clearance from cerebrospinal fluid mediated by organic anion transporters 1 (Slc22a6) and 3 (Slc22a8) at arachnoid membrane of rats. *Mol Pharm*. (2018) 15:911–22. doi: 10.1021/acs.molpharmaceut.7b00852
249. Barar J, Rafi MA, Pourseif MM, Omidi Y. Blood-brain barrier transport machineries and targeted therapy of brain diseases. *Bioimpacts*. (2016) 6:225–48. doi: 10.15171/bi.2016.30
250. Saxena V, Sadoqi M, Shao J. Degradation kinetics of indocyanine green in aqueous solution. *J Pharm Sci*. (2003) 92:2090–7. doi: 10.1002/jps.10470
251. Haglund MM, Berger MS, Hochman DW. Enhanced optical imaging of human gliomas and tumor margins. *Neurosurgery*. (1996) 38:308–17. doi: 10.1097/00006123-199602000-00015
252. Obach RS, Lombardo F, Waters NJ. Trend analysis of a database of intravenous pharmacokinetic parameters in humans for 670 drug compounds. *Drug Metab Dispos*. (2008) 36:1385–405. doi: 10.1124/dmd.108.020479
253. Desmettre T, Devoisselle JM, Mordon S. Fluorescence properties and metabolic features of indocyanine green (ICG) as related to angiography. *Surv Ophthalmol*. (2000) 45:15–27. doi: 10.1016/S0039-6257(00)00123-5
254. Yoneya S, Noyori K. Improved visualization of the choroidal circulation with indocyanine green angiography. *Archiv Ophthalmol*. (1993) 111:1165. doi: 10.1001/archopht.1993.01090090015002
255. Cherrick GR, Stein SW, Leevy CM, Davidson CS. Indocyanine green: observations on its physical properties, plasma decay, and hepatic extraction*. *J Clin Invest*. (1960) 39:592–600. doi: 10.1172/JCI104072
256. Baker KJ. Binding of sulfobromophthalein (BSP) sodium and indocyanine green (ICG) by plasma 1 lipoproteins. *Exp Biol Med*. (1966) 122:957–63. doi: 10.3181/00379727-122-31299
257. Yoneya S, Saito T, Komatsu Y, Koyama I, Takahashi K, Duvoll-Young J. Binding properties of indocyanine green in human blood. *Invest Ophthalmol Vis Sci*. (1998) 39:1286–90.
258. Schaafsma BE, Mieog JS, Hutteman M, van der Vorst JR, Kuppen PJ, Löwik CW, et al. The clinical use of indocyanine green as a near-infrared fluorescent contrast agent for image-guided oncologic surgery. *J Surg Oncol*. (2011) 104:323–32. doi: 10.1002/jso.21943
259. Haglund MM, Hochman DW, Spence AM, Berger MS. Enhanced optical imaging of rat gliomas and tumor margins. *Neurosurgery*. (1994) 35:930–40; discussion 940–31. doi: 10.1097/00006123-199411000-00019
260. Hansen DA, Spence AM, Carski T, Berger MS. Indocyanine green (ICG) staining and demarcation of tumor margins in a rat glioma model. *Surg Neurol*. (1993) 40:451–6. doi: 10.1016/0090-3019(93)90046-4
261. Charalampaki P, Nakamura M, Athanasopoulos D, Heimann A. Confocal-assisted fluorescent microscopy for brain tumor surgery. *Front Oncol*. (2019) 9:583. doi: 10.3389/fonc.2019.00583
262. Eyüpoglu IY, Hore N, Fan Z, Buslei R, Merkel A, Buchfelder M, et al. Intraoperative vascular DIVA surgery reveals angiogenic hotspots in tumor zones of malignant gliomas. *Sci Rep*. (2015) 5:7958. doi: 10.1038/srep07958
263. Martirosyan NL, Cavalcanti DD, Eschbacher JM, Delaney PM, Scheck AC, Abdelwahab MG, et al. Use of *in vivo* near-infrared laser confocal endomicroscopy with indocyanine green to detect the boundary of infiltrative tumor. *J Neurosurg*. (2011) 115:1131–8. doi: 10.3171/2011.8.JNS11559
264. Hollins B, Noe B, Henderson JM. Fluorometric determination of indocyanine green in plasma. *Clin Chem*. (1987) 33:765–8. doi: 10.1093/clinchem/33.6.765
265. Ott P, Keiding S, Johnsen AH, Bass L. Hepatic removal of two fractions of indocyanine green after bolus injection in anesthetized pigs. *Am J Physiol Gastrointest Liver Physiol*. (1994) 266:G1108–22. doi: 10.1152/ajpgi.1994.266.6.G1108
266. Song W, Tang Z, Zhang D, Burton N, Drissen W, Chen X. Comprehensive studies of pharmacokinetics and biodistribution of indocyanine green and liposomal indocyanine green by multispectral optoacoustic tomography. *RSC Adv*. (2015) 5:3807–13. doi: 10.1039/C4RA09735A
267. Jansen PL, van Klinken JW, van Gelder M, Ottenhoff R, Elferink RP. Preserved organic anion transport in mutant TR- rats with a hepatobiliary secretion defect. *Am J Physiol*. (1993) 265:G445–52. doi: 10.1152/ajpgi.1993.265.3.G445
268. Pedersen JM, Matsson P, Bergström CA, Hoogstraate J, Norén A, LeCluyse EL, et al. Early identification of clinically relevant drug interactions with the human bile salt export pump (BSEP/ABCB11). *Toxicol Sci*. (2013) 136:328–43. doi: 10.1093/toxsci/kft197
269. Shibasaki Y, Sakaguchi T, Hiraide T, Morita Y, Suzuki A, Baba S, et al. Expression of indocyanine green-related transporters in hepatocellular carcinoma. *J Surg Res*. (2015) 193:567–76. doi: 10.1016/j.jss.2014.07.055
270. Belykh E, Miller EJ, Hu D, Martirosyan NL, Woolf EC, Scheck AC, et al. Scanning fiber endoscope improves detection of 5-aminolevulinic acid-induced protoporphyrin IX fluorescence at the boundary of infiltrative glioma. *World Neurosurg*. (2018) 113:e51–69. doi: 10.1016/j.wneu.2018.01.151
271. Valdés PA, Roberts DW, Lu FK, Golby A. Optical technologies for intraoperative neurosurgical guidance. *Neurosurg Focus*. (2016) 40:E8. doi: 10.3171/2015.12.FOCUS15550
272. Vasefi F, MacKinnon N, Farkas DL, Kateb B. Review of the potential of optical technologies for cancer diagnosis in neurosurgery: a step toward intraoperative neurophotonics. *Neurophotonics*. (2016) 4:011010. doi: 10.1117/1.NPh.4.1.011010

273. Wei L, Roberts DW, Sanai N, Liu JTC. Visualization technologies for 5-ALA-based fluorescence-guided surgeries. *J Neuro Oncol*. (2019) 141:495–505. doi: 10.1007/s11060-018-03077-9
274. Murray CB, Kagan CR, Bawendi MG. synthesis and characterization of monodisperse nanocrystals and close-packed nanocrystal assemblies. *Annu Rev Mater Sci*. (2000) 30:545–610. doi: 10.1146/annurev.matsci.30.1.545
275. Akerman ME, Chan WC, Laakkonen P, Bhatia SN, Ruoslahti E. Nanocrystal targeting *in vivo*. *Proc Natl Acad Sci USA*. (2002) 99:12617–21. doi: 10.1073/pnas.152463399
276. Matea CT, Mocan T, Tabaran F, Pop T, Mosteanu O, Puia C, et al. Quantum dots in imaging, drug delivery and sensor applications. *Int J Nanomedicine*. (2017) 12:5421–31. doi: 10.2147/IJN.S138624
277. Greish K. Enhanced permeability and retention (EPR) effect for anticancer nanomedicine drug targeting. *Methods Mol Biol*. (2010) 624:25–37. doi: 10.1007/978-1-60761-609-2_3
278. Saxena V, Sadoqi M, Shao J. Enhanced photo-stability, thermal-stability and aqueous-stability of indocyanine green in polymeric nanoparticulate systems. *J Photochem Photobiol B Biol*. (2004) 74:29–38. doi: 10.1016/j.jphotobiol.2004.01.002
279. Massoud TF, Gambhir SS. Molecular imaging in living subjects: seeing fundamental biological processes in a new light. *Genes Dev*. (2003) 17:545–80. doi: 10.1101/gad.1047403
280. Weissleder R, Mahmood U. Molecular Imaging. *Radiology*. (2001) 219:316–33. doi: 10.1148/radiology.219.2.r01ma19316
281. McFerrin MB, Sontheimer H. A role for ion channels in glioma cell invasion. *Neuron Glia Biol*. (2006) 2:39–49. doi: 10.1017/S1740925X06000044
282. Deshane J, Garner CC, Sontheimer H. Chlorotoxin inhibits glioma cell invasion via matrix metalloproteinase-2. *J Biol Chem*. (2003) 278:4135–44. doi: 10.1074/jbc.M205662200
283. Xiang Y, Liang L, Wang X, Wang J, Zhang X, Zhang Q. Chloride channel-mediated brain glioma targeting of chlorotoxin-modified doxorubicine-loaded liposomes. *J Controlled Release*. (2011) 152:402–10. doi: 10.1016/j.jconrel.2011.03.014

Conflict of Interest: The authors declare that the research was conducted in the absence of any commercial or financial relationships that could be construed as a potential conflict of interest.

frontiers in Oncology

ORIGINAL RESEARCH
published: 08 July 2020
doi: 10.3389/fonc.2020.01069

5-Aminolevulinic Acid Multispectral Imaging for the Fluorescence-Guided Resection of Brain Tumors: A Prospective Observational Study

Patra Charalampaki[1,2*†], *Phileas Johannes Proskynitopoulos*[1†], *Axel Heimann*[3] *and Makoto Nakamura*[1,2]

[1] Department of Neurosurgery, Cologne Medical Center, Cologne, Germany, [2] Witten-Herdecke University, Witten, Germany, [3] Institute for Neurosurgical Pathophysiology, Medical University Mainz, Mainz, Germany

OPEN ACCESS

Edited by:
Evgenii Belykh, Barrow Neurological Institute (BNI), United States

Reviewed by:
Constantinos G. Hadjipanayis, Mount Sinai Health System, United States
Marcel A. Kamp, Heinrich Heine University of Düsseldorf, Germany

***Correspondence:**
Patra Charalampaki
charalampaki@yahoo.de

[†] *These authors have contributed equally to this work*

Specialty section:
This article was submitted to Cancer Imaging and Image-directed Interventions, a section of the journal Frontiers in Oncology

Received: *13 February 2020*
Accepted: *28 May 2020*
Published: *08 July 2020*

Citation:
Charalampaki P, Proskynitopoulos PJ, Heimann A and Nakamura M (2020) 5-Aminolevulinic Acid Multispectral Imaging for the Fluorescence-Guided Resection of Brain Tumors: A Prospective Observational Study. Front. Oncol. 10:1069. doi: 10.3389/fonc.2020.01069

Fluorescence-guided surgery with five-aminolevulinic acid (5-ALA) is the state-of-the-art treatment of high-grade gliomas. However, intraoperative visualization of 5-ALA under blue light remains challenging, especially when blood covers the surgical field and thereby fluorescence. To overcome this problem and combine the brightness of visible light with the information delivered with fluorescence, we implemented multispectral fluorescence (MFL) in a surgical microscope, a technique that is able to project both information in real-time. We prospectively examined 25 patients with brain tumors. One patient was operated on two different lesions in the same setting. The tumors comprised: six glioblastomas, four anaplastic astrocytomas, one anaplastic oligodendroglioma, two meningiomas, 11 metastatic tumors, one acoustic neuroma, and one ependymoma. The MFL technique with a real-time overlay of fluorescence and white light was compared intraoperatively to the classic blue filter. All lesions were clearly visible and highlighted from the surrounding tissue. The pseudocolor we chose was green, representing fluorescence, with the surrounding brain tissue remaining in its original color. When blood was covering the surgical field, orientation was easy to maintain. The MFL technique opens the way for precise and clear visualization of fluorescence in real-time under white light. It can be easily used for the resection of all tumors accumulating 5-ALA. Drawbacks of classic PpIX fluorescence such as hidden fluorescence, intraoperative changes could be overcome with the presence of additional white light in MFL technique.

Keywords: brain tumor, 5-ALA = 5-aminolevulinic acid, microscopic surgery, neurological surgery, fluorescence guided surgery

INTRODUCTION

Malignant brain tumors and especially high-grade gliomas (HGG) are characterized by their aggressiveness and incurability. An influential phase III trial was able to show that mean survival of patients diagnosed with glioblastoma (GBM) is only 14.6 months when treated with radiotherapy and temozolomide (1) and that a mere 9.8% survived for 5 years (2). Apart from the use of radio- and chemotherapy, survival, neurological function, and the patients' quality of life highly depend on the extent and safety of neurosurgical resection (3, 4).

For the neurosurgical treatment of HGG, total resection of the tumor while not causing new neurological deficits is the primary goal (4, 5). For this matter, the use of five-aminolevulinic acid (5-ALA) (6) in fluorescence-guided surgery (FGS) has significantly improved HGG therapy (7).

Since the first observational study of 5-ALA fluorescence-guided surgery for the resection of HGG (8) followed by a promising prospective study (9), a prospective phase III trial was able to show that its use significantly improved progression-free survival with 41% in the 5-ALA and 21.1% in the white light group at 6 months (10). Furthermore, 5-ALA has also been **used** for the visualization of other entities like meningiomas and/or metastases, although more appealing and strong evidence for its use in these lesions is needed (11, 12).

Nonetheless, some disadvantages exist. Blue light is used for excitation of the protoporphyrin IX (PpIX) fluorescence and is strongly absorbed by blood cells, as it has a strong attenuation to hemoglobin (6, 13). Even a single layer of erythrocytes can absorb the light and make the underlying PpIX fluorescence invisible to the surgeon. In the literature, this fact is described as a minor problem during surgery when continuous rinsing is applied (6). However, at final inspection of the surgical cavity, coagulated blood can easily masque malignant tumor tissue (6, 14). Hence, the surgeon needs to repeatedly switch between white and blue light in order to both detect bleeding sites and remove the tumor. Furthermore, if blood is lying above the tissue the view under blue light becomes dark and it gets more difficult to remove any blood or remaining tumor. If one does so, there is a high risk of destroying more vulnerable blood vessels existing in malignant tumor tissue when trying to treat bleeding with coagulation. Also, it is easier and more intuitive for the surgeon to pay attention to the total visual field under white light as opposed to blue light. Apart from that, there is an ergonomic problem when it is essential to repeatedly switch between white and blue light especially if heavy bleeding occurs. Hence, one could argue that it would be necessary to combine the advantages of both white and blue light in the setting of brain surgery with 5-ALA in order to diminish their disadvantages.

To do so, the multispectral fluorescence microscopy (MFL) was incorporated into a commercially available microscope (ARveo, Leica Microsystems, Wetzlar, Germany). We have already investigated its use for the combination of indocyanine green (ICG) fluorescence and white light images in the therapy of vascular anomalies of the brain in both an animal model, and on a human cadaver model as well as in clinical use for vascular and tumor applications (15–17). Such a microscope also allows simultaneous visualization of PpIX fluorescence and white light. After merging, this combined image is then delivered via the ocular and shows both the fluorescent properties of the inspected field and the anatomical details as visualized under white light (13, 17).

To the best of our knowledge, no other observational study has used MFL for the intraoperative visualization of brain tumors accumulated with PpIX fluorescence. As the MFL mode uses the information obtained from the blue light image, we hypothesized that the intraoperative assessment of the fluorescence quality and contrasts in the MFL mode would match the fluorescence under blue light. Thus, outcome parameters of this study were the matching information of both fluorescent pictures and intraoperative usability of the MFL mode when assessing and resecting a brain tumor. With this study, we want to get first insights into the use of MFL as a possible tool that could diminish the technological and ergonomical disadvantages of the visualization of PpIX fluorescence under blue light for fluorescence-guided surgery of brain tumors.

MATERIALS AND METHODS

The present study was approved by the ethics committee of the University of Witten/Herdecke, Germany (Nr: 35/2017). All patients participating in this prospective observational study gave written informed consent and were recruited in the Department of Neurosurgery of the Cologne Medical Center, Cologne, Germany. The follow-up was performed in the usual manner for every patient that is treated because of a brain tumor in our clinic.

Inclusion criteria for this study were:

- Primary or secondary brain tumor on an MRI, regardless of WHO grading
- no contraindication for the administration of 5-ALA
- histopathological confirmation of a brain tumor (primary and secondary)
- Written informed consent
- Age 18–75 years although we included also elderly patients if the Karnofsky index higher than 80%.

Exclusion criteria were:

- Severe comorbid diseases that could negatively influence the participation in this study
- Therapeutically uncontrollable arterial hypertension (i.e., systolic pressure above 200 mmHg and diastolic pressure above 120 mmHg)
- Lung diseases that are related to complications during narcosis and anesthesia (such as cystic fibrosis, alpha-1-antitrypsin-deficiency, sarcoidosis, allergic alveolitis, tuberculosis, etc.)
- Patient that received an attenuated vaccine 14 days or the influenza vaccination 7 days prior to their participation in this study
- All comorbid diseases that could influence the participation in this study.

In total, we examined 25 patients (11 women and 14 men) that were operated over the course of 22 months (**Table 1**) between 2018 and 2019. A total of 26 lesions were extirpated and assessed with the novel technique (one patient was operated on two different regions and had two different craniotomies in the same setting). The average age at operation was 62.29 years. The underlying diagnoses that we summarized as HGG were glioblastoma ($n = 6$), anaplastic astrocytoma ($n = 4$), and anaplastic oligodendroglioma ($n = 1$). Apart from that, we investigated the off-label use of 5-ALA in metastases from bronchial carcinoma ($n = 5$), metastasis from colon carcinoma ($n = 3$), metastases from breast carcinoma ($n = 1$), meningioma ($n = 2$), ependymoma (WHO grade II, $n = 1$), acoustic neurinoma

TABLE 1 | List of patients operated on with the additional use of the MFL-technique.

Patient-Nr.	Gender	Age at operation	Tumor entity	Tumor location	Primary tumor or mutation status	Fluorescence quality	Postoperative new neurological deficit	MRI- contrast enhanced resection
1	F	71	Metastasis	Left parietal	Adeno-ca lung	Capsule intensive, content barely	None	Complete
2	F	59	Metastasis	Right temporal	Sigma-ca GI tract	Very intensive	None	Complete
			Metastasis	Right parietal	Sigma-ca GI tract	Very intensive	None	Complete
3	F	83	Metastasis	Right cerebellar	Adeno-ca lung	Intensive but inhomogeneous	None	Complete
4	M	63	Metastasis	Right parietal	Large cell ca lung	Very intensive	None	Complete
5	M	41	Anaplastic Astrocytoma	Right parietal	IDH-mutate, MGMT +	Very intensive	None	Minimal rest near postcentral
6	F	72	GBM cystic	Right temporal	IDH-mutate, MGMT +	Cyst very intensive, content barely	None	Minimal ependymal rest around the ventricle wall
7	F	75	Meningioma WHO I	Left frontal		Very intensive	None	Complete
8	M	50	Anaplastic Oligodendroglioma	Right frontal	MGMT +	Very intensive	None	Complete
9	M	56	Metastasis	Right frontal	Adeno-ca lung	Very intensive	None	Complete
10	M	53	GBM	Right temporal	IDH-wild type, MGMT +	Very intensive	None	Complete
11	M	77	Metastasis	Right frontal	Sigma-ca GI tract	Very intensive	None	Complete
12	F	77	Meningioma WHO I	Right parietal		Very intensive	None	Complete
13	F	51	Acoustic Neuroma	Right cerebelo-pontine angle		Intensive but inhomogeneous	Hypakusis	Complete
14	M	73	GBM	Right frontal	MGMT −	Very intensive	None	Complete
15	M	62	GBM	Right parieto-occipital	IDH-wild type, MGMT −	Very intensive	None	Minimal rest in the calcarine sulcus
16	M	44	Anaplastic Astrocytoma	Left trigonum, thalamus, midbrain	IDH-wild type, MGMT −	Very intensive	None	Incomplete resection due to midbrain thalamus infiltration
17	M	63	Metastasis	4th ventricle	Adeno-ca lung	Very intensive	Diziness	Complete
18	M	73	GBM	right frontal	IDH-wild type, MGMT −	Very intensive	None	No MRI postop
19	M	50	Ependymoma WHO II	4th ventricle		Very intensive	None	Complete
20	M	51	Metastasis	Spinal	Myxoid liposarcoma	Intensive but inhomogeneous	None	Complete
21	F	78	Metastasis	Left temporal	Squamous tongue ca	Very intensive	None	Complete
22	F	32	Anaplastic Astrocytoma	Left frontal precentral	IDH-mutate, MGMT +	Very intensive	None	Complete
23	M	65	Anaplastic Astrocytoma	Left frontal precentral	IDH-mutate, MGMT +	Very intensive	None awake surgery	Complete
24	F	76	GBM	Right frontal precentral	IDH-wild type, MGMT +	Very intensive	Hemiparesis arm 4/5	Minimal rest precentral, intraoperative monitoring + + +
25	F	63	Metastasis	Right frontal	Breast-ca	Very intensive	None	Complete

Ca = Carcinoma, GBM = Glioblastoma, GI = gastrointestinal, IDH = isocitrate dehydrogenase, M = male, MGMT = O^6-methylguanine DNA methyltransferase, F = female.
In patient number 2, two different craniotomies had to be performed as the tumor was metastasized into both the temporal and parietal lobe. Patient 10 in this table is described in case vignette #1, patient 23 in case vignette #2 and patient 21 in case vignette #3.

($n = 1$), metastasis from a myxoid liposarcoma ($n = 1$), and metastasis from tongue carcinoma ($n = 1$) (**Table 1**).

All patients received an oral dosage of 20 mg 5-ALA per kilogram body weight at least 3 h before the surgical procedure. Post-operatively, all patients were treated on the operative intensive care unit of our clinic before being moved to the general ward and kept in an area with low light exposition due to the phototoxic properties of 5-ALA.

Technical Considerations

The MFL system, mounted on a conventional microscope (ARveo, Leica Microsystems, Wetzlar, Germany), consists out of a fluorescence excitation filter covering the absorption spectrum of PpIX in broad range around 405 nm, but blocking the PpIX emission peak at 635 nm to acquire the red fluorescence signal with a separate fluorescence camera. The PpIX fluorescence signal is processed into a pseudo color image with high contrast to the operative field (e.g., green) and transparently overlaid to the stereoscopic, optical view in the eyepieces (Leica Captiview). In addition, the pseudo color fluorescence image can be recorded and observed as embedded information in the white light image on the monitor. The microscope control allowed switching directly from white to blue light or MFL mode or from blue light to MFL mode and vice versa for surgical workflow support and comparison purposes.

Operative Procedure

Following the craniotomy, we continued with a sharp surgical incision of the dura mater. Once the brain parenchyma was visualized macroscopically, we started to continue the procedure under the operation microscope (ARveo, Leica microsystems, Wetzlar Germany). If according to the MRI and intraoperative neuronavigation (Stealth Station, Medtronic, USA) the lesion was on the surface of the brain we continued under blue light in order to assess PpIX fluorescence and coherently visualize and identify the tumor. If the tumor was exposed, we changed to MFL-mode and observed the operation field and evaluated if the fused MFL image matched the different properties of the white light and blue light images. In tumors lying more deeply in the brain parenchyma we first operated under white light until the lesion was exposed. Then, we continued in the same fashion as described before.

When we suspected slight bleeding inside the surgical field during resection under blue light we changed to white light and assessed bleeding. After that, we turned to the MFL-mode in order to evaluate both the fluorescent properties of the tumor tissue and the bleeding. To achieve hemostasis, we switched back to white light. We evaluated the surgical field in the MFL-mode only in the case of slight bleedings that masked the fluorescence under blue light in order to not jeopardize the patient. Larger bleedings were immediately treated under white light. We repeated this procedure in the cases where small bleedings occurred while meticulously resecting the lesion under blue light.

During final inspection of the cavity under blue light we changed to white light to do a final assessment of coagulated blood or small bleeding that both could conceal tumor tissue. Then we switched to the MFL-mode to assess if the bleeding sites were matching the ones identified under white light. After that, we turned to blue light again. If any previously masked lesions were then identified we resected them accordingly until no fluorescent tissue was visible. Following the final inspection, we continued with sufficient hemostasis and closure of the surgical wound under white light. At the end of the operation, we assessed the resected tumor *ex vivo* under blue light and then changed to MFL-mode for the assessment of its fluorescent properties and if the characteristics of both images match. After each operation, the operating surgeon (CC) assessed the raw data (green fluorescence in a black picture, similar to what one sees when using the blue light in the classical way), which is calculated based upon the blue light fluorescence data. This was then compared to the MFL picture regarding matching fluorescence areas and shades.

RESULTS

As the software was installed in a surgical microscope the operative use of the MFL technique was easy to implement in the clinical setting. To correlate the overlay of fluorescence between the traditional blue light mode and the MFL mode the surgeon did an intraoperative assessment. Before switching to the MFL mode, the PpIX fluorescence under blue light was assessed for correspondence to the MFL picture.

In all 26 surgeries, we were able to correlate the pink fluorescence under blue light with the "green" fluorescence in the MFL-mode. The intensity of the green indicated fluorescence was always similar to the intensity of pink seen under blue light. In contrast to the conventional blue mode, under the MFL mode bleeding did not cause any problem as the sources of bleeding were immediately identifiable and were treated accordingly. Thus, periodic switching back to the white light was not necessary during the resection under the MFL fluorescence mode, which facilitated resection and surgical convenience especially in the situations that were ergonomically or surgically challenging (such as when larger bleedings occurred or at the final inspection).

Postoperatively, we reviewed the raw fluorescence signal video recordings and MFL video. Again, the perceived intensities and locations of pseudo colored green fluorescence overlay in the MFL mode corresponded perfectly with the single channel fluorescence recordings in all 26 surgeries. There was no instance when the natural color of the surgical field of view, reflections from the brain tissue or cerebrospinal fluid would impede fluorescence overlay visualization or create a false positive pseudocolored green fluorescence overlay.

In three cases, PpIX fluorescence using the MFL technique was intensive but inhomogeneous (see **Table 1**). In one metastasis from a bronchial carcinoma, the capsule fluorescence was very intense while its content lacked fluorescent intensity. In one GBM case, the cyst capsule displayed a strong fluorescent while the content only slightly fluoresced. In the remaining 20/25, the fluorescence quality was very intensive, while different shades of fluorescence were observed depending on the tumor site, i.e., center vs. periphery. The quality of the fluorescence

signal displayed in the MFL mode was subjectively similar to the fluorescence under blue light using the traditional filter. Hence the different fluorescent shades representing different tumor areas were displayed correctly (**Supplementary Video 1**). This is the case because the data used to generate the MFL picture is taken from the visual information under blue light while simultaneously combining this information with the white light picture.

In 3/25 cases a new neurological deficit was found after the procedure. One patient was operated during awake surgery. In one patient, the intraoperative monitoring was positive and thus the surgeon decided to leave a minimal tumor residual in the precentral region. This patient then presented with a new hemiparesis of the left arm (muscle strength 4/5).

Regarding the degree of resection, postoperative MRI confirmed complete resection in 20/26 lesions. The extent of resection was determined using postoperative T1 weighted MRI scans with contrast. Those were compared with the preoperative MRI scans for residual contrast enhancement. In five lesions, a minimal residual was still present on the MRI. For one patient no postoperative imaging study was available.

Case 1: Glioblastoma (Figure 1)

A 53-year-old male reported to our clinic with persisting headaches, amnesia, concentration deficits, confusion, and coordination deficits on the left side. This was accompanied by a tendency to fall to the left and insecure gait. The initial CT scan obtained showed a lesion in the right temporal-parietal region with significant surrounding edema. The cranial MRI scan revealed a lesion highly suspicious for GBM. We, therefore, scheduled the patient for the resection of the lesion. Prior to the intervention the patient received 20 mg per kilogram bodyweight of 5-ALA. Microsurgical resection of the tumor was performed with the modified microscope and concurring sonographic navigation and neuronavigation. The use of the MFL mode showed a coherent fusion of both white light and blue light images of the highly fluorescent tumor tissue and allowed for easy assessment of any bleedings occurring throughout resection. A tissue sample of the resected tumor was sent to the affiliated department of neuropathology and revealed a GBM. After the operation at the final neurological examination the patient presented himself with no neurological deficits and was totally mobile. Postoperative MRI showed a complete resection of the tumor.

Supplementary File shows a short segment of the operation of this patient.

Case 2: Anaplastic Astrocytoma WHO Grade III (Figure 2)

A 65-year-old male initially presented himself with temporary hemiparesis of the right side accompanied by nausea. An initial MRI showed a hyperintense lesion on T2 in the left medial cingulate gyrus. We scheduled the patient for a biopsy of the lesion, which revealed an anaplastic astrocytoma (IDH-mutation, MGMT+, WHO grade III). After being discharged to his home prior to the elective surgery the patient presented himself through our emergency room with focal epileptic seizures of the right leg, namely the thigh region, causing local pain and cramps. We then decided to resect the lesion as soon as possible. Prior to the intervention the patient received 20 mg per kilogram bodyweight of 5-ALA. We planned neurophysiological monitoring of the right arm and leg during the operation to secure neurological function of the nearby supplementary motoric cortex. Microsurgical resection of the tumor was performed following by neurophysiological monitoring and neuronavigation. After the lesion was identified in the depth of the longitudinal fissure the use of the MFL mode showed a coherent fusion of both the white light and blue light images of the highly fluorescent tumor tissue and was able to assess bleedings occurring throughout resection. The resection was finished without any complications. After the operation, neurological examination revealed a light right leg hemiparesis, which was in remission on the day of discharge. Postoperative MRI showed a complete resection of the tumor.

Case 3: Metastases From a Squamous Carcinoma of the Tongue (Figure 3)

A 78-year-old female suffering from a known squamous carcinoma of the tongue came via the emergency room of our clinic because of a decline in her general condition accompanied by confusion and dizziness for the previous 3 weeks. The conducted MRI showed a necrotic and cystic lesion in the left temporal region with a midline shift. We, therefore, planned resection of the symptomatic temporal lesion. A CT scan obtained for disease staging showed several pulmonary lesions and potential lymph node metastases in the mediastinum as well as a lesion in the left gluteal region and inguinal lymph nodes, all highly suspicious of metastases. The patient received 5-ALA. The use of the MFL mode showed a coherent fusion of both the white light and blue light images of the highly fluorescent metastatic lesion tissue and was able to assess bleedings occurring throughout resection. The resection was finished without any complications and at the end no fluorescence was detected. The histological diagnosis revealed metastatic cells of the squamous carcinoma of the tongue. Postoperative MRI showed a complete resection of the tumor.

DISCUSSION

Even though the use of 5-ALA in neurosurgical patients was reported for the first time almost 20 years ago, fluorescence-guided surgery is, on the one hand, standard of care for brain tumor surgery, while on the other hand, still a developing field, especially in the improvement of fluorescence visibility from the technical point of view. This is highlighted by the fact that 5-ALA has only recently been approved by the FDA (18) and that it is currently used mainly for resection of HGG. Although 5-ALA has improved the outcomes of oncological neurosurgery, it comes with several technical disadvantages that need to be overcome.

To the best of our knowledge, the present observational study is the first investigation that describes a promising new technique that could help to improve PpIX fluorescence-guided tumor surgery while being easy to implement in the operation

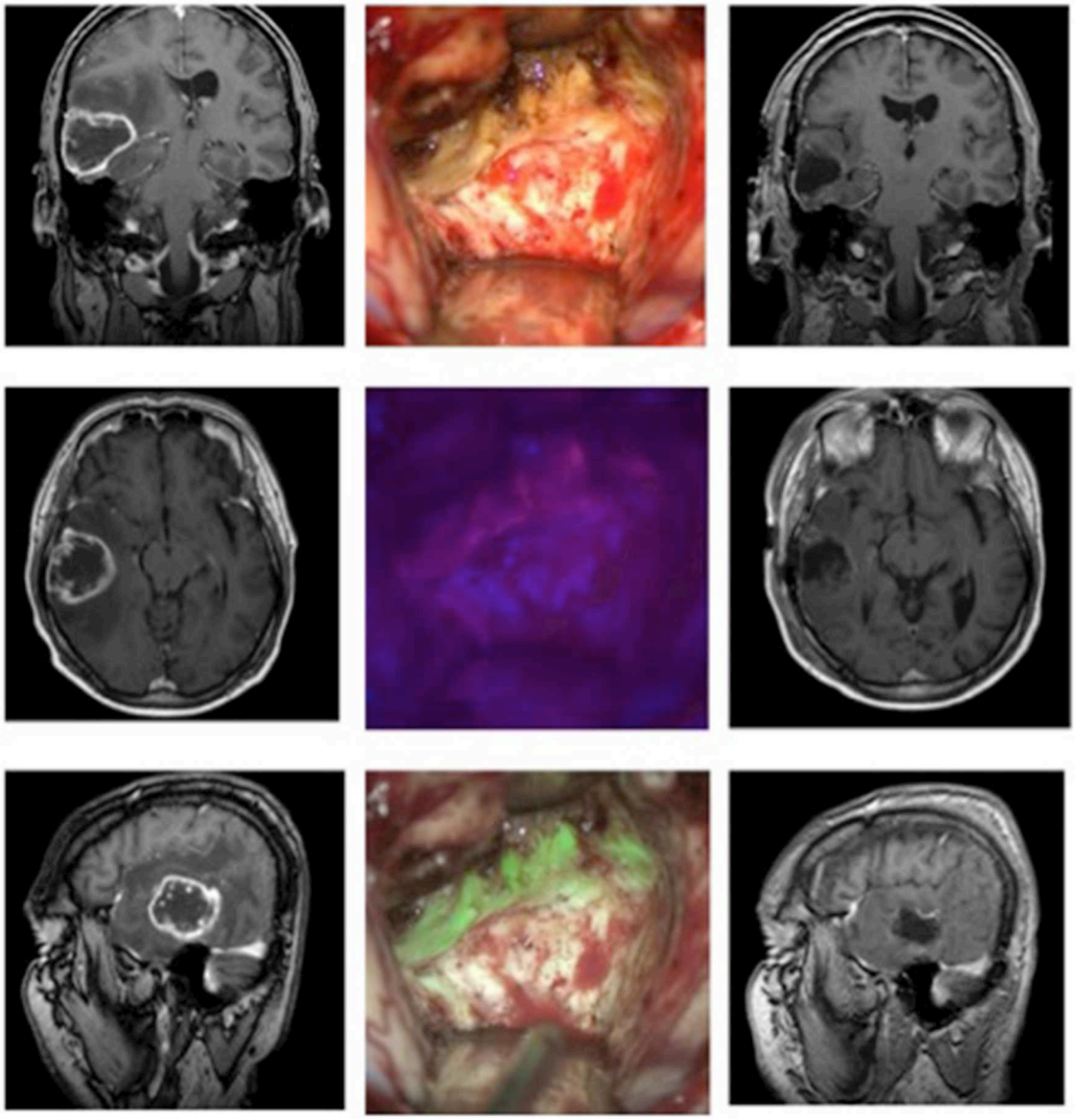

FIGURE 1 | Glioblastoma in a 53-year-old patient. The left column shows the MRI images (T1 weighted with contrast, from top to bottom: coronary, axial, sagittal) before the operation, the right column the postoperative MRI. In the middle column, the top picture shows the surgical field under white light, below it under blue light, and at the bottom the fusion of both images in the MFL-mode.

room. As hypothesized, intraoperative blue light images matched the MFL images while the new visualization technique did not violate operation ergonomics. On the contrary, as we have shown in **Supplementary Video 1**, drawbacks of the traditional blue filter such as blood covering the surgical field were more easily controllable. As we have illustrated in great detail through our small sample and the three illustrative cases, the MFL technique is able to visualize and combine both the picture generated under blue light as well as the white light picture in real-time. Thereby it enables the surgeon to assess the tumor and the surrounding neuroanatomy under white light. Through this, the ergonomic problem of switching between the different light modes and the need to continuously rinse the operation in order to prevent slight bleeding from covering the operation site could be solved. Most importantly, the ability to assess bleeding sites while also operating tumor tissue enables the surgeon to identify regions in real-time that could masque tumor tissue when blood coagulation has happened. Apart from that, learning to resect tumors in this augmented reality setting could prove to be more intuitive as opposed to the traditional way under blue light.

Furthermore, previously to this study we made the observation that this mode is able to sufficiently differentiate

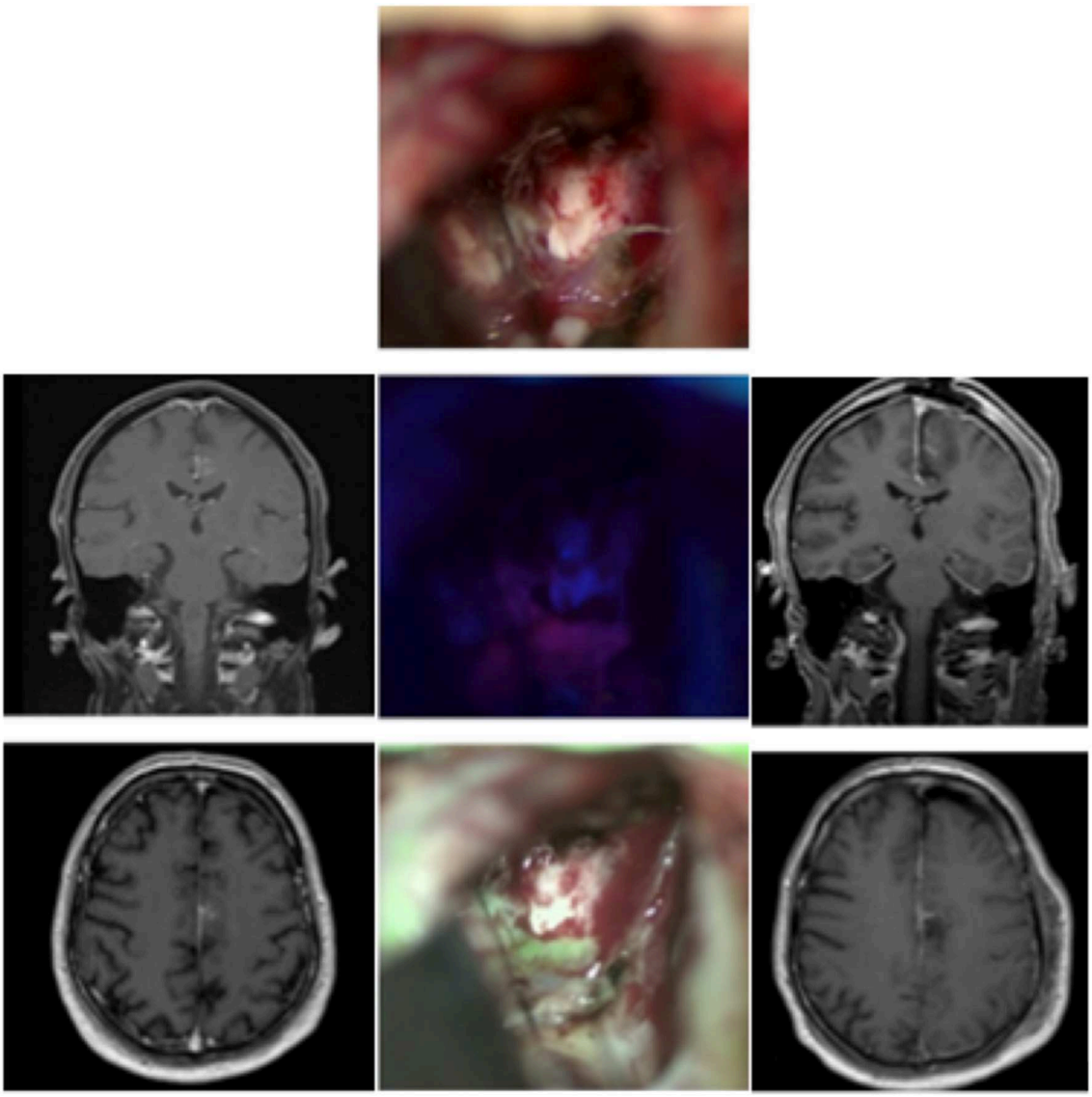

FIGURE 2 | Anaplastic astrocytoma in a 65-year-old patient. The left side shows the preoperative MRI (contrast-enhanced), while the right column shows the early 48 h-postoperative MRI. In the middle column the operative cavity shows the field under white light, below it under blue light, and at the bottom the fusion of both images in the MFL-mode.

between the brain's physiological color and the artificial color chosen (15). This led us to believe that in the clinical setting of tumor surgery it would be easier to identify and resect tumor tissue in this augmented reality setting as opposed to operation under blue light were brain tissue is pretty much dark. We also made the same observation in a previous implementation of the MFL-mode for surgery of vascular malformations as well as tumors with indocyanine green (16).

In a recent paper, it was shown that the intensity of the PpIX fluorescence is related to the light source used, which, according to the authors, could have implications for surgery (19). This is further highlighted by the fact that various surgical microscopes can exhibit "considerably different illumination optical power levels at identical system settings" (20). According to Belykh et al. (20), this is the case because of several factors that are related to [1] the excitation light, as microscopes have variations in excitation light power which are related to several factors, [2] the detection of the emitted light, depending on optical parameters such as the distance between object and objective, sensitivity of the camera chip/eye, etc., and [3] factors related to the tissue itself, such as blood or light scatter, to name a few (21). Being aware of the effect of the light source upon the fluorescence properties of PpIX, we have tried to minimize this effect by undertaking several measures. All operations were

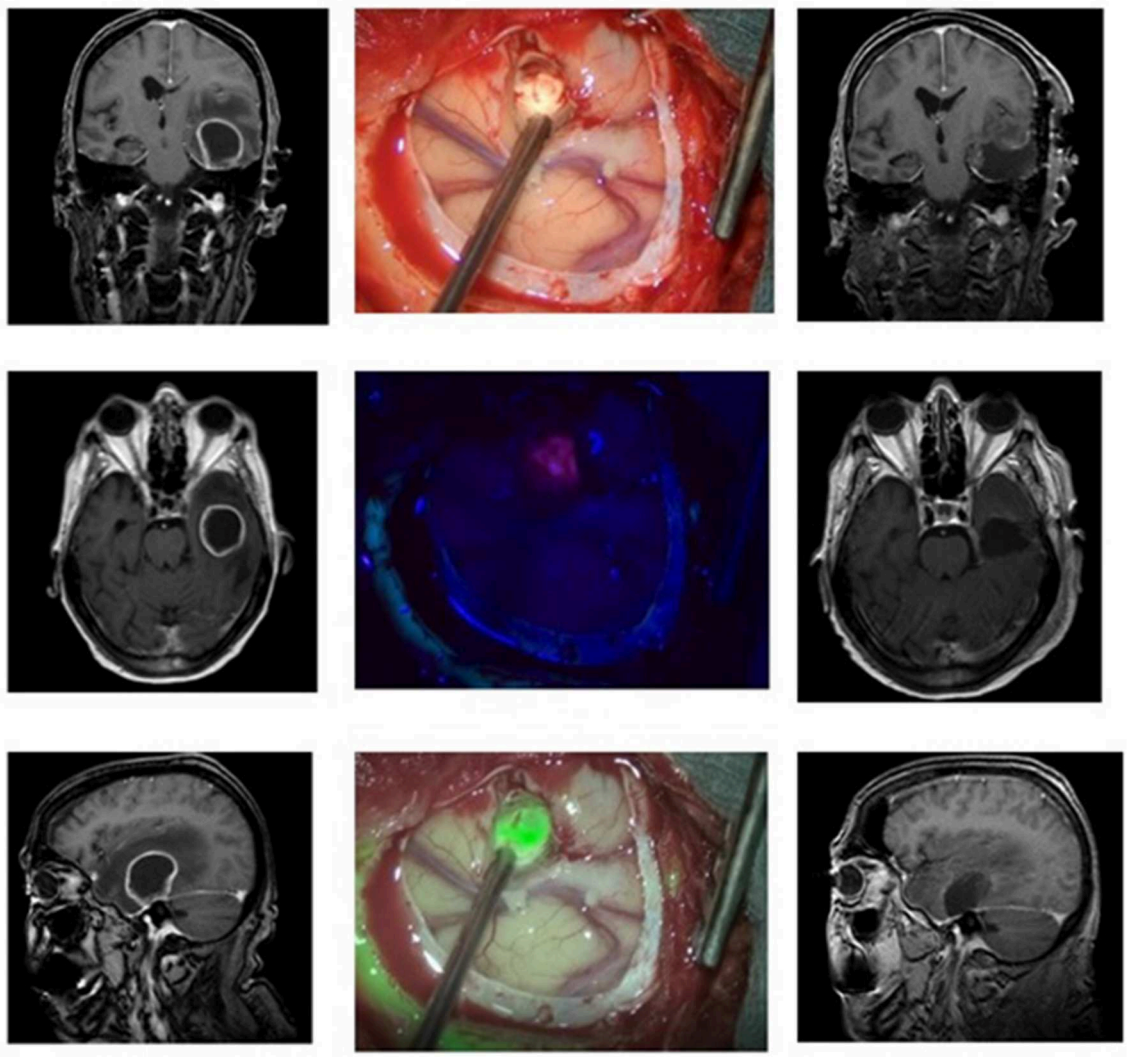

FIGURE 3 | Metastasis from a squamous tongue carcinoma in a 78 old patient. Preoperative (left side) and postoperative MRIs (right side) showing the lesion and the total resection zone, respectively. In the middle column, the operative cavity is seen. The top picture shows the exposed tumor under white light, below it under blue light with pink nuances, and at the bottom the fusion of both images in the MFL-mode ("green" is the tumor in pseudo-color mode).

performed by the same surgeon (CC), the microscope used was always identical, the angle between the light source and the surface of interest was always tried to be kept at 90° for the best illumination effect. Apart from that, the parameters that influence the fluorescence (namely illumination, magnification, and working distance) were tried to be kept as constant as possible. Only if operative challenges had to be met, the surgeon changed them accordingly to her needs.

Apart from the means used by the surgeon to cope with the problem of light intensity depending on the light source used, some technical points have to be mentioned and discussed. PpIX is excited with blue light of a narrow spectral range around 405 nm. Illuminated with such light the healthy tissue can be observed as a blue image. With increasing tumor cell density, the red fluorescence marking is added to the reflected blue light and colorizes the observed tissue detail from pinkish blue to strong pink (tissue with low up to strong PpIX fluorescence).

This color shift is generally independent of the excitation intensity, allowing the interpretation for surgical resection as long as the color visibility is given, but with further decrease of excitation intensity the visibility of the observed color signal becomes too dark and recognition of the faint fluorescence in the resection area is more or less impossible.

Comparing the PpIX MFL-white light fluorescence illumination used in the present study to the blue light fluorescence, the excitation of white light fluorescence is broad and comprising the wavelengths shorter than 400 nm up to

700 nm, excluding the PpIX emission peak around 635 nm for the detection of the PpIX fluorescence.

Because the detected fluorescence intensity is related to the light source excitation level in the absorption range of PpIX and the optical parameters, the MFL system allows the control of the related effects as much as possible to provide correct fluorescence intensity and visibility for the combined digital anatomical white light and fluorescence image on the monitor and for the fluorescence image overlay in the eyepieces.

In this observational study, we also report tumors other than HGG that showed PpIX fluorescence even though we applied 5-ALA in an "off-label" setting. Such lesions were different metastatic processes, meningiomas, acoustic neurinoma as well as ependymoma. Although in the literature, mainly HGGs are regarded as tumors that express the highly fluorescent PpIX and hence have fluorescent properties under blue light evidence exists that other brain lesions can also be visualized with 5-ALA, such as brain metastases (22). Of note, this seems to be only the case in approximately 50% of metastases while, interestingly, in one recent study, neither the primary site of the metastases nor their histologic subtype correlated with fluorescence behavior (22). Hence, we believe that with more knowledge about the different metastases and their 5-ALA metabolism this drug will eventually become more important for the field of neurosurgical oncology. Therefore, s it is crucial to address well-evaluated and documented disadvantages of 5-ALA regarding operation ergonomics and bleeding complications. The described novel MFL technology is able to bring light back to the operating field during the 5-ALA guided surgery, similarly to what we have previously described for fluorescence guided surgery using other fluorophores like ICG even for vascular pathologies (15) or brain tumor treatment (16). For that matter, the presented real time augmented reality setting combined with a commercially available microscope could be a promising tool to improve surgical therapy.

Nonetheless, the present study bears a few limitations. Being an observational study, we were only able to get the first insight into the way the MFL-mode could be used in neurosurgery. All pictures obtained in the MFL-mode were matching the fluorescence pictures under blue light while, however, the fluorescence and its contrast to the surrounding brain tissue was subjectively perceived stronger in the MFL-mode as opposed to the blue light pictures. In other words, we did not include any objective data such as quantitative assessment of fluorescence intensities or histopathological analysis of the tumor zones and the areas that showed different fluorescence intensity. Hence, future studies would need to quantitatively compare blue light and white light pictures to the generated MFL-mode picture regarding factors such as fluorescence intensity, discrimination of different tissues in real-time, or/and simultaneously identification of anatomically relevant structures such as blood vessels, to name a few. Apart from that, it is on our next steps to compare the traditional way of operating with both blue and white light to the sole use of the MFL-mode toward clinical endpoints such as progression-free survival, neurological function, or degree of tumor resection.

CONCLUSION

The MFL technique embedded on a classic surgical microscope opens the way for precise and clear visualization of brain tissue PpIX fluorescence in real-time under white light. It can be easily implemented in the resection of all brain lesions accumulating 5-ALA and producing PpIX. Drawbacks of classic PpIX fluorescence visualization techniques such as difficulty in identification of bleeding sources, operating in dark environment and the necessity to regularly switch off the fluorescence mode could be overcome with the presence of additional white light which allows for clear simultaneous visualization of the exposed brain in natural colors and PpIX fluorescence in green pseudocolor.

DATA AVAILABILITY STATEMENT

All datasets generated for this study are included in the article/**Supplementary Material**.

ETHICS STATEMENT

The studies involving human participants were reviewed and approved by University of Witten/Herdecke, Germany (Nr: 35/2017). The patients/participants provided their written informed consent to participate in this study. Written informed consent was obtained from the individual(s) for the publication of any potentially identifiable images or data included in this article.

AUTHOR CONTRIBUTIONS

PP and PC drafted the manuscript. PC and AH designed the manuscript. All operations were carried out by PC and MN. All authors read and approved the final manuscript.

SUPPLEMENTARY MATERIAL

The Supplementary Material for this article can be found online at: https://www.frontiersin.org/articles/10.3389/fonc.2020.01069/full#supplementary-material

Supplementary Video 1 | Intraoperative video as recorded with the operative microscope. The video was recorded during resection of the glioblastoma described in the case vignette #1. The video shows in the beginning the classic blue fluorescence while later on the multispectral fluorescence (MFL) mode is visible. The fluorescent tissue appears in the pseudo-color green. In this video, the different fluorescent shades are clearly visible, which helps identifying different areas of the lesion. It also shows that any blood covering the surgical field is immediately visible and can then be removed without losing focus of the tissue of interest. Finally, coagulated blood can be identified during dissection and then be removed while immediately seeing any underlying fluorescent tissue.

REFERENCES

1. Stupp R, Mason WP, van den Bent MJ, Weller M, Fisher B, Taphoorn MJ, et al. Radiotherapy plus concomitant and adjuvant temozolomide for glioblastoma. *N Engl J Med*. (2005) 352:987–96. doi: 10.1056/NEJMoa043330
2. Stupp R, Hegi ME, Mason WP, van den Bent MJ, Taphoorn MJ, Janzer RC, et al. Effects of radiotherapy with concomitant and adjuvant temozolomide versus radiotherapy alone on survival in glioblastoma in a randomised phase III study: 5-year analysis of the EORTC-NCIC trial. *Lancet Oncol.* (2009) 10:459–66. doi: 10.1016/S1470-2045(09)70025-7
3. Almenawer SA, Badhiwala JH, Alhazzani W, Greenspoon J, Farrokhyar F, Yarascavitch B, et al. Biopsy versus partial versus gross total resection in older patients with high-grade glioma: a systematic review and meta-analysis. *Neuro Oncol.* (2015) 17:868–81. doi: 10.1093/neuonc/nou349
4. D'Amico RS, Englander ZK, Canoll P, Bruce JN. Extent of resection in glioma–a review of the cutting edge. *World Neurosurgery.* (2017) 103:538–49. doi: 10.1016/j.wneu.2017.04.041
5. Goldbrunner R, Ruge M, Kocher M, Lucas CW, Galldiks N, Grau S, et al. The treatment of gliomas in adulthood. *Dtsch Arztebl Int*. (2018) 115:356–64. doi: 10.3238/arztebl.2018.0356
6. Stepp H, Stummer W. 5-ALA in the management of malignant glioma. *Lasers Surg Med*. (2018). 50:399–419. doi: 10.1002/lsm.22933
7. Hadjipanayis CG, Widhalm G, Stummer W. What is the surgical benefit of utilizing 5-aminolevulinic acid for fluorescence-guided surgery of malignant gliomas? *Neurosurgery.* (2015) 77:663–73. doi: 10.1227/NEU.0000000000000929
8. Stummer W, Stocker S, Wagner S, Stepp H, Fritsch C, Goetz C, et al. Intraoperative detection of malignant gliomas by 5-aminolevulinic acid-induced porphyrin fluorescence. *Neurosurgery.* (1998) 42:518–26. doi: 10.1016/S0303-8467(97)81684-8
9. Stummer W, Novotny A, Stepp H, Goetz C, Bise K, Reulen HJ. Fluorescence-guided resection of glioblastoma multiforme by using 5-aminolevulinic acid-induced porphyrins: a prospective study in 52 consecutive patients. *J Neurosurg.* (2000) 93:1003–13. doi: 10.3171/jns.2000.93.6.1003
10. Stummer W, Pichlmeier U, Meinel T, Wiestler OD, Zanella F, Reulen HJ, et al. Fluorescence-guided surgery with 5-aminolevulinic acid for resection of malignant glioma: a randomised controlled multicentre phase III trial. *Lancet Oncol.* (2006) 7:392–401. doi: 10.1016/S1470-2045(06)70665-9
11. Ferraro N, Barbarite E, Albert TR, Berchmans E, Shah AH, Bregy A, et al. The role of 5-aminolevulinic acid in brain tumor surgery: a systematic review. *Neurosurg Rev.* (2016) 39:545–55. doi: 10.1007/s10143-015-0695-2
12. Motekallemi A, Jeltema HR, Metzemaekers JD, van Dam GM, Crane LM, Groen RJ, et al. The current status of 5-ALA fluorescence-guided resection of intracranial meningiomas-a critical review. *Neurosurg Rev.* (2015) 38:619–28. doi: 10.1007/s10143-015-0615-5
13. Roberts DW, Olson JD, Evans LT, Kolste KK, Kanick SC, Fan X, et al. Red-light excitation of protoporphyrin IX fluorescence for subsurface tumor detection. *J Neurosurg.* (2018) 128:1690–7. doi: 10.3171/2017.1.JNS162061
14. Stepp H, Schnell O. Brain tumor imaging with ALA. In: Hamblin MR, Huang Y, editors. *Imaging in Photodynamic Therapy*. *1st ed*. Boca Raton: CRC Press. (2017). p. 369–406.
15. Athanasopoulos D, Heimann A, Nakamura M, Kakaletri I, Kempski O, Charalampaki P. Real-time overlapping of indocyanine green—video angiography with white light imaging for vascular neurosurgery: technique, implementation, and clinical experience. *Oper Neurosurg.* (2020) opaa050. doi: 10.1093/ons/opaa050
16. Charalampaki P, Nakamura M, Athanasopoulos D, Heimann A. Confocal-assisted multispectral fluorescent microscopy for brain tumor surgery. *Front Oncol.* (2019) 9:583. doi: 10.3389/fonc.2019.00583
17. Nickele C, Nguyen V, Fisher W, Couldwell W, Aboud E, David C, et al. A pilot comparison of multispectral fluorescence to indocyanine green videoangiography and other modalities for intraoperative assessment in vascular neurosurgery. *Operat Neurosurg.* (2019) 17:103–9. doi: 10.1093/ons/opy237
18. Hadjipanayis CG, Stummer W. 5-ALA and FDA approval for glioma surgery. *J Neuro-Oncol*. (2019). 141:479–86. doi: 10.1007/s11060-019-03098-y
19. Kamp MA, Knipps J, Neumann LM, Mijderwijk HJ, Dibue-Adjei M, Steiger HJ, et al. Is the intensity of 5-aminolevulinic acid-derived fluorescence related to the light source? *World Neurosurg.* (2019) 131:e271–e6. doi: 10.1016/j.wneu.2019.07.136
20. Belykh E, Miller EJ, Patel AA, Bozkurt B, Yagmurlu K, Robinson TR, et al. Optical characterization of neurosurgical operating microscopes: quantitative fluorescence and assessment of PpIX photobleaching. *Sci Rep.* (2018) 8:12543. doi: 10.1038/s41598-018-30247-6
21. Belykh E, Nelson LY, Seibel EJ, Preul MC. Factors that influence quantification of fluorescent signal during the 5-ALA-guided surgery. Letter to the editor regarding the paper "Is the Intensity of 5-Aminolevulinic Acid Derived Fluorescence Related to the Light Source? *World Neurosurg.* (2020)
22. Kamp MA, Fischer I, Buhner J, Turowski B, Cornelius JF, Steiger HJ, et al. 5-ALA fluorescence of cerebral metastases and its impact for the local-in-brain progression. *Oncotarget.* (2016). 7:66776–89. doi: 10.18632/oncotarget.11488

Conflict of Interest: The authors declare that the research was conducted in the absence of any commercial or financial relationships that could be construed as a potential conflict of interest.

Advantages of publishing in Frontiers

OPEN ACCESS
Articles are free to read for greatest visibility and readership

FAST PUBLICATION
Around 90 days from submission to decision

HIGH QUALITY PEER-REVIEW
Rigorous, collaborative, and constructive peer-review

TRANSPARENT PEER-REVIEW
Editors and reviewers acknowledged by name on published articles

Frontiers
Avenue du Tribunal-Fédéral 34
1005 Lausanne | Switzerland

Visit us: www.frontiersin.org
Contact us: frontiersin.org/about/contact

REPRODUCIBILITY OF RESEARCH
Support open data and methods to enhance research reproducibility

DIGITAL PUBLISHING
Articles designed for optimal readership across devices

FOLLOW US
@frontiersin

IMPACT METRICS
Advanced article metrics track visibility across digital media

EXTENSIVE PROMOTION
Marketing and promotion of impactful research

LOOP RESEARCH NETWORK
Our network increases your article's readership